P. 615

Lunar and Planetary Science XXV

Abstracts of papers submitted to the Twenty-fifth Lunar and Planetary Science Conference

PART 3 P _

National Aeronautics and Space Administration

Lyndon B. Johnson Space Center
Houston, Texas

LPI / USRA

LUNAR AND PLANETARY INSTITUTE
UNIVERSITIES SPACE RESEARCH ASSOCIATION

LUNAR AND PLANETARY SCIENCE XXV

Abstracts of Papers Submitted to the

TWENTY-FIFTH LUNAR AND PLANETARY SCIENCE CONFERENCE

Sponsored by

National Aeronautics and Space Administration
Lunar and Planetary Institute
NASA Johnson Space Center

March 14–18, 1994

Part 3

Compiled by
Lunar and Planetary Institute
3600 Bay Area Boulevard
Houston TX 77058-1113

The Lunar and Planetary Institute is operated by the Universities Space Research Association under Contract No. NASW-4574 with the National Aeronautics and Space Administration.

Preface

This volume contains abstracts accepted by the Program Committee of the Twenty-Fifth Lunar and Planetary Science Conference.

The Program Committee was co-chaired by Douglas Blanchard (*NASA Johnson Space Center*) and David Black (*Lunar and Planetary Institute*); other members were Nadine Barlow (*Lunar and Planetary Institute*), James Bell (*NASA Ames Research Center*), Donald Bogard (*NASA Johnson Space Center*), Bruce Bohor (*U.S. Geological Survey, Denver*), Bruce Campbell (*Smithsonian Institution*), Mark Cintala (*NASA Johnson Space Center*), Tammy Dickinson (*NASA Headquarters*), Deborah Domingue (*Lunar and Planetary Institute*), Charles Hohenberg (*Washington University*), Walter Kiefer (*Lunar and Planetary Institute*), Marilyn Lindstrom (*NASA Johnson Space Center*), Glenn MacPherson (*Smithsonian Institution*), Renu Malhotra (*Lunar and Planetary Institute*), Scott Murchie (*Lunar and Planetary Institute*), Laurence Nyquist (*NASA Johnson Space Center*), Patricia Rogers (*NASA Headquarters*), Sue Smrekar (*Jet Propulsion Laboratory*), Allan Treiman (*Lunar and Planetary Institute*), Faith Vilas (*NASA Johnson Space Center*), Paul Warren (*University of California, Los Angeles*), and Michael Zolensky (*NASA Johnson Space Center*).

Papers are arranged alphabetically by the last name of the first author. There are four indexes: author, lunar sample number, meteorite, and keyword.

This abstract volume was compiled by the staff of the Publications and Program Services Department of the Lunar and Planetary Institute. Computer service support was provided by the LPI's Computer Center.

Logistics and administrative support for the conference was provided by the staff of the Publications and Program Services Department, Lunar and Planetary Institute.

CONTENTS

Magnetic Properties of Zagami and Nakhla
D. P. Agerkvist, L. Vistisen, M. B. Madsen, and J. M. Knudsen 1

Martian Fluvio-Thermal Erosion: Experimental Project
J. Aguirre-Puente, F. Costard, and N. Makhloufi 3

Radiative Signals from Impact of Shoemaker-Levy on Jupiter
T. J. Ahrens, G. S. Orton, T. Takata, and J. D. O'Keefe 5

Chondrules from Chondrules? An Ion Probe Trace Element Study
C. M. O'D. Alexander 7

Evidence for Short SiC Lifetimes in the ISM
C. M. O'D. Alexander 9

C1 and Alkali Metasomatism in Unequilibrated Ordinary Chondrites
C. M. O'D. Alexander, J. C. Bridges, and R. Hutchison 11

Distributions of the Preatmospheric Sizes of Antarctic and Non-Antarctic Chondrites
V. A. Alexeev 13

On Calculation of Cosmic-Ray Exposure Ages of Meteorites
V. A. Alexeev 15

Short Life of Small Meteorites in the Cosmic Space?
V. A. Alexeev 17

Meteorites as Differential Detectors of Events Over a Long Time Scale
V. A. Alexeev and G. K. Ustinova 19

New Prospects for Analyzing Lunar Pyroclastic Glass
C. C. Allen, L. P. Keller, J. P. Bradley, D. E. Brownlee, and D. S. McKay 21

Reduction of Lunar Mare Soil and Pyroclastic Glass
C. C. Allen, R. V. Morris, and D. S. McKay 23

Calorimetric Thermometry of Meteoritic Troilite: Preliminary Thermometer Relationships
J. H. Allton, S. J. Wentworth, and J. L. Gooding 25

C-, N-, O-, Si-, and Ti-Isotopic Ratios of Low Density Graphite Grains from Murchison Indicate a Supernova Origin
S. Amari, E. Zinner, and R. S. Lewis 27

Lithospheric Controls on the Formation of Valles Marineris
F. S. Anderson and R. E. Grimm 29

Bunte Breccia-like Deposits Within the Manson Impact Structure (Iowa); Evidence for Impact into a Shallow Marine Environment?
R. R. Anderson and B. J. Witzke 31

Surface Characteristics of Steep-Sided Domes on Venus and Terrestrial Silicic Domes: A Comparison
S. W. Anderson, D. A. Crown, J. J. Plaut, and E. R. Stofan 33

Cryptomaria in the Schiller-Schickard, Mare Humorum and Western Oceanus Procellarum Areas: Studies Using Dark-Halo Craters 35
I. Antonenko and J. W. Head

Computer Simulation of Low Pressure Melting in Meteoritic Igneous Systems 37
A. A. Ariskin and M. I. Petaev

Oblique Impact: Atmospheric Effects 39
N. A. Artem'eva and V. V. Shuvalov

Laboratory Simulations of Large-Scale Vortex Flows Generated at Impacts on Venus and on Earth 41
V. I. Artem'ev, V. A. Rybakov, S. A. Medveduk, and B. A. Ivanov

The Surface and Interior of Phobos 43
E. Asphaug and W. Benz

Stratigraphy of Small Volcanoes and Plains Terrain in Vellamo Planitia, Venus 45
J. C. Aubele

Stepping into Space: Getting Involved in Pre-College Outreach 47
J. C. Aubele and P. H. Schultz

A Mercury Orbiter Mission: Report on the European Space Agency's Assessment Study 49
A. Balogh, R. Grard, G. Scoon, and M. Hechler

Gravity Studies of Mead Crater, Venus 51
W. B. Banerdt, N. J. Rappaport, W. L. Sjogren, and R. E. Grimm

Mars Soil: Nanophase Minerals and Formation Processes 53
A. Banin

The Hypsometric Distribution of Impact Craters on Venus 55
M. Banks, S. Emerson, R. G. Strom, and G. G. Schaber

Observational and Computational Evidence for Gravitationally Stable Particle Accretions in the Perseid Meteor Stream 57
J. C. Barentine

Impact Craters as Indicators of Subsurface H_2O on Mars 59
N. G. Barlow

A Quantitative Assessment of an Impact Generated Ring Vortex 61
O. S. Barnouin and P. H. Schultz

Concentric Wrinkle Ridge Pattern Around Sif and Gula 63
A. T. Basilevsky

Preliminary Stratigraphic Basis for Geologic Mapping of Venus 65
A. T. Basilevsky and J. W. Head

Geology and Morphometry of Large Impact Craters of Venus 67
A. T. Basilevsky, B. A. Ivanov, P. G. Ford, and C. M. Weitz

Variations in Mars' North Residual Polar Cap Frost Coverage in Mariner 9 and Viking Images 69
D. S. Bass, K. E. Herkenhoff, and D. A. Paige

Single Agglutinates: A Comparative Study of Compositions of Agglutinitic Glass, Whole-Grain, Bulk Soil, and FMR
A. Basu, R. Robinson, D. S. McKay, D. P. Blanchard, R. V. Morris, and S. J. Wentworth 71

Deep Melting and Residual Garnet in the Sources of Lunar Basalts: Lu-Hf Isotopic Systematics
B. L. Beard, G. A. Snyder, and L. A. Taylor 73

CoMA: A Cometary Matter Analyzer for In Situ Analysis with High Mass Resolution
P. Beck and J. Kissel 75

Solar Wind Gases in a Metal Separate from Lunar Soil 68501: A Followup Study
R. H. Becker and R. O. Pepin 77

The Partitioning of Na Between Melilite and Liquid: An Experimental Study with Applications to Type B CAIs
J. R. Beckett and E. M. Stolper 79

High Spatial Resolution Telescopic Multispectral Imaging and Spectroscopy of the Moon: I. The Serenitatis/Tranquillitatis Border Region
J. F. Bell III and B. R. Hawke 81

High Resolution Visible to Short-Wave Near-Infrared CCD Spectra of Mars During 1990
J. F. Bell III, K. Bornhoeft, and P. G. Lucey 83

Absolute Calibration and Atmospheric vs. Mineralogic Origin of Absorption Features in 2.0 to 2.5 μm Mars Spectra Obtained During 1993
J. F. Bell III, J. B. Pollack, T. R. Geballe, D. P. Cruikshank, and R. Freedman 85

Wavelength Calibration Techniques and Subtle Surface and Atmospheric Absorption Features in the Mariner 6, 7 IRS Reflectance Data
J. F. Bell III, T. L. Roush, T. Z. Martin, and R. Freedman 87

Ordinary Chondrites in Space and Time
J. F. Bell 89

Geologic Map of Callisto
K. C. Bender, R. Greeley, J. W. Rice Jr., and D. E. Wilhelms 91

Pre-Impact Orbital Evolution of P/Shoemaker-Levy 9
L. A. M. Benner and W. B. McKinnon 93

Post-Shock Cooling and Annealing Within L-Group Ordinary Chondrites
M. E. Bennett and H. Y. McSween Jr. 95

Primitive Material in Lunar Highland Soils
P. H. Benoit, J. D. Batchelor, S. J. Symes, and D. W. G. Sears 97

Natural Thermoluminescence Profiles in Meteorites: Cosmogenic and Terrestrial Profiles in Falls and Finds
P. H. Benoit, Y. Chen, and D. W. G. Sears 99

Shoemaker-Levy 9 and the Tidal Disruption of Comets
W. Benz and E. Asphaug 101

Refractory Carbides in Interstellar Graphite
T. J. Bernatowicz, S. Amari, and R. S. Lewis 103

Origin of Amorphous Rims on Lunar Soil Grains
T. J. Bernatowicz, R. H. Nichols Jr., and C. M. Hohenberg 105

Craters in Aluminum 1100 Targets Using Glass Projectiles at 1–7 km/s
R. P. Bernhard, T. H. See, F. Hörz, and M. J. Cintala 107

A Martian Mantle with Peridotitic Versus Chondritic Mg/Si and Al/Ca Ratios: Implications for Mantle Mineralogy and Melting Reactions
C. M. Bertka 109

Thermal Inertias in the Upper mm of the Martian Surface Derived Using the Phobos Shadow
B. H. Betts, B. C. Murray, and T. Svitek 111

Magellan LOS Gravity of Venus Plains Regions: Lithospheric Properties and Implications for Global Tectonics
D. L. Bindschadler 113

The Unique Carbonaceous Chondrite Acfer 094: The First CM3 Chondrite (?)
A. Bischoff and T. Geiger 115

Reflectance Spectra of Mars Soil Analogs Measured Under Reduced Atmospheric Pressures and Temperatures
J. L. Bishop and C. M. Pieters 117

Spectroscopic and Geochemical Analyses of Sediments from Lake Hoare, Antarctica and Applications to Dry Valleys on Mars
J. L. Bishop, P. A. J. Englert, D. W. Andersen, C. Kralik, C. Koeberl, C. M. Pieters, H. Froeschl, and R. A. Wharton Jr. 119

A Mineralogical Instrument for Planetary Applications
D. F. Blake, D. T. Vaniman, and D. L. Bish 121

Infrared Spectrophotometry of Io Between 3 and 13 μm in 1993
D. L. Blaney, M. S. Hanner, R. Russell, D. Lynch, and J. Hackwell 123

Measuring Track Densities in Lunar Grains Using Image Analysis
G. E. Blanford, D. S. McKay, R. P. Bernhard, and C. K. Schulz 125

A Spectral Survey of the Crisium Region of the Moon
D. T. Blewett, B. R. Hawke, P. G. Lucey, and P. D. Spudis 127

Venus: Influence of Surface Roughness on the Threshold for Windblown Sand Derived from Magellan Data
D. G. Blumberg and R. Greeley 129

Mars Cartographic Coverage: Status Prior to Mars-94 Mission
N. N. Bobina and G. A. Burba 131

Geometrical Transformation of Panoramas of Mars Surface Received from Phobos-2 Space Station
I. M. Bockstein, M. A. Kronrod, and Yu. M. Gektin 133

Fe and Mn Systematics in Experimental Analogues of Murchison and a 65% H Chondrite-35% CM Chondrite
J. S. Boesenberg and J. S. Delaney 135

^{39}Ar-^{40}Ar Ages of Four Ureilites
D. D. Bogard and D. H. Garrison 137

Bromine in Interplanetary Dust Particles
J. Bohsung, P. Arndt, and E. K. Jessberger 139

The Solubility of Platinum in Silicate Melts: Experiments Under Oxidizing Conditions
A. Borisov, H. Palme, and B. Spettel 141

Phosphorus Chemistry in the Atmospheres of Jupiter and Saturn
S. Borunov, V. Dorofeeva, I. K. Khodakovsky, P. Drossart, E. Lellouch, and Th. Encrenaz 143

Axial Focusing of Seismic Energy from a Large Impact on Earth: Preliminary Numerical Simulations
M. B. Boslough and E. P. Chael 145

Comet Shoemaker-Levy 9: An Upper Bound on Its Mean Density
A. P. Boss 147

Midplane Temperatures and Solar Nebula Evolution
A. P. Boss 149

Injection of Presolar Grains into the Solar Nebula by a Stellar Shock Wave
A. P. Boss and P. N. Foster 151

Provenance of the Spacewatch Small Earth-Approaching Asteroids
W. F. Bottke Jr., M. C. Nolan, R. Greenberg, A. M. Vickery, and H. J. Melosh 153

Spacing Distributions and Intersection Angles for Kilometer Scale Lineations on the Plains of Venus
D. D. Bowman, C. G. Sammis, and W. B. Banerdt 155

Vapor Transport, Weathering, and the Highlands of Venus
R. A. Brackett, B. Fegley Jr., and R. E. Arvidson 157

Reflectance Spectroscopy of Individual Interplanetary Dust Particles
J. P. Bradley, D. E. Brownlee, and L. P. Keller 159

Rb-Sr Dating of Alkaline and Mafic Intrusives from the Pretoria Saltpan Impact Crater and Environs
D. Brandt, W. U. Reimold, and C. B. Smith 161

Your Own Educational Outreach Program: It's Not as Hard as You Think
R. H. Brazzle, B. M. Barker, L. C. McLeod, and C. M. Hohenberg 163

Metamorphic Effects in the Matrices of CO3 Chondrites: Compositional and Mineralogical Variations
A. J. Brearley 165

Metamorphism in the CO3 Chondrites: Trace Element Behavior in Matrices and Rims
A. J. Brearley, S. Bajt, and S. R. Sutton 167

Pancake Domes on Venus and the Seafloor
N. T. Bridges 169

Release of Light Nitrogen from Apollo 12023 <10 μm Fraction by a Combination of Pyrolysis-Combustion 171
D. R. Brilliant, I. A. Franchi, and C. T. Pillinger

The ^{15}N-rich Low-temperature Nitrogen Component in Lunar Soils—An Ammonia Related Species? 173
D. R. Brilliant, A. D. Morse, J. Higgins, I. A. Franchi, and C. T. Pillinger

'Space Weathering' and the Ordinary Chondrites 175
D. T. Britt and B. E. Clark

Cat Mountain: Spectra and Petrology of an L5 Impact-Melt Breccia 177
D. T. Britt and D. A. Kring

Tectonics of Artemis Corona, Venus: Implications for Formation and Evolution 179
C. D. Brown and R. E. Grimm

Alteration and Formation of Rims on the CM Parent Body 181
L. B. Browning, H. Y. McSween Jr., and M. Zolensky

Eureka!! Aerogel Capture of Meteoroids in Space 183
D. E. Brownlee, F. Hörz, L. Hrubsch, J. A. M. McDonnell, P. Tsou, and J. Williams

Identification and Analysis of Cometary IDPs 185
D. E. Brownlee, D. J. Joswiak, S. G. Love, J. P. Bradley, A. O. Nier, and D. J. Schlutter

Considerations for Planetary Gamma-Ray Spectroscopy of the Surface of Mercury 187
J. Brückner, U. Fabian, and M. Wieder

Lava Flow Rheology: A Comparison of Data and Theory 189
B. C. Bruno, S. M. Baloga, G. J. Taylor, and M. J. Tatsumara

Venus Climate Stability and Volcanic Resurfacing Rates 191
M. A. Bullock, D. H. Grinspoon, and J. B. Pollack

Modified Lava Domes on Venus 193
M. H. Bulmer and J. E. Guest

Thematic Map Types Possible for Mars: Mars-94 Mission Cartographic Perspectives 195
G. A. Burba

Zhamanshin Astrobleme: Review and First Results of 1992 Landscape and Geomorphic Survey 197
G. G. Burba Jr. and V. A. Meshcherskaya

Questions Concerning the Oxidation of Ferrous Iron in Carbonaceous Chondrites 199
T. H. Burbine and R. G. Burns

Are Steep Slopes on Venus Preserved as a Result of Chemical Cementation of Pore-Spaces in Surface Rocks? 201
K. Burke, B. Fegley Jr., and V. L. Sharpton

Schwertmannite on Mars: Deposition of This Ferric Oxyhydroxysulfate Mineral in Acidic Saline Meltwaters 203
R. G. Burns

Crustal Recycling Due to Mantle Flow-Driven Crustal Thickening: A Preliminary Assessment
J. D. Burt, E. M. Parmentier, and J. W. Head 205

Modelling the Formation of Venusian Channels
D. B. J. Bussey, S. A. Sørensen, and J. E. Guest 207

Light Element Isotopic Composition in the Wind of a Typical AGB Star
M. Busso, R. Gallino, C. M. Raiteri, and G. J. Wasserburg 209

Martian Polar Regions: 35-cm Radar Images
B. J. Butler, D. O. Muhleman, and M. A. Slade 211

Fluvial Processes in Ma'adim Vallis and the Potential of Gusev Crater as a High Priority
N. Cabrol, R. Landheim, R. Greeley, and J. Farmer 213

Comparative Results from Giant Impact Studies
A. G. W. Cameron 215

Dielectric Properties of Venus: Results from Emissivity Modeling and Terrestrial Field Measurements
B. A. Campbell 217

Multiple-Wavelength Lunar Radar Images: Analsyis of Regolith Properties
B. A. Campbell and B. R. Hawke 219

Siderophile Trace Elements in Silicate Melts: Significance and Status of Unusual Oxidation States
C. J. Capobianco, J. A. DeAro, M. J. Drake, and V. J. Hillgren 221

Low-Temperature Cooling Histories of Vigarano CAIs: Constraints from Compositions of Metal Particles
I. Casanova and L. Grossman 223

Impact Craters on Mars: The Relative Roles of Atmospheric and Subsurface Volatiles
J. Cave, J. Guest, and N. Barlow 225

Impact Crater Morphology on Martian Volcanoes
J. Cave, J. Guest, B. J. Moore, J. Carroll, and N. Barlow 227

Evidence for Episodic Tectonic Construction of Ovda Regio, Venus
D. J. Chadwick and G. G. Schaber 229

Refined Volcanic and Tectonic History of the Valles Marineris, Mars
D. J. Chadwick, G. J. Leonard, and K. L. Tanaka 231

Wax Modeling of Thermal Erosion in Low-Viscosity Lava Flows
D. Challis, S. Williams, and R. Greeley 233

Lunar Mineral Feedstocks from Rocks and Soils: X-Ray Digital Imaging in Resource Evaluation
J. G. Chambers, A. Patchen, L. A. Taylor, S. J. Higgins, and D. S. McKay 235

First Galileo Image of the Asteroid 243 Ida
C. R. Chapman, M. J. S. Belton, J. Veverka, G. Neukum, J. Head, R. Greeley, K. Klaasen, D. Morrison, and the Galileo Imaging Team 237

3-D Perspective Imaging: A Tool for Geologic Mapping of Venus 239
M. G. Chapman, R. L. Kirk, and J. M. Barrett

Subpixel Resolution from Multiple Images 241
P. Cheeseman, B. Kanefsky, J. Stutz, and R. Kraft

Hypervelocity Impacts and the Magnetism of Small Bodies in the Solar System 243
G. Chen, T. J. Ahrens, and R. Hide

The Abundance of Thallium and Premordial Lead in Selected Meteorites—The Search for ^{205}Pb 245
J. H. Chen and G. J. Wasserburg

The Orbital Evolution of Ordinary Chondrites Over the Last 50 Million Years 247
Y. Chen, P. H. Benoit, and D. W. G. Sears

Exploration of the Morphological Distribution of the Spectral Units in the Gruithuisen Domes Region 249
S. D. Chevrel, P. C. Pinet, and J. W. Head

Determination of Nanogram Amounts of C_{60} by High Pressure Liquid Chromatography 251
L. P. F. Chibante, W. S. Wolbach, and D. Heymann

MORO: A European Moon Orbiting Observatory 253
A. F. Chicarro and G. D. Racca

Formation of IAB-IICD Iron Meteorites 255
B.-G. Choi and J. T. Wasson

Thermal-Infrared Multi-Spectral Observations of Mars 257
P. R. Christensen

Grain Rims on Ilmenite in the Lunar Regolith: Comparison to Vapor Deposits on Regolith Silicates 259
R. Christoffersen, D. S. McKay, and L. P. Keller

Block Distributions on the Lunar Surface: A Comparison Between Measurements Obtained from Surface and Orbital Photography 261
M. J. Cintala and K. M. McBride

Acid Waters as Agents of Change on a Cold Early Mars 263
B. C. Clark

Infrared Spectral Observations of Smaller (50 km) Main Belt S, K, and M Type Asteroids 265
B. E. Clark, J. F. Bell, D. J. O'Connor, and F. P. Fanale

Remote Geochemical Experiment Package for Discovery Class Missions 267
P. E. Clark, L. G. Evans, and J. I. Trombka

Oxygen Isotopes in Kaidun 269
R. N. Clayton, T. K. Mayeda, A. V. Ivanov, and G. J. MacPherson

The Role of Low Temperature Hydrothermal Convection in the Physical and Chemical Evolution of the Martian Crust and Groundwater 271
S. M. Clifford

An X-Ray Diffraction and Reflectance Spectroscopy Study of Iron Sulphides 273
E. A. Cloutis and M. J. Gaffey

Minimum Discharge Rates Required for Sustained Water Flow on the Martian Surface
G. D. Clow 275

Triton's Lineaments: Complex Morphology and Stress Patterns
G. Collins and P. Schenk 277

On the Possible Role of Elemental Carbon in the Formation of Reduced Chondrules
H. C. Connolly Jr., R. H. Hewins, R. D. Ash, G. E. Lofgren, and B. Zanda 279

Astronomy Laboratory Exercise Based on SkyGlobe™
M. Connors 281

Return of an Earth-Grazing Asteroid
M. Connors 283

Has the Tidal Bulge on Ariel Shifted in Longitude?
G. Consolmagno, D. M. Davis, and P. Nyffenegger 285

Unusual Concentrations of Rampart Craters at the Mouths of Outflow Channels, Mars
F. Costard 287

Affinity and Petrogenesis of a Unique Vitrophyric Olivine-Augite Mare Basalt from the Apollo 15 Coarse Fines
T. C. Cox and G. Ryder 289

Geologic History of Isidis Planitia and Syrtis Major Planum, Mars
R. A. Craddock 291

The Origin of Phobos and Deimos
R. A. Craddock 293

The Influence of Body Shape on the Deformation and Breakup of Comet Shoemaker-Levy 9 Fragments as They Enter the Jovian Atmosphere
D. A. Crawford, T. G. Trucano, M. B. Boslough, M. E. Kipp, and J. M. McGlaun 295

Palimpsests on Ganymede: An Endogenic Origin?
S. K. Croft 297

Post-Impact Hydrothermal Systems: Manson Impact Structure, Manson, Iowa
L. J. Crossey, A. M. Kudo, and P. McCarville 299

Geology of the Guinevere Planitia Quadrangle of Venus
D. A. Crown, E. R. Stofan, and J. J. Plaut 301

The Distribution of Hot Spots and Its Relation to Global Geology: Venus, Earth, and Mars
L. S. Crumpler 303

Calderas on Mars: Classification, Characteristics, and Processes Related to Mechanisms of Formation
L. S. Crumpler, J. W. Head, and J. C. Aubele 305

What Initiated Planetesimal Formation?
J. N. Cuzzi, A. R. Dobrovolskis, and R. C. Hogan 307

NMR Spectroscopy of Experimentally Shocked Coconino Sandstone and the Effect of Pore Water
R. T. Cygan, M. B. Boslough, and R. J. Kirkpatrick 309

The Planetary Data System Educational CD-ROM Demonstration 311
M. A. Dale-Bannister

High-Resolution Transmission Electron Microscopy Study of Meteoritic and Terrestrial Nano-Diamond Microstructures 313
T. L. Daulton, D. D. Eisenhour, R. S. Lewis, and T. J. Bernatowicz

Alteration of Allende Type B1 CAIs: When, Where, and How 315
A. M. Davis, S. B. Simon, and L. Grossman

Morphometries and Possible Terrestrial Analogs of Small Martian Volcanoes 317
P. A. Davis and K. L. Tanaka

The Occurence of Blue Luminescing Enstatite in E3 and E4 Chondrites 319
J. M. DeHart and G. E. Lofgren

Ponding and Lacustrine Deposition in Lower Mangala Valles, Mars 321
R. A. De Hon

An Oxygen Fugacity Grid for Nebular and Planetary Geochemistry 323
J. S. Delaney, S. R. Sutton, and S. Bajt

Abundance and Diffusivity of Sulfur in Lunar Picritic Magmas 325
J. W. Delano, B. Z. Hanson, and W. B. Watson

The Fretted Terrain of the Nilosyrtis Mensae Region of Mars: Clues to the Timing of Dichotomy Formation and the Emplacement of the Northern Plains 327
J. E. DeTroye and S. H. Williams

High-Temperature Vaporization of Olivine and Serpentine 329
Yu. P. Dikov, O. I. Yakovlev, M. V. Gerasimov, and F. Wlotzka

Geologic History of the Thaumasia Region of Mars 331
J. M. Dohm and K. L. Tanaka

Magnetic Field in the Protosun and Protostars Vicinities 333
A. Z. Dolginov

Soil Texture at the Lunar Surface: Regional Analysis with Polarimetric Images 335
A. Dollfus

The Role of Hapke's Bidirectional Surface Reflection Model in Determining Atmospheric Abundances at Mercury 337
D. L. Domingue, A. L. Sprague, and D. M. Hunten

A Search for Further Concentrations of Organic Materials in EET A79001 339
C. Douglas, I. P. Wright, C. T. Pillinger, and M. M. Grady

Found: Star and Linear Dunes on Mars 341
K. S. Edgett and D. G. Blumberg

Suggestions for Interaction Between Scientists, K-12 Students and Educators: Mars Education Program in Arizona 343
K. S. Edgett, P. R. Christensen, and S. Schmidt

Heating by Light and the Size Distribution of Chondrules
D. D. Eisenhour, T. L. Daulton, and P. R. Buseck 345

Carrier Phases of Isotopically Anomalous Nitrogen in Acapulco Metal: C- and N-Isotopic Compositions Vary with Graphite Morphology
A. El Goresy, E. Zinner, and K. Marti 347

Carbonates in the CI-Chondrite Ivuna: Implications for Aqueous Alteration Processes on the CI-Parent Body
M. Endress and A. Bischoff 349

Apollo 16 Lunar Glasses: Normative Composition and Origin
W. v. Engelhardt 351

Gamma Ray Spectra from the Mars Observer Gamma Ray Spectrometer: Cruise Data Analysis
P. A. J. Englert, N. Chakravarty, O. Ivanova, E. A. Beck, J. Brückner, S. H. Bailey, F. C. McCloskey, and W. V. Boynton 353

C/O Atomic Ratios in Antarctic Micrometeorites: A Progress Report
C. Engrand, M. Perreau, and M. Maurette 355

Effects of Aerosols Scattering on Spectral Characterization of the Martian Surface
S. Erard 357

Projectile Shape and Velocity: Impact on Ejecta Distribution and Composition
N. J. Evans and T. J. Ahrens 359

Theoretical Analysis of the Explosive Emplacement of Basaltic Magma in Lava Fountain Eruptions: Implications for Pyroclast Dispersal on Earth, Venus and Mars
S. A. Fagents and L. Wilson 361

Mg and Ti Isotopic Compositions of CAI's from the Unusual Chondrite Acfer 214
A. Fahey and F. Wlotzka 363

Will the Real Asteroid Size Distribution Please Step Forward
P. Farinella and D. R. Davis 365

Exopaleontology and the Search for a Fossil Record on Mars
J. D. Farmer and D. J. Des Marais 367

Diaplectic Transformation in Clinopyroxene (Puchezh-Katunky Astrobleme, Russia)
V. Feldman, S. Kotelnickov, L. Sazonova, and E. Guseva 369

Modeling the Space Weathering-Induced Optical Alteration of Lunar Soils: First Results
E. M. Fischer, C. M. Pieters, and S. F. Pratt 371

Grain-Size Fractions of SiC in Murchison ARR: A Method for the Analysis of Carbon and its Isotopes by Stepped Combustion
A. V. Fisenko, A. B. Verchovsky, L. F. Semjenova, J. W. Arden, and C. T. Pillinger 373

Isotopic and Elemental Fractionations Produced During Evaporation of the Allende Carbonaceous Chondrite
C. Floss, A. El Goresy, G. Kransel, W. Rammensee, H. Palme, and E. Zinner 375

Narrow-Field Imaging of the Lunar Sodium Exosphere
B. Flynn and S. A. Stern 377

Does the Kuiper Belt Contribute Significantly to the Zodiacal Cloud and the Stratospheric Interplanetary Dust? 379
G. J. Flynn

Hydrated Interplanetary Dust Particles: Element Abundances, Mineralogies, and Possible Relationships to Anhydrous IDPs 381
G. J. Flynn, S. R. Sutton, S. Bajt, W. Klöck, K. L. Thomas, and L. P. Keller

Nitrogen Solubility in Aubrite and E Chondrite Melts 383
R. A. Fogel

SIMS Analysis of Orthopyroxene in Diogenites: An Attempt to Define a Fractionation Sequence 385
G. W. Fowler, J. J. Papike, and C. K. Shearer

Impact Basins in Southern Daedalia, Mars: Evidence for Clustered Impactors? 387
H. Frey and J. H. Roark

Effects Due to Overlapping Large Impact Basins on Mars 389
H. Frey, A. M. Reidy, J. H. Roark, and S. Stockman

Constraints on the Physical Details of Nakhlite Formation 391
R. C. Friedman, T. J. McCoy, and G. J. Taylor

Estimating Surface Roughness: Evaluation of an Empirical Backscatter Model 393
L. Gaddis

Spectral Unit Map of the Moon with Improved Galileo SSI Mosaics 395
L. Gaddis, A. McEwen, and T. Becker

Influence of Variable Oxygen and Sulfur Fugacity on Partitioning of Ni, Cu and Cr Among Olivine, Silicate Melt and Sulfide Melt 397
G. A. Gaetani and T. L. Grove

Nature and Origins of the Olivine-Dominated A- and S(I)-type Asteroids 399
M. J. Gaffey

Interstellar Graphite in Tieschitz 401
X. Gao, C. Alexander, P. Swan, and R. Walker

Solar Proton Produced Neon in Shergottite Meteorites 403
D. H. Garrison, M. N. Rao, and D. D. Bogard

Quantifying Shapes of Volcanoes on Venus 405
J. B. Garvin

Mesoscale Roughness of Venus 407
J. B. Garvin and J. J. Frawley

Volcano Morphometry and Volume Scaling on Venus 409
J. B. Garvin and R. S. Williams Jr.

Ida: Distribution and Origin of Surface Blocks 411
P. Geissler, J.-M. Petit, and R. Greenberg

High-Temperature Vaporization of Gypsum and Anhydrites: Experimental Results
M. V. Gerasimov, Yu. P. Dikov, O. I. Yakovlev, and F. Wlotzka 413

Trapping of Carbon Dioxide from a Hot Atmosphere by Condensing Silicates
M. V. Gerasimov, Yu. P. Dikov, O. I. Yakovlev, and F. Wlotzka 415

Preliminary Analysis of Associations of Small Volcanic Edifices with Major Geologic Features by Latitude on the Surface of Venus
K. Gerlach, M. Safford, Evergreen High School Astronomical Research Class, Sahuaro High School Astronomical Research Class, G. Komatsu, J. Johnson, J. Lockwood, and M. Ellison 417

Morphological Mapping of Two Distinct Corona Chains
R. C. Ghail 419

Plate Tectonics, Venusian Style
R. C. Ghail and L. Wilson 421

A Reappraisal of Metamorphism in the Vredefort Dome, South Africa, and Its Implications for the Origin and Evolution of the Dome
R. L. Gibson, W. U. Reimold, Th. Wallmach, and W. P. Collison 423

Intratessera Volcanism of Alpha and Tellus Tesserae on Venus
M. S. Gilmore and J. W. Head III 425

Composition and Petrography of a Muong Nong-type Georgia Tektite
B. P. Glass, C. Koeberl, and H. Povenmire 427

A Theoretical Study of SO_2 Transport by Explosive Volcanism on Venus
L. S. Glaze 429

Hot Belts of Venus and the Early Earth
M. Z. Glukhovsky and V. M. Moralev 431

The Linear Polarization of Light Scattered from Icy Satellite Surfaces: The Diagnostic Potential of Galileo PPR Measurements
J. D. Goguen 433

Application of an Alkylammonium Method for Characterization of Phyllosilicates in CI Chondrites
D. C. Golden, D. W. Ming, M. E. Zolensky, and S. V. Yang 435

High Resolution Transmission Electron Microscopy (HRTEM) of Nanophase Ferric Oxides
D. C. Golden, R. V. Morris, D. W. Ming, and H. V. Lauer Jr. 437

Structure and Rheology of Partially Molten Ammonia-Water Ices
D. L. Goldsby and D. L. Kohlstedt 439

Constraints on the Largest Marsquake
M. P. Golombek 441

Extension Across Tempe Terra and Sirenum Provinces on Mars from Measurements of Fault Scarp Widths
M. P. Golombek, K. L. Tanaka, D. J. Chadwick, B. J. Franklin, and P. A. Davis 443

"Flindersite" Bearing Impact Ejecta Layer from South Australia
V. A. Gostin and M. Zbik 445

"Flindersites", Distant Ejecta Impactites from South Australia 447
V. A. Gostin and M. Zbik

Diamonds from Acfer 182: Morphology, C and N Stable Isotopic Composition and Cathodoluminescence Properties 449
M. M. Grady, M. R. Lee, C. M. O'D. Alexander, J. W. Arden, and C. T. Pillinger

A Search for Nitrates in Nakhla 451
M. M. Grady, I. P. Wright, and C. T. Pillinger

A Galileo Multi-Instrument Spectral Analysis of 951 Gaspra 453
J. C. Granahan, F. P. Fanale, M. S. Robinson, R. W. Carlson, L. W. Kamp, K. P. Klaasen, P. R. Weissman, M. Belton, D. Cook, K. Edwards, A. S. McEwen, L. A. Soderblom, B. T. Carcich, P. Helfenstein, D. Simonelli, P. C. Thomas, and J. Veverka

Ganymede and Callisto Spectral Data Cubes 455
J. C. Granahan, K. Polk, and F. P. Fanale

Early Fluvial Degradation in Terra Tyrrhena, Mars: Constraints from Styles of Crater Degradation on the Earth 457
J. A. Grant and P. H. Schultz

Erosion of Ejecta at Meteor Crater, Arizona: Further Constraints from Ground Penetrating Radar 459
J. A. Grant and P. H. Schultz

Solar UV Photon Interaction with the Surface of Mars 461
R. Grard

The Carson Quadrangle, Venus 463
R. Greeley, K. Bender, D. Senske, and J. Guest

Do Lava Flows Erode? Preliminary Assessment 465
R. Greeley, R. S. Harris, S. D. Kadel, D. A. Williams, and J. E. Guest

Dust on Mars: New Values for Wind Threshold 467
R. Greeley, M. Lacchia, B. White, R. Leach, D. Trilling, and J. Pollack

Morphology and Geology of Asteroid Ida: Preliminary Galileo Imaging Observations 469
R. Greeley, R. Sullivan, R. Pappalardo, J. Head, J. Veverka, P. Thomas, P. Lee, M. Belton, and C. Chapman

Constraints on Flash Heating from Melting Kinetics 471
J. P. Greenwood and P. C. Hess

Ratio of First and Second Generation Fold Wavelengths on Lavas May Indicate Flow Composition 473
T. K. P. Gregg and J. H. Fink

$^{40}Ar/^{39}Ar$ Dating of Samples from the Cat Mountain Meteorite 475
J. A. Grier, T. D. Swindle, and D. A. Kring

The Sudbury Structure: Additional Constraints on Its Origin and Evolution 477
R. A. F. Grieve and A. Deutsch

Wanapitei Impact Structure: Reconstruction of the Event
R. A. F. Grieve and T. Ber 479

Mars—It's What's Inside That Counts
L. L. Griffith and R. E. Arvidson 481

Proposal for a Topographic Survey of Gusev Crater
E. A. Grin, N. A. Cabrol, and G. Dawidowicz 483

Dike Emplacement at Zones of Neutral Buoyancy on Venus
E. B. Grosfils and J. W. Head 485

Modes of Origin for Giant Radiating Lineament Systems on Venus
E. B. Grosfils and J. W. Head 487

Radial Lineament Systems on Venus: Constraining Models of Global Stress
E. B. Grosfils and J. W. Head 489

A Possible Atmospheric Water Source for the Fluvial Valleys on Alba Patera
V. C. Gulick and C. P. McKay 491

Ferrosilicate, Fayalite and Magnesioferrite Formation by Isothermal Annealing of an Iron-contaminated Mg-SiO Smoke
F. Guofei and F. J. M. Rietmeijer 493

Meteoritic Constraints on the 500 Ma Disruption of the L Chondrite Parent Body
H. Haack, K. Keil, E. R. D. Scott, M. D. Norman, and P. Farinella 495

X-Ray Diffraction Line Broadening in Experimentally Shocked Orthopyroxenes
K. Hackbarth, A. Deutsch, and D. Stöffler 497

Restoration of a Planetary Gamma-Ray Data Map
E. L. Haines, R. G. Radocinski, C. L. Lawson, and A. E. Metzger 499

The Geology and Evolution of Hecate Chasma, Venus
V. E. Hamilton and E. R. Stofan 501

Are There Correlations Between Emissivity, Topography, and Age at Coronae on Venus?
V. E. Hamilton, P. R. Christensen, and E. R. Stofan 503

Electron Microprobe Analyses of Low Vanadium Basalt Glasses
B. Hanson and J. W. Delano 505

The Refractive Index of the Regolith of Mercury
B. Hapke 507

Investigations of the ^{182}Hf-^{182}W Systematics
C. L. Harper Jr. and S. B. Jacobsen 509

Martian Atmospheric Interaction with Bolides: A Test for an Ancient Dense Martian Atmosphere
W. K. Hartmann and S. Engel 511

Melt Inclusions in PAT91501: Evidence for Crystallization from an L-Chondrite Impact Melt
R. P. Harvey and E. Roedder 513

Spectral and Radar Studies of the Schiller-Schickard Region of the Moon 515
B. R. Hawke, D. T. Blewett, and B. A. Campbell

Atmospheric Effects on the Mapping of Martian Thermal Inertia and Thermally Derived Albedo 517
J. N. Hayashi, B. M. Jakosky, and R. M. Haberle

Effects of Fine Particles (<25 μm) on Reflectance Spectra from 0.3 to 25 μm 519
J. E. Hays and J. F. Mustard

Large Igneous Provinces: A Planetary Perspective 521
J. W. Head III

Lunar Mare Deposits: Mechanisms of Emplacement, Stratigraphy, and Implications for the Nature and Evolution of Source Regions and Secondary Crusts 523
J. W. Head

NOAH: A Program to Visualize Lava Flooding of the Venus Crust 525
J. W. Head and P. Haggerty

Mars: Formation and Evolution of Magma Reservoirs 527
J. W. Head and L. Wilson

Geology of the Lavinia Planitia Area, Venus 529
J. Head, K. Magee, S. Keddie, M. Gilmore, and A. Yingst

Kawelu Planitia, Venus: Geology and Mechanisms for the Formation of a Major Volcanic Region 531
M. B. Helgerud and D. Senske

New Laboratory Measurements of Mid-IR Emission Spectra of Simulated Remote Planetary Surfaces 533
B. G. Henderson, P. G. Lucey, and B. M. Jakosky

Geologic Map of the MTM-85280 Quadrangle, Mars 535
K. E. Herkenhoff

Gravity Analysis of Impact Basins at Spacecraft Altitudes: Lessons from Chicxulub 537
R. R. Herrick and V. L. Sharpton

^{26}Al, ^{10}Be, and Mg Isotopes in the Grant Iron Meteorite 539
G. F. Herzog, A. E. Souzis, S. Xue, J. Klein, and R. Middleton

Overturn of Magma Ocean Ilmenite Cumulate Layer (II): Implications for Lunar Thermal and Magmatic Evolution 541
P. C. Hess and E. M. Parmentier

Possible Origin of Si-bearing Metal in Chondrites 543
R. H. Hewins, B. Zanda, H. C. Connolly Jr., and M. Bourot-Denise

Search for Extractable Fullerenes in Clays from K/T Boundaries of New Zealand 545
D. Heymann, L. P. F. Chibante, W. S. Wolbach, and R. E. Smalley

Petrographic Characterization of Lunar Soils: Application of X-Ray Digital-Imaging to Quantitative and Automated Analysis 547
S. J. Higgins, A. Patchen, J. G. Chambers, L. A. Taylor, and D. S. McKay

Tektites Found in the Ruins of the Maya City of Tikal, Guatemala
A. R. Hildebrand, H. Moholy-Nagy, C. Koeberl, L. May, F. Senftle, A. N. Thorpe, P. E. Smith, and D. York 549

High Pressure and Temperature Metal-Silicate Partitioning Behavior of Moderately Siderophile Elements: Implications for the Early History of the Earth
V. J. Hillgren, M. J. Drake, and D. C. Rubie 551

Possible Spinel Absorption Bands in S-Asteroid Visible Reflectance Spectra
T. Hiroi, F. Vilas, and J. M. Sunshine 553

The Ammonia-Water Phase Diagram and Phase Volumes to 4 Kbars
D. L. Hogenboom, J. S. Kargel, T. C. Holden, and J. Ganasan 555

An Experimental Study of KREEP Basalt Evolution
B. Holmberg and M. J. Rutherford 557

Recipes for Impact Cratering
K. A. Holsapple 559

Galileo Magnetic Field Signature: No Evidence That Gaspra is Differentiated
L. L. Hood and C. P. Sonett 561

Evidence for an Interstellar Nitride Grain with Highly Anomalous Isotopic Compositions of C, N and Si
P. Hoppe, R. Strebel, P. Eberhardt, S. Amari, and R. S. Lewis 563

Shocked Materials from the Dutch Peak Diamictite, Utah
F. Hörz, T. E. Bunch, and V. R. Oberbeck 565

Experimental Impacts into Teflon Targets and LDEF Thermal Blankets
F. Hörz, M. J. Cintala, M. E. Zolensky, R. P. Bernhard, and T. H. See 567

Simulation of Gravity-dominated Collisions
K. Housen 569

On the Formation of Enstatite in Unequilibrated Enstatite Chondrites
W. Hsu and G. Crozaz 571

Group A5 Chondrules in Ordinary Chondrites: Their Formation and Metamorphism
S. Huang, P. H. Benoit, and D. W. G. Sears 573

NIMS Science Objectives and Observational Plans for Ganymede During the Galileo Tour
J. Hui, H. H. Kieffer, and the NIMS Team 575

Characterization of Lava-Flow Surface Textures in Different Eruptive Environments on Venus
L. K. Hultgrien and L. R. Gaddis 577

The Non-Terrestrial Origin of the Moon
M. Humayun and R. N. Clayton 579

Potassium Isotopic Composition of Some Australasian Tektites
M. Humayun, R. N. Clayton, and C. Koeberl 581

Presolar Al_2O_3 with a Large Excess of ^{17}O and Depleted ^{18}O
G. R. Huss, A. J. Fahey, R. Gallino, and G. J. Wasserburg 583

Silicon Carbide in Unequilibrated Ordinary Chondrites 585
G. R. Huss, A. J. Fahey, and G. J. Wasserburg

A Search for ^{26}Al in Chondrites: Chondrule Formation Time Scales 587
I. D. Hutcheon, G. R. Huss, and G. J. Wasserburg

Grain Charging and Plasma Potentials in a Dusty Plasma with a Dust Grain Size Distribution 589
T. W. Hyde and L. A. Bringol

Extended Grain Lattice Formation Within a Dusty Plasma 591
T. W. Hyde and W. M. Richter

Dynamics of Two Interacting Objects Orbiting the Sun 593
S. I. Ipatov

New Phosphides in the Kaidun Meteorite 595
A. V. Ivanov, M. E. Zolensky, G. J. MacPherson, S. V. Yang, and N. N. Kononkova

Dynamic Fragmentation of a Comet in the Jovian Atmosphere 597
B. A. Ivanov and H. J. Melosh

Dynamics of Fluidized Ejecta Blankets on Mars 599
B. A. Ivanov, B. C. Murray, and A. S. Yen

Induced Thermoluminescence Study of Experimentally Shock-loaded Quartz 601
A. I. Ivliev, L. L. Kashkarov, and D. D. Badjukov

Shock-Thermal History of Erevan Howardite Matter on Data of Thermoluminescence Analysis of Silicate Minerals 603
A. I. Ivliev, L. L. Kashkarov, and Yu. Yu. Korotkova

Relationships Among Radar Backscatter, Microwave Emissivity, Altitude, and Geology in Ovda Regio, Venus 605
N. R. Izenberg and R. E. Arvidson

Size and Distribution of Shocked Mineral Grains in the Pierre Shale (Late Cretaceous) of South Dakota Related to the Manson, Iowa, Impact Event 607
G. A. Izett and W. A. Cobban

Dust Evolution from Comets and Asteroids: Their Velocities at Earth Orbit Intersection 609
A. A. Jackson and H. A. Zook

New Sulfur Isotopic Measurements of Meteorites and Possible Nebular Relations 611
T. Jackson, S. G. Bobias, and M. H. Thiemens

Dating the Giant Moon-forming Impact with ^{146}Sm-^{147}Nd Systematics 613
S. B. Jacobsen and C. L. Harper Jr.

Mars Atmospheric Escape and Isotopic Fractionation: Synthesis of Data and Models 615
B. M. Jakosky, J. G. Luhmann, and J. H. Jones

Siderophile and Volatile Elements in Apollo 17 Impact Melt Rocks 617
O. B. James

Life Cycle of Venusian Coronae 619
D. M. Janes and S. W. Squyres

The Structural Changes of Water Ice I During Warmup
P. Jenniskens and D. F. Blake 621

Buoyant Mantle Flow and Rift Associated Volcanism: Application to Venus
K. Jha and E. M. Parmentier 623

Resolution Analysis of Magellan Cycle 5 Gravity Data
C. L. Johnson and D. T. Sandwell 625

Backscatter Cross Sections of Venusian FEB Crater Deposits
J. R. Johnson and V. R. Baker 627

Longitudinal Surface Property Variations Along Venusian FEB Flows: Isabella
J. R. Johnson and V. R. Baker 629

Preliminary Geologic Mapping of Venus Quadrangle V59 (Barrymore)
J. R. Johnson, G. Komatsu, and V. R. Baker 631

Searching for Rare Highland Igneous Rocks at Apollo 14: Fragments of Magnesian-Suite Assemblages
B. L. Jolliff 633

Evidence for the Nature of the Igneous Percursor of Ferroan Plutonic Rocks from North Ray Crater, Apollo 16
B. L. Jolliff and L. A. Haskin 635

Sampling the Apollo 17 Highlands Using Soils and Lithic Fragments
B. L. Jolliff, K. M. Rockow, R. L. Korotev, and L. A. Haskin 637

The Compositional Similarity Between Sioux County and Experimentally Produced Partial Melts of the Murchison Chondrite Favors a Partial Melting Origin for Primitive Eucrites
J. H. Jones, B. Z. Hanson, G. A. McKay, A. J. G. Jurewicz, J. W. Delano, and D. W. Mittlefehldt 639

Reduced, Plagioclase-rich Chondrules in the Lancé and Kainsaz CO3 Chondrites
R. H. Jones and A. J. Brearley 641

An Additional Alba Patera Structure in Tempe Terra, Mars?
H.-P. Jons 643

Textural Constraints on the Formation of Alteration Phases in CM Chondrites
L. H. Joseph, L. B. Browning, and M. E. Zolensky 645

^{14}C Terrestrial Ages of Achondrites from Victoria Land, Antarctica
A. J. T. Jull, E. Cielaszyk, S. T. Brown, and D. J. Donahue 647

Evidence for an Implanted Solar Component of ^{14}C in Lunar Samples
A. J. T. Jull, D. Lal, and D. J. Donahue 649

Partial Melting of the St. Severin (LL) and Lost City (H) Ordinary Chondrites: One Step Backwards and Two Steps Forwards
A. J. G. Jurewicz, J. H. Jones, and D. W. Mittlefehldt 651

Preliminary Results of Sulfide Melt/Silicate Wetting Experiments in a Partially Melted Ordinary Chondrite
S. R. Jurewicz and J. H. Jones 653

Radar Imaging of "Overspread" Bodies Using Coherent Frequency Hopping 655
R. Jurgens, L. Robinett, M. Slade, D. Strobert, and B. Flores

The Effect of Oxygen Fugacity on the Partitioning of Nickel and Cobalt Between Melt and Metal 657
A. A. Kadik

The CO_2 Formation in Terrestrial Magmas During the Fluid-Absent Melting of Carbon-bearing Rocks 659
A. A. Kadik and S. N. Shilobreeva

Compositional Similarities Between Undergrouped Loongana 001 and CV4 Coolidge 661
G. W. Kallemeyn

Geochemistry of LEW88774 and Two Other Unusual Ureilites 663
G. W. Kallemeyn and P. H. Warren

Isotopic, Chemical and Textural Properties of Acid Residues from Various Meteorites 665
N. Kano, K. Yamakoshi, and H. Matsuzaki

An Alluvial Depositional Analog for Some Volcanic Plains on Venus 667
J. S. Kargel

Cosmic-Ray Exposure History of the Erevan Howardite Matter by Track Data 669
L. L. Kashkarov and N. N. Korotkova

Some General Characteristics of the Early Radiation-Thermal History of Carbonaceous and Ordinary Chondrite Matter on Data of Track Studies 671
L. L. Kashkarov, N. N. Korotkova, and G. V. Kalinina

Structural Characteristics and Classification of Double-Type Coronae and Corona-like Features on Venus 673
K. Kauhanen and T. Törmänen

Dione Regio Venus: A Comparison to Other Regional Highlands 675
S. T. Keddie and J. W. Head

The Geology and Stratigraphy of Dione Regio, Venus 677
S. T. Keddie and J. W. Head

Sapas Mons: Evolution of a Type-Shield Volcano on Venus 679
S. T. Keddie and J. W. Head

Structural Evolution of Danu Montes, Venus: Deformation Around a Curved Boundary 681
M. Keep and V. L. Hansen

Xenon Isotopic Measurements in Shallowater: *In Situ* Pulsed Laser Volatilization and the Search for the Carrier of Radiogenic ^{129}Xe 683
K. Kehm, C. M. Hohenberg, and R. H. Nichols Jr.

The Nature of Agglutinitic Glass in the Fine-Size Fraction of Lunar Soil 10084 685
L. P. Keller and D. S. McKay

Electron Energy-loss Spectroscopy of Carbon in Interplanetary Dust Particles 687
L. P. Keller, J. P. Bradley, K. L. Thomas, and D. S. McKay

Compositional Evidence in Favor of a Genetic Link Between the Nysa and Hertha Asteroid Families
M. S. Kelley, M. J. Gaffey, and J. G. Williams 689

Modelling Lava Flow Cooling Using a Finite-Difference Numerical Approximation
R. M. Kent and H. Pinkerton 691

Modelling the Flow and Heat Transfer of Magma in Dikes Using Computational Fluid Dynamics
R. M. Kent and H. Pinkerton 693

Production of Superparamagnetic Fe^0 on the Lunar Surface
J. F. Kerridge 695

Formation of Venusian Crustal Plateaus Over Mantle Downwellings
J. G. Kidder and R. J. Phillips 697

Mantle Plumes on Venus: New High Rayleigh Number Models and Applications to Magellan Observations
W. S. Kiefer 699

Isolation of Cosmic-Ray-produced Nitrogen in Meteoritic Silicates and Some Implications
J. S. Kim, Y. Kim, and K. Marti 701

Genetic Relationship of Acapulcoites and Lodranites? A Study of Nitrogen and Xenon Isotopic Signatures
Y. Kim and K. Marti 703

Splotches on Venus: Distribution, Properties, and Classification
R. L. Kirk and D. J. Chadwick 705

^{57}Fe Mössbauer Studies of the Kinetics of Pyrite Decomposition on the Surface of Venus
G. Klingelhöfer, B. Fegley Jr., and K. Lodders 707

Optimization of the Miniaturized Backscattering Mössbauer-Spectrometer MIMOS
G. Klingelhöfer, P. Held, J. Foh, F. Schlichting, R. Teucher, E. Kankeleit, E. N. Evlanov, O. F. Prilutski, G. V. Veselova, and E. A. Duzheva 709

Geochemical and Mineralogical Constraints on the Parent Objects of Micrometeorites
W. Klöck and T. Presper 711

Heating Experiments Simulating Atmospheric Entry of Micrometeorites
W. Klöck, G. J. Flynn, S. R. Sutton, S. Bajt, and K. Neuking 713

Wave Tectonics on the Moon and Symmetries-Antisymmetries of Mare Orientale Region
G. G. Kochemasov 715

Ni-rich Cr Spinels in Spherule Beds from the Barberton Mountain Land (South Africa) are of Terrestrial Origin: Evidence Against Impact Origin of Spherule Layers
C. Koeberl and W. U. Reimold 717

Mineralogical, Petrological, and Geochemical Studies of Drill Cores from the Manson Impact Structure: A Progress Report
C. Koeberl, R. R. Anderson, R. H. Boer, J. D. Blum, C. P. Chamberlain, A. Kracher, W. U. Reimold, B. Träxler, and A. Vormaier 719

Ames Structure, Oklahoma: An Economically Important Impact Crater
C. Koeberl, W. U. Reimold, and R. A. Powell 721

Magnesium Isotopic Fractionation in the Olivines from Allende Chondrules and Isolated Grains
A. Koga, H. Nagahara, H. Yurimoto, and O. Koike 723

Al-Mg Isotopic and REE Clues to the Formation of a Type B1 CAI from Allende Meteorite
O. Koike, H. Yurimoto, and H. Nagasawa 725

Longitudinal Profiles of Plains Channels on Venus
G. Komatsu and V. R. Baker 727

Geochemical Comparison of Four Cores from the Manson Impact Structure
R. L. Korotev, K. M. Rockow, B. L. Jolliff, and L. A. Haskin 729

The Ionized Luminous Column Created During the Flight of a Comet Through Jovian Atmosphere
I. B. Kosarev and I. V. Nemtchinov 731

Lunar and Planetary Mission Scenario for H-II Launch Vehicle
H. Koshiishi, R. Kouda, K. Matushima, and A. Takano 733

Towards Formation of Shells and Rays in Cometary Ionosphere
N. Ya. Kotsarenko and O. P. Verkhoglyadova 735

Aspect of Lunar Resources Exploration
R. Kouda and H. Koshiishi 737

Mercury: Mid-Infrared (7.3–13.5 μm) Spectroscopic Observations Showing Features Characteristic of Plagioclase
R. W. H. Kozlowski, A. L. Sprague, F. C. Witteborn, D. P. Cruikshank, D. Wooden, and K. D. Snyder 739

Fate of Halogens at the Surface of Tektites
U. Krähenbühl and M. Langenauer 741

Small Grains with High Lead Concentration in Chainpur
J. L. A. M. Kramer, A. C. Kik, and R. D. Vis 743

Uniqueness of a Solution of a Steady-state Photochemical Problem: Applications to Mars
V. A. Krasnopolsky 745

H_2O-H_2SO_4 System in Venus' Clouds and OCS, CO, and H_2SO_4 Profiles in Venus' Troposphere
V. A. Krasnopolsky and J. B. Pollack 747

First Measurement of Helium on Mars: Implications for the Problem of Radiogenic Gases on the Terrestrial Planets
V. A. Krasnopolsky, S. Bowyer, S. Chakrabarti, G. R. Gladstone, and J. S. McDonald 749

Model for Ascending of Mantle Diapirs Forming Coronae on Venus
M. A. Kreslavsky 751

Silica- and Merrihueite/Roedderite-bearing Chondrules and Clasts in Ordinary Chondrites: New Occurrences and Possible Origin
A. N. Krot and J. T. Wasson 753

Ab Initio Calculations of Thermodynamics and Kinetics of Gas-Phase Reactions Relevant to the Early Solar Nebula
J. D. Kubicki, J. R. Beckett, G. A. Blake, and E. M. Stolper 755

Isostasy Models and Correlations of Geoid and Topography Data for Characteristic Highlands on Venus
A. B. Kucinskas and D. L. Turcotte 757

Mars, A Carbon Rich Planet? Behavior of H and C During Early Core Formation
K. Kuramoto and T. Matsui 759

Fractionated Trace Element Abundances in Micrometeorites from Antarctica
G. Kurat, C. Koeberl, and M. Maurette 761

Preliminary Report on Spinel-rich CAIs in an Antarctic Micrometeorite
G. Kurat, P. Hoppe, and M. Maurette 763

Non-Steady Modeling of Comet's Wake in the Rarefied Layers of the Jovian Atmosphere
M. Ju. Kuzmitcheva and O. P. Popova 765

Volcanism and Tectonism in Rusalka Planitia and Atla Regio, Venus
M. G. Lancaster and J. E. Guest 767

Stratigraphic Assessment of Gusev Crater as an Exobiology Landing Site
R. Landheim, N. A. Cabrol, R. Greeley, and J. D. Farmer 769

Mossbauer and Spectral (Visible and Near-IR) Data for Fe^{3+}-Substituted Rutile
H. V. Lauer Jr., R. V. Morris, and R. K. Vempati 771

An Experimental Study of Iron Sulfide Kinetics in H_2-H_2S Gas Mixtures and Application to Iron Sulfide Condensation in the Solar Nebula
D. Lauretta and B. Fegley Jr. 773

The Massive O, B Star of Second Generation May be Source of Interstellar Diamond, SiC and Graphite in Chondrites
A. K. Lavrukhina and A. V. Fisenko 775

On Forming Mg-26 and Cr-53 Anomalies in Some Meteoritic Minerals
A. K. Lavrukhina and G. K. Ustinova 777

Characterizing Errors Using the Spectral Mixture Framework
M. E. Lawler and J. B. Adams 779

Impact-Related Low-Emissivity Anomolies on Venus
S. L. Lawson and J. J. Plaut 781

Project Artist: Integrating Astronomy and Planetary Sciences Into the Elementary and Middle School Curriculum
L. A. Lebofsky and N. R. Lebofsky 783

The Nature of Low Albedo Asteroids from 3-μm Spectrophotometry
L. A. Lebofsky, D. T. Britt, E. S. Howell, and A. S. Rivkin 785

Mapping Regolith and Blocks on Asteroid 243 Ida: The Effects of Photometric Viewing Geometry
P. Lee, J. Veverka, M. J. S. Belton, P. C. Thomas, B. T. Carcich, R. Greeley, R. Sullivan, R. Pappalardo, and the Galileo SSI Team 787

Progress in the Development of the GMM-2 Gravity Field Model for Mars
F. G. Lemoine, D. E. Smith, F. J. Lerch, M. T. Zuber, and G. B. Patel 789

Preliminary Solutions for the Lunar Gravity Field from Analysis of Lunar Orbiter Tracking Data
F. G. Lemoine, D. E. Smith, M. T. Zuber, D. D. Rowlands, and S. K. Fricke 791

Precision Noble Gas Measurements on Presolar Diamonds from the Murchison Meteorite
R. S. Lewis 793

Exploring Meteorite Mysteries: A Teachers' Guide with Activities
M. Lindstrom, J. Allen, A. Treiman, J. Burch, K. Crowell, K. Stocco, B. Swaby, R. Luksch, and K. Tobola 795

Pigeonholing Planetary Meteorites: The Lessons of Misclassification of EET87521 and ALH84001
M. M. Lindstrom, A. H. Treiman, and D. W. Mittlefehldt 797

Thumbprint Terrain in Isidis Planitia: Formed in a Glacial Paleolake Environment
J. F. Lockwood and J. S. Kargel 799

On the Origin of Enstatite Chondrite Chondrules Based on Their Petrography and Comparison with Experimentally Produced Chondrules
G. E. Lofgren, J. M. DeHart, and P. J. Burkett 801

Liquidus Equilibria of Lunar Analogs in the Garnet Stability Field
J. Longhi 803

A Model for Forecasting Lava Flow Lengths
R. Lopes-Gautier and C. R. J. Kilburn 805

Galileo's Near Infrared Mapping Spectrometer (NIMS) Science Objectives and Observational Plans for Io
R. Lopes-Gautier, R. Carlson, W. Smythe, L. Soderblom, and the Galileo NIMS Team 807

Morphology of Meteoroid and Space Debris Craters on LDEF Metal Targets
S. G. Love, D. E. Brownlee, N. L. King, and F. Hörz 809

Scarp Heights of Martian Channels from Shadow Measurements
B. K. Lucchitta and J. Dembosky 811

Small Time Differences in Differentiated Meteorites Recorded by the ^{53}Mn-^{53}Cr Chronometer
G. W. Lugmair, C. MacIsaac, and A. Shukolyukov 813

Terrain Simulator
W. Luo, R. Arvidson, and R. Becker 815

Dry Deformation of Diabase: Implications for Tectonics on Venus
S. J. Mackwell, M. E. Zimmerman, D. L. Kohlstedt, and D. S. Scherber 817

Magnetic Properties Experiments Designed for Use with a Mössbauer Spectrometer and an APX Spectrometer on Mars
M. B. Madsen, J. M. Knudsen, S. Faurschou Hviid, H. P. Gunnlaugsson, D. P. Agerkvist, L. Vistisen, J. Madsen, G. Klingelhöfer, E. Kankeleit, V. N. Khromov, E. Evlanov, O. Prilutski, and B. Zubkov 819

A Model for the Origin of Flood Volcanism and "Passive" Rifting in the Lada Terra-Lavinia Planitia Region on Venus
K. P. Magee and J. W. Head 821

Venus: Morphology and Morphometry of Volcanism in Rifting Environments
K. P. Magee and J. W. Head 823

Alternative Thermal Histories for Type B Ca-Al-rich Inclusions
S. V. Maharaj and R. H. Hewins 825

Radial Compaction of the Dust Subdisk in a Protoplanetary Disk as a Possible Way to Gravitational Instability
A. B. Makalkin 827

Numerical Simulation of Tidal Capture of a Lunar-Mass Planetoid by an Earth-like Planet: Two-Dimensional Limits of a Prograde Stable Capture Zone
R. J. Malcuit and R. R. Winters 829

Extreme Potassium Enrichment in Plagioclase from Lithic Clasts in the Lewis Cliff 86001 Monomict Eucrite
J. L. Mann and J. S. Delaney 831

Geologic Mapping of the Sif Mons Southern Flank, Venus (Preliminary Results)
A. G. Marchenko 833

Apollo—The Next Generation: Activities to Accompany the Lunar Sample Disk
L. Martel and G. J. Taylor 835

Evidence for a Mineralogical Change in Relation with the Martian Global Geomorphic Dichotomy in the Tharsis-Mare Sirenum Region
P. Martin, P. C. Pinet, R. Bacon, and A. Rousset 837

Experimental and Theoretical Investigation of Shock Induced Outgassing of Dolomite
I. Martinez, U. Schärer, F. Guyot, A. Deutsch, and U. Hornemann 839

Trojan Collisional Families as a Source for Short-Period Comets
F. Marzari, V. Vanzani, and P. Farinella 841

Effects of Meteoroid Shape on Cosmogenic-Nuclide Production Rates
J. Masarik and R. C. Reedy 843

Numerical Simulations of Gamma-Ray Emission from the Martian Surface
J. Masarik and R. C. Reedy 845

The Highbury Structure, A New Impact Crater in N.W. Zimbabwe
S. Master, W. U. Reimold, D. Brandt, C. Koeberl, D. Robertson, and L. A. G. Antoine 847

I-Xe Dating of El Taco Inclusions
K. J. Mathew and F. Begemann 849

Production Rate of Nitrogen in Moon and Meteorites 851
K. J. Mathew and S. V. S. Murty

Cosmogenic ^{26}Al in Deep-Sea Stony Spherules 853
H. Matsuzaki and K. Yamakoshi

GVDR Data Product: A Summary of All Magellan Observations of Venus Surface Characteristics 855
M. J. Maurer and R. A. Simpson

Erosion and Deposition in the Martian Highlands: Aeolis and Arabia 857
T. A. Maxwell and R. A. Craddock

Depth of Formation of Lunar and Terrestrial Anorthosites and Gabbros from Compositional Profiles of Exsolved Pyroxenes 859
I. S. McCallum and H. E. O'Brien

Post-Impact Hydrothermal Alteration of the Manson Impact Structure 861
P. McCarville and L. J. Crossey

The Galileo Mission Near Infrared Mapping Spectrometer (NIMS) Investigation of the Galilean Satellites 863
T. B. McCord, R. Carlson, and the NIMS Team

Low-FeO Ordinary Chondrites: A Nebular Origin and New Chondrite Parent Body 865
T. J. McCoy, K. Keil, E. R. D. Scott, G. K. Benedix, A. J. Ehlmann, T. K. Mayeda, and R. N. Clayton

Eureca's Hypervelocity Impact Score: Microcrater Flux Decreases But the Large Crater Flux Increases in Specific Directions 867
J. A. M. McDonnell

Evidence for Pre-Nectarian Impact Basin in Northwestern Oceanus Procellarum 869
A. McEwen, P. Davis, and A. Howington-Kraus

Global Color Views of Mars 871
A. S. McEwen, L. A. Soderblom, T. L. Becker, E. M. Lee, J. D. Swann, R. Aeschliman, and R. M. Batson

V, Cr and Mn Partition Coefficients Between Mantle Minerals and Silicate Melt 873
E. A. McFarlane, M. J. Drake, and D. C. Rubie

Lunar Ferroan Anorthosite Subgroups 875
J. J. McGee

Evolution of a Hot Spot, Central Eistla Regio, Venus 877
G. E. McGill

Production of Ferroan Andesites by the Experimental Partial Melting of an LL Chondrite 879
J. C. McGuire, A. J. G. Jurewicz, and J. H. Jones

Apatite Fission-Track Age of Marquez Dome Impact Structure, Texas 881
J. F. McHone and R. B. Sorkhabi

Synthetic and Natural Nakhla Pyroxenes: Parent Melt Composition and REE Partition Coefficients 883
G. McKay, L. Le, and J. Wagstaff

Venusian Channel Gradients as a Guide to Vertical Tectonics
L. C. McLeod and R. J. Phillips 885

The Distribution and Source of Na in Two Type B1 CAIs
G. P. Meeker 887

Determination of Bulk-Carbon Contents in Seven IIIAB Iron Meteorites
A. Meibom, K. L. Rasmussen, O. S. Hansen, P. Hornshøj, and N. Rud 889

Discovery Day, Introducing Space Science to the High School
R. C. Melchior and J. O. Annexstad 891

Crater Chains on the Moon: Records of Comets Split by the Earth's Tides?
H. J. Melosh and E. A. Whitaker 893

Genetic Links Between Equatorial and South Polar Regions on Mars?
E. Merényi, W. M. Calvin, K. S. Edgett, and R. B. Singer 895

A Successful Planetary Science "SPACE" Education Program for Students in Grades 3–8
J. A. Merrell, D. Kenealy, and D. Nash 897

An Absolute Normalization for Modeled Neutron Flux Distribution
A. E. Metzger, D. M. Drake, E. L. Haines, J. Mazarik, and R. C. Reedy 899

The Pasamonte *Polymict* Eucrite—A Reclassification
K. Metzler, K.-D. Bobe, H. Palme, B. Spettel, and D. Stöffler 901

Isotope Source Table for a 25 $M_{\odot}$ Type II Supernova
B. S. Meyer 903

Textural and Mineralogical Heterogeneity of Silicate Inclusions in Tsarev Chondrite
L. F. Migdisova, A. A. Yaroshevsky, M. A. Nazarov, and N. N. Kononkova 905

Cr, Mn and Ca Distributions for Olivine in Angritic Systems: Constraints on the Origins of Cr-rich and Ca-poor Core Olivine in Angrite LEW87051
T. Mikouchi, G. McKay, and L. Le 907

Mineral Paragenesis of the Ureilites: Evidence for High Pressure in a Large Parent Body
O. B. Mitreikina, O. V. Chryukina, N. G. Zinovieva, and L. B. Granovsky 909

ALH84001 Cumulate Orthopyroxenite: A Previously Unappreciated Martian Meteorite
D. W. Mittlefehldt 911

Two Types of Shocked Quartz and Graphite at Barringer Impact Crater
Y. Miura 913

Lunar Landing Site and Exploration by Japanese Lunar Project
Y. Miura and Lunar Working Group of Japan 915

Japanese Found Meteorites Similar to Antarctic Meteorite Collection
Y. Miura, K. Yanai, and O. G. Iancu 917

New SNC Meteorite ALH84001: Evidence for SNC Meteorite from Noble Gases
Y. N. Miura, N. Sugiura, and K. Nagao 919

Chemical Zoning of Olivine in Several Pallasites Suggestive of Faster Cooling 921
M. Miyamoto and H. Takeda

Partition Coefficients for Al, Ca, Ti, Cr, and Ni in Olivine Obtained by Melting Experiment on an LL6 Chondrite 923
M. Miyamoto, T. Mikouchi, and G. A. McKay

Thermal Infrared Observations of Mars from Palomar Mountain 925
J. Moersch, T. Hayward, J. Houck, P. Lee, J. Miles, P. Nicholson, M. Smith, S. Squyres, and J. Van Cleve

Geology of the Mahuea Tholus Quadrangle, Venus 927
H. J. Moore, S. T. Arriola, and E. J. Israel

Rhenium-Osmium Isotope Systematics in IIAB and IIIAB Iron Meteorites 929
J. W. Morgan, M. F. Horan, R. J. Walker, M. I. Smoliar, and J. N. Grossman

Thermal Conductivity of Planetary Lithospheres: New Estimates from Measurements on Mantle Xenolith Samples 931
P. Morgan and S. Y. O'Reilly

Use of Mars Climate History to Demonstrate Causes and Consequences of Global Change on Earth: A Teaching Module for Middle School Students 933
P. Morgan, R. A. Lynch, and G. P. Johnson

REE Characteristics of an Igneous Inclusion in the Yamato-75097 L6 Chondrite 935
N. Morikawa, K. Misawa, N. Nakamura, and K. Yanai

Ferromagnetic Resonance Spectra of H_2-Reduced Minerals and Glasses 937
R. V. Morris and C. C. Allen

Hematite Formed from Pyroxene on Mars by Meteoritic Impact 939
R. V. Morris, J. F. Bell III, and H. V. Lauer

Mössbauer Mineralogy of Calcined Murchison Meteorite 941
R. V. Morris, M. E. Zolensky, T. Hiroi, and M. E. Lipschutz

Toward Systematic Estimation of the Origins of Regolith Materials that Might be Sampled During a Lunar Highland Geologic Traverse 943
B. E. Moss and L. A. Haskin

Carbon in the Metal of Bishunpur and Other Ordinary Chondrites 945
S. Mostefaoui and C. Perron

Impact Craters on Martian Volcanoes 947
P. J. Mouginis-Mark

Morphology of Venus Calderas: Sif and Maat Montes 949
P. J. Mouginis-Mark

Radar Imaging of the Ice Deposits on Mercury's Poles 951
D. O. Muhleman, B. J. Butler, and M. A. Slade

Photoclinometric Studies of Crater and Groove Morphology on Phobos 953
D. C. Munro and L. Wilson

Spectral Units of Martian Soil: Possible Discrimination of Mobile Sediments and Substrate
S. Murchie and J. Mustard 955

The HST Spectrum of Phobos: Comparison with Mariner 9, Viking, and Phobos 2 Results and with Meteorite Analogs
S. Murchie and B. Zellner 957

He, Ne and Ar from the Solar Wind and Solar Energetic Particles in Metal Separates from Fayetteville and Acfer111
Ch. Murer, H. Baur, P. Signer, and R. Wieler 959

Limits on the Mafic Mineralogy of Mars Through MGM Analysis of ISM Spectra
J. F. Mustard and J. M. Sunshine 961

Mare-Highland Mixing Relationships Along the Southwestern Shores of Oceanus Procellarum
J. F. Mustard, J. W. Head, and I. Antenenko 963

Why Chondrules Do Not Show and Some CAIs Show Significant Isotopic Fractionation
H. Nagahara 965

Diffusion Measurement on Double-Layered Single Crystals of Olivine, Orthopyroxene, and Zircon Synthesized by Epitaxial Overgrowth
H. Nagasawa and M. Morioka 967

High-Temperature Shock Effects on Carbonaceous Chondrites
T. Nakamura, K. Tomeoka, T. Sekine, and H. Takeda 969

Argon Degassing and Crustal Production Rates on Venus
N. Namiki and S. C. Solomon 971

The Impact Crater Density on Volcanoes and Coronae on Venus: Implications for Volcanism and Global Resurfacing
N. Namiki and S. C. Solomon 973

Mid-Infrared Spectra of Condensed SO_2 Phases: Lab Data and Applications to Galileo Mapping of Io
D. Nash and B. Betts 975

Shape, Size, and Distribution of Magnetic Particles in Bjurbole Chondrules
D. F. Nava 977

P-rich Sulfide, Barringerite, and Other Phases in Carbonaceous Clasts of the Erevan Howardite
M. A. Nazarov, F. Brandstätter, and G. Kurat 979

Chemistry of Carbonaceous Xenoliths from the Erevan Howardite
M. A. Nazarov, F. Brandstätter, G. Kurat, B. Spettel, and H. Palme 981

Utilization of ICP-MS Analytical Techniques for Determination of Siderophile-Element Abundances: Potential Uses for the Planetary Geochemist
C. R. Neal and L. A. Taylor 983

The Hermes Mercury Orbiter Mission
R. M. Nelson, L. J. Horn, J. R. Weiss, and W. D. Smythe 985

Atmospheric Oscillations Initiated by the Penetration of a Comet or an Asteroid into Gaseous Envelope of a Planet
I. V. Nemtchinov and T. V. Loseva 987

Waves Created by Comet Impact Into Ocean 989
I. V. Nemtchinov, A. V. Teterev, and S. P. Popov

The Inner Solar System Impact Record: Lunar, Terrestrial-Planet, and Asteroid Size-Frequency Data Comparison 991
G. Neukum and B. Ivanov

Patterns of Brittle Deformation Under Extension on Venus 993
G. A. Neumann and M. T. Zuber

The Depletion of W in the Earth's Primitive Mantle, A Stumbling Block for High Temperature Equilibrium Core Formation? 995
H. E. Newsom, P. D. Noll Jr., S. A. Maehr, and K. W. W. Sims

Trapped Noble Gases in Native Gold; Radiogenic He and Fission Xe in U-rich Minerals Accompanying Placer Gold 997
S. Niedermann, O. Eugster, Ch. Thalmann, R. Frei, J. D. Kramers, L. Bruno, and B. Hofmann

A Search for Solar Energetic Particle Helium in Interplanetary Dust Particles 999
A. O. Nier and D. J. Schlutter

Geology of Akkruva Colles Area on Venus: Venera 15/16 SAR Images Analysis 1001
A. M. Nikishin, N. N. Bobina, and G. A. Burba

Recent Histories of Lunar Cores 15009 and 79002/1 Using Cosmogenic Radionuclides ^{10}Be, ^{26}Al, and ^{36}Cl 1003
K. Nishiizumi, R. C. Finkel, M. W. Caffee, P. Sharma, J. Masarik, R. C. Reedy, and J. R. Arnold

Interstellar Corundum and Spinel from the Tieschitz Ordinary Chondrite 1005
L. Nittler, C. Alexander, X. Gao, R. Walker, and E. Zinner

Sudbury Igneous Complex: Evidence Favoring Endogenous Magma Rather Than Impact Melt 1007
M. D. Norman

Alkali Element Constraints on Earth-Moon Relations 1009
M. D. Norman, M. J. Drake, and J. H. Jones

Formation of Iron Metal and Grain Coagulation in the Solar Nebula 1011
J. A. Nuth III and O. Berg

Measurement of the Decay Rate of the SiH Feature as a Function of Temperature 1013
J. A. Nuth III and G. F. Kraus

Pre-Bombardment Crystallization Ages of Basaltic Clasts from Antaractic Howardites EET87503 and EET87513 1015
L. E. Nyquist, C.-Y. Shih, H. Wiesmann, and B. M. Bansal

New Data Supporting a $^{146,147}Sm$-$^{142,143}Nd$ Formation Interval for the Lunar Mantle 1017
L. E. Nyquist, H. Wiesmann, B. M. Bansal, and C.-Y. Shih

Galileo's Near Infrared Mapping Spectrometer (NIMS) Science Observation Plan for Europa 1019
A. Ocampo, D. Matson, and the NIMS Team

Calorimetric Thermobarometry of Experimentally Shocked Quartz 1021
K. D. Ocker, J. L. Gooding, and F. Hörz

Penetration of Large Bolides into Dense Planetary Atmospheres—Role of Hydrodynamic Instabilities
J. D. O'Keefe, T. Takata, and T. J. Ahrens 1023

Lithophile Element Diffusion Profiles in Phosphate Phases in IIIAB Iron Meteorites: A Clue to Trace Elements in Metal During Core Formation
E. J. Olsen and I. M. Steele 1025

I Don't Believe All the Irregularly Shaped Small Bodies in the Solar System are the Result of Collisions
W. A. Oran 1027

Depositional Patterns at the Mouths of the Martian Outflow Channels (Dao, Harmahkis, Maja, and Ares Valles, Mars)
G. G. Ori 1029

Constraints on the Origin of the Offset Dikes (Sudbury Impact Structure, Canada) from U-Pb Data
M. Ostermann, U. Schärer, and A. Deutsch 1031

Chromium Isotopic Anomalies in Stepwise Dissolution of Orgueil
U. Ott, F. A. Podosek, J. C. Brannon, T. J. Bernatowicz, and C. R. Neal 1033

Refractory Siderophiles in Antarctic Unequilibrated Ordinary Chondrites
H. Ozaki and M. Ebihara 1035

New Thermal Models for High-Latitude Impact Craters on Mercury: Implications for Water Ice
D. A. Paige, S. E. Wood, and A. R. Vasavada 1037

Noble Gas Composition of Tektites from Bedias, Texas
R. L. Palma, K. D. Ocker, and M. N. Rao 1039

Re-Os Calibration for Isochron Determinations
D. A. Papanastassiou, H. H. Ngo, and G. J. Wasserburg 1041

ALH 84001 A "SNC Orthopyroxenite": Insights from SIMS Analysis of Orthopyroxene and Comparisons to Diogenites
J. J. Papike, G. W. Fowler, G. D. Layne, M. N. Spilde, and C. K. Shearer 1043

Orthopyroxene as a Recorder of Lunar Mg-Suite Norite Petrogenesis: Preliminary Ion Microprobe Studies of Apollo 17 Fragments
J. J. Papike, G. W. Fowler, and C. K. Shearer 1045

Extensional Tectonics of Arden Corona, Miranda: Evidence for an Upwelling Origin of Coronae
R. Pappalardo, R. Greeley, and S. J. Reynolds 1047

Modelling the Transition Between Hawaiian-Style Lava Fountaining and Strombolian Explosive Volcanic Activity
E. A. Parfitt and L. Wilson 1049

The Role of Magma Recycling in Controlling the Behavior of Hawaiian-Style Lava Fountains
E. A. Parfitt, L. Wilson, and J. W. Head III 1051

Apron Heights Around "Stepped Massifs" in the Borealis Basin of Mars
T. J. Parker and D. S. Gorsline 1053

Formation of Complex Ridged Terrain Through Progressive Compressional Deformation in the Northern Ovda Region of Venus 1055
T. J. Parker and R. S. Saunders

High Spatial Resolution Sulphur Isotopic Analysis of Troilite in Ordinary Chondrites by Ion Microprobe 1057
B. A. Paterson, H. Y. McSween Jr., and L. R. Riciputi

The Composition of SEPs Implanted in Regolith Minerals Depends on Implantation Ranges 1059
A. Pedroni

Anomalous Metal and Sulfide Abundances in the Regolith-Breccia Acfer111 1061
A. Pedroni, B. Spettel, and F. Wlotzka

A New Imaging Resonance Ionization Mass Spectrometer for Isotopic and Trace Analysis 1063
M. J. Pellin, R. N. Thompson, Z. Ma, A. M. Davis, R. S. Lewis, and R. N. Clayton

Heavy Xenon Isotopes on the Moon and in the Solar Wind 1065
R. O. Pepin

The Thick Festoon Flow and Adjacent Dark Flow, Ovda Regio, Venus 1067
J. L. Permenter and R. L. Nusbaum

Lamellar Olivine in the Divnoe Achondrite: EPMA and TEM Studies 1069
M. I. Petaev and A. J. Brearley

Numerical Model of a Genetic Link Between Acapulco and Y791493 Primitive Achondrites. I: Phase Equilibria and Major Element Constraints 1071
M. I. Petaev, A. A. Ariskin, and J. A. Wood

Numerical Model of a Genetic Link Between the Acapulco and Y791493 Primitive Achondrites. II: Implications to the Origin of Acapulcoites and Lodranites 1073
M. I. Petaev, A. A. Ariskin, and J. A. Wood

Mg and Ti Partition Coefficients for Anorthite-CAI Liquid: Dependence on Oxygen Fugacity and Melt Composition 1075
M. T. Peters, E. Shaffer, and D. S. Burnett

The Distribution of Lithologic Units in the Western Highlands of the Moon 1077
C. A. Peterson, B. R. Hawke, P. G. Lucey, G. J. Taylor, and P. D. Spudis

Venus Resurfacing History: Constraints from Halo Ejecta Deposits 1079
R. J. Phillips, N. R. Izenberg, and J. S. Alexopoulos

FeO and MgO in Plagioclase of Lunar Anorthosites: Igneous or Metamorphic? 1081
W. C. Phinney

Young Vesta (Regolith)? 1083
C. M. Pieters and R. P. Binzel

Geophysical Studies of the Montagnais Impact Crater 1085
M. Pilkington, L. F. Jansa, and R. A. F. Grieve

Arachnoid-like Feature on Oldoinyo Lengai, an Active Carbonatite Volcano in Northern Tanzania 1087
H. Pinkerton, J. B. Dawson, and D. M. Pyle

Lava Flow Morphology and Chemistry
H. Pinkerton, J. B. Dawson, and D. M. Pyle 1089

Topographic and Surface Roughness Properties of Steep-Sided Domes on Venus and Earth from Radar Remote Sensing and Field Measurements
J. J. Plaut, E. R. Stofan, D. A. Crown, and S. W. Anderson 1091

Atmospheric vs. Solar Noble Gas Abundances: Isotopic Fractionation in Low Energy Argon Ion Implantation
K. V. Ponganis, Th. Graf, and K. Marti 1093

Prolonged Biospheric Effects of Sulfur Vaporization by the K/T Chicxulub Impact
K. O. Pope, A. C. Ocampo, K. H. Baines, and B. A. Ivanov 1095

Systematics of Xe Isotopes in a Two-layer Earth with Mass Transport
D. Porcelli and G. J. Wasserburg 1097

Attempt to Observe the Sodium Exosphere of Mercury During the 1993 Solar Transit
A. E. Potter, D. Talent, H. Kurokawa, S. Kawakami, and T. H. Morgan 1099

Discovery and Description of a Muong Nong-type Georgia Tektite
H. Povenmire, B. P. Glass, and R. Strange 1101

Pb Isotopic Systematics of Troctolitic Anorthosite 62237
W. R. Premo and M. Tatsumoto 1103

Young Tectonism and Volcanism on Venus: Age Estimates from Crater Densities
M. Price, J. Suppe, F. Bilotti, and G. Watson 1105

LEW 88774: A New Type of Cr-rich Ureilite
M. Prinz, M. K. Weisberg, and C. E. Nehru 1107

Surface Expression of Gravitational Relaxation of Topography: South Scarp of Lakshmi Planum, Venus
A. A. Pronin and M. A. Kreslavsky 1109

Solid-Solid Trace-Element Partitioning Between Exsolved Pyroxenes in Cumulate Eucrites
A. Pun and J. J. Papike 1111

Studies of Mafic Intrusives in the Vredefort Impact Structure, South Africa: Implications for Craton Wide Igneous Activity at 1.1 Ga Ago
G. Q. J. Pybus, W. U. Reimold, and C. B. Smith 1113

Cytherean Dextral Transform Fault Zone from Concave Arc to Concave Arc?
J. Raitala 1115

Relative Change in Cross-Sectional Area and Albedo with Rotational Phase for 532 Herculina and 45 Eugenia
K. L. Reed, M. J. Gaffey, and L. A. Lebofsky 1117

Cosmogenic-Nuclide Depth Profiles in the Lunar Surface
R. C. Reedy and J. Masarik 1119

First Observations of Shatter Cones in the Direct Vicinity of the Bushveld Complex
W. U. Reimold and R. C. A. Minnitt 1121

The Dynamical Evolution of Magnetized Solar Nebula 1123
M. Reyes-Ruiz and T. F. Stepinski

Terrestrial Polar Beach Processes: Martian Paleolake Analogs 1125
J. W. Rice Jr.

Analogs and Interpretations for the Martian Thumbprint Terrain and Sinuous Ridges 1127
J. W. Rice Jr. and J. D. Mollard

Searching for a Principal Component Mixing Model for Chondritic Interplanetary Dust Particles: The Use of Size Analyses 1129
F. J. M. Rietmeijer

Sulfide and Layer Silicate Grain Size Distributions Constrain the Unique Petrogenesis of a Type CM Interplanetary Dust Particle 1131
F. J. M. Rietmeijer

Lineament Analysis of Fortuna Tessera; A Preliminary Evaluation of a Complex Ridged Terrain, Venus 1133
K. M. Riley and R. C. Anderson

Hydrated E-class and M-class Asteroids 1135
A. S. Rivkin, D. T. Britt, E. S. Howell, and L. A. Lebofsky

The Weathering Process on Venus Takes 2–3 Hundred Million Years: Evidence from Radiothermal Emissivity Signatures at Coronae 1137
C. A. Robinson

SO_2 and CH_4 Levels in the Venusian Atmosphere, Measured by Pioneer Venus: Caused by Plinian-Style Volcanic Activity at Maat Mons? 1139
C. A. Robinson and G. D. Thornhill

Volumes and Depth of Burial of the Lesser Tharsis Volcanoes 1141
M. S. Robinson and H. Garbeil

Mass Spectra of Sputtered Sugars: Testing the Assignment of Polyoxymethylene as a Constituent of Comet Halley 1143
M. S. Robinson and T. J. Wdowiak

Mariner 10 Multispectral Images of the Moon and Mercury 1145
M. S. Robinson, B. R. Hawke, P. G. Lucey, and K. Edwards

The Lesser Tharsis Volcanoes: Clues to Martian Edifice Building Eruptions 1147
M. S. Robinson, P. J. Mouginis-Mark, and S. K. Rowland

Geology and Distribution of Rock Types at the Apollo 17 Landing Site from a 2–4 mm Perspective 1149
K. M. Rockow, B. L. Jolliff, R. L. Korotev, and L. A. Haskin

Compositional Differences Between Impact-Melt Breccias of the North and South Massifs at Apollo 17 1151
K. M. Rockow, R. L. Korotev, B. L. Jolliff, and L. A. Haskin

Luna 24 Regolith Breccias—A Possible Source of the Fine Size Material of the Luna 24 Regolith 1153
O. D. Rode and M. M. Lindstrom

Antarctic Weathering of the CK Chondrites EET90004, 90007, and 90022: Nickel and Sulfur Mobility
C. S. Romanek, R. A. Socki, E. K. Gibson Jr., and J. H. Allton 1155

The Chondritic Regolith Breccia (H3-6) Acfer 153: Petrography and *In-Situ* Nuclear Track Investigations
J. Romstedt and K. Metzler 1157

Thermal Isostasy Process and Lithospheric Structure on Venus
P. Rosenblatt and P. C. Pinet 1159

Thermal Emission Measurements (5–25 μm) of Hawaiian Palagonitic Soils with Implications for Mars
T. L. Roush and J. F. Bell III 1161

Thermal Emission Measurements (5–25 μm) of Palagonite/Fe-substituted Montmorillonite Intimate Mixtures: Applications to Mars
T. L. Roush and J. B. Orenberg 1163

Transmission Measurements (4000–400 cm^{-1}, 2.5–25 μm) of Crystalline Ferric Oxides and Ferric Oxyhydroxides: Implications for Mars
T. L. Roush, J. F. Bell III, and R. V. Morris 1165

More Shock Recovery Experiments on Mesosiderite Analogs
L. R. Rowan and D. W. Mittlefehldt 1167

Contact Metamorphism in Ordinary Chondrite Impact Breccias: Implications for the Impact Heating of Chondrite Parent Bodies
A. E. Rubin 1169

Comparison of Mars Sinous Ridges with Terrestrial Linear Dunes: Observations from the Field
S. W. Ruff 1171

Chondrule Formation in Radiative Shock
T. V. Ruzmaikina and W. H. Ip 1173

Energy Partitioning in Catastrophic Collisions
E. V. Ryan and D. R. Davis 1175

Past Geological Exploration of the Earth and Future Geological Exploration of the Planets
G. Ryder 1177

The Petrogenetic Interpretation of Tiny Fragments of Evolved Lunar Rocks: An Analog Analysis of the Abriachan Granite, Scotland
G. Ryder and J. Gillis 1179

Detectability of Lunar Tephra Deposits: Examples from the Apollo 17 Landing Site
D. E. Sabol Jr., J. B. Adams, M. O. Smith, and P. C. Pinet 1181

Igneous Inclusions from Ordinary Chondrites: High Temperature Residues and Shock Melts
R. O. Sack, M. S. Ghiorso, and M. E. Lipschutz 1183

Search for ^{26}Mg Isotopic Anomaly in Unequilibrated Chondrites and Unique Meteorites
S. Sahijpal, J. N. Goswami, L. L. Kashkarov, N. N. Korotkova, and M. A. Nazarov 1185

Small Volcanic Edifices on Venus: Morphology, Diameter, and Elevation Distributions
Sahuaro High School Astronomical Research Class, J. F. Lockwood, Evergreen High School Research Class, M. Ellison, J. Johnson, and G. Komatsu 1187

Terrestrial Basaltic Counterparts for the Venus Steep-Sided or "Pancake" Domes
S. E. H. Sakimoto 1189

Thermal Gradients and Kirchhoff's Law
J. W. Salisbury, A. E. Wald, and D. M. D'Aria 1191

Formation of Continuous Ridges on Icy Satellites by Cooling Gravity-Current Volcanism
S. Sasaki, R. Kono, and Y. Iwase 1193

Scientific Analysis and Display of Magellan Venus Data with McIDAS-eXplorer
R. S. Saunders, S. S. Limaye, L. A. Sromovsky, R. Krauss, E. Wright, D. Santek, and P. Fry 1195

Genesis and Parameters of Ultramylonite and Pseudotachylite (Puchezh-Katunky Astrobleme, Russia)
L. Sazanova and N. Korotaeva 1197

Venus: Fractured Craters Revisited, and the Evidence for Minimal Geologic Activity Over the Past 300 m.y.
G. G. Schaber, R. G. Strom, and D. J. Chadwick 1199

Venusian Parabolic Halos: Numerical Model Results
C. J. Schaller and H. J. Melosh 1201

Lobate Thrust Scarps and the Thickness of Mercury's Lithosphere
P. Schenk and H. J. Melosh 1203

The Stereo View of the Solar Sytem
P. Schenk, D. Wilson, R. Morris, and T. J. Parker 1205

Hole Size from Impacts at Scaled Velocities of 7 to 21 km/s
R. M. Schmidt and K. R. Housen 1207

Calculation of Hugoniot Curves and Post-Shock Temperatures for H- and L-Chondrites
R. T. Schmitt, A. Deutsch, and D. Stöffler 1209

Chicxulub as an Oblique Impact
P. H. Schultz 1211

Atmospheric Containment of Crater Growth
P. H. Schultz and O. S. Barnouin 1213

Penetrating and Escaping the Atmospheres of Venus and Earth
P. H. Schultz and S. Sugita 1215

Comparative Rock Mass Strengths of Basalt and Tuff and Some Planetological Implications
R. A. Schultz 1217

Outstanding Tectonic Problems in the Valles Marineris Region of Mars
R. A. Schultz 1219

Distribution of Siderophile and Other Trace Elements in Melt Rock at the Chicxulub Impact Structure
B. C. Schuraytz, D. J. Lindstrom, R. R. Martinez, V. L. Sharpton, and L. E. Marín 1221

Preliminary Description of Double Drive Tube 68002/68001
C. Schwarz, R. V. Morris, and R. L. Korotev 1223

1:1 Million-scale Geologic Maps of Mars' Tharsis Montes
D. H. Scott, J. R. Zimbelman, and J. M. Dohm 1225

Evaporation and Recondensation of Volatiles During Chondrule Formation
E. R. D. Scott 1227

Evaporation and Recondensation During Chondrule Formation
D. W. G. Sears and M. E. Lipschutz 1229

Numerical Ocean Tides on Titan: Spherical Case
W. D. Sears 1231

Current Activities and Results of the Long Duration Exposure Facility Meteoroid and Debris Special Investigation Group
T. H. See, K. S. Leago, J. L. Warren, R. P. Bernhard, and M. E. Zolensky 1233

NIMS-Callisto Science Objectives and Observational Plans
M. Segura, J. Sunshine, T. McCord, and the NIMS Team 1235

SEM Study of Metal Grain Surface in Ordinary Chondrites. I. Primary Sculptures
V. P. Semenenko and B. V. Tertichnaya 1237

SEM Study of Metal Grain Surface in Ordinary Chondrites: II. Secondary Sculptures
V. P. Semenenko and B. V. Tertichnaya 1239

Examination of the Relation Between Rifting and Volcanism in the Juno Dorsum Region of Venus
D. A. Senske 1241

Radar Characteristics of Geologic Units in the Carson Quadrangle, Venus
D. Senske, R. Greeley, and K. Bender 1243

The Global Geology of Venus: Classification of Landforms and Geologic History
D. A. Senske, R. S. Saunders, E. R. Stofan, and members of the Magellan Science Team 1245

Pyrolysis Typing of Meteoritic Organic Matter
M. A. Sephton, C. T. Pillinger, and I. Gilmour 1247

Student Explorer Demonstration Initiative: Affordable Access to Space
J. Sevier and P. Coleman 1249

Nebula Matter Differentiation as a Result of Condensation
A. I. Shapkin and Yu. I. Sidorov 1251

The Problem of High Precision Measurements of $^{142}Nd/^{144}Nd$: The Terrestrial Record of ^{146}Sm
M. Sharma, D. A. Papanastassiou, G. J. Wasserburg, and R. F. Dymek 1253

Constraints on Excavation and Mixing During the Chicxulub Impact Event
V. L. Sharpton, L. E. Marín, B. C. Schuraytz, P. D. Spudis, and G. Ryder 1255

Light Lithophile Elements (Li, Be, B) in Lunar Picritic Glasses. Implications for Lunar Mantle Dynamics and the Origin of the Moon
C. K. Shearer, G. D. Layne, and J. J. Papike 1257

The Earth-Moon Connection. Clues Preserved in Lunar Picritic Magmas
C. K. Shearer, J. J. Papike, and H. E. Newsom 1259

Innovative Instrumentation for Mineralogical and Elemental Analyses of Solid Extraterrestrial Surfaces: The Backscatter Mössbauer Spectrometer/X-Ray Fluorescence Analyzer (BaMS/XRF)
T. D. Shelfer, R. V. Morris, T. Nguyen, D. G. Agresti, and E. L. Wills 1261

A Ferroelectric Model for the Low Emissivity Highlands on Venus
M. K. Shepard, R. E. Arvidson, R. A. Brackett, and B. Fegley Jr. 1263

Ion Microprobe Studies of Lunar Highland Cumulate Rocks: Preliminary Results
J. W. Shervais 1265

Remote Sensing Assessment of the Lunar Soil Maturation
V. V. Shevchenko 1267

Tektite-Obsidian-like Glasses from Space
M. Shima, M. Honda, A. Okada, T. Okada, Y. Kobayashi, M. Ebihara, Y. N. Miura, and K. Nagao 1269

Is There Umov Effect for the Moon in Polarization Minimum?
Yu. G. Shkuratov and N. V. Opanasenko 1271

Pu-Xe Ages of Eucrites
A. Shukolyukov and F. Begemann 1273

Unusual Refractory Inclusions from a CV3 Chondrite Found Near Axtell, Texas
S. B. Simon, L. Grossman, and J. F. Wacker 1275

Geoid/Topography Admittance on Venus from Models of Convection with No Crustal Deformation
M. Simons, B. H. Hager, and S. C. Solomon 1277

The Magellan Quasi-Specular Bistatic Radar Experiment
R. A. Simpson, G. H. Pettengill, and P. G. Ford 1279

Venus Gravity Field Determination: Progress and Concern
W. L. Sjogren and A. S. Konopliv 1281

Pre-Allende Planetesimals with Refractory Compositions: The CAI Connection
W. R. Skinner 1283

Rounding of Chondrules by Abrasion: A Cautionary Note Regarding Textural Evidence
W. R. Skinner and H. C. Connolly Jr. 1285

Access to Large Planetary Science Data Bases
S. Slavney, T. Stein, and R. E. Arvidson 1287

The Topography of Mars: A Re-Evaluation of Current Data
D. E. Smith and M. T. Zuber 1289

The Mass of Mars, Phobos, and Deimos, from the Analysis of the Mariner 9 and Viking Orbiter Tracking Data
D. E. Smith, F. G. Lemoine, and S. K. Fricke 1291

The Imager for MESUR Pathfinder (IMP)
P. H. Smith, D. T. Britt, L. R. Doose, R. B. Singer, M. G. Tomasko, F. Gliem, H. U. Keller, J. M. Knudsen, and L. A. Soderblom 1293

Interpretation of Magellan Gravity Data for Large Volcanic Swells on Venus: Implications for Interior Structure
S. E. Smrekar 1295

The Status of Mercury Exploration
W. Smythe, R. Lopes-Gautier, A. Ocampo, and R. Nelson 1297

A Sortie for Pristine Rocks at Mare Tranquillitatis: A Ferroan Anorthosite, A New Group D Basalt, and the Isotopic Composition of Group D High-Ti Basalts
G. A. Snyder, E. A. Jerde, L. A. Taylor, D.-C. Lee, and A. N. Halliday 1299

A Basaltic Safari Across the Cayley Plains and Over the Descartes Mountains: Still Searching for a Pristine Highlands Basalt at Apollo 16
G. A. Snyder, J. Karner, E. A. Jerde, and L. A. Taylor 1301

Silicate Liquid Immiscibility in Anorthosite Suites: Viewing the Moon from Wyoming and Labrador
G. A. Snyder, J. Mitchell, L. A. Taylor, and E. C. Simmons 1303

Petrology and Chemistry of the Magnesian Suite: Further Evidence of Liquid Immiscibility and Metasomatism in the Western Highlands of the Moon
G. A. Snyder, C. R. Neal, L. A. Taylor, and A. N. Halliday 1305

Chronology and Petrogenesis of the Western Highlands Alkali Suite: Cumulates from Quartz Monzodiorite (QMD) Liquids
G. A. Snyder, L. A. Taylor, and A. N. Halliday 1307

Rb-Sr Isotopic Systematics of Lunar Ferroan Anorthosite 62237
G. A. Snyder, L. A. Taylor, and A. N. Halliday 1309

Evolved QMD-Melt Parentage for Lunar Highlands Alkali Suite Cumulates: Evidence from Ion-Probe Rare-Earth Element Analyses of Individual Minerals
G. A. Snyder, L. A. Taylor, E. A. Jerde, and L. R. Riciputi 1311

Journey to the Center of the Regolith: Petrology and Mineral Chemistry of a New Ferroan Anorthosite from Drive Tube 68002/68001
G. A. Snyder, L. A. Taylor, and A. D. Patchen 1313

Crystal Sizes in Magma Oceans: Application to the Suspension Problem
V. S. Solomatov and D. J. Stevenson 1315

Gravity Anomalies over Volcanoes on Venus: Implications for Lithospheric Thickness and Volcano History
S. C. Solomon, P. J. McGovern, M. Simons, and J. W. Head 1317

The Bimodal Size Distribution of Near-Earth Asteroids 1319
D. H. Speidel

Laser Fusion ^{40}Ar-^{39}Ar Dating of Pseudotachylites from the Vredefort Impact Structure: New Evidence for a Major Formation Event at 2.0 Ga 1321
J. G. Spray and S. P. Kelley

Return to Mercury: The Discovery-Mercury Polar Flyby Mission 1323
P. D. Spudis, J. B. Plescia, and A. D. Stewart

^{41}K Excess in Efremovka CAIs 1325
G. Srinivasan, J. N. Goswami, and A. A. Ulyanov

Trajectory Calculation of Individual Particles from LDEF Impacts 1327
F. J. Stadermann

Spectral Variation Within Mare Tranquillitatis: Implications for Stratigraphy and Mixing Mechanisms 1329
M. I. Staid, C. M. Pieters, and J. W. Head

Longitudinal Variations of the Linear Polarization in Jupiter's Polar Regions at the System III and IV Periods 1331
O. M. Starodubtseva, L. A. Akimov, V. V. Korokhin, and V. G. Tejfel

Reflectance Spectra of Particle Size Separates of Lunar Soils: Is the Difference Controlled by Reduced Iron? 1333
L. V. Starukhina, Yu. G. Shkuratov, O. D. Rode, and C. M. Pieters

Chemical Zoning and Exsolution in Olivine of the Pavlodar Pallasite: Comparison with Springwater Olivine 1335
I. M. Steele

Crystal Structure of Chladniite $Na_2CaMg_7(PO_4)_6$, from Carlton (IIICD) Iron Meteorite 1337
I. M. Steele

Oscillatory Zoning in Forsterite from Carbonaceous and Unequilibrated Ordinary Chondrites: Implications for Origin of Some Forsterite 1339
I. M. Steele

New TOF-SIMS Results on Hydrated Interplanetary Dust Particles 1341
T. Stephan, E. K. Jessberger, H. Rulle, K. L. Thomas, and W. Klöck

Carbonate Formation on Mars: Implications of Recent Experiments 1343
S. K. Stephens, D. J. Stevenson, L. F. Keyser, and G. R. Rossman

Noachian and Hesperian Modification of the Original Chryse Impact Basin Topography 1345
S. Stockman and H. Frey

Classification and Nomenclature of Impact Metamorphic Rocks: A Proposal to the IUGS Subcommission on the Systematics of Metamorphic Rocks 1347
D. Stöffler and R. A. F. Grieve

Status of the Small Body Mapping Program 1349
P. J. Stooke

Promoting Planetary Science Among Elementary School Students 1351
M. M. Strait

The Global Resurfacing History of Venus
R. G. Strom, G. G. Schaber, and D. D. Dawson 1353

Impact Ejecta Vapor Cloud Interference Around Venus Craters
S. Sugita and P. H. Schultz 1355

Isotopic Composition of Nitrogen in the PCA91002 Chondrite
N. Sugiura and S. Zashu 1357

New Evidence for Compositional Diversity on the Marius Hills Plateau from Galileo Multi-Spectral Imaging
J. M. Sunshine, C. M. Pieters, and J. W. Head 1359

Microanalysis of Iron Oxidation States Using X-Ray Absorption Spectroscopy
S. R. Sutton, S. Bajt, and J. S. Delaney 1361

Brownlee's Particles of Cosmic Origins in Deep Sea Sediments
Y. Suzuki, M. Noma, H. Sakurai, K. Yamakoshi, H. Matsuzaki, N. Kano, and K. Nogami 1363

Radiation Emitted During the Flight: Application to Assessment of Bolide Parameters from the Satellite Recorded Light Flashes
V. V. Svetsov 1365

The Thermal History of the Lunar Regolith at the Apollo 16 and 17 Sites
S. J. Symes, P. H. Benoit, and D. W. G. Sears 1367

Comet Shoemaker-Levy 9 Impact on Jupiter—The First Ten Minutes
T. Takata, J. D. O'Keefe, T. J. Ahrens, and G. S. Orton 1369

Orthopyroxene with Dusty Core and Clear Rims in Acapulco and Its Related Formation Process to Lodranites
H. Takeda and M. Miyamoto 1371

Mineralogy of Apollo 12 Low-Ti Basalts in Relation to Lunar Meteorites from Mare Region
H. Takeda, T. Arai, and K. Saiki 1373

Inhomogeneous Distribution of Materials in Lodranites-Acapulcoites and IAB Irons and Their Common Formation Processes
H. Takeda, M. Otsuki, A. Yamaguchi, M. Miyamoto, M. Otsuki, M. Tomobuchi, and T. Hiroi 1375

Strain Measurements of Impact Craters on Tempe Terra, Mars
K. L. Tanaka and M. P. Golombek 1377

Eolian History of the Hellas Region of Mars
K. L. Tanaka and G. J. Leonard 1379

Experimental and Theoretical Examination of Cosmic Dust Grain Deceleration
W. G. Tanner Jr., W. M. Alexander, and S. Stephenson 1381

Slow Emplacement of Flood Basalts: Evidence from Fractal Properties of Lava Flows
G. J. Taylor, B. C. Bruno, and S. Self 1383

Planar Deformation Features in Quartz Grains from Resurge Deposit of the Lockne Structure, Sweden 1385
A. M. Therriault and M. Lindström

New Studies of Mass Independent Isotopic Fractionation Processes and Their Occurrence in the Early Solar System, Mars, and the Earth 1387
M. H. Thiemens

First Observation of a Mass Independent Isotopic Fractionation in a Condensation Reaction 1389
M. H. Thiemens, R. Nelson, Q. W. Dong, and J. A. Nuth III

Anatomy of a Cluster IDP (II): Noble Gas Abundances, Trace Element Geochemistry, Isotopic Abundances, and Trace Organic Chemistry of Several Fragments from L2008#5 1391
K. L. Thomas, S. J. Clemett, G. J. Flynn, L. P. Keller, D. S. McKay, S. Messenger, A. O. Nier, D. J. Schlutter, S. R. Sutton, R. M. Walker, and R. N. Zare

The Anatomy of a Cluster IDP (I): Carbon Abundance, Bulk Chemistry, and Mineralogy of Fragments from L2008#5 1393
K. L. Thomas, L. P. Keller, W. Klock, J. Warren, G. E. Blanford, and D. S. McKay

Ida: Topography, Slopes and Grooves 1395
P. Thomas, J. Veverka, M. J. S. Belton, and Galileo Imaging Science Team

Deformation of Large Bolides During Atmospheric Passage: Comparison of SPH and Analytic Models 1397
P. J. Thomas, L. Brookshaw, and G. Starkey

Teaching Planetary Surface Processes and Mapping to Advanced 5th and 6th Grade Students 1399
P. Thompson, S. Murchie, R. Herrick, B. Schuraytz, and G. Ryder

Magellan Mission Progress Report 1401
T. W. Thompson and Magellan Flight Team

A Simple Model for Particle Support in Pyroclastic Flows 1403
G. D. Thornhill

Properties of Lava Flows Associated with Coronae in S.E. Aphrodite Terra, Venus 1405
K.-A. Tomkinson and L. Wilson

Semi-Objective Determination of Lithologic End-Members in Geologic Environment (Spectral Mixture Analysis) 1407
S. Tompkins, J. F. Mustard, C. M. Pieters, and D. W. Forsyth

4.56 Ga U-Th-Pb Age of MET 78008 Ureilite 1409
N. Torigoye, M. Tatsumoto, and K. Yanai

Areal Distribution of Double-Type Coronae and Corona-like Features on Venus, and Their Relation to Topography, Tesserae and Deformation Belts 1411
T. Törmänen and K. Kauhanen

Two Source Areas for the SNC Meteorites: Petrologic, Chemical, and Chronologic Evidence 1413
A. H. Treiman

Chemical Weathering on Venus: Preliminary Results on the Interaction of Basalt with Carbon Dioxide 1415
A. H. Treiman and C. C. Allen

The Parent Magma of Xenoliths in Shergottite EETA79001: Bulk and Trace Element Composition Inferred from Magmatic Inclusions
A. H. Treiman, D. J. Lindstrom, and R. R. Martinez 1417

The Temperature of Nitrogen on Pluto
K. A. Tryka, R. H. Brown, D. P. Cruikshank, and T. C. Owen 1419

Purity and Cleanness of Aerogel as a Cosmic Dust Capture Medium
P. Tsou, R. H. Fleming, P. M. Lindley, A. Y. Craig, and P. Blake 1421

How Does Venus Lose Its Heat?
D. L. Turcotte 1423

Stress and Flexural Modeling of Alba Patera, Mars
E. P. Turtle and H. J. Melosh 1425

Excitation Functions of the Neon Isotopes in Chondrites and Achondrites
G. K. Ustinova 1427

On Possible Disturbance of the Solar Modulation Mechanism Over a Long-Time Scale
G. K. Ustinova and A. K. Lavrukhina 1429

Shock Deformation in Talc and Its Possible Significance for Investigations of Astroblemes
A. A. Valter 1431

A Silicate Lava Model for Io's Hotspots
G. J. Veeder, D. L. Blaney, T. V. Johnson, and D. L. Matson 1433

Nitrogen and Carbon Components in C_δ: A Possible Presence of Nitrogen-Free Diamonds in C_δ
A. B. Verchovsky, J. Newton, I. P. Wright, J. W. Arden, and C. T. Pillinger 1435

Impact Erosion of Atmospheres
A. M. Vickery 1437

A Quick Look Method of Detecting Water of Hydration in Small Solar System Bodies
F. Vilas 1439

Fireworks Around Naked T Tauri Stars
A. V. Vityazev and G. V. Pechernikova 1441

Generalized Coagulation Equation and Mass-Spectrum of Protoplanet
A. Vityazev, Yu. Kukharenko, A. Bashkirov, and G. Pechernikova 1443

Surface Energy Measurements of Comminuted Silicates: Implications for Cosmochemical Processes
R. Voelkel, R. F. Giese, and C. J. van Oss 1445

Depositional Units in Western Maxwell Montes: Implications for Mountain Building Processes on Venus
R. W. Vorder Bruegge 1447

Variation in Compressional Structures Across Maxwell Montes: Evidence for a Sequence of Events in a Venusian Orogeny
R. W. Vorder Bruegge 1449

Rare Earth Element Distributions in Chassigny: Clues to Its Petrogenesis and Relation to the Nakhlites 1451
M. Wadhwa and G. Crozaz

Modeling the Thermal Infrared Directional Emissivity of Large, Close-Packed, Particulate Media 1453
A. E. Wald and J. W. Salisbury

TEM Studies on the Dislocations in Olivine of Taizhou Meteorite from Jiangsu Province China 1455
H. Wang, W. Rong, F. Zheng, and C. Lin

Chemical and Isotopic Fractionation During the Evaporation of the FeO-MgO-SiO_2-CaO-Al_2O_3-TiO_2-REE Melt System 1457
J. Wang, A. M. Davis, R. N. Clayton, and T. K. Mayeda

Kinetic Isotopic Fractionation During the Evaporation of the Iron Oxide from Liquid State 1459
J. Wang, A. M. Davis, R. N. Clayton, and T. K. Mayeda

Coorbital Bending Waves and Inclination Decay 1461
W. R. Ward and J. M. Hahn

Petrologic Insights Regarding Lunar and Planetary Meteorite Launch Processes 1463
P. H. Warren

Petrology of LEW88774: An Extremely Chromium-rich Ureilite 1465
P. H. Warren and G. W. Kallemeyn

Chondrule Magnetic Properties 1467
P. J. Wasilewski and M. V. O'Bryan

The Evolution of Nebular Solids: Evidence from Compound Chondrules and from Igneous Rims on Chrondules in Ordinary Chondrites 1469
J. T. Wasson and A. N. Krot

The Abundance and Stable Isotopic Composition of Volatiles Released from Weathering Products During Stepped Heating of Nakhla and Lafayette 1471
L. L. Watson, S. Epstein, and E. M. Stolper

Morphologic Studies of Contractional Features on Mars Using Photoclinometrically Derived Elevation Profiles 1473
T. R. Watters and M. S. Robinson

Trace Element and Isotopic Measurements of Refractory Inclusions from the Acfer 182 Carbonaceous Chondrite 1475
D. Weber, E. K. Zinner, and A. Bischoff

Origin of "Rubble Pile" Cometary Nuclei 1477
S. J. Weidenschilling

Primitive Trapped Xe in Lodran Minerals and Further Evidence from EET84302 and Gibson for Break-up of the Lodranite Parent Asteroid 4 Ma Ago 1479
A. Weigel and O. Eugster

Agglomeratic Olivine (AO) Chondrules in Ordinary Chondrites 1481
M. K. Weisberg and M. Prinz

Radiophysical Properties of Impact Craters on Venus
C. M. Weitz, J. J. Plaut, and H. J. Moore 1483

Detectability of Carbonate in Unconsolidated and Indurated Sediments
M. L. Wenrich and P. R. Christensen 1485

Provenance of the Terrestrial Planets
G. W. Wetherill 1487

Dark-Floored Crater Elevations on Venus: Implications for Crater-centered Volcanism
R. W. Wichman 1489

Comet Disruption and Crater Chain Formation in the Earth-Moon System
R. W. Wichman and C. A. Wood 1491

Analytical Modeling of Thermal Erosion by Low-Viscosity Lava Flows and Implications for Planetology
D. A. Williams and R. Greeley 1493

Mars: Volcanic Eruption Theory and Relationships to Observed Landforms
L. Wilson and J. W. Head 1495

Clast Sizes of Basaltic Ejecta from Explosive Eruptions on Asteroids
L. Wilson and K. Keil 1497

Lunar LIGO and Gravitational Wave Astronomy on the Moon
T. L. Wilson and N. LaFave 1499

Advanced Technology Lunar Telescope
T. L. Wilson, W.-K. Chu, and P. C. Chen 1501

Numerical Simulation of Scattering by Discrete Objects
P. B. Wong, R. A. Simpson, and G. L. Tyler 1503

A Remotely Operated Planetary Science Observatory to Enhance Space Education
C. A. Wood and P. Abell 1505

An Asteroid Family Among the NEAs?
C. A. Wood, R. Fevig, and J. Nordlie 1507

Occurrences of Low-Emissivity Surface Material at Low Altitudes on Venus: A Window to the Past
J. A. Wood 1509

Identifying Controlling Mineral Phases in Basalt Chemistries: On Beyond Pearce Element Ratio Diagrams
A. Woronow 1511

Parental Magma Compositions of Basalts Using an Artificial Neural Network: Theory
A. Woronow, A. M. Reid, J. H. Jones, and N. E. Pingitore Jr. 1513

Attempts to Produce Carbon-Free Silica Aerogel for Micrometeroid Capture Cells
I. P. Wright, H.-P. Huang, and C. T. Pillinger 1515

Could the Original Sudbury Structure Have Been Circular?
J. Wu, B. Milkereit, D. Boerner, and B. Robertson 1517

Magellan Radar Data for Venus Topographic Mapping 1519
S. S. C. Wu and E. A. Howington-Kraus

Windblown Sand on Mars: The Effect of Saltation Threshold on Drift Potentials Derived from Mars GCM 1521
P. Xu, R. Greeley, S. Williams, and J. B. Pollack

^{26}Al and ^{10}Be Activities and Exposure Ages of Lodranites, Acapulcoites, Kakangari and Pontlyfni 1523
S. Xue, G. F. Herzog, J. Klein, and R. Middleton

Granulitic Matrices in Monomict Eucrites 1525
A. Yamaguchi and H. Takeda

Tidal Disruption of Comet Shoemaker-Levy-9 Nuclei Just Before the Impact on Jupiter 1527
M. Yanagisawa and T. Konno

AEM Study of the Tetrataenite Rim of Metal Phases in Meteorites 1529
C. W. Yang, D. B. Williams, and J. I. Goldstein

Lunar Mare Deposit Volumes, Composition, Age, and Location: Implications for Source Areas and Modes of Emplacement 1531
R. A. Yingst and J. W. Head

Advanced Generation Condensation Calculations: Compositions of Fassaite, Spinel and Plagioclase in the Solar Nebula 1533
S. Yoneda and L. Grossman

Retention of Sodium Under Transient Heating Conditions—Experiments and Their Implications for the Chondrule Forming Environment 1535
Y. Yu and R. H. Hewins

Can Sulfide Minerals Survive the Chondrule-forming Transient Heating Event? 1537
Y. Yu, R. H. Hewins, B. Zanda, and H. C. Connolly

Oxygen Isotope Distribution in Fassaite of Allende CAI 1539
H. Yurimoto, H. Nagasawa, and O. Matsubaya

Spectrophotometry of Martian Satellites with the Hubble Space Telescope 1541
B. Zellner and E. N. Wells

Simultaneous Adsorption of CO_2 and H_2O Under Mars-like Conditions and Applications to the Evolution of the Martian Climate 1543
A. P. Zent and R. Quinn

The Complex Thermal History of Enstatite Chondrites 1545
Y. Zhang, P. H. Benoit, and D. W. G. Sears

The Unique Thermal History of EL Chondrites and a New Means of Classifying Equilibrated Enstatite Chondrites 1547
Y. Zhang, S. Huang, P. H. Benoit, and D. W. G. Sears

Gravitational Relaxation of Planetesimals 1549
I. N. Ziglina

Computer Simulation of Lava Flow Emplacement on the Terrestrial Planets 1551
J. R. Zimbelman

1:5,000,000-scale Geologic Mapping of the Kawelu Planitia Quadrangle (V16) on Venus
J. R. Zimbelman 1553

Mafic Magnetic Volcaniclastic Dunes: A Possible Mars Analog in the Andes of Ecuador
J. R. Zimbelman and K. S. Edgett 1555

Evidence for Extraneous Perovskites in CAIs from the Efremovka (CV3) Meteorite: A Combined Petrographic, Trace Element, and Isotopic Study
E. Zinner and A. El Goresy 1557

Crystallization in the Silicate Part of the Experimental Melted Ordinary Chondrite Tsarev (L5)
N. G. Zinovieva, O. B. Mitreikina, and L. B. Granovsky 1559

Liquid Immiscibility Process of the Experimental Melted Ordinary Chondrite Tsarev (L5)
N. G. Zinovieva, O. B. Mitreikina, and L. B. Granovsky 1561

The Chemical Composition of Acapulco and Acapulcoites
J. Zipfel and H. Palme 1563

Mineralogy of an Unusual CM Clast in the Kaidun Meteorite
M. E. Zolensky, A. V. Ivanov, S. V. Yang, R. A. Barrett, and L. Browning 1565

Minerology of Artificially Heated Carbonaceous Chondrites
M. E. Zolensky, M. E. Lipschutz, and T. Hiroi 1567

Near-Surface Atmosphere of Venus: New Estimations of Redox Conditions Based on New Data
M. Yu. Zolotov 1569

Phase Relations in the Fe-Ti-Mg-O Oxide System and Hematite Stability at the Condition of Venus' Surface
M. Yu. Zolotov 1571

Lunar Horizon Glow and the Clementine Mission
H. A. Zook and A. E. Potter 1573

Rheology, Tectonics, and the Structure of the Venus Lithosphere
M. T. Zuber 1575

Formation of Fold and Thrust Belts on Venus Due to Horizontal Shortening of a Laterally Heterogeneous Lithosphere
M. T. Zuber, E. M. Parmentier, and G. A. Neumann 1577

Author Index liii

Sample Index lxiv

Meteorite Index lxv

Keyword Index lxix

OMIT TO P 1081 PART-3

New Thermal Models for High-Latitude Impact Craters on Mercury: Implications for Water Ice D. A. Paige, S. E. Wood, and A. R. Vasavada (UCLA)

Recent radar observations of Mercury have revealed the presence of anomalous radar reflectivity and polarization features near the north and south poles which are most easily explained by the presence of relatively pure ice deposits (1-5). We have constructed a detailed thermal model which calculates the temperatures of surfaces within bowl-shaped and flat-floored impact craters on Mercury and the Moon that includes the effects of multiple-scattering at solar wavelengths and re-radiation at infrared wavelengths using the radiosity method (6,7). The results confirm the findings of previous studies which show that water ice should be stable to evaporation within the permanently shadowed regions of larger high-latitude impact craters on both bodies. We have also found that because of their orbital and axial orientations, portions of these permanently shadowed regions on both bodies can be viewed directly from earth. These results are particularly significant, given that recently reanalyzed the Arecibo observations show a clear association between the locations anomalous radar reflectivity features and the locations of known impact craters (8).

(1) J.K. Harmon, M.A. Slade, Science 258, 640, (1992). (2) M.A. Slade, B.J. Butler, and D.O. Muhleman, Science 258, 635 (1992). (3) D.A. Paige, S.E. Wood, A.R. Vasavada, Science 258, 643 (1992). (4) A.P. Ingersoll, T. Svitek and B.C. Murray, Icarus 100, 40 (1992). (5) B.J. Butler, D.O. Muhleman and M.A. Slade, J. Geophys. Res. 98, 15003-15023, (1993). (6) R.R. Hodges, Proc. Lunar. Planet. Sci. Conf. 11, 2463 (1980) (7) C.M. Goral, K.E. Torrance, D.P. Greenberg and B. Battaile, Computer Graphics 18, 213 (1984). (8) J.K. Harman, M.A. Slade, R. Velez, A. Crespo, M. Dryer, B. Amer. Astron. Soc. 25 No. 3, 1089 (1993).

NOBLE GAS COMPOSITION OF TEKTITES FROM BEDIAS, TEXAS. R. L. Palma, K. D. Ocker, and M. N. Rao, Dept. of Physics, Sam Houston State University, Huntsville, TX. 77341.

We have determined the composition of noble gases in the Bediasite tektites to examine whether they belong to the splash form tektite group or the impact glass group.

Tektites and impact glasses seem to have been formed due to meteorite impacts on terrestrial surface rocks [1, 2]. We have measured the elemental and isotopic composition of all noble gases in a few dark brown silica rich tektite glasses collected from the strewn field in Bedias, Texas. These samples seem to belong to splash form tektites. The purpose of this study is to distinguish between the impact glasses and tektites based on noble gas data. Heavy noble gas measurements on these Bediasites have not existed before. Noble gas studies may provide clues about the conditions of their formation.

As the noble gas contents in these tektites are generally low [3, 4, 5], we have chosen fairly large sample sizes (up to about 3 grams) for the proposed study. Noble gas measurements were carried out by standard procedures using a Nuclide mass spectrometer at Texas A&M University. Gas extractions were carried out at 1600 °C for 30 minutes. Note that the blank corrections for neon are only a few percent while for all other gases, ^{4}He, ^{36}Ar, ^{84}Kr and ^{132}Xe, the blank corrections range from 20 to 50%.

The ^{20}Ne concentration in Bediasite-2 is 46 x 10^{-8} cc STP/g. This value seems to be higher than those reported by Matsubara *et al.* (1993) for other splash-form tektites. However, this value belongs to the broad range ($\approx 10^{-7}$ cc STP/g) to which other impact glasses and Munong-Nong tektites belong. In the study of the Bediasites, we found large Ne enrichments (of the order of ≈1000) which are characteristically observed in other tektites [3, 4, 5, 6]. This may be due to the high diffusion of Ne in these glasses at the time of solidification [4]. The isotopic composition of neon in the Bediasites is very similar to air and does not show any anomalies. These large neon enrichments seem to be common to both tektites and impact glasses and does not apear to provide criteria to distinguish one from the other.

Even though He is highly diffusive, a significant concentration of ^{4}He, about 4 to 6 x 10^{-8} cc $^{4}He/g$, was observed in the Bediasites measured in this study. It is not clear whether originally more ^{4}He was trapped in these glasses at the time of solidification and was later lost gradually from theses glasses because of diffusion. Note that the range of Ne values in these tektites is much tighter than the range of ^{4}He in

these samples [6]. As pointed out by Matsubara *et al.* [6], He and Ne do not show any characteristic pattern to distinguish between splash form tektites and impact glasses.

We also examined the concentrations and isotopic compositions of the heavy noble gases in the Bediasites. The Ar content of the Bediasites studied here is about 5 x 10^{-10} cc ^{36}Ar/g. Note that the blank correction in these samples is about 25%. The ^{36}Ar content observed in the Bediasites seems to be in between that observed for splash form tektites and impact glasses [6]. In one sample, we observed a larger concentration of ^{40}Ar than that accounted for by the air ratio, calculated using ^{36}Ar. This anomalous increase in ^{40}Ar may be due to the increased content of the radiogenic ^{40}Ar in the pores of the host rock at the time of impact formation of this sample.

The Kr abundance in the Bediasites is about 5 x 10^{-11} cc ^{84}Kr/g sample, and the ^{132}Xe concentration is 7.6 x 10^{-12} cc STP/g. These Kr and Xe concentrations place the Bediasites between impact glasses and splash form tektites.

One explanation for the above observations is that these Bediasites may not belong to either impact glasses or splash form tektites and probably constitute an independent group of impact objects. Alternatively, the boundary between tektites and impact glasses is probably continuous, as pointed out by Matsuda *et al.* (1993) and the Bediasites belong to an intermediate group. More detailed analyses of the Bediasites are in progress.

Acknowledgements: We would like to thank M. W. Rowe, and M. Hyman for their help with this work.

References: [1] Glass B. P. (1990) *Tectonophysics,* **171**, 393-404. [2] Koeberl C. (1990) *Tectonophysics,* **171**, 405-422. [3] Hennecke E. W., Manuel O. K and Sabu D. D. (1975) JG, **80**, 2931-2934. [4] Matsubara K. and Matsuda J. (1991) *Meteoritics,* **26**, 217-220. [5] Matsuda J., Matsubara K. and Koeberl C. (1993) *Meteoritics,* **28**, 586-589. [6] Matsubara K., Matsuda J. and Koeberl C. (1993) *Meteoritics* (abstract), **28**, 392.

Re-Os CALIBRATION FOR ISOCHRON DETERMINATIONS. D. A. Papanastassiou, H. H. Ngo, G. J. Wasserburg, The Lunatic Asylum, Div. Geol. Planet. Sci., California Institute of Technology, Pasadena, CA 91125.

The precise determination of radioactive parent and of daughter element concentrations by isotope dilution requires the use of separated isotope tracers whose concentrations need to be determined relative to gravimetric solutions produced from high purity materials of known stoichiometry. This has been done, for example, for Sm-Nd[1] and nearly 10^2 aliquots of the Sm-Nd mixed normal have been requested and distributed. For the Re-Os system, it is well known that the problem is made acute both by the absence of stoichiometric salts of Os of high purity and by the extreme sluggishness with which Os ions and complexes of different Os oxidation states reach isotope equilibrium. Failure to reach isotope equilibrium between tracer and sample Os is manifested either by drifting isotope ratios during an analysis and/or by nonreproducible results. Calibration of Os tracers has been reported by the use of the ammonium hexachloroosmate salt [cf 2]. This salt is not stoichiometric, as can be readily seen from the certified concentrations for the high purity salt, issued by Johnson and Matthey, which vary by several percent for different batches of the salt and are different than the concentration for the stoichiometric composition. Work in this laboratory has also established that heating aliquots of this salt to a fixed temperature, e.g. 423 K, as recommended [2,3], does not resolve the stoichiometry problem and does not yield consistent results. Problems may also exist for Re; for example, shifts in the Re concentrations by 6% have been reported [4]. We have established that small chunks of Os metal are readily soluble in a heated, sealed glass ampoule, in the presence of H_2SO_4 and CrO_3. The dissolution procedure for Os is identical to the procedures used for the processing of FeNi meteorite samples. This has allowed the dissolution of an Os tracer, composed of sintered metal as well as of pieces of high purity Os metal. For better control of the Re/Os ratio determination, the Os and Re tracers were prepared separately and then aliquots were combined to yield a mixed tracer. Aliquots of solutions of Os and Re normals of known concentrations were used for the calibration of the mixed tracer.

Os tracer and normal Os metal dissolution: Re and Os metals were weighed using a micro-balance with better than 1 ‰ accuracy. The Os metal was placed in H_2SO_4 in a pyrex ampoule with a thin neck; the acid (and metal) was frozen by immersing the ampoule in a mixture of dry ice and ethanol (-72 °C); a CrO_3 solution was added and the neck of the ampoule was sealed by melting the glass while the contents of the ampoule remained frozen. Mixing of the CrO_3 and the H_2SO_4 was observed to occur after the H_2SO_4 thawed. After heating in an oven overnight, the Os was completely dissolved and converted to OsO_4. The ampoule was again frozen, the thin neck was scored, and then broken and the ampoule and the frozen contents were immersed in SO_2-saturated HCl. [Note: for better mixing at this stage, ampoules with two protruding necks were used.] Os^{8+} is expected to be reduced before Cr^{6+}; the Cr was seen to be reduced from Cr^{6+} to Cr^{3+} (from red to blue-green). Re was dissolved in HNO_3 and kept in an HCl solution. *Calibrations:* For calibration of the Re and Os mixed tracer, aliquots of the normal Re and Os solutions were added to an aliquot of the mixed tracer in an ampoule kept in a dry ice-ethanol mixture. Sulfuric acid and CrO_3 were added and the ampoule was sealed and then heated in an oven, as above, in order to oxidize the Os to OsO_4 and to permit tracer and normal Os isotope equilibrium. The ampoule was removed from the oven, the contents were frozen, the ampoule neck broken, and then chloroform was added in the ampoule for liquid/liquid extraction of the OsO_4. The OsO_4 was then back extracted in HCl. The CrO_3 retained with the Re solution was reduced with SO_2. Os and Re were then purified by ion exchange and measured by NTIMS. For Os normal we used two different metal spheres (about 6 mm in diameter) produced by ESPI with a claimed purity of 0.9995. For Re, we used zone-refined Re ribbon filament obtained from H. Cross and a high purity Re foil (0.9995) obtained from ESPI. We analyzed pieces of the Re and Os by electron microprobe and established the level of contaminants, including PGE. For the Os metal I, the contaminants, above detection limits, amounted to about 4‰, including, in ppm, Ru 1550, Rh 300, Re 230, Ir 740, Pt 950. Os metal II was of higher purity with contaminants of less than 2‰, including, in ppm, Pt 840, Ir 610, Re 750. For Re, the contaminants were less than 1‰. However, we feel that we require more reliable measurements of possible contaminants for both Re and Os high purity metals, including for the light elements (e.g. O, C) which have not yet been measured. We note that Re and Os cross-contamination is not significant. The results for Os and Re are shown in Table 1. Results for Os metals I and II are grouped separately. Different dissolutions of Os metal pieces are indicated by capital letters (B-I); different calibration mixtures of the Os-Re tracer and of normal Os and Re are indicated by "Mix". The entries ^{190}Os and ^{185}Re are the concentrations in the mixed tracer as determined by the use of different Os and Re gravimetric normal solutions. The deviations δ (in permil) are calculated relative to the grand averages for Os and for Re, respectively. Using the ESPI Metal I there is a range in the calculated concentration of the tracer from 3.9‰ to 13‰ , if we exclude the outlier from Normal C, Mix-1 at -6.3‰. For Os Metal II we obtain a range from -3.3‰ to -14.1‰.

We note that the average results for the two Os metal samples are offset by 1.6%, from 7.8‰ for Metal I to -8.2‰ for Metal II, where repeat mass spectrometric results are considered as a single determination. These results indicate our intrinsic reproducibility using these techniques to determine the Os tracer concentration to ±5‰; however, there is still the need to resolve the distinct results for the two different Os metal samples and to ascertain the level of impurities (O, C) by better metallurgy and by further chemical analyses. These results constitute a clear improvement over previous efforts and point to the need for further work. For Re the results show a range of ±2.4‰, which is reasonable for a two isotope system. We consider that the Re determination is of good accuracy.

We have used the mixed Os-Re tracer to check our previously reported results [5] on IIA iron meteorites which appeared to yield a well-defined isochron [cf 5,6]. Sawed pieces of the meteorites were first leached in aqua regia to remove surface contamination. Following the experience with Pd-Ag, the samples were leached extensively, with an attendant sample weight loss of up to 50%. The leached FeNi chips were then processed, following the procedures discussed briefly above for the dissolution of Os and for the tracer calibrations. Analyses of Negrillos and of Tocopilla are shown in Table 2. The analyses of Tocopilla show a range in $^{187}Re/^{188}Os$ of 2.3%, which is much larger than the experimental reproducibility seen for tracer calibrations. The range in $^{187}Os/^{188}Os$ is 1.3‰. When these Tocopilla data are combined with the Negrillos data we calculate slopes on the Re-Os evolution diagram of 0.0745 and 0.0776; these are different by 4.2%. We conclude that a) the Re-Os systematics are open on the scale sampled; b) the smaller samples of the iron meteorites used here, as compared to the work of Horan *et al.*[5] who obtained an isochron for IIA irons, are not representative of the whole meteorite; c) our leaching procedure results in differential loss of Re and Os prior to the closed system dissolution of the leached samples; or d) there is an erratic problem with Re-filament blanks. These issues will require further investigation.

Work supported by NASA NAGW-3337. Division Contribution 5359(834). We thank Paul Carpenter for the electron probe analyses.

References:[1]Wasserburg, G.J. et al. (1981) *GCA 45*, 2311 [2]Morgan, J.W. and Walker, R.J. (1989) *Anal. Chim. Acta 222*, 291. [3]Morgan, J.W. (1965) PhD Thesis, ANU, Canberra. [4]Morgan, J.W., Walker, R.J. and Grossman, J.N. (1992) *EPSL 108*, 191. [5]Creaser, R.A., Papanastassiou, D.A, and Wasserburg, G.J. (1993) *LPSC XXIV*, 339. [6]Horan, M.F., Morgan, J.W., Walker, R.J. and Grossman, J.N. (1992) *Science 255*, 1118.

Table 1. Calibration of the Os-Re Double Tracer

Osmium	^{190}Os (nm/g)	$\delta(^{190}Os)$ ‰	Rhenium	^{185}Re (nm/g)	$\delta(^{185}Re)$ ‰
ESPI, Metal I			H. Cross	0.1473	-1.6
Os normal B			ESPI foil		
Mix-1	2.672	10.1	Mix-1	0.1474	-0.9
Mix-2	2.652	4.3		0.1479	2.4
Mix-3	2.665	9.2		0.1477	1.1
	2.663[a]	8.5		0.1472	-2.3
	2.663	8.5		0.1476	0.4
Mix-4	2.653	4.7	Mix-2	0.1477	1.1
Mix-1	2.632	-3.3			
Mix-2	2.631	-3.6			
Mix-3	2.675	13.0			
	2.675	13.0			
	2.675	13.0			
ESPI, Metal II					
Os normal H	2.606	-13.3			
	2.604	-14.1			
Os normal I					
Mix-1	2.622	-7.1			
	2.621	-7.5			
Mix-2	2.606	-13.3			
Os normal G	2.619	-8.2			
Os normal F					
Mix-1	2.632	-3.3			
Mix-2	2.631	-3.6			

Concentrations in nanomoles/g; deviations in permil. [a]Repeat mass spectrometric analyses listed in sequence.

Table 2.

Sample	Weight mg	Os (ppm)	Re (ppm)	$^{187}Re/^{188}Os$	$^{187}Os/^{188}Os$
Negrillos	11[a]	70.5	5.20	0.3565	0.12333±4
			5.23[b]	0.3580	
Tocopilla					
-A	87	1.154	0.2323	0.973	0.16909±5
		1.154[c]		0.973	0.16928±8
-B	103	1.054	0.2078	0.953	0.16940±4
			0.2070[b]	0.949	

[a]Weight losses due to leaching metal chip with aqua regia: Negrillos 24%; Tocopilla -A 17%, -B 44%. [b]Repeat Re run. [c]Repeat Os run.

ALH 84001 A "SNC ORTHOPYROXENITE": INSIGHTS FROM SIMS ANALYSIS OF ORTHOPYROXENE AND COMPARISONS TO DIOGENITES; J.J. Papike, G.W. Fowler, G.D. Layne, M.N. Spilde and C.K. Shearer; Institute of Meteoritics, Department of Earth & Planetary Sciences, University of New Mexico, Albuquerque, NM 87131-1126, U.S.A.

INTRODUCTION. Recently we were informed that thin sections that we had been working on for the last two years labeled ALH 84001,45 and ALH 84001,46 were mislabeled and really are EETA 79002,154 and EETA 79002,155 respectively. We received "the real ALH 84001" on 11/23/93 and discovered (through the receipt of Antarctic Meteorite Newsletter, Vol. 16, No. 3) that ALH 84001 is a SNC orthopyroxenite. Although we are not actively working on SNC meteorites, we thought we could make a contribution by running a set of trace elements by SIMS (Table 1) on orthopyroxene in 84001 using the techniques that we have been using on diogenites.

RESULTS AND DISCUSSION. Selected microprobe and SIMS data are presented in Table 1 and Figures 1, 2, and 3. Table 1 presents data for 11 trace elements for ALH 84001 and for Roda. Roda is the most REE enriched diogenite we have studied [1]. Even though, as Table 1 illustrates, Roda is considerably more REE enriched than 84001, Eu is an exception. Figure 1 presents chondrite normalized [2] REE patterns for orthopyroxene from ALH 84001 and estimates of REE patterns for melts assumed to be parental to the new SNC meteorite. As usual, the choice of partition coefficients (D's) make such calculations approximate. We used a combination of D's used in the Lundberg et al. paper [3, Table 3]. It is informative to compare the REE patterns for orthopyroxene from Roda and ALH 84001 (Figure 3). Even though Roda orthopyroxene is significantly enriched in REE over ALH 84001, it has a larger negative Eu anomaly. The anomaly that we portray is a minimum and is approximate because the point we plot is the detection limit for Eu; the true anomaly could be much greater. We interpret the higher abundance of Eu in ALH 84001 orthopyroxene than in Roda as a direct result of a higher Eu^{3+}/Eu^{2+} in the parental melt of the SNC orthopyroxenite. This, in turn, is likely the result of a higher fO_2 on "Mars" than the HED parent body. Other than the behavior of Eu, most other trace element comparisons are unremarkable. The trace element attributes such as position of ALH 84001 on a Y vs. Zr or a Y vs. Yb plot places ALH 84001 intermediate to high (excluding Roda) in the diogenite fractionation series somewhat like Johnstown and Aioun El Atrouss but less trace element enriched than Ibbenburen, ALHA 77256, LEW 88008 or Roda [4].

Our mineral chemical data, including that for plagioclase (~60% Ab), is in complete agreement with that of Mittlefehldt [5]. We also analyzed several accessory carbonate veinlets and found that the carbonate ranged from $(Mg_{.75}Ca_{.07}Fe_{.18})CO_3$ to $(Mg_{.48}Ca_{.19}Mn_{.02}Fe_{.31})CO_3$. For orthopyroxene, on a diagram of Mn (afu) vs. Fe (afu) 84001 plots about half way along the positive trend but with a slightly lower Mn/Fe ratio than for the average diogenite (approximately 40 microprobe analyses of ALH 84001 compared with approximately 1000 microprobe analyses of a suite of 23 diogenites). Mittlefehldt noted that the albite content of ALH 84001 plagioclase is considerably higher than the albite content of plagioclase in diogenites. Figure 1 illustrates that the higher activity of Na in "Martian" magmas also results in a slight, but probably significant, elevated Na content of ALH 84001 orthopyroxene compared to diogenite orthopyroxene.

ACKNOWLEDGMENTS. SIMS analyses were performed at the UNM/SNL Ion Microprobe Facility, a joint operation of the Institute of Meteoritics, UNM and Sandia National Laboratories. This research was funded by NASA grant NAGW-3347 and the Institute of Meteoritics.

REFERENCES. [1] Papike, J.J. et al. (1993) *EOS*, **74**, 380-381. [2] Anders, E. and Grevesse, N. (1989) *G.C.A.*, **53**, 197-214. [3] Lundberg, L.L. et al. (1990) *G.C.A.*, **54**, 2535-2547. [4] Fowler, G.W. et al. (1994) *LPS XXV*, these volumes. [5] Mittlefehldt, D.W. (1993) Antarctic Meteorite Newsletter, Vol. **16**, No. 3.

Fig. 1

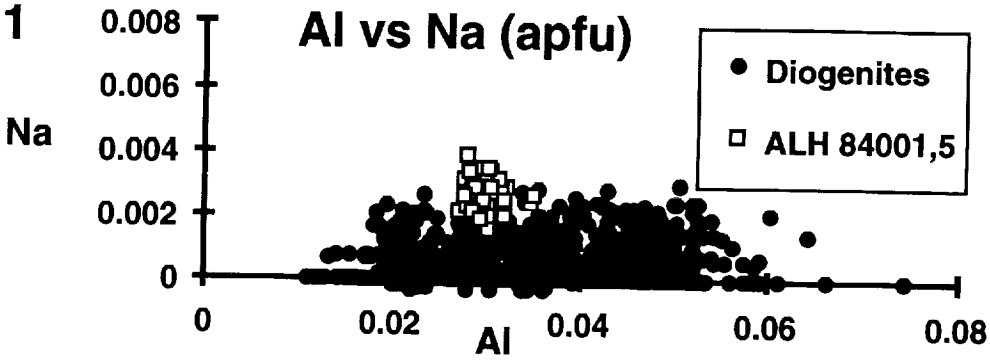

A SNC ORTHOPYROXENITE: Papike, J.J. et al.

Fig. 2

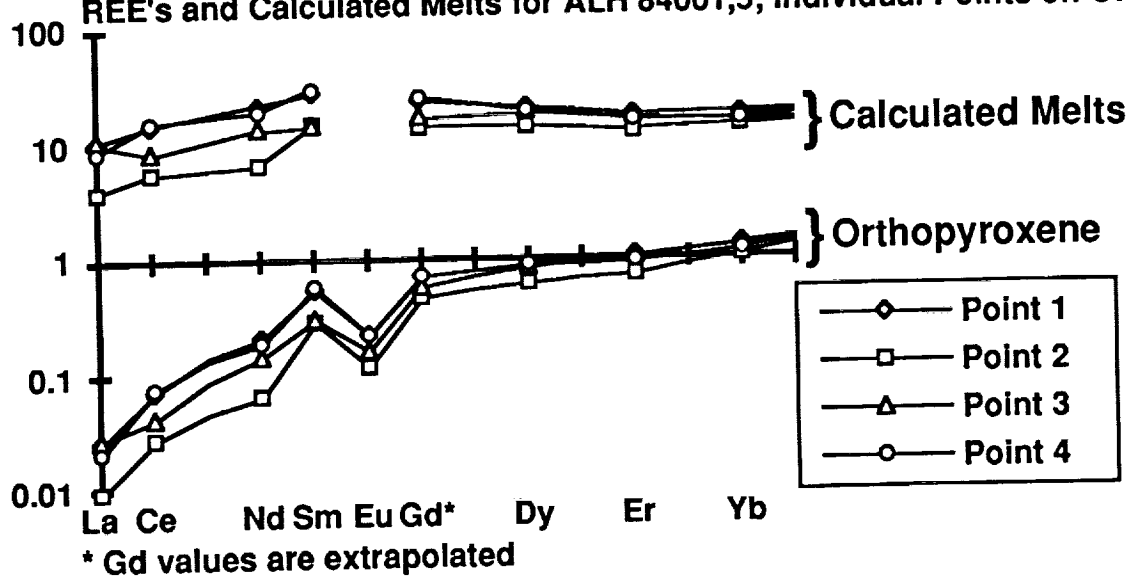

Fig. 3

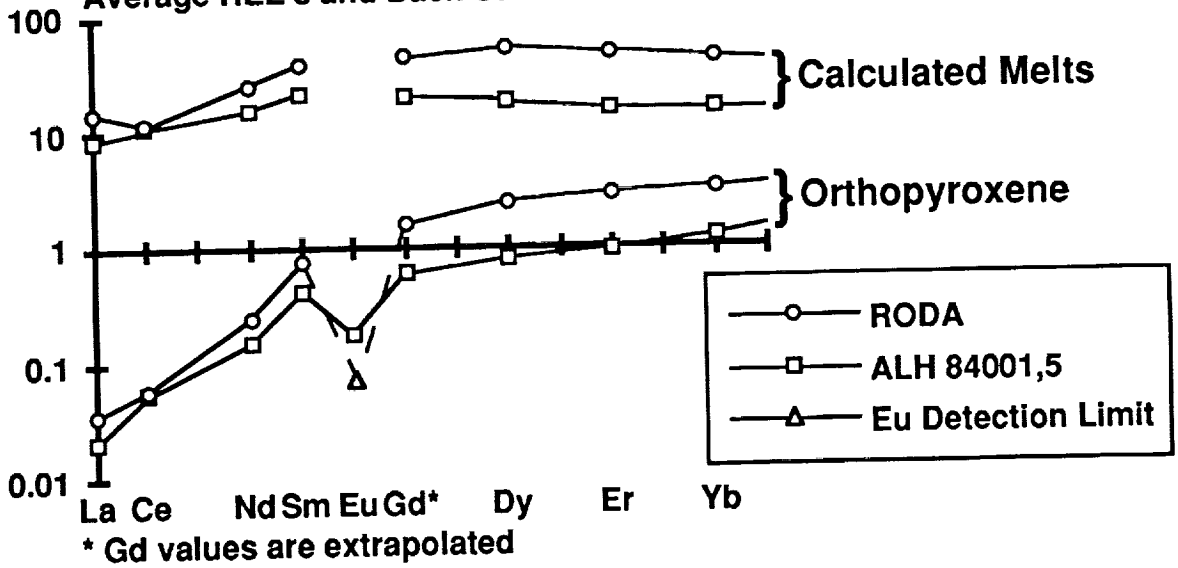

Table 1

ALH 84001 Orthopyroxene (ppm)

		Sr	Y	Zr	La	Ce	Nd	Sm	Eu	Dy	Er	Yb
ALH 84001,5	Point 1	0.148	1.85	4.18	0.006	0.044	0.096	0.079	0.012	0.218	0.163	0.204
	Point 2	0.110	1.41	1.15	0.002	0.017	0.030	0.043	0.007	0.150	0.115	0.169
	Point 3	0.110	1.80	1.90	0.006	0.025	0.064	0.044	0.009	0.207	0.165	0.209
	Point 4	0.137	1.83	3.98	0.005	0.047	0.086	0.086	0.013	0.210	0.145	0.182
Averages:	ALH 84001,5	0.126	1.72	2.80	0.005	0.033	0.069	0.063	0.010	0.196	0.147	0.191
	RODA	0.050	3.99	13.7	0.007	0.035	0.110	0.108	B.D.*	0.575	0.446	0.503

* B.D. = Below Detection.

ORTHOPYROXENE AS A RECORDER OF LUNAR Mg-SUITE NORITE PETROGENESIS: PRELIMINARY ION MICROPROBE STUDIES OF APOLLO 17 FRAGMENTS; J.J. Papike, G.W. Fowler, and C.K. Shearer; Institute of Meteoritics, Department of Earth & Planetary Sciences, University of New Mexico, Albuquerque, NM 87131-1126, U.S.A.

INTRODUCTION. Recent abstracts by S.R. Taylor et al. [1, 2] emphasized that we still have a poor understanding of the lunar Mg-Suite which could make up as much as 20% of the lunar crust. These authors suggest, based on published ages, that the Mg-Suite is 100-200 m.y. younger than the ferroan anorthosites. They point out that the Mg-Suite has two distinct and contradictory components. The suite is Mg-rich with Mg # >90 (implying primitive) but also contains high concentrations of incompatible elements typical of highly evolved rocks. These authors suggest that the primitive component accreted late onto the surface of the moon and mixed with a KREEP component which provided the high incompatible element concentrations.

APPROACH. We became intrigued with this problem and decided to take a "tree before forest" approach rather than the inverse. We were aided greatly by the recent compilation of petrologic information on possibly pristine nonmare rocks by Warren [3]. We used this compilation to select a suite of 24 noritic fragments with a high confidence class indicating a high likelihood of pristine character. The first three fragments we selected to work on are (77035,69), (77215,203), and (78235,39). Sample 78235 was chipped from a glass-coated O.5 meter boulder near the base of Sculptured Hills. An early and complete description of this rock was provided by McCallum and Mathez [4]. Cumulus phases are plagioclase ~50% and orthopyroxene ~50%. We chose noritic lithologies for this study because we believe orthopyroxenes are effective recorders of their parental melt compositions. Diffusion rates for REE are poorly determined but appear to be low and augite exsolution (usually on (100)) is not the serious problem that exists in "inverted pigeonites" where complex exsolution textures greatly compromise the trace element distributions. The approach we use here is very similar to that which we used in our study of diogenites [5].

RESULTS. The grains studied showed limited zoning from core to rim based on electron microprobe traverses. Table 1 presents averages of SIMS data for the three fragments (4 points on 77035, 4 points on 77215, 5 points on 78235). The concentrations are delightfully high (compared to OPX in most diogenites) but nevertheless Eu was usually below detection. The Fe-Mg systematics for the three fragments are illustrated in Figure 1 with Fe increasing in the sequence 78235→77035→77215 which is the same sequence in which the heavy REE increase. Also, 77215 which contains the highest Fe and heavy REE is most depleted in LREE. We attempted to do a preliminary estimate of the parental melt REE patterns. These results are preliminary and approximate because we still have to determine the most appropriate partition coefficients to use. For the calculation we used those of McKay et al. [6]. Nevertheless, the relative positions of the melt REE patterns should be correct. All three fragments could have come from the same or similar magmatic reservoirs that were likely KREEP enriched either during melting (KREEP in the source region) or by assimilation. The calculated melts show a decrease in Mg#, $(Ce/Yb)_N$, and Sr in the sequence 78235→77035→77215. This sequence probably reflects the co-crystallization of orthopyroxene and plagioclase. Significant crystallization of plagioclase was likely the cause of the depleted LREE in the calculated melts relative to what one might expect if a significant KREEP component was present.

REFERENCES. [1] Taylor, S.R. et al. (1993) *LPS XXIV*, 1413-1414. [2] Taylor, S.R. et al. (1993) *Meteoritics*, **28**, 448. [3] Warren, P.H. (1993) *American Mineralogist*, **78**, 360-376. [4] McCallum, I.S. and Mathez, E.A. (1975) *Proc. Lunar Sci. Conf. 6th*, 395-414. [5] Papike, J.J. et al. (1993) *EOS*, **74**, 380-381. [6] McKay, G. (1991) *LPS XXII*, 883-884.

ACKNOWLEDGMENTS. We thank Graham Layne for technical help with the SIMS analyses. SIMS analyses were performed at the UNM/SNL Ion Microprobe Facility, a joint operation of the Institute of Meteoritics, UNM and Sandia National Laboratories. This research was funded by NASA grant NAGW-3347 and the Institute of Meteoritics.

A-17 MG-SUITE NORITES: Papike, J.J. et. al.

Fig. 1

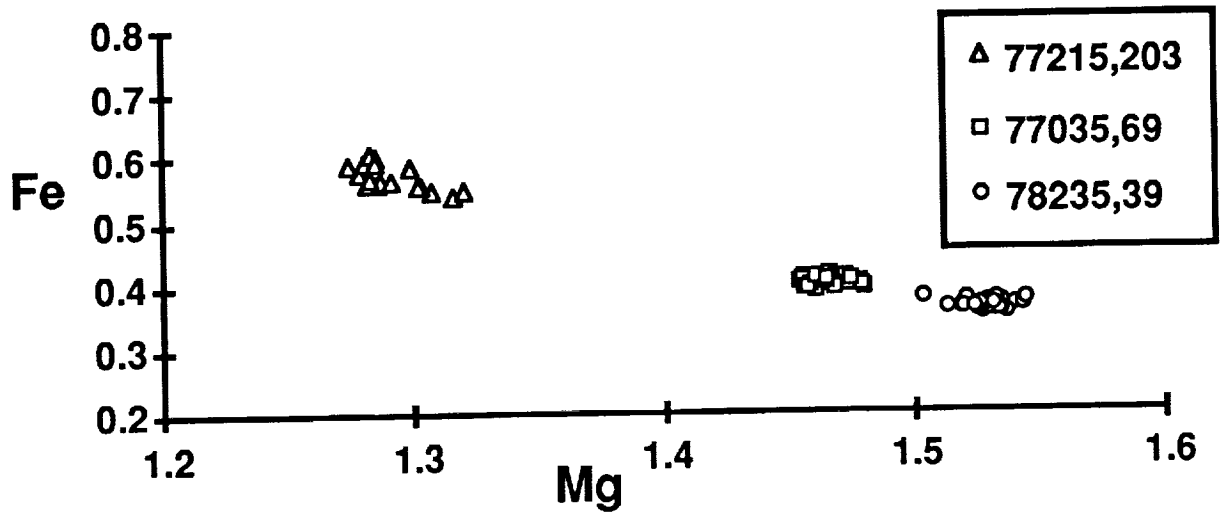

Fig. 2

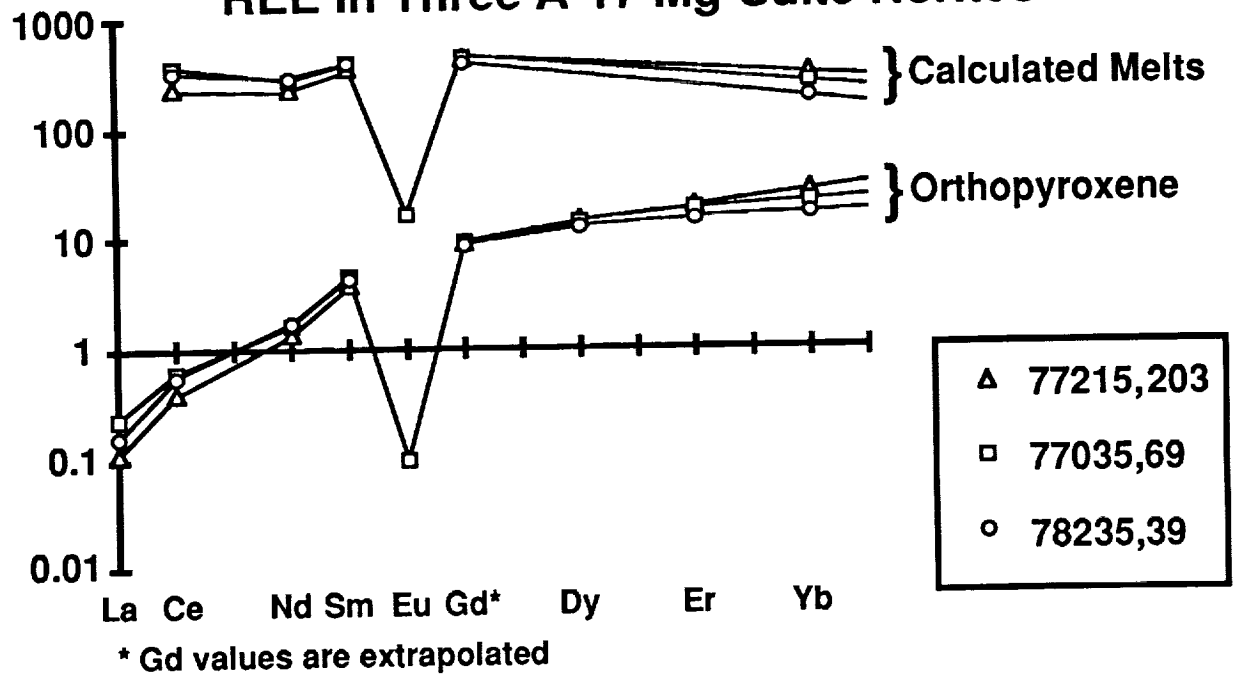

* Gd values are extrapolated

Table 1

Orthopyroxene From Selected A-17 Mg-Suite Norites

AVERAGES in ppm

	Sr	Y	Zr	La	Ce	Nd	Sm	Eu	Dy	Er	Yb
77215,203	0.103	30.2	29.3	0.027	0.245	0.621	0.583	B.D. *	3.58	3.18	4.48
78235,39	0.122	23.3	30.3	0.039	0.336	0.761	0.647	B.D. *	3.07	2.43	2.71
77035,69	0.112	27.7	29.0	0.056	0.372	0.732	0.658	*0.006*	3.49	2.89	3.61

* B.D. = Below Detection.

EXTENSIONAL TECTONICS OF ARDEN CORONA, MIRANDA: EVIDENCE FOR AN UPWELLING ORIGIN OF CORONAE; ***Robert Pappalardo, Ronald Greeley, and Stephen J. Reynolds,*** *Department of Geology, Arizona State University, Tempe, Arizona 85287-1404.*

Subparallel ridges and troughs in Arden Corona on Miranda are interpreted as tilt blocks formed by extension and normal faulting of the satellite's lithosphere. Progressive shallowing of some faults to dips of <20° offers the first evidence for low-angle normal faulting on a body other than Earth. Normal faulting in Miranda's coronae was likely induced by diapiric upwelling during partial differentiation and is inconsistent with a competing model, originally proposed by Shoemaker [see *1*], that invokes catastrophic breakup and reaccretion of the satellite.

Miranda exhibits geology that is unique among the Solar System's natural satellites. Voyager 2 images show the satellite to have three large "coronae" within a rolling cratered terrain [*2*]. These ovoidal to trapezoidal regions consist of an outer belt of subparallel ridges and troughs and an inner region of smooth materials and/or ridges and troughs of multiple orientations. Corona origin is controversial, as they might have resulted from induced downwelling or internal upwelling within Miranda [*1,3,4*].

In the downwelling model, Miranda was shattered in its early history by a catastrophic impact and then reaccreted [*1,3*]. Infalling silicate-rich chunks sank through the satellite's ice-rich mantle and stirred downwelling convection currents, forming the coronae at the surface above. If coronae were formed by downwelling currents, the ridges and troughs of their outer belts should be compressional in origin, expressed as folds or reverse faults [*1*]. In the alternative model, upwelling in Miranda's interior involved internally driven diapirism or solid-state convection [*3,4*]. If coronae were formed by upwelling, Miranda's ridge and trough terrain is predicted to be of extensional-tectonic origin, expressed as horst-and-graben structures or tilt blocks [*5,6*]. Thus, the origin of ridges and troughs within coronae is the principal constraint on corona formation.

Global views of Arden Corona show an inner region of bright and dark materials and an outer belt of ridge and trough terrain. Voyager image FDS 26846.26 reveals a cross-sectional view of the southeastern part of the Arden outer belt, seen along the satellite limb. Because the horizon is perpendicular to the local topographic trend, this view can be translated into a cross-section [*7*] which reveals ≈4 km of total vertical relief in a major depression. A topographic rise outboard of the corona shows a broad convex profile, whereas the inboard rise is sharp. The ridges and troughs within the depression are asymmetric, and ridge-to-trough relief is as great as 2 km [*7*]. More subtly, outward-facing slopes shallow progressively toward the corona's outer boundary. The outward-facing ridge walls display 1 km wide bright and dark striations oriented downslope. Commonly, dark material is concentrated near the top of a striated wall. In western Arden Corona, outer belt ridges and troughs are associated with light and dark albedo banding, with bright-and-dark stripes showing paired widths of about 13 km. Ridges show dark, commonly striated walls that face outward from the corona. A few structures visible in bright material are truncated against neighboring dark stripes, and patches of dark and very bright materials are present.

After considering the detailed morphological expressions of the processes that can create subparallel ridges and troughs on icy satellites [*6*], we interpret the features of the Arden outer belt as due to tilt block style normal faulting in response to extension, the striated walls within Arden Corona being normal fault scarps that dip consistently outward. Subsurface dark material is commonly exposed near the tops of fault scarps and moves downslope. Tilt blocks observed in profile along the limb in southeastern Arden Corona are defined by low angle normal faults. Progressive shallowing of faults toward the outer boundary of the corona requires a listric fault geometry [*8*]. Fault dips at the surface are probably ≈50° before significant fault-block rotation, shallowing to ≈10°. Fault reconstruction shows that the extension across the southeastern Arden rift zone is about 90%. Although not unusual on Earth, this extension is extreme compared to previous estimates of strain on Miranda and other icy satellites, which are typically a few percent [*3,9*].

The convex outer boundary of Arden Corona likely resulted from rollover of the outboard hanging wall, as expected above a listric normal fault [*10*]. The uplifts flanking the depression are probably explained by flexural warping of the lithosphere in response to isostatic buoyancy forces. Following the method of Vening Meinesz [*11*], the ~2 km uplift of the inward rift shoulder can be non-uniquely modeled by a cold elastic ice lithosphere (density = 9200 kg·m^{-3}, Young's modulus = 10^4 MPa, Poisson's ratio = 0.33) of effective thickness 50 km resting on a fluid substrate of density ≈1050 kg·m^{-3}. The outboard uplift might result from similar flexural processes [*12*] or thinning of a "lithospheric mantle" which uplifts isostatically as it thins along a zone of pure or simple shear [*13*].

Ridges and albedo striping in western Arden Corona are likewise interpreted as shaped by normal faults that dip outward from the corona. Bright ridge faces represent original cratered terrain surfaces back-tilted by rotational normal faulting, and dark, commonly striated walls are fault scarps exposing dark subsurface material. This accounts for the pairing of bright and dark albedo stripes, the truncation of structures (craters) in bright material by dark scarps, and the termination style of Arden ridges. This is also consistent with an increase in the ratio of outward-facing (fault scarp)

MIRANDA TECTONICS: Pappalardo, R., R. Greeley, and S. J. Reynolds

slopes to flatter (tilt block) faces visible in western Arden as the Voyager viewing geometry changes from down-looking to highly oblique. Photometric studies show that bright material within the Arden outer belt has an albedo indistinguishable from cratered terrain, suggesting it is the same material [*14*]. This is consistent with tectonic disruption of cratered terrain to form the outer belt, as in the tilt-block model. In eastern Arden Corona, bright outward-facing scarps appear to cut a region of dark material. These scarps appear brighter than their surroundings because of oblique solar illumination or because they reveal bright material that underlies the dark material.

This evidence presents a unified picture of extensional tectonics affecting Arden Corona, in which outward-facing fault scarps shaped its entire outer belt. A tilt-block interpretation of the ridges and troughs in southeastern Arden Corona has been considered by others [*3,7,15*], and it has been suggested that outward-facing normal faults have shaped or modified at least part of Arden Corona's outer belt and that this belt may be extensional [*3*]. However, no one has recognized the low-angle attitude of the normal faulting in southeastern Arden or the general relationship of this region to Arden Corona tectonics; furthermore, we provide specific evidence to conclude that tilt-block style normal faulting accounts for the ridge and trough topography and the albedo striping throughout the corona's outer belt.

Extension in the Arden outer belt indicates an upwelling origin for Arden Corona and is inconsistent with the sinker model of corona evolution. The outward-facing direction of faults suggests doming of the corona interior and sloughing of the outer ridge and trough belt. Support for an upwelling origin for Miranda's coronae also follows from the morphology of ridges and troughs in Inverness Corona and Elsinore Corona, likely shaped by similar volcano-tectonic processes in response to extensional stress [*16*]. Major corona-bounding depressions, analogous to that of southeastern Arden, are likewise observed in limb profiles crossing the western boundary of Arden Corona and the boundaries of Elsinore Corona [*7*]; these depressions and their flanking topographic highs were probably created around each corona by rifting and flexural processes analogous to those described above in response to internal upwelling. A tilt block origin for ridges and troughs in Arden Corona follows a general model in which normal faulting and fissure volcanism can combine to produce a spectrum of possible morphologies that accounts for most ridge and trough terrain on icy satellites [*17*].

Either solid-state convection or large-scale diapirism during partial differentiation might have induced corona formation. Models of convection in a sphere predict that a pattern of four or six symmetrically distributed regions of concentrated upwelling can form at low Rayleigh number and persist as Rayleigh number increases, but only when a significant fraction of heat is supplied from a core below [*18*]. This is marginally possible for a differentiated Miranda that gets the bulk of the ~100 K temperature rise necessary to induce solid state convection from tidal heating which deposits heat within the mantle instead.

Although the riser model predicts a zone of concentric extensional structures surrounding an inner region of disorganized extensional structures, the actual squared shape of Miranda's coronae might be explained by superposition of a concentric upwelling-induced stress field onto a pre-existing structural grid [*19*]. Alternatively, modeling shows that downwelling material confined to a sphere has a slab-like geometry [*18*], and interaction between contemporaneously formed coronae might induce "flattening" of their adjacent sides in response to inter-corona downwelling [cf. *20*].

In summary, the outer belt of Arden Corona on Miranda was shaped by tilt-block style normal faulting, in which outward-facing scarps generally expose dark material. This explains both the topography and albedo patterns in Arden Corona. In a rift that bounds the corona, we recognize the first evidence for low-angle normal faulting on a body other than Earth, and we estimate a local extension of ≈90%. Arden Corona observations contradict the compressional-tectonic predictions of the "sinker" model of corona evolution. Instead, an extensional-tectonic origin supports formation of Arden Corona in response to internal upwelling. Thus, Miranda likely had an endogenic, rather than a catastrophic, geological history.

[1] Janes and Melosh (1988), *JGR* **93**, 3127. [2] Smith *et al.* (1986), *Science* **233**, 43. [3] Greenberg *et al.* (1991), in *Uranus*, p. 693. [4] T.V. Johnson *et al.*, *Sci. Amer.* **256**, 48 (1987). [5] McKinnon, *Nature* **333**, 701 (1988). [6] Pappalardo and Greeley (1994), submitted to *JGR*. [7] P.C. Thomas (1988), *Icarus* **73**, 427. [8] Wernicke and Burchfiel (1982), *J. Struct. Geol.* **4**, 105. [9] Golombek (1982), *JGR* **87**, A77; Squyres and Croft (1986), in *Satellites*, p. 293. [10] Hamblin (1965), *Geol. Soc. Amer. Bull.* **76**, 1145. [11] Heiskanen and Vening Meinesz (1958), *The Earth and Its Gravity Field.* [12] Egan (1992), *Tectonophys.* **202**, 291; Buck (1988), *Tectonics* **7**, 959. [13] Wernicke (1985), *Can. J. Earth Sci.* **22**, 108; Weissel and Karner (1989), *JGR* **94**, 13919. [14] Hillier *et al.* (1989), *Icarus* **82**, 314; Buratti and Mosher (1991), *Icarus* **90**, 1. [15] Plescia (1988), *Icarus* **73**, 442. [16] Pappalardo and Greeley (1992), *LPSC Abstr.* **23**, 1023. [17] Pappalardo and Greeley (1992), *LPSC Abstr.* **23**, 1025. [18] Bercovici *et al.* (1989), *J. Fluid Mech.* **206**, 75; Bercovici *et al.* (1989), *Science* **244**, 950. [19] Pappalardo and Greeley (1993), *LPSC Abstr.* **24**, 1111. [20] Busse (1975), *J. Fluid Mech.* **72**, 67.

MODELLING THE TRANSITION BETWEEN HAWAIIAN-STYLE LAVA FOUNTAINING AND STROMBOLIAN EXPLOSIVE VOLCANIC ACTIVITY; E.A. Parfitt[1] and L. Wilson[1,2] [1]Geological Sciences Department, Brown University, Providence RI 02912. [2]Environmental Science Division, Lancaster University, Lancaster LA1 4YQ, U.K.

Abstract: Basaltic volcanic activity can vary widely in character from passive effusion through strombolian explosions and hawaiian-style lava fountaining to sub-plinian and plinian eruptions. The two end members of basaltic activity - passive effusion and plinian explosion - result from extremes of the gas content, very low gas contents leading to effusion of somewhat vesiculated lavas and very high gas contents causing plinian activity. While these extremes of behaviour are certainly of interest, the volatile contents of most terrestrial basaltic magmas are such that basalts are usually erupted explosively in strombolian or hawaiian-style activity. We show how the volatile content, viscosity and rise speed of the magma control the transition between these two eruption styles.

Background: The processes which give rise to strombolian and hawaiian activity have been investigated by a number of authors [1, 2, 3]. Magma rising towards the surface on Earth usually has sufficient volatiles dissolved within it to become supersaturated in one or more volatile species. When rising magma exsolves volatiles to form gas bubbles, the bubbles are always buoyant relative to the surrounding liquid, and they rise through it at a rate which depends on their size. The sizes of existing bubbles increase as they approach the surface, due to a combination of decompression and continued volatile migration from the liquid [2]. At the same time, new, small (~10 μm diameter) bubbles continue to nucleate as the magma becomes ever more supersaturated at lower pressures. Larger bubbles rise faster than smaller bubbles and may overtake them. If two bubbles come into physical contact they are likely to coalesce. The exact extent to which coalescence takes place in an erupting magma is a complex function of its rise speed, viscosity and total volatile content [3]. It is the degree to which coalescence occurs which is essentially responsible for the strombolian and hawaiian natures of basaltic explosive eruptions. Fig 1 shows the theoretical relationship between bubble diameter and rise speed for a total magma gas content of 0.5 wt% and a magma viscosity of 100 Pa s. In essence, this figure shows the range of gas bubble behaviour which reflects the change from lava fountaining to strombolian activity. At high magma rise speeds, the gas bubbles are unable to move relative to the magma and thus stay strongly coupled to its motion: upon eruption, such a mixture gives rise to a lava fountain in its truest sense (the situation treated in [4]). At low or zero magma rise speed, gas bubbles are able to rise by significant distances through the magma and as they rise they coalesce and form larger bubbles. The bursting of such large bubbles at the surface gives rise to classic strombolian activity [1] For intermediate magma rise speeds, the behaviour of the gas-magma mixture is more complex, with some of the gas forming large bubbles which rise through the residual gas-magma mixture. The energy provided by the expansion of the gas released from these large bubbles will not be very strongly coupled to the motion of the remaining gas-magma mixture, and thus the coalescence and rise of these bubbles essentially depletes the remaining gas-magma mixture of gas.

Coalescence Modelling: Wilson & Head [3] treated the coalescence mechanism by utilising a computer program originally devised by Sparks [2] for simulating bubble growth in rising magmas. They added to this program the extra code needed to allow them to find the diameter of the largest bubble which would form by absorption of smaller bubbles in a magma with given material properties at a given rise speed. We have added to this program the few extra lines of code needed to allow us to keep track, as a function of depth below the surface, of the relative masses of the gas contained in the largest bubble and the gas distributed as smaller bubbles through the residual liquid. The depth at which the residual bubble-liquid mixture attains an average gas volume fraction of 75% (and thus disrupts into released gas and pyroclasts), and the pressure level at that depth, are also noted. The final velocity with which the gas-pyroclast mixture emerges at the surface is then found by simultaneous numerical integration of the energy and continuity equations between the disruption level and the surface using the computer code described in [3] and [5]. We have run this program for rise speeds in the range 0.01 to 1 m/s, magma viscosities of 30, 100 and 300 Pa s and total gas contents of 0.25, 0.5 and 1 wt %. In each case we used the resulting exit velocity to calculate an *energy efficiency factor* (EEF) which we define as the square of the ratio of the actual eruption speed to the speed which would have been attained if no coalescence had occurred. Because the height of a fire fountain is found by equating the kinetic energy of the eruption products leaving the vent to the potential energy they have at the top of the fountain, the energy efficiency factor is also the ratio of the actual fountain height expected when coalescence does take place to the fountain height which would have been reached by a magma with the same total volatile content but a sufficiently great rise speed at depth in its conduit system that coalescence did not take place.

Results: Figs 2 and 3 summarise our results. An EEF value of 1 signifies pure lava fountaining behaviour and an EEF of 0 pure strombolian activity. These results show that where the transition occurs depends on both gas

content and viscosity, lower viscosities and higher gas contents pushing the transition up towards higher rise speeds. Lower viscosity magma makes coalescence easier and therefore allows strombolian behaviour to occur even when the magma is rising beneath the vent at relatively high rates. Similarly, if the gas content of the magma is high the large number of gas bubbles promotes coalescence; thus unless the magma itself rises rapidly enough, coalescence will occur to cause strombolian activity. Using the results in figs 2 and 3 we can predict not only where the transition from strombolian to hawaiian-style activity will occur but also how the fountain height will vary as the rise rate of the magma increases. Consider, as an example, a magma with a gas content of 0.5 wt% and a viscosity of 100 Pa s. If this magma rises below an eruptive vent at rates <0.01 m/s then, from fig 2, the magma has an EEF value of 0 and thus behaves in a strombolian fashion with discrete explosions throwing small volumes of magma to heights of ~150 m above the vent. For an EEF of 1 (rise speeds of >0.05 m/s) the magma will erupt in a fountain ~617 m high. As the rise speed beneath the vent increases from 0.01 to 0.015 m/s there is a dramatic change in the activity with an unsteady lava fountain being produced with a maximum height of 210 m (EEF=0.34). A further increase to a rise rate of 0.018 m/s increases the fountain height further (to 400 m - EEF=0.65) and the fountain is steadier; by the time the rise speed has increased to 0.035 m/s the fountain height is 600 m - close to its maximum possible height of 617 m, i.e., the fountain is now behaving essentially in a purely Hawaiian fashion.

Conclusions: Our results show that, while the transition from strombolian to hawaiian-style eruptive activity can be relatively abrupt, it is not strictly correct to consider these styles of eruptive activity as being discrete. In practice, magma rising beneath a vent at an increasing rate will initially exhibit discrete strombolian explosions which, at low rise speeds, will be infrequent but relatively violent; as the rise speed increases the number of explosions will increase but the individual strength of the explosions will decline. At higher rates still the explosions will give way to a sustained fountain which will initially fluctuate in height quite considerably but as the rise rate continues to increase will stabilise to the maximum height. Our model allows us to simulate this transitional behaviour and thus provide a link between existing models of pure Strombolian [1] and pure Hawaiian [4] activity.

References: [1] Blackburn, E.A., Wilson, L. & Sparks, R.S.J. (1976) J. geol. Soc. Lond. 132, 429. [2] Sparks, R.S.J. (1978) JVGR 3, 1. [3] Wilson, L. & Head, J.W. (1981) JGR 86, 2971-3001. [4] Head, J.W. & Wilson, L. (1987) JGR 92, 13715-13719. [5] Wilson, L., Sparks, R.S.J. & Walker, G.P.L. (1980) Geophys. J. Roy. astr. Soc. 63, 117.

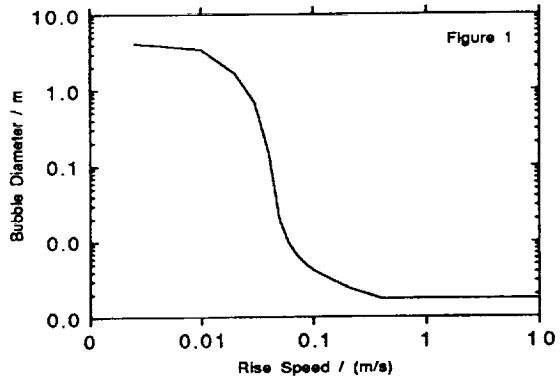

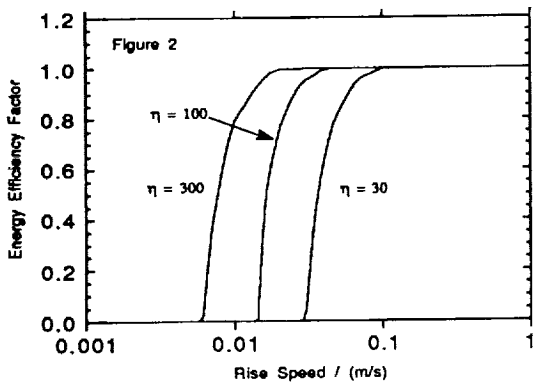

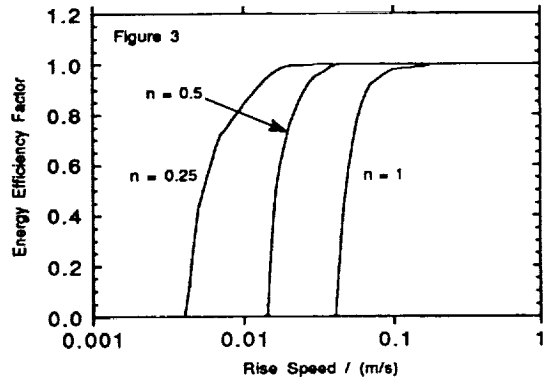

THE ROLE OF MAGMA RECYCLING IN CONTROLLING THE BEHAVIOUR OF HAWAIIAN-STYLE LAVA FOUNTAINS: E.A. Parfitt[1], L. Wilson[1,2], and J.W. Head III[1], [1]Geological Sciences Department, Brown University, Providence RI 02912, U.S.A. [2]Environmental Science Division, Lancaster University, Lancaster LA1 4YQ, U.K.

Introduction: It is common during the explosive eruption of a mafic magma for a lava fountain to form over the vent. The fountain consists of a mixture of liquid clots and magmatic gases, and arises because sufficient volatiles exsolve from the magma during its ascent and decompression to form a population of gas bubbles which occupies more than 75% of the bulk fluid at some finite depth below the surface vent. When this value is exceeded, the magma disrupts and the mixture of gas and pyroclasts emerges from the vent as a jet within which the clasts are suffciently large to behave ballistically. The height, H, of this jet, or lava fountain, is given by:

$$u_a^2 = 2\,g\,H \qquad (1)$$

where u_a is the mean eruption speed in the vent and g is the acceleration due to gravity. In this way, the fountain height can be used to deduce the eruption speed which, as long as the mass eruption rate is known at least approximately, can be used to infer the amount of gas released from the magma [1]. On reaching the ground, the clasts will accummulate and, depending on their temperature and size, will either form hot, mobile, rootless flows and relatively minor vent structures or the lava clasts will have cooled considerably in flight and form a sizeable unwelded cinder cone on landing [2,3]. If any kind of spatter rampart or cinder cone develops, (and one usually does), this provides a topographic constraint on clots and clasts whose trajectories cause them to land close to the vent. In some cases these topographic structures can almost completely surround a localised conduit-type vent, and lead to the development of a distinct lava pond, through which the fountain will punch up (e.g., 4). In a typical fissure eruption the situation is probably less extreme some of the accumulating lava clots sliding back into the fissure along the edge of the fountain. Any recycling of material back into a fountain in this way, either by simple "drainback" or from a lava pond, is likely to have a significant effect on the behaviour of the system because energy must be expended in accelerating the entrained material back up into the fountain, thus causing it to behave as though it were being formed by a magma with a lower exsolved gas content than is actually the case. We have developed a model to investigate the significance of this process in terms of reducing fountain heights and altering eruption style. The details of this model are given in a separate paper [5].

Results: (a) Circular vents: We carried out the modelling for circular vents with magma mass fluxes of 10^4 to 10^8 kg/s, exsolved water mass fractions of 0.03 to 2 wt%, and lava pond depths ranging from zero to 50 m, (values typical for the Earth). Fig. 1 shows the variation of lava fountain height with lava pond depth for a range of erupted mass fluxes at a constant exsolved magma water content of 0.3 wt %. It is readily apparent that a pond only a very few meters in depth can greatly reduce the height of even an energetic lava fountain. For example, a fountain having a mass flux of 10^6 kg/s and an exsolved gas content of 0.3 wt% will have a height of 501 m in the absence of any lava ponding but the height will decrease to 263 m if a pond 5 m deep is present within the vent. For a given gas content the lowest mass flux eruptions are more susceptible to the effects of entrainment than are higher mass flux events. For a constant mass flux and variable gas content we find that the fractional decrease in fountain height as pond depth increases does not vary greatly for different gas contents but higher gas content eruptions are somewhat more susceptible to the effects of entrainment than are low gas content eruptions. (b) Fissure vents: Figure 2 gives the variation of lava fountain height with lava pond depth for a range of erupted mass fluxes per unit length of fissure at a constant exsolved magma water content of 0.3 wt%. Again, ponds only a few meters in depth can greatly reduce lava fountain heights. For example, for a fountain having a mass flux per unit length of 10^5 kg s^{-1} m^{-1} and an exsolved gas content of 0.3 wt% the fountain will have a height of 467 m in the absence of any lava ponding but the height will decrease to 409 m if a pond 2 m deep is present around the fissure. Fig. 2 shows that, as in the central vent case, for a given gas content the lowest mass flux eruptions are more susceptible to the effects of entrainment than are higher mass flux events. For a constant mass flux and variable gas content we find that the fractional decrease in fountain height as pond depth increases is greater for high gas contents than low gas contents, as was the case for the central vent example.

Discussion: Our model results have several important implications for observations of explosive basaltic eruptions. Most basaltic eruptions start as a "curtain of fire", in which magma erupts from a fissure which may be hundreds to thousands of metres in length. As the eruption proceeds, the fissure vents tend to localise so that lava issues from only one or two points along the fissure [4, 6-8]. If the eruption continues for long enough, this localisation will continue to the point where accumulation of spatter and cinders around the vent produces a central cone (e.g., 3,4). If the total mass flux does not decline significantly during the process of localisation, then the mass

MAGMA RECYCLING IN HAWAIIAN-STYLE ERUPTIONS: Parfitt, E.A., Wilson, L. and Head, J.W.

flux per unit length of fissure will increase rapidly as vent localisation occurs. This localisation will have a dramatic impact on the heights of the vent fountains for two reasons. Firstly, as the vent geometry becomes more equant the energy losses due to friction within the vent are reduced [9] and the fountain height will increase. In addition, however, our results demonstrate that fissure vents are more susceptible to the effects of entrainment than are central vents. Thus, we expect that, for the same amount of entrainment, as the vent becomes localised the fountain height will increase by an amount greater than that which can be explained by reduced friction losses alone. For example, for an eruption with a total mass flux of 10^6 kg/s, an exsolved gas content of 0.3 wt%, an initial fissure length of 1 km (and therefore a mass flux per unit length of 10^3 kg m^{-1} s^{-1}) and an equivalent pond depth of 1 m. The fissure fountains are predicted to have an initial height of 32 m; this height increases to 225 m as the fissure length decreases to 100 m and reaches a maximum value of 425 m by the time the vent has become circular. These results are consistent with field observations on historic eruptions (e.g., 8, 10-11). The strong susceptibility of fissure eruptions to the effects of reentrainment makes for the possibility of eruptions in which the behaviour can appear to be strombolian rather than hawaiian in nature, simply because the large degree of entrainment almost completely suppresses steady fountaining. Because strombolian activity normally reflects very low eruptive mass fluxes or very low gas contents (or both) [9,12], the observation of apparent strombolian activity could lead to serious misinterpretation of the magma gas content and eruption dynamics. Finally, although many basaltic eruptions are shortlived and never progress beyond the initial fissure eruption stage, some basaltic eruptions become centralized at a single vent where eruption may continue for many months or years [4,6]. The style of such events varies - some eruptions exhibit vigorous fire fountaining and episodic activity [4] but more commonly such eruptions occur from a central lava pond which overflows intermittently and which exhibits only strombolian spattering and no fountaining [6,13]. As we discuss in a separate paper [14] strombolian eruption from lava ponds is often indicative of low rise speed rather than low gas content and there are cases of eruptions in which, once the rise speed increases, fire fountaining activity is initiated at the vent (e.g., 6,13). In this situation, the vent is partially filled with magma which has largely degassed and which has been cooling for some time and thus has a higher viscosity than fresh magma. Thus, by analogy with our simple entrainment situation, we would expect that this cooling body of degassed magma would inhibit the onset of fire fountaining activity as the rise rate at depth increases to a level at which fountaining should be sustained [14]. Initially, energy is required to set up a circulation pattern in the degassed lava consistent with the upward motion of the new magma through it. As soon as new magma reaches the surface, it will inevitably have entrained some of the old lava, the high density of which will maximise the extent to which fountaining is suppressed. The onset of new activity through the cooling remains of earlier-emplaced lava is therefore always likely to have the appearance of the eruption of new magma which is volatile-poor, and true fire fountaining activity will not be possible until the bulk of the degassed magma has been erupted.

References: [1] Head, J.W. & Wilson, L. (1987) J.G.R. 92, 13715-13719. [2] Wright, J.V., Smith, A.L. and Self, S. (1982) J.V.G.R. 8, 315-336. [3] Head, J.W. & Wilson, L. (1989) J.V.G.R. 37, 261-271. [4] Wolfe, E.W., Neal, C.A., Banks, N.G. & Duggan, T.J. (1988). Ch 1 in U.S.G.S. Prof. Pap. 1463. [5] Wilson, L., Parfitt, E.A. & Head, J.W. (1993) In Prep. [6] Swanson, D.A., et al. (1979). U.S.G.S. Prof. Pap., 1056. [7] Moore, R.B., et al. (1980). J.V.G.R., 7, 189-210. [8] Delaney, P.T. & Pollard, D.D. (1982). Am J Sci, 282, 856-885. [9] Wilson, L. & Head, J.W. (1981) J.G.R. 86, 2971-3001. [10] Richter, D.H., et al. (1970). U.S.G.S. Prof. Pap. 537. [11] Wright, T.L., Kinoshita, W.T. & Peck, D.L. (1968). J.G.R.. 73, 3181-3205. [12] Blackburn, E.A., Wilson, L. & Sparks, R.S.J. (1976) J. geol. Soc. Lond. 132, 429-440. [13] Tilling, R.I., et al. (1987). Ch 16 in U.S.G.S. Prof. Pap. 1350. [14] Parfitt, E.A. & Wilson, L. (1993) In Prep.

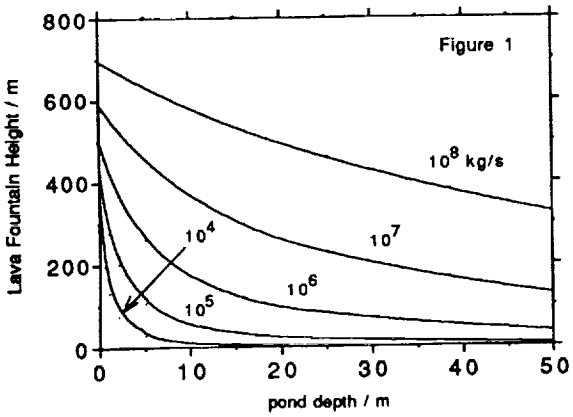

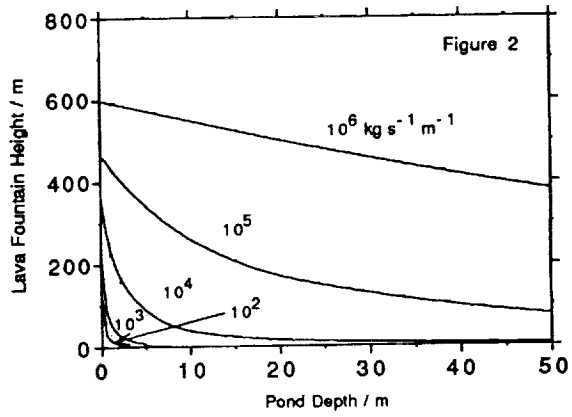

APRON HEIGHTS AROUND "STEPPED MASSIFS" IN THE BOREALIS BASIN OF MARS. T. J. Parker and D. S. Gorsline, University of Southern California, Dept. of Geological Sciences, Los Angeles, CA 90089-0740.

Evidence for large standing bodies of water (ranging from numerous large lakes to a single ocean-size body) or ice sheets within the Borealis Basin of Mars has been described by numerous investigators (1-14). Our own efforts have focused on the identification and regional mapping of possible shore morphology, and point toward an ocean size body with 2 -7 highstands recognizable at Viking image scales (10, 11).

Basin volume estimates currently are tied to the available topography (15) with its very large vertical errors and suggest the possibility that the volumes required to fill the basin may be at or beyond the high end of the estimated volumes available from the major outflow channels. High resolution topography is needed to sort out the common modifiers of shoreline elevation that likely altered the topography of the northern plains after the putative surface water was lost, so that the original topography can be reconstructed. The above studies would have benefited greatly from the the high resolution topography afforded by the Mars Observer Laser Altimeter (16). The best high resolution topography available now - photoclinometry and shadow measurements - cannot be accurately tied to the global datum.

What is needed are a number of measurements of the height of the paleoshoreline(s) distributed across the basin. In addition to delineating the basin, shore morphology appears as steps or benches on knobs ("stepped massifs" 9, 11) within the Borealis Basin. Many of these knobs exhibit multiple benches. Photoclinometric measurements of the heights of these benches can provide a measure of the basin depth in the vicinity of the knob. Similarly, if the observed benches were produced by a mechanism other than shore erosion, such as differential erosion of layered material that once covered the Borealis Basin, then these measurements should reflect the former thickness of the deposit. Beginning with the Cydonia Mensae region, we have found that the height of the most prominent bench, that defining the relatively flat apron surface surrounding most knobs in the region, ranges typically from 100-200m.

REFERENCES:

1) Jöns , H.-P., (1985), Lunar. Planet. Sci. - XVI, 414-415. 2) Jöns , H.-P., (1986), Lunar and Planet. Sci. - XVII, 404-405. 3) Jöns , J.-P., (1990), Geol. Rundsch. 79, 131-164. 4) Lucchitta, B. K. et al. (1986), JGR 91, E166-E174. 5) McGill, G. E., (1985), Lunar and Planet. Sci. - XVI, 534-535. 6) McGill, G. E., (1986), Geophys. Res. Let. 13, 705-708. 7) McGill, G. E. and Hills, L. S., (1992), JGR 97, 2633-2647. 8) Parker, T. J., et al., (1987a), LPI Tech. Rept. 87-01, 96-98. 9) Parker, T. J., et al., (1987b), Rept. Planet. Geol. Prog. - 1986, NASA TM 89810, 502-504. 10) Parker, T. J., et al., (1989), Icarus 82, 111-145. 11) Parker, T. J., et al., (1993), JGR 98, E6, 11,061-11078. 12) Baker, V. R., et al., (1991), Nature 352, 589-594. 13) Scott, D. H., et al. (1991), in Workshop on the Martian Surface and Atmosphere Through Time, Sept. 1991, Lunar and Planet. Inst., 119-120. 14) Rotto S. L., and Tanaka, K. L., (1991), in Workshop on the Martian Surface and Atmosphere Through Time, Sept. 1991, Lunar and Planet. Inst., 111-112. 15) USGS, (1989), Atlas of Mars, 1:15,000,000 Topographic Series, Map I-2030, 3 sheets. 16) Zuber, M. T., et al. (1992), JGR 97, 7781-7797.

BOREALIS BASIN, MARS Parker, T. J. and D. S. Gorsline

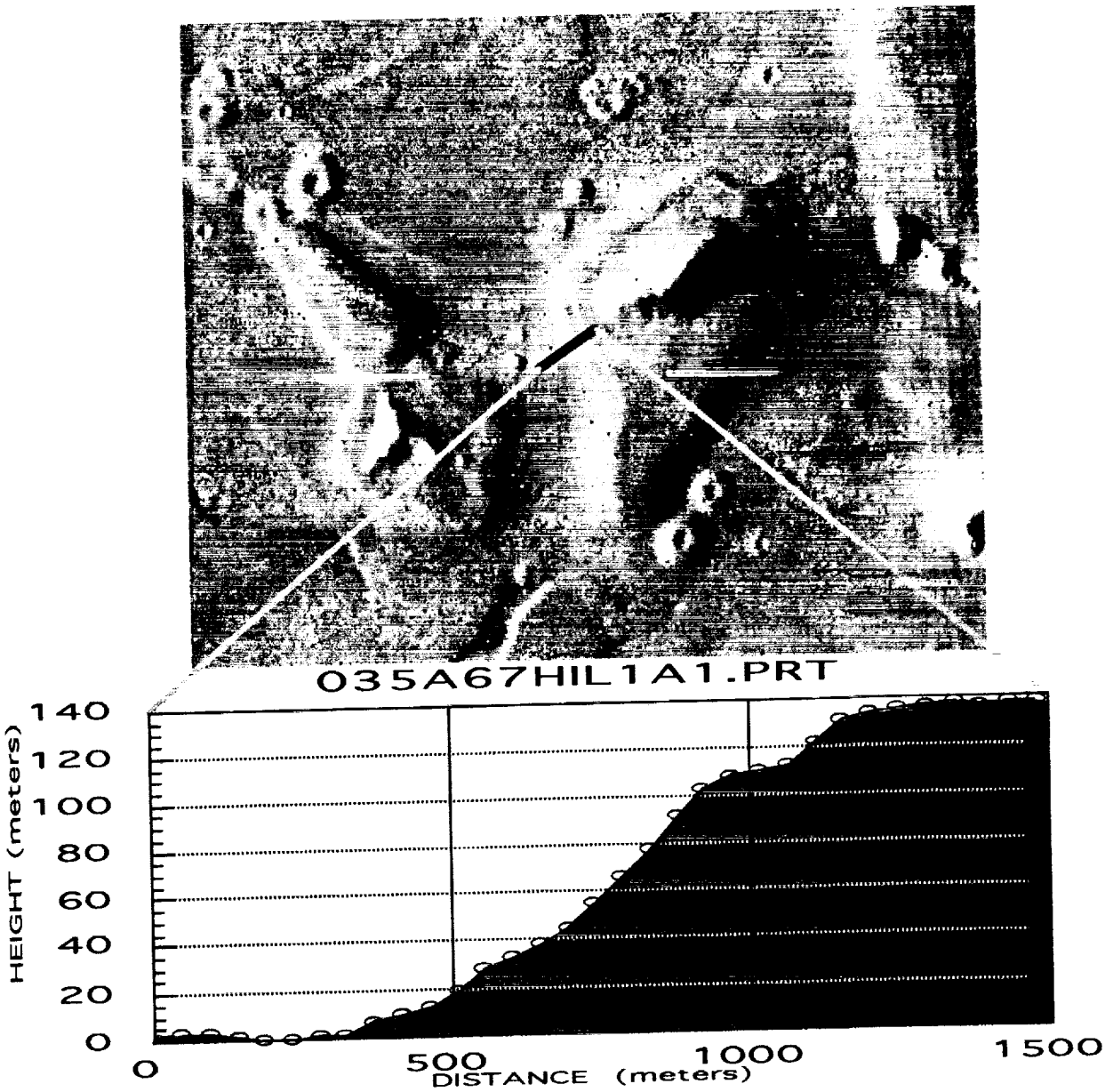

Figure 1: Many stepped massifs in the northeastern Cydonia region exhibit a prominent bench at the outer margin of the apron surrounding the massifs, particularly in the upsun and downsun directions (where shading maximizes their detectability). Photoclinometric profiling has consistently revealed this bench to lie between 20-40 meters below the top of the apron. Because this bench can be identified on massif aprons over many hundreds of kilometers, we have termed it a "marker" bench. Image and asymmetric profile on Viking Orbiter image 035A67.

FORMATION OF COMPLEX RIDGED TERRAIN THROUGH PROGRESSIVE COMPRESSIONAL DEFORMATION IN THE NORTHERN OVDA REGION OF VENUS. T. J. Parker and R. S. Saunders, Jet Propulsion Laboratory, California Institute of Technology, Pasadena CA 91109.

Understanding the development of Complex Ridged Terrain (CRT) on Venus is one key step in the verification (or falsification) of the various competing models for the tectonic evolution of that planet. Achieving this understanding is complicated since, although Venus may lack terrestrial-style plate tectonism, it is nevertheless a geologically complex planet. Most highland regions, and CRT in particular, appear to have been subjected to multiple cross-cutting fracturing or compressional events, such that the structural grain dominates the surface morphology, making determination of surface rock unit emplacement mechanisms difficult or impossible. Stereo image mosaics (at all available standard data product resolutions) on the Magellan CD-Roms provide high-frequency topographic detail that is invaluable in geologic mapping of these complex structures.

Our investigation of CRT on Venus begins with northern Ovda Regio, where individual CRT units appear to exhibit a progressive increase in complexity southward from the CRT/plains contact. The CRT within F-MIDRs 00N082 and 05N082 can be divided into 5 or more morphotectonic units (fig 1). For descriptive purposes, these are termed (from north to south): "Ovda North Slope" (ONS), "'Simple' CRT" (SCRT), "Highly Fractured CRT" (FCRT), and two units of "'Normal' CRT" (NCRT). Locally, these units define arcuate belts up to 100km wide separated by relatively "undeformed" radar-dark plains units up to 75km wide. The belts strike parallel to the topographic boundary between the plains and the CRT (fig 1). Differences between adjacent morphotectonic units are readily apparent in the SAR mosaics and can even be recognized in the altimeter topography when that data is plotted at relatively low resolution (cells on the order of 10km with 100m contours). The ONS consists of radar-bright fold-like ridges trending parallel to the plains/highland boundary and embayed by relatively unmodified, radar-dark smooth plains. The regional slope of this unit is not apparent in the stereo mosaics (due to the regional topography included in the projections), but is obvious in the altimeter-based topography (figure 1b). The plains material embaying the CRT in the ONS may indicate tilting of the unit after embayment by flood lavas. The SCRT unit consists of several large, cross-fractured, parallel fold-like structures approximately 10-20km wide, bounded by numerous narrow (a few km wide) smooth fold-like structures, embayed locally by narrow belts of relatively smooth, undeformed plains (figs 1 and 2). It is these three principle elements of the SCRT unit that, we feel, provide the clearest evidence for progressive deformation in the region. The FCRT and NCRT units are typical of many CRT units on the planet, in which deformation appears so advanced that reconstructing the sequence of events that led to their development is much more difficult.

Figure 1: F-MIDRs 00N082 and 05N082 of northern Ovda Regio with topographic map based on MGN altimeter. Morphotectonic units are indicated.

Figure 2: Stereo image pair of a portion of 'Simple' CRT unit (1°S lat, 80.5° lon, Tile 19 of cycles 1&3 F-MIDR 00N082 on MGN CD-Roms). Geomorphic map superposed on right image, showing evidence for at least three stages of development: (i) - Hills labeled 'CRT' are portions of large, long wavelength fold-like structures that appear to be superposed by smaller, shorter wavelength folds (e.g., CRT at bottom); (ii) - Troughs between 'CRT' hills appear to have been filled by plains material that has itself been folded into short-wavelength (a few km), smooth fold-like ridges and troughs. Note cross-cutting relationships with 'earlier' ridges toward top left and above center. Lack of evidence of additive interference by the earlier ridges to the subsequent ridges, as might be expected in folding previously folded terrain, suggests burial of the earlier ridges by smooth plains, with subsequent folding of those plains; (iii) Troughs between these latter folds appear filled in places with radar-dark, relatively undeformed plains (unit Pl).

OVDA REGIO, VENUS Parker, T. J. and R. S. Saunders

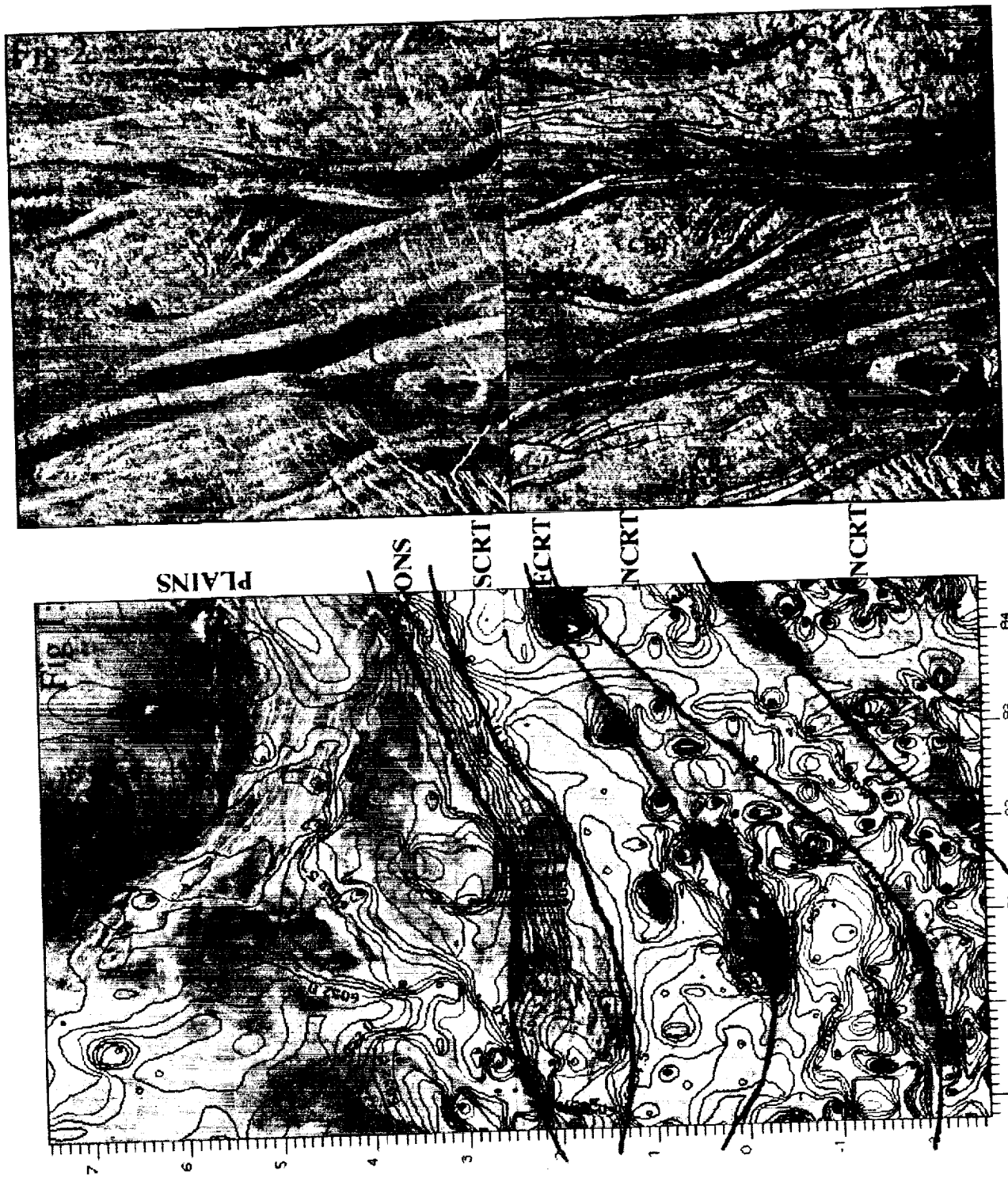

HIGH SPATIAL RESOLUTION SULPHUR ISOTOPIC ANALYSIS OF TROILITE IN ORDINARY CHONDRITES BY ION MICROPROBE

Bruce A. Paterson [1], Harry Y. McSween, Jr. [1] and Lee R. Riciputi [2]. [1] Department of Geological Sciences, University of Tennessee, Knoxville, TN 37996, [2] Chemistry and Analytical Sciences Division, Oak Ridge National Laboratory, Oak Ridge TN 37831.

Rationale. Sulphur is the fifth most abundant element found in meteorites and it occurs in a wide variety of chemical forms, including sulphides, sulphates and organic material. Partly due to the very restricted isotopic composition of S in bulk meteorites of all types [1] (the standard deviation on the range is <0.1‰), there have been comparatively few studies of the composition of constituent phases, although the studies that have been published have observed small but significant differences between phases [2]. In addition to the restricted isotopic composition, the extraction of S for isotopic analysis usually relies on chemical extraction [3] or stepped combustion [4] techniques. There are a number of drawbacks to these methods: 1) it is not always certain which phases are being sampled; 2) spatial information is lost; and 3) the demands of minimum sample size mean that it is virtually impossible to analyse single grains, let alone parts of single grains, and thus it is not possible to detect inter-grain variability within one phase. S isotopic analysis using the ion microprobe can overcome some of these problems, although the precision is poor in comparison with conventional and laser combustion techniques [5]. Here we report initial *in situ* analyses of troilite from ordinary chondrites using an ion microprobe. This has enabled us to study inter and intra-grain variations in S isotopic composition.

Methods. The S isotopic values were obtained with a Cameca ims-4f ion microprobe [6]. A Cs^+ primary beam focussed to a spot of between 25-30μm in diameter, although the secondary ion optics result in only the central 8μm being analysed. The S isotope standard Cañon Diablo Troilite (CDT) was analysed at the beginning and end of each analytical session in order to measure the degree of instrument-induced isotopic fractionation (usually -20 to -25‰, although this varies from session to session), overall reproducibility (usually in the range ±1-1.5‰ (2σ), occasionally better) and to check for drift over the period of an analytical session (~12 hours). None of the standard analyses presented here displayed any such drift. The reproducibility is the measure of the consistency of the instrument conditions over an analytical session, in particular the alignment of the primary beam relative to the secondary ion optics. In any one analytical session the ratio of the number of standard analyses to the number of unknowns is always better than 1:2. In addition to being used to correct the unknown analyses for instrument-induced fractionation, the reproducibility of the measured value of CDT is incorporated in the error for each unknown in order to obtain a measure of the accuracy. All errors are quoted at the 2σ level. The relatively poor precision obtainable using the ion microprobe means that the detection of nucleosynthetic anomalies involving the minor isotopes, ^{33}S and ^{36}S, is not likely.

Results. $\partial^{34}S_{CDT}$ data have been obtained from troilite grains in six ordinary chondrites, three relatively low-shock Antarctic L chondrites (ALH85045 (L3), LEW86024 (L4) and QUE90210 (L5)) and three H chondrites (Tieschitz (H3), Forest Vale (H4) and Limerick (H5)). The results obtained thus far are summarised in Figure 1.

Discussion. For the purposes of discussion the samples can be divided into three categories:

1) Those samples (Tieschitz, Forest Vale and ALH85045) whose absolute $\partial^{34}S_{CDT}$ values are not significantly different from CDT and that show a range of variation not significantly greater than that expected from the reproducibility of the standard. The Forest Vale analyses were obtained on troilite both within chondrules and within the matrix. The Tieschitz analyses came from troilite on chondrule rims and within the matrix.

SULPHUR ISOTOPIC ANALYSIS OF TROILITE: Paterson, B.A. et al.

2) Those samples (Limerick and LEW86024) that show significant differences in absolute values of $\partial^{34}S_{CDT}$, although again the variation within a sample is not significantly greater than would be expected given the standard reproducibility. Limerick gave values consistently heavier than CDT by an average of approximately +2.5‰, and the results from two separate analytical sessions are in agreement. In contrast, troilite in LEW86024 is isotopically light, giving an average of approximately -2.7‰. In both samples troilite was a matrix phase.

3) The only sample which has a significant variation in troilite $\partial^{34}S_{CDT}$ values greater than that observed in the standard analysed concurrently is QUE90210. The 12 standard analyses gave a standard deviation of 1.3‰, and the standard deviation of the 21 unknown analyses, which were all from matrix troilite, was 2.2‰. The last 8 analyses (see Figure 1), which are displaced to lighter isotopic values, were all from a single grain or grain aggregate. At the present scale of study there is no indication of within-grain heterogeneities.

Differences in the S isotopic composition of troilite from that of bulk meteorites could have two extreme interpretations: either the variations observed are due to nebular heterogeneity, or that the they are due to secondary alteration of the primary S-containing phases. The differences in troilite S isotopic composition presented here and in particular the apparent heterogeneities within a single section of QUE90210 support a secondary alteration mechanism. If such small-scale, within-phase heterogeneities commonly exist in chondrites and they are due to variable secondary processes, then it would suggest that similar heterogeneities may exist in coexisting S containing phases and that the internal variations between phases, identified using chemical extraction and stepped combustion techniques, may locally be larger than has previously been reported.

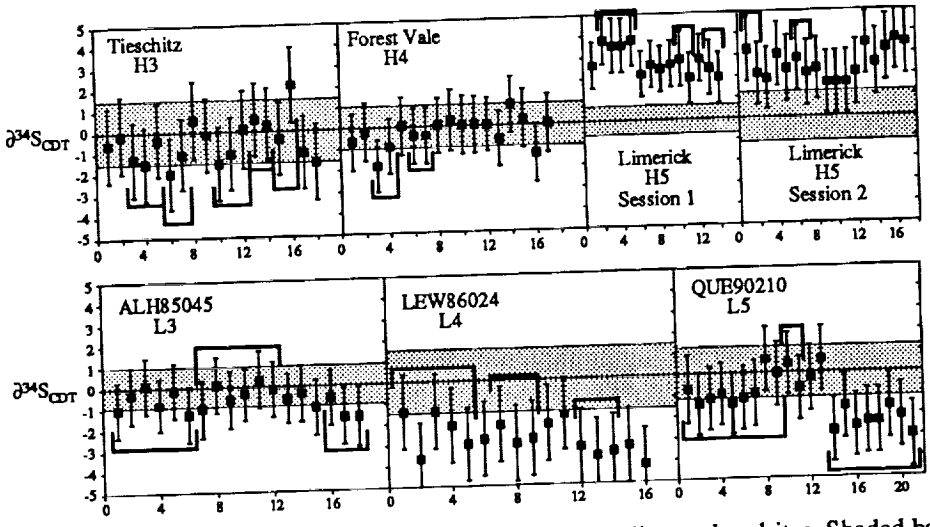

Figure 1. Summary of S-isotope data obtained on troilites from ordinary chondrites. Shaded bands represent the 2σ reproducibility of analyses on the CDT standard. Error bars on the analyses include both the error on the sample and the reproducibility on the standard. Grouped analyses were obtained from different areas on the same grains or grain aggregates.

References. [1] Pillinger (1984) GCA, **48**, 2739. [2] Monster et al. (1965) GCA, **29**, 773. [3] Gao & Theimens (1993) GCA, **57**, 3171. [4] Burgess et al. (1991), Meteoritics, **26**, 55. [5] Kelley et al. (1992) Scanning Microscopy, **6**, 129. [6] Graham & Valley (1991) Chem Geol. 101, 169-172. **Acknowledgements.** NASA grant NAGW 2800, and Geoscience Research Program and Division of Chemical Sciences, Office of Basic Energy Sciences, US Department of Energy under Contract DE-ACO5-85OR21400 with Martin Marietta Energy Systems, Inc.

The composition of SEPs implanted in regolith minerals depends on implantation ranges.

A.Pedroni, Max-Planck-Institut für Chemie, J.J.Becherweg 27, D-55128 Mainz, Germany

Abstract: Different ion species with the same kinetic energy per nucleon have different penetration ranges when stopped in matter. Therefore, when gases are extracted from regolith minerals by depth-sensitive methods (e.g. etching in vacuo), the composition of trapped solar gases should differ with depth and only the integral be identical with the composition of the original Solar Cosmic Ray (SCR). A crude estimate of this effect, presented here, shows that shifts are small for isotopic ratios (a few percent), but important for element ratios. The largest isotopic shift (~15%), predicted for the 3He/4He ratio, seems to be identical with the "Helium problem" reported by Benkert and coworkers [1].

Introduction: Great efforts have been made during the past few decades for measuring the elemental and isotopic composition of solar noble gases implanted in regolith minerals. In-vacuo-etching, which turned out to be the most reliable technique, revealed that besides implanted Solar Wind (SW), there is a further, isotopically heavier and deeper-implanted component [1,2,3 and cit.]. The latter was attributed to Solar Energetic Particles (SEP) of energies above 1 keV/amu. Benkert and coworkers [1] noted that SW and SEP isotopic composition might be related by:

$$R_{sep}/R_{sw} = 1 + a \cdot (m_i/m_j - 1) \qquad (1a)$$

where R_{sw} and R_{sep} are abundance ratios N_i/N_j of isotope pairs "i"-"j" having masses m_i and m_j. In the following we do not discuss (1a), because this expression is a first-order approximation [4] of:

$$R_{sep}/R_{sw} = (m_i/m_j)^a \qquad (1b)$$

When best estimates for SW- and SEP- isotopic ratios [1,2,3] are fitted to (1b), one obtains $a = 2.6 \pm 0.3$. He-isotope ratios are, however, far away to obey the relation (1b). This "He-problem" was noted already by Benkert and coworkers [1]. Here is a preliminary report of how differing implantation ranges of the ions of helium isotopes might generate this problem.

Theoretical considerations: Heavy ions in the Solar Wind are pulled approximately to the average proton speed, by means of the Coulomb drag of the plasma [5]. The mechanism implies that element- and isotope- abundance ratios are (roughly) invariant for particles of the same energy per nucleon. For this reason, the "composition" $R_{ij}=N_i/N_j$ of any component of the SCR's is usually assumed to be the ratio of abundances N_i and N_j of particles "i" and "j" having the same energy E per nucleon. The stopping power for energetic ions in a target material depends on ion species and energy. As shown in the figure for the case of noble gas ions implanted in Ni-Fe, differing ions which are implanted with the *same energy per nucleon*, will *not* end up their path *at the same depth*. Therefore, when atoms of the SCR are extracted from host regolith minerals by a depth sensitive technique, (e.g. stepped etching) the local concentration ratios C_i/C_j measured are slightly different from original SCR-ratios N_i/N_j, because a differing window of the SCR-energy spectrum is sampled for each ion species.

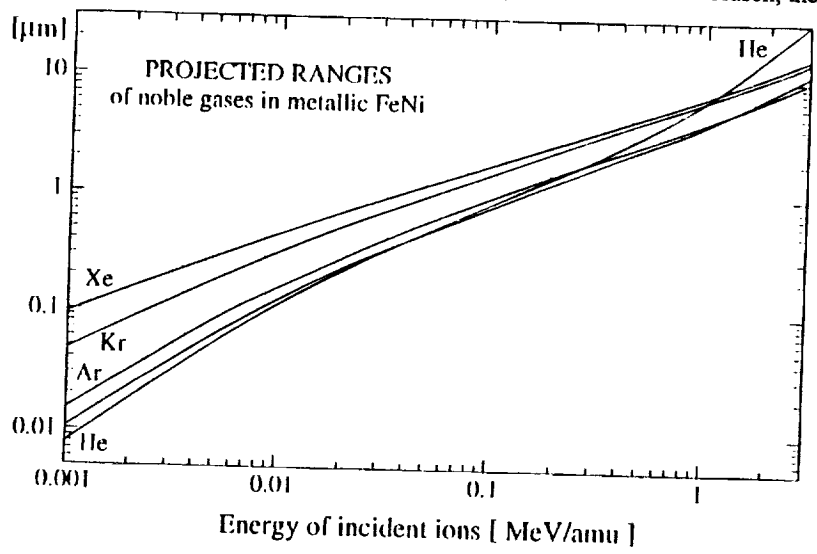

Lindhard and coworkers [6] first formulated an ion-stopping theory (the LSS-theory) which takes into account the stopping on electrons *and* on nuclei of the target material. Analytical implantation-range estimates, such as of the LSS-theory and its later refinements, are accurate to within a factor of 2-3. Half-empirical energy-range relations tabulated by Ziegler [7,8] and Littmark and Ziegler [9] are much more accurate (aprox. ± 10%). Thus, the best way to estimate solar ratios from local concentration ratios is a computer-supported numerical calculation. The method presented here gives a more crude estimate. According to the LSS-Theory, the energy-range relation can be approximated by:

$$D = f \cdot E^{1/q} \qquad (2)$$

where D(E) is the penetration depth, E the energy per nucleon and f a function of masses and charges (m_i, Z_i) of the incident ions and (m_t, Z_t) of the nuclei in the target. "q" is a smooth function of E and, for 1keV/amu<E<100keV/amu, constant to within ± 20%. The SCR-spectra of all ion species above 1 keV/amu are approximated to:

$$\frac{dN}{dE} = k \cdot N \cdot E^{-\gamma} \qquad (3)$$

COMPOSITION OF SEPs AND RANGES. **Pedroni A.**

"k" is assumed to be constant. N are the time integrated fluxes (particles per square centimeter and time unit) for each ion species. The concentration profiles C(D) implanted in a semi-infinite solid, exposed at normal incidence angle to the SCR are then:

$$C = \frac{dN}{dD} = \frac{dN}{dE} \cdot \frac{dE}{dD} = b \cdot f^{e} \cdot D^{-(1+e)} \qquad (4a)$$

where: $b = k \cdot q \cdot N$ and $e = q \cdot (\gamma - 1)$ (4b and 4c)

Local concentrations $C_{i,j}$ of implanted atoms"i" and "j" and abundances $N_{i,j}$ of parent ions from SRC are related by:

$$\frac{C_i}{C_j} = \frac{N_i}{N_j} \cdot \frac{q_i}{q_j} \cdot \left(\frac{E_i}{E_j}\right)^{(1-\gamma)} \qquad (5a)$$

It should be noted that E_i and E_j are not the same function of D, and , therefore , E_i and E_j are not equal. We rewrite (5a) in terms of the average energy $E = (E_i + E_j)/2$ and the energy difference $\Delta E = (E_i - E_j)/2$:

$$\frac{C_i}{C_j} = \frac{N_i}{N_j} \cdot \frac{q_i}{q_j} \cdot \left(\frac{1+\Delta E/E}{1-\Delta E/E}\right)^{(1-\gamma)}$$

and, using the linear approximation $D(E \pm \Delta E) = D(E) \cdot \left(1 \pm \frac{\Delta E}{q \cdot E}\right)$ we obtain:

$$\frac{C_i}{C_j} = \frac{N_i}{N_j} \cdot \frac{q_i}{q_j} \cdot \left(\frac{D_i.q_j.(1+q_i) + D_j.q_i.(1-q_j)}{D_i.q_j.(1-q_j) + D_j.q_j.(1+q_j)}\right)^{(1-\gamma)} \qquad (5b)$$

Projected ranges D_i, D_j are tabulated (e.g. [7,8,9]) and q_i,q_j might be estimated by fitting D_i, D_j to (2). The spectral index γ obtained by satellite measurements might range from 1 to 5, and is typically 2-3. The spectral index obtained from nuclear tracks in regolith minerals lies between 1.1 and 1.6. In the discussion we adopt γ=1.4 according to Blanford et al. [10]. Projected ranges of isotopes cannot be found in tabulated form. Nevertheless an upper limit (which is also a reasonable approximation above 100 keV/amu) can be obtained under the assumption $f = m_i \cdot f^*$, with f^* independent from m_i :

$$\frac{C_i}{C_j} = \frac{N_i}{N_j} \cdot \left(\frac{m_i}{m_j}\right)^{-e} \qquad (5c)$$

Discussion and conclusion:

Isotope ratios of SCR-particles trapped at any depth in regolith minerals do not differ much from isotope abundance ratios in the SCR plasma. The composition of SEP obtained by in-vacuo-etching experiments [1,2,3] is $(4He/3He)_{sep}$=4500; $(20Ne/22Ne)_{sep}$=11.2; $(21Ne/22Ne)_{sep}$= 0.029; $(36Ar/38Ar)_{sep}$=4.9 and $(86Kr/84Kr)$=0.317. When corrected for the implantation-range effect (by means of 5c), these isotope ratios become $(4He/3He)_{sep}$=3850; $(20Ne/22Ne)_{sep}$=11.8; $(21Ne/22Ne)_{sep}$=0.0304; $(36Ar/38Ar)_{sep}$=4.98 and $(86Kr/84Kr)_{sep}$= 0.310. By fittig the corrected ratios to (1b) one obtains a=2.01± 0.015. Correction factors deduced from (5c) might be not better than ±50%, because of the crude approximation and uncertainties of the parameters D, q and γ. Nevertheless, as shown by the smaller uncertainty obtained for "a", corrected ratios fit better to (1b) than measured ratios. Furthermore, it should be noted that corrected He isotope ratios agree to within the experimental error limits to (1b) strongly suggesting that the "He-Problem" reported by Benkert and coworkers [1] is related to the implantation-range effect.

Elemental ratios are more heavily affected by the implantation-range effect than isotope ratios. The energy-range relations for He, Ne and Ar cross over in the window 30-300 keV/amu, and measured He/Ne and Ne/Ar ratios do not differ more than 15% from original SCR ratios. Below and above this energy window differences might exceed 25%. Energy-range relations for Kr and Xe cross over the He-, Ne- and Ar- range relations at higher energies (above 1MeV/amu). Below 100 keV/amu differences between measured and original Ne/Kr and Ne/Xe ratios always exceed 15%, and possibly 50% for E<5keV/amu. It should be noted that the linear approximation presented here is reasonable only for small differences in $D_{i,j}$ *and* $q_{i,j}$, and therefore, elemental abundance ratios of SCR should not be calculated from measured ratios by means of (5b).

Acknowledgement: It is a great pleasure for me to acknowledge many fruitful discussions with Prof. F. Begemann, who also motivated me to acquire a deeper understanding of this problem.

References: [1] Benkert J.-P., Baur H., Signer P., and Wieler R. (1993) *J.Geophys. Res. 98, E7-13*, 147-162; [2] Pedroni A. (1993) *LPSC-XXIV, Houston*,1121-1122; [3] Wieler R., Baur H. and Signer P. (1986) *Geochim. Cosmochim. Acta 50*, 1997-2017; [4] Geiss J. and Bochsler P., (1991) in: *The Sun in Time* (eds Sonett C.P. et al.), Univ. Arizona Press, 98-117; [5]Geiss J. , Hirt P. and Leutwyler. (1970) *Solar Physics 12*, 458-483. [6]Lindhard J., Scharff M. and Schiott H.E. (1963) *Kgl. Danske Vid. Selsk., Math-fys., Medd.33(14)*, 1-42; [7]Ziegler J.F. (1977) *The stopping and ranges of ions in Matter, Vol4* (Pergamon Press); [8]Ziegler J.F. (1980) *Nucl. Instr. Meth. 168*, 17-24 ; [9]Littmark U., and Ziegler J.F., (1980) *The stopping and ranges of ions in matter, Vol6* (Pergamon Press); [10]Blanford G.E., Furland M., and Morrison D.A. (1975) *Proc. Lunar Sci. Conf. 6th*, 3557-3576.

Anomalous metal and sulfide abundances in the regolith-breccia Acfer111.

A. Pedroni, B. Spettel and F.Wlotzka, Max-Planck-Institut für Chemie, J.J. Becherweg 27, 55128 Mainz, Germany.

Abstract: Modal- and INA- analyses of the H3-H6 regolith breccia Acfer111 reveal that the abundance of metal in the host is 20-25% higher than in clasts. Furthermore, sulfides are depleted by some 30% compared to average H-chondritic compositions [1]. We present here some possible mechanism which might enrich the regolith of the Acfer111 parent body in metal, i.e. admixture of foreign material, FeO-FeS reduction through loss of S_2 and SO_2, unrecognized Fe-rich indigenous lithologies, and a sorting mechanism. Each of these possiblities might contribute to the observed feature, but sorting seems to be the most likely mechanism.
Implications for regolith chronology and for the original in-depth structure of the H-chondrite parent body make accurate studies on other gas rich meteorites (like Fayetteville and Noblesville) highly desirable.

Introduction: Acfer111 exibits the typical "dark-light" structure of regolith-breccias: centimeter sized "light"clasts, are embedded in a "dark" host consisting of submillimeter sized, solar cosmic ray irradiated fragments."Matrix" is a current designation for the host, and will be used henceforth. The light clasts are H-chondrite fragments of petrologic type 4-6 (Tab.1). The matrix consists mainly of equilibrated silicates in chondrules and crystal fragments, but it contains also unequilibrated material of type 3 (see below). It is thus generally agreed upon that the host was generated mainly in the regolith of the parent body by impact-comminution of clast-type progenitors. We present here additional evidence for more complex clast-matrix relationships.

Experimental procedure and results: The reflectivity for 20 keV electrons on polished Fe-Ni-metal, sulfide, Fe-oxide, and silicate surfaces is quite different, and these mineral phases can very well be distinguished on a SEM backscattering-image. We examined the modal amounts of these mineral phases on 804 SEM images (each sampling around 1mm²) of polished sections of 7 clasts and 6 matrix samples of Acfer111. Each image was covered by an array of 1500x1800 points, and analysed using the KEVEX 1989 image analysis software. The surface of voids and cracks on the polished sections was taken into account, and a small correction (mostly <<1%) was applied to the modal abundances listed in Tab.1. On each polished section we counted around 10^8 points, nevertheless, the precision is much lower than counting statisics, since the area of the polished section might not be representive for the whole rock. Typically, 5-10 major (>10 μm) and 20-60 minor grains of each mineral species are found in one image area. Counting statistics, applied to the number of mineral grains give a relative error of around 5 %. Standard deviations of the averages listed in Tab.1 confirm our consideration.
The volume occupied by Fe-oxides and -hydroxides is on average 1% and is independent of the texture of the sample. Sulfides are also, on average, equally abundant in matrix and clast samples, but are about 30-40% less abundant than usually found for H-chondrites [1]. This deficiency is less pronounced when all oxides are assumed to be weathering products of sulfides. Nevertheless, we suspect that Acfer 111 is really depleted in sulfides, since oxide rims are observed mainly on metal and rarely on sulfides. The abundance of metal in clasts lies at the lower limit, in matrix close to the mean of the range observed for H-chondrites. In the following discussion we try to explain the higher amount of metal in the matrix under the assumption that the metal content of clasts is the primary feature (wich is accidentally at the lower end of the H-chondrite range [1]).

Discussion: Whatever we assume on the origin of the oxides, metal abundances in clasts and matrix are different, i.e. matrix is not simply a finely comminuted clast-type material.
This peculiar feature of the matrix might have several origins, each contributing to the observed abundances:

1. Metal is introduced into the matrix as a foreign component, i.e. as metal-rich meteoroid which fell into the parent body regolith. Hewins [2] found such foreign material in howardites, where it is much easier identified than in ordinary chondrites. The abundance of foreign material found in any meteoritic regolith breccia [2,3,4,5] is, however, much too low to sum up to the observed abundances.

2. Metal might have formed by reduction of FeO and FeS through loss of S_2 and SO_2 when the regolith was locally heated to 800-1000 °C by impacts, as it was observed in the Camel Donga eucrite [6]. This mechanism looks attractive, since it would also explain the sulfide deficit. But, when we assume the average H-chondrite sulfide abundance of 4.3 vol%, only half of the metal excess we observe could be produced. Intact radiogenic 4He- and 40Ar-inventories as well as an unfractionated solar-gas composition suggest that if any such changes did indeed occur, this must have happened very early. Also the chemical analysis shows that the matrix has a higher content of total iron and siderophile elements (Co, Ni, Ir, Au) than clasts (Tab.2); i.e. the higher metal content of the matrix cannot be explained by a simple reduction-oxidation relationship.

3. Metal might have an indigenous origin, e.g. from a metal core of the Acfer111 parent body. An objection to this hypothesis is that large (>1mm) metal chunks are rare in the matrix. Why are fragments of the brittle chondritic lithology abundant but metal-rich fragments cannot be found? A core-origin of metal looks thus of minor importance, if any.

4. We do not find large (cm sized) H3-chondritic clasts. Nevertheless, the variable composition of olivines (9<Fa<19,5) and pyroxenes (2,5<Fs<16,8), show that an H3-type component is present in the matrix (A.Bischoff, priv. comm. 1991). Noble gases confirm this, since the average 129Xe-concentration of $17\pm5\cdot10^{-11}$ccSTP/g in 31 matrix samples is distinctly higher than $5\pm3\cdot10^{-11}$ ccSTP/g found in 21 clast samples. H3-Chondrites typically have more than $170\cdot10^{-11}$ ccSTP/g 129Xe [7], suggesting that ~10% of matrix might be H3. For an oninon-shell structured H-chondritic parent body, where H3-type lithologies lie originally on the surface, it seems reasonable that the H3-component is more efficiently comminuted by impacts than other, deeper sited components. The absence of large H3-type clasts should thus not be surprising. Nevertheless, we doubt that the metal excess can be attributed to an H3-type component in the matrix, because this would imply an H3-lithology having a factor of two, or so, more metal than average H-chondrites. Such a high-metal lithology has never been observed [1].

5. In a previous study of the Howardite Kapoeta [8] we found some evidence for a sorting mechanism acting on asteroidal regoliths. Metal in the matrix of Acfer111 might also be enriched by sorting. A candidate for a sorting mechanism is the hydrodynamic drag during ejection of impact debris [9]. The mechanism acts on grains of low mass/surface ratio, and it can easily be shown that low-density silicates are preferentially "blown-up" to the escape velocity. The expected metal (and possibly sulfide) enrichments are, however, hard to quantify, already because of the stochastic nature of impacts.

Conclusions and Outlook: Except the last one, none of the hypotheses given above looks completely satisfactory, when taken alone. Possibly, several mechanim contribute to the observed metal excess. We note that indigenous metal sources, such as hypotheses 3 and 4, have important implications for the nature and the structure of the H-chondrite parent body, whereas the sorting mechanism (hypothesis 5) has consequences for the regolith chronology, requiring some refinement of the Housen model [10]. This makes further studies highly desirable, especially of fresh samples like Fayetteville and Noblesville, where ambiguities due to weathering are avoided.

Tab.1: Modal abundances (vol%) for clasts (left panel) and matrix (right panel) of Acfer111.

Clast	Type	Surface mm²	Fe-Ni metal	Fe S	Fe-Oxide
A	H6	75	5.16	2.74	0.99
C	H4	51	5.73	1.89	0.64
D	H6	51	5.54	3.21	1.89
E	H5	69	6.61	2.68	1.07
H	H4	66	6.70	1.64	1.10
K		6	6.60	2.40	0.61
V	H5	60	6.63	1.98	1.44
weighted average			6.08±0.5	2.36±0.5	1.16±0.4
average H-Chondrite (Jarosewich, 1990)			9.4	4.3	-

Matrix	Surface mm²	Fe-Ni metal	Fe S	Fe-Oxide
MA	60	8.49	2.05	0.55
ME	96	8.45	2.58	1.18
MV	48	5.76	2.06	1.24
MW	78	8.65	2.46	0.87
MZ	84	8.53	2.00	0.58
ML	60	8.28	2.38	0.95
weighted average		8.19±0.6	2.28±0.2	0. 89±0.3

Tab.2: INAA of two matrix and two clast samples of Acfer111. Fe_{tot} and Ni abundances in wt. %, all other in ppm.

	Fe_{tot}	Co	Ni	Se	La	Os	Ir	Au
Matrix MA	28.2	859	2.00	9.8	0.30	1.17	0.96	0.25
Matrix MIH	28.0	837	1.90	11.1	0.29	1.02	0.86	0.23
Clast E	25.8	683	1.72	10.9	0.30	0.95	0.77	0.20
Clast C	24.0	681	1.77	6.1	0.28	0.90	0.79	0.19
average H-Chondrite (Kallemeyn et al., 1989)	27.1	830	1.63	8.1	0.30	0.83	0.79	0.22

References: [1] Jarosewich E (1990) *Meteoritics 25*, 323-337; [2] Hewins R. (1979) *Geochim. Cosmochim. Acta 43*, 1663-1673; [3] Wilkening L.L. (1973) *Geochim. Cosmochim. Acta 37*, 1985-1989; [4] Chou C.-L. et al. (1976) *Proc. Lunar Sci.Conf. 7th*, 3501-3518; [5] Pedroni A. (1989) *Ph.D.-Thesis Nr. 8880*, ETH-Zürich; [6] Palme H. et al. (1988) *Meteoritics 23*, 49-57; [7] Loeken Th., Scherer P., Weber H.W. and Schultz L. (1992) *Chem. Erde 52*, 249-259; [8] Pedroni A. (1992) *Lun. Planet Sci. Conf. Houston (abstract)*, 1047-1048; [9] Rehfuss et al. (1977) *Proc. Lunar Sci. Conf. 8th*, 3375-3388; [10] Housen K. et al. (1979) *Icarus 39*, 317-351; [11] Kallemeyn G.W. et al. (1989) *Geochim. Cosmochim. Acta 53*, 2747-2767.

A NEW IMAGING RESONANCE IONIZATION MASS SPECTROMETER FOR ISOTOPIC AND TRACE ANALYSIS*; M. J. Pellin[1], R. N. Thompson[1,2], Z. Ma[1], A. M. Davis[3], R. S. Lewis[3], and R. N. Clayton[2,3,4], [1]Materials Science/Chemistry Divisions, Argonne National Laboratory, Argonne, IL 60439, [2]Department of Geophysical Sciences, [3]Enrico Fermi Institute, [4]Department of Chemistry, University of Chicago, Chicago, IL, 60637

Chemical and isotopic analysis of meteorites, interplanetary dust particles, and other planetary materials increasingly requires microscopic determinations with an accuracy and precision not addressable with current instrumentation. The need for such measurements is clearly at odds with a desire to examine samples whose spatial extent is measured in nanometers. At Argonne National Laboratory, we have developed a resonance ionization mass spectrometer capable of both high useful yields (>10^{-2}) and trace analysis (<100 ppt). The instrument incorporates a high resolution optical microscope that can be used for both sample viewing (illumination is normal to the sample surface) and for laser ablation. There are a number of outstanding problems in the study of stardust that must await improvements in analytical technology: (1) isotopic analysis of many elements in SiC, including Zr, Mo, REE, in order to improve constraints on processes of nucleosynthesis; (2) isotopic analysis of Si and C in individual SiC grains <0.5μm across in order to see whether these grains sample populations not seen so far; (3) Si and Ti isotopic analysis of graphite at high precision, to learn more about the formation conditions of TiC inclusions in graphite; (4) improvement in data on trace element abundances and isotopic compositions of diamond; (5) more thorough searches for and characterization of stardust in situ in meteorites and in interplanetary dust particles collected from the stratosphere, Antarctica and Greenland. Some projects we hope to begin shortly while others will require significant development work before they can be attempted.

Our work has built on the extensive experience and equipment for Resonance Ionization Mass Spectrometry (RIMS) available at ANL. The new machine, named CHARISMA (CHicago Argonne Resonance Ionization Spectrometer for Micro-Analysis), has been constructed to overcome several problems in a previous machine, SARISA IV, which made isotopic analysis of meteoritic samples difficult. These problems include: (1) the difficulty of installing a high-quality microscope in SARISA IV, (2) problems with installation of small spot ion sources in SARISA IV; and (3) the desirability of a higher mass resolution time-of-flight spectrometer.

Historically, the most spectacular example of the power of microbeam analytical methods has been the revelation of details of nucleosynthetic processes from determination of the isotopic compositions of individual grains of circumstellar dust recovered from meteorites[1]. Diamond, silicon carbide and graphite that formed around stars and survived solar system formation and incorporation into meteorite parent bodies have been separated from carbonaceous chondrite meteorites and analyzed by a variety of techniques. They have been found to have anomalous isotopic compositions for every element analyzed in them. Different types of grains have isotopic signatures of different circumstellar environments. Analyses of individual grains reveal correlations between isotopic properties that reveal a great deal about nucleosynthetic processes. Stardust is extremely fine-grained. Diamond has an average grain size of only 16μm and each grain contains only 60 to 1100 atoms. Analyses of individual grains have not been performed because the grains are so small. Silicon carbide grains range from <0.05 to 20 μm across and individual grains greater than 0.5 μm across have been analyzed isotopically by ion microprobe for a limited suite of elements. Graphite grains are 0.8 to 10 μm across and occasionally contain TiC inclusions. Isotopic analyses of C, N, O, Si and Mg have been made by ion microprobe, but precisions of isotopic compositions of minor elements in graphite (O, Si, Mg) have been poor because of the limited sensitivity of the ion microprobe.

As a first step, we plan to measure titanium in individual presolar SiC grains separated from the Murchison meteorite. The titanium isotopic composition has been measured in some of these grains by conventional ion probe techniques[1]. The bulk of the grains have enrichments or depletions of all other isotopes relative to ^{48}Ti. The magnitude of the effects, –40 to +160‰ in ∂^{46}Ti, –40 to +60‰ in ∂^{47}Ti, –40 to +220‰ in ∂^{49}Ti and –60 to +400‰ in ∂^{50}Ti (all normalized

to ^{48}Ti) are adequate to be readily measured by the current generation RIMS-TOF. (Repetition of these measurements is essential to gain confidence in the new technique.) The isotopic pattern for titanium is roughly consistent with the expectations for a contribution from the He-shell *s*-process region of AGB stars. In detail, though, it cannot be that simple as the enrichments, and even the relative enrichments, of each of the isotopes are not constant. Instead, each grain has its own pattern. In addition, most of the data are not consistent in precise detail with the current theoretical production rates in AGB stars. These variations tell us something about the composition and nucleosynthetic history of the stars sampled by these grains, as well as the limitations of the current theory of stellar nucleosynthesis. It seems clear to us that we will have to make correlated measurements on several elements in each grain, if we hope to make progress in disentangling these clues. The higher efficiency of the new RIMS-TOF instrument compared to conventional ion probes will be essential in this endeavor.

References: [1] E. Anders and E. Zinner (1993) *Meteoritics* **28**, 490

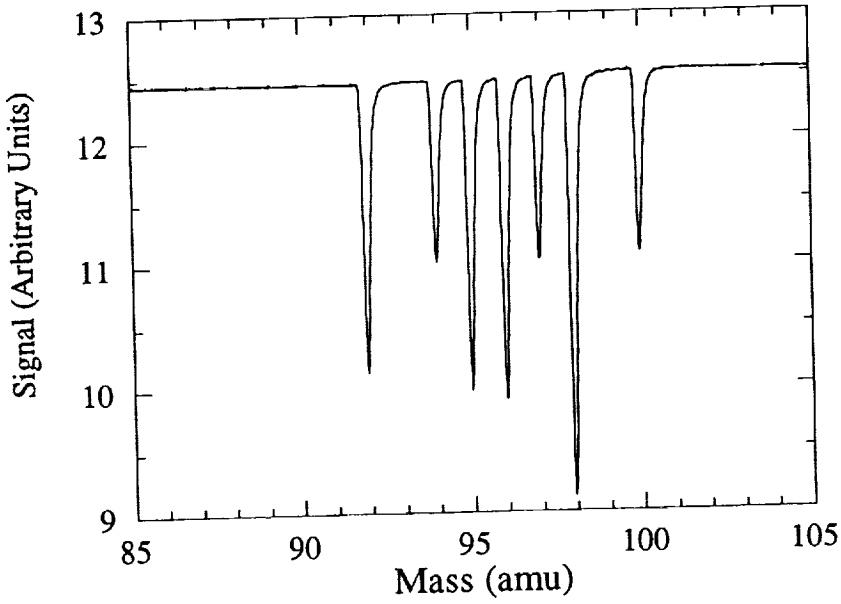

Figure (1): A preliminary mass spectrum obtained from laser ablation of a molybdenum sample. Mass resolution (m/Δm) is 400.

*Work supported jointly by the US. Department of Energy, BES-Materials Sciences, under Contract W-31-109-ENG-38 and by the Planetary and Materials Division of NASA.

HEAVY XENON ISOTOPES ON THE MOON AND IN THE SOLAR WIND. R. O. Pepin, School of Physics and Astronomy, University of Minnesota, Minneapolis, MN 55455.

Evidence for two types of implanted solar particles in noble gases evolved from lunar ilmenites by acid-etch techniques has been presented by the Zürich group [1 and references therein]. Gases initially etched from grain surfaces are identified as shallowly implanted solar wind (SW) species. Later releases from presumably deeper sites are interpreted to represent a higher energy solar particle component (SEP), isotopically related to solar wind by a nonlunar fractionation process favoring the heavier isotopes [1]. However, for at least the heavy Xe isotopes, an alternate interpretation that accounts reasonably well for lunar data trends is mixing of SW-Xe with a ^{244}Pu fission-Xe component known to exist on the moon [2-5]. Analysis of the present data base also suggests that SW-Xe is a mixture of U-Xe [6] with a nucleogenetic Xe component (DME-Xe) containing only the two heaviest isotopes.

A proposed heavy isotope structure for meteoritic Xe [6] is shown in Fig. 1. The U-Xe "parent" composition, originally defined by the intersection of the basaltic achondrite U-Pu and carbonaceous chondrite U-H correlations [7] (data fields indicated by dashed boxes) and later by assumption of a mass-fractionation relationship between U-Xe and nonfissiogenic Earth-Xe [6,8], has since been observationally supported by the measured "NZ" and "ME" data points [9,10]. The presence of an additional component, DME-Xe, containing little or no ^{132}Xe (or ^{131}Xe) was inferred from derived heavy Xe compositions in oxidized residues from three carbonaceous chondrites (open triangles) [6]. On this diagram, the Xe data field for lunar fines and the Pu-Xe-rich [2-5] lunar breccias (open squares) plots near the apex of the U-Pu-DME triangle, and at higher resolution is seen to be bounded by the U-Pu and U-DME lines. This pattern suggests that heavy-isotope lunar Xe could be a mixture of the meteoritic U-Xe, Pu-Xe, and DME-Xe components.

Subtracting the dominant U-Xe component (assuming ^{130}Xe ≡ 100% U-Xe) projects the lunar data field into the DME-Pu region of Fig. 1. Applied to individual temperature and acid-etch fractions of the listed samples [1,11-13], this yields the Fig. 2 pattern, where subtraction residuals at ^{132}Xe and ^{134}Xe have been divided by the ^{136}Xe residual. Spallation corrections, relatively small for these isotopes, assume the U-Xe ratio for nonspallogenic ^{124}Xe/^{130}Xe [14]. About 70% of the 89 total data points appear in Fig. 2; the rest scatter beyond the plot boundaries (20%) or cluster around "Air" (10%), denoting contamination. This data re-mapping inflates analytic error, particularly for Δ^{132}Xe where the measured and U-Xe ^{132}Xe/^{130}Xe ratios are similar. Resulting uncertainties are large enough —on average ≈ ±0.2 and ±0.1 in the horizontal and vertical respectively— that within them most of the points could lie on either the DME-Pu line or the locus ("mf") of linearly mass-fractionated SW-Xe. However the nominal data do appear to trend more closely along a DME-Pu correlation, and to truncate more or less abruptly near Pu-Xe on one end and DME-Xe on the other. The fuzzy ball of 14 ~"Pu-free" points within about ±0.25 of Δ^{132}Xe = 0 (all are within error of 0, and include at least one data point from each of the six samples) averages to the composition labeled SW in Figs. 2 and 3. In this representation it is indistinguishable from DME-Xe; consequently SW-Xe = U-Xe + DME-Xe.

Fig. 3 is a similar Δ-plot of spallation-corrected <u>total</u> Xe from the Fig. 2 samples and others (data references: #1,3 [1]; #2,4 [11]; #5 [13]; #6 [15]; #7 [12]; #8 [14]; #9 [2-5]; #10 [16]). The trend along the DME-Pu mixing line is now more apparent (although the eye is strongly influenced by the #9 breccia samples, not included in Fig. 2 but added here because their Pu-Xe component is directly documented [2-5]). Nominal single-sample uncertainties are again large enough to permit #1 and #3-7 to lie on the "mf" curve between SEP[frSW]-Xe and DME-Xe. However given the collective grouping of all these data around the DME-Pu line, even excluding the breccia samples, this does not seem very likely. The SEP[frSW] point in Figs. 2 and 3 was derived by fractionating SW-Xe by the square of the SW isotope mass ratios, as postulated for SEP-Xe by [1]. One problem with this SEP-Xe hypothesis is the separation in Fig. 3 between the calculated SEP[frSW] point and SEP compositions (I79 SEP and I71 SEP) deduced directly from acid-etch step data [1]. The I79 SEP datum could be understood within error as a mixture of SEP[frSW] with Pu-Xe —although it could also lie on the DME-Pu line— but the position of I71 SEP is harder to explain. At the pure solar-wind end of Fig. 3, one finds agreement, within error, of the proposed U-Xe + DME-Xe composition with those deduced from Fig. 2 (SW) and calculated by [1] from 71501 ilmenite data (I71 SW), and, interestingly, with <u>total</u> Xe in the one mineralogically unique sample in Fig. 3 —#8, the lunar metal. In summary: I propose that pure SW-Xe is a superposition of U and DME components, and that addition of lunar Pu-Xe dominates departures from this composition in lunar soils —without, however, necessarily requiring that SEP-Xe be completely absent.

REFERENCES. [1] Wieler R. & Baur H. (1994) *Meteoritics* (in press). [2] Drozd R. et al. (1972) *EPSL* **15**, 338 (500°C step). [3] Behrmann C. J. et al. (1973) *EPSL* **17**, 446. [4] Reynolds J. H. et al. (1974) *GCA* **38**, 401. [5] Bernatowicz T. J. et al. (1978) *Proc. LPSC 9*, 1571. [6] Pepin R. O. & Phinney D. (1978) Components of Xe in the solar system, unpublished preprint. [7] Takaoka N. (1972) *Mass Spectr.* **20**, 287. [8] Pepin R. O. (1991) *Icarus* **92**, 2. [9] Niemeyer S. & Zaikowski A. (1980) *EPSL* **48**, 335. [10] Michel Th. & Eugster O. (1994) *Meteoritics* (in press). [11] Frick U. et al. (1988) *Proc. LPSC 18*, 87. [12] Rider P. E. & Pepin R. O. (1994) *GCA* (submitted). [13] Rider P. E. (in preparation). [14] Becker R. H. & Pepin R. O. (1994), *Meteoritics* (submitted). [15] Becker R. H. & Pepin R. O. (1989) *GCA* **53**, 1135. [16] Kim J. S. & Marti K. (1992) *Proc. LPSC 22*, 145.

LUNAR AND SOLAR WIND XENON: Pepin R. O.

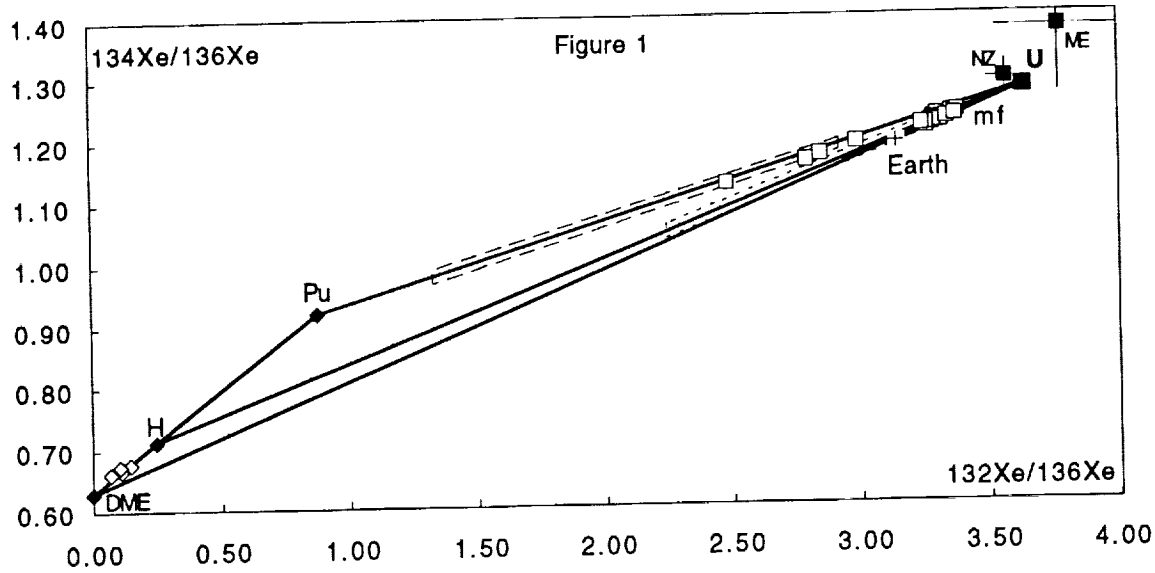

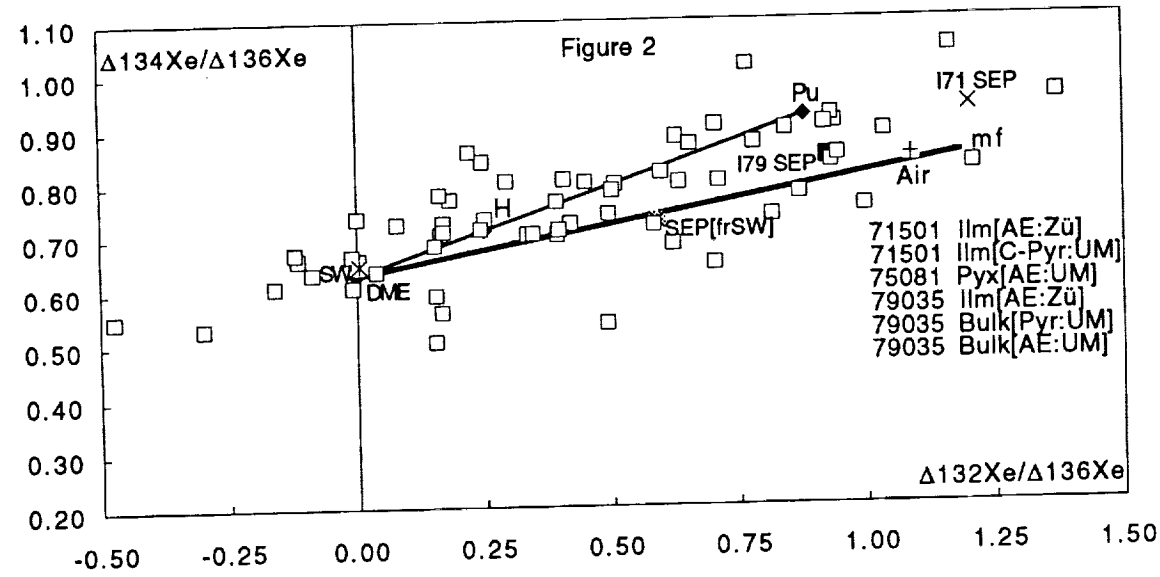

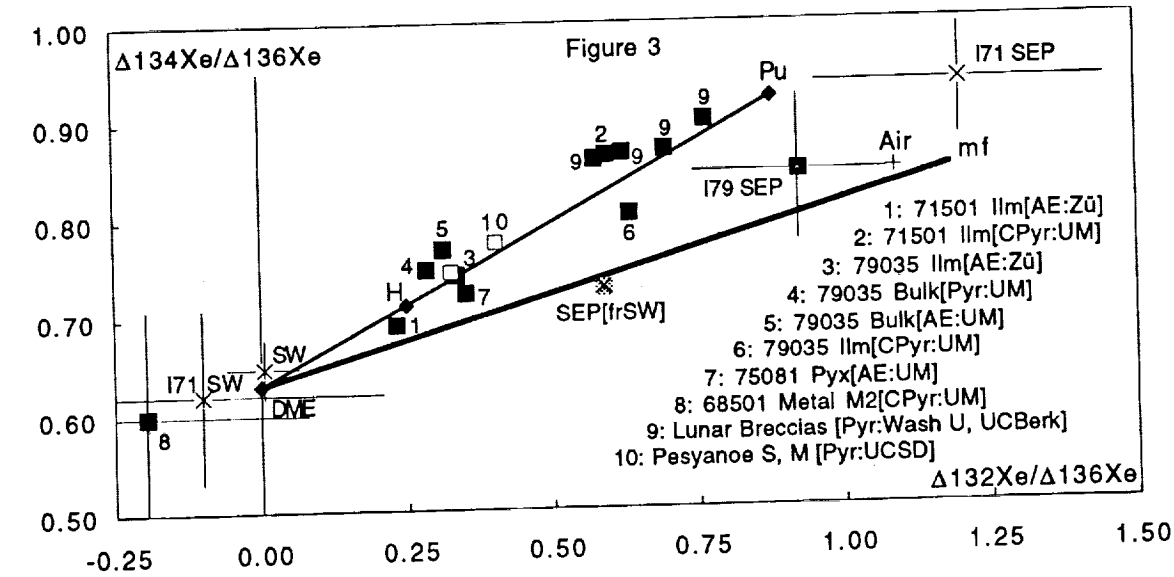

THE THICK FESTOON FLOW AND ADJACENT DARK FLOW, OVDA REGIO, VENUS; *J.L. Permenter* and *R.L. Nusbaum*, Department of Geology, College of Charleston, Charleston, SC 29424

SUMMARY: The thick flow in the Ovda Regio is one of two festoon flows identified on Venus [1,2,3]. From the general appearance of the festoon flow in the Ovda Regio and a dark flow adjacent to the south, it has been postulated that the two flows may be the result of a single volcanic episode, although a source vent was not identified [4]. The thickness of the marginal flow lobes of the festoon flow is suggestive of possible evolved compositions on Venus [5]. We investigated cycle 1 and cycle 2 SAR images of the flows to determine their relative age, source areas, and emplacement histories. Thickness estimates were combined with radar data to calculate the yield strengths and Bingham viscosities of the flows. The results of our study indicate the following: 1) the radar-bright festoon flow was emplaced continuously, from a source near its center; 2) the dark flow is younger than the festoon flow, thick, and originated from a separate source within the dark flow area; 3) proposed sources for both flows are topographic depressions suggesting collapse following magma withdrawal; and 4) yield strengths and Bingham viscosities estimated for the festoon flow are comparable to those of terrestrial silicic lava flows, the Unusual Volcano (Mahuea Tholus) flows [2,3], and some of the 145 steep-sided domes identified on the venusian surface [5].

INTRODUCTION: The radar-bright, festoon flow centered at 6°S 95.5°E in the Ovda Regio has well defined boundaries with the surrounding tessera. Stratigraphic relations with the dark flow adjacent to the south are not apparent, however [4]. The thickness of the festoon flow is unusual on Venus, and suggestive of an evolved composition [5]. We investigated cycle 1 and cycle 2 SAR images of the flows to determine their relative age, source areas, and episodicity of emplacement. Thickness estimates were combined with radar data to calculate the yield strengths and Bingham viscosities of the flows for comparison to other venusian flows and terrestrial flows.

RESULTS AND DISCUSSION: Although irregular in outline, we estimated the aerial extents of the the bright festoon flow and the dark flow to be 150 X 300 km and 75 X 150 km, respectively. Both flows are traversed by NW-SE and NE-SW trending fracture systems which are parallel to fractures within the tessera. The festoon flow is radar bright with prominent flow ridges across much of its surface. Within the body of the festoon flow are lava 'windows' which expose older tessera. These 'windows' have rounded to lobate interior margins suggesting that they are primary features resulting from viscous lava flow. The margins of the festoon flow adjacent to tessera are lobate and readily distinguished from adjacent tessera. Some of the marginal lobes were apparently channeled into lower elevation tessera troughs. The marginal lobe thicknesses and 'window' depths are summarized in Table 1. As we had little success with parallax measurements over the rough terrain, we used a

Table 1. Dimensions of the Flows

Area of flows: Festoon flow	45,000 km^2
Dark flow	9,400 km^2
Festoon flow thickness estimates	
Marginal lobes	52-108 m (n=12)
Flow interior 'windows'	52-144 m (n=12)
Dark flow thickness estimates	
Marginal lobes	69-86 m (n=4)
Festoon flow volume estimate	4,545 km^3

single-look method [6] which assumes symmetry of features being measured. The method was applied to individual marginal lobes and 'windows' as a check of symmetry, using paired left-looking (incidence angle = 43.7°) and right-looking (incidence angle =24.8°) SAR images.

Vectors constructed perpendicular to festoon flow ridges indicate that the flow was emplaced during a single continuous episode, from a source area near the center of the flow. A younger, thick, radar-bright flow is superimposed on the festoon flow near its southern margin. The younger bright flow originated from the dark flow area. The gradational contact between the younger bright flow and the dark flow appears to be elevation dependent, suggesting that the dark flow and the younger bright flow are the same unit. Both proposed sources of the flows are topographic depressions, suggesting collapse after magma withdrawal

Radiothermal emissivity of the dark flow is greater than that of the older festoon flow (Figure 1, Table 2) despite the overall greater elevation of the dark flow [4]. The emissivity increase begins within the area labeled as festoon flow, at approximately the contact with the younger festoon flow (Fig. 1). Most of the festoon and the dark flows are well above the critical elevation for the Ovda Regio, which suggests that the dark flow may contain a large component of unweathered rock [7]. Emissivity and corrected reflectivity mean values for the 'unweathered' dark flow were used to estimate bulk densities of the flows: 3,010 kg/m^3 and 2,550 kg/m^3 , respectively. Both values are within the range expected for mafic to intermediate terrestrial glasses [8].

Table 2. Radar Properties of Units

	Festoon flow	Dark flow	Tessera
Emissivity	0.42±0.06	0.78±0.04	0.37±0.02
Corrected reflectivity	0.46+0.07	0.16+0.05	0.45+0.13

Thickness estimates of the festoon flow, and younger bright flow (and thus, the dark flow) are indicative of viscous lava emplacement. The argument is enhanced by the abundance of flow ridges, particularly for the festoon flow, which have a mean wavelength of 640 m. In an attempt to quantify lava rheology, we estimated yield strength and Bingham viscosity using the bulk density estimates derived in the preceding paragraph. Due to irregular slopes of the 'basement' tessera, we used the slope independent equation of Orowan [9] to estimate the yield strength, which ranges from 1.3 X 10^4 to 1.84 X 10^5 Pa. Viscosity estimates using the equation of Moore and Ackerman [10] range from 2.0 X 10^7 to 2.6 X 10^9 Pa s. These are comparable to those of terrestrial silicic lava flows, the Mahuea Tholus flows [2,3], and some of the 145 steep-sided domes identified on the venusian surface [5]. Based on rheology estimates alone, however, mafic compositions for the thick Ovda flows cannot be ruled out.

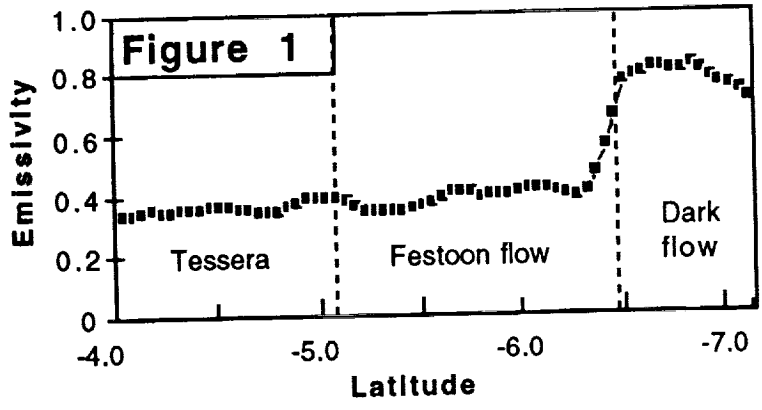

[1] Head, J.W., et al., *J. Geophys. Res.*, **97**, 13,153-13,198, 1992. [2] Moore, H.J., et al., *J. Geophys. Res.*, **97**, 13,479-13,494, 1992. [3] Moore, H.J., et al., LPSC, **XXIV**, 1003. [4] Pettengill G.H., et al., *J. Geophys. Res.*, **97**, 13,091-13,102, 1992. [5] Pavari B., et al., *J. Geophys. Res.*, **97**, 13,445-13,478, 1992.

[6] Leberal, F. et al., *Photog. Engr. Rem. Sens.* **57**, 1561, 1991. [7] Klose, K.B., et al., *J. Geophys. Res.*, **97**, 16.353-16,369, 1992. [8] Carmichael, I.S.E., et al., Igneous Petrology, 739 p., 1974. [9] Orowan, E., *J. Glaciol.*, **1**, 231, 1949. [10] Moore, H.J. and Ackerman, J.A., LPSC, *NASA Tech. Memo*, **TM-4130**, 387-389, 1989. Acknowledgement: This research was funded by grants from the NASA-JOVE Program and the South Carolina Space Grant Consortium.

LAMELLAR OLIVINE IN THE DIVNOE ACHONDRITE: EPMA AND TEM STUDIES Michail I. Petaev[1] and Adrian J. Brearley[2] 1 - Harvard-Smithsonian Center for Astrophysics, 60 Garden St., Cambridge, MA 02138; 2 - Institute of Meteoritics, University of New Mexico, Albuquerque, NM 87131

Abstract. EPMA, optical microscopy and TEM studies of lamellar olivine in Divnoe have revealed several different types of lamellar structure. The lamellar structure seen in BSE images is caused by minor variations in Fe and Mg contents between adjacent lamellae. The lamellae seen in TEM images are caused by linear arrays of dislocations parallel to the olivine c-axis which define the lamellar structure seen in transmitted light. The two types of lamellae have the same orientation within grains studied but do not correspond to each other.

The Divnoe meteorite is a granoblastic olivine-rich primitive achondrite whose textural and mineralogical characteristics suggest extensive recrystallization and slow cooling in the temperature range from ~1000 to ~500°C and lower [1]. In spite of this, in back-scattered electron (BSE) images many, if not all, olivine grains show a lamellar appearance caused by minor chemical variations [1,2] in Fe, Mg and Mn contents between adjacent lamellae. These variations are superimposed on a large-scale compositional zoning in some olivine grains. In three grains studied by EPMA [2] the differences between Fe-richest and Fe-poorest lamellae are found to be 2.7, 3.0 and 3.2 mol.% Fa, with a strong positive correlation between Fe and Mn, which was only the minor element present in significant (> 0.05 wt.%) concentrations. Several mechanisms have been suggested to explain the lamellar structure of olivine, but none of them is satisfactory [1]. In order to understand the nature of chemical variations in lamellar olivines we are carrying out EPMA and TEM studies of other lamellar olivine grains.

Eight grains of lamellar olivine studied here by EPMA and optical microscopy display slightly different structures shown in Fig. 1. An 'ordinary' lamellar appearance in BSE images, where alternating light (Fe-rich) and dark (Fe-poor) lamellae up to some tens of μm in thickness form a regular pattern (Fig. 1A), has been found in many grains, but only grain #1 displays a similar structure in transmitted light (Fig. 1B). Some grains are composed of diffuse lighter and darker areas which contain bright (Fe-enriched) disk-shaped lamellae decorated by dark irregular domains (Fig. 1C). The lamellae have a system of cracks perpendicular to their elongation direction. While some cracks continue to the darker groundmass, they seem to be a distinctive feature of the Fe-rich lamellae in many grains. One of the grains studied has a spotty structure (Fig. 1D) instead of a lamellar one, with some arrangement of light and dark domains. The arrangement may be caused by a crossing of lamellae developing in different directions. Several similar grains has been found in Divnoe earlier [2].

In spite of the structural differences between the grains studied, the compositional variations between lamellae (Fig. 2) display similar patterns with the strong correlation between Fe and Mn. While the compositional ranges of Fe-poor and Fe-rich lamellae overlap, the differences between lamellae richest and poorest in Fe are quite similar (Table 1), suggestive of their formation due to an equilibrium process. The more restricted compositional differences between lamellae within grains #5A and # 6A, which have thinner lamellae, may be caused by contamination of the analysis with the adjacent lamellae. Both the ranges of chemical variations and Fe-Mn correlations are almost the same as those found earlier [2].

Only grain #1 has been studied by TEM so far. It contains an extremely high density of dislocations, which are typically concentrated in very narrow bands parallel to c-axis. These linear arrays of dislocations are rarely continuous and the maximum length observed is of the order of few microns, parallel to c. It is these linear arrays of dislocations which define the lamellar microstructure of the olivine observed optically (Fig. 1B). Despite the linear arrays of dislocations, there are few regions within the olivine where a clear interface has developed as a result of coalescence of dislocations. The olivine lattice in most cases is continuous across the region where the dislocation density is high, but is obviously highly strained. The thickness of the "lamellae" defined by the linear arrays of dislocations is typically of the order of 1 μm, which is much less than the compositional lamellae observed by BSE imaging. It is clear that the arrays of dislocation do not correspond to interfaces between Fe-rich and Fe-poor lamellae. EDS analyses in the TEM confirm that the adjacent lamellae defined by the linear arrays of dislocations have identical compositions. However, the compositions of olivine measured in different places within the grain #1 vary from 24.1 to 27.6 mol.% Fa, which is practically identical to the range observed in EPMA study (Table 1). The nature of the interfaces between compositional lamellae requires further investigation on the TEM scale.

The question now is how this type of microstructure has developed and how it relates to the compositional lamellae. Among several mechanisms discussed by [1], shock and static deformation may be excluded since an exsolved pyroxene adjacent to the grain #1 displays extremely low dislocation densities. Another possibility is that the dislocations are the result of an exsolution process where strain energy in the olivine is generated by the formation of two compositionally distinct lamellae which have different molar volumes. This is in qualitative agreement with the calculated low-temperature miscibility gap in ferromagnesian olivine solid solutions [3], but the volume difference (0.1 -0.2 %) for lamellae only 2 mol.% Fa different does not seem high enough to cause such a high degree of strain energy. Further studies are in progress of other grains in Divnoe to elucidate the origin of these unusual microstructures.

References: [1] Petaev M.I. et al. (1994) *Meteoritics* **29**, in press. [2] Petaev M.I. (1993) *LPSC XXIV*, 1127. [3] Sack R.O. and Ghiorso M.S. (1989) *Contrib. Miner. Petrol.* **102**, 41

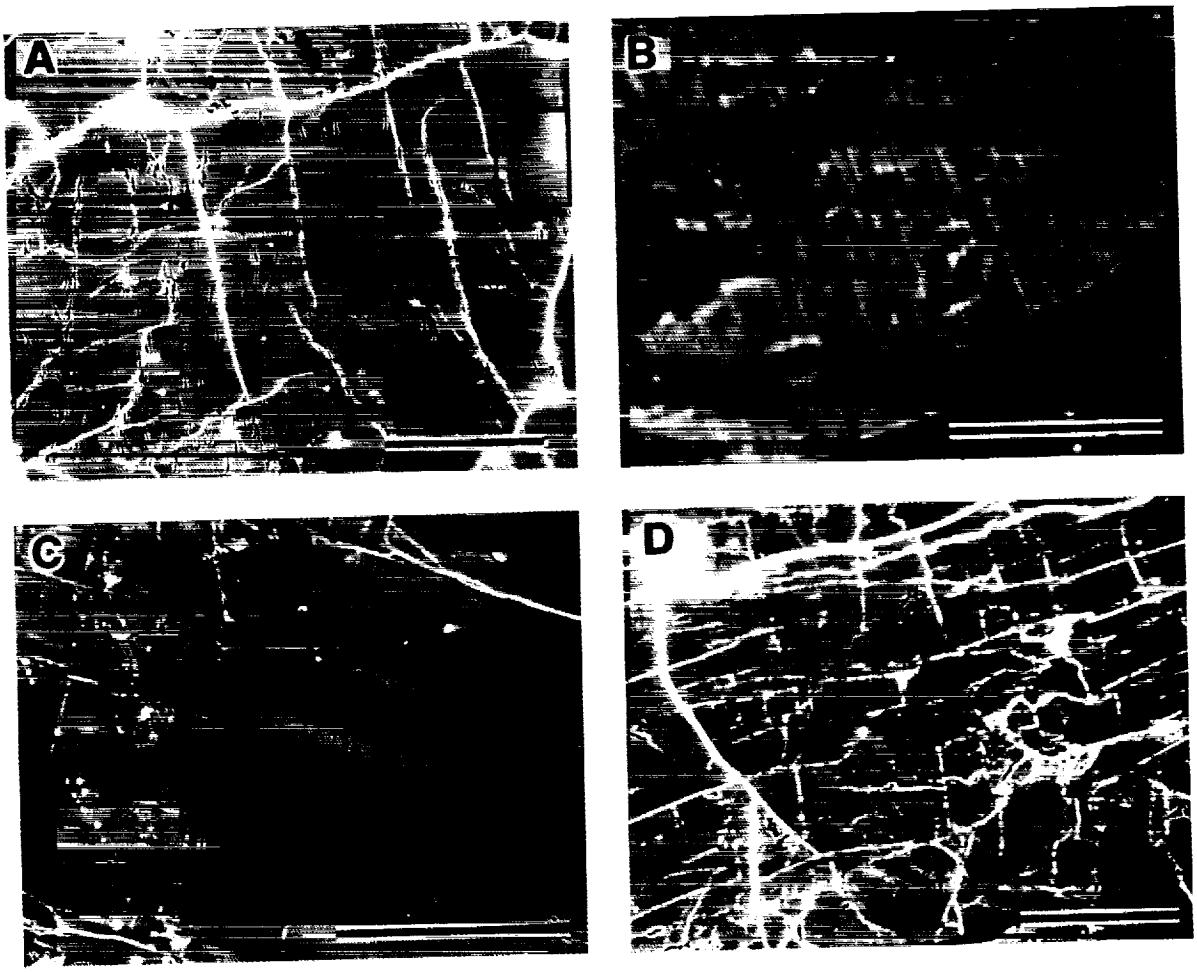

Fig. 1. Microstructures of olivine grains. **A** - "Ordinary" lamellar structure in the grain #1, BSE image. Scale bar 100 μm. Insert is shown in Fig. 1B. **B** - Lamellar structure in the grain #1, transmitted light. Scale bar 20 μm. **C** - Disk-shaped lamellae in the grain #6, BSE image. Scale bar 100 μm. **D** - Spotty structure in the grain #11, BSE image. Scale bar 50 μm.

Table 1. *Chemical variations within lamellar olivines (Fa, mol.%).*

Grain	Fe-poor	Fe-rich	Range
#1	24.6	27.9	3.3
#3	25.6	28.9	3.3
#5	22.8	27.1	4.3
#5A	24.3	28.3	4.0
#5B	25.7	27.2	2.5
#6	25.3	29.1	3.8
#6A	25.2	27.3	2.1
#11	24.2	26.9	2.7

Fig. 2. Fe - Mn correlation within lamellar olivines.

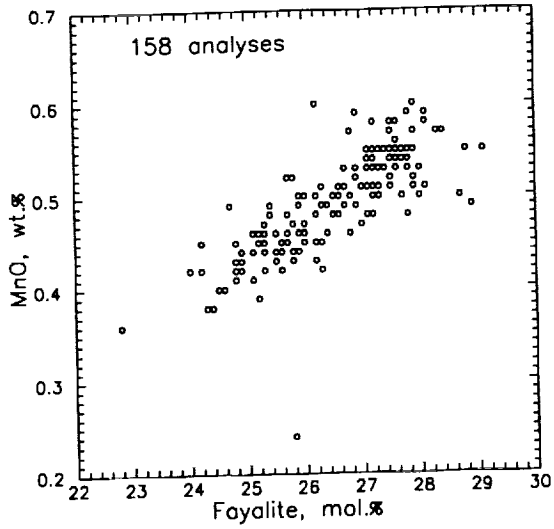

NUMERICAL MODEL OF A GENETIC LINK BETWEEN ACAPULCO AND Y791493 PRIMITIVE ACHONDRITES. I: PHASE EQUILIBRIA AND MAJOR ELEMENT CONSTRAINTS Mikhail I. Petaev[1,2], Alexei A. Ariskin[1], John A. Wood[2]; 1-Vernadsky Institute of Geochemistry and Analytical Chemistry, Russian Academy of Sciences, 19 Kosygin St., Moscow 117975, Russia; 2 -Harvard-Smithsonian Center for Astrophysics, 60 Garden St., Cambridge, MA 02138, USA

Abstract. The Y791493 lodranite can have been produced by partial melting of Acapulco precursor material, followed by removal of ~85% of the liquid (formed by ~6% melting of the precursor) and addition of ~3 wt.% metal. The residuum may then have been further heated and melted to produce 7-10% interstitial liquid, which crystallized *in situ* without further loss.

The acapulcoite-lodranite group of meteorites appear to have been formed in the same parent body [1], which experienced a range of degrees of partial melting. Acapulcoites represent precursor material, and lodranites are residua after partial melting [*e.g.*, 1,2]. To quantify this process, we numerically modeled the relationship between the two members of this group that have been best characterized chemically and mineralogically: Acapulco itself [4], and the lodranite Y791493 [5]. The Meteorite Melting Model computer program of [3] was used to calculate the relationship.

Since Acapulco was assumed to be the precursor material in the system modeled, a series of 1-atm equilibrium melting calculations were carried out for degrees of melting >5 mol.%, at 0.5 mol.% increments, and for values of fO_2 between 1.5 to 2.5 log units below the iron-wüstite (IW) buffer, to estimate the equilibrium fO_2 value in the system. The bulk metal content of Acapulco and the Fo content of its olivine (Table 1, column *ACA*) were found to agree best with the model at $\log(fO_2)$ = IW-2.4. The sequence of mineral assemblages left in the residue as melting proceeds was found to be: Ol+Met+Opx+Pl±Cpx (T=1122°C; 6.1 wt.% melt) → Ol+Met+Opx (T=1140°C; 8.1% melt) → Ol+Met (T=1346°C; 22.6% melt) → Met (T=1686°C; 88.8% melt).

The simplest way to produce a lodranite from an acapulcoite would be to completely segregate partial melt from a residue. We found that the removal of 6.1 wt.% of Al,Na-rich partial melt formed at 1122°C (Table 1, column M_{part}) leaves a residue whose bulk chemistry and mineralogy (Table 1, column R_{part}) are both quite similar to those of the Y791493 lodranite (Table 1, column *Y93*), except that the latter is depleted in Al and Na compared to the model residue. The discrepancy in these elements could be reconciled if a small amount of the partial melt (~15% of the melt) was retained within the residue. The composition of the crystal-melt mixture left as a residue (Table 1, column R_{cont}) is close to that of Y791493 lodranite (Table 1, column *Y93*), with the model residuum showing a minor depletion in Fe and enrichment in SiO_2. A final adjustment between the compositions of 'model lodranite' (to produce column *mLod*, Table 1) and Y791493 lodranite could be made by assuming the addition of ~3 wt.% metal (recalculated to 3.5 wt/% FeO) to the crystal-melt mixture R_{cont}.

While bulk mineralogies of the 'model lodranite' and Y791493 are in very good agreement with one other, additional melting of the 'model lodranite' at temperatures above 1122°C seems to be required in order to reproduce the compositions of Y791493 Ol and Opx. The degree of further partial melting required depends upon the criterion chosen to estimate it. Such a criterion should take into consideration the strong relationship between total metal content, compositions of silicates and the melting degree. Our calculations have revealed the Fe/Mn ratio in olivine seems to be the most sensitive indicator to monitor variations of the parameters listed above. This ratio is found to increase from 15.1 to 41.0 as melting degree increases from 5 wt.% to 85.6%, when olivine dissolves. If the Fe/Mn ratio of mean Y791493 olivine is the criterion (Table 1), then the final phase assemblage in the 'model lodranite' source region (Table 1, column R_{mLod}) before it starts to cool should contain ~10 wt.% melt (Table 1, column M_{mLod}) and slightly more Ol and less Opx

than is now in Y791493. If the modal abundance or Mg/(Mg+Fe) of Y791493 orthopyroxene are used to estimate the final degree of melting in the 'model Iodranite' source region, this could vary from ~1 wt.% (no additional melting compared to *mLod* phase composition) to ~7 %. The effect of crystallization of this melt, retained in the source region as an interstitial liquid, would be to decrease Ol content by ~2 wt.% and add ~4.5% Opx, 3.5% Cpx, and 3% Pl to the mineral assemblage R_{mLod}, improving the agreement in mineralogical composition between the model and Y791493. For this reason, Fe/Mn in olivine seems the preferable criterion to use in modelling.

References: [1] McCoy T.J. et al. (1993) *LPSC XXIV*, 945. [2] Takeda H. et al. (1992) *Proc. Japan Acad. Sci.* **68B**, 115. [3] Ariskin A.A. and Petaev M.I. (1994) *this volume*. [4] Palme H. et al. (1981) *GCA* **45**, 727. [5] Nagahara H. and Ozawa K. (1986) *Mem. Natl. Inst. Polar Res.* **41**, 181.

Table 1. Chemical, mineral and phase compositions of primitive achondrites and modeled melting products (normalized to 100 wt.%)

Comp	Acapulco bulk [4]	Equilibrium melting of ***ACA*** at 1122°C			'Model' Iodranite	Equilibrium melting of ***mLod*** at 1340°C		Y791493 bulk [5]
	ACA[§]	M_{part}[#]	R_{part}[#]	R_{cont}[#]	***mLod***	M_{mLod}	R_{mLod}	***Y93***[§]
SiO_2	38.58	48.48	37.93	38.03	**36.75**	60.81	34.02	**35.94**
TiO_2	0.07	0.71	0.03	0.03	**0.03**	0.21	0.01	**0.05**
Al_2O_3	2.11	24.37	0.66	0.89	**0.86**	7.52	0.10	**0.93**
FeO*	26.33	2.75	28.07	27.83	**30.27**	8.22	32.77	**30.43**
MnO	0.40	0.18	0.41	0.41	**0.40**	0.42	0.40	**0.43**
MgO	29.46	3.68	31.13	31.13	**29.83**	9.59	32.13	**30.41**
CaO	1.98	7.31	1.63	1.63	**1.63**	10.96	0.57	**1.58**
Na_2O	0.88	12.52	0.12	0.12	**0.23**	2.26	>0.01	**0.22**
Phase Assemblages								
Melt, wt.%		6.1		~1	~1	10.2		
Ol. wt.%	25.6		38.5	40.6	39.3		46.8	40-42
Fo	*88.1*		*87.9*	*87.9*	*87.9*		*87.8*	*87-91*
Fe/Mn	*19.6*		*16.6*	*16.6*	*16.6*		*20.2*	*20.4*
Opx, wt.%	35.8		33.3	35.1	34		20.3	34-37
En	*86.2*		*84.5*	*84.5*	*84.5*		*84.3*	*85-86*
Pl, wt.%	9.4		1.5	1.6	1.5			1-5
Met, wt.%	19.1		20.6	21.7	24.1		22.7	17-22

[§] Mineral modes and chemical compositions are recalculated on a chromite, troilite and phosphate-free basis

[#] ***R*** and ***M*** denote Residues and partial Melt compositions (for subscripts see text) : $R_{cont} = R_{part} + 0.92\% M_{part}$; ***mLod*** = R_{cont} + 3 wt.% Fe°

*All Fe as FeO

NUMERICAL MODEL OF A GENETIC LINK BETWEEN THE ACAPULCO AND Y791493 PRIMITIVE ACHONDRITES. II: IMPLICATIONS TO THE ORIGIN OF ACAPULCOITES AND LODRANITES Mikhail I. Petaev[1,2], Alexei A. Ariskin[1], John A. Wood[2]; 1 - Vernadsky Institute of Geochemistry and Analytical Chemistry, Russian Academy of Sciences, 19 Kosygin St., Moscow 117975, Russia; 2 - Harvard-Smithsonian Center for Astrophysics, 60 Garden St., Cambridge, MA 02138, USA

Abstract. Acapulcoites and lodranites could have formed from a common precursor by partial melting up to ~15 % of it. The mineralogical and chemical properties of acapulcoites point to retention of the partial melt in its source region(s), while those of lodranites require removal of the earliest portions of partial melt. In the system modeled by [1], at melting degrees less than ~20%, Mg/(Mg+Fe) ratios in residual olivine and orthopyroxene coexisting with metal *decrease* as the melting proceeds, allowing lodranites to be formed as residua from the partial melting of more magnesian acapulcoites.

The thermodynamic model studied by [1] allows lodranites to be produced from Acapulco by partial melting their source region, followed by the removal of a portion of the melt and addition of small amounts of Fe metal. Apparently the acapulcoite/lodranite parent body contained a partially molten region(s), in which melt and metal moved in opposite directions. Textural and petrofabric studies of the Y791493 lodranite suggest it was formed "in the presence of strong magmatic laminar flow" [2]. The degree of melting required is >6 wt.%, but more likely ~15 %. The latter value is required to explain the Fe/Mn and Mg/(Mg+Fe) ratios of Acapulco olivines. To produce the Y791493 lodranite from the same precursor material, a more complicated history is required (Table 1 in [1]): primary residue (*mLod*) formed by removal of the first ~5% of melt (M_{part}) then needs to be melted by an additional ~10% (M_{mLod}). For the Acapulco composition, the calculated temperature at which 15% partial melting is achieved (1257°C) is close to the temperatures estimated from oxygen isotope thermometry (1300-1400°C, [3]) and metal compositions (1400-1500°C, [4]). The model requires that acapulcoite and lodranite source regions were melted to similar degrees, but the former retained all melt generated within the residue while the latter lost ~85% of the first melt formed (which comprised <~6 wt.% of the total mass of precursor material). Later melt formed in the lodranite source regions was retained with the residue, and ultimately crystallized there.

What happened to the partial melt that was lost from the lodranite source regions? These incompatible-element-rich melts could have been pyroclastically ejected from the parent body altogether, forming Na, Al-rich chondrules or other objects in space [5], or they could have migrated to undepleted precursor material, ending up in the acapulcoites themselves. The enrichment of Acapulco and ALH81261 in REE, especially LREE [6-8], relative to chondrites could be achieved by the addition of small amounts of a melt enriched in incompatible elements. The addition required would not significantly change the bulk mineralogy of acapulcoites, except by increasing their plagioclase contents (as has occurred in the ALH78230, EET84302 and ALH81261 acapulcoites [9-12]). [13] suggested partial melts were lost from lodranites by explosive volcanism. This mechanism could work at low degrees of partial melting, until volatiles (mainly S) were exhausted from the source region. Fe_{sulf} has not been included in the model [1]; if sulfur were removed as a gas rather than as a constituent of Fe-Ni-S-rich melt, the loss of ~1.8 wt.% S from the source region would be equivalent to the addition of ~3 wt.% metal to the residue, which is required by the model of [1]. Thus the removal of S-rich gas or fluid along with silicate melt can be seen as an alternative mechanism of differentiation in the lodranite source region(s).

One of the most important results of our model calculations is the discovery that at degrees of melting <20 wt. %, Mg/(Fe+Mg) in olivine and orthopyroxene equilibrated with melt and metal in the source region *decreases* as melting proceeds (Fig. 1). This resolves an apparent discrepancy between the silicate mineral chemistries of lodranites and acapulcoites [14]: lodranites with Mg/(Mg+Fe) ratios lower than those of acapulcoites can be the solid residua left after partial melting of the latter. Our calculations also suggest that the composition of olivine - *i.e.*, its Fe/Mn and Mg/(Mg+Fe) ratios - are an important source of information about the igneous history of acapulcoites and lodranites, and one that does not depend upon the sections studied petrographically being highly representative. The olivine compositions of both meteorites modeled

plot along the calculated melting curve in Fig. 1, indicating that these meteorites could represent different stages of partial melting of the same precursor material. The importance of the Fe/Mn ratio in silicates coexisting with metal as an indicator of redox conditions and metal/silicate fractionation in achondrite source regions has also been noted by [15,16].

Application of our model to other members of the acapulcoite/lodranite group is limited by the scarcity and incompleteness of published data. The few data on olivine chemistry shown in Fig. 1 suggest that both the degree of melting and fO_2 might vary slightly within the source region(s). Minor differences between calculated and observed chemical and mineral compositions may be attributable to small variations in fO_2 and/or melting degree, but this cannot be tested until more members of the acapulcoite/lodranite group are included into the model. Only samples having thoroughly characterized chemical and mineral compositions can be included in our model calculation, in order to compare the model with 'nature.' The one meteorite that meets these criteria is the acapulcoite Y74063 [17]. The bulk analysis of Lodran [18] does not include SiO_2, which is extremely important in model calculations. While the bulk chemical composition of Y77081 is available [19], the lack of data on mineral chemistry makes it difficult if not impossible to compare the modeled and real mineral assemblages.

References: [1] Petaev M.I. et al. (1994), *this volume*. [2] Nagahara H. and Ozawa K. (1986) *Mem. Natl. Inst. Polar Res.* **41**, 181. [3] Mayeda T.K. and Clayton R.N. (1980) *Proc. LPSC 11th*, 1145. [4] Zipfel J. et al (1992) *LPSC XXIII*, 1585. . [5] Bischoff A. and Keil K. (1984) *GCA* **48**, 693. [6] Palme H. et al. (1981) *GCA* **45**, 727 [7] Davis A. et al. (1993) *LPSC XXIV*, 375. [8] Morikawa N. and Nakamura N. (1993) *18th Symp. Antarc. Meteorites*, 38. [9] Hiroi T. and Takeda H. (1991) *Proc. NIPR Symp. Antarc. Meteorites* **4**, 163. [10] Takeda H. et al. (1992) *Proc. Japan Acad. Sci.* **68B**, 115. [11] McCoy T.J. et al. (1993) *LPSC XXIV*, 945. [12] Yugami K. et al. (1993) *18th Symp. Antarc. Meteorites*, 34. [13] McCoy T.J. et al. (1992) *Meteoritics* **27**, 258. [14] McCoy T.J. et al. (1993) *Meteoritics* **28**, 393. [15] Delaney J.S. and Boesenberg J.S. (1993) *LPSC XXIV*, 391. [16] Walker D. and Grove T. (1993) *Meteoritics* **28**, 629. [17] Yanai K. and Kojima H. (1991) *Proc. NIPR Symp. Antarc. Meteorites* **4**, 118. [18] Fukuoka T. et al. (1978) *LPSC IX*, 356. [19] Haramura H. et al. (1983) *Mem. Natl. Inst. Polar Res.* **30**, 109. [20] Bild R.W. and Wasson J.T. (1976) *Miner. Mag.* **40**, 721

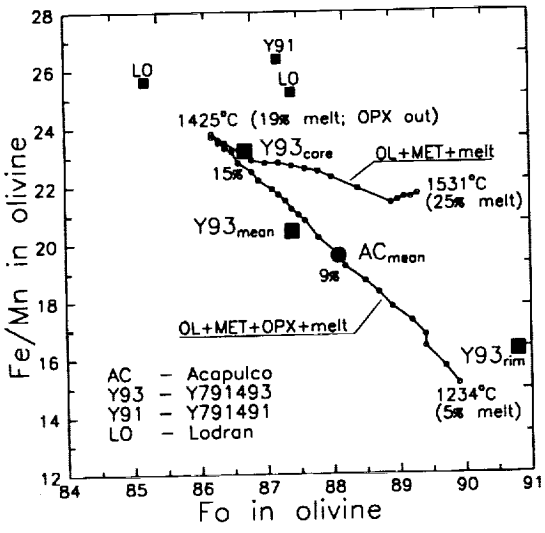

Fig. 1. Variations in olivine composition during partial melting of 'model' lodranite [1]. Open circles are calculated values, with 0.5% melting degree increments. Filled circle: Acapulco olivine [6]; filled squares: lodranites - Y791493[2], Lodran [9,20] and Y791491 [9]. As melting proceeds, Fo content decreases, and Fe/Mn ratio increases, until orthopyroxene is exhausted in the residue; after that the trend reverses. Data for meteorites included in the model (Acapulco and Y791493) plot along the calculated line, suggesting that olivine compositions were established during the melting stage of their evolution. Deviation of the most magnesian rim compositions from the calculated line may be caused by subsolidus reequilibration [2]. Deviations of other lodranites from the calculated trend may result from variation of the degree of melting and/or oxygen fugacity in the lodranite source region(s).

Mg AND Ti PARTITION COEFFICIENTS FOR ANORTHITE-CAI LIQUID: DEPENDENCE ON OXYGEN FUGACITY AND MELT COMPOSITION

Mark T. Peters, Elizabeth Shaffer, and Donald S. Burnett, Division of Geological and Planetary Sciences, Caltech, Pasadena, CA 91125.

Type B CAIs should be ideal for studying trace element partitioning during closed system fractional crystallization; however, despite an abundance of experimental and analytical data, (e.g. 1-3) serious inconsistencies are present. A particularly glaring discrepancy (Fig. 1) involves the Mg and Ti concentrations in CAI anorthite [3]. The Figure 1 calculations assume that, at the low oxygen fugacities (f_{O2}) relevant for CAIs, trivalent Ti substitutes for Ca, but with a very small partition coefficient (D_3=0) following the ionic radius trend set by REE Ds. The fractional crystallization paths, as a function of crystallization (F), fail to describe the observed Mg and Ti abundances. However, if Ti^{3+} can substitute in the tetrahedral site, larger values of D_3 might be possible. Models in which D_3=D_4 for Ti [3] give anorthite concentrations of Ti which are about 4 times higher than those shown on Figure 1, allowing for possible agreement with observations for F>90%. We have conducted a series of partitioning experiments between anorthite and Type B liquid over a range of oxygen fugacity to determine D_3 in order to further constrain models for Type B crystallization. We have also determined Mg partition coefficients in the same experiments. This work also provides information on the dependence of Mg and Ti partitioning on liquid composition, which, in turn, allows assessment of substitution mechanisms of Mg and Ti in anorthite.

Experimental Methods Experiments were done with the source material from which the composition of [3] was prepared. Mechanical mixtures of the component oxides were homogenized to provide a well-defined composition to assess f_{O2} effects on Ti partitioning (H series runs), while some material was not homogenized, producing a range of compositions to assess the liquid composition dependence of partitioning (UH series runs). The thermal history for crystal growth by fractional crystallization consisted of an initial 2 hour hold 30°C above the liquidus, step cooling to 10°C below the liquidus where the charge was held for 24 hours, followed by cooling 2-5°C/hour an additional 60°C below the liquidus with a final 12 hour hold. The experiments were conducted in air using Pt loops or at low f_{O2} using graphite capsules. The low f_{O2} runs were performed in an atmosphere of CO ($f_{O2} \sim 10^{-17}$ atm. at 1350°C) or CO diluted with Ar ($f_{O2} \sim 10^{-19}$ atm.), both of which should approximate conditions of CAI genesis [4]. Quenched low f_{O2} runs were purple, consistent with the presence of Ti^{3+}, which has been verified by preliminary electron spin resonance data; however, the exact determination of Ti^{3+}/Ti^{4+} in the experiments awaits further measurements now in progress. Mg and Ti abundances in anorthite and glass were determined by electron microprobe analysis using operating conditions optimized for acceptable counting statistics.

Results and Discussion The Mg and Ti partition coefficients are presented in Figure 2. Each data point is the average for a single crystal. It is apparent from the H runs that D_{Ti} does not vary systematically with f_{O2}. A range of D_{Ti} from 0.028 to 0.038 is observed in the air experiment (all Ti as Ti^{4+}). The D_{Ti} for the low f_{O2} runs (mixture of Ti^{3+} and Ti^{4+}) are within this range. Assuming that a significant fraction of the Ti is trivalent in our low f_{O2} experiments, this lack of variation suggests that Ti^{3+} does in fact enter the anorthite structure and D_3 is not equal to zero, qualitatively consistent with the D_3=D_4 model of [3].

There are large variations in D_{Mg} (factor of 4) and D_{Ti} (factor of 2), particularly in the UH series runs; moreover, there is a negative correlation of D_{Mg} and D_{Ti}. The partition coefficients exhibit a strong dependence on glass composition (SiO_2 and Al_2O_3 in particular) with D_{Mg} positively correlated with SiO_2 and negatively correlated with Al_2O_3, while D_{Ti} shows the opposite trends. It is well-known that partition coefficients can vary with melt composition, but the anticorrelation of Mg and Ti differs from the results of previous liquid-liquid partitioning studies [5]. The reason for this difference is unclear. Regardless, the dependence of D_{Mg} and D_{Ti} on melt composition, along with the new data on D_{Ti} at a range of f_{O2}, can now be utilized to further improve models for CAI genesis.

In addition, the dependence on glass composition can be used to assess possible substitution mechanisms of Mg and Ti in anorthite using the approach of Longhi et al. [6]. Their thermodynamic methodology suggests that a partition coefficient is proportional to an activity product of oxide components in the melt given by the proposed substitution mechanism (e.g., $CaMgSi_3O_8$ or $Mg^{2+} + Si^{4+} = 2Al^{3+}$). This approach was used to test plausible substitution mechanisms for Mg and Ti in anorthite using our data (Fig. 3). Our results suggest that Mg partitions into anorthite by the exchange reaction, $Mg^{2+} + Si^{4+} = 2Al^{3+}$ (Fig. 3a), which is consistent with the mechanism proposed by previous workers [6,7]. Our data are consistent with Ti^{4+} and Ti^{3+} entering tetrahedral sites in anorthite by the exchange reactions, $2Ti^{4+} = 2Si^{4+}$ (Fig. 3b) and $Ca^{2+} + 2Ti^{3+} = 2Si^{4+}$ + vacancy (Fig. 3c), respectively. Substitution of Ti in tetrahedral sites has been suggested previously [8].

References [1] Beckett J. et al. (1990) Geochim. Cosmochim. Acta 54, 1755. [2] Simon S. et al. (1991) Geochim. Cosmochim. Acta 55, 2635. [3] Simon S. et al. (1994) Geochim. Cosmochim. Acta (in press). [4] Ihinger P. and Stolper E. (1986) EPSL 78, 67. [5] Lesher C. (1986) JGR 91, 6123. [6] Longhi J. et al. (1976) PLSC 7, 1281. [7] James O. and McGee J. (1992) LPSC 23, 603. [8] Smith J.V. (1983) in "Feldspar Mineralogy" ed. P.H. Ribbe, Rev. Min. 2, 281.

FIGURE 1

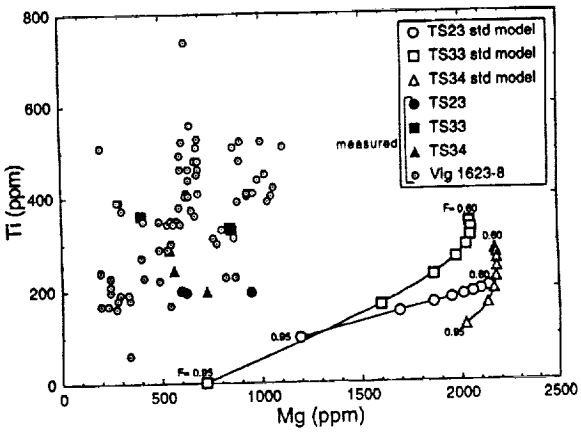

FIGURE 2

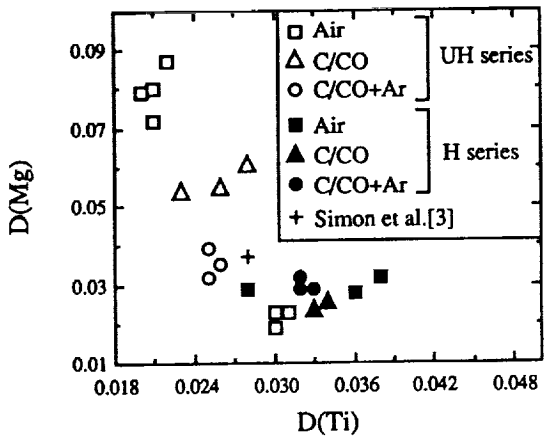

FIGURE 3a

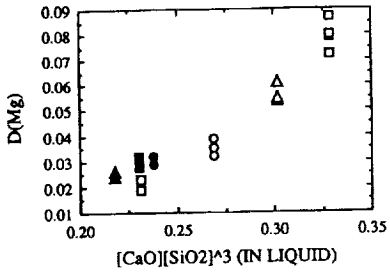

FIGURE 3b

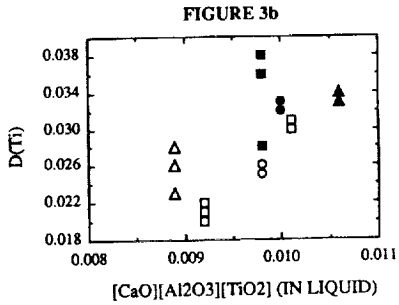

FIGURE 3c

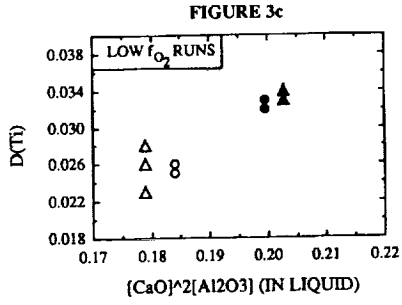

THE DISTRIBUTION OF LITHOLOGIC UNITS IN THE WESTERN HIGHLANDS OF THE MOON; C.A. Peterson, B.R. Hawke, P.G. Lucey, G.J. Taylor, Planetary Geosciences, Univ. of Hawaii, 2525 Correa Rd., Honolulu, HI 96822; P.D. Spudis, Lunar and Planetary Institute, Houston, TX 77058

A number of distinct lithologic units have been identified on the western portion of the lunar nearside. These include deposits of pure anorthosite, gabbroic units, and cryptomare deposits. The Inner Rook ring of the Orientale Basin and at least a portion of the inner ring of Grimaldi Basin and the mare-bounding ring of Humorum Basin are composed of pure anorthosiste. Gabbroic anorthosite which had been buried by ejecta from the Orientale impact event has been exposed by the craters Byrgius A and Prosper Henry. Two craters to the north, near Crüger, may also have excavated gabbroic material from beneath Orientale ejecta. Some unusual properties of the cryptomare and other terrain northwest of Humorum Basin suggest a complicated history for this region. The craters Gassendi G and F expose mare basalt from beneath a highlands-rich surface unit emplaced as ejecta from nearby impact events. Mixing analyses of spectra obtained for the cryptomare unit and the Letronne ejecta deposit indicate that significant amounts of mare basalt are present. The presence of a major mare basalt component could help to explain anomalously low radar returns observed for the terrain northwest of Humorum.

INTRODUCTION: In recent years, we have been conducting remote sensing studies of lunar basin and crater deposits in order to determine the composition and origin of surface units as well as to investigate the stratigraphy of the lunar crust. [1,2,3,4] We have combined both visible and near-IR spectral observations with Earth-based multispectral imagery in order to determine the lithology of relatively small (2-10 km) portions of the lunar surface. Our attention has been focused on the western portion of the lunar nearside in response to the first Galileo spacecraft encounter with the Earth-Moon system. Numerous deposits of pure anorthosite, gabbroic rock, and cryptomare have been identified, and interesting patterns can now be discerned.

RESULTS and DISCUSSION:

A. **Anorthosite Deposits.**

Orientale Basin region. With the exception of the Inner Rook massifs, all the highland units associated with the Orientale Basin appear to be composed of either noritic anorthosite or anorthositic norite. Our spectral data indicate that the Inner Rook ring of the Orientale Basin is a mountain range composed of pure anorthosite. [1,2]

Grimaldi Basin Region. Spectra obtained for the inner ring of Grimaldi indicate that this feature is composed, at least in part, of pure anorthosite. [3] Another anorthosite deposit has been identified just inside the outer Grimaldi ring. This material was excavated from beneath the basin floor material by subsequent impacts.

Humorum Basin region. At least a portion of the mare-bounding ring of Humorum is composed of anorthosite. [2,3] However, the entire ring is not composed of anorthosite, and no anorthosites have yet been identified on the outer Humorum rings.

Other occurrences. Pure anorthosites have also been identified in other portions of the nearside. These include the four innermost rings of Nectaris Basin, the central peaks of Alphonsus and Petavius, and two areas in the northern lunar highlands (within Goldschmidt and west of Thales). [4,5,6,7] To date, anorthosites have only been identified in a relatively narrow belt in the southern highlands, extending from Petavius in the east to the Inner Rook Mountains on the western limb, and at two locations in the far north. Extensive spectral studies of many nearside regions (e.g., north-central highlands, Imbrium) have failed to reveal additional depostis of pure anorthosite. Lunar anorthosite deposits are almost always found on or very near basin rings. This association is significant only for the inner rings of basins such as Grimaldi and Orientale. These rings were derived from beneath more mafic-rich layers in the pre-impact target sites. In contrast, the anorthosites associated with the outer rings of Nectaris and other basins are generally found in the central peaks and walls of large impact craters. It appears that these anorthosites were derived

from layers many kilometers beneath the crater target sites and that the surfaces of these outer rings are not composed of anorthosite.

B. **Gabbroic Units.** A gabbroic province has been identified in the western highlands. The Byrgius A and Prosper Henry impact structures have exposed material that is dominated by gabbroic anorthosite. The spectra obtained for these features have relatively wide "1 μm" absorption bands centered longward of 0.95 μm. [5] It appears that these craters excavated gabbroic material from beneath the Orientale ejecta blanket which is dominated by noritic anorthosite with lesser amounts of anorthositic norites. This gabbroic province may extend to the north of Byrgius A. Two craters near Crüger appear to have exposed gabbroic material from beneath the deposits emplaced as a result of the Orientale impact event.

C. **Cryptomare Deposits.** Both Galileo and Earth-based remote sensing data are being utilized to better understand ancient, pre-Orientale mare basalt deposits that were covered by highlands-rich material emplaced as a result of the Orientale and other impact events. [e.g., 2,3,8,9] Cryptomaria are located in the Schiller-Schickard region, the Mendel-Rydberg region, within the South Pole-Aitken Basin, and northwest of Mare Humorum. Out attention has recently been focused on the cryptomare NW of Humorum because of its possible association with terrain that exhibits anomalously low returns in the 3.8-cm, 70-cm, and 7.5-m radar data sets. [3] The results of our previous spectral studies demonstrated that both Gassendi G and F craters expose mare material from beneath a highlands-rich surface unit that was emplaced as a result of Letronne, Gassendi, and other impact events. Some ancient mare material could have been mixed with this highlands debris either by local mixing by secondary craters during ejecta emplacement or by vertical mixing due to small crater-forming impacts in the area. The presence of a mare basalt component in the surface layer could be responsible for the radar anomaly in the region since a significant amount of mare basalt could alter the bulk dielectric constant of the regolith. However, the spatial extent of the radar anomaly argues against this interpretation because the anomalous radar unit commonly extends to near the rim crests of the craters that apparently covered the ancient basalts with highlands debris. [3] It is unlikely that such a thick layer of ejecta could incorporate enough of the subjacent mare basalt, either through local or vertical mixing, to produce the observed anomaly.

In order to further investigate this question, we have analyzed three near-IR spectra obtained for the terrain NW of Humorum. Two spectra were collected for the surface of the cryptomare unit. The relatively strong "1 μm" absorption bands exhibited by these spectra suggest that significant amounts of mare basalt are present in the areas for which the spectra were obtained. Linear mixing analyses were conducted on the spectra. A mature mare spectrum (MH0) and a typical mature highlands soil (Apollo 16) were used as endmembers. The results indicate that mare material contributed 23% and 40% of the flux measured in these two areas. Hence, significant amounts of mare basalt are present in the surface of the cryptomare unit.

A spectrum was also obtained for a portion of the Letronne ejecta deposit. The area for which this spectrum was collected is just south of the Letronne rim crest; the ejecta should be relatively thick in this area. A mixing analysis indicated that mare basalt contributed approximatedly 42% of the flux. The most straightforward interpretation of this result is that mare basalt was present in the Letronne pre-impact target site and was incorporated into the crater's ejecta deposit. The Letronne impact event may have contributed some mare material to the terrain NW of Humorum, and this basaltic component may be, at least in part, responsible for the low radar returns.

References: [1] P.D. Spudis *et al.* (1984) *PLSC, 15,* C197 [2] B. R. Hawke *et al.* (1991) *GRL, 18,* 2141 [3] B. R. Hawke *et al.* (1993) *GRL, 20,* 419 [4] P.D. Spudis *et al.* (1989) *PLPSC, 19,* 51 [5] C.M. Pieters (1986) *Rev. Geophys. 24,* 557. [6]C.R. Coombs *et al.* (1990) *PLPSC, 20,* 161[7] C.M. Pieters (1993) *LPS XXIV,* 1141[8] J. W. Head *et al.* (1993) *J. Geophysl. Res. 98,* no. E9, 17149 [9] D.T. Blewett *et al.* (1993) *LPS XXIV,* 133.

VENUS RESURFACING HISTORY: CONSTRAINTS FROM HALO EJECTA DEPOSITS; R.J. Phillips, N.R. Izenberg, and J.S. Alexopoulos, Dept. of Earth and Planetary Sciences and McDonnell Center for the Space Sciences, Washington University, St. Louis, MO 63130.

Introduction. A large fraction of impact craters on Venus exhibit low-radar-backscatter halo-like deposits thought to be primary features formed by surface comminution associated with meteoroid shock waves [1,2] or by fallout of relatively fined-grained ejecta from impact events [3]. Because these deposits extend outward up to 10 crater radii, they provide a relatively widespread stratigraphic marker compared to craters and their continuous ejecta blankets [4]. Of a total population of 934, 383 craters have complete halos, 253 have partial halos, and 298 exhibit no halos. The removal of halos is attributed to dispersal by winds, chemical alteration, and burial by volcanic deposits [4]. In this abstract, we reaffirm that the crater population as a whole cannot be distinguished from a spatially random population [5], and show that this is also the case for the crater subsets of halo, no halo, and volcanically embayed, but not for tectonized (faulted). Thus processes that remove halos and that embay craters are apparently themselves spatially random. However, embayed craters have a strong tendency to be devoid of halo deposits [4] and no-halo and embayed craters show significant spatial clustering. Here we propose that the preservation state of halos can be used as a guide to the spatial distribution of volcanism.

Method. We performed Monte Carlo simulations and use "P-P" and "Q-Q" plots [5,6] and a test statistic to examine the spatial randomness (SR) of a single crater subset, or the randomness of one subset relative to another. The P-P plot displays the extremes, amongst m random simulations, of the fraction of crater-to-nearest crater distances less than some distance x versus the expected value of x. The Q-Q plot displays spatial relationships of minimum distances (degrees) between craters. Also shown on each plot are the corresponding measurements for the observed data set(s). A test statistic for the null hypothesis of random distribution on a sphere is given by $A_n = n - (4/n\pi)\sum_{i=1}^{n-1}\sum_{j=i+1}^{n}\psi_{ij}$, where n is the number of craters and ψ_{ij} is the spherical angle between the i-th and j-th craters [7]. We calibrate the Q-Q and P-P plots by comparison to the corresponding test statistic for single data sets (e.g., no-halo craters, tectonized craters), and then use the plots by themselves to assess randomness when comparing one data set to another (e.g., halo vs. no halo, no halo vs. embayed).

Results. The table below gives the confidence levels for rejecting the null hypothesis. The levels depend to some extent on the sizes of the data sets, but the results clearly show that rejection is reasonable only for tectonized craters. The tectonized crater subset is the only case in which the

All	Embayed	Tectonized	Halo	No Halo
66%	46%	99%	70%	14%

observed data are near the simulation extremes over a large fraction of both the P-P and Q-Q plots, and this is taken as a bound for rejecting the null hypothesis graphically. The Q-Q plot indicates that tectonized craters have a non-random clustering up to length scales of about 1200 km.

There are no halos at 52 of the 83 craters that are volcanically embayed. If the two sets were statistically independent, then 26 would be expected. We examined the spatial relationship between the remaining (non-coincident) craters in these two data sets. Figures 1 and 2 show that the null hypothesis is rejected and that there is a strong clustering of no-halo craters with embayed craters at all length scales (heavy dashed lines = simulation extremes, solid line = observed data). This result provides the following hypothesis: Regions of high concentration of no-halo craters are a guide to the space-time distribution of volcanism. If correct, this provides a more robust means to study volcanism than by studying embayed craters alone because no-halo craters make up a third of the total crater population. The thickness of halo deposits is probably a meter or less [2], so the volcanism implied need be only modest and certainly less than that required to remove the associated crater. Figure 3 is a contour plot of the ratio of the spatial density of the no-halo population to the total population where the darkest

shades of gray indicate the highest ratio. High ratio areas include Ovda and Thetis Regiones, a band extending in a northeasterly direction from Aino Planitia to Atla Regio to Hecate Chasma, the Lavinia Planitia–Lada Terra region, and Atalanta and Sedna Planitiae.

Conclusions. This result should be viewed with some caution because of possible altitude-dependent and latitude-dependent (radar incidence angle) biases in the mapped population of no-halo craters. However, this hypothesis can be further explored by examining other ratio distributions (e.g., halos, partial halos, embayed) as well as the spatial density of the overall population.

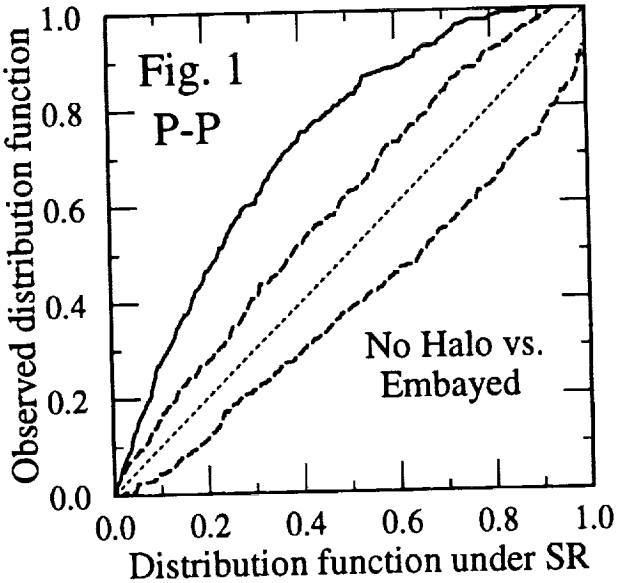

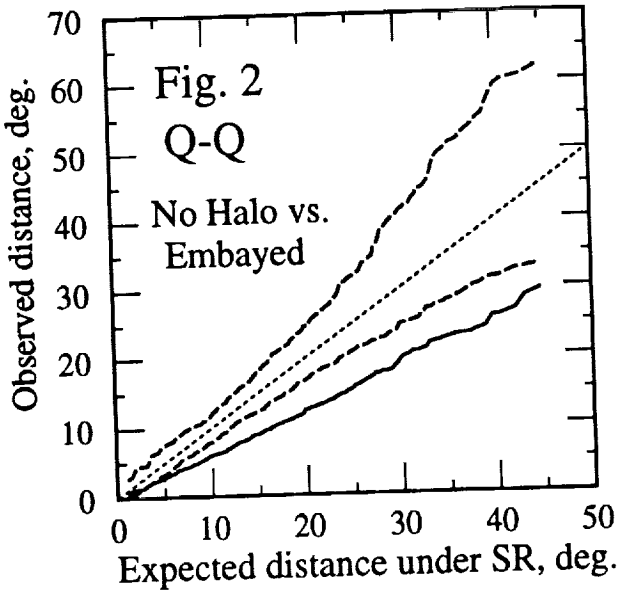

Fig. 3

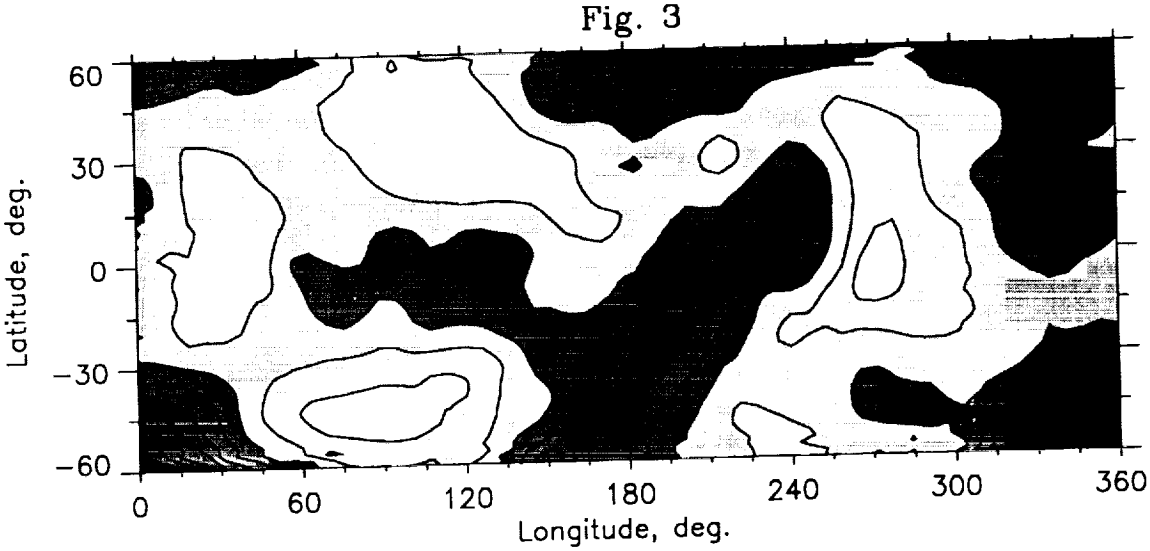

References. [1] B.A. Ivanov *et al.*, *J. Geophys. Res.* **91**, D413 (1986); [2] R.J. Phillips *et al.*, *Science* **252**, 288 (1991); [3] P.H. Schultz, *J. Geophys. Res.* **97**, 16,183 (1992); [4] N.R. Izenberg, R.E. Arvidson, and R.J. Phillips, *Geophys. Res. Lett.*, in press (1994); [5] R.J. Phillips *et al.*, *J. Geophys. Res.* **97**, 15,923 (1992); [6] P.J. Diggle, *Statistical Analysis of Spatial Point Patterns*, Academic, San Diego (1983); [7] N.I. Fisher, T. Lewis, and B.J.J. Embleton, *Statistical Analysis of Spherical Data*, Cambridge University Press, Cambridge (1987).

FeO AND MgO IN PLAGIOCLASE OF LUNAR ANORTHOSITES: IGNEOUS OR METAMORPHIC?

W.C. Phinney, SN2, NASA/JSC, Houston TX 77058

BACKGROUND: The FeO and MgO contents of plagioclase in lunar anorthosites has been recognized as producing anomalously low FeO and MgO in their equilibrium melts when available partition coefficients are utilized for the appropriate calculations[1,2,3]. Determinations of partition coefficients for FeO from experiments both in Fe crucibles that should maintain low oxygen fugacities[4] and in gas mixing furnaces that provide data on changes of the coefficient with f_{O_2}[3] and also from natural assemblages[5] have been consistent. Use of these coefficients with the FeO contents of plagioclase in lunar anorthosites produces melts with FeO contents that are several times lower than expected. Similarly, both natural and experimentally determined partition coefficients for MgO also produce melts that are several times lower in MgO than expected[3,5], the experimental values producing melts almost twice as low in MgO as the natural values. I have explained these anomalies as resulting from redistribution of FeO and MgO during high-grade thermal metamorphism in the early lunar crust[1]. This process is well demonstrated in terrestrial anorthosites that have undergone upper amphibolite to granulite grades of metamorphism[1] and in meteorites that have been recrystallized[6].

In a recent paper McGee[7] maintains that the FeO and MgO contents of plagioclases in lunar anorthosites retain their original igneous concentrations. He argues that the partition coefficients used to calculate the low FeO and MgO in the melts are inappropriate for two reasons: **A.)** they will be lower at the higher An contents of lunar plagioclase (An95 to 98) than were produced in the experimental work (An80 to 85) and **B.)** they will be lower for slowly grown plagioclase as is the case for the plutonic environments that produced lunar anorthosites.

DISCUSSION: In an attempt to resolve argument A.) plagioclases of An90 to 96 have been produced experimentally at the liquidus using previously established procedures[3]. The same starting material from previous work was used, but in order to increase the An content of the plagioclase most of the Na was vaporized under low f_{O_2} and high temperature before commencing the experiments. ***The resulting partition coefficients for FeO and MgO in plagioclases of An91 to 96 and melts with 9 to 19% FeO show no significant change from the values at An80 to 85 (Fig 1).*** Argument B.) ignores the fact that ***plutonic plagioclases contain FeO and MgO at concentrations that are consistent with the partition coefficients of both the experiments and volcanic plagioclases across all An values from 65 to 85***[e.g. 3,5,8]. In fact, the low partition coefficients for FeO that McGee cites from Longhi et al.[4] for plutonic plagioclases are misleading. The only anomalously low partition coefficient for FeO (0.006) from Longhi et al. is from a lunar pink spinel troctolite which has probably undergone a history similar to that of the lunar anorthosites. When partition coefficients for the terrestrial plutonic samples are calculated using the mole % values of [4] they are 0.019, 0.024 and 0.046. However, when converted to weight % values, which is what should have been done for a valid comparison with Phinney's data[1,3], the partition coefficients are 0.024, 0.030 and 0.054, in much closer agreement with the experimental results (~0.03). Furthermore, if one uses the classic Skaergaard study of Wager[9] to select the FeO value in the melt of the LZA section, rather than the olivine-based FeO value of Longhi, the coefficients for Longhi's Skaergaard plagioclases range from 0.029 upward, in excellent agreement with the experimental results. Similar mole% conversions for the MgO partition coefficients produce values of 0.020 to 0.022, in excellent agreement with other values based on natural terrestrial assemblages (0.020-0.023)[5]. Thus, the two arguments that question the validity of the FeO and MgO partition coefficients are found wanting and their application to lunar anorthosites stretches credulity.

McGee[7] includes a figure from an earlier abstract[10] which shows a regular decreasing trend for FeO and MgO in plagioclase with increasing An content in two mare basalts. The trends are headed directly towards the compositions of plagioclases in lunar anorthosite. At first glance this data would suggest that the partition coefficients do decrease drastically with increasing An content. To take the data at face value, however, would require a change in the partition coefficient for FeO by a nearly impossible factor of ~3 from An86 to An94, given a constant liquid composition. A later extended abstract [11] containing figures with further and more detailed data from this same study indicates that such a simple interpretation is not appropriate. MgO values in the later reference display two oppositely sloped trends over the same range of An values and, in contrast to the earlier figure, the lowest MgO values are actually associated with the lowest An values. Also, FeO values are shown to reverse their trends from early to late-stage plagioclases that display complex textures. In fact, there are both late and early plagioclases at about An90 with 0.5 % FeO which are quite compatible with the experimental partition

coefficient of 0.030. A plot of mg number vs. An content shows that with progressive crystallization there is a small decrease in mg number with increasing An values during early formation (the reverse of what is expected if olivine and/or pyroxene coprecipitate with plagioclase) and then an even steeper decrease in mg number with decreasing An values during later formation. Clearly substantial changes occurred in the melt composition during the course of plagioclase formation. Complex textural relationships further indicate that: olivine was involved in the early crystallization of one basalt but not in the other, there was precipitation of pyroxenes with plagioclase in both, late-stage precipitation of oxides and quartz occurred in one, and both reversed and normal zoning occurs in the plagioclases. Clearly there were complicated changes in compositions of the melts during the crystallization history of the plagioclases in these two basalts, perhaps even mixing of liquids occurred. ***In such complicated textures it is extremely difficult to guess which stage of plagioclase growth was in equilibrium with which composition of liquid. Variation of FeO in the melt by a factor of about 2 from 10-12% to 18-20%, which is certainly possible during crystallization of a basaltic melt, could produce the observed variations.*** Thus, given the unknown variation of FeO and MgO concentrations in the melts at the various stages of plagioclase formation, the actual values of partition coefficients are not readily determinable. At this stage of study, the use of these data by McGee in the context of appropriate values for partition coefficients is of questionable utility.

A second point in McGee[7] argues that many lunar anorthosites have not undergone the high temperature metamorphism that would cause redistribution of FeO and MgO. His argument is based on the observation that thin sections of some lunar anorthosites display textural evidence for recrystallization but others do not. To suggest that the textures of a few centimeter-sized chips of lunar anorthosite can be used to determine the recrystallization history of a larger anorthosite unit is to ignore the valuable lessons that are available from large outcrops of terrestrial anorthosites. Terrestrial anorthosites from high grade metamorphic environments may display well preserved igneous textures in numerous enclaves up to a meter across enclosed within totally recrystallized zones[12,13]. ***In thin sections coarse-grained igneous textures are maintained immediately adjacent to totally recrystallized textures. Yet, throughout both textures the FeO and MgO contents of the plagioclases are anomalously low***[1]. The low FeO and MgO contents of the plagioclase, whether in clearly recrystallized grains or large, well-twinned, zoned igneous grains, are consistent throughout not only outcrops having dimensions of tens of meters but also metamorphosed units that may extend for kilometers. Thus, the degree of recrystallization observed in centimeter-sized samples does not necessarily reflect the metamorphic context of an entire outcrop and can be quite misleading if used to interpret the petrogenetic history of a rock unit.

SUMMARY: The combined evidence from terrestrial anorthosites and experimental laboratory studies strongly implies that lunar anorthosites have been subjected to high-grade metamorphic events that have erased the igneous signatures of FeO and MgO in their plagioclases. Arguments to the contrary have, to this point, been more hopeful than rigorous.

Figure 1. FeO D'S for PLAGIOCLASE at 1180°C

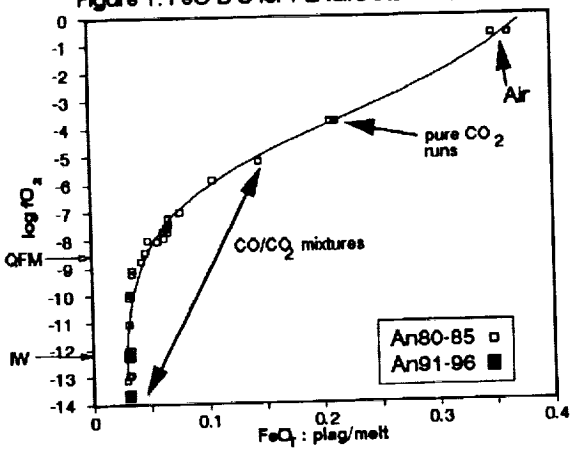

References: [1] Phinney, W.C. (1991) Proc. Lunar & Planet. Sci. 21, 29-49. [2] James, O.B. et al (1991) Proc. Lunar & Planet. Sci. 21, 63-87. [3] Phinney, W.C. (1992) Geochim Cosmochim Acta, 56, 1885-1895. [4] Longhi, J. et al (1976) Proc. Lunar Sci. Conf. 7th, 1281-1300. [5] Phinney & Morrison (1991) Geochim Cosmochim Acta, 55 1639-1654 [6] Phinney, W.C. (1993) Lunar & Planet. Sci. XXIV 1137-1138 [7] McGee, J.J. (1993) J Geophy Res, 98, 9089-9105. [8] Miller, J.D. & Weiblen, P.W. (1990) J Petrology, 31, 295-339. [9] Wager, L.R. (1960) Jour Petrology 1, 364-398. [10] James, O.B. & McGee, J.J. (1991) abstr., Meteoritics, 26, 351-352. [11] James, O.B. & McGee, J.J. (1992), Lunar & Planet. Sci. XXIII, 603-604. [12] Myers, J.S. (1978) Precambr Res, 6, 43-64. [13] Ashwal, L.D. (1993) Anorthosites, Springer Verlag.

C-2.

YOUNG VESTA (REGOLITH)? Carlé M. Pieters[1] and Richard P. Binzel[2]. [1]Dept. Geological Sci., Brown University, Providence, RI 02912, [2]EAPS, Mass. Inst. of Technology, Cambridge, Mass. 02139

For more than two decades asteroid 4 Vesta has presented dilemmas to the asteroid and meteorite communities. Vesta, 500 km in diameter, is one of the largest asteroids in the main belt. On the one hand, Vesta's reflectance spectrum (1, 2, 3) provides clear identification of the mineral composition of the surface: low-Ca pyroxene plus plagioclase. This mineral composition is directly comparable to the HED basaltic achondrites, and the eucrites in particular. In fact, visible to near-infrared spectra of Vesta and this class of meteorites are almost indistinguishable. Yet, while ample HED meteorite falls have been recorded, Vesta remained the only large main belt asteroid observed with HED properties. Vesta's 360 m/s surface escape velocity and location relatively far from any resonances makes it dynamically difficult to deliver fragments from Vesta to the inner solar system. Thus, while the composition of Vesta appeared to provide a direct link between asteroids and meteorites, the actual origin of the HEDs that fall to Earth was unresolved. Furthermore, since the spectrum of Vesta was so similar to spectra of eucrites measured in Earth-based laboratories, it was felt that, unlike the Moon, very little space weathering (alteration) occurred on Vesta, and consequently on small airless bodies in general (4). We consider the opposite argument here. Namely that if space weathering *does* occur on asteroidal surfaces, then the regolith of Vesta would have to be quite young, probably created by a relatively recent (impact) event. This scenario meshes nicely with the discovery of several small Vesta-like asteroids stretching from Vesta to the 3:1 Jovian resonance (5), which reveals a dynamically plausible link between the HED meteorites and Vesta, their preferred parent body.

Hypothesis considered: A major impact event recently occurred on Vesta. This event was energetic enough to eject 4 - 10 km fragments to the vicinity of the 3:1 resonance and also led to a freshly exposed regolith (globally) on the surface of Vesta. More numerous smaller (meteoroid-sized) ejecta sent toward the resonance, or subsequent collisional events on larger Vesta fragments near the resonance, has led to samples from Vesta being delivered to the inner solar system resulting in the occurrence of HED meteorites in Earth-based collections.

Evidence in favor of this scenario: If space weathering does occur in any significant amount on asteroids, a recent event that freshly exposes surface material on Vesta would be an unavoidable consequence since Vesta's spectrum shows no evidence of alteration. The occurrence of space weathering on asteroids is suggested by Galileo spectral observations of the asteroid Gaspra (6) which showed small fresh craters to have optical properties different than surrounding regolith (an effect similar to, but less pronounced than lunar space weathering (7)). The Vesta impact event must be large to redistribute regolith across the 500 km body; the existence of 20 small (<10 km) fragments probably derived from Vesta and trailing to the 3:1

resonance (5) speaks of a large impact event on Vesta. The possible basin suggested by Gaffey's rotational data (8) would be the principal remaining evidence of the impact. The orbits of two (possibly three) small near-Earth asteroids that exhibit Vesta-like composition are very similar, probably poorly evolved (young), and are candidates for part of an asteroid stream (9, 10). These NEA's, which themselves are short lived, were presumably fragments placed in the 3:1 resonance as a result of the impact and quickly joined the near-Earth population.

Evidence against this scenario: The character, magnitude, and rate of space weathering on asteroids is unknown. If the stony-iron meteorites are directly related to the HEDs (e.g. 11), the impact would have to have penetrated to the core mantle boundary while allowing the impactee (Vesta) to remain largely intact.

Discussion: While the discovery of the large "chips" off of Vesta imply one or more major impact events, the timing of any such event is not well constrained. Cosmic ray exposure ages of HED's suggest 10^7 - 10^8 yrs exposure time. Dynamical evolution of near-Earth asteroids suggests a shorter time scale. If the rate of space weathering were known, an upper limit could be set. The properties of the impactor and direction of impact await analysis. Furthermore, if a recent major impact and the young Vesta scenario is correct, then it is more plausible that Vesta is the sole parent body of HED meteorites and may be a unique asteroid--the only large asteroid known to have differentiated that still retains its crust. The young Vesta scenario also contributes to the ordinary chondrite parent body problem: if space weathering produces OC surfaces that mask the OC spectral characteristics, a young Vesta regolith is required to be consistent with Vesta observations.

Conclusions: If space weathering is an active process on asteroid surfaces, then the similarity of spectral characteristics between Vesta and the eucrite meteorites (absorption strength, absorption character, continuum, etc.) would require a recent (relative to the age of the solar system) impact to give Vesta a fresh unweathered regolith. An impact occurring relatively recently is a plausible scenario for forming the observed Vesta family of fragments and for yielding the current flux of HED meteorites.

Acknowledgments: NASA support for this research is greatly appreciated: NAGW-28 (CMP) and NAGW-1450 (RPB)

References:

1. McCord et al. (1970) *Science*, 168, 1445-1447.
2. McFadden et al. (1977) *Icarus*, 31, 439-446.
3. Feierberg et al. (1980) *Geochim Cosmochim Acta* 44, 513-524.
4. Matson et al. (1977) *PLSC 8th*, 1001-1011.
5. Binzel and Xu (1993) *Science*, 260, 186-191.
6. Belton et al. (1992) *Science*, 257, 1647-1652.
7. Pieters et al. (1993) *JGR*, 98, 20817-2-824.
8. Gaffey (1983) *LPS14*, 231-232.
9, Cruikshank et al. (1991) *Icarus* 89, 1-13.
10. Drummond (1991) *Icarus*, 89, 14-25.
11. Wasson (1985) *Meteorites*, Freeman, New York.

GEOPHYSICAL STUDIES OF THE MONTAGNAIS IMPACT CRATER

M. Pilkington, L.F. Jansa* and R.A.F. Grieve, Geophysics Division, Geological Survey of Canada, Ottawa, Canada, *Atlantic Geoscience Centre, Geological Survey of Canada, Dartmouth, Canada.

The Montagnais impact structure is located on the outer continental shelf ~200 km SSW of Halifax, Nova Scotia and is the only crater to have been discovered beneath the ocean [1]. The structure consists of a near-circular disturbed area with a central fault-bounded uplifted basement block with a diameter of ~11-13 km surrounded by an annular trough of down-dropped basement and sediments extending out to a diameter of 45 km, interpreted to be the crater rim [2]. Seismic reflection data suggests that impact breccia up to 800m thick extends outwards from the central uplift to distances of ~8.5 km and overlies the uplifted basement rocks. Although interpreted to be of volcanic origin [3] or due to a combination of tectonic and volcanic processes [4,5], the presence of petrographic indicators such as planar features in quartz and feldspars and geochemical evidence [2] strongly favours an impact origin. $^{40}Ar/^{39}Ar$ dating of the melt rock gives an age of 51 Ma. Extensive multichannel reflection seismic data and drill hole samples from the Montagnais I-94 well located within the central uplift indicate that the Montagnais structure has all the morphological elements expected of a complex terrestrial impact crater.

Two sets of detailed gravity and magnetic data have been collected in the Montagnais area. The first consists of data measured in conjunction with seismic lines carried out by the CSS Hudson [6]. The second consists of additional observations taken in conjunction with a detailed hydrographic survey of the Scotian Shelf. Regional potential fields over the Scotian Shelf are related to the Cambro-Ordovician Meguma Group (metasediments and associated granite plutons) which outcrops in Nova Scotia and underlies the Mesozoic sedimentary basin on the shelf.

The local gravity field in the Montagnais area is dominated by the steep shelf-edge gravity gradient related to the transition from continental to oceanic crust. This regional crustal effect has been removed from the observed data by high-pass filtering which passes all wavelengths less than 56 km and rejects all those greater than 85 km. Hence, any crater related signature of 40-50 km size should be retained. Figure 1 shows that the structure is marked by a gravity anomaly high of ~8 mGal with width ~11 km centered on 42° 52'N, 64° 15'W. The contoured data suggest that no negative anomaly delineates the crater extent (determined from seismic interpretation) as found in the majority of terrestrial impact craters. Radial gravity profiles centered on the gravity anomaly high confirm the absence of a definitive negative anomaly associated with the crater. A small inflection in the radially-averaged gravity anomaly at ~23 km radius could reflect density changes related to the impact and as such, define a negative anomaly of ~1 mGal. However, the magnitude of such an anomaly is within the estimated error in the data and is therefore not justified.

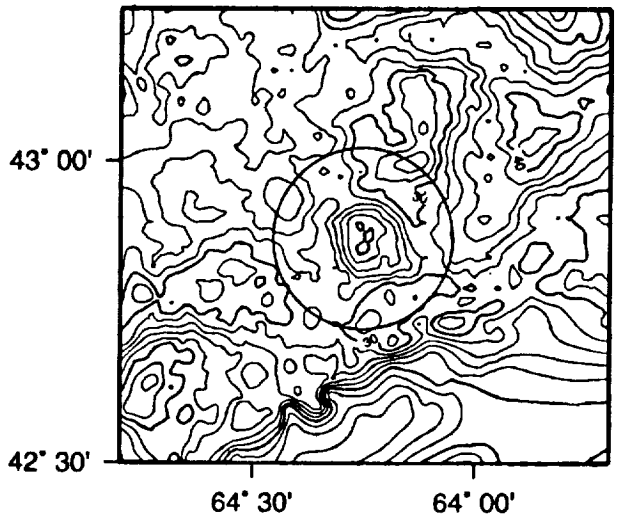

Figure 1. Residual Bouguer gravity anomaly map of Montagnais area after removing regional crustal component associated with the continental shelf edge. Contour interval is 2 mGal. Circle is 45 km in diameter and centered on 42° 52'N, 64° 15'W.

For a structure of the size of Montagnais, we expect a maximum negative anomaly of -5 to -10 mGal and a central gravity high of less than this magnitude [7]. The gravity signature of

Montagnais (only a gravity high associated with the central uplift), however, most resembles those found over heavily eroded structures formed in sedimentary rocks, e.g., Upheaval Dome, Utah; Kentland, Indiana. In these cases, erosion has removed the low density crater lithologies such as impact breccia and fractured/brecciated target rocks that contribute most to the negative gravity anomaly. All that remains is the effect of the uplifted denser root of the central uplift. Montagnais, on the other hand, appears well preserved. We may expect some reduction in the expected gravity anomaly due to the sedimentary component in the Montagnais target stratigraphy [7]. More important is the non-brittle behaviour of saturated unconsolidated material in the target and its more efficient absorption of impact energy compared to more compact targets. This will limit the formation of fractures and hence the size of the low density zone.

The total magnetic field intensity over the Montagnais region is given in Figure 2. The impact is located at the southern end of a NNE-trending magnetic high. The close association of this high with a gravity low suggests that the causative body may be a Devonian granite pluton such as that interpreted for other shelf anomalies. The field within the interpreted crater rim shows no expected features related to the impact process such as truncation of regional trends nor reduced field intensities [7]. However, a small magnetic high occurs ~3 km east of the central gravity anomaly. Depth estimates from the magnetic data give values of <2 km for the eastern part of this small central anomaly and 3-5 km for the western part. The latter depths are similar to those estimated for the larger (granite?) magnetic high to the NNE, while the shallower depths correspond to the average basement depth in the surrounding region. Although zones of melt rock have been found in the I-94 drill core, these units are unlikely to be responsible for the central magnetic anomaly. Melt sheets at impact craters generally produce a zone of several high-amplitude short-wavelength magnetic features with a greater areal extent than the Montagnais anomaly. The simple form of the central anomaly and the estimated source depth suggests a cause related to uplift of more magnetic basement material at depth.

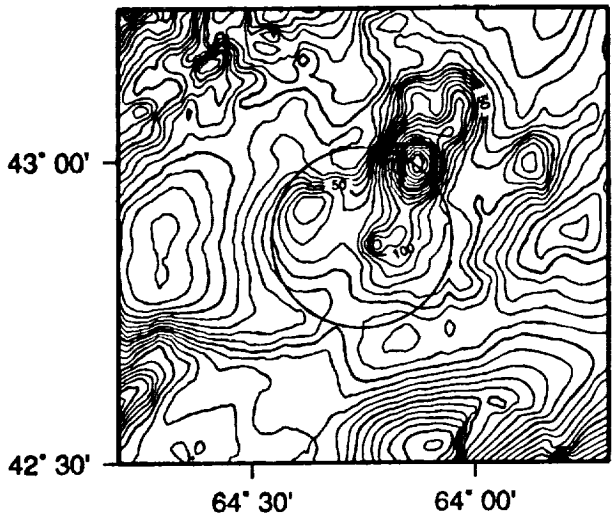

Figure 2. Total magnetic field intensity map of Montagnais area. Contour interval is 20 nT.

The unusual gravity signature of the Montagnais crater has important consequences for the location/detection of impact structures formed in offshore regions, particularly on continental shelves. The usual case of a gravity anomaly low which outlines the crater extent and is modified by a central anomaly high related to the central uplift is replaced by simply a positive anomaly whose size reflects the dimensions of the central uplift. Similarly, the existence of any associated magnetic anomaly will depend on whether crystalline basement is shallow enough to be involved in the impact process.

REFERENCES: [1] Jansa, L.F. and G. Pe-Piper, Nature, 327, 612-614, 1987. [2] Jansa, L.F. et al., Geol. Soc. Am. Bull. 101, 450-463, 1989. [3] Jansa, L.F. and J.A. Wade, Geol. Surv. Can. Pap. 74-30, v.2, 51-105, 1975. [4] Edwards, A., Soc. Explor. Geophys. Expanded Abstracts, 535-538, 1989. [5] Wade, J.A. and B.C. MacLean, in M.J. Keen and G.L. Williams (ed.); Geology of Canada, no. 2, p. 167-238, 1990. [6] Loncarevic, B. et al., Atlantic Geoscience Centre, Int. Rep., 80pp., 1988. [7] Pilkington, M. and R.A.F. Grieve, Rev. Geophys., 30, 161-181, 1992.

ARACHNOID-LIKE FEATURE ON OLDOINYO LENGAI, AN ACTIVE CARBONATITE VOLCANO IN NORTHERN TANZANIA; H. Pinkerton, IEBS, Lancaster University, LA1 4YQ, U.K., J.B. Dawson, Department of Geology, University of Edinburgh, Edinburgh EH9 3JW, U.K. and D.M.Pyle Department of Earth Sciences, Downing Place, Cambridge CB2 3EQ, U.K.

Summary

A structure resembling an arachnoid was discovered during a recent study of the active carbonatite volcano Oldoinyo Lengai, northern Tanzania. We mapped the radial and circumferential fractures, and we examined the folded circumferential folded zones around the outer margins of a shallow moat close to the edge of the structure. A structural interpretation of these features supports a mode of formation similar to that suggested by previous workers who have examined the much larger coronae and arachnoids on Venus.

Introduction

Oldoinyo Lengai was continuously active between April 1983 and June 1993 [1,2]. In spite of the lower eruptive temperatures and viscosities of the lavas [3], the volcanic processes occurring on this volcano are identical to those occurring on silicate volcanoes. During previous work on this volcano, we made the first detailed measurements of thermal erosion beneath active lava flows [3,4]. Until mid-June, activity was characterised by the quiet extrusion of low-volume lava flows. These were erupted from small, open vents which lasted for periods of a few hours to several years. Mild strombolian activity was a characteristic of these vents, though mapping in 1988 revealed breadcrust bombs up to 800 mm long, evidence of occasional more explosive activity from some of the centres.

Recent activity on Oldoinyo Lengai

Between 14 and 25 June 1993 small explosive eruptions occurred, and ash was deposited on the upper flanks of the volcano. Following partial collapse of major ash cones, 3 large lava flows were extruded in the southern (previously inactive) part of the crater, and a structure with an unusual fracture pattern developed (figures 1,2). This period of unusual activity was followed by the more common eruption of small, fluid carbonatite lava flows.

Arachnoid-like feature on Oldoinyo Lengai

The structure with the unusual fracture pattern bears a striking resemblance to arachnoids on Venus, apart from its smaller size (140 m diameter, compared with diameters of ~90 km for arachnoids and > 200 km for coronae [5]). Radial and circumferential fractures are well developed; radial fractures extend well beyond the circumferential fractures; the structure has a depression like the moats on Venus; there are circumferential compression ridges on the outer rim of the structure; and the structures are associated with extrusive volcanic activity.

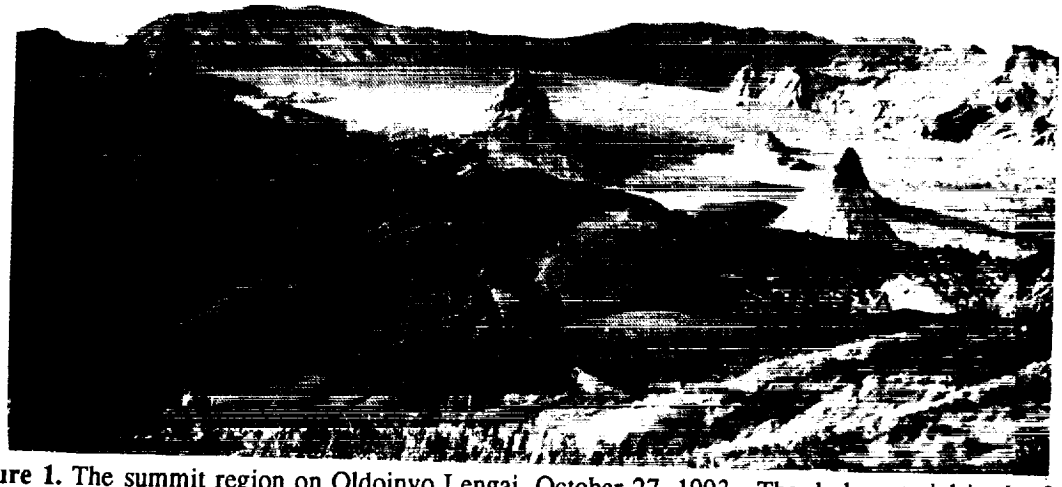

Figure 1. The summit region on Oldoinyo Lengai, October 27, 1993. The dark material in the foreground is covered by viscous flows and ash. A viscous lava flow can be seen emerging from a breached cone in the right (east) foreground. The lighter coloured material in the far side of the crater consists of fluid carbonatite lavas. The arachnoid-like feature dominates the left (south) foreground. Radial and circumferential fractures and circumferential fold structures on the 'arachnoid' are clearly visible.

The radial fractures and circumferential fractures around the arachnoid-like feature on Oldoinyo Lengai were typically 1.5 to 3 m deep and 1 m wide. The compressional ridges which were arranged circumferentially around the volcano occurred on the outer edge of a small moat, and the ridges were typically 1 m wide and 1 m high.

Formation of Terrestrial arachnoids

Several models for the formation of arachnoids and coronae have been proposed [6,7,8]. Most involve the diapiric uplift and subsequent spreading of a viscous magma. These models are compatible with our observations for the formation of the structure on Oldoinyo Lengai. We envisage the slow ascent of a low density, crystal-rich mush of carbonatite magma through the pyroclastic pile on the southern part of the active crater. The tensile radial fractures formed in response to uplift as the magma neared the surface. During subsequent radial spreading of the near-surface mush, the radially outward shear stresses induced by the flowing magma resulted in the formation of the small moat and the circumferential folds on the outer side of the moat. At the same time, circumferential fractures formed by fracturing due to the downward flexure of the central region of the structure as the magma migrated outward. The radial fractures continued to propagate outwards as the magma moved laterally away from the centre of the structure.

As far as we are aware, this is the first identification of any arachnoid-like structure on Earth. While this structure was observed in a carbonatite volcano, we are not inferring that this has any bearing on the compositions of rocks underlying the much larger arachnoids on Venus.

In conclusion, Oldoinyo Lengai has considerable potential for extending our knowledge of terrestrial and planetary volcanism. In addition to the discovery of the structure referred to in this contribution, a study of the proximal channels on the 1988 [3,4] and 1993 flows, has confirmed the importance of thermal erosion beneath proximal lava flows. We intend to carry out further detailed studies of the structures and plumbing system of this remote laboratory volcano during the next few months.

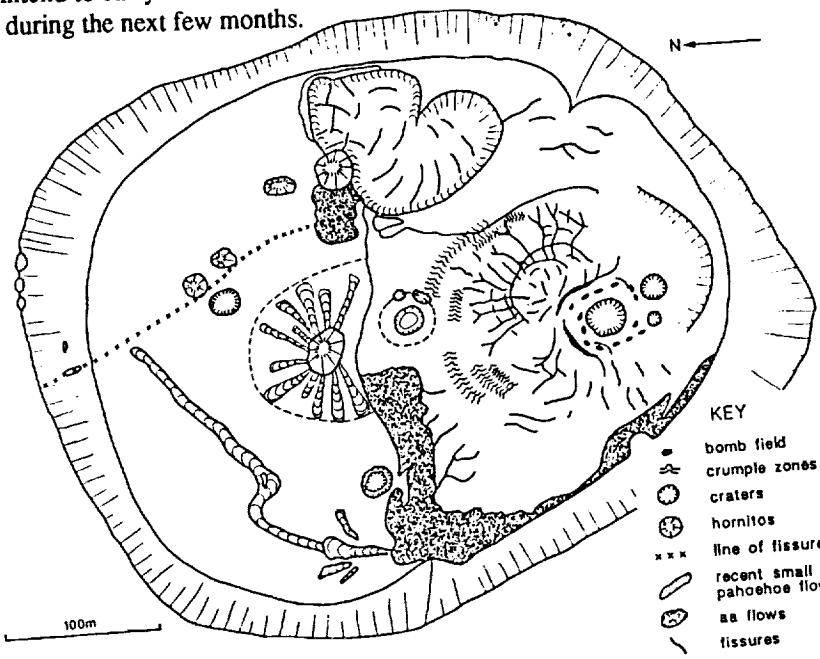

Figure 2. Map of the active crater in Oldoinyo Lengai, October 25-28, 1993. The arachnoid-like structure referred to in this contribution is the obvious feature with radial fractures in the S part of the crater. The large viscous flow referred to in figure 1 is the fractured flow emerging from a breached cone in the E part of the crater.

References: [1] Dawson J.B. et al., 1990. *Geology* 18: 260-263. [2] *Carbonatite volcanism of Oldoinyo Lengai - petrogenesis of natrocarbonatite*. Eds Bell K., Keller J. Springer-Verlag, Berlin (in the press). [3] Pinkerton H. et al., 1994. Field observations and measurements of the physical properties of Oldoinyo Lengai alkali carbonatite lavas, November 1988. *Carbonatite volcanism of Oldoinyo Lengai - petrogenesis of natrocarbonatite*. Eds Bell K., Keller J. Springer-Verlag, Berlin (in the press). [4] Pinkerton H. et al., 1990.*Lunar and Planetary Science* XXI: 964-965. [5] Head J.W. et al., 1992 *J Geophys Res* 97: 13153-13188. [6] Basilevsky A.T, et al., 1986. *Proc Lunar Sci Conf 16th, Part 2, J Geophys Res* 91, Suppl D399-D411. [7] Squyers SW, et al., 1992. *J Geophys Res* 97: 13611-13634. [8] Janes DM, et al., 1992. *J Geophys Res* 97: 16055-16068.

LAVA FLOW MORPHOLOGY AND CHEMISTRY; H. Pinkerton, IEBS, Lancaster University, LA1 4YQ, U.K., J.B. Dawson, Department of Geology, University of Edinburgh, Edinburgh EH9 3JW, U.K. and D.M.Pyle Department of Earth Sciences, Downing Place, Cambridge CB2 3EQ, U.K.

Summary

An examination of recent aerial photographs of the northern crater on Oldoinyo Lengai, an active carbonatite volcano in northern Tanzania, revealed flows with morphological properties unlike any previously seen in the crater. An increase in explosive activity, coupled with the eruption of a 6 m thick flow with crevasse structures in June 1993 suggested that there may have been an abrupt change in the chemistry of the eruption products at that time. Methods currently applied to planetary lava flows suggest that the thick flow had higher apparent viscosities and yield strengths than those erupted previously on Oldoinyo Lengai. The inference that follows from these calculations is that the lavas are highly evolved silicates. However, thin section examination of the rocks collected from the Chaos Crags flow during a study of the volcano in October 1993 have shown that the unusual flow morphology of the Chaos Crags flow was not the result of a change from carbonatite to silicate chemistry; it was a consequence of the eruption of high crystallinity carbonatites. In this contribution, we question the usefulness of remote sensing measurements in assessing the composition of this and other lava flows.

Introduction

Oldoinyo Lengai has been erupting carbonatite lavas between April 1983 and June 1993 [1,2]. Prior to an explosive event in mid-June, activity was characterised by the quiet extrusion of low-viscosity lava flows. The thick, viscous lavas erupted in June 1993, hereafter referred to as the Chaos Crags flow, were clearly different. As part of our investigation of the plumbing and petrological development of this volcano, we wished to establish whether the changes in June reflected an input of silicate magma into the summit crater. This study has obvious planetary implications, not only for assessing the usefulness of remote sensing methods in determining composition from lava flow morphology; but also because some Venusian lavas are highly alkaline, particularly the sample from Venera 13 which resembles olivine nephilinite [3]. The close association between nephilinites and carbonatites supports the view that some of the lavas on Venus may be carbonatites; consequently any terrestrial information on flow morphology of carbonatites and related rocks is of potential planetary interest.

Compositional data based on the interpretation of aerial photographs

A study of aerial and ground-based photographs taken in June and October 1993 reveal some of the features that characterise the Chaos Crags flow (see figs 1 & 2 in Pinkerton et al., this volume). The flow, which was 6 m thick at the snout and had a length of 150 m, emerged from a the breached cinder cone on the E side of the crater; it has well developed fissures parallel and transverse to the flow direction.

We agree with previous workers that the lengths of lava flows provide little useful compositional information; while most rhyolitic lava flows are only a few km long, some have lengths in excess of 30 km [4]. Similarly, some phonolite flows with SiO_2 contents in the range 52% to 59% are 250 km long [5]. Recent modelling [6-8] suggests that rhyolitic lava flows have the potential to travel as far as the most extensive basaltic lava flows. In addition, the lengths of lava flows are functions of erupted volume, eruption rate and other physical and environmental properties including viscosity [6,8]. Thus the short length of the Chaos Crags flow is not, on its own, evidence of a high viscosity.

Most workers use the dimensions of levees or lobes to extract compositional information from lava flows. For example, if we approximate lava flows as Bingham fluids, the yield strengths of the lavas can be calculated from $\tau = \rho gh/w$ where the mean flow thickness, width and density are denoted by h, w and ρ respectively [4]. Applying this equation to the Chaos Crags lava flow on Oldoinyo Lengai the calculated yield strengths range from 4000 to 8000 Pa. This is several orders of magnitude higher than the measured yield strengths of carbonatite lavas, and it is 2 to 3 times greater than the mean value for basalts [4].

Using the methods developed by Crisp & Baloga [9] and relevant physical properties of natrocarbonatites in [1] & [10-13], calculated emplacement times for the Chaos Crags flow range from 46 hrs to 1160 hrs. However, observations of the volcano indicate maximum emplacement time of 336 hrs. Using emplacement times of 46-336 hrs, advance rates of the flow front range from 0.45 to 3.3 m hr^{-1}. Inserting these into the Jeffreys equation, calculated viscosities range from 3.10^7 to 7.10^8 Pas. These viscosities place it within the range considered to be appropriate for rhyolites (3, 14), though the yield strengths would suggest a composition closer to basaltic andesite.

Flow morphology and chemistry: Pinkerton H. Dawson J.B. and Pyle D.M.

Field and laboratory observations and measurements, October, 1993

Field measurements confirmed that the flow front was 6 m thick, though the general level of the upper surface of the flow was 12 m above the older underlying lava flows. The flow front contained metre-sized fragments of the breached cinder cone. In addition to the crevasse structures seen in the aerial photographs, well developed grooves and slickensides were an obvious feature on the flow; these had not been found previously on carbonatite lava flows. Indeed the structures encountered on the flow are reminiscent of similar structures observed on andesitic flows [15]. However, field and subsequent laboratory investigations showed that the lavas were carbonatites. Why does the Chaos Crags flow have such a different morphology compared with 'normal' carbonatite flows?

Previous investigations have shown that two basic types lava flows are erupted on Oldoinyo Lengai. Gas-poor pahoehoe lavas are Newtonian with viscosities in the range 1 to 5 Pas whereas gas-rich lava flows are viscoplastic with unit strain rate apparent viscosities of 70 to 120 Pas [1,12,13]. The presence of gas clearly has a marked effect on the rheology of carbonatites. However, the vesicularity of the Chaos Crags lavas is less than 5%, and cannot explain the high viscosities. Aternative explanations for the anomalous rheology are that the lavas contained an immiscible silicate fraction, and hence behaved as an emulsion during flow, or that they had an unusually high crystallinity. Thin section examination show that the rocks were natro-carbonatites with up to 60% crystals and occasional silicate globules. A detailed study of these has revealed unequivocal evidence of magma unmixing; however, the presence of small percentages of globules will not have a significant effect on the rheology of these flows, and the chemical effects of the silicate component on the viscosity of the melt are negligible. Field and laboratory rheological measurements on carbonatites from Oldoinyo Lengai show that the viscosity of these rocks increases from 1 Pa s to 245 Pa s as the temperatures drop from 636 C to 544 C [12,13]. While we have not yet measured the rheological properties of natrocarbonatite lavas with the high crystallinities that characterise the Chaos Crags lavas, the apparent viscosities and yield strengths of lavas increase exponentially once the crystallinity exceeds 55% [16]; thus the anomalous rheology during emplacement of the Chaos Crags flow can be explained simply by the high crystallinity of the lava.

Discussion

The reasons for the high crystallinity of the Chaos Crags lavas are, as yet, unclear. However, an examination of the flow has revealed that the lava occupied the source cinder cone for some time prior to breaching. During that time, a 50 cm thick crust developed on the surface of the flow; it is this crust that fractured to form the crevasse structures and other fractures during flow. The observed grooves and slickensides formed at the junction between the crust and the underlying cool plastic lava. Crustal formation time calculated from measured crustal thickening rates in 1988 [13] is 10 hours. These times are compatible with the aerial observations of the crater during the eruption. However, they are considered to be too short to permit 60% crystallisation. We are currently investigating the relationship between the 'normal' natrocarbonatites and those erupted at Chaos Crags.

This study has confirmed the conclusions reached by previous workers [e.g. 17,18] that rheological properties calculated using methods currently used to study planetary lava flows will not always reveal useful compositional data; without detailed field and subsequent laboratory investigations of the lavas on Oldoinyo Lengai, invalid conclusions would have been reached about the composition of the rocks erupted from this volcano.

References:

[1] Dawson JB et al., 1990. *Geology* 18: 260-263. [2] Bell K, Keller J (Eds)*Carbonatite volcanism of Oldoinyo Lengai - petrogenesis of natrocarbonatite*. Springer-Verlag, Berlin (in the press). [3] Baker VR et al., 1992 *Geophys Res* 97:13421-13444. [4] Moore HJ et al., 1992. *Geophys Res* 97:13479-13494. [5] Lippard SJ, 1973. *Geol Mag* 110:543-549. [6] Pinkerton H, Wilson L, 1988. *Lunar Planet Sci* XIX:937-938. [7] Manley CR ,1992. *J Volcanol Geotherm Res* 53:27-46. [8] Pinkerton H, Wilson L, 1994. *Bull Volcanol* (in the press) [9] Crisp JA, Baloga SM, 1990. *J Geophys Res* 95:1255-70. [10] Pinkerton H et al., 1990. *Lunar Planet Sci* XXI:964-965. [11] Norton GE et al., 1990. *Lunar Planet Sci* XXI:901-902. [12] Norton GE, Pinkerton H, 1992. *Lunar Planet Sci* XXIII:1001-1002. [13] Pinkerton H et al., 1994. In *Carbonatite volcanism of Oldoinyo Lengai - petrogenesis of natrocarbonatite*. Eds Bell K, Keller J Springer-Verlag, Berlin (in the press). [14] Pavri et al. 1992. *Geophys Res* 97:13445-13478 [15] Naranjo JA et al., 1992. *Geol Mag* 129:17-28. [16] Pinkerton H, Stevenson RJ, 1992. *J Volcanol Geotherm Res*. 53:47-66. [17] Fink JH, Griffiths RW, 1990. *J Fluid Mech* 221:485-501. [18] Bridges N, Fink JH, 1991. *Lunar Planet Sci* XXII:137-138.

TOPOGRAPHIC AND SURFACE ROUGHNESS PROPERTIES OF STEEP-SIDED DOMES ON VENUS AND EARTH FROM RADAR REMOTE SENSING AND FIELD MEASUREMENTS.
Jeffrey J. Plaut, Ellen R. Stofan, Jet Propulsion Laboratory, California Institute of Technology, Pasadena, CA 91109, David A. Crown, Department of Geology and Planetary Science, University of Pittsburgh, Pittsburgh, PA 15260, Steven W. Anderson, Black Hills State University, Spearfish, SD 57799-9102.

Introduction

Several hundred volcanic features with roughly circular planforms and steep margins were detected in Magellan radar images of Venus. First-order similarities in appearance led some workers to suggest that these Venusian domes were analogous to terrestrial silicic domes, in composition, lava viscosity and eruptive style [1-6]. In their detailed characteristics of size, shape and surface morphology, however, Venusian and terrestrial steep-sided domes are considerably different, prompting a re-evaluation of the use of silicic domes as direct analogs for the Venusian features [7-9]. We report here on efforts to constrain the gross shape, morphology of surface structures, and mean slope and roughness characteristics of steep-sided domes on Venus and Earth using radar remote sensing, as well as field measurements at several terrestrial sites. An understanding of geometric characteristics at scales from centimeters to tens of kilometers can be used to infer eruptive conditions and emplacement processes. Data sets used in the analysis include: for Venusian domes, Magellan SAR image and backscatter data, altimeter-derived roughness measurements, and stereo-derived topographic data; for terrestrial domes of the Inyo-Mono chain, California, AIRSAR multiple-angle, -wavelength and -polarization SAR image and backscatter data, TOPSAR interferometric radar digital elevation models, and field measurements of topography at 25-cm horizontal intervals and surface block size distributions.

Planform and profile shape

The planform shape of both Venusian and terrestrial domes appears to be controlled by pre-existing topography, with circular planforms occurring when domes are erupted on terrain with small topographic gradients. Irregular planforms are more common on Earth, while circular planforms are more common on Venus. Venusian domes are most abundant in plains regions, which typically are quite flat, while terrestrial domes are often found in volcanic and tectonic settings that contain significant relief, such as the Long Valley Caldera / Sierra Front region. Venusian domes often display scalloped margins, thought to result from slope failure on the outer flanks, possibly associated with secondary eruptions [5]. This phenomenon is limited on Earth to domes developed on steep topography, such as the flanks of large edifices. Dome diameters are ~ 5 to 100 km on Venus, and ~ 0.5 to 5 km on Earth.

Multiple-cycle Magellan SAR data acquired at different viewing angles were used to obtain high resolution topographic profiles and digital elevation models for many of the Venusian domes. Preliminary analyses indicate that Venusian domes typically show an overall concave profile, with elevated rim areas and depressed centers. In contrast, topographic profiles derived fron TOPSAR digital elevation models show that terrestrial dome profiles in the Inyo chain are typically convex, with elevated central summit vent areas that show considerable local relief. The concave profiles of many Venusian domes imply post-eruptive deflation of their central zones, which is rarely observed on terrestrial silicic domes.

Surface roughness characteristics

Venusian steep-sided domes exhibit surface roughness properties in Magellan SAR backscatter data that are comparable to those of typical Venusian plains. Multiple-incidence angle backscatter cross section data (scattering "laws") indicate that the upper surfaces of Venusian domes are only slightly rough at the 12-cm wavelength scale, and that the dielectric constants do not differ significantly from typical Venus values. As noted in [2], altimeter-derived rms slope estimates are primarily in the range of 1°-5°, and these values typically differ from those of the surroundings by only ± 2°.

In contrast, the scattering laws of the Inyo-Mono dome surfaces show little dependence on incidence angle, consistent with their extremely rough appearance in the field. Backscatter cross

section values in AIRSAR data interpolated to a 12-cm wavelength are 5 to 10 dB higher than values obtained on Venusian domes at similar incidence angles.

25-cm-interval topographic transects 30-100 m in length were acquired at 25 sites on silicic domes in the Inyo-Mono and Medicine Lake Highland areas, and for comparison, on basalt flows in the Cima volcanic field. Data reduction included: detrending, rms height (standard deviation of surface heights relative to the mean), rms slope (standard deviation of point-to-adjacent-point slopes), and correlation length (offset for which autocorrelation function falls to 1/e). Block size distributions were also obtained along each transect. Table 1 shows results for several sites (see [9] for unit descriptions). Most of the roughness parameters of silicic domes far exceed those of basalt flows, except for some of the roughest a'a sites. Blocks larger than 20 cm commonly cover over 50% of the surface, indicating that large-scale facets will predominate over subwavelength scatterers in SAR backscatter measurements. Rms slope values are generally over 20°, significantly higher than published values for basalt flows [10] and than Hagfors-modeled Magellan altimetry values for Venusian domes [2].

Summary

Differences in the geometric characteristics of terrestrial silicic and Venusian steep-sided domes at scales from centimeters to tens of kilometers are revealed by detailed analysis of radar-derived topographic and surface roughness information. Field measurements of terrestrial domes support the interpretation that the upper surfaces of terrestrial and Venusian domes are vastly different in their textural properties. The differences require a re-evaluation of the silicic model of origin for the Venusian features: either the Venusian domes do not consist of silicic lavas, or silicic volcanism does not operate in the same fashion on the two planets.

References

[1] Head, J.W. et al., 1991, Science 252, 276-288. [2] Pavri, B. et al., 1992, JGR 97, 13445-13478. [3] McKenzie, D. et al., 1992, JGR 97, 15967-15976. [4] Head, J.W. et al., 1992, JGR 97, 13153-13198. [5] Guest, J.E. et al., 1992, JGR 97, 15949-15966. [6] Fink, J.H. et al., 1993, GRL 20, 261-264. [7] Crown, D.A. et al., 1993, Lunar Planet. Sci. Conf. XXIV, 355-356. [8] Plaut, J.J. et al., Eos Trans. Am. Geophys. Union 74, 379. [9] Anderson, S.W. et al., 1994, this volume. [10] Campbell and Garvin, 1993, GRL 20, 831-834.

TABLE 1. SURFACE ROUGHNESS CHARACTERISTICS

Site	Rms Height, cm	Rms Slope, degrees	Correlation Length, cm	Arctan (h/l), degrees	Blocks, % < 10 cm	Blocks, % > 20 cm
Obsidian Dome, ridges	54.31	34.51	150.0	19.90	44	31
Obsidian Dome, jumbled	30.09	35.52	50.0	31.04	10	64
Obsidian Dome, vent	82.29	40.01	125.0	33.36	7	73
Obsidian Dome, slabs	50.86	23.76	200.0	14.27	31	50
Cima, a'a channel	32.49	22.33	400.0	4.64	50	26
Cima, a'a margin	53.18	32.68	175.0	16.90	28	51
Kilauea, pahoehoe[10]	7.70	3.92	350.0	1.27		
Venus, steep-sided domes[2]		< 5.0				

ATMOSPHERIC VS. SOLAR NOBLE GAS ABUNDANCES: ISOTOPIC FRACTIONATION IN LOW ENERGY ARGON ION IMPLANTATION; K. V. Ponganis, Th. Graf, and K. Marti, Dept. of Chemistry, UC San Diego, La Jolla, CA 92093-0317

Possible mechanisms driving the evolution of planetary volatiles from original compositions in the solar accretion disk were considered by Suess in 1949 [1] and are still poorly understood. Modeling of noble gas compositional histories requires knowledge of fractionating processes that may have operated through the evolutionary stages. Since these gases are chemically inert, they can be used as probes for studies of fractionating processes. The importance of understanding these processes extends well beyond "noble-gas planetology."

Absolute abundances of noble gases in the terrestrial planets' atmospheres reflect a differential depletion with respect to solar abundances.[2] Isotopic signatures are distinct for each terrestrial planet and from solar wind compositions.[3] Furthermore, although measured $^{20}Ne/^{36}Ar$ ratios are roughly the same for Earth and Mars, which may imply a common source, isotopic uniformity is missing.[4] The $^{20}Ne/^{22}Ne$ ratio on Venus is higher and the inferred $^{38}Ar/^{36}Ar$ ratio on Mars is lower than on the other terrestrial planets.[5] Terrestrial xenon is positively mass-fractionated (that is, enriched in the heavy isotopes) almost 3.5% per amu, while terrestrial Kr is unchanged or slightly lighter than solar.[6] The central issue to the origin and evolution of terrestrial planets' atmospheres is how, when, and from what sources did the accreting planetesimals get their gaseous elements. Volatile sources may include the solar nebula, the solar wind, comets and meteorites along with their parent bodies.

Fractionation mechanisms involving ion implantation have received scant attention after Bernatowicz and coworkers concluded that the isotopic fractionation was too small to account for the large isotopic shifts of Xe observed in the terrestrial atmosphere.[7][8] However, we reexamined low-energy, ion implantation and found significant fractionation of argon isotopes.[9]

Our initial studies were similar to those discussed by Bernatowicz and Hagee[8], but we could degas the W ion collector of a Bayard-Alpert device directly by resistive heating.

Using a well-degassed and annealed collector wire at a potential of -50 V, a large, ≥3% per amu, isotopic fractionation was observed. As the ion collector voltage increased, the trapped fraction of Ar increased, while the isotopic fractionation decreased. The fractionation effects are due to either ion implantation, gas sputtering or diffusive loss after ion implantation or a combination of these processes. Since ion implantation with the reaction chamber at 200°C produced the same extent of isotopic fractionation, but yielded a lower trapping efficiency than with a chamber initially at room temperature, fractionation cannot be simply due to diffusion.

While ions are implanted, some can be subsequently ejected from the collecting surface by ion bombardment or by sputtering. Gas sputtering becomes possible at very low energies, generally about 25 eV. [10]

The relevant processes may be approximated with a simple model. The concentration of trapped gas C after a time t is written as [7]:

$$dC/dt = \alpha(C_0-C) - \beta C$$

Here, C_0 is the total amount of gas initially available for implantation, α and β are rate constants for the trapping and release of gas. In the simplest case where α and β depend only on the type of the incident particles and the target material, the solution to this equation is:

$$C = C_0 (\alpha/[\alpha+\beta]) [1-e^{-(\alpha+\beta)t}]$$

In many cases, α and β will also depend on the extent of damage produced in the crystallographical structure during the bombardment. Further, during the experiment the collector surface is contaminated with the residual gas molecules of the chamber and this also may affect the rate constants. However, if the effects of such processes can be minimized, it should become possible to determine experimentally α, β and their dependence on isotopic mass.

In our initial implantation chamber for a 100 V run, it took approximately 20 hours to obtain a quantitative release of the trapped argon. Bernatowicz and Hagee [8] reported a diminished uptake of gases over time and suggested that this behavior may be due to lattice damage caused by sputtering. Our prolonged resistive-heating procedure anneals some of the lattice damage, as well.

Our implantation chamber was redesigned to eliminate some ambiguities caused by our original design. In particular, the area for ion implantation onto the collector wire was targeted to the inside area of the grid and to the central part of the collector wire. This ensures uniform heating when degassing. A more focused beam of electrons was obtained by adding a shield with a 1 x 4 mm slit and a coiled tungsten filament. We can measure the electron emission current between the shield and grid.

THE ARGON EXPERIMENTS A modified static VG 5400 mass spectrometer was used for isotopic analyses, using both a Daly detector and Faraday detectors. The mass spectrometer is connected to an all-metal vacuum line that includes two getters, one of titanium sponge and one of SAES NP10. There are also two stainless-steel mesh frits used for cryogenic separation of argon fractions using liquid nitrogen.

The walls of the implantation chamber were heated to 250°C for at least 12 hours before the procedural

blanks were run. Both the grid and the ion collector were degassed several times before use. The grid and shield were kept at ground potential and the filament at -34 V. The electron emission current was 500 μA (±10 μA) during the ion implantation and the ion collector was at -75 V.

Procedural blanks were run before every experiment and blank corrections are only significant at the shortest implantation times. The free phase was first collected, then the reaction chamber was closed and the ion collector was heated to ~1000°C to release the trapped phase. The ion collector remained at this temperature for approximately 20 hours as required for complete degassing, although ~85% of the gas was released in the first 30 minutes.

Figure 1. shows the argon trapping as a function of ion implantation time. As the time of ion implantation increases, the amount of trapped argon increases. However, it is interesting to note from Figure 1. that the isotopic fractionation of argon changes little.

To test the effects of gas sputtering on our system, argon was implanted for two hours with the getter open (normal procedure) and then two more hours with the getter closed in order to increase the hydrogen partial pressure substantially. This experiment yielded only slightly more trapped argon (3.36%) than the normal two-hour ion implantation (3.13%). Obviously, ion implantation tapered off as the hydrogen pressure increased in the reaction chamber, but gas sputtering did not decrease the amount of implanted argon that is observed in a normal two-hour experiment. At present it is not possible to resolve the relative contributions of charge-transfer, energy loss and of gas sputtering. With the getter closed during a four-hour experiment, very little gas is implanted (0.24%).

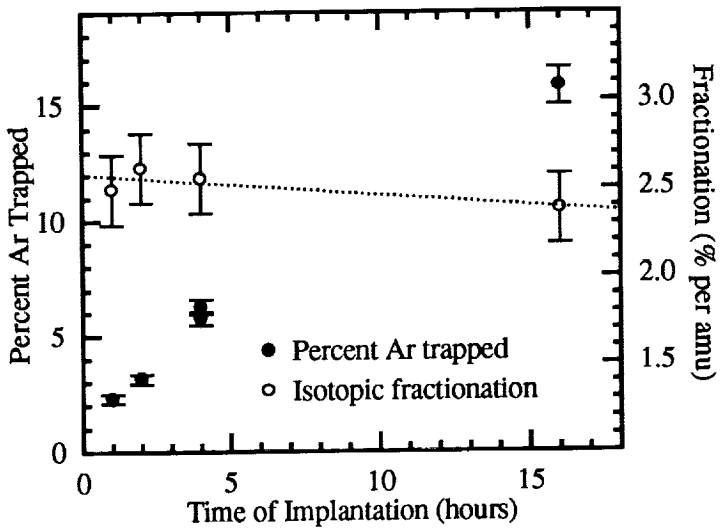

Figure 1. The percent of trapped Ar for different ion implantation times (left scale) as well as the resulting isotopic fractionation (right scale) is shown. The potential of the ion collector is -75 V.

One initial experiment was performed to assess Ar diffusion after implantation. After a two-hour Ar implantation the voltage on the ion collector was set to zero for another two hours. The trapped Ar was 76% of a normal two-hour implantation and of similar isotopic fractionation. This result shows, in agreement with the previously discussed 200°C implantation experiment, that diffusive losses decrease trapping efficiencies, but cannot be the sole process affecting the isotopic fractionation of argon in these experiments.[9]

We conclude that in a natural environment where low-energy, ion implantation processes are possible, isotopic fractionation of argon (and other gases) has to be expected. Low-energy ion implantation also provides a mechanism for considerable gas loading. The potential implications of this process in the origin of the terrestrial planetary atmospheres and meteoritic material needs to be considered and requires further study. We also obtain an order of magnitude estimate of 10^{-3} for the collecting efficiency (ions collected per incident ions) in our experiments at -75 V. The largest uncertainty arises from the fact that we have to calculate the ion current. This value may be compared with collecting efficiencies of 2×10^{-2} reported for He implantation into Pt at -75V interpolated from data by Filleux **et al.** [11] and with a value of 7×10^{-4} obtained by Kornelson for Ar implantation into a W target at 100 eV.[12]

REFERENCES

[1] H. Suess (1949) *J. Geol.* 57, 600. [2] R. O. Pepin (1949) *Icarus* 92, 2. [3] D. M. Hunten, R. O. Pepin, T. C. Owen, in *Meteorites and the Early Solar System* J. Kerridge, M. Matthews, Eds. (University of Arizona Press, Tucson, AR, 1988) pp. 565-591. [4] T. M. Donahue, J. B. Pollack, in *Venus* D. Hunten, L. Colin, T. Donahue, V. Moroz, Eds. (University of Arizona Press, Tucson, AR, 1983) pp. 1003-1036. [5] R. O. Pepin, in *Origin and Evolution of Planetary and Satellite Atmospheres* J. Atreya, J. Pollack, M. Matthews, Eds. (University of Arizona Press, Tucson, AR, 1989) pp. 291-305. [6] M. Ozima, F. A. Podosek, *Noble Gas Geochemistry* (Cambridge University Press, Cambridge, 1983). [7] T. J. Bernatowicz, A. J. Fahey (1986) *Geochim. Cosmochim. Acta* 50, 445. [8] T. J. Bernatowicz, B. E. Hagee (1987) *Geochim. Cosmochim. Acta* 51,1599. [9] K. V. Ponganis, T. Graf, K. Marti (1993) *Lunar Planet. Sci.* XXIV, 1163. [10] R. V. Stuart, G. K. Wehner (1962) *J. Appl. Phys.* 33, 2345. [11] C. Filleux, et al. (1980) *Radiation Effects* 46, 1. [12] Kornelsen (1964) *Can. J. Phys.* 42, 364.

PROLONGED BIOSPHERIC EFFECTS OF SULFUR VAPORIZATION BY THE K/T CHICXULUB IMPACT; K.O. Pope, Geo Eco Arc Research, 2222 Foothill Blvd. Suite E-272, La Canada, CA 91011 USA.A.C. Ocampo and K.H. Baines, Jet Propulsion Laboratory, 4800 Oak Grove Dr., Pasadena, CA 91109 USA, and B.A. Ivanov, Russian Academy of Sciences in the Institute for Dynamics of Geospheres, Leninskij prospect 38, korpus 6, Moscow, Russia.

One of the most potentially devastating biospheric effects of the Cretaceous/Tertiary (K/T) Chicxulub impact was the attenuation of sunlight by a massive sulfuric acid aerosol cloud created by the vaporization of anhydrite target rocks (1-3). Our previous studies (3) indicated that the sulfuric acid aerosol may have extended global blackout condition several months beyond that proposed for the dust, but these calculations were based on the assumption of rapid conversion of impact-generated stratospheric SO_2 to H_2SO_4 aerosol. We developed a more sophisticated model for our current study by incorporating more realistic H_2SO_4 production rates derived from studies of Venusian atmospheres and the scaling-up of Earth volcano models. Our results indicate that the Chicxulub impact caused prolonged, severe cooling, lasting many decades to several centuries. Temperatures gradually cooled to well below freezing for many years in regions not buffered by the heat released from the warm Cretaceous oceans.

We applied the results of our previous model of impact vaporization (3) with only slight modifications. This model predicts the mass of sulfur injected into the stratosphere by a 10 km or 20 km diameter asteroid. These two bolide diameters correspond to craters with diameters of about 180 km and 300 km, which bracket the proposed dimensions of the Chicxulub crater (4,5,6). The amount of SO_2 produced by the model impacts, given the two bolide diameters and total vaporization occurring between 30 and 60 GPa, ranged within an order of magnitude of 10^{18} g.

The conversion rate of 10^{18} g of SO_2 to H_2SO_4, when scaled-up using the rates established for large volcanic eruptions (7), gives a SO_2 lifetime of 200 yrs. The lifetime of SO_2 on Venus is also estimated to be 200 yrs (8), and the Venusian atmosphere has a sulfur mass similar to that produced by the Chicxulub impact. The relatively slow rate of acid production is due to limits on the photochemical oxidation of SO_2 caused in part by the attenuation of sunlight by the sulfur cloud (9).

We adapted our previous (3) atmospheric model to incorporate a range of potential SO_2 lifetimes from 50 to 1000 years. Our 1 D model predicts the reduction in solar energy reaching the Earth's surface based on radiative transfer calculations including the processes of SO_2 to H_2SO_4 conversion, coagulation of acid aerosol droplets, and sedimentation. The model contains 12 stratospheric layers, and tracks the optical properties of the aerosol particles as they coagulate and fall, which on average takes about 1 yr. The final model results include predictions of surface temperature changes that would occur if equilibrium with incoming solar radiation was achieved (i.e. black body calculations neglecting the thermal reservoir effect of the oceans).

PROLONGED BIOSPHERIC EFFECTS OF CHICXULUB IMPACT: Pope et al.

Our baseline prediction of 10^{18} g of SO_2 converting completely to H_2SO_4 in 200 years would reduce the amount of solar radiation reaching the Earth's surface by about 90% for the 200 yr period. Faster conversion rates (i.e. SO_2 lifetimes of 100 or 50 yrs) would reduce solar input slightly more. An SO_2 lifetime of 1000 years would still reduce solar input by more than 75%. The equilibrium (black body) surface temperature for all these scenarios falls between 50-100° C, which would have dropped surface temperatures well below freezing if equilibrium was achieved. Our model shows that even if only 1% of the SO_2 converted to H_2SO_4 over the proposed 200 yr lifetime (i.e. if there is another sulfur sink not accounted for in our model), equilibrium temperatures would still fall well below freezing.

Actual surface temperatures are difficult to estimate, and for a period the ocean thermal reservoir would have kept temperatures above freezing. General Circulation Models (GCMs) of temperature perturbations with impact aerosol loadings similar to our estimates predict actual surface freezing conditions in middle to high latitudes and continental regions within a month of the impact (10). Therefore it is reasonable to assume that within the first few years following the Chicxulub impact permanent freezing conditions would have developed in many continental regions, and that this cooling would have been much more severe than recent impact models have prtedicted (10). The GCMs have not been run for prolonged perturbations of decades to centuries, a time interval in which the oceans would cool significantly and freezing conditions may have expanded throughout much of the globe.

REFERENCES

(1) Sigurdsson H., D'Hondt, S., and Carey, S. (1992), Earth and Planetary Science Letters 109, 543-559.
(2) Brett, R. (1992), Geochimica et Cosmochimica Acta 56, 3603-3606.
(3) Pope, K.O., Ocampo, A.C., Baines, K.H., and Ivanov, B.A.(1993), LPSC XXIV, 1165-1166.
(4) Hildebrand, A.R., Penfield, G.T., Kring, D.A., Pilkington, M., Camargo Z., A., Jacobsen, S.B., and Boynton, W.V. (1991), Geology 19, 867-871.
(5) Sharpton et al. 1993, Science 261, 1564-1567.
(6) Pope, K.O., Ocampo, A.C., and Duller, C.E., (in press), Earth, Moon, and Planets.
(7) Pinto, J.P., Turco, R.P., and Toon, O.B., 1989, Journal of Geophysical Research 94, 11,165-11,174.
(8) Prinn, R.G., and Fegley Jr., B., 1987, Annual Review of Earth and Planetary Science 15, 171-212.
(9) Winick, J.R., and Stewart, A.I.F., 1980, Journal of Geophysical Research 85, 7,849-7,860.
(10) Covey, C., Ghan, S.J., Walton, J.J., and Weissman, P.R., 1990, GSA Special Paper 247, 263-270.

This project was funded by the Exobiology Program of the National Aeronautics and Space Administration.

SYSTEMATICS OF Xe ISOTOPES IN A TWO-LAYER EARTH WITH MASS TRANSPORT

D. Porcelli and G. J. Wasserburg, The Lunatic Asylum, California Institute of Technology, Pasadena, CA 91125.

We present a model of steady-state transport of Xe through the upper mantle. A steady-state upper mantle supplied by a flux from a deeper reservoir has been modelled previously for He [1,2] and Pb [3]. In such a system, upper mantle Xe reflects the isotopic characteristics of the deeper source altered by present production of radiogenic isotopes, in contrast to the standard model [4] in which upper mantle Xe is residual from atmosphere removal. This model satisfies earlier arguments for deeper storage of Xe [5,6] and it will be shown here to account for observed MORB data. We will show that consideration of the transport equations yields the following conclusions: 1) ^{136}Xe excesses generated in the lower mantle are derived from Pu and may be augmented by U decay in the upper mantle; 2) the ^{129}Xe excess is stored in the lower mantle; 3) the upper mantle is greatly depleted in Xe; and 4) the observed MORB isotopic compositions can be accommodated. A subducted Xe flux is also considered. The source of the atmospheric Xe is not addressed. The mantle is divided into upper (D) and lower (P) reservoirs. No assumptions are made of the initial state of Xe in P. Xe transfer is advective, with mass fluxes into the upper mantle by subduction and from P through material rising in hotspots. For a steady state upper mantle, following of [1]:

$$C_P^i \dot{M}_{PD}(1 - r) + C_S^i \dot{M}_{SD} + C_D^U M_D P_D^i = r a C_D^i \dot{M}_{PD} + C_D^i \dot{M}_{MOR} \quad (1)$$

with $\dot{M}_{PD}$ = mass transfer rate from P to D; $\dot{M}_{SD}$ = mass subduction rate; $\dot{M}_{MOR}$ = rate of processing D at ridges; P_R^i = production of i per gram of U per year; C_R^i = concentration of i in reservoir R (D, P, or subducted materials; (1-r) = fraction of rare gases not lost directly to the atmosphere at hotspots; a = degree of entrainment of upper mantle material at hot spots. Rearranging with $\gamma = \dot{M}_{SD}/\dot{M}_{MOR}$ and $C_D^U/C_P^U = f$:

$$C_D^i/C_P^i = \frac{(1 - r)\dot{M}_{PD}}{(ra\dot{M}_{PD} + \dot{M}_{MOR})}\left(1 + \frac{C_S^i \gamma \dot{M}_{MOR}/C_P^i}{(1 - r)\dot{M}_{PD}} + \frac{C_P^U f M_D P_D^i/C_P^i}{(1 - r)\dot{M}_{PD}}\right) \quad (2)$$

The second and third terms in the parentheses are the fractional increase of i in D due to subduction (δ_{SD}^i) and production in D (δ_{SF}^i), respectively. For ^{136}Xe, $C_P^{136} = C_{PO}^{136} + C_{P_{SF}}^{136}$. Although C_{PO}^{136} is not known, $C_{P_{SF}}^{136}$ can be calculated:

$$C_{P_{SF}}^{136} = C_P^U[3.5 \times 10^{-8} + 1.4 \times 10^{-4} C_O^{244}/C_O^{238}] = 3.3 \times 10^7 \text{ atoms/g} \quad (3)$$

For $C_O^{244}/C_O^{238} = 6.8 \times 10^{-3}$ [7] and $C_P^U = 5.5 \times 10^{13}$ atom/g (22 ppb U). For ^{129}Xe:

$$C_P^{129} = C_O^{129} + I_P^{129} = C_O^{129} + \left(C_P^{129I}/C_P^{127I}\right)_O \left(C_P^{127I}/C_P^U\right)_\odot g F C_P^U = C_O^{129} + (3.2 \times 10^{11}) g F \quad (4)$$

where g is $(I/U)_P/(I/U)_\odot$ and F is the depletion factor of ^{129}I due to early losses of radiogenic ^{129}Xe. Note that for estimated g of $\sim 10^{-2}$ for I [8], ^{129}I has generated $\sim (3 \times 10^9)$F atoms ^{129}Xe/g in P. There will be a larger number of radiogenic ^{129}Xe atoms to $^{136}Xe_{SF}$ for F>0.01.

Equation 2 has a term common to all *i*, $(1 - r)\dot{M}_{PD}/(ra\dot{M}_{PD} + \dot{M}_{MOR})$. This is the ratio of C_D^i/C_P^i if there are no sources in D. From estimates of $\dot{M}_{PD}, \dot{M}_{MOR}, a$, and r > 0.7 [1], there must be at least two orders of magnitude decrease in concentration in D relative to P. If the atmosphere was formed by earlier degassing of D, then the fraction of radiogenic ^{129}Xe that may be remaining in D can be compared to the Xe in D derived from P. For the present steady state with a residence time of 1.4Ga[1], the amount of Xe remaining is $C_D^{129^*} = C_P^{129^*} e^{-4.55/1.4} = 0.03\, C_P^{129^*}$. This can be compared to the amount in D from P of $C_D^{129^*} \sim C_P^{129^*} 10^{-2}$. However, if upper mantle cycling was more vigorous in the past and has diminished on a timescale of 2.5 Ga, then the $C_D^{129^*}/C_P^{129^*} = 5 \times 10^{-5}$ [1].

The fractional shifts in C_D^{136} due to radiogenic production in D and subduction are shown in Fig. 1. Due to the depletion of D and the timescales of extraction, significant shifts are possible. For an estimated range of $M_D/\dot{M}_{PD} = (1\text{-}5) \times 10^{10}$ [1], the fraction of radiogenic ^{136}Xe to the total radiogenic ^{136}Xe concentration ($\delta_{SF}^{136^*}$) is substantial (10-50%). The effect of radiogenic production in D on the total ^{136}Xe inventory, δ_{SF}^{136} (and so the effect

SYSTEMATICS OF Xe ISOTOPES: Porcelli D. and Wasserburg G.J.

on the isotopic composition of Xe), cannot be determined without an estimate of C_P^{136}. To examine the potential effects, an estimate will be used initially of $N_{Atm}^{136}/M_D = 3.8\text{x}10^8$ atoms/g. For the estimated range of $M_D/\dot{M}_{PD}$, shifts of several percent are obtained. The fraction of subducted ^{136}Xe to total ^{136}Xe (δ_{SD}^{136}) for various values of $C_S^{136}\gamma$ (the number of atoms subducted per gram of processed D at ridges) is plotted. Significant effects are found for $C_S^{136} > 5\text{x}10^5$. For comparison, a value of $5.0\text{x}10^7$ is obtained from data in [9] for material approaching trenches. Although much of this may be removed at subduction zones, only 0.2% is required to be subducted to have a significant impact on the upper mantle Xe budget. Combining eq. 2 for ^{136}Xe and ^{130}Xe and no subducted flux, $(^{136}Xe/^{130}Xe)_D - (^{136}Xe/^{130}Xe)_P = (C_D^U P_D^{136} M_D)/[(1 - r)\dot{M}_{PD} C_P^{130}]$. In Figure 2 the shifts in ^{136}Xe/^{130}Xe ratio due to production in the upper mantle are plotted agains C_P^{130}. For the estimated range of $M_D/\dot{M}_{PD}$ of (1-5)x 10^{10} [1], the relatively large excesses seen in Harding Co. well gas [10] and some MORB [e.g.4] can be generated for a value of C_P^{130} that is 10 times lower than N_{atm}^{130}/M_D. To explain the same shift in ^{136}Xe/^{130}Xe, $M_D/\dot{M}_{PD} = 3\text{x}10^{11}$ would then require C_P^{130} $= 4\text{x}10^8$ atoms/g. The evolution of Xe isotopic compositions is shown in Fig. 3 along with the effects of subduction. Decay of ^{129}I and ^{244}Pu in the lower mantle (P) generates ^{129}Xe and ^{136}Xe excesses. Entrainment of material from P into D is followed by U-derived increases in the ^{136}Xe excess. Subduction of Xe will reduce the ^{129}Xe and ^{136}Xe excesses on a trajectory towards atmospheric compositions. The MORB array is due to either atmospheric contamination during emplacement, though alteration, or by exposure on the seafloor. Division Contribution 5355(830). Work supported by NASA NAGW-3337. Refs.[1]Kellogg & Wasserburg (1990) *EPSL 99*, 276. [2]O'Nions and Oxburgh (1983) *Nature 306*, 429. [3]Galer and O'Nions (1985) *Nature 316*, 778. [4]Allègre et al. (1983) *Nature 303*, 762. [5]Ozima et al. (1985) *Nature 315*, 471. [6]Porcelli et al. (1986) *LPSC XVII*,674. [7]Hudson et. al. (1989) *Proc. 19th LPSC*, 547. [8] Wänke and Dreibus (1988) *Phil. Trans. R. Soc. Lond A325*, 545. [9]Staudacher and Allègre (1988) *EPSL 89*, 173. [10]Phinney et al. (1978) *JGR 83*, 2313.

FIGURE 1

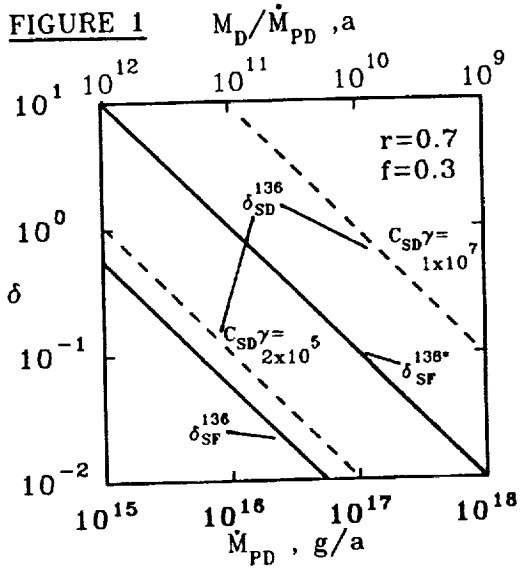

FIGURE 2

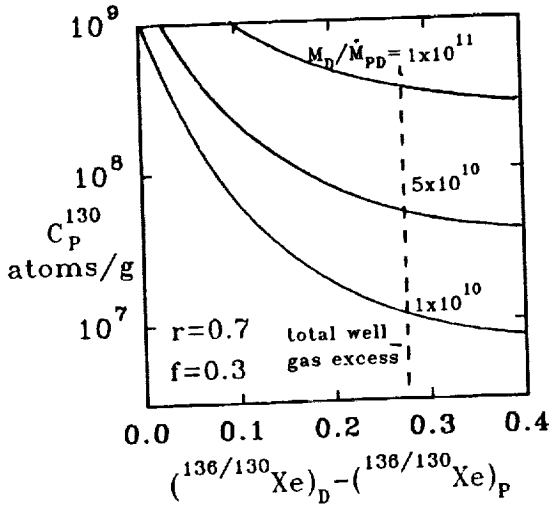

FIGURE 3

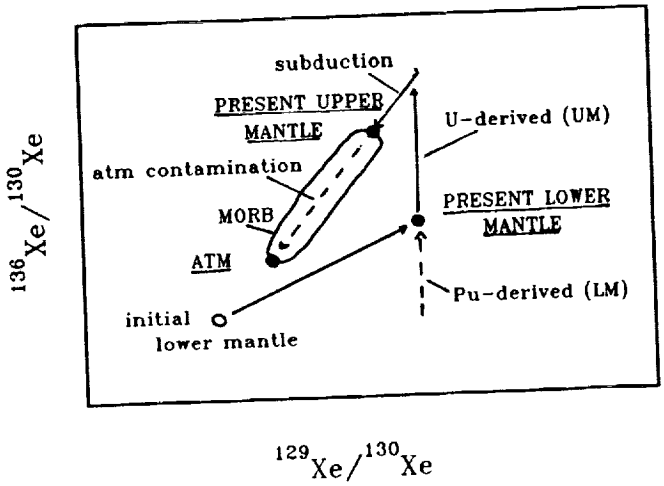

ATTEMPT TO OBSERVE THE SODIUM EXOSPHERE OF MERCURY DURING THE 1993 SOLAR TRANSIT: A.E. Potter, NASA Johnson Space Center, D. Talent, Lockheed Engineering and Science Co., H. Kurokawa, Hida Observatory, Japan, S. Kawakami, Osaka Museum of Science, Japan, and T.H. Morgan, Southwest Research Institute.

Introduction. High-resolution spectra of the region around the shadow of Mercury during its transit across the Sun can yield information about the altitude distribution of sodium in the Mercury exosphere. Measurements of sodium resonance emission have shown that both Mercury and the Moon possess sodium vapor exospheres [1,2]. In the case of the Moon, the sodium exosphere can be detected up to 1500 km above the subsolar point [3], and there is evidence for a "tail" of sodium vapor extending behind the Moon [4]. The lunar measurements give rise to a speculation that a similar extended exosphere might exist for Mercury. Efforts to detect such an exosphere using conventional ground-based spectroscopy have not been successful, perhaps because of the relatively poor spatial resolution of such measurements. Transit of Mercury across the face of the Sun gives an opportunity to look for an extended exosphere by observation of sodium vapor in absorption above the Mercury surface. Our measurements of the sodium D resonance emission from the Mercury sodium atmosphere have shown that sodium vapor is optically thick near the poles [5], so it was reasonable to expect that this sodium could be detected in absorption during transit of Mercury across the Sun.

Transits of Mercury are not common-- only fifteen transits occur in the hundred-year interval from 1951 to 2050. The transit of interest here occurred on 03:57 UT on 6 November 1993. The previous transit was on 04:07 UT 13 November 1986, and the next one will be on 21:41 UT 15 November 1999. The 1993 transit was best observed in Asia and Australia. The Hida Solar Observatory in Japan was well placed geographically for observation of the transit, and was equipped with a high-resolution solar spectrograph, capable of resolution 1,250,000 in fifth order.

Our approach was to use an imaging detector placed at the exit slit of the solar spectrograph. One dimension of the image was spatial, the other spectral. By using a slit length longer than the planetary angular width, we could obtain spectra across the planet, and into the region above and below the planet. By orienting the spectrograph slit north-south, and east-west, we could measure the spectrum across the polar and equatorial regions. We prepared two detection systems for observation of the transit. A CCD detector was provided by the Science Museum of Osaka, Japan, and an intensified video system was provided by NASA Johnson Space Center. The CCD detector provided calibrated photometric data, but with a rather slow exposure time of about 1 second, while the intensified video system was capable of collecting thirty frames per second. It was expected that selected video frames would provide very high spatial resolution. The transit time was predicted to be about 1 hour 30 minutes, so

that sufficient time was available to collect images with both types of detectors.

Results. Although eastern Japan remained clear during the transit, the weather did not cooperate at the Hida Observatory site in the Japanese alps west of Osaka. Observations were possible for only a short time at the beginning of the transit. However, useful measurements were done in the short time available. The observations began with the CCD detector, and spectra across Mercury were obtained at a resolution of 840,000 for both north-south and east-west orientations of the slit. Following this, video observations were attempted, but by this time, cloud cover greatly reduced the quality of the measurement.

A sample of the CCD spectra obtained is shown in Figure 1. where the sodium D_2 solar Fraunhofer line is plotted. This particular spectrum was taken from the north polar edge of the shadow of Mercury on the Sun, and we expected to see sodium resonance absorption, Doppler-shifted by the radial velocity of Mercury at the time of the transit. The position of the absorption expected from the sodium resonance line is marked on this spectrum. There is no evidence for sodium absorption in this, or any other of the spectra that we obtained. This result means that sodium density at altitude above the surface the planet must be small, in spite of the fact that sodium vapor is found to be optically thick over the illuminated surface of the planet in the polar regions. Evidently, the sodium exosphere of Mercury is not extended in the same way as the Moon. Further analysis of the data is expected to yield upper limits to the sodium abundance at altitude above the surface.

References. [1]Potter, A.E. and T.H. Morgan (1985) Science, 229, 651 [2]Potter, A.E. and T.H. Morgan (1988) Science, 241, 2097 [3] Potter, A.E. and T.H. Morgan (1988) GRL 15, 1515 [4] Mendillo, M, J. Baumgardner,and B. Flynn (1991) GRL 18, 2097 [5]Killen, R.M., A.E. Potter, and T.H. Morgan (1990) Icarus 85, 124

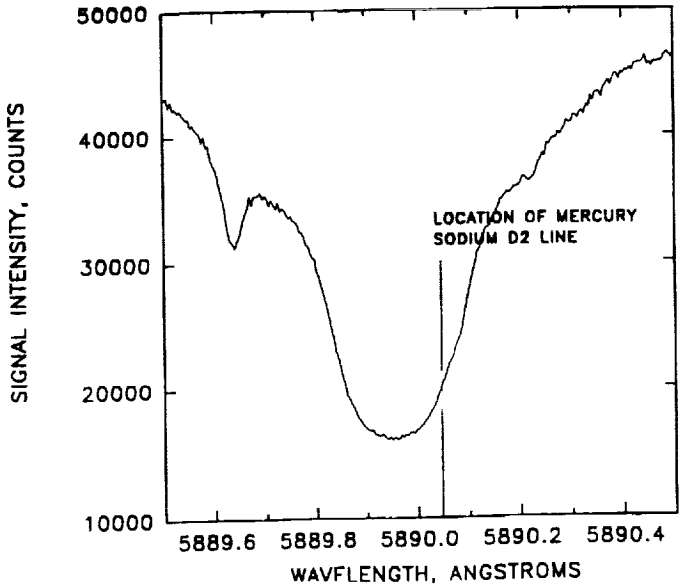

Figure 1. Solar Spectrum at the Edge of Mercury During Transit

DISCOVERY AND DESCRIPTION OF A MUONG NONG-TYPE GEORGIA TEKTITE; Harold Povenmire, 215 Osage Drive, Indian Harbour Beach, FL 32937; B. P. Glass, Geology Department, University of Delaware, Newark, DE 19716; Robert Strange, Sandersville, GA 31082.

One of us (RS) found an unusually large, blocky, layered tektite just south of Riddleville, Washington County, Georgia (32° 53′ N. Lat., 82° 40′), on July 31, 1993. This specimen weighs 130 g and measures approximately 4 x 5.5 x 6 cm. Layering is evident on the surface of the specimen due to differential solution. Layering is also evident in four 1-2 mm thick slices that were cut from the specimen (Fig. 1); it occurs as streaks or layers of dark (olive brown) glass in a pale green transparent glass. Vesicles are abundant, but generally less than 200 μm in diameter. Lechatelierite is common. Several translucent to opaque white inclusions, generally between 20 and 60 μm in size, were also observed in the slices. These inclusions are apparently zircon and/or baddeleyite [1]. Major oxide compositions of polished grain mounts, determined by energy dispersive x-ray analysis, show that the specimen is generally similar in composition to previously analyzed North American tektites (Table 1), but with a much greater range in composition [1].

This specimen is unique for several reasons: 1) it was found in the extreme northeastern part of the Georgia strewnfield [2]; 2) it is larger than any previously reported Georgia tektite (prior to the discovery of this specimen the largest known Georgia tektite weighed 70.5 g [3]); 3) it is the only known Muong Nong-type or layered tektite found in Georgia; and 4) it is the only North American tektite known to contain zircon grains as well as baddeleyite.

Because of the unique nature of this specimen, a consortium was set up to study it. The major element composition and petrography are being determined by B. P. Glass, the Rb-Sr and Sm-Nd systematics by J. Blum, the ^{39}Ar-^{40}Ar age by G. A. Izett and J. D. Obradovich, the water content and trace element composition by C. Koeberl, and the magnetic properties and iron oxidation state by F. E. Sentfle.

References: [1] Glass, B. P. et al. (1993) LPS XXV (this volume); [2] Povenmire, H. (1982) Meteoritics, 17, 145; [3] Povenmire, H. (1980) Meteoritics, 15, 85; [4] O'Reilly, T. C. (1983) LPS XIX, 580; [5] Cuttitta, F. (1967) JGR, 72, 1343; [6] Glass, B. P. (1989) Meteoritics, 24, 209.

Table 1. Major oxide compositions of Muong Nong-type Georgia tektite and splash form Georgia tektites, the Martha's Vineyard (MV) tektite, and Site 612 tektite glass.

	MN Georgia Tektite (this study)			Georgia Tektites LET-4 [4]	(this study)	MV-2082 [5]	Site 612 [6]
SiO_2	77.6	80.5	87.4	77.5	80.4	80.5	77.5
Al_2O_3	13.2	11.7	7.06	12.54	11.4	11.2	13.1
FeO*	2.80	2.17	0.93	2.95	2.74	2.65	2.82
MgO	0.93	0.82	0.47	0.71	0.81	0.69	0.95
CaO	0.62	0.56	0.33	0.71	0.54	0.69	0.68
Na_2O	0.80	0.65	0.56	1.98	0.66	1.00	0.92
K_2O	2.65	2.45	2.36	2.36	2.40	2.37	3.10
TiO_2	0.68	0.50	0.26	0.63	0.47	0.53	0.46

*All iron reported as FeO.

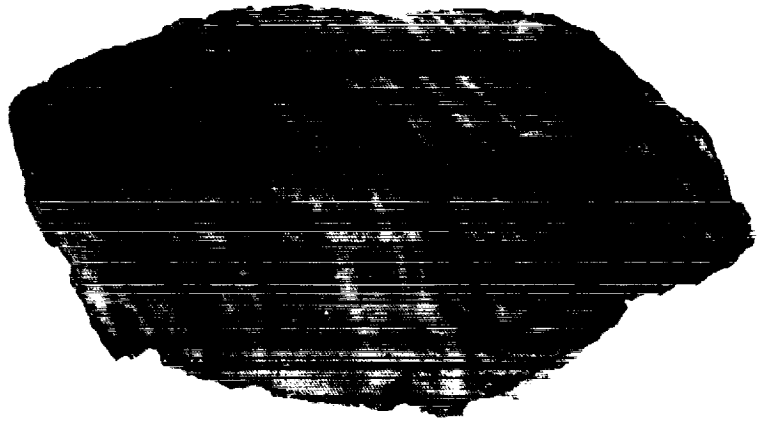

Figure 1. Photograph of millimeter-thick slice of MNGaTek showing layering. Scale bar equals one centimeter.

Pb ISOTOPIC SYSTEMATICS OF TROCTOLITIC ANORTHOSITE 62237;

W.R. Premo and M. Tatsumoto, U.S. Geological Survey, Denver, Co. 80225

Preliminary Pb isotopic data for two mineral separates, plagioclase and pyroxene, from troctolitic anorthosite 62237 yield an age of 4103 ±110 Ma, although there may be reason to suspect that this rock is as old as 4343 Ma. An olivine separate from previous work tends to support an isochron that identifies an old radiogenic source for this rock. Assuming either age, the single-stage $^{238}U/^{204}Pb$ (μ) for the anorthosite source is >1000, a value similar to KREEP sources and larger than those for sources of most other anorthosites and high-Mg suite rocks. High-μ magmas may have been derived from a residual, highly-evolved portion of the upper lunar mantle that developed in the late stages (~4.4 to 4.45 Ga ?) of primary lunar differentiation of a magma ocean. A combination of Pb partitioning into a dominantly plagioclase-rich crust (relatively low-μ anorthosites) and a sulfide-metal-rich core probably helped produce such an evolved upper mantle reservoir.

Most anorthositic and noritic rocks sampled by the Apollo missions exhibit excess radiogenic Pb (i.e. Pb that cannot be attributed to the in-situ decay of U and Th). This excess Pb, usually considered "initial" Pb, varies from sample to sample, implying that either some samples represent rocks derived from sources with different U/Pb values, or the rocks have acquired Pb of various compositions and proportions after formation [1,2,3]. Although many of the anorthosites have been described as pristine [4,5] with mainly igneous textures [6,7], undoubtedly most, if not all, samples are actually conglomerates or breccias. The fact that some samples have clasts that preserve primary igneous textures only attests to their mode of origin. Most anorthositic samples have been analyzed for U-Th-Pb as whole-rocks and plagioclase mineral separates, and sometimes as bulk mineral separates; for example, magnetic, non-magnetic, or mafic fractions. Whereas the actual analytical data for these whole-rock and mineral separates may be precise, they often do not behave as a linear array as one might expect from truly primary igneous rocks. Scatter is not uncommon in the U-Pb results from lunar anorthosites [8,9,10], and may point out the fact that the individual mineral grains may not actually be derived from a single source region, or may contain secondary Pb of various compositions and proportions.

We have, therefore, continued our search for a well-behaved anorthosite by analyzing Apollo 16 Type II clastic anorthosite 62237. This troctolitic anorthosite has been described as relatively pristine and monomict in its mineralogy and chemistry [4,6]. It is very light gray, moderately friable, with ~83 % shattered and broken anorthitic plagioclase grains and a notably higher olivine content (~16 %) than other Apollo 16 anorthosites. Plagioclase and olivine form what appears to be a primary igneous texture, and the other trace minerals occur mainly as inclusions in plagioclase and olivine [6]. Our analytical procedures are not very different than those used previously [10,11]. The original subsample of one piece weighed approximately 1.76 gm and was shaken in a sealed quartz vial until no further disaggregation occurred. The largest chips were removed, crushed, and sieved. The entire sample has been split into several fractions; however, Pb isotopic data for only three separates have been collected thus far. Those separates include a magnetically-separated plagioclase (PL), a hand-picked (+80-μm-size) pyroxene (PYR), and a -80-μm-size pseudo-whole-rock (WR). These fractions were subjected to alcohol washing and three dilute acid leachings (two HBr and one HNO_3) designed to remove terrestrial contamination and strip the grain surfaces of any adsorbed Pb component [2]. The Pb isotopic results from only the residues of these separates (washes and leaches will be analyzed soon) are shown in Figure 1 and compared to results from previous work on 62237 [10] and other lunar highland rocks [11,12,13,14,15,16]. We have more mineral separates and whole-rocks to measure and the U-Pb isotopic results are not complete at present.

The residues (solid circle, square, and diamond) of 62237 do not form an linear array (Fig. 1). Plagioclase from this study plots to the upper-left portion of the data near the results from anorthosites 67075 [15] and 15415 [14], indicating its derivation from a very radiogenic source. The PYR separate exhibits a very radiogenic Pb composition and plots near the y-axis at a $^{207}Pb/^{206}Pb$ value of ~0.538 that yields an age of 4.34 Ga. The fine-grained pseudo-whole-rock separate, however, does not conform to a linear array between PL and PYR, but instead plots toward some non-radiogenic Pb composition, suggesting mixing with a material derived from a relatively low-μ source. Similar Pb isotopic data were obtained from anorthosites 62237 and 67075 [10,17], and indicate the mixing of Pb components from different sources. Nonetheless, PL and PYR probably represent accurate compositions for these assemblages. The Pb isotopic data for the two mineral separates yield an age of 4103 ±110 Ma (dashed line), and an olivine separate from previous work [10] tends to support this isochron. However, PYR does not lie very far from the y-axis and subtracting a few more pg of blank Pb from this analysis dramatically alters the y-axis intercept and age. For example, the addition of 5 pg of blank yields an age of 4164 Ma and 10 more pg, an age of 4231 Ma. Although we attempt to establish a constant Pb blank during sample processing, usually there is some variation (this study: between 34 and 45 pg). Bearing this in mind, it is possible that the pyroxene-plagioclase line may indicate an age as old as 4343 Ma, assuming all the ^{204}Pb is removed as blank Pb. Assuming either age, 4.1 or 4.34 Ga, the single-stage, source $^{238}U/^{204}Pb$ (μ) for the anorthosite is >1000

Pb ISOTOPES IN ANORTHOSITE 62237: Premo, W.R. and Tatsumoto, M.

(intersection of dashed line with the evolution lines), a value indicative of KREEP sources and larger than those for sources of most other anorthosites and high-Mg suite rocks. It is also possible that 62237 is a polymict breccia in that the plagioclase is mixed with or contaminated by Pb produced from early-formed, high-μ magma sources rather than derived from them.

In contrast to the high-μ data, an alternative array(s) is defined by whole-rock and plagioclase separates from anorthosite 60025 that yield ages ~4.41 to 4.43 Ga and indicate derivation from a low-μ (~35 to 100; [13]) source. Pb data from other anorthosites, including 67075 and 15415, lie between low-μ Pb compositions for 60025 plagioclase and the high-μ-derived, high $^{207}Pb/^{206}Pb$ compositions, implying that these polymict breccias are composed of plagioclase derived from both sources.

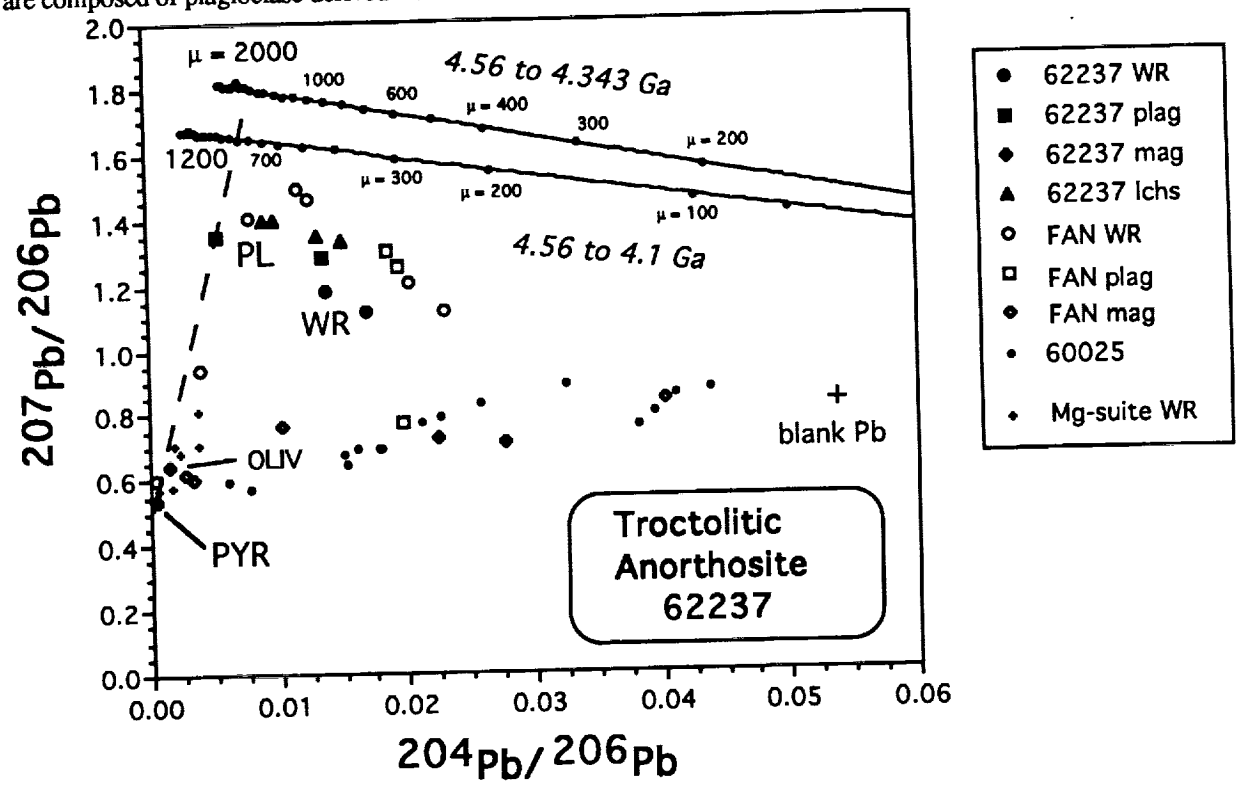

Figure 1: Pb-Pb isotopic data for troctolitic anorthosite 62237. Pb evolution isochrons show the loci of Pb values for lunar sources with μ ($^{238}U/^{204}Pb$) values between ~100 and ~2000 calculated from 4.56 Ga as the age of the Moon to both 4.1 Ga (isochron age of anorthosite 62237) and 4.343 Ga (possible age of pyroxene separate).

High-μ magmas may have been derived from a residual, highly-evolved portion of the upper lunar mantle that developed in the late stages (~4.4 to 4.45 Ga ?) of primary lunar differentiation of a magma ocean. A combination of Pb partitioning into a dominantly plagioclase-rich crust (relatively low-μ anorthosites) and sulfide-metal-rich core probably helped produce such an evolved upper mantle reservoir. Early bombardment probably played a role in the mixing of cumulates derived from both high-μ and low-μ sources, although intuitively it would seem that later impacting events caused the kind of brecciation that is the rule in most lunar samples. It shouldn't be surprising that nearly all of the lunar highland samples are breccias or soils composed of rocks produced at various crustal levels that at one time underwent extreme geochemical as well as isotopical variations.

References: [1] Silver L.T. (1970) Proc. Apollo 11 LSC, 1533. [2] Tatsumoto M. (1970) Proc. Apollo 11 LSC, 1595-1612. [3] Tera F. and Wasserburg G.J. (1972) EPSL 17, 36-51. [4] Warren P.H. and Wasson J.T. (1977) PLSC 8, 2215-2235. [5] Warren P.H. and Wasson J.T. (1980) Proc. Conf. Lunar Highlands Crust, 81-99. [6] Dymek R.F. et al. (1975) PLSC 6, 301-341. [7] McCallum I.S. et al. (1975) EPSL 26, 36-53. [8] Nunes P.D. et al. (1973) PLSC 4, 1797-1822. [9] Tera F. and Wasserburg G.J. (1974) PLSC 5, 1571-1599. [10] Premo W.R. et al. (1989) PLPSC 19, 61-71. [11] Premo W.R. and Tatsumoto M. (1991) PLPSC 21, 89-100. [12] Premo W.R. and Tatsumoto M. (1992) PLPSC 22, 381-397. [13] Premo W.R. and Tatsumoto M. (1993) LPS XXIV, 1173-1174. [14] Tatsumoto M. et al. (1972) in The Apollo 15 Lunar Samples (J.W. Chamberlain and C. Watkins, eds.), 391-395. [15] Oberli F. et al. (1979) LPS X, 940-942. [16] Hanan B.B. and Tilton G.R. (1987) EPSL 84, 15-21. [17] Premo W.R. and Tatsumoto M. (1989) LPS XX, 866-867.

Young Tectonism and Volcanism on Venus: Age Estimates from Crater Densities

Maribeth Price (1), John Suppe (1), Frank Bilotti (1), and Geoff Watson (2)
(1) Dept. of Geological and Geophysical Sciences, Princeton University, Princeton, NJ 08544
(2) Dept. of Mathematics, Princeton University, Princeton, NJ 08544

Abstract: We have found that it is feasible to estimate ages for geologic features on Venus using impact crater densities. Although [1] demonstrated that the crater population appears spatially random, areas defined on geologic criteria can have density variations that are significantly different from the mean global density. We have estimated mean ages for rifts, large volcanoes, lava flow fields, and wrinkle ridges. Our preliminary analysis suggests that volcanism, rifting, and wrinkle ridge formation have all been active within the last 100 Ma.

Observations: Using impact density to estimate age is an accepted technique for Mars, Mercury, and the Moon, but has been considered inappropriate on Venus due to the low number (~900) and apparent randomness of craters. However, there are indications that this technique can be useful on Venus. First, Figure 1 shows that rifts and large volcanoes roughly correlate with low crater density. Second, when areas are delineated on geologic criteria, their crater densities differ from the global density at a confidence level of over 95%. Table 1 shows the crater densities for lowland plains, rifts, large volcanoes, and lava flow fields. Volcanic features were mapped from locations provided by [2]. Impact crater locations were provided by [3].

We have argued [4] that the impact data support a globally synchronous resurfacing of Venus [1], and that subsequent resurfacing is associated mainly with tectonism and volcanism in the highlands. It follows that the relatively quiescent lowland plains record a background crater density reflecting the age of the global event. By comparing the densities of geologic areas to the background density (D/Do), we can estimate the ages of deformation and volcanism as a fraction of the mean global age **T**. In the following discussion, we report ages both as a fraction of **T** and in Ma, assuming that **T** = 500 Ma [1].

Model: The number of impacts in a geologic area is a function of the original age of the undeformed surface, and the timing and extent of: 1) changes in area due to deformation, and 2) resurfacing by volcanism and tectonism. This simple model assumes: 1) the plains record a background density reflecting the age of global resurfacing, 2) the cratering process is spatially random and rate-constant over the past **T** Ma, 3) the deformation and volcanism occurs instantaneously, and 4) the geologic terrain is all the same age. Clearly assumptions (3) and (4) are gross generalizations, but the model is a starting point for comparing ages of tectonic and volcanic events. Model ages represent the weighted sum of a mixture of ages in the terrain.

In volcanic terrains, little deformation is involved, and the model age is simply (D/Do)**T**. Large volcanoes have a density of 0.48 ± 0.13 (craters/million sq. km.), giving a mean age of 0.2**T** (100 ± 30 Ma). A density this low cannot be produced by steady-state volcanism over the past **T** Ma; an increasing rate or recent pulse of volcanism is required. Local stratigraphic relations between volcanoes and the surrounding features suggest that some volcanoes are older and others may be quite young. Lava flow fields have a density of 0.89 ± 0.31, or a model age of 0.4**T** (200 ±75 Ma).

We have modelled the crater density of rifts as a whole, although preliminary mapping suggests that at least two ages of rifting are present. Based on preliminary mapping, we estimate that 30% ± 10% of the rifts are occupied by syn- or post-rift volcanic deposits, that <5% of the rifts have been resurfaced tectonically to the point of obliterating craters, and that the overall fractional change in area of old target due to deformation, averaged over the rift system, is 1.2 ± 0.1. The crater density of the rifts is 1.50 ± 0.20. From these ranges of values we obtain a model age of 0.4**T** (200 Ma (+ 100 Ma, -200 Ma)), as shown in Figure 2. However, many of the large volcanoes are contemporaneous with rifting based on local field relations; hence we suspect that some of the rifts are less than 100 Ma old.

Although the linear nature of wrinkle ridges does not lend itself to an area-based analysis, we have considered the proportion of impacts which post-date the ridges. Initial attempts have been made to determine relative ages of impact craters vs. wrinkle ridges in the plains surrounding Aphrodite Terra. By observing the interactions of crater ejecta and outflow deposits with small scale topography, we find that 20% of the craters postdate wrinkle ridge formation. This initial estimate places the age of wrinkle ridge formation around Aphrodite at about 0.2**T** (100 Ma).

Young Tectonism and Volcanism on Venus: Age Estimates from Crater Densities: Price, M. et al.

Conclusions: Geologically defined areas on Venus can have significant variations in crater density relative to the global mean. We used simple models to estimate ages for rifts, large volcanoes, lava flow fields, and wrinkle ridges. Although these model ages generalize complex age relationships, they clearly indicate the presence of young (~100 Ma) rifting and volcanism on Venus. Furthermore, the associations which have been observed between gravity highs, rifting, wrinkle ridges, and volcanism on Venus [5], combined with these data, make it very likely that Venus is an active planet today.

References: [1] Schaber et al., (1992) JGR 97:E8, pp. 13257-13302. [2] Head et al. (1992) JGR 97:E8, pp. 13153-13198. [3] Herrick and Phillips (1994), Icarus, in review. [4] Price and Suppe, EOS 74:43, p. 379. [5] Bilotti, Connors, and Suppe (1993) EOS 74: pp. 191.

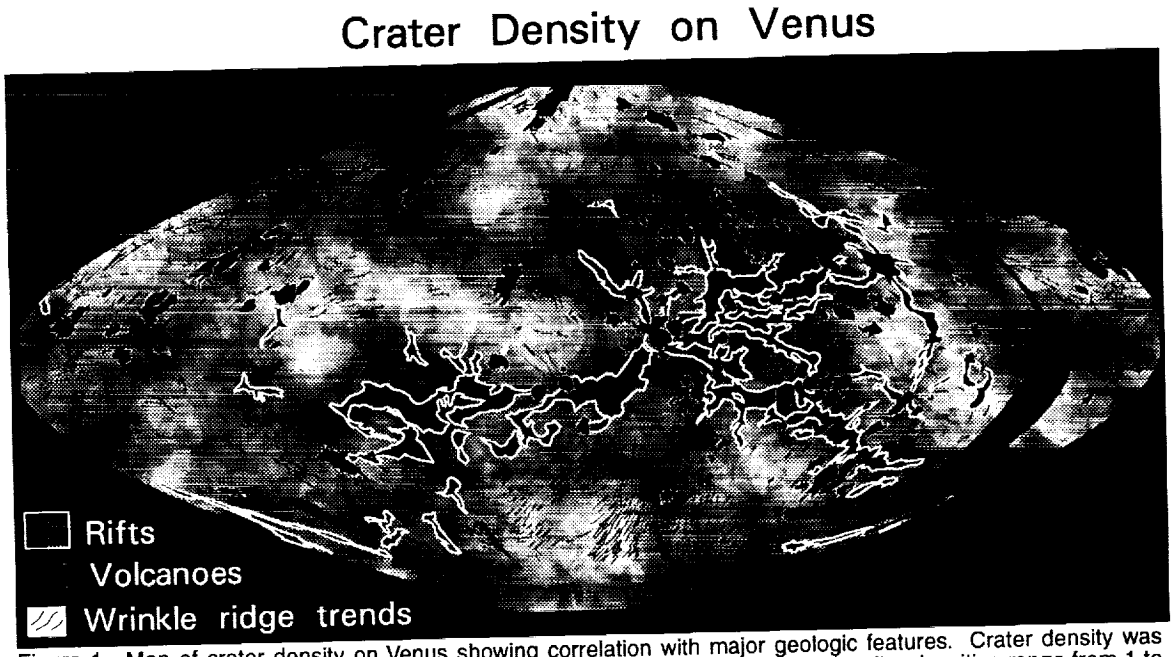

Figure 1. Map of crater density on Venus showing correlation with major geologic features. Crater density was computed using a moving 1300 km radius circle. Dark area represent low crater density--densities range from 1 to 3.5 craters/million sq. km.

Terrain	Area	Crater Density	Model Age (Ma)
Plains	344	2.06 ± 0.08	500 [1]
Rifts	36	1.50 ± 0.20	200 +100,-200
Volcanoes	25	0.48 ± 0.13	100 ± 30
Flow Fields	9	0.89 ± 0.31	200 ± 75
Wrinkle ridges	n/a	n/a	100 ± ??

Table 1. We have mapped the areas of several features, calculated their crater densities, and estimated mean ages using a simple model and assuming a global background age of 500 Ma. Areas are given in millions of sq. km.

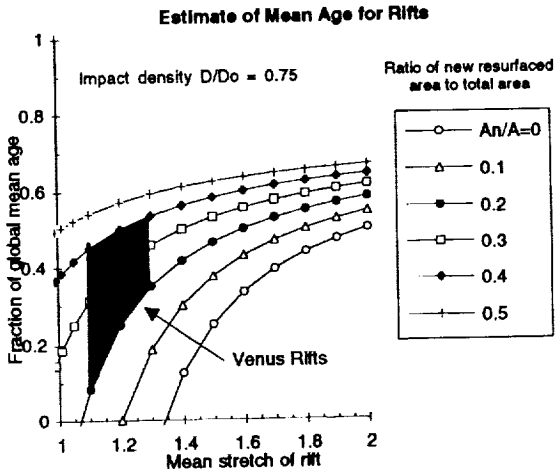

Figure 2. We have developed a simple model to estimate ages of tectonic features from the ratio of the crater density to the background global density (D/Do), the fraction of resurfaced area to the present area (An/A), and the fractional change in area of old target due to deformation (stretch). The black area shows the range of ages from preliminary estimates of these parameters for rifts with a crater density of 1.5 craters/million sq. km.

LEW 88774: A NEW TYPE OF Cr-RICH UREILITE. M. Prinz[1], M.K Weisberg[1], and C.E. Nehru [1,2]. (1) Dept. Mineral Sci., Amer. Museum Natural History, New York, NY 10024. (2) Dept. Geology, Brooklyn College, CUNY, Brooklyn, NY 11210.

LEW 88774 is a monomict ureilite that differs sharply from all other ureilites. The major mineral assemblage is a coarse-grained olivine-opx-cpx-chromite-carbon rock. Silicates and oxygen isotopes are those of Fe-rich ureilites, but the presence and abundance (6%) of chromite, the high pyx/(pyx+ol) ratio (0.9), and the coarsely exsolved pyx are unique. In addition, chromite-carbon reactions produced a new phase near $[Fe,Cr]_2C$, rare brezinaite (Cr_3S_4),and blades of eskolaite (Cr_2O_3) along chromite rims. Fine-grained interstitial in situ shock melt consists of feldspathic glass, silica, chromite and chromian pyx. The major minerals may be a residua that formed from a Cr-, C-enriched nebular component, at a depth of ~100 bars, by extensive smelting at lower P and pO_2 than that of the ol-pigeonite ureilites. This resulted in the formation of chromite and the reaction of some of the ol to produce more pyx. After extensive burial time, resulting in pyx exsolution, the assemblage was excavated by impact, resulting in in situ shock melting of the interstitial plag (plus some chromite and silicates). Due to the still lower P and pO_2, a second and incomplete phase of reduction took place, due to a rapid cooling rate, resulting in reduction rims on the silicates, and the reaction of the chromite with C to produce $[Fe,Cr]_2C$ and Cr_2O_3.

Introduction. LEW 88774 consists of a major mineral assemblage of 78.8 vol.% large (5mm) pyx crystals with equal amounts of exsolved opx and cpx; lamellae are ~20μm wide, but irregular crystals are also present. These are bounded by olivine (12.1%), chromite (5.8%), and carbon (3.8%), all up to 1mm in size. Olivine, chromite and carbon are also included in pyx. The pyx/(pyx+ol) ratio of 0.9 is greater than that of all other ureilites (0-0.5). Interstitial melt (1.2%) is present along grain boundaries and consists of SiO_2-enriched feldspathic glass and micron-sized grains of chromite plus chromian opx and cpx; tiny crystals of corundum (Al_2O_3) are also present. The margins of the large crystals of chromites and pyx are resorbed, and new chromite and pyx are grown onto them, as are fine symplectic intergrowths of all of these phases. Large olivine and pyx have reduction rims, and chromites are reduced along chromite-carbon contacts to blades (10μm) of eskolaite (Cr_2O_3). Chromite-carbon reactions also result in forming a new phase (1.3%), near $[Fe,Cr]_2C$ in composition, and rare grains of brezinaite Cr_3S_4).

Mineral Chemistry. The major mineral assemblage is equilibrated, with olivine at Fo_{74}, low-Ca pyx at Wo_4En_{75}, and cpx at $Wo_{33}En_{14}$. Olivine has a typical ureilite CaO of 0.25%, but "Cr_2O_3" at 0.35% is low. Chromites have compositions that differ from those of all other meteorites. They are zoned by reduction and range from $FeCr_2O_4$- to $MgCr_2O_4$- to $MgAl_2O_4$-rich, with increasing reduction (Fig. 1). Interstitial melt is a quench assemblage that includes mainly feldspathic glass, SiO_2, opx and cpx low in Fe and high in TiO_2 (1%), Al_2O_3 (2-3%), Cr_2O_3 (4-5%), chromite, and skeletal (1μm) crystals of corundum; symplectitic intergrowths are too fine to resolve. The $[Fe,Cr]_2C$ phase has (in wt. %) Fe (53-67), Cr (22-33), Ni (0.2-0.8). and C (10-12). Eskolaites have 71-77 Cr_2O_3, 20-26 Al_2O_3, and 3-4 TiO_2.

Discussion. Ureilites are a primitive achondrite group with seemingly irreconcilable chondritic and achondritic characteristics. LEW 88774 presents new aspects to the petrology/geochemistry of this group and thus provides constraints on previous hypotheses as to their origin. The formational history of this ureilite may be divided into three stages.

Stage 1. Nebular Processing. If originally of carbonaceous chondritic parentage, this ureilite would require not only reduction and partial melting, but must be followed by extensive fractional crystallization, to form a pyx- and chromite-rich cumulate. This is difficult to reconcile with oxygen isotopic data [1]. If it is a residua, the assemblage can form from chondritic abundances by reduction and partial melting (smelting with C) only if

the starting material is Cr- and C-enriched. This is necessary in order to provide adequate Cr to form the high chromite content, and provide a higher pO_2 than that of the other ureilites so that the chromite is stable. The mg# (74) of this ureilite is lower than that of any other ureilite as a result of the higher pO_2. The additional C would make the reaction $Fe_2SiO_4 + C = FeSiO_3 + CO$ procede further to the right than in other ureilites, resulting in the higher pyx/ol ratio. Krot et al. [2] proposed a nebular scenario involving incomplete evaporation of presolar material to explain chromite-rich chondrules. This type of presolar processing may be required to enhance the initial Cr content because planetary processes would not be adequate without extensive melting and crystal accumulation. Heterogeneity in the starting compositions of ureilites has already been indicated by large isotopic variations, especially in polymict ureilites. **Stage 2. Smelting and Equilibration.** Smelting relationships were determined by Walker and Grove [3] for the common ol-pigeonite ureilites, which are only slightly different from this Cr-pyx-rich ureilite. These data indicate that LEW 88774 underwent complete equilibration at depth in the ureilite parent body at T ~1200°C, at P ~100 bars, and with pO_2 at ~10^{-13}. The ol-pigeonite ureilites equilibrated at a slightly lower pO_2 (~$10^{-13.5}$ to $10^{-14.5}$), at which chromite was not stable; they also cooled rapidly after their high T formation, freezing in the pigeonite in most cases. As a result of the extremely slow cooling of LEW 88774 (millions of years) to the conditions described above, chromite was stable, more pyx formed at the expense of some of the olivine, exsolution of pyx to opx and cpx took place, and the texture was equiliibrated. **Stage 3. Excavation and Requilibration.** The major mineral assemblage of LEW 88774 was excavated by a major impact that resulted in bringing the meteorite closer to the parent body surface. This decompression and increase in T resulted in in situ melting of all of the minor interstitial plag, as well as some of the chromites and silicates, along the grain boundaries. This resulted in the resorbed margins of the chromites and silicates. This interstitial melt was quenched to produce the unusual fine-grained assemblage. The interstitial melt in other ureilites may be of similar origin, rather than trapped liquid. After excavation, the lower P (~ 25 bars), at high T, resulted in a highly reduced state, with a pO_2 of ~10^{-15}. This resulted in incomplete smelting, due to the rapid cooling rate (probably 10-15°C/hr), and produced reduction rims on the olivines and pyx, but also reactions between the chromite and C. This reaction may be expressed as: $2FeCr_2O_4+6C = 2[Fe,Cr]_2C+Cr_2O_3+5CO$. The aluminous eskolaite equilibrated at a T of ~850°C, based on the corundum-eskolaite solvus [4].

References. [1] Clayton, R.N. and Mayeda, T. (1988) GCA 52, 1313-1318. [2] Krot, A. et al. (1993) EPSL 119, 569-584. [3] Walker, D. and Grove, T. (1993) Meteoritics 28, 629-636. [4] Chatterjee, N.D. et al. (1982) Am. Min. 67, 725-735.

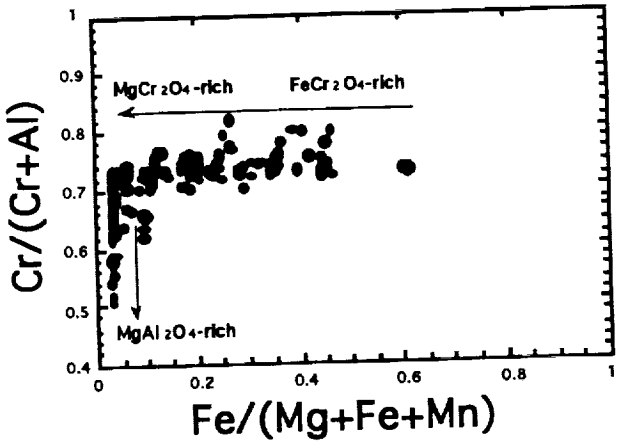

Fig. 1. Chromites in LEW 88774, with arrows indicating compositions with increasing reduction.

SURFACE EXPRESSION OF GRAVITATIONAL RELAXATION OF TOPOGRAPHY: SOUTH SCARP OF LAKSHMI PLANUM, VENUS; **A. A. Pronin,** Vernadsky Institute, Kosygina 19, Moscow, Russia and **M. A. Kreslavsky,** Astronomical observatory of Kharkov University, Sumskaya 35, 310022 Kharkov Ukraine

Study of recently formed tectonic features in a region of Eastern part of South scarp of Lakshmi Planum on Venus was carried out basing on Magellan radar images and altimetry. In the frame of a simple model for gravitational spreading of ductile crust of different thicknesses a distribution of surface stresses was calculated for the region. Patterns of observed deformations and modeled stress field coincide for crustal thickness of 45 km or somewhat greater.

Introduction. High temperature of venusian surface causes lower part of the crust to be relatively weak (e.g. [1]), that promotes gravity driven relaxation of topography. On the other hand low rate of exogenic resurfacing on Venus promotes surface manifestation of the relaxation to preserve and appear on radar images as small-scale tectonic features. This paper continues our work on modeling of surface expression of gravitational relaxation in Ishtar Terra [2,3] using high resolution Magellan data [4]. Eastern part of South scarp of Lakshmi Planum (**Fig. 1**) was chosen for this study because of its steep complex slope and good coverage with Magellan topography data and images.

Observations. Advanced geomorphological study of the region was focused on establishing signatures of the most recent tectonic deformations. Small-scale most recent tectonic features crossing others were treated. Sets of subparallel fissures situated at the upper parts of the scarp indicate on local extension in direction across the fissures. Sets of subparallel sinuous ridges on dark lava plain at the foot of the scarp reveal local compression (like shown in **Fig. 2, 3**). Areas of extension concentrate predominantly above the main scarp, while compression is usually below it (**Fig. 1**); It allows to consider tectonic features to be related with gravity-driven processes.

Model. The crust was modeled as a uniform viscose layer of thickness H lying over a rigid substrate modeling strong upper shell of the mantle. Relief of free surface of the layer was taken from Magellan altimetery data for the region under consideration. Equations of linear fluid dynamics was used to calculate distribution of strain rate caused by gravity driven flow (e.g., [1, 5]). An example of results for H = 45 km is shown in **Fig. 4**. An attempt to apply less simplified models with two-layer structure of the crust showed that only slightly does resulting pattern of strain signature depend on details of crust structure. Pattern of compression and extension depends first of all on depth of transition from less viscose to more viscose (or rigid) material. That is why we use the simplest model with only one parameter H.

Conclusions. Comparison of pattern of recent deformation signatures observed in studied region with model strain rate distributions reveals good coincidence for H=45 km or somewhat greater. The coincidence evidences the spreading origin of recent tectonic deformations and gives an estimate of crust thickness in the region.

References.

[1] Bindshadler D.L and Parmentier E.M. (1990) *J. Geophys. Res., 85,* 21329 - 21344
[2] Pronin A. and Kreslavsky M. (1992) *LPSC-23,* 1113 - 1114
[3] Pronin A.A. and Kreslavsky M.A. (1992) *Astronomicheskij Vestnik, 26,* 26 - 43
[4] Ford P.G. (1991) Altimetric and Radiometric Global Data Records. Project Magellan. Software Interface Specification.M.I.T. Center of Space Research
[5] Ramberg H. (1981) *Gravity, deformations and Earth's crust,* Academic press, London.

GRAVITATIONAL RELAXATION ON VENUS; Pronin A.A. and Kreslavsky M. A.

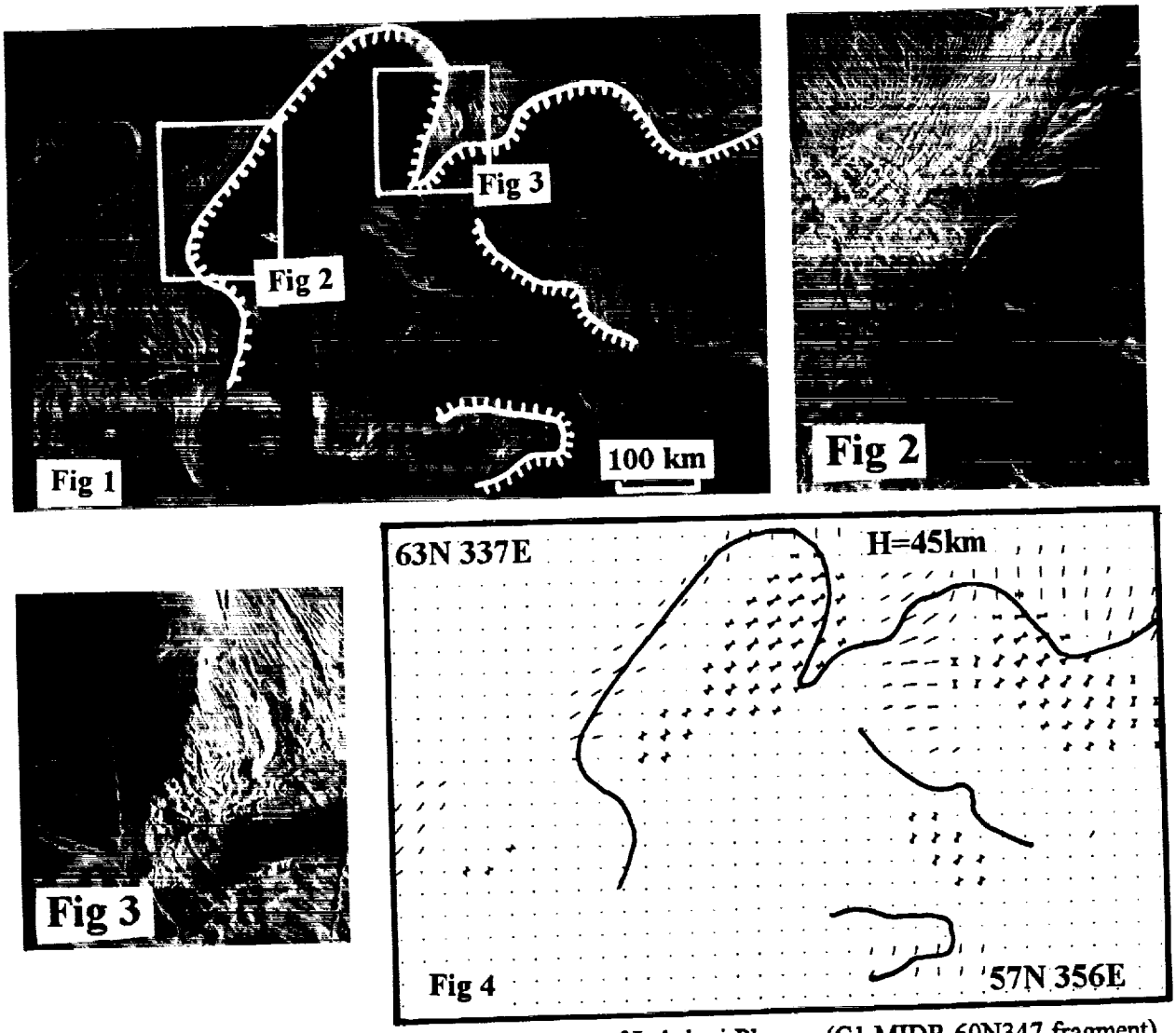

Fig. 1. Radar image of Eastern part of South scarp of Lakshmi Planum (C1 MIDR 60N347 fragment). Location of main scarp and areas shown in Fig. 2 and 3 are outlined.

Fig. 2. High-resolution radar image showing a set of fissures (upper left corner) indicating recent NE-SW extension (F MIDR 60N344 fragment).

Fig. 3. Another example of high-resolution radar image showing a set of extensional fissures and compressional ridges indicating recent NE-SW deformations (F MIDR 60N344 fragment).

Fig. 4. Model stress field for crustal thickness H=45 km. Directions of principal stresses and their relative values are shown. Thin lines designate extension, triangles - compression. Location of the main scarp is outlined by solid line.

SOLID-SOLID TRACE-ELEMENT PARTITIONING BETWEEN EXSOLVED PYROXENES IN CUMULATE EUCRITES; Aurora Pun and James J. Papike, Institute of Meteoritics, Department of Earth and Planetary Sciences, University of New Mexico, Albuquerque, NM 87131-1126, USA.

We have increased the database in our continuing study of understanding trace-element partitioning during pyroxene exsolution processes. In addition to Binda [1], we have examined Moore county, Moama and Serra de Mage'. SIMS analyses of both the high-Ca augite lamellae and their corresponding orthopyroxene or pigeonite hosts show that augite is an important repository for REE during the exsolution process. Distribution and abundances of the REE in the augite lamellae and orthopyroxene or pigeonite host are consistent among these eucrites and reflect the different crystal structures of the pyroxenes. We also determined the solid-solid major, minor, Sr, Y, and Zr partition coefficients between the lamellae and host pairs.

All four of these meteorites are monomict cumulate eucrites that show textural evidence of extensive subsolidus reequilibration of pyroxenes. Binda is the only one of the four meteorites that is brecciated. Orthopyroxenes from Binda, Moama, and Serra de Mage' typically show coarse "remnant (001)" exsolution lamellae of augite formed before inversion of primary monoclinic pigeonite to orthopyroxene. Later and thinner (100) augite exsolution lamellae are formed in the host orthopyroxene as temperatures decrease. These solid state reactions lead to the characteristic exsolution texture, called "inverted pigeonite" texture. Unlike the other cumulates, Moore County contains (001) augite lamellae in host pigeonite; most primary pigeonite did not undergo inversion to orthopyroxene in the sample we studied.

A few pyroxene grains from each meteorite were selected for trace-element analyses using SIMS. These analyses were performed on a Cameca 4f ion probe at the UNM/SNL Ion Microprobe Facility, a joint operation of the Institute of Meteoritics, UNM and the Sandia National Laboratories. Complimentary major element analyses were measured using a JEOL 733 electron probe with an Oxford-Link imaging system.

The spidergrams in Figure 1 show the results of the trace-element analyses normalized to CI chondrite (average CI, [2]). Points for Gd have been estimated. All four cumulates show similar patterns and indicate similar distribution behaviors of the trace-elements during the exsolution process. All of these patterns are consistent with those expected for high-Ca/low-Ca pyroxene partitioning. There is a HREE enrichment over LREE in the low-Ca pyroxenes and abundances of REE in augite are greater than those found in the hosts. This reflects the pyroxene crystal chemistry whereby the Ca in the M2 site of augite "prop" open their structures to incorporate more REE, the "Ca effect" [3,4]. The ionic radii of the LREE are too large to be incorporated easily into the M2 sites of the orthopyroxenes and this is reflected in their depleted LREE patterns. Sr abundances behave systematically by following the Ca ions reflecting the geochemical similarity of the two elements.

The higher abundances of the REE found for Moore County pyroxenes may reflect higher initial enrichments of the trace-elements in the Moore County melt. This is consistent with the higher Fe# found in the pyroxenes of Moore County (Figure 2). Also, the higher abundances and flatter slope of LREE in Moore County pigeonite host reflect the fact that the pigeonite structure is more receptive to these large REE than orthopyroxene.

Solid-solid partition coefficients were determined for the high and low-Ca pyroxenes of the cumulates. They were calculated based on the elemental weight percents of the components involved. The Ca content of the low-Ca pyroxenes are determined to be in the sequence Moore County > Moama > Binda >Serra de Mage'. The partition coefficients for the HREE are found to be the same among the cumulates. Slight variations of the partition coefficients may reflect the differences in subsolidus reequilibration temperatures. Temperatures were calculated for the lamellae-host pairs using a geothermometry program, QUILF, provided by Don Lindsley [5]. Average temperatures calculated for all four meteorites range from approximately 850°C to 950°C. The orthopyroxenes of Serra de Mage' are the most depleted in Ca and contain the most complicated exsolution textures, suggesting the melt equilibrated further down the pyroxene solvus, in agreement with the lowest calculated temperatures.

The pyroxenes from these cumulate eucrites are a natural example of pyroxenes from an almost pure Wo-En-Fs system. The pyroxene chemistries contain very little "other" components [6] and all fall closely within the pyroxene quadrilateral. As a result, these pyroxenes required very little corrections in calculating subsolidus temperatures. Independent of the fact that these trace-element measurements were for cumulate eucrites, these are a good estimate of the solid-solid trace-element partition coefficients between high-Ca and low-Ca pyroxenes.

PARTITIONING BETWEEN EXSOLVED PYROXENES: A. Pun and J.J. Papike

Acknowledgements: We thank M.N. Spilde for technical assistance on the electron probe and Graham D. Layne and Grant Fowler for technical assistance on the SIMS. We also thank the Smithsonian Institution for the thin sections of Binda, Moore County and Moama. This work is supported by NASA grant NAGW-3347 (J.J.P.) and NGT-70223 (NASA GSRP training grant for A.P.).

References: [1] Pun A. *et al.* (1993) *Meteoritics*, **28**, 402. [2] Anders E. and Grevesse N. (1989) *GCA*, **53**, 197-214. [3] Papike J.J. *et al.* (1988) *LPSC*, **19th**, 901-902. [4] Shearer C.K. *et al.* (1989) *GCA*, **53**, 1041-1054. [5] Andersen D.J. *et al.* (1993) *Computers & Geosciences*, **19**, 1333-1350. [6] Papike J.J. and Cameron M. (1976) *Rev. Geophy. Space Phys.*, **14**, 37-80.

Figure 1:

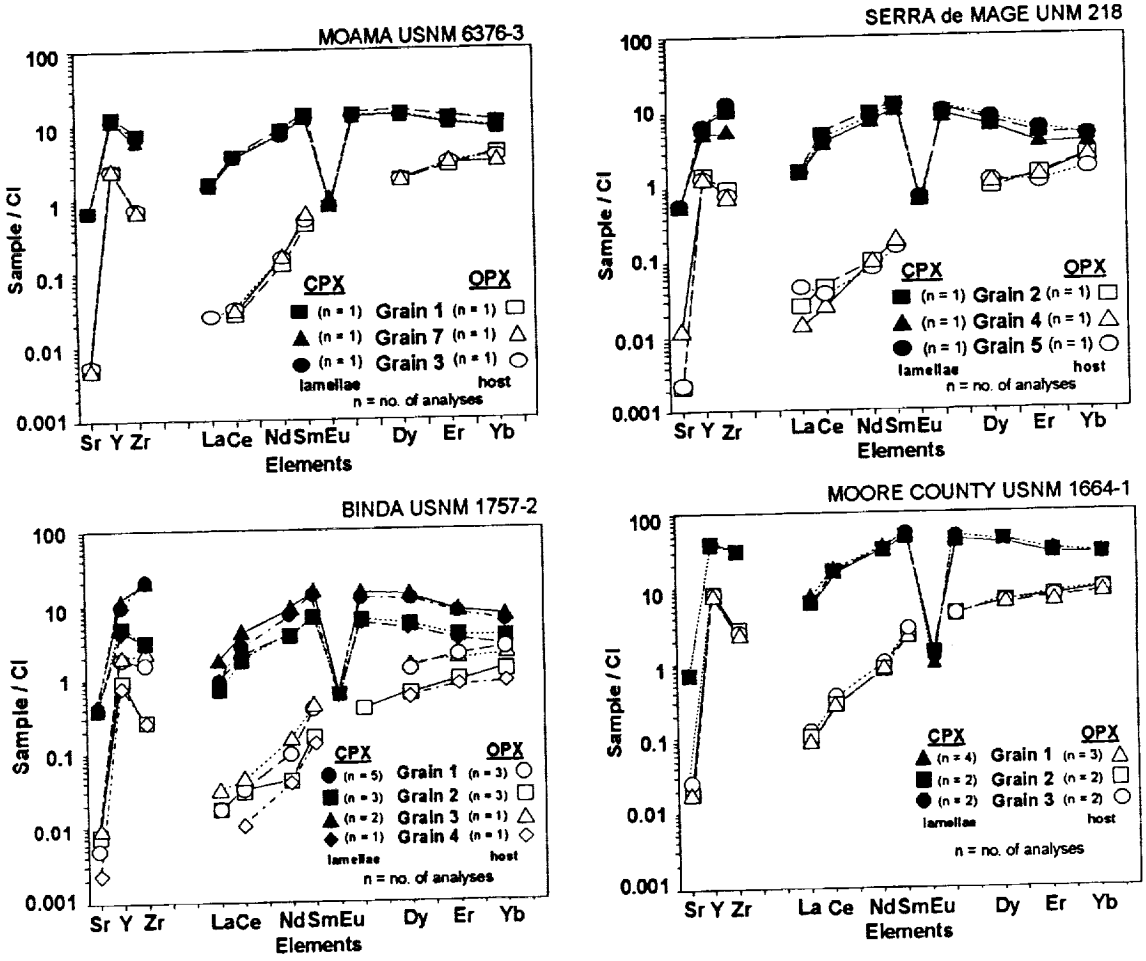

Figure 2:

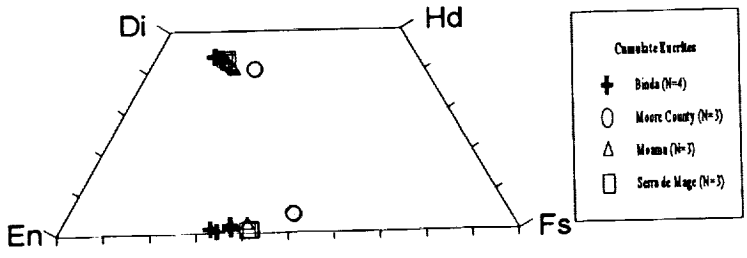

STUDIES OF MAFIC INTRUSIVES IN THE VREDEFORT IMPACT STRUCTURE, SOUTH AFRICA: IMPLICATIONS FOR CRATON WIDE IGNEOUS ACTIVITY AT 1.1 Ga AGO. G.Q.J. Pybus[1], W.U. Reimold[1], and C.B. Smith[2], [1]Econ. Geol. Res. Unit at the Dept. of Geology, [2]Isotope Div., BPI Geophysics, Univ. of the Witwatersrand, P.O. Wits 2050, Johannesburg, R.S.A..

We investigated the different populations and generations of the mafic intrusives abundant in the region of the Vredefort impact structure. A 100-m-thick gabbroic intrusion was recognized throughout the dome and dated at 1054 Ma. Recognition of this magmatic event has strong implications for the tectonomagmatic history of the whole of the Kaapvaal Craton and for the interpretation of thermochronological data from the Vredefort dome itself and from the surrounding Witwatersrand basin.

The Vredefort structure, 120 km southwest of Johannesburg, has long attracted attention because of the controversy about its origin by either internal or external processes [1] and its position in the centre of the economically important Witwatersrand basin. The genetic controversy has recently been resolved when new, definitive evidence in favour of impact was discovered [2,3]. However, this does not mean that Vredefort research has become obsolete. With an estimated diameter of 180-300 km [4] this structure is one of the three largest recognised terrestrial impact structures and clearly warrants further multidisciplinary study. Furthermore, it has been suggested [5] that the formation of the Vredefort dome had significant effects on the whole Witwatersrand basin and its gold mineralization. Our group continues with structural mapping of the dome and has begun a comprehensive mineralogical, chemical and isotopic study of the numerous mafic intrusives occurring in core and collar of the dome. The main objectives for this project are to identify the different populations and generations of intrusives in order to contribute to the general understanding of the tectonomagmatic history of this region, to investigate the thermal effects of these various magmatic events in the region of the Witwatersrand basin, and to investigate the possibility that the results of discrimination analysis could be of use to the mining and exploration activities in the Witwatersrand basin.

Five types of mafic intrusives were previously identified in the region of the dome: (1) primitive mafic-ultramafic meta-intrusives, (2) relatively old epi-diorites, (3) unmetamorphosed gabbros and diorites, (4) evolved high Fe-Ti diorites, and (5) Karoo dolerites [6-8]. With the exception of the Karoo dolerites, these types are transected by pseudotachylite. A sixth group, which is also not cut by pseudotachylite, but displays a chemical composition very similar to that of the high Fe-Ti group of [7], has now been identified. Correlation and classification of the various types of intrusives is achieved by petrographic study and whole rock chemical analysis (Table 1). The new rock type occurs in the Anna's Rust Sheet (ARS), the Vredefort Mafic Complex (VMC), and on the farms Hester 98 (H) and Oceaan 99 (O) and adjoining farms (Fig. 1). In addition, this material was detected in an 80 m thick section of a borehole into the Inlandsee pan and was intersected in several boreholes into the southwestern collar of the dome. It appears likely that an intrusive reported from another borehole in the vicinity of the Inlandsee [9] also represents this type. It was established that the ARS, VMC and borehole occurrences from Inlandsee and environs are approximately horizontally oriented.

Previous attempts at establishing a chronological framework for the formation of the mafic intrusives in the Vredefort area have been limited to correlations of specific rock types with regional magmatic events, such as the 2.7 Ga Ventersdorp, 2.065 Ga Bushveld and the 170-180 Ma Karoo events, on the basis of field and petrographic observations [6,10]. Palaeomagnetic work [11] on the ARS and several other small bodies in the Vredefort dome indicated similar pole positions to the Umkondo Dyke Swarm (1080 +140/-25 Ma) in Zimbabwe and to some of the post-Waterberg diabases [12]. We carried out Rb-Sr dating on whole rock and mineral samples from the ARS and the VMC (Table 2). For four biotite fractions and two plagioclase separates an errorchron was obtained corresponding to an age of 1054 +- 13 Ma (I_{Sr} = 0.7052 -+ 0.0002), cf. Fig. 2. The fact that whole rock and pyroxene data fall off the regression line can be explained by alteration effects. These results confirm a temporal relationship between Group 6 Vredefort and Umkondo Dyke intrusives and implies Kaapvaal and Zimbabwe craton-wide igneous activity around 1100 Ma ago which is coincident with the collisional tectonics in the Namaqua-Natal thrust belt at the southern/southwestern margin of the Kaapvaal Craton. Other evidence for this event was provided by workers on alkaline rocks that established widespread alkaline magmatism in the central part of the Kaapvaal Craton between 1100 and 1300 Ma ago [e.g.,13]. In the context of late thermal events in the region of the Vredefort dome [14-16], it needs to be evaluated whether the dome-wide gabbro sheet could have caused effective thermal overprinting at that time. Trieloff et. al. [17] have recently noted minor resetting of argon isotopic systematics of 2 Ga old pseudotachylites from the northern and northwestern parts of the Witwatersrand basin during the time interval 1200-1600 Ma, and the U-Xe results from Witwatersrand uraninites of Meshik et. al. [18] also indicate thermal/hydrothermal (?) activity around this time.

Refs.: [1] Reimold W.U.(1993), J.Geol.Ed.,**41**,p.106-117; [2] Leroux et al.(1993), A T.E.M. investigation of shock metamorphism in quartz from the Vredefort dome, South Africa. Tectonophys. (in press); [3] Koeberl et al.,in prep. [4] Therriault et al.(1993), LPS XXIV, p.1421-1422; [5] Reimold W.U.(1994), Epithermal Witwatersrand gold mineralization-caused by the Vredefort mega-impact event? K/T event and other Catastr. in Earth History Conf.,Houston,Febr.1994 (in press); [6] Bischoff A.A.(1972a),Trans.Geol.Soc. S.Afr.,**75**,p.23-34; [7] Jackson M.C. et al.(1992), Geocongr. 92, Bloemfontein, p.213-215,Geol.Soc.S.Afr.; [8] Pybus G.Q.J. et al. (1993), 16th Coll.Afr.Geol.,Mbabane,p.291-293; [9] Hart R.J. et al.(1990),Chem.Geol.,**82**,p.233-248; [10] Bisschoff A.A. (1972b), Trans.Geol.Soc. S.Afr.,**75**,p.34-45; [11] McDonald A.J. and Anderson H.T. (1974), unpubl Hons. Diss. Univ. Witwatersrand; [12] Allsop H.L.(1989), S.A.J.Geol.,**92**,p.11-19; [13] Brandt D. et al., this volume; [14] Reimold W.U. et al.(1990), Tectonophys.,**171**, p.139-152; [15] Reimold W.U. et al.(1992),S.A.J.Sci.,**88**,p.563-573; [16] Allsop H.L. et al.(1991), S.A.J.Sci.,**87**,p.431-442; [17] Trieloff M. et al.(1994), ^{40}Ar-^{39}Ar thermochronology of the VCR, Witwatersrand Basin, S.A.J.Geol.(in press); [18] Meshik A. et al.,(1994), Fission track dating of Witwatersrand uraninites: implications for 1 Ga geological activity in the Kaapvaal Craton (MS. in prep).

MAFIC INTRUSIVES IN THE VREDEFORT IMPACT STRUCTURE: Pybus G.Q.J. et al.

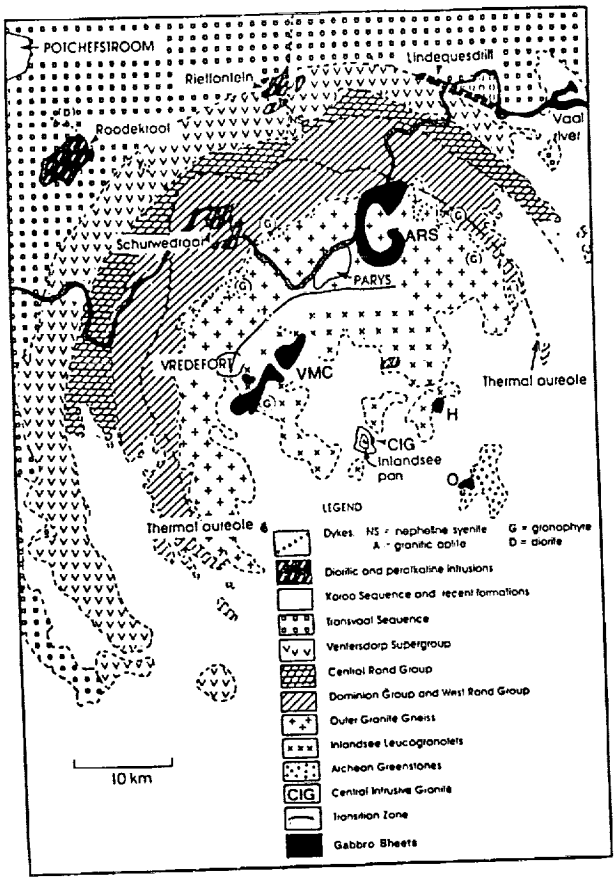

FIGURE 1 :Simplified geological map of the Vredefort Structure.

Sample	Weight (g)	Rb (ppm)	Sr (ppm)	$^{87}Sr/^{86}Sr$	$^{87}Rb/^{86}Sr$
GP18-WR	0.06501	25.40	167.7	0.71280	0.4383
GP18-PL	0.00543	1.744	297.2	0.70558	0.0170
GP18-PY	0.03828	1.520	11.97	0.71260	0.3675
GP18-B1	0.00511	377.1	7.093	3.72689	199.20
GP18-B2	0.00943	100.4	4.868	1.71801	65.564
GP18-B3	0.00291	405.8	6.624	4.29976	239.49
GP18-B4	0.00246	143.4	5.504	1.94616	84.479
UP16-PY	0.02902	1.206	12.16	0.71148	0.2870
UP16-PL	0.00316	1.574	315.6	0.70537	0.144
UP16-WR	0.06438	20.25	174.7	0.71142	0.3354

TABLE 2. Analytical results of Rb-Sr isotopic analysis from samples UP16 and GP18. (WR = whole rock, PY = pyroxene, PL = plagioclase, B(1-4) = biotite). All data blank corrected, Rb Blank = 2ng; Sr Blank = 2.5ng.

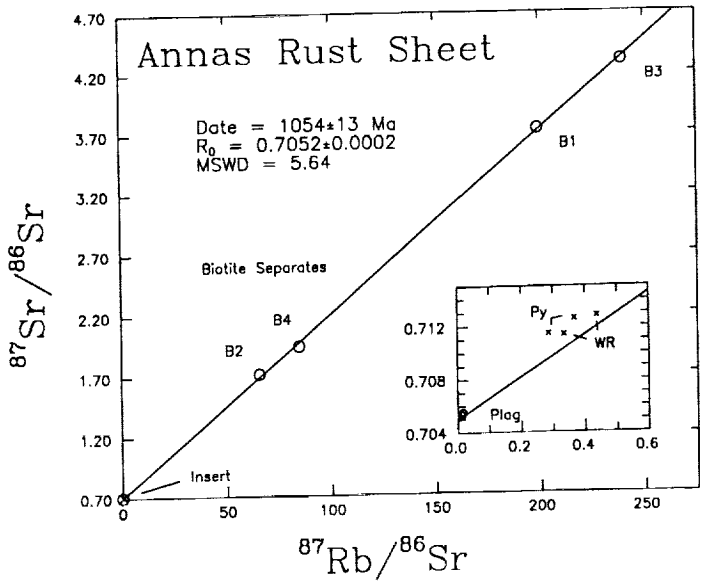

FIGURE 2 :Errorchron for the four biotite separates from an ARS sample. Regression includes two plagioclase samples, (see insert), one of which is from the VMC (sample UP16). The insert shows the offset of the pyroxene and whole rock samples not included in the regression. (B=Biotite, Py=pyroxene, WR=whole rock, Plag=plagioclase).

	ARS	VMC	HESTER	OCEAAN
SiO_2	51.0	51.3	49.9	50.8
TiO_2	1.49	1.32	1.46	1.43
Al_2O_3	14.8	15.2	15.8	15.2
Fe_2O_3[2]	13.4	12.7	13.1	13.3
FeO	na	na	na	na
MnO	0.20	0.19	0.19	0.19
MgO	6.53	6.88	6.46	6.60
CaO	9.77	10.2	9.87	9.77
Na_2O	2.08	1.78	1.81	2.15
K_2O	0.72	0.60	0.65	0.66
P_2O_5	0.16	0.14	0.17	0.15
LOI	0.14	0.24	0.37	0.23
Total	100	100	99.7	100
Ba	223	200	206	211
Rb	41	31	38	41
Sr	170	178	176	178
Y	29	26	29	29
Zr	123	107	118	115
Nb	8	8	8	8
V	300	313	253	284
Cr	133	165	251	141
Co	44	40	41	45
Ni	93	95	107	104
Cu	109	98	109	106
Zn	122	114	124	105
N[1]	29	3	4	2

TABLE 1. Whole rock chemical compositions for the four localities in Figure 1.
[1] - Number of samples; [2] - Total Fe as Fe_2O_3, na - not analysed.

¿CYTHEREAN DEXTRAL TRANSFORM FAULT ZONE FROM CONCAVE ARC TO CONCAVE ARC?;
J. Raitala, Dept. of Astronomy, University of Oulu, 90570 Oulu, Finland; e-mail: jouko@hiisi.oulu.fi

Even if the paradigm of plate tectonics can not be adopted to Venus some of its structures may be understood in terms of plate tectonics (pseudo-plates etc. [1, 2, 3, 4]).

Compression at Salme Dorsa: Multiple compressional ridge belts of the Salme Dorsa area represent various ages or tectonic phases indicating complex, repetious tectonics of the Ishtar Terra foreland crust [3, 5]. The N-S ridges of Ausra Dorsa are connected to E-W compression as well as the west-facing, thrust-front scarp of arcuate Salme Dorsa. The scarp-parallel trough and bulge to the west of the scarp are bent partly by the ridge belt load and partly by compressional crustal movements [3, 6, 7] letting the weakest part to bend under the compression. Even some subduction, or overthrust, may have taken place within the area [8]. This area supports the idea of multitemporal, or long-lasting, horizontal compressional stresses [9]. Ridge belt deformation has been thrust faulting and folding of the uppermost surface due to compression transmitted through the uppermost rigid crust and due to relative dynamical movements of crustal units, or domains [6].

Dextral srike-slip fault: The E-W Manto Fossae fault zone along southern Fortuna Tessera is oriented from Meshkenet Tessera in the east towards Salme Dorsa in the west. Topography of the fault zone varies but due to structures indicating dextral strike-slip movements this zone may have formed by relative side-sweeping movements of crustal units. The network of various order fault structures along the main fracture zone indicates that the crust of the southern planitia moved from east to west relative to Ishtar Terra [5].

Bar-like crustal blocks: The en echelon outlook of Meshkenet Tessera is explained by differential movements of crustal blocks. The northernmost blocks leaned against eastern Ishtar Terra at Tusholi while southern Meshkenet Tessera was able to move to the west [6]. The movement rate depended on faulting and surface age estimations. The original shape and dimensions of the 1600 km long Meshkenet Tessera are not known but the age estimation of 500 m.y. [10, 11, 12, 13, 14] and a 200 km displacement from a more rectangular shape give a preliminary estimation of a 0.04 cm/year movement between middle and southern areas. The appropriate numbers may be 400 km and 0.08 cm/year if the northernmost area is also included. Because ages of tessera material, morphology and fault activity are, however, unknown [6] the movement rate is rather uncertain. These may be maximum movement rates while older surface ages give lower relative movements. The movement rate becomes smaller if the tessera was originally NE-SW -directed and larger if fault activity lasted only part of the surface age.

Corona activity: Nightingale and Earhart Coronae, with a connecting N-S ridge belt locate to the east of Meshkenet Tessera. Some main faults and the most recent graben structures of Meshkenet Tessera are radial or concentric to Nightingale indicating some structural connections to it as if an active corona centre may have contributed to additional crustal stresses. Vertical energy and stresses due to the plume or hot spot activity [15, 16, 17, 18, 19, 20] below a corona are transformed into horizontal ones and transmitted radially through the surrounding crust breaking it by resulting in radial and/or consentric structures. Surface deformations, fractures and ridges between adjoining coronae may indicate pre-existed zones of weakness or stress-induced structures between the active centres due to horizontal corona-related forces [9, 21, 22, 23, 24, 25, 26]. Changes in activity or relative mantle-crust movements may result in an irregular, elongated, double etc. corona formation [16, 27, 28].

Discussion: The Cytherean crust is divided into units [or domains or (micro/pseudo)plates] which have moved related to each other. The complexity of the tectonic zone, here displayed by various fault, ridge belt and thrust structures, indicates movements of such units. Compression from east-southeast against Ishtar Terra resulted in ridge belt formation and surface bending at Salme Dorsa along the seam between two crustal domains. Structures of this area indicate multitemporal or long-lasting deformation of the planitia crust. The middle Manto Fossae part of the zone consists of conjugate faults with numerous second and third order en echelon ones. These all indicate dextral, or westward, strike-slip shear of the planitia crust related to Ishtar Terra. In the east, faults of Meshkenet Tessera indicate differential movements with the same dextrality. The southernmost bar-like block of Meshkenet Tessera has had the largest westward movement. The northenmost Meshkenet Tessera was compressed against Tusholi Corona resulting of foreland bending which resembles that at Salme Dorsa.

The tectonic zone resembles a dextral transform fault extending from a concave arc in the west to another concave arc in the east. Salme Dorsa and Tusholi Corona locate on the edges of crustal units, or domains, not too much unlike to crustal plates. Some faults of the Meshkenet area are at least geometrically related to one or more of the near-by coronae partly explaining their wide structural, spatial and temporal diversity. At the coronae mantle

DEXTRAL TRANSFORM FAULT ZONE?: **Raitala, J.**

penetrated vertically against, or into the crust with vertical stresses being transformed into horizontal ones [9, 29, 30, 31]. Understanding of these processes is needed to gain a better idea of origin of crustal deformations and reason(s) for movements of crustal, or uppermost lithosphere, domains able to transmit stresses over distances.

Acknowledgments: For the Venera and Magellan data I thank Vernadsky Institute and NASA, respectively.

References: [1] Herrick, R. R. (1993). Lunar Planet. Sci. XXIV: 645-646. [2] McKenzie, D.et al. (1992). JGR 97: 134533-13544. [3] Suppe, J. & Connors, C. (1992). JGR 97: 134545-13561. [4] Lenardic, A. & Kaula, W. M., 1993. Lunar Planet. Sci. XXIV: 865-866. [5] Raitala, J. & Törmänen, T. (1989). Earth, Moon, and Planets 45: 237-263. [6] Raitala, J. et al. (1993). Lunar Planet. Sci. XXIV: 1191-1192. [7] Brown, C. D. & Grimm, R. E. (1993). Lunar Planet. Sci. XXIV: 107-108. [8] Burt, J. D. & Head, J. W. (1993). Lunar Planet. Sci. XXIV: 235-236. [9] Banerdt, B. (1993). Lunar Planet. Sci. XXIV: 57-58. [10] Basilevsky, A. T. & Head, J. W. (1988). Ann. Rev. Planet. Sci. 16: 295-317. [11] Phillips, R. J. et al. (1992). JGR 97: 15923-15948. [12] Malin, M. C. et al. (1993). Lunar Planet. Sci. XXIV: 919-920. [13] Solomon, S. C. (1993). Lunar Planet. Sci. XXIV: 1331-1332. [14] Turcotte, D. L. (1993). Lunar Planet. Sci. XXIV: 1447-1448. [15] Schilling, J. G. (1985). Nature 314: 62-67. [16] Schilling, J. G., Thompson, G., Kingsley, R. & Humphris, S. (1985). Nature 313: 187-191. [17] Head, J.W. & Crumpler, L. S. (1987). Science 238: 1380-1385. [18] Crumpler, L. S. & Head, J. W. (1988). J. Geophys. Res. 93: 301-312. [19] Janes, D. M. et al. (1992). JGR 97: 16055-16067. [20] Phillips, R. J. & Hansen, V. L. (1993). Lunar Planet. Sci. XXIV: 1135-1136. [21] Muller, O.P. & Pollard, D.D., (1977). Pure and Applied Geophysics 115, 69-86. [22] Raitala, J. (1980). Earth, Moon, and Planets 23: 307-321. [23] Head, J. W. (1988). Lunar Planet. Sci. XIX: 467-468. [24] Head, J. W. et al. (1989). Lunar Planet. Sci. XX: 396-397. [25] Parfitt, E. A. & Head, J. W. (1993). Lunar Planet. Sci. XXIV: 1113-1114. [26] Roberts, K. M. & Head, J. W. (1993). Lunar Planet. Sci. XXIV: 919-920. [27] Pronin, A. A. & Stofan, E. R. (1988). Lunar Planet. Sci. XIX: 953-954. [28] Janle, P.; unpublished Brown-Vernadsky meeting presentation. [29] Morgan, P. & Phillips, R. J. (1983). J. Geophys. Res. 93: 8305-8317. [30] Coombs, C. R. & Wood, C. A. (1989) EOS Trans. AGU 70: 1185. [31] Nikishin, A. M. & Marchenkov, K. I. (1989). Vernadsky-Brown Microsymposium 10, Abstract Vol. 1: 36-37. [32] Wilson, J. T. (1965). Nature 207: 343-347.

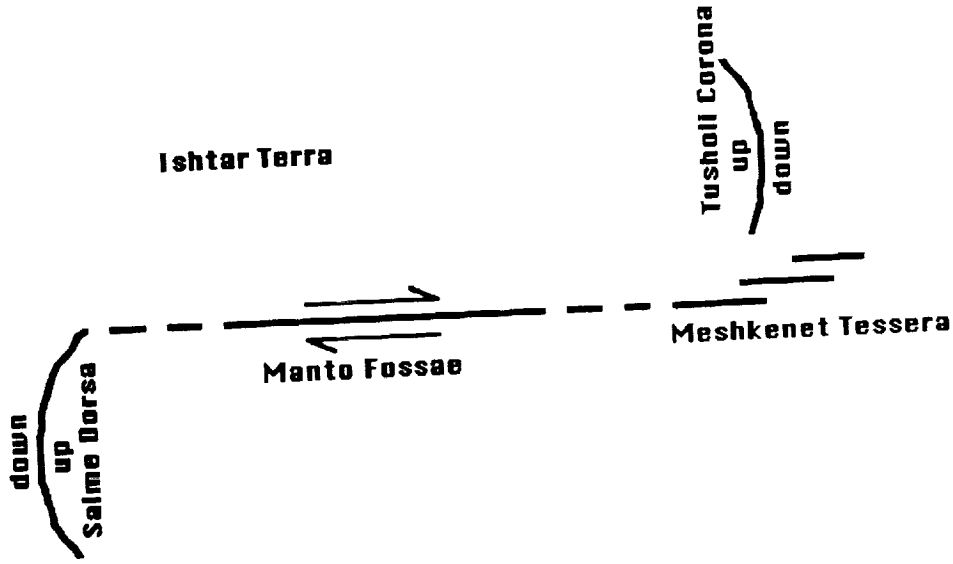

A sketch of the tectonic zone of the Salme Dorsa ridge belt in the west, the Manto Fossae fault zone in the middle and Meshkenet Tessera and Tusholi scarp in the east resembles a dextral transform fault extending from a concave arc in the west to another concave arc in the east [32]. In the both ends of the fault zone there are similar ridge belts with scarps and foredeep troughs in front of them. Major coronae are located around the eastern end.

RELATIVE CHANGE IN CROSS-SECTIONAL AREA AND ALBEDO WITH ROTATIONAL PHASE FOR 532 HERCULINA AND 45 EUGENIA; K. L. Reed and M. J. Gaffey (Rensselaer Polytechnic Institute), L. A. Lebofsky (University of Arizona)

Simultaneous reflected and thermal infrared lightcurves were obtained in 1987 in order to solve the question of whether the lightcurve variations for 532 Herculina and 45 Eugenia are a consequence of shape or albedo spots [1,2,3]. The in-phase behavior of their lightcurves pointed to a mainly shape-derived lightcurve with only a minimal possibility of major albedo spots [3]. Using data from simultaneously-obtained near-infrared and thermal wavebands plus a simple technique of relating the incoming solar flux at an asteroid with the outgoing measured flux, an estimate of the minimal changes in relative cross-sectional area and maximum relative albedo changes was found. The comparatively large change in relative cross-sectional area and small change in relative albedo confirms the original findings that the lightcurve variations for these two asteroids are shape-dependent and not albedo-dependent.

The data used was first digitized from the graphs given in Figures 2 through 6 of [3]. The accuracy of the digitization was estimated to have a maximum error of ±0.01 magnitude. The digitized magnitudes were then converted to fluxes relative to α Lyrae using the logarithmic magnitude-flux relation.

One filter's data set was then interpolated to the same rotational phase values as the other using a cubic spline technique in order to achieve rotational simultaneity for the data. The lightcurve data set with the most rotational coverage was interpolated to the other in order to obtain consistent and continuous data while not having to interpolate too far between points. The only exception to this is the data for 45 Eugenia taken in March of 1987. The breaks in coverage for the J flux data were too large to accurately spline the N flux data smoothly, so the J flux data were splined to the N flux data rotational phases. Relative cross-sectional area and albedo were calculated in each data set only for rotational phases for which there were actually closely-obtained near-infrared (J and K) and N flux data.

The filter fluxes relative to α Lyrae were then converted to absolute fluxes by multiplying them by conversion factors for each standard filter supplied by the IRTF Photometry Manual [4]. This transformed the relative fluxes through the filters into energy units.

In order to calculate the relative cross-sectional area and relative albedos, the total reflected and emitted fluxes from the body needed to be found. Conversion factors transforming flux through the J and K filters into total reflected flux were calculated by dividing the solar constant value (integrated from solar flux curve data by [5]) by the same solar flux curve which was multiplied by each filter's (J and K) bandpass. This procedure gives the ratio of total reflected flux off the body to that reflected flux measured through each respective filter. Converting the flux measured through the N filter to total emitted flux, was accomplished by assuming the body to be spherical with an emissivity of 1 and that the standard non-rotating thermal model applied to the body, then finding total emitted flux curves using this model at various solar distances and albedos. The components of this two-dimensional array of flux curves were then each integrated to get the total flux, then multiplied by the N filter bandpass and integrated to get the flux through the filter. The ratio of these two values was then taken and a two-dimensional look-up table was formed of these conversion factors.

Two simple equations were then used to iteratively find the effective cross-sectional area and the effective albedo:

I. $\text{TOTAL FLUX}_{\text{EMITTED}} = \text{AREA} * (1 - \text{ALBEDO}) * \text{SOLAR CONSTANT}$
II. $\text{TOTAL FLUX}_{\text{REFLECTED}} = \text{AREA} * \text{ALBEDO} * \text{SOLAR CONSTANT}$
Note: The albedo is here defined as the fraction of incident flux reflected into space at all wavelengths.

Knowing the solar distance of the asteroid, an albedo was assumed and the various values were substituted into equation I in order to calculate the effective cross-sectional area. This area value was then substituted into equation II in order to calculate the effective albedo. This albedo value was used to look up a new value for the emitted flux conversion and the whole process was repeated until the cross-sectional area and albedo converged to singular values within errors (taken as within 5% of the previously calculated values). It was known that using the standard thermal model would produce a large systematic error but that it should be consistent within each data set such that the relative change over any one data set could be found. According to [6], the use of the standard spherical, non-rotating thermal model would underestimate the cross-sectional areas and overestimate

the albedos for an elliptical body. Therefore, the results from this technique should give us the minimum relative change in cross-sectional area and maximum relative albedo change for each object.

Since actual areas and albedos are highly model-dependent [6,7], each area and albedo value was divided by the average for each data set in order to obtain a relative value. This makes the values less susceptible to the large systematic errors of absolute measurements. This said, the absolute effective albedo values were found to be quite close to the accepted geometric albedo values (the worst case was 20% too low). This circumstance helped lend credence to the technique but will require further investigation. The absolute cross-sectional area values calculated did have large systematic errors associated with them compared to accepted values for the asteroids' diameters - in line with the model-dependent nature of absolute value calculations.

The data for 532 Herculina show a minimum change in cross-sectional area of between 23 - 25% across a full rotation with a maximum change in albedo of 14%. This result is confirmed through the use of both the K filter (for the January data) and the J filter (for the data from March and May) data giving similar results. The data for January and March show an inverse relation of albedo to cross-sectional area which may be an example of a radius-of-curvature effect on the effective albedo [6]. In the January data, the first maximum shows a broad hump which may possibly indicate a larger radius of curvature for that end than at the opposite end (it is slightly "egg-shaped"). The second maximum in area is slightly out of phase with the second minimum in albedo (by approximately 0.1 rotational phase). This may possibly indicate (1) a varying radius of curvature for this end, (2) a limb shadowing effect of some sort, or (3) a real albedo change across the surface. The other data sets show a varied relationship between the areas and albedos with the March data in inverse relation but with a mild phase off-set and with the May data in phase. This behavior would be more indicative of (1) and (2) above since (3) should be more consistent between data sets and should not have a possible relation to aspect angle.

The data for 45 Eugenia show a minimum 25% change in relative cross-sectional area, though this minimum may be larger since the lightcurve coverage was not complete for both filters. The relative albedo change was minimal, being only slightly measurable at the least significant digit (at 0.001 albedo) which suggests a maximum relative change of 10%. A mild inverse relationship of albedo and cross-sectional area was noticed in the May data set, again possibly indicating a radius-of-curvature effect.

An extension to the present analysis would use total-emitted-flux conversion factors based upon an ellipsoidal shape that corresponded to the relative changes in area presented here in order to see if the relative cross-sectional areas are altered. This would also better constrain the relative albedo and if used iteratively, using the model to find a shape and then using the shape to calculate a model, may be used to converge to a true shape.

Using this technique in concert with rotational spectral variations would lead to a powerful tool with which to study the surface mineralogy and petrology of an asteroid as a unique planetary body. This would give a better understanding of how individual asteroids formed and evolved and how they are interconnected not only among any family relationship, but among the asteroid population as a whole. A knowledge of how mineralogy and petrology changes with shape and albedo would help in the study of asteroid evolution, both of their parent bodies and their collisional evolution. Much work needs to be done with this technique in order to gain a deeper understanding of asteroids as individual worlds.

ACKNOWLEDGEMENTS: This work was supported under NASA Grant NAGW-642. L.A. Lebofsky was Visiting Astronomer at the NASA Infrared Telescope Facility which is operated by the University of Hawaii under contract to NASA.

REFERENCES: [1] Taylor *et al.* (1988) *Icarus* **73**: 314-323, [2] Taylor *et al.* (1987) *Icarus* **69**: 354-369, [3] Lebofsky, L.A. *et al.* (1988) *Icarus* **75**: 518-526, [4] Tokunaga, A.T., IRTF Photometry Manual (1986), [5] Neckel, H. and Labs, D. (1984) *Solar Phys.* **90**: 205-258, [6] Brown, R.H. (1985) *Icarus* **64**: 53-63, [7] Lebofsky, L.A. *et al.* (1978) *Icarus* **35**: 336-343

COSMOGENIC-NUCLIDE DEPTH PROFILES IN THE LUNAR SURFACE.*

R. C. Reedy and J. Masarik, Astrophysics and Radiation Measurement Group, Mail Stop D436, Los Alamos National Laboratory, Los Alamos, NM 87545, USA.

Depth-dependent production rates of ^{10}Be, ^{26}Al, ^{36}Cl and ^{53}Mn in the lunar surface were calculated using evaluated cross sections and the LAHET Code System for particle fluxes. Good agreement with experimental data were obtained for all investigated radionuclides down to 400 g/cm^2 for a primary galactic-cosmic-ray particle flux of 4.56 nucleons/cm^2/s. The nature of the reactions making a nuclide strongly affects the amount of the production-rate increase from the surface to the peak and the depth of this peak but has little effect on the rate of decrease below 200 g/cm^2.

The study of cosmogenic nuclides in extraterrestrial bodies allows us to study the histories of cosmic rays and the irradiated object. In order to use cosmogenic nuclides as such a tool, it is essential to understand how production rates depend on the shielding of the sample in which the nuclide is measured. Because of their low energies, most solar cosmic rays (SCR) are stopped by ionization loses in the outermost few g/cm^2. We did not simulate the contribution of SCR to the total production rates and therefore have underestimated nuclide production near the surface. The galactic cosmic rays (GCR) have much higher energies and penetrate very deep inside the irradiated body and produce many secondary particles that contribute to nuclide production. The nuclear processes involved in the interaction of GCR particles with matter are simulated in our model with the LAHET Code System (LCS) [1], which is a system of coupled Monte Carlo codes that treats the relevant physical processes of particle production and transport. LCS and its adaptation to meteorite applications are described in [2]. Production rates calculated in meteorites using LCS-calculated fluxes have agreed well with various measurements [2–4].

We simulated the irradiation of the lunar surface with an isotropic GCR particles flux of 1 proton/cm^2/s with an energy distribution corresponding to the GCR primary particle flux averaged over a solar cycle. The Moon was modeled as a sphere with the average lunar radius, and the bulk composition and density were from the Apollo 15 deep-drill core (15001/6). To map the depth dependence of production rates, we divided the model sphere into concentric shells with thickness 6 g/cm^2. In each shell, neutron and proton fluxes were calculated. Simulation of 50,000 primary GCR particles gives calculated particle fluxes with statistical errors less than 3%. Having calculated the particle fluxes, the production rates of cosmogenic nuclides were calculated by integrating over energy the product of these fluxes with cross sections for the nuclear reactions making the investigated nuclide [2]. Cross sections were those evaluated for extraterrestrial studies: ^{10}Be [5], ^{26}Al [6], ^{36}Cl (like in [7] but with 0.8 of all Ca cross sections below 1 GeV), and ^{53}Mn [8,9].

We first determined the flux of GCR particles over the few last Myr by fitting the calculated depth profiles for the production of ^{26}Al and ^{53}Mn in the Apollo 15 drill core to the experimental data [10–12] (cf., Figs. 1 and 2). The ^{26}Al measurements of [13] are ~0.81 of the others. Fairly good agreement was found over the whole depth region with an effective incident GCR particle flux of 4.56 protons/cm^2/s. The agreement with the ^{10}Be and ^{36}Cl lunar measurements [14] are also fairly good (Figs. 3–4). This flux is slightly less than the one of 4.8 protons/cm^2/s we found for these radionuclides in meteorites [3], implying that the average GCR flux at meteorites are ~5% greater than that at 1 AU. This effective flux includes contributions from the alpha particles in the GCR (~13%) [2] and is equivalent to a primary GCR proton flux of 3.04 protons/cm^2/s. Our GCR flux of 4.56 protons/cm^2/s is slightly less than the lunar ones of [15] (4.72) and [16] (5.5) calculated with a similar code, the differences probably due to the cross sections used.

The figures present the total calculated production rates and the contributions of protons and neutrons. Contributions of other particles (e.g., pions) are negligible [2]. Neutron production is dominant for all depths and nuclides except for ^{10}Be near the surface. The neutron contributions vary from ~60% at the surface (only ~30% for ^{10}Be) to about 90% at depths $\gtrsim$400 g/cm^2.

A characteristic feature of all production-rate-versus-depth profiles is an increase from the surface to a peak value and then an approximately exponential decrease to greater depths. The depth of the peak production and the steepness of increase from surface to the peak are determined by characteristics of the nuclear reactions making the nuclide [17]. The highest energy product investigated in this study, ^{10}Be, has a peak production rate at a depth about 20 g/cm^2 and the difference between peak and near surface production rates is less than 1 atom/min/kg. The flat experimental ^{10}Be profile [18] together with our calculations imply that the SCR contribution to

LUNAR NUCLIDE DEPTH PROFILES Reedy R.C. and Masarik J.

the ^{10}Be production is ~1 atom/min/kg. The steepest increase from surface to the peak production rate is observed for ^{26}Al, which like ^{36}Cl and ^{53}Mn reach peak production rates near 50 g/cm^2. The e-folding lengths for depths of 200–450 g/cm^2 are 179 g/cm^2 for ^{10}Be and ^{53}Mn and 182 g/cm^2 for ^{26}Al and ^{36}Cl, in very good agreement with measured values [13,14]. Over the depth range of 150–450 g/cm^2, the e-folding lengths of these four radionuclides decreases with increasing depth, with the biggest rate of change nearest the surface and the least change for ^{10}Be.

These calculations for the production of cosmogenic nuclides are in good agreement with measured data and with other model calculations [8,15] with respect to the absolute magnitude as well as the shape. Our inferred GCR flux for the last few Myr are similar to modern fluxes, indicating no significant change of the GCR intensity during the last few million years.

References [1] Prael R.E. and Lichtenstein H. (1989) *Los Alamos Report LA-UR-89-3014*. [2] Masarik J. and Reedy R.C. (1994) *GCA*, submitted. [3] Reedy R.C. *et al.* (1993) *LPS XXIV*. p. 1195. [4] Michlovich E.S. *et al.* (1994) *JGR*, submitted. [5] Tuniz C. *et al.* (1984) *GCA* **48**,1867. [6] Reedy R.C. (1987) *NIM* **B29**, 251. [7] Nishiizumi K. *et al.* (1989) *PLPSC-19*, p. 305. [8] Reedy R.C. and Arnold J.R. (1972) *JGR* **77**, 537. [9] Nishiizumi K. (1988) (priv. comm.). [10] Rancitelli L.A. *et al.* (1975) *PLSC-6*, p. 1891. [11] Nishiizumi K. (1992) (priv. comm.). [12] Imamura M. *et al.* (1973) *EPSL* **20**, 107. [13] Nishiizumi K. *et al.* (1984) *EPSL* **70**, 164. [14] Nishiizumi K. *et al.* (1984) *EPSL* **70**, 157. [15] Michel R. *et al.* (1991) *Meteoritics* **26**, 221. [16] Dagge G. *et al.* (1991) *PLPSC-21*, p. 425. [17] Masarik J. and Reedy R.C. (1993) *Meteoritics* **28**, 391. [18] Nishiizumi K. *et al.* (1988) *PLPSC-18*, p. 79. * Work supported by NASA and done under the auspices of the US DOE.

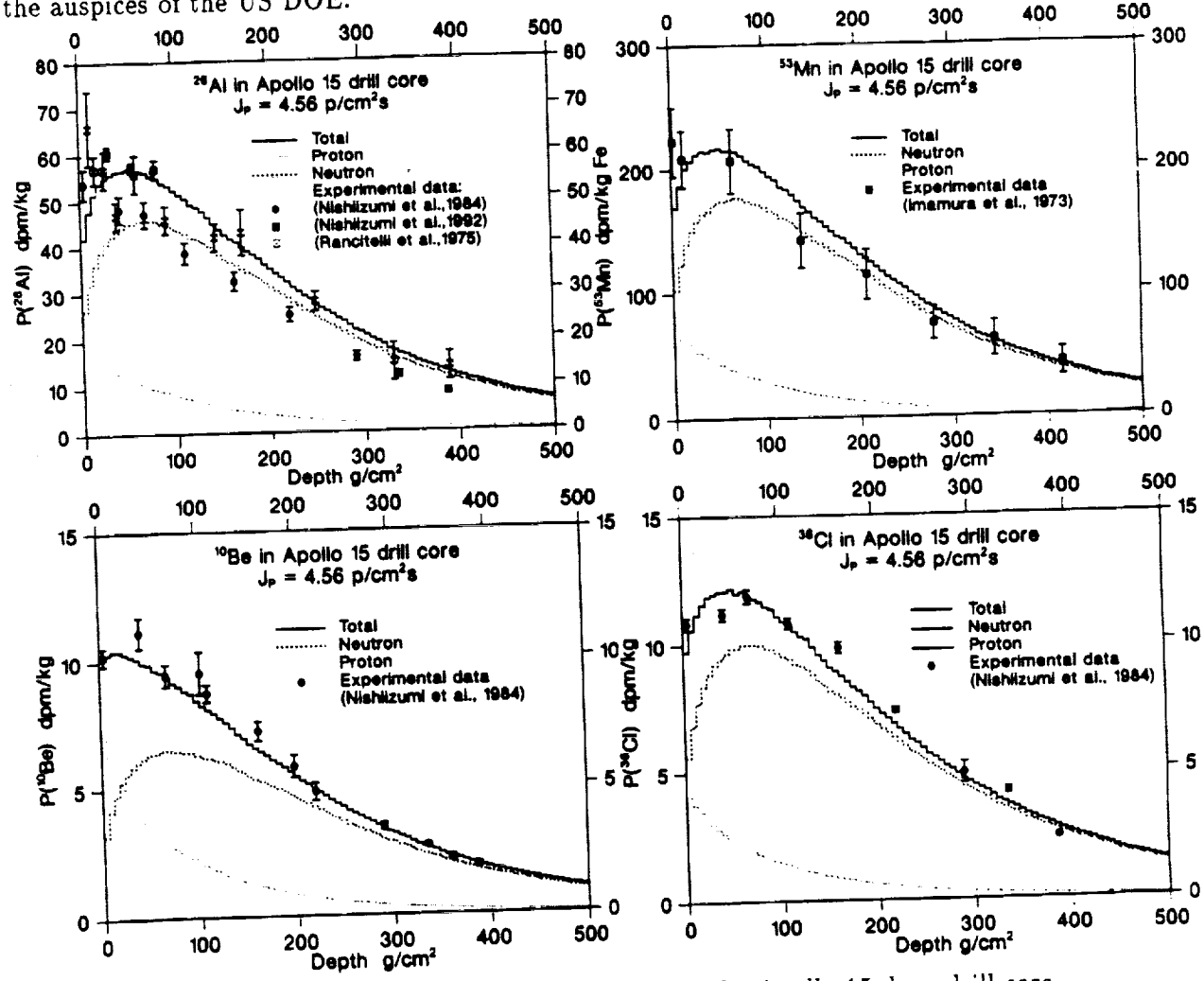

Figs. 1-4. Calculated and measured production rates in the Apollo 15 deep drill core.

FIRST OBSERVATIONS OF SHATTER CONES IN THE DIRECT VICINITY OF THE BUSHVELD COMPLEX. **W.U. Reimold[1] and R.C.A. Minnitt[1,2]; [1]E.G.R.U., Dept. of Geology, Univ. of the Witwatersrand, P.O. Wits 2050, Johannesburg, R.S.A.; [2]Cons. Geol., GEOBASEcc, P.O. Box 1423, Florida 1710, RSA.**

Findings of shatter cones are reported for the first time from two localities in the Nooitgedacht (Klapperkop) Member of the 2.25-2.35 Ga Timeball Hill Formation near Lydenburg in the Eastern Transvaal - about 25 km from the eastern margin of the Bushveld Complex. Spatial distribution of cone fractures in these river-bed exposures and cone appearances favor their interpretation as true shatter cones and not as sedimentary percussion (impact) marks. An origin by bolide impact has been suggested in the past for the Bushveld Complex (B.C.), however to date no firm evidence in support of this hypothesis has been offered. It may now be speculated whether the Klapperkop shatter cones are related to the formation of the Bushveld Complex, or, alternatively, to a local impact structure in the Proterozoic rocks of the Eastern Transvaal. Be it as it may, further search for such rock deformation around the perimeter of the Bushveld Complex is clearly indicated.

Several workers suggested earlier that the expansive and ore resource-rich Bushveld Complex in South Africa (Fig. 1) could be the result of one or more large impact events [e.g., review by 1]. However, to date no firm evidence in the form of shock metamorphic effects or of macroscopic impact indicators, such as shatter cones that are widely, but not uniformly believed to be diagnostic of impact, could be obtained in support of this hypothesis [2]. The main arguments in favor of Bushveld impact stem from morphological interpretation. It is believed that diagnostic shock effects should not be recognizable, because all exposures of "fragments" of pre-Bushveld crust are distal with respect to impact sites or completely annealed [1].

In 1992, one of us (R.M.) during a hiking-trip accidentally came across an exposure of the Nooitgedacht (also known as Klapperkop) Quartzite Member [3] of the ca. 2.2-2.3 Ga old Timeball Hill Formation of the Transvaal Sequence. He recognized unique near-circular, sometimes raised and cone-shaped fractures (Figs. 2,3) in this riverbed pavement exposure and suggested [4] a possible relationship to similar deformation in shatter-coned Hospital Hill quartzite (Fig. 4) that had just been mapped by him. The Klapperkop exposure is located in the bed of the Houtbosloop streamlet on farm Kantoorbos 263JT, some 27 km SSE of the town of Lydenburg (Fig.1). Individual cones or abraded cone fractures generally measure between 2 and 12 cm in diameter. Poles to striations (Fig. 5) for several well-preserved cones plot along a circle (Wulff net, lower hemisphere) defining a (master) conical angle of 125°. However, some data (small circle in Fig. 6) are clearly not reconcilable with this projection of a master-cone trace. Orientations of apical axes (Fig. 6) scatter widely between near-vertical and subhorizontal attitudes. This scenario is similar to our observations in the Vredefort structure. Close comparison of Figures 3 and 4 reveals that the cone features in both cases are produced by intersecting multiple sets of curvilinear fractures (MSJS [5], cf. Fig. 6).

Exposures of Klapperkop quartzite are rare in this difficult, mountainous terrane and are generally restricted to high, inaccessible cliff-faces and to pavements in river-beds that are often only accessible just above water-falls. Despite these unfavorable circumstances we discovered a second exposure of 'coned' Klapperkop quartzite in the bed of the Beestekraalspruit on the forest farm Uitzoek 260JT, only 3 km NE of the first site. Subsequent surveys failed to yield other accessible outcrops in this area. No cone features could so far be discovered in under- or overlying argillaceous units. The fact that both coned exposures are in river-beds and near water-falls prompted the critique that our 'cones' could represent sedimentary percussion (impact) marks. However, literature studies on this topic provided no support for this suggestion, as our cones are regularly shaped, are sometimes still recognizable as definite 3D, cone-shaped features (Fig. 2), are generally much larger than percussion marks, and are, just like Vredefort and Sudbury shatter cones, related to MSJS. For these reasons we conclude that true shatter cones have been discovered < 25 km from the eastern margin of the Bushveld Complex. Currently it can only be speculated whether these shatter cone occurrences can be linked to the B.C. or are perhaps the result of a local impact event. Only further fieldwork in the environs of the B.C. will potentially resolve this problem. We hope that this report will not trigger a flood of speculative contributions related to the origin of the B.C., but will generate awareness amongst field-workers along the > 1500 km periphery of the Complex of the possibility that shatter cones could occur in their study areas.

Refs.: [1] Elston, W.E., 1992, LPI Contr. No. 790 (Sudbury 92), 23-24; [2] French, B.M., 1990, Tectonophys. 171, 287-301; [3] S. Afr. Comm. for Stratigr., 1980, Geol. Surv. Hdb. 8, p.192-194; [4] Minnitt, R.C.A. et al., 1992, Geocongr. 92, GSSA, Bloemfontein, 274-277; [5] Nicolaysen, L.O. and Reimold, W.U., 1987, Contrib. to Cryptoexpl. and Catastr. in the Geol. Rec. Worksh., Section N2, 8pp.

SHATTER CONES NEAR THE BUSHVELD COMPLEX: Reimold W.U. and Minnitt R.C.A.

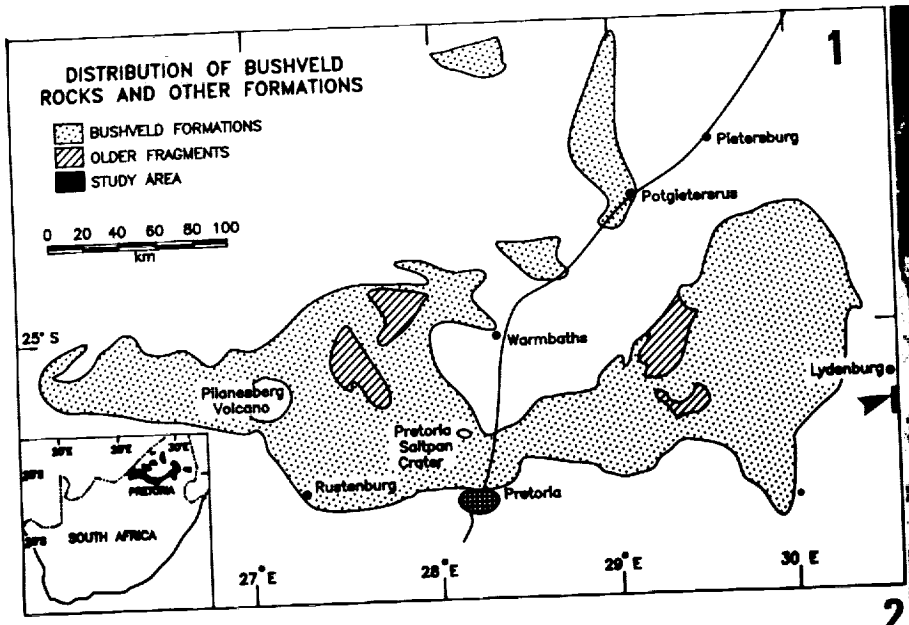

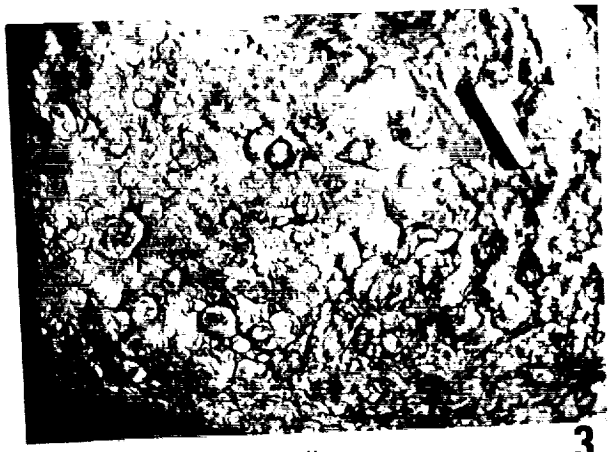

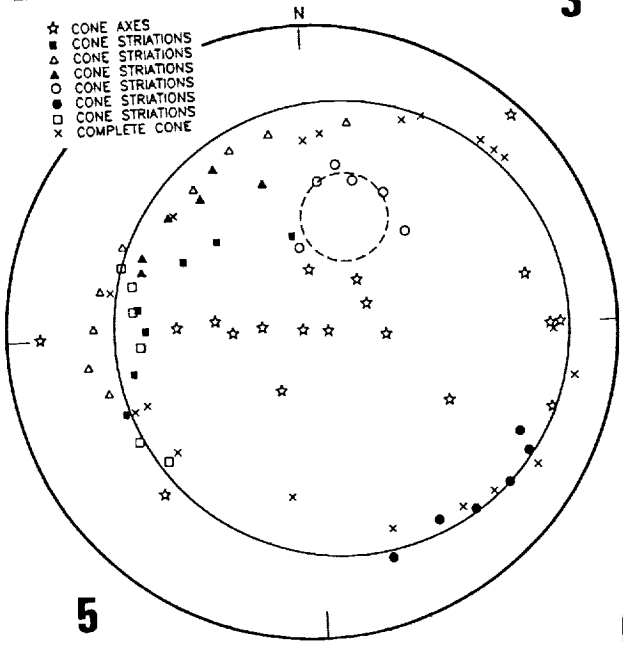

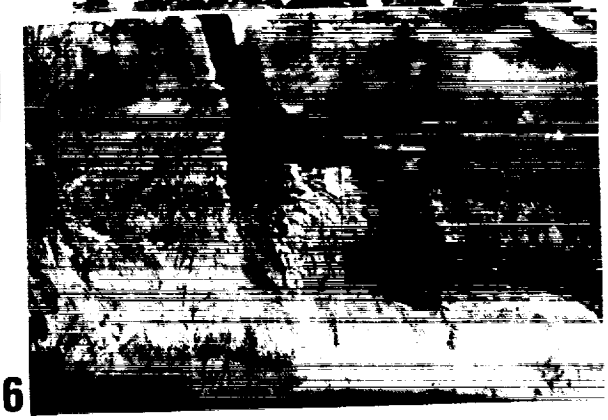

THE DYNAMICAL EVOLUTION OF MAGNETIZED SOLAR NEBULA M. Reyes-Ruiz, Dept. of Space Physics and Astronomy, Rice Univ., Houston, Texas, and T. F. Stepinski, Lunar and Planetary Institute, 3600 Bay Area Blvd., Houston, TX 77058

It is now widely accepted that our solar system, at the solar nebula stage of its evolution, could be best described as Keplerian accretion disk (AD). In ADs, it is usually assumed that the turbulent viscosity is solely responsible for the outward transport of angular momentum and inward mass accretion. In addition to turbulence, a magnetic field embedded in a AD may also transport angular momentum. In a typical AD, the timescale for magnetic field dissipation is orders of magnitude smaller that the typical disk lifetime, so for a magnetic field to persist long enough to be dynamically or otherwise important it must be regenerated by a dynamo cycle. It has been shown [1] that such a dynamo-generated magnetic field is indeed likely to exist in the solar nebula and may significantly contribute to the accretion evolutionary process and physical structure of the nebula. Such fields would supplement rather then replace turbulence in transporting angular momentum. In this paper we present the results of calculations of the global dynamical evolution of a AD solar nebula that take into consideration the existence of a large-scale, dynamo-generated magnetic field.

For our calculations we chose a fiducial case of an AD [2], which is based on the α_{ss} prescription of viscosity. A solution is obtained under the assumption that the Rosseland mean opacity is adequately described by a piecewise continuous power-law [3]. The degree of ionization is calculated from the balance between sources (thermal ionization, cosmic rays, radioactive isotopes) and losses (recombination on ions and grains) of free electrons. It is assumed that all grains are spherical and have the same size equal to $50\mu m$, a maximum value still consistent with the opacity calculations. The evolution of the nebula structure is obtained numerically following the method described in [4]. The numerical experiment starts with a disk of mass equal to $0.225 M_{\odot}$ distributed uniformly from $R_{in} = 0.04$ AU to $R_{disk} = 15$ AU, and having an angular momentum equal to 5.2×10^{52} g cm^{2}sec^{-1}. At each timestep we first calculate the structure of the non-magnetic nebula. We then calculate the spatial distribution of degree of ionization and the resulting ohmic diffusivity, find the regions of a disk where the dynamo process maintains a magnetic field and estimate the magnitude of the magnetic field, as well as the ratio between the horizontal and vertical components of the magnetic field. The disk structure is now calculated taking into account the structure of magnetic field. Magnetic effects are taken into account by modifying the standard disk equations in the following manner: (1) magnetic pressure is added to the gas pressure, (2) magnetic tension is incorporated by defining an effective viscosity parameter α_{eff}, which encapsulates both the turbulent and magnetic contribution to angular momentum transport.

A magnetized nebula evolves faster than a nebula in which turbulent viscosity is the sole mechanism of angular momentum transport. The initial distribution of mass is forgotten after less than 10^4 years. A new feature, directly related to the presence of a magnetic field, is the surface density bulge located in the region of the disk that cannot support a magnetic field. The bulge persists for about 3×10^5 years, moving gradually inward. The density within the bulge is increased by a factor of 3-4 (for $\beta = 20$), more for a stronger magnetic field. The location, size, and lifetime of the bulge depend on a choice of α_{ss}, and initial disk mass; however, the example shown here is representative for most models of the solar nebula. The presence and persistence of the surface density bulge in the disk may have important implications for the process of formation of giant planet cores. A surface mass density of solids in the range of 15-30 g/cm^2 appears to be needed to allow Jupiter's core of about 15 – 20 $M_{\oplus}$ to form by rapid runaway growth of planetesimals on a timescale of 5×10^5 - 10^6 years [5]. Such surface density is about 5-10 times greater than predicted by the minimum mass nebula model. One can postulate a more massive disk, but then the surface density increases everywhere. This is a problem because, whereas the formed Jupiter can remove the "unused" material from the solar system, the terrestrial planets cannot, so there would be a lot of planetesimals left in the inner solar system. In a magnetized nebula, however, this difficulty seems to have a natural solution. The bulge remains mostly unaltered in the region of Jupiter formation for about 10^5 years. During this time the surface density of solids within the bulge is enhanced to about 15-20 g/cm^2, but the density of solids in the inner solar system is on average about as high as predicted by the minimum nebula model. Therefore, the formation of Jupiter may be the simple consequence of a density bulge rather than the reflection of the existence of the so-called "snow line," the radius at which water ice adds to the density of solids.

EVOLUTION OF MAGNETIZED SOLAR NEBULA M. Reyes-Ruiz and T. F. Stepinski

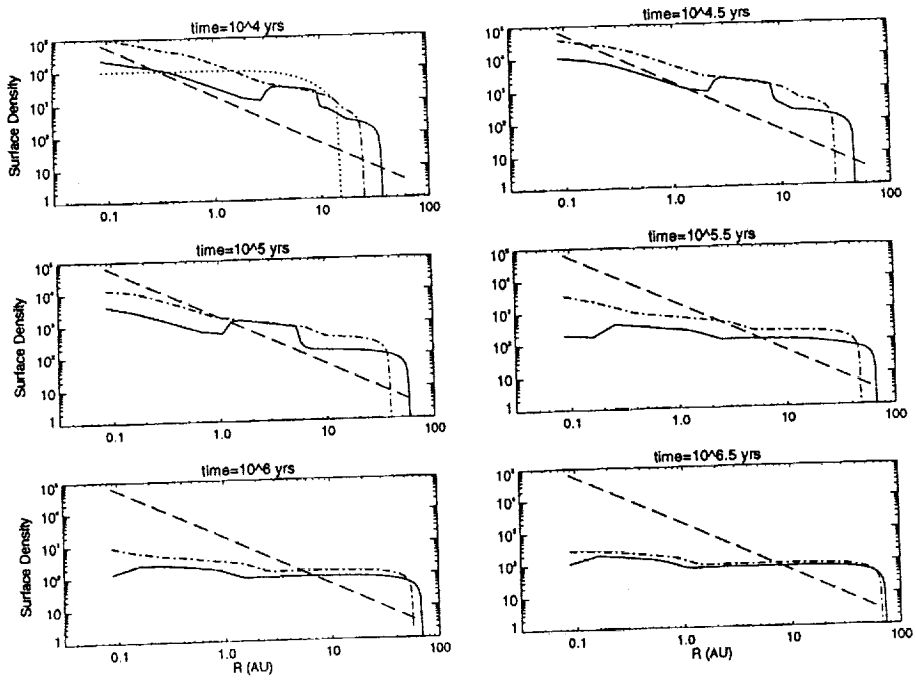

FIGURE 1. Radial distribution of the solar nebula surface density at selected times for the case with $\alpha_{ss} = 0.01$ and the ratio of gas to magnetic pressure $\beta = 20$ (which corresponds to a magnetic field strength such that the Lorentz force on the turbulent eddy equals the Coriolis force on it, and the dynamo process is presumably saturated). Solid lines show the surface density for the magnetized nebula; dash-dotted lines show the surface density for the unmagnetized nebula. The dotted line shows the initial condition, and the dashed line show the distribution of surface density in the minimum mass, phenomenological model of the solar nebula. Surface density is given in grams/cm^2, and the radial coordinate is given in AU.

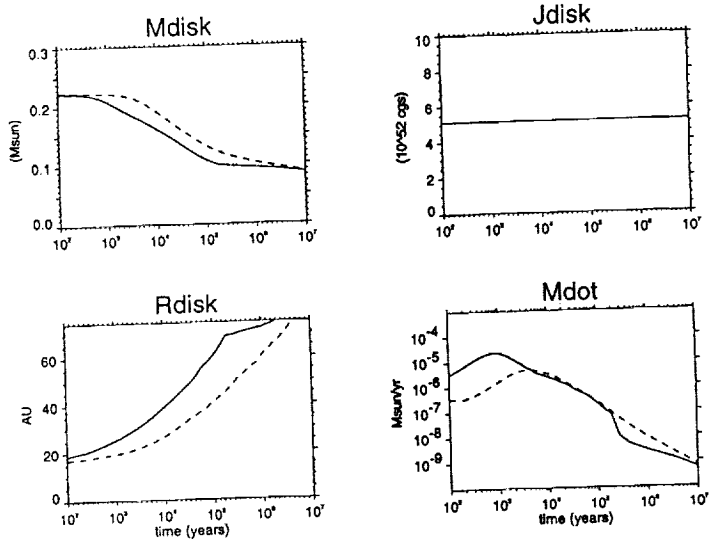

FIGURE 2. Solar nebula mass, total angular momentum, outer radius, and mass flux onto the protosun as a function of time for the case with $\alpha_{ss} = 0.01$ and $\beta = 20$. Solid lines are for a magnetized nebula, and dashed lines are for an unmagnetized nebula. Angular momentum stays constant throughout the time of calculation, pointing to the accuracy of the numerical scheme.

References:[1] Stepinski *et al* (1993), *Icarus*, **106**, 77;[2] Shakura, N.J. and Sunyaev, R.A. (1973) *Astron. Astrophys.*,**24**, 337; [3] Ruden and Pollack, 1991, *ApJ*, **375**, 740; [4] Bath and Pringle (1981, *MNRAS*, **194**, 967; [5] Lissauer, 1987, *Icarus*, **69**, 249.

TERRESTRIAL POLAR BEACH PROCESSES: MARTIAN PALEOLAKE ANALOGS; J.W. Rice Jr., Department of Geography, Arizona State University, Tempe, AZ 85287, USA

The perennial ice covered lakes of the Antarctic are considered to be excellent analogs to lakes that once existed on Mars. Field investigations of ice covered lakes, paleolakes, and polar beaches have been conducted in the Bunger Hills Oasis, Eastern Antarctica.

Important distinctions have been made between ice covered and non ice covered bodies of water, in terms of the geomorphic signatures produced. Field investigations have revealed that the classical lacustrine landforms created by non ice covered lakes (spits, bars, berms, cusps, tombolos, and wave cut platforms) are absent in an ice covered lake regime. The features mentioned above are the result of the direct coupling of wind and the free water surface. The ice cover acts as a geomorphically protective agent. Therefore, the shores of ice covered bodies of water are low energy environments i.e. poorly sorted, due to restricted or nonexistent wave action. However, regions of open water may exist for 1-2 months a year, but the proximity of the permanent pack ice severely limits the distance of fetch and consequently the magnitude of wave action. Another curb to any wave action effectiveness is the presence of a narrow strip of ice frozen to the shore which is unaffected by tidal movements. This narrow fringe of ice attached to the shore is an ice foot. It is composed of sea ice, frozen snow, and frozen spray (1). In non tidal regimes, a frozen swash layer with interbedded sediments is termed a kaimoo (2). From a geologic perspective, the ice foot and kaimoo are very important in that they additionally protect the beaches from any limited wave action that may exist. Consequently, Polar beaches are very poorly developed and narrow. These processes (along with age and resolution limits) may help explain why paleoshorelines on Mars are hard to discern.

The most notable landforms produced by ice covered lakes are ice shoved ridges. These features form discrete segmented ramparts of boulders and sediments pushed up along the shores of lakes/seas. The shorelines are generally planated with the ramparts defining the inner edge of the shoreline. These ridges usually have a heterogeneous veneer of boulders, pebbles, sand and gravel mantling an ice core. The ice core normally melts out and leaves behind its mantle of material in the form of irregular discontinuous ridges. The ice core can persist for years if it is sufficently insulated, by its mantle of material.

The ice shoved features observed in the Bunger Hills Oasis were up to 83m long, 2m high, and 4m wide. Ice shoved ridges up to 300m long and 10m high have been reported (1).

POLAR BEACH PROCESSES: Rice, J.W.

Other unique landforms associated with polar beaches are frost cracks and mounds, patterned ground, pingos, pitted beaches, coastal striated bedrock, and ventifacts.

References:

(1)Nichols R. L. (1961)Am.Jour.Sci., 259, 694-708.
(2)Embelton C. (1975)Periglacial Geomorphology, 203p.

ANALOGS AND INTERPRETATIONS FOR THE MARTIAN THUMBPRINT TERRAIN AND SINUOUS RIDGES; J.W. Rice Jr.[1] and J.D. Mollard[2],Department of Geography, Arizona State University, Tempe Arizona 85287, USA [1]; Mollard and Associates Ltd., 2002 Victoria Ave., Regina, Sask., S4P 0R7, Canada [2].

Large Scale Retrogressive Slope Failures On Mars:

A new explanation for certain types of Martian "thumbprint" terrain is that these landforms are ribbed retrogressive earth flows. Several possible terrestrial analogs have been located in the Interior Plains region of Canada. Retrogressive slope failures are a mass movement landform and process characterized by downslope translation of soil and weathered rock over a discrete basal shear surface. The failed slopes can be rather shallow, flattening out as a result of slow creep movements to gradients as low as 9.5 to 4 degrees (1).

The Canadian slope failures occur most commonly in Upper Cretaceous bentonitic marine clay shale, silty shale, and claystone, commonly with siltstone and sandstone interbeds. These earthflows form multiple, arcuate, elongate ridge and depression topography that may extend for several kms and cover areas many tens of square kms (1). The location of these flows usually occur near the reaches of active lateral river erosion and on the flanks of mesa like uplands in the Interior Plains region.

In most places where there are slope failures, clay and silt deposited during transgression and regression of the Champlain Sea are covered by fluvial and deltaic fine - medium grained sand with some gravel. Postglacial uplift resulted in stream incision into the plains sediments forming sand terraces at different elevations. Locally, the terraced sands show features of abandoned shorelines, dunes and blowouts.

The style of failure and repetitive pattern of transverse ribs was explained by plastic flow and extrusion which takes place in a soft layer underlying a stiffer layer that in turn underlies surficial saturated sand. It has been proposed (2) that the extrusion of the underlying, remolded soft clay very rapidly transported successive and intact slices of the stiff layer away from the retreating backscarp. Elongate crescent shaped slices then subside intact as the softened clay is extruded with ridges and pinnacles of the remolded clay being squeezed upward between successive blocks. Slope failure is usually initiated by snowmelt runoff thus causing high pore pressure, but active stream erosion at the toe of slopes and earthquakes can also start failures.

Raised Channel Systems On Mars:

Raised channel systems are alluvial stream deposits that have been cemented and differentially exposed by weathering and erosion to form a series of upstanding, multistorey, linear ridges and sheets representing an area of inverted drainage (3). Raised channel deposits have been identified in numerous terrestrial desert regions (Saudi Arabia, Oman, Egypt, Transvaal, New Mexico, and Texas) and have been described under various terms such as suspendritic drainage lines, bas relief, pseudo-eskers,

MARTIAN GEOMORPHIC ANALOGS: Rice, J.W. and Mollard, J.D.

gravel capped ridges, gravel trains, perched wadis, wadi ridges, and suspenparallel drainage.

The raised channels systems of Oman will serve as the prime example of these features for this study. The system in Oman represents over 12 seperate episodes of fluvial activity such that the ridges intersect one another and successive paleochannel deposits are superimposed on one another (3). Work by Maizels has differentiated paleofluvial deposits by contrasts in elevation, morphology, sedimentology, and lithology.

The fluvial deposits are cemented during periods of high water tables, associated with rapid evaporation rates and precipitation of salts within the gravel sequence. The deposits once cemented are more resistant to erosion, additionally, the deposits are protected from deflation by the concentrations of gravel on the channel floor. Initial burial of the fluvial deposits can be achieved by fluvial accretion, overbank facies, and eolian deposition. The subsequent exhumation of these deposits can be accomplished by fluvial, eolian, or marine activity.

The raised channel systems extend across low gradient alluvial fans for a distance of up to 250 km from the Eastern Oman Mountains. The Plio-Pleistocene period raised channel systems are comprised of heavily varnished chert and ophiolite rich gravels. The channels are sinuous, broad, gravel topped ridges 1 to 2 km wide, several hundred km long, and rising over 35 m above the adjacent desert floor (3).

There are numerous examples of raised channels systems on Mars. Some locations are the Mangala Vallis region, and the Auqakah Vallis region. It is also proposed here that the ridges in Argyre Planitia and Dorsa Argentea are raised channels. The sinuous ridges in Argyre and Dorsa Argentea have been explained in the past as eskers, longitudinal dunes, lacustrine spits and bars, wrinkle ridges, and clastic or igneous dikes (4-8). Additonally, inverted stream beds have been mentioned but dismissed by one researcher and only mentioned in passing by the other. In addition to the regions listed, I have located raised channels along the the inner rim of Moreux crater and east of Argyre Planitia.

References:

(1)Mollard,J.D.(1973) Canadian Jour. Earth Sci.10,324-26.
(2)Mollard, J.D.(1977) GSA 3,29-56.
(3)Maizels,J.(1990)Paleo,Paleo,Paleo,76,241-277.
(4)Kargel,J.S.;R.G.Strom(1990)LPSC 21,598-99.
(5)Ruff,S.W.;R Greeley(1990)LPSC 21, 1047-48.
(6)Parker,T.J.(1992)LPSC 23, 1031-32.
(7)Metzger,S.M.(1991)LPSC 22, 891-892.
(8)Howard, A.D.(1981)NASA TM 84211,286-88.

SEARCHING FOR A PRINCIPAL COMPONENT MIXING MODEL FOR CHONDRITIC INTERPLANETARY DUST PARTICLES : THE USE OF SIZE ANALYSES.

Frans J.M. Rietmeijer, Department of Earth and Planetary Sciences, University of New Mexico, Albuquerque, NM 87131, USA.

At a recent workshop on interplanetary dust particles (IDPs), I have proposed a scheme for chondritic IDP classification [1] that is founded on two observations, *viz.* (1) many chondritic IDPs are mixtures of three *principal components* [2], and (2) chondritic IDPs may have bulk carbon contents in excess of CI-abundances [3]. Principal components were first recognised in the fluffy granular matrix of a carbonaceous chondritic porous (CP) IDP which gave rise to the granular units (GUs) [4]. The ratio of carbon materials to silicates plus sulfides in GUs can vary from pure carbon ('tar balls', ref. 5) to carbonaceous chondritic material [2,4,5]. Various investigators have used a different terminology. I propose the following *principal components*,

(1) **carbonaceous units** [CUs],
(2) **granular units** [GUs], *i.e.* carbonaceous chondritic material, and
(3) **polyphase units** [PUs], *i.e.* carbon-free chondritic material [2].

I have suggested that the principal components are nebula dust that accreted into chondritic IDPs. Different mixing ratios yield variable carbon content of chondritic IDPs and broadly determine the morphology, e.g. a low (CU+GU)/PU ratio characterises chondritic smooth IDPs [2]. The mixing ratios also affect the amount of amorphous material, or micron-sized olivine, pyroxene, feldspar and layer silicates crystals and fragments in IDPs [2] (Figure 1).

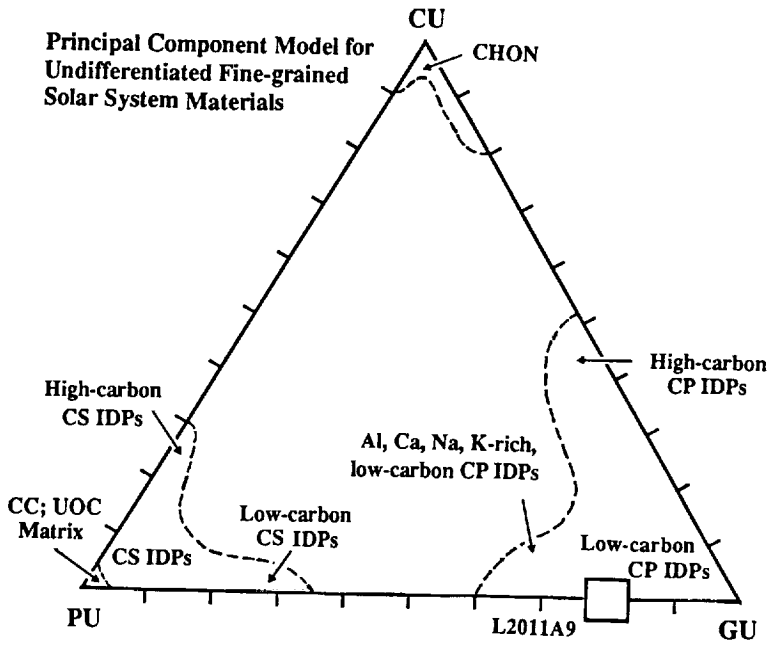

Figure 1: A proposed ternary principal component mixing model of CUs, GUs and PUs. The dashed lines delineate guestimated fields of IDP types with markers to compositional variations within the CP and chondritic smooth IDP fields. The position of CP IDP L2011A9 is determined by the observed relative abundance of its GUs and PUs. The true field boundaries and the reality of miscibility gaps remain to be determined. They potentially contain information on solar nebula conditions during dust accretion.

In a principal component model its basic component sizes should be similar among chondritic IDPs and the constituent minerals in GUs and PUs from different IDPs should have a similar history. To this effect I use size distribution analyses of principal components and their constituent minerals. The sizes were measured on calibrated transmission electron microscope negatives from ultrathin IDP sections and they are expressed as the root-mean-square size [6]. This size analysis study continues with the analysis of CP IDP L2011A9 with granular matrix of GUs and PUs that contains a few large (~810 nm) Fe-sulfide xenocrysts [7] and a large (2.7 x 0.8 μm) PU [1]. Small Fe-oxide crescents and dispersed nanocrystals throughout the IDP are evidence for atmospheric entry heating and its extraterrestrial origin. The clustering of pyrrhotite compositions and scarcity of vesicular sulfides show that heating was not severe [8].

OBSERVATIONS. Principal Components in L2011A9. The GUs are discrete units. The (rms) size range for 130 GUs is 43-509 nm with a mean of 168 nm that also represents the basic unit

A PRINCIPAL COMPONENT MODEL : Rietmeijer, F.J.M.

size. Five larger GUs are fused units. These data compare with a GU size range of 64-7,580 nm (mean = 585 nm) and a basic unit of 128 nm in size in CP IDP W7010*A2 [2]. In both IDPs the basic size of ~0.1 μm (real size) in diameter is similar to the proposed size of composite interstellar dust [9]. The polyphase units form well-defined, partial or holocrystalline clusters. The latter are slightly porous (ΔV crystallisation). Other units are open clusters with isolated single-crystal grains "fading" into the matrix [cf. 2]. The sizes of 34 recognisable PUs range from 190.4 nm to 1,972 nm. They define two Gaussian distributions: (1) mean = 532.8 nm (range: 190.4-797.9 nm; cf. ref. 8)(N=25), and (2) mean = 1,138.3 nm (range: 869.7-1,445.9 nm) (N=8). The data constain the PU/(PU+GU) ratio of this IDP at ~0.21 but it probably somewhat higher as the isolated single crystal-grains should be included in this calculation.

Constituent Minerals. Data for 274 ultrafine minerals in these GUs are shown in Table 1. The grain size distribution is a composite of two lognormal distributions. Its steady-state profile is consistent with second order growth by Ostwald ripening in a closed system [cf. 10] due to surface free energy driven nucleation and growth of ultrafine minerals [6]. The ultrafine grains have an unevolved size distribution. This size analysis of all grains in the GUs [Table I, (a)] included dispersed Fe-oxide nanocrystals formed during atmospheric entry heating. These nanocrystals (N=114) have a lognormal size distribution ranging from 1.0 to 12.4 nm; mean = 2.3 nm. The exponential steady-state profile is transitional from a nucleation- to a ripening-controlled distribution and consistent with a single event not followed by size adjustment. When the size distribution for the constituent GU minerals is "corrected" for the Fe-oxide nanocrystals, population II [Table 1; (b)] becomes consistent with the other two particles.

Table 1: rms-sizes (nm) of platey grains in granular units in CP IDPs W7010*A2 and U2015*B [from ref. 2] and U2011A9.

	range	mean
	Population I	
W7010*A2	1.4 - 4.2	3.5
U2015*B	2.1 - 6.4	4.2
U2011A9	no data	
	Population II	
W7010*A2	5.6 - 17.0	8.9
U2015*B	7.1 - 17.2	9.4
U2011A9	1.4 - 29.0	8.1 (a)
	5.7 - 18.6	10.3 (b)
	Population III	
W7010*A2	21.2 - 127.0	49.6
U2015*B	a few grains	
U2011A9	32.2 - 49.8	37.8 (a)
	14.7 - 48.9	26.8 (b)

See text for (a) and (b). All populations are lognormal distributions. CP IDPs W7010*A2 and U2015*B do not have a (partial) Fe-oxide rim or dispersed Fe-oxide nanocrystals.

The size range of 143 fine-grained silicate and sulfide grains is 8.7 - 2,903 nm in diameter. They define three Gaussian distributions (1) mean = 25.5 nm (range: 8.7-73.8 nm), (2) mean = 113.8 nm (range: 74.6-163.2 nm), and (3) mean = 308.4 nm (range: 171.5-571.0 nm). The jagged steady-state profile for all grains generally supports coarsening of an original size distribution. This result is not signifcantly diffferent when corrected for the Fe-oxide nanocrystals.

CONCLUSIONS. One *principal component* in two CP IDPs, the **granular units**, have a similar basic unit size of 0.1 μm (real size). The PUs are larger than GUs, and probably also CUs. The constituent minerals in PUs are larger than those in the GUs. This size difference may reflect different diffusion rates in amorphous carbon-free and *ibid* carbonaceous chondritic materials to form similar Mg,Fe-silicates and Fe-sulfides. These (ultra)fine constituents support *in situ* nucleation and surface free energy driven Ostwald ripening in all three IDPs. The largest size range occurs W7010*A2 that shows evidence for aqueous alteration [11], *i.e.* the operation of a heat-carrying fluid. The physical meaning of the lognormal distributions, if any, is unclear. They may support *in situ* size sorting rather than by a large-scale process. A model of *principal components* in chondritic IDPs is viable. The main challenge will be to establish the true extent of mixing and the reality of miscibility gaps in the ternary diagram [Figure 1].

REFERENCES. 1. Rietmeijer FJM (1994) IAP Conf. Proc, in press; 2. Rietmeijer FJM (1992) Trends Mineral. 1, 23-41; 3. Thomas KL et al. (1993) GCA 57, 1551-1566; 4. Rietmeijer FJM (1989) Proc. 19th LPSC, 513-521; 5. Bradley JP (1988) GCA 52, 889-900; 6. Rietmeijer FJM (1993) EPSL 117, 609-617; 7. Rietmeijer FJM (1994) companion abstract, this volume; 8. Rietmeijer FJM (1993) LPS XXIV, 1201-1202; 9. Mathis JS & Whiffen G (1989) Astrophys. J. 341, 808-822; 10. Eberl DD & Srodon J (1988) Amer. Mineral. 73, 1335-1345; 11. Rietmeijer FJM (1991) EPSL 102, 148-157. This work was supported by NASA Grant NAGW-3626.

SULFIDE AND LAYER SILICATE GRAIN SIZE DISTRIBUTIONS CONSTRAIN THE UNIQUE PETROGENESIS OF A TYPE CM INTERPLANETARY DUST PARTICLE.

Frans J.M. Rietmeijer, Department of Earth and Planetary Sciences, University of New Mexico, Albuquerque, NM 87131, USA.

It is believed that the interplanetary dust particles (IDPs) collected in the lower stratosphere are a cross-section of the asteroid belt. If it is not an artifact of stratospheric dust collection, the dearth of chondritic IDPs with a distinct link to any meteorite type is then at least surprising. There is one IDP is linked to type CI meteorites [1], two IDPs are linked to type CM meteorites [2,3], and three IDPs show CAI affinity [4]. The unique carbon-rich chondritic porous [CP] and chondritic smooth [CS] IDPs, particularly CP IDPs, show accretion textures of granular and polyphase units (GUs & PUs) [5,6]. I report analytical electron microscope observations on serial ultrathin sections of IDP L2011O3 lacking the typical carbon-rich GUs and PUs of carbon-rich IDPs. This lack of GUs indicates a low bulk-carbon content of this particle wherein Si and CM normalised abundances are Mg = 0.38, Fe = 0.67, Ni = 0.33, S = 0.80 and Al = 0.30. A a narrow (< 110 nm) discontinuous polycrystalline Fe-oxide rim and the vesicular texture of its sulfides indicate atmospheric entry heating of the extraterrestrial particle L2011O3 [7]. The sizes of sulfide and layer silicate grain are measured on calibrated transmission electron microscope negatives and expressed as the root-mean-square size [cf. 8]. The size ranges here reported refer to the mean +/- one standard deviation.

OBSERVATIONS. The surface of this angular, elongated (about 26.4 x 10.4 μm) IDP is quite irregular. The dense, poorly-lineated, matrix is characterised by lens-shaped and equant-angular domains of Mg,Fe-material (< 500 nm in diameter) and rare, large single-crystal Fe-sulfide grains (488 x 268 nm; 885 x 577 nm) that are both surrounded by coarse-grained layer silicates. These layer silicates plus associated coarse-grained sulfides are part of a poorly-crystalline matrix that also includes amorphous, microporous patches with ultrafine layer silicates and *ibid* sulfides. These two layer silicate and sulfide occurrences are distinctly different although they show no clear boundary. Locally the ultrafine patches are dominant. The proportion of Mg,Fe-domains to matrix varies among ultrathin sections. All matrix analyses were obtained on optically sulfide-free locations. The IDP bulk, matrix and Mg,Fe-domain compositions are shown Figure 1. The average Al_2O_3 content in the matrix is ~5 wt%.

Sulfides. The compositions cluster at ~53 at% (pyrrhotite) with < 3 at% Ni with rare grains up to 8 at% Ni. The cluster is smeared towards FeS_2 which is common to sulfides in unmelted IDPs that were flash-heated on atmospheric entry [7]. Rare high-Ni (19-27 at%) pentlandite grains occur close to the Fe-oxide rim. The coarse-grained sulfides form eu- to subhedral grains but (ultra)fine-grained sulfide grains are typically (sub-)circular. The size-frequency distribution of the sulfide grains does not reflect an original grain size distribution. Its ragged, skewed pattern suggests continued ripening of the original grains towards greater grain sizes. The steady-state size profile supports second-order growth Ostwald ripening transitional between a *nucleation-controlled* distribution and a *ripening-controlled* distribution [cf. ref. 9]. Statistical analysis of sizes for 244 grains shows at least three Gaussian populations, *viz.* (1) mean = 7.7 nm, range = 2.9-25.8 nm, (2) mean = 40.7 nm, range = 31.5-49.5 nm, (3) mean = 127.5 nm, range = 118.8-136.8 nm, and possibly (4) mean = 221.1 nm, range = 199.8-242.4 nm. Ultrafine layer silicates often decorate the smallest sulfide grains.

Layer Silicates. The coarse-grained (up to 410 nm x 80 nm) anastomosing layer silicates generally flow around the Mg,Fe-domains and coarse pyrrhotite grains. They are smectite with a basal spacing of 1.37 nm (range: 0.88-1.87 nm) and may show turbostratic layer stacking. The ultrafine- and fine-grained layer silicates in the poorly-crystalline matrix form (*a*) spikey and curved grains up to ~30 nm long and 1-2 unit cell layers thick, (*b*) long (up to ~60 nm) sinuous grains and 2-5 unit cell layers thick, and (*c*) stubby grains of more than 7-10 unit cell layers. The size-frequency distribution for 92 grains shows a poor fit to any type of distribution but it generally supports ripening in a closed system. These layer silicates include both smectite, d = 1.23 nm (range: 1.0-1.7 nm) and illite-smectite, d = 2.5 nm (range: 1.9-3.1 nm) (on average 6.4

nm thick). The smectite particle thickness is a narrow, slightly skewed (0.62), distribution with mean 3.65 nm (range: 1.8-5.5 nm). When crystallite growth occurs by addition of unit cell layers, this distribution reflects the original particle thickness [cf. ref. 9]. The smectites in this IDP are, probably iron-rich, saponite.

Mg,Fe-Domains. The zoned domains have a granular core surrounded by an amorphous zone with short-range order and an amorphous zone that may contain scattered ultrafine layer silicates. The core is a polycrystalline aggregate of randomly-oriented single-crystals of ~2-20 nm in diameter. The Fe-content of these three units is almost constant but Mg continually increases, and Si decreases, from the core outwards. The reconstructed composition of the Si-free core is MgO = 33wt% and Fe_2O_3 = 67wt% which suggests the hematite-magnesioferrite solid solution. Lattice fringes with 0.585 nm spacing might be the magnesioferrite (110) plane.

Discussion. IDP L2011O3 is uniquely different from carbon-rich CS IDPs. The grain size pattern and morphology of layer silicates and sulfides in an amorphous to poorly-crystalline matrix of the Bells CM2 meteorite [Brearley, pers. comm.] are similar to this IDP. Thus, IDP L2011O3 is a third particle showing a type CM *petrogenesis*. Its most conspicuous feature is the persistent co-occurrence of similarly-sized sulfides and smectites although layer silicates are invariably younger than the associated sulfides. The grain sizes of both minerals define a size continuum albeit with distinct populations due to continued nucleation and ripening. The observations support aging of the IDP under diagenetic conditions (as opposed to aqueous and/or thermal alteration). The present data cannot constrain these conditions but they may not require 'elevated', or increased, temperatures. The surface free energy of the nanocrystals provides sufficient driving force for Ostwald ripening. Continued grain growth might establish solute concentrations conducive to trigger matrix nucleation. The staged smectite formation does not necessarily require high amounts of water. For example, ultrafine smectites might be a result of protonisation [10]. These diagenetic changes require residency in a parent body capable of sustaining an 'elevated' thermal regime at a geological timescale. The size continuum with distinct groups of layer silicate and sulfide grain sizes in IDP L2011O3 and the matrix texture are consistent with crystallisation of amorphous precursor material. This grain size analysis also allows the recognition of exotic constituents. For example, rare sulfide single-crystals are well outside the size continuum which shows that they did not grow *in situ*. Similarly, the granular Mg,Fe-material may be nebular grains that accreted into this IDP.

CONCLUSIONS. IDP L2011O3 is a third particle collected in the lower stratosphere with a type CM *petrogenesis*. It shows evidence for surface free energy driven diagenesis in amorphous and ultrafine-grained extraterrestrial materials prior to 'traditional' aqueous and/or thermal alteration. The finding of this unique IDP raises the question of a new type of parent body outside the asteroid belt. Conceivably extinct comet nuclei show this distinct petrogenesis.

REFERENCES. 1. Keller LP et al. (1992) GCA 56, 1409-1412; 2 Bradley JP & Brownlee DE (1991) Science 251, 549-552; 3. Rietmeijer FJM (1992) LPS XXII, 1153-1154; 4. Zolensky ME (1987) Science 237, 1466-1468; 5. Rietmeijer FJM (1992) Trends Mineral. 1, 23-41; 6. Rietmeijer FJM (1994) AIP Conf. Proc., in press; 7. Rietmeijer FJM (1993) LPS XXIV, 1201-1202; 8. Rietmeijer FJM (1993) EPSL 117, 609-617; 9. Eberl DD & Srodon J (1988) Am. Mineral. 73, 1335-1345; 10. Tazaki K (1986) Contrib. Mineral. Petrol. 92, 86-88. This work is supported by NASA Grant NAGW-3626.

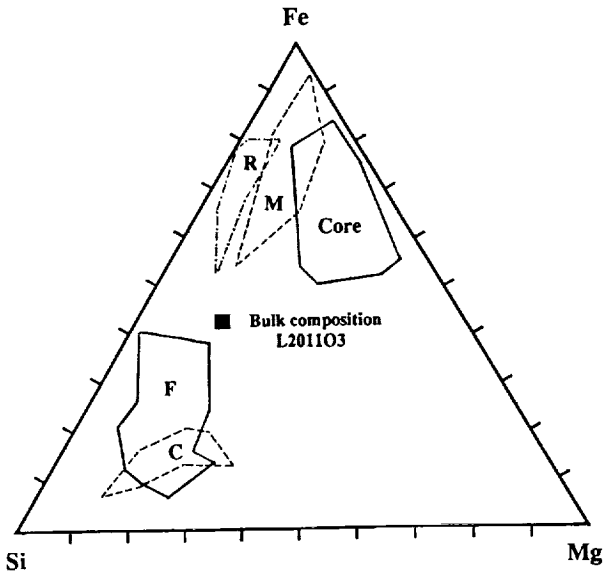

FIGURE 1. The ternary Si-Fe-Mg (wt% element) diagram showing the compositions of the amorphous to poorly-crystalline layer silicate matrix (C=coarse-grained; F=fine-grained layer silicates) and the zoned Mg,Fe-material (C=core; M=marginal zone; R=amorphous border.

LINEAMENT ANALYSIS OF FORTUNA TESSERA; A PRELIMINARY EVALUATION OF A COMPLEX RIDGED TERRAIN, VENUS.

Kevin M. Riley and Robert C. Anderson. Department of Geology and Planetary Science, University of Pittsburgh, Pittsburgh, PA 15260.

It is essential to identify the structural pattern of a region in order to fully understand its tectonic history . A method commonly used in terrestrial studies is to map lineaments and identify dominant trend directions. The purpose of this project is to identify major and minor lineament trend directions for Fortuna Tessera and its immediate surroundings. In this presentation, we will be showing results obtained from ongoing research.

Fortuna Tessera and other complex ridged terrains (CRT) are extremely deformed, elevated regions found on the surface of Venus. CRT comprise 10% of the surface, and are distributed widely across the planet (Solomon, et al., 1992). They generally contain sets of structural features (ridges, faults and grabens) of diverse orientations with various geometric relations.Truncation of these features by smooth plains material indicates that CRT may be some of the oldest surfaces in existence on the planet.

Fortuna Tessera is an irregularly shaped elongate region of complex ridged terrain located within the eastern portion of Ishtar Terra, 65° to 70.3° latitude., 14.7° to 82.1° longitude. Surrounding Fortuna are a variety of volcanic and tectonic features.Volcanic plains lie to the north, south and east of Fortuna. Adjacent to Fortuna in the west is Maxwell Montes,the highest mountain on Venus, which has been interpreted as a compressional feature. Just further west are other high, compressional mountain belts that surround Laksmi Planum. The elevation of Fortuna above the planetary datum (6054 km) decreases from west to east: about 6 km in the west near Maxwell Montes to about 3 km on the eastern edge (Vorder Bruegge and Head, 1989).

Features typically found in CRT, including Fortuna, have the following general properties: (1)The **ridges** can have a range of widths from about 1 km across to as much as 20 km across. The fine ridges are usually only a few ten of kilometers long, while the broad ridges can be up to 100 km long. Broad ridges are spaced about 10-20 km apart, and the fine ridges are usually spaced much closer (Solomon, et al., 1992). Ridges are typically the oldest structures in CRT. (2) **Zones of disruption** that cut across ridges are common in CRT. These zones are thought to be caused by small degrees of shear or strike-slip motion (Bindschadler et al., 1992, Solomon et al., 1992). (3) **Grabens** and other extensional features are an integral component of complex ridged terrain. These structures cut across the ridges and disruption zones, and are thus interpreted to have formed last. The graben are up to hundreds of kilometers long, vary in width from under a kilometer to several kilometers wide, and are 1-10 km apart (Bindschadler et al, 1992).

One problem regarding CRT is the mechanism of formation and their high persistence to survival. One way to attack this problem is to delineate structural features and to classify these features by trends and cross-cutting relationship. A

mathematical method used to identify dominate lineaments trends on Mars (Anderson, 1993) has been applied in this study.

Four Magellan C1 MIDR photoproducts, which include all of the available image data for Fortuna Tessera, were examined, and the lineaments were traced onto mylar overlays at photo scale. Each lineament was digitized, and the endpoints were measured and recorded in an X-Y reference coordinate. Several analytical methods have been applied to the dataset, including length-weighted frequency contour diagraming and dominate trend analysis. Rose diagrams were also constructed from the data in order to identify the dominate lineament trends.

References

Anderson, Robert .1993 Lineament Analysis and Tectonic Interpretation for the Tharsis Region, Mars. abstract submitted to the *Lunar and Planetary Science XXIV. Vol.1 p. 33.*

Bindschadler, Duane L., Annette DeCharon, Kathi K. Beratan, Suzanne E. Smrekar and James W. Head. 1992. Magellan Observations of Alpha Regio: Implications for Formation of Complex Ridged Terrains on Venus. *J. Geophys. Res..*, 97, 13,563–13,577.

Solomon, Sean C., Suzanne E. Smrekar, Duane L. Bindschadler, Robert E. Grimm, William M. Kaula, George E. McGill, Roger J. Phillips, R. Stephen Saunders, Gerald Schubert, Steven W. Squyres and Ellen R. Stofan. 1992. Venus Tectonics: An Overview of Magellan Observations. *J. Geophys. Res..*, 97, 13,199–13,255.

Vorder Bruegge, R. W. and James W. Head. 1989. Fortuna Tessera, Venus; Evidence of Horizontal Convergence and Crustal Thickening. *Geophys. Res. Lett.*, 16, 699-702.

HYDRATED E-CLASS AND M-CLASS ASTEROIDS;

Andrew S. Rivkin*, Daniel T. Britt*, Ellen S. Howell* and Larry A. Lebofsky*, Lunar and Planetary Laboratory, University of Arizona 85721

For airless bodies like asteroids and meteorites, the 3-μm region of the spectrum is diagnostic for hydrated minerals. Reflectance studies in this region can determine the hydration state of surface minerals, and by inference, thermal histories. We have made spectrophotometric observations of nine E-class and M-class asteroids in August 1993 using the IRTF on Mauna Kea, Hawaii. We confirm the presence of a 3-μm absorption band on 92 Undina (Figure 1) and on 44 Nysa (Figure 2) and have possibly detected this feature on the M-asteroid 201 Penelope. Because the 3-μm band is diagnostic of water of hydration, these discoveries and confirmations demonstrate for the first time that high-albedo objects such as E- and M-asteroids need not be of igneous origin. The discoveries also suggest that current interpretations of asteroid surfaces may not be completely accurate.

Based on their moderately high albedos (0.15–0.25) and red-sloped featureless spectra, M-asteroids have been thought to be composed of metals such as iron and nickel. E-asteroids, with similar spectral features but a higher albedo (0.4–0.5) have been thought to be composed of enstatite [2][3]. M-asteroids were thought to be the cores of disrupted, differentiated asteroids and E-asteroids were thought to have formed and differentiated under more reducing conditions in the solar nebula. However, observations done over the past several years in many different wavelength regions seem to contradict these interpretations [1][4][5][6]. Jones et al. (1990) found evidence of hydrated silicates on two M-class asteroids in the 3-micron region of the spectrum. Unfortunately, the lack of strong absorption features in the near-IR on M-asteroids has hampered our ability to identify any non-metallic contribution to their surface composition. In 1992 Howell and Nolan found evidence of hydrated silicates on the E-asteroid 44 Nysa. This surprising result shows us that the E-asteroids as a class are also not homogeneous in composition.

Because hydrated minerals are not stable at even moderately high temperatures (above 500 K) they are not expected to be present on igneous bodies [1]. These discoveries imply either that some E- and M-asteroids are *not* igneous and have little in common with other members of their current taxonomic classes, or that currently unknown post-igneous aqueous alteration processes have occurred. However, it is worth noting that there *cannot* have been any free metal on the surface on these asteroids, or it would have been oxidized in the alteration episode, giving these asteroids an ultraviolet absorption feature that is not present.

These results open a series of questions: 1) what percentage of high-albedo objects have this hydration feature, 2) what mineral or minerals are creating it, 3) what relationship might these bodies have to hydrated minerals in our meteorite collection, 4) what relationship (if any) is there between these high-albedo hydrated asteroids and heliocentric distance, 5) what do these asteroids imply about the conditions in the early solar system, and 6) what do these asteroids imply about metamorphic processes and mineral evolution in the solar system?

References:

[1] Jones et al. (1990) *Icarus* **88**, 172-192. [2] Gaffey et al. (1989) in *Asteroids II*, U. of Arizona Press, Tucson. [3] Tholen (1984) Ph.D. Thesis, University of Arizona. [4] Lupishko and Belskaya (1989) *Icarus* **78**, 395-401. [5] Ostro et al. (1985) *Science* **229**, 442-446. [6] Lebofsky and Britt (1992), Preprint.

---

* Visiting astronomer at the Infrared Telescope Facility which is operated by the University of Hawaii under contract to NASA.

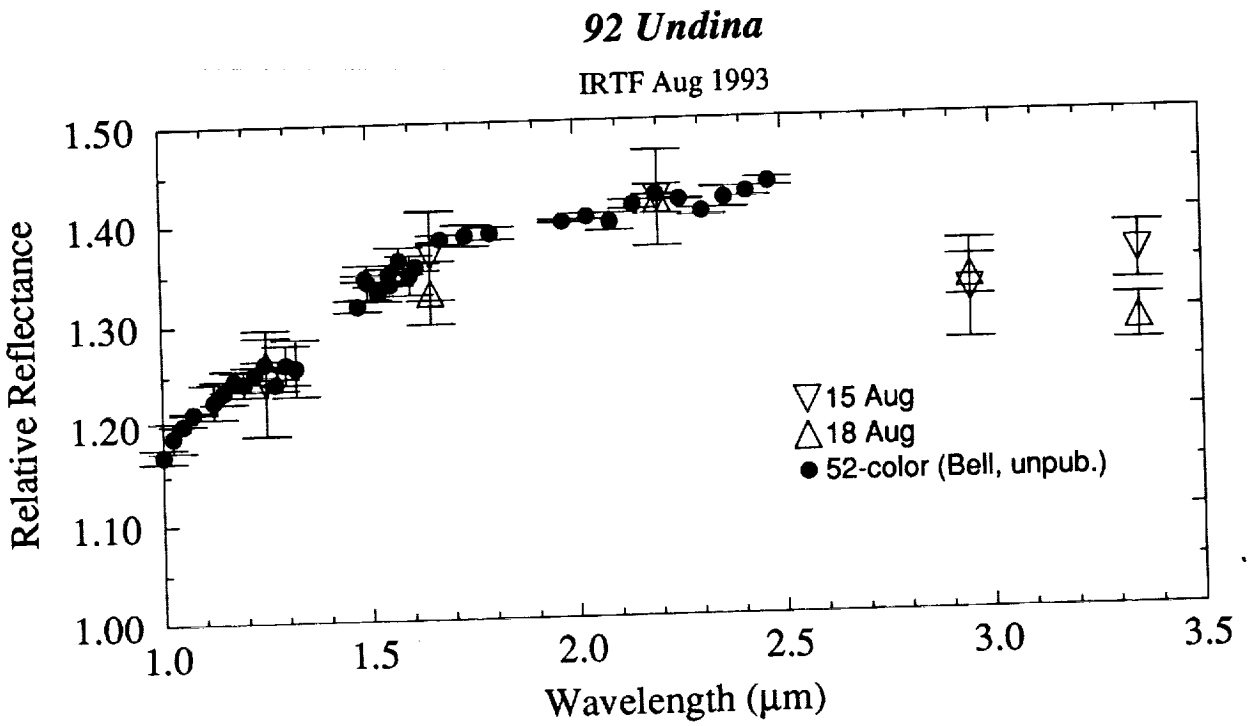

Figure 1: Spectrum of M-class asteroid 92 Undina from IRTF, with spectrum from Bell's 52-color survey. The IRTF data is scaled to be equal to the 52-color data at 2.2 μm.

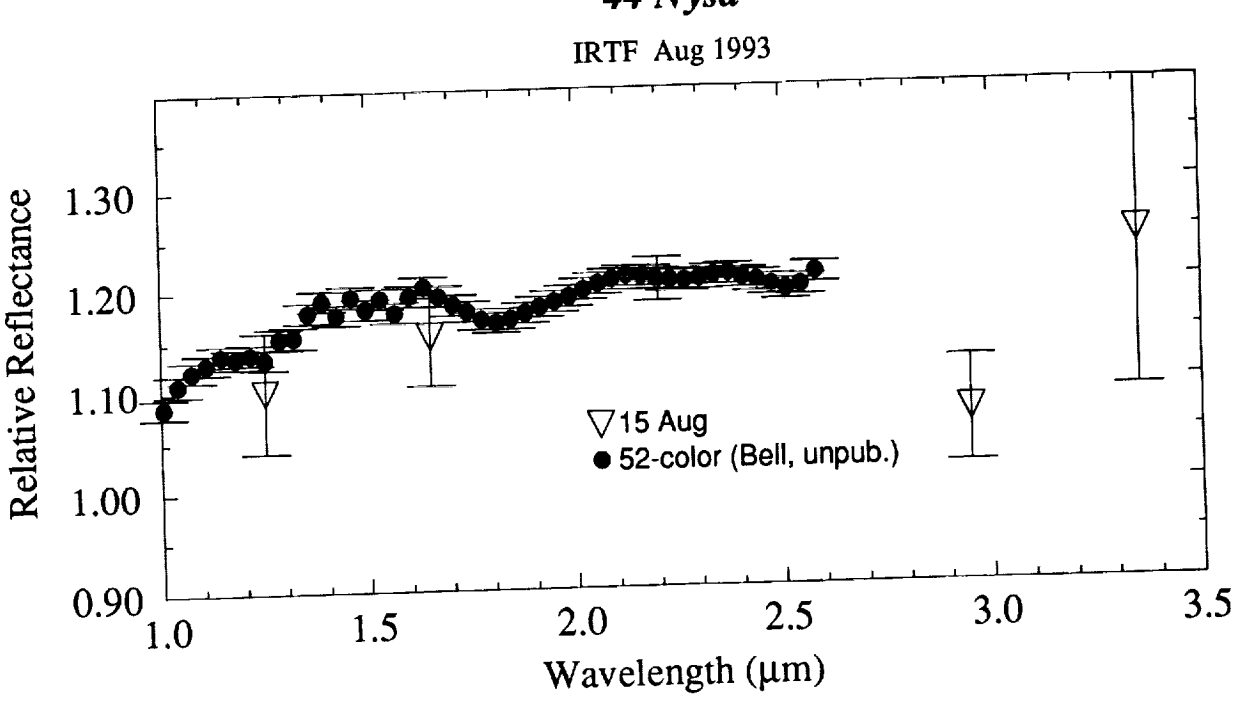

Figure 2: Spectrum of E-class asteroid 44 Nysa, scaled with Bell's data as above.

THE WEATHERING PROCESS ON VENUS TAKES 2-3 HUNDRED MILLION YEARS: EVIDENCE FROM RADIOTHERMAL EMISSIVITY SIGNATURES AT CORONAE.

C.A. Robinson (Harvard-Smithsonian Center for Astrophysics, Cambridge, MA 02138).

The surface material on most Venus mountain summits (> ~2.5 km above plains level) displays much lower radiothermal emissivity than the plains material [1,2,3]. This is thought to result from weathering of the primary basaltic rock, which at high altitudes (thus, relatively low temperatures) produces a distinctive pyrite-bearing mineralogical assemblage that causes the observed reduction in emissivity [1,3]. The timescale for weathering is not known. [3] suggested it may be on the order of tens to hundreds of millions of years, owing to the lack of water on Venus: water is an essential ingredient of weathering on Earth, and its near absence on Venus must greatly hinder the process.

The presence or absence of weathering effects may explain some deviations from the nominal altitude-emissivity pattern allowing older landforms to be distinguished from features created by relatively recent activity – recent tectonism or volcanism, or volcanic gas emission that has continued until recent time. A study of the radiothermal emissivity of coronae ($\geq$350 km in diameter), which uses anomalous weathering effects as a chronological tool [4], has shown two coronae have unweathered or little-weathered surface material at high altitudes, implying tectonic uplift so recent that weathering has been minimal. Two other coronae display low emissivity associated with volcanic domes, at altitudes lower than that at which the pyritic low-emissivity mineral assemblage normally appears: this is attributed to seepage of sulfurous volcanic gases in the vicinity of the domes, which would produce pyritic soil, until recent time (perhaps the present) [4,5]. Thus, four coronae appear to have been volcanically and/or tectonically active in the recent past.

[6] have suggested coronae formation is initiated by large impact events. If so, the frequency of large cratering events that appears to hold for the inner solar system [7] must also apply to coronae; this allows the timescale for weathering to be estimated. Four impacts large enough to give rise to the coronae which appear to have been recently active would have been produced in the past 2-3 x 10^8 Yr [7]. This would mean surface weathering on Venus (to a depth of a few m) takes place on a timescale of 2-3 x 10^8 Yr, and the "recent" volcanic and tectonic activity could have occurred anywhere within this period. [8] also

concluded that surface weathering takes 2-3 x 10^8 Yr, on the basis of the time apparently needed for weathering to reduce the Fresnel reflectivity of crater ejecta blankets they observed by ground-based radar.

References: **1.** Pettengill, G.H. *et al.* (1988) *J. Geophys. Res., 93,* 14,881. **2.** Garvin, J.B. *et al.* (1985) *J. Geophys. Res., 90,* 6859. **3.** Klose, K.B. *et al.* (1992) *J. Geophys. Res. 97,* 16353. **4.** Robinson, C.A., and J.A. Wood (1993) *JGR-Planets*, submitted. **5.** Robinson, C.A., and J.A. Wood (1993) *Icarus, 102,* 26. **6.** Stewart, C.A. *et al.* (1993) *EOS, Supplement, Oct. 26,* 80. **7.** Gault, D. E. (1970) *Radio Science, 5,* 273. **8.** Jurgens, R. F. *et al.* (1988) *Science, 240,* 1021.

SO_2 AND CH_4 LEVELS IN THE VENUSIAN ATMOSPHERE, MEASURED BY PIONEER VENUS: CAUSED BY PLINIAN-STYLE VOLCANIC ACTIVITY AT MAAT MONS?

C.A. Robinson (Harvard-Smithsonian Center for Astrophysics, Cambridge, MA 02138) and G. D. Thornhill (Brown University, Providence, RI 02912).

Magellan (and PVO) found high mountain terrains on Venus (~2.5 km above 6051 km planetary radius) exhibit anomalously low radiothermal emissivity [1,2,3]. This is thought to result from weathering of primary Venus rock, which at high altitudes produces a high-dielectric-constant, low-emissivity mineral assemblage [1,3]. Deviations from the nominal altitude-emissivity pattern have been used as a crude chronometric tool with which to date Venusian landforms [4,5]. This technique indicates Maat Mons (an unusually large, basaltic shield volcano, standing 9.17 km above 6051 km planetary radius, at 2.1^0N, 194.3^0E) has undergone a "recent" episode of large-scale volcanic activity [3,4]. The timescale for weathering defines "recent" to be anywhere in the past 2-3 My [5]. Recent volcanic activity is also implied morphologically with impact crater-free flanks, and young, medium-bright flow fields that emanate from the summit region and overlie all other landforms in their paths [4]. The presence of possible, stratigraphically-young ash flows on the northern flanks [3] and at the summit of Maat Mons [6] indicate the recent volcanic activity was explosive and, therefore, gas rich.

We investigated whether a plinian eruption at Maat Mons could explain the enhanced concentrations of SO_2 and CH_4 gas in the middle (~26 km above 6051 km planetary radius) and upper atmosphere (~50 km above 6051 km planetary radius) of Venus, as detected by the Pioneer Venus atmospheric probes [7,8, 9, 10]. Modelling of the eruption plume is based on the mathematics of [11] and adapted for the Venusian environment [12]. A plinian-style eruption at Maat Mons is considered appropriate since plinian eruptions are characterised by explosive activity at the vent. Our results show for a minimum vent radius of 156 m and minimum eruption temperature of 1200 K (Fig. 1), a plinian eruption at Maat Mons can explain the anomalous SO_2 and CH_4 concentrations recorded by PVO. This would mean Maat Mons is an active volcano.

References: 1. Pettengill, G.H. *et al.* (1988) *J. Geophys. Res., 93,* 14,881. 2. Garvin, J.B. *et al.* (1985) *J. Geophys. Res., 90,* 6859. 3. Klose, K.B. *et al.* (1992) *J. Geophys. Res. 97,* 16353. 4. Robinson, C.A., and J.A. Wood (1993) *Icarus, 102,* 26. 5. Robinson, C.A., and J.A. Wood (1993) *JGR-Planets*, submitted. 6. Robinson, C.A. *et al.* (1994)

VENUS: CH_4, SO_2, AND MAAT MONS, Robinson, C.A. and Thornhill, G.D.

in preparation. **7.** Donahue, T.M., and R.R. Hodges (1992) *LPI, 789*, 29. **8.** Donahue, T.M., and R.R. Hodges (1993) *Geophys. Res. Lett., 20, No. 7*, 591. **9.** Esposito, L.W. (1984) *Science, 233*, 1072. **10.** Esposito, L.W. *et al.* (1988) *J. Geophys. Res., 93*, 5267. **11.** Woods, A.W. (1988) *Bull. Volc., 50*, 169. **12.** Thornhill, G.D. (1993) *J. Geophys. Res., 98, No. E5*, 9107.

Fig. 1. Graph of plume heights as a function of vent diameter and eruption temperature (1200 K and 1400 K). H_2O is the magmatic volatile. 0 height datum represents the vent height - this is 9.17 km for Maat Mons.

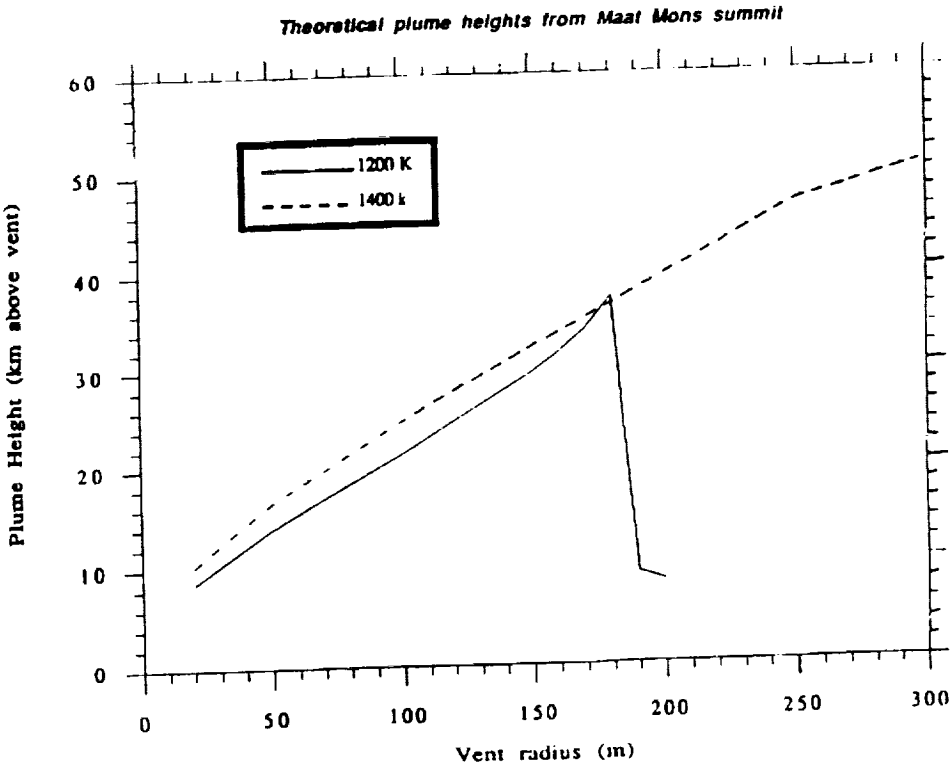

VOLUMES AND DEPTH OF BURIAL OF THE LESSER THARSIS VOLCANOES, M.S. Robinson, H. Garbeil, Planetary Geosciences, SOEST, University of Hawaii, 96822.

Utilizing the newly released USGS Mars global digital terrain model, DTM, we have calculated the volumes of the edifices and calderas of the lesser Tharsis volcanoes (LTV; Biblis Patera-BP, Ceraunius Tholus-CT, Jovis Tholus-JT, Tharsis Tholus-TT, Ulysses Patera-UlP, Uranius Patera-UrP, Uranius Tholus-UrT) which occur in the Tharsis volcanic province on Mars. These data were collected in order to compare the relative volumetric significance for each of these volcanoes, as well as to aid in comparison with other martian and terrestrial volcanoes. To augment the global DTM, we have also taken high resolution shadow measurements of the relief of each caldera where possible. From these new measurements we find that the caldera floors of five of these volcanoes (BP, JT, TT, UlP, UrP) actually lie below the level of the surrounding, embaying, lava plains [1, 2, *3]. An extreme case of burial is exhibited at Ulysses Patera, where the volume of the caldera is actually larger than that of the exposed edifice (Table). This is unusual in that the volume of a caldera represents a minor percentage of the total volume of the whole edifice for terrestrial basaltic shield volcanoes [4]. Estimates of the thickness of these LTV embaying lavas range from a few hundred meters [5] to 1000-1500 m [6,3]. In support of the upper estimate of burial we interpret that the caldera floor elevations (relative to the surrounding plains) of these five volcanoes indicates >1km of burial, on average, on the basis of the observation that there are no large terrestrial shield volcanoes with the caldera floor lying below the pre-existing terrain.

To further constrain the depth of burial for these martian volcanoes, we examine the relationship between height of volcanic edifice to caldera depth (H/d). This was considered due to the fact that five of the lesser Tharsis volcanoes have caldera floors that lie below the surrounding plains (Table). Additionally, these five calderas are also deep (compared with other martian and terrestrial examples) thus indicating that significant portions of the original caldera remain unfilled. Typically, the ratio of volcano height to caldera depth is greater than 20 for terrestrial shield volcanoes [4]. Volcanoes with a low height to depth ratio (H/d) would be less likely to have experienced large scale infilling, while volcanoes with a large H/d may have experienced large amounts of infilling. Simply put, volcanoes with a small H/d are probably most representative of types that have experienced relatively little infilling since their formation. In this context it is useful to examine the terrestrial volcanoes of the Galapagos Islands as they contain a significant H/d range (H/d = 4-22). In particular the caldera of Fernandina (H/d = 4) and Volcan Wolf (H/d = 6) exhibit low H/d not only within the Galapagos Island examples, but also for terrestrial basaltic shields in general [4]. It is also instructive to compare the H/d for the four major Tharsis shields and Apollinaris Patera with these terrestrial examples. For martian and Galapagos volcanoes the lower limit is about four (Apollinaris Patera and Fernandina). Since no large scale terrestrial basaltic shields have H/d of one or lower, this value (H/d = 1) is considered an extreme lower bound, in all likelihood the real value of H/d should be higher. The depths of the calderas of the predominately effusive lesser Tharsis volcanoes are great by any standard (average 2400 m), and thus it is reasonable to apply the low end H/d range to estimate their preburial height (H/d of 1-4). The depth of burial is determined by the product of the respective (H/d) and measured caldera depth (dm), minus the measured height of the edifice above the surrounding terrain (hm), b = [(H/d) x dm] - hm. BP is a particularly useful example to apply this method, since it has what appears to be a relatively unfilled caldera . The reconstructed depths of burial for BP are 1, 4 and 10 km for H/d of 1, 2 and 4, respectively. The greater estimate of 10 km is nearly equivalent to the height of the Tharsis rise, and thus is probably an overestimate [c.f. *9]. The mid-range estimate of burial, 4 km, is consistent with both constructional and mixed constructional/upwarping models [9] for the origin of the Tharsis rise. The lower reconstructed burial, 1 km, is probably too low on the basis of terrestrial H/d values and the sparsity of neighboring impact craters with diameters of 5 km and greater (they are buried). Thus, it is here proposed that the average depth of burial lies in the range of 1-10 km, with the estimate of 4 km being the most reasonable.

The reconstructed burial of UlP (3.5 km, from H/d = 2) is consistent with the depth of burial of BP (Table). UlP and BP are spatially close (<50 km), so it is reasonable to assume that their depth of burial should be similar if they were both emplaced prior to all the embaying lavas. Stratigraphic mapping by [7] indicates that BP and UlP predate all embaying lavas. Thus, it is

consistent to infer that the thickness of the embaying lavas around BP and UlP is on the order of 3-4 km. The mid-range estimate of burial (H/d = 2) for UrP (2.4 km burial) is significantly greater than the previous estimate of 500-600 m [6] and essentially equivalent to the 2.1 km estimate of [3]. This depth of burial (2.4 km) is consistent with those of BP and UlP in that UrP is further (400 vs. 900 km, respectively) from the putative source of the Tharsis flood lavas, the Tharsis Montes. It is reasonable to expect a radial thinning of the flood lavas from the source, resulting in less burial outward from the Tharsis Montes. Consistent with a radial thinning of the Tharsis flood lavas, is the depth of burial of JT (3.0 km; H/d = 2). This depth of burial is intermediate to those of BP, UlP (3.5-4.0 km) and UrP (2.4 km). JT has a correspondingly intermediate distance from the Tharsis Montes (700 km). The neighboring volcanoes to UrP, CT and UrT, both have shallow calderas that appear to be relatively infilled and are proposed to be dominantly of explosive origin, hence, it is not appropriate to apply the H/d method. However, due to their close spatial location to UrP it is assumed that their depth of burial is similar (2.4 km). Due to the highly irregular shape of TT, it is difficult to apply the H/d method due to uncertainties regarding a valid edifice height (relief above the surrounding terrain) and depth of caldera. However, using the eastern caldera wall height of 2.4 km, and applying the H/d method, the corresponding depths of burial for H/d of 1, 2 and 4 are 1.0, 3.5 and 8.5 km, respectively. The mid-range burial estimate (H/d = 2) of 3.5 km is consistent with the other lesser Tharsis volcanoes, on the basis of relative proximity to the Tharsis Montes (600 km). Clearly these estimates are rough and are subject to unconstrained errors, probably 1 to 2 km. However, these estimates indicate that the commonly inferred average thickness of 500-1500 m [6, 7, 8] for the lavas on the Tharsis rise are low. The observation that the calderas of BP, JT, TT, and UlP are all at least 1 km below the surrounding plains argues strongly that only the upper range (1500 m) of the previous estimate is plausible. In support of a greater total thickness of the Tharsis flood lavas is the observation that the flood basalts of the Deccan Traps, India, have an average thickness in excess of 2 km [10]. Similar or greater thicknesses, of similar type martian deposits are not unreasonable, and possibly even expected, due to gravity differences. Individual lava flows that compose a flow unit should have greater thicknesses on Mars relative to the Earth [11]. On the basis of this new model, the caldera elevations, and terrestrial analog, it is plausible to assume that the average thickness of lavas on the Tharsis rise is greater than 1500 m, and may be as much as 4 km locally. For the LTVs this means that the volume of the buried portion, for the minimum H/d of one, is greater than the volume of the exposed portion for BP, JT, UlP and UrP. The mid-range estimate of H/d of two indicates the buried volume for each of the LTVs (excluding TT) is, on average, greater than 15x the exposed volume (Table).

References:[1] Plescia and Saunders (1979), *PLPSC* 10, p. 2841.[2],Greeley and Spudis (1981), *RGSP* 19, p. 13. [3] Whitford-Stark, (1982), *JGR* 87, p. 9829. [4] Pike and Clow, (1981), *USGS OFR*-81-1038. [5] Plescia, (1993), abstract *LPSC* XXIV, p. 1155. [6] Plescia and Saunders, (1980), *PLPSC* 11, p. 2413. [7] Scott and Tanaka (1980), *JGR* 87, p. 1179. [8] DeHon, (1982), *JGR* 87, p. 1179. [9] Solomon and Head (1982), *JGR* 87, p. 9755. [10] Cas and Wright, (1988), *Volc. Succ. Modern Ancient,* p. 369. [11] Wilson and Head, (1983), *Nature* 302, p. 663.

	E D	E H	E Vol	B, V	C D	C d	C Vol
BP	184	2000	22	*4.0, 350*	52	3000	4.0
CT	115	6000	27	*--, 59*	24	1000	0.4
JT	54	1000	1	*3.0, 23*	26	2000	0.4
TT	114	6000	22	*3.5, --*	30	2400	2.2
UlP	97	1000	2	*3.5, 83*	55	2240	4.2
UrP	264	2000	33	*2.4, 292*	100	2200	7.5
UrT	61	3000	4	*--, 16*	21	220	<0.1

Table. Pertinent measurements of the lesser Tharsis volcanoes. E=edifice, D=Diameter (km), H=edifice height (m), Vol=volume (10^3 km^3), B=depth of burial estimate from H/d=2 (km), V=reconstructed volume from H/d=2 (10^3 km^3), C=caldera, d=depth (m).

MASS SPECTRA OF SPUTTERED SUGARS: TESTING THE ASSIGNMENT OF POLYOXYMETHYLENE AS A CONSTITUENT OF COMET HALLEY; M. S. Robinson and T. J. Wdowiak, Department of Physics, Astro and Solar System Physics Program, University of Alabama at Birmingham, Birmingham AL 35294

The mass spectrum of the coma of Comet Halley obtained by the *Giotto* spacecraft in March 1987 has a regularity which suggests that it is due to the breakdown products of a single polymer. Due to the ubiquitous presence of formaldehyde in interstellar space, the ease with which formaldehyde polymerizes into polyoxymethylene (POM), and the stability of this polymer it has been suggested that the mass spectrum observed by *Giotto* was the breakdown product of POM [1, 2]. Experiments conducted by M. Moore and T. Tanabe in 1990, in which a sample of POM was irradiated by a beam of 700 keV protons, resulted in a mass spectrum which in all principal features correlated to that obtained by *Giotto* [3]. The result obtained by Moore and Tanabe is shown in figure 1. This paper reports on the mass spectra obtained by irradiating some simple sugars, similar in atomic constituents to POM, by a beam of H_2^+ ions accelerated through a potential of 250 kV. The mass spectra obtained are also very similar to the mass spectrum of the coma of Comet Halley.

We have used a Van de Graaff accelerator to accelerate ions under a potential of up to 400 kV into a target chamber to which a quadrupole mass spectrometer is attached. The mass spectra of sputtered fragments from five different compounds were obtained: POM, Ribose, Xylose, Arabinose and Sucrose. In the experiments a small sample (approximately 0.1 g) of the material was placed on the target substrate, which consisted of a fine mesh screen on a copper disk, and pressed into the mesh of the screen using a laboratory press. The target was then mounted in the sample chamber and the chamber evacuated to a pressure of 10^{-6} torr. The sample was then irradiated with a beam of H_2^+ ions at a current of 0.5 to 1.0 μA for 1 to 2 minutes during which time the mass spectrum of the sputtered fragments was monitored. Prior to irradiating the target a background mass spectrum was taken and saved in the mass spectrometer. Our background spectrum is significantly different from that obtained for any sample. The results shown in figure 2 are the result of subtracting the background mass spectrum from the mass spectrum obtained while the target was being irradiated.

As can be seen, for all materials tested at UAB the mass spectra are quite similar, they all consist of a prominent set of peaks in the regions 44-48 amu, 59-63 amu, 73-76 amu and 87-89 amu. These features correspond very well with the features in the mass spectra obtained by Moore and Tanabe and this also correlates well with the *Giotto* results. The experimental data so far supports the conclusion that polyoxymethylene is a component of cometary comas. However, our results also indicate that this assignment must rest upon the greater likelihood of formation of POM in comets as compared to the likelihood of formation of simple sugars.

This research was supported by NASA grant NAGW-749

[1] Huebner, W. F. (1987) *Science, 237,* 628 ; [2] Mitchell, D. L., et. al. (1987) *Science, 237,* 626 ; [3] Moore, M. H., and Tanabe, T. (1990) *Ap. J., 365:*L39

MASS SPECTRA OF SPUTTERED SUGARS: **Robinson M. S. and Wdowiak T. J.**

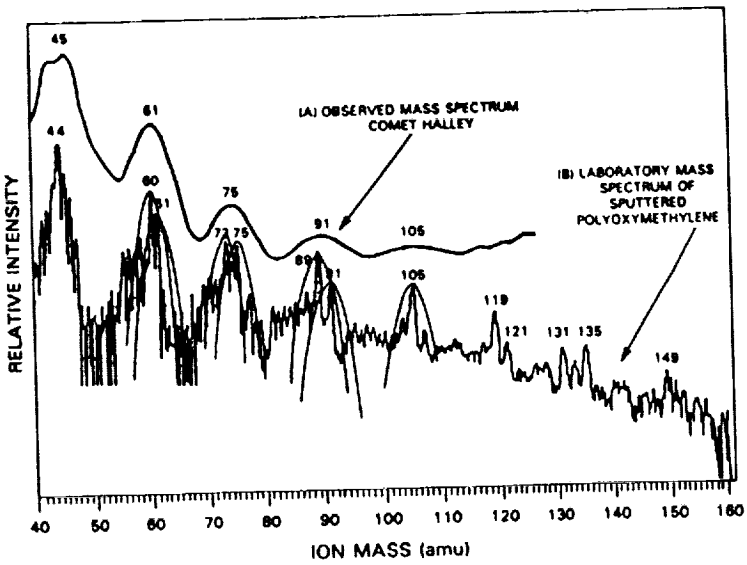

Fig. 1. The upper curve reproduces the mass spectrum measured by the PICCA instrument on board the *Giotto* spacecraft. This is compared with the laboratory mass spectrum of fragments produced during sputtering of polyoxymethylene at 300 K with 700 keV protons. From Moore and Tanabe [3].

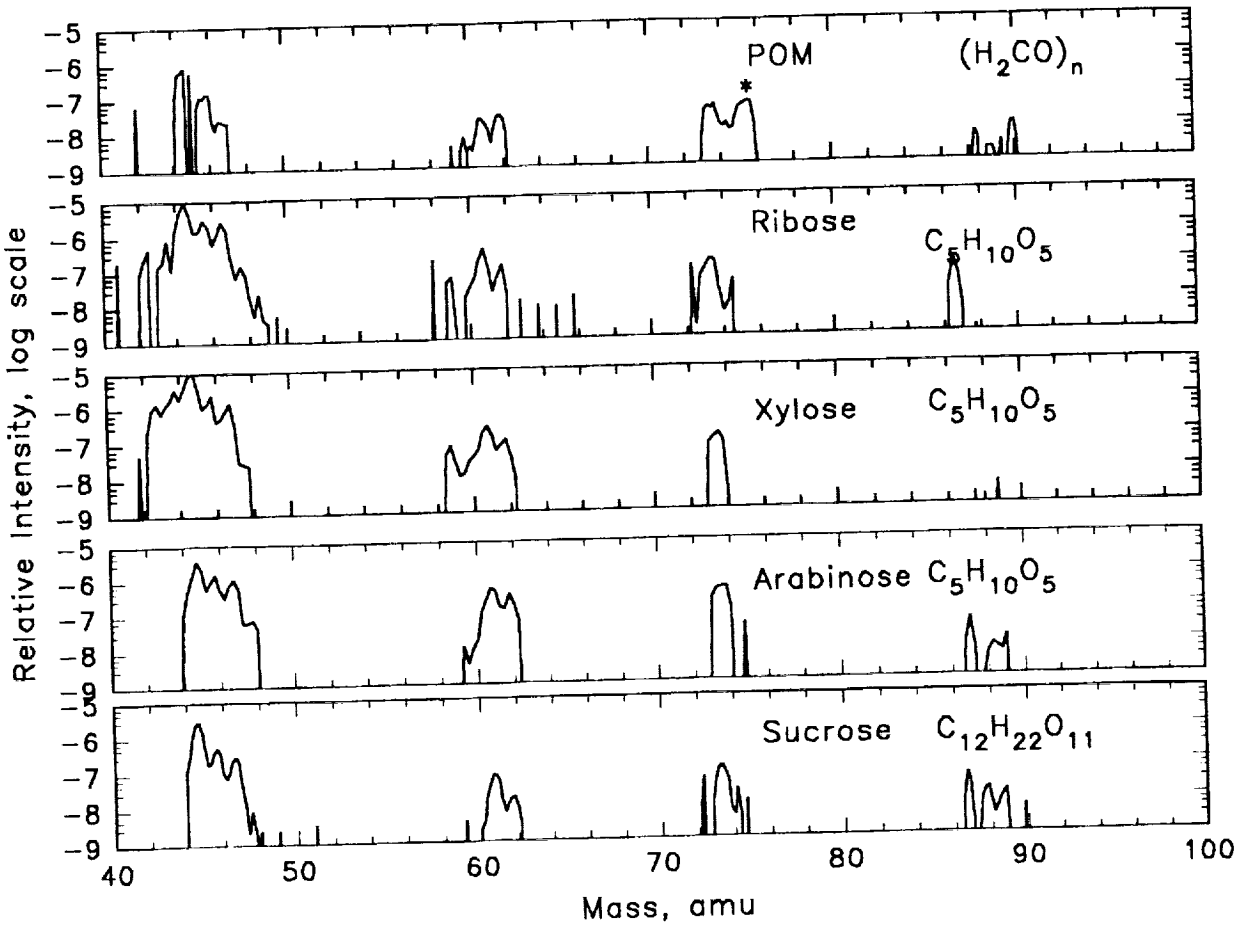

Figure 2. Mass spectra of fragments sputtered from targets made of POM or of various sugars. As indicated by the asterisk the 73-75 amu feature in the POM spectrum is much more noticeably bimodal, the only significant difference between the POM spectrum and that of the sugars. This is also observed in the data by Moore and Tanabe.

MARINER 10 MULTISPECTRAL IMAGES OF THE MOON AND MERCURY M.S. Robinson, B.R. Hawke P.G. Lucey, Planetary Geosciences, SOEST, University of Hawaii, Honolulu, HI, 96822, K. Edwards, U.S. Geological Survey, 2255 N. Gemini Dr., Flagstaff, AZ, 86001.

The Mariner 10 spacecraft acquired multispectral images of both the Moon and Mercury [1]. We have developed a calibration scheme to make these images useful for quantitative color studies [2]. This radiometric calibration includes dark current removal and a nonuniformity/nonlinearity correction [2]. Our initial calibration work included Mariner 10 image data of the eastern limb and farside of the Moon. These newly calibrated lunar images provide color data that are consistent with earlier measurements where the data overlap. On the basis of this consistency, compositional interpretations from Mariner 10 data are extended to areas previously not examined with spectral instruments. From these data there was no indication of the existence of basaltic soils with TiO2 in excess of 5% in the region of the Moon covered by the Mariner 10 images. Comparison of these new data, Earth-based spectral measurements, lunar meteorite compositions, and lunar mare emplacement models lead to the predication that no high titanium mare basalts were extruded in regions of the Moon with thickened crust (most of the farside). Additionally, these newly calibrated color data allowed a spectral confirmation of the presence of widespread cryptomare deposits northeast of Mare Marginis.

However, this lunar color effort is just a beginning. We are currently processing the rest of the Mariner 10 lunar image data. The remaining data cover portions of the eastern limb, at a resolution of ~1 km, in four wavelengths (orange, blue, ultraviolet and ultraviolet polarized) and provide excellent views of regions of the Moon poorly seen from the Earth. These include the Frigoris, Humboldtianum, Marginis, and Smythii regions. Initial analysis of these data indicates that the sensitivity of the Mariner 10 vidicons changed between the time of the acquisition of the low resolution color data and these high resolution images. This is most likely due to a change in the temperature of the instrument during closest encounter with Moon. Examination of overlapping images shows that this change is most likely confined to the edges of the frame; thus it may be possible to mask these "bad" areas. A preliminary mosaic constructed of masked images resulted in a nearly seamless image of the northeast nearside (NEN) region.

In addition to the radiometric calibration we have also developed a scheme to improve the pointing geometry for both the lunar and mercurian frames. This process involves limb fitting and minimizing camera angle discrepancies between each frame within a mosaic. In order to better control the color frames we are currently constructing

a clear filter mosaic at a resolution of about 1 km for all of Mercury imaged during the first encounter.

Not only will these high resolution color image data of the moon provide new compositional information, they will also give further insight into the dynamic nature of the Mariner 10 vidicon calibration. This is important because we are also processing the Mariner 10 images of Mercury. Initial color work [3, 4] of Mercury, utilizing Mariner 10 orange and ultraviolet images, relied on a calibration that was based solely on pre-launch characterization of the vidicon response [5]. Our initial examination of the low resolution approach color images of Mercury reveals that the Mariner 10 vidicon dark current response changed from the time of the lunar encounter. Learning from the lunar experience, we are calibrating the mercurian images, taking into account changes in the dark current. Similar to the Mariner 10 lunar images, we have found that for the high resolution ultraviolet mosaic of Mercury, we can produce a nearly seamless mosaic after applying our new calibration and masking the edges of the frames (camera B frames). We have developed calibrations for the orange, blue and ultraviolet-polarized images for analysis of the mercurian surface. It will be quite useful to have the Mariner 10 lunar images to use as a comparison with the Mariner 10 mercurian frames. Since much is known of the Moon, having a like dataset for the two bodies will allow for the direct color comparison of morphologically similar features. For example, the inter-crater plains on Mercury are morphologically similar to plains found on the Moon. Currently, the mercurian plains are mostly thought to have a volcanic origin, while many of the lunar inter-crater plains are proposed to be impact related [6, 7]. Using the two Mariner 10 datasets we will investigate this apparent contradiction as well as other important issues of mercurian geology.

References: [1] Danielson et al., (1975) *JGR* 80, p. 2357. [2] Robinson et al., (1992) *JGR* 97, p. 18265. [3] Hapke et al., (1980) *PLPSC* 11, p. 817. [4] Rava and Hapke, (1987), *Icarus* 71, p. 397. [5] Soha et al., (1975) *JGR* 80, p. 2394. [6] Trask and Guest, (1975) *JGR* 80, p. 2461. [7] Strom et al., (1975) *JGR* 80, p. 2478.

THE LESSER THARSIS VOLCANOES: CLUES TO MARTIAN EDIFICE BUILDING ERUPTIONS. M.S. Robinson, P.J. Mouginis-Mark, S.K. Rowland, Planetary Geosciences, Univ. Of Hawaii, Honolulu, HI, 96822.

Seven smaller volcanoes (Biblis Patera-BP, Ceraunius Tholus-CT, Jovis Tholus-JT, Tharsis Tholus-TT, Ulysses Patera-UP, Uranius Patera-UrP, Uranius Tholus-UrT) occur amongst the giant martian volcanoes in the Tharsis province. These lesser Tharsis volcanoes (LTV) exhibit a diversity of landforms that give clues to the mode of emplacement of the materials that compose their flanks. The identification (and lack thereof) of incised valleys or lava flow lobes are the key lines of evidence used to identify the emplacement mechanisms on martian volcanoes [1, 2].

The LTVs exhibit morphologies consistent with both explosive and effusive eruptions. Ceraunius Tholus is characterized by an oval shape, relatively small caldera, lack of lava flows, and incised valleys on the flanks. The two distinct types of valleys on Ceraunius Tholus [3] are those that appear relatively steep sided and deep, Type I, and those that appear relatively flat floored and shallow, Type II. The Type I valleys are generally accepted to be the result of lava processes [c.f. 4]. The Type I valleys truncate Type II valleys, thus establishing that at least some of the Type II valleys are older. The Type I valleys all occur on the western half of the volcano, consistent with an origin due to overflow of late stage effusive activity from within the caldera. The Type II valleys are generally less than a kilometer in width and are relatively flat floored (compared to the Type I valleys). Reimers and Komar [1] interpreted the hummocky flanks and fine valleys (Type II) to be the result of explosive eruptive processes (density currents). This interpretation was based on the observation that in all cases these valleys lack levees, and exhibit discontinuous sections cutting through pre-existing topography. Gulick and Baker [3] thought that the coalescence (tributary network) exhibited by some of the Type II valleys was indicative of pluvial runoff, possibly later modified by sapping. However, the essential point of both of these hypotheses is that the flanks are mostly composed of relatively friable explosive deposits (ash and/or cinder). Similar to the caldera of Olympus Mons [5], the caldera floor of UrP exhibits sharply slanting subsidence blocks, a gently sloping floor, and wrinkle ridges; all consistent with a basaltic, effusive shield volcano. The flanks of UrP are characterized by raised linear deposits with lobate terminations. A high resolution frame covering the flanks just east of the caldera confirms the lobate materials in this area to be lava flows (626A41). Flank slopes are on average 3° [6, 7], however the flanks just below the caldera on the western side are about 9° which is comparable to slopes on CT [U.S. Geological Survey map, I-2111]. This slope dichotomy at UP could possibly indicate early, large scale explosive eruptions that resulted in relatively steep flanks which were later buried.

From these examples, it is inferred that certain martian volcanoes initiated as dominantly explosive, then evolved to late stage effusive activity. Admittedly this idea is speculative, but it is consistent with observations at other martian volcanoes. The basal scarp of Olympus Mons has been proposed to be the result of erosion along a basement of friable ash under the upper, more competent, effusive edifice [8, 9]. Apollinaris Patera exhibits a morphology that is consistent with early stage explosive eruptions, and late stage effusive activity that covers a significant portion of its flanks [10]. Alba Patera [11], Elysium Mons [12], Tyrrhena Patera and Hadriaca Patera [13, 14] all show evidence for early explosive and late stage effusive activity. Thus, it seems to be common among martian volcanoes to initiate explosively, and later evolve to a predominately effusive style. If true, this hypothesis raises the question, what was the nature of the explosive eruptions; magmatic or hydromagmatic? With the currently available data it is impossible to directly determine which process was most responsible for the martian eruptions. Large scale, juvenile volatile driven martian eruptions are theoretically possible. Due to the weaker martian gravity field and lower martian atmospheric pressure, explosive eruptions would be favored on Mars relative to the Earth given similar magmatic conditions [15]. Analysis of rocks ejected from Mars and delivered to the Earth (e.g. SNC meteorites) reveals that martian magmas do contain juvenile water in amounts consistent with this hypothesis [c.f. 16]. It is reasonable to postulate that early degassing of upwelling magma could be responsible for initial explosive activity, thus accounting for the observed transition from explosive to effusive activity. Such explosive activity would most likely be similar to terrestrial plinian eruptions [15]. Ceraunius Tholus and Uranius Tholus may also have been formed by large scale phreatomagmatic eruptions. Such an eruption scenario was considered for Hadriaca Patera [14]. However, it is open to question whether martian eruptions could be continuously supplied with

groundwater for a period long enough to build large volcanoes such as Ceraunius Tholus and Hadriaca Patera [14]. Specifically, it is not clear if enough groundwater can be transported to the vent for sustained periods of time, and it is also likely that the upcoming magma would eventually be sealed off from the water table as the edifice grew. A pertinent terrestrial example arguing against such large scale phreatomagmatic eruptions is the Hawaiian volcanoes. Hawaiian volcanoes exhibit <1%, by volume, hydromagmatic deposits [17] despite their unlimited source of water (the Pacific Ocean). On the basis of this example, it is not plausible that groundwater pathways can remain open to upcoming magma for extended periods of time. Thus, it is most likely that the putative explosive activity was dominantly the result of juvenile volatiles. Whatever the case, magmatic or hydromagmatic explosive activity, it appears that edifice building explosive deposits are common and volumetrically significant on Mars. Gregg and Williams [18] are currently investigating terrestrial analog deposits for comparison with martian volcanoes, and they have found significant basaltic Plinian airfall deposits as well as basaltic ignimbrite deposits (Maysaya, Nicaragua and Ambrym, Vanuatu). Thus, by terrestrial analogy [18] and numerical modeling [15], it is reasonable to assume that large scale mafic explosive eruptions did occur on Mars. The processes that formed the LTVs may be similar to those of the larger Tharsis Montes and Olympus Mons. If these larger volcanoes also underwent extended periods of earlier explosive activity, then we can infer that, in general, martian edifice forming magmas have relatively high volatile contents, and the eruptive episodes that formed these volcanoes must have contributed significantly to the martian atmosphere [19, 20].

References [1] Reimers and Komar, (1979), *Icarus* 39, p. 88. [2] Mouginis-Mark et al., (1982), *JGR* 87, p. 9890. [3] Gulick and Baker, (1990), *JGR* 95, p. 14325. [4] Carr, (1974), *Icarus* 22. [5] Mouginis-Mark and Robinson, (1992), *Bull. Volc.* 54, p. 347. [6] Pike et al., (1980), *NASA TM-81776*, p. 192. [7] Blasius and Cutts, (1981), *Icarus*, 45, p. 87. [8] King and Riehle, (1974), *Icarus* 23, p. 300. [9] Head et al., (1976), Nature 263, p. 667. [10] Robinson et al., (1993), *Icarus* 104, p. 301. [11] Mouginis-Mark et al., (1988), *Bull Volc.* 50, p. 361. [12] Malin, (1977), *GSA Bull.*, 88, p.908. [13] Greeley and Crown, (1990), *JGR 95*, p. 7133. [14] Crown and Greeley, (1993), *JGR 98*, p. 3431. [15] Wilson and Head, (1983), *Nature* 302, p. 663. [16] Banin et al., (1992), *Mars*, Univ Ariz. Press, p. 594. [17] MacDonald, (1972), *Volcanoes*, Prentice Hall, p. 355 [18] Gregg and Williams (1993), abstract *LPSC XXIV*, p. 491. [19] Wilson and Mouginis-Mark, (1987), *Nature* 273, p. 730. [20] Postawko et al., (1988), abstract *LPSC XIX*, p. 943.

Figure. Digital mosaic of the martian volcano Ceraunius Tholus (23°N 97°) from Viking frames 516A21-24. The morphology of the flanks is dominated by two types of valleys incising a hummocky, finely textured surface. The Type I vallleys (arrows) are inferred to be the result of late stage effusive activity, while the Type II valleys (not labeled - fine striations running perpendicular to flank slope) are interpreted to be the result of erosion into an ash substrate by either water or volcanic density currents. The morphology of this volcano suggests that the edifice was dominantly formed by explosive activity followed by late stage effusive activity, possibly associated with caldera formation. Total width of image is 150 km, north to the top.

GEOLOGY AND DISTRIBUTION OF ROCK TYPES AT THE APOLLO 17 LANDING SITE FROM A 2–4 MM PERSPECTIVE. KAYLYNN M. ROCKOW, BRADLEY L. JOLLIFF, RANDY L. KOROTEV, AND LARRY A. HASKIN, DEPARTMENT OF EARTH AND PLANETARY SCIENCES & MCDONNELL CENTER FOR THE SPACE SCIENCES, WASHINGTON UNIVERSITY, ST. LOUIS, MO 63130.

We have analyzed over 500 particles from the 2–4 mm splits of three Apollo 17 soils, 76503, 72503 and 72443, in order to determine the diversity and proportions of rock types recorded within the soils, to compare the relative diversity of North and South Massif soils, and to compare lithologic diversity within the soils to that of large-rock samples. In this abstract, we compare the known distribution of rock types at the Apollo 17 site to what we have found in the soil particles. The floor of the Taurus Littrow Valley, located on the southeastern rim of the Serenitatis Basin, is underlain by high-Ti mare basalt and covered by a thick regolith which is intermixed with pyroclastic orange-glass deposits. The valley is bordered by tall massifs consisting of Serenitatis impact-melt-breccia and pre-Serenitatis ANT-suite materials; many samples of impact-melt breccia were obtained from boulders near the base of the massifs. Most melt-breccias fall into two compositionally similar groups: the more abundant poikilitic-matrix breccias, presumably formed by the Serenitatis impact, and the aphanitic-matrix breccias, of uncertain origin [1,2]. The ANT-suite rocks are generally less coherent than the impact-melt breccias and are represented by small rocks and lithic fragments in the soils. They are dominated by granulitic breccias and norite, dunite, troctolite, and anorthositic gabbro of igneous origin; ferroan anorthosite is extremely rare [3]. A "light-mantle" surge deposit lies at the base of South Massif [4]. The 2-4 mm fraction of a typical sample of this soil, in this case, 72503, is predominantly melt breccia: 65% noritic breccia matrix, 17% ITE-poor highlands rock types, 12% agglutinates and regolith breccias, and 5% others. In contrast, North Massif soil, represented by 76503, has a much greater portion of ITE-poor highlands rocks and mare basalt fragments: 29% ITE-poor highlands, 24% melt-breccia matrix, 13% mare basalt, 30% agglutinates and regolith breccias, and 4% orange-glass breccia and others. The greater percentage of melt breccia in the South Massif light-mantle soil is due to stratigraphy and poor mixing; the light mantle, from the noritic top portion of the massif, did not mix well with the pre-existing regolith of the lower massif slopes, which is presumably similar to that of North Massif. Additional differences between the massif soils include (1) compositions of poikilitic melt breccias from the two massifs differ slightly [2]; (2) North Massif regolith contains magnesian troctolitic anorthosite and possibly other magnesium-rich, ITE-poor components that are not represented in South Massif soils.

Mare basalts. At least three compositionally distinct groups of high-Ti basalts are distinguished on the basis of geochemical parameters such as Ba/Rb or Sr/Rb (groups A-C, [5]), and further subdivisions have been based on REE ratios (B1 & B2, [6]). A chemically distinct type D basalt has also recently been characterized [7]. Samples of groups A and B are abundant and come from many location on the valley floor; however, the few group C samples are all from Shorty Crater (Sta. 4). The type D basalt sample is from the Van Serg drive tube. Of the 2-4 mm particles from sample 76503, 13% by mass are basalt. A third of the particles belong to Gp. A and another third, to Gp B2. One coarse-grained basalt particle is compositionally similar to Gp. C and two fine-grained particles have tentatively been assigned to Gp D. Remaining basalt particles are too coarse-grained to be representative and cannot be assigned to one of the known groups without further petrographic study.

Very-low-Ti basalt (VLT) has been found only as small fragments in the deep drill core [8] and as clasts in impact melt breccias 73255 [9] and 72215 and 72235 [10], although spectral reflectance data indicate that a VLT type basalt flow may cover the central Serenitatis basin [8]. In addition to TiO_2 concentrations less than 2%, VLT basalts have low REE concentrations and distinctive REE patterns. Among the particles in 76503, there is VLT basaltic breccia (hypabyssal?) rich in augite and with ~0.8% K_2O. Its relationship to other VLT basalts is uncertain and merits further investigation.

Orange Glass. Spheres and broken fragments of orange and black glass were found in and around Shorty Crater and in some places constitute entire soil horizons (e.g., 74220) within the gray soil that otherwise characterizes the valley floor. The compositions and morphologies of these glasses are consistent with an origin by fire-fountaining of primary, mantle-derived magma [11, 12]. All of the regolith breccias found in sample 76503 contain orange-glass as well as mare-basalt components and four of the particles consist almost entirely of orange and black-glass breccia. Two of the particles from sample 72503 are rich in orange-glass. Presumably, these samples have been delivered to the massif soil by small impacts on the valley floor.

Impact melt breccias. The melt breccias from Apollo 17 have been classified mainly into two groups, aphanitic and poikilitic, based on a combination of petrographic and compositional characteristics [1]. The majority of analyzed melt breccias belong to the compositionally tight poikilitic group and it is generally accepted that this group formed during the Serenitatis basin-forming impact [1,4,15,23]. The aphanitic melt-breccia group is compositionally more variable and is distinguished from the poikilitic group by lower Ti, Na, Eu, Ni/Co and

more variable Sc [1, 2]). The aphanitic melt breccias also tend to be more aluminous [13]. It has also been noted that the clast content of the two groups of melt breccias are different [1]; clasts of the poikilitic melt breccias are dominantly of the ANT suite, commonly granulites and plutonic norites and troctolites [14, 15]. In addition to ANT suite lithologies, aphanitic melt breccias contain clasts of felsite, basalt, feldspathic breccia, and more abundant shocked mineral clasts [10,16,17,18]. The Apollo 17 impact melt breccias are very coherent and form the boulders that have rolled or slid down the massif slopes. The station 6 boulders came from the lower third of North Massif whereas those at the base of South Massif are from near the top [4]. All of the large aphanitic melt breccia samples are from the South Massif, but poikilitic melt breccias were found at the base of both massifs.

Roughly one fourth of the particles from 76503 are fragments of melt breccias, whereas the majority of those from 72443 and 72503 are fragments of melt breccia. Most of these are of the poikilitic type based on compositional characteristics and limited petrography. This group generally forms a compositional trend between a mafic ITE-rich melt and incompatible-trace-element (ITE) poor highlands rock types. The low ITE component does not appear to be dominated by any one particular type of clast. There appear to be subtle differences between poikilitic melt breccias from North Massif and those from South Massif [2]. Four particles from 76503 appear to belong to the aphanitic group and are the first of this group found in a North Massif sample. Approximately 13% of the station 2 melt-breccia particles appear to be of the aphanitic type. In addition to the aphanitic and poikilitic breccias, we have found a third compositional group of melt breccias among the soil particles. They are characterized by higher REE concentrations, and a lower Cr/Sc ratio than either the poikilitic or aphanitic breccias, but a Eu/Sm ratio similar to the aphanitic breccias. Some of these breccias were visually observed to bear notable feldspathic clasts.

ITE-poor highlands rock types. Highlands granulitic breccias and monomict igneous rock types occur in the sample collection as small rocks, clasts in melt breccias, and as fragments in the soils. Less than ten of these among the returned rocks have masses exceeding 50g. The majority of the igneous rocks belong to the magnesian suite; only a few small samples have ferroan or alkaline mineral compositions [e.g. 19], although some of the well-studied lunar granites were found as clasts in Station 2 [20] and Station 3 [18] boulders. Of the igneous rock types, troctolites and norites are most abundant and about equally represented. Granulitic breccias with compositions ranging from noritic/gabbroic anorthosite to anorthositic gabbro are also abundant.

Among the 2-4 mm fragments, granulitic breccias are found in samples from both massifs, although they are more abundant in North Massif sample 76503. Magnesian and ferroan granulitic breccias are present at Station 6 whereas Station 2 appears only to have magnesian granulitic breccias. Lithic fragments of igneous magnesian-suite samples are scarce in the Station 2 samples, but there are several that have ferroan compositional characteristics. Lithic fragments of magnesian-suite igneous rocks are found in the station 6 sample, but they are dominated by crystalline fragments of plagioclase, plagioclase plus olivine, and brecciated equivalents, which, taken as a group, indicate a troctolitic anorthosite precursor [21]. Another compositionally distinct group of samples found in soil particles from both stations 2 and 6 are regolith breccias that lack mare basalt and noritic impact melt components. These we consider to be samples of the pre-Serenitatis surface [22].

Sample 76503, from a submature soil, reflects the lithologic diversity of the Taurus Littrow Valley and the surrounding highlands massifs better than rock particles from the mature station 2 soils. Thus, more important than a soil's maturity in this regard is the length of time it is exposed to the effects of small-scale lateral mixing from impacts coupled with its proximity to lithologically diverse geologic units. The lithic fragments in these soils, particularly 76503, do not simply reflect comminuted products of the nearest boulders or large rocks.

Acknowledgments. Funding for this work was through NASA grant NAGW-3343.

References [1] Spudis P.D. and Ryder G. (1981) In *Multi-ring Basins, PLPSC 12A*, 133-148. [2] Rockow et al., this Vol. [3] James O.B. (1992) in *Workshop on Geology of the Apollo 17 Landing Site*. LPI Tech. Rpt. 92-09, 17-20. [4] Wolfe E. et al. (1981) *USGS Prof. Paper 1080*, 280 pp. [5] Rhodes J.M. et al. (1976) *PLSC 7th*, 1467-1489. [6] Neal C.R. et al. (1990) *GCA*, *54*, 1817-1833. [7] Ryder G. (1990) *Meteoritics, 25*, 249-258. [8] Vaniman D.T. and Papike J.J. (1977) *PLSC 8th*, 1443-1471. [9] James O.B. and McGee J.J. (1980) *Proc.LPSC 11th*, 67-86. [10] Ryder G. et al. (1975) *The Moon 14*, 327-357. [11] Heiken G.H. and McKay D.S. (1974) *GCA 38*, 1703-1718. [12] Delano J.W. (1992) in *Workshop on Geology of the Apollo 17 Landing Site*. LPI Tech. Rpt. 92-09, p. 5-7. [13] Ryder G. (1992) in *Workshop on Geology of the Apollo 17 Landing Site*. LPI Tech. Rpt. 92-09, 49-50. [14] Simonds C.H. (1975) *PLSC 6th*, 641-672. [15] Dymek R.F. et al (1976) *PLSC 7th*, 2335-2378. [16] Blanchard D.P. and Budahn J.R. (1979) *Proc.LPSC 10th*, 803-816. [17] James O.B. (1976) *Proc. LSC 7th*, 2145-2178. [18] James O.B. and Hammarstrom J.G. (1977) *Proc.LSC 8th*, 2459-2494. [19] Warren P.H. et al (1991) *PLPS 21*, 51-61. [20] Ryder G. et al. (1975) *Proc. LSC 6th*, 435-449. [21] Jolliff B.L. et al. (1992) in *Workshop on Geology of the Apollo 17 Landing Site*. LPI Tech. Rpt. 92-09, 24-27. [22] Jolliff B.L. and Bishop K.M. (1993) In *LPS XXIV*, 727-728. [23] Winzer S.R. et al. (1977) *EPSL 33*, 389-400.

COMPOSITIONAL DIFFERENCES BETWEEN IMPACT-MELT BRECCIAS OF THE NORTH AND SOUTH MASSIFS AT APOLLO 17; *KAYLYNN M. ROCKOW, RANDY L. KOROTEV, BRADLEY L. JOLLIFF, and LARRY A. HASKIN,* Department of Earth and Planetary Sciences, Washington University, St. Louis, MO 63130

Based on analysis of numerous 2–4 mm particles in the regolith [1,2], the average composition of impact-melt breccias from station 6 on the North Massif at Apollo 17 differs subtly from the average composition of impact-melt breccias from station 2 on the South Massif. The differences are not simply a result of the previously recognized differences in distribution of textural types between the massifs. About 23 of 172 (13%) melt-breccia particles studied from station-2 soils 72443 and 72503 are characterized by low ratios of Eu/Sm (average 0.8 times as great) compared to typical particles, whereas about 4 of 54 (8%) North Massif particles from 76503 have similarly low Eu/Sm ratios. Particles with low Eu/Sm also tend to have low Na/Sm (Fig. 1). The low-Eu samples appear to correspond to the aphanitic melts described in earlier studies [3,4] whereas the Eu-normal samples correspond to the poikilitic melts. The differences in Eu and Na must represent a significant difference in a plagioclase component of the two types of melt breccia (clasts or matrix components). The only significant compositional difference between the two types of melt breccia previously noted was in TiO_2 concentration [3,4]. However, even when only the most normal (presumably poikilitic) particles are considered (80% of North Massif and 70% of South Massif melt-breccia particles), the North Massif samples are distinct from the South Massif samples in having higher mean concentrations of Na and Eu (by a factor of 1.06–1.07) and lower mean concentrations of Sc and Cr (by 0.92–0.94) (Figs. 2,3). Another striking compositional difference is that among the Eu-normal particles, Ni concentrations are distinctly lower in the North Massif samples (mean and median: 200 and 95 μg/g) compared to the South Massif samples (mean and median: 297 and 270 μg/g) (Fig. 3). If the samples studied are representative of the melt breccias of the massifs, the results imply lateral variation in the composition of Serenitatis impact-melt breccia on the scale of the Apollo 17 site.

A number of samples, mostly from the South Massif are unusual compared to samples described in the literature in having high concentrations of ITEs (incompatible trace elements), e.g., >18 μg/g Sm (Fig. 2). However, most of these samples have low Eu/Sm ratios, similar to the aphanitic melt (Fig. 1), thus they may be ITE-rich variants of the aphanitic melt or samples with unusually ITE-rich clasts (we have not yet examined these particles petrographically).

The differences observed here probably do not result simply because the melt-breccia particles from a given massif derive primarily from a single boulder and the boulders differ in composition. Although for *aphanitic* melt breccias, compositional differences exist among samples from different boulders [3], no such compositional differences have been reported among samples of *poikilitic* melt from different boulders, and our results imply a subtle compositional difference between poikilitic melts of the two massifs. Note also that the North Massif particles studied here are from 76503, a sample collected 25 m from the station-6 boulder cluster, and that most (78%) of the Eu-normal particles from the South Massif studied here are from 72503, which was collected distant from the station-2 boulders. However, it is likely that the two massifs are stratified [5], in which case the particles may not be representative of the respective massifs because even if the two massifs are structurally identical, most of the melt-breccia particles studied here from the North Massif may derive from a different stratigraphic position than the melt-breccia particles of the South Massif. Thus, the differences may reflect vertical instead of lateral variation in a thick deposit of melt. In either case, the compositional variability noted here in what are presumably samples of poikilitic melt breccia diminish somewhat the arguments that compositional difference between the aphanitic and poikilitic breccias require that they were formed in separate impacts [3]. It is likely that the differences in lithophile-element concentrations relate to differences in clast abundance or distribution, but it is unlikely that this is the cause of the difference in Ni concentrations.

APOLLO 17 IMPACT MELT BRECCIAS: *Rockow K. M., Korotev R. L., Jolliff B. L. & Haskin L. A.*

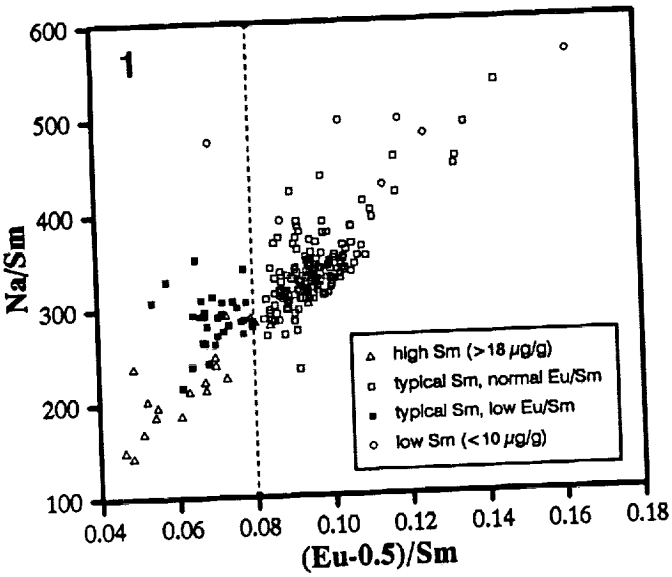

Fig. 1. "Low-Eu/Sm samples" are defined here (somewhat arbitrarily) as those for which the ratio $(C_{Eu}-0.5)/C_{Sm}$ (concentrations in µg/g) is less than 0.08 and $C_{Sm} < 18$ µg/g. The constant factor of 0.5 µg/g is applied because on a plot of Eu *vs.* Sm (Fig. 2), the trend extrapolates to ~0.5 µg/g Eu at 0 µg/g Sm.

Fig. 2. (a) The majority of melt-breccia samples analyzed here form a tight cluster corresponding to the poikilitic melts of previous studies; the low-Eu/Sm samples, however, fall mainly in the field of aphanitic melts [2]. The dashed diagonal line represents the same demarcation as the dashed vertical line of Fig. 1. **(b)** Within the field of poikilitic melts, samples from station 6 tend to have higher concentrations of Eu (and Na).

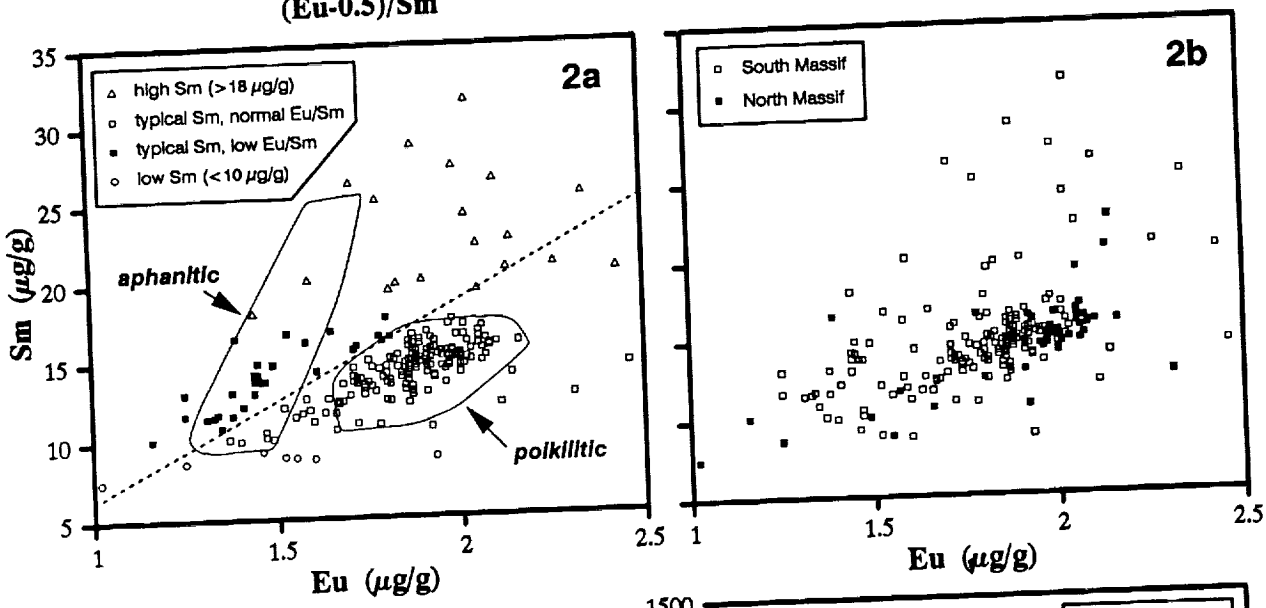

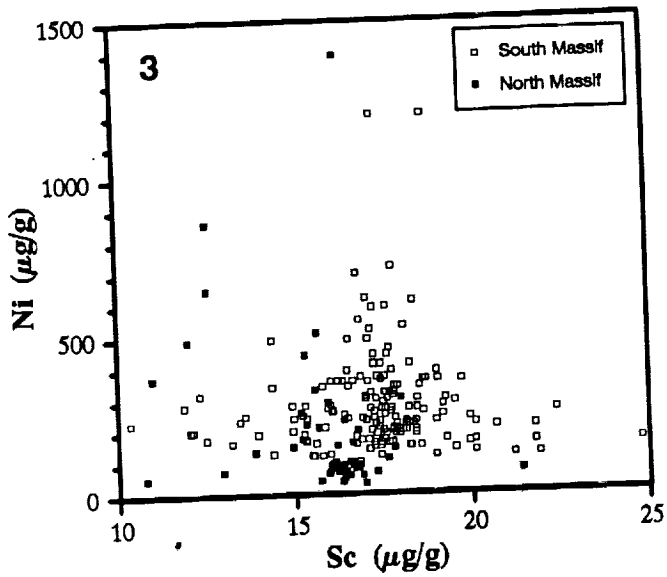

Fig. 3. Melt breccias (mostly Eu-normal) from the North Massif tend to also have lower concentrations of Sc, Cr (not shown), and Ni than those from the South Massif.

REFERENCES: [1] Jolliff B. L., Rockow K. M., Korotev R. L., & Haskin L. A. (this volume); [2] Rockow K. M., Jolliff B. L., Korotev R. L., & Haskin L. A. (this volume); [3] Spudis P. D. & Ryder G. (1981) *Multi-ring Basins*, (P. H. Schultz & R. B. Merrill, eds.), 133–148; [4] James O. B., Hedenquist J. W., Blanchard D. P., Budahn J. R., & Compston W. (1978) *PLPSC9*, 789–819; [5] Rhodes J. M., Rodgers K. V., Shih C., Bansal B. M., Nyquist L. E., Wiesmann H., & Hubbard N. J. (1974) *PLSC5*, 1097–1117.

52-91 ABS. ONLY
2068

p. 2

LUNA 24 REGOLITH BRECCIAS - A POSSIBLE SOURCE OF THE FINE SIZE MATERIAL OF THE LUNA 24 REGOLITH, O.D. Rode, V.I. Vernadsky Instit. of Geochem. and Analytic Chem., Moscow, Russia; M.M. Lindstrom, NASA Johnson Spase Center, Houston, TX. 77058.

We analyzed the regolith breccias from the Luna 24 core. The Luna 24regolith is a mixture of fine and coarse grain materials. The comparable analysis of the grain size distributions, the modal and chemical compositions of the breccias and the regolith from the same levels shows, that the friable slightly litificated breccia with a friable fine grained matrix may be a source of fine grain material of the Luna 24 present day regolith.

Regolith breccia - a second lunar rock forming by a shock lithification of lunar regolith and containing all its component. Regolith breccias are formed from older regolith and may differ from present-day regolith. They may contain very interesting information on the evolution of surface soils.

We analyzed the regolith breccias from the Luna 24 regolith core. As well known the Luna 24 core is mixture of a coarse, immature component and a finer, submature component [1, 2 and oth.]. The investigation of the Luna 24 regolith breccias may give very usefull and important data which can help to understand the forming of the Luna 24 regolith. For our investigations we selected breccias from the enriched in breccias 133 and 165 cm level of the Luna 24 core. We studied the polish thin sections of the breccias themselves and the grain size fractions. For dissagregation we selected two typical regolith breccias from 143 and 160 cm levels and applyed the method descriebed in [3] using also ultrasonic techniques.The samples were sieved in ethanol. We did a study of modal petrology and chemical compositions of grain fractions (using INAA). The obtained data we compare to the data on the Luna 24 regolith samples from the same levels.

Investigating the thin sections we found out two large groups of regolith breccias which appreciable differ in matrix: 1) group A - friable,very poorly consolidated breccias with matrix consisting of finely comminuted clasts of mineral and containing a little glass, and 2) group B -more compact, porous breccias with dark glass matrix including angular rock and mineral clasts of different sizes. According to the grain size distribution data (presented in table 1) breccia A is considerable more fine grained compared to breccia B and especially to the regolith. Table 2 demonstrates the modal data of the 250-100 and 100-45 μm fractions. The grain fractions of the breccias have very high contents of monomineralic grains; among them pyroxene predominates. Breccia A is more rich in plagioclase than breccia B. In breccia B we observe the increase of glass and lithic fragments (especially mare basalt) compared to breccia A.The agglutinates are nearly absent in the breccias perhaps because of destruction under lithification. Both breccias contain spherules.In the modal analysis of the grain size fractions we can observe the same systematic trends which are peculiary to regolith: the increase of plagioclase and pyroxene and decrease of lithic fragmens with decreasing of particle size.

The chemical composition data show the compositional similarity of the regolith breccias (Table 3). The chemical element distributions in the grain size fractions have the same trends as in regolith samples:with decreasing of grain size the fine fractions become slightly enriched in the feldspathic elements (Na2O, CaO) and depleted in mafic elements(FeO, Sc). However in the regolith this trend is more strongly marked than in the breccias. It is also necessary to note that the fine fraction of breccia A is more enriched in the feldspathic elements than the regolith from the same level. The similarity of the chemical compositions of both breccias and the regolith shows that all of them are of local origin.

We suggest that breccia A was formed by impact lithification from well developed mature local previous regolith. Now this breccia is one of the possible source of the finest material in present day regoliththat is a result of space weathering of local rocks excavated after breccia A forming.

References: [1] Rode O.D. and Ivanov A.V. (1984) LPS XY, 691;[2] McKay D.S. et al. (1978) Mare Crisium: The View from Luna 24, 125-136;[3] Rode O.D. and Ivanov A.V. (1984) Solar System Res., 18, N1,1-4.

Table 1. The size fractions of Luna 24 regolith and breccia, %

size fraction, μm	24143,26 regolith	24143,26 breccia	24160,26 regolith	24160,26 breccia
200-370	8.5	0.6	10.6	2.6
100-200	22.3	13.8	22.7	38.3
45-100	24.2	31.1	26.5	24.3
10- 45	33.3	17.9	30.0	19.9
< 10	11.7	36.6	10.2	14.9

LUNA 24 REGOLITH BRECCIAS: Rode O. D. and Lindstrom M.M.

Table 2. Particle types and relative abundances in size fractions (μm) of Luna 24 regolith and breccias.

	24143				24160			
	regolith		breccia		regolith		breccia	
	250-100	100-45	250-100	100-45	250-100	100-45	250-100	100-45
Agglutinat.	2.3	2.2	0.0	0.0	7.4	2.1	2.2	0.0
Breccia reg.	27.1	17.3	8.4	5.6	22.9	12.4	14.9	10.1
Plagioclase	8.4	12.1	16.0	19.8	4.1	6.1	9.0	12.2
Olivine	6.2	3.7	7.7	10.3	5.5	6.6	4.7	3.2
Pyroxene	31.0	44.2	48.8	49.1	30.3	50.1	24.2	35.4
Opaque	3.9	3.8	2.1	2.9	1.0	2.4	5.1	6.3
Glass	5.4	5.3	4.7	5.2	2.0	3.4	18.5	21.2
Spherules	0.5	1.2	1.7	2.6	1.7	1.8	0.9	1.4
Mare basalt	11.7	7.4	3.0	2.1	18.7	9.8	12.0	8.8
Gabbro	2.9	2.5	3.0	0.0	6.2	3.3	4.9	0.0
Others	0.6	0.3	0.6	0.0	0.2	2.0	3.6	1.4

Table 3.Chemical composition of the size fractions of Luna 24 breccia[1] and regolith[2]

	24143 breccia/regolith				24160 breccia/regolith			
	200-100	100-45	45-10	<10	200-100	100-45	45-10	<10
Na2O,%	0.23	0.25	0.28	0.45	0.22	0.22	0.27	0.42
	0.15	0.18	0.18	0.37	0.20	0.18	0.31	0.38
K2O,%*	<0.06	0.04	<0.11	0.06	<0.10	<0.04	0.05	<0.16
CaO,%	11.0	11.3	11.4	11.4	10.9	10.9	10.7	11.6
	6.0	6.0	6.1	6.7	6.1	6.1	6.5	7.0
FeO,%	19.9	20.4	19.2	15.9	20.3	20.5	18.7	16.0
	22.8	19.6	17.1	14.3	22.6	21.2	20.8	15.4
Sc,ppm	48.9	46.6	42.0	30.3	51.8	50.0	41.4	30.0
	47	46	35	29	59	52	43	30
Cr,ppm	2800	2950	2990	3050	2820	2840	2760	3060
	4100	3800	4000	3100	3900	4200	2800	5500
Co,ppm	54.4	54.3	50.3	45.2	57.0	55.7	49.6	46.3
	50	55	43	44	52	50	50	41
Ni,ppm*	290	217	260	240	240	159	180	740
Sr,ppm*	100	97	<180	180	<190	100	<100	90
Ba,ppm	46	39	<120	65	<80	54	46	49
	40	40	100	100	75	95	95	125
La,ppm	3.02	3.07	2.98	5.03	3.54	3.28	3.58	4.00
	1.9	2.3	4.7	4.9	1.4	2.1	3.5	5.5
Ce,ppm	9.4	10.6	8.4	13.4	9.7	9.9	10.6	11.0
	7.7	17.2	14.1	18.3	6	7	14	20
Sm,ppm*	2.04	2.07	1.89	3.01	2.41	2.26	2.39	2.25
Eu,ppm	0.61	0.64	0.71	0.94	0.62	0.64	0.70	0.88
	0.54	0.51	0.60	0.84	0.61	0.69	0.81	1.1
Tb,ppm	0.51	0.54	0.43	0.77	0.67	0.60	0.60	0.51
	<1	<1	<1	0.9	<1	<1	0.6	0.9
Yb,ppm	1.94	1.99	1.92	2.23	2.29	2.14	2.15	1.93
	1.8	2.3	2.1	2.9	2.1	1.6	2.3	2.5
Th,ppm*	0.63	0.73	0.41	1.39	1.21	0.79	1.14	0.51
Ir,ppm*	8.1	5.1			11	7.4	<9	12
Au,ppm*	26.1	<3.3	<8		6.8	2.7	27.5	7.8

[1]The data of M.M.Lindstrom [2]The data of O.D.Rode *The data only for the breccias

53-90 ABS ONLY
3069

P. 2

ANTARCTIC WEATHERING OF THE CK CHONDRITES EET90004, 90007, AND 90022: NICKEL AND SULFUR MOBILITY; C.S. Romanek, R.A. Socki†, E.K. Gibson Jr. and J. H. Allton†, Planetary Science Branch/SN4 and LESC†, JSC/NASA, Houston, TX 77058

CK chondrites are a relatively new class of carbonaceous chondrite that have been described in the literature [1]. Most meteorites that comprise the CK group are restricted to Antarctic finds; therefore terrestrial weathering processes can influence the geochemical records contained within these chondrites. The paired CK chondrites EET90004, 90007, and 90022 share not only a common heritage but similar weathering histories since all three meteorites were found on Antarctic ice covered with thick evaporative coatings. Additional material has grown on these samples during curation at the Antarctic Meteorite Lab at JSC, NASA. At present, efflorescence up to a millimeter thick coats the surface of EET90004 and 90022, with less material coating EET90007. The chemistry, mineralogy and isotopic composition of efflorescence on EET90004 and 90022, described here, provide valuable information regarding the fate of meteoritic components in the Antarctic environment.

SEM photo-micrographs of grain mounts from EET90004 and 90022 surface coatings show that the efflorescence is composed of crystal aggregates up to 500 μm in length. Individual grains are composed of columnar to bladed crystals ~ 10 to 100 μm long with prismatic or pyramidal terminations. Crystal faces commonly contain desiccation cracks. Qualitative energy-dispersive x-ray analyses with a thin window detector show that the solid is composed solely of Ni, S and O, ± minor Mg and Ca.

The mineralogy of the efflorescence is the hydrated nickel sulfate retgersite ($NiSO_4 \cdot 6H_2O$) on EET90022 and retgersite plus nickel hexahydrite (both $NiSO_4 \cdot 6H_2O$) on EET90004, determined by standard x-ray diffraction techniques. All diffractogram lattice spacings from each sample can be attributed to one of these two minerals.

Differential scanning calorimetry (DSC) heat flow curves were taken of the samples and reagent grade synthetic analogs to confirm the mineralogy and determine the temperature release of structural water within the meteoritic efflorescence. Gas speciation from the effluent of synthetic analogs was determined using a quadrupole mass spectrometer. Mass scans were recorded for mass/charge ratios of 18, 32, 33, 34, and 64, to monitor for H_2O, S, HS, H_2S, and SO_2 release. All five species were detected during the heating of synthetic retgersite from ~ 60°C to 720°C, with only trace quantities of S-bearing gas species being detected. Reaction kinetics probably inhibit significant S-volatilization over the time interval of a single run. Observed total mass loss (45% by wt.) was in slight excess of the theoretical value for dehydration (41% by wt.), supporting the observation of minor gaseous sulfur release. Weight loss for EET90022 (45%) was identical to that for synthetic retgersite while that for EET90004 was slightly less (41%). Since EET90004 contains a significant proportion of nickel hexahydrite, perhaps the differences in weight loss can be attributed to mineral-specific reaction kinetics associated with S-volatilization.

DSC heat flow curves of efflorescence on EET90004 and 90022 are similar despite their distinct mineralogies. Curves display three common peak interval ranges that occur at 60° to 130°C, 130° to 240°C, and 300° to 450°C. Peak positions are similar to those from synthetic retgersite although peak shapes and areas differ. Since little to no S-bearing gases were generated during the runs, peaks probably represent the loss of water at different structural sites within the crystal framework. Previous work has shown that water in $NiSO_4 \cdot 6H_2O$ is principally bound to the Ni cation [2]. Upon heating, five water molecules

are lost at ~100°C and the sixth is lost at 280°C. The second two peaks observed in the DSC heat flow curves of the meteoritic efflorescence probably represent the release of these six structural water molecules, albeit shifted to slightly higher temperatures than those reported in the literature. The low-temperature peak observed in the meteoritic efflorescence and synthetic retgersite is probably related to a highly mobile seventh water molecule that forms a hydrogen bond with SO_4. DSC curves for the synthetic analog $NiSO_4 \cdot 7H_2O$ display an intense peak that occurs precisely over this temperature interval. The shape and area of peaks from curves of EET90004 and 90022 are intermediary between synthetic retgersite and $NiSO_4 \cdot 7H_2O$, suggesting that some water is hydrogen-bonded to SO_4 in the efflorescence. These results place constraints on the interpretation of the H-isotopic composition of efflorescence reported below.

Hydrogen isotope analysis of the efflorescence was determined by pyrolysis of the solid at 625°C. All evolved gas was trapped in a cold finger held at -197°C. After 4 hours the temperature of the trap was raised to -80°C and evolved gas was isolated for chemical speciation on a quadrupole mass spectrometer. SO_2 was the only gas trapped at this temperature suggesting that, unlike other meteoritic efflorescence [e.g., 3], carbonates did not form. The remaining H_2O was sealed in a Pyrex tube containing Zn for reduction to H_2 at 450°C and analysis on an isotope ratio mass spectrometer. The δD for EET90022 efflorescence was -25‰ (SMOW) while that for 90004 was +25‰ (SMOW). Efflorescence is significantly enriched in deterium compared with the ambient Antarctic water from which it precipitated (i.e., -425‰), suggesting that evaporative processes strongly influence isotopic composition. Mass balance calculations reveal this to be a reasonable scenario. Isotopic exchange of SO_4-bonded water with local water vapor (~-80‰ SMOW) may have increased the δD of the solid but it could not have produced the excessive enrichments observed in the efflorescence.

The mobility of Ni and S play active roles in the terrestrial weathering of these CK chondrites. The most probable source for Ni and S is pentlandite $[(Fe,Ni)_9S_8]$ which occurs as small 10 to 20 μm grains that are dispersed throughout these meteorites. Freeze-thaw action of water could promote the migration of oxidizing fluids into the meteorite during sunny periods on the ice sheet [4]. Reduced solid phases that border fractures, such as pentlandite, would be highly soluble under these conditions and could contribute aqueous nickel and sulfur to the migrating fluid during mineral dissolution. The absence of Fe in efflorescence is explained by the formation of goethite pseudomorphs replacing pentlandite along meteorite fractures. Aqueous nickel and sulfur are deposited on the surface of the meteorite in the soluble phases, retgersite and nickel hexahydrite, during periods of extreme evaporation. The hydrogen isotopic signature of the efflorescence records the extreme levels of evaporation required to enrich the hydrate in deuterium by 400‰. The chemical, mineralogical and isotopic signature of evaporative weathering products can provide valuable clues about the processes responsible for the alteration of the pre-terrestrial record contained within CK chondrites.

REFERENCES

[1] Kallemeyn et al. (1991) *Geochim. Cosmochim. Acta* 55, 881-892.
[2] Busch et al. (1973) **Chemistry**, Allyn and Bacon, Boston, p.501.
[3] Socki et al. (1993) *Meteoritics* 28, 440.
[4] Gibson and Andrawes (1980) *LPSC* 11, 1223-1234.

omit to R116

THE CHONDRITIC REGOLITH BRECCIA (H3-6) ACFER 153: PETROGRAPHY AND *IN-SITU* NUCLEAR TRACK INVESTIGATIONS J. Romstedt[1] and K. Metzler[2], [1]Institut für Planetologie, Wilhelm-Klemm-Str. 10, 48149 Münster, Germany; [2] Museum für Naturkunde der Humboldt-Universität, Invalidenstr. 43, 10115 Berlin, Germany.

A single piece of this meteorite weigh ing ~211 g was discovered in the Algerian Sahara. This meteorite is one of 400 individuals found during the last four years in this area. At first this meteorite was classified as an ordinary H 3.8 ordinary chondrite (1), but our recent petrographical and nuclear track investigations revealed that this sample represents a chondritic breccia containing exotic clasts, solar flare irradiated grains in addition to a considerable amount of solar wind implanted noble gases (pers. com. SCHULTZ 1993). Hence, this meteorite should be classified as a H3-6 regolith breccia.

Results and conclusions:

Petrography This meteorite consists of chondrules and chondrule fragments with minor amounts of identifiable lithic clasts, embedded in a fine-grained clastic matrix. One lithic clast (clast A; Fig.5) represents a H6 fragment with equilibrated olivines (Fa Ø = 20.5 mol %) and feldspar intergrowths (Ø = $Ab_{80}An_{10}Or_{10}$) with sizes of single feldspar grains in the order of 100 µm. Due to the scarcity of lithic clasts of high petrologic type and their small size, the typical dark and light structure of chondritic regolih breccias is not visible in handpieces of this meteorite.

Two exotic lithic clasts were discovered, one of which (clast B; Figs.1, 5) represents an amoeboidal shaped impact-melt breccia clast with spinifex texture. Its skeletal, unequilibrated olivines (Fa = 13-22 mol %) are embedded in a glassy mesostasis that partly shows devitrification features like dendritic pyroxenes. This clast contains several angular olivine fragments that seem to have been admixed to the melt. The second exotic clast (Fig.2) represents a fragment of a friction breccia vein. This fragment shows a layered texture of alternating clastic and crystallized layers. The latter contain finely distributed metal/sulfide beads indicating the immiscibility of metal/sufide melt and silicate melt.

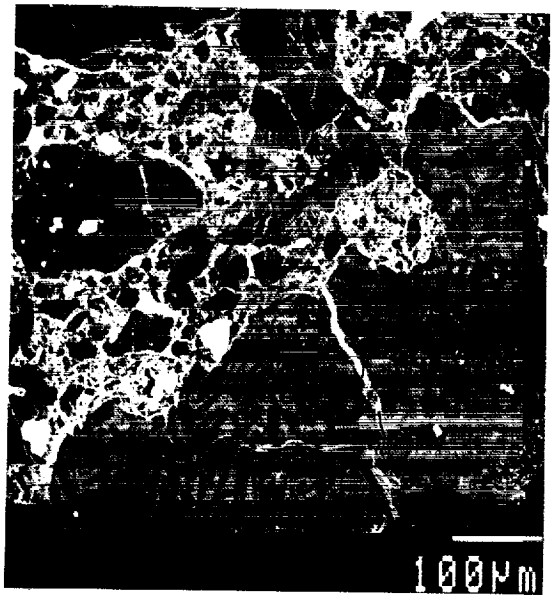

Fig.1 BSE image of a melt-breccia.

Fig.2 BSE image of a friction-breccia.

THE CHONDRITIC REGOLITH BRECCIA (H3-6) ACFER 153: Romstedt J. and Metzler K.

Nuclear track investigations The track investigations were performed using both grain separates and thin sections (for in situ studies). 110 transparent olivines were picked from a 60-200 µm sieve fraction, mounted in epoxy, polished and etched for about 4 hours in boiling WN solution (2). The etching time for the thin sections was reduced to 1 hour to preserve small and/or heavily irradiated olivine grains from destruction. The grain separate does not contain preirradiated grains. The observed track density distribution (40 grains, Fig.3) with a mean track density of about 1.5×10^6 and a variation factor of 3.9 can be traced back exclusively to the meteroid transit irradiation.

One large thin section (~ 2.6 cm^2) contains only two preirradiated grains, both of which have grain sizes below 10 µm. These two grains are located in a small inclusion that can be interpreted as a breccia-in-breccia structure. In the smaller section (~ 0.7 cm^2) we identified an elongated area of ~2 mm wideness containing 39 heavily irradiated mineral and lithic fragments (Fig.5). This area, that contains the H6 clast and the impact-melt breccia clast (clasts A, B; Fig.5) described above, is petrographically indistinguishable from other parts of the meteorite. Whereas the H6 clast does not show any indication for a preirradiation, the impact-melt breccia clast was clearly irradiated by solar flares at some time at the parent body surface, prior to its final incorporation into the present regolith breccia. The solar flare irradiation of this clast is indicated by a steep track density gradient (Fig. 4) of about one order of magnitude (2×10^8 to 3×10^7 tracks/cm^2) on a 100 µm scale.

The reason for the missing preirradiated olivines among the 40 separated and epoxy mounted grains is their scarcity. This observation underscores the importance of *in-situ* nuclear track investigations of meteorites *using large polished thin sections*.

References: (1) Bischoff A. et al. (1992), LPS XXII, 107. (2) Krishnaswami S. et al. (1971), Science 174, 287.

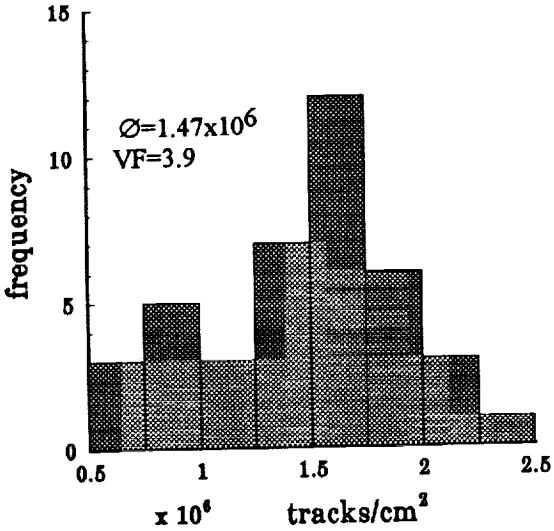

Fig.3 Track densities determined in a separate of olivine grains. Tracks were only produced during transit.

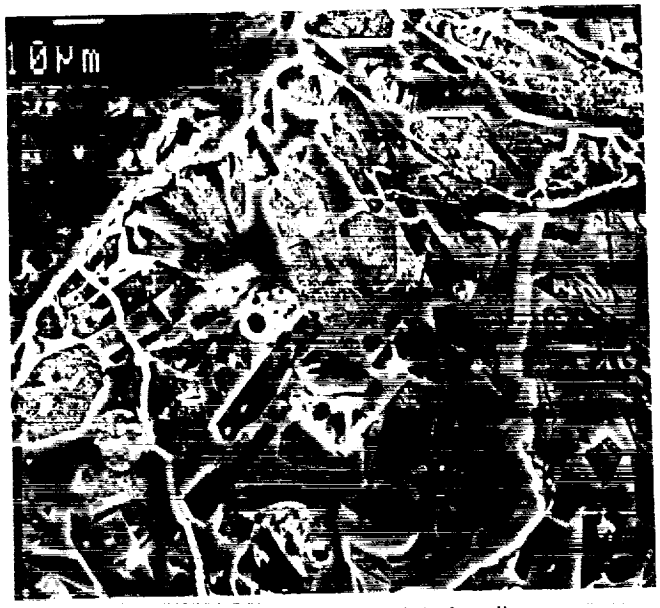

Fig.4 SE image of a solar flare irradiated melt-breccia.The steep track density gradient from the edge to the centre is clearly visible.

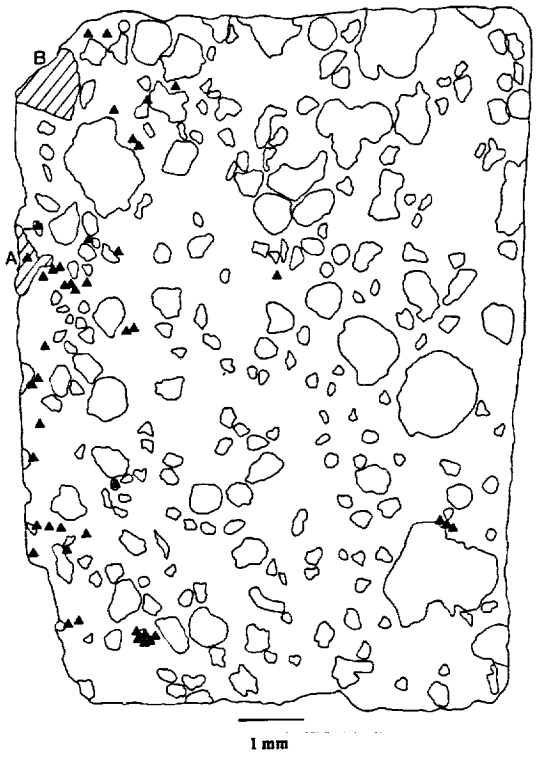

Fig.5 Sketchmap of a thin section. The triangles show the inhomogenious distribution of preirradiated grains.

THERMAL ISOSTASY PROCESS AND LITHOSPHERIC STRUCTURE ON VENUS.

P. Rosenblatt, and P. C. Pinet: UPR 234/CNRS, Groupe de recherche de Géodésie Spatiale, Observatoire Midi-pyrénées, Toulouse France.

The hypsometric analysis of Earth and Venus topography has revealed that the hypsometric curve shows a linear trend for both planets (1), defining a topographic domain (called as the linear domain) with an elevation range of about 2000 m. It corresponds, on one hand, to the nearly global oceanic domain for the Earth and, on the other hand, to the most part of the venusian surface. For the planetary areas so defined a model of thermal isostasy adapted from (2) is applied in order to take account for the relief distribution. It leads to the estimates of the thermal lithospheric thickness L and of the surface heat flux Φ, parametrized by the mantle temperature Tm, by means of the following relationships:

$$L = 2\,D/\,\alpha\,\Delta T \qquad \Phi = k\,\Delta T\,/\,L$$

where α is the coefficient of thermal expansion, k is the thermal conductivity. The numerical values of these constants are taken from (3). ΔT is the drop of temperature between the bottom and the top of the thermal lithosphere.
On this ground, the upper elevation of the linear domain is assumed to correspond, in terms of lithospheric structure, to the planetary level for which the thermal lithospheric thickness tends toward zero, and D represents the elevation difference with respect to this particular level.
Figure 1 and 2 show different distributions of the lithospheric thickness and the surface heat flux respectively, when investigating the effect of the mantle temperature parameter ranging from 900 °C (taken as the reference isotherm of the thermal lithospheric base) to 1450 °C (a maximum estimate for the oceanic lithosphere basal temperature (4)). When ranging from 1250 °C to 1450 °C, the modal value of the thermal lithospheric thickness varies from 112 km to 90 km, the modal heat flux varies from 22 to 34 mW/m2 and the mean global heat flux varies from 50 to 63 mW/m2 as the mantle temperature is increasing. In the case the mantle temperature is 900 °C, it is found a modal thermal lithospheric thickness of about 200 km and a modal heat flux of around 7 mW/m2.
Applied to the Earth, this model gives the surface heat flux by interval of depth from the upper to the lower elevation of the linear domain (e.g. the nearly global oceanic surface). For the greatest depths, the heat flux estimates agree in the standard deviation with the observational data (5). The mean heat flux obtained by averaging the heat flux of each depth interval weighted by the respective percentage of area varies from 120 mW/m2 to 162 mW/m2 as the mantle temperature beneath the lithosphere varies from 1250 °C to 1450 °C. But the thermal isostasy model gives a heat flux value rapidly divergent as the elevation tends to the upper elevation of the linear domain, corresponding to the mean depth of the mid-oceanic ridges. In order to avoid this divergence, the mean global heat flux is recalculated when excluding the heat flux values of the first depth intervals from the ridge level, yielding to a mean heat flux of about 100 mW/m2

THERMAL ISOSTASY ON VENUS: P. Rosenblatt and P.C. Pinet

which is in good agreement with the value of (5) for the mean oceanic heat flux. This good agreement is obtained for 93 % and 88 % of the oceanic surface with a mantle temperature of 1350 °C and 1450 °C respectively.

REFERENCES: (1) Rosenblatt et. al. (submitted); (2) Morgan P. and R.J. Phillips (1983) *jGR, 88*, 8305; (3) Johnson H.P. and R.L. Carlson (1992) *GRL,19*, 1971; (4) Stein C.A. and S. Stein (1992) *Nature, 359*, 123; (5) Pollack H. N. et. al. (1993) *Rev. of Geophys. 31*, 267.

Figure 1

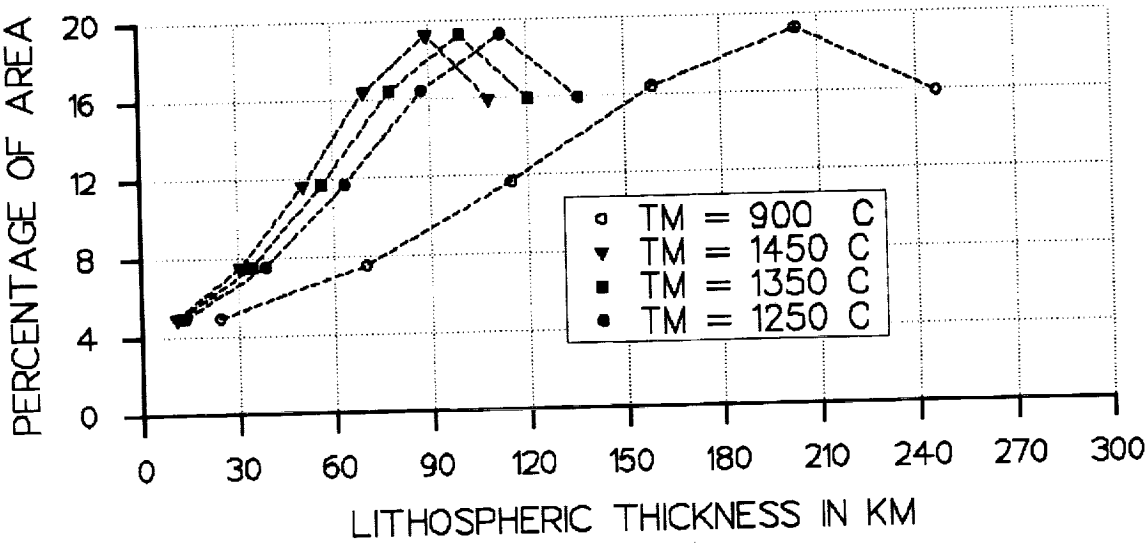

Figure 2

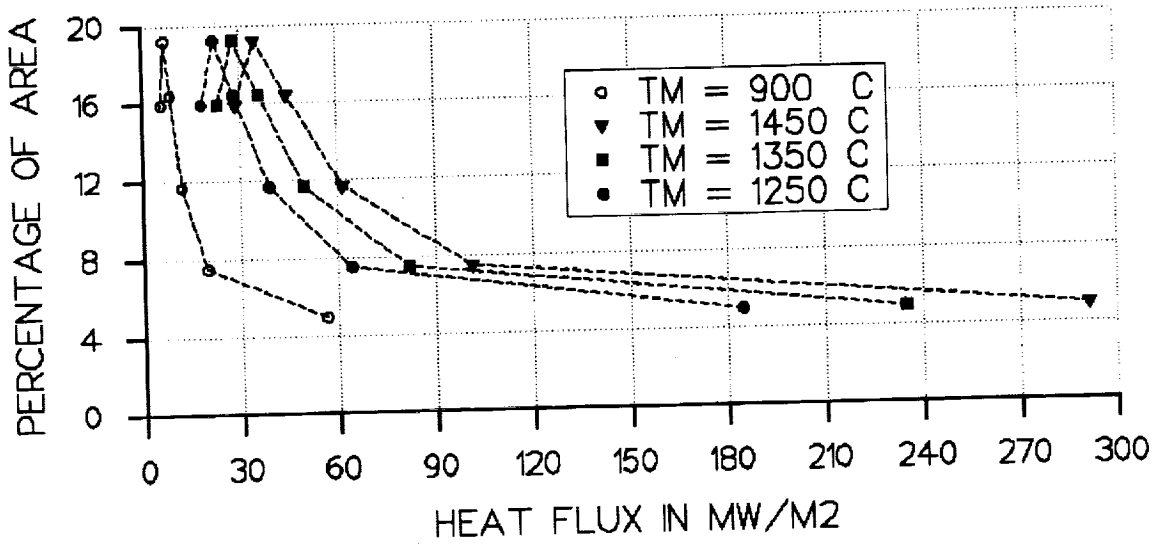

54-46 ABS ONLY
3070

N94-35452

P. 2

Thermal Emission Measurements (5-25 μm) of Hawaiian Palagonitic Soils With Implications for Mars; Ted L. Roush[1] and James F. Bell III[2], [1]San Francisco State Univ. and NASA Ames Research Center, MS 245-3, Moffett Field, CA 94035-1000, [2]NRC/NASA Ames Research Center, MS 245-3, Moffett Field CA 94035-1000

Background: There is ample evidence that abundant iron-bearing minerals are present on Mars. This evidence takes the form of in situ analyses [1-4], previous and continuing Earth-based telescopic spectroscopic observations [e.g. 5,6], Viking Lander and Orbiter multispectral imaging [7-10], and Phobos-2 multispectral imaging [11,12]. Information regarding the crystalline or amorphous nature of the iron-bearing (and other) surface materials on Mars can provide insight into the availability of liquid water at the surface and the duration, mode, and extent of weathering.

Data from Viking X-ray fluorescence analyses, magnetic experiments, and aerosol imaging were interpreted as indicating the presence of a variety of iron-rich materials, including iron oxides [1-4,13]. However, since the Viking Landers did not carry any instruments capable of determining mineralogy, the exact mineralogical form of the iron-bearing material remains uncertain.

Interpretations of continuing visual, near-, mid- and far-infrared spectroscopic observations of Mars from the Earth and spacecraft over the past 20 years have revealed that the ferric mineralogy occurs in two distinct forms: (1) nanophase or truly amorphous Fe^{3+}-bearing materials [14,15] that spectrally resemble certain terrestrial palagonites [e.g. 16-20]; and (2) well-crystalline ferric oxides like hematite (α-Fe_2O_3), maghemite (γ-Fe_2O_3), or magnetite (Fe_3O_4) [1,13,15, 21-24]. The available data indicate that the poorly-crystalline "palagonite-like" phases are spectrally dominant [e.g. 5,6] and that the well crystalline ferric oxides cannot constitute an abundance of more than about 4-8 wt. % [24].

The research presented here represents the initial phase of a broader project that is intended to provide data in the mid- and far-infrared spectral region for both well-characterized iron oxides/oxyhydroxides and poorly crystalline or amorphous materials (e.g. palagonites). Such information can be used in the interpretation of past and future thermal infrared observations of Mars.

Spectral Studies: In the middle infrared (5-25 μm), spectral features arise from vibrational motions of atoms and molecules which compose the materials. These fundamental modes are much more intense than any associated combination and/or overtones of these modes and hence remote sensing observations in the infrared are extremely sensitive to minor concentrations of these absorbing species [25].

Careful laboratory studies have shown that the coloring agent in certain Mars analog Hawaiian palagonitic soils is nanophase iron oxide [18,19,26]. We have measured the emissivity of two Mauna Kea palagonitic soils whose transmission spectra exhibit different spectral features [27] and of a thermally-altered volcanic tephra sample that exhibits a wide range of crystallinity and degree of alteration (from black cinders to fully hematitic) [19]. Both of these samples may represent analogs for formation mechanisms involving the production of highly-altered secondary weathering products on Mars. The emission spectra of all samples were measured at the TES spectroscopy laboratory [28] at Arizona State University with the cooperation of Dr. Phil Christensen. The data were converted to emissivity using blackbody measurements combined with measurements of each sample at different temperatures [29].

Results: Emissivity spectra for coarse and fine particle size separates of each sample are shown in Figure 1. Several trends are immediately obvious. First, the finer particle size fractions exhibit increasingly lower emissivity than the coarser sizes at wavenumbers above 1400 cm^{-1}. This effect may be a manifestation of the increased importance of multiple scattering at these frequencies rather than Fresnel-like reflections at lower frequencies. Second, emissivity peaks in the 1000-1400 cm^{-1} region in the fine fraction samples are shifted to higher frequencies relative to the same feature in the coarse fraction samples. This may be a particle size effect, or it may be due to variations in the silicate and/or iron-bearing mineralogy between the coarse and fine samples [e.g., 19]. While we do not make specific mineralogic assignments for the various spectral features seen in these data, we note that a broad

emissivity peak possibly due to silicates is present near 1200-1300 cm^{-1} and that narrower features near 1400-1600 cm^{-1} and near 400 cm^{-1} are possibly consistent with crystalline iron oxide minerals like hematite and/or goethite [30,31].

This preliminary study has demonstrated that naturally-occurring palagonites, thought to be good visible to near-IR spectral analogs for Mars, exhibit complex emissivity spectra at thermal wavelengths. Disentangling the various spectral signatures that make up the emissivity spectra of these complex assemblages may prove quite important in the interpretation of mid-IR Mars data sets.

References: [1] R.B. Hargraves et al. (1977) JGR, 82, 4547. [2] P. Toulmin et al. (1977) JGR, 82, 4625. [3] B.C. Clark et al. (1977) JGR, 82, 4577. [4] B.C. Clark et al. (1982) JGR, 87, 10059. [5] L.A. Soderblom (1992) in Mars (H.H. Kieffer et al., eds.), 557. [6] T.L. Roush et al. (1993) in Remote Geochemical Analysis (C. Pieters and P. Englert, eds), 367. [7] L.A. Soderblom et al. (1978) Icarus, 34, 446. [8] T.B. McCord et al. (1982) JGR, 87, 10129. [9] J.B. Adams et al. (1986) JGR, 91, 8098. [10] R.E. Arvidson et al. (1989) JGR, 94, 1573. [11] S. Murchie et al. (1993) Icarus, in press. [12] J.F. Mustard et al. (1993) JGR, 98, 3387. [13] J.B. Pollack et al. (1977) JGR, 82, 4479. [14] R.V. Morris and H.V. Lauer Jr. (1990) JGR, 95, 5101. [15] R.V. Morris et al. (1989) JGR, 94, 2760. [16] R.B. Singer et al. (1979) JGR, 87, 10159. [17] D.L. Evans and J.B. Adams (1980) PLPSC 11, 757. [18] R.V. Morris et al. (1990) JGR, 95, 14427. [19] J.F. Bell III et al. (1993) JGR, 98, 3373. [20] A. Banin (1992) LPI Tech. Rpt. 92-04, 1. [21] R.V. Morris et al. (1985) JGR, 90, 3126. [22] J.F. Bell III et al. (1990) JGR, 95, 14447. [23] R.B. Hargraves et al. (1979) JGR, 84, 8379. [24] J.F. Bell III (1992) Icarus, 100, 575. [25] J.F. Bell III and T.L. Roush LPI Tech Rpt 93-06, 2 [26] D.C. Golden et al. (1993) JGR, 98, 3401. [27] T.L. Roush (1992) LPI Tech. Rpt. 92-04, 32. [28] D.L. Anderson et al. (1991) LPSC XXII, 21. [29] P.R. Christensen and S.T. Harrison (1993) JGR, submitted. [30] J.W. Salisbury et al. (1991) Infrared (2.1-25 μm) Spectra of Minerals, Johns Hopkins Univ. Press, 267 pp [31]T.L. Roush and J.F. Bell III, this volume

Acknowledgements: This research is supported by funding from: Mars Observer Participating Scientist Program; NASA's Geology and Geophysics Program via RTOP 151-01-60-01 and NAGW 2212; and from NASA's Exobiology program via RTOP 185-52-62-07.

Figure 1. Emissivity spectra of Hawaiian palagonitic samples PH-1 (a thermally altered palagonitic tephra from Mauna Kea) and 91-1 (a palagonitic tephra from South Point, island of Hawaii). Both coarse and fine size fraction spectra are shown. Arrows indicate subtle shifts in emissivity peak position between the two particle size regimes shown. The vertical line shows the frequency of the strong H-O-H bending fundamental caused by molecular water associated with these samples.

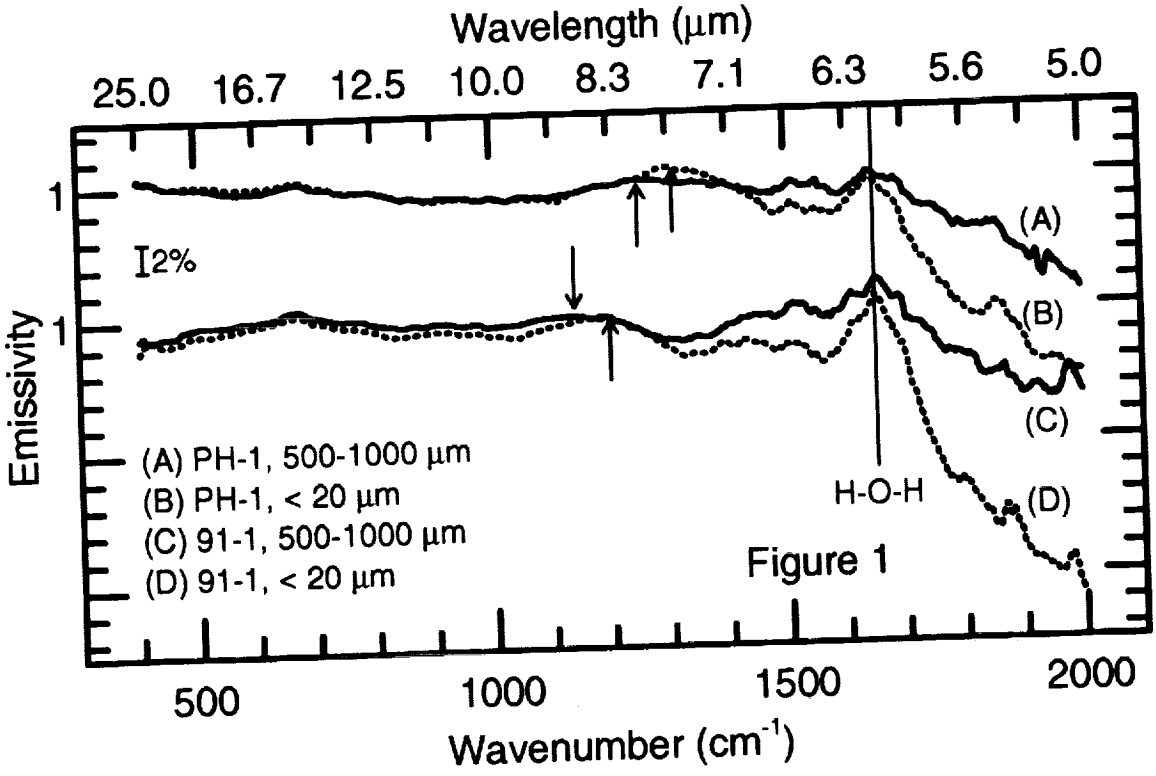

55-46 ABS ONLY 3071

N94-35453

Thermal Emission Measurements (5-25 μm) of Palagonite/Fe-substituted Montmorillonite Intimate Mixtures: Applications to Mars: Ted L. Roush[1] and James B. Orenberg[2], [1]San Francisco State Univ. and NASA Ames Research Center, MS 245-3, Moffett Field, CA 94035-1000, [2]Dept. Chemistry & Biochemistry, San Francisco State Univ., 1600 Holloway Ave., San Francisco, CA 94132

Background: Based on Viking Lander x-ray fluorescence analyses Si and Fe are the two most abundant elements constituting 44% and 19%, respectively, of the martian soil when recast as their oxide equivalents [1-3]. Simulations of the relative elemental abundances have included smectite clays, iron oxides, sidromelane, chlorides, and sulfates [1-3]. The Viking Landers also performed experiments designed to address the question of biological activity on Mars [e.g. 4]. Mineralogical interpretation of these results include smectites [5-8] and palagonite/smectite mixtures [9]. However, since the Viking Landers did not carry any instruments capable of determining mineralogy, the exact mineralogical form of the surface materials remains uncertain.

Interpretations of continuing visual and near-infrared spectroscopic observations of Mars from the Earth and spacecraft over the past 20 years [10,11] have revealed that the ferric mineralogy occurs in two distinct forms: (1) nanophase or amorphous Fe^{3+}-bearing materials [12,13] that spectrally resemble terrestrial palagonites [e.g. 14-18]; and (2) well-crystalline ferric oxides [13,19-23]. The available data indicate that the poorly-crystalline "palagonite-like" phases are spectrally dominant [e.g. 10,11] and that the well crystalline ferric oxides cannot constitute an abundance of more than about 4-8 wt.% [22].

Spectral analyses of the 2.2 μm Al-OH absorption feature suggests that AL-OH-bearing materials have abundances $\leq$0.008 wt.% if they are present as the pure phase [24]. Fe-substituted montmorillonites (FeM), smectite clays where the interlayer cations have been chemically replaced by Fe, have also been suggested as a mineralogical analog for martian bright soils [5-9]. Since these smectites all exhibit the 2.2 μm feature, the extreme constraint imposed for Al-OH materials is likely applicable to the pure FeM. Spectral analyses of physical mixtures of palagonite and FeM suggest that up to 15 wt. % FeM may be present on Mars and remain undetected [25]

In the middle infrared (5-25 μm), spectral features arise from vibrational motions of atoms and molecules which compose the materials. These fundamental modes are much more intense than associated combination and/or overtones of these modes occurring at shorter wavelengths. Hence, remote sensing in the infrared is extremely sensitive to minor concentrations of these absorbing species. FeM transmission spectra exhibit typical clay absorption features in the mid-infrared (2.5-25 μm) [26]. Palagonites also have absorptions in the mid-infrared although they appear less complex than the clay features [11,27]. The research presented here represents a portion of a broader project that is intended to investigate the detectability limits for the minerals containing the biogenic elements. Such information can be used in the interpretation of past and future thermal observations of Mars.

We have measured the emissivity of a Mauna Kea palagonitic soil mixed with an Fe-substituted montmorillonite. The emission spectra of all samples were measured at the TES spectroscopy laboratory [28] at Arizona State University with the cooperation of Dr. Phil Christensen. The data were converted to emissivity using blackbody measurements combined with measurements of each sample at different temperatures [29].

Results: Emissivity spectra for the two pure end members and two mixtures are shown in Figure 1. The spectrum of the FeM sample exhibits greater emissivity variations than the palagonite sample spectrum. Several emissivity peaks are present in the FeM sample near 500, 1130, and 1880 cm^{-1}, indicated by arrows, that are not present in the palagonite spectrum. These peaks may serve to identify the presence of FeM when mixed with palagonite. For example, the spectrum of the 85% palagonite, 15% FeM mixture exhibits the 500 cm^{-1} peak and a hint of the 1130 cm^{-1} feature. In the spectrum of the 75% palagonite, 25% FeM mixture both of these features are more pronounced and an additional feature near 1880 cm^{-1} is also present. We had planned to measure mixture of 90% palagonite and 10% FeM as part of this study. However, the sample was destroyed during shipping.

Thermal Emission of Palagonite/Fe-Montmorillonite Mixtures; Roush, T.L. and J.B. Orenberg

This preliminary study has demonstrated that both naturally-occurring palagonites, thought to be good visible to near-IR spectral analogs for Mars, and FeM exhibit complex emissivity spectra at thermal wavelengths. FeM exhibits greater emissivity variations than palagonite, and emissivity peaks observed in the FeM spectrum allows its identification for abundances $\geq$ 15% when mixed with palagonite. Smaller abundances of FeM are potentially identifiable when mixed with palagonite, but this remains to be determined.

References: [1]P. Toulmin et al. (1977) JGR, 82, 4625 [2] B.C. Clark et al. (1977) JGR, 82, 4577 [3]B.C. Clark et al. (1982) JGR, 87, 10059 [4]H.P. Klein (1979) Rev. Geophys., 17, 1655 [5]A. Banin and J. Rishpon (1978) Life Sci. Space. Res., 17, 59 [6]A. Banin and J. Rishpon (1979) J. Mol. Evol., 14, 133 [7]A. Banin et al. (1985) PLPSC 15, JGR suppl., 90, C771 [8]A. Banin et al. (1988) Origin Life Evol. Biosphere, 18, 239 [9]R. Quinn and J. Orenberg (1993) Geochim. Cosmochim. Acta, 57, 4611 [10]L.A. Soderblom (1992) in Mars (H.H. Kieffer et al., eds.), 557 [11]T.L. Roush et al. (1993) in Remote Geochemical Analysis (C. Pieters and P. Englert, eds), 367 [12]R.V. Morris and H.V. Lauer Jr. (1990) JGR, 95, 5101 [13]R.V. Morris et al. (1989) JGR, 94, 2760 [14]R.B. Singer et al. (1979) JGR, 87, 10159 [15]D.L. Evans and J.B. Adams (1980) PLPSC 11, 757 [16] R.V. Morris et al. (1990) JGR, 95, 14427 [17]J.F. Bell III et al. (1993) JGR, 98, 3373 [18]A. Banin (1992) LPI Tech. Rpt. 92-04, 1 [19]R.V. Morris et al. (1985) JGR, 90, 3126 [20]J.F. Bell III et al. (1990) JGR, 95, 14447 [21]R.B. Hargraves et al. (1979) JGR, 84, 8379 [22]J.F. Bell III (1992) Icarus, 100, 575 [23]J.B. Pollack et al. (1977) JGR, 82, 4479 [24]R.N. Clark (1992) BAAS, 24, 986 [25]J. Orenberg and J. Handy (1992) Icarus, 96, 219 [26]T.L. Roush, unpublished data [27]T.L. Roush (1992) LPI Tech. Rpt. 92-04, 32 [28]D.L. Anderson et al. (1991) LPSC XXII, 21 [29]P.R. Christensen and S.T. Harrison (1993) JGR, submitted.

Acknowledgements: This research is supported by funds from: Mars Observer Participating Scientist Program; NASA's Geology & Geophysics Program via RTOP 151-01-60-01; and NASA's Exobiology Program via RTOP 185-52-62-07.

Figure 1. Emissivity spectra (top two curves) of Hawaiian palagonitic soil (dotted line) and an Fe-substituted montmorillonite (FeM), solid line) and mixtures of palagonite and FeM (bottom two curves). The spectra are offset for obscurity. For the mixtures, the dotted line is 85% palagonite and 15% FeM while the solid line is for 75% palagonite and 25% FeM. The vertical line shows the frequency of the strong H-O-H bending fundamental caused by molecular water associated with these samples, while the arrows indicate emissivity features associated with the FeM.

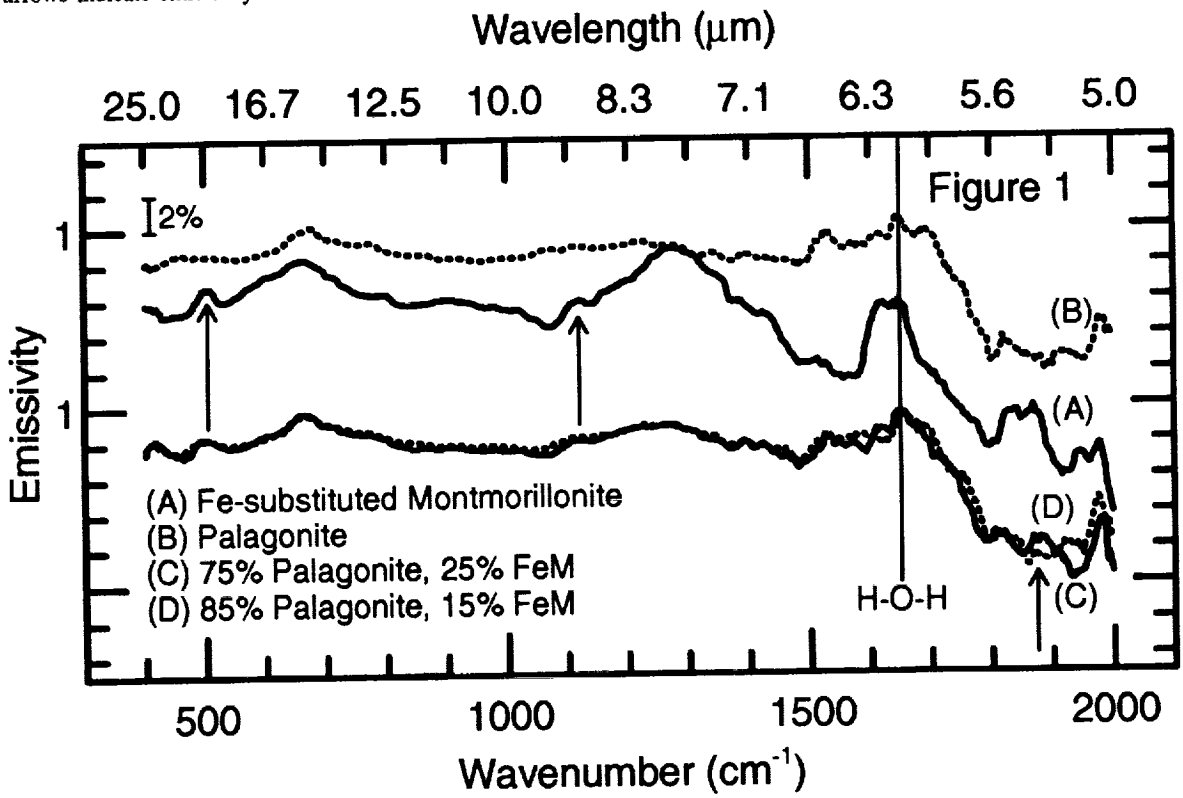

Transmission Measurements (4000-400 cm^{-1}, 2.5-25 μm) of Crystalline Ferric Oxides and Ferric Oxyhydroxides: Implications for Mars; Ted L. Roush[1], James F. Bell III[2], and Richard V. Morris[3], [1]San Francisco State Univ. and NASA Ames Research Center, MS 245-3, Moffett Field, CA 94035-1000, [2]NRC/NASA Ames Research Center, MS 245-3, Moffett Field CA 94035-1000, [3]Code SN4, NASA Johnson Space Center, Houston TX 77058.

Ample evidence exists indicating abundant iron bearing minerals are present on Mars. In situ analyses performed by the Viking Landers were interpreted as indicating the presence of iron-rich materials, including iron oxides [1-5]. However, since the Viking Landers did not carry any instruments capable of determining mineralogy, the specific iron-bearing phases remains uncertain. Interpretations of continuing visual, near-, mid- and far-infrared spectroscopic observations of Mars from the Earth [e.g. 6,7] and spacecraft over the past 20 years [6-13] have revealed that the ferric mineralogy occurs in two distinct forms: (1) nanophase or truly amorphous Fe^{3+}-bearing materials [14,15] that spectrally resemble certain terrestrial palagonites [e.g. 16-20]; and (2) well-crystalline ferric oxides like hematite (α-Fe_2O_3), maghemite (γ-Fe_2O_3), or magnetite (Fe_3O_4) [1,5,15, 21-24]. The available data indicate that the poorly-crystalline "palagonite-like" phases are spectrally dominant [e.g. 6,7] and that the well crystalline ferric oxides cannot constitute an abundance of more than about 4-8 wt. % [24]. Information regarding the crystalline or amorphous nature of the iron-bearing (and other) surface materials on Mars can provide insight into the availability of liquid water at the surface and the duration, mode, and extent of weathering. The research presented here represents the initial phase of a broader project that is intended to provide data in the mid- and far infrared spectral region for both well-characterized iron oxides/oxyhydroxides and poorly crystalline or amorphous materials (e.g. palagonites). Such information can be useful in the interpretation of both past and future thermal infrared observations of Mars.

In the near- to middle infrared (2.5-25 μm), spectral features arise from vibrational motions of atoms and molecules which compose the materials. These fundamental modes are much more intense than any associated combination and/or overtones of these modes, and hence remote sensing in the infrared is extremely sensitive to minor concentrations of these absorbing species [25].

We have measured the transmission spectra of three ferric oxides (2 α-Fe_2O_3 samples, and 1 γ-Fe_2O_3 sample) and two ferric oxyhydroxides (α-FeOOH and γ-FeOOH). The physical and chemical properties of these samples have been previously reported along with measurements of their reflectance in the 0.3- to 2.1 μm spectral region [21]. A small amount (approx. 1 mg) of each sample was mixed with KBr powder while both were immersed in alcohol. After the alcohol evaporated, 200 mg of the resultant mixture was pressed into a cohesive pellet using a standard 13 mm KBr pellet die. Using the facilities at the NASA Ames Astrochemical Laboratory, with the cooperation of Drs. Robert Bohn, Scott Sandford and Louis Allamandolla, the transmission of each pellet was measured at a resolution of 4 cm^{-1} using a Nicolet 7199 Fourier transform spectrometer in the 4000 to 400 cm^{-1} spectral domain, and was subsequently ratioed to the transmission of a pure KBr pellet. The resulting measurements of the ferric oxides are shown in figure 1 and of the ferric oxyhydroxides in figure 2.

Transmission spectra of both hematites exhibit strong absorptions with minima located at $\approx$ 18.3 and 20.9 μm separated by a maximum near 20 μm. All are consistent with previous measurements [26,27,28]. Additional transmission minima occur near 2.9, 6.1, 7.1, 8.8, 9.5, 11.4, and 17.3 μm for HMS3. The transmission spectrum of γ-Fe_2O_3 exhibits several minima located near 14.4, 15.7, 18.2, 20.8, 22.7, and 23.7 μm, and several weaker features located near the same positions as those of HMS3.

The transmission spectrum of α-FeOOH exhibits minima located near 3.2, 5.6, 6, 8.8, 11, 12.5, 16.6, 21.2, and 23.6 μm, and a hint of a feature near 15 μm that is obscured by imperfect correction for atmospheric CO_2. All of these, except the 5.6 μm band, are comparable to previously reported features [26,29,30]. The transmission spectrum of γ-FeOOH exhibits minima located near 3.2, 5.0, 6, 8.6, 9.8, 13.3, 16.8, 18.9 20.8, and 23.9 μm. The bands at 3.2, 8., 9.8, 1.8, 18.9, and 23.9 μm are

similar to bands previously reported [29].

This preliminary study has demonstrated that crystalline ferric oxides and ferric oxyhydroxides exhibit complex spectral features at thermal wavelengths. Some of these features suggest that thermal infrared observations of Mars can provide significant insight into the ferric mineralogy of that planet. The results of this study suggest that emissivity spectra of crystalline ferric oxides and ferric oxyhydroxides may prove quite important for the interpretation of thermal infrared spectral observations of Mars.

References: [1]R.B. Hargraves et al. (1977) JGR, 82, 4547 [2]P. Toulmin et al. (1977) JGR, 82, 425 [3] B.C. Clark et al. (1977) JGR, 82, 4577 [4]B.C. Clark et al. (1982) JGR, 87, 10059 [5]J.B. Pollack et al. (1977) JGR, 82, 4479 [6]L.A. Soderblom (1992) in Mars (H.H. Kieffer et al., eds.), 557 [7]T.L. Roush et al. (1993) in Remote Geochemical Analysis (C. Pieters and P. Englert, eds), 37 [8]L.A. Soderblom et al. (1978) Icarus, 34, 44 [9] T.B. McCord et al. (1982) JGR, 87, 10129 [10]J.B. Adams et al. (198) JGR, 91, 8098 [11]R.E. Arvidson et al. (1989) JGR, 94, 1573 [12]S. Murchie et al. (1993) Icarus, in press [13]J.F. Mustard et al. (1993) JGR, 98, 3387 [14]R.V. Morris and H.V. Lauer Jr. (1990) JGR, 95, 5101 [15]R.V. Morris et al. (1989) JGR, 94, 270 [16] R.B. Singer et al. (1979) JGR, 87, 10159 [17]D.L. Evans and J.B. Adams (1980) PLPSC 11, 757 [18]R.V. Morris et al. (1990) JGR, 95, 14427 [19]J.F. Bell III et al. (1993) JGR, 98, 3373 [20]A. Banin (1992) LPI Tech. Rpt. 92-04, 1 [21]R.V. Morris et al. (1985) JGR, 90, 312 [22]J.F. Bell III et al. (1990) JGR, 95, 14447 [23]R.B. Hargraves et al. (1979) JGR, 84, 8379 [24]J.F. Bell III (1992) Icarus, 100, 575 [25]J.F. Bell III and T.L. Roush (1993) LPI Tech Rpt. 93-06, pt. 1, 2 [26]J.W. Salisbury et al. (1991) Infrared (2.1-25 μm) Spectra of Minerals, Johns Hopkins Univ. Press, 27 pp [27]Farmer, V.C. (1975) Infrared Spectra of Minerals, (V.C. Farmer, ed.) Mineral. Soc. Monograph 4, 183-204 [28]J.A. Gadsden (1975) Infrared Spectra of Minerals and Related Compounds, Butterworths, 277pp [29]Y.I. Ryskin, Infrared Spectra of Minerals, (V.C. Farmer, ed.) Mineral. Soc. Monograph 4, 137-181 [30]R.A. Nyquist and R.O. Kagel (1971) Infrared Spectra of Inorganic Compounds, Academic Press, NY, 495pp

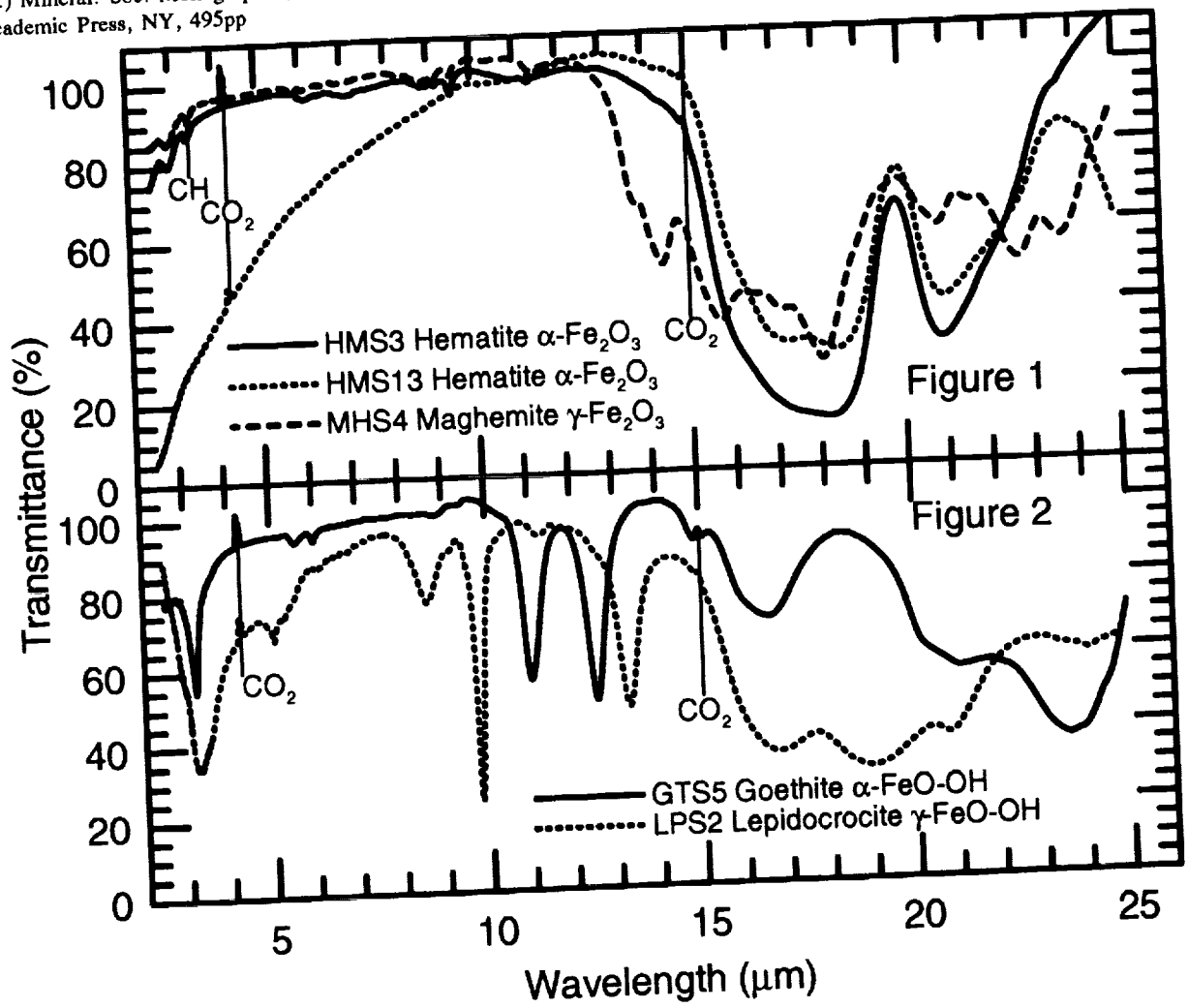

MORE SHOCK RECOVERY EXPERIMENTS ON MESOSIDERITE ANALOGS

L. R. Rowan, NASA-Johnson Space Center, SN4, Houston, TX, 77058 and D. W. Mittlefehldt, Lockheed ESC, 2400 Nasa Rd. 1, Houston, TX, 77058

Mesosiderites, a small but unique group of stony-iron meteorites with affinities to howardites, eucrites and pallasites [1], remain enigmatic in terms of their petrogenesis. They are composed of approximately equal weight proportions of Fe-Ni metal plus troilite and gabbroic, basaltic and orthopyroxenitic materials. The metal and silicates, which display variable grain sizes and shapes, are delicately intermingled, forming irregular grain boundaries that have been attributed to a wide range of origins from subsolidus metamorphism [1] to supersolidus igneous processes [2]. Perhaps the most relevant question regarding the petrogenesis of mesosiderites is: what is the source and duration of heating that could produce the unequilibrated textures and chemistry of these meteorites? A leading candidate appears to be impacts of metallic core fragments with a differentiated asteroidal surface [2, 3]. This provides not only a suitable source of heat, but also the metal component uniquely required by mesosiderites. We have continued a series of shock recovery experiments on mesosiderite analogs initiated earlier [4] and have found textural and chemical similarities that support an impact-derived origin for these unusual meteorites.

Method: The experiments involved shock loading a metal-silicate powder mixture in a 20 mm bore propellant gun following the techniques described in [4, 5]. The silicate fraction for all of our experiments was a Bushveld gabbro [5] ground and sieved to 75-150 μm. Three series of experiments were performed in which the metal fraction (sieved to 75-150 μm) was varied from 1. Stainless steel 304 (SS304), 2. SS304 plus troilite and 3. Meteoritic Fe-Ni metal. For the first two series, the starting mixtures consisted of equal weight proportions of gabbro and SS304. The troilite in the second series was added to each gabbro-SS304 mixture in 5% increments from 5 to 15%. For the last series, the starting mixture was equal weight proportions of gabbro and Fe-Ni metal from Antarctica mesosiderite RKPA79015. Thin sections were made of the recovered samples for textural studies (optical microscope and scanning electron microscope) and chemical analyses (electron microprobe).

Results: In the first series of experiments (SS304) the overall textures ranged from a compacted, non-porous, non-melted network of interlocking grains in which the metal filled the spaces around the silicates (104 kbars) to a frothy, vesicular mixture of melted metal and silicates (436 kbars). The first evidence of melting of the metal appeared at 148 kbars where some metal formed minute, rounded veinlets and even rarer sponge metal. Sponge metal as defined in the preliminary work [4] consists of rounded metal blebs full of elliptical to spherical silicate inclusions. The size of the inclusions is variable from sub-micron to tens of microns in diameter and some of the larger inclusions (>10 μm) contain metal spheres. The silicates in the 148-kbar sample were brecciated and generally subhedral. In the 302-kbar sample, melted SS304 is common as veinlets, sponge metal and isolated metal spheres. Zones of elongated sponge metal blebs and streams of spheres are evidence that flow developed in the sample. The streams of spheres are usually contained in melted pyroxenes that have surrounded and partially invaded plagioclase grains. Some of the silicates have melted and tend to be vesicular. In the 436-kbar sample these melt textures are more abundant. Chemical analyses of the sponge metal showed depletions in Cr and Mn and small enrichments in Si, Cu and Co relative to Fe. Some of the silicates showed highly variable enrichments of FeO and Cr_2O_3, but negligible additions of NiO. Analyses of silicate inclusions in the sponge metal of the 436-kbar sample showed consistent enrichments in Cr_2O_3 and MnO and depletions in SiO_2. These chemical variations suggest that the SS304 was being oxidized and mixed with the silicate.

ANALOGS OF MESOSIDERITES; Rowan, L.R. and Mittlefehldt, D. W.

In the second series (SS304 + troilite), the textural changes as a function of increasing pressure were similar to the first series. In the low pressure (~150 kbars) samples most of the troilite occurs as sub-angular, pitted, isolated grains that have not reacted with the SS304 or silicates. The higher pressure (~300 and 450 kbars) samples show increasing degrees of melting and mixing of the troilite with the SS304, such that Fe-Cr-S-rich rims were formed around the melted SS304. Some of these rims branched out from the main metal masses to form thin veins along cracks and grain boundaries in the silicates.

In the third series (meteoritic metal), the textures are similar to those seen in the first series, but the pressures required for significant melting are higher. The first evidence of melting is observed in the 280-kbar sample which has similar textures as the ~150 kbars samples from the first two series. Abundant melt textures are seen in the 710-kbar sample versus the ~300-450 -kbar samples from the first two series. Preliminary chemical analyses revealed enrichments of FeO and NiO in some of the melted silicates.

Conclusions: Our textural and chemical analyses indicate that the shocked analogs possess some significant similarities to mesosiderites, particularly when comparing the unique and intricate metal textures. An impact origin of these meteorites seems plausible, although not conclusive. The sponge metal and veins as noted previously [4] are similar to some mesosiderite textures. The sponge metal and the streams of metal spheres would also help provide a way to prevent efficient metal-silicate segregation that models involving the formation of large impact-melt sheets [2, 6] require. The isolated troilite that is abundant in the lower pressure samples is similar to the troilite in mesosiderites described by [1] that led to a subsolidus metamorphic model, while the Fe-Cr-S rims and veins found in higher pressure samples are texturally similar to the anastomosing troilite veins in mesosiderites described by [2] that led to an impact-melt model. These comparisons suggest that different mesosiderites may be showing different degrees of shock pressure and subsequent heating. Finally the compositional variations in the sponge metals and silicates within the sponge metals suggest that redox reactions produced these changes; these observations fit well with the theory that FeO reduction occurred simultaneously with metal-silicate mixing in mesosiderites [7].

REFERENCES: [1] Powell (1971) *Geochim. Cosmochim. Acta 35*, 5-34. [2] Floran *et al.* (1978) *Proc. Lunar Planet. Sci. Conf. 9th*, 1083-1114. [3] Wasson and Rubin (1985) *Nature 318*, 168-170. [4] Mittlefehldt *et al.* (1991) *Lunar Planet. Sci. XXII*, 903-904. [5] Hörz *et al.* (1984) *Proc. Lunar Planet. Sci. Conf. 15th, JGR 89*, C183-C196. [6] Hewins and Harriott (1986) *Proc. Lunar Planet. Sci. Conf. 16th, JGR 91*, D365-D372. [7] Mittlefehldt (1990) *Geochim. Cosmochim. Acta 54*, 1165-1173.

ACKNOWLEDGEMENTS: We wish to acknowledge the technical support of Frank Cardenas who conducted the experiments at the JSC experimental impact laboratory. L.R.'s work was supported by a National Research Council - NASA/JSC Research Associateship.

CONTACT METAMORPHISM IN ORDINARY CHONDRITE IMPACT BRECCIAS: IMPLICATIONS FOR THE IMPACT HEATING OF CHONDRITE PARENT BODIES.

Alan E. Rubin, Institute of Geophysics and Planetary Physics, University of California, Los Angeles, CA 90024, USA.

A key problem in meteorite research is the identification of the heat source responsible for the metamorphism of chondrites. Although there are several arguments against impacts being the primary mechanism responsible for heating meteorite parent bodies [1], there are numerous examples of chondrites containing impact-melted materials. These range from small melt pockets in some ordinary chondrites (OC) to OC impact-melt breccias that contain no relict chondritic material. In order to determine the relationship between chondritic clasts and adjacent impact melt, I examined thin sections of seven OC impact-melt breccias. The melted regions of Rose City and Chico contain 20-300 μm polycrystalline olivine aggregates composed of ~20-μm faceted olivine crystals with 120° triple junctions, indicative of a high degree of textural equilibrium. These aggregates formed from mosaicized olivine grains by contact metamorphism with the surrounding impact melt. A total of 11 OC are impact melt-breccias that contain significant amounts of both impact melt and relict chondritic material; nine are type 6; two are type 5. This distribution of petrologic types differs from that of observed falls at the 75% confidence level, suggesting that the chondritic portions of these breccias were metamorphosed by impact heating. These impact events probably heated a larger fraction of OC to subsolidus temperatures.

The olivine aggregates with the 120° triple junctions constitute ~5 vol.% of the melt in some sections of Rose City and Chico; many of the aggregates have resorbed margins indicating that they were entrained in the melt long enough to be partially digested. In most aggregates the individual olivine grains have undulose extinction, but lack planar fractures and have not been darkened by finely dispersed opaques. Besides olivine aggregates, the Rose City melt contains a few 100-200-μm-size olivine grains that exhibit extensive darkening and strong mosaic extinction indicative of shock stage S5. It seems likely that the olivine aggregates with the 120° triple junctions formed from the mosaicized olivine grains by contact metamorphism with the surrounding 1500 K melt. Although it is difficult to discern the precise degree of metamorphic recrystallization in highly shocked OC, it appears that contact metamorphism may also have affected the portions of Rose City that border the melt. These regions contain few discernable chondrules and appear to be type 6, suggesting an equilibration temperature of ~1120 K [2]. At a distance of >1 cm from the melt, the chondritic structure is more pronounced, suggesting type 5 (~1000 K).

Eleven OC breccias have been reported to contain substantial amounts of both solidifed melt and relict chondritic material; these include H5 Rose City [3], L6 Shaw [4], L6 Paranaiba [5], H6 Yanzhuang [6], L6 Belle Plaine [7], L6 Chico [8], LL6 Y790964 [9-11], LL6 Y790143 [9], L5 Cat Mountain [12], L6 Orvinio [13] and L6 Taiban (this study). (Although Taiban is listed as L5 [14], I reclassified it as L6.) There are two type-5 OC (18%) and nine type-6 OC (82%) among these melt breccias. In contrast, the distribution of petrologic types among 609 well characterized OC falls is 26 type 3 (4%), 78 type 4 (13%), 185 type 5 (30%) and 320 type 6 (53%) [14]. A χ^2 goodness-of-fit test shows that χ^2=4.16 with 3 degrees of freedom, indicating that the distribution of petrologic types among the melt breccias differs from that of observed falls at the 75% confidence level. It thus is probably not a coincidence that the relict chondritic material in these OC impact-melt breccias is so metamorphosed; it seems likely that the material was heated by shock processes, either by contact metamorphism with the adjacent melt or by residual impact heat.

CONTACT METAMORPHISM IN ORDINARY CHONDRITE IMPACT BRECCIAS: Rubin A.E.

I estimate that approximately 3000 independent OC have been reported worldwide to date. The total number of OC impact-melt breccias reported includes the 11 listed above as well as rocks that have been so extensively melted that little or no chondritic material remains; among the latter samples are "L7" Ramsdorf [15], "LL7" Y74160 [16], "L7" LEW88663 [17,18] and "L7" PAT91501 [18]. This survey is undoubtedly incomplete because of the many poorly characterized OC. I estimate that the total number of OC impact melt-breccias is twice that listed above, implying that impact melt-breccias constitute ~1% of OC. Although some of these breccias (e.g., Chico) have relatively young ^{39}Ar-^{40}Ar ages [8], others (e.g., Shaw) formed by impacts 4.4-4.5 Ga ago [19]. This is consistent with the ^{39}Ar-^{40}Ar data of heavily shocked OC which show that about 50% formed ≥4.4 Ga ago [20]. I therefore assume that 0.5% of OC are impact breccias that formed 4.4-4.5 Ga ago.

Geothermometric calculations indicate that the melt portions of the OC impact melt-breccias reached temperatures of ~1500 K [e.g., 18]. It is probable that during these impact events some larger fraction of OC reached subsolidus temperatures that were sufficient to cause significant metamorphism. The specific heat of an average L chondrite is about 0.18 cal g^{-1}; assuming that the initial temperature of the OC parent body was 250 K and that the OC melting temperature was 1500 K, I find that the amount of heat required to bring an L chondrite to the melting temperature is 225 cal g^{-1}; the heat of fusion requires an additional ~75 cal g^{-1} to actually cause melting. Thus, early-solar-system impact events provided 300 cal g^{-1} to 0.5% of the OC. In order to model the percentage of OC affected by diminishing impact heat, I took the inverse approach and assumed that these early impact events were responsible for metamorphosing all of the type 4-6 OC; I also assumed that all OC received at least 25 cal g^{-1} from these impact events. Given the distribution of type 4-6 OC among observed falls [14], a thermal model can be derived. The model indicates that 7% of the OC reached temperatures of ≥1500 K (although most did not receive the additional input of heat necessary to actually cause melting), 21% reached ≥1300 K (where metallic Fe-Ni and troilite should be molten), 53% reached ≥1120 K (equivalent to petrologic type 6), 83% reached ≥1000 K (equivalent to type≥5), and 96% reached ≥920 K (equivalent to type≥4). The major prediction of this model is that 21% of OC were heated sufficiently 4.4-4.5 Ga ago to mobilize substantial amounts of metallic Fe-Ni and troilite. Such OC would be "black chondrites" exhibiting extensive silicate darkening. Britt [21] found that 14% of OC falls are black chondrites; if regolith breccias are included, this increases to 17%. Given the uncertainties, these values are in good agreement with that predicted by the model. Thus, impact events seem to be a viable mechanism for metamorphosing ordinary chondrites.

References: [1] Wood J.A. and Pellas P. (1991) in *The Sun in Time*, Univ. Arizona, 740-760; [2] Dodd R.T. (1981) *Meteorites*, Cambridge; [3] Fruland R.M. (1975) *Meteoritics* **10**, 403-404; [4] Taylor G.J. et al. (1979) *GCA* **43**, 323-337; [5] Keil K. et al. (1977) *Rev. Bras. Geo.* **7**, 256-268; [6] Xie X. et al. (1991) *Meteoritics* **26**, 411; [7] Reimold W.U. et al. (1985) *LPS* **16**, 693-694; [8] Bogard D.D. et al. (1990) *LPS* **21**, 103-104; [9] Sato G. et al. (1982) in *LPI Tech. Rpt.* **82-02**, 120-122; [10] Takeda H. et al. (1983) *LPS* **14**, 771-772; [11] Miyamoto M. et al. (1984) *JGR* **89**, 11581-11588; [12] Kring D.A. (1993) *LPS* **24**, 823-824; [13] Smith B.A. and Goldstein J.I. (1977) *GCA* **41**, 1061-1072; [14] Graham A.L. et al. (1985) *Catalogue of Meteorites*, Arizona Press; [15] Begemann F. and Wlotzka F. (1969) *GCA* **33**, 1351-1370; [16] Takeda H. et al. (1984) *EPSL* **71**, 329-339; [17] Harvey R.P. (1993) *Meteoritics* **28**, 360; [18] Mittlefehldt D.W. et al. (1993) *Meteoritics* **28**, 401-402; [19] Enright M.C. and Turner G. (1977) *Meteoritics* **12**, 217; [20] Wasson J.T. (1985) *Meteorites--Their Record of Early Solar-System History*, Freeman; [21] Britt D.T. (1991) *The Meteorite Record as Clues to Asteroidal Regolith Processes*, Ph.D. thesis, Brown University.

COMPARISON OF MARS SINUOUS RIDGES WITH TERRESTRIAL LINEAR DUNES: OBSERVATIONS FROM THE FIELD; *Steven W. Ruff, Department of Geology, Arizona State University.*

Sinuous ridges observed in the Dorsa Argentea region near the south pole of Mars (Figure 1) are the subject of continuing inquiry and debate [1,2] The characteristics of the ridges have been described in some detail [3] but the mode of formation for these unusual land forms remains elusive. The two most often cited terrestrial analogs for the ridges are glacial eskers [2] and linear dunes [1]. Observations of linear dunes from field work are the subject of this study.

An important clue to the origin of the ridges may lie in the understanding of ridge intersections which give rise to the braided and dendritic patterns seen in the Viking images. These intersections can be described as either an 'X' or 'Y' shape. On the earth, Y-junction linear dunes are a common dune type in many of the great deserts of Australia [e.g. 4]. X-shaped junctions in linear dunes, though rarely described, are evident in photographs of some of these deserts. In the literature, descriptions of dune intersections are few and the mechanism for their formation is apparently undocumented. The lack of information on linear dune junctions and the potential for this knowledge to shed light on the origin of martian ridges makes a case for field work. A little known dune field in west central Arizona is providing the author with the opportunity to pursue this work.

An area known as the Cactus Plain east of Parker Arizona is host to a small dune field containing a variety of dune forms (Figure 2) [5]. Most significant for this study are the linear dunes. These dunes have many of the same features as their Australian counterparts, namely, similar intersections and notable sinuosity. This contrasts with the more parallel, non-intersecting linear dunes found in northern Arizona as well as many African deserts. The Cactus Plain linear dunes differ from the Australian dunes in scale, both in the area covered by the dunes as well as the size of individual dunes. Many Australian linear dunes are tens of kilometers long and a tens of meters high [e.g. 6]. The Cactus Plain variety are approximately an order of magnitude smaller; a few kilometers in length and several meters high. In both cases, the dunes are vegetated. The role of vegetation in the formation and evolution of linear dunes is still controversial [e.g. 7,8].

In previous work [3], some of the Mars ridge intersections were described as overlapping. It appears as if one ridge actually rests on top of another (arrows in Fig 1). This observation is difficult to explain. But visible in the photo of the Cactus Plain are similar intersections which give the appearance of overlapping. The goal of the first field visit to the dunes was to examine two of these intersections.

Upon inspection in the field, both of these intersections show a different situation than

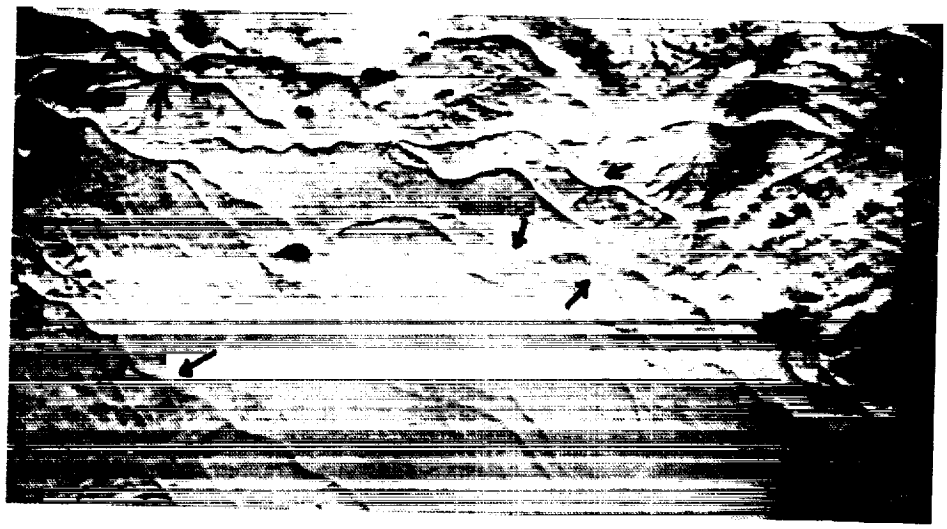

Figure 1. Sinuous ridges in Dorsa Argentea. Arrows indicate ridge intersections of interest. (VO 421B53)

MARS RIDGES: COMPARISONS FROM EARTH FIELD WORK; S.W. Ruff

was interpreted from the photo. In one case (arrow A, Fig 2) the dune stops short of the apparent intersection. On the other side of this failed intersection, a short dune branches off the main one, forming a Y-junction with just the right orientation to give the appearance of continuity with the non-intersecting dune segment.

The other intersection (arrow B, Fig 2) proved to be more interesting. In this case the intersection is real, though it appears to be the result of one dune migrating into another and touching along a small segment of each dune. The evidence for this scenario comes from an obvious difference in sand color from one dune to the other. Each dune maintains the same color along its length. This color distinction does not cross the intersection into opposite dune segments. Rather, sand color is continuous into adjacent segments of the intersection. If sand color is assumed to be a unique characteristic of a given dune, then it appears that these two dunes have merged.

Though intuitively appealing, lateral migration of linear dunes has been difficult to document [see 9]. In fact, lateral sand transport is contrary to the accepted morphodynamic description of linear dunes as *longitudinal* dunes where sand transport is roughly parallel to the dune. Evidence of lateral migration does exist [9] but this mechanism, to my knowledge, has not been proposed to explain the formation of dune junctions. In this context, the apparent lateral migration of the two Cactus Plain dunes to form an X-junction is noteworthy.

The failure to verify the photogeologic interpretation of overlapping dune intersections results in two conclusions: 1) overlapping intersections may exist but not at the two candidate sites of this study or 2) overlapping intersections do not exist and are simply the result of misleading images. In either case, a re-examination of the Mars ridges is in order.

Photogeologic interpretations of the Mars sinuous ridges are hampered by the relatively low resolution of the Viking images and the obscuration of some of the ridges by a mantle of lighter material. But in light of results from the Cactus Plain study, the significance of overlapping intersections is reduced. Instead, a mechanism by which simple linear dunes can evolve into more complex patterns is available. If the Mars ridges are linear dunes, the complexity of their patterns can be explained by the action of lateral migration and merging of adjacent dunes.

REFERENCES: [1] Ruff, S. W. (1992) In Haberle, R. M. et al., eds. *Workshop on the Martian Surface and Atmosphere Through Time.* LPI Tech. Rpt. 92-02, Lunar and Planetary Institute, Houston, 126-27. [2] Kargel J.S. and Strom, R.G. (1992) *Geology,* **20**,3-7. [3] Ruff, S. W. and Greeley, R. (1990) *Lunar Planet. Sci. Conf.,* **XXI**, 1047-48. [4] Mabbutt, J. A. (1968) *Austr. Geogr. Stud.* **6**, 139-50. [5] Breed, C. S. et al. (1984) In Smiley, T. L. et al. eds. *Landscapes of Arizona,* University Press of America, 505 pp. [6] Breed, C.S, and Grow, T. (1979) In Mckee, ed. *A Study of Global Sand Seas,* U.S.G.S. P.P. 1052, 253-302. [7] Ash, J.E. and Wasson, R.J. (1983) *Zeit. Geomorph. Suppl.,***45**, 7-25. [8] Thomas, D.S.G (1988) In Dardis, G.F. and Moon, B.P. eds. *Geomorphological Studies in Southern Africa.* [9] Rubin, D. M. (1990) *Earth Surf. Proc. Land.* **15**,1-14.

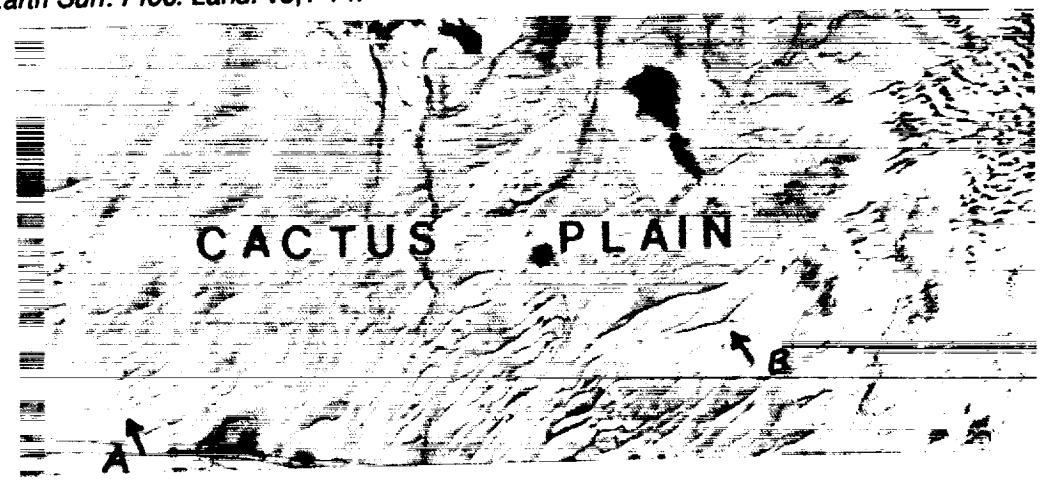

Figure 2. Linear dunes of the Cactus Plain. Arrows indicate field sites.

CHONDRULE FORMATION IN RADIATIVE SHOCK

T.V. Ruzmaikina (Lunar and Planetary Laboratory, University of Arizona, Tucson 85721), and **W.H. Ip** (Max-Planck-Institut für Aeronomie, D-3411 Katlenburg-Lindau, Germany)

Introduction The most abundant constituent of most groups of chondrite meteorites are chondrules - those are sub-millimeter to millimeter-sized, spherical-shaped grains, composed of silicates [1]. Physical, mineralogical, and isotopic properties of chondrules strongly indicate that they were formed by rapid melting and resolidification of preexisting solids composed from primitive material. The chondrule precursors were heated to temperature about 1800 K in short high temperature events, followed by cooling with a rate 10^2 to 10^3 K/hr. A significant abundance of chondrules in almost all types of chondrites reveals high efficiency of the energy sources in conversion of precursor material into liquid droplets. Lightning discharges and flayers in the solar nebula [2], and melting of chondrule precursors by the interaction with the gas in an adiabatic accretional shock [3,4] or in the shocks (of unspecified nature) within the solar nebula [5] were discussed as possible mechanisms for chondrule formation.

Summary. In this paper we reconsider heating of chondrule precursors in an accretional shock, i.e. in a shock produced by infalling gas, when it hits the solar nebula. This shock had inevitably developed at the stage of solar nebula formation, and a significant fraction of infalling gas and dust had been reprocessed in this shock [6]. In contract to earlier papers, we took into account cooling of the postshock gas. We took into account cooling by dissociation of hydrogen molecules, rotational cooling by dipole molecules H_2O, OH, CH, CO, HCl, HD (according to [7]), and radiative cooling by small dust particles. We assume that the material has a solar bulk composition and that 0.05% (of the mass) of the condensible elements is concentrated in small dust particles, which include in the gas cooling. For the abundance of dipole molecules, we assume that the bulk of atoms of O and half of C are in a molecular form, and that less abundant elements are equally distributed between different molecules containing them. Other parameters were taken as follows: the mass and angular momentum of protosolar cloud $M_{PC} = 1.1\ M_\odot$, $J_{PC} = 2 \cdot 10^{52}$ g cm^2 s^{-1}, the surface density of the solar nebula $\Sigma = 10^4\ (R/1\,\mathrm{AU})^{-1}$ g cm^{-2}, and temperature in the solar nebula, far from the shock front, is $T_r = \left(T_{en}^4 + T_{eff}^4\right)^{1/4}$. where $T_{en} = 1200\ (R_{ce}/R_{p\odot})^{1/2}\ (R/1\,AU)^{-1}$ K, $R_{p\odot}$ $(= 3\,R_\odot)$ is the radius of protosun, R_{ce} is the centrifugal radius of infalling material which is ≤ 2 AU in our case, and T_{eff} is a photospheric temperature of viscous disk, which is approximated as $T_{eff} \simeq 475\ (R/1\,\mathrm{AU})^{-3/4}$ K.

We found that shocked gas cools fast by dipole molecules and small dust particles, and it results in a sharp increase of gas density in the postshock region. Sub-millimeter and larger grains cross the region of cooling and penetrate in cooled and compressed postshock gas. As a result the grains are heated by the drag stronger than in the shock without cooling. This makes possible melting of dust aggregates (chondrule precursors) in the radiative accretional shock during formation of the solar nebula, even when the matter is transparent for the thermal radiation of the aggregates. The maximal radius of region of chondrule formation increases with the density of infalling gas. Clumpy accretion [8,9], and enhancement of density in the vicinity of the centrifugal radius of infalling gas [4,10] could provide the necessary densities of the infalling gas at distances of the asteroid belt.

Postshock region of cooling. Fig. 1a÷1c shows distribution of gas density in the postshock region for the normal component of infall velocities 15; 18; 21; 24; 27; 30; and 33 km s^{-1}. These velocities are equal to parabolic ones (for 1 $M_\odot$) at distances 8.73; 6.07; 4.46; 3.41; 2.70; 2.18; and 1.80 AU, respectively. The average densities of the preshocked gas at these distances are $0.61 \cdot 10^{10}$; $0.11 \cdot 10^{11}$; $0.17 \cdot 10^{11}$; $0.25 \cdot 10^{11}$; $0.36 \cdot 10^{11}$; $0.49 \cdot 10^{11}$; $0.65 \cdot 10^{11}$ cm^{-3}, assuming accretion rate $1 \cdot 10^{-5}\ M_\odot$ yr^{-1} (Fig. 1a). (For the fragmented accretion, density of clumps could be significantly larger while the average rate of infall is the same.) The density of the infalling gas is assumed 10 times larger (b), and 50 times larger (c) than for the case (a); velocities and the distances are the same.

Grain Heating: Results. Evolution of temperature of 1-mm grains is determined by a balance between their heating due to gas drag and UV radiation from the shock front, and cooling of grains by their thermal radiation. When particles are melted or evaporated, the latent heat of these phase transitions is an additional important sink of energy. We assume, that the region of grain heating is transparent for their thermal radiation. In the cooling postshock region heating of grains by UV-

C-3.

radiation is the same as in an adiabatic shock, with the same parameters, while the postshock region is transparent for UV radiation emitted by the shock front. Figure 2(a-c) shows the evolution of the temperature of 1 mm solid grain in the postshock region with the cooling for the postshock gas density distribution 1(a-c), respectively. Dotted lines are marked the temperature 1600 and 1800 K.

Formation of chondrule precursors. Models of chondrule formation in the accretional shock, associated with formation of the solar nebula, generate a question: as it possible that grains (as big as ~ 1 mm in size, and ~ 1 to a few 10^{-3} g in mass) could be formed before entering the solar nebula. A detailed (both analytical and numerical) consideration of the coagulation of interstellar dust particles in protostellar clouds, seem to, give a positive answer [11]. If the aggregate has a constant density, then $r_d \propto t^2$ for large t. Fractal aggregates with dimensions $D = 2.5, 2.3$, and 2.11, with the initial radii 10^{-5} cm reach 1 cm in $\leq 10 \cdot 10^6$ yrs for the fractals with $D \leq 0.54$, and 1 cm for $D \leq 2.43$. If the initial radius of grains is 10^{-4} cm and 10^{-4} cm, they reach 1mm and 1 cm in 8.0, 2.7, and $0.7 \cdot 10^6$ yrs, respectively. The typical mass of cm-size aggregates is comparable or exceeds that of chondrules. Grain coagulation is also effective in the inner part of infalling envelope, provided that the turbulence is amplified during collapse, because of transference into collapse of a fraction of the kinetic energy of the infall.

References

[1] Grossman, J.N. 1988. Formation of Chondrules. In *Meteorites and the Early Solar System*, (J.F. Kerrige, and M.Sh. Matthews, Eds.), pp.680-696. Univ. of Arizona, Tucson.

[2] Levy E.H. 1988. In *Meteorites and the Early Solar System*, (J.F. Kerrige, and M.Sh. Matthews, Eds.), pp.697-714. Univ. of Arizona, Tucson.

[3] Wood, J. (1984). *Earth Planet. Sci. Lett.*, **70**, 11–26.

[4] Ruzmaikina, T.V. 1990. *Lunar Planet. Sci. XXI*, 1053–1954.

[5] Hood, L.L., and M., Horanyi 1991. *Icarus* **93**, 259–269.

[6] Ruzmaikina, T.V., I.V. Khatuncev, and T.V.Konkina 1993. *Lunar Planet. Sci. XXIV*, 1225–1226.

[7] Hollenbach, D., and McKee, C.F. 1979. *Astrophys. J.,Suppl.*

[8] Graham, J.A. 1992. *Publ. Astron. Soc. Pacific* **104**, 479–488. **41**, 555–592.

[9] Boss, A.P., and J.A. Graham 1993. *Lunar Planet. Sci. XXIV*, 153–154.

[10] Cassen, P.M., and Moosman, A. 1981. *Icarus* **81**, 353–376.

[11] Weidenschilling, S.J., and T.V. Ruzmaikina 1993. *Astrophys. J.*, in press.

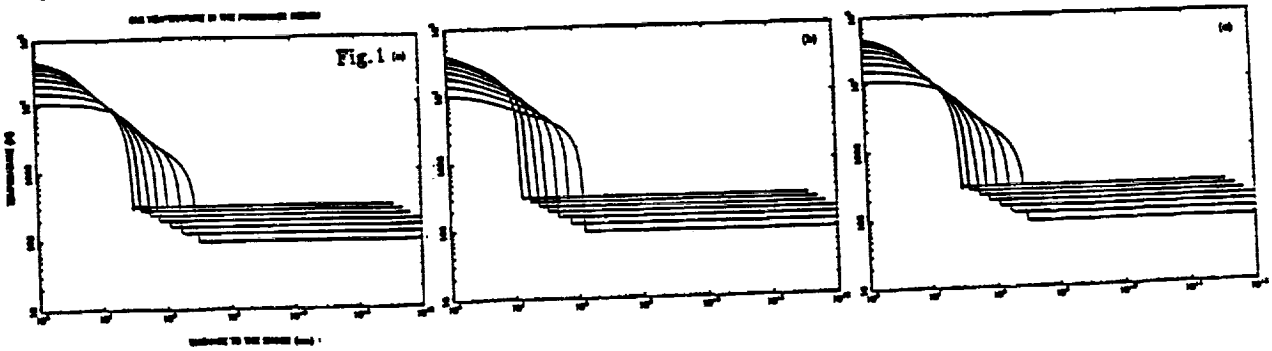

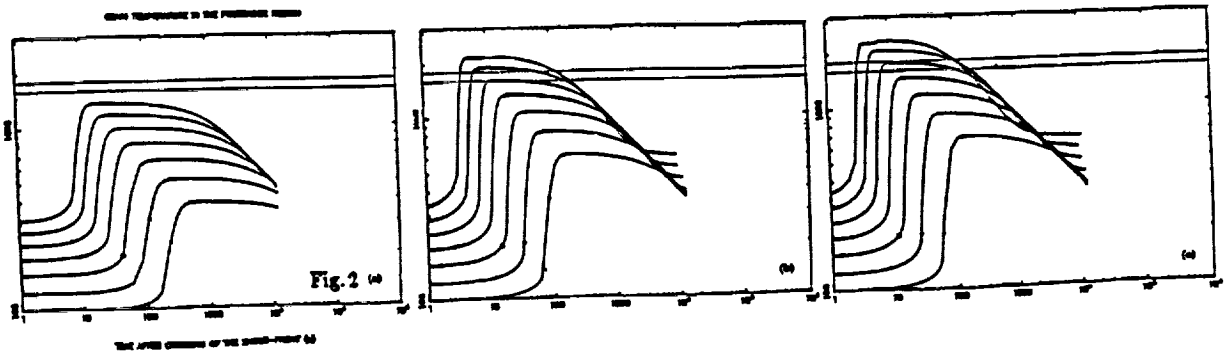

ENERGY PARTITIONING IN CATASTROPHIC COLLISIONS

Eileen V. Ryan and Donald R. Davis (Planetary Science Institute)

When two bodies collide, it is not clear how the kinetic energy is partitioned between the target and projectile. Previous studies [1, 2] have indicated that half the available energy goes into each of the impacting bodies, regardless of size, when both target and projectile are made of the same material. However, the partitioning that occurs for bodies made of different materials is unknown. Since different materials certainly exist in the solar system, among the main-belt asteroids, for example, it is important to understand how strength differences might affect collisional outcome. To discover the fragmentation energy partitioned into each body, we perform laboratory impact experiments using similar and different strength materials, and examine the fragment mass distributions that result from the disruption of both the target and the projectile. Results indicate that, indeed, there is equipartitioning of energy when identical materials are used. However, if a strong body is impacted into a weak one, more energy is partitioned into the weaker body.

Laboratory impact experiments [3] have shown that the degree of fragmentation undergone by a target body is dependent upon the projectile material used, as well as target/projectile material differences. For example, when strong cement mortar targets are impacted with weak mortar or ice projectiles, no damage is done to the target, even at specific energies large enough to produce a supercatastrophic fragmentation outcome using steel or aluminum projectiles. However, if the strong mortar target is hit with a projectile made of the same material, the damage produced is similar to that seen using aluminum, pyrex, or steel projectiles [4]. These variations in fragmentation outcome are possibly due to a change in the amount of collisional energy that is being partitioned into the target body for different material combinations.

The concept of energy partitioning is particularly important when determining a material's impact strength [5], or resistance to fragmentation in a collisional event. The impact strength of a body should be defined in terms of the fraction of collisional energy that is partitioned into it. However, it has been difficult to quantify how the energy is divided for dissimilar materials, so experimental determination of impact strengths has usually been made assuming 100% of the incoming kinetic energy is partitioned into the target body. This actually results in an upper limit to the impact strength, since the true energy partitioned into the object must be less than the total energy. A more accurate determination of impact strength can be made only when energy partitioning is more clearly understood.

Impact experiments using cement mortar in different target/projectile strength combinations were performed at velocities ranging from 100 - 229 m/s. For (6) of the (21) shots, it was possible to collect and measure 75% or greater of the fragment masses for each body, and we limit the present analysis to those experiments. Coloring is added to the mortar mixture so that target and projectile fragments can be distinguished. Figure 1 shows the resulting mass distributions (shot 930522) when strong mortar is impacted with strong mortar. The projectile is more comminuted than the target, consistent with an equal division of energy, but the projectile is somewhat less fragmented than expected. However, the scatter in collisional outcomes means that a more definitive result awaits further experimental results. A weak mortar target disrupted by a strong mortar projectile (shot 930503) is shown in Figure 2. The stronger projectile suffers far less damage than the weak target, in fact, too little damage for the assumption of equipartition of energy to hold. This implies that more than 50% of the kinetic energy is being partitioned into the weaker (target) body, and less than 50% into the projectile. Through additional analysis, the actual partitioning will be determined.

ENERGY PARTITIONING IN CATASTROPHIC COLLISIONS, E.V. Ryan and D.R. Davis

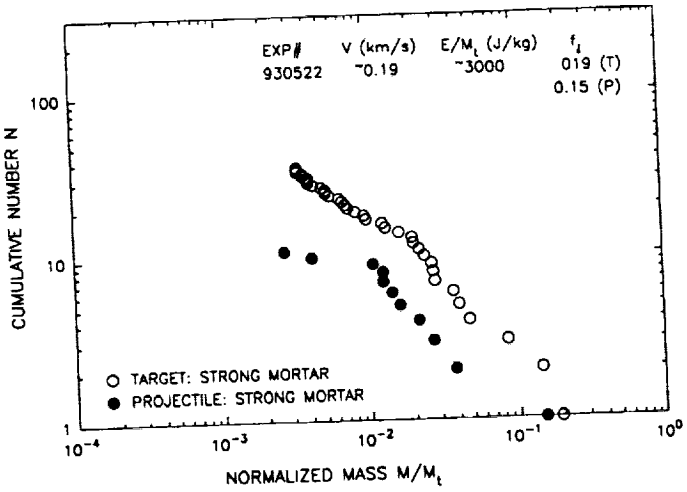

Figure 1: Cumulative fragment mass distributions for both target (open circles) and projectile (filled circles), resulting from the low-velocity impact (V_I = 190 m/s) of a strong cement mortar projectile into a target made of the same material. The mass of each fragment has been normalized to the original mass of the appropriate body, either the target (t) or projectile (p).

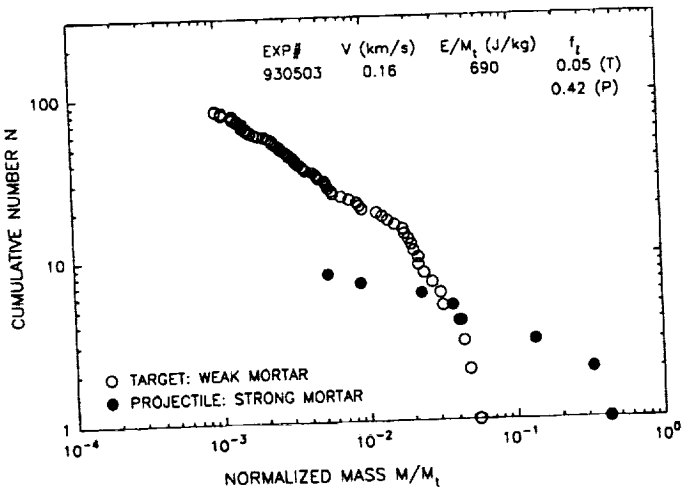

Figure 2: Cumulative fragment mass distributions for both target (open circles) and projectile (filled circles), resulting from the low-velocity impact (V_I = 160 m/s) of a strong cement mortar projectile into a weak cement mortar target. The mass of each fragment has been normalized to the original mass of the appropriate body, either the target (t) or the projectile (p).

References: [1] Hartmann, W.K. (1980), *Lunar Planet. Sci. XI*, [abstracts], 404-406. [2] Hartmann, W.K. (1988), *Lunar Planet. Sci. XIX*, [abstracts], 451-452. [3] Davis, D.R., and E.V. Ryan (1990), *Icarus* **83**, 156-182. [4] Martelli, G., et al. (1993), *submitted to Planetary and Space Science*. [5] Ryan, E.V., et al. (1991), *Icarus* **94**, 283-298.

PAST GEOLOGICAL EXPLORATION OF THE EARTH AND FUTURE GEOLOGICAL EXPLORATION OF THE PLANETS. Graham Ryder, Lunar and Planetary Institute, Center for Advanced Space Studies, 3600 Bay Area Blvd., Houston, TX 77058-1113.

The necessary predominance (and predilection) of sophisticated analyses of samples and observations from spacecraft characterizes the current exploration of the solar system, and appears to dominate some thinking about the future (e.g. [1]). However, exploration must eventually include *in situ* geological exploration of the planets (e.g. [2]), unless we are content to remain largely uncertain of inventories, histories, and processes. Many reviews (e.g. [3-6)] refer to geology, but their subject is generally either geomorphology or the geology of the very last events. Much of geological history is hidden within rock units. The geological exploration of planets must be undertaken with an understanding of how geological knowledge has been obtained on the earth, taking into account current and reasonably-soberly-projected technologies. A case study of the acquisition of geological knowledge in the classic area of NW Scotland provides a background for understanding some limitations of remote-sensing, spot landers or observations, and transect investigation. Terrestrial experience clarifies limitations in potential robotic investigation and the necessity of iteration, and suggest that human presence will be necessary [2] if geology is to be adequately understood. Non-epistemic factors will undoubtedly have a powerful influence on the methodology and schedule of planetary geological exploration.

Current Exploration Methodology and Limitations: Undeniably spectacular advances were made during the Golden Age of Planetary Exploration (e.g. [7]) in promoting the planets from obscure tiny discs to describable and "comfortably familiar" [4] bodies. The objectives of the exploration of the solar system include understanding the evolution of planets, and much of this is, or is interpreted from, their geological history. However, most of our information has come from observations made at a distance of several tens of kilometers at least, from flybys or orbit; only a few spot landings have provided direct contact information. We use landforms, supplemented to some extent by a little information on physical and chemical characteristics of the surface at a fairly gross scale, to interpret the geology [8]. This has been supplemented for Mars by meteorites from unknown locations. Our information about the Moon is more advanced, including observations by humans at the surface, sample analyses, and some *in situ* geophysical measurements. Nonetheless, if we studied the Earth only in that way, we would be far from understanding even the major processes currently operating. For processes and events that took place epochs ago a close investigation at the surface is necessary. Plate tectonics was not discovered from orbit and even if orbital data available in the '60s had suggested plate tectonics, it could not have been confirmed without contact investigations. Geological processes that took place in the Silurian Period cannot be determined from orbit, nor in any but the most superficial way from the analysis of samples alone.

Particularly important questions pertain to choices among conflicting hypotheses, iteration of observations, and knowing when a controversy is resolved. Sparse data lead not only to little constraining and multiplicity of concepts but allow no means of checking which (if any) are correct; they also of course hide real complexity. Thus even for the Moon we have no way to know whether its history prior to about 4.0 Ga was rather simple or rather complex, what tectonic and magmatic processes dominated, or whether a readable record even exists. Even for a subject as simple (?) as the origin of lunar granites, we have virtually no testable concept of generation of magma, crystallization processes, depth or size of magma bodies, or physical and tectonic aspects of intrusion (indeed, we do not know that intrusion, in the sense that there was magma movement, occurred at all). Yet these would be seen as essential components of studies of terrestrial granitic rocks.

In this age of detailed chemical and isotopic measurements on samples, it is easy (apparently) to overlook the geological context that must be determined both to obtain relevant samples and to interpret the data, and which is fundamental in its own right. The geological context has inevitably been derived from geological field work, which never has been (and is not now) foremost a sample collecting expedition. To properly plan future planetary exploration, one must be aware of how geological knowledge has been, is, and can be obtained, and both the advantages and limitations of particular strategies and techniques. It is important to know how geology is done (and not done), and the comparative information and cognitive response acquired with orbiting sensors, landed robots, and human sensors and manipulative abilities. The comparative information levels of *in situ* analysis, sample returns, selected transects, and detailed geological mapping must be assessed. Yet with the

GEOLOGICAL EXPLORATION OF THE PLANETS: Ryder G.

growth of Planetary Geology as a distinct field, increasing numbers of participants have little or no significant experience of terrestrial field studies such as geological mapping. Studies of how geological knowledge has been obtained on the earth provide the basis for understanding both the advantages and the limitations of possible methodologies of constructing planetary geological knowledge.

Acquisition of geological knowledge in NW Scotland: Oldroyd [9] made a definitive study of how the structure and geological history of the classic NW Highlands of Scotland were deciphered (up to ~1890). His study documents participants, methodologies, and controversies. I have used both his analysis and my own conclusions from visiting important sites at Assynt and Eriboll to attempt to construe how the geological history of the area might have been addressed by hypothetical planetary-style exploration. I have been more concerned with the cognitive aspects of field work than with the mechanical ones, and attempted to imagine what the participants might have been thinking when they made their observations. This was difficult insofar as it is almost impossible to suppress knowledge that those participants did not have.

NW Scotland is an appropriate example: classic significance, Oldroyd's study [9], my familiarity with it, reasonable exposure, general lack of fossils, and remoteness (though it is accessible). As now recognized, pre-Cambrian Lewisian gneiss is overlain by Torridonian arkosic sediments and then quartzite and limestone of Cambrian age. Overthrust from the east are the Moines (mainly meta-shales and -sandstones). All dip roughly to the south-east. The interpretation of the units and their relationships, hence the essential geological history, went through several shifts before the true nature was recognized. Although units could be reasonably described and correlated, there were two *main* sources of contention: a) whether the Moine and the Lewisian (modern names) were the same, b) the nature of the boundaries between units. Murchison inferred a continuous upward succession, at least partly for non-epistemic reasons, and was able to override objections about overlying metamorphic rocks and the need for faults; this extension of "Siluria" held sway for twenty years. Lapworth (among others) used a different working hypothesis, different methodology (including the use of right-way-up structures and exceptionally detailed mapping) to show that the boundary between the Moine and the rocks to its west was a zone of thrusting, with several thrust planes and numerous imbricate sheets. However, the resolution was a compromise as well as a new creation, and depended on the acquisition of better and more relevant data.

The distinction of the Moine from the Lewisian could probably not be made from orbital geochemistry. While ground chemical traverses could probably distinguish all the main units, the relationships could not be seen without examination of the boundaries themselves and the detailed mapping of their outcrop. Murchison saw the Moine thrust; he just never recognized it from his spot checks. It would have been clear to him perhaps if he had followed its trace and not been led too strongly by preconception.

Conclusions: Knowledge results from an interplay of data and cognition, and scientists are continuously involved in a series of feed-back loops within an agonistic field. The problem of underdetermination (sparse data) is particularly well demonstrated in historical geology, which is different, both methodologically and epistemologically, from most other sciences. Critical evidence for genetic interpretation (such as the nature of a boundary) might exist only in a few spots, and not be apparent in a broad view e.g. a rover traverse or a brief field survey. This was one of the reasons that Murchison was wrong in his interpretation of NW Scotland: generalized theory-induced limited sections and no detailed mapping. Many critical types of information, such as the nature of a contact, are unlikely to be definitively acquired with remote sensing, even from smart and sophisticated robots of a type we can reasonably envisage. One can argue that the planets have a more simple geological history than does the earth, and that less detail is necessary to understand them, but unless we do the detailed studies, we will not know that they are indeed more simple.

References: [1] U.S. Congress, OTA (1991) *Exploring the Moon and Mars: Choices for the Nation*, OTA-ISC-502, US Govt. Print. Off., 104 pp. [2] National Academy of Sciences, Space Studies Board (1988) *Space Science in the 21st Century, Planetary and Lunar Exploration*, National Academy Press. [3] Short N. (1975) *Planetary Geology*, Prentice-Hall, 361 pp. [4] Carr M. et al. (1984) *The Geology of the Terrestrial Planets*, NASA SP-469, 317 pp. [5] Mutch T. et al. (1976) *The Geology of Mars*, Princeton University Press, 400 pp. [6] Guest J. et al. (1979) *Planetary Geology*, Halsted Press, 208 pp. [7] Hinners N. (1989) *in The New Solar System* (Eds. Beatty J. and Chaikin A), Sky Publ. Corp./Cambridge U. Press. p. 3. [8] Greeley R. (1985) *Planetary Landscapes*, Allen and Unwin, 265 pp. [9] Oldroyd D. (1990) *The Highlands Controversy*, Chicago U. Press, 438 pp.

THE PETROGENETIC INTERPRETATION OF TINY FRAGMENTS OF EVOLVED LUNAR ROCKS: AN ANALOG ANALYSIS OF THE ABRIACHAN GRANITE, SCOTLAND. Graham Ryder and Jeffrey Gillis, Lunar and Planetary Institute, Center for Advanced Space Studies, 3600 Bay Area Blvd., Houston, TX 77058-1113.

Many lunar evolved plutonic rocks such as quartzmonzodiorites and granites exist only as small fragments. Most chemical analyses are performed on very tiny fragments, rarely as much as 50 mg and commonly much less. Frequently these analyses are interpreted as if they are representative of a much larger volume of rock, and quite specific petrogenetic constraints have been placed on the lithologies, the inferred parental magmas, and the evolutionary processes of the Moon from these fragments. We are studying splits of 5 small handsamples from a single exposure of the Abriachan granite (Scotland) in an attempt to see how much can really be inferred from the chemistry of such tiny fragments. We are making chemical analyses of splits in a hierarchy of sizes to see what inferences that are made from analyses of large fragments can still be reasonably inferred from analyses of small fragments. We are using multiple subsamples from each sample that are 1g, 50mg, and 20 mg, as well as mineral separates and thin sections from each sample. We report our first work on chemical analyses. The results suggest that petrogenetic interpretations made even on 50 mg samples should be treated with caution.

The Abriachan granite is one of the smaller of the Newer Caledonian Granites of Scotland, which are dominantly between 410 and 390 Ma old. Samples were collected at a roadcut on the NW shore of Loch Ness. Their grain size is similar to many lunar "granitic" rocks, major phases (quartz, feldspars, biotite, and hornblende) being about 1mm across. All 5 small handsamples (~4 to 7cm) were collected within about 10m of each other. We assume that all have an essentially common origin. Although part of the Abriachan granite is fenitised with secondary crocidolite infilling fractures along with aegirine and hematite [1,2], the outcrop was in the unfenitised part, and did not contain any obvious fenitisation features. Our analyses show that our samples are similar to those of "unaltered" Abriachan granite [2], not fenitised i.e. not enriched in any of Fe, Na, K, or Ba, nor depleted in Rb. The data show that the Abriachan granite is a fairly typical Newer Caledonian Granite, with a sloping rare earth pattern enriched in the light rare earths, and lacking a Eu anomaly (Figs. 1,2).

We have so far subjected 29 subsamples to neutron activation analysis for a typical suite of elements at the Johnson Space Center using the standard irradiation, counting, and reduction techniques. Each sample was broken up. For each sample, two subsamples each with a total mass of about 1g (A1, A2, B1, etc.), and two subsamples each about 50mg (A1-50, A2-50, B1-50, etc.) were taken. From sample D, 7 subsamples of about 20 mg (D1-20, D3-20, etc.) were also taken. Subsamples were selected only on the basis of appropriate size and freshness. All samples were ground to a homogenized fine powder for analysis. For the powders from the 1g samples, about 50mg was irradiated, with duplicates for sample D. Smaller subsamples were entirely irradiated. The Figures show only some of the rare earth element (REE) comparisons. (Because of higher uncertainties and some yet-to-be-explained anomalies in the Tb data, these are not included.)

We have not yet had time to fully investigate the data, and must be content to make general statements. Fig. 1 shows the REE abundances for all subsamples, normalized to chondritic abundances, and Fig. 2 those for the 1g subsamples alone. The REEs vary among subsamples by a factor of about 4 in abundance, although the patterns are reasonably similar; other incompatible elements such as Th vary similarly. The extremes are not 20 mg subsamples but 50 mg samples (A2-50 lowest and C2-50 highest). However, the range in the 1g samples is not much less than the range among all samples, and this is not much less than the range reported among average different rock types from zoned Newer Granites [e.g. 3]. The average for all 50mg subsamples is only slightly different from the average for all 1g samples. Among other elements, Fe varies by factor of 2.7, K by 2.7, Na by 2.5, and Rb by 2.3. In Figs. 3 to 6, the average of the 1g subsamples is used as the normalizing factor because that allows the differences to be seen more clearly.

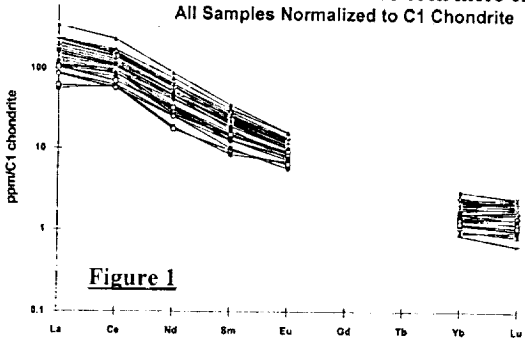

Figure 1

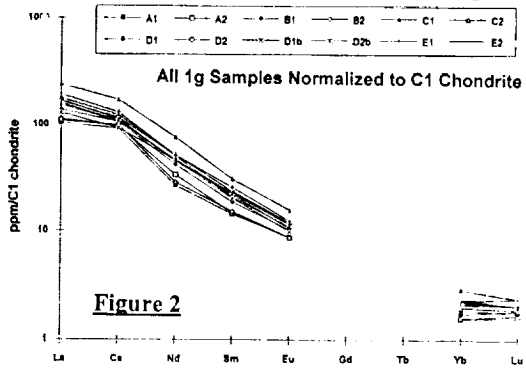

Figure 2

PETROGENETIC INTERPRETATION ABRIACHAN GRANITE: Ryder G. and Gillis J.

Differences among 1g samples: There are clear differences among the 5 samples that contribute significantly to the total variation. Figs. 2 and 3 show that each of the subsamples from one sample (e.g. A1 and A2) are more similar to each other than to the other samples, although there is some overlap. The duplicate subsamples of D are reasonably similar, though not within analytical uncertainty. Among all 1g subsamples, REE abundances roughly correlate positively with Fe and K, showing some mineralogical or modal contribution to the variation. Subsamples with higher incompatible element abundances have a slight comparative enrichment in light REEs.

Differences among 1g and 50mg samples: Because of the differences among the samples, the 50mg subsamples are best compared with the 1g samples from the same sample. Figs. 4 to 6 for subsamples from A, C, and D (with 1g samples shown in bolded lines) show that the 50mg subsamples tend to retain roughly the REE pattern of the 1g subsamples. However, this is not very consistent, and the abundances are erratic, varying by a factor of at least 2. Subsamples from B and E are more consistently like the average in pattern.

Differences among 1g and 20mg samples: Only subsamples from D have been analyzed at the 20mg size (Fig. 6). The REEs vary in abundance by a factor of 2 to 3. They deviate in pattern slightly from average D in being slightly more enriched in light rare earths.

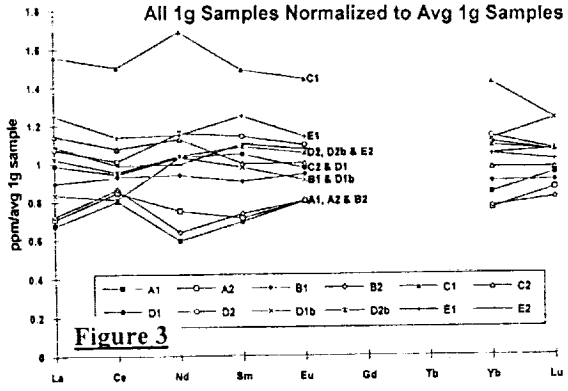

Figure 3

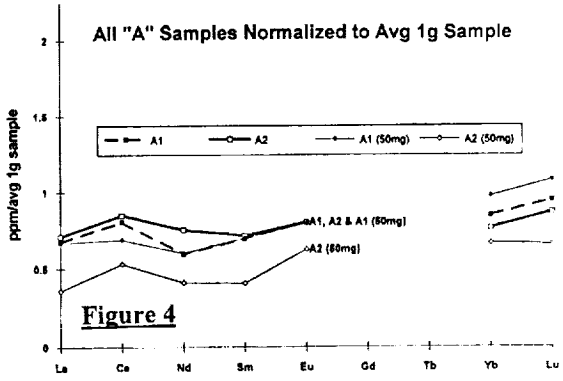

Figure 4

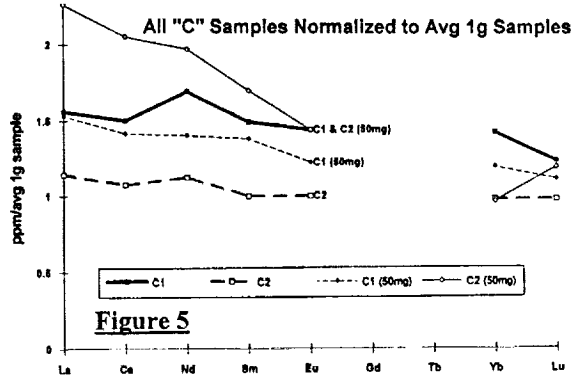

Figure 5

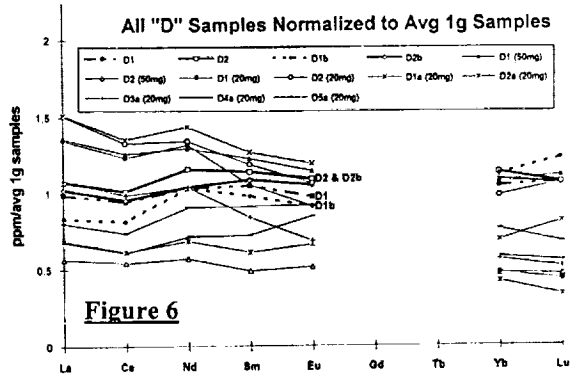

Figure 6

Preliminary conclusions: Small subsamples of the Abriachan granite show that there are significant differences in chemistry at the handsample level even though the samples were collected from a homogeneous-appearing outcrop and from within a few meters of each other. Tiny subsamples deviate from the handsample abundances by factors up to 2 or 3, and to some extent in REE patterns. Without further constraints from the mineralogy and petrography, it is clear that caution should be used in making petrogenetic inferences from the chemistry. We plan to further model the data in terms of petrogenetic constraints, to make analyses of more 20 mg samples, to analyze mineral separates, and to study thin section of each sample to evaluate pitfalls in the interpretation of tiny subsamples of granites.

References: [1] Deans T. et al. (1971) Nat. Phys. Sci. 234, p 145. [2] Garson M. et al. (1984) J. Geol. Soc. London 141, p. 711. [3] Harmon R. et al. (1984) Phil. Trans. R. Soc. London A 310, p. 709.

DETECTABILITY OF LUNAR TEPHRA DEPOSITS: EXAMPLES FROM THE APOLLO 17 LANDING SITE; Donald E. Sabol Jr., John B. Adams, Milton O. Smith (Department of Geological Sciences University of Washington, Mail Stop AJ-20, Seattle WA 98195), and Patrick C. Pinet, (UPR 234/GRGS/OMP, 14, Av. E. Belin, 31400 Toulouse, France)

Introduction: Lunar samples have provided evidence that a variety of types of volcanic glasses are present on the surface of the moon. Although petrographic evidence indicates that they are volcanic in nature, their exact origins are not well known. The spatial distributions of these glassy materials, can provide a valuable key for determining both their origins and processes of deposition[1]. The main types of lunar volcanic glasses (black, orange, and green) are spectrally distinctive in the visible and near-infrared [2,3] and may be mapped using multispectral images. To map small quantities of each of these glasses, it is critical to determine their detectabilities relative to the (background) regolith. The purpose of this study is to: 1) determine the minimal amount of each glass that would have to be present to be detectable by applying detection threshold analysis, an analytical technique based on spectral mixture analysis [4] , and then 2) apply these detection thresholds to a multispectral telescopic image of the Apollo 17 landing site.

Methods: Detection threshold analysis is used to predict the spectral detectability of a target material under given conditions of target-background spectral contrast and system noise. Two detection thresholds are determined for each target-background combination. The first is Continuum Analysis, where the target is included as a spectral endmember. In this case, the detection threshold is the smallest fraction of the target that can be measured above system noise. The second is Residual Analysis. Here, the target is not included as an endmember and is detected as deviations of the observed mixed spectrum (including the target) from spectral mixtures of "background".

For this study, the detection thresholds were determined for orange (74220), green (15401), and black (74001) glasses in backgrounds composed of mature upland (74241) and mare (70051) soils using spectral measurements of lunar samples. "Shade" was included as an additional background endmember to account for shading due to the lighting geometry of the surface. Both linear and non-linear mixing models were employed to account for both macroscopic and intimate mixtures between the glasses and regolith. Signal-to-noise (SNR) levels of both 20/1 and 100/1 as well as a confidence level of 90% were used. The detection thresholds were then applied to fraction images (derived from CCD image data) to create detectability maps of the glasses for the Apollo 17 landing site. To determine the "best case" for detecting these glasses, we initially used high resolution laboratory spectra (1076 bands between 0.350 μm and 2.500 μm). The analysis was then repeated using these laboratory spectra convolved to the 9 bands of a telescopic CCD image data set (bands at 0.560, 0.730, 0.91, 0.95, 0.97, 0.98, 0.99, 0.102, an 0.105 μm). These images were collected at the 2-meter telescope (F/D=25) of the Pic du Midi Observatory in France.

Results: Detection threshold analysis showed that the three glasses were more detectable using continuum than residual analysis. Detection thresholds (continuum analysis) for the laboratory spectra of the glasses were generally low; ranging from 2% to 13% at 20/1 SNR and from 1% to 6% at 100/1 SNR (Figure 1). The thresholds for these same materials, as measured by the CCD camera, were reduced to levels ranging from 3% to being undetectable. Of the glasses, the green glass showed the greatest detectability.

Conclusions: This study indicates that the volcanic glasses can be spectrally detected at relatively low abundances when using high-resolution, hyperspectral data. The detectability of the glasses (particularly the black and orange glasses) is reduced in the CCD images because: 1) only a few bands were used, and 2) the target spectra have relatively low spectral contrast with mixtures of the background materials at the wavelengths collected.

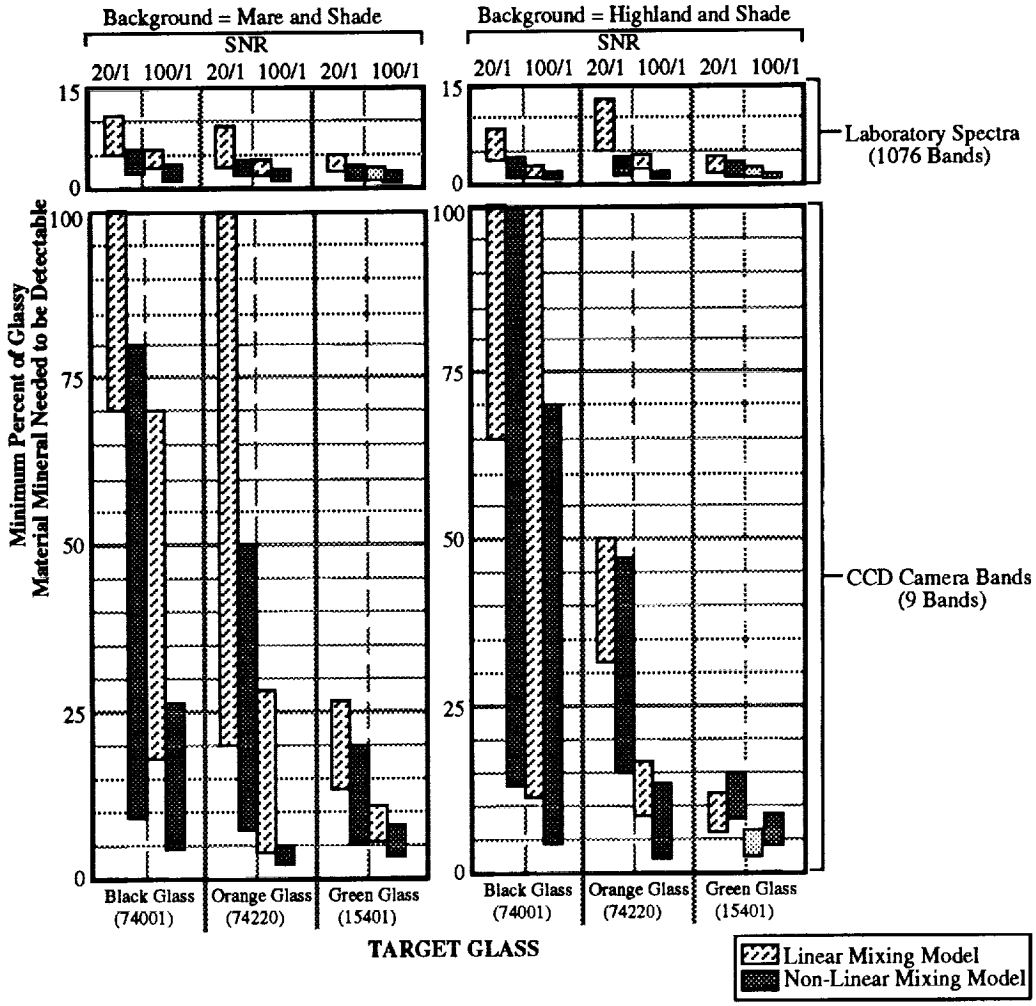

Figure 1: Continuum detection thresholds of black, orange, and green volcanic glasses against backgrounds of: 1) a mature mare soil and shade and 2) a mature highland soil and shade. The range of detection thresholds for each glass varies with the fractional composition of the background. The results for both linear and non-linear models are shown at both 20/1 and 100/1 signal-to-noise ratios.

References: [1] Coombs, C.R. and B.R. Hawke (1992) LPSC XXII, 303., [2] Adams, J.B., and T.B. McCord (1973) LPSC IV, 63., [3] Adams, J.B., and T.B. McCord (1974) LPSC V, 1171., [4] Sabol, D.E. Jr., J.B. Adams, M.O. Smith (1992) JGR, 97, 2659.

IGNEOUS INCLUSIONS FROM ORDINARY CHONDRITES: HIGH TEMPERATURE RESIDUES AND SHOCK MELTS; Richard O. Sack[†#], Mark S. Ghiorso[#] and Michael E. Lipschutz[*], [†]Departments of Earth and Atmospheric Sciences and [*]Chemistry, Purdue University, W. Lafayette, IN 47907-1393, and [#]Department of Geological Sciences, University of Washington, Seattle, WA 98195.

As part of a consortium formed to investigate genetic links between achondrites and ordinary chondrites we have studied the mineral chemistries of three igneous inclusions and their host Antarctic ordinary chondrites from the following PTS: Y 75097, 86-4 (L6 chondrite host and igneous inclusion); and Y 793241,91-1 (L6 host) and ,94-2 (inclusion); Y 794046,71-5 (H host) and ,53-3 (inclusion). The igneous inclusions of Y 75097 and Y 793241 are troctolites with achondritic textures and minor amounts of chromite, merrillite, and trace secondary ilmenite intimately intergrown with chromite. The igneous inclusion in Y 75097,86-4, which resembles Brachina [1], is about 70% olivine, 22% plagioclase, 6% merrillite, and 2% chromite, and Y 793241,94-2 is about 82% olivine and 16% plagioclase, with about 2% chromite and merrillite. Olivine compositions in these inclusions [2] are nearly identical to those in their hosts (Fig. 1), while plagioclases in the inclusions, particularly in Y 793241,94-2, are more Ca-rich than in their hosts (Fig. 2). Pyroxenes in the L6 hosts are primarily orthopyroxenes, with minor fine-grained and lamellar high-Ca clinopyroxenes (Fig. 3): the compositions of coexisting olivine, pyroxenes, and chromites [2] are consistent with equilibration temperatures between 700 and 900°C according to Fe-Mg and Ca-Mg exchange geothermometers [3-5]. Although differences in spinel and feldspar compositions, and rare earth elements (REE) and phosphorous contents [6], provide convincing evidence that Y 75097 and Y 793241, in particular, are not paired with each other, it appears that the inclusions from these two L6 chondrites originated by a similar genetic process involving magma formation elsewhere in the parent body. The magma formed by melting of chondritic parent, together with some alkali-rich material. The resultant magma crystallized olivine, chromite, and feldspars more Ca-rich than L6 hosts, and these residues accumulated to form the igneous inclusions.

Y 794046,53-3 differs from the igneous inclusions of Y 75097 and Y 793241 texturally and in mineral assemblage and chemistry. From microprobe modal analysis (n=875), the igneous inclusion in Y 794046,53-3 is 44.7 % olivine, 40.6 % pyroxene, 14.4 % plagioclase, and 0.34 % chromite, with minor to trace amounts of Fe-metal, troilite, and secondary ilmenite and rutile: the remaining portion of Y 794046,53-3 contains several coarse grains of Fe-metal and troilite, and distinctly less Ca-pyroxene. In the main portion of Y 794046,53-3, coarse pyroxene laths up to about 1 mm in length poikolitically enclose olivine. These laths have cores of Ca-poor orthopyroxene, rims of subcalcic augite (and/or pigeonite?), which are set in a matrix of medium to fine-grained olivine, and ophitic to sub-ophitic feldspar. The feldspars of this inclusion are substantially poorer in calcium than its H host and the igneous inclusions and L6 hosts of Y 75097 and Y 793241 (Fig. 2). The olivines of this inclusion are slightly more ferroan than its host (Fig. 1), and its clino- and orthopyroxene pyroxenes are respectively more Ca-poor, and more variable in Ca- and Mg-contents than those in its H host or the L6 hosts of Y 75097 and Y 793241. The mineral chemical data for Y 794046,53-3 indicate that the inclusion crystallized rapidly, under disequilibrium conditions, with various mineral-pair thermometers indicating temperatures of 1200 to 800°C [2-5, Figs. 1,3]. This conclusion is consistent with results of calculations obtained with the MELTS program of Ghiorso and Sack [7]. These calculations demonstrate that under equilibrium conditions, the high-Ca pyroxenes which would crystallize would have Ca-contents significantly greater than those observed (Fig. 4). In situ fractionation (with consequent Fe-enrichment of liquids) must have occurred to produce pyroxenes with the Ca/(Ca+Fe+Mg) ratios observed. Secondary Fe-Mg exchange during subsolidus annealing must also have occurred to reequilibrate the Fe/(Fe+Mg) ratios of these pyroxenes. The chondrite host is strongly brecciated, and its mineral compositions suggest derivation of the igneous inclusion from its host, given severe heating and the reactions consequent therefrom. Hence, the igneous inclusion Y 794046,53-3 formed in situ from a melt produced by severe shock heating of the host. This melting was accompanied by loss of metal and sulfide, presumably in Fe-FeS eutectic with a threshold temperature of ~988°C. Compositional data for siderophiles and chalcophiles [6] accord with this conclusion. Cooling times for the inclusion Y 794046,53-3 can be estimated as days to months, demonstrating that the shock-heated assemblage now represented by Y 794046, was near the surface of a breccia regolith, but was insulated by overburden on the meter-scale.

These three meteorites have brought to Earth samples of three parent regions. The inclusions in Y 75097 and Y 793241 sample at least two parts of the same magma pool or two pools, each of which was on the path to producing achondrites. These meteorites, like the LL7 chondrite Y 74160 [8], contain important clues to parent body processes that converted chondritelike parent material to achondrites.

References: [1] K. Yanai *et al., Proc. 8th Symp. Antarctic Meteorites, 30*, 29 (1983). [2] R. O. Sack and M. E. Lipschutz, *18th Symp. Antarctic Meteorites (abstract)*, 68 (1993). [3] R. O. Sack and M. S. Ghiorso, *Am. Mineral., 76*, 827 (1991). [4] R. O. Sack and M. S. Ghiorso, *Contrib. Mineral. Petrol., 102*, 41 (1989). [5] R. O. Sack and M. S. Ghiorso, *Contrib. Mineral. Petrol.*, in press (1994). [6] M. S. Wang *et al., Proc. 9th Symp. Antarctic Meteorites*, submitted (1993). [7] M. S. Ghiorso and R. O. Sack, *Contrib. Mineral. Petrol.*, submitted (1994). [8] H. Takeda *et al., Earth Planet. Sci. Letters, 71*, 329 (1984).

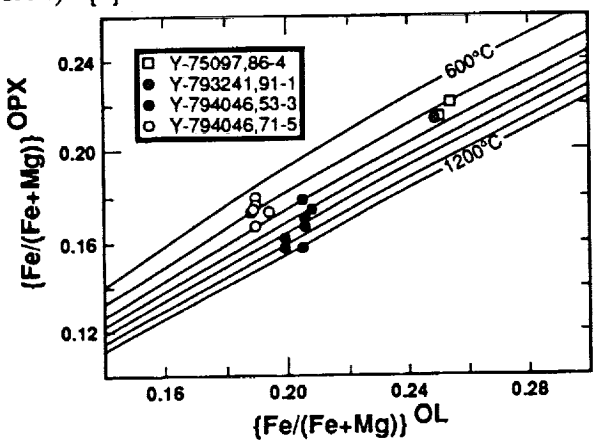

Fig. 1. Molar Fe/(Fe+Mg) ratios of olivines and low-Ca pyroxenes in Y 75097, Y 793241, and Y 794046 compared with the calibration for the Fe-Mg exchange reaction between orthopyroxenes with Ca/(Ca+Fe+Mg) = 0.16 and Fe-Mg olivines given by Sack and Ghiorso [4-5].

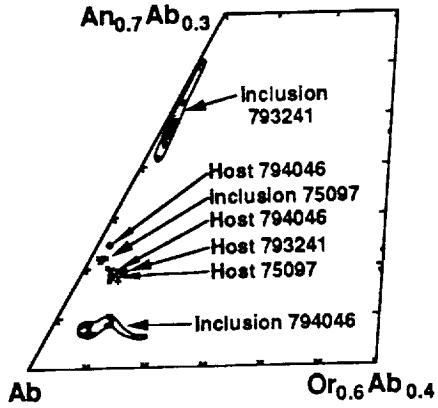

Fig. 2. Molar Ca/Na and Ca/K ratios of feldspars in Y 75097, Y 793241, and Y 794046 compared with a portion of the composition triangle defined by $NaAlSi_3O_8$ (Ab), $CaAl_2Si_2O_8$ (An), and $KAlSi_3O_8$ (Or) components.

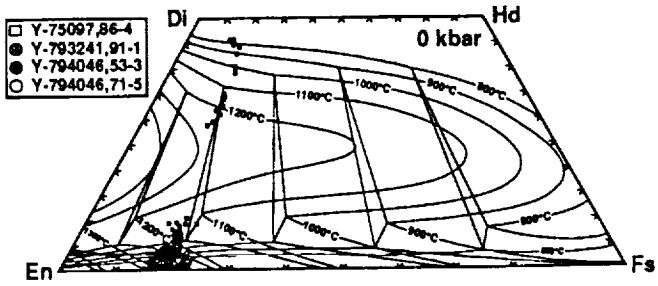

Fig. 3. Molar Ca/Fe and Ca/Mg ratios of Y 75097, Y 793241, and selected Y 794046 pyroxenes compared with the 1 atm calibration for stable and metastable phase relations between Pbca and C2/c pyroxenes in the $Mg_2Si_2O_6$ (En) - $CaMgSi_2O_6$ (Di) - $CaFeSi_2O_6$ (Hd) - $Fe_2Si_2O_6$ (Fs) system of Sack and Ghiorso [5].

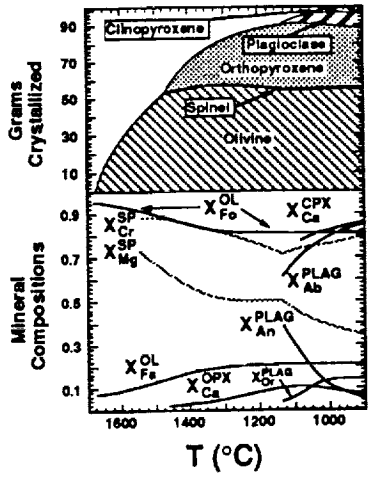

Fig. 4. Relationships between temperature, grams of minerals crystallized, and mineral composition variables for 100 grams of Y 794046 igneous inclusion bulk composition calculated for equilibrium crystallization from the MELTS program [7].

SEARCH FOR ^{26}Mg ISOTOPIC ANOMALY IN UNEQUILIBRATED CHONDRITES AND UNIQUE METEORITES; S.Sahijpal and J.N.Goswami, Physical Research Laboratory, Ahmedabad-380009, India. L.L.Kashkarov, N.N.Korotkova and M.A.Nazarov, Vernadsky Institute of Geochemistry and Analytical Chemistry, Moscow-117975, Russia.

We have looked for excess ^{26}Mg in plagioclase phases of an igneous object found in the H3 chondrite Severnyi Kolchim and in anorthite grains separated from the Kaidun meteorite. A small ^{26}Mg excess is seen in a couple of anorthite grains from Kaidun. Plagiclase in the igneous object from Severnyi Kolchim has normal magnesium isotope composition. Widespread signature of ^{26}Al heating of planetesimals in the early solar system is still elusive.

^{26}Al and ^{60}Fe are now considered to be the two short-lived radionuclides that can provide the thermal energy necessary for melting and differentiation of the meteorite parent bodies and for thermal metamorphism taking place in these objects. The presence of ^{60}Fe in the differentiated meteorites Chervony Kut and Juvinas has been established recently [1,2]. Even though the presence of ^{26}Al in the early solar system is well established, its widespread presence in meteoritic object of igneous origin is yet to be established conclusively [3,4,5]. Here, we report the results of our Mg isotopic studies of well characterized igneous objects found in unequilibrated H chondrites and also in separated phases from an unique meteorite.

The samples analysed include plagioclase phases from an igneous object found in the Severnyi Kolchim (H3) chondrite [6], an angular clast with crystalline structure from the Dengli (H3) chondrite [7] and a basaltic inclusion from the L chondrite Tsarev [8]. In addition anorthite grains separated from the carbonaceous matrix of the unique meteorite breccia Kaidun [9] was also analysed. The Mg isotopic measurements were carried out using an ion microprobe (Cameca ims 4f) at a mass resolution of ~4000, sufficient to resolve the hydride and other interferences. ^{27}Al was not included in the measurement routine and the ^{27}Al/^{24}Mg ratios of the analysed phases were independently determined before and after each analysis. The analysis of the glassy plagioclase phases in Dengli and Tsarev was hampered by interference in the magnesium signal from surrounding Mg-rich, low-Al phases. This could be inferred from the much lower value for ^{27}Al/^{24}Mg obtained from the ion probe data than those obtained by the electron-probe. Analysis with a small beam diameter eliminated this problem to some extent, however, the low magnesium signal resulted in large uncertainties in the measured ratios. No detectable excess in ^{26}Mg (above the limits of our experimental uncertainty) could be seen in both these samples.

The results obtained from the analysis of plagioclase phases from the igneous objects in the Severnyi Kolchim chondrite and anorthite grains from the Kaidun meteorite are shown in Figure 1. Two anorthite grains from Kaidun have definite excess in ^{26}Mg with δ^{26}Mg of 4.2 ± 1.6‰ and 4.0 ± 2.4‰ respectively (2σ errors). Two other grains have normal magnesium composition and the fifth grain, whose measured ^{27}Al/^{24}Mg values before and after the analysis showed a significant difference, also has a near normal isotopic composition. As the source and origin of these anorthite grains isolated from the cabonaceous matrix of the Kaidun multicomponent breccia is not very clear, it is difficult to argue the case of ^{26}Al as a heat source based on these data. If the analysed anorthites represent fragments from refractory inclusions that could have been present in the carbonaceous matrix, some or all the grains must have undergone different degree of isotopic exchange with a reservior of normal magnesium composition.

The Mg isotopic compositions of the plagioclase phases in the igneous object from the Severnyi Kolchim chondrite are normal within the limits of our experimental uncertainties. The relatively large experimental uncertainty in this data set resulted from the use of a smaller primary beam spot (low primary current) to avoid interference from the Mg-rich phases surrounding the plagio

clase. Nazorov et al.[6] proposed this igneous object to be of nebular origin although some of the mineralogical characteristics suggest its formation on a differentiated parent body by igneous process. If we consider the first alternative our data suggest isotopic exchange and equilibration with a normal solar system magnesium composition. On the other hand if it represents igneous object from a parent body, there is no clear signature of ^{26}Al at the time of its crystallization.

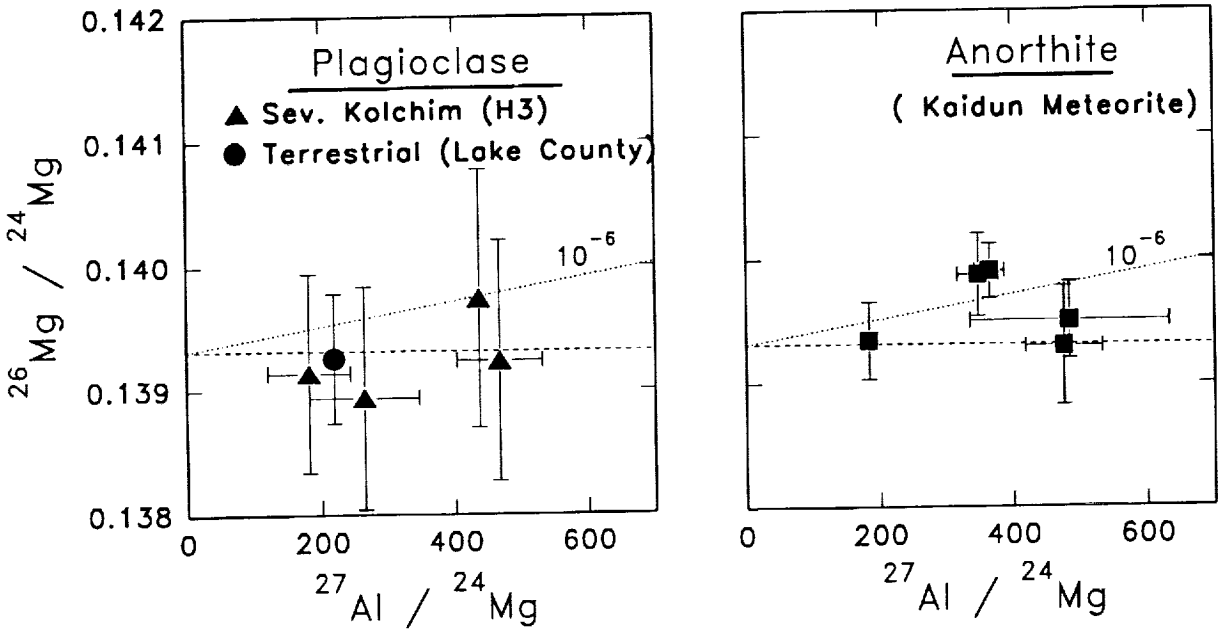

Fig.1 Al-Mg isotopic composition in plagioclase and anorthite from Severnyi Kolchim and Kaidun meteorite, respectively. The normal magnesium isotopic composition and the expected evolution line for an initial ^{26}Al/^{27}Al of 10^{-6} are also shown. The magnesium isotopic composition of the lake county plagioclase was measured under the same experimental conditions used for the analysis of Sev. Kolchim plagioclase.

The possibilty of ^{60}Fe acting as a heat source for melting, differentiation and thermal metamorphism of meteorite parent bodies [1] relaxes to some degree the need for a high initial ^{26}Al/^{27}Al ($>10^{-6}$), at the time of retention of radiogenic ^{26}Mg in meteoritic objects of igneous origin, to argue the case of ^{26}Al as an effective heat source. In fact the measured initial ^{26}Al/^{27}Al in plagioclase from the Ste. Marguerite chondrite is only 2×10^{-7} [5]. Such an initial ratio will lead to an excess ^{26}Mg signal of $< 1.5‰$ for phases with Al/Mg < 1000, like the phases analysed in this work, which is not distinguishable within the limit set by our experimental uncertainty. However, the absence of widespread evidence for excess ^{26}Mg in meteoritic component of igneous origin may also be due to postformation isotopic exchange and/or reequilibration of most or all of these objects with normal solar system material. This has already been suggested as a plausible cause for the absence of ^{26}Mg excess in differentiated meteorites [4].

REFERENCES: [1] Shukolyukov A. and Lugmair G.W., Science 259, 1138 (1993). [2] Shukolyukov A. and Lugmair G.W., EPSL 119, 159 (1993). [3] Hutcheon I.D. and Hutchison R., Nature 337,238 (1989). [4] Bernius M.T. et al., LPSC XXII, 93 (1991). [5] Zinner E. and Göpel C., Meteoritics 27, 311 (1992). [6] Nazarov M.A. et al., LPSC XXIV, 1055 (1993). [7] Ivanova M.A. et al., Meteoritics 27, 463 (1992). [8] Migdisova L.F. et al., LPSC XXIII, 909 (1992). [9] Ivanov A.V., Geochem. International 26, 84 (1990).

Small Volcanic Edifices on Venus: Morphology, Diameter, and Elevation Distribution Sahuaro High School Astronomical Research Class[1], Tucson, AZ, J. F. Lockwood, teacher, Evergreen High School Research Class[2], Vancouver, WA, Mike Ellison, teacher, Advisors: J. Johnson, G. Komatsu, (Lunar and Planetary Laboratory, University of Arizona, Tucson, AZ 85721)

Introduction: It appears that volcanic features are not evenly distributed on the surface of Venus.[3] Head et al. [4,5] theorizes that the sparcity of volcanic features in the lowlands may be due to an altitude dependent inhibition of volatile exsolution, and the resulting production of neutral buoyancy zones sufficient to form magma reservoirs and favoring flood lava's at lower elevations. The astronomy research classes of Evergreen and Sahuaro High Schools surveyed a slice of Venus Magellan data to investigate the frequency of edifice type, the frequency distribution of edifice diameters, and the frequency distribution of edifices by elevation.

Observations: Student researchers from the two high schools located and measured small volcanic edifices (1 to 20 km) in 15 FMIDRS taken from five Venus Magellan Mosiacked Image Data sets. These FMIDRS are located in a strip from 70^0 N to 60^0 S latitude and centered at 0^0 longitude.

Students used the four classifications (shield-shaped, dome-shaped, flat-top, and cone-shaped) described in Aubele, 1993.[6]

Using a 1.49 PDS program, the volcanic edifices were located by centering the cursor on calderas and recording the latitude and longitude. The diameters were measured in kilometers by averaging the distance across the x and y axes.

The elevation was recorded by using the GXDR Elevation and Altimetry Disk. To find the elevation, the latitude and longitude of the edifices were located on the topographic image and the elevation was recorded directly form the results box in Image 1.49.2.

Results: The total number of volcanic edifices per class and the percentage in each class was plotted in Figure 1. Shield-shaped volcanoes appear to be the most dominant with over 50% of the total number of edifices measured. Cone-shaped and dome-shaped edifices were both 20% and flat-tops were only 2%. This compares to a similar study by Head and Aubele who reported 85% of the small volcanic edifices measured to be shield-shaped.[7] They did not report, however, on the percentages of the other classes.

The distribution of volcanic cone diameters is shown in Fig. 2. Of the 2221 cones sampled, 41% fell in the 2-3.5 km size range. The graph peaks at the 2.5 km bin with 320 cones. A 200 cone sample of terrestrial submarine cones by R.C Searle (Fig. 3) shows a distinct peak (30% of sample) between edifices with diameters of two to three kilometers.[8] Both graphs show similar and gaussian-like distribution to about ten kilometers (Fig. 2 and 3).

The 15 FMIDR sample represents about 1% of the Venusian surface area. Given that one data set is a rough approximation of the various topographic levels on Venus, we project that the number of small volcanic cones may range from 400,000 to 600,000 if the polar regions are included.

Our sampling area's distribution by elevation (Fig. 4) shows very few cones in the lowland areas, a result similar to Head et. al.,1992[4], and it implies that cones are most densely populated in the plateau regions. The graph shows an even distribution from the Mean Planetary Radius (6051.4 km) to 6052.2 km However, there is no single peak in contrast to a previous distribution by elevation produced by last year's Sahuaro Astronomical Research class, which peaked at 6051.8 km. Our findings also showed a larger percentage of cones at higher elevation than last year's study. Figure 4 makes a dramatic downward turn at elevation 6052.4 km. We found very few cones located above elevation 6053.8 km. These findings could be a result of the number and type of F-MIDR's we chose for our sample.

The configuration of Figure 4 is strikingly similar to the results of Keddie et. al., 1993.[9] Their results show that the majority of large cones in his sample fall between 6051.5 km and 6052.5 km. There was also a paucity of edifices in both the lowlands and highlands, and an abundance of edifices in the mid-altitude regions. These results, which agree with our own, may be due to the fact that 70% of the Venusian surface is classified as rolling uplands or plateau.

Conclusion - Volcanic edifices are not uniformly distributed on the surface of Venus. This study shows that the distribution by elevation follows the neutral buoyancy theory of Head, et. al., 1992.[4] The percentage of edifice in each of the four classes may vary across different topographic regions while the distribution of small edifice diameters appears to be very uniform, peaking between 2 and 3 km. This distribution is very similar to the size of small cones on Earth. A more comprehensive sample is necessary to fix the percentages of small volcanic edifices on the surface of Venus as well as total number of these constructs.

SMALL VOLCANIC EDIFICES: Sahuaro High School Research Class

References: [1]K. J. Arbeit[a], J. T. Blee[a], P. J. Borns[a], O Bretschger[a], R. J. Brown, C. C. Crowson[a], V. A. Duke[a], J. K. Eppley, A. S. Falgiano, T. J. Griffith, S. D. J. Hiller, A. R. Lucas, D. R. McCanse, C. F. McGinley[a], B. A. Newell, C. H. Philips, K. A. Rathbun[a], R. L. Root, D. M. Stoflet, B. V. Tucker, S. Woods, [2] K. Gerlach[a], C. Peterson[a], A. Fosse[a], [3]Saunders, S., et. al., 1992, JGR, v. 97, 8, pp. 13067-13090, [4] Head, J., et. al., 1992, JGR, v. 97, E8, pp. 13153-13197, [5] Head, J., Wilson, L., 1992, JGR, v. 97, E8, pp. 3877-3903, [6] Aubele, J. C., 1993, LPSC XXIV, LPI/USRA, pp. 47-48, [7] Head, J. Aubele, J., 1991, LPSC XXII, LPI/USRA, pp. 545-546, [8]Searle, R., 1981, Marine Geol., v. 53, p. 57, [9] Keddie, S., 1993, LPSC XXIV, LPI/USRA, p. 499-500.
a = principal investigator

Fig. 1- Total Edifices by Class

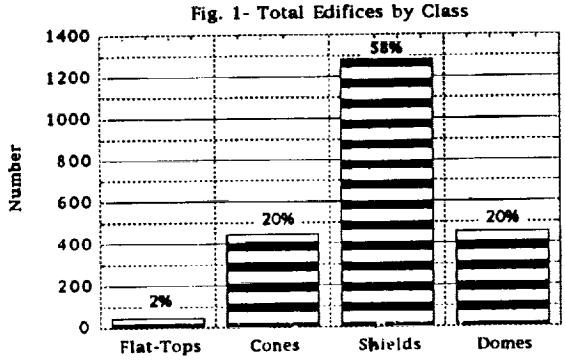

Figure 2-Number of Edifices vs. Diameter

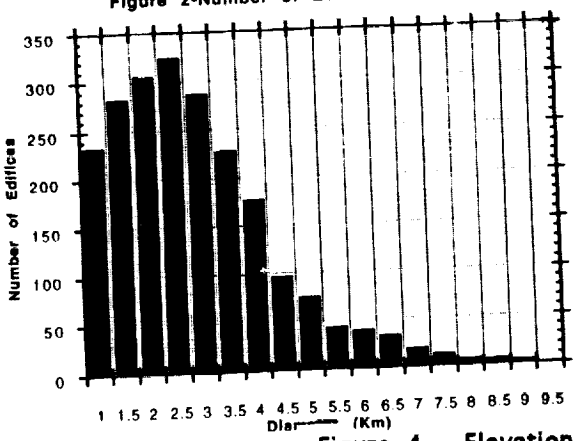

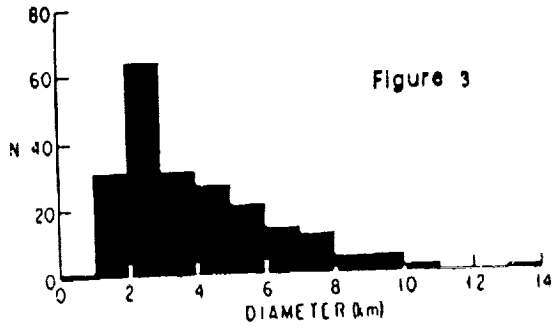

Figure 3

Figure 4 - Elevation vs. Number of Edifices

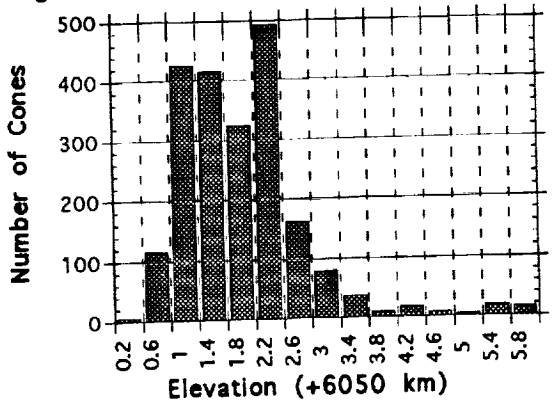

TERRESTRIAL BASALTIC COUNTERPARTS FOR THE VENUS STEEP-SIDED OR "PANCAKE" DOMES; *S. E. H. Sakimoto,* Department of Earth and Planetary Sciences, The Johns Hopkins University, Baltimore, MD 21218-2681.

The Magellan Images of Venus have revealed a number of intriguing volcanic and tectonic features, including the steep-sided or "pancake" domes. These volcanic domes or flows have morphologies that suggest formation by a single continuous emplacement of magma with a higher viscosity than that of the surrounding basaltic plains. Since the majority of studied terrestrial volcanic domes are silicic, numerous investigators have compared the domes to terrestrial silicic volcanic domes and suggested that such high viscosity is due to high silica content, leading to the conclusion that the domes are evidence of evolved magmatic products on Venus. However, the majority of volcanic features on Earth are basaltic seafloor features, and thus little studied and not often used for interplanetary volcanologic comparisons. Nevertheless, the Venus domes may have a greater resemblance to terrestrial basaltic submarine domes than to the terrestrial silicic subarial domes.

Modeling of Venus volcanic dome formation indicates that it is probably feasible to produce the steep-sided domes from a variety of compositions—including basalt—and thus their morphology is not necessarily an unambiguous indication of their composition [1, 2]. Several studies comparing their morphology to terrestrial features have been made [3, 4, 5], however, the overwhelming majority of terrestrial features selected for comparison to the Venus pancake domes are silicic, small, and subarial. Since the Venus domes are usually at least one magnitude larger in both diameter and in volume than the terrestrial subarial features, and possibly made of basaltic material similar to that of the plains [2, 6], it seems reasonable to compare Venus domes to terrestrial seafloor volcanic features; specifically, seamounts. While the terrestrial seafloor has many features comparable to Venus volcanic features such as extensive basaltic plains, shield-like small edifices, and large volcanic constructs, seamounts such as those recently described by [7] seem the most promising analogs of the Venus pancake domes. Three particularly interesting seamounts (figure 1), as imaged in the SEABEAM 2000 data of [7], are approximately 5 km across and 1 km high, basaltic, with flat to bowl-shaped tops. The Venus steep-sided domes, as characterized by Pavri et al. [3], generally have steep sides, relatively flat tops, and radial symmetry. Individual dome morphologies range from low shield-like shapes with flat tops to steep-sided "pancakes" with concave tops. Thus, the Venus domes and the seamounts are morphologically very similar as well as having the low aspect ratios and high volumes in common. Possible differences include seamount flanks that are somewhat less steep than those of the Venus domes due to talus slope formation, which appears to be generally less prevalent on Venus than on Earth. Also, sediment cover obscures the tops of the terrestrial seamounts and precludes observations of a presence or lack of the concentric and radial fracturing patterns observed on some of the Venusian domes. Due to resolution limitations in both the Magellan Venus data and the terrestrial bathymetric data, it is not possible to absolutely determine if either feature type is composed of individual flows or a single flow. However, Pavri et al. [3] considered the smooth margins, radial symmetry, and lack of evidence for multiple flows indications that the Venus domes were the result of a single eruptive episode.

The similarities between the Venus domes and the seamounts may be the result of similarities between Venus and oceanic thermal lithosphere conditions. Generally, the probability of transport and/or eruption of a magma of a particular crystallinity is a function of the time it spends at that crystallinity during the cooling process [12]. If the heat flux out of a magma is reduced and the cooling process lengthened, the time a magma has to erupt or be transported before it is too crystalline to move (approximately 60% crystals [12]), is correspondingly longer also. Probability of transport and/or eruption for a given magma is enhanced on Venus relative to Earth [11] as the result of a reduced heat flux out of the magma caused by the higher surface temperature and higher near-surface thermal gradient [8, 9, 10, 11] in the Venus thermal lithosphere relative to terrestrial oceanic thermal lithosphere

conditions. A similar but smaller magnitude effect may exist for terrestrial oceanic lithosphere conditions in comparison to terrestrial continental lithosphere conditions. In both cases, this effect would increase the probability of eruption of all magmas, as well as the probability of eruption of higher crystallinity (20-50%) basalts. These basalts could then either spread as a single unit [1, 2, 13] or as a series of units [14] and form steep-sided basaltic domes instead of the more common basaltic shields. If this is the case, than the terrestrial seafloor is probably a more appropriate region than the continents for Venus comparative planetary volcanology studies of the steep-sided or "pancake" domes as well as other features.

References:

[1] Sakimoto, S. E. H. and M. T. Zuber, LPSC XXIV, 1993
[2] Sakimoto, S. E. H. and M. T. Zuber, in preparation.
[3] Pavri, B., et al., *J. Geophys. Res.*, **97,** 13445-13478, 1992.
[4] Fink, J. H., N. T. Bridges, and R. E. Grimm, *Geophys. Res. Let.*, **20**, 261-264, 1993.
[5] Bridges, N. T. and J. H. Fink, *LPSC XXIII,* 1992.
[6] Ford, P. G. and G. H. Pettengill, *Papers Presented to the International Colloquium on Venus,* LPI Contribution No. 789, 34, Pasadena, CA, 1992.
[7] Schierer, D., and K. Macdonald, *EOS Trans. AGU*, **74,** No. 43, p. 593, 1993.
[8] Zuber, M. T., *J. Geophys. Res.*, **92**, E541-E551, 1987.
[9] Grimm, R. E. and S. C. Solomon, *J. Geophys. Res.*, **93**, 11911-11929, 1988.
[10] Zuber, M. T. and E. M. Parmentier, *Icarus*, **85**, 290-308, 1991.
[11] Sakimoto, S. E. H. and M. T. Zuber, *J. Volcanol. Geotherm. Res.*, in press.
[12] Marsh, B. D., *Contrib. Mineral. Petrol.*, **78**, 85-98, 1981.
[13] Huppert, H., E., et al., *J. Volcanol. Geotherm. Res.*, **14**, 199-222, 1982.
[14] Fink, J. H. et al., *Geophys. Res. Letts.*, **20**, 261-264, 1993.

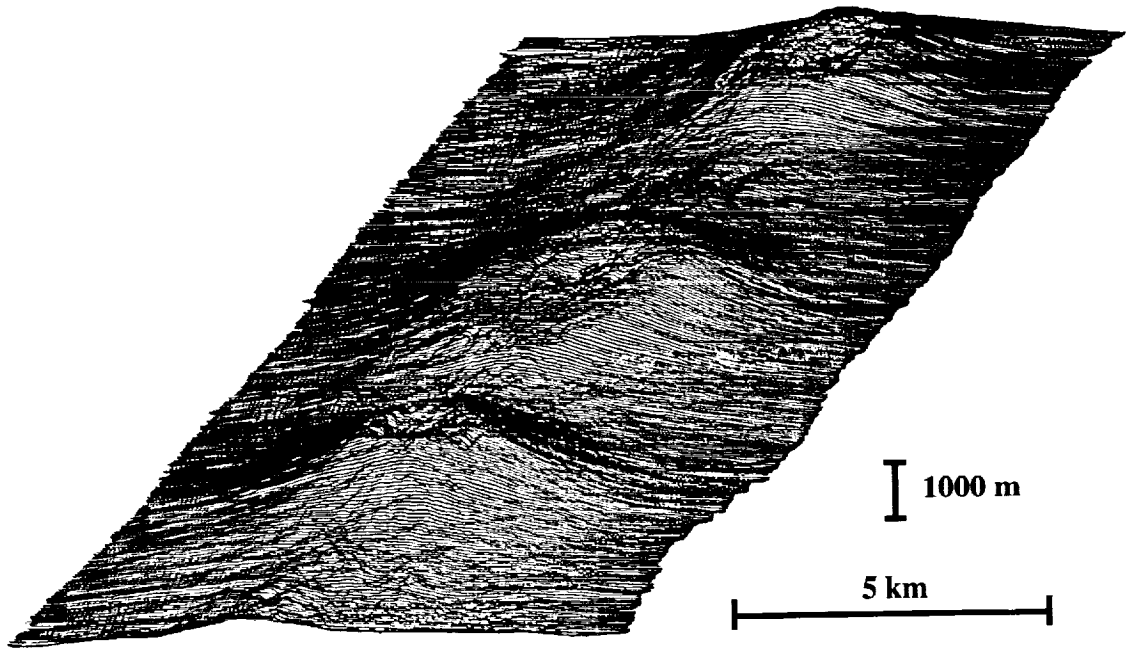

Figure 1. Topography of the "Three Wisemen" seamounts at latitude -18 17.2 and longitude -114 44.2 near the northern East Pacific Rise. No vertical exaggeration (figure after [7]). See text for discussion.

THERMAL GRADIENTS AND KIRCHHOFF'S LAW; J. W. Salisbury, A. E. Wald, and D. M. D'Aria, Department of Earth and Planetary Sciences, Johns Hopkins University, Baltimore, MD 21218

Kirchhoff's Law (ε=1-R) strictly applies when the radiating material is isothermal. Laboratory experiments have indicated that steep thermal gradients exist in particulate surface materials on airless bodies like the Moon, or on planets with thin atmospheres, such as Mars [1,2]. These gradients significantly increased the spectral contrast compared to that measured for more isothermal samples, showing that Kirchhoff's Law did not apply. Henderson and Jakosky [3] have modeled heat transfer in a particulate medium under different atmospheric pressure conditions to determine the magnitude of near-surface gradients and their effect on emission spectra. Their model indicates gradients steep enough to cause significant spectral effects on bodies like Mars and the Moon, in agreement with the earlier laboratory experiments. These gradients occur because near-surface heat transport is dominated by radiation to cold space on airless, or near-airless, bodies. On bodies with thick atmospheres like the Earth, however, their model shows that heat transport by interstitial gas dominates heat transport between grains, and tends to mitigate near-surface thermal gradients. We have made the first quantitative laboratory measurements of emissivity and directional hemispherical reflectance under terrestrial atmospheric conditions, to test the applicability of Kirchhoff's Law. We find that most materials obey the Law, despite the occurrence of weak thermal gradients. Fine materials that form underdense structures at the surface (the "fairy castle structures" of Hapke [4]), however, may develop a thermal gradient that significantly distorts the spectrum.

This result can be illustrated by comparison of spectra predicted from directional hemispherical reflectance measurements with actual emittance spectra. Figure 1 shows this comparison for a solid sample of fused silica heated from below (the condition of the Henderson and Jakosky model), which should minimize thermal gradients. Predicted and measured emissivity agree within experimental error. Figure 2 shows the same comparison for a soil sample, which has a similar agreement, despite the occurrence of a weak gradient. Figure 3 shows this comparison for a fine quartz powder having fairy castle structures on its surface, which displays a significant difference between predicted and measured emissivity. This difference in spectral contrast indicates that a significant thermal gradient has formed within the fairy castle layer, suggesting that some improvement is needed in the Henderson and Jakosky thermal model. Specifically, they need to incorporate a decreasing density in the fairy castle layer, which appears to be the factor that causes samples with fairy castle surfaces to display significant thermal gradients.

References:

[1] Logan, L. M., and G. R. Hunt, *Journal of Geophysical Research*, 75, 6539-6548, 1970.

[2] Logan, L. M., G. R Hunt, J. W. Salisbury, and S. R. Balsamo, *Journal of Geophysical Research*, 78, 4983–5003, 1973.

[3] Henderson, B. G., and B. M. Jakosky, Lunar and Planetary Science Conference XXIV, 639-640, 1993.

[4] Hapke, B., I*carus*, 67, 264-280, 1986.

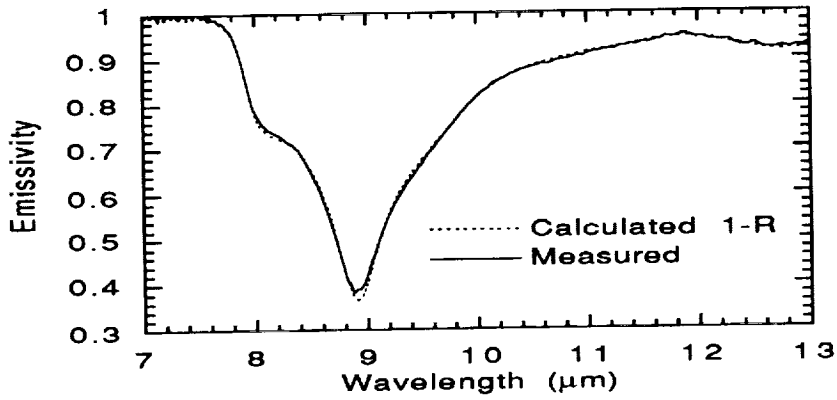

1. Comparison of measured spectral emissivity with emissivity calculated from directional hemispherical reflectance of a solid sample of fused silica.

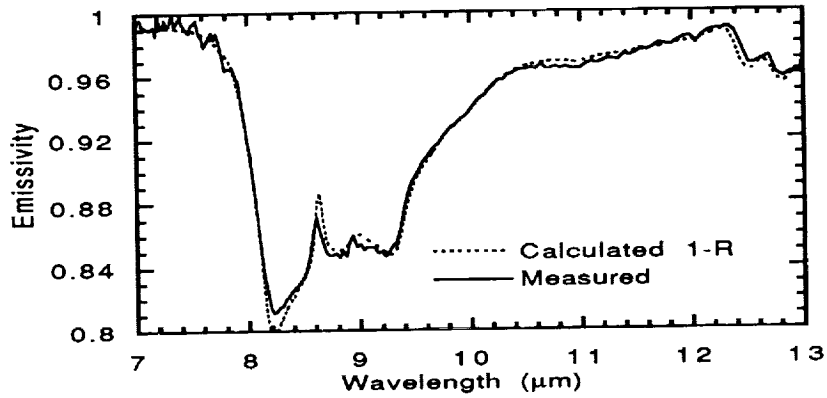

2. Comparison of measured spectral emissivity with emissivity calculated from directional hemispherical reflectance of soil 0133.

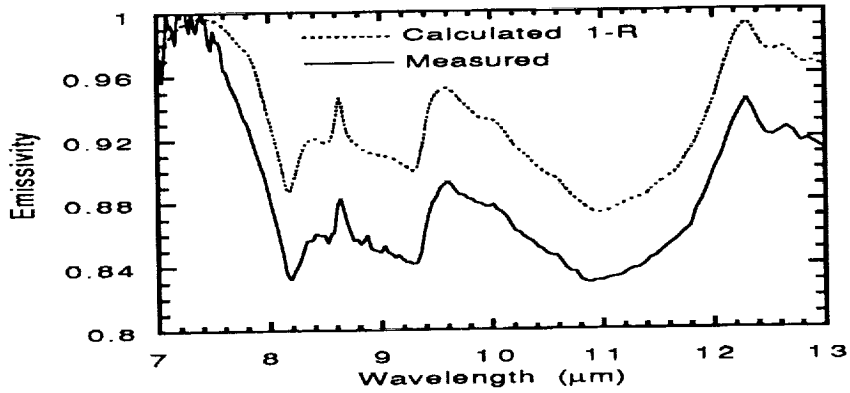

3. Comparison of measured spectral emissivity with emissivity calculated from directional hemispherical reflectance of a sifted, 0-75 μm, quartz powder.

FORMATION OF CONTINUOUS RIDGES ON ICY SATELLITES BY COOLING GRAVITY-CURRENT VOLCANISM; Sho Sasaki[1], Ryuji Kono[2*], and Yasuyuki Iwase[2]. [1]Geological Institute, Univ. Tokyo, Tokyo 113 Japan, [2]Department of Earth and Planetary Systems Sciences, Hiroshima Univ., Hiroshima 734, Japan, *currently at PASCO Coop.

Formation of continuous ridges in grabens of icy satellites is numerically analyzed to estimate viscosity of erupted icy materials. Uranian satellites Ariel and Miranda have morphological structures where a continuous swell fills graben (chasma) floor. The continuous ridge runs parallel to the graven walls. In several chasmas (Kewpie, Vallis, Pixie) on Ariel, a continuous fracture run on the top of the swell. Jankowski and Squyres presented the model that erupted materials along the axis of the valley should spread a short distance laterally by gravity [1]. This "gravity current" model was originally considered as an explanation of lava domes and flows [2].

For constant volume and viscosity, the outer boundary of the flow proceeds in proportion to $t^{1/5}$. Asignment of flow timescale should give the final shape of the structure. Jankowski and Squyres adopted a cooling time by heat conduction $\tau_{cool}=h^2/\kappa$ (h and κ being flow height and thermal diffusivity) and obtained high (in solid state) viscosity (~10^{16}[Pas]). They advocated that solid-state cryovolcanism is dominant on Uranian icy satellites. On the other hand, Schenk [3] used a cooling time by radiation from the surface $\tau_{cool}=\rho h C_p/\varepsilon\sigma T_o^3$ and obtained ~10^{12}[Pas] as flow viscosity. We consider that cooling time should not be directly applied to the time scale of the gravity current, which is controlled by viscosity. Since temperature dependence of viscosity is approximated by $\mu \propto \exp(E/RT)$ (E and R being activation energy and ideal gas constant, respectively), the typical time is expressed by

$$\tau_{stop} = \left|\frac{1}{\mu}\frac{d\mu}{dt}\right|^{-1} = \left|-\frac{E}{RT^2}\frac{dT}{dt}\right|^{-1} = \frac{RT}{E}\tau_{cool} \equiv \frac{1}{\alpha}\tau_{cool}$$

The parameter α is about 30 (silicate), 30 (H_2O ice), and 20 (H_2O-NH_3 ice) when temperature is just below the melting temperature [4]. The flow timescale should be 1/20 - 1/30 of the cooling time. Then for the same aspect ratio of the final shape, required initial flow viscosity should be lower than previous estimates.

We simulated a two-dimensional gravity current taking into account change of viscosity with time: $\nu = \nu_0 \exp(t/\tau_{stop}) = \nu_0 \exp(\alpha t/\tau_{cool})$. Timescale is normalized by $\tau = (12\nu_0/g)(\bar{x}^2/\bar{h}^3)$ where $\bar{x}$ and $\bar{h}$ are nominal lateral distance and vertical height, respectively. Figures 2 show the case where the total volume is constant. At high α, the flow should stop moving quickly to give a lower aspect ratio for the final shape. Figures 3 show the case where there is fluid injection at x=0. Change of the aspect ratio for different α is larger. We also calculated the case where eruption rate decays. Comparing with actual landforms, we can obtain the initial viscosity of the flow for each case. In the constant volume case where α=30 (10), ν_0 can be 100 (22) times smaller than those of the previous estimates.

Several efforts have been done to explain the difference of theoretically-estimated higher viscosity and experimentally (and observationally) obtained lower lava viscosity: effect of compressibility [5] and Bingham characteristics of the flow of solid-liquid mixture [3, 6]. Stereo pictures clearly show that the height of some ridges should be much lower than the original estimate [7], which would be in favor of lower viscosity. Combined with these effects, we consider that the erupted material should have lower viscosity, not being in solid state.

Ref. 1. Jankowski D. G. and Squyres S. W. (1988) Science 241,1322-1325.
2. Huppert H. E. et al. (1982) J. Volcanol. Geotherm. Res. 14, 199-222.
3. Schenk, P. M. (1991) J. Geophys. Res. 96, 1887-1906.
4. Kargel, J. S. et al. (1991) Icarus 89, 93-112.
5. Jaupart, C. (1992) Bull. Volcanol. 54, 1-9.
6. Melosh, H. J. and Janes, D. M. (1988) Science 245, 195-196.
7. Croft, S. K. and Soderblom, L. A. (1991) in Uranus pp.561-628.

COOLING ICY FLOW: Sasaki S., Kono R., Iwase Y.

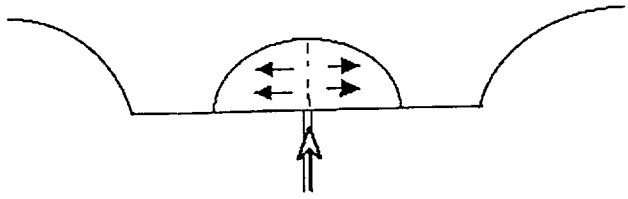

Figure 1 Schematic figure of a gravity current model.

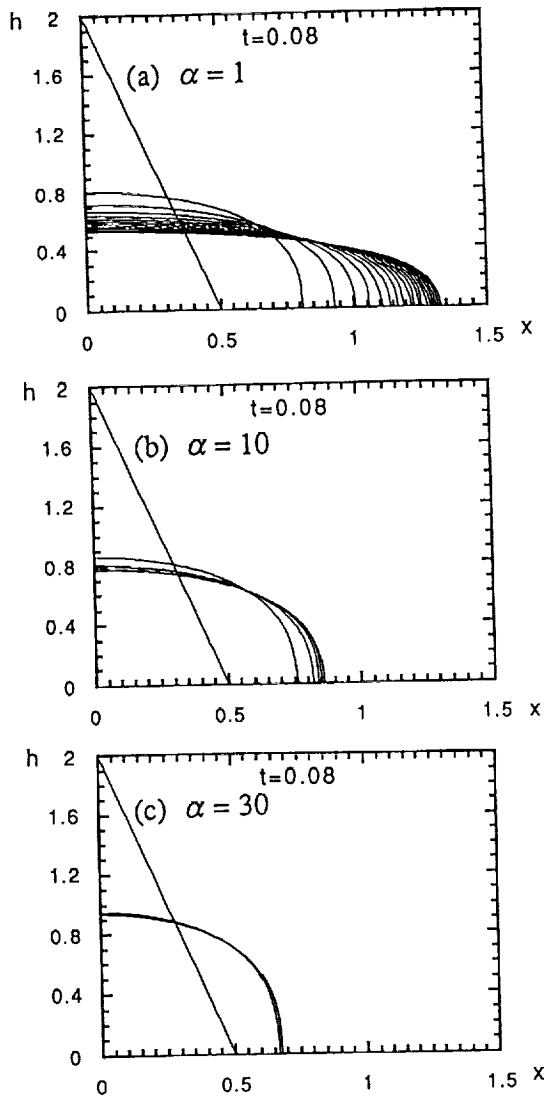

Figure 2 Change of the flow shape: constant volume case.

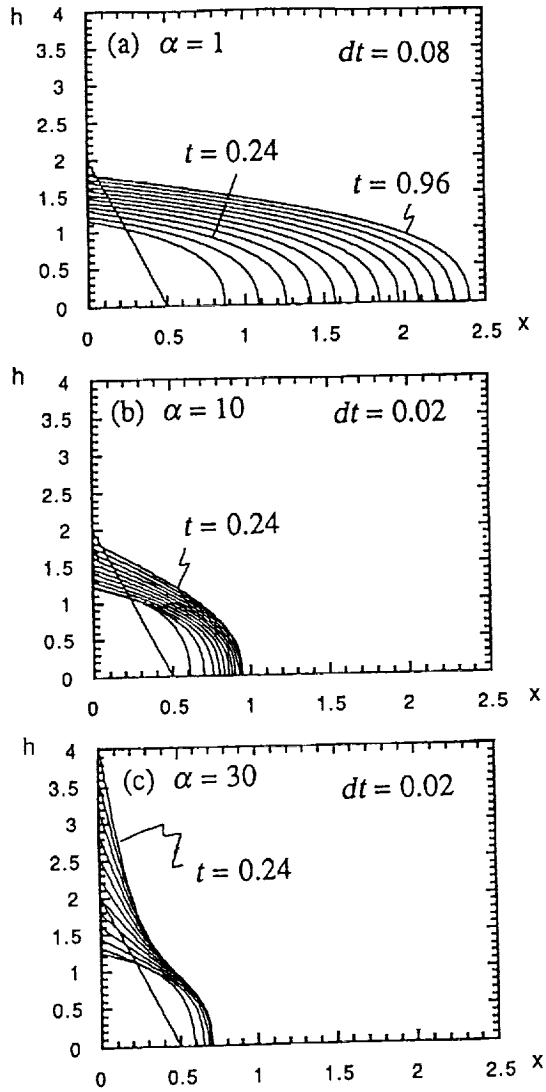

Figure 3 Change of the flow shape: increasing volume case ($V = 1 + 10t$).

SCIENTIFIC ANALYSIS AND DISPLAY OF MAGELLAN VENUS DATA WITH McIDAS-eXplorer; R.S. Saunders, Jet Propulsion Laboratory, California Institute of Technology, Pasadena, CA, Sanjay S. Limaye, L. A. Sromovsky, R. Krauss, E. Wright, D. Santek, and P. Fry, Space Science and Engineering Center, University of Wisconsin-Madison

The compilation of radar observations of the Venus surface from the Magellan mission data has resulted in over 70 gigabytes of radar reflectivity and radiometry images and altimetry profiles covering over 98% of the surface of Venus. The Magellan image data are available from the Planetary Data System on 129 CD - ROM volumes, the altimetry data on 15 CD-ROM volumes and the global topography, radiometry and surface slope compsite data are available on a set of 2 CD-ROM volumes. To facilitate access, analysis and display of these data, a software environment, McIDAS-eXplorer has been developed. This planetary image system is based on a mature system that is used extensively for Earth weather satellite observations and the extensions now allow analysis of most solar system targets for which spacecraft and ground based telescopic data are available in a large number of recognizable formats. Navigation, registration and calibration of the planetary data are an integral part of the environment. Designed to run on most UNIX workstations supporting X-windows, the environment is user extensible allowing addition of user developed applications and includes both a Graphical User Interface and a command line interface, multi-frame display and animation capability and tools for most image processing applications such as digital enhancements, filters, cartographic projections, graphical overlays, and color composites.

McIDAS-eXplorer is a multi-processing environment and can run as many applications or user sessions as practical under the computing, memory and peripheral storage resources available. Batch processing is supported as well as the ability to create or use different user interfaces such as a function key template, a graphical user interface or the command window. A simple macro facility allows quick creation of specific command sequences that are used repetitively.

In order to fully exploit the navigation, calibration, display and animation capabilities of McIDAS-eXplorer, the data are first imported into McIDAS-eXplorer along with all available navigation and calibration data and stored in the workstation in a specific format. Processing history records are kept for each image imported along with the entire text label that the image was tagged with (e.g. the PDS or the VICAR label). The supplementary calibration information for the radar images to convert raw data numbers into radar reflectivity is accessible to the system, such that while roaming (with the use of a mouse controlled cursor) in a displayed

image, the full calibrated and navigated data (incidence angle and radar reflectivity in dB, latitude and longitude) can be retrieved at the cursor location. The altimetry and radiometry data can be found and plotted over an image. All the Venus nomenclature is available for inserting into the plots.

These capabilities will be demonstrated using Magellan data at the conference.

This work is funded at the University of Wisconsin-Madison under Contract # NAS5-31347 from NASA's Applied Information Systems Research Program and was performed, in part, at the Jet Propulsion Laboratory, California Institute of Technology, under contract with NASA.

Genesis and Parameters of Ultramylonite and Pseudotachylite formation (Puchezh-Katunky astrobleme, Russia).

L.Sazonova, N.Korotaeva. Moscow State University, Geological Department, Moscow, 119899, Russia.

In this work we have tried to estimate genesis and some parameters of ultramylonites (UM) and pseudotachylites (PT) formation in the central uplift of Puchezh-Katunky Astrobleme on the basis of super deep core hole studying made in that uplift.

The central uplift of this astrobleme is formed by Archean amphibolite, gneisses, plagiogneisses, different schists. All these rocks are embedded with dolerite and ultrabasite dykes. Central uplift rocks bear traces of shock metamorphism showing that maximum shock loading in the Astrobleme exceeded 50 GPa. In these rocks there is a network of branching veins, lenses (varying in width from several mm to several tens of cm) of solid brown rocks of aphanitic structure where tiny rocks fragments are practically not deserved.

Such formations from biotite- and biotite-garnet gneisses and dolerites have investigated with the help of scanning electron microscopy (CamScan-4DV) with energy-dispersive analyzer (An-10000). In the process of investigation with the help of electronic microscope it has been found that such rock formation are ultra thin fractional and in dependence of glass content refer to UM or PT. In UM a small quantity of glass fragments is present (first %) and in PT the fragment content is 30-40% of the rock, the rest is glassy cement matrix. In both types of rocks the fragments are those of surrounding rocks, their sizes varying from first tens of mkm to fist mkm often to tenth mkm. We have noticed characteristic features of impact mineral transformation neither in UM nor in PT. Both UM and PT are formed **in situ** without noticible replacement of fractional and fused material.

With the help of Px-Gr and Amf-Px geotermometers and geobarometers [1] we have found the parameters of UM formation. The formation temperatures of UM in dolerites vary from 860° to 1290° C, pressures from 0.36 to 1.46 GPa. The formation temperatures of UM in Bi-Gr gneisses vary from 660-700° C.

PT are observed in central uplift of Puchezh-Katunky Astrobleme more seldom than UM. PT have been found in Bi- and Bi-Gr gneisses. In such rocks with completely fused matrix fractions of quartz, orthoclase, garnet, plagioclase, apatite, sphenel are present. A very important feature of PT is that they are transformed into UM in some localities that is the quantity of fused material sharply decreases while that of fractional one increases. Thus a direct connection between UM and PT is quite clear. The fused matrix of PT is microporous, glassy, often with great quantity of dendrites. These dendrites are enriched by Ti, P, Al and their composition corresponds to Px. In reference to 6 atoms of O these dendrites have the formula: $(Ca_{0.57}Mg_{0.39}Fe_{0.40}Ti_{0.23}Al_{0.12}P_{0.10})_{1.81}[Si_{1.40}Al_{0.60}]$.The cation sum in reference to 6 atoms of O is depleted which is often observed in crystals having great growth velocity. Dendritic pyroxenes with high P content are described in silicate inclusions in natural iron-carbon alloy (Disco Island, Greenland). P-enriched olivines are found in the same silicate inclusions and in Zaisho meteorite [2,3]. The studies of formation conditions of these minerals as well as the results of experimental works [2-5] show that formation of such unusual pyroxenes (P, Ti, Al-rich) require the combination of conditions which are seldom found together. These conditions are low f_{O2} , high velocity of crystal growth, low Si-content, high P_2O_5 - concentration in the melt. No doubt sharp melt super cooling together with its sharp superheating is of great importance. The combination of all these factors takes place in this case. UM and PT chemical compositions are sharply Si, Na-poor and P, Ti, Fe, Mg, Ca-rich in comparison with the surrounding rocks . Maximum difference is observed for PT, the least-for dolerite UM (tabl., fig.) The same regular composition PT changes in comparison with surrounding rocks have been observed before [6]. So far as we have got proofs that UM and PT are formed **in situ** we are led to conclude that dark colour minerals and among them most of all biotite were the first to take part in UM and PT formation processes.

Um and PT formation results from the rock resistance to shear strength. In UM fraction melting just begins on the account of heat in friction process, friction sliding. In PT wchich appeared those places where rock loading were greater complete fusion of fine grained crystalline rocks take place at friction sliding. The resistance to shear strength for dark colour minerals is less than that for quartz and field spar [7]. Among the dark colour minerals biotite has the least resistance to shear strength.

Therefore UM and PT are enriched with the components of dark colour minerals. Thus in UM and PT of Puchezh-Katunky features of shock metamorphism are absent. On the other hand numerous traces of plastinic deformation and friction fusion notifying that the genesis of these rocks results from the resistance to

shear strength. The parameters of UM formation agree with such a conclusion. Though the nature of shear strength in the studied rocks is undoubtedly connected with shock wave processes UM and PT presence is not in general a sigh of impact processes.

1. Perchuk L.L., Rjabchickov J.D. Phase correspondence in mineral systems. Moscow, 1976, 287p. (IN Russian). 2. Goodrich C.A. - Geochim. Cosmochim.Acta, 1984, 48, 2769-2771. 3. Buseck P.R., Clark J. - Mineralogical Magazine, 1984, 48, 229-235. 4. Newson H.E., Drake M.J. - Geochim. Cosmochim. Acta, 1983, 47, 93-11. 5. Donaldson C.H. - Contrib. Mineral. Petrol., 1976, 57, 187-243. 6. Thompson L.M., Spray J.G. - International Conference on Large Meteorite Impact and Planetary Evolution. Sudbury, Canada. - 1992, 73-74. 7. Allen A.R. J. of structural Geology, 1979 1, 3, 231-243.

Table

Chemical Composition of ultramylonites, pseudotachylites and surrounding rocks.

	dolerite	UM in dolerite	Bi-Gr gneisses	UM in gneisses	PT in gneisses
SiO_2	52.06	51.05	68.34	44.90	41.41
TiO_2	1.0	1.43	0.41	1.00	1.25
Al_2O_3	17.43	17.03	16.36	19.50	18.63
FeO	9.46	11.04	2.61	11.71	15.80
MnO	0.19	0.22	0.13	0.10	0.12
MgO	5.64	6.48	0.73	7.07	8.98
CaO	10.11	9.86	2.01	10.45	6.38
Na_2O	2.83	1.35	6.44	0.36	0.77
K_2O	0.72	1.32	2.49	2.45	5.42
P_2O_5	0	0	0.1	0.1	3.2

Fig. The rocks of target: (1) Bi-Gr gneisses; (2) dolerites. Ultramylonites: (3) in gneisses; (4) in dolerites. pseudotachylites: (5) in gneisses

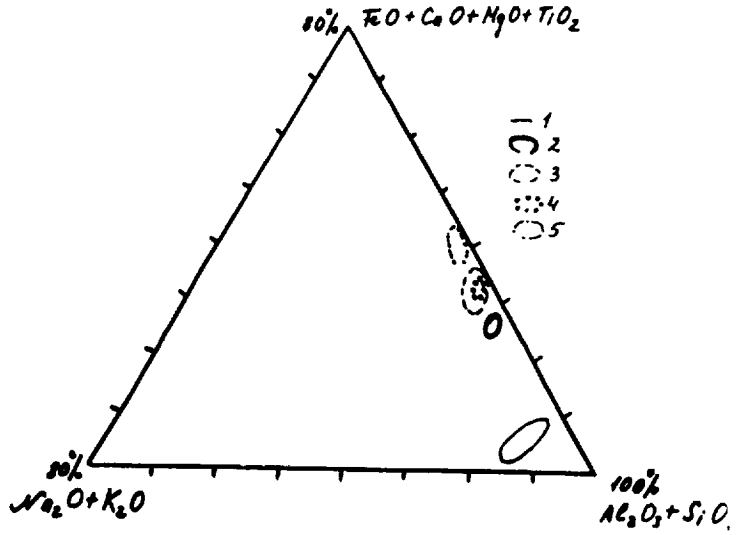

VENUS: FRACTURED CRATERS REVISITED, AND THE EVIDENCE FOR MINIMAL GEOLOGIC ACTIVITY OVER THE PAST 300 M.Y.; **G.G. Schaber**, U.S. Geological Survey, Flagstaff AZ, R.G. Strom, U. of Arizona, Tucson AZ, and D.J. Chadwick, U.S. Geological Survey, Flagstaff AZ

Fractured Craters-A total of 932 impact craters have been identified on 98% of the surface of Venus. This impact record constitutes a virtually complete survey of the Magellan data as well as the Venus cratering record. A recent reassessment of the modification classes of these craters using the Magellan image dataset has revealed that a remarkable 84% of all craters have pristine morphologies [1]. Only 12% of the craters are now classified as clearly fractured (8.5% slightly fractured; 3.5% heavily fractured); only 3.5% of the craters are embayed by volcanic deposits. It is no surprise, considering the higher elevation of the major fracture belts, that we find that the mean elevation of the heavily fractured craters is highest (6052.86±2.03 km), followed by elevation of slightly fractured craters (6052.19±1.50 km), lava-embayed craters (6052.17±0.83 km), and pristine craters (6051.74±0.83 km). These mean elevations for different crater classes are in general agreement with [2]. The percentage of craters interpreted as fractured has been reduced by half from our original estimate of 33% [3]. According to our new methodology for assessing modification, craters are classified as fractured only if one or more fractures are clearly observed to transect the crater rim and floor. Because crater floors on Venus are commonly flat, smooth, and therefore radar-image dark, they provide an optimal contrast in radar backscatter to crosscutting, radar-bright fractures. Upon examination of the entire Magellan image dataset, we found, for example, that many lineaments earlier recognized within the ejecta of craters on highly fractured terrains do not actually cross the floor deposits and are, in fact, pre-existing structures only thinly blanketed by ejecta.

Using standard statistical methods, we have confirmed that the distribution of impact craters on Venus is consistent with a completely random one (including stochastic variations), both spatially (as originally shown by [4]) and hypsometrically (i.e., with regard to elevation) [1] (See poster talk [5].) These results are not in agreement, however, with a report of possible ancient terrains on Venus [6], or with the suggestion that the craters are distinctly nonrandom with elevation [2]. As a result of the paucity of impact craters on Venus and their completely random distribution, it is not possible to determine surface ages, even on a regional basis. Nevertheless, three separate regions (covering 25±10% of Venus' surface) with distinct surface ages have been proposed by [7].

We find that about 9% (13 of 147) of all craters ≥35 km in diameter and 11% (47 of 428) of all craters ≥16 km in diameter lie on tesserae. These percentages agree very well with the percentage of the planet's surface (10%-11%) estimated to be occupied by tesserae [8]. Given the spatially and hypsometrically random distribution of impact craters, these results for the larger craters are interpreted to indicate that the average surface age of the tesserae is statistically the same as that for the entire planet (about 300 m.y.). The results do not support the older average age (900+430-330 m.y.) for tesserae suggested by [8], based on their independent tesserae crater counts. We agree with [8], however, that there is a deficiency (of about half) of impact craters <16 km in diameter on tesserae, and that most of these missing craters may be unrecognized on the rough terrain.

We have shown that a global resurfacing event ending 300±200 m.y. ago best accounts for (i) the random spatial and hypsometric distribution of the impact craters, (ii) the low crater density (1 per 500,000 km^2), and (iii) the paucity of impact-related features (craters, haloes and splotches) that have been embayed by volcanic lava flows [1,3]. In the global resurfacing model, extreme tectonic and volcanic activity prior to about 300 m.y. ago acted together to obliterate the pre-existing record of early heavy bombardment and later light bombardment. The extensive lowland plains on Venus were resurfaced dominantly by volcanism, while at the same time the less abundant, higher tesserae were resurfaced dominantly by tectonism [1,3]. There is evidence from studies of tectonic deformation

within some tesselated uplands that global-scale resurfacing may have been episodic throughout Venus' history [9], as earlier suggested by some thermal evolution models [10].

Minimal Geologic Activity Over the Past 300 m.y. The record of geologic activity on Venus over the past 300 m.y. is well preserved. It suggests much lower levels of tectonism and especially volcanism than the levels of earlier periods, which completely erased the preexisting cratering record. Recent modification of the Venusian surface has been largely the result of simple fracturing (with limited extension) and regional volcanism on such a low level that the cratering record has been left virtually intact.

In general, the most recent geologic activity postdating the proposed global event has occurred along broad fracture belts that criss-cross the middle latitudes of the planet and were first described from Pioneer Venus altimetry [11,12]. Three broad tectonic "disruption zones" were named the Aphrodite-Beta, Themis-Atla, and Phoebe-Atla zones and attributed at that time to limited extension [12]. The Magellan data support this interpretation and show the disruption zones to be complex, anastamosing belts of closely spaced fractures, grabens, coronae, and volcanic eruption centers. Where the three disruption zones broadly intersect in the vicinity of Maat and Ozza Montes in Atla Regio and near Thela Mons in Beta Regio, there is evidence of ongoing shield volcanism. High-emissivity volcanic peaks at high elevations, combined with spatially related, low-emissivity, volcanic domes on the plains, have been interpreted to indicate recent volcanic activity [13]. Sites of such activity are in the Beta-Atla-Themis (BAT) region, which has been described as having the highest density of volcanic landforms on Venus [14]. Three of the larger shield volcanoes (Sapas, Maat, and Ozza Montes), all in Atla Regio, are grouped together and are closely associated with five embayed craters (the densest concentration of such craters on the planet); Maat Mons is thought to have been the most recently active [13]. Thus, the general region at the intersection of the Themis-Atla and Aphrodite-Beta tectonic belts may have been the locus of the most recent volcanic activity on Venus. Also, this region was likely the location of a significant fraction of the estimated 20 or so craters actually destroyed since the last global resurfacing event. The 33% of Venus' surface bordered by lat ±30°, long 60°-300° E. contains twice as many heavily fractured impact craters as the planetary average and 1.4 times more lava-embayed craters [1,3]. This region includes most of the major tectonic belts in the equatorial region. Given that the craters are statistically random both spatially and hypsometrically, this concentration of heavily fractured craters and embayed craters is statistically significant and indicative of a continuing low level of limited extension and volcanic activity in this region over the past 300 m.y. For tesserae craters ≥16 km in diameter, 15% (7 of 47) are slightly fractured and 13% (6 of 47) are heavily fractured; thus, the tesserae areas appear to have been slightly more tectonically active than the planetary average over the past 300 m.y. We must keep in mind that the modified craters on Venus are simply fractured and/or embayed, and very few have been subjected to complete tectonic disruption, complete burial, and subsequent removal from the surface as was the case during the latest global resurfacing event. Nothing other than global resurfacing, followed by the present level and style of geologic activity, could have produced the observed cratering record.

References Cited: [1] Strom, R.G., Schaber, G.G., and Dawson, D.D., *J. Geophys. Res.-Planets*, in press; this conference; [2] Herrick, R.R. (1993) LPSC XXIV, 645-646; [3] Schaber, G.G., et al. (1992) *J. Geophys. Res.*, 97, E8, 13,257-13,301; [4] Phillips, R.J. et al., (1992) *J. Geophys. Res.*, 97, E10, 15,923-15,948; [5] Banks, M. et al., this conference; [6] Schultz, P. (1993) LPSC XXIV, 1255-1256; [7] Phillips, R.J. (1993) Supplement to EOS, Spring Meeting, 74, no. 16, 187; [8] Ivanov, B.A. and Basilevsky, A.T. (1993) LPSC XXIV, 693-694; [9] Chadwick D.J. and Schaber, G.G., this conference; [10] Arkani-Hamed, J., Schaber, G.G., and Strom, R.G. (1993) *J. Geophys. Res.*, 98, E3, 5309-5315; [11] Masursky et al. (1980) *J. Geophys. Res.*, 85, A13, 8232-8260; [12] Schaber, G.G. (1982) *Geophys. Res. Lettr.*, 9, 499-502; [13] Robinson, C.A., and Wood, J.A. (1993) *Icarus*, 102, 26-39; [14] Head, J.W., et al. (1992) *J. Geophys. Res.*, 97, E8, 13,153-13,197.

VENUSIAN PARABOLIC HALOS: NUMERICAL MODEL RESULTS. C. J. Schaller and H. J. Melosh, Lunar and Planetary Laboratory, The University of Arizona, Tucson, AZ 85721.

Magellan SAR images have revealed roughly 50 craters which have large, parabolic halos associated with them [1]. Using a numerical model in which impact ejecta is sorted by the Venusian atmosphere [2], we have successfully modeled half of these. Results seem to be supported by the terrestrial crater Chicxulub.

Briefly, the model (from [2]) requires the crater-forming impact to be large enough to form an atmosphere-piercing vapor plume. Particles carried aloft by the plume may then follow ballistic trajectories back into the atmosphere, where they will fall at terminal speed. Atmospheric winds will affect the particles' paths; in the case of Venus, the strong, westward-moving winds will tend to carry particles westward. Smaller particles, with a smaller terminal speed, will tend to travel greater distances than larger particles.

It is assumed that the particles are distributed radially from the center of the crater in the form of a power law [2]:

$$\bar{d} = \bar{d}_c \left(\frac{r}{r_c} \right)^{\alpha} \qquad (1)$$

where $\bar{d}$ is the mean particle diameter, $\bar{d}_c$ is the mean reference size which scales the law, r is the distance from the center of the crater, r_c is the crater radius, and α is the empirical power. In order to fit the model to the observed halos, we must choose the correct values for the reference size and the power.

It should be noted that not all Venusian impacts will generate a plume large enough to pierce the atmosphere; Vervack and Melosh [2] have calculated that craters less than 16 km in diameter are not large enough. The ejected particles will not leave the atmosphere, and equation 1 will not necessarily hold.

For each halo to be modeled, we used a crater radius as determined from [3]. We started the calculations (arbitrarily) at 100 km from the crater's center. Since the model has particles traveling only westward, it is reasonable to use the width of the halo as a stopping criterion. Thus, when the initial particle distance, used in equation 1, reached 10% more than half of the halo's maximum width as reported in [1], we stopped the calculations.

There are several potential dimensions to which we could attempt to fit the model. Inspection of the Venusian halos suggests that the best-defined borders are near the crater's end of the halo. We therefore used the distance from the crater's center to the tip of the halo as our primary target dimension. As a secondary dimension, we used the halo's width at the longitude of the crater. The overall lengths and widths of the halos were less important to the fitting process.

We must also consider the depth to which we can see the halos. Campbell et al. [1] suggest a depth on the order of centimeters to meters. We attempted to fit halos at two minimum thicknesses, 1 cm and 10 cm. At thicknesses less than the minimum, the radar does not detect ejecta.

We found that halos with craters less than about 20 km in radius could not be fit to our model, which agrees well with [2]. In addition, although it was possible to match the primary and secondary dimensions to within 10%, at a minimum thickness of 10 cm, we could not match

the lengths and widths of the halos. At a minimum thickness of 1 cm, however, we were successful.

We had success with 19 halos at the 1 cm thickness level: Abington, Adivar, Akeley, Akiko, Aurelia, Austen, Ban Zhao, Bassi, Boleyn, Boulanger, Caldwell, Carson, Faustina, Frank, Pimiko, Stowe, Stuart, VonSchuurman, and Yablochkina. From successfully fitting these halos, we find $\alpha = 2.65 \pm 0.03$. For Chicxulub, a range of 2.0 to 2.5 was determined [2] using microtektite data.

We found that the reference sizes for these halos follow a power law of their own, according to crater radius. (See the accompanying figure.) The reference size relationship determined is

$$\log \bar{d}_e = (3.18 \pm 0.34) + (-1.56 \pm 0.26) \log r \qquad (2a)$$

or

$$\bar{d}_e \approx 1500 r^{-1.56} \qquad (2b)$$

with the scaling coefficient ranging (to one standard deviation) between 3300 and 690 and the power ranging between -1.30 and -1.82.

This power law (2b) fits Chicxulub quite well. With a crater radius of 90 km, Chicxulub's reference size was determined to be between 0.4 and 1.7 m [2]. The dashed line on the figure shows this. The model presented in [2] appears to hold up.

REFERENCES

[1] Campbell D. B. et al. (1992) *JGR*, *97*, 16,249. [2] Vervack R. J. and Melosh H. J. (1992) *Geophys. Res. Lett.*, *19*, 525. [3] Schaber G. G. et al. (1992) *JGR*, *97*, 13,257.

1 cm Minimum Detectable Thickness

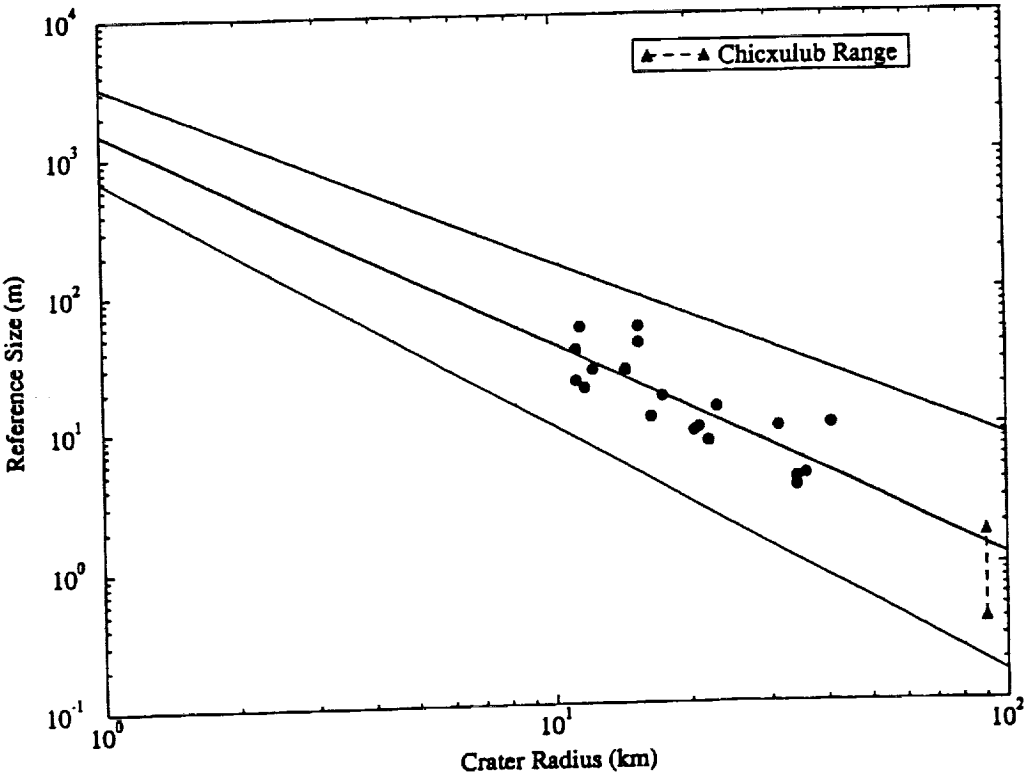

LOBATE THRUST SCARPS AND THE THICKNESS OF MERCURY's LITHOSPHERE;

P. Schenk, Lunar and Planetary Institute, Houston, TX; and H.J. Melosh, Lunar and Planetary Lab, Univ. of Arizona, Tucson, AZ

The thermal history and structure of the lithosphere of the planet Mercury is still a matter of some conjecture [1]. Despite its Moon-like appearance, Mercury has had a complex geologic history and probably has had an unusual thermal history as well. Constraints on thermal history can be obtained by determining lithospheric thicknesses at discrete times. Deformation that penetrates the lithosphere can be used to constrain lithospheric structure, especially thickness. Mariner 10 revealed numerous lobate scarps on Mercury (Fig. 1), and shortening of craters across these ridges indicate they are thrust scarps, generally attributed to lithospheric shortening during a period of global contraction [e.g., 2]. If so, these thrusts probably penetrate the lithosphere. Thrust faulting of this type produces a flexural response in the lithosphere. The wavelength of this topographic response is governed by the flexural parameter $\alpha = (4D/\rho g)^{1/4}$ where D is the flexural rigidity, $D = Eh^3/12(1-\nu^2)$, E is Young's modulus, ν is Poisson's ratio, and h is lithospheric thickness. The observed topography of many of these scarps is consistent with such a flexural response (Fig. 2).

Although thin-plate flexure models give some qualitative insight into the flexure induced by thrust faulting, they cannot be used in detailed modeling because of the loading conditions created by the fault extending over a horizontal distance comparable to the plate thickness, and thus violates the approximations made in deriving thin-plate theory. We have used the finite element code TECTON [e.g., 3] to model thrust scarp topography on Mercury. The code is designed for tectonic problems and includes well-tested methods for introducing fault discontinuities (here using 'slippery nodes' which permit free slip on a specified fault plane). Also, isostatic restoring forces are automatically developed in the large strain formalism employed by TECTON.

Mercury is one of the few places in the solar system where this type of modeling can be attempted, because the thrust scarps are well developed here and have not been seriously degraded by erosion. We selected Discovery Rupes (Fig. 1) for modeling. The scarp is several hundred kilometers long and ~2 kilometers high. The topography of Mercurian lobate scarps has been determined using photoclinometric profiles from calibrated Mariner 10 images. Our finite-element grid incorporated a fault dipping at 30°. Horizontal shortening of 20 kilometers was introduced into the 900 km wide grid, which was then allowed to relax over several Maxwell times. Lithospheric thicknesses of 10, 20, and 50 km were modeled, with faults penetrating the lithosphere either fully or halfway through. The best match to the actual topography of Discovery Scarp is given for the case of a fault dipping at 30° extending 10 km into a 20 km thick lithosphere (Fig. 3), subject to a final analysis of scarp topography on Mercury. The flexural parameter for this case is α=61 km, close to the wavelength of the scarp topography.

Lobate thrust scarps are relatively young features, geologically, although occasional young craters are superposed on them [e.g., 2, 4]. The present lithosphere of Mercury is probably >100 km thick [4]. Our modeling of lobate thrust scarps on Mercury indicates that the lithosphere was ~20 km thick at the time of faulting, and is the first observational support that the early lithosphere of Mercury was rather thin (much less than 100 km thick). This is consistent with indirect arguments that the lithosphere was <100 km thick at the time of despinning [5], prior to thrust fault formation. In contrast, the Moon's lithosphere was at least 25 to >75 km thick at the end of mare basalt flooding [6]. Implications of these results for Mercury's thermal history will be discussed.

REFERENCES: [1] Schubert, G., et al., in *Mercury*, p. 429, 1988. [2] Strom, R., et al., *J. Geophys. Res.*, 80, 2345, 1975; Dzurisin, D., *J. Geophys. Res.*, 83, 4883, 1978. [3] Melosh, H.J., and A. Raefsky, *Geophys. J. R.A.S.*, 60, 333, 1980. [4] Leake, M., NASA TM-84894, 1982. [5] Melosh, H.J., and W. McKinnon, in *Mercury*, p. 374, 1988. [6] Solomon, S., and J. Head, *Rev. Geophys. Space Phys.*, 18, 107, 1980.

MERCURY'S LITHOSPHERIC THICKNESS: Schenk, P., and Melosh, H.J.

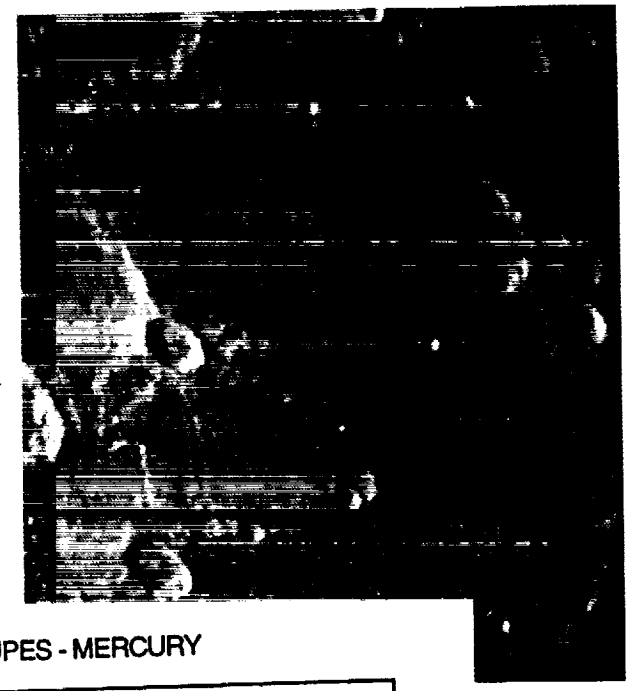

Figure 1. Mariner 10 image (FDS 27399) of Discovery Rupes. Image is ~300 kilometers across. Black line indicates location of topographic profile in Figure 2.

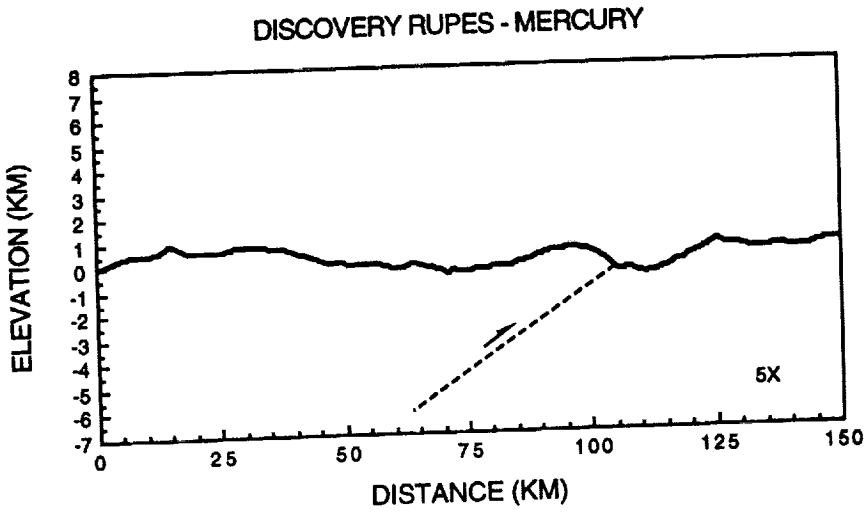

Figure 2. Topographic profile of Discovery Rupes, Mercury. Dashed line indicated inferred location and orientation of thrust fault. Upthrown block is to the left.

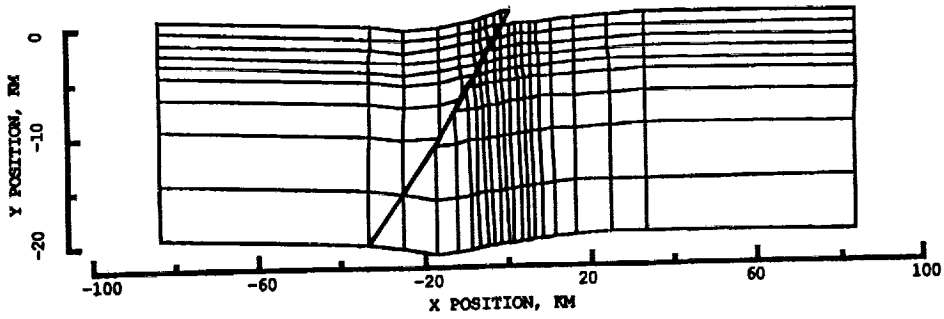

Figure 3. Finite-element grid for 20-kilometer thick lithosphere. Grid is shown after thrust faulting has occurred along a 30° dipping fault extending to a depth of 10-kilometers. Surface topography clearly shows a flexural response that matches well the actual topography of Discovery Rupes in Figure 2.

THE STEREO VIEW OF THE SOLAR SYSTEM; Paul Schenk, Daniel Wilson, and Robert Morris, Lunar &Planetary Institute, Houston, TX 77062; Timothy J. Parker, Jet Univ. of Southern California, Los Angeles, CA 90089.

Stereo imaging can literally transform our perception of planetary bodies. It is of primary importance in distinguishing topography from albedo, namely in areas where high sun angle or complex albedo variations make topography ambiguous. This is especially true for Io, Triton, and Mars where volcanic and aeolian deposits have complex color and albedo patterns. Polar regions, where nonuniform frosts can confuse topographic information, are also good stereo candidates, as are fresh crater deposits. Determination of relief is also important in specific investigations. For example, in physical volcanology where regional slopes can control flow morphology, or thermal studies where topography across craters is a measure of lithospheric viscosity and heat flow.

Stereo can be used as an interpretive tool when viewing images taken under different illumination or filters. Our brain works best stereoscopically and by merging two images optically feature recognition and 'effective' resolution is improved. In areas with variable albedo photoclinometry (PC) will not work in monoscopic images. PC will not produce reliable topography over broad areas due to accumulated errors and unaccounted for albedo variations. As with Magellan, the only way to obtain reliable pixel-scale topography (digital elevation models) over large areas in the outer solar system for future planned missions will be by stereo. It should also be possible to map the global geoid figure using a properly acquired data set, as has been attempted for Io. To this end, we are in process of generating a stereo image catalog of the solar system, with particular emphasis on the outer solar system. Work has also begun in earnest on Viking stereo imagery of Mars, and Mariner 10 stereo of Mercury.

STEREO: Processing & Problems

The Voyager image library contains numerous untapped stereo targets on the icy satellites. However, because of planetary curvature, changes in viewing geometry and target-spacecraft distances it is not possible to optically fuse most Voyager stereo pairs in their original format. The production of useful stereo pairs requires a complex set of procedures. Once a set of images with suitable stereo parameters is selected, the images are calibrated for vidicon effects and spatially filtered to enhance detail. The images are then co-registered and projected to a common orthographic map format centered on the feature(s) of interest. To mosaic multiple frames without forming distracting image boundary 'scarps' it was necessary to update the camera pointing vectors for all the images with subpixel accuracy, which has proved time consuming. The images are assembled into left and right mosaics that are high-pass filtered to remove the global brightness variation and contrast stretched for optimal retention of dynamic range and viewing pleasure.

Voyager images were not targeted for stereo, however. To achieve suitable stereo separation it was sometimes necessary to use images with significantly differing spatial resolution, or filters, depending on image sequencing. Solar illumination angles changed during some imaging sequences, although this was mostly a problem for the small inner satellites of Saturn. The positions of some vidicon reseaus are not accurate or remappable with extreme precision, resulting in some ambiguity regarding very-long-wavelength topography. Image smear during the Voyager 1 Jupiter flyby reduced the potential stereo targets for Io, Ganymede, and Callisto. Finally, relief on the icy Galilean satellites rarely exceeds 2 km, and image resolution is relatively low, requiring greater angular separation between images to produce stereo.

STEREO COVERAGE AND RESULTS

In the outer solar system, the best stereo occurs on Miranda, Rhea, and Io. The best Io stereo pairs often required use of green filter wide-angle images. Differences in photometric properties and colors of geologic units should be remembered when interpreting these stereo pairs. Up to 20% of Io can be mapped with stereo at resolutions ranging from 500 m to 2 km. Additional coverage at lower resolution exists, and a search for undiscovered plumes will be possible. Several previously unknown prominent mountain structures have been identified. Relief on large volcanic constructs is variable. At Ra Patera, relief is unexpectedly low, implying very shallow slopes or late-stage topographic subsidence. On Rhea, most of the lit northern hemisphere is visible in stereo. The surface is extremely rough: no smooth terrains of any kind are apparent. Evidence for large ringed structures is ambiguous, but global scale linear structures are apparent. Particularly impressive are craters, which have steep rimwalls and prominent central peaks, consistent with earlier results based on photoclinometry. Image targeting permitted stereo coverage of ~8% of Ganymede's surface, with vertical exaggeration factors ranging from ~2 to 6. Examples of major features on Ganymede seen in stereo include craters, grooves, smooth terrain, palimpsests, and the large basin Gilgamesh. Despite low resolution and low relief, portions of the Valhalla ring structure on Callisto can be seen stereoscopically. 'Flows' emanating from ring scarps appear to be thicker than anticipated.

Geologic mapping based on these and other stereo products is in progress. Stereo results for Mars have a high scientific potential, if pointing problems can be overcome. Preliminary products will be presented.

STEREO ON FUTURE MISSIONS

Operational and planned missions offer many excellent stereo opportunities in the coming decades. In many cases, proper planning can produce selected stereo with a minimum number of additional images. In some cases, combination of new mission images with Voyager or other older data sets can produce 'cheap' but high quality stereo results. Here, image resolution appropriate viewing angle separation and particularly solar illumination must be considered so that scientifically useful stereo can result. Combination of stereo with color data can be of special importance, as shown by our Io results.

HOLE SIZE FROM IMPACTS AT SCALED VELOCITIES OF 7 TO 21 KM/S

R. M. Schmidt and K. R. Housen, Boeing Defense and Space Group, M/S 87-60, Seattle WA 98124

Holsapple (1993) and Schmidt *et al.* (1993, 1994) have shown that cadmium surrogates provide a viable technique for simulation of aluminum-aluminum impacts at velocities up to 21 km/s using conventional light gas guns. Theoretical and experimental studies support a magnification factor of 3.1 on velocity based upon the specific energy required for melt and vapor phase transitions. Cadmium has a density approximately 3.1 times larger than aluminum; consequently the total projectile momentum is identical for tests of the same projectile size as the aluminum prototype of interest. The hole size data used here are from experiments described by Schmidt *et al.* (1993, 1994) and performed at the University of Dayton Research Institute by Messrs Piekutowski and Poorman.

The diameter, D, of the hole produced by an impact on a thin plate is expressed as

$$D = f(d,U,\delta,b,\beta,Y) \quad (1)$$

where d, U, and δ are the impactor diameter, velocity, and density, and b, β, and Y are the thickness, density, and strength of the plate. This expression can be written in terms of four dimensionless parameters as

$$\frac{D}{d} = f\left(\frac{d}{b}, \frac{U}{\sqrt{Y/\rho}}, \frac{\delta}{\beta}\right). \quad (2)$$

Note that for fixed plate and impactor materials, the terms $\sqrt{Y/\rho}$ and δ/β are constant.

Figure 1 shows the results of cadmium tests plotted as D/d vs d/b, for fixed values of scaled velocity, U. Figure 2 shows a subset of these results plotted as D/d vs U, for fixed values of d/b. These two plots show a remarkable power-law dependence of hole size on both impactor diameter/plate thickness and velocity.

The power-law dependence on velocity can be explained by noting that these phenomena have been found to be well-approximated by an equivalent point-source coupling parameter by Arione and Bjorkman (1987a,b) and Holsapple and Schmidt (1987). For plate impacts, the coupling parameter, C, is expected to be a function of d, U, δ and b and, therefore, must be of the form $C = dU^{\mu}\delta^{\nu}f(d/b)$. If the hole diameter is a function of C, β, and Y, then for fixed materials, Eq. (1) simplifies to

$$\frac{D}{d} = U^{\mu} f\left(\frac{d}{b}\right) \quad (3)$$

which explains the power-law dependence on velocity shown in Fig. 2, but does not require the power-law for d/b shown in Fig. 1.

To obtain an expression that can be used for estimating hole size, the data shown in Fig. 1 were used in a linear regression, assuming a power-law for the function f:

$$\frac{D}{d} = 2.14\ U^{0.354\pm0.014}\left(\frac{d}{b}\right)^{-0.510\pm0.012} \quad (4)$$

where U is in km/s. This expression was used to construct the lines shown in Figs. 1 and 2.

The cadmium results also show good agreement with existing aluminum data at 6 to 7 km/s, which are represented by the "+" symbol in Fig. 1. This gives credibility to using Eq. (4) as a preliminary velocity dependence, which can used to extend some of the results of Hörz *et al.* (1993) to explain observed hole size distributions on aluminum panels returned from LDEF.

Arione S. E. and Bjorkman M. D. (1987a) Scaling of hole diameter from perforating impacts of plates, *APS Topical conference on shock Waves in Condensed Media*, Monterey, CA.

Arione S. E. and Bjorkman M. D. (1987b) Scaling flow fields from the impact of thin plates, Int. J. Impact Engng

Holsapple K. A. (1993) Hypervelocity impact experiments in surrogate materials, *Int. J. Impact Engng* Vol.14, pp.335-345.

Holsapple K. A. and Schmidt R. M. (1987) Coupling parameters in cratering mechanics, *J. Geophys. Res.* 92(B7), 6350.

Hörz F., Cintala M. J., Bernhard R. P. and See T. H. (1993) Dimensionally scaled penetration experiments to extract projectile sizes from space exposed surfaces, *Int. J. Impact Engng* Vol.14, pp. 347-358.

Schmidt R. M., Housen K.R., Piekutowski A.J. and Poormon K.L. (1994) Cadmium simulations of orbital debris shield performance to 18 km/s. Accepted for publication in *Journ. Spacecraft Rockets.*

Schmidt R. M., Housen K.R., and Ahlstrom H.G. (1993) Experiments and analysis of orbital debris shock-induced penetration of pressure vessels in space. *Proceedings of 19th International Symposium on Shock Waves, Marseilles, France, Springer-Verlag.*

HOLE SIZE FROM IMPACTS AT SCALED VELOCITIES OF 7 TO 21 KM/S **Schmidt & Housen, Boeing Co.**

Fig. 1 Hole size as a function of d/b for fixed velocity.

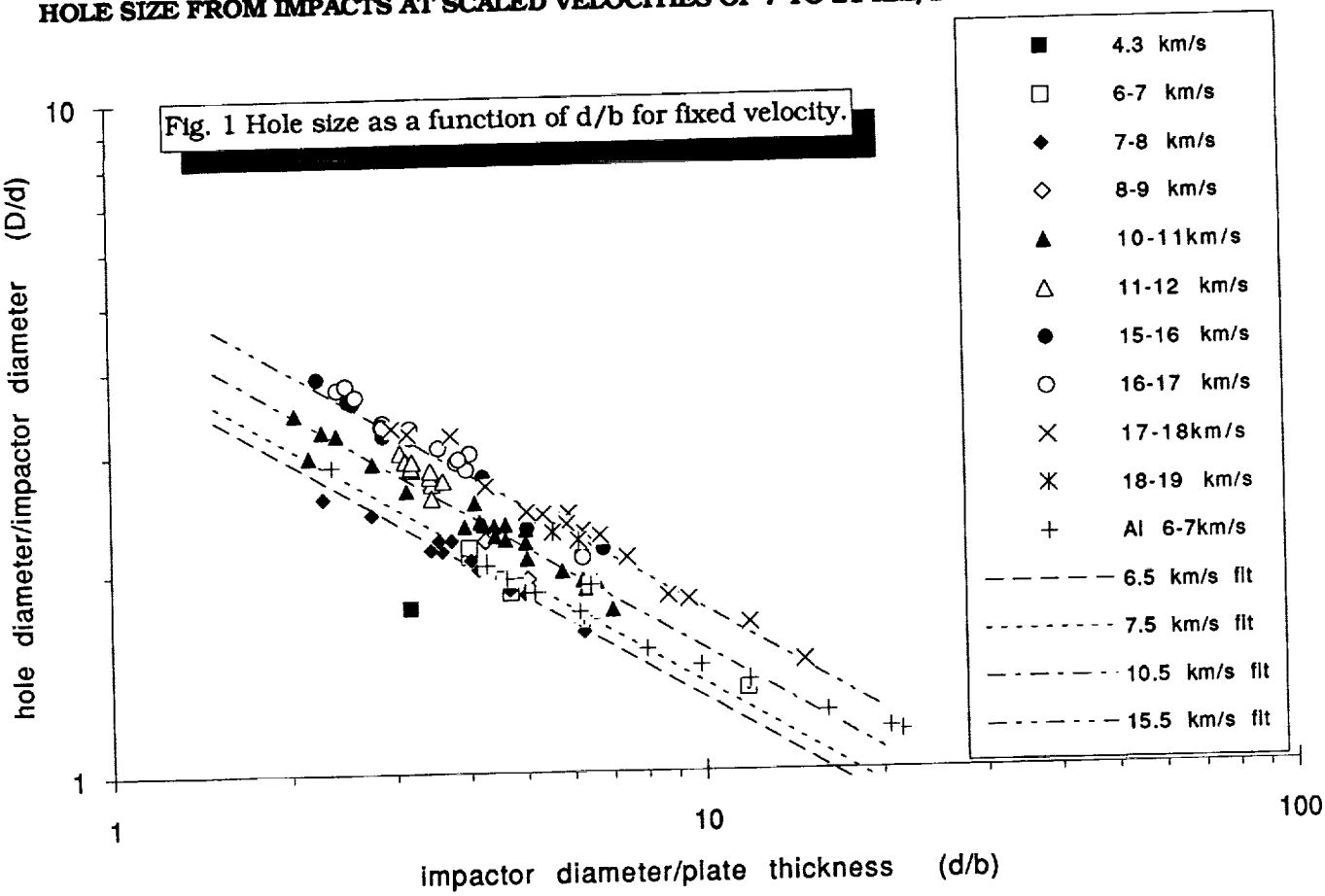

Fig. 2 Hole size as a function of velocity for fixed d/b.

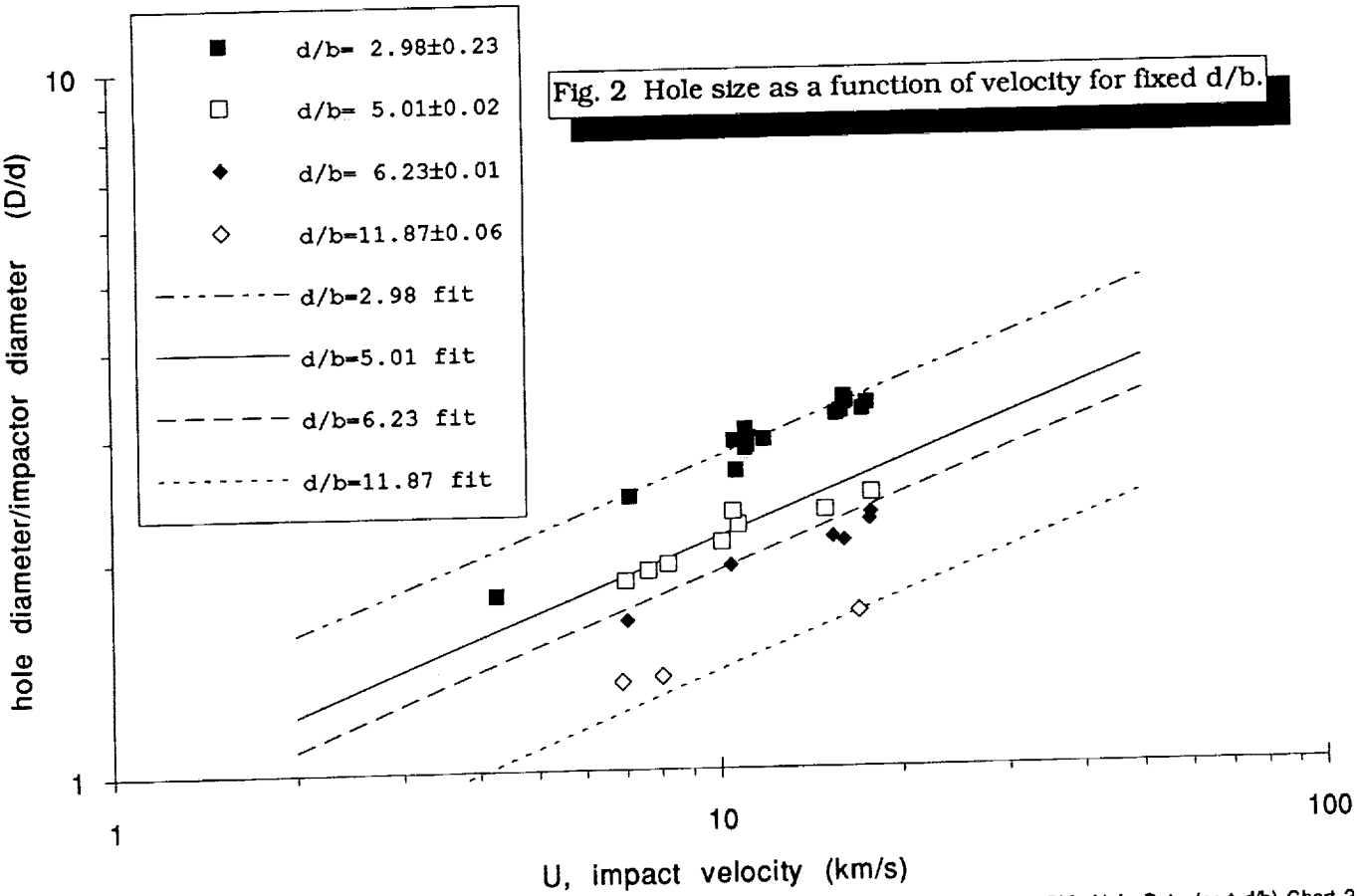

1/6/94 1:08 PM Hole Data (sort U) Chart 19

1/6/94 1:10 PM Hole Data (sort d/b) Chart 24

CALCULATION OF HUGONIOT CURVES AND POST-SHOCK TEMPERATURES FOR H- AND L-CHONDRITES

R. T. Schmitt[1], A. Deutsch[1] and D. Stöffler[2], [1]Institut für Planetologie, Wilhelm-Klemm-Str. 10, Westfälische Wilhelms-Universität, D-48149 Münster, Germany, [2]Institut für Mineralogie und Petrographie am Museum für Naturkunde, Humboldt-Universität, Invalidenstr. 43, D-10115 Berlin, Germany.

Introduction. The shock metamorphism of chondrites provides important information on the collisional and geologic history of asteroidal parent bodies [1]. The most important physical properties for the study of this phenomenon are Hugoniot data. So far, however, Hugoniot curves for only a few chondrites have been measured experimentally [2, 3]. These Hugoniot data are inconsistent, which apparently is an effect of the inhomogeneity of the chondritic samples used in these experiments. For this reason, we have developed a method for calculating Hugoniot curves of H- and L-chondrites. Based on these Hugoniot curves post-shock temperatures can be estimated.

Calculation of the Hugoniot curves. The following assumptions were made for the calculation: (1) The chondritic material is nonporous and behaves hydrodynamic. (2) The constituent minerals are arranged in monomineralic layers. (3) Phase changes of the minerals were disregarded. (4) The average mineral compositions of H- and L-chondrites given by [4] were used for calculation. First, the modal composition was calculated based on the CIPW-norm using mineral densities of [4]. For each shock pressure, the particle velocity of the chondrite was calculated with the formula given by [5]. Pressure dependent densities of the individual minerals, as required by this formula, were calculated from data compiled in [6], using a linear relation between shock wave velocity and particle velocity, and the density of the unshocked mineral. The shock wave velocity and pressure dependent density were than calculated from the particle velocity on the basis of the Hugoniot equations [7]. The results of the calculation are shown in Fig. 1.

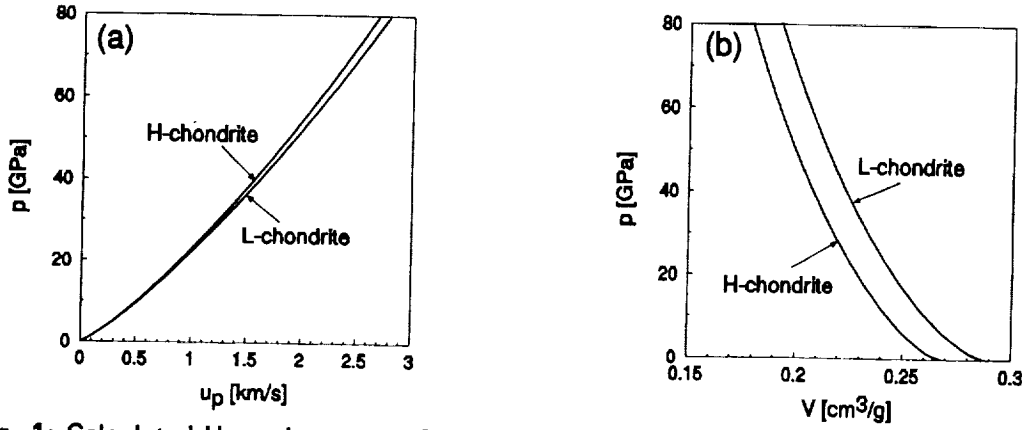

Fig. 1: Calculated Hugoniot curves for H- and L-chondrites: (a) pressure - particle velocity plot, and (b) pressure - specific volume plot.

Calculation of post-shock temperatures. The following assumptions were made in the calculation: (1) Release adiabats were approximated by the Hugoniot curve. (2) Phase changes of the minerals were disregarded. The post-shock temperatures were calculated by using the residual energy, which corresponds to the area between the Rayleigh line and the release adiabat [8]. In the case of nonporous chondrites, the area between p_0V_0, p_1V_1 and the Hugoniot curve (Fig. 2; cross-hatched) was used for calculation. For porous chondrites the area between p_0,V_{0P} (specific volume of the unshocked porous chondrite), p_1V_1 and the Hugoniot curve of the same chondrite without porosity (Fig. 2; hatched) was assumed for the residual energy. Average porosities of 8 % for H5-/ H6-chondrites, and 11 % for L5-/ L6-chondrites, as estimated by [4, 9], were used for the calculation. Given the residual energy (E_R), the post-shock temperature (T) can be calculated by the

equation $E_R = \int_{293K}^{T} c_p dT$ [8]. The specific heat capacities (c_p) for H- and L-chondrites (Fig. 3) were calculated from the mineral composition of the chondrites [4] and specific heat capacities of the minerals [10, 11]. Fig. 4 illustrates the results of the calculation.

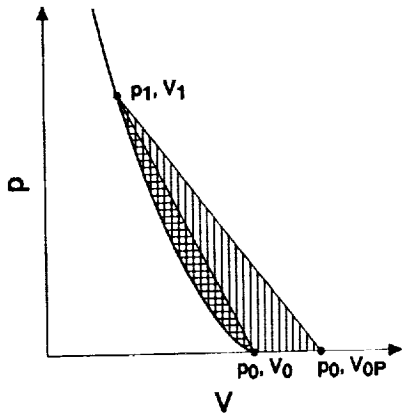

Fig. 2: Different residual energy for nonporous (cross-hatched) and porous (hatched) chondrites.

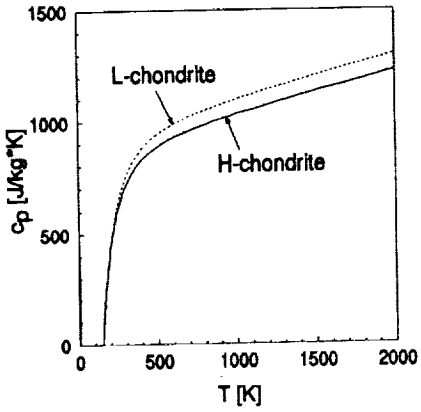

Fig. 3: Specific heat capacities calculated for H- and L-chondrites.

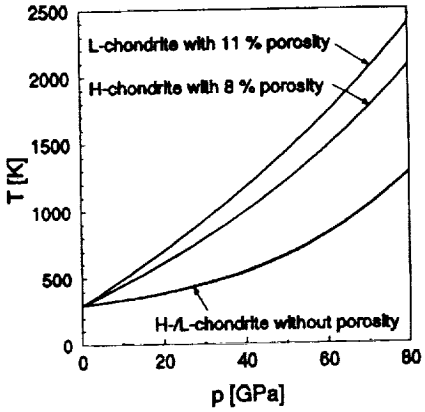

Fig. 4: Post-shock temperatures calculated for H- and L-chondrites.

Results and discussion. The distinct difference between the Hugoniot curves of H- and L-chondrites (Fig. 1) is mainly due to the different metal content of both types of chondrites. The Hugoniot curves are most strongly influenced by the metal and feldspar, as their Hugoniot curves are very different from those of olivine, the predominant mineral constituent. The calculated post-shock temperatures for nonporous chondrites are quite similar for H- and L-chondrites, since the difference in the metal content of both types of chondrites has no distinct effect on the post-shock temperatures. The most important factor for the post-shock temperature of a chondrite is the porosity of the sample (Fig. 4).

The calculated post-shock temperatures for nonporous chondrites are about 100 K lower than measured temperatures for nonporous silicates [12]. This is a result of the metal content of chondrites, because the post-shock temperatures of metals [13] are much lower than those of silicates. In comparison with post-shock temperatures for L-chondrites estimated from metal textures [14], the calculated post-shock temperatures for porous L-chondrites are about 250 K higher. This might be an effect of the inaccuracy of the porosity data available for L-chondrites. The results of the calculation could help explain different shock features in some chondrites of shock stage S3 - S5 [15]. These shock features, which include the occurrence of significant amounts of shock-induced melts and metal textures like coarse plessite or martensite [15], require a high post-shock temperature. Such a high temperature could be a result of a high initial porosity.

References: [1] STÖFFLER, D. et al. (1991) *GCA*, **55**, 3845-3867. [2] LIN, W.-Z. (1984) *Chin. J.Space Sci.*, **4**, 338-346. [3] MATSUI, T. et al. (1986) ***11th.Symp.Antarc.Met.***, 150-151. [4] YOMOGIDA, K. & MATSUI, T. (1983) *JGR*, **88**, 9513-9533. [5] MUNSON, D.E. & SCHULER, K.W. (1971) in BURKE, J.J. & WEISS, V. (ed.) *Shock waves and the mechanical properties of solids*, 185-202. [6] STÖFFLER, D. (1972) in *Landolt-Börnstein - Numerical data and functional relationships in science and technology, new series, group V: Geophysics and space research*, Vol. **1**, Sub.-vol. **A**, 120-183. [7] McQUEEN, R.G. et al. (1970) in KINSLOW, R. (ed.) *High-velocity impact phenomena*, 293-417. [8] GIBBONS, R.V. & AHRENS, T.J. (1971), *JGR*, **72**, 5729-5742. [9] YOMOGIDA, K. and MATSUI, T. (1981) *LPSC*, **XII**, 1227-1228. [10] ROBIE, R.A. et al. (1979) *U.S.Geol.Surv.Bull.*, **1452**. [11] BABUSHKIN, V.I. et al. (1985) *Thermodynamics of silicates*. [12] RAIKES, S.A. & AHRENS, T.J. (1979) *Geophys.J.Roy.Astron.Soc.*, **58**, 717-747. [13] MEYERS, M.A. & MURR, L.E. (1981) *Shock waves and high-strain-rate phenomena in metals*. [14] BENNETT, M.E. & McSWEEN, H.Y. (1993) *Meteoritics*, **28**, 322. [15] SCOTT, E.R.D. et al. (1991) *Meteoritics*, **26**, 393.

Chicxulub as an Oblique Impact. Peter H. Schultz, Department of Geological Sciences, Brown University, Providence, RI 02912.

Introduction: The discovery (1), confirmation (2), timing (3), and analyses of the geophysical expression (2, 4) of the Chicxulub structure establish a major impact at the end of the Cretaceous. These data also provide important clues for the nature of the collision based on analogy with well-preserved craters on other planets and an understanding of the impact process. Previous studies speculated about the effects a major oblique impact on the Earth (1, 2) but the new geophysical data contain substantive evidence that Chicxulub was formed by an object 10-15 km in diameter at an angle of 20-30° from the southeast. Such a perspective is important for appreciating the devastating atmospheric/biospheric stress.

Oblique Impacts--Mapping Time into Space: The impact cratering process can be subdivided into three stages (5): penetration, excavation, and modification. These stages are witnessed in laboratory and computational experiments of vertical impacts, but are largely masked in the final crater appearance as each successive stage supersedes the next. Oblique impacts, however, spread these time-dependent stages along the trajectory and preserve related asymmetries. *Penetration:* The penetration stage for oblique impacts changes with time along the trajectory. Laboratory experiments using the NASA-Ames Vertical Gun Range (AVGR) reveal that projectile failure occurs prior to significant penetration of the surface. Spallation of the uppermost surface results in a string of fragments along the downrange trajectory for very low angle impacts (< 10°). Higher impact angles (15-30°) result in ricochet rays subtending larger angles with increasing impact angle (from horizontal). For example, the Rio Cuarto crater in Argentina and Messier exhibit ricochet rays subtending only 5-10°, consistent with very low impact angles. Schrödinger (Moon) exhibits a pronounced pair of chains subtending about 45°, consistent with a higher angle. The 2-ring basin Bach (Mercury, Fig. 2a) and multi-ring lunar basin Orientale (Fig. 2b) exhibit similar patterns. In each case, the chains converge close to the first point of contact. The rate of energy transfer to the target depends on impact angle and velocity. Hypervelocity collisions result in the greatest penetration uprange with shallower penetration downrange due to "sibling" (projectile ricochet) collisions at lower angles. This early penetration stage is recognized both in laboratory experiments and at much larger planetary scales by: secondary and sibling crater chains extending back uprange; greatest shock damage at depth (penetration) but least surface failure uprange; elongate or breached penetration zones (expressed as elongate or breached central rings at planetary scales); downrange impact melt and vapor condensate preserving a portion of the impactor momentum; and asymmetric profile (deepest uprange in simple craters; uprange-offset central peaks in complex craters). The dimensions of the penetration zone have been found to be independent of impact angle and can be used to estimate impactor size consistent with other scaling relations (6, 7). Due to gravity-limited growth, the penetration stage comprises an increasing fraction of the excavation stage (20%) at very large scales (> 100 km). *Excavation:* The energy transfer from impactor to target resembles a moving source for oblique impacts. The pronounced penetration asymmetry becomes more symmetrical during the later stage of ballistic excavation. Consequently, a more radial pattern of ejecta emplacement centered downrange superposes the earlier non-radial pattern reflecting impactor failure centered uprange. The center of symmetry, however, is offset downrange from the region of deepest penetration. Fracture patterns generated by oblique impacts at the AVGR dramatize these two centers of symmetry (Fig. 1). The outer failure zone forms an incomplete, subarcuate fracture uprange but is centered downrange from the region of maximum penetration. Depth of excavation decreases with impact angle and may be significantly less downrange. *Modification:* The modification stage is difficult to document directly at laboratory scales. Nevertheless, this stage should reflect responses to both the region of deepest penetration and near-surface failure (Fig. 1). Deeper penetration results not only in rebound offset uprange but also enhanced rim/wall collapse uprange for craters above a critical size (6). This "circularizes" the crater outline in part, but the shallow depths of excavation downrange undergo less readjustment.

Chicxulub: The geophysical patterns and surface expressions of Chicxulub (2, 4) are consistent with formation by an oblique impact from the southeast. The inner gravity high is relatively symmetrical but is flanked by a horse shoe-shaped low with extensions northeast and northwest. Such a pattern is consistent with asymmetric excavation preserving the early stages of penetration and failure by an impactor from the southeast at an angle from 20-30°. Similar patterns are found on Venus (6), Mercury, and the Moon (see Fig. 2). The limits of the central gravity high provide a signature of the penetration zone, which may provide a measure of the impactor. The only analog clearly linking a gravity high to preserved crater features in the 2-ring basin Grimaldi on the Moon (8). The dimensions of this central anomaly closely match the diameter of the interior peak ring, which falls on the empirical relation between diameters of other central relief structures (Fig. 3a). Plotting the diameter of gravity highs of other terrestrial craters onto the diameter of central peaks and rings of craters on Venus (Fig. 3b) reveals a consistent relation. On this plot, the 60 km diameter of the central gravity high of Chicxulub suggests that its crater diameter should be about 130-150 km. Although this is considerably smaller than the outermost rings of Chicxulub (4), the disparity is proposed to reflect more extensive rim/wall collapse and failure zones uprange that can extend well beyond the original excavation rim, as on the Moon and Mars. Scaling of the penetration zones and central peak

Chicxulub as an Oblique Impact, P.H. Schultz

dimensions (6, 7) yield an impactor size between 10 and 15 km in diameter depending on the assumed impact velocity. If these interpretations are correct, then the northern hemisphere could have been subjected to much greater atmospheric stress. Moreover, this region would have received multi-staged impact products reflecting separate stages of impactor-driven vaporization, high-speed ballistic ejecta and secondary products, and dispersed target vapor/melt products.

(1) Penfield, G.T. and Camargo, Z.A. (1981), *Mtg. Soc. Explor. Geophys. Abstr., 51*, 37. (2) Hildebrand, A.R. *et al.* (1991), *Geology, 19*, 867-871. (3) Sharpton, V.L. *et al.* (1992), *Nature, 359*, 819. (4) Sharpton, V.L. *et al.* (1993) *Science, 261*, 1564-1567. (5) Gault, D.E. et al. (1968) in *Shock Metamorphism of Natural Materials*, pp. 87-100, Mono Books, Baltimore, MD. (6) Schultz, P.H. (1992), *J. Geophys. Res., 97*, 16,183-16,248. (7) Schultz, P.H. and Gault, D.E. (1993), *Lunar Planet. Sci. XXIV*, 1257-1258. (8) Phillips, R.J. and Dvorak, J.(1981), in *Multi-Ring Basins*, pp. 91-104, Pergamon, NY. (9) Scott, D.H., McCauley, J.F., and West, M.N. (1977), US Geol. Survey Map I-1034.

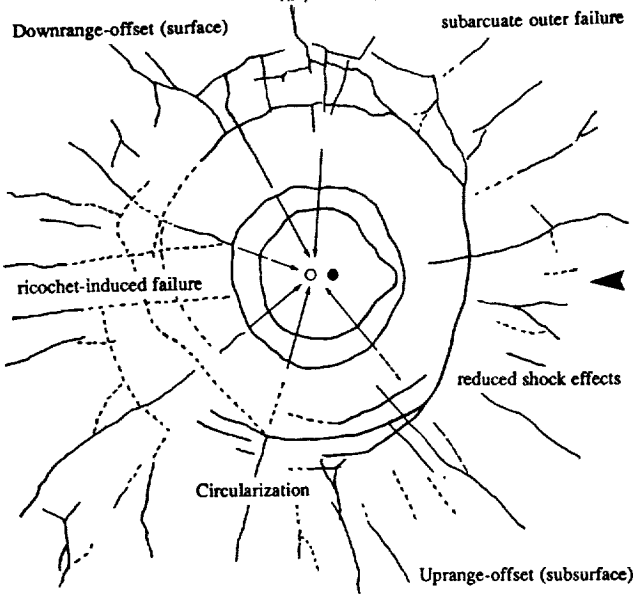

Figure 1. Fracture pattern created in a dry-ice block from a 30° impact (from horizontal) by a 0.635 cm aluminum sphere at 1.6 km/s. The deepest penetration (solid dot) occurs uprange but the radial and concentric failure pattern at the surface is centered downrange. An outer subarcuate fracture reflects the combined effects of reduced shock uprange and the time-dependent energy coupling downrange, thereby producing a mach-like boundary cone in the target (but pointing uprange). Similar patterns occur in basalt and lucite targets.

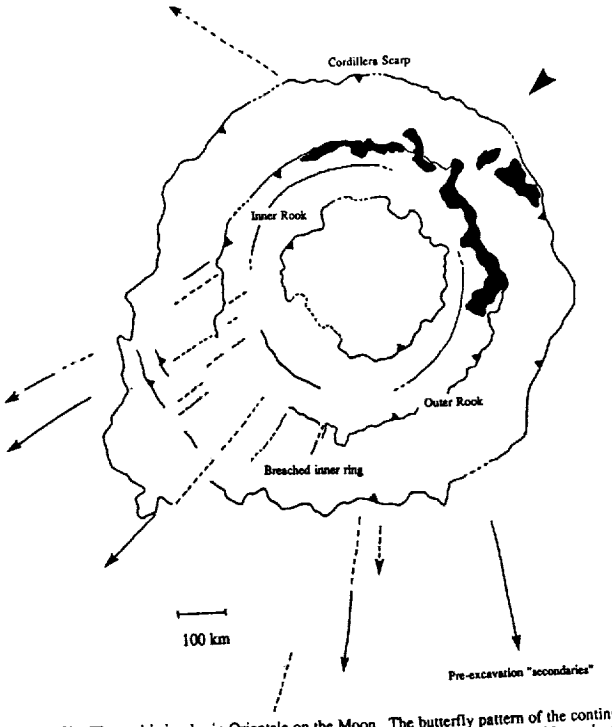

Figure 2b. The multi-ring basin Orientale on the Moon. The butterfly pattern of the continuous ejecta deposits of Orientale suggest an oblique impact (9). This is further indicated by early-stage "secondaries" converging on the uprange inner Rook, the downrange breach of the Rook ring, downrange extension of the Cordillera, and deep-seated failure uprange leading to mare emplacement (consistent with enhanced uprange collapse).

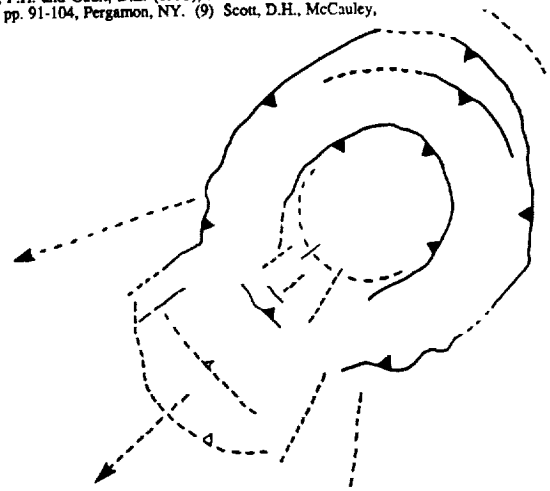

Figure 2a. The 2-ring basin Bach on Mercury displaying a breached inner ring, downrange sibling or secondary craters related to impactor failure (converges on uprange inner ring) and enhanced uprange rim/wall failure producing fractures beyond the crater rim. The inner ring preserves asymmetry during penetration; the outer rings reflect crustal response to a time/space-evolving energy source and enhanced rim/wall collapse uprange.

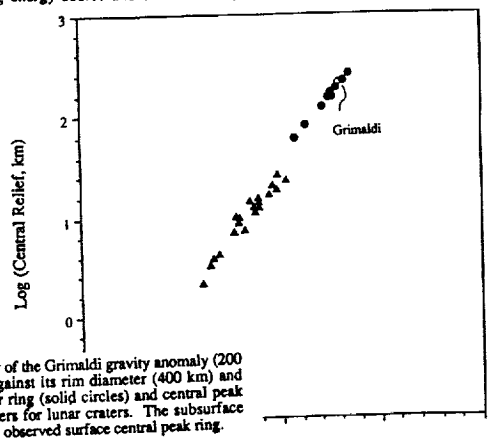

Figure 3a. The diameter of the Grimaldi gravity anomaly (200 km) from (8) plotted against its rim diameter (400 km) and superposed on the inner ring (solid circles) and central peak (solid triangles) diameters for lunar craters. The subsurface uplift correlates with the observed surface central peak ring.

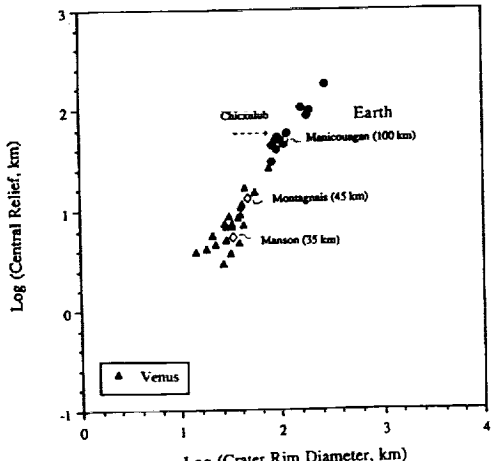

Figure 3b. Central gravity anomaly diameters for three terrestrial craters (open triangles) plotted with central peak (solid triangles) and peak ring (solid circles) diameters on Venus against their rim diameters. The diameter of the central gravity anomaly of Chicxulub is consistent with an uplift diameter only slightly larger than Manicouagan. The additional larger diameter rings at Chicxulub may reflect failure beyond the excavation crater rim, rather than the limit of the excavation crater.

Atmospheric Containment of Crater Growth. Peter H. Schultz and Olivier S. Barnouin, Department of Geological Sciences, Brown University, Providence, RI 02912.

The presence of an atmosphere can dramatically reduce cratering efficiency in particulate targets in the laboratory, provided that critical values of dimensionless static and dynamic pressure ratios are exceeded (1, 2). Although these dimensionless ratios also accommodate diverse empirical combinations of atmospheric, projectile, and target variables, they do not provide a clear model for the process. Here we explore a model where the atmosphere dynamically decelerates outward motion of the ejecta curtain, thereby shutting down crater growth somewhat analogous to the role of gravity.

Laboratory Experiments: Reduction in cratering efficiency has been shown (1, 2) to depend on a dimensionless Euler number ($P/\delta v^2$ for ambient pressure P, bulk target density δ, and impact velocity v) and a dimensionless ratio of aerodynamic drag to gravity forces acting on individual particles comprising the target ($d/g = 1/2C_D\rho v_e^2/\delta g a$ for drag coefficient C_D, atmospheric density ρ, ejection velocity v_e, target particle density δ, gravity g, and particle size a). Cratering efficiency includes both crater diameter and depth. Laboratory experiments reveal, however, that atmospheric forces reduce crater diameter but not depth (3). This process is preserved in targets with sufficient internal cohesion (e.g., pumice) to retain the unstable crater profile. Nevertheless, it is also clearly documented in quarter-space experiments using particulate targets with very low strength. The outward limit of crater growth temporarily matches growth for impacts into pumice but the crater subsequently collapses to a shallow profile (3, 4). Consequently, atmospheric forces restrict the gravity-controlled ballistic excavation stage of crater growth with strength playing only a secondary role.

Crater growth in water (5) closely resembles growth in low-strength particulates. Because water is not a particulate, the dynamic forces must act on the entire cratering flow field, not just individual particles. These observations led to a conceptual model where the coherent portion of the ejecta curtain resembles an inclined plate moving outward against a viscous medium (4). In such a model, the lower portion of the curtain transmits hydrostatically the forces retarding an incompressible inertial flow field. A simple analytical model illustrates some key aspects. Deceleration of a flat plate from an initial velocity v_o to a value v_x is simply expressed by:

$$ln(v_x/v_o) = -C_D\rho X/m_A \quad (1)$$

for a distance traveled X and curtain mass in a unit area m_A. Crater ejecta do not come out in a single massive block but comprise a relatively thin curtain having a large surface area at a given time. Curtain mass in a unit area is proportional to $\delta_e W_e$ for a curtain width W_e and bulk density δ_e. Because X depends on crater radius R and because W_e at a given time will map out as ejecta thickness, t_e, at a corresponding given ballistic range, the right side of equation (1) is proportional to $-C_D\rho(R/t_e)$. Since t_e depends on $(gR)^{1/2}$, equation (1) becomes $-C_D\rho(R/g)^{1/2}$. When v_x in equation (1) reduces to a limiting value, lateral crater growth ceases. The relative importance of shut-down should actually increase as $R^{1/2}$ for a given atmospheric density. This counter-intuitive result is simply analogous to the contrasting drag effects on a small brick and a large thin sheet (or a boulder versus a glider) of equivalent mass.

Model: A model of ejecta curtain thickness through time provides a more realistic assessment of possible dynamic pressure effects on crater growth. The ejecta curtain was assumed to be a frustum of a cone that widens with time at a rate constrained by computational and analytical models of crater growth (6, 7). The ejecta flux within the frustum surface was further constrained by matching the excavated ejecta mass at a given time to the mapped ejecta thickness decaying with distance. A Runge-Kutta iteration scheme generated a 2-D (but axisymmetric) model of ejecta curtain evolution with cumulative errors less than 1% for ballistic emplacement in a vacuum. Curtain height varied as a function of time and was considered "porous" to the atmosphere (unaffected by drag forces) when the curtain width reduced to only two ejecta particles thick; consequently, curtain height depends on the size and density of ejecta particles comprising the target.

Figure 1 shows the results for curtain deceleration for No. 24 sand and pumice (or microsphere) targets under vacuum conditions and at a one bar atmosphere at laboratory scales (final apparent crater diameter of 20 cm). The coarse, porous sand is hardly affected by the atmosphere. Curtain deceleration for the pumice target, however, essentially ceases when the crater has expanded to only 75% of its final diameter, or about a factor of two in cratering efficiency. Both results are consistent with empirical observations (2). While craters in pumice retain this arrested limit, craters in microspheres collapse. As a test for the assumption that deceleration of the ejecta curtain can transmit this information to crater growth, a solid plate was placed at different heights above the target surface. The projectile passed through a hole in the plate, and ejecta during crater formation were deflected laterally away from the cavity. The resulting crater was arrested in lateral growth, just as in cratering in an atmosphere, even without any evidence for fall back.

Implications: Atmospheric reduction in cratering efficiency is proposed to represent dynamic deceleration on an incompressible cratering flow field represented by the ejecta curtain during growth. This process is controlled by the pressure difference in front of and behind an impermeable curtain, which exhibits a large surface area but

Atmospheric Containment of Crater Growth, P.H. Schultz and O.S. Barnouin

relatively little mass at any given time. Because permeability depends on the number of ejecta particles per unit volume within the curtain at any given time, cratering efficiency will depend on size, density, and velocity of individual particles comprising the curtain as well as atmospheric density. Such a perspective helps to resolve the dilemma that air drag does not prevent individual particles from being ballistically ejected (6), yet their parameters are observed to be important (2). Moreover, it allows for atmospheric reduction of crater growth in non-particulate targets (e.g., water). For purposes of illustration, Figure 2 shows the possible implications for crater growth in different planetary settings at larger scales, without inclusion of other complicating effects (see 8, 9). The atmospheres of Mars and the Earth are insufficient to limit crater growth, whereas the atmosphere of Venus could have a significant effect. This is consistent with the anomalously high rim profiles and unexpected diameter/depth relations.

(1) Schultz, P.H. (1988), *Lunar Planet. Sci. XIX*, 1037-1038. (2) Schultz, P.H. (1992), *J. Geophys. Res., 97*, 975-1005. (3) Schultz, P.H. (1990), *Lunar Planet. Sci. XXI*, 1097-1098. (4) Schultz, P.H. (1993), *Int. J. Impact Eng.,14*, 659-670. (5) Gault, D.E. & Sonett (1982), in *Geol. Soc. Amer. Sp. Bull. 190*, pp. 69-92. (6) Schultz, P.H. and Gault, D.E. (1979), *J. Geophys. Res., 84*, 7669-7687. (7) Schultz *et al.* (1981), in *Multi-Ring Basins*, pp. 181-195, Pergamon, NY. (8) Ivanov et al., (1986), *Proc. Lunar Planet. Sci. Conf. 16th, J. Geophys. Res., 91*, D413-D430. (9) Schultz, P.H. (1992), *J. Geophys. Res., 97*, 16,183-16,248.

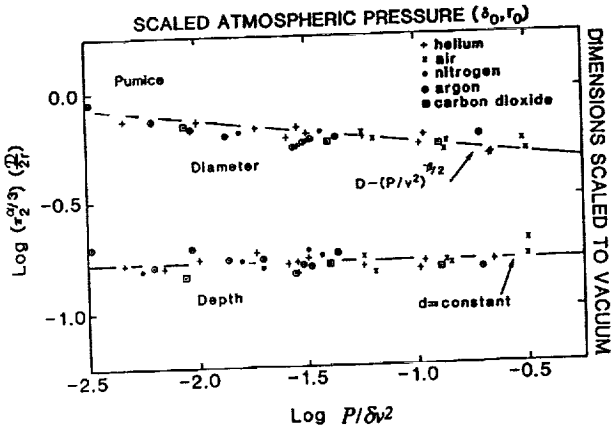

Figure 1. Effect of atmospheric pressure on crater diameter and crater depth. Dimensionless pressure is given by an Euler number with pressure P, bulk target density δ, and impactor velocity v. Pressure reduces crater diameter, not depth. The same reduction occurs in targets of microspheres and water with little or no strength but the cavity collapses after formation. Particle size, however, also has a profound effect (2) by controlling the permeability of the ejecta curtain.

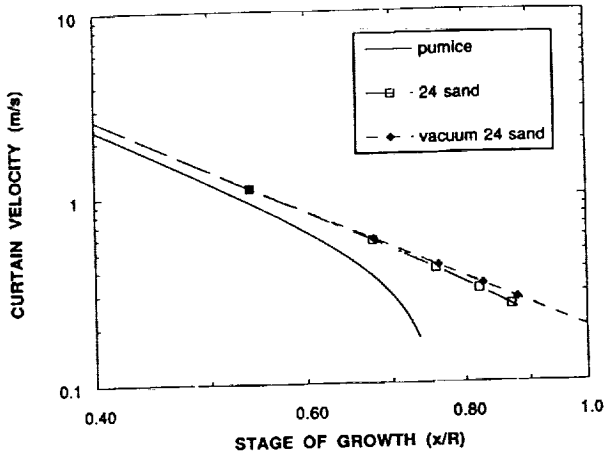

Figure 2a. Calculated dynamic deceleration of ejecta curtain created by impacts into targets with particle sizes for pumice and No. 24 sand. The ejecta curtain composed of coarse No. 24 sand exhibits little deceleration due to its high permeability, whereas the less permeable curtain of finer grained pumice rapidly decelerates after the crater has grown to 75% of its final diameter under vacuum conditions.

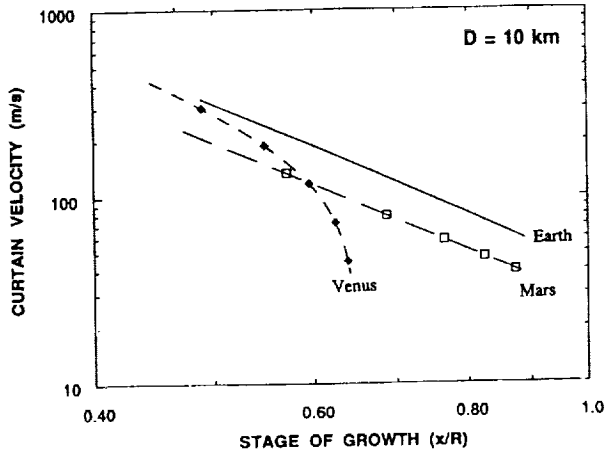

Figure 2b. Dynamic deceleration of ejecta curtains for 10 km-diameter craters on Mars, Earth, and Venus. Dynamic forces are insufficient to decelerate curtains (crater growth) on either Mars or Earth but could have a profound effect on Venus. Although the total ejected mass is large relative to the atmosphere, dynamic retarding forces at any given time are large due to the large outward velocity and large surface area of the curtain. Even supersonic velocities experience significant retarding forces.

Penetrating and Escaping the Atmospheres of Venus and Earth. Peter H. Schultz and Seiji Sugita, Department of Geological Sciences, Brown University, Providence, RI 02912.

The smallest single crater on Venus is only about 2 km in diameter (1), even though various models suggest that much larger objects should disrupt, decelerate, and disperse (2). Moreover, inversion of Tunguska-like blast limit dimensions indicate that the largest objects failing to reach the surface without catastrophic failure approach 4 km (3). The contrast between limiting sizes of "survivors" and "blasters" suggests that atmospheric entry may affect different types of objects differently. An important clue for resolving this paradox can be found in laboratory experiments documenting the dispersal and deceleration of hypervelocity debris clouds during atmospheric entry (3, 4). Such experiments and theoretical considerations reveal that interacting shocks act to collimate (rather than disperse) fragments below a critical size, which depends on the lateral velocity and atmospheric density. Schlieren imaging using the NASA-Ames Vertical Gun reveals that smaller fragments "surf" the inner shock front, and the entire debris cloud reshapes to a needle-shape form, thereby reducing deceleration by minimizing the drag coefficient. These results have significance not only for surviving entry to low altitudes but also for atmospheric escape of high-speed ejecta and siblings following low-angle impacts.

Laboratory Experiments: Hypervelocity debris clouds were produced by passing intact pyrex or aluminum spheres through thin mylar or aluminum sheets, respectively (5). Spall velocities spread the resulting fragments into a cluster that expands with time. Under low atmospheric densities, fragments dispersed due to interacting bow shocks as described in (2); however, under high densities (air at one bar) the fragments became tightly collimated with little deceleration (3, 4). Witness plates placed at various distances along the trajectory document the pattern, but Schlieren imaging allows witnessing the process. Schlieren imaging uses collimated light focused on a knife edge to reveal subtle variations in atmospheric density. A short duration flash freezes the image on film. The large impact chamber and side-viewing ports at the NASA-Ames Vertical Gun are ideal for this approach. Effects of ionization and impact flash preclude use at very high velocities (M~> 10), but comparison of dispersal patterns on witness plates up to M = 20 establish the similarity of the process over a wide range of velocities.

Figure 1a provides reference for the shock pattern around a single projectile just before impact under 1 bar atmospheric pressure (air). Figure 1b reveals the separate mach cones around individual fragments under an atmosphere pressure of 0.125 bars. Because schlieren imaging projects three dimensions onto a two-dimensional plane, overlapping mach cones do not necessarily represent interactions. Figure 1b reveals the effect of differential drag acting on different size fragments with larger mach angles documenting lower velocities. At one bar pressure (air), however, individual fragments are contained within a mach cone generated by a leading cluster (Fig. 1c). Differential pressure along the gradient within the boundary shock force individual fragments inwards toward the lower density wake, i.e., they "surf" the mach cone.

Witness plates demonstrate that the same process occurs at M = 18 while high-frame rate photography reveals that the leading front of the debris cloud undergoes little deceleration over the 2 m path length (see 5). Different combinations of ambient pressures, densities, and sound speeds (e.g., use of a helium atmosphere) reveal that the dispersal pattern of the projectile during disruption is not affected by the pressure differential at the break-up diaphragm situated between the evacuated launch tube and impact chamber.

Collimation within a mach cone also occurs for high-speed ejecta and ricochet debris after impact. Such a process was previously inferred from the contradiction between theory and experiments (6). Theory predicted that drag deceleration should prevent sufficiently small ejecta from escaping the cavity, whereas experiments demonstrated that this process was defeated by ballistic shadowing. Schlieren imaging documents this process (Fig. 2). Again a key requirement is that lateral dispersion velocity is small relative to the translational velocity.

Modeling the Process: Containment by the mach surface can be modeled by balancing forces along the pressure gradient across the shock front. Figure 3 illustrates the results for three different planetary environments using the ambient surface pressure for reference. A fragment will escape if the outward force (due to its lateral velocity and diameter relative to the bow shock thickness) exceed the pressure barrier created by the shock boundary, i.e., below the relevant curve. Conditions leading to collimation, therefore, depend on the style of failure and fragment size. Catastrophic disruption resulting in numerous small fragments and high dispersion velocities will escape into ambient conditions outside the mach cone (actually a column at hypervelocities). Non-catastrophic disruption or dispersal of a weak brecciated or regolith-covered object should result in collimation. For example, a bow shock thickness of 100 m (10% of the leading mass) will retain smaller fragments provided that the dispersal velocity due to disruption is less than 33 m/s (Mars), 0.44 km/s (Earth), or 4.5 km/s (Venus) if disruption occurs just above the surface. In reality, a weak object will begin to fail at a high altitude during entry (e.g., comparable to Martian surface conditions) and undergo successive failure as it penetrates to lower altitudes. Collimation of smaller fragments reshapes the debris cloud, thereby further reducing drag (i.e., pressure forces and deceleration).

Implications: High-velocity natural objects may be able to penetrate dense atmospheres to greater depths than previously expected if they undergo disruption at altitude before developing large dispersal velocities generated by

Penetrating/Escaping Atmospheres, P.H. Schultz and S. Sugita

high dynamic pressures. This process allows smaller disrupted objects to reach the surface at velocities much higher than allowed simply by deceleration of rigid bodies. When the effective density of the debris cloud approaches the compressed atmospheric density at lower altitudes, however, catastrophic deceleration should occur. Conversely, this process provides a mechanism by which high-speed ejecta can escape a dense atmosphere with minimal deceleration and without the need for wholesale atmospheric blow-off. Ricocheted debris and ejecta streams created by lower angle impacts provide escape routes for subsequent ejecta, perhaps contributing to ray-like patterns of impact glass and tektites on Earth.

(1) Phillips, R.J. *et al.* (1991), *Science, 252*, 288-296. (2) Melosh, H.J. (1981) in *Multi-Ring Basins*, pp. 29-35, Pergamon, NY. (3) Schultz, P.H. (1992), *J. Geophys. Res., 97*, 16,183-16,248. (4) Schultz, P.H. and Gault, D.E. (1992), *Lunar Planet. Sci. XXIII*, 1235-1236. (5) Schultz, P. H. and Gault, D.E. (1985), *J. Geophys. Res., 90*, 3710-3732. (6) Schultz, P.H. and Gault, D.E. (1979), *J. Geophys. Res., 84*, 7669-7687.

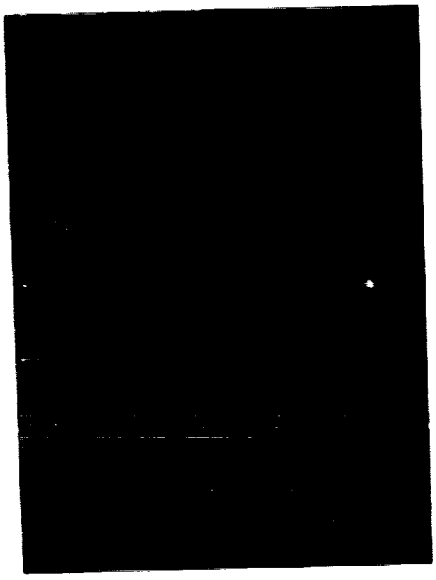

Figure 1a. Mach cone associated with a single 0.635 cm diameter aluminum projectile traversing a 1 bar (air) atmosphere at 1.8 km/s.

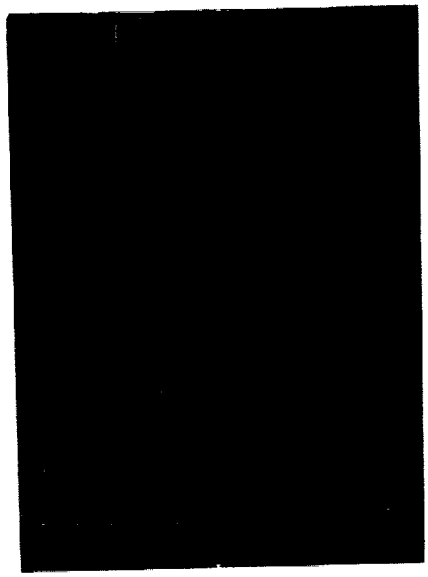

Figure 1b. Separate mach cones associated with larger fragments of a disrupted pyrex sphere traversing a 0.125 bar (air) atmosphere at 1.8 km/s. Fragments spread apart relative to vacuum conditions due to interacting bow shocks; trailing smaller fragments have yet to appear.

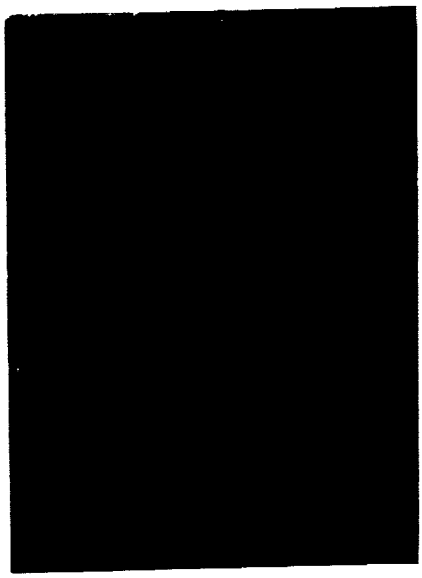

Figure 1c. Collimation of 1.7 km/s impactor fragments within a mach cone created by a group of leading fragments in a 1 bar (air) atmosphere. This process occurs only at higher atmospheric pressures when differential forces created along the shock front exceed the lateral momentum of each fragment. Deceleration of the entire cloud is substantially reduced

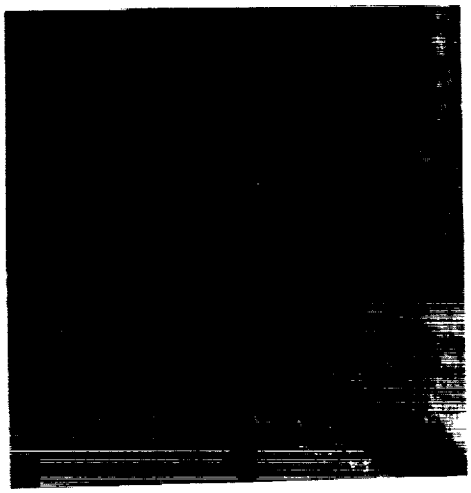

Figure 2. Ballistic shadowing created by downrange ejecta from a slightly oblique impact (60°) into a carbonate target at 1.6 km/s under 1 bar (air). Impact point is to lower right; impactor mach surface (only downrange half) extends to right. Vaporization at impact creates downrange "bubble". High-speed ejecta break through the vapor-induced blast downrange within overlapping mach cones

Figure 3. Conditions leading to mach collimation of debris for different planetary environments (for illustration, assumed to be surface pressure). Fragment sizes (scaled to width of shock front) will be contained by the mach cone (mach column for hypervelocity) if the lateral velocity due to breakup falls below the plotted envelope.

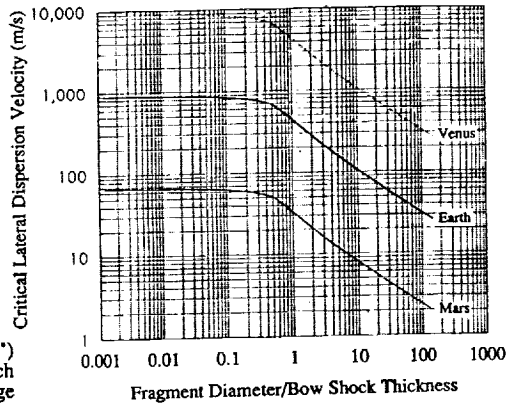

COMPARATIVE ROCK MASS STRENGTHS OF BASALT AND TUFF AND SOME PLANETOLOGICAL IMPLICATIONS

Richard A. Schultz, Geomechanics–Rock Fracture Group, Mackay School of Mines, University of Nevada, Reno, NV 89557-0138.

Summary.

Basalt and impact crater ejecta are thought to be two important rock types on Mars. Pyroclastic deposits (tuff) have sometimes been used to approximate the mechanical properties of impact crater ejecta, and may also represent a locally significant rock type as well. The strength and deformation properties of basalts and tuffs differ considerably from an ideal frictional model (Byerlee's law) and from each other. Systematic estimates of the relevant properties of basalt and tuff rock masses provide useful new constraints on the stresses required to fracture, fault, or buckle strata composed of these materials.

Introduction.

Jointed basaltic rock units such as those found on the Columbia Plateau in Washington State provide a well constrained example of a highly fractured rock mass that also has a high modulus intact material [1]. A complementary example at the other extreme is that of Calico Hills tuff, a highly fractured rock mass characterized by low modulus rock. This tuff unit consists primarily of pyroclastic airfall material locally reworked into bedded sequences [2]. Calico Hills tuff underlies the Topopah Spring member of the Tertiary Paintbrush Tuff, which is currently undergoing engineering evaluations for the proposed high-level nuclear waste repository at Yucca Mountain, Nevada.

The Hoek-Brown criterion [3] is used to represent the bulk properties of basalt and tuff on Mars. The tuff of Calico Hills is relatively weak; it provides an estimate of the strength and deformability of cold, poorly lithified impact crater/basin ejecta, which probably comprises a substantial part of the near-surface rock mass. Mohr envelopes for intact basaltic rock, a rock mass, and Byerlee's law are compared in Figure 1.

Strength parameters for Calico Hills tuff and basalt are very different, both from their intact equivalents and from each other. Fracturing of either rock type is associated with a marked reduction in the properties of the respective rock masses. For example, the bulk tensile and compressive strengths are reduced by one order of magnitude relative to the values for the intact material, as is the bulk cohesion. The deformation modulus is reduced by perhaps 50% from Young's modulus; however, Poisson's ratio and friction coefficient are not markedly affected by fracturing.

Mohr envelopes for basalt and tuff are compared in Figure 2. As can be seen from the figure, the envelopes for large exposures (e.g., outcrop scale and greater) of basalt and Calico Hills tuff are significantly different than those which are based only on the properties of the intact rock. The slopes of the rock mass envelopes for basalt ($\sigma > 20$ MPa) are comparable to the widely cited Byerlee's law, implying similar values of friction angle or coefficient. However, the tuff rock mass exhibits much lower angles or coefficients of friction, on the order of 10–15° and $0.2 < \mu < 0.3$ respectively.

The dramatic examples of landslides in the Valles Marineris troughs of Mars have been used to constrain the mechanical properties (cohesion and friction) of the failed wallrock in an effort to infer indirectly the underlying lithology [4]. Based on a simple slope stability model, values of cohesion between 0.05 and 5 MPa, and friction angles of 15–40°, separate stable and unstable wallrock; smaller values are associated with failure and landsliding. The values of bulk cohesion, 1–4 MPa (basalt) and 1.7–4.4. MPa (tuff), along with friction angles of ~30° for basalt [5] and 10–15° for tuff [2], suggest that a basalt rock mass would be marginally stable, whereas the tuff rock mass would be unstable. Although the inversion noted above neglects certain factors such as changes in rock-mass properties with depth, the bulk properties suggest in addition that the interior layered deposits in Valles Marineris, which have been interpreted by some as volcanic or pyroclastic material [6] and lack landslides, are stronger than Calico Hills tuff. If those deposits are pyroclastic, they probably contain material having higher Young's modulus and frictional properties.

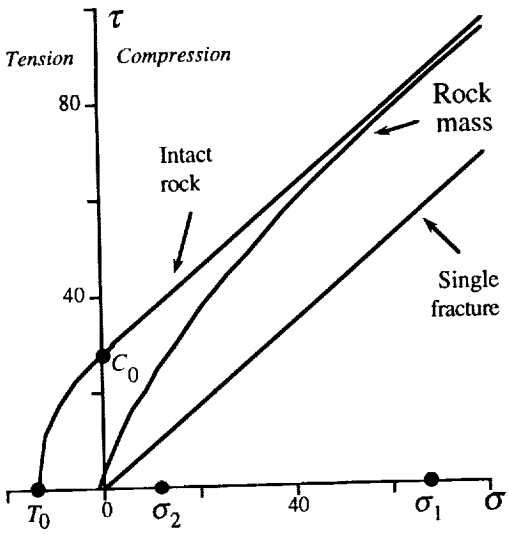

Fig. 1. Mohr diagram showing commonly used representations of intact and fractured rock strengths. The intact envelope, consisting of a parabolic Griffith envelope for tensile normal stress and a linear Coulomb envelope for compression, assumes that microcracks and other flaws are minute compared to the size of the rock specimen. The "sliding-line" envelope, defined by the frictional properties of a single joint, fault, or artificial saw-cut surface, implies that a single fracture plane completely cuts the rock. Most rocks would probably fall between these two extremes.

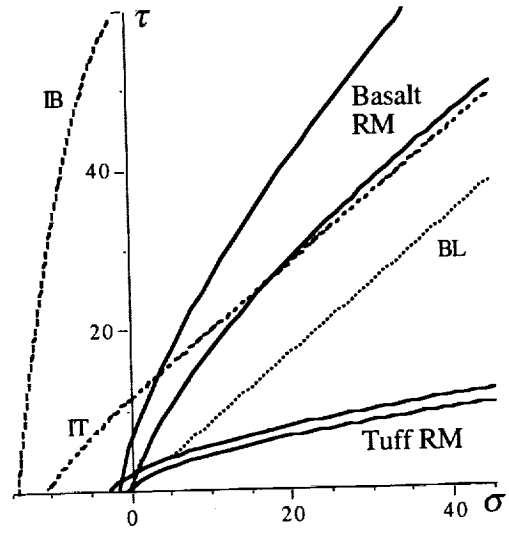

Fig. 2. Brittle strength envelopes for basalt and tuff. Bold curves, Mohr envelopes for basalt or tuff rock masses; dashed curves, Modified Griffith envelopes for intact basalt (IB) and tuff (IT) rock. Dotted curve, Byerlee's law (BL) for pre-existing fractures assuming $C_0 = 0$ and coefficient of friction of 0.85; curve appropriate for $\sigma > 5$ MPa. Note reduction in tensile strength and cohesion for the rock masses relative to their intact equivalents.

TABLE 1. STRENGTH OF BASALT AND TUFF ROCK MASSES

Property	Basalt	Basaltic RM	Tuff	Tuff RM
Uniaxial compressive strength, MPa	262	12–63	22–29	3.3–7.1
Young's modulus, GPa	73	–	5–6	–
Deformation modulus, GPa	–	5–50	–	<6
Poisson's ratio	0.25	≈ 0.3	0.16–0.29	≈ 0.2
Tensile strength, MPa	–14	–0.2 to –2	–11.8	–0.8 to –2.6
Cohesion, MPa	66	1–4	12	1.7–4.4

Conclusions.

Fractures having a variety of scales are present in most rock units larger than several meters in size. These fractures are associated with marked reductions in strength properties and moduli of rock masses relative to an unfractured hand sample or core. Mohr envelopes for fractured rock masses of basalt and nonwelded tuff indicate that Byerlee's law should not be used indiscriminately as an indicator of rock mass strength near the surface for these rock types.

References. [1] Schultz, *JGR*, **98**, 10,883–10,895, 1992. [2] Lin et al., SAND92–0450, 1993. [3] Hoek and Brown, *J. Geotech. Div. ASCE*, **106**, 1013–1035, 1980. [4] Lucchitta et al., in *Mars*, 453–492, 1992. [5] Goodman, *Introduction to Geomechanics*, 1989. [6] Lucchitta, *Icarus*, **86**, 476–509, 1990.

OUTSTANDING TECTONIC PROBLEMS IN THE VALLES MARINERIS REGION OF MARS

Richard A. Schultz, Geomechanics–Rock Fracture Group, Mackay School of Mines, University of Nevada, Reno, NV 89557-0138.

Summary.

A number of important problems in Martian tectonics can be addressed using the existing image and topography data. Of these, a detailed understanding of the dynamics of extension at Valles Marineris and lateral crustal deformation in the Coprates Strike-slip Province to the south will provide an improved basis for modeling the evolution of stress states in those regions.

Valles Marineris.

The significance of many large-scale structures on Mars, such as Valles Marineris, remain enigmatic despite continued intensive study. For example, *Tanaka et al.* [1] have pointed out the inherent paradox between coeval Tharsis-radial structures 1000's of km long, which are observed, and results of stress models of Tharsis tectonism that require more than one scenario to predict the faulting. Recent work [2] indicates that much of the normal faulting in the Valles Marineris trough system may be contemporaneous, which makes the tectonism there similar to other long Tharsis-radial grabens in the region. One way out of the dilemma is to propose a different stress model, which has been done qualitatively by Tanaka et al. Another appealing solution is to invoke a number of smaller tectonic centers that are superimposed on regional Tharsis tectonism, such as lithospheric uplift and bending as a stress center at Valles Marineris. Thus a comprehensive understanding of the structural sequence in Valles Marineris is fundamental to a comparison of stress models and observed tectonics.

Further, as noted by *Schubert et al.* [3] in their discussion of post-SNC global thermal models of Mars, new models of global differentiation and cooling must also be constrained by the observed tectonics. In this context the spatial interplay between compressional structures (wrinkle ridges) and extensional structures (normal faults in Valles Marineris), including their stress implications, will bear on various speculations on the relationship between the two sets of structures and the thermal history of the planet.

Structurally, many of the rectangular troughs in central Valles Marineris are best interpreted as large grabens [4,2,5]. Thus they are indicative of a significant amount of *localized* crustal extension, but the relationship between this extension and driving forces has always been somewhat obscure. A general relationship to Tharsis can and has been invoked on the basis of radial orientation and orthogonality to calculated stress trajectories [e.g., 6,7,8], but as *Tanaka et al.* [1] point out, Tharsis models require a two-stage, sequential process to form the trough system. This theoretical problem is inconsistent with the observation [2] that faulting was essentially synchronous along Valles Marineris (Upper Hesperian), given the resolution of crater statistics, unless a rapid evolution of stress states in Tharsis is assumed. On the other hand, the available stress models, which are based on the entire Tharsis load, may have shortcomings when used to predict structures formed early in the loading process. Identification of the sequence of faulting in places such as Valles Marineris may help document changes in the regional stress state that might be due to evolution of the load/lithosphere system.

Another concept for producing or augmenting local extension in the Valles Marineris region is uplift [6,9,1]. However, this mechanism cannot be easily reconciled with the topography and trends of large troughs such as Coprates Chasma. According to this hypothesis, crustal uplift would bend the lithosphere so that normal faults and structural troughs would be oriented parallel to the trend of the uplift; this geometric relationship is violated by several major structures in Valles Marineris. Notwithstanding these difficulties, the proximity of Valles Marineris to high regional topography underscores the need to evaluate the contribution of uplift to trough extension.

Strike-slip Faulting.

Strike-slip faulting is a fundamental mechanism for localizing horizontal shear strain in the upper brittle lithosphere of many planets and satellites. Until relatively recently, strike-slip faulting not been seriously considered as an important planetary process on bodies other than the Earth. However, examples on Mars [10,11] suggest that this deformation mechanism was important on a local to regional scale. Excellent examples of discrete strike-slip faults occur southeast of Valles Marineris in association with wrinkle ridges. However, the faults are not simple tear faults or accommodation structures [11], and not all ridged plains show evidence for strike-slip faulting. Thus the exposures in the Coprates Strike-Slip Province are special,

particularly in light of a surprising paucity of comparable discrete structures on Venus [e.g., 12]. It is possible that deformation in this Province was related to the development of the Thaumasia plateau, which was apparently a major precursor to Tharsis deformation [e.g., 13]. Study of the strike-slip faults will provide a more thorough understanding of the tectonics of the south Tharsis region and its development during a period of widespread volcanism and contractional deformation [e.g., 14–17].

Curiously, very few unequivocal occurrences of strike-slip faults based on photogeologic observations have been reported for Mars. Indeed, strike-slip faults are rare and are prominently developed only in one province near eastern Thaumasia and Coprates [18]. Why do these structures occur there, and what is their relationship to wrinkle ridges, stress models, and Tharsis evolution?

Several important statements can be made by inspection of the faults in this region. First, the strike-slip faults do not represent tear faults or minor accommodation structures between segments of wrinkle ridges, because (*a*) the strike-slip faults are not orthogonal to ridges, as required by this hypothesis; and (*b*) the faults can extend beyond the ridges. Second, strike-slip faulting is locally younger than the main development of wrinkle ridges, so the process of strike-slip faulting was at least partly decoupled from that of wrinkle ridges. Third, not all regions that exhibit wrinkle ridges show evidence of strike-slip faulting. Further, the structures record multiple, superimposed phases of strike-slip and wrinkle ridge deformation [18] that locally suggest a consistent pattern of bulk strain [19].

Of all the expanses of ridged plains on Mars, only the Coprates Strike-slip Province clearly shows arrays of strike-slip faults. One is compelled to ask why this region deformed differently than adjacent areas such as Lunae Planum that also contain numerous wrinkle ridges. Discrete strike-slip faults also seem to be somewhat rare on Venus, a planet whose surface has experienced considerable horizontal strain (extension and compression), making the faults in Coprates remarkable. Detailed mapping and analysis are required to explain the dynamics of this special region on Mars.

References. [1] Tanaka et al., *JGR*, **96**, 15,617–15,633, 1991. [2] Schultz, *JGR*, **96**, 22,777–22,792, 1991. [3] Schubert et al., in *Mars*, pp. 147–183, 1992. [4] Blasius et al., *JGR*, **82**, 4067–4091, 1977. [5] Lucchitta et al., in *Mars*, pp. 453–492, 1992. [6] Wise et al., *Icarus*, **38**, 456–472, 1979. [7] Banerdt et al., *JGR*, **87**, 9723–9733, 1982. [8] Schultz, *JGR*, **90**, 7849–7860, 1985. [9] Witbeck et al., USGS Map I-2010, 1991. [10] Forsythe and Zimbelman, *Nature*, **336**, 143–146, 1988. [11] Schultz, *Nature*, **341**, 424–426, 1989. [12] Solomon et al., *JGR*, **97**, 13,199–13,255, 1992. [13] Frey, *JGR*, **84**, 1009–1023, 1979. [14] Tanaka et al., *Proc. Lunar Planet. Sci. Conf.*, **18th**, 665–678, 1988. [15] Frey et al., *Proc. Lunar Planet. Sci.*, **21**, 635–644, 1991. [16] Greeley and Schneid, *Science*, **254**, 996–998, 1991. [17] Watters, *JGR*, **98**, 17,049–17,060, 1993. [18] Schultz, *LPSC XXI*, 1109–1110, 1990. [19] Watters, *Geology*, **20**, 609–612, 1992.

58-90 ABS ONLY

N94-35456

2 3074

DISTRIBUTION OF SIDEROPHILE AND OTHER TRACE ELEMENTS IN MELT ROCK AT THE CHICXULUB IMPACT STRUCTURE; B. C. Schuraytz[1], D. J. Lindstrom[2], R. R. Martinez[3], V. L. Sharpton[1], and L. E. Marín[4]. [1]Lunar and Planetary Institute, Houston, TX 77058; [2]Planetary Science Branch, SN4, NASA Johnson Space Center, Houston, TX 77058; [3]Lockheed Engineering and Science Co., C23, Houston, TX 77058; [4]Instituto de Geofisica, UNAM, Mexico City, Mexico 04510.

Recent isotopic and mineralogical studies [1-4] have demonstrated a temporal and chemical link between the Chicxulub multiring impact basin [5] and ejecta at the Cretaceous-Tertiary boundary. A fundamental problem yet to be resolved, however, is identification of the projectile responsible for this cataclysmic event. Drill core samples of impact melt rock from the Chicxulub structure contain Ir and Os abundances and Re-Os isotopic ratios indicating the presence of up to ~3% meteoritic material [2,6,7]. We have used a technique involving microdrilling and high sensitivity instrumental neutron activation analysis (INAA) [8] in conjunction with electron microprobe analysis to characterize further the distribution of siderophile and other trace elements among phases within the C1-N10 melt rock.

Initial studies of whole rock INAA for eleven melt rock fragments reported Ir abundances ranging from <1.5 ppb to 13.5 ± 0.9 ppb [2,6]. Furthermore, variations in Ir concentration (~2×) between splits (≤100 mg) of finely-ground powder from single fragments (~1 g) suggest that the Ir is concentrated in a trace phase that is not uniformly disseminated in the melt rock. Because sulfides, ranging in size from 10 to 300 μm, were observed in thin section as heterogeneously distributed trace phases (<1%), and because significant siderophile element enrichments have been found in association with sulfide particles at other impact structures [9-11], these sulfides, variably enriched in Co and Ni (e.g. Fig. 1a), were considered potential carrier phases for the Ir [6]. The principal objective of this study was to test that hypothesis.

Microcores of four pyrite grains (e.g. Fig. 1b) were obtained from a thin section of C1-N10. Chalcopyrite, though present, was not sampled because of the elevated background expected from high Cu concentrations. Samples of pyroxene, plagioclase, magnetite, and mesostasis were also drilled to investigate trace element partitioning among the more abundant phases of the melt rock. Because the cores (40 to 400 μm dia. × 50 μm thick) are too small to weigh accurately, their masses have been estimated by calibrating the Fe concentration determined by INAA with the FeO content obtained by microprobe analyses prior to removal from the thin section. Comparison of INAA values for Na_2O, K_2O, CaO, and relevant minor elements to corresponding microprobe analyses indicate that, in most cases, the cores are of reasonable purity with respect to the phase of interest. Two of the pyrite cores were known to contain significant (melt?) inclusions and/or adhering silicate material, and their analyses are compromised by relatively high concentrations of alkali and rare earth elements.

Analyses of the two relatively pure pyrite cores are compared to C1-N10 whole rock abundances in Figure 2. These results confirm the elevated concentrations and variable distribution of Co and Ni, and show analogous variations for Au and As. However, no measurable Ir was found in either sample, and 2σ upper limits of <50 ppb and <34 ppb place severe constraints on the feasibility of pyrite as a significant sink for the Ir. Considering average Co concentrations of 4720 ppm for pyrite and 15 ppm for the whole rock limits the maximum pyrite abundance to ~0.3%, whereas at least 25% would be required to account for the whole rock Ir abundance even if one assumed an Ir concentration for pyrite to lie between the noted upper limits. Cobalt concentrations of 40 ppm in pyroxene suggest that the pyrite abundance is probably much lower than 0.3%. Based on these results, the hypothesis that sulfides are a carrier phase for Ir must be rejected. We note, however, that these samples constitute only four of the 125 sulfide grains observed in the thin section, and it is possible that a sulfide phase other than pyrite and chalcopyrite (e.g. Irarsite, Iridarsenite, etc.) is among that population. Nevertheless, it is clear that alternative hypotheses for the Ir carrier phase should be explored. There are numerous submicron particles with high backscatter electron intensity scattered throughout the melt matrix yet to be characterized.

REFERENCES [1] Swisher C. C. *et al.* (1992) *Science,* **257,** 954-958. [2] Sharpton V. L. *et al.* (1992) *Nature,* **359,** 819-821. [3] Blum J. D. *et al.* (1993) *Nature,* **364,** 325-327. [4] Krogh T. E. *et al.* (1993) *Nature,* **366,** 731-734. [5] Sharpton V. L. *et al.* (1993) *Science,* **261,** 1564-1567. [6] Schuraytz B. C. and Sharpton V. L. (1994) *Conf. on New Develop. Regarding the KT Event and Other Catastrophes in Earth Hist.,* in press. [7] Koeberl C. *et al.* (1994) *Geochim. Cosmochim. Acta,* in press. [8] Lindstrom D. J. (1990) *Nucl. Instr. Meth. Phys. Res.* **A299,** 584-588. [9] Palme H. *et al.* (1979) *Proc. Lunar Planet. Sci. Conf. 10th,* 2465-2492. [10] Grieve R. A. F. *et al.* (1980) *Contrib. Mineral. Petrol.,* **75,** 187-198. [11] Reimold W. U. *et al.* (1992) *Geology,* **20,** 1079-1082. [12] Wasson J. T. and Kallemeyn G. W. (1988) *Phil. Trans. R. Soc. Lond.* A **325,** 535-544.

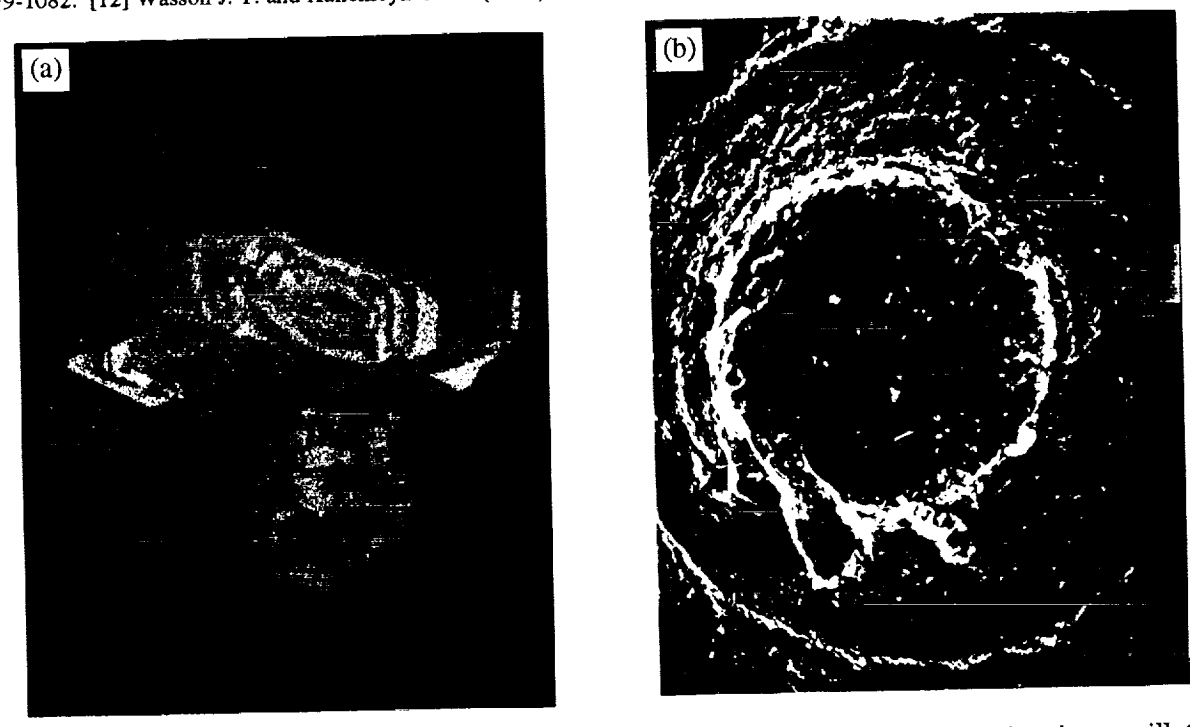

Figure 1. Thin section photomicrographs of pyrite C1-N10 S85. (a) X-ray map showing oscillatory zoning of Co. (b) SEM image of microcore volume.

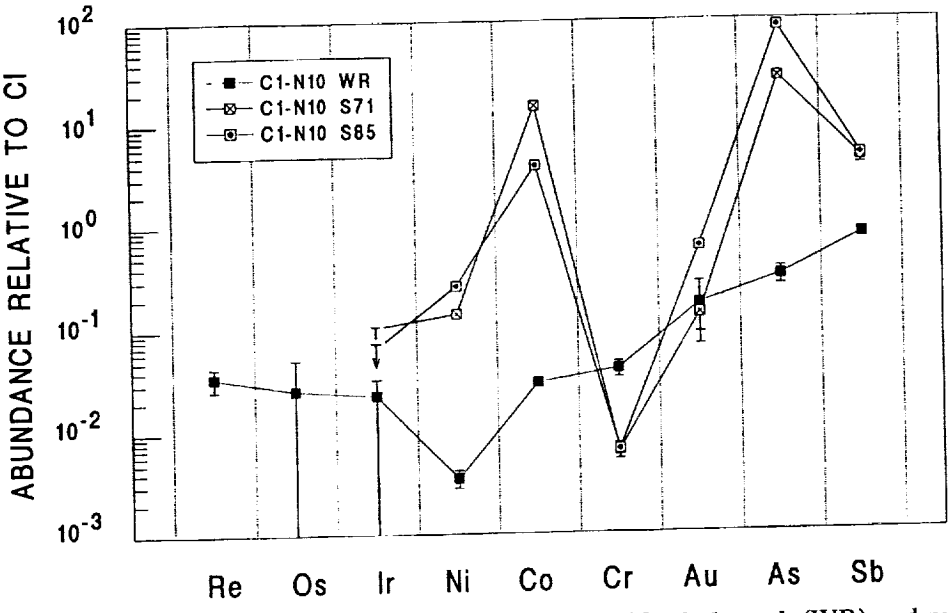

Figure 2. Siderophile and chromium abundance ratios in C1-N10 whole rock (WR) and pyrite cores (S71 and S85) relative to CI chondrites [12]. 2σ upper limits for Ir are shown for the pyrite cores. Rhenium and Os data for C1-N10 WR from [7].

59-91 ABS. ONLY
3075

N94-35457

PRELIMINARY DESCRIPTION OF DOUBLE DRIVE TUBE 68002/68001; Carol Schwarz[1], Richard V. Morris[2], and Randy L. Korotev[3], [1]Lockheed-ESC, 2400 NASA Road 1, Houston, TX, [2]NASA-JSC, Houston, TX, and [3]Dept. of Earth and Planetary Sciences, Washington University, St. Louis, MO.

Apollo 16 double drive tube 68002/68001 has been opened and information on its contents and structure is now available. The sample was taken in April 1972 at Station 8, a gently undulating surface of South Ray Crater ejecta material. The tube was driven into the surface about 2 m from the edge of a 10-15 m diameter crater in an area where small (<0.5 m diameter) craters are common [1]. Fragments of the <1 cm diameter size are most abundant in this area [2]. 68002, the top section, and 68001, the lower section, have a combined length of about 61 cm.

68002 was extruded in February 1993. The apparent length of the core before extrusion, from x-rays, was 27.4 cm. The length after extrusion was 26.7 cm; thus compaction during the extrusion was 0.7 cm. A weight of 583.13 g was calculated from previously weighed core hardware.

The color of the soil of 68002 was determined to be 10YR 5/1 on the Munsell color scale and no distinct color boundaries were observed during dissection. A void was present from the lunar surface to about 3.5 cm depth. The top 4 cm was loose and below that the soil was noticeably more coherent and compact. Friable soil clods were abundant from 9.5 to 14.5 cm from the lunar surface.

A close examination of particles >1 mm from the first and third dissection passes showed that about 80% (by number) of the particles are in the 1-2 mm size range, 18% are 2-4 mm, <1% are 4-10 mm, and <1% are greater than 10 mm in diameter. Lithology of the >1 mm fraction was determined by binocular examination of the particles from the first and third passes and is summarized as follows: 58% are various types of breccias, 16% are dark, coherent, fine-grained particles, 14% are glasses including glass shards, agglutinates, and glass coated breccias, 11% are white or light gray (anorthositic), and less than 1% are basalts.

Eight particles given individual split numbers included several small glass spheres, a chip with a possible metallic coating, a 14 g anorthositic rock, a flat black fine-grained rock, and several breccias. Three bulk samples were taken from the third pass under red light conditions for future thermoluminescence studies.

68001, the bottom section of the core, was extruded in December 1993. The apparent length of the core before extrusion was 34.9 cm. The length after extrusion was 34.1 cm, for a compaction of 0.8 cm. A weight of 839.7 g was calculated from previously weighed hardware. The color of the soil of 68001 varied from 10YR 5/1 to 7/1 with several color boundaries observed after derinding. A void present after extrusion extended from the top end to about 1.5 cm. 0 to 10 cm from the top end was a dark layer, approximately 10YR 5/1 on the Munsell color scale. From 10 cm to about 13 cm is lighter colored soil which contrasts along the upper boundary adjacent to the top layer. The color of this layer is approximately 10YR 7/1 to 6/1 with mm-sized light gray fragments visible. At 13 cm the color darkens to about 10YR 5/1, lightening gradually towards the bottom. More information on 68001 will be available as dissection passes are completed.

FeO and I_s/FeO depth profiles for section 68002 are shown in Figures 1 and 2. To smooth out sampling artifacts, the data are three point sliding averages, except for the anomalous point in the FeO data. The anomalous point probably represents a chance occurrence of a large metallic iron particle in that particular sample. The FeO content is nearly constant and averages 5.63(20) wt. %. All of the soil in the upper core section is mature [3]. There are no significant discontinuities, although the maturity generally decrease from the lunar surface.

References: [1] LSPET (1972), in *Apollo 16 Preliminary Science Report*, p. 7-43; [2] Apollo Lunar Geology Investigation Team (1972), in *Interagency Report: Astrogeology 51*, p. 125; [3] Morris, *PLPSC9*, 2287, 1978.

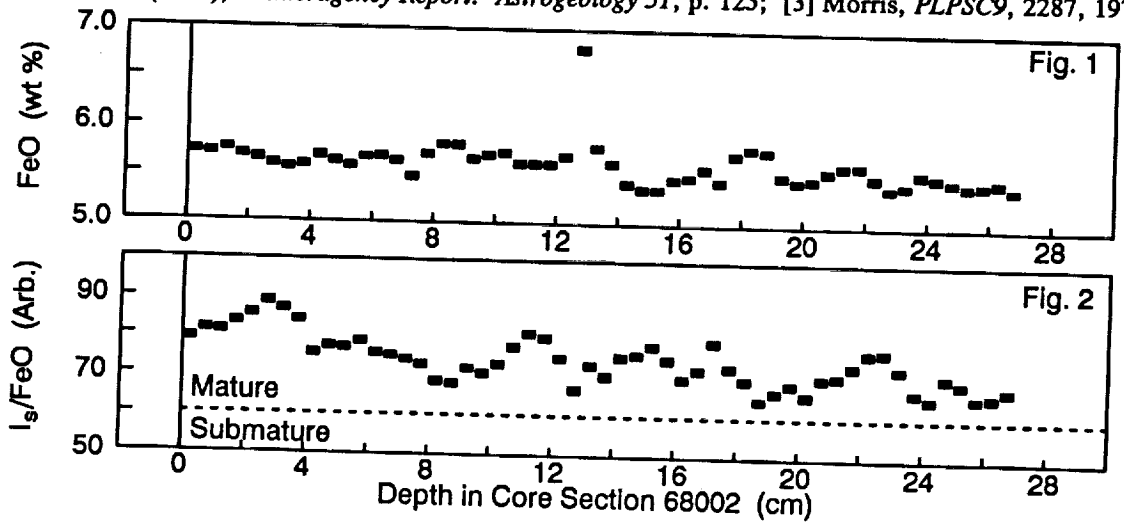

omit to P 233

1:1 MILLION-SCALE GEOLOGIC MAPS OF MARS' THARSIS MONTES. D.H. Scott[1], J.R. Zimbelman[2], and J. M. Dohm[1]; [1]U.S. Geological Survey, 2255 N. Gemini Dr., Flagstaff, AZ 86001; [2]CEPS/NASM, Smithsonian Institution, Washington, D.C. 20560.

Geologic maps of selected areas on Mars are being compiled at 1:500,000 scale by investigators in NASA's Mars Geologic Mapping Program. As originally planned, these maps were to be published at full scale as U.S. Geological Survey Miscellaneous Investigations Series I-Maps. Although there is an advantage in mapping the geology on large-scale bases, many of the maps could be published at half scale (1:1,000,000) without sacrificing geologic detail; moreover, although several map sheets may be required to cover a particular area at 1:500,000 scale, the same area can often be shown on one sheet at 1:1,000,000 scale (e.g. Fig. 1). The reduced-scale version is more readily displayed, and the geologic relations can be better appreciated when viewed on one map rather than on several larger scale maps. We have just completed the geologic mapping of six contiguous quadrangles of Mars' Arsia Mons region at 1:500,000 scale. We then reduced the scale of these maps to 1:1,000,000 and combined them on one sheet. As a result, relations between geologic features can be more easily compared, such as in the enigmatic fan-shaped deposits on Arsia's western flank and lava flows of the Tharsis Montes Formation elsewhere in the map area. Another important result is the savings in time and production cost. A similar approach will be used for publishing the geologic maps of the other Tharsis volcanoes, Pavonis and Ascraeus Montes.

The three shield volcanoes of the Tharsis Montes have interested planetary scientists since their discovery during the Mariner 9 mission [1-7]. These volcanoes have been shown as a single geologic unit on most maps of the region, regardless of the scale [2,8-10]. Olympus Mons and its aureole deposits also have received considerable attention by many investigators [e.g. 11-21], and the volcano has been generally thought to be a larger version of its smaller Tharsis neighbors to the southeast. However, our detailed mapping (in progress) of Arsia and Pavonis, along with previous investigations of Ascraeus [22] and Pavonis [23], has revealed striking differences as well as similarities among the four large shield volcanoes.

Fourteen individual Mars Transverse Mercator (MTM) quadrangles cover the three Tharsis volcanoes and their fan-shaped deposits (Fig. 1). Scott has concentrated on the fan-shaped deposits while Zimbelman has focused on the volcanic constructs. During the Arsia mapping, Scott recommended that the six individual MTM quadrangles be reduced to make a single map. This plan has proven to be both time and cost efficient. Future mappers should consider combining adjacent maps when, as here, such a combination does not compromise the science results.

REFERENCES: [1] McCauley J.F. et al. (1972) Icarus **17**, 289-327. [2] Carr M.H. (1973) JGR **78**, 4049-4062. [3] Carr M.H. et al. (1977) JGR **82**, 3985-4015. [4] Crumpler L.S. and Aubele J.C. (1978) Icarus **34**, 496-511. [5] Greeley R. and Spudis P.D. (1981) Rev. Geophys. Sp. Phys. **19**, 13-41. [6] Mouginis-Mark P.J. (1981) Proc. LPS **12B**, 1431-1447. [7] Zimbelman J.R. and Edgett K.S. (1992) Proc. LPS **22**, 31-44. [8] Carr M.H. (1975) U.S.G.S. Misc. Invest. Series Map I-893, scale 1:5,000,000. [9] Scott D.H. and Carr M.H. (1978) U.S.G.S. Misc. Invest. Series Map I-1083, scale 1:25,000,000. [10] Scott D.H. and

1:1 MILLION-SCALE MAPS OF MARS' THARSIS MONTES: D.H. Scott et al.

Tanaka K.L. (1986) U.S.G.S. Misc. Invest. Series Map I-1802A, scale 1:15,000,000. [11] King J.S. and Riehle J.R. (1974) Icarus **23**, 300-317. [12] Head J.W. et al. (1976) Nature **263**, 667-668. [13] Hodges C.A. and Moore H.J. (1979) JGR **84**, 8061-8074. [14] Lopes R.M.C. et al. (1980) Moon **22**, 221-234. [15] Scott D.H. and Tanaka K.L. (1981) Icarus **45**, 304-319. [16] Lopes R. et al. (1982) JGR **87**, 9917-9928. [17] Hiller K.H. et al. (1982) JGR **87**, 9905-9915. [18] Morris E.C. (1982) JGR **87**, 1164-1178. [19] Tanaka K.L. (1984) PhD diss., U.C. Santa Barbara. [20] Tanaka K.L. (1985) Icarus **62**, 191-206. [21] Zuber M.T. and Mouginis-Mark P.J. (1992) JGR **97**, 18295-18307. [22] Zimbelman J.R. (1984) PhD diss., A.S.U. (in NASA TM-88784, 1986, 271-572. [23] Edgett K.S. et al. (1987) LPS XVIII, 254-255.

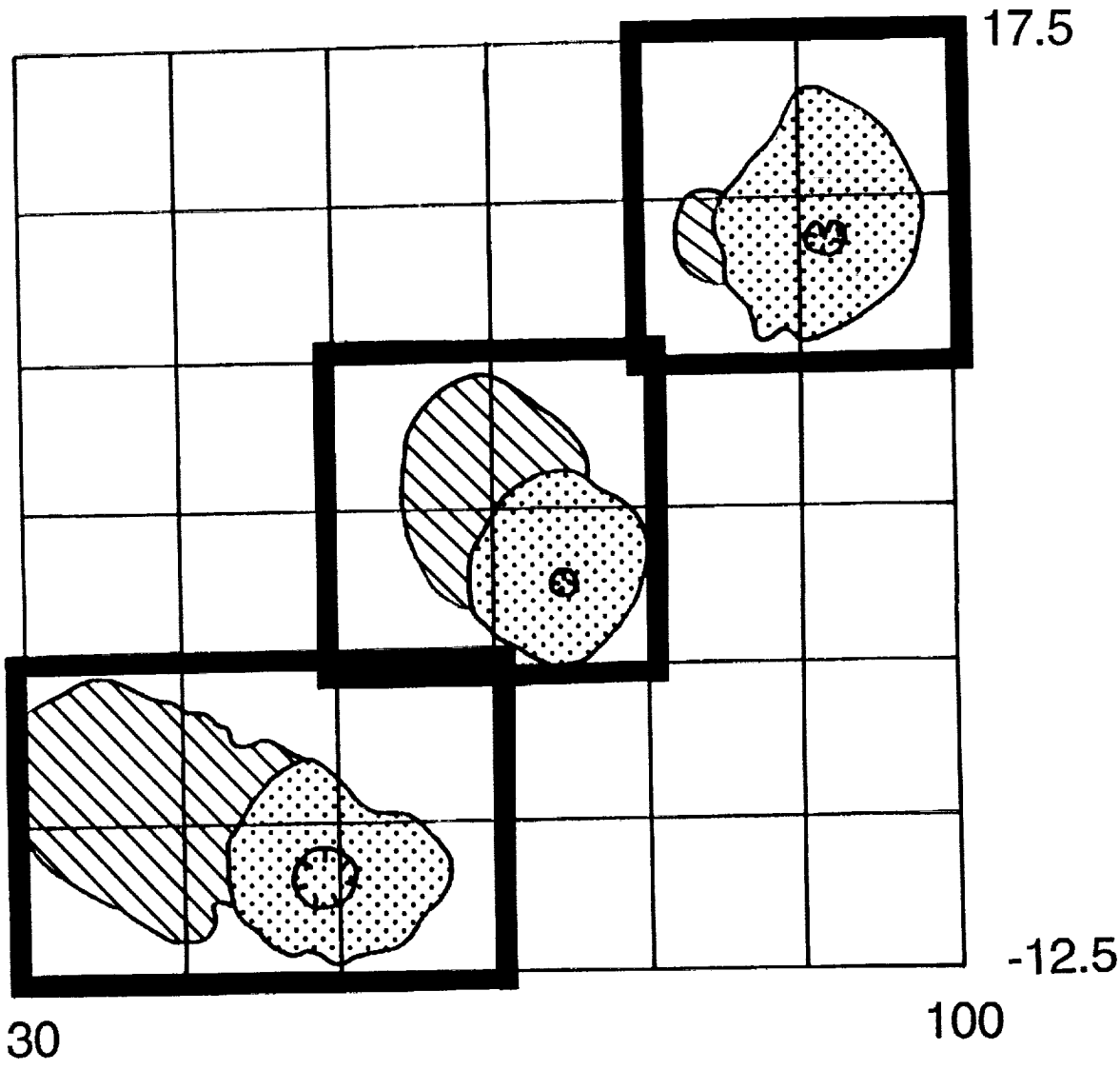

Figure 1. Sketch map of the Tharsis Montes region showing major volcanoes, boundaries of individual MTM 5° quadrangles (thin lines), and boundaries of areas covered by the three composite maps (heavy lines). Volcanoes shown by dot pattern; associated fan-shaped deposits by line pattern.

EVAPORATION AND RECONDENSATION OF VOLATILES DURING CHONDRULE FORMATION; Edward R.D. Scott, Planetary Geosciences, Department of Geology and Geophysics, SOEST, University of Hawaii, Honolulu, HI 96822.

Chemical compositions of chondrules are controlled by precursor grain compositions and liquid-gas exchange during chondrule formation. The relative importance of these two factors is controversial [1-3]. Most chondrules in O and C chondrites show only minor volatile depletions [4], but a few ungrouped chondrites show significant volatile depletions in most chondrules [5, 6]. Like Sears and coworkers [3, 7], I argue that for type I chondrules there is considerable circumstantial evidence for volatile loss and partial recondensation. Chondrites composed largely of type I porphyritic or barred chondrules that failed to reacquire volatiles should be grossly deficient in volatiles; Bencubbin and Weatherford may be examples of such chondrites rather than products of impacts on planetary surfaces [5, 6]. Iron meteorites lacking volatile siderophiles, e.g., IVB irons, probably formed from these kinds of chondrites. Evaporation and recondensation processes during brief high-temperature nebula events may be common to many CAIs and some chondrules [8].

Type I chondrules

Type IA porphyritic chondrules in Semarkona have concentrations of Na and K that are typically only 30% of the concentrations in type II chondrules. Jones [9] showed that type IA chondrules in Semarkona could be derived from type II by loss of 80% of Na and 20% of Si, but she considered fractionation of precursor grains and volatile loss to be equally plausible. Jie et al. [7] and Hewins [10] argued respectively for and against volatile loss during the formation of type I chondrules. Most of the 30-odd type I chondrules that have been studied in detail show little direct evidence for nebula-chondrule interaction. Exceptions include the fayalite rims on certain Allende chondrules [11] and a Semarkona type IA chondrule [12] that shows core-edge zoning in the mesostasis. Matsunami et al. [12] infer that the enrichments of Si, Na and Mn at the rim by factors of 1.1-6 are due to recondensation of volatiles during crystallization.

Bulk compositions of type IA chondrules show positive correlations among the refractories, Ca, Al, and Ti, and among the volatile elements, Si, Fe, Na, K, Cr and Mn, but refractories and volatiles are not related [13 and this work]. Mean volatile abundances are depleted in type IA relative to type II by amounts which are qualitatively consistent with evaporation experiments [14] and equilibrium condensation calculations [15], suggesting that these elements have been lost during chondrule formation, though Fe is also lost by reduction. Hewins [10] argued against volatile loss from type IA chondrules in part because some type IA chondrules had higher concentrations of Na than some type II chondrules. However this may result from recondensation of volatiles as most of the volatiles listed above are also enriched at the edge of the Matsunami chondrule [12]. The absence of a volatile-refractory relationship in the bulk compositions of type IA chondrules could be due to an absence of a relationship between the duration or peak temperature of the heating event and the subsequent cooling rate. But some variation in the refractory abundances may be due to variability in the precursor grains.

The Cr, Mn and Fe enrichments at the edges of many olivine phenocrysts in type IA chondrules [13] may also be due in part to recondensation during crystallization. Ca and Al, which are depleted in the mesostasis at the edge of the Matsunami chondrule [12], are also depleted at the edges of many olivines, contrary to fractional crystallization models. This may be due to dilution of Ca and Al by recondensed material.

Volatile-poor chondrites

If type I chondrules experienced major loss of volatiles as a result of chondrule formation, as argued above, and the proportions of type I and type II chondrules vary significantly because of different nebular conditions or because of sorting processes [16], we should expect to find chondrites that are significantly depleted in volatiles as a result of chondrule formation. Such chondrites may be composed of type I porphyritic or type I barred

olivine chondrules that cooled rapidly and did not reacquire volatiles during any subsequent nebular processing. Bencubbin and Weatherford probably formed in this way and are not impact melts [6] but true chondrites [17].

Volatile-poor irons

We do not know whether volatile siderophiles can be preferentially removed during chondrule formation. However, Cr and Si levels in metal in type I chondrules were modified during chondrule formation [18]. In addition, metallic and silicate "chondrules" in Bencubbin show large depletions of volatile siderophiles and lithophiles, respectively [6]. Thus, the large depletions of volatile siderophiles in certain irons might be inherited from chondrites that experienced major loss of volatile siderophiles and lithophiles during chondrule formation.

Most irons, like most chondrites show minor depletions of volatile siderophiles. But group IVB shows a 10^4-fold depletion of Ge [19]. Mean abundances of volatile siderophiles in iron meteorite groups and abundances in ungrouped irons are correlated, and depletions relative to Ni and CI chondrites increase in the order Co, Au, P, As, Cu, Ga, Ge [20]. This sequence corresponds closely to the order of decreasing equilibrium condensation temperature in the nebula and the order of increasing depletion in chondrites [19, 21]. An alternative explanation to nebula-wide heating [22] is that brief high-temperature, chondrule-forming events caused the volatile depletions in the precursor chondrites of certain irons.

CAI-chondrule relationships

Many CAI are believed to have formed by partial evaporation from silicate melts during brief nebular heating processes [23]. I suggest that certain chondrules also lost volatiles in the same way. Chemical, mineralogical and isotopic properties of CAIs and chondrules commonly show a small but significant overlap suggesting that their formation processes are not fundamentally dissimilar. For example, chondrules in Dhajala (H3) show Si mass fractionation effects analogous but much smaller than those in CAI and Allende chondrules [24]. The small Dhajala chondrules found to be enriched in heavy Si isotopes are probably largely type I chondrules that experienced a net evaporative loss of Si.

CAI in Allende and other oxidized CV3 chondrites have been altered by the addition of Na and other alkalies, apparently by nebular condensation processes below ~1000 K [23]. One CO3 chondrite has chondrules and CAI that appear to have suffered similar nebular alteration processes [25]. The absence of CAI alteration in many CO3 and CV3 chondrites suggests that nebula alteration was a local process. I suggest that nebular pressures may have been enhanced briefly as a result of evaporation from zones with high dust-gas ratios and that CAI and chondrule alteration processes were related. Evidence in CAI for multiple stages of alteration and melting [26] and in chondrules for several high temperature events [4] suggests that volatile abundances may have been controlled by multiple evaporation and recondensation events.

References: [1] Anders E. (1977) EPSL 36, 14. [2] Wasson J.T. (1977) EPSL 36, 21. [3] Sears D. (1993) Meteoritics 28, 607. [4] Wasson J.T. (1993) Meteoritics 28, 14. [5] Wasson J.T. and Kallemeyn G.W. (1990) EPSL 101, 148. [6] Kallemeyn G.W. et al. (1978) GCA 42, 507. [7] Jie L. et al. (1992) LPS XXIII, 813. [8] Sheng Y.J. et al. (1991) GCA 55, 581. [9] Jones R.H. (1990) GCA 54, 1785. [10] Hewins R.H. (1991) GCA 35, 935. [11] Hua X. et al. (1988) GCA 52, 1389. [12] Matsunami S. et al. (1993) GCA 57, 2101. [13] Jones R.H. and Scott E.R.D. (1989) Proc. 19th LPSC, 523. [14] Hashimoto A. (1983) Geochem. J. 17, 111. [15] Wood J.A. and Hashimoto A. (1993) GCA 57, 2377. [16] Haack H. and Scott E.R.D. (1993) Meteoritics 28, 358. [17] Weisberg M.K. et al. (1990) Meteoritics 25, 269. [18] Zanda B. et al. (1993) Meteoritics 28, 466. [19] Wasson J.T. (1985) Meteorites: Their Record of Early Solar-System History, W.H. Freeman. [20] Scott E.R.D. (1979) Mineral. Mag. 43, 415. [21] Wai C.M. and Wasson J.T. (1979) Nature 282, 790. [22] Palme H. et al. (1988) in Meteorites and the Early Solar System, J.F. Kerridge and M.S. Matthews eds, p. 436, Univ. of Arizona. [23] MacPherson G.J. et al. (1988) ibid. p. 746. [24] Clayton R.N. et al. (1985) in Protostars & Planets II, D.C. Black. and M.S. Matthews eds, p. 755, Univ. of Arizona. [25] Tomeoka K. (1993) 18th Symp. Antarctic Met. p. 19. [26] MacPherson G.J. and Davis A.M. (1993) GCA 57, 231. This work was partly supported by NASA grants NAG 9-454 and NAGW-3281 (K.Keil, PI).

EVAPORATION AND RECONDENSATION DURING CHONDRULE FORMATION. Derek W.G. Sears[†] and Michael E. Lipschutz[‡]. [†]Cosmochemistry Group, Department of Chemistry and Biochemistry, University of Arkansas, Fayetteville, Arkansas 72701. [‡]Department of Chemistry, Purdue University, West Lafayette, Indiana 47907.

The composition of eight chondrules from Semarkona, seven from Bishunpur and seven from Chainpur have been determined by radiochemical neutron activation analysis (RNAA) to better understand chondrule formation and history. The elements determined include some of the most mobile ones, which are therefore of greatest potential value in deciphering the details of thermal processing. Elemental abundances decrease as lithophiles > siderophiles > chalcophiles. While lithophile element abundances decrease, chalcophile and sometimes siderophile element abundances of the chondrules increase with increasing element mobility (as determined from laboratory heating experiments on Krymka). The behavior of the major host phases during chondrule formation largely controls trace element abundances, but there was also considerable evaporative loss of the volatile lithophiles while the mobile chalcophile (and sometimes siderophile) elements experienced both loss and recondensation. There was clearly considerable redistribution of major mineral phases and trace elements during the formation of all chondrule groups.

Chondrule formation was clearly a major process in the early solar system (1) and chondrules play an important role in determining chondrite properties (2). While considerable effort has been placed in documenting the range of compositional and textural properties displayed by the chondrules (2-6), no attempt had been made to determine the abundance in them of some of the most volatile trace elements like In, Tl and Bi. These elements show very large abundance variations in ordinary chondrites (7-8) and have been crucial in our efforts to understand chondrite formation and metamorphic history. For the present study, chondrules were hand-picked from three low petrologic type ordinary chondrites and analyzed by RNAA for 15 groups elements, including some of the most highly volatile. The chondrules were assigned to compositional classes using the criteria of ref. 9. A number of related studies on the same chondrules have been briefly reported (10-12).

The data are shown in Fig. 1, in which chondrules have been grouped by compositional class and the data plotted by cosmochemical group in order of increasing mobility as determined by heating experiments on Krymka (LL3.1, 13). Despite the volatility of most of these elements, the concentrations determined were high (near CI values) and the patterns remarkably reproducible from chondrule to chondrule, independent of group. Contents decrease in a fashion similar to major elements, lithophile > siderophile > chalcophile (2), but while concentrations of lithophile elements decrease with increasing mobility, contents of chalcophile (and sometimes siderophile) elements increase with mobility.

The difference in abundance of the cosmochemical groups indicates that, to a first approximation, the abundance of these elements depends on the amount of host phases, silicate, metal and sulfide. The lithophile > siderophile > chalcophile trend therefore reflects the relative abundance of metal and sulfide in the precursor mix or the loss of metal and sulfide during chondrule formation. The decrease of lithophile concentrations with increasing mobility most probably reflects evaporative loss of these elements during chondrule formation, since there is no obvious reason why they should vary in this way in the precursor. We argue that the increase in abundance of the chalcophiles reflects recondensation of volatiles during chondrule cooling, following labile element loss at peak temperatures of chondrule formation. These elements are so

mobile, mainly by virtue of their volatility, that they must have been lost during chondrule formation, even assuming the mildest thermal history (13); yet Cd and In now have the highest chalcophile element abundance. Evaporation and recondensation almost certainly accompanied formation of group A chondrules, producing the rims on these chondrules which often contain sulfide and metal rich layers (14, 15). Apparently, evaporation and recondensation also occurred among the more mobile elements in group B chondrules. The present data indicate that there was considerable redistribution of major host phases and trace elements associated with chondrule formation.

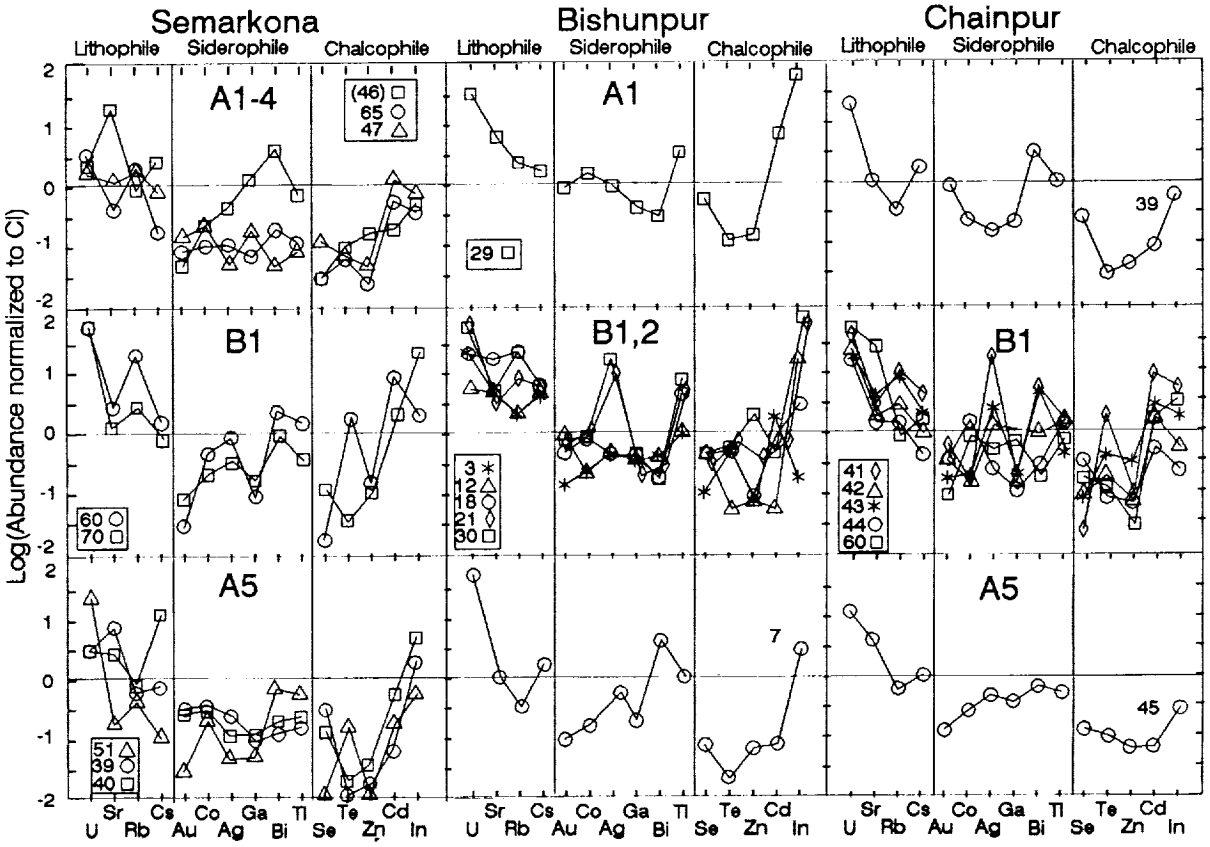

Fig. 1. Abundance of 15 elements, mainly highly mobile trace elements, in chondrules from three low petrologic type ordinary chondrites. Within the cosmochemical groups, elements are plotted in order of increasing mobility which was determined from heating experiments on the Krymka LL3.1 ordinary chondrite. The numbers by each symbol refer to individaul chondrule identifications. Electron microprobe data are not available for the classification of chondrules 7 and 39.

(1) J.A. Wood (1985) In *Protostars and Planets II* (eds. D.C. Black and M.S.Matthews) pp. 687-702. (2) J.N. Grossman (1988) In *Meteorites and the Early Solar System* (eds. J.F.G. Kerridge and M.S. Matthews) pp. 619-659. (3) S.W. Kieffer (1975) *Science* **189**, 333-340. (4) R.T. Dodd (1981) *Meteorites: A Petrologic-Chemical Synthesis*. (5) H.Y. McSween (1977) *Geochim. Cosmochim. Acta* **41**, 477-491. (6) E.R.D. Scott and G.J. Taylor (1983) *Proc. Lunar Sci. Conf.* **14**, *Jour. Geophys. Res.* **88** B275-286. (7) C.M. Binz *et al.* (1976) *Geochim. Cosmochim. Acta* **40**, 59-71. (8) S.N. Tandon and J.T. Wasson (1967) *Science* **158**, 259-260. (9) D.W.G. Sears *et al.* (1992) *Nature* 357, 207-210. (10) A.D. Morse *et al.* (1987) *Meteoritics* **22**, 465-466. (11) D.W.G. Sears *et al.* (1988) *Lunar and Planetary Sci.* **19**, 1051-1052. (12) D.W.G. Sears *et al.* (1988) *Meteoritics* **23**, 30. (13) M. Ikramuddin *et al.* (1975) *Geochim. Cosmochim. Acta* **41**, 393-401. (14) D.W.G. Sears *et al.* (1993) *Meteoritics* **28** 669-675. (15) S. Huang *et al.* (1993) *Meteoritics* **28** 367-368. Supported by NASA grants NAGW 3519 (DWGS) and NAG 9-48 (MEL) and DOE grant DE-FG07-80ER1 0725J (MEL)

NUMERICAL OCEAN TIDES ON TITAN: SPHERICAL CASE; William D. Sears, Department of Planetary Science, University of Arizona, Tucson, AZ 85721

Sagan and Dermott [1] discussed an analytical model of tidal dissipation in the proposed ocean on Titan. A numerical hydrodynamic differential equation (HDE) model of a methane ocean on Titan has been used to check the analytical results. It shows dissipations about six times greater than the analytic model. This reinforces the argument that the ocean must be deep or non-existent.

The analytical model presented by Goldreich and Soter [2] was used in [1] to show that oceans less than $400m$ deep would have dissipated enough energy over the age of the Solar System to have cicularized Titan's orbit. This was a conservative estimate in that velocities were thought to be underestimated by at least a factor of two and the initial orbital eccentricity was barely constrained.

I adapted the earth ocean model described by Zahel [3] for Titan. This is a full, non-linear HDE model with coriolis terms, bottom friction, and eddy viscosity. I used a 2° grid and the second order spherical harmonic disturbing potential with both the radial and libration tides, assuming synchronous rotation. I neglected tidal loading and the ocean self-attraction and I assumed a spherical solid Titan. This latter assumption implies that there has been no hydrostatic relaxation in the solid body but is necessary for proper comparison to [1].

The table shows the period-averaged bottom friction dissipation calculated by the numeric model and compares it with that calculated using the formulas in [1] and [2]. Parameters are taken from [1] with the exception of the coefficient of skin friction which is taken as 0.003 after [3]. As can be seen the dissipation from the numeric model is approximately six times larger than the analytic model, but does approximately follow the Depth^{-3} relationship derived by [1]. To one and a half significant figures the relationship would be $\text{Dissipation} = 1.5 \times 10^{18} (W \cdot m^3)/\text{Depth}^{-3}$. For the same conditions as given in [1], a six times greater dissipation would imply a $6^{1/3}$ or 1.8 times deeper ocean giving a minimum depth of about $700m$.

The numerical HDE model shows a markedly higher dissipation than the analytic model which uses only radial tides. This is due to the addition of coriolis terms and the libration tide which accounts for approximately half of the total dissipation, according to a libration only numeric run. The figures show the displacements and velocities for a full $400m$ depth ocean numeric run.

Increased ocean dissipation argues even more strongly that an ocean must be deep or non-existent. However, there are many other factors which must be considered to obtain an overall picture of Titan's tides. It is likely that the solid Titan is hydrostatically relaxed, and this will probably change the dissipation. Also, there is still the question of exactly what partial land coverage would do to the dissipation. The HDE model will be used to investigate these issues. Then there is the interior dissipation, which may be more important than previously thought. Tides on Titan is still an active area of research.

ACKNOWLEDGMENT.

This work was supported by NASA's Graduate Student Researchers Program.

REFERENCES.

[1] Sagan, C. and Dermott, S.F. (1982) *Nature, 300*, 731–733.

[2] Goldreich, P. and Soter, S. (1966) *Icarus, 5*, 375–389.

[3] Zahel, W. (1978). In *Tidal Friction and the Earth's Rotation*, eds. P. Brosche and J. Sündermann, pp. 98–124.

NUMERICAL TITAN TIDES: Sears W.D.

TABLE.
Tidal energy dissipation for a methane ocean on Titan.

Ocean Depth (m)	Numeric Model Dissipation (W)	Analytic Model Dissipation (W)
100	1.7×10^{12}	2.4×10^{11}
400	2.2×10^{10}	3.7×10^{9}
600	6.1×10^{9}	1.1×10^{9}
1000	1.2×10^{9}	2.4×10^{8}

FIGURES.

Depth relative to spherical.

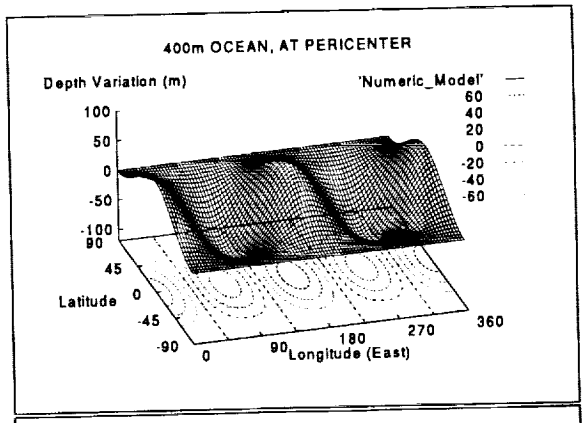

Northward tidal currents.

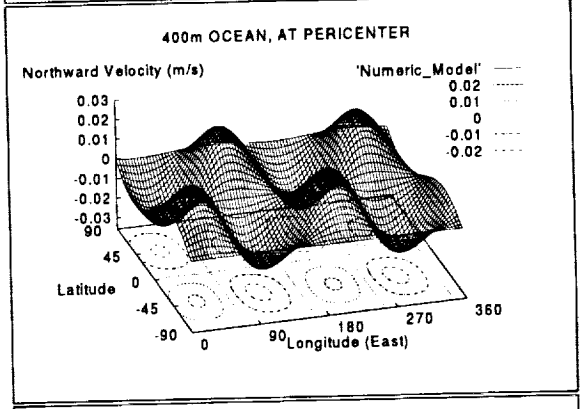

Eastward tidal currents.

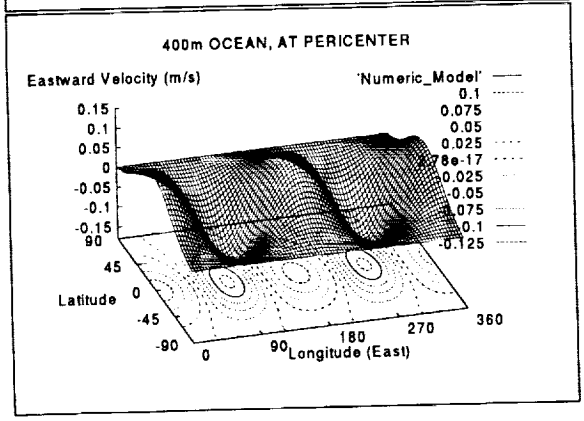

N94-35458 LPSC XXV 1233

CURRENT ACTIVITIES AND RESULTS OF THE LONG DURATION EXPOSURE FACILITY METEOROID & DEBRIS SPECIAL INVESTIGATION GROUP

Thomas H. See*, Kimberly S. Leago*, Jack L. Warren*, Ronald P. Bernhard* and Michael E. Zolensky**,* C23, Lockheed-ESC and **SN2, NASA/JSC, all in Houston, Texas 77058.

INTRODUCTION: Fiscal Year 1994 will bring to a close the initial investigative activities associated with the Long Duration Exposure Facility (LDEF). LDEF was a 14-faced spacecraft (*i.e.*, 12-sided cylinder and two ends) which housed 54 different experimental packages in low-Earth orbit (LEO) between April, 1984 to January, 1990 (*i.e.*, for ~5.75 years). Since LDEF's return, the Meteoroid & Debris Special Investigation Group (M&D SIG) has been examining various LDEF components in order to better understand and define the LEO particulate environment. Members of the M&D SIG at the Johnson Space Center (JSC) in Houston, Texas have been contributing to these studies by carefully examining and documenting all impact events found on LDEF's 6061-T6 aluminum *Intercostals* (*i.e.*, one of the spacecraft's structural frame components). Unlike all other hardware on LDEF, the frame exposed significantly large surface areas of a single homogeneous material in all (*i.e.*, 26) possible LDEF pointing directions. To date, 28 of the 68 *Intercostals* in the possession of the M&D SIG have been documented. This data, as well as similar information from various LDEF investigators, can be accessed through the M&D SIG Database which is maintained at JSC.

IMPACT FREQUENCY: Figure 1 shows the cumulative size-frequency distribution for craters as determined from examination of the *Intercostals* carried out in the Facility for the Optical Inspection of Large Surfaces (FOILS) at JSC. For the sake of clarity, only the average flux for the four cardinal pointing directions of LDEF are plotted. Each curve represents the average flux for the primary row (*i.e.*, 3, 6, 9 & 12) from each cardinal direction, along with the adjacent rows on either side (*i.e.*, East represents the average flux for Rows 8, 9 & 10). LDEF's forward-facing rows continue to reveal the highest cratering frequencies, while the rearward-facing rows exhibit the lowest. The northern facing rows (1, 12 & 11) exhibit a slightly higher overall flux than do their southern-facing counterparts, at least for craters >30 μm in diameter. The minor differences between these two pointing directions are most likely due to the fact that LDEF's velocity vector was yawed ~8° toward the Row-12 direction (*i.e.*, Rows 1, 12, and 11 pointed ~8° more into the velocity vector, while Rows 5, 6, and 7 were ~8° further removed from the velocity vector [1]). However, as data from more impact features are accumulated, the overall differences between the northern- and southern-facing *Intercostals*, excluding the difference below ~30 μm, have become smaller, to the point where the impact frequency for these surfaces are essentially the same. The elevated flux for impact features below 30 μm on the southern-facing rows is due to the unusually high frequency of small features documented on *Intercostal* F07F02.

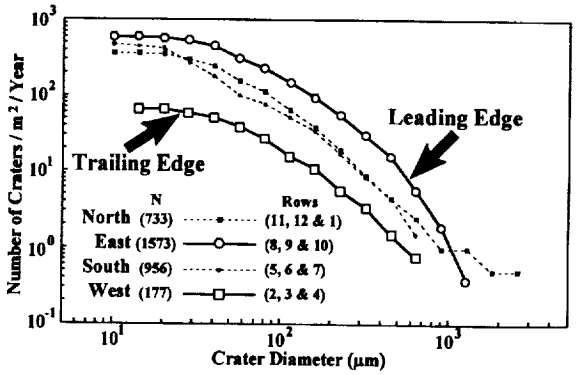

Figure 1. Average cumulative size frequency distributions for the four cardinal pointing directions on LDEF. Row 9 was the leading edge of the spacecraft in its gravity-gradient stabilized orbit.

The ratio of the production rate of impacts on the leading edge to that on the trailing edge seems to vary slightly depending on the impact-crater diameter. Comparing the averages of the east- and west-facing directions the ratios range from ~8:1 to ~10:1 for the smallest size bins, and drops to ~6:1 for the larger features. Is the large-particle population more isotropically distributed, are these differences related to the sources, and hence the associated velocities of the different particle-population sizes, or is this simply a statistical effect from the reduced number of impacts at successively larger diameters? We are currently investigating these possibilities.

INTERCOSTAL F07F02: High-magnification optical examination of 28 *Intercostals* has revealed an anomalous number of craters ≤40 μm in diameter on *Intercostal* F07F02 [2]. In an effort to understand this phenomenon and to identify the source of these features, the M&D SIG has analyzed some of these craters, the associated projectile residues, and associated contamination by Scanning Electron Microscopy (SEM) and Energy Dispersive X-ray Analysis (EDXA). The objectives were to evaluate the chemical variability and possible clustering of discrete particle types and determine their source(s). Detectable projectile residues were classified as either micrometeoritic or as man-made debris, while sources of surface contamination were identified whenever possible.

The occurrence of the various projectile types resulting from this investigation has been tabulated in histogram form and is illustrated in Figure 2, which displays the relative frequencies of micrometeoritic, man-made debris particles (*i.e.*, paint and electrical components), indeterminate, and contaminated impacts for the smaller size bins. We analyzed 251 of the 540 craters from F07F02, or ~46%. A higher occurrence of all types of particles is evident in the 20 to 40 μm size range. However, there is a particular increase in the relative amount of paint-type residues as compared to residues found on tray clamps and the gold surfaces from experiment A0187-1 [3, 4]. SEM examination of impact-feature morphology shows that the depth to diameter ratios, the crater rim characteristics, and the residue remnants are similar within this suite of impact features. The chemistry of the paint-impact residues tend to be Si-, Cl-, Ti-rich paint, all exhibiting an absence of Zn. This may indicate that the projectiles originated from a common source, yet the exact nature of this source remains unknown. One possibility is that the paint particles

may have been traveling as a dense cloud or group of orbital debris; if so, the occurrence of this phenomenon on LDEF has only been found in this one very localized area thus far. In fact, *Intercostals* C07F02 from the other end of the same row, and F08F02 from the adjacent row do not exhibit this anomalous flux behavior. An orbiting debris cloud would have to have been extremely compact to have caused such a localized phenomenon. The craters could represent secondaries from some localized impact event. However, attempts to identify a source related to LDEF have been unsuccessful. This leads us to believe that the primary source for these particles was an impact event into a painted Shuttle surface (*e.g.*, the Remote Manipulator System or arm), which occurred either during deployment or retrieval of LDEF.

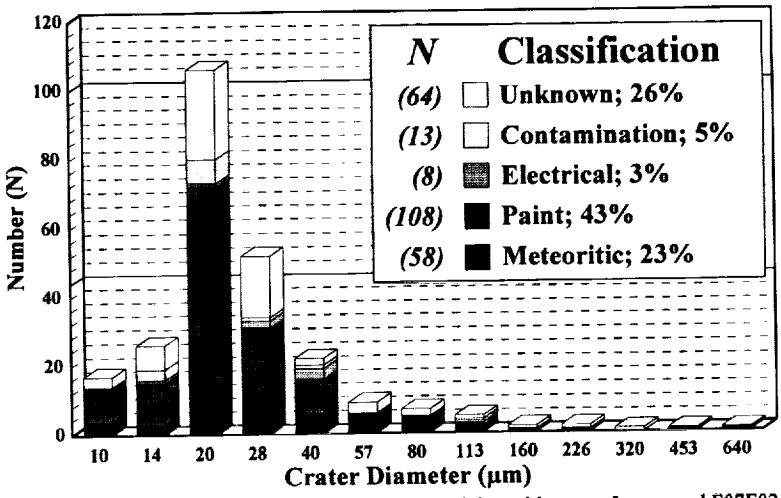

Figure 2. Relative occurrence of the various particle residues on *Intercostal* F07F02. Percentages given are for all crater sizes.

M&D SIG ACTIVITIES FOR FY 94: With FY 94 bringing to a close the initial investigative phases of LDEF, the M&D SIG is active on several fronts. In a continuing effort to make all M&D data available to the general user community, the M&D SIG at JSC is constantly updating the M&D Database with data from all possible sources, including data generated at JSC, as well as data provided by various LDEF investigators. However, the M&D SIG would like to receive more data from all potential sources and are requesting that anyone having such data forward it to T.H. See or M. Zolensky.

Members of the M&D SIG at JSC continue to gather data from the detailed scans of the LDEF *Intercostals*; these activities will continue as long as funding permits. In related matters, the past year saw the return of the EURECA spacecraft, as well as the Hubble Space Telescope (HST) repair mission. The M&D SIG has already acquired sections of EURECA's thermal insulation materials and plans to scan or examine this hardware during the upcoming months. Prior to the HST repair mission the M&D SIG had requested pieces of the return solar panels for examination. However, during the repair activities one of the two solar panels would not completely fold to a configuration permitting it's return to Earth, and thus, was jettisoned over the side of the Shuttle. Whether or not the M&D SIG will still acquire any of this material for examination has yet to be determined. Nevertheless, LDEF will serve as a useful baseline or snap shot of the LEO particulate environment for the time period of April, 1984 to January, 1990. Future data will be compared to the data acquired from LDEF to evaluate how the LEO particulate environment is evolving with time.

Another activity presently underway at JSC involves the long-term storage and availability of the ~4,500 stereo images of various LDEF impact features taken during the initial deintegration and examination of LDEF at the Kennedy Space Center, as well as all of the subsequent images acquired at JSC. All of these images have been converted to a TIFF file format and are being transferred on to CD-ROM. Copies of these CDs are available on a temporary loan basis from the Office of the LDEF Curator at JSC. In addition, the LDEF Science Office located at Langley Research Center, Hampton, Virginia is considering doing the same thing with the on-orbit LDEF survey and general-view pictures, and the post-flight deintegration and experiment tray stand pictures for the purpose of long-term archiving and general access. The exact format in which these files will be written to CD has not been determined. Finally, along this same line, the M&D SIG plans on archiving all LDEF M&D data it can acquire on CDs. This will only occur if the various LDEF investigators provide the M&D SIG with their data.

Lastly, the M&D SIG is in the process of putting together a final report summarizing all results, and what they mean to the survivability of both manned and unmanned spacecraft in LEO. This report will include recommendations for further M&D-type activities and investigations on future spacecraft, as well as a long-term outlook as to ways in which the population of LEO particles can be monitored, as well as possible mitigation of it's orbital-debris components.

FUTURE ACTIVITIES: Although FY 94 will conclude the initial LDEF activities, it will not mean an end to M&D-type studies and investigations. At the recently held 3rd LDEF Post-Retrieval Symposium in Williamsburg, Virginia, NASA Headquarters and the LDEF Science Office presented plans for the formation of a Space Environments & Effects (SEE) program. This program would encompass the various LDEF SIGs, as well as private industry and academia, and would be customer-oriented, focusing on issues related to designing, placing and safely maintaining both manned and unmanned payloads into orbit.

REFERENCES: 1) Peters and Gregory, 1993 Att. Stab. LDEF: Ref Resu. from the Silver Pinhole Cam. *LDEF - 69 Mths Sp. 2nd Post-Ret. Sym., NASA CP-3194*, p. 3-12. 2) See *et al.*, 1994, Comp. Anal. of Proj. Res. on LDEF Inter. F07F02, *3rd LDEF Post-Ret. Sym., Abstracts*, p. 54. 3) Bernhard and Zolensky, 1994, Anal. of Imp. Res. on LDEF Clamp Sur. by SEM, *3rd LDEF Post-Ret. Sym., Abstracts*, p. 56. 4) Hörz *et al.*, 1994, Comp. and Freq. of Hyper. Part. <1 mm in LEO, *3rd LDEF Post-Ret. Sym., Abstracts*, p. 57.

NIMS - CALLISTO SCIENCE OBJECTIVES AND OBSERVATIONAL PLANS; M. Segura (Jet Propulsion Laboratory, Caltech), J. Sunshine and T. McCord (SETS Technology), and the NIMS team

Callisto will be observed by the Galileo Near Infrared Mapping Spectrometer (NIMS) for the first time on September 9, 1996. This paper describes the current observation plans which focus on surface composition identification and a thorough investigation of both ice and non-ice materials. Focused observations will include the Asgard and Valhalla multi-ring structures.

The Galileo Near Infrared Spectrometer (NIMS) provides a combination of spectroscopic and imaging observations. For geological studies of Callisto, NIMS can perform regional mapping while simultaneously determining composition and mineralogy, thus providing data to help determine the surface evolution. The NIMS instrument covers the spectral range from 0.7 to 5.2 microns. This spectral region contains diagnostic spectral signatures of minerals and ices known or suspected to be present on planetary and satellite surfaces.

The primary science objective for NIMS at Callisto is to identify the composition and spatial distribution of surface units. A key question for NIMS is the composition, variability, and origin of the "non-ice" material residing on Callisto's surface. NIMS is well suited to search for hydroxilated silicates, opaque minerals, and organic material. Along with the well known water ice features, ground based spectral observations of Callisto have indicated additional absorption features present at 2.8, 2.9,and 3.4 microns, and potentially a 3.1 micron feature which could indicate the presence of ammoniated clays [1]. In particular, NIMS can detect absorptions due to a range of iron bearing minerals. Minor volatile species may be detectable in observations with good spatial and spectral resolution. In addition, the H_2O temperature dependent feature at 1.6 microns may be used to estimate temperatures within icy surface features [2,3].

A study of the mineralogy and chemical composition of Callisto's surface features may give some insight into the processes which caused their formation. For example, the domes of central pit craters and palimpsests could be a result of excavated material. With the support of NIMS, the "bright" areas at the base of Valhalla's rings may provide insight into the formation of the multi-ring structure itself, the state of the central structure and lithosphere at the time of formation, and the composition of subsurface materials.

Galileo's two year tour consists of eleven orbits of Jupiter, including three close encounters and two moderate distance passes near Callisto. Global context maps with moderate spectral resolution of 51 wavelengths coupled with high spectral traverses of 204 to 408 wavelengths will be obtained in each of the five

orbits containing Callisto observations. Approximately seventy-five percent of Callisto's surface will be mapped at 50 to 210 km spatial resolution. Regional observations with moderate spectral resolution of 51 to 102 wavelengths but higher spatial resolution will be made of specified target areas such as the Asgard basin and multi-ring structure. "Postage stamp" size observations having high spatial and spectral resolution of 204 wavelengths will be made of a small subset of the regional observations. Northern latitudes will be observed to determine the composition of the "dark" areas and possible evidence of early volcanism. All known types of Callisto's terrain will be observed by NIMS.

References: [1] Calvin and Clark 1993. Icarus, 104, 69 - 78. [2] Kieffer and Smythe 1974. Icarus, 21, 506 - 512. [3] Fink and Larson, 1975. Icarus, 24, 411 - 420.

SEM STUDY OF METAL GRAIN SURFACE IN ORDINARY CHONDRITES. I. PRIMARY SCULPTURES. V.P.Semenenko, B.V.Tertichnaya. Institute of Geochemistry, Mineralogy and Ore Formation. Ukr.A.S., Palladin 34, Kiev, 252142, Ukraine.

Surfaces of chondrules and mineral grains of chondrites may contain sculptural features that are direct imprints of cosmic events [1-8]. Formation of these features is either connected with physical-chemical properties of the mineral or with conditions of their interaction with environments. The surface of iron nickel particles in contrast to other minerals offers the best perspective for sculptural investigations due to plastic properties of their grains. SEM-study of metal grains allows us to get important information on very small samples (< few mg) of meteorites.

The sculpture of metal particles was studied in 13 ordinary chondrites with different shock history [1]. Metal grains are kamacite, rarely taenite, and have generally irregular and sometimes globular shape. Regular metal crystals were observed by Christophe Michel-Levy in the Sena (H4) chondrite [2]. Four types of surface of the irregular metal particles can be distinguished: smooth, polygonal-concave (Fig.1), lamellar (Fig.2) and fine-granular. Particles with smooth and polygonal-concave surfaces are shining and the other are mat. The latter is typical of intensively shocked grains. Polygonal-concave surfaces contain imprints of near-by grains and are observed in some metal particles from equilibrated chondrites.

Primary and secondary sculptures of the metal grains are defined according to their history before and after agglomeration of parent body. Most of the sculptural features are located on free surfaces of grains that were not in tight contact with other minerals. The sculpture caused by internal factors is developed as the result of slow cooling of the metal particles and may be connected with primary or secondary origin. There are inclusions, crystallographic elements (vicinals, growth steps) and voids. Occurence of mineral inclusions (usually chromite) (Fig. 3) on the grain surface is connected with their preferable formation on the mineral phase boundaries during slow cooling of the metal particles containing dissolved minor elements such as Cr, P, Cu, etc... Relatively slow growth of metal grains promoted the formation on their surface of more or less developed vicinals (Fig.4) or growth steps (Fig.5). The presence of small spherical voids ($\leq 1\mu m$) on the surface and inside the metal particles could indicate possibly some gas inclusions.

The primary sculptures caused by the external factors are sticked globules (Fig.6), microcraters (Fig. 7) and melt sparks (Fig.8). The same sculptures were also observed on chondrules surface [3-6,8]. Their formation could result from collision with solid particles at different velocities other before or during agglomeration. However, some could result of interaction with associated grains during shock metamorphism on the parent body. Features of the melt sparks distribution testify to different moistening of the metal grain surface caused by the various temperature and composition of melt drops.

CONCLUSIONS: 1. The presence of the same sculptural features on metal grains and chondrules surface of chondrites indicates their common history under conditions of intermixing and interaction with each other before or during agglomeration of parent body. 2. The presence of metal grains with polygonal-concave surface found only in equilibrated chondrites confirms their origin as high temperature agglomerates. They are not found in unequilibrated chondrites. 3. Conservation of some primary sculptures on the metal surface

of equilibrated chondrites suggests, that heating was not high enough to anneal them during agglomeration or metamorphism of the parent body.

REFERENCES: [1]. V.P.Semenenko, B.V.Tertichnaya, this volume. [2]. Jedwab J. (1972) Meteoritics 7, 537-546. [3]. M.C.Michel-Levy (1977). Meteoritics, 12, 3, 194. [4]. S.P. Das Gupta et al. (1978). Meteoritics, 13, 435. [5]. M.Christophe Michel-Levy (1981). Earth Planet. Sci. Lett., 54, 67. [6]. V.P.Semenenko, E.V.Sobotovich (1983). Mineral.J., 5, 1, 63 (In Russian). [7]. V.P.Semenenko et al., (1987a). Meteoritika, 46, 73 (In Russian). [8]. V.P.Semenenko et al. (1987b). In: The meteorites of Ukraine, 218p. (In Russian).

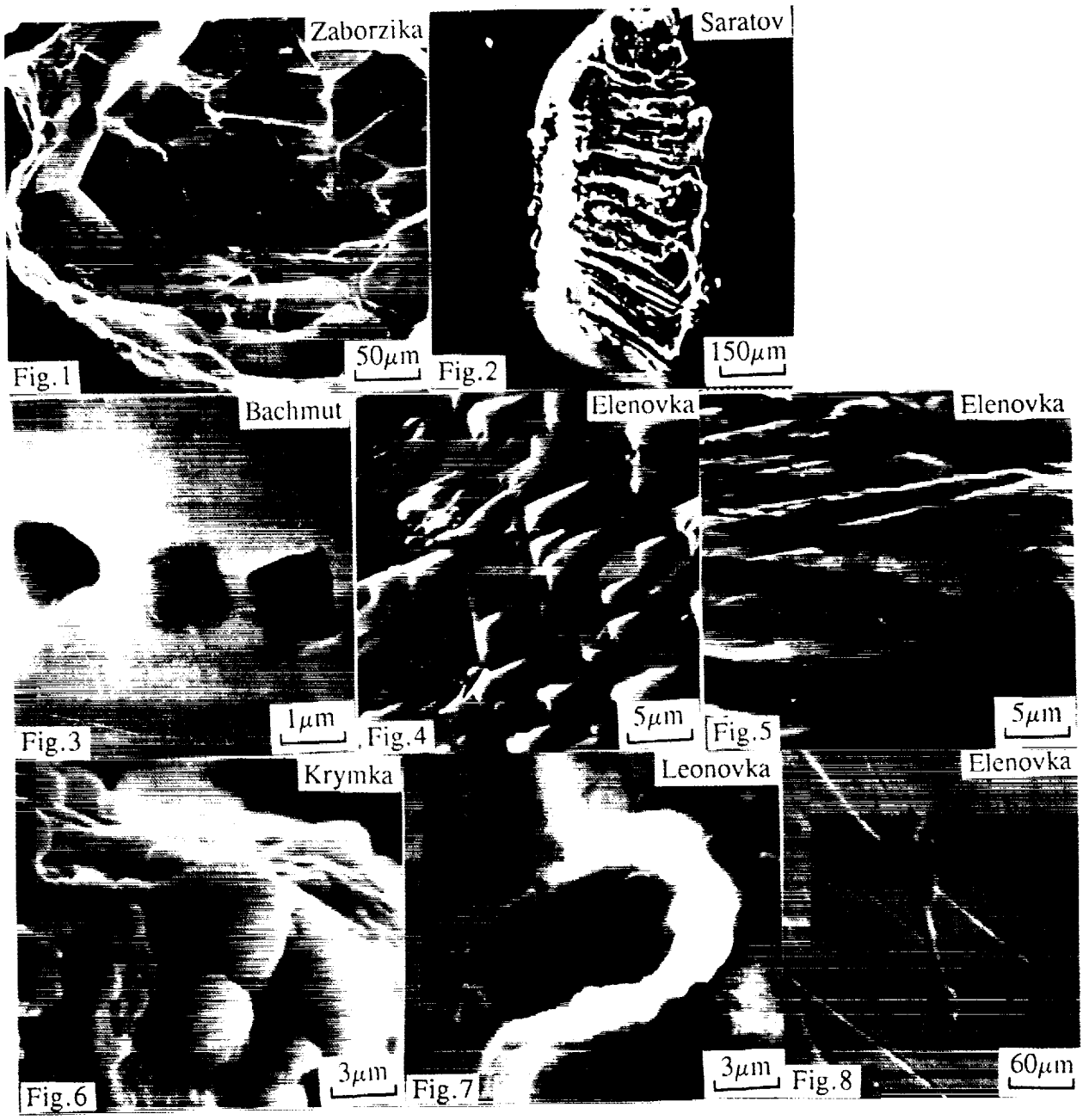

SEM STUDY OF METAL GRAIN SURFACE IN ORDINARY CHONDRITES. II. SECONDARY SCULPTURES. V.P.Semenenko, B.V.Tertichnaya. Institute of Geochemistry, Mineralogy and Ore Formation. Ukr.A.S., Palladin 34, Kiev, 252142, Ukraine.

Secondary sculptures are more widespread than primary one's [1] and are visible on the surface of metal grains from the ordinary chondrites as following features: voids, friable (fracturing, disruption, brecciation) and plastic (linear, lamellar, bending) deformations and sculptures of shock heating (healing of deformation sculptures, recrystallization and disintegration) [2,3]. The studied chondrites suffered different shock pressure and heating which vary in range 15-50GPa and 400->500°C, respectively [3]. Straight correlation between abundance of the secondary sculptures and degree of shock-transformation of the chondrites testifies to their origin during shock metamorphism.

The surface of the metal particles contains voids which in comparison with primary one's are characterized by larger sizes (≥1μm) and irregular shape (Fig. 1). A straight correlation between void size and degree of shock metamorphism and their absence inside the grains suggest that they formed during shock, possibly as result of a coagulations of defects and dislocations [4,5] or as surface corrosion.

In spite of plastic features, the surface of some metal particles shows evidences of brittle deformation that allows us to conclude about collisions of parent bodies in space at low temperatures (≤-100°C) when plastic metal becomes brittle [5]. The plastic deformation sculptures are developed along certain crystallographic directions and are characterized by the regular orientation that permits to determine them as the surface tracks of shear deformations. F.Begemann and F.Wlotzka [6] noted similar features on surface of metal particles from the Ramsdorf chondrite. They are visible on some free surfaces of particles and are characterized by deformation lamellas (width ≤10μm) (Fig. 2). Some of them are splited. Sometime, the higher degree of shock metamorphism caused brecciation of lamellas (Fig. 3) and their recrystallization (Fig. 4).

Some relationship between deformation and sculptures produced by heat effects is observed. The formation of these "heating sculptures" is caused by the shock and partial healing of deformations during shock heating. The surface sculpture of the recrystallized metal grains varies according to the possibility of free crystal growth. On areas of free growth the particle's surface is granular with regular crystals shape. In case of compact contact with surrounding minerals the surface is smooth with visible boundaries of the kamacite crystals which have regular shape inside polycrystalline grains. The SEM-study of disintegrated metal grains which have undergone the highest degree of shock metamorphism is difficult. These grains are characterized by their high brittleness and fine-globular structure that did not permit to clearly observe them (Fig. 5). The study of interrelation of the sculptural elements gives some information about the sequence of cosmical processes. For example, the presence of relicts of deformation lamellas visible as bands on the surface of some metal particles which have been broken by brittle cracks indicates at least two shock events at different temperatures during the meteorite history (Fig. 6).

CONCLUSION: 1. Surface of metal grains of the chondrites is more sensitive to shock metamorphism than their inner part. 2. Sensitiveness of the metal grain surface to shock

deformation allows us to range the studied chondrites in the following sequence which correlates with their shock pressure (15→50GPa) and temperature (400→>500°C): Elenovka (L4-5), Zhigailovka (LL6), Leonovka (L6), Zaborzika (L6), Zvonkove (H5), Bachmut (L6), Kuleschovka (L6), Andreevka (L3-4), Bielokrynitschie (H4), Saratov (L4), Krymka (LL3), Gorlovka (H4), Tsarev (L4). 3. The secondary sculptures of metal grains of the studied chondrites is more widespread in unequilibrated one's than in equilibrated. This may be connected with different level of their shock transformation and/or with different cooling rates after the shock heating.

REFERENCES: [1]. V.P.Semenenko, B.V.Tertichnaya, this volume. [2]. V.P.Semenenko et al. (1987). Meteoritika, 46, 73 (In Russian). [3]. V.P.Semenenko et al. (1987). In: The meteorites of Ukraine, 218p. (In Russian). [4]. J.Blakemore (1972). In: Physic of solid state, 488p. (In Russian). [5]. R.W.K.Honeycombe (1972). In: The plastic deformation of metals, 408p. (In Russian). [6]. F.Begemann, F. Wlotzka (1969). GCA, 33, 1351.

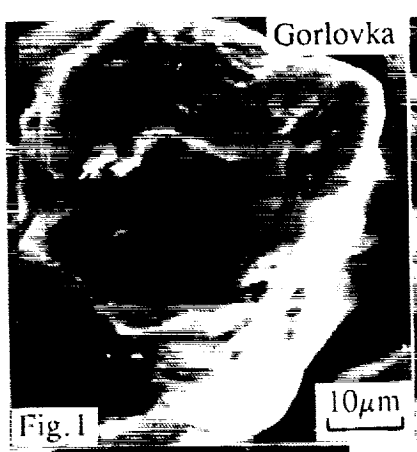

Fig.1

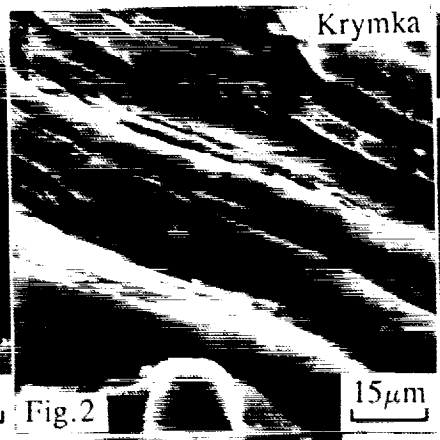

Fig.2

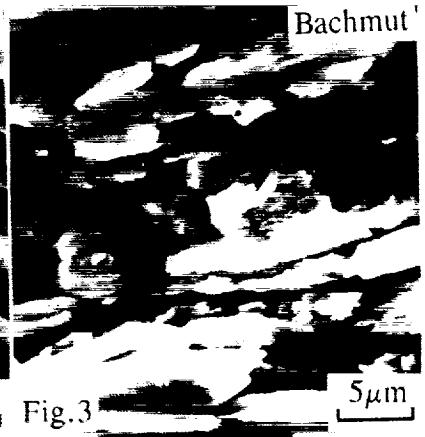

Fig.3

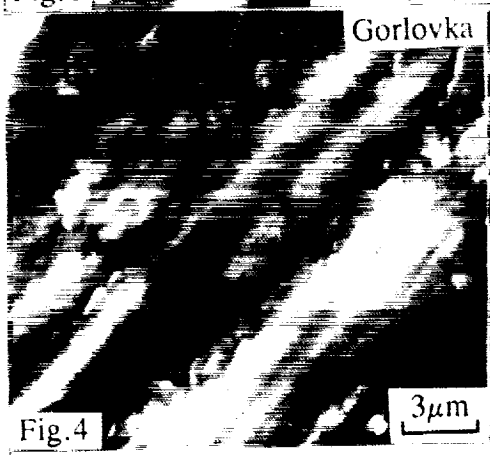

Fig.4

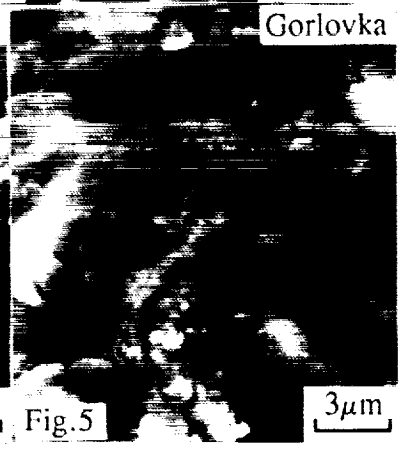

Fig.5

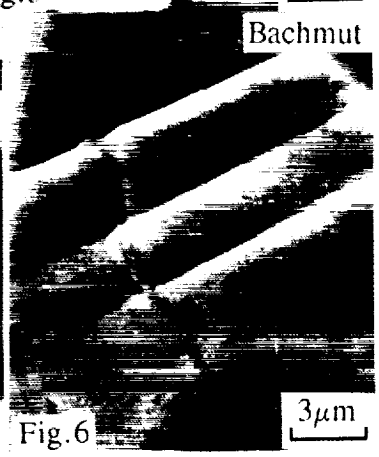

Fig.6

EXAMINATION OF THE RELATION BETWEEN RIFTING AND VOLCANISM IN THE JUNO DORSUM REGION OF VENUS, D. A. Senske, Jet Propulsion Laboratory, California Institute of Technology, Pasadena, CA 91109.

Introduction. Zones of extension and rifting on Venus are located in belts that extend northeast from the south pole to Aphrodite and along the equatorial region to Beta Regio and Atla Regio [1]. In general, volcanism is concentrated at the ends of trough segments or at nodal points where the rifts form branching patterns. In many cases, major graben are located on broad, regional, rises (Beta, Atla, Western Eistla, and Imdr Regiones), sites interpreted to be associated with mantle upwelling [2,3,4,5]; at others, such as Ganis Chasma and Juno Dorsum, rifts lie on the crest of linear rises without apparent domical swells. Along with regional topographic information, Magellan altimetry data show the details of the raised flanks of the rifts, suggesting lithospheric flexure. To understand better the relation between extension and volcanism and to examine properties of the lithosphere, the Juno Dorsum region is mapped and a simple lithospheric flexure model is evaluated. These results are compared to other areas of the planet where major rifts are present.

Geology of the Juno Dorsum Region. Juno Dorsum, a linear topographic rise, reaches an elevation of 1.0 km above the surrounding plains. Located along the highest topography is a 60 to 90 km wide, 1.0 to 2.0 km deep, graben that is bound by normal faults. Like many of the other rifts on Venus, this one is generally empty of volcanic filling [5,6]. Geologic mapping shows the Juno region to be dominated by six major units (Fig. 1). The most pervasive, undivided plains, are made up of dark, homogeneous, material and in many places contains low, sinuous ridges. Lineated plains, irregular shaped areas of dark material contain numerous lineaments/fractures. Contacts with the undivided plains are sharp, indicating that the lineated plains have been flooded by more recent volcanism. Isolated occurrences of complex ridged terrain (CRT), elevated radar-bright areas with multiple directions of deformation, are also extensively embayed by the undivided plains. The western end of the Juno rift is abruptly truncated at a large volcano. Lava flows on the eastern flank of this edifice are deflected around a preexisting ridge belt. Other lava deposits, located in the eastern part of the area, form flow fields that originate at a corona. In addition to coronae, other structures identified in this area include fractures, impact craters, ridges, and major fault scarps. Stratigraphically, the oldest units are the CRT, lineated plains and the ridge belt. These are all embayed by the undivided plains. Superposed on these regional plains is the Juno rift, coronae, and the flow fields. Fractures from the rift cut across part of the flow fields, indicating extension occurred subsequent to the formation of the corona and its deposits. The large volcano is superposed on the rift and does not appear to be deformed by it, indicating that this edifice is one of the most recent features in this area.

Modelling the structure of the uplifted rift flanks using a plate flexure model provides insight into the properties of the Venus lithosphere. These type of analyses have been carried out for both coronae and rifts [7,8,9]. In this study, the deflection of a thin elastic plate due to the mass deficit at the rift is calculated using the relation:

$$w(x) = \left[\frac{\rho_m}{\rho_c} + \frac{D}{\rho_c g}\left(\frac{2\pi}{\lambda}\right)^4\right]^{-1} h_o \sin 2\pi\frac{x}{\lambda}$$

where ρ_m and ρ_c are the mantle and crustal densities, g is the acceleration of gravity, $h_o \sin 2\pi (x/\lambda)$ is the topography and D is the flexural rigidity, $Eh^3/12(1-\upsilon^2)$, which is a function of the plate thickness, h, and E and υ, Young's modulus and Poisson's ratio respectively. Plate thicknesses of 10 to 15 km provide a relatively good fit to the topography on southern the southern flank of the rift (Fig. 2). These values are consistent with those obtained for this area by Evans *et al.* [8] and are less than the 20 to 40 km thicknesses at Beta Regio [9]. The fit to the northern flank is much poorer, showing substantial residual topography. This suggests that additional forces, not accounted for here (possibly related to variations in lithospheric structure), may be producing some of the observed topography.

Conclusions. Stratigraphic relations indicate that recent volcanism in the Juno Dorsum area is focused at coronae and a large volcano. Like other parts of the planet, these structures are located at the end of trough segments, producing a characteristic chain of volcanic centers [10]. Results from evaluating a plate flexure model are consistent with those obtained by Evans *et al.* [8] and suggest that the elastic lithosphere is thin relative to that at Beta Regio. The larger thickness and the presence of areally extensive occurrences of CRT at Beta may be relate to differences in lithospheric structure. Further geologic mapping and analysis using Magellan Cycle 4 gravity data is aiding to better establish the sequence of events in rifting and to characterize the properties of the Venus lithosphere.

References. [1] Senske *et al.*, this volume, 1994. [2] Stofan, E. R., *et al.*, *Geol. Soc. Am. Bull.* , *101* , 143-156, 1989. [3] Grimm, R. E. and R. J. Phillips, *J. Geophys. Res.*, 97, 16035-16054, 1992. [4] Senske, D. A., *et al.*, *J. Geophys. Res.*, 97, 13395-13420, 1992. [5] Senske, D. A., *et al.*, *LPSC XXIV*, 1279-1280, 1993. [6] Solomon, et al., *J. Geophys. Res.*, 97, 13199-13255, 1992. [7] Sandwell, D. T. and G. Schubert *J. Geophys. Res.*, 97, 16069-16083, 1992. [8] Evans, S. A., *et al.*, *International Colloquium on Venus*, 30-32, 1992. [9] Senske, D. A., *LPSC XXIV*, 1277-1288, 1993. [10] Stofan, E. R. and V. E. Hamilton, *LPSC XXIV*, 1361-1362, 1993.

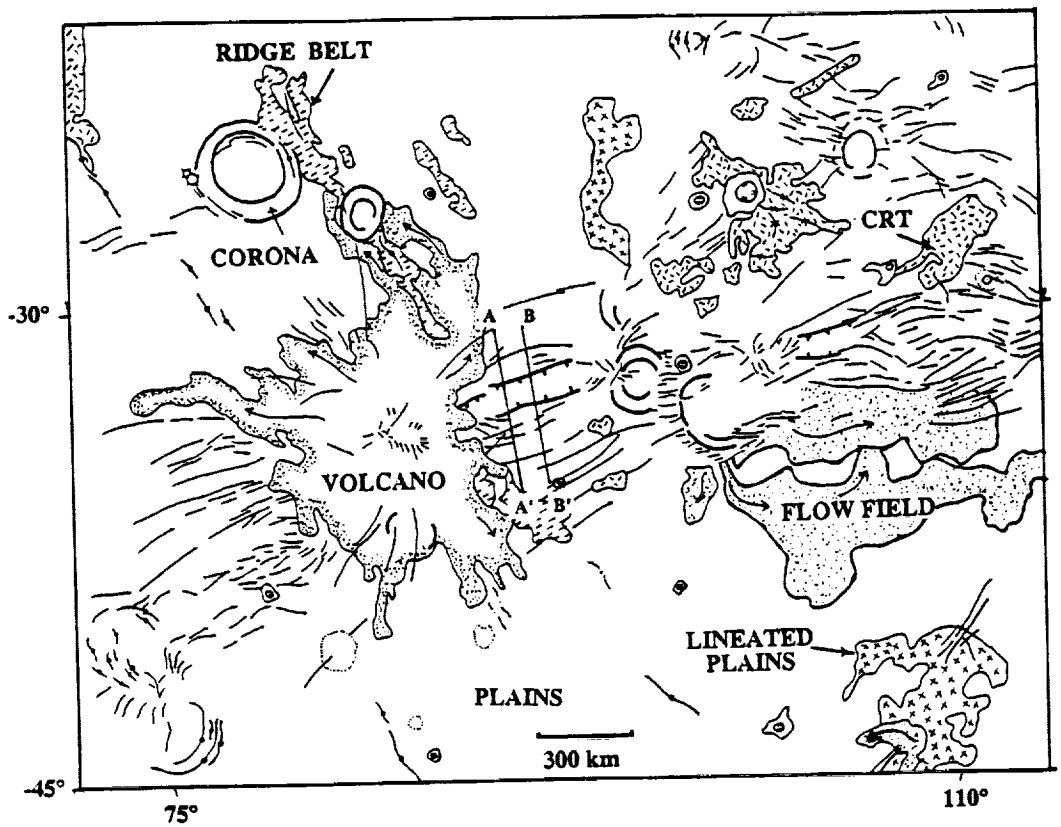

Figure 1. Sketch map of the Juno Dorsum area. The ground track for orbits (665 and 668) for which plate flexure models are evaluated are indicated.

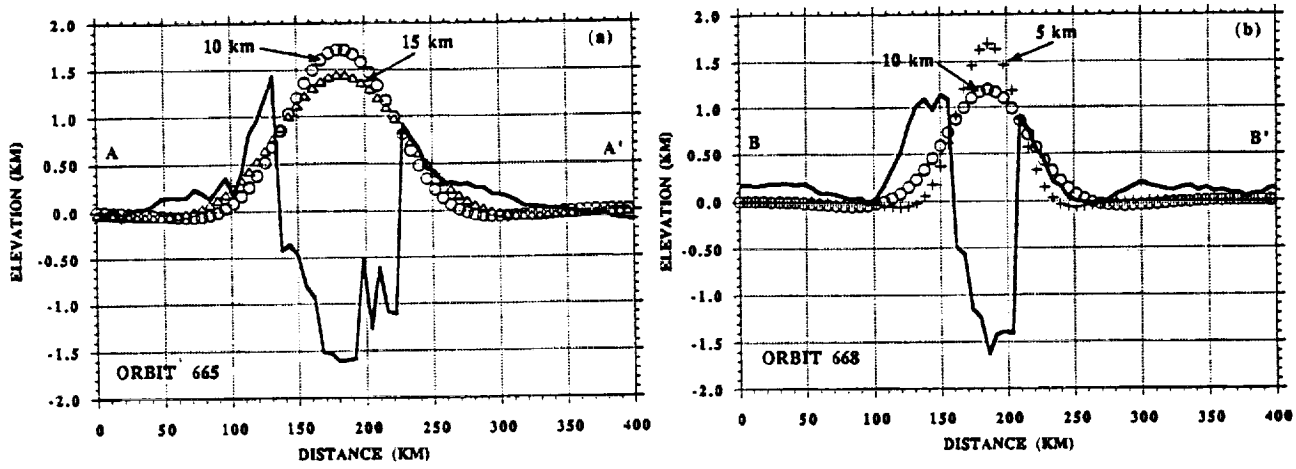

Figure 2. Elastic plate models fit to topographic profiles (solid line) across the Juno rift, orbits 665 (a) and 668 (b). For these models, E= 70 x 10^9 Pa, υ =0.25, ρ_m =3300 kg/m^3, ρ_c =2800 kg/m^3, and g =8.8 m/s^2. The southern flank is best fit with a plate with an effective elastic thickness of 10 to 15 km.

RADAR CHARACTERISTICS OF GEOLOGIC UNITS IN THE CARSON QUADRANGLE, VENUS

D. Senske[1], R. Greeley[2], K. Bender[2], [1]Jet Propulsion Laboratory, California Institute of Technology, Pasadena, CA 91109, [2]Arizona State University, Tempe, AZ, 85287,

Introduction. Geologic mapping of the Carson Quadrangle, southeast Guinevere Planitia (0° N to 25° S; 330° to 0°), shows this part of Venus to contain a wide array of landforms [1]. To understand better the properties of surface features and styles of lava emplacement, the radar scattering behavior of various units is examined. This information allows comparisons to be made with terrestrial lava flows and geologic units mapped elsewhere on the planet [2,3].

Geology of the Carson Quadrangle. Geologic units identified in the Carson Quad can be divided into three classes: (1) volcanic, (2) tectonic, and (3) impact related [1]. When defining units, the angle that Magellan viewed the surface is important to understanding the mechanism by which the incident radar signal is scattered. For features in the latitude range discussed here, these angles vary from 46° at 0° N to 35.5° at 25° S. The returned signal is therefore strongly controlled by surface roughness, diffuse scattering [4], at the 12.6 cm radar wavelength and units defined as bright are generally rough while dark units are smooth. Of the eleven units identified in the Carson Quadrangle, we examine the characteristics of seven [Fig.1]. These include, a dark diffuse deposit (dark "splotch"), crater material (ejecta, bright outflow material associated with the crater Carson, and bright deposits), complex ridged terrain (CRT), regionally extensive reticulate and undivided plains, bright lava flows within a flow field, and dark lava flows within shield fields.

Radar Scattering Characteristics. The large incidence angle scattering behavior of geologic landforms on Venus has been studied previously on both global and regional scales [2,3]. Ford and Senske [2], used Pioneer Venus radar data to characterize units in the equatorial region of the planet mapped from Arecibo images (1- to 2-km resolution). The high resolution Magellan data (120 to 300 m) allows these results to be compared with backscatter from units identified on other areas of the Venus. Scattering curves for several of the Arecibo units are shown in Fig. 2a along with values for features in the Carson region. These initial results show that the roughness of material making up bright crater outflows, CRT, and ejecta from Carson are comparable to that of CRT mapped elsewhere, indicating the presence of a large number of sub-wavelength-scale scatterers. Bright lava flows, relatively fluid lavas that fill fissures within the lineated plains, and regional plains units show characteristics similar to the planetary average and are similar to the Arecibo units of mottled and bright plains. Dark lava flows and a dark "splotch" (dark diffuse deposit) contain few sub-wavelength-scale scatterers and are comparable to the dark plains unit.

Bright diffuse deposits cover a range of σ_0 over a small incidence angle interval. This variability may be due to differences in the thickness, or the amount of wavelength-scale material in the deposit. For several units it is possible to make comparisons with terrestrial lava flows [2] (Fig. 2b). Backscatter values for CRT are similar to rough pahoehoe while the bright outflow deposits at Carson have similarities to terrestrial A'a. In comparison, the dark lava flows, dark diffuse deposit, regional plains units, and some of the bright deposits have scattering behaviors similar to, or are smoother than pahoehoe flows.

Conclusions. Examination of the scattering characteristics of units mapped in the Carson Quadrangle show that a wide range of surface roughness is present, reflecting the style of lava emplacement or is related to surface modification. Comparisons to units mapped from Arecibo data show that lava flows and tectonic units are similar to landforms identified elsewhere on the planet. Backscatter information for individual units provides a basis to better characterize geology from radar data. The results presented here represent a small part of the area being studied. Continuing analysis is focusing on comparisons to other terrestrial lava flows along with incorporating other radar property data (i.e. reflectivity, rms slope, and emissivity information).

References. [1] Greeley *et al.*, *LPSC XXV*, this volume, 1994. [2] Campbell, B. A. and D. B. Campbell, *JGR.*, 97, 16293-16314, 1992. [3] Ford, P. G. and D. A. Senske, *GRL*, 17, 1361-1364, 1990. [4] Ulaby, *et al.*, *Microwave Remote Sensing*, vol 2, 1982.

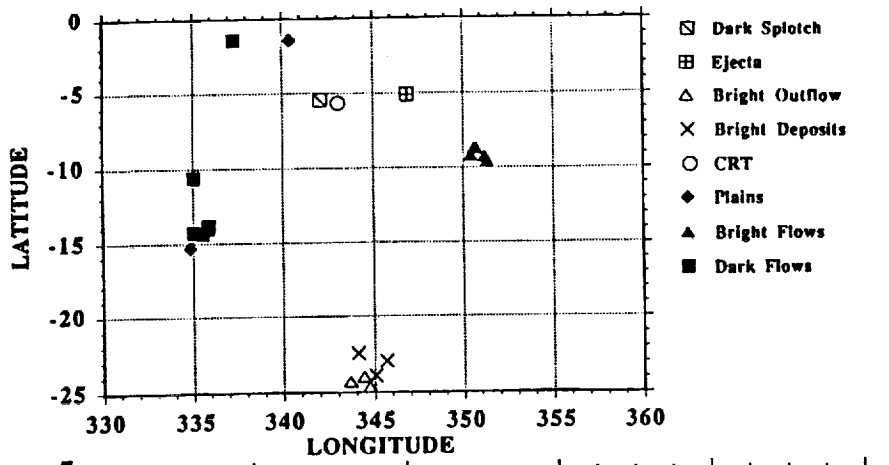

Fig. 1 Map showing the location of areas in which backscatter cross section has been extracted and plotted in Fig. 2.

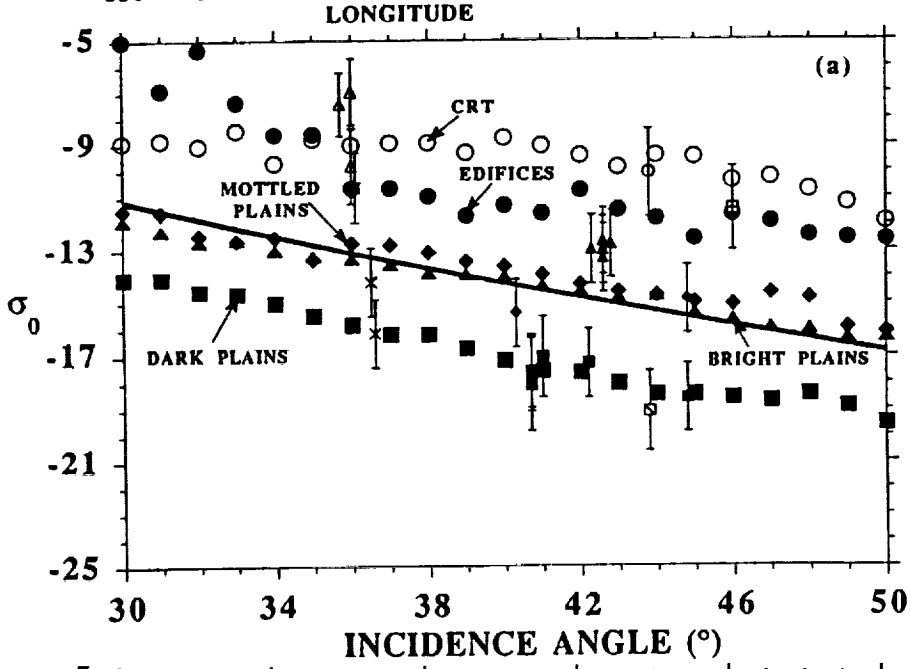

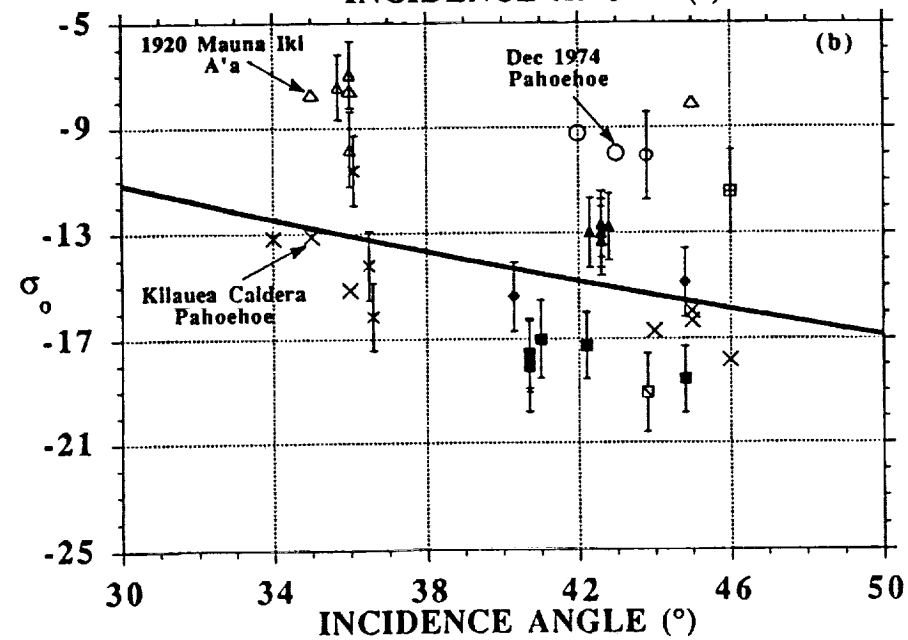

Fig. 2 (a) Comparison of backscatter cross section for several areas in the Carson Quad with units mapped from Arecibo data [3]. (b) Comparison of units mapped on Venus with Terrestrial lava flows. The terrestrial data is from Campbell and Campbell [2]. In both plots, the average scattering curve for Venus is indicated by the solid line.

THE GLOBAL GEOLOGY OF VENUS: CLASSIFICATION OF LANDFORMS AND GEOLOGIC HISTORY. D. A. Senske, R. S. Saunders, E. R. Stofan, and Members of the Magellan Science Team, Jet Propulsion Laboratory, California Institute of Technology, Pasadena, CA 91109.

Introduction. The Magellan Mission to Venus successfully imaged 98% of the surface of the planet at a resolution of 120 to 300 m [1]. To better understand the distribution of landforms and identify general stratigraphic relations, a geologic map (Fig. 1) is produced from a global image (scale of 1: 50,000,000).

Unit Classification. Global-scale geologic mapping of Venus has been carried out previously by several investigators [2,3,4]. These studies defined units on the basis of variations in radar backscatter, surface textures, topography, and morphology. Unit classification in this survey uses much of this criteria along with superposition and cross cutting relations to preserve as much stratigraphic information as possible. General age relations are identified, but in cases where units do not touch each other the stratigraphy is not always clear. Since the Magellan viewing geometry varied as a function of latitude during each of its three mapping cycles [1,5] care must be taken when identifying units at different latitudes.

Sixteen units are identified along with a variety of structural features. The most abundant units, plains, correspond to low land areas that cover in excess of 75% of the surface of the planet. Six classes of plains are mapped and distinguished stratigraphically as: (1) *lineated plains*, areas of moderate, homogeneous, radar brightness containing abundant fractures that in some places form a gridded or orthogonal pattern. (2) *Reticulate plains*, areas of intermediate, homogeneous, radar brightness that typically contain abundant, low, sinuous ridges. (3) *Dark plains*, localized areas of homogeneous, radar-dark, material found mainly adjacent to ridge belts and interpreted to be smooth pahoehoe-like lava flows. (4) *Bright plains*, areas of homogeneous, radar-bright, material typically found adjacent to fracture belts and interpreted to be associated with lava flooding related to extension and rifting. (5) *Mottled plains*, extensive areas of radar-bright and dark material found in the region bound by Atla Regio to the west, Themis Regio to the south, and Beta Regio to the north and east. The mottled texture is due to the presence of abundant small shields (diameters of several to 10's of km) and their associated deposits. (6) *Digitate plains* (lava flow fields), concentrations of radar-bright and dark deposits, arrayed in digitate patterns and generally associated with coronae. Centers of constructional volcanism include large edifices and shield/dome fields. Features mapped as *volcanic edifices* are isolated, circular to oval, areas of radar-bright and dark material that form a radial, digitate, pattern centered on a topographic rise. The largest concentration of these shields is found in an area bound by Beta, Atla, and Themis Regiones [6]. *Shield/dome fields* are isolated concentrations, 100's of km across, of small (several to 10's of km in diameter) shields and domes and their associated deposits.

Geomorphic units, defined by assemblages of structural features, include: (1) *complex ridged terrain* (CRT or tesserae), localized elevated areas made up of ridges and fractures with multiple directions of deformation [7]. (2) *Ridged and fractured terrain*, localized areas 100's of km across contain closely spaced fractures or ridges and are often associated with coronae. This unit differs from CRT in that there is a single, dominate, direction of deformation. (3) *Ridge belts* (including a sub unit of *mountain belts*) are distinguished by linear, elevated, zones of parallel to anastomsing ridges arrayed in belts 10's to 100's of km wide and 100's of km long. Like the ridge belts, mountain belts, located exclusively in Ishtar Terra, are collections parallel ridges forming boundaries with CRT. Unlike the ridge belts, the mountain belts typically have high values of Fresnel reflectivity. (4) *Fracture belts* are dense collections of parallel lineaments/fractures forming belts 10's to 100's of km wide and 1000's of km long. These zones, concentrated in the equatorial region and southern hemisphere, extend northeast from the south polar region, link up at Artemis with a belt that lies along the southern edge of Aphrodite and continues east toward Atla Regio where it splits to the northeast (Hecate Chasma) and to the southeast (Parga Chasma).

Deposits associated with impact events are identified as: (1) *crater material*, radar-bright (rough at the 12.6 cm radar wavelength) ejecta deposits. (2) *bright diffuse deposits* , made up of radar-bright material distributed asymmetrically about impact craters forming a "wispy" pattern. These deposits form gradational boundaries with adjacent units and are interpreted to be wind blown ejecta. (3) *dark diffuse areas* are radar-dark, parabola shaped, regions that typically open to the west and extend for 100's of km from an impact crater. These areas, including numerous dark "splotches", are sites where the surface has been smoothed by an impact event.

Discussion and Conclusions. Stratigraphic relations indicate that the oldest units on Venus, lineated plains, CRT, and ridged/fractured terrain preserve early episodes of deformation. These units are typically embayed by regionally extensive reticulate plains. Due to the absence of identifiable individual flows the reticulate plains are interpreted to be associated with widespread lava flooding. Plains emplaced more recently include, bright, digitate, dark, and mottled plains and are linked to volcanism associated with individual vents, fractures, and coronae. Other features associated with recent volcanism are large edifices and shield/dome fields. In a number of areas, ridge belts and fracture belts deform older plains, corresponding to some of the most recent tectonic activity. The distribution of units on Venus is not uniform. The region bound by Atla, Themis, and Beta Regiones is dominated by fracture belts (corona chains), mottled plains, and volcanic edifices. Occurrences of CRT are relatively minor in this area and

is found primarily along the periphery of the Beta rise and at Phoebe Regio. In comparison, the area bound by Ishtar Terra to the north and Aphrodite to the south contains large concentrations of CRT, fractured plains, and reticulate plains, with few large volcanic edifices present. Like the north polar region where there is a large concentration of ridge belts (longitudes 180° to 240°), a second major ridge belt province is located near the south pole (180° to 270°, Helen Planitia and 0° to 330°, Lavinia Planitia). In addition, this part of the planet contains the greatest concentration of large lava flow fields (digitate plains). This area, and the Beta, Atla, Themis area contain some of the stratigraphically most recent lava deposits. In general, many of the youngest features on Venus are found along fractures belts (corona chains) in these regions.

References. [1] Saunders, R. S., *et al.*, *JGR*, 97, 13067-13090, 1992. [2] Sukhanov, A. L., *et al.*, *U.S.G.S. Misc. Inv., Map I-2059*, 1989. [3] Senske, D. A., *et al.*, *Earth, Moon and Planets*, 55, 163-214, 1991. [4] Senske, D. A., *et al.*, *Earth, Moon, and Planets*, 55, 97-161, 1991. [5] Tyler, L. G., *et al.*, *JGR.*, 97, 13115-13139, 1992. [6] Head, J. W., *et al.*, *JGR*, 97, 13153-13197, 1992. [7] Barsukov, V. L., *et al.*, *JGR*, 91, D378-D398, 1986.

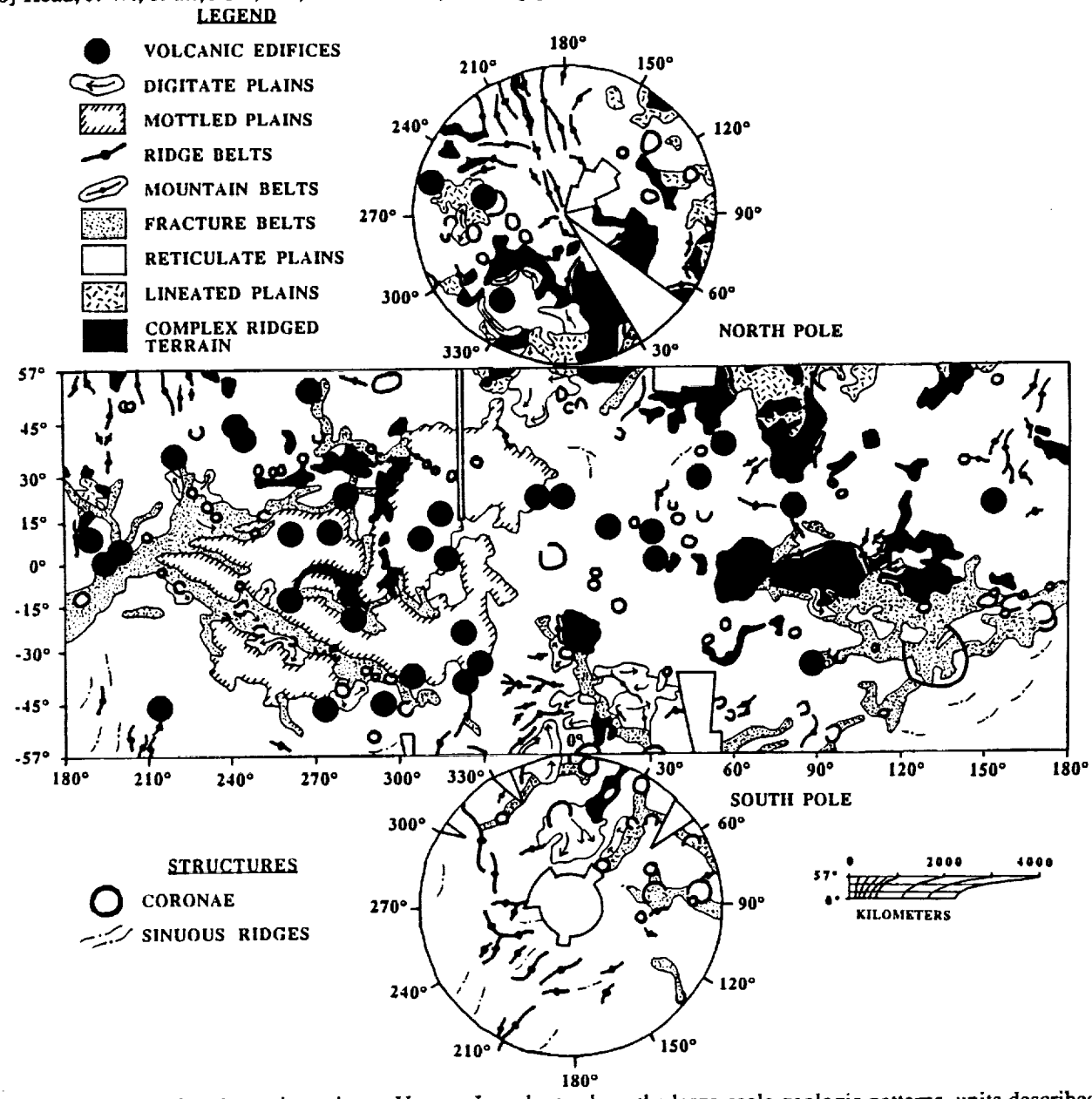

FIG. 1 Map showing the major units on Venus. In order to show the large-scale geologic patterns, units described in the text, but not shown on this map include: dark plains, bright plains, shield/dome fields, ridged and fractured terrain, crater material, bright diffuse deposits, and dark diffuse areas.

PYROLYSIS TYPING OF METEORITIC ORGANIC MATTER: M.A. Sephton, C.T. Pillinger and I. Gilmour, Planetary Sciences Unit, Dept. of Earth Sciences, The Open University, Milton Keynes, MK7 6AA.

The complex organic macromolecule that constitutes the bulk of the organic matter in CM chondrites is a heterogeneous material that contains evidence of both a solar nebula and pre-solar origin; the latter indicated by an enrichment in D [1, 2]. It is structurally composed of condensed aromatic, hetroaromatic and hydroaromatic ring systems and as such is similar to the more aromatic (so called type III) terrestrial kerogens [3, 4]. However, the polycyclic aromatic hydrocarbons solvent extractable from the meteorites are apparently not the precursors of the macromolecule as their isotopic compositions are relatively enriched in ^{13}C [5].

Various degradative methods have been used to study meteoritic macromolecular carbon [4, 6] including pyrolysis and chemical oxidation; on-line pyrolysis-gas chromatography-mass spectrometry (Py-GCMS) a technique long used for the chemical characterisation of terrestrial kerogens (eg.[7]; and refs therein) has not been used on meteorites to any extent. We have applied this latter technique combined with off line hydrous and anydrous pyrolysis in an attempt to characterise further the chemical structure of the macromolecule, to examine the effects of aqueous and thermal processing, to develop a method to produce fragment compounds suitable for isotopic analysis by isotope ratio monitoring-GCMS, and ultimately to provide a relatively quick means of comparison between the macromolecular material in primitive chondrites of different class.

Table 1. Relative abundances (%) of pyrolysis fragments.

Compound	Murchison Whole (W)	Murchison Residue (R)	Anhydrous Pyrolysis (A)	Hydrous Pyrolysis (H)
Naphthalene	41	33	31.5	27.5
Methyl-naphthalene	17	20	4	19
Phenol	5	7	4	21.5
Methyl-phenol	17	16	13	20
Benzaldehyde	17	18	27	0
Benzonitrile	3	6	16	12
Benzoic acid	0	0	4.5	0

A powdered, whole-rock sample of Murchison that had previously been solvent extracted [5] and a Murchison HF/HCl residue (also solvent extracted) were used for trial experiments. Anydrous pyrolysis was carried out at 310°C for 24 hours in pyrex vessels sealed under N_2 on samples of 200 mg of HF/HCl residue. Hydrous pyrolysis experiments were undertaken using a stainless steel high pressure bomb (Parr 4740, 71ml); samples of 200 mg of residue together with 30 ml of high purity water were loaded into the bomb in a pyrex tube, the bomb sealed under nitrogen, and heated at 310°C for 24 hours. Bulk meteorite and the residues resulting from the pyrolysis were pyrolysed on-line to a GCMS as dry pellets (typically 1mg) using a pyrojector at 500°C (S.G.E, Ltd); GCMS conditions were as in [5].

The major compounds released on pyrolysis are listed in Table 1 as are their relative abundances compared to that of the bulk untreated meteorite. Little difference was observed in the on-line 500°C pyrolysis of whole-rock meteorite compared with that of an unpyrolysed HF/HCl residue implying that the mineral matrix is having a negligible effect on the pyrolysis products.

Figure 1 shows the relative abundances of benzonitrile, phenol, benzaldehyde and naphthalene plotted on a ternary diagram. It is evident that hydrous pyrolysis results in a marked increase in the relative abundance of phenol presumably due to a partial hydroxylation of the macromolecule. Interestingly, thermal processing alone produces markedly different results with a relative increase in the abundance of both benzaldehyde and benzonitrile. Perhaps the most obvious bivariate indicator of thermal history is the benzaldehyde/phenol ratio which increases and decreases markedly when heated under anhydrous and hydrous conditions (5.7 and 0.9 respectively, compared to 3.5 when unheated). The increase in alkyl-naphthalenes together with a decrease in the abundance of alkyl phenols seen in the hydrously pyrolysed sample mirrors changes that have been observed during the diagenesis of bituminous coals [8]. The trivariate analysis (Fig. 1) illustrates the potential of the technique as samples with common thermal histories can be seen to group together. The success of this kind of molecular "typing" relies on the different thermal stabilities of the chosen compound's precursors and has been used successfully for many years on terrestrial kerogens [7].

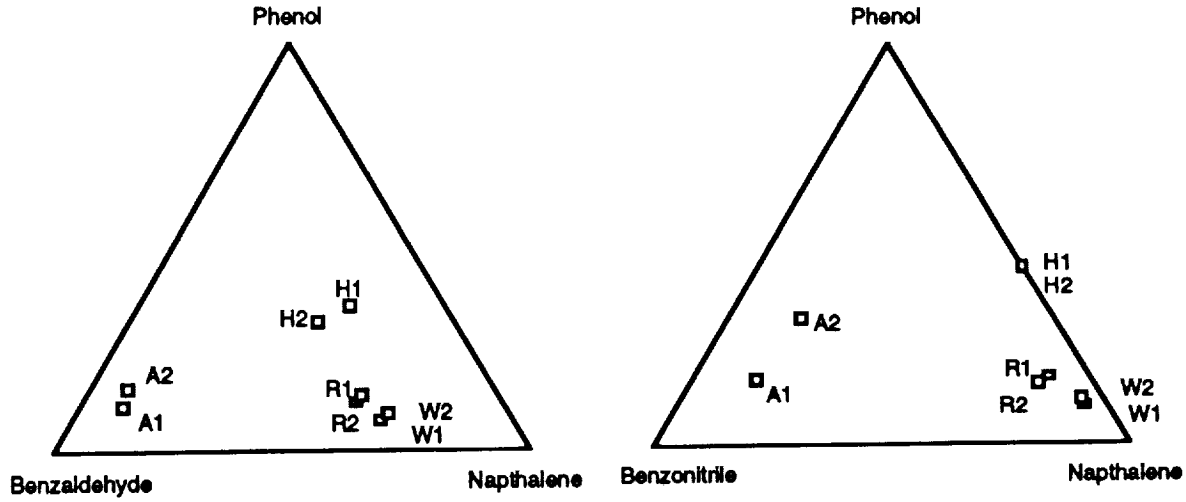

Fig1. Relative abundances from 500°C pyrograms. W1, W2: whole Murchison; R1, R2: Murchison residue; A1, A2: Anhydrously pyrloysed samples; H1, H2: Hydrous pyrolysis.

References

1. Kerridge, J.F. (1983) *Lunar Planet. Sci.*14, 365-366. 2. Kerridge, J.F. et al. (1987) *Geochim. Cosmochim. Acta* 51, 2527-2540. 3. Cronin, J.R.et al. (1987) *Geochim. Cosmochimi. Acta* 51, 299-303. 4. Hayatsu, R. et al. (1977) *Geochim. Cosmochim. Acta* 41, 1325-1339. 5. Gilmour, I. & Pillinger, C.T. (1994) *Mon. Not. R. Astron. Soc. In Press* 6. Bandurski, E.L. & Nagy, B. (1976) *Geochimi.Cosmochim. Acta* 40, 1397-1406. 7. Larter, S.R. (1984) in *Analytical methods and applications* (eds. Vorhees, K.) 212-275 (Butterworths, London). 8. Allan, J. & Larter, S.R. (1983)*Advances in Organic Geocgemistry* , 534-545 (Wiley, Chichester).

Student Explorer Demonstration Initiative: Affordable Access to Space

Jack Sevier and Paul Coleman, Universities Space Research Association

The high cost of access to space for science payloads, together with the long lead times from the inception of a project to when it is actually launched, preclude meaningful involvement of students and entry level professionals in a project from beginning to end. This is in contrast to the early days of space science when projects were less complicated and lead times were much shorter. It is also in contrast to the way university sounding rocket programs are done today. The Universities Space Research Association has long been endeavoring to find affordable means through which university investigators and their graduate students can have frequent access to space for their payloads and on a lead time that spans the typical graduate period. The Student Explorer Demonstration Initiative (STEDI) was conceived as a first step towards a new way of doing business for small payloads. The STEDI program will utilize surplus ballistic missiles from the U.S. stategic weapons inventory (which would otherwise be destroyed under the terms of the START treaty) as the launch vehicle,and will invite proposals for scientific payloads (including the spacecraft, instruments, data analyses, and everything else except for the launch vehicle and launch operations). Total mission costs are capped at $8 million, of which roughly half would go toward the launch vehicle and launch operations, with most of the remainder going to the cost associated with the payload. Using a modified three stage Minuteman missile, a payload of 350 lbs. can be placed in a 200 n.mile polar orbit. NASA Administrator Dan Goldin has agreed to place high priority on funding in the FY95 budget for three such missions ($24M). The schedule is to launch all three missions within two years of go-ahead and that the missions be completed within three years of go-ahead. Six candidates will be selected for a four month Phase I study, after which three of them will be selected for continued development.

Nebula matter differentiation as a result of condensation

A.I.Shapkin, Yu.I.Sidorov

Vernadsky Institute, Academy of Sciences of Russia,

117975, Kosygin street 19, Moscow, Russia

Nonisothermal condensation of nebula matter is considered in terms of a system **O-H-Si-Mg-Fe-Ca-Al-Ti-Ni-Na-K-C-S** [1] at $P=10^{-4}$ bar. It is assumed that only one refractory interstellar dust particle being a condensation nucleus is existing within the pre-assigned volume of the initial instant of time. The thermodynamic condensation model is based on two assumptions. Firstly, the cooling of nebular gas is rather fast (1K/1000 years); secondly, the diffusion layer volume at the surface of a condensing particle is substantially less in relation to the reaction volume of the bulk chemical system. Thus a condensed matter flux at the surface of a condensation nucleus is determined as a solid phase fraction of equilibrium heterogeneous assemblage which is being formed in a gaseous system exclusive of preceded condensed mass. Our model of condensation sequence as a result of condensation is differing from the models of [2-5] in a following point: we assume the evolutionary depletion of a gas fraction of the bulk chemical system in elements incorporated in the condensed matter.

The numerical experiments carried out in a framework of our model lead to the following conclusions: 1. If the concentration of refractory interstellar dust is evaluated as 10^{-14} g/cm^3 [6] appropriate to a given particle radius of 0.1 μm within 1 cm^3 parcel of nebular gas, the maximal radii of condensed matter particles should have been not above 1-3 μm ("*high temperature*" condensates,Fig.1). 2. We assume that at 1000 K the process of mononuclear condensation was changed by the multinuclear condensation at newly formed condensation nuclei. Thus the mononuclear condensation was ceased and new sort of particles were formed appropriate to the condensation sequence of nebular gas of given chemical composition. 3. Condensed particles are assumed to have a distinct phase zoning (Fig. 2). 4. Surface layer at the mononuclear condensation is assumed to have **forsterite-enstatite-iron-quartz** composition with **Fe** metal film. At the case of multinuclear condensation the appropriate particles are formed in the assemblage of **Fe** metal submicrone particles. 5. The surface of particle comprises a series of thin films consisting of **enstatite, quartz, Fe** metal, **Ni** metal, **rutile** etc. 6. The gaseous phase (below 800K) consists only of H_2O, **sulfur oxides, carbon oxides** and **metane. At** the successive cooling these phases could form separate particles and/or aggregates ("*low-temperature*" condensates). 7. Postcondensation evolution of nebula matter could be involved in convective, gravitational or electromagnetic separation of particles and correspondingly to the depletion or enrichment by "*high-temperature*" or "*low-temperature*" condensation.

Nebula matter differentiation...A.I.Shapkin, Yu.I.Sidorov

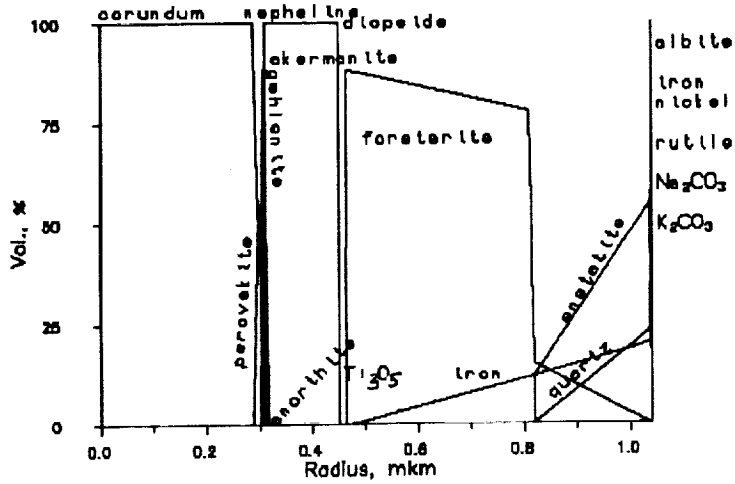

Fig. 1a

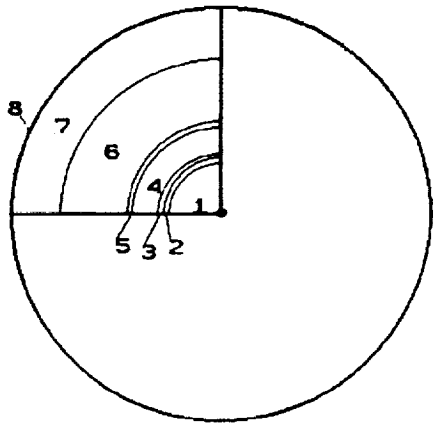

Fig.2

	Thickness, μm	Composition	Vol.,%
1.	< 0.28	corundum	100
2.	0.28-0.31	perovskite	30
		gehlenite	70
3.	0.31-0.32	nepheline	100
4.	0.32-0.46	akermanite	100
5.	0.46-0.48	diopside	100
6.	0.48-0.81	forsterite	85
		Fe, (Ti_3O_5, anorthite < 1%)	15
7.	0.81-1.0	enstatite	40
		Fe	15
		forsterite	10
		quartz	20
		albite, rutile	15
8.	surface	Fe, Ni, quartz, albite, rutile, Na_2CO_3, K_2CO_3	

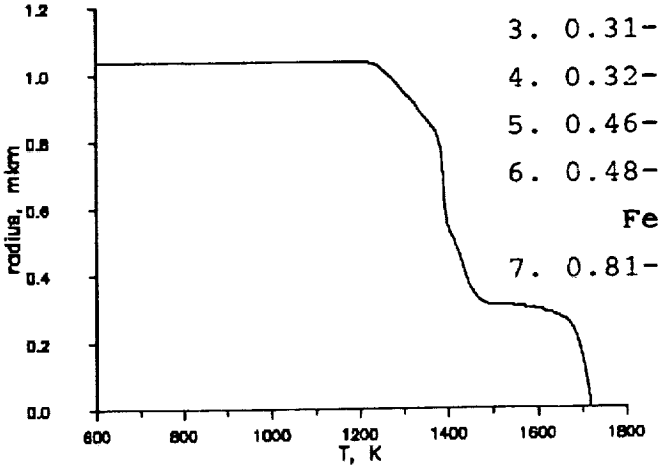

Fig.1b

References: 1.*Anders E., Grevasse N.*//Geochim. et cosmochim acta. 1989. V.53. P.197. 2.*Grossman L.*// Ibid. 1972. V.36. P.597. 3.*Saxena S.K., Ericsson G.*//Chemistry and Physics of Terrestrial Planets.N.Y. Springer=Verlag, 1986. P.30. 4.*Wood J.A., Hashimoto A.*//Geochim et cosmochim. acta. 1993. V.57. P.2377. 5.*Shapkin A.I., Sidorov Yu.I.*//Geokhimia. 1994. N2. (in Russia). 6.*Shklovsky I.S.* Stars. Its formation, existing and destruction. Moscow: Nauka, 1984. 383p. (in Russia).

THE PROBLEM OF HIGH PRECISION MEASUREMENTS OF $^{142}Nd/^{144}Nd$: THE TERRESTRIAL RECORD OF ^{146}Sm. M. Sharma[1], D. A. Papanastassiou[1], G. J. Wasserburg[1] and R. F. Dymek[2], [1]The Lunatic Asylum, Division of Geological and Planetary Sciences, Caltech, Pasadena, CA 91125. [2]Dept. of Earth and Planetary Sci., Washington University, St. Louis, MO 63130.

There is abundant evidence of the widespread occurrence of ^{146}Sm ($\bar{\tau}$ = 0.149 Æ) in the early solar system. This is established by correlated Sm/Nd and $^{142}Nd/^{144}Nd$ in meteorites [1-6]; the largest excess of ^{142}Nd (9.6 εu) is found in an opx separate from a mesosiderite with $f_{Sm/Nd}$ of 3.7 [6]. The initial $^{146}Sm/^{144}Sm$ ratio is 0.008 ± 0.001 at 4.56 Æ [cf 5-7]. It follows that if early (between 4.5 and 4.3 Æ) differentiation processes on the earth produced reservoirs with high $f_{Sm/Nd}$ and if samples were preserved it should be possible to see ^{142}Nd excesses. For example, for differentiation at 4.4 Æ, a reservoir with $f_{Sm/Nd}$ of +0.4 would yield about 36 μu excess in ^{142}Nd (μ = ((Rock/Standard)-1)*10^6); if the age of differentiation were 4.2 Æ this would yield a 9 μu excess in ^{142}Nd. Harper and Jacobsen [8-9] have reported a 33 ± 4 μu ^{142}Nd excess in a 3.8 Æ felsic gneiss (IE 715-28) from Isua, Greenland. This is relative to the Caltech Nd β Standard. If the above results could be substantiated they would indicate an early planetary differentiation with large $f_{Sm/Nd}$ and the existence of mechanisms that preserved these effects in a 3.8 Æ old rock. This interesting observation prompted other workers to search for ^{142}Nd excesses in other samples from early Archean terrains. But so far no evidence in support of this claim has been found [10-11]. We present results of $^{142}Nd/^{144}Nd$ measurements at Caltech with a F-MAT 262 multicollector mass spectrometer. This instrument is similar to that used by Harper and Jacobsen [9]. Results were obtained on two Isua samples, including the one analyzed by Harper and Jacobsen [8-9]. In order to resolve ~30 μu effects we need to measure $^{142}Nd/^{144}Nd$ ratios to about 10 μu (2σ) which is a factor of 3 below the manufacturer's specification for the instrument. Therefore, we have expended considerable effort in trying to identify key parameters that may improve the machine performance. We experimented with NdO^+ and Nd^+ beams and decided to obtain the data in static mode with Nd^+. The reliability of such a measurement depends on (1) high beam intensity to reduce the equivalent ion counting statistics and the effect of the electrometer feedback resistor noise, (2) reproducible effective cup efficiency, which may depend on ion beam focusing conditions in the source, (3) electrometer relative gains and (4) the detailed ion optical trajectories in the instrument. Equivalent ion counting statistics imply that a 2V ^{142}Nd beam with $10^{11}\Omega$ resistor (1.25 x 10^8 cps) integrated for 4 hours will yield 1.4 ppm uncertainty (2σ). For a 64 s integration, the noise of the $10^{11}\Omega$ resistor is 8 μV (2σ) corresponding to 4 ppm per measurement. An individual ratio corrected for fractionation would be expected to show a 10 ppm 2σ distribution with the mean of 100 ratios defined to 1 ppm. The F-MAT 262 employs $10^{11}\Omega$ resistors to measure the ion current. The outputs of the electrometer are digitized by voltage to frequency convertors (= 2000 counts/V); we have chosen a 64 s beam integration in order to reduce this V to F quantization uncertainty to ~4 ppm per measurement. *Collector Gains:* In a static measurement the amplifier gains on each of the collectors have to be precisely determined. The $^{142}Nd/^{144}Nd$ ratio corrected for instrumental mass fractionation depends upon the gain ratios of three Faraday detectors (F5 = ^{146}Nd, F7 = ^{144}Nd, F9 = ^{142}Nd). In Figure 1A we show the frequency distribution of a set of 100 gain measurements conducted over a period of 12 hours. Figure 1B shows the frequency distribution of 21 gain sets measured over one month (total number of data = 2600). The F9/F7 gain ratios vary more than for F5/F7. It appears that the grand means are well defined and that the distributions are not skewed. The uncertainties that may be propagated in $^{142}Nd/^{144}Nd$ due to the distribution of collector gains shown in 1B are examined in Figure 1C using each of the 21 data sets. Based on extensive tests we believe that the relative gains do not show a significant temporal drift. Therefore, we have chosen to use the grand average of the gains and to monitor that the relative gains do not drift. *Focusing and Ion Optics:* Ion beams near the optic axis of the instrument may be expected to provide repeat analyses to the desired level of reproducibility. In this hope, the ion source exit and magnet entry apertures were carefully aligned and fixed. Further, we investigated the effects of sample position and of the applied lens potentials in the ion source on the $^{142}Nd/^{144}Nd$ ratios. These experiments showed the need for a protocol which includes rigid control on the applied potentials in the X-Y and Z directions, along with several iterative steps for the filament position optimization using the ion beam intensity as the principal guide. Using the above protocol a series of Nd β Standards were run for the zero standard. In addition gravimetric standards were prepared with excesses in ^{142}Nd; analyses of the 30 μ standard were interleaved with the zero standard. The samples analyses were also interleaved with either the 0 or 30 μ standards. Typically the isotope fractionation is less than 1‰ per amu and within run precision of $^{142}Nd/^{144}Nd$ (100 to 150 ratios) is 6 ppm (2σ). Our results on samples and standards are presented in Figure 2 in a time sequence. It is known that a single mass spectrometer run under constant and optimum conditions yields an "internal" precision which is far better than the precision of repeat analyses, the so called "external" precision. While it is necessary to have excellent "internal" precision, the "external" precision defines our ability to resolve differences in isotope ratios between samples. Note that the 0 μ standards (Fig. 2) have a substantial spread with means ranging from -10 to +12 μ. Also, two successive analyses of standards can have substantial variation. These shifts do not appear to be related to smooth "drifts" in time. The external reproducibility of the 0 μ standard is 12 ppm (2σ) about two times the in run statistics (see Fig 3A). Similar behavior was found for the 30 μ standard (Fig 3B). It appears that the 30 μ difference is well resolved but that there is a broad distribution of these standards each with ± 12 ppm (2σ). Because of our concern regarding the validity of our focus protocol, we ran a 0 μ standard by optimizing the filament position only once and not iteratively and with some nominal change in X-Y focusing and found that this run gave 30 ± 5 μ value for the 0 μ standard (0A in Fig 2). After collecting this data we then optimized the ion beam with the same filament using our standard operating procedure (SOP) and carried out a set of measurements (0B) which gave -3 μ . The ion beam was then again optimized repeating our SOP and the filament run again (0C) yielding -2 μ. It would appear that

TERRESTRIAL RECORD OF ^{146}Sm: Sharma, M. et al.

departures from the strict but arbitrary optimization procedures caused large shifts. We then ran a 30 μ standard using SOP which gave 30 μ . A rock from Isua (ID 27-2A) was then measured again using SOP. No Ce or Sm interference was found in this or any other run reported below. This sample gave 48 ± 5 μ (1A Fig 2). Using the same filament the ion beam was again optimized using our SOP and yielded 47 ± 5 μ (1B Fig 2). A 0 μ standard was then analyzed which gave +4 ± 5 μ (SOP). We then analyzed a split of the sample (IE 715-28P; powder) used by Harper and Jacobsen [8-9]. Following SOP this gave 31 ± 6 μ . A 0 μ standard was then analyzed using SOP which gave +12 ± 5 μ . Following this we ran IE 715-28R, a piece of the parent rock of IE 715-28P. This gave us 26 ± 7 μ . To check the robustness of our running conditions we defocused the beam by re-initializing the focus settings and moving the filament; about 30 % of the ion beam was lost this way. Under these conditions the sample gave 54 ± 9 μ (3B Fig 2). This effect is similar to that noted above for a 0 μ standard. After collecting this data we re-focused the ion beam using our SOP and obtained 43 ± 7 μ. This comprises the summary of our most recent attempts to precisely measure the ^{142}Nd/^{144}Nd ratios to about 10 ppm level. Figure 3 is a histogram of the samples and standards run under established conditions. The conclusions that we can draw are (1) the 30 μu standard shows distinct separation from the 0 μu standard and is in agreement with gravimetry; (2) the Isua supracrustals appear to lie close to the 30 μ standard; and (3) changes in beam focusing can engender large shifts. There is a strong indication of ^{142}Nd excess in the two Isua rocks analyzed. This result would be a direct and independent confirmation of the claims made by the Harvard group. However, we consider the results to be still ambiguous given the present technical limitations. Further analyses of these and other early Archean rocks are justified. Unless the running conditions are rigidly controlled and shown to yield good reproducibility, substantial artifacts can and will creep in the data. Nevertheless, why a quartzo-feldspathic meta-sedimentary crustal rock with $f_{Sm/Nd} < 0$ should show ^{142}Nd excesses is not evident to us.

References: [1] Lugmair et al (1975) *Earth Planet Sci Lett* 27, 79-84. [2] Lugmair et al (1983) *Science* 222, 1015-1018. [3] Prinzhofer et al (1989) *Astrophys J* 344, L81-L84. [4] Prinzhofer et al (1992) *Geochim Cosmochim Acta* 56, 797-815. [5] Nyquist et al (1994) *Meteoritics*, in press. [6] Stewart et al (1993) Submitted to *Geochim Cosmochim Acta*. [7] Lugmair & Galer (1992) *Geochim Cosmochim Acta* 56, 1673-1694. [8] Harper & Jacobsen (1992) *Lunar Planet Sci* XXIII, 487-488. [9] Harper & Jacobsen (1992) *Nature* 360, 728-732. [10] Goldstein & Galer (1993) *EOS*. [11] McCulloch and Bennett (1993) *Lithos* 30, 237-255. Work supported by NASA (NAGW-3337). Division Contribution No. 5363 (837).

Figure 1

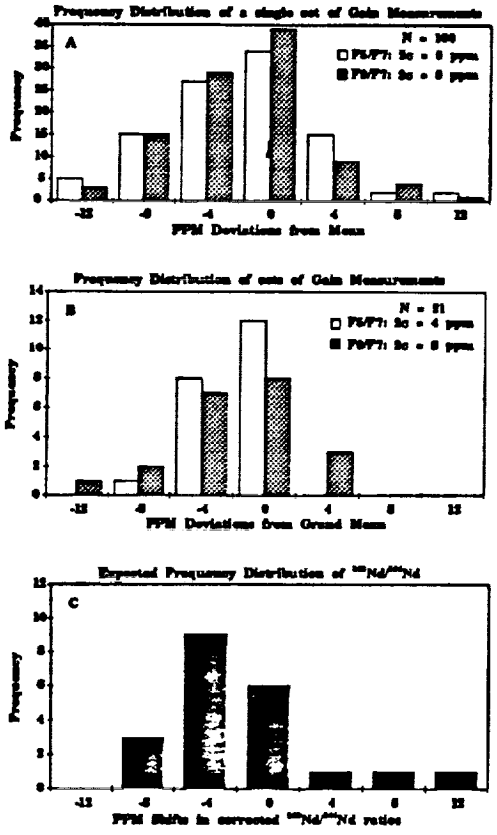

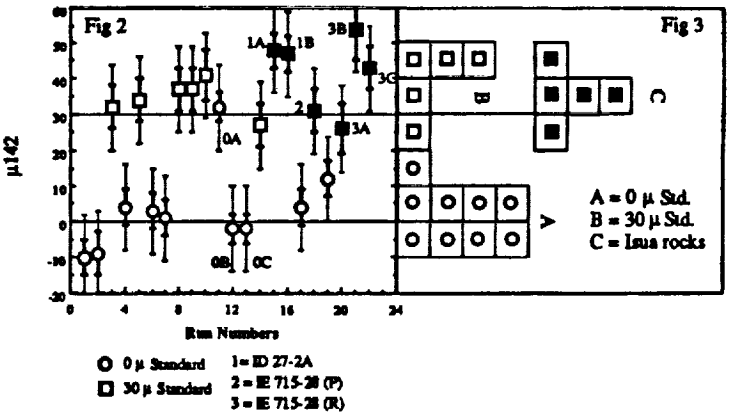

CONSTRAINTS ON EXCAVATION AND MIXING DURING THE CHICXULUB IMPACT EVENT; Virgil L. Sharpton[1], Luis E. Marín[2], Benjamin C. Schuraytz[1]; Paul D. Spudis[1], and Graham Ryder[1], [1]*LPI, 3600 Bay Area Blvd, Houston, TX 77058 (713-486-2111);* [2]*Instituto de Geofisica, UNAM, Mexico City, Mexico 04510*

The only direct information on crater excavation depth (d_e) comes from estimating the amount of uplift on the central structures of complex craters formed in sedimentary rocks on Earth. Structural uplift (SU), as a proxy to d_e, has been estimated for 13 craters ranging in final crater diameter (D) between 3 and 25 km, and a power law fit to these data indicate that $SU = 0.06D^{1.1}$[1]. Although this is approximately the mean trend, and therefore preferred, there are substantial problems with extrapolating this trend to large basins. To estimate d_e at D=300 km, for example, would require extrapolating the trend over more than 10 times the total diameter range of the observations. Furthermore, analysis of the input data (Figure 1) shows considerable variability in SU over small D increments, *e.g.*, two D=24 km craters, Strangways and Ries, differ in estimated SU by 50%. This may be related to difficulties both in estimating SU and D for these heavily modified craters. But such scatter could also reflect real variations in SU at a given diameter. In either case, uncertainties of at least ±0.3 SU are probable. Because no single trend can account for all the measurements in the data set, a range of power law fits to these data are equally appropriate; *i.e.*,

$$SU = 0.07(^{+0.09}_{-0.03})D^{1.0(^{-0.1}_{+0.3})}.$$

This imparts substantial uncertainties to d_e measurements, particularly for large-basin-scale events of planetary significance. For example, the excavation depth of a 300 km basin conceivably could vary between 10 km and 100 km based on the SU data set. Clearly it would be useful to have an independent estimate of excavation depth for much larger impact basins to test the relationship from the smaller craters of [1].

Breccias and melt rocks produced during impact contain information on their depth of origin and if the target stratigraphy can be constrained, excavation depth can be estimated from the proportions of each protolith required to form the breccia or melt. For the D=180-300 km [2,3] Chicxulub structure, target stratigraphy is constrained by drill cores to a depth of ~3 km [4]. Seismic refraction studies and geophysical modeling [*e.g.*, 5] provide additional information on the depths to lower crust and mantle (Figure 1). Figure 2 shows feldspar compositions in lithic clasts from Chicxulub breccia samples. These feldspars are similar to those from the KT sections of the western U.S. [6] and indicate a granitic protolith. No indications of mantle lithologies or gabbroic clasts have been detected to date. Clasts with granulitic textures are present but rare; nonetheless, these clasts may indicate a minor component of lower crustal origin. Consequently, we have so far found no evidence that the impact event excavated mantle or substantial quantities of lower crust. This places a maximum constraint on d_e of ~25 km.

Major element chemistry [*e.g.*, 2,3] and isotope analysis [7] demonstrates that the ejected glasses found in KT outcrops in Haiti and the Chicxulub melt rocks are identical. Multiple linear regression analysis on major oxides of Chicxulub melt rocks and breccia clasts indicate that the melt rock is composed of $\geq$90% granite and $\leq$10% platform sediments. This is in close agreement with isotopic studies [7] that indicate both the Chicxulub melt rocks and Haitian glass spherules could be formed by a mixture of ~94% silicate basement and ~6% platform carbonate rocks. Given an

average pre-impact thickness of ~2 km for the platform cover in this region [8], and allowing for vaporization of carbonates near the impact point, silicate basement would have to be melted to a minimum depth of 15 to 20 km to provide these proportions. This provides the additional constraint that $d_e \gtrsim 15$ km.

Figure 1

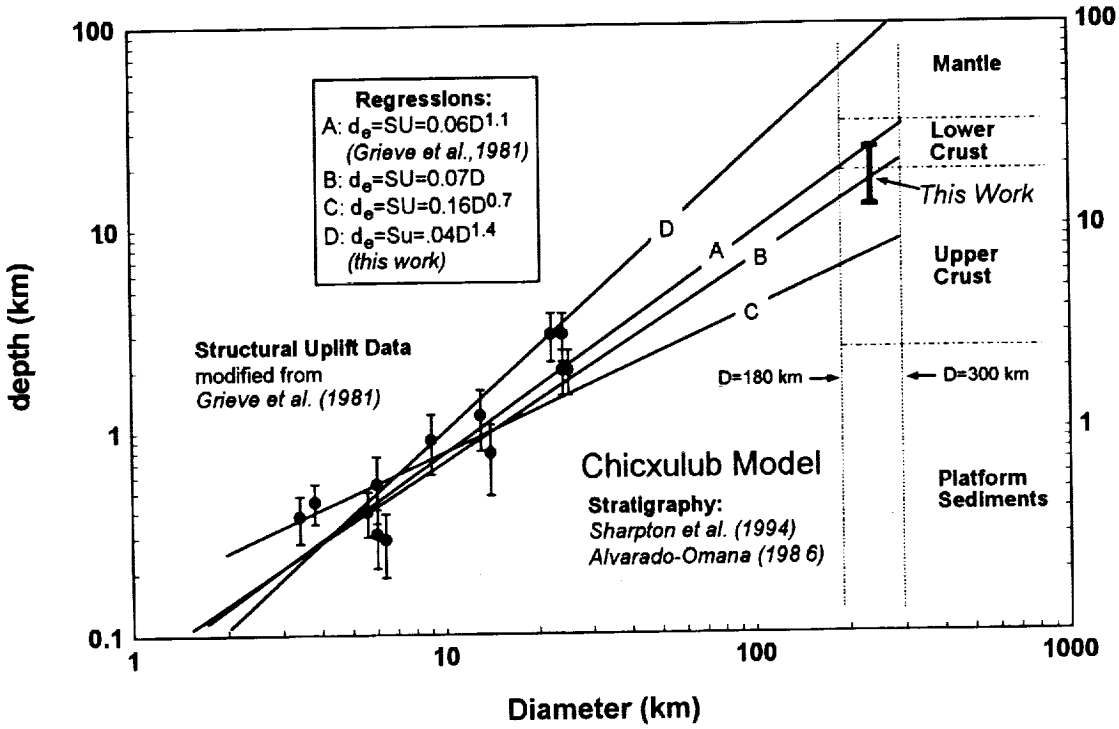

Conclusions. The current constraints on d_e (15-25 km) of the Chicxulub impact basin are in good agreement with the estimate provided by the SU data of [1], suggesting that the relationship derived from the small terrestrial craters, $SU \simeq 0.07D$, is valid to diameters of at least a few hundred kilometers. With additional evaluation of Chicxulub samples and better stratigraphic constraints it may be possible to improve on this information.

Figure 2

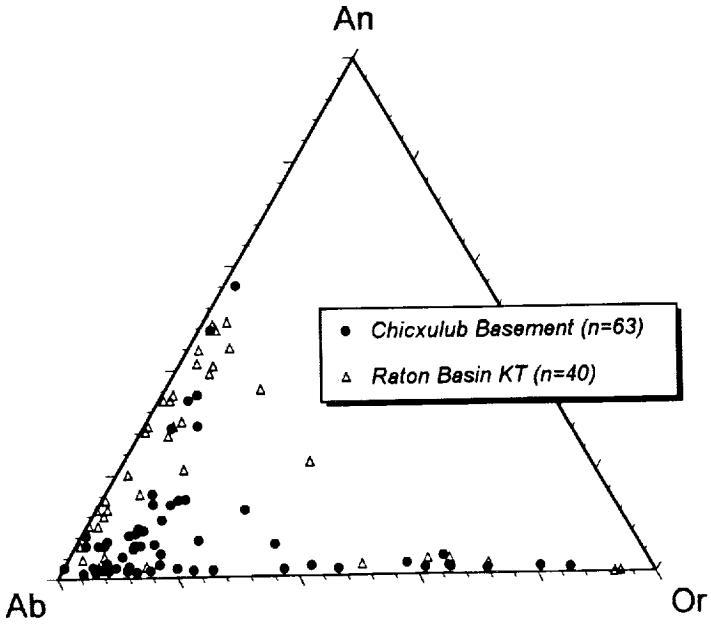

References: **[1]** Grieve, R.A.F. *et al.*, *Multi-ring Basins*, 19 (1981). **[2]** Hildebrand, A.R. *et al. Geology 19*, 867 (1991). **[3]** Sharpton, V.L. *et al. Nature 359*, 819 (1992). **[4]**Lopez-Ramos, E., *Geologia de Mexico*, UNAM (1979). **[5]** Alvarado-Omana, M.A., *M.S. Thesis*, U. Oregon (1986). **[6]** Sharpton, V.L. *et al., Geol. Soc. America Sp. Paper 247*, 349, (1990). **[7]** Blum, J.D. et al., *Nature 364*, 325 (1993). **[8]** Sharpton V.L. *et al.*, *Snowbird III abstract*, 1994.

LIGHT LITHOPHILE ELEMENTS (Li, Be, B) IN LUNAR PICRITIC GLASSES. IMPLICATIONS FOR LUNAR MANTLE DYNAMICS AND THE ORIGIN OF THE MOON. C. K. Shearer, G. D. Layne, and J. J. Papike. Institute of Meteoritics, Department of Earth and Planetary Sciences, University of New Mexico, Albuquerque, New Mexico, 87131-1126.

INTRODUCTION. Lunar picrites represented by high Mg volcanic glasses are thought to be products of either partial melting of the deep lunar mantle followed by rapid ascent [1,2] or polybaric partial melting initiated in the deep lunar mantle [3]. The near primary compositions of these volcanic glasses provide us with a unique perspective for evaluating basaltic magmatism, the characteristics and evolution of the lunar mantle and the origin of the moon. The light lithophile elements (Li, Be, B) in planetary materials have been used to estimate planetary compositions and evaluate magmatic processes. Based on the available Li and Be data, [4] calculated the primary proportion of Mg-silicates (non-refractory) and high temperature condensates (refractory) during the accretion of the Earth, Moon, and Eucrite Parent Body (EPB). Recent studies [5,6,7] of LLE in terrestrial basaltic systems have yielded several important insights into terrestrial mantle magmatism and LLE characteristics of the terrestrial mantle. In all cases cited, basalts analyzed were not of primary magma composition. Here, we present LLE data on the lunar picrites and offer insights based on their behavior.

ANALYTICAL TECHNIQUES. Ion microprobe analyses of the glasses were conducted using a Cameca 4f ion microprobe operated on the UNM campus by a UNM-Sandia National Laboratory consortium. Standards for Li, Be, and B in basaltic glass matrices were kindly provided by Dr. J. Ryan. Precision for Li is better than 1.0% and for Be and B it is better than 2.0%. Calibration curves (LLE/^{30}Si x wt% SiO_2 versus LLE concentration) were originally defined by a minimum of five standards for each element and are linear for the concentration ranges found in the picritic lunar glasses. Picritic glasses analyzed in this study were from the Apollo 11, 12, 14, 15, and 17 sites and were previously analyzed for major and selected trace elements by electron microprobe and ion microprobe. This suite of glass beads ranged in TiO_2 from 0.3 to 17 wt% and covers most of the groups defined by [1]. A total of 70 individual glass beads were analyzed for the LLE. In addition, core-rim analyses of individual glass beads were made.

RESULTS. The LLE show a wide range of variability with Li ranging from 1.2 to 23.8 ppm, Be ranging from .06 to 3.09 ppm, and B ranging from .11 to 3.87. B/Be ranges from 0.40 to 4.6. Li/Be ranges from 2.7 to 41.7 although 90% of the Li/Be values range from 14 to 30. Both B/Be and Li/Be values for the picritic glasses are less than chondrite. Be/Nd for the glasses ranges from .04 to .06 and are similar to that of chondrites (.058). Traverses across individual beads indicates that they are generally homogeneous with regards to LLE regardless of TiO2 content (Fig. 1 and 2). Beads that exhibited textural evidence for slower cooling (i.e. A17 Orange glass ⇒ A17 Black glass) generally show a increase in LLE from core to rim. Except for the A-17 VLT glasses and the A-15 Yellow glasses, the individual glass groups show limited variations in LLE characteristics. Even these anomalous glass groups plot in clusters with limited deviations from the cluster. At individual sampling sites, the LLE content is positively correlated to TiO_2. LLE concentrations also parallel the enrichment of other lithophile elements such as Ba, Zr, Sr, and REE. As noted by [2] for other trace element characteristics, glasses from each sampling site have similar LLE signatures. For example, the Apollo 14 glasses generally have higher LLE concentrations relative to glasses of similar TiO2 content from other sites. As shown in Figure 1 and 2, this LLE enrichment appears to fall along a mixing lines between LLE depleted glasses (i.e. A15 Green C) and KREEP. Also shown in Fig. 2, is that the high Ti glasses are displaced toward higher Li at similar B and Be relative to the very low Ti glasses.

DISCUSSION: The LLE data also support mantle inhomogeneity and cumulate overturn models suggested by previous studies [i.e. 2]. A KREEP component had been

incorporated into some of these picritic glasses. This is consistent with other trace elements [2] and probably reflects the recycling of KREEP and/or other late stage LMO cumulates into the deep lunar mantle. Other variability in associated glass groups (i.e. Apollo 15 Green glasses) suggest local mixing of cumulates may be responsible for LLE systematics. The relative enrichment in Li relative to B in the high TiO_2 glasses relative to the very low TiO_2 glasses (Figure 2) most likely reflects the bulk partition coefficients for the residuum. The picritic glasses are compositionally distinct from the crystalline mare basalts in LLE. Fractional crystallization or partial melting trajectories calculated using partition coefficients suggested by [5,6,7] indicate that they are not related by either of these processes. This suggests that they were derived from distinctly different mantle sources or at least have slightly different mantle components.

In their approach to estimate the bulk compositions of the earth and the moon, [4] suggested that the ratio of Li to Be is a direct measure of the ratio of the Mg-silicates to the high temperature condensates (HTC) in a planet. Based on the available Li and Be data, [4] calculated that the abundance of high temperature condensates during the planetary accretion of the Earth, Moon, and the EPB. The proportion of HTC was calculated to be 40% for the Moon, 22% for the Earth and 13% for the EPB. It is apparent that if Li/Be is to be used to estimate bulk moon composition, the picritic glasses provide a better estimate than the crystalline mare basalts. Differences in D for Li and Be indicate that fractional crystallization and partial melting will modify the Li/Be ratio. Estimates based on the picritic glasses imply a higher Li/Be from the bulk Moon than estimated from the mare basalts. This would indicate that the bulk Moon is less refractory than previously calculated by Li/Be.

FIGURE 1.

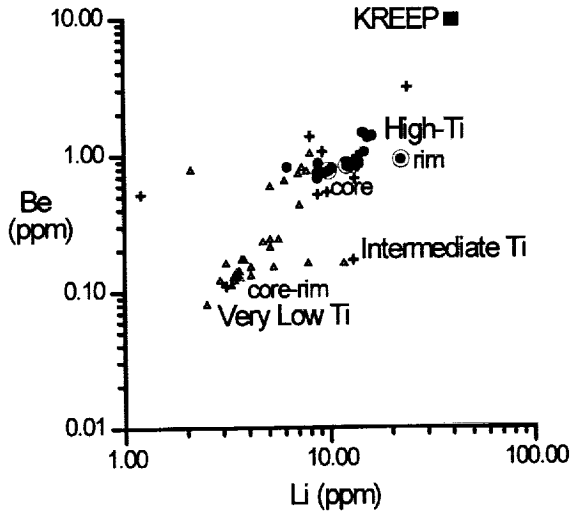

FIGURE 2.

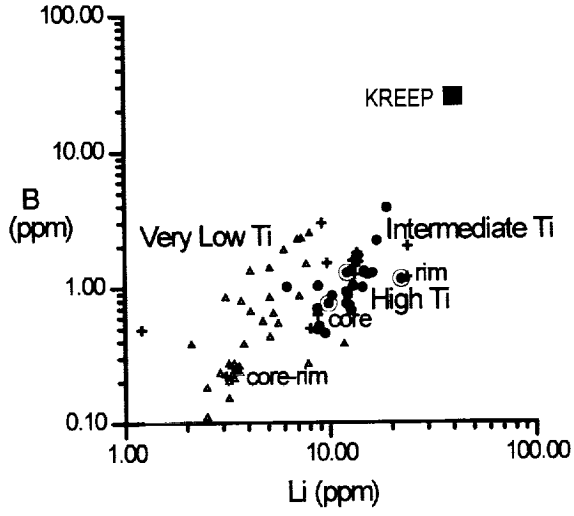

ACKNOWLEDGEMENTS: This research was funded by NASA Grant NAGW-3347 and the Institute of Meteoritics.

REFERENCES: [1] Delano, J. W. (1986) Proc. 16th LPSC, D201 - D213. [2] Shearer, C.K. and Papike, J.J. (1993) GCA, 57, 4785-4812. [3] Longhi, J. (1992) GCA, 56, 2235-2252. [4] Dreibus et al. (1976) Proc. 7th LSC, 3383-3396. [5] Ryan, J.G. and Langmuir, C.H. (1987) GCA, 51, 1727-1741. [6] Ryan, J.G. and Langmuir, C.H. (1988) GCA, 52, 237-244. [7] Ryan, J.G. and Langmuir, C.H. (1993) GCA, 57, 1489-1498.

THE EARTH-MOON CONNECTION. CLUES PRESERVED IN LUNAR PICRITIC MAGMAS.
C.K. Shearer, J. J. Papike, and Newsom, H. E. Institute of Meteoritics, Department of Earth and Planetary Sciences, University of New Mexico, Albuquerque, New Mexico, 87131-1126.

INTRODUCTION. Numerous models have been proposed concerning the origin of the Moon and its relationship to the Earth [1,2,3,4,5]. Recent models suggest that theMoon was probably formed as a result of collisions between the proto-Earth and bodies up to 10% of its mass during the last stages of planetary accretion [2,3,4,5]. Available data from the lunar highlands and mare basalts define some similarities and dissimilarities between the early Earth and the Moon, but the isotopic and chemical relationships between the lunar mantle and that of the Earth remain clouded. It appears that primary lunar magmas (largely represented by lunar volcanic glass beads) produced in the deep lunar mantle may provide addition information concerning this connection.

PICRITIC MAGMAS.

Primary Composition and Depth of Origin. The high Mg# values of the picritic magmas relative to mare basalts [6, 7] make them the best candidates for approximations of primary melts. This is also confirmed by their relative position on major element liquid lines of descent and their trace element characteristics (i.e. higher Ni). High pressure experiments may be interpreted as indicating that the picritic magmas were generated at a depth greater than most mare basalts and that the wide compositional range of picritic glasses were generated at similar depths (400 to 1000 km).

Relationship to Mare Basalts. Major and trace element and isotopic signatures suggest than the picritic magmas, represented by the glass beads, are not parental to the mare basalts. [7,8]. This evidence includes chemical differences in liquid lines of descent, trace element characteristics, isotopic signatures, depths of multiple saturation, and mode of eruption. These data may be interpreted as indicating that the picritic glasses are derived from a mantle source different from the mare basalts. More likely, the source for the picritic glasses represent a "mixture" of lunar magma ocean (LMO) cumulates and a more fertile (less refractory, more-volatile rich) mantle. This "mixture" of components may be a result of mantle overturning [7] or polybaric melting [9].

Light Lithophile Elements. In their approach to estimate the bulk compositions of theEarth, Moon, and Eucrite Parent Body (EPB), [10] suggested that the ratio of Li to Be is a direct measure of the ratio of the Mg-silicates to the high temperature condensates (HTC) in a planet. Based on the available Li and Be data, [10] calculated that the proportion of high temperature condensates during the planetary accretion was 40% for the Moon, 22% for the Earth and 13% for the EPB. It is apparent that if Li/Be is to be used to estimate bulk moon composition, the picritic glasses provide a better estimate than the crystalline mare basalts. Differences in $D^{olivine}$ for Li and Be indicate that fractional crystallization and partial melting will modify the Li/Be ratio. Alternatively, the picritic glasses provide an estimate of a different portion of the Moon. Estimates based on the picritic glasses imply a higher Li/Be for the bulk Moon than estimated from the mare basalts. This indicates that the bulk Moon is less refractory than previously calculated by Li/Be.

Volatile Element Characteristics. The nature of the eruptive mechanism (volatile driven fire-fountaining) for the picritic glasses, the presence of volatile coatings, and enrichment of some volatile elements in the glass beads relative to the crystalline mare basalts is circumstantial evidence that suggests that the source for the picritic glasses was enriched in volatiles relative to the sources for the crystalline mare basalts. This conclusion based on this data alone, is somewhat compromised in that the extent of volatile loss during eruption of the lunar basalts is not known. Other lines of evidence for the volatile nature of the mantle source for the picritic glasses are the lower $^{238}U/^{204}Pb$ and the relatively unfractionated ratios of volatile elements in volatile coatings [6].

Siderophile Element Characteristics. The picritic glasses have been used to constrain the composition of the lunar metallic core. The high Ni contents of the A15 and A17 Green Glasses, compared to the Mare Basalt source regions imply a Ni content for the lunar core of 38 wt% to 44 wt% [11]. This composition is very Ni-rich compared to chondritic metal, and the question still remains of how representative of the lunar mantle is the source of these glasses. Ringwood [12] argued that the high siderophile element abundances in the source regions of the lunar volcanic glasses implied that these regions did not experience a core formation event in the Moon at all, but were derived from the Earth's mantle. Additional tantalizing evidence is beginning to emerge suggesting that different reservoirs in the Moon have different siderophile element signatures. The abundance of Ge has been shown to be variable, with substantial enrichments in

Apollo 14 samples attributed to mobilization by a volatile phase [13]. Studies of lunar meteorites in comparison with the Apollo samples suggests, for example, that the high Ni content of the Apollo 16 regolith is not a general feature of the Moon's crust [14]. As pointed out many times by A.E. Ringwood, the difference in siderophile element abundances in the Earh's primitive mantle and the lunar mantle can provide critical constraints on the relationship between the Earth and Moon. However, additional data for refractory and volatile siderophile elements on a wide range of lunar materials , including picritic glasses, along with a geophysical determination of the size of the lunar core are needed to resolve this issue.

Isotopic Systematics. In comparison with the Earth (μ= 1 to 5), lunar highland and basalt samples have very high initial lead compositions requiring derivation from source regions with μ values ($^{238}U/^{204}Pb$) of greater than 100. In contrast, picritic glasses from the A-15 and A-17 sites require a source region with μ values of between 19 and 55. The high Ti and very low Ti glasses from these sites overlap. The $^{232}Th/^{238}U$ for these magmas ranges from 3.57 to 3.83 and are similar to that of the bulk silicate Earth ($\approx$ 3.9).

Comparison to Early Basaltic Magmatism on the Earth. There are a number of similarities and differences between terrestrial Archean komatiitic magmatism and lunar picritic magmatism. The mantle thermal regimes under which melting occurred to produce the near primary terrestrial mantle magmas (i.e. komatiites) and lunar picrities were vastly different. The komatiites are considered to be generated by high degrees of melting (greater than 30%) in a energetic thermal mantle system. In contrast, the lunar picritic magmas were probably produced by low degrees of partial melting (less than 10%) in a declining thermal environment. Mg# for the lunar picrites (48 to 70) are lower than their Archean terrestrial equivalents (greater than 75). The Al content of the lunar picrites is lower than modern picrites but similar to komatiites. In addition, komatiites and lunar picrites have similar Cr enrichments relative to modern terrestrial primitive magmas. In contrast to early terrestrial basaltic magmatism, the lunar picritic magmas have a much wider range in TiO_2, and incompatible elements (i.e. REE), have a characteristic Eu anomaly throughout this wide range, and are depleted in Ni. The very low Ti picritic glasses have Co, Sr, Ba, Cs, and Rb similar to the komatiites.

DISCUSSION. The picritic magmas represented by the high Mg glasses (there is another suite of picritic magmas that are parental to the mare basalts) have isotopic (i.e. $^{238}U/^{204}Pb$) and chemical characteristics (i.e. Li/Be, volatile elements) that contrasts with that of mare basalts. These differences may be attributed to partial melting in the LMO cumulate pile with the addition in the case of the picritic glasses of a less refractory mantle component. This component may have been incorporated into the mantle source through cumulate overturn or incorporated into the picritic magma through polybaric melting of a variety of mantle lithologies. The existence of a lower μ, less refractory, and more volatile-rich component in the lunar mantle presents some interesting alternatives to potential models for the origin and evolution of the early Moon. There are several intriguing possibilities for the origin of this lowμ mantle component. (1) It may reflect an early accretionary component derived from the proto-Earth through less energetic impacts that may have resulted in smaller degrees of volatile loss. The more dominant, higher μ, more refractory, volatile-depleted component of the lunar mantle is the result of more energetic impacts. (2) Alternatively, this component may reflect an early accretionary component derived from the proto-Earth that did not experience terrestrial core formation. Within the context of impact driven core formation models proposed by [5], small impacts into the proto-Earth may have resulted in not only smaller degree of volatile loss but also limited melting and impact related differentiation. In this scenario, the more dominant, higher μ component of the lunar mantle reflects material derived from massive impact driven volatilization, melting and core formation. (3) The high μ lunar component is derived through massive impact-volatilization of the proto-Earth followed by lunar core formation. The lower μ lunar component must have partially escaped both extensive volatilization and episodes of lunar core formation.

ACKNOWLEDGEMENTS. This research was funded by NASA Grant NAGW-3347 and the I.O.M.

REFERENCES. [1] Wood (1986) in *Origin of the Moon*, 17, [2] Cameron (1986) in *Origin of the Moon*, 609, [3] Newsom and Taylor (1989) *Nature 338*, 29, [4] O'Neill (1991) *GCA 55*, 1135, [5] Melosh and Tonks (1993) EOS, 74, 654, [6] Delano (1986) Proc. 16th LPSC, D201, [7] Shearer and Papike (1993) GCA 57, 4785, [8] Longhi (1987) Proc. 17th LPSC, E349, [9] Longhi (1992) GCA, 56, 2235, [10] Dreibus et al. (1976) Proc. 7th LSC, 3383, [11] Seifert et al. (1988) *GCA 52*, 603 [12] Ringwood (1992) *EPSL 111*, 537, [13] Dickinson et al. (1989) *Proc. 19th LPSC*, 189, [14] Warren et al. (1989) *EPSL 91*, 245.

5/1-25 ABS. ONLY
3077
P. 2

N94-35459

INNOVATIVE INSTRUMENTATION FOR MINERALOGICAL AND ELEMENTAL ANALYSES OF SOLID EXTRATERRESTRIAL SURFACES: THE BACKSCATTER MÖSSBAUER SPECTROMETER/X-RAY FLUORESCENCE ANALYZER (BaMS/XRF); T.D. Shelfer (NRC), R.V. Morris, Code SN4, NASA Johnson Space Center, Houston, TX, 77058, T. Nguyen, Lockheed Engineering and Sciences Co., Houston, 2400 Nasa Rd. 1, TX, 77058, D.G. Agresti, and E.L. Wills, Department of Physics, University of Alabama at Birmingham, Birmingham, AL, 35294.

SUMMARY. We have developed a four-detector research-grade backscatter Mössbauer spectrometer (BaMS) instrument with low resolution x-ray fluorescence analysis (XRF) capability. A flight-qualified instrument based on this design would be suitable for use on missions to the surfaces of solid solar-system objects (Moon, Mars, asteroids, etc.). Target specifications for the flight instrument are mass < 500 g, volume < 300 cm^3, and power < 2 W. The BaMS/XRF instrument would provide data on the oxidation state of iron and its distribution among iron-bearing mineralogies and elemental composition information. This data is a primary concern for the characterization of extraterrestrial surface materials.

INTRODUCTION AND BACKGROUND. A primary concern for future missions to solid planetary surfaces is the development of instrumentation for *in-situ* mineralogical and elemental analyses. Such analyses would provide the fundamental data required for the characterization and identification of surface materials and offer insights into their origins and subsequent modification processes. In terms of naturally occurring materials, the element iron is particularly important due to its abundance and multivalent nature (primarily 0, +2, +3 oxidation states).

Mössbauer spectroscopy is a nuclear resonance technique which provides detailed information about the local electromagnetic environment of individual ^{57}Fe nuclei. The resulting resonance pattern (Mössbauer spectrum) provides diagnostic information on the oxidation state of iron and its distribution among iron-bearing mineralogies, which tightly constrains the types of materials present. For remote use, backscatter geometry (Mössbauer source and detector(s) on same side of sample) is preferable over transmission geometry (Mössbauer source and detector on opposite sides of sample, commonly used in the laboratory) because no sample preparation is required. Backscatter geometry also allows energy-dispersive x-ray fluorescence elemental analysis to be performed simultaneously with the Mössbauer analysis requiring no additional hardware.

In 1988 we proposed and began an instrument development project designed to produce a flight-qualified combined backscatter Mössbauer spectrometer/x-ray fluorescence analyzer (BaMS/XRF) instrument [1]. Here we present our work on the BaMS/XRF project to date. A similar instrument development project is underway in Europe [2].

RESULTS AND DISCUSSION. This instrument development project has been divided into three distinct phases: 1) Design and construct a prototype two-detector brassboard BaMS/XRF instrument to demonstrate proof-of-concept. 2) Design and build a research-grade laboratory-quality four-detector instrument based on data gathered in phase one. 3) Develop a flight-qualified BaMS/XRF instrument suitable for use on upcoming lander missions. Last year we reported the results of our completion of the first phase of this project [3].

The second phase required research efforts in three main areas to make the step from brassboard to research-grade instruments. The first area of work was to optimize the detector preamplifier/shaping amplifier and the velocity transducer electronics to maximize the signal-to-noise ratio and velocity linearity of the instrument respectively. This step was accomplished through unique circuit designs, specially selected components, and carefully designed printed circuit board layouts.

The second area of research completed for phase two was the optimization of the Mössbauer source-collimator-sample-detector(s) geometry. This was a critical step in maximizing the signal-to-noise ratio of the instrument. An aluminum instrument chassis and graded collimator were designed and machined based on these considerations. A cross-sectional view of the phase two research-grade BaMS/XRF instrument design is shown in Figure 1.

The final area of research completed on the research-grade instrument was the development of a computer-based control and data storage unit. Due to wide availability and speed of software implementation using C/C++ programming, we are using a transputer (INMOS T805-20) for the heart of this unit. The transputer has been programmed to operate as a multichannel analyzer (MCA) with up to 16 separate detector input channels. Each detector channel has its own single channel analyzer (SCA) capable of multiple window settings. For a given input channel, two Mössbauer spectra and one pulse height analysis (PHA) spectrum will be stored in separate memory groups. The two Mössbauer spectra represent the data gathered from the 6.4 keV Fe x-ray SCA window and the 14.4 keV Mössbauer γ-ray window. Due to the different escape depths of these two energies, a limited amount of depth selective BaMS is possible, which should allow investigation of weathering rinds and other thin-coating phenomena. The PHA spectrum will contain the XRF data collected.

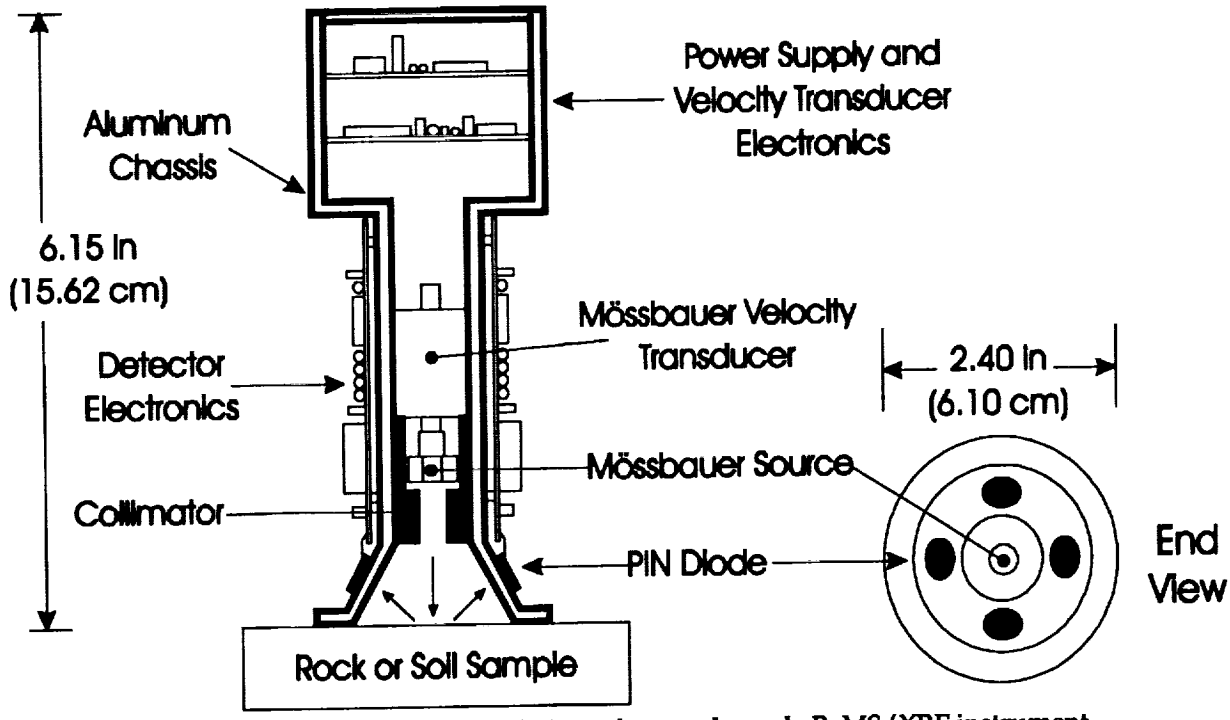

Figure 1. Cross-section and end view of research-grade BaMS/XRF instrument.

ACKNOWLEDGMENTS: This work was done while T.D. Shelfer held a National Research Council-NASA/JSC Research Associateship and support was provided by a grant from the NASA Planetary Instrument Definition and Development Program. We would also like to thank Jerry Sewell (Scientific instrument maker and machinist, Physics Dept., U.A.B.).

REFERENCES: [1] Morris R.V. et al. (Nov. 14-16, 1988) *SAAP Instr. Tech. Workshop*, Houston, TX. [2] Klingelhöfer G. et al. (1992) *Hyp. Int., 71*, 1449. [3] Shelfer T.D. et al. (1993) *Lunar Planet. Sci. XXIV*, 1291.

Omit 7J P-1289

A FERROELECTRIC MODEL FOR THE LOW EMISSIVITY HIGHLANDS ON VENUS;

Michael K. Shepard, Raymond E. Arvidson, Robert A. Brackett, and Bruce Fegley Jr., McDonnell Center for the Space Sciences, Washington University, St. Louis, MO, 63130

A model to explain the low emissivity venusian highlands is proposed utilizing the temperature dependent dielectric constant of ferroelectric minerals. Ferroelectric minerals are known to occur in alkaline and carbonatite rocks, both of which are believed to exist on Venus. Ferroelectric minerals possess extremely high dielectric constants (10^5) in a small range of temperatures and therefore require only minor (<<1%) abundances to explain the observed emissivities. The ferroelectric model simply explains: (1) the observed trends in emissivity with altitude, (2) the sharp transition back to normal emissivities at the highest elevations, (3) the variations in the critical elevation observed from region to region, and (4) emissivity polarization properties.

An interesting feature observed on Venus is the transition from areas of 'normal' emissivity (i.e., 0.8-0.9) and radar cross section at wavelengths of 12.6 cm over most of the planet to anomalously low emissivities (as low as 0.3-0.4) above a critical altitude, typically around 6054 km of planetary radius [1]. Because the temperature and pressure are functions only of altitude, one mechanism proposed for this observation is that pyrite (FeS_2) becomes thermodynamically stable at higher elevations [2,3] where, when incorporated in a rock matrix, it acts as a 'loaded dielectric' and raises the effective dielectric permittivity of the surface. One difficulty with this model is that the measured dielectric permittivity of pyrite is only ~10 [4] whereas the value at high altitudes on Venus is ~65. In addition, experimental studies show that pyrite rapidly decomposes under the entire range of venusian surface conditions [5]. An alternate proposal is that perovskite ($CaTiO_3$) is found only at high elevations on Venus where its destruction by reactions involving CO_2 and SO_2 is kinetically inhibited [6]. Perovskite has a dielectric constant of 170 at microwave frequencies and may be able to explain the observed low emissivities; however, a significant amount of perovskite is probably required. Additionally, the rates of perovskite destruction by CO_2 and SO_2 are currently unknown.

Textural changes have also been invoked to explain the low emissivities, including decimeter-scale voids interior to the surface which would mimic high dielectric permittivities via multiple scattering [1] or scattering from a matrix of igneous rocks in low loss soils [7]. However, no mechanisms have been proposed to explain why these textural changes occur with elevation. In part, textural changes (and the resulting volume scattering) have been proposed to explain the correlation between venusian topography and observed depolarized to polarized (LL/LR) backscatter ratios [7]. However, studies of terrestrial surfaces demonstrate that surface roughness can explain this correlation [8]. Furthermore, scattering theory implies that an increasing surface dielectric constant (with altitude) will also increase LL/LR ratios, independent of roughness [8].

Ferroelectric minerals are a subset of the piezoelectric minerals with permanent polarizations that can be reversed upon the application of an electric field, analogous to the behavior of ferromagnetic minerals. Also like ferromagnetic minerals, this behavior disappears above a certain critical temperature which is referred to as the Curie or transition temperature. The term ferroelectric is misleading in that these minerals are not metallic and the presence of iron is not common [9]. Below the Curie temperature, the dielectric permittivity of a ferroelectric is typically 10^2 - 10^3. At the Curie temperature, however, the dielectric permittivity sharply (often discontinuously) increases to values as high as 10^5 and then decays inversely proportional to the temperature. This behavior can be expressed with the Curie-Weiss equation:

$$\varepsilon_S = \frac{C}{T - T_C} \quad \text{for } T > T_C \qquad (1)$$

where ε_s is the dielectric permittivity of the ferroelectric, C is the Curie constant which is a function of the composition of the material, T is the temperature, and T_c is the Curie temperature [10]. Minerals which display ferroelectric behavior include many of the perovskites (although not pure $CaTiO_3$) and pyrochlores [11]. These minerals are of interest because perovskites and pyrochlores occur naturally in alkaline basalts and carbonatites, both of which have been proposed to exist on Venus [6,12].

We have developed a model utilizing ferroelectric minerals which can be directly compared to venusian observations of the distribution of emissivity with altitude. Several assumptions are made in the model: (1) ferroelectric minerals are ubiquitous (though this is not required), (2) ferroelectric minerals are present only in small concentrations (i.e. 0.1% - 1%), and (3) the Fresnel equations can be used to relate the surface dielectric constant to observed emissivities. We utilize the Polder - van Santen dielectric mixing model to calculate the effective dielectric constant of a basalt matrix (ε = 3-6) with small concentrations of ferroelectric inclusions (ε given by eq. 1) [13]. We

A FERROELECTRIC MODEL FOR THE HIGHLAND OF VENUS: Shepard M. K. et al.

find that concentrations of only 0.06-0.2% by volume are required to give an effective dielectric constant of 65, where the range represents tabular and acicular endmember mineral forms, respectively. Figure (1) shows model predictions (line) for emissivity as a function of temperature (and therefore altitude) plotted with Magellan emissivity (horizontal polarization) and elevation observations (small dots) over Ovda Regio. The scatter about the curve is due to uncertainties in altimetry measurements over rough topography, variations in ferroelectric abundance and T_c (caused by solid-solution compositional variations), and averaging over the large emissivity and altimetry footprints. Figure 1 also shows emissivity data (larger dots) over an area of Ovda Regio for which high resolution elevation data were obtained from a digital elevation model (DEM). The DEM was made using stereophotogrammetric analysis of Cycle 1 and 3 Magellan F-MIDR's (F05S098;1 and F05S099;301) [14]. The additional data points on Figure 1 show a sharp demarcation from low emissivity to normal emissivity in a narrow altitude range about 6056 km. This observation is consistent with the ferroelectric model in that the temperature at this elevation corresponds to the Curie temperature of the ferroelectric mineral. Regional variations in the critical elevation are caused by variations in the Curie temperature, which is known to vary with the solid-solution composition of the ferroelectric mineral [11].

The ferroelectric model can also explain the observed emissivity polarization properties. Figure 2 shows vertically polarized emissivity (EV) observations (small dots) from 6 orbits at longitudes of 93-98° and latitudes of 20° to -20°. EH data (coincident with EV data but not shown for clarity) were fit with the ferroelectric model (dashed-line). The EH model curve was then used to calculate expected EV behavior, assuming perfectly smooth surfaces and Fresnel reflection. The predicted EV model curve (solid-line) is quite close to the EV observations. If the surface was "perfectly rough" (i.e., Lambertian), EV observations would be identical to EH observations [15]. Thus, the proximity of the smooth surface EV model curve to the observations indicates that the ferroelectric model is viable and that emission is only weakly controlled by roughness.

To summarize, several observational features of the highlands are simply explained by a ferroelectric mineral model: (1) the observed trends of emissivity with elevation are due only to the change in temperature and not compositional or textural changes; (2) the sharp return to normal emissivity at the highest elevations observed in some regions (e.g, Maat, Sif, Ozza Mons; Ovda Regio) occurs where local temperature equals T_c and the ferroelectric behavior switches off; (3) regional variations in the critical altitude are due to slight compositional changes in the ferroelectric solid-solution phase which changes T_c; and (4) observations of horizontally and vertically polarized emissivity are consistent with a temperature (and therefore elevation) dependent surface dielectric constant and low to moderate surface roughness. Acknowledgements. We thank J. Alexopoulos and R. Phillips for providing the DEM.

Figure 1

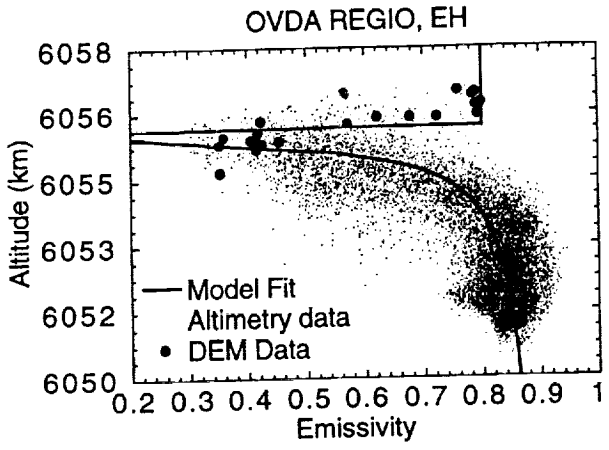

Figure 2

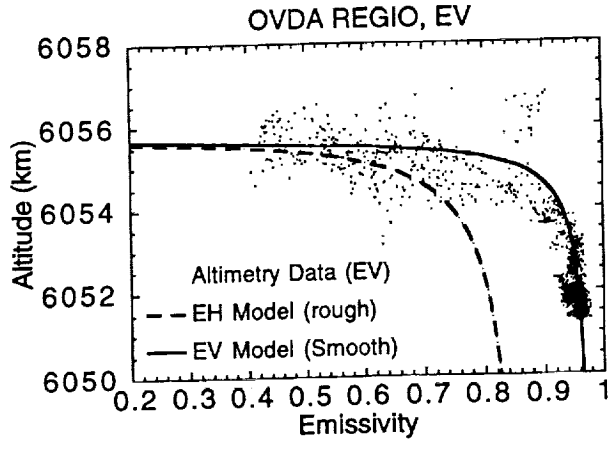

[1] Pettengill et al. (1992) JGR, 97, 13091. [2] Pettengill et al. (1988) JGR, 93, 14881. [3] Klose et al. (1992) JGR, 97, 16353. [4] Husk and Seehra (1978) Solid State Commun., 27,147. [5] Fegley et al. (1993) Bull. Amer. Ast. Soc., 25, 1094. [6] Fegley et al. (1992) Proc. LPSc, 22, p. 3. [7] Tryka and Muhleman (1992) JGR, 97, 13379. [8] Campbell and Campbell, (1992) JGR, 97, 16293. [9] Burfoot (1967) Ferroelectrics, Van Nostrand. [10] Rupprecht and Bell (1964) Phys. Rev. Lett., 135A, 748. [11] Lines and Glass, (1977) Principles and Applications of Ferroelectrics and Related Materials, Clarendon. [12] Kargel et al. (1991) LPSc XXII, p. 685. [13] Sihvola and Kong (1988) IEEE Trans. Geosc. Remote Sens., 26, 420. [14] Leberl et al. (1992) JGR, 97, 13675. [15] Ulaby et al. (1982) Microwave Remote Sensing, vol II, Addison-Wesley.

ION MICROPROBE STUDIES OF LUNAR HIGHLAND CUMULATE ROCKS: PRELIMINARY RESULTS; John W. Shervais, Department of Geological Sciences, University of South Carolina, Columbia, SC 29208.

Introduction: Deciphering the origin and evolution of the lunar highland crust is crucial to our understanding of the Moon's early magmatic history and, by inference, the early history of other terrestrial planets. This task is especially difficult in the western lunar highlands because of the small size of the highland rock clasts recovered from breccias, and because it is impossible to calculate parent magma compositions from whole rock chemical data on cumulate rocks. In this report I present preliminary data from a new effort to characterize the parent magmas of lunar cumulates through ion microprobe analyses of their cumulus phases.

The composition of cumulate plutonic rocks, such as those which comprise the lunar highlands, are a function of primocryst composition, the proportions of cumulate phases, and the proportion and composition of trapped melt. Subsequent reactions between the trapped melt and primocrysts can alter the compositions of both. The trapped melt may crystallize to form overgrowths on the primocrysts (causing its exclusion from the final rock, i.e., adcumulate growth) or lower temperature mineral assemblages which reflect continued cotectic crystallization (i.e., orthocumulate crystallization). Producing a chemical analysis which is representative of the bulk rock can be a challenge even with large terrestrial samples. When the samples are less than a centimeter in diameter and sample aliquots are 100 mg or less, the task is clearly impossible, even with relatively fine-grained basalt samples (e.g., [1,2]).

Another approach for characterizing the chemical composition of lunar cumulate parent magmas is to analyze the major and trace element composition of primary cumulus phases ("primocrysts") and to use equilibrium crystal/liquid partition coefficients to calculate possible parent magma compositions. This approach eliminates the need for "representative" bulk rock samples, and is even effective for texturally pristine samples which are known only in thin section.

Results: Four samples have been analyzed in reconnaissance: enstatite-bearing troctolite 14305 ,347 [3,4], diopside-bearing troctolite 14305 ,301 [5], alkali anorthosite 14305 ,303 [5], and enstatite-bearing troctolite 14321 ,1237 [6]. Analyses were performed on the UNM-SNL Cameca 4f SIMS ion microprobe, located at the University of New Mexico, under the supervision of Dr. Graham Layne. Because of the limited machine time available for this exploratory work, only two-three spots were analyzed on each sample for the REE, Sr, Zr, and Y. Phases analyzed include clinopyroxene, orthopyroxene, and plagioclase. Plagioclase standards were not available at the time, so only the pattern of LREE in plagioclase can be considered reliable. Orthopyroxene in sample 14321 ,1237 has extremely low concentrations of REE and produced a very unstable signal with high uncertainties. This sample was not used for equilibrium melt calculations.

Despite these problems, it is possible to make some preliminary observations with the data currently in hand. Melts in equilibrium with phases analyzed in the subsamples of 14305 were calculated using experimental and empirical partition coefficients for pyroxene and plagioclase [7-10]; chondrite-normalized magma compositions are shown in the figures below. Two samples are members of the magnesian suite (,301 and ,347). The parent magma of troctolite ,347 is slightly depleted in LREE (La/Yb = 0.6 x chondrite) with La concentrations around 100 x chondrite. The parent magma of troctolite ,301 is slightly enriched in LREE (La/Yb =

1.5-2.5 x chondrite) with La concentrations around 200-300 x chondrite. The highest REE concentrations in ,301 are indicated by the Cpx analysis; Opx and plagioclase both indicate lower overall REE, although the relative abundance patterns are remarkably consistent. Sample ,303 is an alkali anorthosite which contains REE-rich whitlockite [5] and post-cumulus Cpx. Warren et al [5] showed that if the whitlockites are cumulate, REE concentrations in the whitlockites imply a parent magma with around 2000 x chondrite La. Alternatively, they suggest that whitlockite could have formed from trapped liquid with La = 3300 x chondrite, based on mass balance considerations [5]. In contrast, the data presented here show that a calculated parent magma in equilibrium with the cumulus plagioclase is much lower in REE, with La roughly 450 x chondrite. Post-cumulus Cpx is in equilibrium with an LREE-depleted melt, suggesting it formed after post-cumulus crystallization of whitlockite.

The data presented here show that ion microprobe analyses of primary cumulus phases in lunar highland cumulates can be used to determine the composition and petrologic history of their parent magmas independently of bulk rock compositional data. Further, these data suggest that analyses of post-cumulus accessory phases which form from evolved trapped liquid do not result in accurate determinations of parent magma composition.

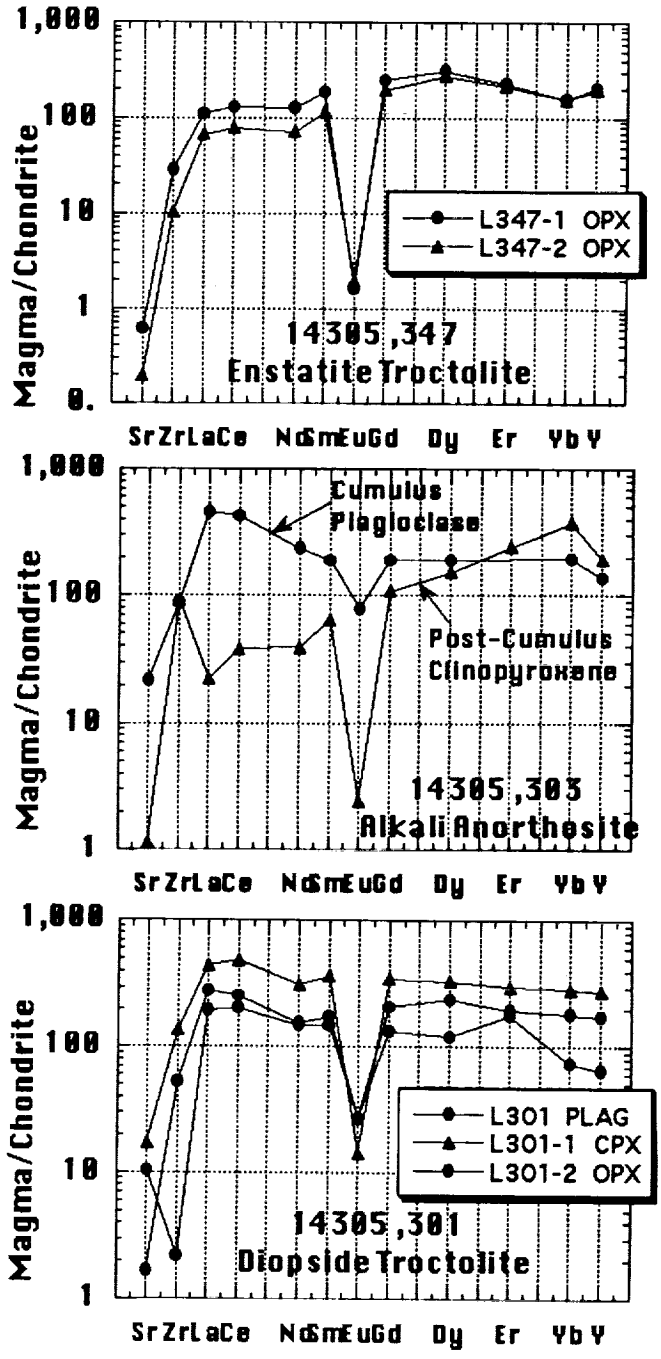

References: [1] Shervais et al, 1990, Proc. LPSC 20th, 109-126; [2] Shervais and Vetter, 1991, LPSC XXII, 1237-1238; [3] Shervais et al, 1983, Proc. 14th LPSC, JGR Supl. v88, B177-B192; [4] Shervais et al, 1984, Proc. 15th LPSC, JGR Supl. v89, C25-C40; [5] Warren et al, 1983, Proc. 14th LPSC, JGR Supl. v88, A615-A630; [6] Lindstrom et al, 1984, Proc. 15th LPSC, JGR Supl. v89, C41-C49; [7] Grutzeck et al, 1974, Geophys. Res. Lett., v1, 273-275; [8] McKay, 1982, LPS XIII, 493-494; [9] Phinney and Morrison, 1990, Geochim. Cosm. Acta, v54, 1639-1654; [10] Phinney, 1991, Proc. 21st LPSC, v21, 29-49.

REMOTE SENSING ASSESSMENT OF THE LUNAR SOIL MATURATION; V.V.Shevchenko, Sternberg State Astronomical Institute, Moscow University, Moscow 119899, Russia

The amount of fused glassy particles in the lunar soils is a direct index of the amount of micrometeorite reworking of surface layer and hence of soil maturity. The surface exposure (maturity) index as rate of agglutinates and glassy fragments in lunar soils was proposed by Florensky et al. [1]. The values of the maturity index I_m range between 0 (start of regolith forming) and 1.0 (saturation of regolith by reworked particles) units. Other quantitative index of surface maturity was proposed by Morris [2]. This maturity index I_f is the ratio of the value of the intensity in arbitrary units of the FMR resonance to the value of the FeO concentration. Comparison of the lunar samples data from [3] and [4] let us to construct the following equation showed correlation between I_m and I_f values (r = 0.971): $I_m = - 0.0139 + 0.0121 I_f$. The mean values of maturity indices for lunar samples from six Apollo landing sites were used (Fig. 1).

The increasing rate of fused glassy fragments in regolith leads to changing average value of refraction index of the surface layer substance. Therefore polarimetric and spectropolarimetric properties of the regolith must be varied by the reworking soil in course of time. On the base of known laboratory results and telescopic data it was found that spectropolarization ratio $r = P_{max}(B)/P_{max}(R)$ for blue and red spectral region could be used as remote sensing parameter of lunar soil maturity. It correlates with value of maturity index derived from morphological or ferromagnetic methods. Using lunar samples data for nine Apollo and Luna landing sites and spectropolarimetric telescopic data for these sites it was obtained correlation of the spectropolarimetric ratio $P_{max}(0.42\mu m)/P_{max}(0.64\mu m)$ from [5] with morphological index of the lunar soil maturity from [6]. This correlation is shown in Fig. 2. The least-squares method gives the following relationship for linear regression (r = - 0.932): $I_m = 2.401 - 1.111\ r$. Relationship based on the spectropolarimetric ratio $(0.42\mu m/0.70\mu m)$ has analogous form but the correlation is not so strong in this case (r = -0.883).

As it was expected, a strong correlation between maturity index I_m and exposure age **T** was found. Using 15 lunar samples data the dependence of the maturity index (values of I_m for 15 different lunar samples was taken out from [3, 7]) from exposure age (values of **T** for the same samples was taken out from [7- 11]) was obtained. The least-squares method gives the following equation: $I_m = 0.226 + 0.243 \ln T$, where **T** is in units of million years. The data are plotted in Fig. 3 (r = 0.938).

Table 1 lists the derived values of maturity index and exposure age for a number of lunar morphological features. Column of **D** lists the values of telescope diaphragm projection on the lunar surface (km) [5].

Table 1. Soil maturity and exposure age of lunar formation surfaces.

Formation name	I_m	T	D	Formation name	I_m	T	D
Reiner-gamma	0.273	7.8	6	Mare Serenitatis	0.789	65.2	14
Mare Fecunditatis	0.440	15.5	14	Reiner	0.859	84.4	6
Plinus	0.456	16.6	6	Gassendi	0.880	94.7	28
Proclus	0.524	21.9	6	Clavius	0.901	103.3	28
Aristarchus	0.549	24.3	6	Lansberg	0.914	109.2	6
Flamsteed	0.676	40.9	3	Arzachel	0.938	120.3	14
Mare Imbrium	0.760	57.8	14	Grimaldi	1.042	184.5	14

Table 1 lists both mare and highland formation data for different morphological type features. The most immature soil was found in area of a swirl like Reiner-gamma formation. According to classification of Morris [4] a such type of immature soil material includes not more than only 28% of agglutinates. The immature regolith ($I_m < 0.35$) is observed on the surface of mare bright rays and inside youngest bright craters. The submature soils ($0.35 < I_m < 0.70$) are associated with fresh dark mare material. The mature regolith ($I_m > 0.70$) is located within old mare and highland craters. When residence time of soil in the upper layer of regolith is equal 150 - 160 million years it is occurred the saturating soil by agglutinates (I_m is near 1.0).

REMOTE SENSING LUNAR SOIL MATURATION; V.V.Shevchenko,

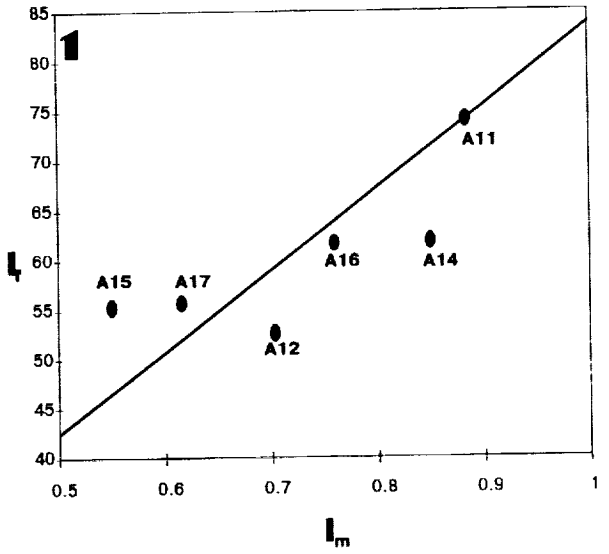

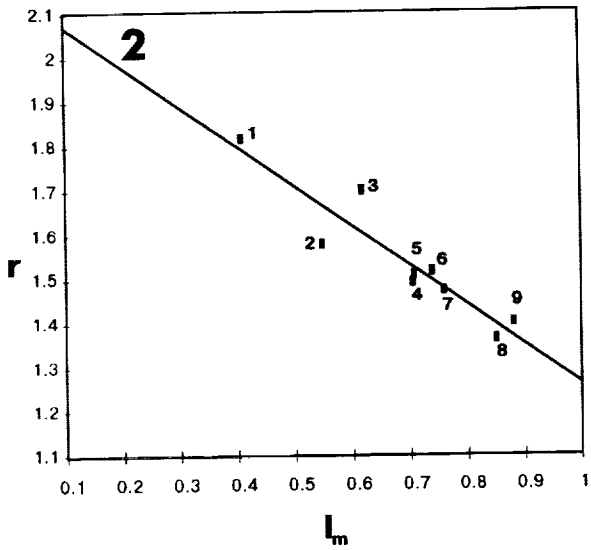

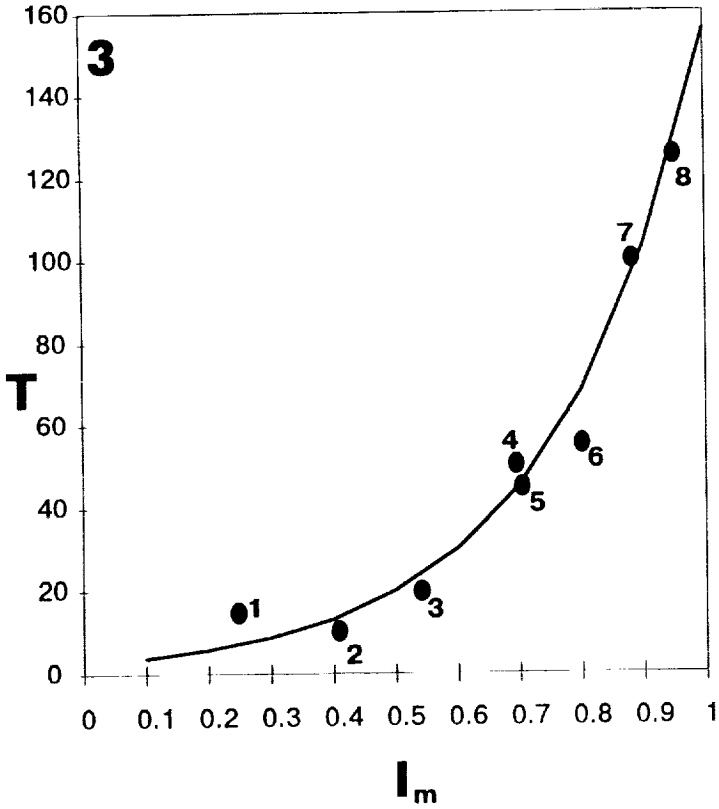

Figure 1. The correlation between morphological index of the lunar soil maturity I_m and magnetometric maturity index I_f. The points are average data for lunar samples from landing sites of Apollo-11, -14, -15, -16, 17, respectively. Values of I_m are taken out from [3], values of I_f are taken out from [4].

Figure 2. The correlation between morphological index of the lunar soil maturity I_m and spectropolarization ratio $r = P_{max}(0.42\mu m/0.64\mu m)$ The points are data for areas of the following spacecraft landing sites: 1 - Luna-20, 2 - Apollo-15, 3 - Apollo-17, 4 - Apollo-12, 5 - Luna-24, 6 - Luna-16, 7 - Apollo-16, 8 - Apollo-14, 9 - Apollo-11.

Figure 3. The correlation between maturity index I_m [3, 7] and exposure age T (10^6 yr) [7-11]. The points are lunar sample data: 1-12037(Apollo-12), 2 - 2001-2004(Luna-20), 3 - 74220, 74240, 74260 (Apollo-17), 4 - 67701(Apollo-16), 5 - 14141(Apollo-14), 6 - 67601(Apollo-16), 7 - 10010-10011(Apollo-11), 8 - 60009-60010(Apollo-16).

REFERENCES: [1] Florensky K.P. et al. (1974). *Lunar Soil from Mare Fecunditatis. Nauka Press*, 38-43. [2] Morris R.V.(1976). *Proc.Lunar Sci. Conf. 7th*, 315-335. [3] Stakheev Yu.I. (1979). *Soil from Lunar Highland. Nauka Press*, 77-82. [4] Morris R.V. (1978) *Proc. Lunar Planet. Sci. Conf. 9th*, 2287-2297. [5] Kvaratskhelia O.I. (1988). *Byull. Akad. Nauk. Gruz. SSR Abastumans. Astroph. Obs.*, No. 66, 159-168. [6] Stakheev Yu.I., Lavrukhina A.K. (1979). *Soil from Lunar Hihgland. Nauka Press*, 74-76. [7] Kashkarov L.L. et al. (1979). *Soil from Lunar Highland. Nauka Press*, 659-663. [8] Poupeau G. et al (1980). *Lunar Soil from Mare Crisium. Nauka Press*, 263-279. [9] *The Geologic History of the Moon. US GSPP 1348.* (1987). 269-270. [10] Crozaz G. (1978). *Proc. Lunar Planet. Sci. Conf. 9th.*, 2001-2009. [11] Becker R.H. & Clayton R.N. (1978). *Proc. Lunar Planet. Sci. Conf. 9th.*, 1619-1627.

Q-4.

TEKTITE-OBSIDIAN-LIKE GLASS FROM SPACE;

Masako Shima and M. Honda, Department of Science and Engineering, National Science Museum, A. Okada, T. Okada and Y. Kobayashi, Institute of Physical and Chemical Research, M. Ebihara, Department of Chemistry, Faculty of Science, Tokyo Metropolitan University, Yayoi N. Miura, Department of Earth and Planetary Physics, Faculty of Science, University of Tokyo, K. Nagao, Institute for Study of the Earth's Interior, Okayama University.

On March 25, 1993, around 2pm, tektite-obsidian-like glass, 122.2g, fell on the balcony of the office at 7th floor of the tall building in the center of Kyoto City. The external appearance is a duplicate of the "Tektite". Determination of cosmogenic radioactive nuclides, petrographical characteristics, major and trace elements by EPMA and INAA, Mössbauer Effects and noble gases were performed. As the results, it is concluded that the glass is neither like as tektite nor similar to terrestrial natural glases such as obsidian. It could be originated in the moon. It was temporaly named as Kyotite.

Circomstances of Fall: Just after Miss K. Sawai, Interior coordinator, was aware strange sound like a peal of thunder in her office, something hit and broke down flower pot which left on air conditioner sitting on the end of balcony. Her assistant, Miss Ishikawa, went there and found black glassy stone like duck-egg in size and shape. It seems to enter the balcony from southwest. It is well known that in the center of Kyoto City, low, one or two-storied, old houses stand side by side. The office is only the tall building, so it cannot be the results of somebody's practical Joke!

Gamma-ray measurements: The next day evening, this was informed to one of the authors, M. S. Immediately she hastened to there, brought back it to the Museum and put into the gamma-ray counter. It was noticed that Kyotite has trace peak in the place of 1274.5keV, while in others, nothing are observed. The peak area were compared with the moc sample and calculated as 20±10dpm-^{22}Na/kg-sample. The K, U and Th contents of Kyotites as well as tekties and obsidians were also determined by gamma spectrometry.

Petrographical characteristics: Polished thin sections, about 30micrometers thick, were made for the microscopic observation of petrographic characteristics of the Kyotite both in the transmitted and reflected lights. For comparison, tektites and obsidians were also investigated. The Kyotite is petrographically similar to obsidian. In the thin section, numerous globular-shaped, irregular hair-shaped, opaque crystallites which are submicron-sized in diameter, and colorless microlites are present. Flow structure is noticed by the oriented arrangment of crystallites and microlites in the Kyotite, but is quite different of that observed in tektite. In the reflected light, numerous magnetite grains, submicron to 20 microns in size, some of them accompanied partly reduced metals, are observed.

Table 1. Examples of EPMA analysis of the glassy area of Kyotite, tektites and obsidian(wt%)

	Kyotite	Australite	Bediasite	Indochinite	Moldavite	WadaPass	Koshidake	Shiratake
SiO_2	77.5	72.8	74.5	75.1	78.7	77.4	77.1	76.9
Al_2O_3	13.4	13.7	14.5	11.9	8.85	11.9	12.5	12.0
FeO	0.59	4.30	4.12	4.31	1.64	0.63	0.77	0.68
Na_2O	3.53	0.83	1.52	0.90	0.28	3.36	3.35	3.23

Refractive index of Kyotite is 1.485, which is equal to that of obsidians, 1.485-1.486, but is lower than that of tektites, 1.493-1.506.

Electron probe microanalysis of the glassy area of Kyotite, tektites and obsidians were carried out by using a Shimadz EMX-SM7 EPMA. Results for main components are shown in Table 1, as an example.

^{57}Fe Mössbauer spectrum of the finely pulverized sample of Kyotite was taken at room temperature. Because of low abundance of iron in the sample, the measurement was performed for about 700 hours. ^{57}Fe Mössbauer spectrum of Kyotite in Fig 1 shows that it consists of a mixture of five kinds of iron components, *i.e.* magnetite(Fe_3O_4), metallic iron, and tetrahedral Fe^{2+}, octahedral Fe^{2+} and octahedral Fe^{3+} in silicate network structure of the glass. The presence of

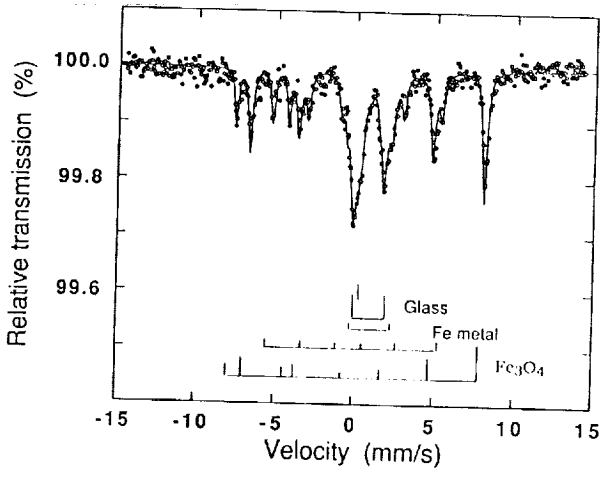

Fig.1. Mössbauer spectrum of Kyotite.

metallic iron in Kyotite is noticeable. Metallic iron is not present in obsidians, while metallic iron spherules have been reported in tektites, philippinites and indochinites [1].

Chemical Analyses by INAA of Kyotite were performed along with obsidians as well. REE abundances for Kyotite and obsidians are plotted against C1 value in Fig.2. Tektites have a similar REE pattern with an enrichment of light REE[2], but its inclination from light to heavy is steeper and the degree of negative Eu anomary is less prominent compared with those for Kyotite. From a viewpoint of chemical composition, the Kyotite is similar to an obsidian rather than a tektite. The chemical compositon of the Kyotite is also similar to those of terrestrial granites as well as lunar high-SiO_2 glasses[3].

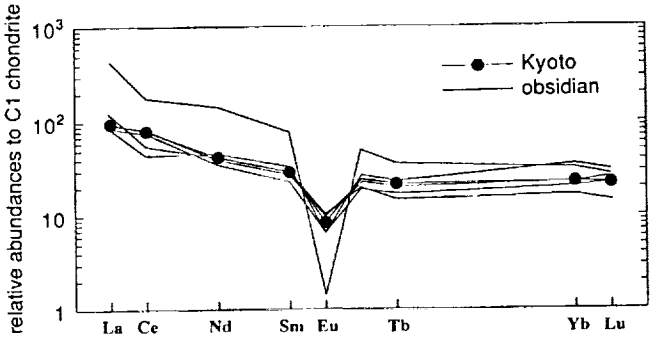

Fig.2 REE pattern of Kyotite and obsidians.

Noble gases of Kyotite were measured as usual manner. Isotopic composition of each element are similar to that of terrestrial atmosphere. Results are shown in Table 2 together with literature data of tektite[4], impact glass[5] and obsidian[6]. Kyotite has unique elemental abundances, low in He, High in Ar and heavy noble gases.

Table 2. Isotopic Composition of Noble Gases in Kyotite, tektite, impact glass and obsidian

	$[^4He]$	$^3He/^4He$	$[^{20}Ne]$	$^{20}Ne/^{22}Ne$	$^{21}Ne/^{22}Ne$	$[^{36}Ar]$	$^{38}Ar/^{36}Ar$	$^{40}Ar/^{36}Ar$
Kyotite	9.15	n.d.	69.0	9.832(24)	0.0290(8)	105	0.1873(8)	296.58(31)
Moldavite[4]	9.49		152	9.91(11)	0.0293(7)	0.0824		
Aouelloul[5]	423		470	9.80(8)	0.0270(4)	41.1	0.189(3)	346(5)
WadaPath[6]	7.4	< 4	12	10.06(32)	0.0290(5)	0.19	0.1889(39)	996(4)
	$[^{84}Kr]$	^{78}Kr	^{80}Kr	^{81}Kr	^{82}Kr	^{83}Kr	^{86}Kr	
Kyotite	1.070	0.624(61)	4.06(30)	n.d.	20.18(62)	20.48(60)	30.26(1.16)	
Moldavite[4]	< 0.00508							
Aouelloul[5]	0.917							
WadaPath[6]	0.0067	0.625(30)			20.16(21)	20.28(7)	30.85(14)	
	$[^{132}Xe]$	^{124}Xe	^{126}Xe	^{128}Xe	^{129}Xe	^{130}Xe	^{131}Xe	^{134}Xe	^{136}Xe
Kyotite	0.0279	0.34(3)	0.35(3)	7.27(14)	98.0(1.1)	15.3(3)	78.7(9)	38.6(5)	32.8(5)
Moldavite[4]	<0.0027								
Aouelloul[5]	0.0428								
WadaPath[6]	0.0012	0.35(3)	0.33(3)	7.07(8)	99.1(4)	15.2(2)	78.1(6)	38.6(3)	32.9(2)

Unit of concentrations of noble gases, symbol [N], are $10^{-9}cm^3STP/g$. Each Kr and Xe data are given against ^{84}Kr=100 and ^{132}Xe=100.

Discussion: Through whole examination of Kyotite, it is concluded that this is somewhat different object from tektite, and natural terrestrial glasses. Kyotite has somehow small visible peak of cosmogenic ^{22}Na and five kinds of irons exist together. Further it shoud be emphasized that metallic iron is present with magnetite in silicate matrix. This is hard to believe in natural terrestrial glasses. Taylor described existence of metallic iron in lunar regolith in his review[7]. He wrote that metal particles produced from reduction of ferrous iron induced by exposure, such metal ranges 40-330 A in size. This is just applicable in the case of occurence of iron metal of Kyotite, which glow side of small size of magnetite. From these aspects, we concluded that Kyotite should came from space, where not far from the earth, probably it originate in the moon.

Acknowledgement: Authors are indebted to Miss K Sawai, who provides us Kyotite sample for the present study immediately after its fall. Authors thank to Dr. R. Hutchison, British Museum, for supplying us several tektite sample for comparison.

[1] Chao E. C. T. *et al.* (1962) *Science, 135,* 97 and (1964) *GCA, 28,* 971. [2] Koeberl C. (1986) *Ann. Rev. EPS, 14,* 323. [3] Kempa M. J. and Papike J. J. (1980) *Proc. LPSC 11th,* 1635. [4] Matubara K. and Matsuda J-I (1991) *Meteoritics 26,* 217. [5] Matsubara K. *et al.* (1991) *GCA, 55,* 2951. [6] Miura, Yayoi and Nagao K. (1991) *Geochem. J., 25,* 163. [7] Taylor S. R. (1982) *Planetary Science; A Lunar Perspective,* p.142

IS THERE UMOV EFFECT FOR THE MOON IN POLARIZATION MINIMUM ?

Yu. G. Shkuratov and **N. V. Opanasenko** Astron. Observ. Kharkov Univ., Kharkov, 310022, Ukraine

The first polarimetric image of the central part of the lunar disk at a phase angle of about 10 degrees is presented. Regions of an intermediate albedo which are associated with mare / highland transition zones show increased values of $|P_{min}|$. The correlation diagram P_{min} - albedo has a horseshoe shape, which can be explained by the coherent backscatter mechanism of the negative polarization.

This paper continues our publications devoted to "exotic" characteristics of the lunar surface on the base of photometric and polarimetric data [2,3,7].

The Umov effect is an inverse correlation between polarization degree (P) and albedo (A) of a light-scattering surface. This effect is known to be revealed for the Moon at large enough phase angles when a positive polarization is observed [1-4]. The correlation is linear on a log-log scale. Recently, a similar dependence was also found for degree of the negative polarization ($|P_{min}|$), though, as turns out, it is justified only for regions with high enough albedo, being linear. For very dark regions the dependence is directly proportional. Thus, the dependence $P_{min}(A)$ has a horseshoe form. This result has been obtained on the base of discrete photopolarimetric observations of a few hundreds of lunar sites and of laboratory measurements of samples which are structure analogs of lunar regolith [3,4]. It is necessary to confirm the findings using more representative data, e.g., images of parameters $|P_{min}|$ and A.

Until recent time, the parameter P_{min} of the Moon had been considered as a characteristic which has practically no regional variations [5]. For the first time such variations were suspected by Kvaratskhelia [4]. Later they were confirmed in [3] where it was shown that the variations are in the interval 0,5 - 1,5%. To take an image of P_{min} we decided to use the photographic method in combination with discrete photopolarimetric data needed for calibration and photometric correction of original photographic images. The original images corresponding to two orientations of polaroid were taken by a 60 cm telescope in red light at a phase angle of about 10 degrees. These images were put in a computer memory by the special microdensitometer [6] which provides us with suitable quantization (of about 2000 photometric levels). Image calibration and photometric corrections were made using the data from [3]. Some details of the procedure of preparation of the image of polarization degree can be found in [7]. The P_{min} image of the central part of the lunar disk is shown in Fig.1. This is the first image of the Moon in the parameter P_{min}.

One can see that young craters and the ray systems show up. These units are characterized by low values of P_{min} (dark tone in the figure). Immature soils of the units have coarse regolith which is optically homogeneous as compared to the mare regolith. It agrees with the data of our laboratory studies of structure imitators of lunar grounds [3]. Regions with an intermediate albedo which are associated with mare/highland transition zones reveal increased values of $|P_{min}|$. According to the laboratory data [3] this feature can be due to the effect of mixing of optically contrasting (mare and highland) grounds.

Having images of $|P_{min}|$ and A, we can study the correlation diagram $|P_{min}|$-A (see Fig.2). Indeed, it has the horseshoe form which is explained in the frame of the so-called coherent backscatter mechanism of the negative polarization [8].

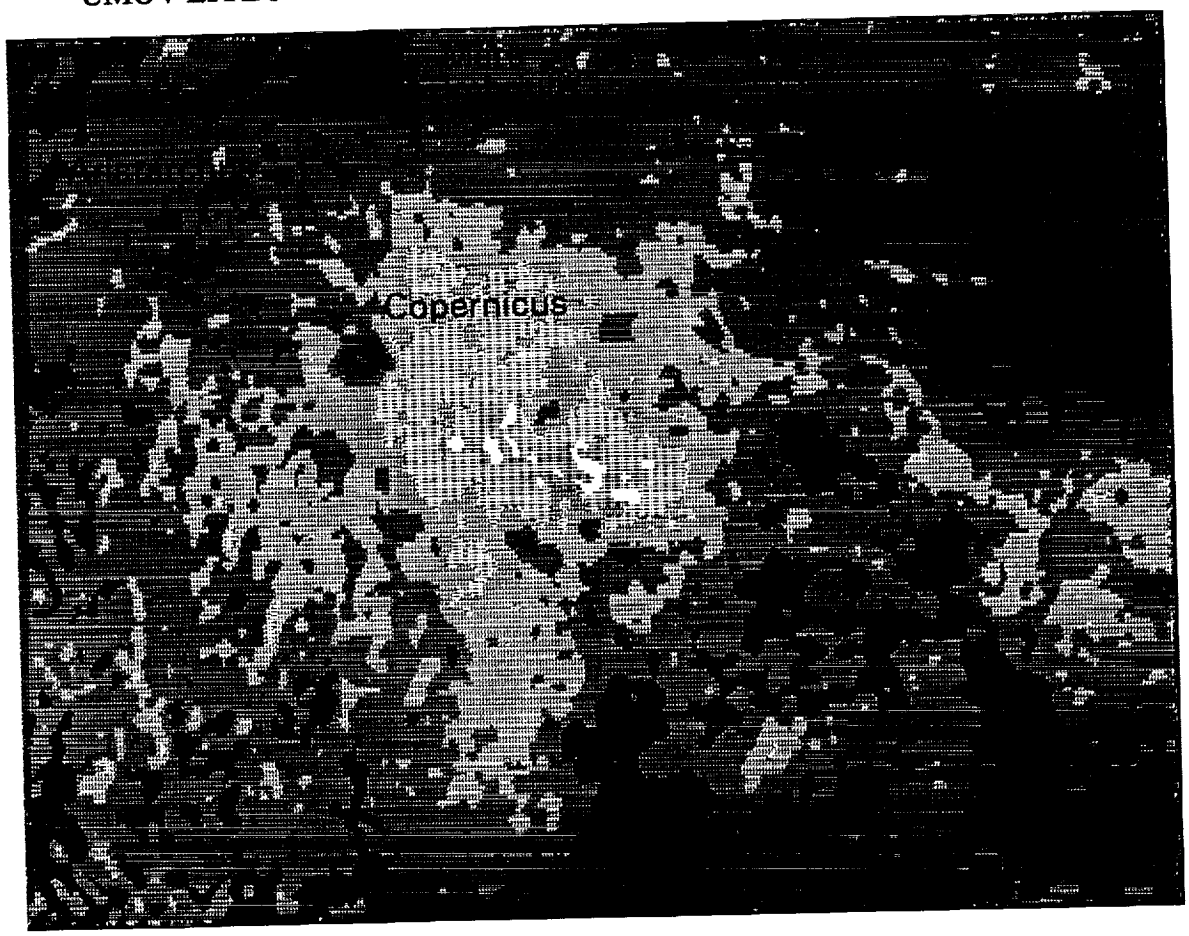

Fig.1. Image of P_{min} for central part of lunar disk

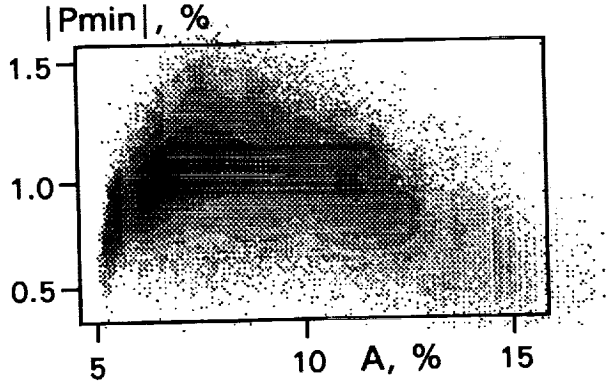

Fig. 2. Diagram $|P_{min}|$ - Albedo

References:

[1]. Dollfus A., Bowell E. (1971) *Astron. Astrophys., 10*, 29.

[2]. Shkuratov Yu. G., Opanasenko N.V. (1992) *Icarus, 99*, 468.

[3]. Shkuratov et al. (1992) *Icarus, 5*, 283.

[4]. Kvaratskhelia O. I. (1988) *Bull. Akademii Nauk Gruzinskoy SSR, B4*, 312 pp. (In Russian)

[5]. Bowell E. et al. (1972) In: *Proceedings of 3rd Lunar Sci. Conf.*, 3103.

[6]. Parusimov V. G.(1981) *Astrometriya i Astrofizika, 45*, 75. (In Russian)

[7]. Opanasenko N.V. et al. (1994) *Astronomicheskiy Vestnik*, in press.(In Russian)

[8]. Shkuratov Yu. G. (1991) *Astronomicheskiy Vestnik, 25*, 152 (in Russian).

Pu - Xe AGES OF EUCRITES A.Shukolyukov and F.Begemann, Max-Planck-Institut für Chemie, 55122 Mainz, Germany

^{244}Pu decays by α-emission and spontaneous fission with a half life of $T_{1/2}(\alpha)$ = 82 Ma. The former existence in meteorites of ^{244}Pu is indicated from the presence of characteristic spontaneous fission Xe. The ^{244}Pu-Xe isotope system offers a possibility for the chronology of various objects, provided the abundance of trapped Xe in these objects is small so that reliable measurements of fission Xe are feasible. What hampers its usefulness for chronological estimates is the absence of a stable, or long-lived, Pu reference isotope. This problem, however, can be avoided if the former abundance of ^{244}Pu is referenced to an element which behaves coherently with Pu. Lugmair and Marti [1] have shown that Pu must have been closely associated with light REE and used Nd as a reference element. The time difference of Xe retention for two meteorites is obtained [2] from: $\Delta T=1/\lambda\times$ $\times\ln[(^{244}Pu/^{150}Nd)_1/(^{244}Pu/^{150}Nd)_2]$ (1), where λ is the decay constant of ^{244}Pu and ^{244}Pu/^{150}Nd is the initial ratio at the time when fission Xe began to be retained. The content of ^{244}Pu is calculated from the measured Xe concentration. The main problem in the application of this traditional method of Pu-Xe dating is that Nd conentrations vary from sample to sample within a meteorite. Reliable data can be obtained only in cases when Xe and Nd concentrations are measured in the same sample. An additional source of error is due to the uncertainties in absolute instrumental sensitivity for Xe. Hohenberg et al. [3] therefore suggested to determine ^{244}Pu/REE ratios based on the $^{136}Xe_{Pu}/^{126}Xe_{REE}$ ratios, where $^{126}Xe_{REE}$ is the fraction of spallation ^{126}Xe from REE. While this method avoids problems of sampling heterogeneity and uncertainties in absolute instrumental sensitivity, it requires a reliable procedure for the partitioning of $^{126}Xe_{sp}$ into Ba- and REE-components.

Our work is an attempt to develop Pu-Xe dating and to explore the possibilities this isotope system can offer to shed light on the evolution of eucrites. We have analyzed noble gases in samples from Bereba(BER), Moore County(MC), Pasamonte(PAS), Pomozdino(POM), and Sioux County(SC) eucrites. Available literature data for these and other eucrites as well as from angrites are also considered.

Time differences of Xe retention are derived from:

$$\Delta T = 1/\lambda \ln \frac{[(^{136}Xe_{Pu}/^{126}Xe_{sp})\,(1+(P_{Ba}/P_{REE})\,([Ba]/[REE]))]_1\,(P_{REE}\,T)_1}{[(^{136}Xe_{Pu}/^{126}Xe_{sp})\,(1+(P_{Ba}/P_{REE})\,([Ba]/[REE]))]_2\,(P_{REE}\,T)_2}, \qquad (2)$$

where $^{136}Xe_{Pu}$ is the portion of ^{136}Xe originating from the fission of ^{244}Pu, $^{126}Xe_{sp}$ is total spallation ^{126}Xe, P_{Ba} and P_{REE} are production rates for ^{126}Xe on Ba and REE respectively, [Ba] and [REE] are Ba and La+Ce+Nd concentrations, T is the cosmic ray exposure age. Eq. (2) is similar to that suggested by Hohenberg et al.[3], the difference being that we calculate fractions of $^{126}Xe_{REE}$ via the [Ba]/[REE] ratios rather than from the isotopic composition of spallation Xe. The advantage of eq.(2) compared to the traditional method of Pu-Xe dating (eq.(1)) is that we avoid the determination of any absolute concentrations. Firstly, fractions of $^{136}Xe_{Pu}$ and $^{126}Xe_{sp}$ in total ^{136}Xe and ^{126}Xe can be calculated without a knowledge of the absolute amount of Xe. Secondly, although REE concentrations may vary from sample to sample within a meteorite, the [Ba]/[REE] *ratio* remains constant within several percents. Thirdly, the ^{81}Kr-Kr dating method provides radiation ages based also on the measurements of isotope ratios only. Although an exact mathematical analysis of possible errors associated with the use of eq.(2) is complicated, we can estimate a reasonable limit for the total uncertainty. The sources of the uncertainties are: 1) determination of the isotopic composition of Xe; 2) calculation of the spallation component; 3) subtraction of ^{238}U fission Xe; 4) variation of the [Ba]/[REE] ratio within a meteorite; 5) uncertainties in the isotopic composition of trapped Xe; 6) determination of the radiation ages; 7) variation in P_{Ba} and P_{REE} due to different shielding. (The experimentally detemined P_{Ba}/P_{REE} of 1.8±0.3 [4] is in agreement with the value of 1.8±0.1 obtained in thin-target simulation experiments for Ba and REE targets [5].) The analysis of the available data has shown that the uncertainties associated with the items 1)-5) are small, usually 2 - 6% from each source. To evaluate a range of the variations of the production rates we plotted $^{126}Xe_{sp}$eff. versus ^{81}Kr-Kr radiation age (Fig.). $^{126}Xe_{sp}$eff. is the amount of $^{126}Xe_{sp}$ normalized to Ba and REE concentrations. To reduce uncertainties due to the absolute instrumental sensitivity calibration we used data obtained in our laboratory only (this work and [6]). The data points for BER, Bouvante(BOUV), Juvinas(JUV), POM, SC form a straight line which is an indication that the production rates were the same (within ~10%) for this group of samples. The data for the angrites [3,7], presented for comparison, belong to the same line. Thus, a limit for the uncertainties associated with production rate variations in these samples is ~10%. The data points for MC and Stannern(STAN) fall below the line. Most likely, this is a result of smaller production rates for these samples. If true this would result in an overestimation of the ages calculated by eq.(2). The apparent ages, however, can be corrected using the correlation on the Fig.. In sum, in the most-favorable cases (large $^{136}Xe_{Pu}/^{136}Xe_{trapped}$ ratio, precisely

Pu-Xe AGES OF EUCRITES: Shukolyukov A. and Begemann F.

determined radiation age, etc.) error propagation yields a total uncertainty of 13-14%, or 14-15 Ma, for the time differences.

To tie the relative Pu-Xe ages to an absolute time scale we use Angra dos Reis(ADOR) for normalization. A precise absolute Pb-Pb age of 4.5578±0.0004 Ga for this meteorite has recently been determined [8]. The average $^{136}Xe_{Pu}/^{126}Xe_{sp}$ ratio for ADOR was calculated from the data for two bulk samples and three pyroxene separates [1,7,9,10]. Fractions of $^{126}Xe_{REE}$ for eucrites and angrites were determined using [Ba]/[REE] ratios from [2,4,11].

The results of our calculations are presented in the table. The ΔT_{ADOR} are the average values calculated from the data obtained in different laboratories. The total range of ΔT for the same meteorite is in the most cases *less* than the listed uncertainties for a single calculation. The "+" signs imply ages younger than that for ADOR. Available Pb-Pb and Sm-Nd ages are also shown for comparison. Pu-Xe ages indicate an existence of two distinct clusters. The BOUV, Ibitira(IBIT), JUV, MC, PCA82502, PAS, POM ages are close to those for ADOR and LEW86010 (and generally agree with the available Pb-Pb and Sm-Nd ages). Since we can not exclude a potential fission Xe loss during the long history of these eucrites (for example, during brecciation events), Pu-Xe ages are only lower limits for the crystallization ages. On the other hand, the true crystallization ages can not be much older because formation of the earliest condensates in the solar system occured ~4.566 Ga ago [8]. Thus, at least some of the eucrites retained their fission Xe almost completely and their crystallization ages are, most likely, very close to those of angrites. The old Pu-Xe age for the unbrecciated cumulate MC implies its formation contemporaneous with non-cumulate eucrites at ~4.56 Ga while the young Sm-Nd age for this meteorite is probably a result of deep-crustal burial and exposure to elevated temperatures, above Nd closure temperature, for a long period of time [12]. STAN is a heavily metamorphized and brecciated meteorite and its young Pu-Xe age (which is in a good agreement with its Sm-Nd age), most likely, indicates the time of a metamorphic event. The Pu-Xe ages for BER, SC, Nuevo Laredo(NL), Millbillillie(MIL) form another cluster. These ages are also in a reasonable agreement with the Pb-Pb ages. Since the Rb-Sr data on BER and SC do not reveal metamorphic disturbances [13], it is not clear yet whether these ages are true crystallization ages or rather reflect complete melting and recrystallization which resulted in resetting of the Pu-Xe and Pb-Pb chronometers.

Table. Pu-Xe, Pb-Pb, and Sm-Nd ages for eucrites and angrites (in Ma).*

Sample	ΔT_{ADOR}	T_{Pu-Xe}	T_{Pb-Pb}	T_{Sm-Nd}
LEW[1]	+1±14	4557±14	4557.8±0.5	4550±30
PAS[2]	-8±16	4566±16	4530±30	4580±120
PCA[3]	-6±25	4564±25		
IBIT[4]	-5±25	4563±25	4560±3	
MC[5]	-2±17	4560±17		4457±25
POM[6]	+4±14	4554±14		4540±90
BOUV[7]	+9±14	4549±14	4514±4	
JUV[8]	+15±14	4543±14	4539±4	4560±80
NL[9]	+49±30	4509± 30	4534±2	
MIL[10]	+51±17	4507±17		
SC[11]	+54±15	4504± 15	4526±10	
BER[12]	+57±18	4501±18	4522±4	
STAN[13]	+107±20	4451±20		4480±70

* - Pb-Pb and Sm-Nd data are from reviews [12,13].
Xe data from: 1-[2,3], 2-this work(tw),[14,16,17], 3-[15], 4-[9], 5-[tw], 6-[tw], 7-[6], 8-[6,14], 9-[10], 10-[18,19], 11-[tw,6,14,16], 12-[tw,16], 13-[6,14,16,20].

Fig. Correlation between the amounts of effective (normalized to Ba and REE concentrations) spallation ^{126}Xe and ^{81}Kr-Kr radiation ages.*

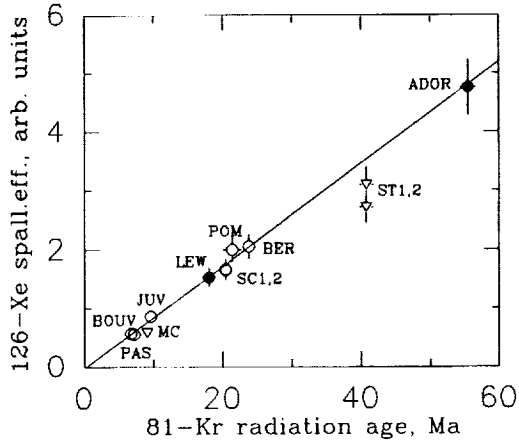

** - The radiation age of LEW86010 is the average of its ^{3}He, ^{21}Ne, ^{38}Ar, ^{83}Kr ages [2].

References: [1] Lugmair G.W. and Marti K.,(1977),EPSL,35,273. [2] Eugster O. et al.,(1991),GCA,55,2957. [3] Hohenberg C.M. at al.,(1991),EPSL,102,167. [4] Hohenberg C.M. et al.,(1981),GCA,45,1909. [5] Shukolyukov A.,(1989),Meteoritika,48, 94. [6] Freundel M.,(1983),MPI für Chemie,Mainz,Ph.D. thesis. [7] Hohenberg C.M.,(1970),GCA,34,185. [8] Lugmair G.W. and Galer S.J.G.,(1992),GCA,56,1673. [9] Wasserburg G.J. et al.,(1977),EPSL,35,294. [10] Munk M.N.,(1968),EPSL,3,457. [11] Warren P.H.,Eucrite Database,(1992),pers.comm. [12] Warren P.H.,(1991),JGR,96,5909. [13] Smoliar M.I.,(1993),Meteoritics,28,105. [14] Kuroda P.K.,(1966),Nature,212,241. [15] Schultz L.,pers.comm. [16] Hudson B.G.,(1981),Washington Univ.,St.Louis,Ph.D. thesis. [17] Hohenberg C.M. et al.,(1967),JGR,72,3139. [18] Eugster O. and Michel Th.,(1993),Meteoritics(in press). [19] Miura Y.,pers.comm. [20] Marti K. et al.,(1966),Z.Naturforsch.,21A,398.

UNUSUAL REFRACTORY INCLUSIONS FROM A CV3 CHONDRITE FOUND NEAR AXTELL, TEXAS; S.B. Simon[1], L. Grossman[1,2]. and J.F. Wacker[3], [1]Department of the Geophysical Sciences, [2]The Enrico Fermi Institute, University of Chicago, Chicago, IL 60637, [3]Battelle, Pacific Northwest Laboratories, Richland, WA 99352

Abstract. A CV3 chondrite reportedly found in Texas in 1943 has recently become available for study. It resembles Allende in texture but is heavily weathered, and its ^{60}Co activity (<1 decay per minute/kg) is lower than that of Allende (1-7 dpm/kg). Six of eight CAIs studied are unusual in some way compared to those in Allende, including: a CTA with a spinel-perovskite core; a CTA with a rare, unnamed Ca-, Ti-rich silicate; a B1 with melilite sprays in the mantle; and a fluffy Type A containing abundant palisade bodies.

A CV3 chondrite reportedly found near Axtell, Texas (31°42'N, 96°49'W) in 1943 has recently become available for study. From the original mass of 6.2 kg, five slabs were cut. Its texture resembles that of Allende, but the meteorite is heavily weathered and most of the chondrules exhibit iron oxide staining. Refractory inclusions, amoeboid olivine aggregates, and dark inclusions are also exposed on the slab surfaces. The oxygen isotopic composition of Axtell, $\delta^{18}O = +1.61$, $\delta^{17}O = -2.54$ (R.N. Clayton, pers. comm.), is identical to that of Allende. Cosmogenic ^{26}Al and ^{60}Co activities were determined by counting a 101 g sample of the Axtell specimen and a piece of Allende for 7000 min. The ^{26}Al activities of both specimens are typical of chondrites, 50 ± 6 dpm/kg for Axtell and 54 ± 4 dpm/kg for Allende. The Axtell sample, however, had <1 dpm/kg ^{60}Co while Allende had measurable ^{60}Co. When Allende fell in 1969, its ^{60}Co activity ranged from 23-180 dpm/kg, with most values > 100 dpm/kg [1]. The current-day activity of ^{60}Co is only ~4 % of that in 1969, i.e. 1-7 dpm/kg, with most values >4 dpm/kg. The ^{60}Co results thus suggest that Axtell is not a piece of Allende. On the basis of these data, however, we cannot rule out the possibility that Axtell is a fragment from near the surface of the pre-atmospheric mass of Allende.

After examination of ten slab surfaces, we selected eight coarse-grained refractory inclusions for study. Although all can be classified as either Type A or B, six are unusual in some way, compared to those we have seen in Allende.

The most unusual inclusion in our suite is AX-4, a 4 × 3.5 mm compact Type A (CTA) with a remarkable spinel-perovskite core, in which spinel is so abundant that many grains are intergrown with one another, forming large, nearly monomineralic regions. In some parts of the core, spinel grains are enclosed in perovskite or interstitial melilite. With increasing distance from the core, the melilite/spinel ratio increases, and the core grades into an outer zone dominated by melilite laths that are typically 50-100 μm wide and 200-400 μm long. The texture of this zone also contrasts with that of typical CTAs, which generally have blocky, more equant melilite crystals. The laths are unzoned, and generally range from $Åk_{22}$ to $Åk_{29}$ except at the rim, where the melilite is more aluminous ($Åk_{13}$). This zone also contains sparsely distributed grains of perovskite, 10-70 μm across, and euhedral spinel crystals, mostly 10-30 μm across. Except for several large (up to 300 μm across) patches of fine-grained anorthite, alteration products (mostly grossular) are restricted to melilite grain boundaries. Although Allende CTA TS12 has a spinel-, perovskite-rich area which resembles the outer part of the core of AX-4 in that melilite encloses abundant spinel, an inclusion with a melilite mantle and a spinel-perovskite core has not been previously reported.

AX-1 is an irregularly shaped, 3.3 × 1.8 mm CTA which is dominated by anhedral to blocky melilite and its alteration products. The inclusion also contains heterogeneously distributed spinel crystals, fine-grained (5-10 μm) except for those in a large palisade body [2] in which they are up to ~50 μm across. In the palisade body and elsewhere in the inclusion, spinel contains ~ 1.2 wt % V_2O_3. Perovskite occurs as blebs in symplectite, and as coarser anhedral to subhedral grains up to 120 μm across. Some of the latter have inclusions of melilite. What is unusual about this inclusion is the presence of a rare, unnamed Ca-, Ti-rich silicate that has only one other reported occurrence [3], in an Allende Type A inclusion. Here, as in Allende, the phase is associated with perovskite. It occurs as anhedral grains, 10-50 μm across, some with perovskite cores or enclosing multiple grains of perovskite. The phase contains ~ 1 wt % MgO, 4 % Al_2O_3, 29 % SiO_2 and 33 % CaO, all within the ranges reported for the Allende material [3], and up to 1 wt % ZrO_2. TiO_2 contents are more variable; they range from 21.6 to 31.2 wt % and are anticorrelated with Sc_2O_3 (0.41-3.8 wt %) and V_2O_3 (0.82-4.3 %), suggesting that these cations compete for the same crystallographic site. This phase may also be present in Allende CTA TS19, where it occurs with fassaite between perovskite and a Fremdling. In this case, however, the phase is very rich in V_2O_3 (~ 6.9-10 wt %), which was probably supplied by the Fremdling. It is not clear that this phase is simply a product of alteration of perovskite, however, because in at least one place in AX-1, a perovskite-free grain occurs adjacent to unaltered perovskite. Also, it is strongly enriched in Sc_2O_3 relative to perovskite, its TiO_2/Sc_2O_3 ratio being <100, and that in perovskite is >900. On the other hand, if it is primary, it is curious that fassaite did not form instead. Perhaps

there was insufficient Al_2O_3 and/or Ti_2O_3 available or the f_{O_2} was too high to allow fassaite formation.

The two Type B1 inclusions in the suite, AX-5 and AX-7, cannot be considered typical of this type of inclusion. AX-5, 3.2 × 2.5 mm, has a melilite-rich mantle with coarse, euhedral, radially oriented laths up to 640 μm long, and most are 50-100 μm wide. In a rather striking departure from the normal B1 structure, in which the mantle is a solid, continuous shell of melilite, the mantle in AX-5 is only ~70 % melilite, and many laths diverge inward from the rim, forming sprays, with fassaite (4.6-8.1 wt % TiO_2^{tot}) and anorthite between the laths. In the interior, melilite is interstitial to fassaite and anorthite, and is generally more Mg-rich ($Åk_{40-50}$) than in the mantle ($Åk_{14-42}$). Small, rounded grains of spinel are poikilitically enclosed in all phases, but it is much more abundant in the interior than in the outer part of the inclusion. Also abundant in the interior are small (~5-10 μm) grains of NiFe metal and pentlandite, and at least one grain of an Fe-free Ni-sulfide, perhaps heazlewoodite, is present.

AX-7, 6.4 × 5.3 mm on the slab surface, has a continuous, 500 μm-wide melilite mantle ($Åk_{20-40}$) and is extremely spinel-rich. Fassaite is mostly subhedral, 300-500 μm across, and is much more abundant than melilite in the interior of the inclusion. Opaque assemblages are generally ~10 μm across, rounded, enclosed in fassaite, and made of magnetite + NiFe metal. The largest assemblage, 80 μm across, contains magnetite and FeS. Unlike most B1s, which have spinel-poor mantles, spinel in AX-7 is uniformly distributed and very abundant, dominating the entire inclusion except for the outermost 100 μm and one spinel-poor island. The spinel grains are small (mostly 5-20 μm). Although experiments show that, for most Type B compositions, spinel should be the first phase to crystallize [4,5], most B1s have spinel-poor mantles and spinel-rich cores, suggesting that spinel crystals were pushed inward, rather than incorporated, by melilite crystals as they grew. For some reason, this did not occur in AX-7, perhaps due to an unusual cooling history, bulk composition or both. The great abundance of tiny spinel crystals may be due to an unusually high bulk Al_2O_3 content, giving AX-7 a higher liquidus temperature and allowing it to retain more crystal nuclei.

Two inclusions are notable for the abundances of palisade bodies in them, especially AX-2, a 5.3 × 2.7 mm, irregularly-shaped, heavily altered "fluffy" Type A inclusion [6]. Melilite is fine-grained (5-70 μm) with much subgrain development, indicating recrystallization. Except for a few spinel-rich areas, the melilite generally encloses little spinel. Wark and Lovering [2] found no palisade bodies in any of the Allende Type A inclusions they studied, but in AX-2, most of the spinel is present in palisade bodies, which range from about 50 to 300 μm across. Most are round, but several are oval or flattened, as if they were deformed. They consist of rings of spinel grains enclosing melilite and spinel ± fassaite ± perovskite. In the largest one, melilite ranges from $Åk_{12}$ to $Åk_{40}$ and fassaite has ~10 wt % TiO_2^{tot}. AX-9, 4.6 × 3.7 mm on the slab surface, is a heavily altered, possibly brecciated Type B2 with abundant palisade bodies. Some are large (>250 μm across) and contain anorthite, in addition to the usual melilite and spinel. Some have thick spinel shells, whereas others have incomplete rings that appear to have been frozen in the act of formation. Also consistent with *in situ* formation is the fact that their rims are jagged, not smooth as would be expected if the spinel crystals had nucleated on the edges of liquid droplets that were later incorporated as solids into the host CAIs [2]. They may instead be chains of crystals brought together by surface tension during crystallization of their liquid hosts.

Spinel is very heterogeneously distributed in AX-9. The interior is fairly rich in coarse spinel (up to ~40 μm). Most of the rest of the inclusion is virtually spinel-free except for the palisades and the outermost ~200 μm along part of the rim, where melilite and fassaite enclose numerous, small (~5 μm) spinel grains. Fassaite and anorthite are anhedral and as large as 500 μm across. Much of the melilite exhibits wavy extinction and development of subgrains (~10 μm across), indicating that the inclusion has been shocked. There are also patches where fassaite or anorthite poikilitically enclose subhedral melilite grains 10-20 μm across, a texture observed in some Leoville [7] and Vigarano inclusions (but rare in Allende) and attributed to remelting of the inclusions.

Comment: We have been unable to substantiate the claim that this meteorite was found in 1943, but of eight CAIs we studied, six are unusual in some way when compared to analogous Allende inclusions. The likelihood of this occurring during an investigation of a similar amount of Allende is low. In light of this and the ^{60}Co results, we believe that the Axtell specimen is a new, previously undescribed CV3 chondrite.

References. [1] Evans J.C. *et al. JGR 87*, 5577-5591. [2] Wark D.A. & Lovering J.F. (1982) *GCA 46*, 2595-2607. [3] Floss C. *et al.* (1992) *Meteoritics 27*, 220. [4] Stolper E. (1982) *GCA 46*, 2159-2180. [5] Stolper E. & Paque J.M. (1986) *GCA 50*, 1785-1806. [6] MacPherson G.J. & Grossman L. (1984) *GCA 48*, 29-46. [7] Simon S.B. & Grossman L. (1991) *LPS XXII*, 1261-1262.

Geoid/Topography Admittance on Venus from Models of Convection with No Crustal Deformation; Mark Simons[1], Bradford H. Hager[1], and Sean C. Solomon[2], [1]Department of Earth, Atmospheric, and Planetary Sciences, Massachusetts Institute of Technology, Cambridge, MA 02139, [2]Department of Terrestrial Magnetism, Carnegie Institution of Washington, Washington, DC 20015.

Introduction. Global maps of the spatial and spectral variation of the geoid/topography admittance of Venus are now available from recent Magellan data [1]. The admittances varies between about 0 and 35 m/km, in contrast to the range -6 to 12 m/km derived for Earth. Two different scenarios for convection-driven lithospheric deformation fit the admittance observations [1]. In the first, compressive highland plateaus are expressions of present mantle downwelling, broad volcanic rises are expressions of mantle upwelling, and the lowlands overly regions with no substantial vertical motion in the upper mantle. This model is characterized by active ongoing crustal deformation. In the second scenario, compressive highland plateaus are remnants of an earlier regime of high crustal strain, the crust presently does not thicken or thin significantly in response to mantle-convective tractions, and most long-wavelength topography not associated with the earlier regime arises from normal convective tractions at the base of the lithosphere. Here, we explore models that specifically address this second scenario with negligible lithospheric deformation.

Admittance Curves. Values of the admittance for selected geographic regions are shown in Figure 1. The admittances are calculated from a spherical harmonic expansion of topography based on Magellan altimetry [2,3] and a spherical harmonic expansion of the geoid (MGN40D) based on Magellan spacecraft tracking data [3]. At both long (~3000 km) and medium (~1500 km) wavelengths, the globally averaged admittance is approximately 15 m/km. The lowest admittances calculated thus far occur in highlands characterized by extensive compressional tectonic deformation. For example, Ishtar Terra, and Ovda and Alpha Regiones, have admittances of 3 - 10 m/km (Fig. 1). Under the hypothesis of the variable regime, such regions are interpreted to be tectonic fossils of a previous period of deformation. In contrast, highland regions such as Beta, Atla, and Eistla Regiones, characterized by high admittance values, extensive volcanism and rifting, are interpreted as sites of current mantle upwelling [4-9], while the lowest regions such as Atalanta and Lavinia Planitiae are sites of current mantle downwelling. The admittance over the volcanic swells is typically more than 30 m/km at long wavelengths, as shown in Figure 1. The plains and lowlands also have admittances greater than 15 m/km. Airy isostatic models for these areas require unreasonably large apparent depths of compensation, approximately 200 km [7]. Furthermore, the spectral behaviour of the admittances for most of these regions is inconsistent with a purely Airy compensation mechanism [5].

Convection Models. We are conducting a series of finite element convection calculations designed to test the consistency of the variable regime against the admittance constraints. We use a 2-dimensional cylindrical domain (infinite in the z direction) with either depth-dependent or fully temperature-dependent viscosity. These are time-dependent whole-mantle models. We calculate topography, geoid, and the resulting admittance as functions of time, position, and wavelength. We explore the sensitivity of the admittance to the Rayleigh number, the degree of internal heating, and the variation in upper mantle viscosity structure.

References. [1] M. Simons et al., *Science*, submitted, 1993; [2] P.G. Ford and G.H. Pettengill, *JGR, 97*, 13091, 1992; [3] A.S. Konopliv et al., *GRL, 20*, 2403, 1993; [4] R.J. Phillips and M.C. Malin, in *Venus*, Univ. Arizona Press, 158, 1983; [5] R.R. Herrick et al., *GRL, 16*, 543, 1989; [6] W.S. Kiefer and B.H. Hager, *JGR, 96*, 20947, 1991; [7] S.E. Smrekar and R.J. Phillips, *EPSL, 107*, 582, 1991; [8] D.A. Senske et al., *JGR, 97*, 13395, 1992; [9] S.C. Solomon et al., *JGR, 97*, 13199, 1992; [10] R.J. Phillips and K. Lambeck, *Rev. Geophys. Space Physics, 18*, 27, 1980; [11] B.H. Hager, *EPSL, 63*, 97, 1983.

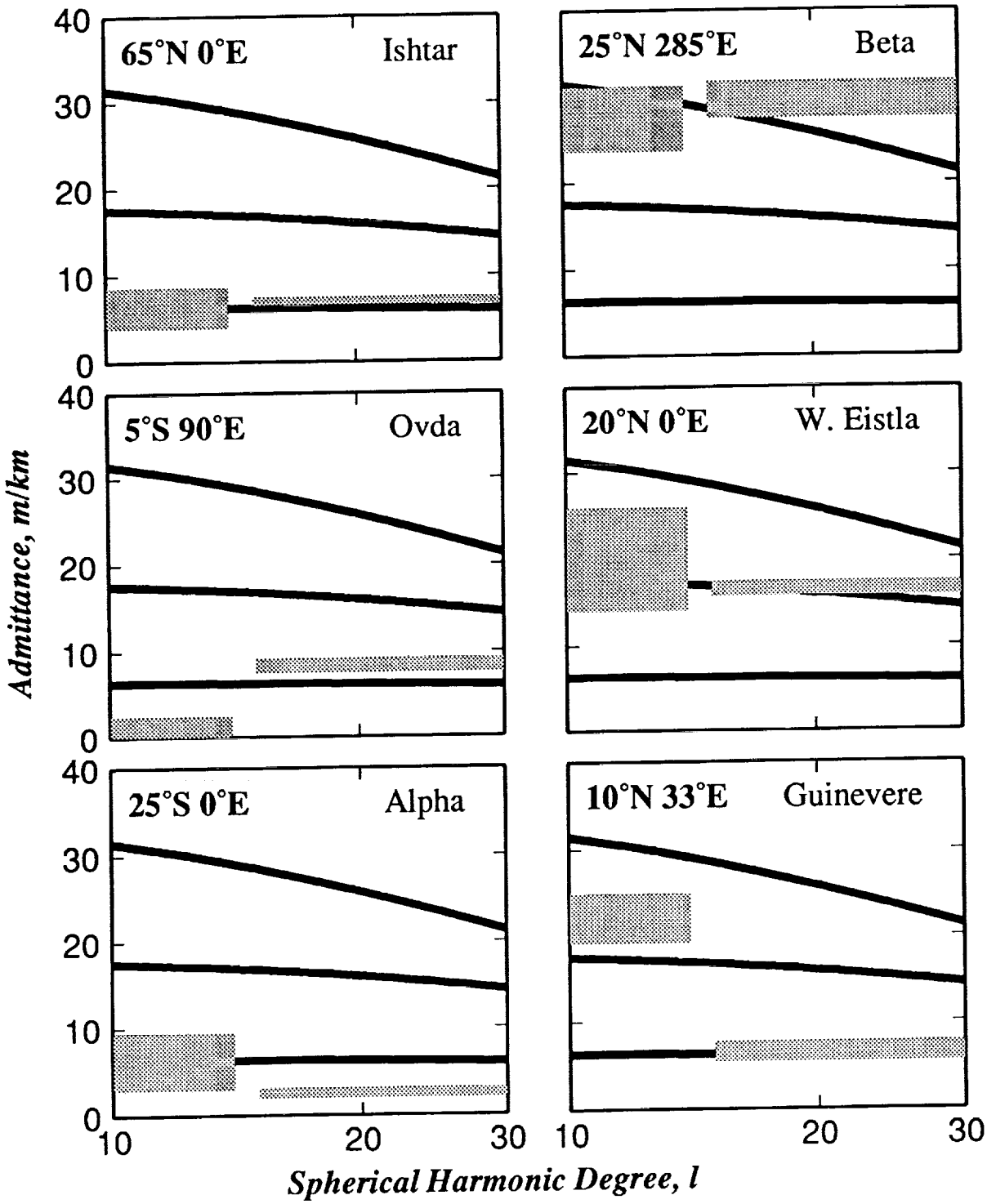

Figure 1. Geoid/topography admittances for selected regions of Venus. The admittances are shown as shaded rectangles whose horizontal extent represents the limits of the harmonic degree band and whose vertical extent corresponds to two standard deviations in the admittance estimate. For reference, theoretical geoid/topography admittance curves for Airy isostasy with different compensation depths (50, 150, and 300 km in bottom-to-top order) are shown [10, 11].

THE MAGELLAN QUASI-SPECULAR BISTATIC RADAR EXPERIMENT;
R. A. Simpson, Center for Radar Astronomy, Stanford University, Stanford, CA 94305-4055, G. H. Pettengill and P. G. Ford, Center for Space Research, Massachusetts Institute of Technology, Cambridge, MA 02139-4307

Bistatic radar experiments, where the reflecting surface element is illuminated and viewed from different directions, allow a wider variety of useful measurements (particularly of the polarization dependence) of the scattering process than is available in the more usual monostatic geometry. The Magellan spacecraft, now in low circular orbit around Venus, was used to carry out a set of bistatic observations of that planet in Nov, 1993, by illuminating the surface simultaneously with its telemetry transmitters at X and S bands; the illuminated region was chosen to satisfy the geometric requirements for specular reflection as viewed from Earth. The echo signals were received at the 70-m DSN site in Madrid, using dual circularly polarized receiving channels at both wavelengths. Preliminary analysis shows a 2-kHz-wide, approximately 50% linearly polarized echo at S-band, but no evidence of a signal at X-band, where the Venus atmospheric absorption is severe.

The S-band telemetry downlink radiation is linearly polarized at transmission; by adjusting the orientation of the spacecraft, the illumination of the surface was maintained at 45° to the incidence plane. Thus, the power striking the surface in both the *in-plane* and *out-of-plane* linearly polarized components was equal. Two effects dominate the scattering process: a) wavelength-scale roughness scatters the incident energy incoherently over a wide range of emerging angles and largely destroys its polarization; and b) smooth surfaces reflect the incident energy coherently in the specular direction (towards Earth) and impose a polarization on the reflected signal that depends strongly on the dielectric properties of the surface (1). The use of dual orthogonally polarized receiving channels permits full reconstruction of the echoes' Stokes Parameters. Where the surface is rough, we expect the observed echoes to weaken, since the scattered energy is diffused over a wide range of solid angles. Where it is reasonably smooth, the signal is concentrated in the specular direction and remains highly polarized. Spectral broadening is expected in both circumstances, with the degree depending on the surface undulations, as well as on the extent of the illuminated surface region (1). In the present experiment, the width is determined primarily by the antenna "footprint," and remains remarkably constant at about 2 kHz.

Data analyzed to date cover an arc over the Venus surface moving from the "horns" of eastern Ovda Regio (roughly 0° lat, 67°E lon) up to about 77°N, 150°E, a total strip length of about 8500 km. During this interval, the angle of incidence to the surface varied slowly from about 75° to 80°. For comparison, the Brewster angle (at which the *in-plane* scattering component vanishes for specular reflection) corresponding to a surface dielectric permittivity of 4.5 is 77°. Over this interval, the degree of linear polarization varies from a minimum of 20% up to a maximum of 80%. Further analysis will parametrize the surface track properties, to retrieve estimates of wavelength-scale roughness, RMS meter-scale slopes, and dielectric permittivity.

(1) Simpson, R. A., "Spacecraft studies of planetary surfaces using bistatic radar," *IEEE Trans. Geosci. and Rem. Sensing*, **31**, 465-482, 1993.

VENUS GRAVITY FIELD DETERMINATION: PROGRESS AND CONCERN;
W.L. Sjogren; A.S. Konopliv, Jet Propulsion Laboratory/California Institute of Technology, Pasadena, CA 91109

New gravity data from the Magellan spacecraft are continuing to be acquired and reduced, revealing new results for the high latitude regions. There is a big concern that NASA may terminate Magellan before complete uniform gravity coverage is obtained, leaving sizable data gaps over very important features.

The Magellan spacecraft has been producing excellent gravity data since September 1992 when periapsis was lowered to 180 km and daily coverage was obtained for 360° of longitude. However the eccentricity of that orbit produced high altitudes over the polar regions such that the gravity signals were greatly attenuated. As a result the resolution above 40° N latitude and 20°S latitude is very poor. To achieve complete uniform gravity coverage, the Magellan project successfully executed a 70 day aerobraking plan from May 1993 to August 1993, which produced a near circular orbit having a periapsis altitude of 180 km and an apoapsis altitude of 550 km. To date, again, excellent gravity data have been acquired. In the near circular orbit good data are obtained from both apoapsis and periapsis tracking, unlike the eccentric orbit where only good gravity data are obtained near periapsis. So we should be in fat city. Not so. Due to the laws of celestial mechanics and some unfortunate timing the data coverage is not obtained in a nice continuous block as was the case for the previous coverage in cycle 4. It turns out that when either periapsis or apoapsis become occulted from the earth, that the data obtained from the now visible portion of the orbit is greatly redundant with the previous tracking. This is shown in figure 1 where at the end of cycle 5, April 15, 1994 there will exist a longitude gap of 125° over very important geophysical features such as Artemis, Atalanta, Tethus Regio, Aino Planitia, and Lada Terra. If the mission continues until Oct. 5, 1994, (It is now NASA's thinking to terminate operations on April 16, 1994) this gap will be reduced to 55°. To obtain complete coverage the mission should be continued until March 1, 1995. (See figure 2).

We are presently acquiring data having the lowest possible altitudes over Ishtar Terra. However the spacecraft is also approaching solar conjunction and we may lose a sizable portion of these data due to high noise levels from the sun. We will discuss and display the results from these data with our best 40th degree and order spherical harmonic solution. We expect to have improvements over previous models in the areas of Beta, Metis, Guinwere, Sedna and Ishtar.

VENUS GRAVITY FIELD DETERMINATION: W.L. Sjogren and A.S. Konopliv

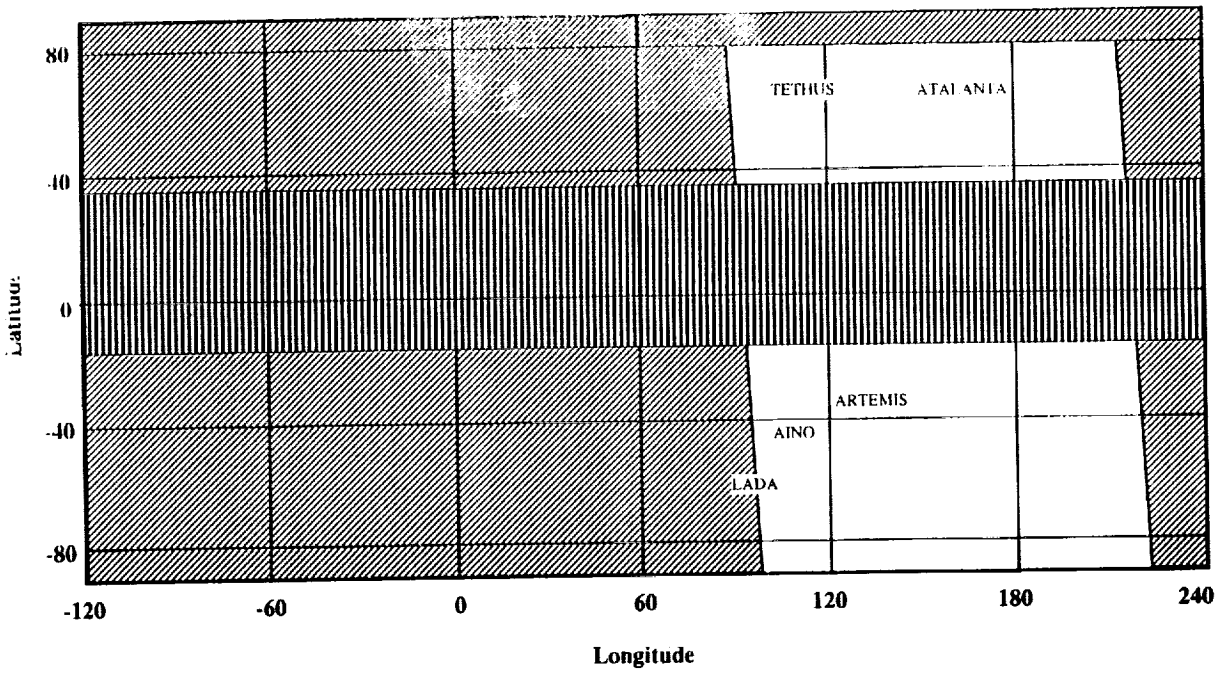

Figure 1 Magellan High Resolution Gravity Coverage
Vertical hash is good gravity data from cycle 4; the slant hash is anticipated coverage from cycle 5 by April 16, 1994.

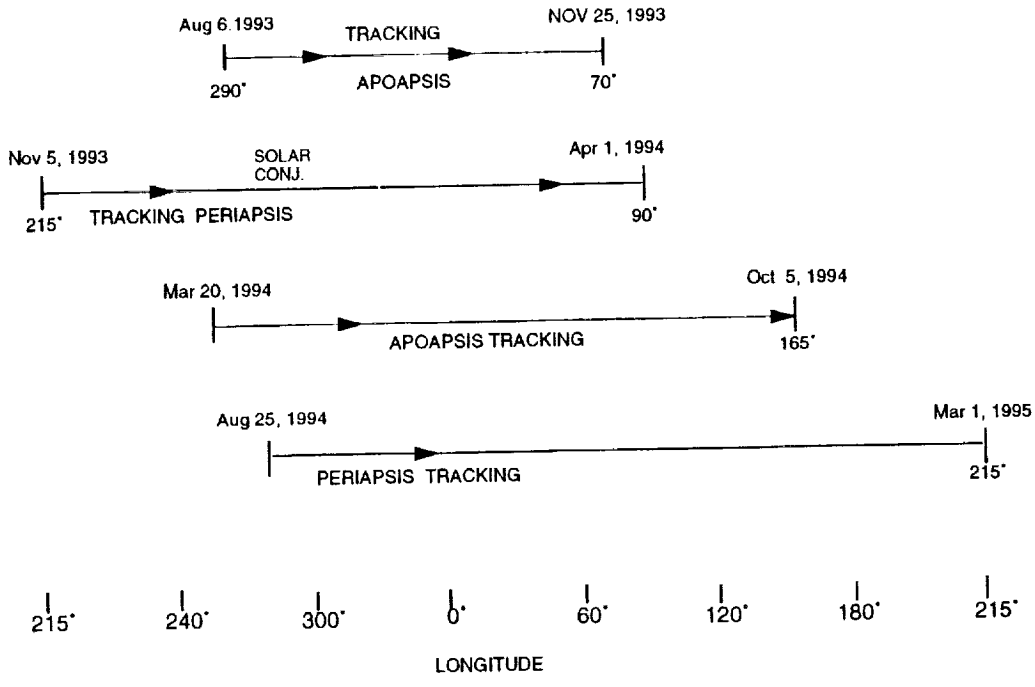

Figure 2 Maximum Gravity Data Coverage
Achievable in the near circular orbit
NOTE: considerable redundancy is obtained before 360° of longitude is covered.

PRE-ALLENDE PLANETESIMALS WITH REFRACTORY COMPOSITIONS: THE CAI CONNECTION. William R. Skinner, Department of Geology, Oberlin College, Oberlin, OH 44074-1044.

Refractory inclusions (also called calcium-aluminum-rich inclusions or CAI) are abundant in some carbonaceous chondrites, and at least some of them give evidence of complex histories that exceed a million years prior to their inclusion in those meteorites [1, 2]. CAIs also exhibit deformations and recrystallizations that are not recorded in the mixture of chondrules and matrix in which they now occur. The additional dynamical problem of preserving centimeter-sized objects for long periods of time in an active accretion disk [3], suggests that CAIs might have been stored in one or more larger objects prior to their inclusion in meteorite parent bodies. These observations, together with interpretations of textures and deformational structures observed in coarse-grained Allende CAIs, lead to the conclusion that these objects must have once resided in one or more pre-Allende planetesimals that probably had overall refractory composition(s). Furthermore, these CAIs, as small objects, have experienced at least two separate exposures to nebular gases: an early high-temperature exposure and a later low-temperature one. The textures and structures preserved in Allende CAIs reveal a sequence of events and environments which allows the reconstruction of their evolution. The evolutionary sequence developed here seems to be compatible with isotopic and geochemical data reported in the literature.

This paper presents a model of CAI evolution; it does not attempt to address the original formation of these objects or their precursor materials. The proposed model is based on physical (textural) evidence that very clearly defines a sequence of events -- that is, it outlines a history of the CAIs. It is essentially what G. J. Wasserburg has called "early solar system stratigraphy" based on the laws of superposition, intersection, and inclusion. The physical evidence also has implications for the environments associated with each event. The history of Allende CAIs can be modeled in several stages, beginning with the formation of objects up to centimeter-scale with highly refractory compositions. The complexities of their formation are not necessary to the following argument, but may be explored by reference to the literature (e.g., [4]).

Stage 1: During this stage, coarse-grained CAIs up to a centimeter or more in size were formed. The refractory nature of these objects and the slow cooling rates implied by their mineralogies and textures [5], as well as their extreme ages, suggest that this stage may represent an early, high temperature phase of nebular history [4]. For CAIs, this stage ended with their accretion into one or more planetesimals, producing large refractory objects and isolating the CAIs, by burial, from further reaction with nebular gases (including Fe and Mg which are major constituents of chondrules and meteorite matrix).

Stage 2: The refractory planetesimal(s) would have had to be more than a kilometer in diameter to survive in the solar accretion disk for more than a million years [3]. On the other hand, the planetesimal(s) could not have exceeded a few kilometers in diameter because Al-26 was still alive at this time [6] and would have produced melting and/or extensive recrystallization, giving rise to densely lithified rock in the planetesimal(s). Had this occurred, the integrity of mantled type B-1 CAIs would have been lost, and the occurrence of two or more type Bs welded together would be an expected result, but such compound objects have not been reported. More likely, there was weak lithification of the accreted material so that it easily broke up into the original objects (like a poorly cemented pebble conglomerate) when the planetesimal was disrupted. Direct evidence for this stage and the necessity to postulate a refractory planetesimal is found in deformation structures widely reported in type A and B CAIs. Kink banding in Allende CAIs as reported and illustrated by [7] is a deformation feature. Collision of centimeter-sized objects in the nebula would produce fragmentation, not internal kinking. This structure indicates that stress was applied while the objects were confined, i.e., buried within a planetesimal. This could not have been the Allende parent body, however, because the next stage in the evolution of these CAIs is a nebular one. The triple-junction mosaic textures noted in some coarse-grained CAI (e.g., by [7]) probably developed at this time as well. The mosaic textures I have observed in CAIs from Allende look like subgrains that formed from larger grains in response to stress, similar to those seen in many deformed quartz and feldspar grains in terrestrial rocks. Replacement textures associated with little or no evidence of an Al-26 signature [1] may have formed late in this planetesimal stage, or shortly after it, and may provide a means of estimating its duration. It is not yet clear whether low temperature alteration occurred during this stage or only during the following one. Stage 2 ended with the disruption of the refractory planetesimal(s).

Stage 3: Disruption of the refractory planetesimal(s) was probably due to one or more collisions that released whole CAIs and fragmental debris into a nebular environment that was now cooler than that in

which these refractory solids had formed. Recrystallization, neocrystallization, and low temperature alteration (metasomatism) may have occurred during this stage and/or during the disruption event that formed the transition from Stage 2 to Stage 3. A most important process associated with Stage 3 was the formation of thin Wark-Lovering rims on coarse-grained CAIs [8], probably during a transient heating event. This heating event may have been a fireball created by the collision(s) that destroyed the refractory planetesimal(s). The Wark-Lovering rims are ubiquitous and completely encase individual coarse-grained CAIs, except where they have been removed by later fracturing [8]. They formed on CAIs in the nebula before these objects acquired accretionary dust rims and before they were accreted onto the meteorite parent bodies, e.g., the Allende parent body [9]. The rims are not affected by the kinkbands that are found in some CAI interiors. Fine-grained CAIs which resemble fragmented refractory debris that was altered, surrounded, and cemented into aggregate masses by Wark-Lovering rim-like material [8] also probably formed at this time. Amoeboid olivine aggregates (AOAs) do not exhibit Wark-Lovering rims but were probably formed during this stage, possibly by condensation of olivine around refractory dust [10], perhaps released into the nebula by collisional disruption of refractory planetesimal(s).

Stage 4: Coarse-grained CAIs with Wark-Lovering rims, fragments of such objects, fine-grained CAIs, and AOAs were accreted and buried on the Allende parent body along with much larger proportions of chondrules and fine-grained matrix. Some minor low temperature alteration and fragmentation may have occurred during this stage.

Stage 5: Impact on the Allende parent body produced interplanetary debris, some of which became the Allende meteorite. The textures seen within the Allende meteorite probably do not record this stage in the sequence of events, and textural evidence of previous events was not affected.

How does the history of CAIs, as determined largely from those in Allende, relate to the general question of CAIs in chondritic meteorites? Allende and other CV chondrites are unusual in that they contain CAIs of greater maximum size than those found in other meteorites [4]. Also, the compositions and mineralogies of CAIs are not the same in different meteorites, e.g., the CAIs in Murchison, a CM chondrite, are smaller and more refractory than those in the CV group [11], and there is some variation among various CVs [12]. All, however, seem to have been subjected to the size sorting process that operated on chondrules [13].

It is not clear what determines the differences in CAI compositions among the various groups of chondrites. It may be related to disruption of planetesimals with different compositions that formed at different locations/times during Stage 1, or it may be related to some other process as yet undetermined. An important observation, however, is that CAIs are absent from CI chondrites, abundant in other carbonaceous chondrites, and rare in ordinary and enstatite chondrites. This suggests sudden influx of refractory material from one or more stochastic events, with carbonaceous chondrites (except for CIs) being especially close in time and location to those event(s).

I believe that the physical history developed here can assist in sorting out the chemical and isotopic complexities of refractory inclusions. Conversely, this physical model must be compatible with the chemical and isotopic characteristics of these objects if it is to survive as a useful construct. Theoretical studies of accretion and growth of refractory objects in the hot, early stages of the nebula and experimental studies on the production of kink-bands and other deformational structures in melilite would provide further insights into the conditions under which CAIs formed and evolved.

Acknowledgments: I wish to thank Pat Cassen, Jeff Cuzzi, Julie Paque, and Ted Bunch for their hospitality and for stimulating conversations at Ames Research Center that helped to develop these ideas.

References: [1] Podosek F. A. et al. (1991) *GCA 55*, 1083-1110. [2] MacPherson G. J. and Davis A. M. (1993) *GCA 57*, 231-243. [3] Weidenschilling S. J. (1977) *Mon. Not. Royal Astr. Soc. 180*, 57-70. [4] MacPherson G. J. et al. (1988) in Kerridge J. F. and Matthews M. S., *Meteorites and the Early Solar System*, 746-807. [5] Stolper E. and Paque J. M. (1986) *GCA 50*, 1785-1806. [6] Wasserburg G. J. and Papanastassiou D. A. (1982) in Barnes C. A. et al., *Essays in Nuclear Astrophysics*, 77-140. [7] Meeker G. P. et al. (1983) *GCA 47*, 707-721. [8] Wark D. A. and Lovering J. F. (1977) *Proc. LPSC 8*, 95-112. [9] MacPherson G. J. et al. (1985) *GCA 49*, 2267-2279. [10] Grossman L. and Steele I. M. (1976), *GCA 40*, 149-155. [11] Ekambaram V. et al. (1984) *GCA 48*, 2089-2105. [12] Sylvester P. J. et al. (1993) *GCA 57*, 3763-3784. [13] King T. V. V. and King E. A. (1978) *Meteoritics 13*, 47-72.

ROUNDING OF CHONDRULES BY ABRASION: A CAUTIONARY NOTE REGARDING TEXTURAL EVIDENCE. **William R. Skinner, Department of Geology, Oberlin College, Oberlin, OH 44074, and Harold C. Connolly Jr., Department of Geological Sciences, Rutgers University, New Brunswick, NJ 08903.**

It has been proposed by several investigators that significant numbers of chondrules in primitive meteorites have been rounded and/or reduced in size by the abrasion of their surfaces. We challenge some of the textural arguments used to support the concept that chondrules have been abraded. Specifically, we do not believe that the truncation of crystal outlines or compositional zoning of crystals by the surface margin of a chondrule is sufficient to prove that the surface was created by abrasion, because these truncation textures can be produced purely by crystallization of chondrule compositions in the laboratory.

The concept of chondrule abrasion was elaborated and proposed as a major process affecting a large proportion of chondrules by King and King [1]. Their Figure 2 illustrates the truncation of otherwise euhedral crystal shapes by the surface margins of chondrules as seen in thin section. They interpret this truncation as evidence that the chondrules, and the crystals within them, have been abraded. Kitamura and Watanabe [2], apparently unaware of this earlier study, used the same textural argument to demonstrate that chondrules, both lithic and droplet types, had been rounded by abrasion. They assigned chondrules to three major groups defined by surface characteristics and internal geometry. Their "Group C" includes chondrules with crystal outlines, and in some cases compositional zoning within crystals, that are truncated by the chondrule margin. Their Figure 3 includes several excellent photomicrographs illustrating this truncation. They report that the Group C chondrules make up a large proportion, in some cases more than half, of the chondrules in their unequilibrated chondrites, but that Group C chondrules do not occur in the equilibrated chondrites which they studied. Bunch, et al., [3] also illustrate the concept of abrasion of chondrules by drawing the hypothetical extensions of crystals truncated at the chondrule margin (see their Figure 3).

Abrasion of chondrules, if it occurs in the nebula, has important implications for chondrule number density (concentration) as well as for energy considerations. If abrasion occurs during accretion or within the regolith of a parent body, there are implications for process and energy as well. Thus if abrasion occurs at all, the process must be accommodated within models of chondrule formation and evolution, and the concept will influence the formulation of such models [4, 5].

The point we wish to emphasize is that chondrule textures that exhibit crystal outlines and zonation patterns truncated by a chondrule surface do not, of themselves, demonstrate that abrasion has occurred. Figures 1 and 2 shown here are synthetic chondrules that were produced by the junior author in the laboratory. In each of these figures it is clear that the olivine crystal outlines as well as the compositional zonation within them are truncated at the surface of the synthetic chondrule, *even though no abrasion has occurred.* The chondrule surfaces and the crystal morphologies shown here were solely determined by the bulk compositions and the heating and cooling histories of the two synthetic chondrules. This is not to say that such textures could not be produced by abrasion of larger objects, but it does clearly demonstrate that such textural relationships are not sufficient to prove abrasion. Where abrasion is proposed, additional arguments must be presented to support it, as was done, for example, by Bunch, et al. [3].

References: [1] King T. V. V. and King E. A. (1978) *Meteoritics 13*, 47-71. [2] Kitamura K. and Watanabe S. (1986) *Mem. NIPR, Spec. Issue 41*, 222-234. [3] Bunch T. E. et al. (1991) *Icarus 91*, 76-92. [4] Hewins R. H. (1989) *Proc. NIPR Symp. Antarctic Meteorites 2*, 200-220. [5] Hewins, R. H., personal communication, Aug. 1993.

ABRASION OF CHONDRULES: W. R. Skinner and H. C. Connolly, Jr.

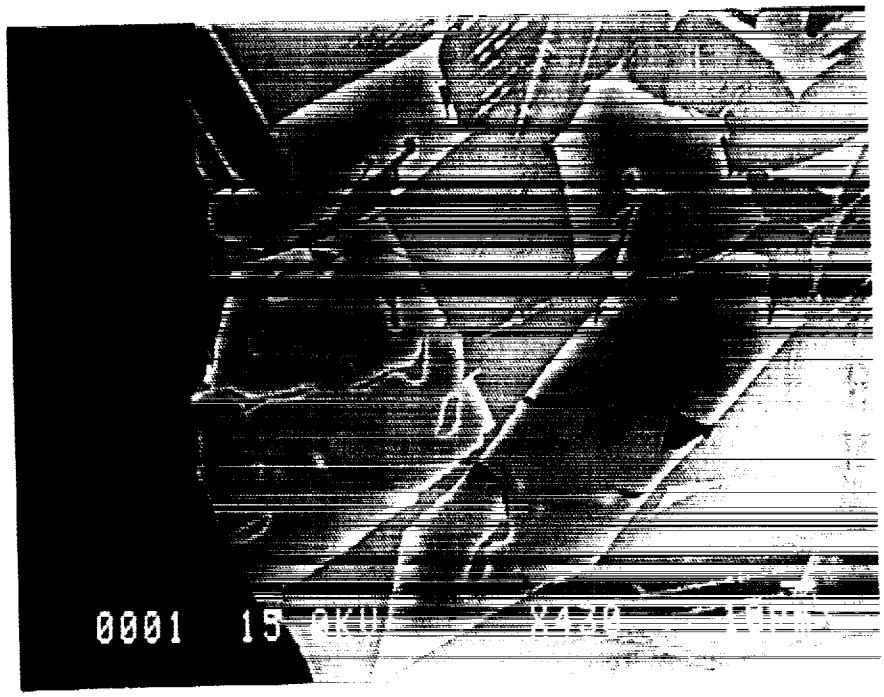

Figure 1. Compositionally zoned olivine crystals in a glassy mesostasis as grown in a synthetic charge. The large, almost euhedral crystal at the edge of the chondrule is truncated by the surface margin of the chondrule, as is the compositional zoning within the crystal. (Backscattered electron image.)

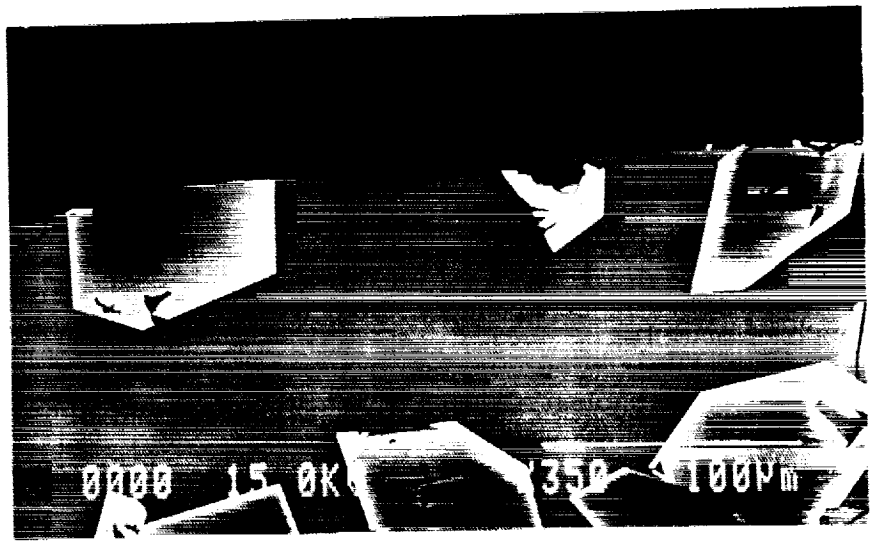

Figure 2. Compositionally zoned olivine crystals in a glassy mesostasis as grown in a synthetic charge. Note that the otherwise euhedral crystals are truncated by the margin of the chondrule. The compositional zoning in these crystals is truncated as well. (Backscattered electron image.)

ACCESS TO LARGE PLANETARY SCIENCE DATA BASES; S. Slavney, T. Stein, and R.E. Arvidson, McDonnell Center for the Space Sciences, Earth and Planetary Sciences Department, Washington University, St. Louis, MO 63130

Technological advances in recent years have made it possible for planetary missions such as Magellan to generate datasets of many gigabytes in size. Upcoming missions will result in equivalent data volumes. Cost-effective archiving and timely distribution of such large data bases require careful planning based on an understanding of the demand for the data. A large dataset for which there is great demand, such as the Magellan MIDRs (Mosaicked Image Data Records), is a good candidate for distribution on CD-ROMs, each disk being sent directly from the factory to a list of subscribers as soon as it is produced. On the other hand, a high-volume dataset that is only occasionally in demand can be stored on write-once compact discs (CD-WOs) and distributed electronically upon request. In this abstract we illustrate an approach to distributing Magellan F-BIDR (Full Resolution Basic Image Data Record) products based on the latter model.

The Magellan F-BIDR dataset consists of several thousand individual products ranging in size from 20 to about 140 megabytes. The original products are stored on 9-track tapes. In order to preserve the dataset on a more stable medium, and at the same time make it accessible to the science community, the Planetary Data System (PDS) Geosciences Node at Washington University is currently working to transfer the complete Magellan F-BIDR dataset to CD-WOs. Two copies are made of each CD-WO volume, one of which is sent to the National Space Science Data Center for deep archive. The other is kept at Washington University where it can be made available upon request for electronic file transfer over the Internet. The process of ordering data products is automated using a system of three Kodak Professional PCD CD-ROM jukeboxes, each holding 100 disks, accessed through the Magellan Standard Products Catalog based on the Sybase relational data base management software. The catalog enables the user to select products based on location, time, orbit, product ID, and Magellan Experimenter's Notebook parameters. The catalog currently contains information for Magellan data from Cycle 1, and by the end of January 1994 will include information for Cycles 2 and 3 and for gravity data from Cycle 4. Users may place orders for selected products electronically, and may choose to have them delivered via FTP (File Transfer Protocol) over the Internet. The viability of electronic delivery has been demonstrated by experiments conducted with Rand Corporation and Stanford University. Results show that this method is reliable and reasonably fast; as of December 1, 1993, a total of 1690 products (over 93 gigabytes) had been transferred with an average rate of 5 megabytes per minute during the day and 10 megabytes per minute at night, with no loss of data.

The Geosciences Node and the PDS Image Node are currently planning a similar approach to archive and distribute data from the Clementine mission. Clementine's 3.5 million images of the lunar surface and the asteroid Geographos will be stored on CD-WOs and made accessible on the Internet via an electronic catalog.

THE TOPOGRAPHY OF MARS: A RE-EVALUATION OF CURRENT DATA; *D.E. Smith*[1], and *M.T. Zuber*[2,1], [1]Laboratory for Terrestrial Physics, NASA/Goddard Space Flight Center, Greenbelt, MD 20771, [2]Dept. of Earth and Planetary Sciences, Johns Hopkins University, Baltimore, MD 21218.

Our present knowledge of the topography of Mars is completely inadequate for addressing a wide range of geophysical, geological, and atmospheric problems. The data acquired to date by several techniques has not provided us with reliable and consistent values for even the equatorial and polar radii and large uncertainties exist in the altitudes of many of the major volcanic constructs. While much of this can be blamed on a lack of reliable data, we feel that much more could be done to improve the analysis of the present data in a consistent global system that would necessarily involve the re-analysis of early spacecraft and Earth-based data in conjunction with more recent models of Mars' gravity field.

Current topographic knowledge of Mars is based entirely on measurements obtained by the early Mariner and Viking spacecraft and on Earth-based radar measurements [1-4]. Radio occultation measurements of the Mariner 9 spacecraft and the Viking 1 and 2 Orbiters are the primary near-global data sets. The principle behind these observations is that knowledge of the time when the signal from a spacecraft is "lost" behind the planet can be used (in conjunction with knowledge of the position of the spacecraft and the planet) to estimate the radius of the planet at the time of occultation. These data have formed the basis of several determinations of global Mars topography [3,5,6] but only about 400 measurements from the primary and extended phases of these missions are available. The principal sources of error in these data are the spacecraft position [4] at the km level, the timing of the actual loss of signal at the hundreds of msecs of time (~1 km) and the actual location of the grazing ray at the time of occultation due to local topography [1]. Depending on the orbital radius of the spacecraft at the time of occultation, the geometry of the spacecraft and planet, and the topography of the limb, these errors can amount to several kilometers in the planetary radius, although this is often not the case. The effect of refraction through the 6 mbar atmosphere contributes up to a maximum of a few tens of meters to the error in radius, even if neglected completely. Figure 1 shows how 300 Mariner 9 and Viking orbiter occultation measurements [1,4] are distributed across the planet, ranging in latitude between approx. 75N and S and spread across all longitudes. If these data were uniformly distributed across the planet they would have a mean separation of approximately 800 km, equivalent to a spherical harmonic representation of degree and order 17. Even if each value only had an accuracy of only 1 km, the basic shape of the planet at the sub-kilometer level would not be in doubt and the mean equatorial planetary radius known to a few hundred meters even in the absence of other data.

The Earth-based radar data [7,8] provide a direct measure of the distance to the surface of the planet from Earth and by inference of the planetary surface from its center. The measurement is the distance to the point on the surface normal to the incoming wave and has a resolution of 10 to 30 km in longitude and 80 to 120 km in latitude, depending the distance of Mars from Earth and on transmitter power [8]. Because of the limitations in the variation in geometry of the orbit of Mars and its spin axis direction from Earth, radar observations are generally limited to 25 degrees of the Mars equator. A typical observation period will produce radar returns from a strip of almost constant latitude [7] with a range precision of better than 100 meters. The primary source of error appears to be the planetary ephemeris which was thought to be at the kilometer level in the late seventies and early eighties when most of the calculations of Mars topography were performed. This error is of particular significance for estimating the global scale topography and must be accounted for when combining radar data with occultation data by the estimation of biases or adjustments to the ephemeris directly. At a lesser level are errors introduced by the solar plasma, which depend on the radar frequency, and are typically at the tens of meters level. The radar data are an orthogonal data set to the occultation data and together provide the strongest measurements of the global shape of Mars.

The third data set that has been used in deriving the global topography is from the infrared and ultraviolet sensors on the Mariner 6, 7 and 9 spacecraft [9-12]. These sensors provided data about the total atmospheric column content of carbon dioxide thus enabling the topography of the planet's surface to be inferred with respect to an equipotential surface (usually the 6.1 mbar surface) based upon a model of the atmosphere. The instrumental precision of the measurements for a clear atmosphere is probably equivalent to a few hundred meters in altitude above the reference surface [9] with a spatial resolution of a 10x30 kilometers for the UV measurements and 125x125 kilometers for the IR. Over thirty thousand measurements were obtained globally by Mariner 9 [11,12]. Systematic effects arising from assumptions about the atmosphere and its constancy over space and time introduce much larger errors on a global scale thus making the measurements of greater value in some local region but limited in their ability to provide geodetic control on a planetary scale. Further, these measurements only provide altitude

deviations from the reference surface and are unable to independently describe the planet in terms of areocentric radii. In contrast to these data providing strong information about the shape of Mars, it is clear [B. Jakosky, pers. comm.] that an improved topographic model would make the atmospheric data from these instruments even more valuable. More recently the infrared spectrometer on board the Phobos spacecraft obtained nine spectral images of Mars [13]. From the measurement of carbon dioxide absorption, topographic data of 150 meter quality has been derived for certain local regions. These results show some systematic differences with both radar and the occultation data at the few hundred meter level and suggest more major discrepancies for the altitudes of some of the major volcanoes which are not easily observed at their peaks by either the occultation or Earth based radar. The most significant limitation of all these instrumental observations is that they are all referenced to the 6.1 mbar surface and therefore are not providing any topographic information on planetary scales of a 1000 km or larger.

On regional and local scales photogrammetric techniques have been used extensively to derive the topography [6,14-18]. Photogrammetry provides precise detailed information on a local level that requires little or no long wavelength control. However, its obvious strength at local scales is its inherent weakness on the planetary scale and, indeed, in nearly all global models the photogrammetric results have been treated as detail that is added to the long wavelength geodetic control provided by other data, usually occultation and radar. Thus, issues of compensation and isostasy are difficult or impossible to address with the photo data and little progress has been made in this respect for over a decade. A further limitation is the lack of validity of the reference areoid on all medium and shorter length scales. Even the most recent models of the gravity field of Mars [19] contain only minimal information at wavelengths less than 500 km. Thus, even regional problems requiring slope information with respect to the areoid cannot be reliably addressed. Further discussion of Mars topography and its limitations can be found in [20-23].

It is our opinion that all the data that contribute to our knowledge of Mars topography should be re-analyzed. This would include the occultation data, which would benefit from significantly improved orbits for the spacecraft now available, the Earth-based radar data, the incorporation of improved global gravity models [19] and planetary ephemerides, the application of *a priori* information based on the present topographic models, the use of consistent and improved reference models and parameters of the planetary coordinate system, incorporation of lander atmospheric data and position, and the application of computing techniques and facilities not available a decade ago. We might then be reasonably sure of the extent to which our ignorance of Mars topography is limited by the data.

Fig.1 Mariner 9, Viking 1 & 2 Orbiter Occultation Data

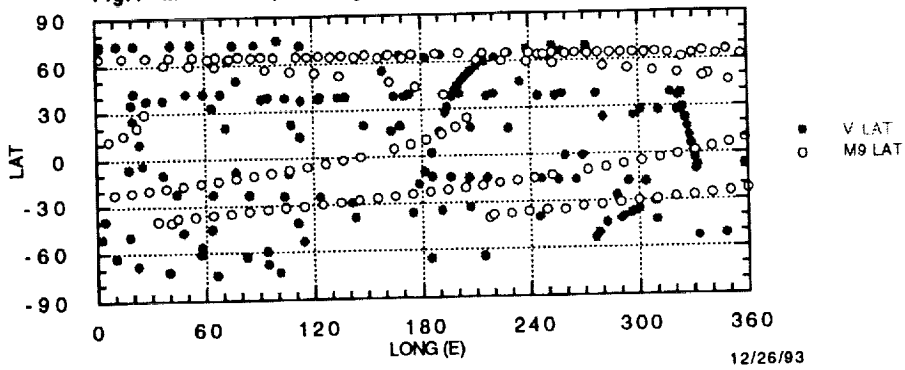

References: [1]Kliore, A.J. et al. (1972) *Icarus, 17,* 484. [2]Kliore, A.J. et al (1973). [3]Christensen, E. (1975) *JGR.,78,* 4411. [4]Lindal, G.F. et al. (1979) *JGR,* 8443. [5]Wu, S.S.C. (1977) *XV International Congr Surveyors, Comm.. V* Stockholm, Sweden. [6]Bills, B.G. and A.J. Ferrari, (1978) *JGR,83,* 3 497.[7]Roth et al., (1980) *Icarus, 42,* 287. [8]Downs et al, (1982) *JGR, 87,* 9747.[9]Herr, et al., (1970) *Astron. J., 75,* 883. [10]Barth, and Hord, (1971) *Science, 173,* 197. [11]Hord, et al, (1972) *Icarus, 17,* 443. [12]Hord, et al, (1974) *Icarus, 21,* 292. [13]Sotin, C. et al (1992) *LPSC, XX111,* 1335, LPI, Houston. [14] Blasius, K.R. (1973) *JGR, 78,* 4411, [15]Wu, S.S.C. (1978) *Icarus, 33,* 417. [16]Wu, S.S.C. (1979) *JGR, 84,* 7955. [17]Blasius, K.R. and J.A. Cutts, (1981) *Icarus, 45,* 87. [18]Davis, P.A. and L. Soderblom, (1984) *JGR, 89,* 9449. [19]Smith, D.E. et al (1993) *JGR, 98,* 20,871. [20]Zuber, M.T. et al. (1992) *JGR, 97,* 7781. [21]Esposito, P.B. et al (1992) in *Mars,* Kieffer et al,(edit), Univ. Ariz. Press. [22]Banerdt, W.B. et al (1992)in *Mars,* Kieffer et al,(edit), Univ. Ariz. Press. [23]Davies, M.E. et al. (1992) in *Mars,* Kieffer et al,(edit), Univ. Ariz. Press.

THE MASS OF MARS, PHOBOS, AND DEIMOS, FROM THE ANALYSIS OF THE MARINER 9 AND VIKING ORBITER TRACKING DATA;

D.E. Smith[1], *F.G. Lemoine*[1,2], and *S.K. Fricke*[3] [1]Laboratory for Terrestrial Physics, NASA/Goddard Space Flight Center, [2]Astronomy Department, University of Maryland, College Park, MD 20742, [3]RMS Technologies Inc., Landover, MD 20706.

We have estimated the mass of Phobos, Deimos and Mars using the Viking Orbiter and Mariner 9 tracking data. We divided the data into 282 arcs, and sorted the data by periapse height, by inclination and by satellite. The data were processed with the GEODYN/SOLVE orbit determination programs, which have previously been used to analyze planetary tracking data[1,2]. The *a priori* Mars gravity field applied in this study was the 50th degree and order GMM-1 (Goddard Mars Model-1) model [2]. The subsets of data were further carefully edited to remove any arcs with close encounters of less than 500 km with either Phobos or Deimos. Whereas previous investigators have used close flybys (less than 500 km) to estimate the satellite masses[3-6], we have attempted to estimate the masses of Phobos and Deimos from multiday arcs which only included more distant encounters. The subsets of data were further edited to eliminate spurious data near solar conjunction (November-December 1976, and January 1979). In addition, the Viking-1 data from October through December 1978 were also excluded because of the low periapse altitude (as low as 232 km) and thus high sensitivity to atmospheric drag.

During the Mariner 9 mission, the majority of Phobos flybys were at distances of 3,750 to 4,500 km whereas the Deimos flyby distances averaged 5,500 to 7,000 km. In contrast, the flyby distances between Viking 1 and Phobos ranged mostly from 1,000 to 4,000 km, whereas the encounter distances between Viking-1 and Deimos ranged mostly from 6,000 to 13,000 km. Nevertheless, during 17 arcs (out of approximately 150 arcs), the flyby distance between VO-1 and Deimos reached 1,000 to 5,000 km. Our solutions indicate that the Viking Orbiter 2 arcs at 300 km periapse altitude are only weakly sensitive to both Phobos and Deimos, an apparent consequence of a poor flyby geometry, and large residual signals from both Mars gravity and atmospheric drag.

In units of km^3/s^2, we find that the *GM*, or universal constant of gravitation multiplied by the planet or satellite mass, for Mars, Phobos, and Deimos are:

Satellite & Periapse Ht.	Mars (km^3/s^2)	Phobos (10^{-3} km^3/s^2)	Deimos (10^{-3} km^3/s^2)
VO-1 1500 km (30 arcs)	42828.40205 ± 0.052	0.539 ± 0.046	0.061 ± 0.072
Mariner 9 (32 arcs)	42829.30448 ± 0.57	0.562 ± 0.065	0.157 ± 0.109
VO-2 1500 km, 55 deg inclin., (12 arcs)	42820.93202 ± 31.04	0.696 ± 0.095	0.046 ± 0.285
VO-2 1500 km, 75 deg inclin., (6 arcs)	42787.98356 ± 21.37	0.619 ± 0.306	1.282 ± 0.646
VO-2 800 km (51 arcs)	42832.05436 ± 4.85	0.770 ± 0.581	0.103 ± 0.291
VO-1 300 km (81 arcs)	42828.23235 ± 0.071	1.172 ± 0.871	1.053 ± 0.859

The Viking-1 spacecraft dominates the determination of the Mars *GM* because of the tight standard deviations. The solutions from the Viking-1 300 km, and Viking-1 1500 km data are close to those found by Null [7] from the Mariner 4 hyperbolic flyby of 42828.32 ± 0.13 km^3/s^2 and Anderson et al. [8] from the Mariner 6 Mars hyperbolic flyby of 42828.22 ± 1.83 km^3/s^2. The Mariner 9 data manifests a large bias in the Mars *GM* estimate with respect to the values from Null [7] and the Viking-1 Orbiter estimates. We believe this bias may be an artifact of an as yet unidentified force or measurement modeling error associated with the Mariner 9 Doppler data.

It is interesting that the subset solutions utilizing the distant encounters yield estimates of the Phobos *GM* reasonably close to the published values from Christensen et al. [3] of (0.66 ± 0.08) 10^{-3} km^3/s^2, and from Koluyka et al. [6] of (0.722 ± 0.005) 10^{-3} km^3/s^2. Using the Phobos volume estimate of 5,680 ± 250 km^3 from Duxbury [9], our high altitude periapse Phobos *GM* estimates yield a density ranging from 1.42 to 1.83 g/cm^3. The solutions for Deimos from the distant encounters are intrinsically weaker. If the data from the high altitude (1500 km and 800 km periapse orbits) are combined we obtain a Deimos *GM* of (0.076 ± 0.055) 10^{-3} km^3/s^2. Conversion of this *GM* to an estimate of satellite density is more problematical given the large uncertainty in the estimate for the volume of this satellite [9]. This estimate agrees with the value of (0.12 ± 0.01) 10^{-3} km^3/s^2 from the close flybys [4,5]. Nevertheless, we find that analysis of the distant encounters provides more robust estimates of the Phobos *GM* than the Deimos *GM*.. We also find that the estimates for the *GM* of Mars are largely uncorrelated with the *GM* 's for the natural satellites, since the satellite values change minimally whether or not the Mars *GM* is adjusted in any of the subset solutions.

References: [1]Nerem et al., (1993), *GRL* 20, 599. [2]Smith et al., (1993), *JGR-Planets* , 98, 20871. [3]Christensen et al., (1977), *GRL* 4, 555. [4]Hildebrand et al., (1979), *Natural and Artificial Satellite Motion,* The Univ. of Texas Press. [5] Williams et al., (1981), *AGU Abstract G21-A-11* , San Francisco. [6] Koluyka et al., (1991) *Planet Space Sci.,* 39, 355. [7] Null, G.W., (1969), *Bull. Amer. Astron. Soc..*, 1, 356. [8] Anderson, J.D. et al., (1970), *Science,* 167, 277. [9] Duxbury (1991), *Planet. Space Sci.,* 39, 355.

omit to P.1345

THE IMAGER FOR MESUR PATHFINDER (IMP). P.H. Smith, D.T. Britt, L.R. Doose, R.B. Singer, M.G. Tomasko (LPL), F. Gliem (TUB, Germany), H.U. Keller (MPAE, Germany), J.M. Knudsen (Orsted Institute, Denmark), L.A. Soderblom (USGS).

The Imager for MESUR Pathfinder (IMP) team under Peter H. Smith (PI) was selected in May 1993 after a NASA AO selection process to provide the imaging system for the MESUR Pathfinder Mars lander. The IMP instrument, shown in **Figure 1**, is a binocular CCD-based imager with a 12-position filter wheel and full azimuth/elevation pointablity. Design characteristics of the camera are shown in **Table 1** and for comparison the corresponding characteristics of the Viking Lander Camera system are also listed. The IMP team has five major science objects for imaging on the Martian surface: (1) Map the morphology of MESUR Pathfinder landing site. (2) Determine the mineralogy of the exposed crustal rocks and the mineralogy of the weathering products in the soil, dust, and on the surface of the rocks. (3) Study the time-variable phenomena observable at the landing site including imaging cloud formations, wind velocity and direction (by imaging a calibrated "wind-sock"), frost, and the formation of eolian features. (4) The study of the properties of the Martian atmosphere including measurement of the quantity of atmospheric water vapor and the quantity and size distribution of atmospheric dust. (5) Study the magnetic properties of the Martian dust by multispectral imaging of dust accumulations on or more magnetic arrays.

IMP Geological Investigations: The capabilities of the IMP system allow for a broad range of science investigations on the Martian surface. Panoramas of the landing site will be taken both before and after the camera mast deployment. These images will map the landing site for rover operations, as well as study the large-and small-scale structure of the landing site, rock and dune features, and any erosional features. Additional images will be taken to study time variable phenomena as discussed above, as well as rover track marks and the settling of dust on the lander. Filter-wheel spectral mapping using eight filters spanning 0.45 to 1.0 μm will determine the compositional variation of the landing site and identify mineralogical units as targets for further investigation using the rover-based Alpha/Proton/X-ray spectrometer. Spectral mapping will also study weathering processes and products in the dust, soil, and rock. Tests have been done at LPL with commerical filters and a testbed CCD camera to demonstrate the ability of the IMP bandpasses to distinguish the diagnostic spectral features of minerals in Martian analog material. Nighttime multispectral observations of Phobos and Deimos can enhance the limited spectral data available on these small moons. Included in the instrument package is J.M. Knudsen's magnetic properties experiment that will use several arrays of magnets of differing strengths to collect different magnetic minerals in the Martian airborne dust. Spectral images of the accumulated dust on the magnets will should provide diagnostic mineralogical identification of these magnetic species.

IMP Atmospheric Investigations: IMP is also designed for a number of significant atmospheric studies. Atmospheric water vapor will be measured by ratioing solar images through two narrow band filters, one at the 0.935 μm water band and one on the continuum at 0.925 μm. Additional solar images using ratios of narrow band filters at 0.45 and 0.925 μm will provide data on the size distribution and quantity of atmospheric dust. These measurements will be made at a number of airmasses from zenith to horizon to provide an hourly history of water vapor, dust loading, and particle size variability for each day of the Pathfinder mission. The 8 geology filters can be used to take multispectral sky images for several applications. Sky brightness measured at various angles from the Sun at multiple wavelengths can determine atmospheric particle size and shape. As the sun sets illumination is restricted to progressively higher zones in the atmosphere and a series of multispectral sky brightness measurements can give us a picture of the vertical structure of the aerosols in the Martian atmosphere. Finally multispectral measurements of Phobos and its aureole can detect nighttime condensation and early morning fogs. Another atmospheric experiment images several "wind socks" giving to estimates of wind direction and velocity at various heights from the surface to 1.5 meters.

Figure 1: Cutaway drawing of the IMP camera.

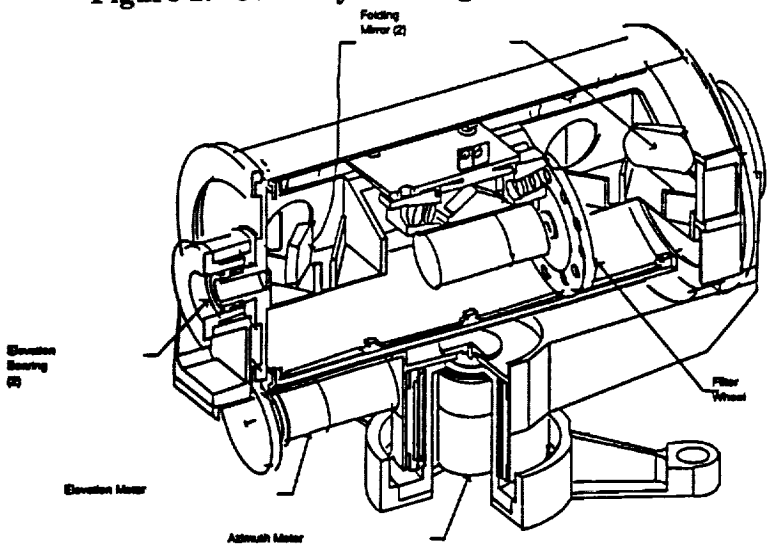

Table 1: Comparison of IMP and Viking Lander Cameras

	IMP	VIKING
Filter set	8 filters - 40 nm FWHM, standard filters	6 filters - 100nm, >20% leakage
Calibration	1 % relative 5% absolute	Loss of calibration: Autoclave (113°C) RTG neutrons
Solar filters	3: 450, 925, 935 nm, NB (5nm), measure water and dust	1: red, no pre-amp, dust only
Stereo	Broadband only, 15 cm horiz., 86 cm vertical. Complete field	All filters, 80 cm horiz., limited field
Height above surface	1.5 meters	1.3 meters
FOV	IFOV = 0.057° Frame = 14.4°x14.4°	B&W = 0.04°, Color = 0.12° Line scan
Depth of focus	0.65m to ∞	1.7 m to ∞
Exposure time/pixel	1 msec - 32 sec, 200 msec typical	fast = 0.4 msec, slow = 25 msec
Pointing	Altitude: -79° to +90° Azimuth: 0° to 360°	Altitude: -60° to +32° Azimuth: 2.5° to 342.5°
Data compression	JPEG and Rice	none
Detector	Loral CCD, 512x512 pixels, frame transfer, 23x23 μm pixels includes 6x23 μm anti-blooming well	12 Si photodiodes
Mass	3 Kg	2*7.3 Kg
Power	Standby 1.7W Motor drive 3W Image acquisition 2.6W	Standby 22W Motor drive 111W Image acquisition 34W
Bits/pixel	12	6
Cost	$5 million, 1992US$	$27 million, 1975 US$
Calibration targets	Radiometric, wind vector, magnetic properties	Radiometric, magnetic properties (limited usefulness: saturated)
Data rate (bits/sec)	175-700 Earth	16K relay, 250 Earth
Development time	2 yr	4 yr

INTERPRETATION OF MAGELLAN GRAVITY DATA FOR LARGE VOLCANIC SWELLS ON VENUS: IMPLICATIONS FOR INTERIOR STRUCTURE; Suzanne E. Smrekar, California Institute of Technology, Jet Propulsion Laboratory, Pasadena, CA, 91109.

Introduction. Numerous large volcanic swells on Venus have been interpreted as likely sites of mantle upwelling, or hotspots [e.g. 1,2]. In the absence of terrestrial-style spreading ridges, these swells provide one of the most conspicuous manifestations of mantle heat loss. As such they offer important information about the thermal history of Venus. In this study I use Magellan line-of-site (LOS) gravity data to investigate the interior structure beneath two large volcanic swells: Atla and Bell Regiones. Initial interpretation of the admittance spectra (the ratio of the gravity to the topography in the Fourier transform domain) in these areas shows that flexural compensation is important in both regions. Although absolute values of the effective elastic thickness, Te, are not well determined, the elastic thickness appears to be smaller at short wavelengths than at long wavelengths in both areas. This is consistent with thinning beneath the large volcanic edifices, which load the plate at wavelengths shorter than those of the broad topographic swells. A thinned plate further suggests that a thermal perturbation, presumably due to a mantle plume, is (or was once) located beneath the swells.

Data Analysis. To facilitate forward modeling and interpretation, I employ a linearized, least-squares approach to invert the LOS data to obtain a vertical gravity field [3]. The vertical gravity field is used to produce admittance (Figures 1 and 2). As the interpretation of gravity data alone is non-unique, the admittance is compared to three different models: Airy (or crustal) compensation, flexure plus Airy compensation, and a hotspot compensation model. The hotspot model [4] assumes that the crust and elastic plate are loaded from above at short wavelengths by a volcanic edifice (or edifices), and that a deep thermal anomaly loads the crust and elastic plate from below at wavelengths comparable to that of the swell. Thus the hotspot model differs from the flexure model in that it assumes a specific loading scenario and it includes a second compensation depth, referred to as the swell compensation depth, in addition to the crust-mantle boundary.

Results. Airy compensation does not provide a good fit to the admittance spectra at Bell and Atla Regiones. The Airy compensation depth varies from 5 to 50 km at Bell Regio. At Atla Regio the longer wavelength data are fit by Airy compensation depths of 50-100 km; Airy compensation does not fit the shorter wavelength data. When flexural compensation is included, the longer wavelengths are still isostatically compensated. The vertical position of the model curve is controlled by the Airy compensation depth. Loading of the elastic plate controls the shape of the model curve at shorter wavelengths; loading from above or below the plate produces a very different admittance curve [5]. When the longest wavelength value of the spectrum at Bell Regio is fit with a crustal compensation depth of 50 km, the short wavelength part of the spectrum gives $T_e = 35 \pm 5$ km and a ratio of bottom to top loading of 2 (Fig. 1a). Since the long wavelength portion of the admittance spectrum does not fit a single Airy compensation depth, the vertical position of the model curve is not well constrained. Thus a model with a thinner crust, a thinner elastic plate, and top loading alone will also fit the data. At Atla Regio, the best fitting depth of Airy compensation at long wavelengths is 110 km (Fig. 1b). The short wavelengths require dominantly bottom loading with $T_e = 80 \pm 5$ km. The best fitting hotspot model at Bell Regio has a short wavelength T_e = 5-15 km and a long wavelength value of 50 km, with a swell compensation depth of 100-150 km (Fig. 2a). Since the crustal thickness is unknown and the thickness of the crust and swell compensation depth trade off, I assume a crustal thickness in the range of 10-50 km and find a corresponding range of swell compensation depth. A swell compensation depth of 100-175 km with $T_e = 30$ km fits most of the spectrum at Atla Regio (Fig. 2b). The shortest wavelength admittance value is consistent with top loading and $Te \leq 20$ km.

Discussion. Modeling of the admittance spectra at Bell and Atla Regiones shows that Airy compensation at a single depth is unlikely. Flexural compensation is evident in both areas. In the absence of the additional constraints, it is difficult to accurately determine the absolute value of T_e. Both the flexure and hotspot models provide a reasonable fit to the data at Bell and Atla Regiones. The hotspot model is preferred at Atla Regio, since a crustal compensation depth of 110 km is implausible for Venus. As a crustal thickness of 50 km is at least plausible, the choice of hotspot vs. flexure models at Bell Regio is less clear. The long wavelength portion of the hotspot model

is poorly determined (with only two data points), yet it does provide a better fit to the data than the flexure model. If we make the case that the hotspot model is most appropriate at Bell Regio as well as at Atla Regio, T_e at short wavelengths is somewhat less than that for long wavelengths (5-35 km vs. 50 km at Bell and <20 km vs. 30 km at Atla). This interpretation implies possible local thinning of the elastic plate beneath the volcanos and the presence of a thermal anomaly. Further work is underway to improve estimates of T_e and to include additional hotspots in this study.

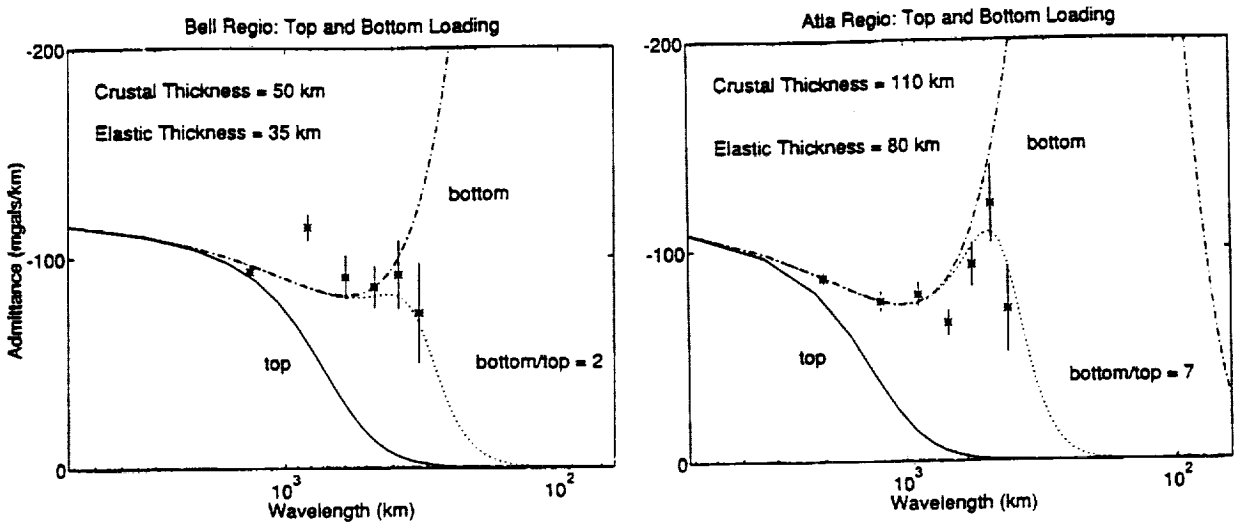

Figure 1. Admittance spectra calculated from the Bouger gravity and topography for (a) Bell and (b) Atla Regiones with combined crustal and flexural compensation models. Solid lines are for top loading only, dash-dot lines are for bottom loading only, and dotted lines are for a models with both bottom and top loading.

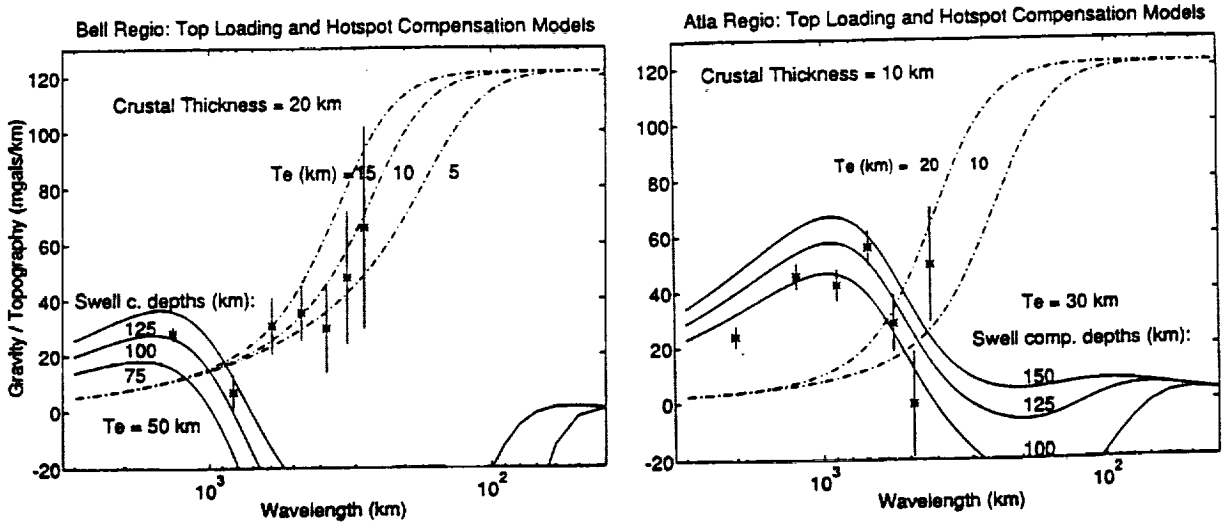

Figure 2. Admittance spectra calculated from the free air gravity and topography for (a) Bell and (b) Atla Regiones with hotspot compensation models. Dash-dot lines are for top loading only, and solid lines are for swell compensation depths. Note that the best fitting effective elastic thickness at short and long wavelengths differs.

References. [1] S.C. Solomon et al., *JGR, 97*, 13,199, 1992; [2] S.E. Smrekar and R.J. Phillips, *EPSL, 107*, 582, 1991; [3] R.E. Grimm and R.J. Phillips, *JGR, 93*, 11,911, 1988; [4] M.K. McNutt and L. Shure, *JGR, 91*, 13915, 1986; [5] D.W. Forsyth, *JGR, 90*, 12,623, 1985.

THE STATUS OF MERCURY EXPLORATION W. Smythe, R. Lopes-Gautier, A. Ocampo, R. Nelson (Jet Propulsion Laboratory, California Institute of Technology, Pasadena, CA 91109).

Mercury's proximity to the Sun has inhibited the number and diversity of Earth-based observations, which makes its exploration by planetary probes particularly important. In spite of this, Mercury is among the few solar system bodies which has been visited only once. Mercury's position as an end member of the solar system makes knowledge of its evolution particularly relevant to solar system studies. This paper discusses the scientific issues which need to be addressed by missions which follow Mariner 10.

The highest priority observational objectives for next Mercury missions include (i) completion of the surface mapping started by Mariner 10; (ii) acquire the stereo coverage and photometric dataset necessary for deriving the surface topography; (iii) mapping the planet's magnetic and gravity fields; (iv) searching for the presence of iron in surface materials. Additional desirable objectives include (i) measuring bulk composition and mineralogy of surface materials; (ii) verifying the suggested presence of ice on the pole [1]; and (iii) measuring the structure of the tenuous atmosphere.

Mariner 10 mapped approximately half the planet during two fly-bys utilizing a vidicon camera. The instrument package also included an infrared radiometer, an airglow ultraviolet spectrometer, and a fields and particle package. The spacecraft trajectory's geometry prevented good phase angle and stereo coverage of the surface and detailed mapping of the magnetic and gravity fields. The spectral range of the instrument package was not suited for determining the presence of iron in surface materials. Difficulties with temperature control and linearity in the vidicon camera limited the photometric studies of the surface.

Studies by Chen-wan Yen [2] have shown that it is feasible to mount both orbital and fly-by missions to Mercury using modest launch vehicles having payload capacities which can complete and enhance the survey initiated by Mariner 10. This makes Mercury a prime candidate for near-term exploration within the resources expected to be available within NASA's planetary program.

REFERENCES: [1] Butler, B.J., Muhleman, D.O., and Slade, M.A. (1993): J. Geophys. Res. 98, E8, 15,003-15,023. [2] Belcher, J.W. et.al. (1991): Mercury Orbiter: Report of the Science Working Team, NASA Tech. Mem. 4255, 136pp.

A SORTIE FOR PRISTINE ROCKS AT MARE TRANQUILLITATIS: A FERROAN ANORTHOSITE, A NEW GROUP D BASALT, AND THE ISOTOPIC COMPOSITION OF GROUP D HIGH-Ti BASALTS

Gregory A. Snyder, Eric A. Jerde, Lawrence A. Taylor, Der-Chuen Lee*, and Alex N. Halliday*, Planetary Geosciences Institute, Dept. of Geological Sciences, University of Tennessee, Knoxville, TN 37996-1410; *Dept. of Geological Sciences, University of Michigan, Ann Arbor, MI 48109.

Mare basalts comprise only a small fraction of the rocks found at the Moon's surface. However, the study of these basalts is of paramount importance to an understanding of the evolution of the mantle of the Moon. The high-Ti basalts at the Mare Tranquillitatis have provided important constraints on the mineralogy, chemistry, and depth of upper mantle cumulate sources. Previous studies have delineated five separate basalt groups at Mare Tranquillitatis, including the rare Group Ds [1,2]. This group is represented by only a few small 2-4 mm samples, but is crucial in advancing our knowledge of those basalts which contain significant whitlockite (0.2-0.8 wt.%) and, yet, may represent the inititiation of extrusive activity at Mare Tranquillitatis. Therefore, we have undertaken a sortie of 2-4 mm fragments from several other soils at the Apollo 11 landing site in the hope of uncovering other pristine basaltic rocks (possibly even some more group Ds). The first of three sets of analyses (of 12 rock fragments each) are presented in this abstract and do, indeed, include one "new" Group D high-Ti basalt. This proposed Group D basalt was then analyzed for its Nd and Sr isotopic composition, along with one other known group D basalt. Both Group D rocks indicate time-averaged LREE-enrichment (Sm/Nd decrease) when compared to other low-K high-Ti basalts. This enrichment is interpreted as being due to the earliest melting of a source, which contains a small proportion of KREEPy trapped liquid, and, due to its lower temperature of melting compared to the enclosing cumlate, makes up a larger proportion of the first small percentage partial melt. In order to fit these rocks into the lunar chronology, Ar-Ar ages currently are being determined for these rocks.

Table 1: Elements Analyzed by INAA for 2-4 mm Fragments from Soil 10002

Sub-samp	,1006	,1008	,1009	,1010	,1011	.1012	,1013	,1014	,1015	,1016	,1017	,1018
Na (ppt)	2.81	3.13	3.83	2.04	2.89	2.62	3.10	1.95	3.42	2.00	2.32	2.10
Ca	76.8	----	100	----	----	----	----	94.9	97.3	----	----	54.1
Fe	146	172	113	149	171	43.4	175	40.8	139	146	143	84.1
K (ppm)	779	488	644	270	675	538	523	127	877	268	148	455
Mn	2130	2280	1870	2030	2260	630	2240	575	2100	2120	1920	1080
Sc	81.6	80.3	91.6	75.9	96.3	9.10	76.7	6.84	99.3	87.7	74.4	53.3
Cr	1610	1460	918	3150	1370	935	1260	893	1700	3250	2790	578
Co	14.3	13.9	11.2	20.5	12.0	18.1	13.9	19.1	12.2	20.3	19.6	7.88
Ni	----	187	----	50	50	110	60	200	----	----	----	----
Zn	60	----	----	----	----	14	43	18	74	----	----	99
Ga	5.1	5.5	6.3	3.1	4.3	3.7	4.3	4.6	6.0	3.9	3.6	2.9
Rb	4.8	----	6.8	----	5.4	----	----	7.1	10.8	----	----	5.9
Sr	162	89	----	63	64	150	39	92	242	----	----	----
Zr	388	282	337	188	214	75	396	----	300	113	41	455
Cs	----	----	0.4	----	0.06	0.1	0.26	----	0.18	----	----	0.1
Ba	333	----	96	117	104	101	124	11	119	45	----	31
La	30.8	19.6	8.83	5.3	8.14	4.83	18.3	0.72	10.1	3.08	3.79	4.73
Ce	91.4	54.5	30.5	18.5	26.9	11.3	50.4	2.76	38.9	11.8	13.3	17
Nd	60.4	41.4	20.7	14.6	24.5	12.1	37.5	----	29.8	9.6	9.9	14.3
Sm	21.7	18	13.6	7.83	12.2	2.15	16.2	0.32	16.2	5.39	6	6.48
Eu	1.99	2.22	2.71	1.66	2.21	0.89	2.15	0.69	2.82	1.32	1.64	1.35
Tb	4.73	3.98	3.47	1.91	2.95	0.36	3.69	0.07	4.25	1.38	1.66	1.54
Dy	31.2	23.2	21.9	12.5	20.9	1.4	24.7	----	27.6	9.7	11.6	10.1
Ho	8.4	7.1	5.6	3.3	5.3	0.9	5.9	----	6.1	2.4	2.5	2.1
Tm	2.4	2.2	1.6	1.2	1.6	0.3	1.9	0.03	2.0	1.0	1.1	----
Yb	16.3	13.0	11.4	7.13	10.3	1.6	13.1	0.32	13.2	5.39	5.83	6.1
Lu	2.30	1.90	1.46	1.18	1.55	0.233	1.72	0.046	1.81	0.795	0.854	0.794
Hf	12.0	10.8	7.8	7.11	9.29	1.21	10.7	0.22	10.4	5.00	6.34	4.93
Ta	1.45	1.43	0.94	1.45	1.64	0.18	1.45	0.08	1.56	1.03	1.16	1.10
Th	2.81	1.44	0.68	0.21	0.52	0.66	0.83	0.09	0.76	0.17	0.26	0.31
U	0.45	----	0.26	----	----	----	----	----	0.17	----	----	0.15
Ir (ppb)	nd	8.0	nd	nd	4.0	7.6	17.6	5.3	nd	8.8	11.2	nd

nd = not detected (below detection limit [3 ppb]).

CHEMISTRY OF 2-4 MM FRAGMENTS FROM SOIL 10002 -- Twelve 2-4 mm fragments were carefully chosen from soil 10002 and analyzed by INAA methods for their trace-element contents (Table 1). Of these twelve, five contain no detectable Ir and are, therefore, considered tobe pristine. Two others contain relatively low abundances of Ir (,1011 and ,1014) and could possibly be pristine. These seven rocks are plotted in Figure 1and on a K vs. La diagram. The REE for these rocks are plotted relative to C1 chondrites on figure 2.

Of particular interest is clast **,1014** , which is comprised of mostly plagioclase and could be a **ferroan anorthosite** (FAN). It contains the lowest REE, Sc, Na, K, Ba, and Mn abundances of any of the clasts analyzed (e.g., see Figure 1) and high abundances of Ca. The most diagnostic characteristic of this clast is the large positive Eu anomaly (Figure 2), which again lends credence to its designation as a FAN.

Clasts **,1009**; **,1010; ,1011; ,1015; and ,1018** also plot within the field for **Group B3 basalts (,1015 could be a B1**; Figure 1), although they are coarser-grained than basalt ,1006. Thin-sections are being prepared by the Curatorial Staff at the Johnson Space Center and mineral chemistry will be determined on the electron microprobe to confirm or deny these designations. Rock **10002,1006 plots within the field for Group D basalts from Apollo 11** in Figure 1. The remaining 50 mg portion of this sample was then analyzed for its Nd and Sr isotopic composition (Table 2), along with one other Group D basalt.

Nd AND Sr ISOTOPIC COMPOSITION OF GROUP D HIGH-Ti BASALTS -- For the first time, two proposed Group D basalt rocklets were analyzed for their Nd and Sr isotopic compositions (Table 2).

Nd & Sr ISOTOPE CHEMISTRY OF APOLLO 11 GROUP D BASALTS: Snyder, Jerde, Taylor, & Halliday

Table 2: Nd and Sr Isotopic Composition of Apollo 11 Group D Basalts

Rock	Grp.	wt.(mg)	Rb (ppm)	Sr (ppm)	$^{87}Rb/^{86}Sr$	$^{87}Sr/^{86}Sr$	$^{87}Sr/^{86}Sr_{(i)}$	T_{LUNI} (Ga)	Sm (ppm)	Nd (ppm)	$^{147}Sm/^{144}Nd$	$^{143}Nd/^{144}Nd$	$\varepsilon_{Nd}(T)$	T_{CHUR}
10002,98	D?	31	4.67	168	0.0799	0.703751±13	0.69932±2	4.09	18.8	54.3	0.2089	0.513053±12	2.0±0.4	5.07
10002,1006	D	21	1.35	139	0.0279	0.700709±20	0.69916±3	4.17	19.6	60.2	0.1972	0.512715±12	1.2±0.6	18.5

The two samples do exhibit some variability in their initial Nd and Sr isotopic ratios (although the initial ε_{Nd} values are within analytical uncertainty). However, the Nd and Sr isotopic compositions of these Group D basalts are within the ranges for the Group B2 basalts from Apollo 11 ($^{87}Sr/^{86}Sr$ = 0.69920 to 0.69921 and ε_{Nd} = +2.0 to +3.9 at 3.85 Ga; [3,4,5] Figure 3). Rock 10002,98 does exhibit a slightly higher $^{87}Sr/^{86}Sr$ initial ratio than other B2 or D samples. However, because of the relatively large Rb/Sr ratio of this sample, a slight increase in either the Rb/Sr ratio (by no more than 2%) of the rock, or age (by less than 0.08 Ga) yields an initial ratio which is in line with other D and the B2 basalts. The similarity in Nd and Sr initial ratios is consistent with the model of Jerde et al. [6], whereby the **Group D basalts were derived from the Group B2 basalts by the simple addition of the mineral whitlockite**, either through metasomatism or the trapping of a residual liquid component.

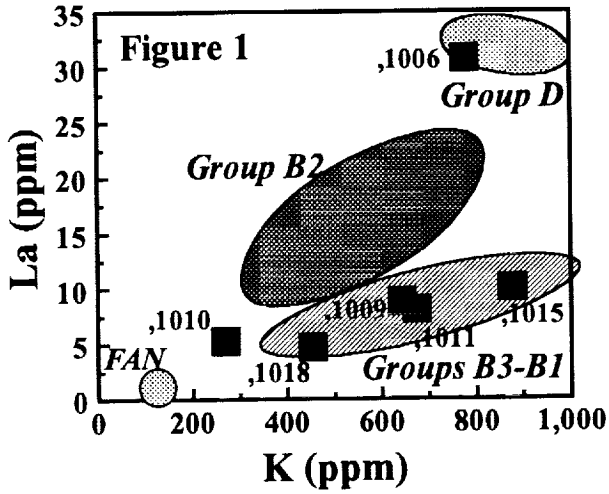

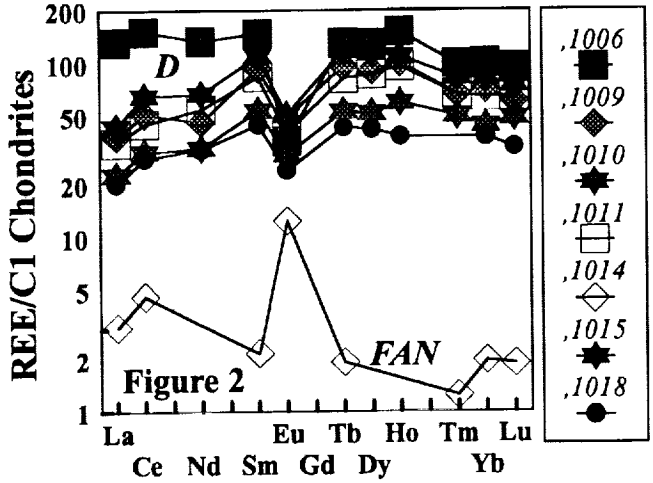

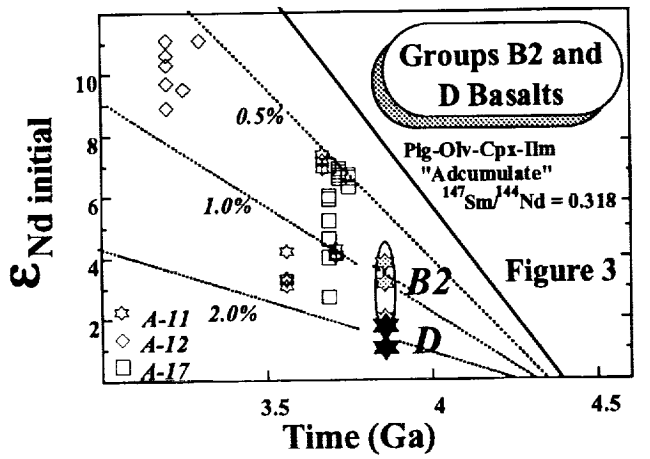

EARLIEST MELTING BENEATH MARE TRANQUILLITATIS: HIGH-Ti BASALTS OF GROUPS B2 AND D -- Nd and Sr isotopic heterogeneities in the sources of low-K high-Ti mare basalts (such as Groups B2 and D) could be the consequence of events unique to the Moon. In the late stages of LMO crystallization, when ilmenite was a liquidus phase, upper mantle cumulates trapped variable yet small amounts of residual LMO liquid [5,7]. A lack of recycling in the lunar environment would allow these slightly different portions of essentially the same source to diverge along separate isotopic evolutionary paths. Adcumulates with more trapped liquid would have higher contents of the heat-producing elements U, Th, and K and would likely melt first. Therefore, the earliest phase of volcanism at the Mare Tranquillitatiis (3.85 Ga ago, Group B2 and possibly D) involved the melting of a source which was relatively enriched in this KREEPy trapped liquid and the resultant magmas were slightly more aluminous, less titaniferous, and possessed a lower Mg# than the later B3 basalts [5]. These observations are consistent with these basalts being melted from a source which was relatively enriched in trapped KREEPy liquid. The volume of this KREEPy trapped liquid would be small, but, because of its high LILE content, could greatly affect the isotopic ratios of basaltic magmas that would have intruded through the upper crust en route to the surface of the Moon.

REFERENCES: [1] Beaty, D.W. and Albee, A.A. (1978), *PLPSC 9th*, 359-463; [2] Beaty, D.W. et al. (1979), *PLPSC 10th*, 41-75; [3] Papanastassiou, D.A. et al. (1977), *PLPSC 8th*, 1639-1672; [4] Unruh, D.M. et al. (1984), *PLPSC 14th*, B459-B477; [5] Snyder, G.A. et al. (1994), *GCA*, submitted; [6] Jerde, E.A. et al. (1993), *GCA*, in press; [7] Snyder, G.A. et al. (1992), *GCA 56*, 3809-3823.

A BASALTIC SAFARI ACROSS THE CAYLEY PLAINS AND OVER THE DESCARTES MOUNTAINS: STILL SEARCHING FOR A PRISTINE HIGHLANDS BASALT AT APOLLO 16

Gregory A. Snyder, James Karner*, Eric A. Jerde, and **Lawrence A. Taylor,** Planetary Geosciences Institute, Dept. of Geological Sciences, University of Tennessee, Knoxville, TN 37996-1410; *Natural Sciences, Bemidji State University, Bemidji, MN 56601.

We have made a petrographic reconnaissance of currently known "basaltic" samples from the Apollo 16 landing site and have found four samples (61249,2; 62245,6; 65905,8; and 64515,5) which are indeed basaltic in hand specimen. These four samples have been analyzed for trace-elements by INA (including siderophiles to determine their pristinity). Ir abundances are high (13.5-18.8 ppb) for all four samples, indicating that they are not pristine. Careful study of the whole-rock chemistry of these four samples shows that they are elevated in Ca, Al, and Sr relative to typical lunar basalts, indicative of mixing with a plagioclase-rich component such as highlands anorthosite. A true, pristine, basalt has yet to be found at the Apollo 16 landing site.

INTRODUCTION -- It is believed that mare volcanism was an important process during the early evolution of the highlands. We have evidence for volcanism at all landing sites, including Apollo 14, but have not been able to find true basalts at the Apollo 16 site. It has also been shown that the character of basaltic volcanism at the Apollo 14 site was quite different that at the mare sites of Apollos 11 and 12. If basalts were found in the highlands, its character is likely to be vastly different than that found in the mare. Such is the case on Earth, where oceanic basalts are found to be demonstrably different in chemistry and character from continental basalts.

We have undertaken a two-pronged approach, in an attempt to find true basalts from the Apollo 16 landing site. First, we carefully combed through the Apollo 16 sample catalogs and requested thin-sections be made (for those that had no sections made) of all samples which appeared to be basaltic from preliminary descriptions. The results of this petrographic reconnaissance will be reported next year. Second, we had allocated a group of existing thin-sections of possible basaltic rocks and four whole-rock splits of samples classified as subophitic, 'basaltic" melt rocks for trace-element analyses, the results of which are reported below.

PETROGRAPHY & MINERAL CHEMISTRY OF APOLLO 16 SUBOPHITIC IMPACT MELTS -- Sample ***67948*** is a mesostasis-rich basalt with abundant plagioclase grains subophitically enclosed in pyroxene. The plagioclase grains are anhedral to acicular and range from 0.5 mm to 0.3 mm in longest dimension. The mesostasis contains glass, metal, and ilmenite. No olivine is present in the sample. Pyroxene varies in composition from En_{65} to En_{85}. Plagioclase exhibits a bimodal distribution in composition of An_{90-95} and An_{75-80}. One FeNi metal grain contained 2.6% Ni.

Nearly 80% of rock ***67559*** in plagioclase of relatively uniform compostion, An_{90-96}. The plagioclase occurs as subophitic, accicular grains about 0.5 mm long. Pyroxene is common and exhibits a broad range from En_{60} to En_{80}. Olivine is rare and has a composition of Fo_{60}. Small grains of metal and ilmenite are also present. The dominant mineral in ***65795*** is coarse-grained lath-like to tabular, subophitically enclosed plagioclase with a composition of An_{95-97}. Fine-grained olivine, metal, and ilmenite are also present. Olivine has a composition of ~Fo_{70} and pyroxene ranges in compositions from En_{60} to En_{80}. Rock ***67747*** is also rich in plagioclase (An_{90-95}) which comprises aproximately 80% of the sample. Large (> 1mm), poikilitic olivine (Fo_{83-86}) grains are common. Pyroxene is interstitial and also occurs in the mesostasis and ranges in composition from En_{70-80}. Rock ***60635*** is an especially coarse-grained section with large, phenocrystic plagioclase laths up to 2.5 mm in longest dimension. Smaller plagioclase (An_{93-97}) and pyroxene (En_{60-80}) grains are also interstitial. Olivine is absent from this section.

Although all of the rocks above exhibit pristine, subophitic igneous textures, the chemistry of the minerals and their relative proportions suggest that they are impact-generated mixtures of basaltic and highlands rocks. The samples are too rich in plagioclase and often exhbit bimodal distribution of mineral composiitions within a given rock. Furthermore, the anorthite content of most samples is in the range of ferroan anorthosites (An_{92-97}), not typical mare basalts. Only rock 67498 contains plagioclase with a composition in the range of typical mare basalt (An_{60-80}).

WHOLE-ROCK CHEMISTRY -- A careful search through the Apollo 16 Catalogs [1] led us to request four rock samples which had previously been classified as subophitic, 'basaltic", melt rocks -- 61249, 62245, 64515, and 65905. We postulated that, since trace-elements had not been analyzed on these rocks, they could still be

'true', pristine, basalts. Sub-samples were allocated and then analyzed by INA for trace-element abundances, including the siderophile element Ir (Table 1).

As can be seen, all four samples contain a high level of Ir (13.5-18.8 ppb) and **cannot be considered chemically pristine**. Although the rare-earth element (REE) patterns of these rocks are similar to many lunar basalts, REE and K abundances are much higher, ranging from 100 to 300x chondrites La (Figure 1) and suggesting the addition of a REE- and K-enriched component (KREEP?).

THE REGOLITH AT APOLLO 16: "BASALTS" VS. IMPACT MELTS -- It is perhaps not surprising that these impact melts are comprised of mostly highlands material. High Al and modal plagioclase (up to 80 vol.%) in these rocks are indicative of the large proportion of anorthositic highlands component in these impact melts. In fact, very little evidence of a true mare basaltic component is found in the rocks studied from Apollo 16. Furthermore, it is likely that if mare basalt were found at the site it would not be indigenous to the Apollo 16 site, but could have been transported there by meteorite impact. Only rock 67498 contains plagioclase which is evolved enough to have been derived from a mare basalt. Conversely, this range in plagioclase (An_{60-80}) is also characteristic of Alkali Suite rocks.

Reimold et al. [2,3] determined that rocks 67948, 67559, and 67447 were indeed impact melts. They suggested that impact melts from Apollo 16 could be grouped into 22 distinct melt sheets with ages ranging from 3.72 to 3.94 Ga, but grouped into two separate events. Rb-Sr and Sm-Nd isotopic modelling pointed to the age of the Descartes formation as 4.1 Ga and that of the Cayley formation as 3.81-3.86 Ga. The range in mineral chemistries exhibited by these impact melts is also suggestive of the polymict nature of these rocks. The high Ir values for the four INAA samples also indicate that Apollo 16 impact melts contain a significant, albeit minor, meteoritic component.

Table 1: Trace-Elements Analyzed by INAA for Apollo 16 Impact Melts

Sample	61249,2	62245,6	64515,5	65905,8
Na (ppt)	3.59	3.76	3.85	4.06
Ca	95.5	91.3	95.6	103
Fe	61.4	71.0	64.4	71.4
K (ppm)	1360	1670	1910	2850
Mn	728	785	791	906
Sc	11.0	13.1	13.4	16.8
Cr	1090	1360	1240	1170
Co	46.3	63.5	43.9	46.0
Ni	865	955	671	439
Zn	18	15	22	10
Ga	3.8	4.9	5.3	5.8
Rb	4.9	8.9	9.9	6.4
Sr	153	151	172	202
Zr	478	414	461	1010
Cs	0.18	0.32	-----	0.44
Ba	236	306	316	602
La	24.1	31.5	31.8	61.9
Ce	64.1	89.8	84.0	177
Nd	33.8	49.4	45.1	93.5
Sm	11.4	14.8	14.8	28.7
Eu	1.44	1.69	1.76	2.33
Tb	2.27	2.94	2.99	5.86
Ho	2.74	3.65	4.01	8.88
Tm	0.98	1.28	1.27	2.78
Yb	8.83	11.1	11.1	21.5
Lu	1.01	1.27	1.28	2.30
Hf	8.48	9.88	10.1	20.6
Ta	1.09	1.27	1.29	2.68
Ir (ppb)	18.8	13.5	18.8	17.2
Th	3.82	4.99	4.81	10.1
U	0.98	1.25	1.28	2.23

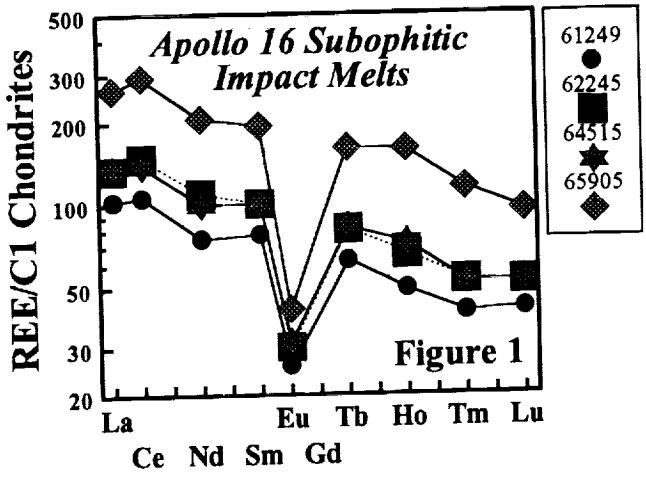

Figure 1

Only two known basalts, both clasts in breccias, have been reported from the Apollo 16 sample collection -- 60639,4 (,5) [4,5] and 60255,21 [6,7]. Clast 60639,4(,5) was classified as a high-Ti mare basalt [5], although its TiO_2 content is only 7.3 wt.%, much less than typical mare basalts from Apollo 11 and Apollo 17. Ir was not measured on this sample, but Au contents of 14 to 19 ppb make the pristinity of this sample suspect. Hughes et al. [7] claimed that clast 60255,21 is a low-Ti mare basalt, although its trace-element content was found to be distinctly different from other low-Ti basalts at Apollo 12 and Apollo 15. Furthermore, the chemical pristinity of this clast is still in question as siderophile elements were not analyzed. Therefore, we conclude that pristine basalts have yet to be unequivocally confirmed at the Apollo 16 landing site. The search continues.

REFERENCES: [1] Ryder, G. and Norman, M.D. (1980) Catalog of Apollo 16 Rocks: Parts I, II, and III, 1144 pp. [2] Reimold, W.U. and Reimold, J.N. (1984), *Fortschr. Miner. 62*, 269-301; [3] Reimold, W.U. et al. (1985), *PLPSC 15th*, C431-C448; [4] Dowty, E. et al. (1974) *PLSC 5th*, 431-445; [5] Murali, A.V. et al. (1976), *LPSC XII*, 583-584; [6] Simon, S.B. and Papike, J.J. (1987), *LPSC XVIII*, 922-923; [7] Hughes, S.S. et al. (1988), *LPSC XIX*, 515-516.

SILICATE LIQUID IMMISCIBILITY IN ANORTHOSITE SUITES: VIEWING THE MOON FROM WYOMING AND LABRADOR

Gregory A. Snyder, Jeremy Mitchell, Lawrence A. Taylor, and **E. Craig Simmons***, Planetary Geosciences Institute, Dept. of Geological Sciences, University of Tennessee, Knoxville, TN 37996-1410; *Dept. of Geochemistry, Colorado School of Mines, Golden, CO 80401.

There is mounting evidence that silicate liquid immiscibility (SLI) plays an important role in the evolution of late-stage liquids in terrestrial anorthosite massifs. Evidence for its importance is found in the ubiquitous occurrence of ferrodiorites (jotunites) and monzodiorites which are suggested to be the mafic and silicic end-members of SLI in terrestrial massif anorthosites. Importantly, these two rock types must be proven to be contemporaneous for the SLI model to be valid. In some instances, similar rocks are found comingled as pillows (i.e., liquids) in the plutonic environment, thus suggesting both synchronicity as well as consanguinity. Similar processes could have been operable during lunar anorthosite evolution in the early crust of the Moon.

INTRODUCTION -- Silicate liquid immiscibility (SLI) has been observed in experimental studies of various initial compositions [1]. Furthermore, trace- and major-element two-liquid partition coefficients have been established between the mafic and silicic end-members of SLI [2]. Two natural examples where bulk compositions are appropriate for liquid immiscibility to occur are Proterozoic anorthosite complexes and Fe-enriched basalts. There is clear petrographic evidence that SLI does occur naturally in Fe-enriched basalts, but direct evidence is sparse for its importance in the origin of anorthosite complexes.

TERRESTRIAL ANORTHOSITE MASSIFS -- On Earth, massif anorthosites are restricted mostly to the mid-Proterozoic. They are comprised chiefly of plagioclase and hypersthene with compositions ranging from An_{40} to An_{80} and En_{30} to En_{80}, respectively [3]. Associated rocks include granites, leuconorites, troctolites, gabbros, and monzodiorites. Fe-enriched dioritic rocks are a ubiquitous, albeit volumetrically small, component of Proterozoic anorthosite complexes. They commonly occur as dikes and pods within anorthosite and as cumulates in intrusions.

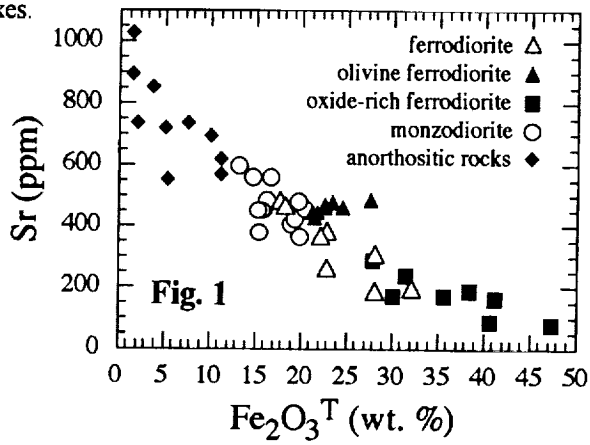

Fig. 1

In the **Laramie Anorthosite Complex, southeastern Wyoming**, these dioritic rocks form two distinct groups. The first group, referred to as ferrodiorite, ranges from oxide-rich varieties (up to 40 vol.% Fe-Ti oxide) to more felsic ferrodiorite (olivine-free) and olivine ferrodiorite. Experiments show that these oxide-rich rocks are close to liquid compositions [4]. P and Ti enhance the solubilities of apatite and Fe-Ti oxide in a silicate melt and lead to a very dense melt, capable of readily segregating from the host [4]. The second group, called monzodiorites, is much more potassic and felsic than the ferrodiorites. On major and trace-element variation diagrams, both groups of diorites typically form one smooth trend, ranging from silicic monzodiorite to silica-poor oxide-rich ferrodiorite, implying a single differentiation sequence (Fig. 1). This interpretation is complicated by the fact that ferrodiorite samples have compositions that are similar to mafic pegmatoids within the anorthosite which are composed of melts residual to the anorthosites. This implies that the melt remaining after extensive plagioclase fractionation is ferrodioritic in composition. *How, then, could there be a single evolutionary trend resulting both in Fe-enrichment to oxide-rich ferrodiorite and silica-enrichment to monzodiorite?* When plotted on the SLI diagram of Roedder [5], these groups of rocks form a smooth trend with oxide-rich ferrodiorite at the mafic end, ferrodiorite and olivine ferrodiorite in the middle, and monzodiorite at the "granitic" end (Fig. 2). Although this evidence of an immiscible relationship between the ferrodiorites and monzodiorites is not conclusive, it is strongly suggestive from experimental data on these rocks [6]. It is likely that the anorthosite residual magmas will evolve to one side or the other of a gently sloping immiscibility field as a function of oxygen

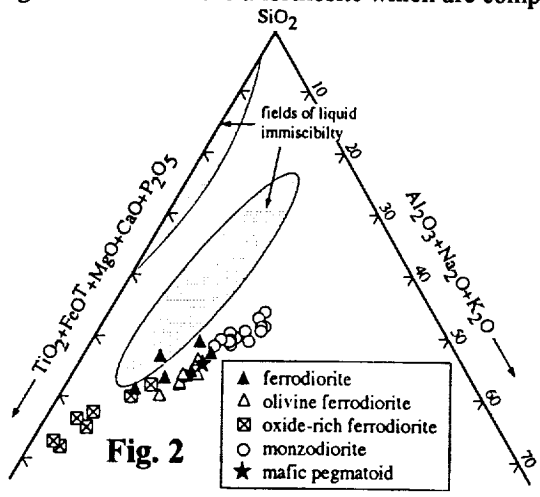

Fig. 2

fugacity, silica activity, crystallization history, and crustal contamination.

Ferrodiorites are also common in the **southern Nain Anorthosite Complex, Labrador** as layered rocks along Fox Inlet and as pillows in a hydrous granitic matrix on Tunungayualuk Island [7,8]. Wiebe [7,8] suggested that these ferrodiorites were late-stage products of fractional crystallization of an anorthositic (leuconorite) magma. However, whereas quartz and alkali feldspar were important interstitial phases in the leuconorite parent, these phases did not occur in the ferrodiorites. Wiebe [7,8] postulated that these phases were absent in evolved ferrodiorites due to separation of an immiscible granitic liquid containing the quartz and alkali feldspar. Indeed, anhydrous granitic pillows do occur and are likely contemporaneous with ferrodiorite pillows on Tunungayualuk Island [7,8]. Furthermore, plagioclase and pyroxene phenocrysts in these granitic pillows have major-element compositions comensurate with ferrodiorite pillows. Rb-Sr isotopic systematics of contemporaneous granitic and ferrodioritic pillows from Tunungayualuk Island [9,10] are broadly consistent with the immiscibility relationship (Fig. 3). Ferrodiorites with relatively low Fe lie along a trend of increasing Fe, Ba and initial $^{87}Sr/^{86}Sr$ suggesting combined crustal assimilation and fractional crystallization of a parental leuconorite magma [9,10]. However, high-Fe ferrodiorite pillows and anhydrous granitic pillows plot off of this trend at much lower Rb/Sr and higher Rb/Sr ratios, respectively. The high-Fe ferrodiorite pillows also exhibit higher Na_2O/K_2O and $Al_2O_3/(Na_2O + K_2O)$ values and P_2O_5, TiO_2, MgO, and MnO contents and lower K_2O, Na_2O, and Al_2O_3 contents than coexisting anhydrous granitic pillows, while mantaining similar Mg#s and MnO/FeO values [11], consistent with their relationship as complementary immiscible liquid pairs.

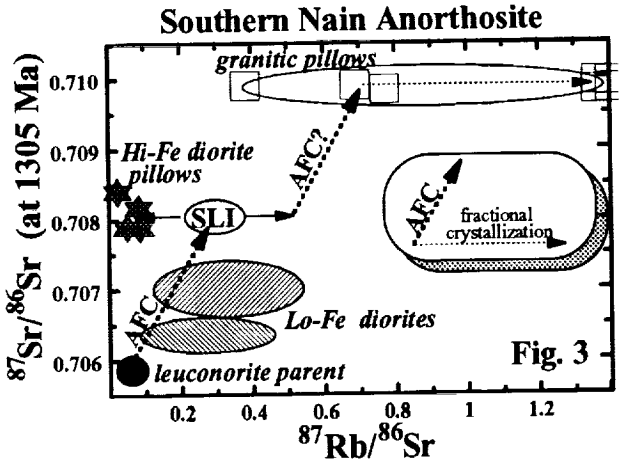

Fig. 3

LUNAR ANORTHOSITES -- Anorthosites on the Moon can be subdivided into three types: 1) Ferroan -- characterized by high-Ca plagioclase (An_{92-96}) evolved mafic mineral compositions (Mg# = 40-70), and primitive incompatible trace-elements; 2) Magnesian -- exhibiting variable (yet still high-Ca) plagioclase compositions (An_{83-96}), primitive mafic mineral compositions (Mg# = 65-92), and evolved incompatible trace-elements; and 3) Alkali -- comprised of relatively low-Ca plagioclase (An_{65-86}), evolved mafic minerals (Mg# = 35-70), and evolved, albeit quite varible, incompatible trace-elements [12].

Ferroan anorthosites likely were precipitated from a global magma ocean early in the Moon's history (prior to 4.4 Ga; [13]) and are comprised of extremely calcic plagioclase. Therefore, ferroan anorthosites are not likely analogs for terrestrial massif anorthosites, although they may share genetic similarities with rare Archean anorthosites [e.g., 14]. Magnesian anorthosites are mineralogically more primitive than terrestrial massif anorthosites. **Lunar Alkali Suite anorthosites most closely resemble terrestrial massif anorthosites in terms of mineral chemistry.** The currently favored model for Alkali Suite anorthosite genesis is the precipitation from an evolved quartz monzodiorite-like liquid [15]. How, and if, this liquid fits into a scheme of SLI is not known. Lunar granites are known to be the crystallization products of the complementary acidic liquid of SLI (e.g., [16-20], however, the complementary basic liquid has been elusive. Neal and Taylor [20] suggested that the phosphate phases seen in lunar highlands rocks represent a portion of the complementary basic liquid of SLI. However, the place of SLI in the evolution of anorthosites on the Moon is still unknown. Further work is needed in the areas of chemical modelling and experimental petrology in order to answer these questions.

REFERENCES: [1] Roedder, E. (1951), *Amer. Mineral. 36*, 282-286; [2] Watson, E.B. (1976), *Contrib. Mineral. Petrol. 56*, 119-134; [3] Morse, S.A. (1982), Amer. Mineral. 67, 1087-1100; [4] Lindsley, D.H. (1991), In IGCP 290: Proterozoic Anorthosite Massifs, abstract; [5] Roedder, E. (1979), In Yoder, H.S. (editor) The Evolution of the Igneous Rocks, 15-57; [6] Lindsley, D.H. (1994), *GCA*, submitted; [7] Wiebe, R.A. (1978), *Can. Jour. Earth Sci. 15*, 1326-1340; [8] Wiebe, R.A. (1979), Jour. Petrol. 20, 239-269; [9] Simmons, E.C. et al. (1980), Trans. Amer. Geophys. Union 61, p. 410; [10] Snyder, G.A. and Simmons, E.C. (1985), Trans. Amer. Geophys. Union 65, p. 305; [11] Naslund, H.R. (1983), *Amer. Jour. Sci. 283*, 1034-1059; [12] Snyder, G.A. et al. (1994) *GCA*, submitted; [13] Carlson, R.W. & Lugmair, G. (1988), *EPSL 90*, 119-130; [14] Myers, J.S. (1988), *Prec. Res. 38*, 309-323; [15] Snyder, G.A. et al. (1994), *LPSC XXV*, this volume; [16] Hess, P.C. et al. (1975), PLSC 6th, 895-909; [17] Rutherford, M.J. et al. (1976), PLSC 7th, 1723-1740; [18] Taylor, G.J. et al. (1980), In Papike, J.J. & Merrill, R.B. (editors), Proc. Lunar Highlands Crust, 339-352; [19] Shih, C-Y. et al. (1985), GCA 49, 411-426; [20] Neal,C.R. and Taylor, L.A. (1989), GCA 53, 529-541.

PETROLOGY AND CHEMISTRY OF THE MAGNESIAN SUITE: FURTHER EVIDENCE OF LIQUID IMMISCIBILITY AND METASOMATISM IN THE WESTERN HIGHLANDS OF THE MOON

Gregory A. Snyder, Clive R. Neal*, Lawrence A. Taylor, and **Alex N. Halliday****, Planetary Geosciences Institute, Dept. of Geological Sciences, University of Tennessee, Knoxville, TN 37996; *Dept. of Civil Eng. & Geol. Sci., Univ. of Notre Dame, Notre Dame, IN 46556; **Dept. of Geological Sciences, University of Michigan, Ann Arbor, MI 48109

The lunar magma ocean (LMO) was probably formed at the Moon's birth (at 4.5 Ga) and persisted for 150-200 Ma. After 60-80% of the LMO had crystallized, plagioclase became a liquidus phase and subsequently floated to form the ferroan anorthosites of the nascent lunar crust. During the latest stages of LMO crystallization, at approximately 4.36 Ga [1], the residual liquid was enriched in Fe, Si, P, K, and the REE and was trapped in the upper mantle and/or lower crust of the Moon where it crystallized to form urKREEP. This evolved residual LMO liquid is ripe for splitting into two immiscible silicate liquids and may have done so at that time. Being enriched in radioactive heat-producing elements such as K, U, and Th, this urKREEP could also readily re-melt at some later date and differentiate until it underwent silicate liquid immiscibility (SLI). The basic portion of SLI (which was REE- and P-rich, so-called "REEP-frac") was then available to metasomatize portions of the lunar crust. At least as early as 4.2 Ga, the interior of the Moon was also beginning to melt and produce primitive mafic magmas [2]. These mafic magmas could have precipitated troctolitic, gabbroic, and anorthositic cumulates in the crust and were also variedly metasomatized by the available REEP-frac. This produced Mg-suite rocks which contain primitive mineral compositions, are enriched in the REE and P, but are depleted in the alkali metals K, Rb, and Cs. Alkali anorthosites also were produced at about this time (possibly a little later), but were formed directly from the re-melted urKREEP as cumulates.

INTRODUCTION -- The study of rocks from the Apollo 14 landing site has led to important discoveries of evolved samples (e.g., [3,4]) which have added to our understanding of such processes as liquid immiscibility and metasomatism in the lunar environment. Mg-suite rocks are enigmatic in that they exhibit primitive mineral chemistry and evolved trace-element compositions. Lindstrom et al. [5] pointed out the problems with the urKREEP assimilation hypothesis for Mg-suite anorthosites, namely that other incompatible elements (besides the REE) such as Zr, Hf, Rb, and Cs are not enriched in the Mg-suite anorthosites and that interstitial mafic grains should be more Fe-rich, only if they crystallized from an evolved trapped liquid. These problems led them to postulate that REE-rich metasomatic fluids had infiltrated primitive troctolitic plutons in the lunar crust and percolated upwards into the anorthositic portions. These anorthositic portions of the plutons then were sampled as the magnesian anorthosites. The presence of phosphates (especially whitlockite) in the magnesian anorthosites were the only petrographic evidence of this metasomatic event [5].

CHRONOLOGY OF Mg-SUITE CUMULATES -- Nyquist and Shih [6] compiled age information from the lunar highlands Mg-suite and indicate that these ages range from 4.61 ± 0.07 to 4.17 ± 0.02 Ga. However, ages (with the exception of one Rb-Sr determination) for the most plagioclase-rich clasts (troctolites) fall in a range from 4.27 to 4.16 Ga. A compilation of U-Pb zircon ages for Apollo 14 Mg-suite rocks (14066,47: gabbronorite = 4141 ± 5 Ma; 14305,91: norite = 4211 ± 5 Ma; 14306,150: troctolite = 4245 ± 75 Ma; 14306,60: gabbronorite = 4200 ± 30 Ma; [7]) yields a possible range of 4136 to 4320 Ma and a weighted average age of 4191 ± 4 Ma. Thus, an age of ~4.2 Ga is considered reasonable for Apollo 14 magnesian suite rocks and is used in calculating initial isotopic ratios.

Shih et al. [8] recently have determined precise Sm-Nd ages for two Mg-suite norites (15445,17: 4.46 ± 0.07 Ga; 15445,247: 4.28 ± 0.03 Ga) and a Rb-Sr age on one other (15455,228: 4.55 ± 0.13 Ga) from the Apollo 15 landing site; these ages indicate that at least some magnesian suite rocks are in excess of 4.4 Ga old. Obviously, precise age information is needed for more Mg-suite rocks. Current isotopic data indicate that magnesian suite rocks were produced by a variety of parental magmas over an extended period of early lunar history, although *the bulk of magnesian suite rocks are younger than the ferroan anorthosites*.

Furthermore, as Figure 1 suggests, it is possibile that Mg-suite magmatism was initiated at different times in different regions of the Moon. In fact, the pattern in Figure 1 could lead to the interpretation that Mg-suite magmatism on the near-side occurred first in the northeast and then swept slowly to the southwest over a period of some 300-400 Ma. Granted, reliable age data are sparse, especially at landing sites 14, 15, and 16. However, if this age pattern is found to be real, we speculate that this regional progression could be due to the progressive freezing, and release of latent heat needed for melting, of the final residual liquids of the lunar magma ocean. This final liquid layer spread beneath the surface on the lunar near-side and was deepest, and therefore hottest, where the largest

Fig. 1: *Mg Suite Ages*

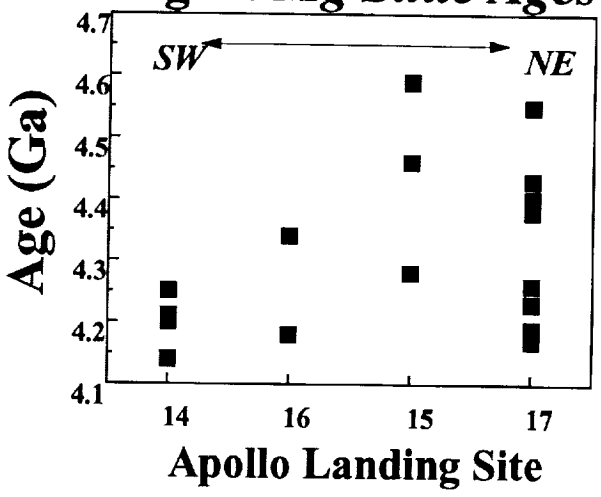

concentration of urKREEP has been found -- at Apollo 14. As this final liquid layer crystallized, it did so from northeast to southwest, and culminated in the production of the most evolved KREEPy liquids beneath the Apollo 14 landing site.

PETROGENESIS OF Mg-SUITE CUMULATES -- Magnesian anorthosites exhibit mineral chemistry consistent with their derivation from a primitive source, have REE contents consistent with an evolved parentage, but are relatively depleted in the alkali metals (e.g. K and Rb). REE contents vary widely, but in all cases, the REE are at least an order of magnitude higher than those in ferroan anorthosites [5]. The enriched Nd isotopic signature for anorthosite 14303,347 (ε_{Nd} = -1.0 at 4.2 Ga) obviates a derivation from depleted mantle cumulates alone (which would have exhibited *positive* ε_{Nd} values at 4.2 Ga) and suggests the possible presence of some KREEP-like component, from which its Nd isotopic signature (ε_{Nd} = -1.0) is indistiguishable at this time. Therefore, the Mg-suite could represent re-melted portions of the Moon's deep interior which have been contaminated (assimilated? metasomatized?) by a component which is enriched in the REE. However, KREEP is not only enriched in the REE, but also in other incompatible elements such as the alkali metals, K and Rb [9]. The very low K (in many cases below detection limit by INAA of <0.055 wt.% K_2O; [5]) and Rb (0.494 ppm for 14304,347) contents and low $^{87}Sr/^{86}Sr$ initial ratio (0.69915 at 4.2 Ga) of the magnesian anorthosite, preclude KREEP as an important component. [Note that this $^{87}Sr/^{86}Sr$ ratio at 4.2 Ga is indistinguishable from that of alkali anorthosites, suggesting a similar source for the two types of anorthosites]. Furthermore, other evolved rock-types, such as QMD and lunar granite which have much higher K_2O and Rb abundances (1.4-2.1 wt.% and 28-52 ppm, and 1.6-6.5 wt.% and 37-152 ppm, respectively; [10-12]) can also be ruled out as the added component.

An appropriate component, albeit only hypothesized, is found in the basic liquid fraction produced during the process of silicate liquid immiscibility (SLI). Neal and Taylor [12,13] have argued that some phosphates in some lunar highlands rocks are indicative of the process of metasomatism. Rb, Sr, and REE abundances, along with an enriched Nd isotopic signature, of 14304,347 support this conclusion for the metasomatism of the magnesian anorthosites.

Lindstrom et al. [5] noted that "magnesian anorthosites have larger negative and smaller positive Eu anomalies than the alkali anorthosites." Warren et al. [14] and Snyder et al. [15] have shown that the mineralogy and trace-element characteristics of alkali anorthosites can be explained by precipitation of plagioclase from an evolved QMD-like liquid with up to 20% of the liquid trapped in the cumulate. The greater the proportion of trapped liquid, the larger the negative Eu anomaly. However, the alkali anorthosite with the greatest proportion of trapped QMD-like liquid has a Eu/Eu* (0.24) which is still in excess of that for the more evolved magnesian anorthosites (0.094; Figure 2). Therefore, the magnesian anorthosites indicate addition of a component which has a Eu/Eu* that is as low, or even lower, than QMD (which has Eu/Eu* = 0.05-0.10). This component also has an elevated Sm abundance as indicated by the well-defined mixing hyperbola (r^2 = 0.916) traced by magnesian anorthosites on Figure 2 [this mixing hyperbola also includes two troctolites (circles) and several gabbronorites (diamonds)]. Only one component is known in the lunar environment which has a high Sm abundance combined with such a large negative Eu anomaly -- the mineral whitlockite.

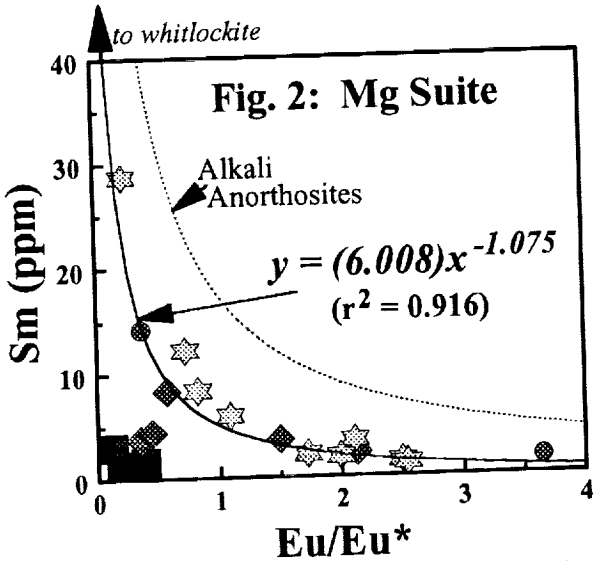

Lindstrom et al. [16] measured REE concentrations in lunar whitlockites from magnesian anorthosite 14321,1211 (,1273 = ion probe sample) using the ion microprobe and found average Sm abundances of 3315 ppm and a Eu/Eu* of 0.015. Assuming the Sm abundance of this whitlockite to be that of the component alluded to in Figure 2, one can calculate the Eu/Eu* value of the component. The calculated Eu/Eu* = 0.0028, approximately 5x smaller than actual measured whitlockites from anorthosite 14321,1211. Although, Eu values for whitlockite are exceedingly small relative to the other REE, they are actually quite large (27-54 ppm; [17]) when compared to any other lunar mineral (except possibly plagioclase). Therefore, the addition of small amounts of other minerals could lead to an extremely REE-enriched component with a lower Eu/Eu* than that of whitlockite. Therefore, it is considered likely that the trace-element abundances in the magnesian anorthosites are determined in large measure by whitlockite which may have been precipitated by the upward percolating REEP-fraction of Neal and Taylor [12].

REFERENCES: [1] Taylor, S.R. (1993), *LPSC XXIV*, 1413-1414; [2] Taylor, L.A. et al. (1983), *EPSL 66*, 33-47; [3] Warren, P.H. et al. (1983), *PLPSC 13th*, A615-A630; [4] Shih, C.-Y. et al. (1985), *GCA 49*, 411-426; [5] Lindstrom, M.M. et al. (1984), *PLPSC 15th*, C41-C49; [6] Nyquist, L.E. and Shih, C.-Y. (1992), *GCA 56*, 2213-2234; [7] Meyer, C. et al. (1989), *LPSC XX*, 691-692; [8] Shih, C.-Y. et al (1993), *GCA 57*, 915-931; [9] Warren, P.H. (1989), Workshop on the Moon in Transition, *LPI Tech. Rpt. 89-03*, 149-153; [10] Jolliff, B.L. et al. (1991), *PLPS 21*, 101-118; [11] Marvin, U.B. et al. (1991), *PLPS 21*, 119-135; [12] Neal, C.R. and Taylor, L.A. (1989), *GCA 53*, 529-541; [13] Neal, C.R. and Taylor, L.A. (1991), *GCA 55*, 2965-2980; [14] Warren, P.H. et al. (1990), *PLPSC 17th*, E303-E313; [15] Snyder, G.A. et al. (1992), *PLPS 22*, 399-416; [16] Lindstrom, M.M. et al. (1985), *LPSC XVI*, 493-494; [17] Jolliff, B.L. (1993), *GCA 57*, 4069-4094.

CHRONOLOGY & PETROGENESIS OF THE WESTERN HIGHLANDS ALKALI SUITE: CUMULATES FROM QUARTZ MONZODIORITE (QMD) LIQUIDS

Gregory A. Snyder, Lawrence A. Taylor, and Alex N. Halliday* Planetary Geosciences Institute, Dept. of Geological Sciences., Univ. of Tennessee, Knoxville, TN 37996; * Dept. of Geological Sci.ences, Univ. of Michigan, Ann Arbor, MI 48109.

Several rocks of alkalic affinity from the western highlands of the Moon have been analyzed for their Nd and Sr isotopic compositions. A noritic alkali anorthosite (14304,267) yields a Sm-Nd mineral isochron of 4108 ± 53 Ma and an ε_{Nd}(T) of -1.0±0.2, and two other alkali norite whole-rocks (14304,270 and 14304,272) yield similar ε_{Nd} (-1.0) values at this time. This age, in conjunction with U-Pb zircon ages for two other alkalic rocks from the Apollo 14 landing site, suggests a distinct western highlands alkalic "event" which was 100-120 Ma in duration and pre-dated widespread mare volcanism. Since the last dregs of the lunar magma ocean (LMO) likely crystallized prior to 4300 Ma, this alkalic "event" could not represent a direct remnant of the late LMO, but may have included the re-melting of evolved portions of the Moon. The resultant melts were similar in composition to lunar quartz monzodiorites (QMD). These evolved melts crystallized to form cumulate gabbros, norites, and anorthosites of the alkali suite, with the proportion of trapped QMD-like liquid determining the LILE enrichment of the rock.

INTRODUCTION -- Alkalic lithologies, such as granites and felsites, have been known from the Moon since the earliest days of the Apollo lunar sample returns [1]. However, not until 1977 [2] were alkali-rich rocks recognized from typical highlands suites such as ferroan anorthosites and norites (FAN) and Mg-suite rocks. Hunter and Taylor [3] suggested, based on plagioclase and mafic mineral compositions, that these rocks represent cumulate crystallization products of evolved magmas, possibly related to the Mg-suite. Conversely, these evolved magmas could represent either the "dregs" of the early lunar magma ocean, or alkalic magmatism that occurred later in the Moon's history. However, until these alkalic rocks are placed into a chronological framework, their significance to lunar petrology and geochemistry will remain enigmatic.

Alkalic rocks may have attained their character through the operation of two types of processes: either 1) primary igneous processes (e.g., small-degree partial melting of a mafic source, advanced fractional crystallization, or melting of a differentiatated protolith), or 2) the character has been imparted to the rock through later metasomatism. To be considered part of the **Alkali Suite** from the lunar highlands, only samples which are determined to have attained this character through primary igneous processes will be included. Therefore, criteria must be developed to distinguish between these two disparate types of processes. Criteria for inclusion in the alkali suite include evolved (elevated) large-ion lithophile elements (LILE) in the whole-rock chemistry combined with evolved mineral chemistry (plagioclase, An < 90; pyroxene, En < 70).

GEOCHRONOLOGY AND ISOTOPE GEOCHEMISTRY -- Nd and Sr isotopes have been reported on three separate clasts of alkali anorthosite from Apollo 14 breccia 14304 [4-5]. One clast (,267) is moderately enriched in Rb and the REE, whereas the others exhibit extreme enrichment for lunar rocks. A four-point Sm-Nd mineral isochron, including whole-rock, plagioclase, clinopyroxene, and a picking residue yields an age of 4108 ± 53 Ma [4-5]. The low MSWD (0.06) of this regression is a strong indication that this is a true crystallization age. The initial ε_{Nd} (relative to CHUR) from this line is -1.0, similar to that of evolved KREEP rocks at this time (e.g., [6]). A four-point Rb-Sr "isochron" yields a somewhat older, poorer precision, "age" of 4336 ± 81 Ma and an initial ratio of 0.69909±3 [4-5]. The high MSWD (12.3) for this line is an indication that the "age" should be considered suspect. The similarity of the ε_{Nd} values calculated for 4.1 Ga is consistent with all samples being of similar age.

WHOLE-ROCK CHEMISTRY AND THE ORIGIN OF ALKALI SUITE HIGHLANDS ROCKS -- Consideration of major- and trace-element systematics for the lunar highlands alkali suite indicate that a single simple process, such as fractional crystallization, cannot explain the wide range in data. Instead, a more complicated scenario, possibly involving several parental magmas, or a magma system which exhibits considerable variation, must be invoked. The actual composition of the original liquid from which the alkali anorthosites fractionated was undoubtedly KREEP-like. Some samples, notably 14160,217, 14305,283, and 14321,1060, contain significant whitlockite, and Warren et al. [7] stated that the presence of whitlockite in an anorthosite may complicate its interpretation. However, Snyder et al. [8] have contended that the whitlockite may have precipitated from the trapped liquid. Late-stage trapped liquids (mesostases) in basalts and highlands rocks often contain Ca-phospates, including whitlockite.

Previous workers (as summarized in [7]) have provided mounting evidence for a relationship between KREEP (as represented by QMD) and the alkali anorthosites. Ryder postulated that QMD is the final crystallization product of a KREEP basalt magma [9]. Hess showed that a Ti-rich KREEP basalt could produce a residual liquid similar to QMD after 60% fractional crystallization [10]. Marvin et al. presented semi-quantitative modelling of QMD clasts from breccias 15403 and 15405 which supported this conclusion[11]. Warren et al. suggested that alkali anorthosites are plagioclase cumulates from this late-stage Super-KREEP, QMD-like residual liquid with variable proportions of the liquid trapped in the rock [7]. In fact, Snyder et al. [8] have shown that analyses of coarse-grained plagioclase in QMD [12] are similar in composition to those in alkali suite rocks. Snyder et al. [8] have also calculated that alkali anorthosites indicate generally <20% trapped, intercumulus, KREEPy (QMD-like) liquid. The alkali gabbros and norites may also be products of QMD liquid fractionation [5].

Modelling of trace-element *abundances* in order to confirm a relationship between QMD and the alkali suite is fraught with problems. First, textures of QMD clasts indicate that these rocks are not chilled liquids, but consist of accumulated mineral assemblages. Second, QMDs are mineralogically and chemically quite variable with elemental abundances varying by a factor of 3-4. Therefore, as pointed out by Marvin et al. [11] any abundance modelling must be considered semi-quantitative. However, elemental *ratios* in the QMDs are relatively uniform and modelling of elemental ratios could prove useful. Plagioclase (and thus anorthosite) and K-feldspar have by far the largest *positive* Eu anomalies of any minerals, whereas lunar KREEP and QMD exhibit very large *negative* Eu anomalies. Therefore, the ratio Eu/Eu* is a sensitive indicator of the two end-member components plagioclase and QMD. In fact, the Eu/Eu* vs. REE (as represented by 1/Sm) abundance data do indicate two separate, tightly constrained

mixing lines for the alkali suite rocks (Figure 1). One of the arrays contains all of the alkali anorthosite data and yields a correlation coefficient (r^2) of 0.973. The other array is comprised of all gabbronorite data and yields a correlation coefficient of 0.944. The two arrays project from high Eu/Eu*, low REE abundance (or high 1/Sm), plagioclase-rich cumulates to a high REE (or low 1/Sm), low Eu/Eu* component. Assuming that this latter component has REE abundances similar to QMD (and that the actual y-intercepts for these two lines are zero), the two linear equations can be solved to yield the Eu/Eu* value of the component. QMD clasts contain variable abundances of Sm from 77 to 121 which gives Eu/Eu* values of 0.28 to 0.18 and 0.13 to 0.08, from the alkali anorthosite and alkali gabbronorite linear equations, respectively. These calculated values are at the upper end of actual measured values for QMDs (0.05-0.10). Considering that QMDs are not liquids and have accumulated small amounts of whitlockite, it is reasonable to assume that any liquid would exhibit a higher Eu/Eu*. Clast 15405,170 lies along an extension of the gabbronorite mixing array, albeit at higher REE abundances (higher even than actual QMD) and lower Eu/Eu*. Again, only the accumulation of whitlockite, common as a trace constituent in alkali suite rocks, could cause such deviation. It is also interesting to note that this clast is the sole gabbronorite (possibly troctolite) sample from Apollo 15 and was extracted from the same breccia which yielded three separate QMD clasts.

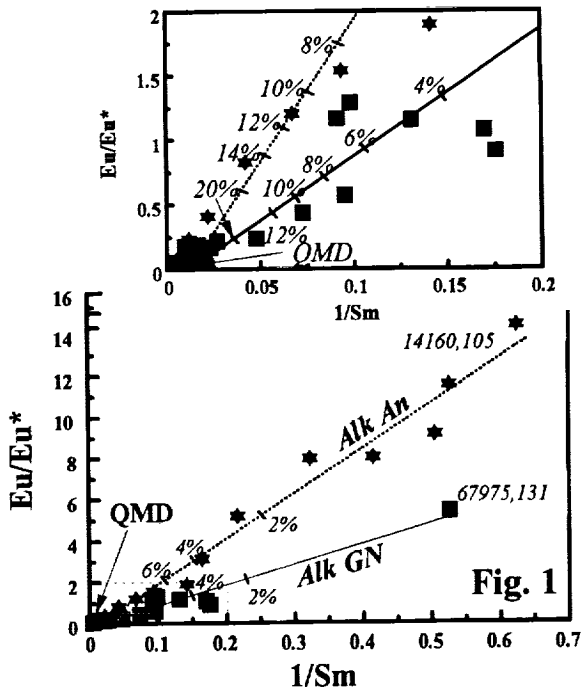

The proportion of QMD trapped liquid in the cumulate can also be estimated from Figure 1. Most alkali gabbronorites and alkali anorthosites contain less than 10% trapped liquid. In fact, the vast majority of alkali suite rocks cluster between 2-15% trapped liquid. However, several rocks indicate in excess of 20% trapped liquid and two gabbronorites (15405,170 and 67975,136) and one anorthosite (14305,283) indicate significant accumulation of a REE-rich, yet Eu-poor, mineral such as whitlockite.

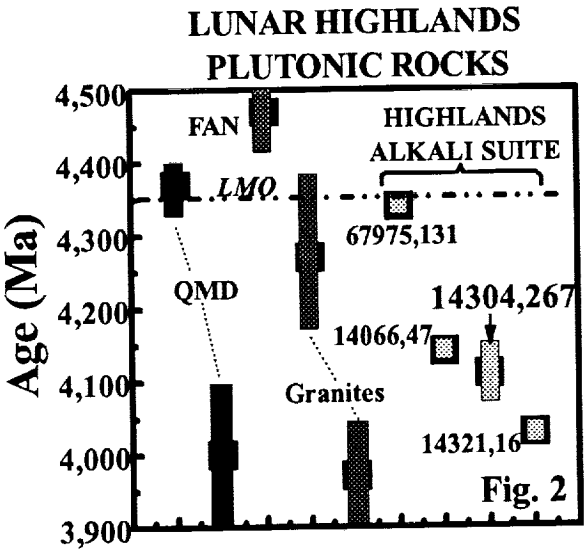

Based on similarities in mineral chemistry and modelling of trace-element ratios, the interpretation of a kinship of the highlands alkali suite with QMD seems plausible. However, the ages of the western highlands alkali suite rocks obviates their direct derivation from a residual QMD liquid of the lunar magma ocean. This early magma ocean could not have persisted beyond 4360 Ma ago [13]. In a study of zircons from various lunar rock types, Meyer et al. [14] achieved precise ages for two Apollo 14 rocks of alkalic highlands affinity: alkali anorthosite 14321,16 and Mg alkali gabbronorite 14066,47 yielded ages of 4028 ± 6 Ma and 4141 ± 5 Ma, respectively. These two ages bracket the age obtained for 14304,267 (4108 ± 53 Ma) presented herein and suggest alkalic magmatism over about 100 Ma duration on the western limb of the Moon (Figure 2). Therefore, the parental liquid(s) for the alkali suite rocks must be a later melt of either an evolved pluton, or the crystallized products of residual KREEPy magma ocean. Evidence that these rocks are indeed melts of a KREEP source rock (original urKREEP residuum?) is found in the initial $^{143}Nd/^{144}Nd$ of the three alkali anorthosites analyzed in this study [4-5]. The initial ε_{Nd} of the mineral isochron is -1.0, indistinguishable from KREEPy rocks at this time [6].

REFERENCES: [1] Brown, G.M. et al. (1972), *PLSC 3rd*, 141-157; [2] Warren, P.H. and Wasson, J.T. (1977), *PLSC 8th*, 2215-2235; [3] Hunter, R.H. and Taylor (1983), *PLPSC 13th*, A591-A602; [4] Snyder, G.A. et al. (1993), *LPSC XXIV*, 1325-1326; [5] Snyder, G.A. et al. (1994), *GCA*, submitted; [6] Shih, C.-Y. et al. (1992), *EPSL 108*, 203-215; [7] Warren, P.H. et al. (1990), *PLPSC 20th*, 31-59; [8] Snyder, G.A. et al. (1992) *PLPS 22*, 399-416; [9] Ryder, G. (1976), *EPSL 29*, 255-268; [10] Hess, P.C. (1989), Workshop on the Moon in Transition, *LPI Tech. Rpt. 89-03*, 46-52; [11] Marvin, U.B. et al. (1991), *PLPS 21*, 119-135; [12] Jolliff, B.L. (1991) *PLPS 21*, 101-118; [13] Taylor, S.R. et al. (1993), *LPSC XXIV*, 1413-1414; [14] Meyer, C. et al. (1989), *LPSC XX*, 691-692.

Rb-Sr ISOTOPIC SYSTEMATICS OF LUNAR FERROAN ANORTHOSITE 62237

Gregory A. Snyder and **Lawrence A. Taylor**, Planetary Geosciences Institute, Department of Geological Sciences, University of Tennessee, Knoxville, TN 37996-1410; **Alex N. Halliday**, Deptartment of Geological Sciences, University of Michigan, Ann Arbor, MI 48109.

Ferroan anorthosites (FAN) are likely the oldest crustal rocks on the Moon and may represent flotation cumulates from an early Moon-wide magma ocean. However, an age has been successfully determined on only one such rock to date (60025; 4.44 ± 0.02 Ga; [1]) which confirmed the antiquity of FAN. We report preliminary Rb-Sr isotopic analyses for another FAN from Apollo 16 -- 62237. However, the Rb-Sr systematics for this FAN have been severely disturbed. Sm-Nd isotopic analyses are being determined in order to obtain a reliable age.

INTRODUCTION -- Based primarily on their complementary relationship to mare basalts, as well as primitive plagioclase compositions (An_{92}-An_{96}), and evolved mafic-mineral compositions, FANs are thought to be flotation cumulates from the early lunar magma ocean. Since mare basalts are younger, remelted portions of the cumulates precipitated from the magma ocean, they cannot yield direct information on the age of the Moon. However, if FANs indeed are flotation cumulates from the early lunar magma ocean, then their ages would provide important constraints on the age and duration of the lunar magma ocean, and, thus, the Moon itself. Norman et al. [2] have obtained some Sm-Nd and Rb-Sr isotopic evidence, albeit sketchy, that a noritic ferroan anorthosite clast from breccia 67016 is quite old (possibly in excess of 4.4 Ga). To date, however, only FAN 60025 has provided a reliable age (4.44 ± 0.02 Ga).

Determing ages for FAN samples is an analytical challenge for several reasons. First, most FAN samples, though chemically pristine, are often cataclastic. Because of the antiquity of the samples (>4.3 Ga), they have likely undergone extensive meteoritic bombardment, including the proposed lunar cataclysm at 3.9 Ga; the timing of which allowed most mare basalts (which are largely < 3.9 Ga) to remain unscathed. Second, because of this extensive bombardment of surface samples and possible remobilization of Rb, Rb-Sr age determinations have not proven particularly fruitful (see below). Third, the low U and Pb abundances of the Moon in general and FANs in particular, along with the volatility of Pb, have negated the use of this system. Fourth, although Sm-Nd sytematics are more likely to remain undisturbed during meteoritic bombardment and metamorphism [3], the FANs generally consist of >98% plagioclase with extremely low abundances of Sm and Nd. Mafic minerals are rare and difficult to separate, but essential in obtaining a sufficient spread in $^{147}Sm/^{144}Nd$ ratios for a reliable Sm-Nd isochron. These challenges are formidable, though not insurmountable, as evidenced by the lack of good age information on FANs, although many have been known from the Apollo collections for over twenty years.

Rb-Sr ISOTOPIC SYSTEMATICS OF 62237,37 -- The sample was ground in acetone in a tungsten carbide mortar until individual grains were mostly monomineralic. The sample was then dried, a 50 mg whole-rock split was separated, and the remaining sample sieved into three fractions (< 75 μm; 75-140 μm; and > 140 μm). The larger two fractions (most of the sample) were then passed through a Frantz Isodynamic Separator (FIS; tilt = 15°). A current of 0.2 amps was initially employed and magnetic and non-magnetic fractions kept separate. The magnetic fraction contained a large proportion of olivine and oxides and the non-magnetic fraction was rich in plagioclase and was again passed through the FIS at a current of 0.6 amps. The non-magnetic separate from this current setting was rich in pure plagioclase, whereas the magnetic fraction contained an abundance of impure plagioclase containing oxide inclusions. The non-magnetic plagioclase separate was then hand-picked to achieve >98% purity. The 0.2 amp magnetic fraction was also hand-picked to achieve >95% pure olivine. The magnetic plagioclase separate was then leached for four hours in 20% HF; a white flocculant precipitate was formed which was decanted into a separate vial. This precipitate was then washed with 6 N HCl and H_2O and the washings added to the leachate. All separates and the whole-rock were then dissolved in HF-HNO_3 and Sm, Nd, Rb, and Sr separated using conventional cation exchange procedures.

Rb-Sr ISOTOPIC SYSTEMATICS OF FERROAN ANORTHOSITE 62237: Snyder, Taylor, & Halliday

The Rb and Sr abundances and Sr isotopic composition of these four separates and the whole-rock split are given in the Table. As indicated in Figure 1, the four separates and whole-rock do not form an isochron. Indeed, no arbitrary collection of any three points yields a line with a low error. Two- and three-point regressions yield lines which define "ages" in excess of the age of the Moon. Model ages (T_{LUNI}) for all separates, except plagioclase, are greatly in excess of the age of the Earth-Moon system, likely indicating volatilization of Rb during meteoritic bombardment; plagioclase seems to indicate post-crystallization enrichment of Rb. Even though it contains the lowest abundance of Rb, olivine has by far the highest $^{87}Rb/^{86}Sr$ by virtue of its low Sr content. Therefore, olivine also exhibits the most radiogenic $^{87}Sr/^{86}Sr$. Again, this may be due to extensive meteoritic metamorphism and redistribution of Rb within the samples. The remaining separates and whole-rock have very similar $^{87}Rb/^{86}Sr$ (0.0117-0.0129), and thus, form a vertical array on Figure 1. Sm-Nd isotopic analyses have yet to be completed for this rock, but will hopefully yield reliable age information on this important FAN sample.

Table: Rb-Sr Isotopic Data for 62237,37

sample	Rb(ppm)	Sr(ppm)	$^{87}Rb/^{86}Sr$	$^{87}Sr/^{86}Sr$	T_{LUNI}(Ga)
whole-rock	0.458	109	0.0121	0.700203 ± 17	6.60
olivine	0.190	6.35	0.0861	0.705812 ± 14	5.41
plagioclase	0.524	121	0.0125	0.699733 ± 17	3.90
mag-resid (0.6a)	0.212	47.4	0.0129	0.700172 ± 17	6.05
mag-leach	2.21	189	0.0117	0.700897 ± 27	10.6

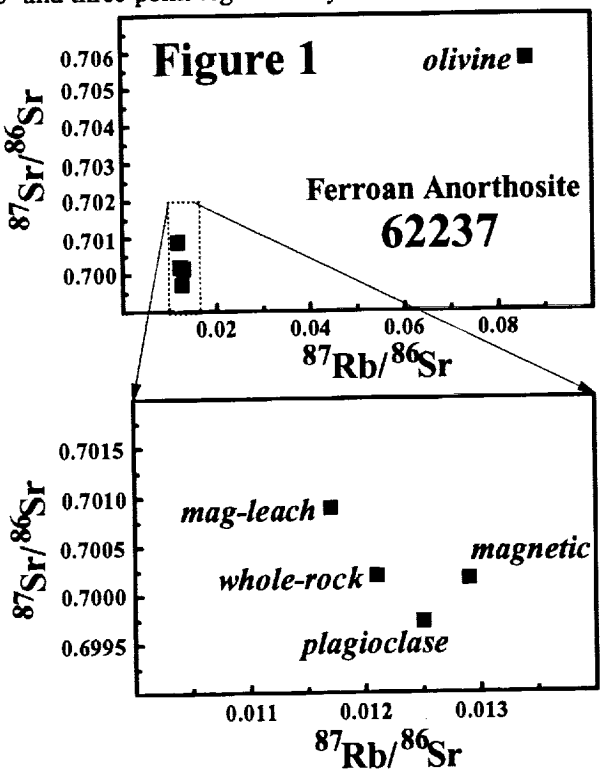

FERROAN ANORTHOSITES: EVIDENCE OF A "YOUNG" MOON? -- Carlson and Lugmair [1] assumed that the Sm-Nd age of rock 60025, being one of the oldest reliable ages on rocks returned from the Moon (4.44 ± 0.02 Ga), was that of the formation of the Moon. However, lunar magma ocean models do not allow plagioclase on the liquidus until the magma ocean is approximately 65-80% solid [4,5], consistent with the evolved mineral chemistry of mafic minerals found in FANs. Calculations of the persistence of this magma ocean suggest that it could have remained molten for 100-250 Ma [6,7]. This means that plagioclase would not have started to crystallize to form flotation cumulate FANs until after 60-200 Ma had passed. Therefore, FANs would be expected to be no older than 4.50 Ga and no younger than 4.36 Ga. The age for FAN 60025 lies within the middle of this postulated range. Therefore, there is no need for special pleading for a "young" Moon [1].

REFERENCES: [1] Carlson, R.W. & Lugmair, G. (1988) *EPSL 90*, 119-130; [2] Norman, M.D. et al. (1993) *LPSC XXIV*, 1089-1090; [3] Nyquist, L.E. et al. (1988) *LPSC XXIX*, 875-876; [4] Snyder, G.A. et al. (1992), *GCA 56*, 3809-3823; [5] Mueller, S., Taylor, G.J., & Phillips, R.F. (1988), *JGR 93*, 6338-6352; [6] Herbert, F. (1980) *Proc. Lunar Planet. Sci. Conf. 11th*, 2015-2030; [7] Warren, P.H. (1985) *Ann. Rev. Earth Planet. Sci. 13*, 201-240.

EVOLVED QMD-MELT PARENTAGE FOR LUNAR HIGHLANDS ALKALI SUITE CUMULATES: EVIDENCE FROM ION-PROBE RARE-EARTH ELEMENT ANALYSES OF INDIVIDUAL MINERALS

Gregory A. Snyder, Lawrence A. Taylor, and **Eric A. Jerde**, Planetary Geosciences Institute, Dept. of Geological Sciences, University of Tennessee, Knoxville, TN 37996-1410; **Lee R. Riciputi** Oak Ridge National Lab, Chemistry and Analytical Sciences Division, Oak Ridge, TN 37831-6365.

Rare-Earth Element analyses have been performed on cores of single grains of pyroxene, olivine, and plagioclase from several Apollo 14 Alkali Suite rocks using the SIMS technique. The ion probe analyses indicate that plagioclase is not only enriched in the REE (La = 15-30x chondritic), but can exhibit either a small positive Eu anomaly or the total lack of an Eu anomaly (14304,212). Pyroxene and olivine both exhibit large negative Eu anomalies. The evolved REE compositions of most lunar Alkali Suite rocks cannot be due to metasomatism or the accumulation of REE-rich minerals, such as whitlockite, and could have been inherited from their parental liquids. Furthermore, these analyses indicate that the minerals were precipitated from extremely evolved parental liquids, similar in REE composition to quartz monzodiorites (QMDs).

INTRODUCTION -- Alkali-rich rocks were first recognized from typical highlands suites such as ferroan anorthosites and norites (FAN) and Mg-suite rocks by Warren and Wasson [1]. Highlands Alkali Suite rocks exhibit evolved (elevated) large-ion lithophile element (LILE) whole-rock chemistry combined with evolved mineral chemistry (plagioclase, An < 90; pyroxene, En < 70), and are distinguished from metasomatized Mg suite rocks (also with evolved LILE chemistry) by their mineral chemistry (FAN-type plagioclase: An91-97 or Mg-suite-type pyroxene: En > 70). Only those samples which are determined to have attained this character through primary igneous processes are included in the Highlands Alkali Suite.

Warren and Wasson [2] and Warren et al. [3] concluded that the Alkali Suite rocks either were evolved differentiates of the Mg-suite or represent a separate, unique group. Hunter and Taylor [4] suggested, based on plagioclase and mafic mineral compositions, that these rocks represent cumulate crystallization products of evolved magmas, possibly related to the Mg-suite. Based on whole-rock trace- and major-element chemistry, and Nd and Sr isotopic systematics, Snyder et al. [5,6,7] postulated that the Highlands Alkali Suite represents a group of cumulates from evolved QMD-like liquids. We present REE chemistry of individual minerals from three Alkali Suite rocks (14304,210; 14304,212; and 14318,149) which support this hypothesis.

The petrography and mineral chemistry of probe mounts 14304,210 and 14304,212 are described in detail in Snyder et al. [7]. These probe mounts are considered to be portions of the the same large clast, designated clast "b" (14304,100) by Goodrich et al. [8]. This clast is anorthositic, but contains minor amounts of low-Ca pyroxene. Probe mount 14304,210 contains a larger proportion of low-Ca pyroxene and is classified strictly as a norite. Clast 14318,149 was studied in detail by Warren et al. [9]. He described this large clast (~1.5 g) as an "Mg-rich norite", but it has since been re-classified as part of the Alkali Suite [7]. The clast consists of 55% plagioclase, 35% low-Ca pyroxene and 12% olivine (thus, it is not truly a norite, but a gabbro) with traces of ilmenite, troilite and Fe-Ni metal [9].

ION PROBE REE DATA -- Rare-Earth Element contents have been determined in different minerals from three Alkali Suite samples, norite 14304,210, anorthosite 14304,212 and gabbro 14318,149. Plagioclase from anorthosite 14304,212 shows a considerable amount of variability in REE abundances, especially in the HREE (Fig. 1). These three analyses were taken from within a large maskelynitized plagioclase "clump" (2-3 mm) and could constitute separate grains (and/or generations) of plagioclase. The cause of the extreme variability in these analyses is not known, but either could have been inherited from a heterogeneous source (impact melt?) or could have been caused by the meteorite impact which maskelynitized the plagioclase.

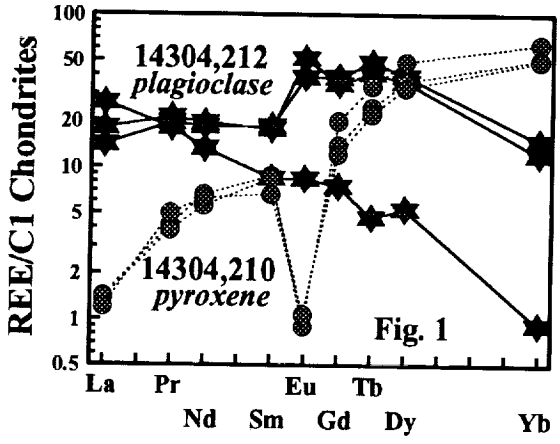

Fig. 1

Pyroxene was analyzed in two different samples, 14304,210 and 14318,149 and was found to be remarkably uniform in both REE abundances and pattern (Fig. 1 & 2). The major striking difference between the two samples

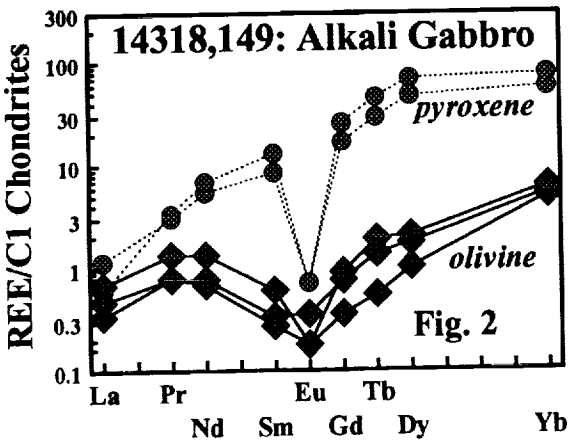

is the deeper negative Eu anomaly in norite 14304,210. Olivine in gabbro 14318,149 contains relatively low REE abundances (0.5-10 x chondrites) and exhibits a negative Eu anomaly (Fig. 2).

CALCULATED EQUILIBRIUM LIQUIDS -- Using the simple partition coefficient relation, $k_D = C_{mineral}/C_{melt}$, and the measured abundances of the REE in individual minerals, we can calculate melts which could have been in equilibrium with each mineral. These calculated liquids are shown in Fig. 3 relative to a field for actual whitlockite-free quartz monzodiorites (QMD). QMDs which contain even small amounts of whitlockite exhibit similar $(La/Yb)_n$ ratios to whitlockite-free QMDs, albeit with higher REE abundances (La = 2000-5000x chondrites) and larger negative Eu anomalies. As can be seen in Fig. 3, all of the melts calculated from pyroxene analyses, along with one calculated from plagioclase analyses, plot within or near the field of QMDs and have similar $(La/Yb)_n$ ratios. The HREE and Eu abundances of all but two calculated liquids plot within or near the QMD field.

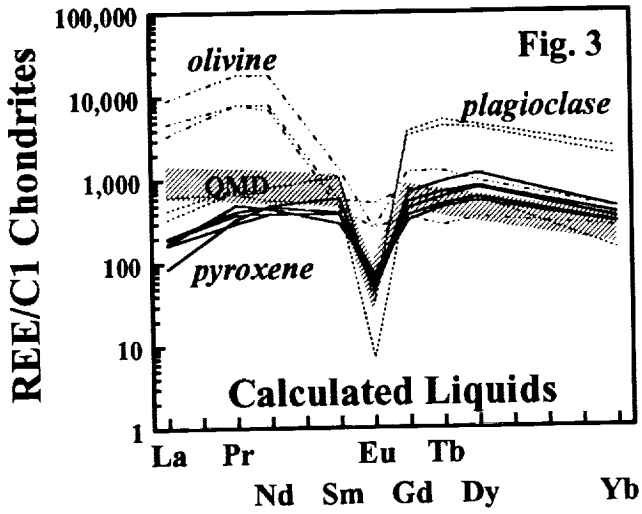

The LREE of calculated melts show considerable variability (i.e., two orders of magnitude, La = 100-10,000x chondrites). This may be due to the extremely low abundances of the LREE in both the olivine and the pyroxene analyses. Differences in only a few tens of ppb would make a large difference in the REE abundances of these minerals, and thus, a large difference in the LREE of the calculated liquids. The HREE in both pyroxene and olivine are 10-50x more abundant than the LREE and would, therefore, not be as subject to error in the analysis (which are, comparatively, quite large for the LREE at such low abundances). The HREE are a more robust indicator of actual REE composition in each mineral. We find it compelling that the HREE abundances calculated for all minerals generally plot within or near the field of QMDs.

QMD-MELT PARENTAGE FOR ALKALI SUITE ROCKS -- Snyder et al. [6,7] have shown major- and trace-element modelling which points to QMD-melt heritage for highlands Alkali Suite rocks. Furthermore, isotopic analyses have also confirmed this link [6]. Analyses of the REE in minerals of Alkali Suite rocks indicates that these minerals precipitated from evolved liquids which have undergone extensive plagioclase fractionation and thus, contain high REE concentrations (La = 100-2000x chondrites) and large negative Eu anomalies. The REE character of these calculated liquds are similar to that of QMDs. This evidence, combined with previous isotopic, trace-, and major-element modelling [6] is consistent with the scenario whereby Alkali Suite rocks are precipitation cumulates of an evolved melt similar in composition to lunar QMDs.

REFERENCES: [1] Warren, P.H. and Wasson, J.T. (1977), *PLSC 8th*, 2215-2235; [2] Warren, P.H. and Wasson, J.T. (1980), *PLPSC 11th*, 431-470; [3] Warren, P.H. et al. (1981), *PLPSC 12th*, 21-40; [4] Hunter, R.H. and Taylor, L.A. (1983), *PLPSC 13th*, A591-A602; [5] Snyder, G.A. et al. (1993), *LPSC XXIV*, 1325-1326; [6] Snyder, G.A. et al. (1994), *LPSC XXV*, this volume; [7] Snyder, G.A. et al. (1994), *GCA*, submitted; [8] Goodrich, C.A. et al. (1986), *PLPSC 16th*, D305-D318; [9] Warren, P.H. et al. (1983), *PLPSC 13th*, A615-A630.

JOURNEY TO THE CENTER OF THE REGOLITH: PETROLOGY AND MINERAL CHEMISTRY OF A NEW FERROAN ANORTHOSITE FROM DRIVE TUBE 68002/68001

Gregory A. Snyder **Lawrence A. Taylor**, and **Allan D. Patchen**, Planetary Geosciences Institute, Dept. of Geological Sciences, University of Tennessee, Knoxville, TN 37996-1410.

We report the first petrographic and mineral-chemical analyses of rock fragments from double drive tube 68002/68001. Two clasts were allocated; one is a basaltic impact melt with acicular, calcic plagioclase (An_{86-93}), microphenocrysts in a devitrified glass matrix. The other fragment is a granular ferroan anorthosite (An_{92-94}) with orthopyroxene compositions of En_{52-58}.

INTRODUCTION -- Double drive tube 68002/68001 was collected near South Ray crater, along the rim of Wreck crater, by Apollo 16 lunar module pilot Charles M. Duke, Jr. [1]. Over twenty years later, sample 68002 (the upper part of the core) was extruded from the drive tube on February 17, 1993 and several dissection passes were made by the Curatorial Staff at Johnson Space Center, Houston. A large anorthositic fragment was discovered in the second pass from 0.4-3.7 cm from the lunar surface, and a smaller, basaltic fragment was found 4.5 to 5.0 cm from the lunar surface. Probe mounts were made and allocated of both fragments ("anorthosite" = 68002,2131; "basalt" = 68002,229) and a 215 mg sample of the "anorthosite" (68002,2128) was allocated at the same time. INAA analyses (for siderophiles) will be performed on this "anorthosite" sample to determine its chemical pristinity.

PETROLOGY AND MINERAL CHEMISTRY -- Sample ***68002,229*** is an oval-shaped fragment approximately 2 mm across and consists of devitrified glass and fine skeletal grains hosting acicular, plagioclase microphenocrysts (< 1mm in longest dimension; Figure 1: field of view is 2 mm across). The plagioclase microphenocrysts comprise approximately 30% of the fragment and vary in composition from $An_{93.7}$ to $An_{95.3}$ although rims of more equant grains can have compositions as low as An_{85}. Olivine is rare and equant and has a composition of Fo_{78}. FeNi metal is present and contains Ni and Co abundances of 5 to 7 wt.% and 0.5 to 0.6 wt.%, respectively. The texture, mineralogy, and mineral chemistry of sample ***68002,229*** lead to the preliminary conclusion that it is an **impact melt**.

Figure 1

Sample ***68002,2128*** is an equigranular, hypidiomorphic, granulated fragment measuring 7 mm in longest dimension (Fig. 2: next page; field of view is 2.5 mm across); the parent sample (68002,2117) was much larger, measuring ~35 mm in longest dimension and weighing 13.7 g. The fragment is ~85% plagioclase with a uniform composition of $An_{91.5-91.9}$. Orthopyroxene occurs in granular clusters (where, locally, it comprises 60-70% of the area) with plagioclase at either end of the fragment and comprises ~15% of the sample. The orthopyroxene varies in composition from $Wo_{17}En_{52}Fs_{31}$ to $Wo_4En_{58}Fs_{38}$ (with some of the higher Wo contents attributable to fine clinopyroxene lamellae) and shows little core to rim variation (Figure 3; next page). Clinopyroxene occurs both as exsolution lamellae ($Wo_{40}En_{41}Fs_{19}$) in orthopyoxene and as less common individual grains ($Wo_{36-40}En_{41-43}Fs_{18-21}$). Individual clinopyroxene grains also contain exsolution lamellae of orthopyroxene. Using mineral-chemical criteria [2,3], this sample is likely a **ferroan anorthosite**.

Figure 2

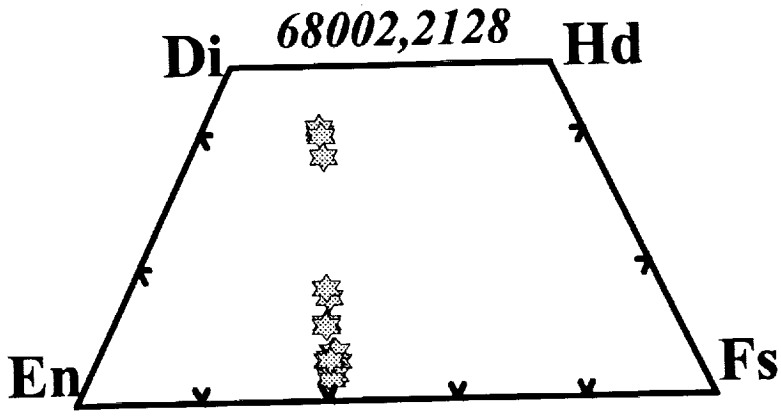

Figure 3: Pyroxene Quadrilateral

FUTURE STUDIES OF "FERROAN ANORTHOSITE" ***68002,2128*** -- This fragment could be classified as a ferroan anorthosite. The granular texture is suggestive of metamorphism due to meteorite impact, but its uniform texture and mineral-chemical compositions suggest that it is monomict. However, INA analyses are being performed in order to confirm the pristinity of the sample and determine if the incompatible elements are in line with those of ferroan anorthosites [4]. The high mafic mineral content (~15%) of this sample, relative to other known ferroan anorthosites, may also allow the age of this rock to be accurately determined using the Sm-Nd isotopic technique. Since a precise age has been determined on only one ferroan anorthosite (60025; [5]), such a determination would be paramount to an understanding of early lunar crustal genesis.

REFERENCES: [1] Ulrich, G.E. et al., editors (1981) *USGS Prof. Paper 1048*, 539 pp.; [2] Warren, P.H. (1990), *Amer. Mineral. 75*, 46-58; [3] McGee, J.J. (1993), *JGR-Planets 98*, 9089-9105; [4] Warren, P.H. and Wasson, J.T. (1978), *PLPSC 9th*, 185-217; [5] Carlson, R.W. and Lugmair, G. (1988), *EPSL 90*, 119-130.

CRYSTAL SIZES IN MAGMA OCEANS: APPLICATION TO THE SUSPENSION PROBLEM; V. S. Solomatov, and D. J. Stevenson (Division of Geological and Planetary Sciences, 170-25, California Institute of Technology, Pasadena, CA 91125)

The size of the crystals in magma oceans is crucial for the models of differentiation of the early Earth and Moon. The crystal size is controlled by internal nucleation in descending convective flows and by Ostwald ripening at the latest stages of crystallization. The theory of nucleation and crystal growth is developed in a general case for the systems undergoing continuous cooling. The theory explains the results of laboratory experiments and is used to estimate the crystal sizes in magma oceans. The crystals can grow to about 0.1-1 cm diameter. Crystals of such sizes can be suspended by convection but only in limited amounts. Sedimentation of a fraction of the crystals might result in a partial differentiation of magma oceans.

Crystallization of a deep magma ocean starts at the bottom and proceeds upward. This is because the melting curve of the perovskite [1] and, thus, the liquidus of the perovskite-magnesiowüstite lower mantle, is much steeper than the adiabatic temperature curve of the magma ocean [2]. When the adiabat drops below the liquidus, the fraction of the solid phase is small and initially the crystals form a suspension. According to [3], if the crystals in the suspension are large enough they settle down and the magma ocean undergoes a chemical differentiation; if they are sufficiently small, they remain in suspension and the magma ocean crystallizes in equilibrium although it can differentiate later [2]; in an intermediate case, the magma ocean undergoes a partial differentiation.

The crystal size is controlled by internal nucleation in descending convective flow and by Ostwald ripening which might be important at the latest stages of crystallization [4]. Nucleation in descending convective flow occurs at the depth where the temperature of the magma becomes equal to the liquidus temperature. This process can be described in terms of an effective cooling rate:

$$\dot{T} = (\nabla T_{liq} - \nabla T_{ad}) u_c \approx 10^{-4} - 10^{-2} \text{ K/s}, \quad (1)$$

where $\nabla T_{liq} \approx 2$ K/km is the gradient of the liquidus [1], $\nabla T_{ad} \approx 0.5$ K/km is the adiabatic gradient [2], and $u_c \approx 6 - 600$ cm/s is the convective velocity [3]. The smallest values of u_c correspond to the case of the slowest convection because of the greenhouse effect and rotation. In such a formulation, $\dot{T}$ is similar to the cooling rate in usual laboratory experiments on nucleation and crystallization under continuous cooling. Fig. 1 shows available laboratory data on the dependence of the crystal size on the cooling rate for various systems and a possible range of cooling rates and crystal sizes for the magma ocean. The crystal size depends on the diffusion coefficient D, cooling rate $\dot{T}$ and the effective surface tension σ for nucleation approximately as

$$d \propto \sigma D^{1/2} \dot{T}^{-1/2}, \quad (2)$$

which explains, for example, the slope of the data sets in Fig. 1.

CRYSTAL SIZES IN MAGMA OCEANS; V. S. Solomatov and D. J. Stevenson

We find that for the composition, temperature and pressure conditions of magma oceans, the diameter of the crystals is likely to be about 0.1-1 cm. Crystals of this size can be suspended in magma oceans [5]. However, energetics limits the amount of solids which can be suspended without sedimentation [3,5]. The crystals might settle down when the crystal fraction is only a few percent or less. This implies a partial differentiation of the magma ocean.

References. 1. Zerr A. and R. Boehler (1993) *Science, 262,* 553-555. 2. Solomatov V. S. and D. J. Stevenson (1993) *J. Geophys. Res., 98,* 5391-5406. 3. Solomatov V. S. and D. J. Stevenson (1993) *J. Geophys. Res., 98,* 5375-5390. 4. Solomatov V. S. and D. J. Stevenson (1993) *J. Geophys. Res., 98,* 5407-5418. 5. Solomatov V. S., P. Olson and D. J. Stevenson (1994) *Earth Planet. Sci. Lett.*, in press. 6. Solomatov V. S. (1994) submitted to *J. Crystal Growth.*

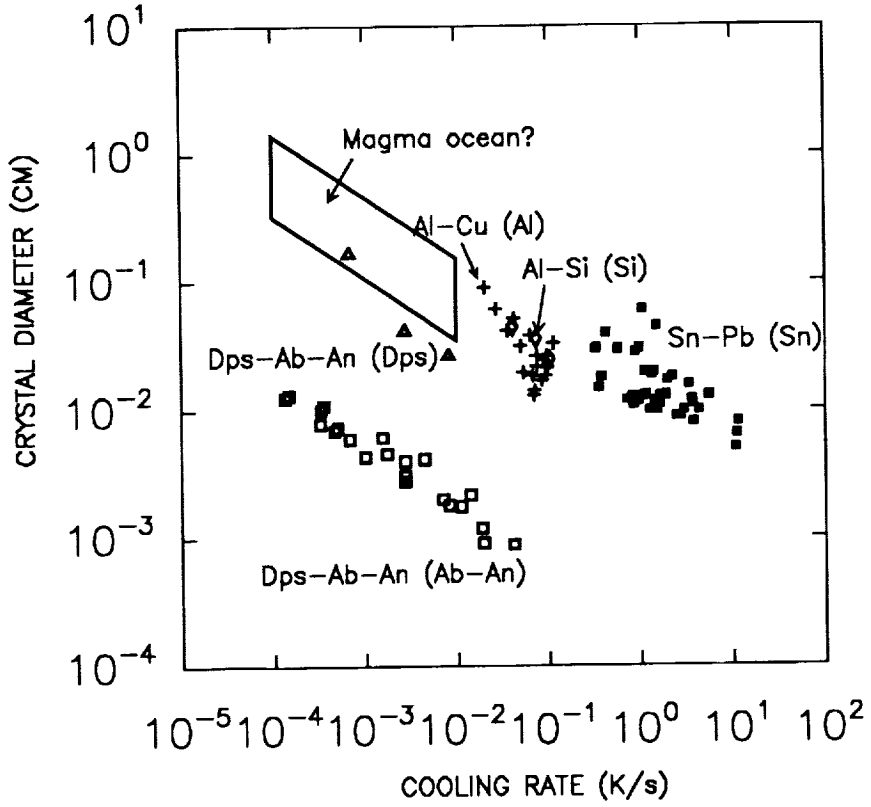

Fig. 1. The dependence of the crystal diameter on the cooling rate in the diffusion regime (from [6]). The experimental data are shown for Sn – Pb (Sn) (solid boxes), Al – Cu (Cu) (crosses), Al – Si (Si) (diamonds), Dps – An – Ab (Dps) (triangles), and Dps – An – Ab (An – Ab) (open boxes). The crystallizing phase is shown in parenthesis. A possible location of the magma ocean is indicated. It is calculated from the theoretical model assuming a peridotite-like composition. The nucleation kinetics is assumed to be similar to that of plagioclase and diopside.

GRAVITY ANOMALIES OVER VOLCANOES ON VENUS: IMPLICATIONS FOR LITHOSPHERIC THICKNESS AND VOLCANO HISTORY; Sean C. Solomon, Department of Terrestrial Magnetism, Carnegie Institution of Washington, Washington, DC 20015; Patrick J. McGovern and Mark Simons, Department of Earth, Atmospheric, and Planetary Sciences, Massachusetts Institute of Technology, Cambridge, MA 02139; and James W. Head, Department of Geological Sciences, Brown University, Providence, RI 02912.

Introduction. High-resolution gravity anomaly measurements by the Magellan spacecraft indicate that a number of the largest volcanoes on Venus are sites of significant positive free air anomalies. Volcanoes are of interest both as manifestations of magmatism and volcanic eruptive phenomena and as loads of known magnitude and dimensions on a planetary lithosphere. The gravitational signature of a volcano provides constraints on both issues that are independent of those obtained only from topography, imaging, or physical modeling. In this paper we utilize the latest representations of the gravity field of Venus to characterize the gravity anomalies of large volcanoes on the planet, to infer from those anomalies the effective elastic lithosphere beneath the volcanic loads, and to discuss the implications for the evolution of volcanic edifices on Venus.

Approach. For each volcano greater than 100 km in diameter identified from Magellan radar images [1], we have assessed whether a free air anomaly is resolvable on current representations of the free air gravity anomaly field. Both unfiltered and bandpass-filtered gravity fields have been examined. For those volcanoes with a resolvable anomaly, we have estimated the excess mass of the volcano through the application of Gauss's theorem to a bandpass-filtered map of the free air gravity field. From the excess mass and the edifice volume calculated from topography subjected to the same bandpass filter, we estimate an effective density for each volcano. These effective densities are compared with forward-model predictions of a simply parameterized compensation model (e.g., local Airy isostasy, elastic plate flexure) to derive the key model parameter for each volcano with a gravity anomaly signature.

Gravity Fields. Our principal source of gravity field information for Venus is the latest spherical harmonic representation of the geoid [2]. The results cited below were obtained using geoid PMGN60I, complete to harmonic degree and order 60 and including tracking data from both the Pioneer Venus Orbiter and Magellan through the end of cycle 4 in May of this year [2]. These results will be updated as improved fields at comparable resolution incorporating tracking data obtained since August, when Magellan achieved its present nearly circular orbit, become available. Where appropriate, regional field representations obtained by direct inversion of line-of-sight tracking data [e.g., 3] will also be used.

Because most of the power in the geoid is at the longest wavelengths [2] and because many volcanoes are associated with larger-scale features in both the topography and free-air gravity fields, it is necessary to filter these fields to isolate the anomalies attributable to individual volcanoes. A highpass filter is necessary to remove the effects of longer wavelength features, and a lowpass filter is desirable to avoid the effect of angular order truncation in harmonic field representation. We have utilized a bandpass filter applied in the wavenumber domain to the harmonic free air gravity and topography fields. The filter is defined by two half-Gaussian curves in angular order; the cutoff and half width of each half-Gaussian are free parameters.

Gravity Anomalies and Effective Densities. For a filter in which the highpass edge has a half-amplitude at harmonic degree 32 and zero amplitude for degrees 20 and less and for which the lowpass is simply the original truncation of the harmonic field, a total of 14 free air gravity anomalies of 25 mgal or greater can be associated with large volcanoes on Venus. Surface free air anomalies for these features range up to 90 mgal, with magnitudes sensitive to the passband applied to the geoid. All of the volcanoes with resolved gravity anomalies are located on or associated with one of the broad volcanic rises: Beta, Phoebe, Dione, Eistla, Bell, and Atla Regiones. On the basis of their broad topographic swells, large ratios of long-wavelength geoid to topography [4], rifting, and magmatism, such rises are generally held to overlie sites of upper mantle upwelling [e.g., 5]. The edifices of these volcanoes range from about 200 to 500 km in diameter, and the associated flow aprons range in diameter from 250 to 1000 km.

The excess masses derived from the 14 resolved free air highs over volcanoes are $(1\text{-}3)\times10^{17}$

kg, and the edifice volumes calculated from similarly filtered topography are (0.5-1.5)x10^{14} m^3. The effective volcano density, equal to the band-limited excess mass divided by the similarly band-limited volume, varies from 1100 to 2400 kg/m^3 and displays a weak inverse correlation with edifice volume (Figure 1). While excess mass and edifice volume depend on the details of the bandpass filter, effective density is relatively robust with respect to filter parameters.

Elastic Plate Flexure Models. Because the present gravity field yields at most only a few independent pieces of information about the gravity signature of individual volcanoes, we choose to make quantitative inferences on the basis of comparisons with simple analytic forward models. The most reasonable simple model is that of loading of an elastic plate from above. We have calculated the effective density of conical volcano loads of a given radius and height for a range of thicknesses of a low-density crustal layer and of the elastic lithosphere. The effective density is obtained from the theoretical gravity field and from the predicted topography (load plus flexural response) subjected to a similar bandpass filter as the observed fields. Solutions for one set of models are shown in Figure 2. The effective density is strongly dependent on elastic lithosphere thickness T_e and only weakly dependent on crustal thickness T_c. The effective density also depends on load radius (increasing for smaller loads) and, less strongly, on load magnitude.

Inferences. The effective densities inferred from the free air gravity anomalies over large volcanoes on Venus require elastic plate thicknesses of 30-70 km. Such values for the elastic plate thickness are in the upper range of those reported on the basis of topographic profiles, interpreted in terms of lithospheric flexure, outward of several different types of large-scale feature on the planet [6-8]. This result supports the view that the growth and maintenance of large volcanic edifices requires both a thick elastic or mechanical lithosphere, to support the mass of the load, and a strong lower crust, to resist ductile flow driven by the differential stresses associated with the large topographic relief [9]. Large volcanoes on Venus, with heights of several kilometers and diameters of hundreds of kilometers, must therefore have been restricted to times and locales when the above conditions were satisfied. That the large volcanoes with resolvable free air gravity anomalies are all associated with broad rises, sites of presumed mantle upwelling and therefore heat flux at least as great as the planetary norm, suggests that the conditions of thick elastic lithosphere and strong lower crust may have held over most of the globe and over much of the history preserved in the geological record of the last 500 My [10].

References. [1] J.W. Head et al., *JGR, 97*, 13153, 1992; [2] A.S. Konopliv et al., *GRL, 20*, 2403, 1993; [3] S.E. Smrekar, *Eos Trans. AGU, Fall Mtg. Suppl., 74*, 374, 1993; [4] M. Simons, B.H. Hager and S.C. Solomon, *Science*, submitted, 1993; [5] S.C. Solomon et al., *JGR, 97*, 13199, 1992; [6] S.C. Solomon and J.W. Head, *GRL, 17*, 1393, 1990; [7] D.T. Sandwell and G. Schubert, *JGR, 97*, 16069, 1992; [8] P.J. McGovern and S.C. Solomon, in *Inter. Colloq. on Venus*, p. 68, LPI, 1992; [9] S.E. Smrekar and S.C. Solomon, *JGR, 97*, 16121, 1992; [10] G.G. Schaber et al., *JGR, 97*, 13257, 1992.

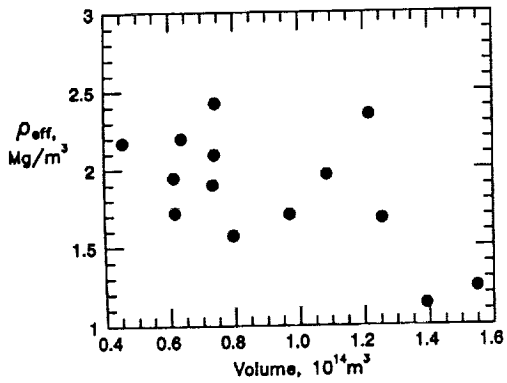

Fig. 1. Effective density ρ_{eff} versus bandpass-filtered edifice volume for 14 large volcanoes with resolvable free air gravity anomalies.

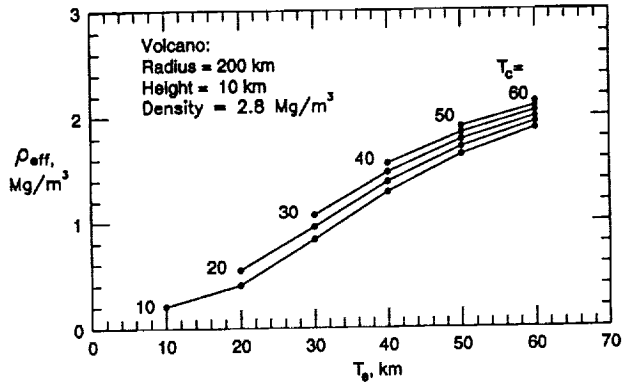

Fig. 2. Effective density for a flexurally compensated volcano load versus elastic plate thickness T_e and crustal thickness T_c.

THE BIMODAL SIZE DISTRIBUTION OF NEAR-EARTH ASTEROIDS; D.H. Speidel, Dept. Geology, Queens Coll., CUNY, Flushing, NY 11367

Probability graph analysis of 153 near-Earth asteroids identified through May 1993 supports the contention that the size distribution of such asteroids can be well described as two populations with diameters that display a log normal distribution. The larger has a mean diameter of 1.2 km and is well defined. The smaller has a mean diameter of 0.013 km and is not as well constrained. These findings are consistent with multiple-sized populations of fragments previously noted in impact experiments.

The diameters of the 153 NEAs were taken from the appendix in *The Spaceguard Survey* [1] with more recent additions as reported by Rabinowitz *et al* [2]. The asteroids are rank-ordered by decreasing diameter and plotted on probability graphs as cumulative percent larger. This technique is well-known in exploration geochemistry [3] and has recently been applied to size distributions of asteroids [4], impact craters [5], and even earthquake magnitudes [6]. The curve that is produced is a composite of, in this case, two populations present in the ratio 90:10. Clearly this ratio will change with concomitant change in the appearance of the curve as more small NEAs are identified.

The NEA diameter populations that can be deaggregated from the composite are [1.2; 2.8/0.5] and [0.013; 0.023/0.007] given in the form [mean; $+1\sigma/-1\sigma$]. The boundary between the bottom of the larger population and the top of the smaller population is distinct because limited overlap occurs at less than the 3σ values for each population. There have been ample discoveries at both larger and smaller diameters so the "gap" can not be explained as an artifact of the measurement/discovery process.

Recent impact experiments provide support for two populations of product fragments. Nakamura and Fujiwara [7] stated that "fragments could be divided into ... the core, fine fragments .. and larger fragments other than the core." Probability graph analysis indicates that the normalized fragment mass of their fractured basalt target is normally distributed. Evans *et al* [8] report on an experiment where the results are a normal distribution of main fragments coupled with additional much smaller fragments. Probability graphs of her raw data (graciously shared) confirm the normal distribution of the larger fragments and support the argument for a normal distribution of the finer fragments as well.

References: [1] Morrison, D.,ed. (1992) *The Spaceguard Survey, Report of the NASA International Near-Earth-Object Detection Workshop* NASA-TM-107979. [2] Rabinowitz, D.L. *et al*, (1993) *Nature*, 704-706. [3] Sinclair, A. J. (1976) *Application of Probability Graphs in Mineral Exploration*, Assoc. Exploration Geochemists. [4] Speidel, D.H. (1991) *GSA Abstracts with Programs Annual Meeting*, A474-475. [5] Speidel, D.H. (1993) *Lunar Planetary Sci. XXIV*, 1333-1334. [6] Speidel, D.H. and Mattson, P.H. (1993) *Bull. Seismo. Soc. Am.* **83**, 1893-1901. [7] Nakamura, A. and Fujiwara, A. (1991) *Icarus* **92**, 132-146. [8] Evans, N.J. *et al* (1993) *Lunar Planetary Sci. XXIV*, 457-458

LASER FUSION ^{40}Ar–^{39}Ar DATING OF PSEUDOTACHYLITES FROM THE VREDEFORT IMPACT STRUCTURE: NEW EVIDENCE FOR A MAJOR FORMATION EVENT AT 2.0 Ga

John G. Spray, Department of Geology, University of New Brunswick, Fredericton, Canada
Simon P. Kelley, Department of Earth Sciences, Open University, Milton Keynes, U.K.

Six pseudotachylyte samples from the Vredefort Structure of South Africa have been dated using the laser probe Ar-Ar technique. This recent development of the conventional K-Ar and Ar-Ar step heating techniques allows for the microanalysis of small (<150 μm) diameter areas within polished specimens. This is particularly useful for pseudotachylyte dating, as enclosed clasts and other wallrock material can be carefully avoided during the analysis of pseudotachylyte matrices. Following irradiation, polished 1 mm thick, 1 cm^2 tiles of selected pseudotachylytes were probed using a Spectron SL902 CW Nd-YAG laser. Gases extracted from 100 μm diameter pits using short laser pulses were analyzed with a MAP 215-50 noble gas spectrometer. On the basis that most if not all the selected pseudotachylytes comprise matrices formed by frictional melting, dating the matrix material should indicate their time(s) of formation (i.e. supercooling or crystallization of microlites).

Pseudotachylyte material was selected from six different field locations having a maximum separation of 40 km. Four of the dated samples occur within the 'outer granite gneiss' and fall within a crude ring located approximately 15 km from the centre of the 'dome'. These include the Otavi Quarry, Leeukop Quarry, Lesotakraal and Broodkop localities. The two remaining samples are located within (a) quartzites of the Johannesburg Subgroup, 20 km ENE of Parys and (b) in association with bronzite granophyre dykes near Lesotaspruit. All samples show evidence of resetting to varying degrees. Resetting is most evident at the margins of pseudotachylyte veins, especially the thinner (cm or less thick) samples. Within about 1 mm of margins, ages of 1.3-1.4 Ga are prevalent. We attribute this alteration/resetting to fluid migration along pseudotachylyte-host rock margins and to resultant partial degassing. However, within the centres of veins 2.0 Ga is the dominant age. The centre of the sample from Leeukop Quarry gives the best age at 2.01 Ga and all five samples yield single maximum ages of 2.0 Ga. This age concurs with that of Walraven et al. [1] for bronzite granophyre (2.0 Ga) which, as a root to an original overlying melt sheet [2], is purported to date the Vredefort impact event.

On the basis of the above data, we conclude that most of the pseudotachylytes in and around the Vredefort Dome were generated by the impact process at 2.0 Ga. This probably occurred during the modification stage of the impact process when ring- and radial fault/fracture structures developed in the basement target lithologies. Our conclusions are contrary to those of Reimold et

VREDEFORT PSEUDOTACHYLYTES

SPRAY, John G.

al. [3], who propose that the pseudotachylytes were formed during several independent (i.e. endogenic) high strain rate events. We attribute their spread of pseudotachylyte ages (1.09 to 2.25 Ga) to the effects of their analyzing crushed, whole rock pseudotachylyte samples. Such material would have included partially degassed pseudotachylyte margins, as well as older wallrock components resulting in artificial (mixed) ages being obtained. The one exception to this is their sample USA-29 which yields a plateau age of 2.01 Ga [3].

We conclude that most of the Vredefort pseudotachylytes, and especially the thicker bodies (> 1 m), were generated by comminution and frictional melting within discrete slip zones. The slip zones were faults systems generated or reactivated in response to meteorite impact. On this basis, the laser probe Ar-Ar technique of dating pseudotachylytes can be used to constrain the timing of impact. In the case of Vredefort, our data indicate a major 2.0 Ga event. Subsequent thermal pulses and/or retrogression resulted in the localized partial resetting of the original 2.0 Ga formation age.

References

[1] Walraven, F., Armstrong, R.A. and Kruger, F.J. 1990. *Tectonophysics* **171**, 23-48.

[2] French, B.M. and Nielsen, R.L. 1990. *Tectonophysics* **171**, 119-138.

[3] Reimold, W.U., Jessberger, E.K. and Stephan, T. 1990. *Tectonophysics* **171**, 139-152.

RETURN TO MERCURY: THE DISCOVERY-MERCURY POLAR FLYBY MISSION Paul D. Spudis, *Lunar and Planetary Institute, Houston TX 77058*; Jeffrey B. Plescia, *Jet Propulsion Laboratory, Pasadena CA 91109*; Alan D. Stewart, *The Boeing Company, Seattle WA 98124*

Mercury is one of the last pieces of unknown real estate in the Solar System. There have been no missions to Mercury since the three flybys of Mariner 10 two decades ago. That spacecraft mapped about 40 percent of Mercury's surface and determined that the planet possesses a weak global magnetic field [1]. Since then, the planet has been studied with Mariner data and through Earth-based optical and radar observatories. These studies have demonstrated that Mercury possesses a tenuous sodium atmosphere [2], has surface properties comparable to the moon [3], and apparently has polar caps composed of water ice [4]. As near-infrared spectra are ambiguous [5], the surface composition of Mercury, a key parameter towards understanding the chemistry of the Solar System [6], is completely unknown. We are proposing a polar flyby mission to Mercury. In accordance with the philosophy of the *Discovery* Program, our scientific objectives are focused: 1) Investigate the physical and compositional state of Mercury's polar caps; and 2) Complete the geological reconnaissance of Mercury begun by Mariner 10 by mapping the morphology and composition of units on the previously unseen hemisphere of the planet. To conduct this exploration, our payload consists of neutron, X-ray fluorescence, and thermal infrared spectrometers, a radar scatterometer, and a narrow angle camera.

We believe that a flyby mission is adequate for achieving the most significant science objectives and requires a simpler and less costly spacecraft. Such a mission simplifies requirements for the spacecraft thermal design because spacecraft perihelion is close to Mercury's aphelion (thermal flux = 4.6 suns), whereas an orbiter must be designed to survive Mercury perihelion (thermal flux = 10 suns, as well as receiving thermal radiation from the planet's surface). Moreover, a flyby spacecraft does not have to carry fuel to burn into orbit and its propulsion subsystem is smaller and much simpler; the additional mass available to a flyby spacecraft as compared to an orbiter is on the order of 300 kg. Such a mass margin permits a much larger, more robust, and diverse payload to be flown, greatly increasing the scientific return of the mission.

Launch opportunities for MPF occur every two years, but to observe the hemisphere opposite to the one seen by Mariner 10, our baseline windows occur in 1996 and 2000. The MPF mission uses a Venus gravity assist to achieve a solar-resonant orbit, thus permitting multiple flybys of the planet at little propulsive cost. The nominal MPF mission consists of three flybys, each at about 500 km altitude. The first encounter occurs approximately 10 months after launch and subsequent encounters take place approximately every 6 months; thus, the entire mission of three flybys will be completed in less than 2 years, thus greatly lowering operations cost. The first Mercury flyby will be across Mercury's north pole, seen only obliquely by Mariner 10. This pass allows us to address our primary science goal, the extent and properties of the polar cap, in addition to imaging the heretofore unseen hemisphere of Mercury. The second flyby is equatorial and completes the mapping of the hemisphere opposite the one studied by Mariner 10. The third encounter will continue these observations over the south pole of Mercury.

The MPF spacecraft is 3-axis stabilized with a scan platform to support and point the science instruments (Figure 1). The design includes articulated solar arrays, hydrazine propulsion, X-band communications, modular structure with 8 avionics bays, and a rigidly mounted, pre-deployed sun shade. The bus combines flight-proven, off-the-shelf subsystems and components along with high-technology items (such as the use of composite materials and solid state data recorders) into a simple, low-cost versatile design. The spacecraft has a dry mass of about 400 kg (including science payload and margins), produces up to 470 watts of power, and has about 1500 m/s total delta-v capability. This design provides significant growth margin and flexibility in meeting the mission requirements.

The principal science goals of the MPF mission are addressed through the analysis of multiple data sets. On all passes, both approach and departure imaging will thoroughly map the unknown hemisphere of Mercury. We will obtain full disk images of the planet at eight wavelengths between 200 and 1000 nm, permitting major color provinces to be mapped across the planet. Image mosaics will complete the surface mapping of the planet and will have an average resolution of about 200 m/pixel, comparable to existing Mariner 10 coverage of the other hemisphere. Closest approach (from about 1000 to 500 km) will yield selected images of the surface at resolutions of 5-10 m/pixel.

For the polar deposits, we want to know their extent, composition, and physical properties; from these observable facts, we hope to be able to determine deposit origin and evolution through time. On the polar passes (encounters 1 and 3), the neutron spectrometer will permit us to identify and measure hydrogen if present in amounts greater than 100 ppm. The radar scatterometer will transmit pulses in right circularly polarized (RCP) radiation and receive pulses in both RCP and left circularly polarized (LCP) modes. The ratio of LCP/RCP in the reflected power is diagnostic of surface material -- ratios greater than unity are characteristic of ice, whereas ratios of much less than unity (0.1) represent silicates [4]. Thus, the radar instrument will determine the presence and map the extent of the Mercurian polar ice caps. The thermal emission spectrometer (TES) will measure the physical properties of the polar deposits, including temperatures, which are around 60° K in the permanently shadowed areas of the Mercurian pole.

On the equatorial pass (encounter 2), geoscience will be emphasized by mapping the composition and morphology of the unknown hemisphere of Mercury. An X-ray fluorescence spectrometer will determine the abundance of the principal rock-forming elements in the crust; Al, Mg, and Si are easily measured to about 10% precision and during periods of active Sun (our year 2000 opportunity), we anticipate also determining Ca, Fe, and possibly Ti to about 20% precision. The TES will obtain mid-IR spectra for the variety of terrain units observed on the planet from which we can identify and determine the abundance of the major silicate minerals of the mercurian crust. Both of these data sets will characterize the chemistry and mineralogy of the color provinces mapped during approach and departure by imaging, thus permitting a complete assessment of the composition and stratigraphy of Mercury's surface.

Through the use of the heritage provided by the Mariner 10 spacecraft and mission design and the use of off-the-shelf instruments, we have created a low-cost, *Discovery*-class mission that effectively does the job of a *Mariner*-class mission, which would probably cost over half a billion dollars in today's fiscal climate. In contrast to some limited objective *Discovery* missions that return a few pieces of first-order information, the MPF mission will obtain hemispherical, multi-wavelength data sets for an entirely unmapped and unknown region of the Solar System. The Mercury Polar Flyby mission blazes new trails in the exploration of the planets by mapping and characterizing one of the last unknown and mysterious members of the solar family.

References [1] Mariner 10 special issues: *Science* v. 185, no.4146, 12 July, 1974; *JGR* vol. 80, 2341-2514, 10 June, 1975. [2] Potter A. and Morgan T.H. (1985) *Science* 229, 651. [3] Clark P.E. et al. (1987) in *Mercury*, Univ. Arizona Press, 77; Harmon J.K.and Campbell D.B. (1987) in *Mercury*, Univ. Arizona Press, 101. [4] Slade M.A. et al. (1992) *Science* 258, 635. [5] McCord T. B. and Adams J. B. (1972) *Science* 178, 745; Villas F. (1987) in *Mercury*, Univ. Arizona Press, 59. [6] Taylor S.R (1992) *Solar System Evolution*, Cambridge Univ. Press, 307 pp.

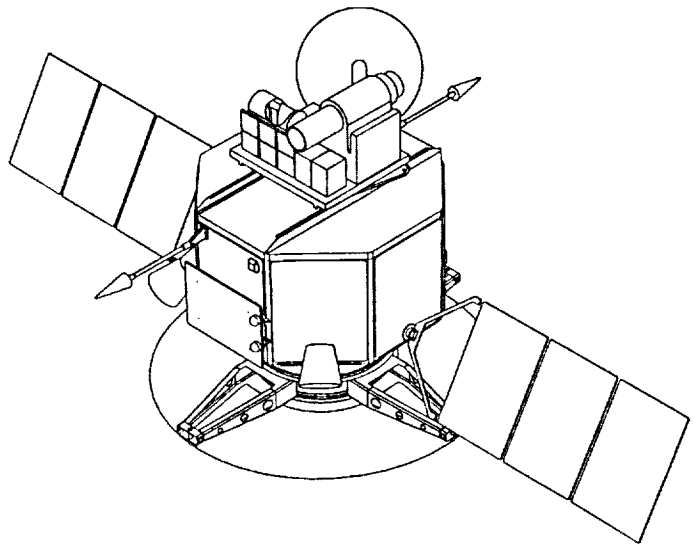

Figure 1. Spacecraft configuration, *Discovery* Mercury Polar Flyby Mission

^{41}K EXCESS IN EFREMOVKA CAIs; G. Srinivasan and J.N. Goswami, Physical Research Laboratory, Ahmedabad 380 009, India. A.A Ulyanov, M.V. Lomonosov Moscow State University, Moscow 119 899, Russia.

Studies of potassium and calcium isotopic composition in Efremovka CAIs have provided evidence for excess ^{41}K from the decay of short-lived radioisotope ^{41}Ca ($\tau \sim 0.14$Ma) and an initial (^{41}Ca/^{40}Ca) of $(1.3 \pm 0.2) \times 10^{-8}$. Our observation suggest a time interval of <1Ma between the injection of freshly synthesised ^{41}Ca into the solar nebula and the formation of Efremovka CAIs.

Ion microprobe studies of K-Ca isotopic composition of terrestrial and meteoritic phases were carried out at a mass resolution of $\sim$ 5000, sufficient to resolve the hydride interference (^{40}CaH) at mass ^{41}K. However, the $(^{40}Ca^{42}Ca)^{++}$ interference cannot be resolved at this mass resolution. Since the expected ^{41}K signal for high Ca/K (10^5 - 10^7) phases is extremely low $\leq$ 1(c/s), possible contributions from the doubly charged interference, tail of the hydride peak and the dynamic background of the counting system were monitored during isotopic measurements by obtaining count rates at masses 41.5[$(^{40}Ca^{42}Ca)^{++}$], ^{43}Ca-δM (δM = ^{40}CaH - ^{41}K) and 40.7 repectively. Measurements of terrestrial and meteoritic pyroxenes gave a value of $(2.6 \pm 0.06) \times 10^{-5}$ for the ratio [$(^{40}Ca^{43}Ca)^{++}/^{43}Ca^{+}$] . The dynamic background (at mass 40.7) is typically $\leq$0.01(c/s). We have analysed several terrestrial minerals (microcline, pyroxene, perovskite and anorthositic glass) with extreme Ca/K values ranging from $< 10^{-3}$ to 3×10^6 and all of them yielded normal potassium isotopic composition (Fig. 1). An ion yield factor of 3.2 favouring K over Ca was also determined from these analyses. The meteoritic phases (pyroxenes and perovskite) analysed in this work are from two Efremovka CAIs: E65 (type B1) and E50 (multizoned hibonite rich inclusion). Both the CAIs have ^{26}Mg excess with initial (^{26}Al/^{27}Al) close to 5×10^{-5} [1,2]. The pyroxenes, particularly those with Ca/K $\geq 5 \times 10^5$, have clearly resolvable excess ^{41}K which correlate well with their ^{40}Ca content. A best fit through the data yields a value of $(1.35 \pm 0.2) \times 10^{-8}$ for initial (^{41}Ca/^{40}Ca) and the initial (^{41}K/^{39}K) is close to the solar system value of 0.072.(Fig 1).

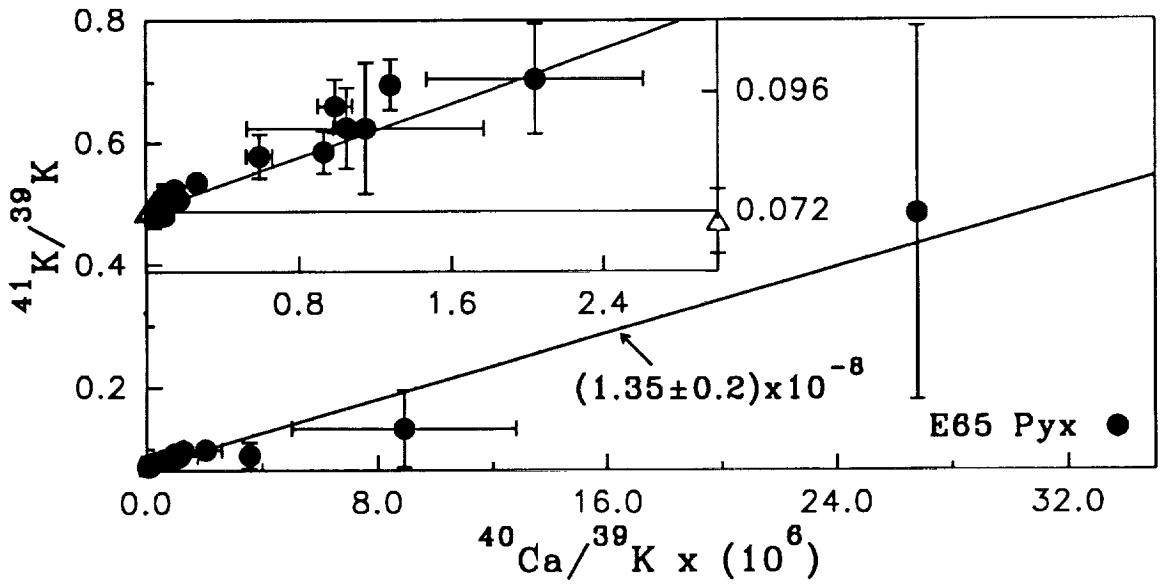

Fig 1. K-Ca isotopic systematics in pyroxene from Efremovka CAI E65. All error bars are $2\sigma_m$. The data points for the terrestrial samples are shown by open symbols.

^{41}K EXCESS IN EFREMOVKA CAIs; Srinivasan G. et al.

The observed ^{41}K excess in Efremovka CAIs can result from several possibilities: (i) production by secondary neutrons during the cosmic ray exposure of Efremovka via the [^{40}Ca(n,γ) $\rightarrow$ ^{41}Ca] reaction (ii) 'fossil' ^{41}K locked in refractory interstellar dust that are part of the initial components in the solar nebula from which CAIs are formed (iii) presence of ^{41}Ca in early solar system that was incorporated live into the CAIs during their formation and its in-situ decay. The first and the third alternative can explain the observed correlation between excess ^{41}K and (^{40}Ca/^{39}K) while it is difficult to explain this in the ' fossil' scenario.

We can rule out secondary neutron induced production of the excess ^{41}K, as the required neutron fluence ($\sim 3 \times 10^{16}$ cm^{-2}) is much higher than that expected for the Efremovka meteorite. Although the neutron fluence experienced by Efremovka has not been measured directly, one can make a fairly good estimate by considering the neutron fluence of $\leq 10^{15}$cm^{-2} experienced by the Allende meteorite belonging to the same CV3 group [3]. The recovered mass of Allende (> 2 tons) is much larger than that of Efremovka ($\sim$ 21Kg) and one does not expect the preatmospheric size of Efremovka to exceed that of Allende. Since the cosmic ray exposue age of Efremovka is only twice that of Allende the neutron fluence experienced by it cannot be more than twice the value determined for Allende. This falls short by more than an order of magnitude from the required thermal neutron fluence to explain the observed ^{41}K excess.

The possible fossil record of extinct nuclide decay products and particularly the presence of excess ^{41}K in meteoritic CAIs was first proposed by Clayton [4]. The 'fossil' scenario assumes mixing of stardust having excess ^{41}K with normal solar system matter during the formation of CAIs. One can estimate the magnitude of this excess by assuming interelement fractionation during the formation of stardust and the mixing ratio of stardust and normal solar system matter during the formation of CAIs. While we cannot completely rule out the possibility of the presence of minor amount of 'fossil' ^{41}K in the samples analysed by us, the excellent correlation between (^{41}K/^{39}K) and (^{40}Ca/^{39}K) is extremely difficult to explain in this scenario.

We therefore consider the ^{41}K excess seen in Efremovka CAIs to be a result of in-situ decay of ^{41}Ca in these objects. An earlier attempt to measure ^{41}K excess in Allende inclusions [5] suggested a somewhat lower value of $(8 \pm 3) \times 10^{-9}$ for the initial (^{41}Ca/^{40}Ca) in these objects. ^{41}Ca is the shortest lived radionuclide whose presence in the early solar system can be considered to be established from our data. Its presence places an important constraint on the time interval between the last injection of freshly synthesised ^{41}Ca into the solar nebula and the formation of CAIs. If we consider appropriate stellar production ratio for (^{41}Ca/^{40}Ca) [6], the Efremovka data suggest a value of 1.5Ma for this interval in the absence of nebular dilution. Assuming a possible dilution factor of 10^4, this time interval turns out to be less than 1Ma.

References: [1] Goswami J.N. et al. GCA 57(1993). [2] Goswami J.N. et al. Meteoritics 26, 339 (1991). [3] Göbel R.et al. GCA 46, 1777 (1982). [4] Clayton D.D. EPSL 36, 181 (1977). [5] Hutcheon I.D. et al. Meteoritics 19, 243 (1984). [6] Woosley S.E. et al. APJ 26, 231 (1973).

TRAJECTORY CALCULATION OF INDIVIDUAL PARTICLES FROM LDEF IMPACTS;
F. J. Stadermann, TH Darmstadt, Hilpertstr. 31 (Geb. H), 64295 Darmstadt, Germany.

The capture cells from LDEF experiment A0187-2 were designed to determine the number and the chemical composition of particles that impacted the surface of the satellite. During routine investigations elliptical discolorations of the target material were observed adjacent to impact features. In a method demonstrated here, these elliptical features are interpreted as results of erosion by atomic oxygen through holes in a cover foil. Based on this assumption, it becomes possible to determine the pre-impact trajectories of individual particles in addition to their original chemical composition. What makes this method particularly intriguing is the fact that it was unexpected and that the experiment was not specially designed for this kind of investigation. It is the *only* experiment on LDEF that offers this kind of combined trajectory and chemistry information of individual particles.

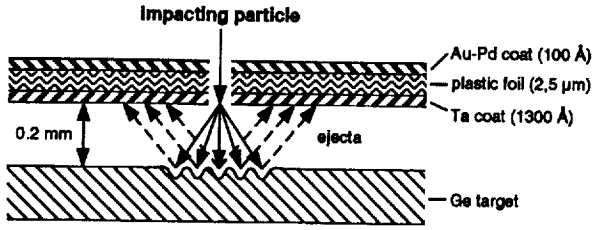

Figure 1: Schematic of LDEF capture cell experiment A0187-2.

INTRODUCTION. The LDEF experiment A0187-2 consisted of germanium target plates and a thin plastic foil, separated by 200 µm (Fig. 1). Impacting particles were partly disrupted and decelerated while passing through the foil and fragments of the particle were then collected both on the germanium plate and the back side of the foil. The extended impact features found on the germanium plates have typical diameters of several hundred µm, although the sizes of the corresponding projectiles (and of the holes in the foil) are only around 10 µm. Secondary ion mass spectrometry was then used to determine the composition of impact deposits and to infer the origin (natural or man-made) of individual particles [1]. Several extended impacts are accompanied by elliptical features (discolorations) of unknown origin on the target plate [2]. These elliptical features have diameters of around 400 µm and are always directly adjacent to or overlapping impact features. Although trays from experiment A0187-2 with identical setups were located on various differently oriented LDEF surfaces, the elliptical features are only found on tray E08 on the leading edge. On this leading edge tray none of the cover foils survived the extended exposure of the satellite, but at the time of the impacts the foils must still have been intact. The elliptical features may be explained as surface erosion effects by atomic oxygen *through the impact holes* in the foils at a time when the latter were still intact. Based on this assumption it is possible to determine (a) the exact positions of the impact holes in the foils, (b) the actual distances of the foils from the germanium plates, and (c) the trajectories of individual projectiles upon impact.

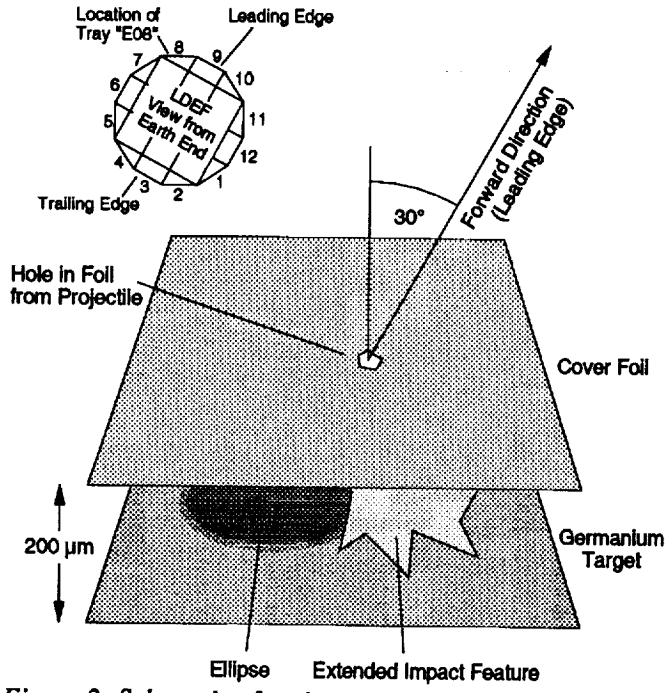

Figure 2: Schematic of an impact event on tray E08 through the cover foil. The orientation of tray E08 relative to the LDEF flight direction is shown in the insert.

GEOMETRIC CONSIDERATIONS. The LDEF satellite was exposed to atomic oxygen, which hit the surface with a collision energy of 4-5 eV almost directly from the forward (ram) direction. Tray E08 was facing sideways from the leading edge at an angle of 30° as shown in Figure 2. Oxygen atoms entering the capture cell through an impact hole from ram direction spread inside in the shape of a circular cone (Fig. 3). The vertex of this cone corresponds to the hole in the foil, which is assumed to be significantly smaller than the features on the target plate. The area where this cone intersects with the surface, *i.e.*, where the oxygen atoms collide with the germanium has the

TRAJECTORY CALCULATION OF INDIVIDUAL PARTICLES FROM LDEF IMPACTS: Stadermann F. J.

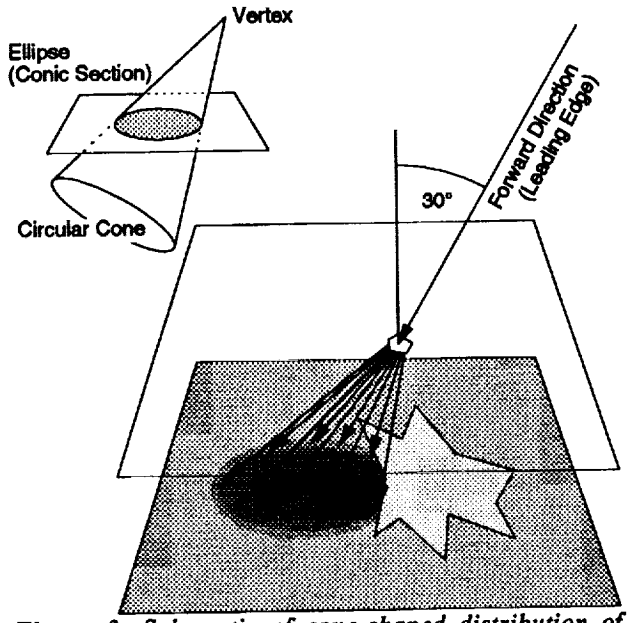

Figure 3: Schematic of cone-shaped distribution of atomic oxygen inside the capture cell and geometric interpretation of the elliptical feature as a conic section.

shape of an ellipse. The visible discolorations on the target show the range of physical or chemical reactions between atomic oxygen and germanium. Since all foils on the leading edge failed eventually, the entire surface (also outside of the ellipses) was subject to atomic oxygen at the end of the flight. Therefore the ellipses can only be understood as temporal features due to the longer exposure.

Mathematically an ellipse in a plane can be expressed as a conic section from a circular cone. With one additional piece of information – either the direction of the axis of the cone or the distance of the vertex from the surface – the cone's geometric properties can unambiguously be determined. After the location of the vertex of the cone (*i.e.*, the location of the penetration hole in the foil) has been calculated, the original trajectory of the particle before the impact can be calculated. For this the approximate location of the center of the impact feature has to be determined arbitrarily. The assumption that the 'center of gravity' of the visible extended impact feature lies on the extrapolated line of original particle trajectory may be a good first order approximation. From this information the impact angles α and ϑ (as shown in Fig. 4) can be calculated.

CONCLUSIONS. The method demonstrated here appears to be a viable way to determine individual particle trajectories from a record stored in the impact and oxygen erosion features on germanium targets from LDEF experiment A0187-2. It is possible to calculate particle trajectories *relative to LDEF* and – since LDEF was stabilized in its orbit – *relative to the Earth*. This information is not sufficient to determine individual projectile origins in the solar system by simply tracing back individual trajectories, because no information on the *timing* of the impacts is available. However, it is possible to distinguish between circular and elliptical orbits, and different entrance angles into the atmosphere. All this information can then be correlated with the measurements of the chemical compositions of the same particles and, thus, lead to a comprehensive understanding of individual particle histories. In previous studies [1, 2] the distribution of different extended impact features could not be explained, nor could the directions of the impacts be determined from the observed features on the germanium. A detailed analysis of the impacts with ellipses may lead to a better understanding of the extended impact features and may make it possible to deduce the approximate angle of impact solely from the shape of the impact feature. Once this step is reached, the study of individual particle trajectories can be extended to all impacts on germanium – even on the trailing edge. This would lead to the most complete database of particle trajectories and chemistry on LDEF.

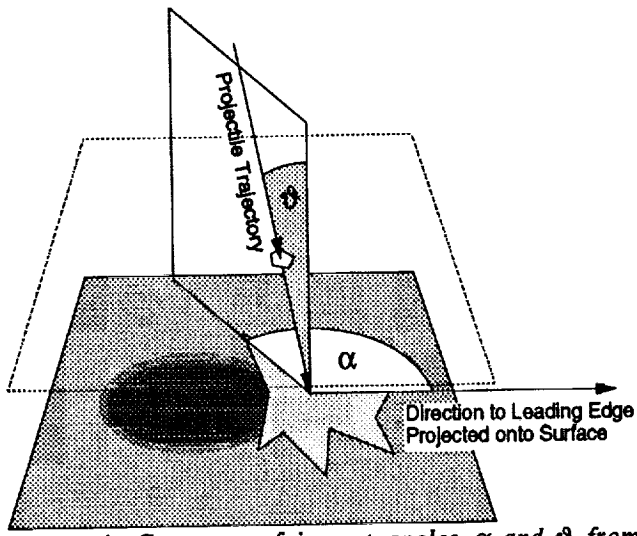

Figure 4: Geometry of impact angles α and ϑ from projectile trajectory.

REFERENCES. [1] Amari S. et al. (1992) Proc. 1st LDEF Post-Retrieval Symposium [2] Amari S. et al (1993) Proc. 2nd LDEF Post-Retrieval Symposium

SPECTRAL VARIATION WITHIN MARE TRANQUILLITATIS: IMPLICATIONS FOR STRATIGRAPHY AND MIXING MECHANISMS

Matthew I. Staid, Carle M. Pieters, James W. Head, Dept. Geol. Sci., Box 1846, Brown University, Providence, RI 02912

Introduction: Galileo's second lunar flyby in 1992 produced low and high phase angle images of the Tranquillitatis and Serenitatis basins with the Solid State Imaging (SSI) system (1). The SSI detector possesses seven channels within the wavelength range of 0.4 - 1.0 μm from which a set of compositionally sensitive ratios have been developed to identify surface units (2). These ratio images show significant spectral variation within the lunar basalts of Mare Tranquillitatis. These variations may result from compositionally distinct flows or the mixing of different highland and mare lithologies. A linear spectral mixing analysis was performed on six channels of a low phase angle (~ 25°) SSI image sequence of the basin in order to identify and map distinct spectral components. Results of this analysis were registered to higher spatial resolution telescopic images obtained at low sun lighting in order to evaluate the distribution of compositional endmembers in their geologic setting and to assess mixing mechanisms.

Data Analyses: Three standard color composite images of the Tranquillitatis region were created from ratios of the SSI data: a UV/VIS ratio (0.41/0.76 μm blue), its complement (red), and a 0.76/0.99 μm ratio (green). The intensity of the blue (0.41/0.76 μm) ratio has been empirically correlated to the titanium content of basaltic materials within the mare (3). The complement of this ratio, or the red intensity, corresponds to less titanium rich mare flows. The green component of this color display is an approximate estimate of the strength of the 1 μm iron absorption band of pyroxenes and olivines. This ratio is greatest for freshly disturbed crater materials because of a relative lack of optical alteration (4). While the color ratio images are fairly homogeneous for Mare Serenitatis, Mare Tranquillitatis shows significant spectral variations across its basin. High spatial resolution mapping of mare UV/VIS ratios in Tranquillitatis using earth-based telescopes have also observed this spectral heterogeneity (5).

A linear spectral mixing analysis was performed on the SSI data to determine what materials could mix to explain observed spectral variations. The mixing technique decomposes the reflectance signal of each pixel into fractions of individual endmember components. A number of fraction images equal to the number of endmembers in the analysis is created from the least squares solution to this mixing problem. Each fraction image displays the relative abundance of one endmember for each pixel in the image (6). Initial endmembers for mixing were selected from within the image after a detailed analysis of the spectra of the mare basalts and surrounding regions. In order to improve the results of the spectral mixing analysis, the SSI data were preprocessed to mask areas of relatively pure highland material to eliminate variations unrelated to the mare region. Sources of spectral variation within the mare, such as mixtures of highland material within the basin and bright mare craters, were preserved in the preprocessed image. The best solution in this spectral mixture analysis required the use of four endmembers: a very blue (high titanium) mare basalt from central Tranquillitatis, a red (low titanium) basalt from Serenitatis, highland material, and material rich in iron-bearing minerals from a bright mare crater in Tranquillitatis (Jansen B 26°40'E,10°50'N). Relative reflectance spectra of these endmembers are plotted in figure 1 and resulting endmember fraction images are shown in figure 2. An important step in the data analysis was registering the ratio images and the results of the mixing analysis to low illumination angle telescopic images of higher spatial resolution. These combined data allowed endmember abundance and spectral variance to be placed in the context of the regional topography of the basin. Of particular interest were the relationships of the endmembers to geologic features such as mare-highland contacts, craters, wrinkle ridges and mare domes.

Discussion: The spectral variation seen in Mare Tranquillitatis can be attributed to compositionally distinct basaltic units as well as to the effects of impact gardening into a shallow and stratigraphically complex basin. Data analysis suggests at least two distinct mare flow types. Stratigraphically younger titanium rich flows are found most abundantly in the central western portion of Tranquillitatis, while less titanium rich flows dominate significant sections of the north-eastern and south-eastern portion of the basin. Photogeologic and crater-count analysis of regions containing the higher titanium basalts indicate that these flows overlay adjacent less blue basalts (5, 9). Depending on location in the mare, impact gardening has caused vertical mixing of both highland and lower titanium underlying basalts into overlying higher titanium flow units. As expected, the mare crater endmember centers around the recent impact structures in the basin. This endmember is insensitive to boundaries between lower and higher titanium units, adding to the spectral variation of flows with similar composition.

Potential sources for the Tranquillitatis basalt flows are being investigated relative to the proximity of mare dome features (7). Since two large domes (21°30'E, 7°40'N and 21°30'E, 6°20'N) north-west of the Lamont feature are found in the titanium poor unit, the domes could be volcanic sources related to these flows. A likely source for the higher titanium basalts is a string of smaller dome features between Arago and Maclear which lie within a region of very high titanium basalts (5). Since the higher titanium flows are interrupted by islands of

lower titanium basalts that are not a result of impact mixing, it is likely that the location of the high titanium flows is a result of both source location and the topography of the basin when they were extruded.

The distribution and mechanisms of highland mixing allows evaluation of the depth of the mare units and the proximity of the underlying basin highland topography. The highland endmember fraction image shows a notable association with mare/highland boundaries although mixing of the highland endmember is more prevalent in the southwestern portion of Tranquillitatis than at the eastern mare-highland contact. In the southwestern portion of the basin, craters such as Sabine and Ritter which have been previously hypothesized as volcanic structures (8) can clearly be seen as impact features excavating shallow highland material. The highland endmember has been excavated by the large crater Arago and also maps abundantly along protruding peaks of highland northeast of that area. South of Arago, a significant portion of the highland endmember occurs on the eastern side of a set of wrinkle ridges east of the Lamont feature. High resolution Lunar Orbiter images do not show any evidence of significant impact events in this region. It is possible that these compressional wrinkle ridge features are upthrusting highland material from short distances below to mix with the surface mare. However, thrusting is not a necessary mechanism since shallow underlying highland topography along with minor impact gardening may be solely responsible for this highland component. The distribution of the highland endmember along with structural features indicate that the underlying highland topography lies unusually close to the surface below these regions. This distribution of highland material supports the existence of shallow sub-mare basin topography, perhaps relating to the proposed inner ring of Procellarum which has been mapped through the center of the basin from its south-western edge up to the northeast portion of the basin just east of southern Serenitatis (9).

Figure 2: Endmember fraction images of the Tranquillitatis region

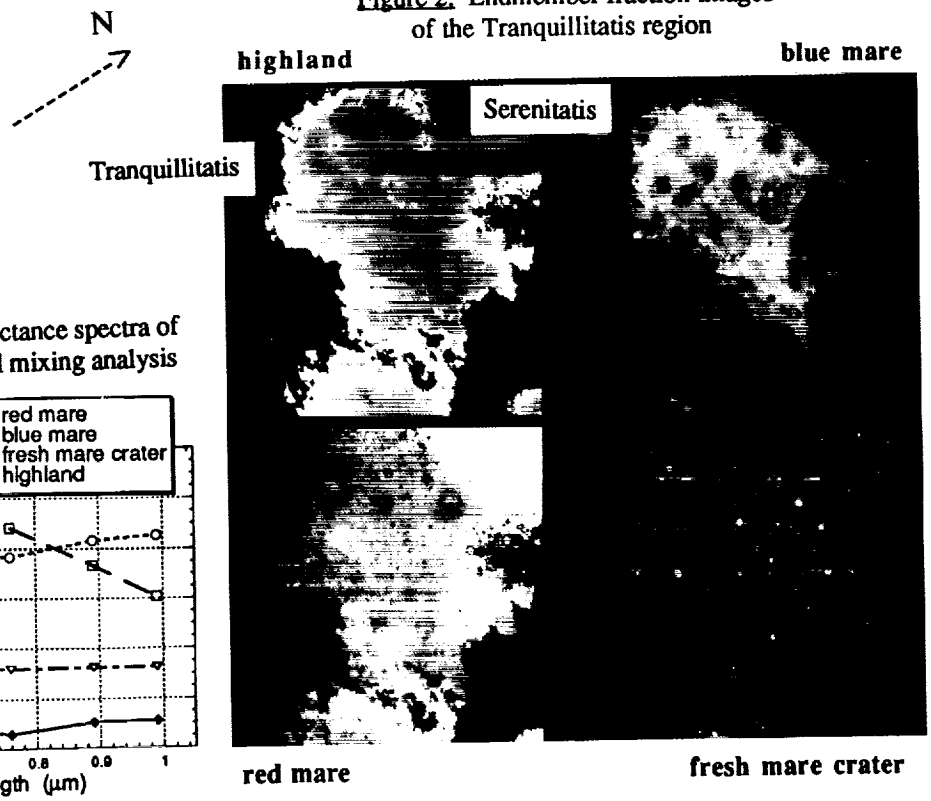

Figure 1: SSI relative reflectance spectra of endmembers used in spectral mixing analysis

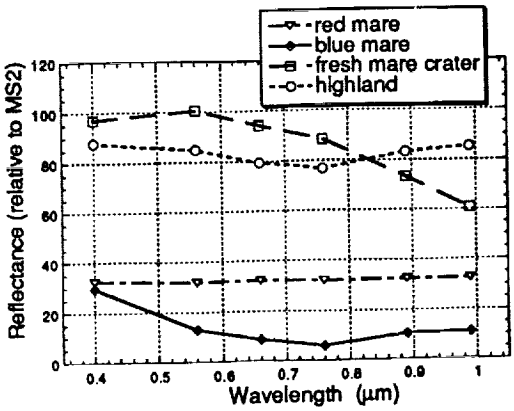

References: 1) Belton et al. (1994) *Science*, in press; 2) Belton et al. (1992) Lunar impact basins and crustal heterogeneity: New western limb and farside data from Galileo, *Science*, 255, 570; 3) Charette, M.P. et al (1974) Application of remote spectral reflectance measurements to lunar geology classification and determination of titanium content of lunar soils, *JGR*, 79, 1605; 4) Fischer, E.M. and Pieters, C.M. (1993) *LPSC XXIV*, 477-478; 5) Melendrez, D. E. et al (1994) Remote sensing of potential lunar resources 2. High spatial resolution mapping of spectral reflectance ratios and implications for near side mare TiO_2 content, *JGR*, in press; 6) Adams, J.B. et al (1993) in Remote geochemical analysis: elemental and mineralogical composition. Cambridge U. Press, N.Y.; 7) Head, J.W. and Gifford, A. (1980), Lunar mare domes: classification and modes of origin, *Moon and Planets* 22, 235; 8) De Hon, R.A. (1971) Cauldron subsidence in lunar craters Ritter and Sabine, *JGR* v76, 23, 5712; 9) Wilhelms, D.E. (1987) The geologic history of the moon, *USGS Prof Paper* no. 1348.

Acknowledgments: NASA support for this research is gratefully acknowledged: NAGW-28 (CMP), NAGW-713 (JWH). Data analysis was performed using a facility provided by the W. M. Keck Foundation.

LONGITUDINAL VARIATIONS OF THE LINEAR POLARIZATION IN JUPITER'S POLAR REGIONS AT THE SYSTEM III AND IY PERIODS: O.M.Starodubtseva, L.A.Akimov, V.V.Korokhin (Astron.Obs.Kharkov Univ.), V.G.Tejfel (Astrophys.Institute Kazakhstan Akademy Sci., Alma-Ata)

The polarimetric observations of Jupiter were carried out during several Jupiter apparitions using different technique: photographic pictures in 1981 and spectrograms in 1985 and 1986 were obtained through two-refracting crystal; the polarimetric equipment with CCD-line was used in 1989. Most of these observations were made with the 40-inch telescope of the high-altitude observatory near Alma-Ata. All observations were made in the visible spectral range. Measurements of the linear polarization degree along the central meridian were obtained for different longitudes.

Behaviour of polarization in polar latitudes (between 55 and 75 degrees) shows the following characteristics. All observations reveal the modulation of polarization if polarization is plotted versus the longitude in system III (rotation of Jovian magnetosphere). But this modulation shows the systematic phase shift about 50 degrees per year to smaller longitudes. One possible natural explanation for such yearly drift is that the rotation period in polar regions is about 5,6 sec less than the period in system III rotation. But other values for the period are also feasible because of the possibility of other values for yearly phase shift, namely $50 \pm 360*n$ deg. (n is an integer). This ambiguity is related to the intervals of year and several years between particular sets of observations.

There are some magnetospheric phenomena which either show no particular organization in system III or drift in system III [1]. In order to organize these phenomena Sandel and Dessler [1] have offered hypothesis about dual periodicity of the Jovian magnetosphere and defined longitude system IY whith the rotation period being 3% larger than the period for system III. The difference of -25,486 degrees between rotation rates for III and IY systems results in the drift of 51,2 degrees per year (365,25 days). This is almost the same yearly phase shift that we have observed in our data, presented in the system III period.

LONGITUDINAL VARIATIONS OF POLARIZATION: Starodubtseva O.M. et al.

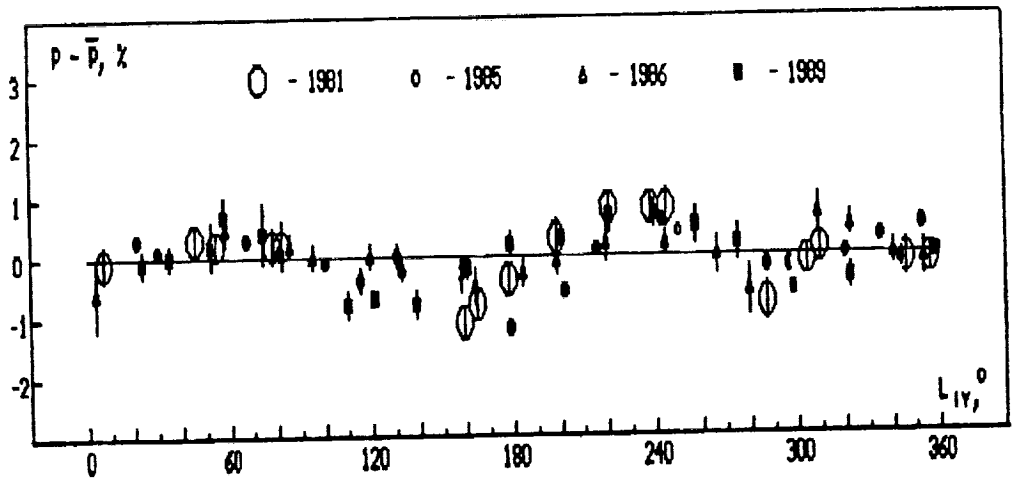

In figure our data are presented as a function of system IV central meridian longitude. The polarization in this figure is shown as the deviation from the mean for each year. Each point is a value averaged over the 40 degrees longitude interval with the 20 degrees step. The figure indicates explicitly that the phase of modulation is stationary if polarization is plotted as a function of the system IV central meridian.

We suggest that there is a possible relationship between the magnetospheric processes and variations of the aerozol concentration in the polar stratosphere of Jupiter which may be the reason of the observed variations of polarization. On the other hand the fact that variations of polarization are organized in system IV is the evidence of validity of system IV because the data described here exhibit the phenomenon in the spectral and time intervals which are different from those used by Sandel and Dessler.

References: (1) Sandel B.R., Dessler A.J. J.Geoph.Res., 1988, 93, N A6, 5487.

REFLECTANCE SPECTRA OF PARTICLE SIZE SEPARATES OF LUNAR SOILS: IS THE DIFFERENCE CONTROLLED BY REDUCED IRON?

L. V. Starukhina, Yu. G. Shkuratov Astron. Observ. of Kharkov Univ., 310022, Kharkov, Ukraine, **O. D. Rode** Vernadsky Institute, Moscow, 117975, Russia, and **C. M. Pieters** Brown Univ., Box 1846, Providence, RI 02912 USA.

Reflectance spectra of particle size separates of mare and highland lunar soils were measured. The finest < 45 μm fractions turned out to be responsible for the pronounced red slope of the spectra of the bulk samples, the spectral curves for the other fractions being far from those for the bulk samples. Our calculations have shown that the distinction between the spectra of the fine and the coarse fractions cannot be due to difference in particle size only but can be explained by presence of reduced iron in the superficial layers of the regolith particles at reasonable values of the depth of the layer containing reduced iron (1000 A) and volume concentration of the iron (4% for mare soil and 2% for highland one).

Because of the high surface/volume ratio fine particles of lunar regolith are expected to be the most sensitive to the processes resulting from exposure to space environment. The fact may show in optical characteristics. To study this effect we prepared particle size separates of mare (Luna 16) and highland (Luna 20) lunar soils and measured reflectance spectra of each fraction (Fig.1). As shown in Fig.1 the ain carrier of the optical properties of lunar soils, in particular, the red slope of the spectra, is the finest fraction < 45 μm. Spectral curves for coarse fractions (*3 - 5* in Fig.1) are rather distant from that for the bulk one and close to each other. This indicates that fine particles probably surround coarse ones forming aggregates and thus shielding coarse particles from direct surface exposure. Among processes due to surface exposure the formation of fine (< 300 A) grains of reduced iron in superficial layers of particles is known to take place. As particle size itself affects the spectra of transparent materials the question arises: is the distinction of the spectra of the finest fraction due to particle size only or to the processes on the surface as well?

To separate the effect of composition from that of particle size we used a model [1] which enables one to calculate spectrum of imaginary part κ of refractive index of a sample using its reflectance spectrum and vice versa. For calculations the only parameter of a sample is used - the average size *l* of light scattering element. For particles with complex structure, such as coarse particles of lunar soils can be, the size *l* is less than that of the particles and equals to grain size that is not known. We suppose the most of particles of the < 45 μm fractions to consist of one grain and be approximately round-shaped so the size *l* of light scattering element for them is assumed to be 40 μm. To estimate *l* for coarse fractions we supposed the values of κ for the finest fraction to be at least not smaller than those for the coarser ones in the whole spectral range. This assumption is supported by the consideration that fine particles should be the most sensitive to the processes resulting from surface exposure which are known to darken lunar soils. In this assumption the size of light scattering element for the 45 - 94 μm fractions is about twice as large as the that for < 45 μm ones, which suggests that the particles of both fractions are probably homogeneous. We calculated the spectra of the 45 - 94 μm fractions as they would be if their particles were as small as those of < 45 μm fractions. As shown in Fig.1 (curves *6*) if the particles of the < 45 μm fractions were chemically identical to those of the 45 - 94 μm ones the < 45 μm fractions would be 1) much lighter in the visible range, 2) with more pronounced 1 μm feature, 3) with less red spectral slope.

We supposed the difference to be due to the fact that external layer of fine particles contains submicron particles of reduced metals, mostly iron. Their effect can be accounted substituting instead of κ the value $\kappa + (d / l)\, g$, where *d* is the thickness of the iron containing layer, and $g = c\, n\, Im\, [(\varepsilon - 1) / (\varepsilon + 2)]$, *c* being volume concentration of reduced iron, $n = 1.55$ - refractive index of the matrix (soil particle), and ε - the relation of complex dielectric constant of iron to that of matrix. As one can see from the expression for the effective value of κ contribution of the colloid iron increases with decreasing grain size so the spectra of the finest fraction are expected to be the most affected by presence of reduced iron.

REDUCED IRON IN SPECTRA OF LUNAR FINES: Starukhina L.V. et al.

We calculated the spectra of the material of 45 - 94 μm fraction with particles of 40 μm size surrounded by a layer $d = 1000$ A with colloid iron, taking the optical constants of iron from [2,3]. Calculated spectra (curves *7* in Fig.1) turned out to be close to the spectra of the < 45 μm fractions at $c = 4\%$ for the mare and 2% for the highland one. The values seem to be somewhat great, which may be due to the difference in structure of the iron in lunar fines and that measured in [2], the optical constants being structure sensitive. But the values of thickness d and relation between concentrations for mare and highland soils are about the observed ones [4,5].

Thus the red spectral slope for the lunar soils may be accounted for by presence of reduced iron in the outer layers of the < 45 μm particles due to solar wind irradiation. The less the grain size the more absorption by iron in the visible and UV ranges darken the lunar fines and weaken their absorption bands. This is, perhaps, the reason of the inversion of the order of spectral curves *3* - *5* for the coarse fractions in the visible range as compared to the IR one.

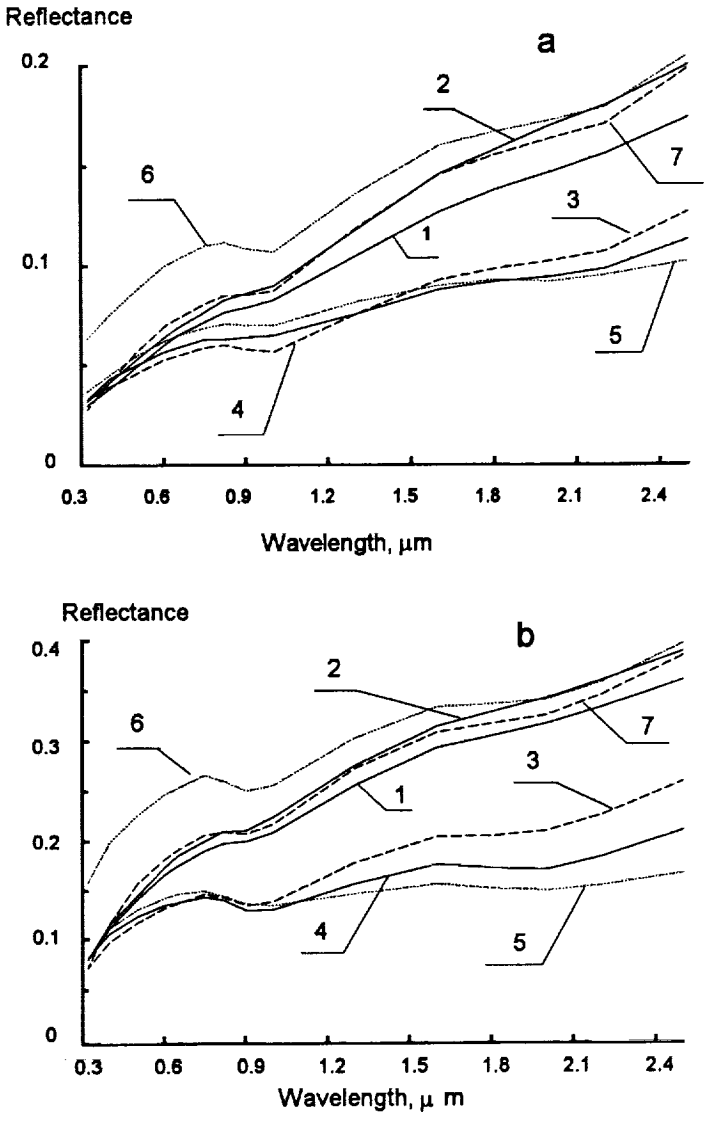

Fig.1. Reflectance spectra of particle size separates of lunar soils:

a - mare (Luna 16),

b - highland (Luna 20);

1 - bulk samples (a - 1637, b - 2014);

2 - fraction < 45 μm,

3 - fraction 45 - 94 μm;

4 - fraction 94 - 250 μm;

5 - fraction 250 - 1000 μm;

6 - calculated spectra for samples of the same composition as 45 - 94 μm fractions (curves *3*) but with particle size < 45 μm;

7 - the same as 6 but with particles surrounded by a 1000 A thick layer of colloid reduced iron particles, their volume concentration being 4% for mare soil (a) and 2% for highland one (b).

References.

[1]. Shkuratov Yu.G. (1987), *Kinematika. i fizika nebesnykh tel, 3*, 39 (in Russian).

[2]. Johnson P.B. and Cristy R.W. (1974), *Phys. Rev. B, 9*, 5056.

[3]. Weaver J.H. *et al.* (1979), *Phys. Rev. B, 19*, 3850.

[4]. Dikov Yu.P. *et al.* (1978), *LPSC 9-th*, 2111.

[5]. Gold T. *et al.* (1975), *LPSC 6-th*, 3285.

CHEMICAL ZONING AND EXSOLUTION IN OLIVINE OF THE PAVLODAR PALLASITE: COMPARISON WITH SPRINGWATER OLIVINE. Ian M. Steele, Department of Geophysical Sciences, University of Chicago, 5734 S. Ellis Ave. Chicago IL 60637.

While the olivine within a pallasite meteorite is generally considered to be of uniform composition based on major elements [1], detailed studies of the minor elements with the ion microprobe [2,3] and electron microprobe [4] have shown that olivines are zoned in the outer approximately 200-400 microns. Qualitatively this zoning is consistent with reequilibration of the olivine with surrounding metal at subsolidus temperatures. Of the 4 elements analyzed with the electron probe in Springwater, Ca, Cr and Al are all show progressive depletion toward olivine boundaries while Mn is enriched. The depletion distance qualitatively corresponds to estimated diffusion rates with Ca>Cr>Al [4] reinforcing a diffusion rather than growth mechanism. Similar data are reported here for Pavlodar olivine chosen because it is an anomalous pallasite [5], because it has olivine compositions like main group pallasites [5,6], because of its unusual apparent exsolution features [6,7], and because its olivine grain size and shape are similar to those of Springwater olivine.

Exsolution features: A conspicuous feature of Pavlodar olivine are numerous oriented, linear features less than about 5 microns in width and up to several mm long. These are oriented in three directions parallel to [001], [100] and [010] of the host olivine as shown by optical and x-ray precession study. Their density near the center of the olivines appears uniform while they are absent in the outer 200 micron rim of each olivine. Between the rim and interior the density increases to the uniform level. Reflected light observation showed that on polished surfaces intersected by these features the linear features were bright relative to host olivine. Examination with BSE (backscattered electron) images showed hexagonal high-Z cross sections which have a uniform brightness at the 0.25 micron scale. Qualitative EDS spectra showed the presence of major Si, Cr, Mg, Ca and Fe with minor Al, Mn and V. Quantitative analyses of the largest cross-sections showed a near constant composition with little change as smaller areas were analyzed suggesting essentially no contamination from surrounding olivine in the analyses. The table presents representative analyses. Within the 15 analyses obtained, Ca-Cr and Fe-Ca show weak negative correlations while Fe-Cr shows a positive correlation (Fig.1). It is assumed that Cr is trivalent to give totals near 100%. The atomic proportions based on 4 oxygens are near:

$Cr_{0.52}Mg_{0.54}Ca_{0.45}Fe_{0.23}Si_{0.98}O_4$ or $M^{+2} = 1.22$, $M^{+3} = 0.52$. No Cr silicate was identified which matches this stoichiometry. A possibility is that this represents a mix of two phases, possibly chromite and diopside, but these should show high contrast in a BSE image. Identification must be made by electron diffraction.

Minor element concentration profiles: Electron microprobe operating conditions were selected (360sec count times, PHA set, focused beam, 200nA incident current, 20kV) to provide sensitivity sufficient to detect Al, Ca, Cr and Mn in Pavlodar olivine. Scans were made from edge toward center for distances ranging from 200 to 500 microns at 5 or 10 micron steps. Approximate interior concentrations (ppmw) are: Al - 28; Ca - 39; Cr - 155; Mn - 2700. These compare favorably with previous electron probe determinations [3]: Al - 26; Ca - 28; Cr - 130; Mn - 2850. Bulk olivine analyses [8] for Mn (2630ppmw) agrees well while Cr (=552ppmw) is 3.5x higher. This is easily explained by the bulk analysis including Cr of the inclusions to give the higher concentration. Pavlodar olivine has the highest bulk Cr concentration of analyzed pallasites [8] which may in part result in exsolution from olivine.

Figs. 2 and 3 show details of two concentration profiles in two olivine grains of Pavlodar. These are similar to each other and to 5 other profiles; the crystallographic orientation of the olivine grains is not known. As with similar data for Springwater, Al, Ca and Cr all show depletion at the edge of the olivine grain. In contrast, however, Mn has a constant concentration in all profiles with no indication of an increase as was observed in Springwater. The Pavlodar profiles extend to about 500 microns whereas Springwater profiles reached constant values near 250 microns. Relative to Ca and Cr, the Al profile appears to be restricted to a distance of about 250 microns in Pavlodar consistent with Al diffusion being slower than either Ca or Cr. The Ca profile for Fig. 3 appears to extend farther than that of Cr before a near constant concentration is reached while in Fig. 2 this is less certain due to an irregular variation near the 450 micron position possibly due to a nearby inclusion acting as a local sink for Cr and Ca. The absence of a flat profile for Mn suggests complete equilibration with other Mn-bearing phases, mainly metal.

Conclusions: The minor element profiles of Pavlodar, like Springwater, are consistent with known or inferred diffusion rates for Ca, Cr, and Al in olivine. The profiles for Pavlodar extend for a greater distance compared to Springwater suggesting more extensive diffusion. The absence of Mn variation in Pavlodar also suggests complete equilibration with respect to Mn in contrast to Springwater. The occurrence of Cr-rich inclusions are consistent with exsolution of a Cr-rich phase(s) lowering the Cr content of the olivine. Because these inclusions are not present near the olivine boundaries, it is concluded that diffusion within a homogeneous olivine occurred with later precipitation of the Cr inclusions. There is no visual indication of exsolutions near the olivine boundary. The later Cr exsolution may have been triggered by an oxidation event where original high Cr^{+2} in the reduced olivine was converted to Cr^{+3} which is not readily accepted by the olivine structure.

References: [1] Buseck, PR. and Goldstein, J.I. (1969) BGSA 80, 2141-2158; [2] Reed, S.J.B. et al. (1979) EPSL 43, 5-12; [3] Leitch, C.A. et al. (1979) LPS X, 716-718; [4] Zhou, Y. and Steele, I. M. (1993) LPS XXIV, 1573-1574; [5] Scott, E.R.D. (1977) GCA 41, 349-360; [6] Buseck, P.R. (1977) GCA 41, 711-740; [7] Scott, E.R.D. (1977) GCA 41, 693-710; [8] Davis, A.M. (1977) Thesis, Yale University.

Acknowledgement: NASA NAGW-3416 for support.

Table. Inclusions in olivine.

SiO_2	31.3	35.7	35.3	36.9
Cr_2O_3	28.9	24.0	23.5	22.5
Al_2O_3	0.05	0.05	0.06	0.06
V_2O_3	0.31	0.30	0.26	0.20
MgO	12.3	13.0	13.0	13.0
FeO	11.6	10.4	10.3	9.8
MnO	0.62	0.55	0.54	0.57
CaO	14.2	15.4	16.1	16.8
Total	99.28	99.40	99.10	99.83

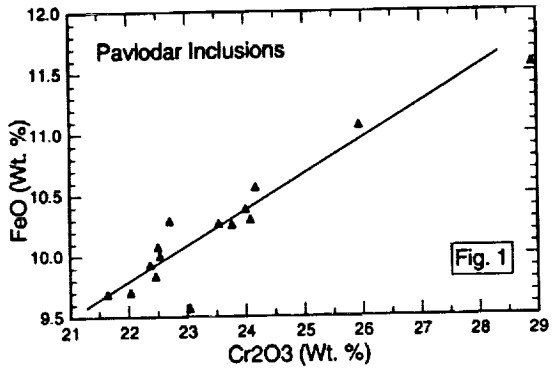

Fig. 1. Near linear variation of Cr and Fe in Pavlodar inclusions.

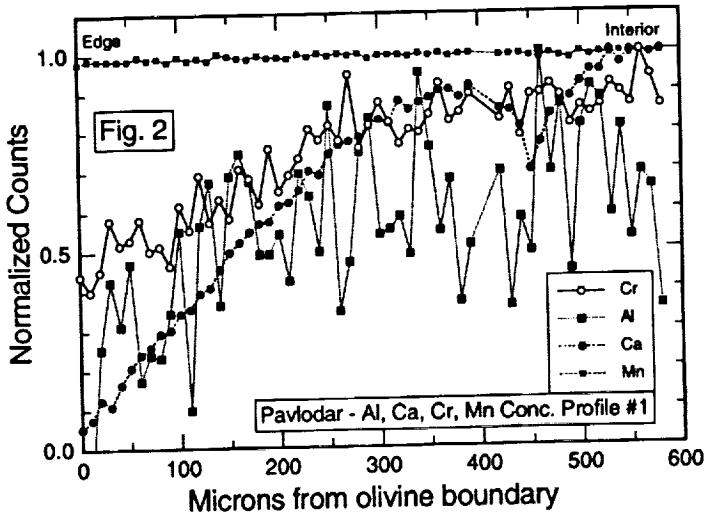

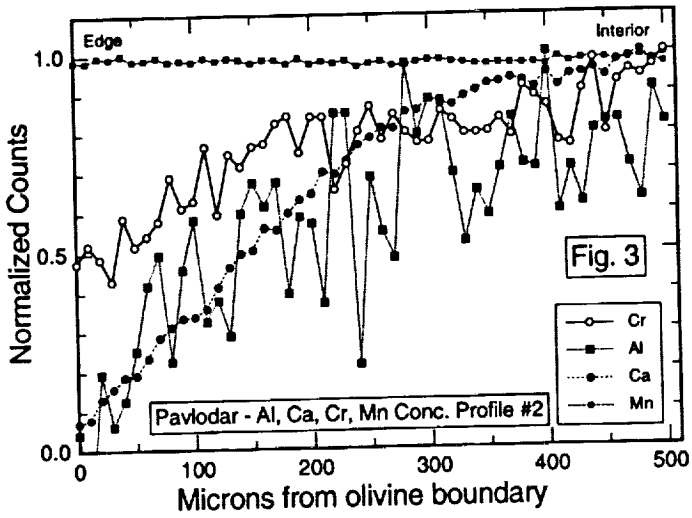

Figs. 2,3. Minor element variation in two olivine grains in Pavlodar from edge (left) toward center (right). Cr, Ca and Al are clearly depleted near the edge while Mn is nearly constant. This suggests diffusion of some incompatible elements out of the olivine structure and complete equilibration of Mn.

CRYSTAL STRUCTURE OF CHLADNIITE, $Na_2CaMg_7(PO_4)_6$, FROM CARLTON (IIICD) IRON METEORITE. Ian M. Steele, Department of Geophysical Sciences, University of Chicago, 5734 S. Ellis Ave., Chicago IL 60637.

A new phosphate occurring in the Carlton (IIICD) iron meteorite has been described [1] with a composition and cell parameters reminescent of terrestrial fillowite [2]. This phase has been named chladniite and has been approved by the Committee on New Minerals. A single crystal structure refinement has been completed confirming the fillowite structure as reported here. In addition, a third composition has been reported [5] from El Sampal (IIIAB) analogous to terrestrial johnsomervilleite and its structure determination is in progress.

Compositions: The ideal compositions of the three phases are:

Fillowite -	$Na_2\ Ca\ Mn_7(PO_4)_6$	,occurs in terrestrial pegmatites
Chladniite -	$Na_2\ Ca\ Mg_7(PO_4)_6$	,only one occurence in Carlton IIICD
Johnsomervilleite-	$Na_2\ Ca\ Fe_7(PO_4)_6$	,occurs terrestrially and in meteorites

The structure of terrestrial fillowite (composition based on structure: $Na_{1.95}Ca_{0.77}Mn_{5.94}Fe_{1.34}(PO4)_6$) has been determined [2] while that of an isostructural synthetic orthophosphate phase, $Na_4Ca_4Mg_{21}(PO_4)_{18}$, has also been determined [4]. This composition ($Na_{1.33}Ca_{1.33}Mg_7(PO4)_6$) is similar to that of Carlton chladniite [1] ($Na_{1.77}Ca_{0.98}Si_{0.08}Mg_{6.96}Fe_{0.26}Mn_{0.04}(P_{0.98}O_4)_6$) except with respect to Ca and Na.

Experimental: Single crystal x-ray intensities were obtained with a four circle diffractometer using CuKα radiation. Cell parameters were obtained by least squares refinement using 20 centered diffractions, each the average of automatic centering of eight equivalent settings. The resulting cell parameters are: a = 14.967±0.002, c = 42.595±0.004Å, $\beta = 120^o$ with space group R3 . A total of 5651 diffractions gave 1880 independent diffractions after averaging. Full-matrix isotropic refinement using initial parameters of fillowite [2] and varying site occupancy gave a final R-factor of 0.04. Structural parameters, isotropic temperature factors, and occupancies are in Table 1.

Discussion: Chladniite is isostructural with fillowite. It is anticipated the meteoritic johnsomervilleite will also be isostructural based on the similar composition and cell parameters of terrestrial johnsomervilleite [3] to those of fillowite. The site occupancy refinement of chladniite shows that the 8-coordinated site labeled Ca is actually partially occupied by Na both in terrestrial fillowite [2] (Table 2) and in chladniite in an almost identical Ca:Na ratio near 0.67:0.33. This may be fortuitous but may represent partial ordering violating the R3 space group. This mixed occupancy also can explain the consistent analytical results giving high Na and low Ca relative to the above ideal stoichiometry (E. Olsen, personal comm.). The Na(1) site appears partially vacant in both synthetic and natural chladniite.

References: [1] McCoy et al. (1993) Meteoritics **2 8**, 394; [2] Araki, T. and Moore, P.B. (1981) Am. Mineral. **6 6**, 827-842; [3] Livingstone, (1980) Min. Mag **4 3**, 833-836; [4] Domanskii, A.I. et al. (1982) Sov. Phys. Crystallogr. **2 7**, 535-537; [5] Olsen, E. and Steele, I. (1993) Meteoritics **2 8**, 415.

Acknowledgements: NASA NAGW-3416 for financial support, E. Olsen for comments, and J. Pluth for data collection and refinement.

TABLE 1. POSITIONAL AND ISOTROPIC DISPLACEMENT PARAMETERS FOR CHLADNIITE.

Site	Occupancy	*x*	*y*	*z*	$^{*}U_{eq}$
M(1)	1.00 Ca	0.0	0.0	0.0	0.022(2)
M(2)	1.00 Mg	0.0	0.0	0.5	0.005(3)
M(3)	1.00 Mg	0.0	0.0	0.1039(3)	0.013(2)
M(4)	1.00 Mg	0.0	0.0	0.3248(3)	0.014(2)
M(5)	1.00 Mg	0.0	0.0	0.3966(3)	0.010(2)
M(6)	1.00 Mg	0.4304(3)	0.2529(3)	0.0521(2)	0.012(1)
M(7)	1.00 Mg	0.1113(3)	0.5728(3)	0.0392(2)	0.010(1)
M(8)	1.00 Mg	0.0022(3)	0.3229(3)	0.0819(1)	0.012(1)
M(9)	1.00 Mg	0.2599(3)	0.3276(3)	0.0862(1)	0.009(1)
M(10)	1.00 Mg	0.5733(3)	0.0796(3)	0.1235(2)	0.015(1)
M(11)	1.00 Mg	0.2222(3)	0.1092(3)	0.1341(2)	0.015(1)
Na(1)	0.81 Na	0.0	0.0	0.1760(4)	0.017(6)
Na(2)	1.00 Na	0.0	0.0	0.2481(3)	0.014(3)
Na(3)	1.00 Na	0.0790(4)	0.4278(4)	0.1650(2)	0.028(2)
Ca	0.69 Ca, 0.31 Na	0.2657(2)	0.2923(2)	0.0008(1)	0.019(2)
P(1)		0.1895(3)	0.4342(3)	0.0283(1)	0.011(1)
P(2)		0.5327(3)	0.1164(3)	0.0382(1)	0.011(1)
P(3)		0.5441(3)	0.0926(3)	0.1991(1)	0.013(1)
P(4)		0.2201(3)	0.1259(3)	0.2105(1)	0.012(1)
P(5)		0.2247(3)	0.4621(3)	0.2226(1)	0.014(1)
P(6)		0.4674(3)	0.2154(3)	0.2782(1)	0.014(1)
O(1)		0.1619(6)	0.3829(6)	0.9956(3)	0.012(2)
O(2)		0.2532(6)	0.5532(6)	0.0260(3)	0.013(3)
O(3)		0.2554(6)	0.3973(6)	0.0459(3)	0.012(3)
O(4)		0.0893(6)	0.4106(6)	0.0448(3)	0.010(2)
O(5)		0.4570(6)	0.1299(6)	0.0591(3)	0.014(3)
O(6)		0.5547(6)	0.0337(6)	0.0511(3)	0.013(3)
O(7)		0.6382(6)	0.2159(6)	0.0385(3)	0.009(3)
O(8)		0.4893(6)	0.0925(6)	0.0044(3)	0.016(3)
O(9)		0.5431(6)	0.0347(6)	0.1697(3)	0.016(3)
O(10)		0.6318(6)	0.2057(6)	0.1982(2)	0.009(2)
O(11)		0.4402(5)	0.0910(6)	0.2025(2)	0.008(3)
O(12)		0.5495(6)	0.0366(6)	0.2290(3)	0.011(3)
O(13)		0.2353(6)	0.0866(7)	0.1786(3)	0.031(3)
O(14)		0.1280(5)	0.1427(6)	0.2090(3)	0.010(3)
O(15)		0.8919(6)	0.2363(5)	0.1145(3)	0.008(2)
O(16)		0.1985(6)	0.0410(6)	0.2348(3)	0.014(2)
O(17)		0.2668(6)	0.5282(6)	0.1936(3)	0.016(3)
O(18)		0.1035(5)	0.3969(5)	0.2206(2)	0.009(2)
O(19)		0.2553(6)	0.3778(6)	0.2234(3)	0.011(3)
O(20)		0.2542(6)	0.5244(6)	0.2531(3)	0.015(3)
O(21)		0.5290(7)	0.2449(6)	0.2482(3)	0.025(3)
O(22)		0.3778(6)	0.1011(6)	0.2737(3)	0.011(3)
O(23)		0.4176(6)	0.2828(6)	0.2830(2)	0.014(3)
O(24)		0.5258(7)	0.2149(6)	0.3073(3)	0.031(3)

$^{*}U_{eq}$ is defined as $\frac{1}{3}\sum_{i=1}^{3}\sum_{j=1}^{3} U_{ij}\mathbf{a}_i^{*}\mathbf{a}_j^{*}(\mathbf{a}_i\cdot\mathbf{a}_j)$

TABLE 2. SITE OCCUPANCIES OF OTHER REFINEMENTS.

Fillowite[2]	Orthophosphate[4]
0.62 Mn,0.38 Ca	1.00 Ca
1.00 Mn	1.00 Mg
1.00 Fe	1.00 Mg
1.00 Fe	1.00 Mg
1.00 Mn	1.00 Mg
1.00 Mn	1.00 Mg
1.00 Mn	1.00 Mg
0.67 Fe, 0.33 Mn	1.00 Mg
1.00 Mn	1.00 Mg
1.00 Mn	1.00 Mg
1.00 Mn	1.00 Mg
0.91 Na, 0.09 Ca	-
0.90 Na, 0.10 Ca	1.00 Na
1.00 Na	1.00 Na
0.65 Ca, 0.35 Na	1.00 Ca

OSCILLATORY ZONING IN FORSTERITE FROM CARBONACEOUS AND UNEQUILIBRATED ORDINARY CHONDRITES: IMPLICATIONS FOR ORIGIN OF SOME FORSTERITE. Ian M. Steele, Department of Geophysical Sciences, University of Chicago, 5734 S. Ellis Ave., Chicago IL 60637.

Oscillatory zoning is difficult to recognize in terrestrial olivine but has been described from olivines from phenocrysts in lavas [1]. The compositional contrast is brought out in polished section by acid etching and viewing by Nomarski interference microscopy. More recently oscillatory zoning has been observed in forsterites from the Allende meteorite [2] where cathodoluminescence (CL) contrast reveals compositional differences. Below are reported additional observations of oscillatory zoning in Allende and an unequilibrated ordinary chondrite, details of zoning as revealed by image processing techniques, and compositional correlations among elements measured with high sensitivity. It is concluded that the proposal that all forsterites formed within chondrules is inconsistent with the observed oscillatory zoning which by analogy with terrestrial and lunar occurrences is restricted to slowly growing crystals in contrast to rapidly cooled chondrules.

Occurrence of oscillatory zoning: The recognition of oscillatory zoning using CL is limited to nearly pure forsterite with less than about 2 wt.% FeO because higher Fe content quenches CL. Oscillatory zoning is recognized by linear bands of varying CL intensity. The occurrence is relatively rare possibly due to the small size of most forsterites, most grains are not whole but rather fractured, and luminescing forsterite is only a small fraction of the total sample. While descriptions here apply to forsterite, oscillatory zoning may occur in more Fe-rich grains but could not be recognized by CL. While numerous examples of linear CL features have been seen in Allende forsterites, one grain is particularly interesting because of its large size (1mm), euhedral form, and repeated zoning with a 5μm period (Fig. 1). Another example which shows repeated linear CL features is a forsterite of ALHA 76004 (H3) but does not represent a complete grain and is embedded in a devitrified matrix. Oscillatory zoning has not been recognized in C2 forsterites which is added evidence that C2 forsterites differ from those of C3 and UOC meteorites both with respect to composition [3] and with respect to crystallization dynamics which is thought to cause oscillatory zoning.

Imaging of the CL texture was done by beam scanning and obtaining a digital CL image [4]. This allowed image enhancement using image processing filters to clearly show the bands and recording of the image from a computer screen. Simultaneous BSE images were recorded to allow recognition of gross zoning changes; no indication of the oscillatory zoning is seen on these BSE images.

Correlation of composition and zoning: Electron microprobe traverses were made perpendicular to the CL zoning with 0.5μm steps. Counting times, current, kV and PHA were selected to obtain near 10ppm detection limits for Al, Ca, Sc, Ti, V, Cr, Mn and Fe. These data extend those reported earlier [2] and show an excellent correlation of Al, Ti, Sc and V with each other and with the CL zoning. In contrast, Ca, Fe, and Mn showed no change correlated with the CL pattern but rather a monotonic change consistent with normal zoning in a growing crystal. The variation in Cr showed one compositional step which did not correlate with any other observation.

OSCILLATORY ZONING ..... : Steele, I.M.

The elements measured can be divided into two groups: 1) the high charge ions including Al^{+3}, Sc^{+3}, Ti^{+3}, V^{+3} are incompatible with the olivine structure and all correlate with CL intensity; Al and Ti which are in high enough concentration to give good statistics correlate with the oscillatory zoning shown by CL. 2) the second group of elements Fe, Ca, Cr and Mn are all divalent (it is assumed that conditions are sufficiently reducing for Cr to be predominently divalent), compatible with the olivine structure, and show only monotonic changes (Fig. 2).

Discussion: By analogy with terrestrial and lunar samples of plagioclase, olivine, and pyroxene oscillatory zoning is restricted to slowly cooling samples typified by phenocrysts within lava flows [5]. The conclusion that the forsterites originate from chondrules [6] which have a cooling rate on the order of hundreds of degrees/hour [7] is difficult to rationalize. These textural observations suggest that at least some forsterites, and possibly more Fe-rich olivines, were from a source that cooled slowly on the time scale of terrestrial lava flows. The compositional variation across the oscillatory zoning is similar to that observed for terrestrial samples where Ca, Mn, Fe and Mg did not correlate with the zoning [1]. Measurements have not been made for incompatible minor elements in terrestrial samples. It is proposed that the trivalent ions have a relatively low diffusion rate in the silicate melt and distribution coefficients such that they are not incorporated into the olivine structure. This combination causes a local concentration increase adjacent to the growing olivine which at some point is great enough to force high levels of these elements into the growing olivine. Similar explanations exist for terrestrial examples. If correct, some forsterites must also have grown from a melt in contrast to a vapor. From the many observations made for forsterite, it appears that there is no one process for their formation.

References: [1] Clark et al. (1986) Amer. Mineral. **71**, 734-741; [2] Steele, I.M. (1990) LPS **XXI**, 1196-1197; [3] Steele, I.M. and J.V. Smith. (1986) LPS **XV**, 822-82; [4] Steele, I.M. (1992) Scanning Microscopy **5**, 611-618; [5] Allegre, C.J. et al. (1981) Nature **294**, 223-228; [6] Jones, R.H. (1992) Geochim. Cosmochim. Acta **56**,467-482; [7] Hewins, R.H. (1983) "Chondrules and their origins,122-133.

Acknowledgement: NASA NAGW-3416 for support.

Fig. 1. CL intensity as a function of position. The region showing oscillatory zoning is indicated with 6 peaks labeled. The width of scan is 75 microns.

Fig. 2. Variation of Cr, Ca, and Fe across the same region of Fig. 1. While CL, Al, and Ti show distinct maxima and minima, the 3 elements shown show no indiaction of oscillatory zoning.

Fig. 1

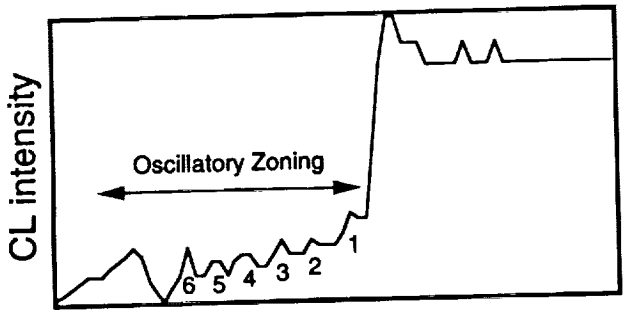

Fig.2

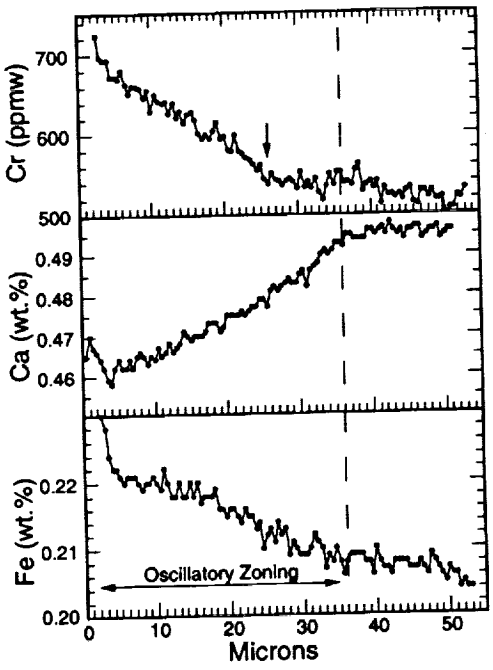

NEW TOF–SIMS RESULTS ON HYDRATED INTERPLANETARY DUST PARTICLES; **T. Stephan** and **E. K. Jessberger,** Max–Planck–Institut für Kernphysik, P.O. Box 103980, D–69029 Heidelberg, Germany; **H. Rulle,** Physikalisches Institut der Universität Münster, Wilhelm–Klemm–Straße 10, D–48149 Münster, Germany; **K. L. Thomas,** Lockheed, 2400 NASA Rd. 1, Houston, TX 77058, USA; **W. Klöck,** Institut für Planetologie der Universität Münster, Wilhelm–Klemm–Straße 10, D–48149 Münster, Germany.

In continuation of our previous studies [1–3], we analyzed sections of two carbon–rich hydrated interplanetary dust particles, L2006E10 and L2006G1, with TOF–SIMS (Time–Of–Flight Secondary–Ion–Mass–Spectrometry). High–resolution TOF–SIMS images yield the lateral element distribution on a scale of ~ 0.2 μm. In addition to imaging, positive secondary ion spectra from selected areas were taken to obtain quantitative element ratios. Because of the low sample destruction — during a typical analysis only a few atomic monolayers of the samples are consumed — subsequent analyses with other techniques are possible. Therefore TOF–SIMS is ideally suited for the analyses of small samples like interplanetary dust.

For the quantitative analysis we determined TOF–SIMS sensitivities relative to Si for O, Na, Mg, Al, K, Ca, Ti, V, Cr, Mn, and Fe from analyses of a homogeneous glass standard (lunar analogue glass) [2]. The Ni sensitivity was measured with the San Carlos olivine [4]. For that of H, Co, and Zn only literature values [5] are available and for C we used a rough estimate based on the analysis of an IDP (L2006J14) with known carbon abundance [6]. Fig. 1 comprises the quantitative results for L2006E10 and L2006G1.

Secondary ion images of **L2006E10** (Fig. 2) show a homogeneous and rather similar distribution of Mg^+, Al^+, Si^+, K^+, Cr^+, Fe^+, Ni^+, O^-, OH^-, and S^- ions (*cf.* the Si^+ image of Fig. 2). Ca is concentrated in a small 4×1 μm^2 region. This very spot is also highly enriched in P^- as well as PO_3^- and $CaOH^+$ (and to a lesser extend OH^-). The source of Ca and P is most likely an apatite grain. This is to our knowledge the first reported occurrence of apatite in a smectite type IDP. Na^+ and F^- are concentrated in two distinct regions on either ends of the elongated particle. Because of lack of F sensitivity no speculation on the responsible mineral is possible yet. The quantitative results (Fig. 1) reveal overall chondritic abundances for many elements within a factor of two, the typical bulk deficiency of Ca and a slight enrichment of Ti and V. Carbon resides mainly in the Ca,P–rich portion of the particle whereas the major part has a C deficiency, in contradiction to SEM studies which showed a C enrichment in the bulk [6]. Zn is highly enriched in the bulk particle as well as in the "apatite"–spot.

The element distribution in **L2006G1** is even more complex. The TOF–SIMS images (Fig. 3) of most ions resemble a ring structure. Only C and H are observed in its center. However, they are also not evenly distributed there but concentrated in a few 1–3 μm sized spots. This is in accordance with the observation by TEM studies that C in this IDP occurs as distinct carbonate grains [6]. Silicone oil as a possible source for H and C in the particle can be excluded from the TOF–SIMS spectra [3]. Overall the IDP looks like a hollow silicate sphere filled with C–rich material. Cl and F are concentrated on one side of the rim of the particle. Here we also found some Br. This finding supports our earlier contention that some elements can be enriched by the interaction of IDPs with halogen–containing aerosols in the stratosphere [1, 3, 7, 8]. Element ratios (Fig. 1) show chondritic abundances for most elements. Na/Si and K/Si are higher than CI ratios by factors of 4 and 7, respectively. The V enrichment ($7\times$CI) might be due to an unresolved interference at mass 51 in the mass spectrum. Fe and Ni are both slightly depleted (0.4 and $0.3\times$CI) whereas Zn is enriched to a similar degree as in the other IDP.

High resolution ion images of IDPs reveal a wealth of information some of which, however, as yet is still difficult to interpret in detail. It is expected that the combination of TOF–SIMS with other techniques like *e.g.* SEM, TEM, PIXE, and SYXFA will shed light on the history of interplanetary dust particles.

References: [1] T. Stephan *et al.* (1992) *Meteoritics* **27**, 292. [2] T. Stephan *et al.* (1993) *Lunar Planet. Sci.* **24**, 1349–1350. [3] T. Stephan *et al.* (1993) *Meteoritics* **28**, 443–444. [4] S. Weinbruch *et al.* (1993) *Eur. J. Mineral.* **5**, 37–41. [5] C. Meyer, Jr. (1979) *Proc. Secondary Ion Mass Spectrometry, SIMS II* (eds. A. Benninghoven *et al.*), 67–69. Springer, New York. [6] L. P. Keller *et al.* (1993) *Lunar Planet. Sci.* **24**, 785–786. [7] E. K. Jessberger *et al.* (1992) *Earth Planet. Sci. Lett.* **112**, 91–99. [8] J. Bohsung *et al.* (1994) *Lunar Planet. Sci.* **25**, this conference.

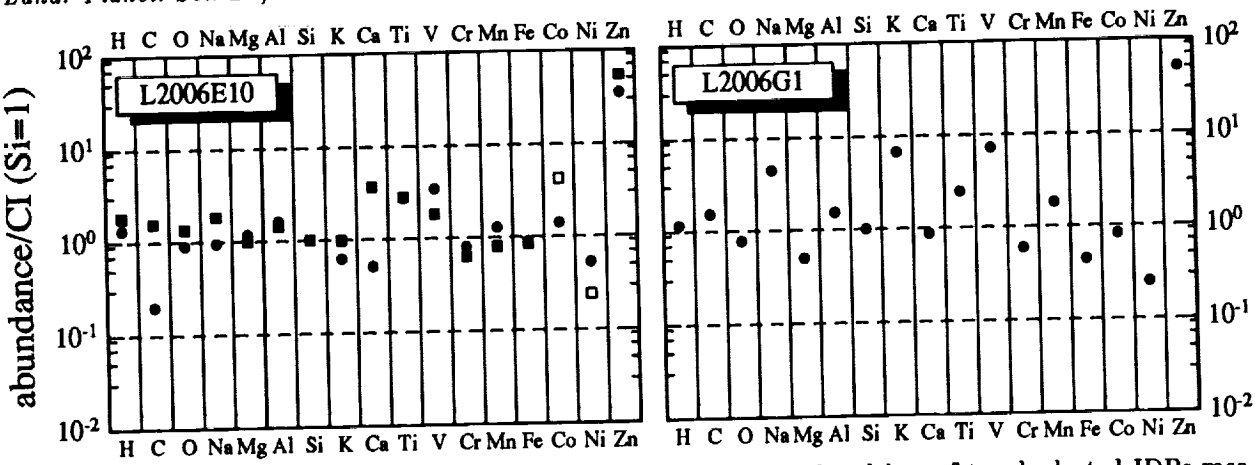

Figure 1: Element abundances relative to Si and normalized to CI chondrites of two hydrated IDPs measured with TOF-SIMS. Open symbols are upper limits. For L2006E10 the Ca,P–rich region was analyzed separately (squares).

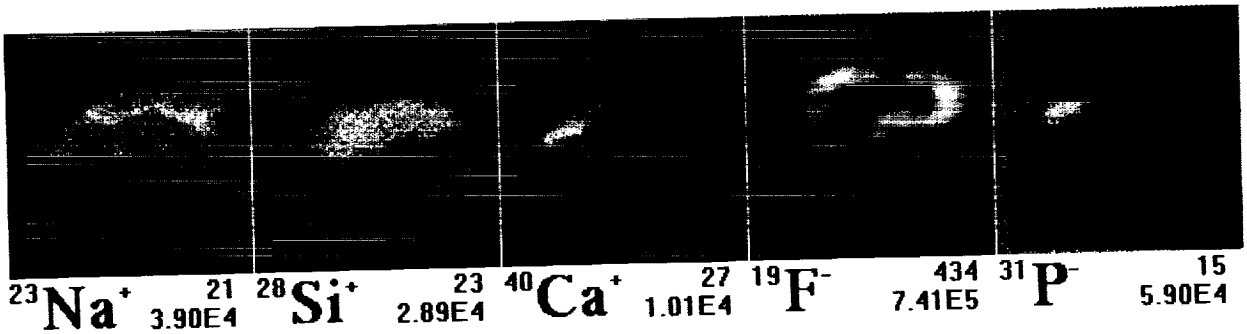

Figure 2: TOF-SIMS images for 5 different ion species from sample L2006E10. The field of view is 25 × 25 μm^2. The sample was rastered with a Ga^+ primary ion beam (128 × 128 pixels, 1000 primary ion pulses per pixel). The subscripts below each image give the secondary ion species, the maximum number of counts per pixel and the integral number of counts for the total image. For each image a linear grey scale was used where white corresponds to the maximum count rate of each image.

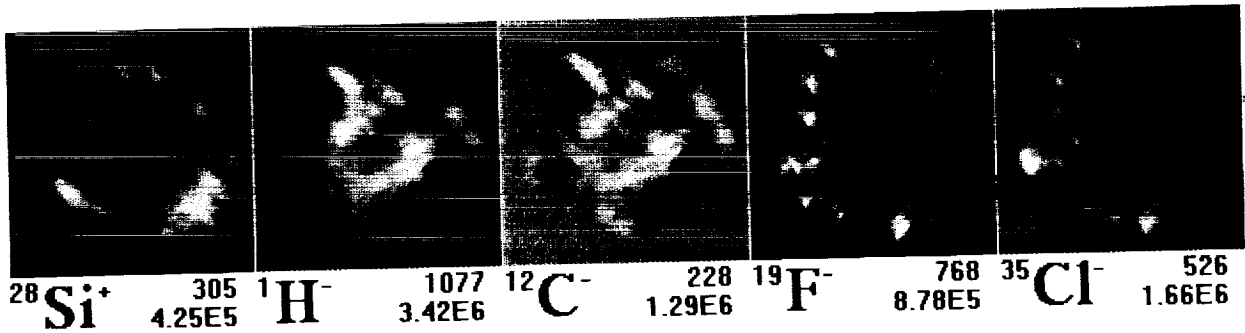

Figure 3: TOF-SIMS images from sample L2006G1 (30 × 30 μm^2, 600 primary ion pulses per pixel).

CARBONATE FORMATION ON MARS: IMPLICATIONS OF RECENT EXPERIMENTS.

S.K. Stephens[1], D.J. Stevenson[1], L.F. Keyser[2], and G.R. Rossman[1], [1]Division of Geological and Planetary Sciences, 170-25, California Institute of Technology, Pasadena, CA 91125, [2]Earth and Space Sciences Division, 183-901, Jet Propulsion Laboratory, California Institute of Technology, Pasadena, CA 91109.

Summary: Could carbonate formation have reduced Martian CO_2 pressure from >1 bar to the present 7 mbar in 3-4 b.y.? Since our previous report [1], we have performed additional experiments which monitor the uptake of CO_2 by powdered basalt. Together with results from post-experimental infrared spectroscopy, these new data support the hypothesis that the kinetics and mechanism of carbonate formation under low-T and low-$P(CO_2)$ conditions (-25°C and 100 mb) are amenable to storing significant amounts of Martian CO_2 in carbonate minerals over geologic time. This claim requires that we verify that carbonate *is* formed in our experiments, and that we support a model involving something like *log t* behavior for CO_2 uptake.

Pressure-Drop Experiments: A sensitive manometer recorded the pressure drop of CO_2 due to uptake by powdered basalt (Kilauea tholeiite, ~98% glass) for periods of days to weeks [1]. (See also [2] for details of experimental procedure.) Runs were performed at warm (~22°C) and cold (-25°C) temperatures, CO_2 pressures of 950, 100, and 34 mb, and H_2O contents equivalent to 0-5000 monolayers. Results are shown below.

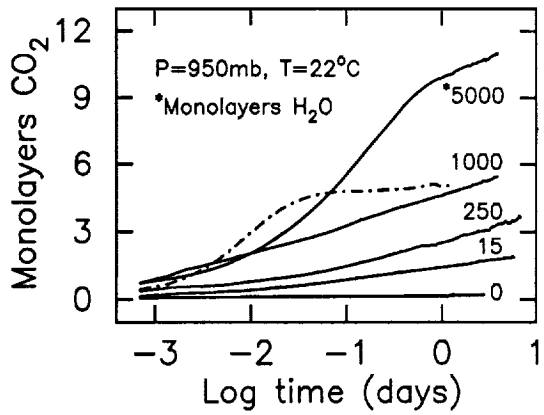

Figure 1. *Pressure-drop results for crushed basalt (0.65 m^2/g) under* warm *conditions at ~1* bar, *where H_2O content (introduced at start of experiment) and CO_2 uptake (measured as a function of log t) are expressed in "equivalent monolayers" deposited uniformly on the surfaces. The broken curve shows the effect of CO_2 dissolution in H_2O without any sample (scaled to 5000 monolayers) and may explain rapid uptakes before ~1 day. Curves then become ~linear.*

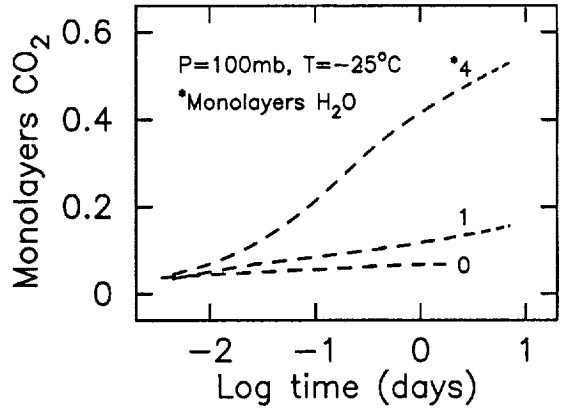

Figure 2. *Basalt (1.85 m^2/g) under* cold *conditions at* 100 mb. *As in Fig. 1, H_2O content varies, and similar behavior is observed. Most H_2O vapor has condensed onto grain surfaces at -25°C. A dry run (0 monolayers) shows only minor uptake after very rapid CO_2 adsorption. The two vapor experiments exhibit curves nearly linear in log t from ~1 to ~10 days, and extrapolation gives a tentative upper limit on CO_2 uptake for geologic timescales (see text).*

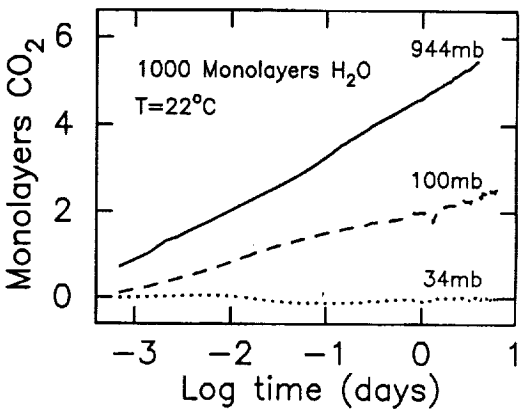

Figure 3 (left). *Basalt (0.65 m^2/g) under* warm *and* damp *conditions (1000 monolayers H_2O). CO_2 uptake after ~0.01 days at 100 mb is roughly half that at 944 mb. A sole experiment run at 34 mb yielded no signal (except fluctuations due to changes in lab temperature), suggesting a possible low-P limit for CO_2 uptake under these conditions. Otherwise, we see from Figs. 1-3 that T and H_2O content influence CO_2 uptake considerably more than $P(CO_2)$. Additionally, at least ~1 monolayer H_2O appears to be necessary for any reaction to occur.*

(text continues overleaf)

XPS (X-ray Photoelectron Spectroscopy): If pressure-drop results are due to carbonate formation and deposition, then added phases should be detectable with suitably sensitive spectroscopic or microscopic techniques. Using XPS, in which electrons generated by incident X-rays allows quantitative identification of surface elements and chemical states from binding energy spectra, we analyzed both crystals of diopside ($CaMgSi_2O_6$) and chips of the same basalt glass used as powders in pressure-drop experiments. Both were exposed for 2 to 4 weeks to a 1-bar CO_2 atmosphere saturated with H_2O vapor, and then compared with controls exposed to N_2. Oxidized carbon, representing carbonate, would have been detected under XPS as a carbon signature shifted to higher binding energy relative to, e.g., adventitious or organic carbon. However, none was detected on either diopside or basalt, suggesting that any carbonate formation in pressure-drop experiments may be related to the surface or subsurface texture of crushed powders. We are presently using XPS to analyze powdered samples.

FTIR (Fourier Transform Infrared Spectroscopy): Infrared spectroscopy was used to test for added carbonate in experimental basalt powders. After pressure-drop runs under warm conditions at ~1 bar CO_2 with H_2O vapor, diopside and basalt were analyzed and compared with known carbonate spectra:

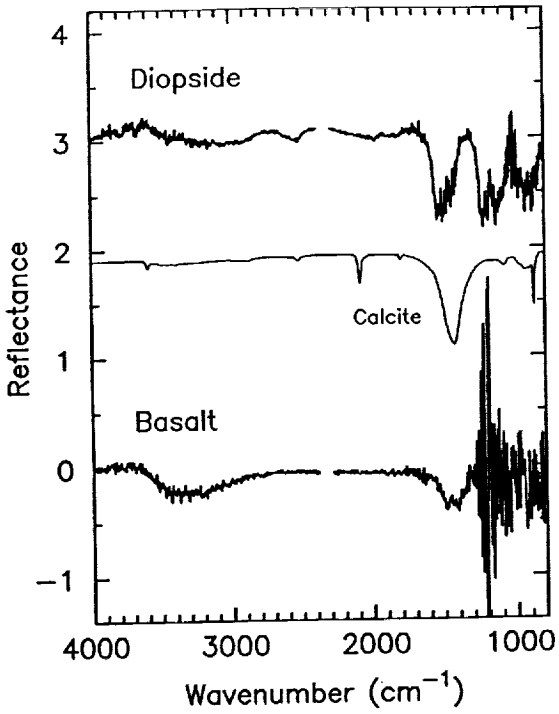

Figure 4. *Ratioed spectra for basalt (corresponding to 15 monolayers H_2O on the previous page) and diopside (also warm, 1-bar, vapor conditions) are shown compared to a calcite transmission spectrum. Ratioing was done relative to control samples which were not subjected to experimental conditions (reflectance is in arbitrary units and the upper two curves are displaced for readability). Controls or dry-run powders would show flat ratioed spectra, expect for noise (e.g., silicate absorptions <1300 cm^{-1}), atmospheric signal (CO_2 band at 2350 cm^{-1}), and water condensation on the detector (>2800 cm^{-1}). We notice prominent absorptions for both diopside and basalt (at ~1500 and 1450 cm^{-1}) which lie on or close to the principal calcite absorption (~1450 cm^{-1} or 6.9 μm). There is a second absorption for diopside (~1200 cm^{-1}) which may be due to a silicate reaction byproduct. The discrepancy between the ~1500 cm^{-1} calcite absorption and the diopside spectrum may be due to a crystal structure other than calcite (e.g., aragonite) or to another carbonate (e.g., dolomite).*

Absorptions at ~1450-1500 cm^{-1} are very suggestive of added carbonate in both diopside and basalt. The apparent inconsistency of FTIR analysis and XPS results may be due to the difference in sampling depths of the two techniques (~1 μm for IR and ~1 nm for XPS). Whatever is causing CO_2 to be stored in pressure-drop experiments and seen with IR may be deep enough that XPS is not seeing it at the surface of bulk samples.

Modeling and Implications for Mars: The apparent functional dependence of CO_2 uptake on ~ log t in pressure-drop experiments suggests a model for aqueous chemistry that involves reaction rate proportional to 1/t. A diffusive process (e.g., simple non-aqueous diffusion through a reaction rind) will give reaction rate ~ $1/t^{1/2}$. However, reaction rate ~ 1/t is a natural outcome of a situation in which the source of a crucial reactant is a dissolving surface that can be encroached upon by deposition of the product. Thus, a scenario involving aqueous chemistry (perhaps as little as a monolayer of H_2O), in which reaction rate is limited by available dissolving surface (yielding cations), yields log t behavior for $P(CO_2)$ after ~1 day. If such a model holds, it is interesting because it is extrapolatable to geologic timescales. For example, log t is such a weak function that, for the -25°C, 100 mb, 4 monolayers H_2O case for basalt shown in Fig. 2, we can derive an upper limit for the CO_2 uptake: In 10^{12} days (3-4 b.y.), a global regolith of basalt powder 100 m in thickness will take up ~10-100 mb. The log t behavior avoids the problem of extrapolating laboratory reaction rates directly.

References: [1] Stephens S.K. et al. (1993) *LPI Tech. Rpt. 93-06, Part 1*, 46-48. [2] Stephens S.K. et al. (1992) *LPI Tech. Rpt. 92-04*, 34-36.

5/4-91 ABS ONLY N94-35462

P-2 3080

NOACHIAN AND HESPERIAN MODIFICATION OF THE ORIGINAL CHRYSE IMPACT BASIN TOPOGRAPHY:

Stephanie Stockman[1] and Herbert Frey[2], [1]Science Systems and Applications, Inc., Lanham, MD 20706, [2]Geodynamics Branch, Goddard Space Flight Center, Greenbelt, MD 20771

Introduction

We propose a new center (35.5°W, 32.5° N) and ring assigment for the original Chryse impact basin based on photogeologic mapping and re-examination of the published geology. Noachian features in the Chryse Planitia area are the best indicators of the ***original*** ancient multiringed impact structure. While other workers have centered the Chryse impact on the topographic low associated with Hesperian volcanic and fluvial deposits, we suggest that the center of the original Noachian-age excavation cavity was located 800 km farther NE and the basin topography was significantly modified over time.

Evidence for Modification of the Topographic Low

Previous workers [1,2,3] proposed a center for the Chryse impact at 45-46.5°W, 22-24°N. This center generally coincides with the locus of Hesperian outflow channel drainage and with the present day topographic low. However, there are two channels which do not drain toward the Hesperian low, Ares Vallis and Kasei Valles.

Ares Vallis exhibits a sudden direction change within Chryse Planitia. The southern portion of the channel and its associated flow features trend toward the present day topographic low. However, where Ares Vallis debouches into the Chryse Basin the direction is N to NE (not NW). Teardrop shaped bars associated with this part of the channel indicate flow was toward the north-northeast away from the (present-day) Chryse topographic low and more toward the lowlying portions of Acidalia Planitia. Additional flow features are also present between 30°N and 40°N in Chryse Planitia, which suggest flow to the NNE, away from the present Chryse Basin low and toward Acidalia.

Kasei is the widest channel debouching into the Chryse Basin. Where it approaches the basin, channel orientation is E-W, trending N of the topographic low. The bars within Kasei are asymmetric and indicative of flow to the SE, toward the present-day topographic low. Kasei Valles is the only channel in the region where channel orientation and fluvial features contrast, suggesting that the channel structure and flow direction has been controlled by separate factors.

New Center and Ring Assigments

Because Hesperian-age features such as the outflow channels suggest different locations for the topographic low of the Chryse Basin, we considered only the distribution of Noachian-age structures in attempting to locate the original impact basin. From photogeologic mapping and the distribution of Noachian-only units, we propose the original Chryse impact basin is centered at 35.5°W, and 32.5°N (Fig. 1), significantly N and E of previously published centers (Fig. 1,). Four rings (diameters 1850, 2650, 3200, 3950 km) were identified.

Previous studies and this study all have at least one ring that intersects Noachian basement (*Nb*)massifs and Noachian Hilly units (*Nplh*) in the SW region of the impact basin, and a second ring that includes the *Nplh* and Noachian plateau sequence cratered unit in Xanthe Terra (Fig. 1). However, restriction to oldest structures yeilds rings fitting the entire Chryse Basin, not just the southern portions. For example, our 1850 km ring follows the contact between Noachian and Amazonian material in NE Chryse, and the contact between Noachian and Hesperian units in NW Chryse. Previous studies did not explain the arcuate Noachian-Amazonian contact in E Chryse.

Conclusion

The original center of the impact basin (35.5°W, 32.5°N), indicated by Noachian age features, is significantly north and east of the low marked by Hesperian-age flow features (45-46.5°W, 22-24°N). The early (Noachian) geologic history of the Chryse Planitia region was

MODIFICATION OF THE CHRYSE BASIN: Stockman, S. and Frey, H.

probabably strongly influenced by two major impacts. The second impact, centered farther N in Acidalia [1,4], overlapped and destroyed the northern portion of the Chryse impact rings and uplifted the central region of the Chryse impact basin. We suggest at least two Acidalia rings may pass through the central portion of the Chryse impact basin. The central topographic depression shifted S and W between the Late Noachian and Hesperian, due in part to the effects of topographic barriers associated with the Acidalia Basin rings [1,4] which restricted volcanic and sedimentary deposits derived from the south to the southern half of the original Chryse Basin. Ponding in this region led to subsidence, shifting the topographic low and controlling the later Hesperian deposition, which became centered on 45-46.5°W, 22-24°N.

References: [1] Schultz, R.A. and Frey, H. V., JGR., 95(B9): 14,175-14,189; 1990. [2] Schultz, P.H. et al., JGR, 87(B12): 9803-9820; 1982. [3] Pike, R. J. and Spudis, P.D., Earth, Moon & Planets 39: 129-194; 1987. [4] Craddock, R. A., et al.., LPSC., XXIV: 335-336; 1993.

Figure 1. Simplified Geologic Map of the Chryse Planitia Region, Mars showing the center and ring assignments for the Chryse Basin multiringed impact structure (a) [2], (b) [3], (c) [1], (d) Stockman and Frey (this study). **Key to Geologic Units**: NPL- Noachian plains units (*Npl_1, Npld, Nple, Npl_2*); NB -Noachian basement material (*Nplh, Nb, Nm, HNu*) HV- Hesperian volcanic plains units; HCH-Hesperian channel deposits and chaotic terrain; AP- Amazonian plains units.

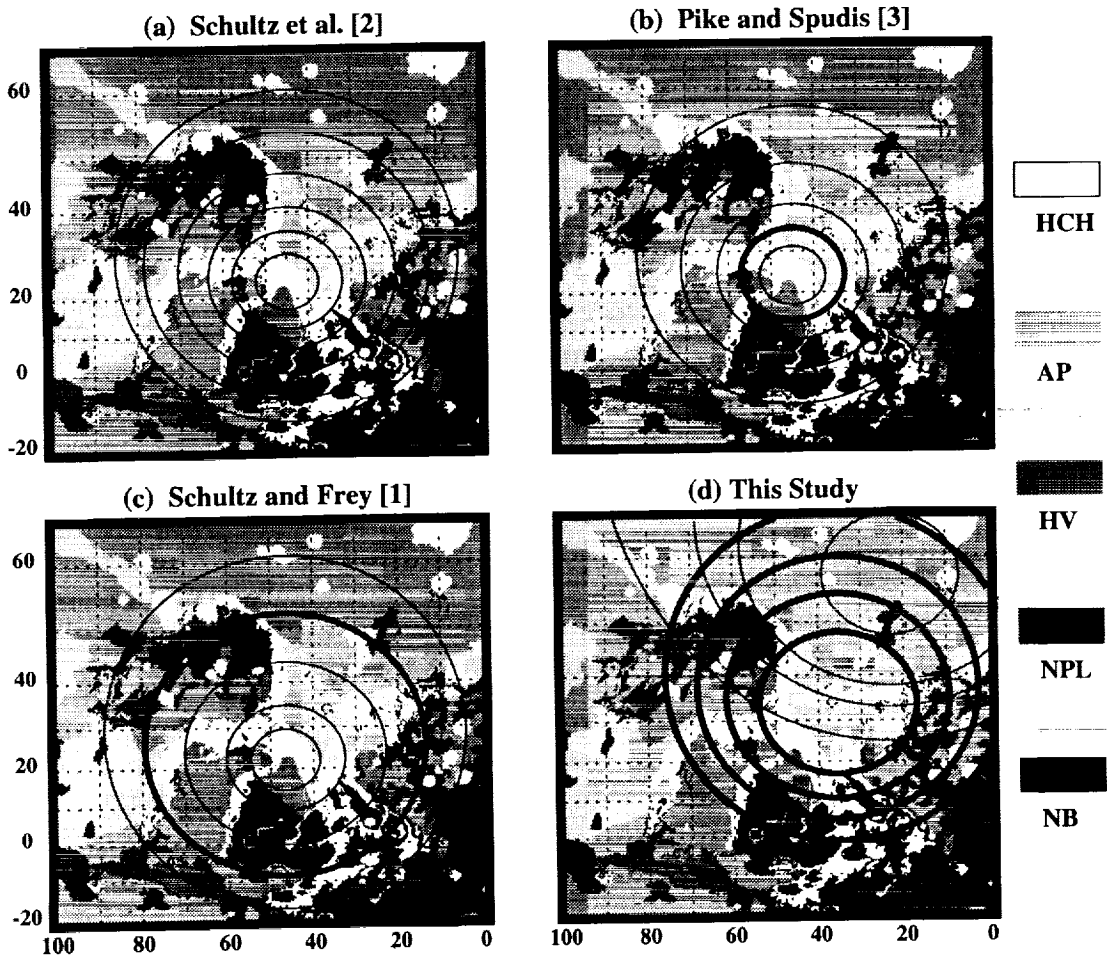

OMIT TO P 1375

CLASSIFICATION AND NOMENCLATURE OF IMPACT METAMORPHIC ROCKS: A PROPOSAL TO THE IUGS SUBCOMMISSION ON THE SYSTEMATICS OF METAMORPHIC ROCKS; D. Stöffler[1] and R.A.F.Grieve[2], [1]Museum für Naturkunde der Humboldt-Universität zu Berlin, Invalidenstr. 43, D-10115 Berlin, Germany, [2]Institut für Planetologie, Universität Münster, Wilhelm-Klemm-Str. 10, D-48149 Münster, Germany, and Geological Survey of Canada, Geophysics Division, 1 Observatory Crescent, Ottawa, Ontario K1A OY3, Canada.

The Subcommission on the Systematics of Metamorphic Rocks (SSMR) of the International Union of Geological Sciences (IUGS) has established a Study Group on "Impactites" composed of several scientists from different countries and chaired by the first author. As a final agreement on the systematics of impact metamorphic rocks has not yet been reached, we are presenting a tentative proposal for the classification and nomenclature of such rocks as a basis for further discussion and input from scientists outside the Study Group.

Introduction and principles of classification. The following members of the Study Group on "Impactites" of the SSMR have made proposals on the classification and nomenclature of impact metamorphic rocks: W. von Engelhardt (Tübingen), V. I. Feldman (Moscow), F. Hörz (Houston), K. Keil (Honolulu), R .A. F. Grieve (Ottawa), and D. Stöffler (Berlin). Two members have not responded. The following proposal is presented to the planetology community in order to seek additional input and final agreement. It is proposed to redefine the term "impactite" as a collective term for all rocks being affected by (an) impact(s) resulting from collision(s) of planetary bodies. The classification distinguishes between products of single and multiple impacts and is meant to be applicable to terrestrial and extraterrestrial rocks. Two parallel sets of classification criteria have been used: (A) a combination of lithological components, texture, and degree of shock metamorphism, and (B) mode of occurrence.

Proposed classification and nomenclature. Our proposal is presented in Table 1. Irrespective of their geological setting (which is not known for most extraterrestrial rocks such as meteorites and lunar rocks) impactites from a single impact fall into 3 major groups: 1. Shocked rocks, 2. Impact melt rocks, and 3. Impact breccias. Shocked rocks are defined as non-brecciated rocks which show unequivocal effects of shock metamorphism (shock pressure in excess of the Hugoniot elastic limit) exclusive of whole rock melting. The terms monomict and polymict refer to lithology *and* degree of shock, e.g. "monomict" means in-situ brecciation of a particluar lithology and uniform (low) degree of shock in all clasts, "polymict" refers to a mixture of one or more lithological types of clasts of different degree of shock which in case of impact melt breccias are embedded in impact melt resulting from shock melting, mixing and homogenizing of one or more target lithologies. This origin of the melt holds also for clast-free impact melt rocks which, therefore, can be considered polymict unless the shock-melted target consisted of only one type of lithology. For illustration of the genetic relations between the various types of impactites a flow diagram is presented in Table 2. The authors would appreciate to receive comments and suggestions concerning this proposal.

Table 1: Classification and nomenclature of impactites

I. Impactites from single impacts

A. Classification according to components, texture and shock metamorphism

1. Shocked rocks
2. Impact melt rocks (clast-free)
   - 2.1 Glassy impact melt rocks (impact glasses)
   - 2.2 Hypocrystalline impact melt rocks
   - 2.3 (Holo)crystalline impact melt rocks
3. Impact breccias
   - 3.1 Monomict (cataclastic) impact breccias
   - 3.2 Polymict clastic impact breccias
     - 3.2.1.1 Fragmental impact breccias (without melt particles)
     - 3.2.1.2 Suevite breccias (with melt particles)
   - 3.3 Impact melt breccias (clast-bearing)
     - 3.3.1 Glassy impact melt breccias
     - 3.3.2 Hypocrystalline impact melt breccias
     - 3.3.3 (Holo)crystalline impact melt breccias

B. Classification of impactites according to mode of occurrence

1. Massive impactites (irregular bodies, layers, lenses, blocks)
   - 1.1 Autochthonous (authigenic)
   - 1.2 Allochthonous (allogenic)
     - 1.2.1 Inside crater rim (crater fill)
     - 1.2.2 Outside crater rim (ejecta blanket)
2. Impact breccia dikes
   - 2.1 Fragmental breccia dikes
   - 2.2 Suevite breccia dikes
   - 2.3 Melt breecia dikes (clast-bearing impact melt)
   - 2.4 Pseudotachylite (calst-bearing frictional melt)
3. Impactoclastic air fall beds and tektite strewn fields

II. Impactites from multiple impacts

1. Impact regolith (unconsolidated impactoclastic debris)
2. Shock lithified impact regolith (consolidated impactoclastic debris)
   - 2.1 Regolith breccias (with matrix melt and melt particles)
   - 2.2 Fragmental breccias (without matrix melt and melt particles)

CLASSIFICATION OF IMPACTITES: Stöffler, D. and Grieve, R.A.F.

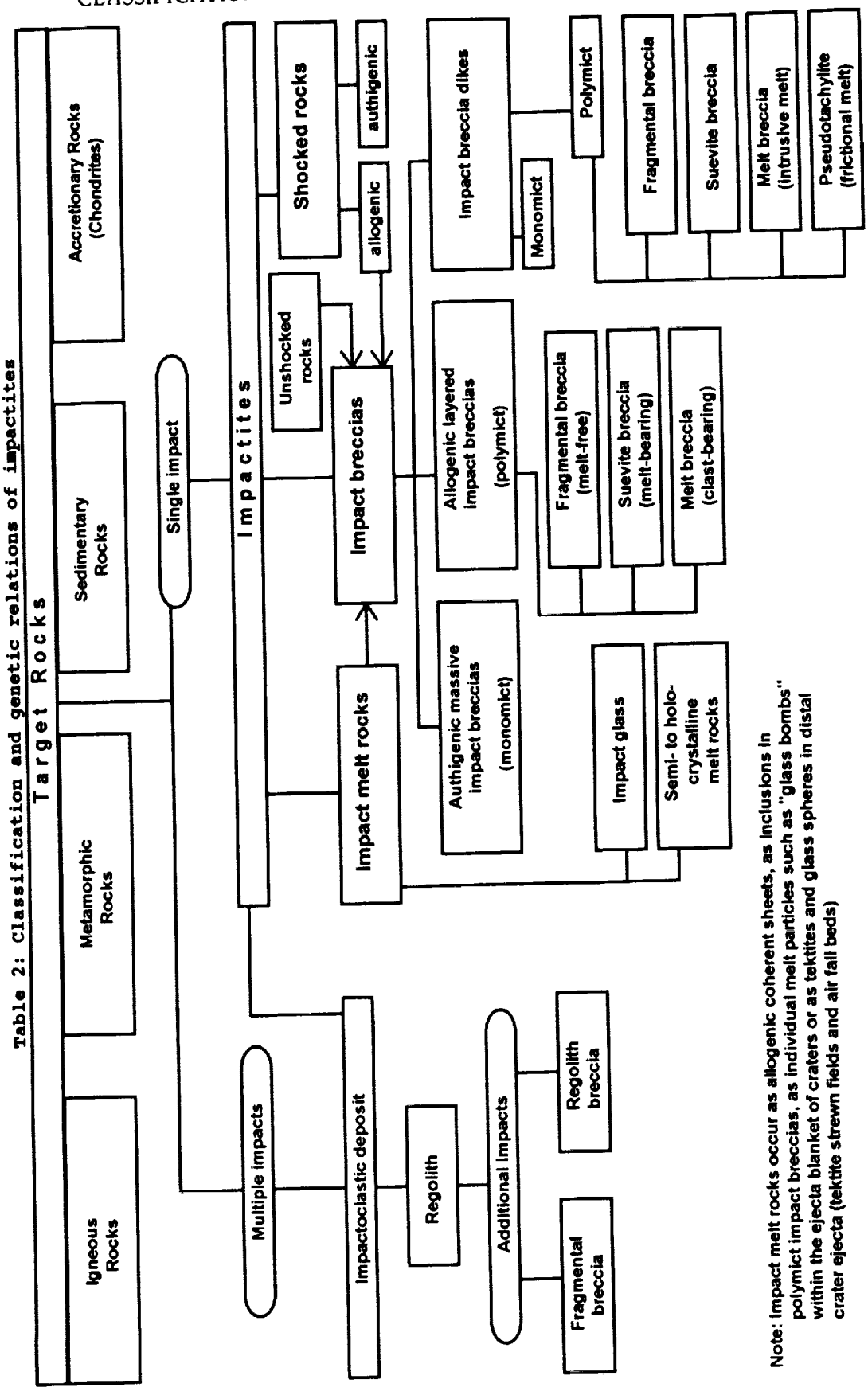

Table 2: Classification and genetic relations of impactites

Note: Impact melt rocks occur as allogenic coherent sheets, as inclusions in polymict impact breccias, as individual melt particles such as "glass bombs" within the ejecta blanket of craters or as tektites and glass spheres in distal crater ejecta (tektite strewn fields and air fall beds)

STATUS OF THE SMALL BODY MAPPING PROGRAM, Philip J. Stooke, Department of Geography, University of Western Ontario, London, Ontario, Canada N6A 5C2 (stooke@vaxr.sscl.uwo.ca).

INTRODUCTION. I have developed shape modelling methods and map projections for non-spherical bodies (**1,2,3,4**). The shape modelling method, which duplicates limbs and terminators using interactive modification of a digital radius model, is a precursor of the greatly extended SPUD software developed by the Galileo imaging team (**5,6,7**). In the **Small Body Mapping Program** I am applying these techniques consistently to all bodies for which data are acquired. Sources include NASA planetary images (e.g. Voyager), ESA and russian spacecraft (e.g. Giotto, VeGa), Earth-based radar (**8**), star occultations (**9**) and HST images. Shapes derived by the SPUD team and others can be imported for mapping. Results for the nucleus of Comet Halley, Amalthea, Prometheus, Pandora, Janus and Epimetheus have been published. Work is in progress on Larissa, Proteus, Puck, Phoebe and Hyperion.

RESULTS TO DATE. These techniques were used to map the nucleus of Comet Halley (**10**) and Amalthea (**11**). The Halley model was based on a rotation state now known to be incorrect. It will be repeated when the rotation is better understood, as now seems to be within reach. The Amalthea map (**11**) was drawn using earlier versions of the software, and has been improved (paper submitted). The new shape is being used to model the gravitational field (**12**).

Since then, models and maps have been derived for the F Ring shepherd and co-orbital satellites of Saturn (**13,14,15**) and for Larissa and Proteus, the inner satellites of Neptune (submitted for publication). Experience indicates that global maps greatly facilitate the interpretation of geology. The process of shape modelling gives a far greater familiarity with the object than can be obtained from simple inspection of images. Thus I was able to describe grooves and a major trough on Epimetheus, find parallel ridges and a large but poorly imaged crater on Prometheus, and note that Prometheus appears smoother than the other three nearby satellites (**16**). For Proteus, lower resolution image pairs were merged to improve SNR, revealing new details including a massive apparent valley on the leading side, and strongly confirming prograde synchronous rotation. Many lineaments are seen, apparently grooves (Figure 1).

WORK IN PROGRESS. Models and maps of Phoebe, Hyperion and Puck are in progress. For Phoebe many images were taken over nearly three rotations at low resolution (10 to 11 pixels across the disk). Despite low resolution and noise, features can be recognised in successive views and in images taken at intervals of one or two rotations. The limb shape varies systematically (Figure 2) and a simple shape model is possible. Preliminary indications are that several large (40 km diameter) craters can be reliably distinguished, and that bright markings are located on ridges rather than around craters.

For Hyperion, two indicators of rotation are found in resolved images: (A) features are seen to cross the terminator in the last few views (arrows, Figure 3), giving a rough indication of the pole position (40° to 80° beyond the centre of the terminator in Figure 3). (B) Images 43883.11 to 43883.31 show small but real brightness variations indicating the position of a large crater well seen in later images. Motion of the crater shows the sense of rotation about the pole described above (counterclockwise in Figure 3). The images show grooves or valleys near the terminator, and many more craters than have been described previously. Hyperion is not lacking in craters as suggested in ref. **17**. Preliminary indications are that the rotation state at the time of the Voyager 2 flyby was as described in ref. **17** (13 day period, axis near the orbit plane) and that the rotation axis was significantly inclined to the short body axis.

Puck was resolved in a single small image. Two dark 'lanes' have been mapped (**18**), but I find only one convincing. It is surrounded by two bright bands and is most likely a single large groove or trough, comparable to that seen on Epimetheus. The bright bands are its walls, the dark lane is its floor (Figure 4). The trough was probably caused by a large impact, at the formation of Puck by fragmentation or later.

FUTURE WORK. These techniques will be applied to all bodies for which data are obtained. The shape modelling method will be modified to work with delay-doppler images of NEAs. The Phoebe experience is directly applicable to HST images of main belt asteroids. Shapes modelled by other researchers will be analyzed independently to help assess duplicability of such models, and maps in a consistent style will be prepared for all suitable worlds.

REFERENCES. (1) Stooke, P.J., 1986. Proc. 2nd Int. Symp. Spatial Data Handling, 523-536. (2) Stooke, P.J., 1988. Ph.D. Diss., Univ. of Victoria, 169 pp. (3) Stooke, P.J. and Keller, C.P., 1990, Cartographica, 27: 82-100. (4) Stooke, P.J., 1992. Proc. ACM '91, LPI, Houston, 583-586. (5) Simonelli, D.P., et al., 1993. Icarus 103: 49-61. (6) Thomas, P.C., 1993, submitted to Icarus. (7) Thomas, P.C. et al., 1993, submitted to Icarus. (8) Ostro, S.J. et al., 1990. Science 248: 1523-1528. (9) Dunham, D.W., Sky & Tel. Jan. 1992, 71-77. (10) Stooke, P.J. and Abergel, A., 1991. Astron. Astrophys. 248: 656-668. (11) Stooke, P.J., 1992. Earth, Moon, Plan. 56: 123-139. (12) Gozdziewski, K. et al., in preparation. (13) Stooke, P.J., 1993a. Earth, Moon, Plan. 62: 199-221. (14) Stooke, P.J. and Lumsdon, M.P., 1993. Earth, Moon, Plan. 62: 223-237. (15) Stooke, P.J., 1993b. Earth, Moon, Plan. 63: 67-83. (16) Stooke, P.J., 1993c. LPSC XXIV (abstract), 1363-1364. (17) Thomas, P. and Veverka, J., 1985. Icarus 64: 414-424. (18) Croft, S.K. and Soderblom, L.A., 1991. in Uranus (Bergstralh et al., eds), U. Arizona Press, pp. 561-628.

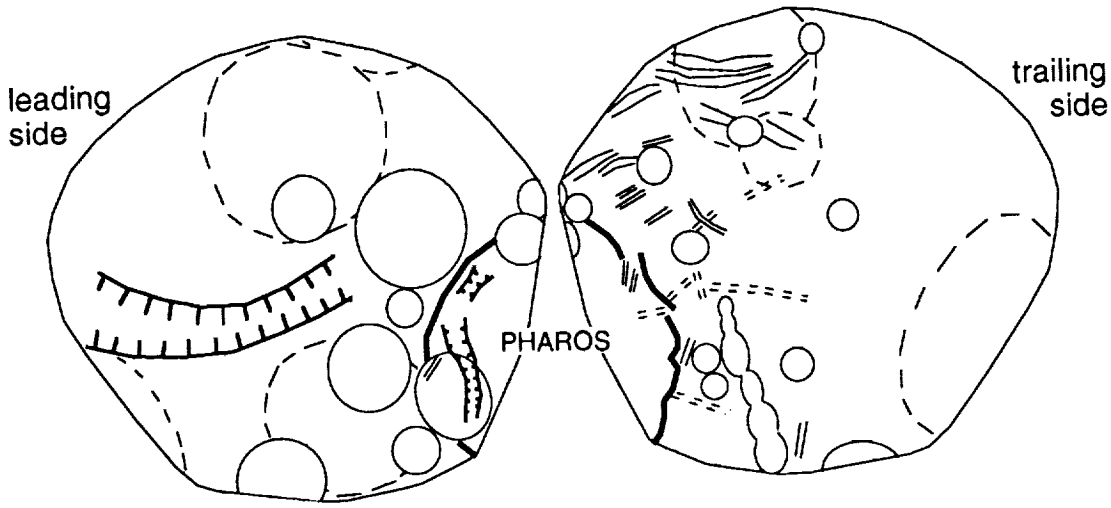

Figure 1. Map of major features of Proteus (morphographic conformal projection), showing grooves (double lines, dashed if uncertain), larger valleys (heavy double lines), large craters (solid loops), degraded craters or facets (dashed loops) and the large crater Pharos (thick arcs).

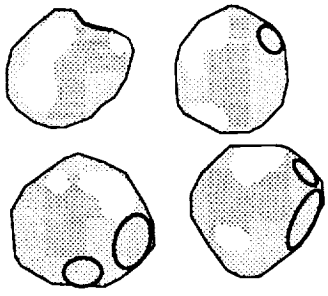

Figure 2. Sketches of Voyager images of Phoebe showing variations in limb shape, possible large craters and bright markings.

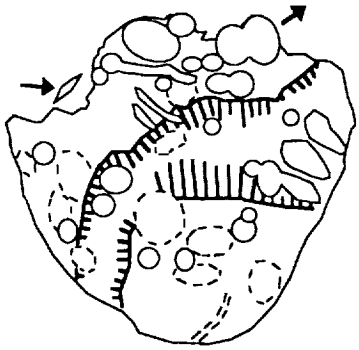

Figure 3. Sketch of Voyager image 43972.11 of Hyperion showing craters, grooves (top centre), motion of craters relative to the terminator (arrows), and major scarps (walls of a large trough).

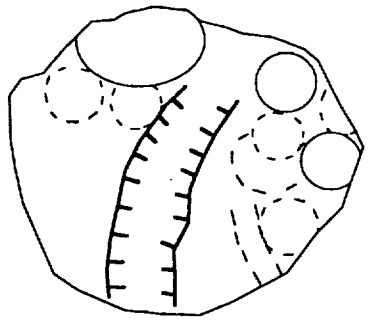

Figure 4. Sketch of Voyager image 26837.16 of Puck showing craters and the possible large trough (centre).

PROMOTING PLANETARY SCIENCE AMONG ELEMENTARY SCHOOL STUDENTS
M. M. Strait, Department of Chemistry, Alma College, Alma,MI 48801.

A good way to enthuse primary school students about science is to use planetary science. The kindergarden to second grade age group is wildly enthusiastic about any outside visitor to their class and amazingly knowledgeable about space. Combined with a multimedia, interactive presentation, this background provides a good platform to talk about education (staying in school, studying hard) and science (what scientists do, how everyone needs to know some science) to these students.

As part of the outreach portion of the Alma College NASA/ Joint Venture grant, I was invited to talk about "space" to students in one of the rural elementary schools in Gratiot County, Michigan. A specific topic was unimportant, and as my background is in meteoritics I used that as a launch point for an interactive presentation to bring space science to the students in their own classroom.

A half-hour presentation was developed using the following basic outline:

I. Introduction -	What do you know about space? What is in Outer Space?
II. Story Time -	Relate the origin and evolution of the Solar System in story form using poster illustrations.
III. The Facts -	Show pictures of the planets and a few other bodies and relate one or two facts about each. Try to address topics brought up in I.
IV. Show and Tell -	Pass around meteorite and terrestrial hand samples and talk about what they tell us. Field questions while waiting for samples to go around.
V. Conclusion -	Settle down the younger kids by talking about what is not in space. "Feel" zero gravity. Hand out line drawings of planets on colored paper for them to color.

The introduction not only introduced the topic for the students, but also let me get a feel for their knowledge base. It also provided a way to address certain topics and their concerns. For example, "aliens" was a popular response to "What is in Outer Space?". This answer was not treated as wrong, but used as a theme when we later looked at the planets. We would talk about living conditions on each individual planet and the students would decide on their own that aliens could not live in our solar system, so must live on planets around another sun.

Posters and pictures were used to illustrate the story of the solar system and the look at the planets. Hand samples of rocks are always popular, so, in addition to space rocks

PROMOTING PLANETARY SCIENCE: Strait M. M.

(i.e., meteorites), I bring a selection of terrestrial rocks including basalt and granite. Flashy rocks (i.e., malachite, specular hematite, etc.) are also very popular, but tend to distract from the main thrust of the talk. (They can be left for another presentation on terrestrial geology.)

At the end, something is usually required to calm everyone down and I have discovered this age group is still willing to believe they can feel zero gravity if they pretend hard enough. So, we sit very still and feel ourselves floating along in space.

This basic format was used in each class and needed surprisingly little modification for each grade level. There was no need to "dumb down" anything, and only judicious trimming of the amount of material related was needed in going from preschool to second grade classes. Everyone was quite well informed about what was in space in general as well as some specifics, such as the names of the planets. As the grade level increased, the amount of knowledge increased from knowing the names of a few planets (Pluto in particular!) to knowing not only the names of all the planets, but also their order and a little about each of them.

Two key considerations lead to success in doing a presentation for this age group. One was to stay on their level - literally. I usually sat in the storyteller's chair with the students in a big circle on the floor. The other consideration one must make is to "go with the flow". You need to respond to what they know and can comprehend, as well as respond to what they want to know, and fit it into the basic format.

This presentation was done for about sixteen preschool through second grade classes over two days in successive weeks. There was only one bad experience, and that was with a kindergarden class on the Tuesday before Thanksgiving. (Oddly, the preschool class that same day was all ears!) Overall, it was an exhausting and time consuming experience, but very rewarding. The impression on the students was great enough that one young man who saw me several weeks later in a completely different setting remembered me as "the lady who talked to us about space".

It is all to often stated that interest in science by American students is at a deplorable level, and that the space program is particularly ridiculed and unsupported by the taxpayer. Among the majority of ordinary people that I have known and worked with, I have rarely found the latter to be true, and this series of presentations has shown me that the former is also false. At rural Ithaca South Elementary School in central Michigan, the students were both enthusiastic and very knowledgeable about space. Somewhere between the second grade and high school they appear to lose this interest in science (although not necessarily space) and it is this loss of interest that we need to be addressing. Programs such as the above should be continued as the students progress through their education in order to improve science education in America.

THE GLOBAL RESURFACING HISTORY OF VENUS; R.G. Strom, Univ. of Arizona, Tucson, AZ, G.G. Schaber, U.S.G.S., Flagstaff, AZ, and D.D. Dawson, Univ. of Arizona, Tucson, AZ

The resurfacing history of Venus is constrained by the following 7 characteristics of the impact cratering record: (1) the areal distribution of the craters cannot be distinguished from a random distribution (Phillips *et al.*, 1992), (2) the hypsometric (elevation area/crater density) distribution of the craters cannot be distinguished from a random distribution (Banks et al, these abstracts), (3) the random crater distribution is independent of size; small craters are generally as randomly distributed as large craters (Phillips *et al.*, 1992; Schaber *et al.*, 1992), (4) fully 84% of the craters are in pristine condition, (5) only 2.5% of impact-related features (crater deposits and craterless splotches) have been embayed by lava, and only 3.5% of the craters are highly fractured, (6) there is no definitive evidence that the parabolic features (covering about 9% of the surface) or the halos surrounding craters have been embayed by lava, and (7) the lava embayed craters are concentrated in zones of recent volcanism and the highly fractured craters are associated with major rift systems along the equatorial highlands.

A global resurfacing event simply and easily accounts for all constraints on resurfacing imposed by the cratering record. It is consistent with (1) the spatially random crater distribution and its diameter independence, (2) the random hypsometric crater distribution, (3) the very low abundance of embayed craters and crater-related features, and (4) the low abundance of fractured craters. Further, the model is consistent with the concentration of embayed and highly fractured craters at zones of recent volcanism and tectonism. Price and Suppe (1993) also find the crater distribution is inconsistent with equilibrium resurfacing, and instead reflects a production population modified by limited tectonism and volcanism. The global resurfacing model proposes that a global resurfacing event involving both tectonism and volcanism occurred about 300 m.y. ago and obliterated the pre-existing cratering record. Its duration is unknown, but it must have ended suddenly relative to the crater production rate. Otherwise, there would be significant variations in the crater density and size/density distribution. The very small number of fractured and lava embayed craters, most of which are concentrated in zones of recent tectonism and volcanism, suggests that it ended in a short time compared to the cratering rate. An estimate of the rapidity with which the global resurfacing event ended can be determined by Monte Carlo simulations using the estimated cratering rate , and an initially high resurfacing rate that declines with time over the period since the global resurfacing event. In these simulations the interval between resurfacing events was increased as the simulation progressed. For a given initial resurfacing interval the rate of this increase was determined by varying it in multiple runs. The rate of increase that results in the observed percentage of embayed craters and crater-related features (2.5%) sets the upper time limit for terminating the global resurfacing event. For a wide range of initial resurfacing intervals, the Monte Carlo simulations suggest that the global resurfacing event ended within a time interval no greater than 10 m.y. It may have ended within a shorter period of time, but more accurate results cannot be determined because of the current uncertainties in the data. This event was followed by greatly reduced tectonism and volcanism on a global scale; however, these processes clearly did not cease entirely (Schaber *et al.*, 1992). The observed crater population has accumulated up to the present time, and the present stratigraphy of the volcanic plains and highland surfaces is largely, but not entirely, the result of the latest resurfacing event. Modification of those surfaces over the past 300 m.y. or so has been dominantly the result of simple fracturing (with limited extension) and regional volcanism at such a low level that the cratering record was left virtually intact (Shaber et al, these abstracts).

VENUS GLOBAL RESURFACING, Strom et al.

Monte Carlo simulations indicate that the number of volcanic events required to cause about 2.5% embayed craters and related features ranged from 400 to 600, and the percentage of the planet resurfaced ranged from 4% to 6%. In reality each of the 400 to 600 events would probably consist of more than one eruption, so that the cumulative number of eruptions could have been much more. One or two eruptions at one site might result in a lava thickness of about 100 m, but multiple eruptions at one site could build an edifice about 1 km thick or more (there are not 400 to 600 volcanoes 1 km high on Venus). If we consider all the deposits to be 100 m thick, or all of them to be 1 km thick then this should span upper and lower limits of deposit thicknesses. Thus, the probable minimum and maximum lava production rate on Venus is 0.01 to 0.15 km^3/yr since the global event. This is about 10 times less to slightly more than the lava-production rate (0.11 km^3/yr) of Kilauea alone, one of the most active volcanoes on Earth (Holcomb, 1987). Thus, the estimated eruption rates since the global resurfacing event are less than estimated current rates of intraplate volcanism on Earth (0.33 to 0.5 km^3/yr), and orders of magnitude less than the Earth's magmatic output (intrusive and extrusive) of 26-34 km^3/yr (Crisp, 1984).

The global resurfacing event involved both tectonism and widespread volcanism that probably operated in concert. The various terrains have complex relative ages; (1) plains have a variety of stratigraphically different ages, (2) fracture belts transect plains and highlands and, in turn, are locally embayed by plains, (3) in some areas, e.g., Ishtar Terra, the folded margins of highlands postdate the adjacent plains, and (4) coronae show a variety of relative ages.

In general, most of the plains surrounding tesserae appear to embay these units, and are, therefore, younger. This suggests that intense crustal disruption generally, but not wholly, preceded widespread plains volcanism. The average age of the tesserae is the same as the average age of other terrains (Schaber et al, these abstracts). Tesserae, however, are the most highly disrupted terrain on Venus and may be the only terrain that has survived the last global resurfacing event, although it has been severely disrupted by it. It is the only terrain that has circular features that may be highly disrupted impact craters that survived the global resurfacing event. Detailed geologic mapping of this terrain will help place it within the context of the global resurfacing model, and may show multiple episodes of major deformation events that coincide with earlier global resurfacing events.

The subtle stratigraphic age differences that occur on most of the Venusian plains likely date from late stages of the global resurfacing event (Komatsu *et al.*, 1993). Komatsu *et al.* (1993) have also suggested that the global resurfacing event may be responsible for the formation of the remarkable canali-like channels on the planet. Unfortunately, these differences in age cannot be determined by crater statistics because of the low overall density and statistically random spatial and hypsometric distribution of craters. Refinement of the relative chronology of events within this global resurfacing episode and the limited activity that followed will require detailed geologic mapping using established stratigraphic methods.

References: Banks, M., these abstracts; Crisp, J.A.,*Volcano. Geotherm. Res.*, *20*, 177-211, 1984; Holcomb, R.T, Vol. 1, Chaper 12, Eds. R.W. Decker, T.L. Wright, and P.H. Stauffer, *U.S. Geological Survey Prof. Paper 1350*, 261-350, 1987; Komatsu, Goro, et al., *Icarus*, *102*, 1-25, 1993; Phillips, R.J., et al., *J. Geophys. Res.*, *97, E10,* 15,923-15,948, 1992; Price, M.H. and J. Suppe, *Supplement to EOS, 74*, No. 43, 379, 1993; Schaber, G.G. et al., *J. Geophys. Res., 97, E8*, 13,257-13,301, 1992; Schaber et al., these abstracts.

Impact Ejecta Vapor Cloud Interference Around Venus Craters

Seiji Sugita and Peter H. Schultz, Dept. of Geological Sci., Brown Univ. Providence, RI, 02912; e-mail address, sugita@stout.geo.brown.edu

Both experimental and theoretical studies indicate that large scale hypervelocity impacts produce significant amount of impact vapor during cratering [1, 2]. Most of the impact vapor escapes a planet without an atmosphere or with a thin atmosphere [3]; even the terrestrial atmosphere cannot contain vapor cloud [4]. The extremely dense atmosphere of Venus, however, can contain the vapor cloud generated by a lower angle impact [5]. A portion of the impact vapor retains the energy, mass, and translational momentum largely decoupled from later stage vapor/melt generation and excavation of the target. The present study assesses the dimensions of the zone on Venus where the impactor-driven vapor cloud interferes with later ejecta emplacement. The purpose is to derive constraints on the vapor cloud motion including the downrange velocity and expansion velocity.

Impact Vapor Clouds on Venus: Runout flows on Venus indicate an origin initially controlled by the impactors. Runout flows of oblique impact craters occur downrange with some examples climbing up slope before redirected by gravity. Such observations led to the hypothesis that an impact vapor cloud produced by an oblique impact has a large translational downrange momentum [5]. A hemispherical shock formed by the impact vapor explosion expands radially, carrying away the kinetic energy of the vapor cloud. This energy coupling between inner vapor cloud and surrounding air cools the vapor cloud and results in vapor condensation. The vapor condensates contribute runout flows on the surface but represent only a portion of the total energy partitioned to internal energy (impact melt/vapor) of the target. The downrange motion decelerates very quickly due to drag forces. Interference between this early-stage process and later stage ballistic ejection produces an interference zone exhibiting turbulent emplacement styles. This interference zone resembles a parabola open downrange with a shape qualitatively related to impact angle (based on the asymmetry of later stage ejecta deposites).

Observation: Selected craters with well defined ejecta interference zones provide a quantitative measure of the relative effects of lateral expansion and downrange deceleration. Impact angle is estimated by uprange ejecta missing zone according to [5] with an error of ±20%. Projectile size is estimated using both the scaling law for crater diameter [7] including 25% of crater widening and a scaling law based on dimensions of central structure of a crater [8]. But the derived sizes agree very well. Runout distance of a flow is defined as the distance from the uprange edge of the interior structure of the crater (central peak and peak ring) and the point where the flow direction begins to be controlled by topography. The uprange edge of the central structure of the crater is a first-order indicator of first contact point between the impactor and the target [5].

Even though the estimate of impact angle is only approximate, a systematic increase in runout distance relative to width of ejecta interference zone with decreasing impact angle is observed: The ratio of runout distance of the flow to width of ejecta interference zone increases from about 1.1 for relatively high impact angle (~40°) to 1.4 for lower angle (~10°). The ratio for an extremely low angle (<7°) elongate crater approaches 2.5. This supports the hypothesis that the downrange motion of vapor cloud is controlled by an initial momentum inherited from the impactor.

Fluid dynamic Calculation: An analytical fluid dynamical model calculation provides an estimate of the downrange velocity of vapor clouds for the selected craters. The radial expansion of the vapor is described by Taylor's approximation [9]. The shock front expands in proportion to $t^{2/5}$ where t is time. But when shock detaches from the vapor/air interface,

the interface expands with time raised to a power of $2/5\gamma$. This provides the vapor cloud dimensions. The deceleration of translational motion of a vapor cloud is described by

$$m\frac{du}{dt} = -\pi C_D \rho_{air} R^2 u^2 \qquad (1)$$

where m, u, C_D, ρ_{air}, and R are mass, translational velocity, drag coefficient, and radius of the vapor cloud, respectively. Drag coefficient, C_D, depends on shape of the vapor cloud, which is assumed to approximate a sphere with C_D about 0.5 [10]. But if the cloud hydrodynamically reshapes itself, C_D can be much smaller and vary with time [11].

This simple analytical model reproduces the observed quasi-parabolic shape of ejecta interference zone, which becomes more elongate with decreasing impact angle due to a higher initial translational velocity. But absolute values for the derived initial translational vapor cloud velocities required to fit the observed interference zones typically appear to be higher than reasonable values of the impactor velocities. This result possibly indicates that the drag coefficient for the vapor cloud is much smaller due to aerodynamic reshaping during deceleration.

Summary: Dimensions of the ejecta interference zone were measured for a number of selected craters. Runout distances increase as impact angle decreases, but very high initial vapor cloud velocities are derived. These observations are consistent with a vapor cloud has a significant impactor component, which is physically decoupled from later stage excavations for lower angle impacts (<30°). More detailed analyses should allow inverting observations to give better estimates of initial impact conditions.

References: [1] Schultz, P. H. and Gault, D. E. (1990) *GSA Special paper*, **247**, 239-261; [2] O'Keefe, J. D. and T. J. Ahrens (1982) *JGR*, **87**, 6668-6680; [3] Vickery, A. M. (1986) *JGR*, **91**, 14139-14160; [4] Vickery, A. M. and H. J. Melosh (1990) *GSA Special paper*, **247**, 289-300; [5] Schultz, P. H. (1992) *JGR*, **97**, 16183-16248; [6] Sleep, N. H. et. al., *Nature*, **342**, 139-142; [7]Schmidt, R. M. and K. R. Housen (1987) *Int. J. Impact Eng.* **5**, 543-567; [8] Schultz, P. H. (1994) New Development Regarding the K/T Event and Other Catastrophics in Earth History; [9] Taylor, F. R. S.(1950) *Royal Soc. London, Phil. Trans.*, **201**, 159-174; [10] e.g., Shapiro, A. H. (1953) *The dynamics and thermodynamics of compressible fluid flow*, The Ronald Press Com., New York; [11] Schultz, P.H. and S. Sugita (1994) *LPSC* abstract, this volume.

ISOTOPIC COMPOSITION OF NITROGEN IN THE PCA91002 CHONDRITE; N.Sugiura and S.Zashu, Dept. of Earth and Planetary Physics, Univ. of Tokyo

PCA-91002 is a CL(Carlisle Lakes) group chondrite. The CL group is a newly identified chondrite group which is characterized by distinct oxygen isotopic composition and highly oxidized mineralogy [1]. Since it has been recognized that nitrogen isotopic composition is quite distinct for many groups of meteorites, and hence it may serve as a useful criterion for identifying meteorite groups, the nitrogen isotopic composition of this new chondrite group is of special interest. Furthermore, isotopic compositions of nitrogen (and oxygen) are useful tools in revealing the relationship between source materials of chondrites, because isotopic compositions can not be changed easily by processes which occurred in the solar system. In particular, if an extreme isotopic composition is obtained, it may serve as an end member of source materials which were mixed and processed to form various chondrites. Bearing these purposes in mind, isotopic composition and abundance of nitrogen in the PCA91002 chondrite were measured. Isotopically light nitrogen (delta ^{15}N=-60 permil) was found in this chondrite. This is the lowest value ever found in bulk chondrites.

The details of the nitrogen measurements have been published elsewhere [2]. Neon and Argon were also measured to get information on the cosmic-ray-exposure age (and hence cosmogenic nitrogen abundance) and solar wind gases which could affect the isotopic composition of nitrogen. A bulk sample and a H_2O_2 treated sample were measured.

From the isotopic composition of Ne and Ar, this chondrite is a gas-rich chondrite. Ne and Ar show bimodal release patterns of solar gases which probably corresponds to solar wind (low temperature release) and solar energetic particle (S.E.P.: high temperature) components, respectively. Since solar rare gases are probably accompanied by solar nitrogen, care has to be taken in deciphering nitrogen results (Fig.1). A large amount of nitrogen is released from the bulk sample at low temperatures. Most of this nitrogen is removed by H_2O_2 treatment. Therefore, it is likely that this is organic nitrogen. This nitrogen is isotopically light (-60 permil). In the case of the bulk sample, the delta ^{15}N value at intermediate temperatures is around -30 permil, while at low and high temperatures it is around -60 permil. This is explained as a result of mixing of isotopically heavier components with a presumably indigenous (-60 permil) component. According to our previous experience, it is likely that at 400-600 C, terrestrial organic nitrogen (delta ^{15}N=+15 permil) is the isotopically heavy component. At 700-1000C, solar nitrogen could be the isotopically heavy component. In the case of the H_2O_2 treated sample a presumably indigenous component (-60 permil) is observed around 900C. This is explained as a result of nearly complete removal of solar nitrogen by the treatment, while some terrestrial organic nitrogen persisted. The delta ^{15}N values (-60 permil) in the H_2O_2 treated sample (around 900 C, nitrogen in metal?) and in the bulk sample (at low temperatures, organic nitrogen?) are quite similar. This suggests that this nitrogen is widely distributed among various minerals in this chondrite. This is important because it suggests that this is not a presolar component which is often observed in primitive ordinary chondrites.

The PCA91002 chondrite contains isotopically light nitrogen (-60 permil) which seems to be distributed among various minerals including organic

materials. This nitrogen isotopic composition is the lightest value ever observed for bulk chondrites (Fig.2; data sources are [3,4,5,6]), although lighter values have been observed in iron meteorites and Acapulco type meteorites. Previously, the lightest nitrogen in bulk chondrites was observed in E chondrites. But there was a gap in the delta value between that of E chondrites (-30 permil [3]) and that in Acapulco types (-150 permil [7]) or that in iron meteorites. Now the gap was partially filled by the CL type chondrites. The CL chondrite is located at the upper left corner on the nitrogen-oxygen isotope ($\Delta^{17}O$) systematics (Fig.2). Such a location for a newly defined chondrite group has an important implication; our collection of chondrites on the Earth may be a rather limited collection of a much broader spectrum of asteroids at the main asteroidal belt. This view is supported by the presence of iron meteorites and Acapulco type meteorites whose nitrogen isotopic values extend down to -150 permil. It is quite likely that chondrite parent bodies with such a light nitrogen isotopic composition still exist among the main belt asteroids. There seems to be no significant correlation between nitrogen and oxygen isotopic composition (Fig.2). It seems that there is no reason to expect that oxygen isotopic composition of chondritic meteorites should be limited to the range observed for the present collection of chondrites. In fact it is expected that the ^{17}O value of the solar nebula gas could be as high as 8.6 permil [8]. Therefore, we can expect that the chondrite data points will extend to delta ^{15}N=-150 permil and $\Delta^{17}O$=8.6 permil on the diagram of Fig.2, which means that there is a lot of room for discovery of new groups of chondrites.

REFERENCES

[1]A.Rubin and G.W.Kallemeyn (1989) Geochim. Cosmochim. Acta,53,3035.
[2]K.Hashizume and N.Sugiura (1990) Mass Spectroscopy, 38, 269.
[3]C.C.Kung and R.N.Clayton (1978) Earth Planet. Sci. Lett., 38, 421.
[4]J.F.Kerridge (1985) Geochim Cosmochim. Acta, 49,1707.
[5]K.Hashizume (1993) Ph.D. Thesis, Univ. of Tokyo.
[6] R.N.Clayton (1993) Ann. Rev. Earth Planet. Sci., 21,115.
[7]G.Sturgeon and K.Marti (1991) Proc. Lunar Planet. Sci. 21, 523.
[8]R.N.Clayton and T.K.Mayeda (1984) Earth Planet. Sci. Lett., 67,151.

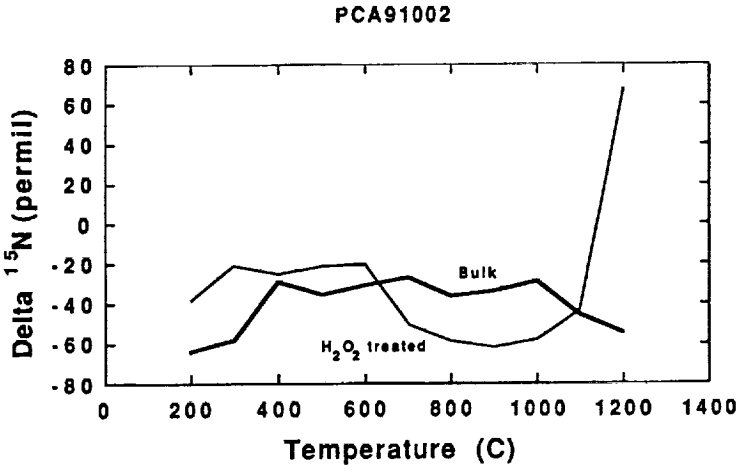

Fig.1

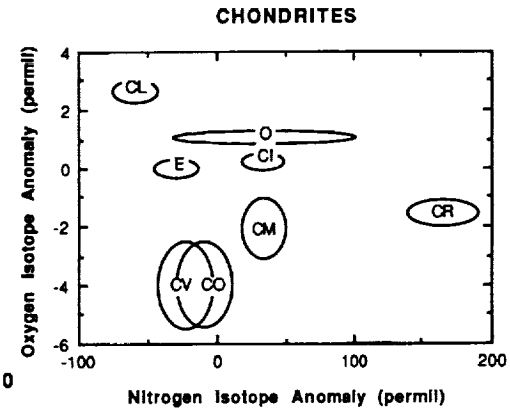

Fig.2

New Evidence for Compositional Diversity on the Marius Hills Plateau from *Galileo* Multi-Spectral Imaging. J. M. Sunshine[1], C. M. Pieters, and J. W. Head, Dept. of Geo. Sci., Brown University, Providence, RI, 02912. [1]Now at SETS Technology Inc., 300 Kahelu Ave., Mililani, HI, 96789.

Introduction The Marius Hills Plateau (MHP), located on the western lunar nearside in central Oceanus Procellarum, is the site of some of the most abundant and varied concentrations of volcanic features on the Moon [e.g. 1-2]. In addition to numerous volcanic features, a series of larger scale mare deposits are also exposed on MHP. Earth-based telescopic studies [3-4] have shown these MHP maria, like the surrounding plains of Oceanus Procellarum, to have relatively high ultra-violet (UV/VIS) ratios. Based on the empirical correlation with titanium content [5-7], these high UV/VIS mare deposits are inferred to be Ti-rich. However, regional stratigraphic studies [8] and relative crater ages [9], indicate that the high-Ti maria of MHP and nearby Oceanus Procellarum are younger than the high-Ti basalts sampled on the eastern nearside. Furthermore, Earth-based telescopic spectra also suggest that these western high-Ti mare are compositionally distinct from the well sampled Ti-rich basalts of the eastern nearside [10]. The recently acquired *Galileo* multi-spectral images, collected by the Solid State Imaging (SSI) camera at six wavelengths between 0.4 and 1.0 μm [11-12], provide an opportunity to re-assess the compositional variability within MHP. By combining the *Galileo* SSI images with a variety of pre-existing data sets, MHP is evaluated both in its regional context and in relationship to other well known Ti-rich volcanic units.

EM1 Results In previous studies [13], multi-spectral images from the first Earth-Moon encounter (EM1-12/90) were used to compare MHP to the surrounding deposits of Oceanus Procellarum. EM1 UV/VIS ratios (0.41/0.56μm and 0.41/0.76 μm) confirm Earth-based results and indicate that MHP has high UV/VIS ratios, comparable to nearby units. However, in 0.76/0.99 μm ratios, MHP is seen to be have distinctly lower values than the surrounding maria. Although at the limit of resolution, the EM1 data also suggest variability in the 0.76/0.99 μm ratio within MHP. Given the similarities in albedo and UV/VIS values, these differences in 0.76/0.99 μm ratios are attributed to a changes in the relative strength of the overall absorptions near 1.0 μm due to Fe^{+2} in mafic minerals and/or glass. As such, the low 0.76/0.99 μm signatures are interpreted as indications of relatively weak 1.0 μm absorptions.

EM2 Results Data from the second encounter (EM2-12/92) confirm that MHP has relatively low 0.76/0.99 μm signatures. In addition, the increased resolution and signal-to-noise of the EM2 data clearly indicate that MHP includes two types of 0.76/0.99 μm signatures: one suggesting relatively strong absorptions (comparable to the surrounding maria) and one suggesting relatively weak absorptions. Yet, even with the improvement over EM1 data, the EM2 data are not at sufficient resolution to allow for clear unit definition. Higher resolution *Lunar Orbiter (LO) IV* images are, however, available. To facilitate comparisons with the *Galileo* SSI data, *LO IV* images were digitized, processed to remove framlet boundaries, mosaiced, and coregistered with the *Galileo* images (as detailed in [14]). Analysis of the combined SSI/*LO* data reveal that the variability in the 0.76/0.99 μm images corresponds to regions on MHP which are larger in scale than any individual volcanic feature. Furthermore, there is a direct correlation between brightness in the *LO IV* images and 0.76/0.99 μm ratios. Using brightness boundaries in the *LO IV* mosaic (as mapped on **Figure 1**), two distinct MHP units are definable: (1) mhW, which is dark in *LO IV* images, has low 0.76/0.99 μm values, and high UV/VIS values, and (2) mhS, which is bright in *LO IV*, has high 0.76/0.99 μm values, and high UV/VIS values.

Spectral Comparisons Using all of the spectral information from EM2 and previous Earth-based telescopic data [3,15,16], the MHP units can now be directly compared to other high UV/VIS deposits. As shown in **Figure 2**, mhS has a relatively strong absorption approaching 1.0 μm and has similar spectral proprieties to nearby western high-Ti maria, as typified by the Flamsteed Basalt. In contrast, mhW has a relatively weak absorption towards 1.0 μm and has affinities to eastern high-Ti basalts, as represented by Apollo 11. In addition, as shown by the spectrum of Black Spot 5, certain dark mantle pyroclastic deposits also have similarities to mhW.

Discussion Synthesis of available data support three general compositional interpretations of the relative differences between the two units exposed on MHP. (1) mhW includes a pyroclastic component not present in

mhS. However, to be consistent with radar [17] and spectral observations, this pyroclastic component must be mixed with other materials and thus may represent finely disseminated pyroclastics mixed in the regolith. (2) mhS is typical of young western high-Ti basalts (e.g., Flamsteed), while mhW is similar in composition to the sampled eastern high-Ti basalts (e.g., Ap. 11). However, because mhW does not appear to be as old as the eastern basalts, the scenario suggests greater diversity in the compositions of Ti-rich basalts in both space and time. (3) Alternatively, mhW could represent a new type of mare basalt. Although data with greater spectral range and resolution, as well as higher spatial resolution, are required to distinguish among these possible scenarios, each suggests significant variations in volcanic activity and that MHP should remain a prime target for future research.

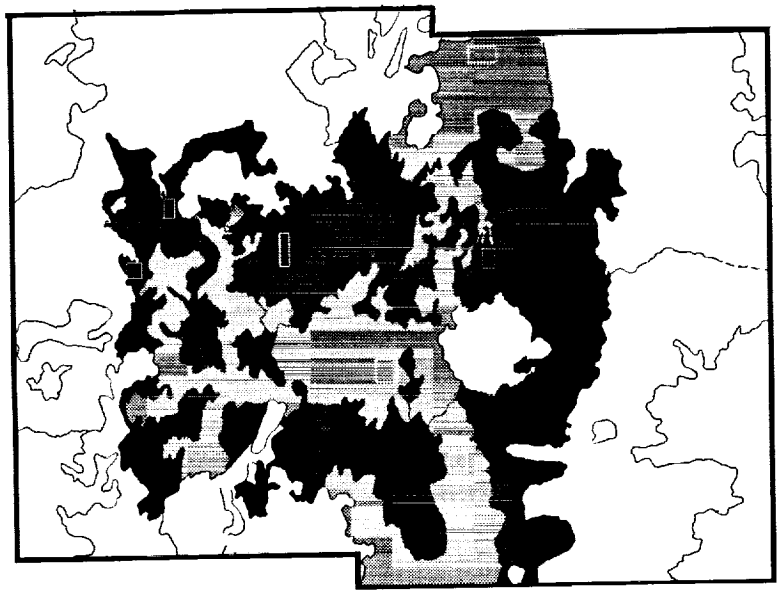

Figure 1: Sketch map of brightness units (dark, intermediate, and light) based on a digitized *LOIV* mosaic. Boxes are locations for spectra of the mhW and mhS units shown in Figure 2.

Figure 2: Comparison of Marius Hills spectra with other high UV/VIS units. The telescopic spectra have been convolved with the *Galileo* SSI filters. All spectra are normalized to 0.56 μm and shown relative to the MS2 standard area [7,15,16].

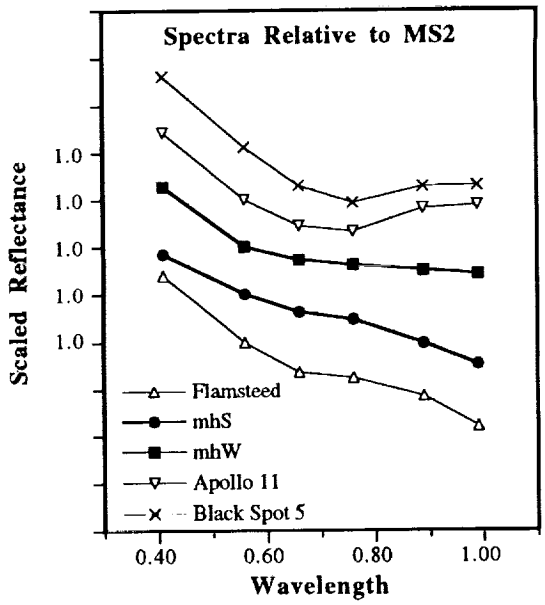

References:

[1] Whitford-Stark and Head, *PLSC 8th*, 2705-2724, 1977.
[2] McCauley, *USGS MAP I-491*, 1967.
[3] McCord *et al.*, *Moon*, **5**, 52-89,1972.
[4] Johnson, *et al.*, *PLSC 8th*, 1013-1028, 1977.
[5] Charette *et al.*, *JGR*, **79**, 1605-1614, 1974.
[6] Johnson, *et al.*, *JGR*, **18**,861-18,882, 1991.
[7] Pieters, *JGR*, **98**, 17,127-17,148, 1993.
[8] Whitford-Stark and Head, *JGR*, **85**, 6579-6609, 1980
[9] Boyce and Johnson, *PLSC 9th*, 3275-3284, 1978.
[10] Pieters, *PLPSC 9th*, 2825-2849, 1978.
[11] Belton *et al.*, *Science*, **255**, 570-576, 1992
[12] Belton, *Science*, in press, 1994.
[13] Sunshine *et al.*, *LPSC XXI* , 1387-1388, 1992.
[14] Sunshine *et al.* , *JGR*, in prep.
[15] Pieters and McCord, *PLSC 7th*, 2677-2690, 1976
[16] Pieters *et al.*, *JGR*, **78**, 5867-5875, 1973.
[17] Zisk *et al.*, *Moon*, **10**, 17-50, 1974.

Acknowledgments: Support for this research, a NASA Graduate Student Fellowship, NASA grants NAGW-28 and NAGW-713, and JPL contract JPL-958512 are greatly appreciated. Image processing facilities at Brown University were generously provided by a grant from the W. M. Keck Foundation.

MICROANALYSIS OF IRON OXIDATION STATES USING X-RAY ABSORPTION SPECTROSCOPY S. R. Sutton[1], S. Bajt[1], and J. S. Delaney[2]. [1]Dept. Geophys. Sci. and CARS, The Univ. of Chicago, Chicago, IL 60637; Dept. Applied Science, Brookhaven National Laboratory, Upton, NY 11973; [2]Dept. Geol. Sci., Rutgers Univ., New Brunswick, NJ 08903.

Abstract: Initial results are reported on a new microanalytic technique for determining $Fe^{3+}/\sum Fe$ in iron oxides and Fe-bearing silicates in conventional thin sections. The technique is based on the monotonic energy shift of a pre-edge peak in x-ray absorption near edge spectra obtained using the synchrotron x-ray microprobe. Reasonable results were obtained for pallasitic olivine, altered magnetites and synthetic wüstite.

Introduction: Oxygen fugacity is one of the most important parameters in determining the cosmochemical and geochemical evolution of a system. Petrogenetic models generally assume particular oxygen fugacities based on indirect evidence. Independent methods for the determination of oxygen fugacity have been unavailable. The oxidation states of minor and trace elements in specific phases can be used to directly probe oxygen fugacity, however, no microanalytical technique currently is available with this capability. We report here progress on development of synchrotron-based techniques to determine the oxidation states of 3d transition metals in individual mineral grains in conventional thin sections based on X-ray Near Edge Absorption Spectroscopy (XANES). This report focuses on the determination of $Fe^{3+}/\sum Fe$ in iron oxides and Fe-bearing silicates. The oxidation state of iron is of fundamental interest. Iron's ubiquity in rock-forming minerals means that it is frequently possible to study the chemical state of iron in a variety of co-existing minerals. Equally significant, iron-dominated phase relations are important chemical controls under the reducing conditions that exist in cosmochemical systems.

XANES Determination of Oxidation State: The basis of XANES is the mapping of the x-ray absorption cross section of the element of interest with high energy resolution. The precise energy of the main absorption edge and associated structural features provide information on the oxidation state(s) and bonding environment of that element [1-3]. A pre-edge peak in transition metal K-edge spectra is typically due to $1s \rightarrow 3d$, bound-state, electronic transitions. Previously, we have used the intensity of the pre-edge peak to infer $Cr^{6+}/\sum Cr$ in waste encapsulation media [4]. The present work is the first attempt to use the pre-edge peak energy to quantify the proportions of various oxidation states in mixed-valence samples. The basis of this technique is the derivation of an oxidation state versus pre-edge peak energy calibration curve using fayalite (Fe_2SiO_4; $Fe^{3+}/\sum Fe=0$), magnetite (Fe_3O_4; $Fe^{3+}/\sum Fe=0.67$), and hematite (Fe_2O_3; $Fe^{3+}/\sum Fe=1.0$). The main complication in this approach is decoupling energy shifts due to oxidation state from those due to coordination geometry. The expectation is that pre-edge peak energies will be determined largely by the former because the resonances involve bound state transitions and therefore molecular effects are minimized. However, one of the main purposes of this initial work on relatively well characterized specimens is to determine experimentally the magnitude of *matrix effects*.

Analytical Technique: The synchrotron x-ray fluorescence microprobe on beamline X26A at the National Synchrotron Light Source (NSLS) was used in its normal configuration (see e.g., [5]) including a Si (111) channel-cut monochromator (energy bandwidth $\Delta E/E=10^{-4}$) and x-ray focusing mirror (ellipsoidal 8:1). A focused monochromatic x-ray beam size of 100 μm x 150 μm was used in the present work. An ion chamber was located down stream of the slit assembly for incident beam intensity normalization. The detector was a Si(Li) energy dispersive instrument with an area of 30 mm^2 mounted at 90° to the incident beam (i.e., incident and takeoff angle at 45°).

XANES spectra were obtained by recording the Fe K_α fluorescence intensity as the incident monochromatic beam energy was scanned in 0.2 eV intervals over the range approximately -30 to +40 eV relative to the main absorption edge energy. Each energy interval

was counted between 3 and 5 live seconds for a total XANES spectrum acquisition time of ≤ 30 minutes. Counting times were adjusted to obtain at least 10^4 counts per pixel above the absorption edge. This resulted in about 10^3 counts at the maximum of the pre-edge peak (about 10^4 counts integrated peak area). Under these conditions, the minimum Fe concentration for which a useable Fe K XANES spectrum could be obtained was about 400 ppm. The energy of the pre-edge peak was defined to be the centroid of a Gaussian fit to the peak after background subtraction. All XANES energies were computed relative to the centroid of the pre-edge peak for a pure magnetite which had been characterized by the Mössbauer method.

Results: Four samples with well-defined Fe oxidation states by other methods (e.g., Mössbauer spectroscopy) were used to generate a calibration curve of "pre-edge peak energy" versus "$Fe^{3+}/\sum Fe$". These standards were: a pure hematite ($Fe^{3+}/\sum Fe$=1.0), two pure magnetites ($Fe^{3+}/\sum Fe$=0.67) and a synthetic fayalite ($Fe^{3+}/\sum Fe$=0.0). The resulting calibration curve (Figure 1) yielded a linear regression line with a correlation coefficient of 0.99 indicating that the pre-edge peak energy shift was monotonic. Several "unknowns" were also analyzed. Six altered magnetites gave reasonable results for $Fe^{3+}/\sum Fe$ based on the calibration curve: Mineville (0.75 ± 0.09), Snarum (0.78 ± 0.07), Sterling (0.83 ± 0.09), Elba (0.86 ± 0.09), Warwick (0.91 ± 0.07) and Monroe (0.95 ± 0.07). A fine-grained, synthetic pigment yielded a $Fe^{3+}/\sum Fe$ value of 0.68 ± 0.09, in exact agreement with the Mössbauer spectroscopy result. A pallasitic olivine gave $Fe^{3+}/\sum Fe$=0.02 ± 0.06. A synthetic wüstite sample ($Fe_{(1-x)}O$) yielded $Fe^{3+}/\sum Fe$= 0.18 ± 0.10 suggesting a reasonable value of x = 0.06. These initial results are encouraging particularly in terms of the apparent insensitivity of the pre-edge peak energy to bonding environment.

Acknowledgments: This research was supported by the following grants: NASA NAG9-106 and NAGW-3651 (SRS) and NAG9-304 (JSD), US DOE DE-FG02-92ER14244 (SRS) and DE-AC02-76CH00016 (BNL).

References: [1] Manceau A., et al. (1992) Amer. Mineral. 77: 1133-1143. [2] Sutton S. R., et al. (1993) Geochim. Cosmochim. Acta 57: 461-468. [3] Waychunas G. A., et al. (1983) Phys. Chem. Minerals 10: 1-9. [4] Bajt, S., et al. (1993) Anal. Chem. 65, 1800-1804. [5] Sutton, S. R., et al. (1993) Nucl. Instrum. Methods B75, 553-558.

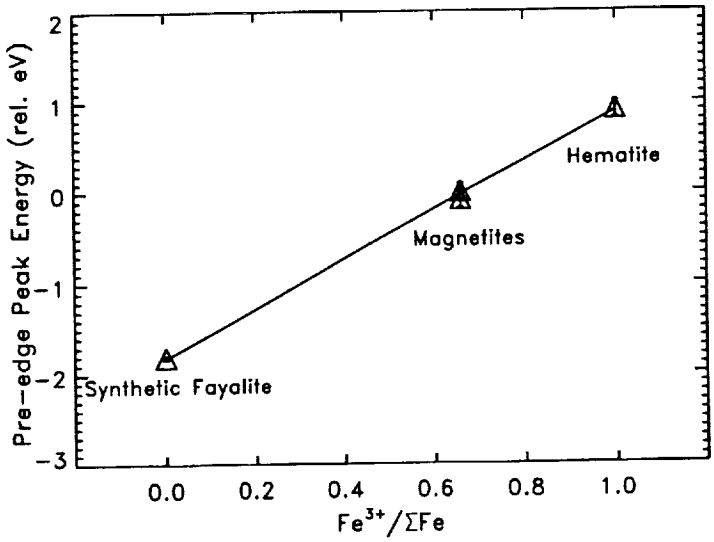

Figure 1: Plot of "pre-edge peak energy" vs "$Fe^{3+}/\sum Fe$" for well-characterized standards: a pure hematite ($Fe^{3+}/\sum Fe$=1.0), two pure magnetites ($Fe^{3+}/\sum Fe$=0.67) and a synthetic fayalite ($Fe^{3+}/\sum Fe$=0.0). The trend is linear with a correlation coefficient of 0.99.

BROWNLEE'S PARTICLES OF COSMIC ORIGINS IN DEEP SEA SEDIMENTS; Yoshimi Suzuki[1], Motosaku Noma[1], Hirohisa Sakurai[1], Kazuo Yamakoshi[2], Hiroyuki Matsuzaki[2], Naoki Kano[2], and Ken'ichi Nogami[3], [1]Dept. Physics, Yamagata Univ., Yamagata, [2]Inst. Cosmic Ray Research Univ., Tokyo 188, [3]Lab. Phys. Dokkyo Univ. School Medicine, Mibu, Shimotsuga-gun, Tochigi, Japan

Recently Several particles have been discovered among strongly magnetized grains gathered from deep sea sediments, whose compositions are muchsimilar to those of Brownlee's particles (stratospheric) of the category "C" in the Cosmic Dust Catalog compiled by CDPET of NASA. The used deep sea sediments were dredged by R/V Hakurei-Maru at off Hawaiian Isl-ands at a depth of 4500 m.

Suzuki et al.(1993) [1] have been searching extraterrestrial grains witha high sensitive x-ray microanalyzer among several hundred magnetc grains, whose sizes exceed 74 μm in the magnetic fraction. A picture ofthe samples is shown below;

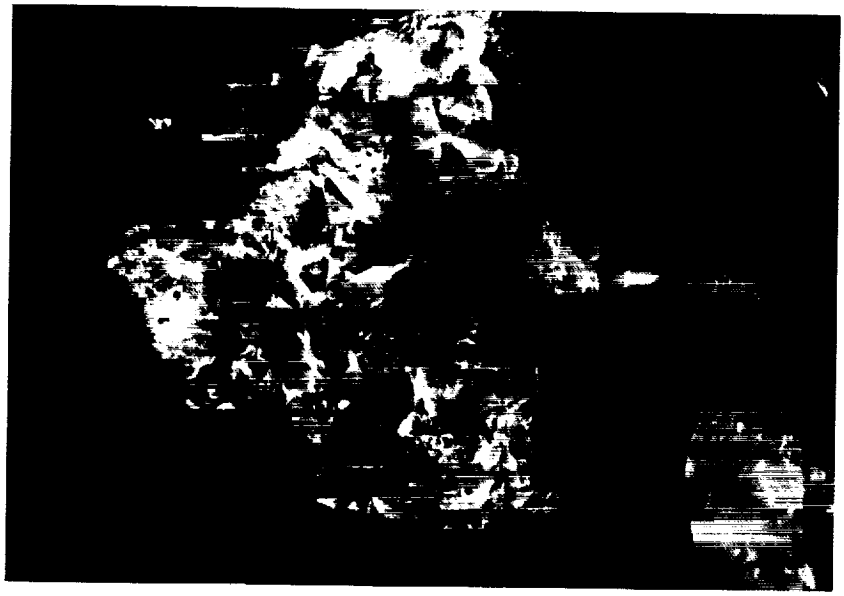

Fig.1 SEM(Scanning Electron Microscope) picture of a typical grain. The size is 100x90 μm.

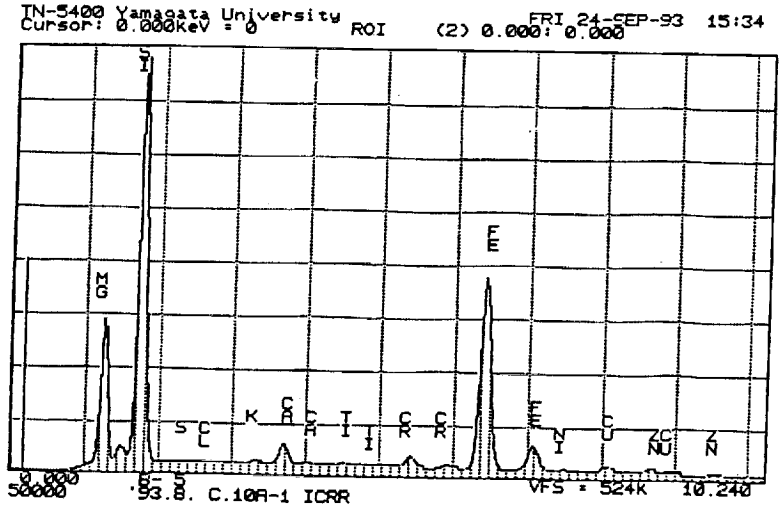

Fig.2 The diagram of the chemical composition of the grain shown in Fig.1. In the diagram Cu and Zn peaks are originated from base materials (brass) of the devices.

BROWNLEE'S PARTICLES IN DEEP SEA SEDIMENTS: SUZUKI Y.et al.

The samples were weighed with an electrobalance(Cahn #29, accuracy; 0.1 μm). Preliminary results of major chemical compositions of a few grains, whose data were obtained using a TEM device.
The results were averaged with the data of 10 point measurements overallthe sample. (% by weight)

Sample Code	Weight (μg)	(Si)	(Fe)	(Mg)	(Ca)	(Cr)	(Ti)	(Ni)	(Al)	(S)
#A	3.8	38.7	32.2	20.9	2.2	1.8	--	--	--	--
#C	6.7	4.0	75.1	0.7	0.7	--	0.9	5.7	1.4	11
#D	1.8	1.8	81.5	--	0.7	--	4.0	5.3	3.5	--

The rare and noble metals are much enriched and the measurements were performed by INAA using Allende powder as a reference.
The samples are so small that the statiatical errors($\pm$ σ) were not better than 50~60% .

Sample Code	(Ir)	(Pt)	(W)	(ppm by weight)
#A	--	103	45	
#C	2.4	--	--	
#D	43	72	--	

(Significant values of Au contents were obtained, however,it is possible, Au-pollution could happen in vacuum devices of SEM and XMA.)

Up to now, fragile, unmelted and thermally-ungenerated grains of comic origins have been discoverd in the stratosphere [2] and arctic ice layers [3,4]. In this work large-sized, unmelted grains could be discovered from deep sea sediments, so that it is expected, some fruitful comparisons between deep sea spherules and deep sea Brownlee's particles [5].

REFERENCES

1 Suzuki Y.et al.(1993) presented at the Fall Meeting of the Jap. Soc. Planet.Sci.
2 Compiled by CDPET of NASA; Cosmic Dust Catalog.
3 Maurette M.et al.(1991) Nature 351, 44.
4 Koeberl C. et al.(1992) LPSC XXIII 709.
5 Yamakoshi K.(1993) EXTRATERRESTRIAL DUST,Kluwer Acad. Publ.

RADIATION EMITTED DURING THE FLIGHT: APPLICATION TO ASSESSMENT OF BOLIDE PARAMETERS FROM THE SATELLITE RECORDED LIGHT FLASHES

Svetsov V.V. (Institute for Dynamics of Geospheres, Russian Academy of Sciences, 38 Leninskii Prospekt, build.6, Moscow, 117979, Russia)

Radiation plays a key role in the performance of bodies entering the atmosphere. At the certain altitudes the radiation flux is greater than the hydrodynamical energy flux, and the shock becomes supercritical [1]. In such a radiation dominated regime of flight the great portion of energy is emitted from the narrow temperature peak behind the shock wave, and the volume of preheated air is many times the volume of the meteoroid [2]. Stony bodies 1 to 10 meters in diameter can reach the altitudes of 20 - 40 km. In this case the radiation of the hot air in the shocked compressed region and in the wake constitutes the major portion of the whole light impulse. The previous 1D numerical computations of the thermal structure and optical luminosity of strong shock waves in air of reduced density [3] have shown that from 10 to 30 % of hydrodynamical energy flux can be emitted by the shock wave.

Calculations of the whole light impulse emitted during the flight offer a substantial challenge for 2D codes because the equations for radiation transport coupled with hydrodynamics should be solved on an adaptive mesh with different scales, which vary from millimeters in the spike at the shock front to meters in the thermal precursor and to hundreds of meters in the wake. Instead, I have developed a 1D approach using the gasdynamical analogy between the flight of an axially symmetric body and an action of an infinite cylindrical piston on gas [4]. Taking the piston's velocity and the work done by the piston equal to those of the meteoroid, one can gain a reasonable approximation to the flow pattern around the body and the more so in the wake. In this procedure, the piston radius at the end point matches the meteoroid size R. We have carried out a set of calculations for R=1 m and R=10 m in the range of velocities V from 10 to 50 km/s and the altitudes H from 20 to 50 km. The main portion of energy, released at a fixed point, is radiated within the time interval 0.01 - 0.05 s. A fraction of the emitted energy has been obtained as a function of R, V and H. The R and H dependencies of f prove to be not as strong as V dependence. For H=30 km and R=10 m f varies from 0.13 at V = 10 km/s to 0.43 at V = 50 km/s.

Using the derived dependence of f, one can estimate a light power during the flight as

$$P(t) = -MVf(R,H,V)dV/dt \qquad (1)$$

where M is the meteoroid's mass. This equation in combination with two equations of the single-body model of drag and ablation [5]:

$$MdV/dt = -C_d\rho(H)V^2\pi R^2 \qquad (2)$$

$$dM/dt = -C_h\rho(h)V^3\pi R^2/Q \qquad (3)$$

RADIATION EMITTED DURING THE FLIGHT: Svetsov V.V.

(C_d is the drag coefficient, C_h is the heat transfer coefficient and Q is the specific energy of vaporization) can give predictions of the meteoroid behavior in flight.

Recently, the light curves obtained via satellites equipped by optical sensors were demonstrated in [6] for the October 1 1990 event. The altitude of 30 km for the peak signal was detected by the companion locator. Using these data and assuming various initial velocities V and entry angles ϑ, I have solved Eqs. (1) to (3) for several values of C_h (from 0.01 to 0.1 [7]) to derive the initial energy and the time dependencies of M and R. Values of V = 30 km/s to V = 50 km/s and C_h = 0.1 lead to contradictions in the behavior of the meteoroid: R grew with time while the major portion of the body was burnt out due to thermal ablation. Moderate values of V from 15 to 20 km/s, being more justified, give the preentry kinetic energy from 3.8 to 5.8 ktons. These values depend only slightly on ϑ.

In Fig.1 predictions of V(H) are plotted for different initial values of V on the assumption that $\vartheta=\pi/4$ and C_h=0.03. In Fig.2 the effective radius of the body is shown as a function of H for V = 20 km/s and different C_h: 0.01 (solid lines), 0.03 (dashed lines) and 0.1 (dotted lines). The essential growth of the radius and effective cross section might be caused by fragmentation and subsequent lateral expansion of the meteoroid (see [8-10]).

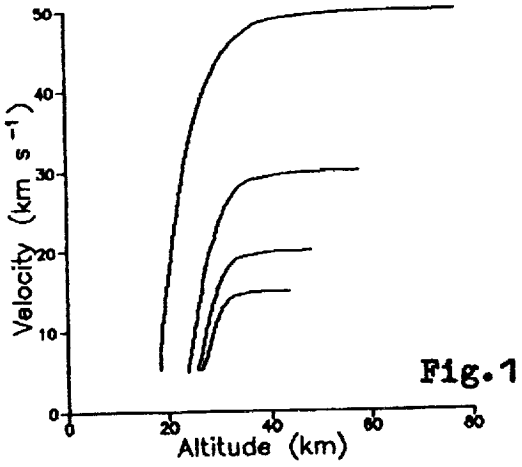

Fig.1

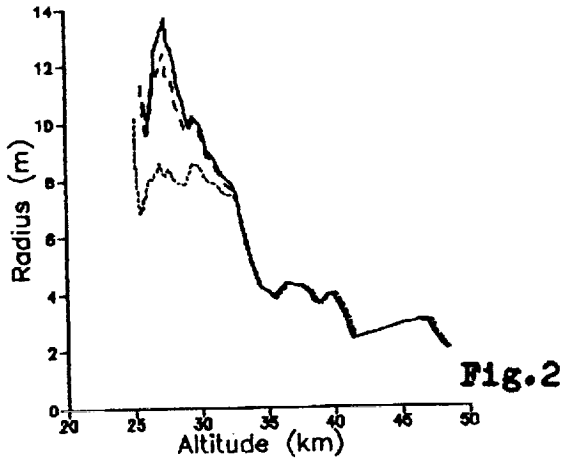

Fig.2

References: 1. Zel'dovtch,Ya.B. and Raizer,Yu.P. (1967) Physics of shock waves and high temperature hydrodynamic phenomena. Academic Press, NY. 2. Nemtchinov,I.V. and Popov,S.P.(1983) Sov. Phys. Doclady **269**, 578. 3. Nemtchinov et al. (1989) Prikl. Mech. Tehn. Fiz. No.1, 35. 4. Hayes,W.D. and Probstein,R.F. (1959) Hypersonic flow theory. 5. Bronsten,V.A.(1983) Physics of meteoric phenomena. D.Reidel, Dordrecht. 6. Reynolds,D.A. (1993) In Proc. Near-Earth-object interception workshop, Los Alamos, p.221. 7. Biberman,L.M. et al. (1980) Acta Astron. **7**, 53. 8. Melosh,H.J. (1989) Impact cratering: a geological process. Oxford Univ. Press, NY. 9. Hills,J.G. and Goda,M.P. (1993) Astron J. **105**, 1114. 10. Chyba,C.F. et al.(1993) Nature **361**, 40.

C1-5

THE THERMAL HISTORY OF THE LUNAR REGOLITH AT THE APOLLO 16 AND 17 SITES. S. J. Symes, P. H. Benoit, D. W. G. Sears, Cosmochemistry Group, University of Arkansas, Fayetteville, AR 72701 USA.

In order to explore the thermal history of the lunar regolith we have measured the induced thermoluminescence (TL) properties of samples from the Apollo cores 60009/10, 60013/14, and 70001-70009. We observe a decrease in TL sensitivity and an increase in TL peak temperature with increasing maturity as measured by magnetic, petrographic, and inert gas measurements. The decrease in TL sensitivity with increasing maturity reflects the conversion of crystalline feldspar to nonluminescent glass and the increase in TL peak temperature reflects the partial or complete disordering of the structural state of the feldspar. Similar TL properties are displayed by basaltic meteorites and chondrite regolith breccias. Our results are consistent with considerable variations in maturity of the soil in lunar cores obtained at the Apollo 16 and 17 sites and they provide a quantitative evaluation of the temperatures associated with regolith processing.

Introduction. The Moon's heavily cratered surface is one indication that planetary bodies have been subjected to a continuous bombardment by external objects ranging from small dust specks to large bodies tens of kilometers in diameter. Depending on the magnitude of the event, impacts can cause shock deformation, heating, melting, and even vaporization of the surface materials. The small scale evolution of the lunar surface is dominated primarily by small impactors which both develop and garden the lunar regolith. Lunar core samples provide the only means for studying variations in regolith properties with depth. Estimated regolith thicknesses are 4-5 m in mare regions and 10-15 m in the highlands while the longest core is ~3m (70001-70009), thus the available cores sample a significant fraction of the regolith.

Experimental. We measured the induced thermoluminescence (TL) properties of samples from the lunar cores 60009/10, 60013/14, and 70001-70009 using the techniques and apparatus described by ref. 1. The maximum intensity of the luminescence (*i.e.* the TL sensitivity) and the temperature at which this occurs (the TL peak temperature) were measured. The TL sensitivity is primarily related to the abundance of crystalline feldspar, which is the major TL phosphor in ordinary and carbonaceous chondrites [2,3], HED achondrites [1,4], and lunar meteorites [1,4]. The TL peak temperature is related to the structural state (specifically the degree of order) of feldspar. Since feldspar melts at about 1500°C, and the temperature related to the order-disorder transition for calcic feldspar is ~600-800°C [13], both TL sensitivity and TL peak temperature are strongly affected by thermal history.

Results and Discussion. Figure 1 shows our results with the data coded according to maturity as determined by ferromagnetic resonance (Is/FeO) [5,6,7] and agglutinate measurements [8] for regions of the core adjacent to the TL samples. As expected, the TL sensitivity decreases and the TL peak temperature increases with increasing maturity at both sites. Similar changes in TL properties with maturity are observed for ordinary chondrite regolith breccias [9]. The agreement between TL properties and other maturity indices is not exact (*e.g.* some of the samples considered "submature" on the basis of Is/FeO are "immature" in terms of TL peak temperature), but sample heterogeneity and genuine variations in maturity between samples would explain these small differences.

We also observe a factor of ~4-5 difference in the mean TL sensitivity of the regolith at the Apollo 16 and 17 sites. Both highland and mare material contain plagioclase feldspar, consisting mainly of anorthite and lesser amounts of albite. However, the proportion of feldspar in the highlands is greater than that in the maria, consistent with flotation of this relatively light mineral in a magma ocean. This is probably the major cause of the higher TL sensitivity at the Apollo 16 site. However, the higher albedo of feldspar-rich materials will increase the apparent TL sensitivity (due to multiple scattering of the light in the sample pan prior to detection [14]) and there may be differences in the trace element content of the feldspars which would contribute slightly to the TL sensitivity difference between the sites. The same TL sensitivity relationship between highlands and mare basalts is observed for whole-rock lunar samples [10], but the core samples have peak temperatures < 160°C while the whole-rock samples have peak temperatures > 160°C. This implies that the whole-rock samples are in general more mature than the soil and suggests that

forming soil from breccias is a less violent process than producing the rocks by the consolidation of soil [11].

The non-linearity in the data for the Apollo 16 core samples suggests that there are changes occurring during regolith processing which can be observed along the length of a single core, although it is not yet clear what is causing the non-linearity. Comminution tends to concentrate feldspar in the finest fractions [12] which might contribute to this effect because it would cause a small increase in the amount of feldspar in the more mature samples. Alternatively, since the non-linearity is observed only in Apollo 16 samples, it could be a compositional effect. Consistent with this, we have found a correlation between TL sensitivity and the amount of anorthositic component, as determined by mixing models, in our 60009/10 data but not in the Apollo 17 data.

Conclusion. We have found that the TL sensitivity decreases and TL peak temperatures increase with increasing regolith maturity. These changes reflect very different processes being experienced by the feldspar, namely, conversion to nonluminescent glass and structural disordering, respectively. The TL data confirm petrographic and magnetic data which indicate considerable variations in the degree of regolith maturity along the length of these lunar cores and they provide new insights to the temperatures involved during regolith processing.

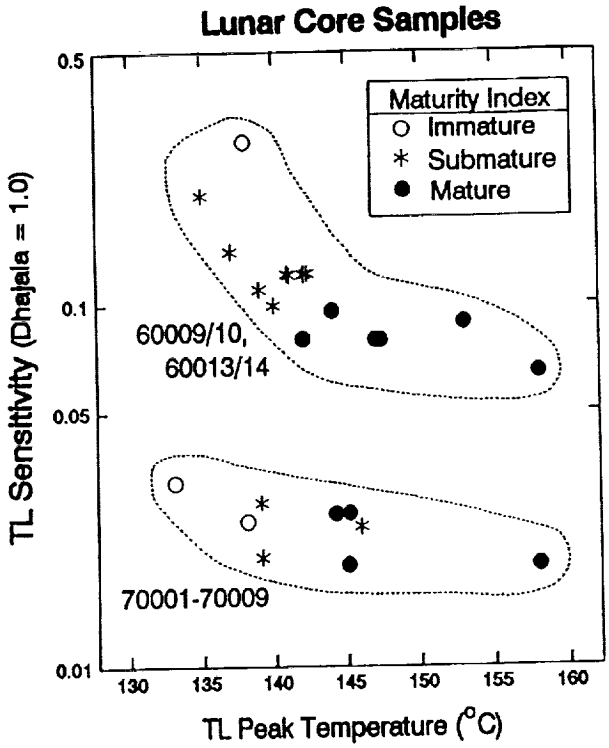

Fig. 1. Plot of TL sensitivity against TL peak temperature for lunar cores from the Apollo 16 and 17 sites with the data coded to indicate regolith maturity. With increasing maturity the TL sensitivity decreases as feldspar is destroyed and the TL peak temperature increases as feldspar is transformed to the disordered phase.

[1] Batchelor J. D. and Sears D. W. G. (1991) *Geochim. Cosmochim. Acta* **55**, 3831-3844. [2] Lalou C. *et al.* (1970) *C.R. Hebd. Seanc. Acad. Sci. (Paris) Serie D* **270**, 2401-2404. [3] Keck B. D., and Sears D. W. G. (1987) *Geochim. Cosmochim. Acta* **51**, 3013-3021. [4] Batchelor J. D. (1992) Unpublished Ph.D. Thesis, University of Arkansas. [5] Morris R. V. and Gose W. A. (1976) *Proc. Lunar Sci. Conf.* **7th**, 1-11. [6] Morris R. V. *et al.* (1979) *Proc. Lunar Planet. Sci. Conf.* **10th**, 1141-1157. [7] Morris R. V. and Lauer Jr. H. V. (1992) *Lunar Planet. Sci.* **23**, 935. [8] McKay D. S. *et al.* (1977) *Proc. Lunar Sci. Conf.* **8th**, 2929-2952. [9] Haq M. *et al.* (1989) *Geochim. Cosmochim. Acta* **53**, 1435-1440. [10] Symes S. *et al.* (1992) *Meteoritics* **27**, 294. [11] Benoit *et al.* (1994) *Lunar Planet. Sci.* **25** this volume. [12] Devine *et al.* (1982) *Proc. Lunar Planet. Sci. Conf. 13th*, in *J. Geophys. Res.* **87** A260-A268. [13] Hartmetz C. P. and Sears D. W. G. (1986) *Meteoritics*, **21** 388-389. [14] Sears D. W. G. (1980) *Icarus*, **44** 190-206.
This work supported by NASA grant NAGW-3519.

COMET SHOEMAKER-LEVY 9, IMPACT ON JUPITER - THE FIRST TEN MINUTES : Toshiko Takata, John D. O'Keefe, Thomas J. Ahrens, and Glenn S. Orton*, Division of Geological and Planetary Sciences, Caltech, Pasadena, CA 91125, * : Jet Propulsion Laboratory, Caltech, Pasadena, CA 91109

We have employed three-dimensional numerical simulations of the impact of Comet Shoemaker - Levy 9 (SL9) on Jupiter and the resulting vapor plume expansion using Smoothed Particle Hydrodynamics (SPH) method. An icy body with a diameter of 2 km can penetrate to an altitude of -350 km (0 km = 1 bar) and most of the incident kinetic energy is transffered to the atmosphere between -100 km to -250 km. This energy is converted to potential energy of the resulting gas plume. The unconfined plume expands vertically and rises a few tens of atmospheric scale heights in $\sim 10^2$ seconds. The rising plume reaches the altitude of $\sim$ 3000 km, however no atmospheric gas is accelerated to the escape velocity ($\sim$ 60 km/s) in our calculations.

Fragments of Comet, SL9 are predicted to impact Jupiter in July 1994 [1,2]. Observations of the Hubble Space Telescope indicates the maximum fragment size is $\sim$ 4 km, and approximately 10 fragments are $\sim$ 3 km [3]. The total energy released to the Jovian atmosphere upon impact of all of the comet fragments (CF's) will be 10^{29-31} erg.

We modeled the impact of CF's onto Jupiter and the resulting plume expansion using the Lagrangian method called Smoothed Particle Hydrodynamics (SPH) [4]. A tillotson equation of state for ice was used for the cometary materials [5] and an ideal gas with $\gamma = 1.4$ is employed for the atmosphere. We used the atmospheric structure observed by Voyager. This model atmosphere is extended adiabaticlly into the interior of Jupiter. We performed calculations for two sizes of CF's, 2 and 10 km in diameter with an impact velocity of 60 km/s and impact angle of 40° from the zenith. These sizes characterize the range of maximum sizes and energy of the Comet SL9 fragments as perceived since discovery [3,6,7,8].

As the CF penetrates the atmosphere, the gas in its wake expands as a cylindrical blast wave and the CF is flattened by drag forces [fig. 1]. The lateral spreading of the CF is constrained by the strong bow shock surrounding the comet and its cross sectional area approaches 2.3 times its initial value. The CF can penetrate to an altitude of -350 km ($\sim$ 200 bar), in the case of an initial diameter, D = 2 km and to the altitude of -550 km ($\sim$ 800 bar), in the case of D = 10 km. The energy transfer from the CF to the atmosphere occurs mostly in the altitude range from -100 km ($\sim$ 10 bar) to -250 km ($\sim$ 100 bar) in the case of D = 2 km and -350 km ($\sim$ 200 bar) to -480 km ($\sim$ 500 bar) in the case of D =10 km [fig. 2].

Next, we carried out the calculation of a plume expansion [fig. 3]. We distributed $\sim 10^5$ atmospheric particles in model atmospheric box of 550 km width extending from 350 to -400 km altitude in the case of the CF of D = 2 km. The energy density of deposition shown in figure 2 is placed on atmospheric particles along the trajectory. The fireball, whose temperature is reduced to $\sim 10^3$ K in $\sim 10^2$ seconds after the impact, can easily rise a few tens of atmospheric scale heights and the unconfined plume expands vertically rather than horizontally in an inhomogeneous atmosphere. Buoyancy forces result in the upward motion of the plume. Some 25% of the energy deposited in the deep atmosphere can be transported above 100 km in 10^2 seconds and most of the energy is brought up above 100 km in $\sim$ 200 seconds. The impact energy is ultimately released to space by thermal radiation. A mass of atmospheric gas equal to 10 times of the CF mass is transported from below the cloud deck to above 100 km in 10^2 seconds and a total of $\sim$ 20 times the initial CF mass is elevated above 100 km. The rising plume achieves an altitude of $\sim$

3000 km, however no atmospheric gas is accelerated to escape velocity in our calculations. The plume transport results in the vertical mixing of deep atmospheric constituents, such as, NH_3, H_2O, and CH_4, in addition to the vaporized cometary materials. Subsequent condensation of both deep atmospheric and cometary materials may be a source of dust condensates in the upper atmosphere.

The energy released by the impact and subsequent expanding plume can be observed by optical and infrared instruments on the Galileo space craft and the plume, upon rising to $\sim 10^3$ to $\sim 10^4$ km may be promptly observed with optical and infrared earth - based instruments before the impact point is in direct view of the earth.

Acknowledgements : All the calculations are carried out on the CRAY - YMP at JPL.

References : [1] Shoemaker C.S. et al.(1993) IAU Circ.,5725. [2] Yeomans D.K. & Chodas P. (1993) *Minor Planet Circ.*, 22197. [3] Weaver H.A. et al.(1993) *Bull. Am. Astron. Soc.*, 25, 1042. [4] Gingold R.A. & Monaghan J.J.(1977) *Month. Not. Astr. Soc.*, 181, 375. [5] O'Keefe J.D. & Ahrens T.J. (1982) *JGR*, 87, 6668. [6] Scotti J.V. & Melosh H.J, (1993) *Nature*, 365, 7333. [7] Chapman C.R. (1993) *Nature*, 363, 492. [8] Sekanina Z. et al. (1993) *submitted to Astron. J.*. [9] Bronshten V. A. (1983) *Physics of meteoric phenomena* 356 pp.

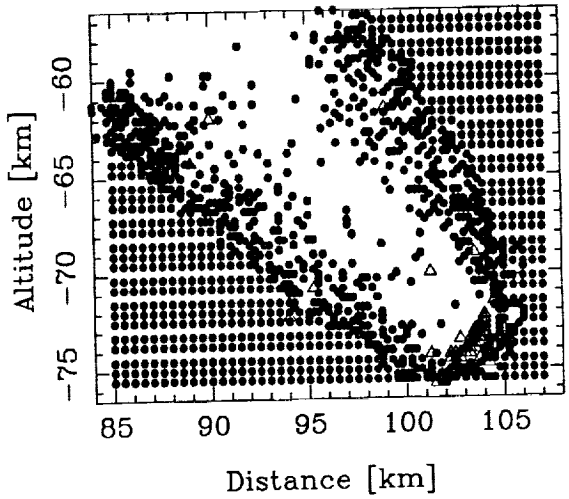

Figure 1. The position of particles at t = 2.6 s for the entry of the 2 km size - cometary fragment into the Jovian atmosphere. Triangles and circles represent cometary particles and atmospheric particles, respectively.

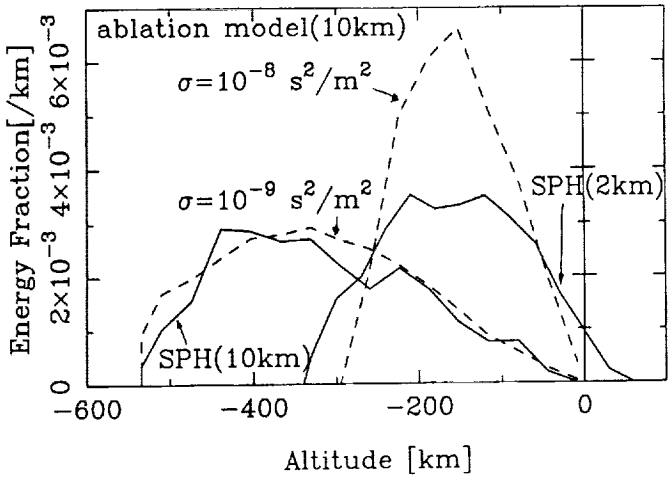

Figure 2. The fractional energy deposition of the initial kinetic energy of the comet as a function of altitude in the case of 2 and 10 km diameter - cometary fragments. The results of SPH calculation are shown by the solid lines, and the results of meteoric ablation model [9], with the ablation coefficients, σ, of 10^{-9} and $10^{-8}s^2/m^2$ for D = 10 km, are shown by dashed lines.

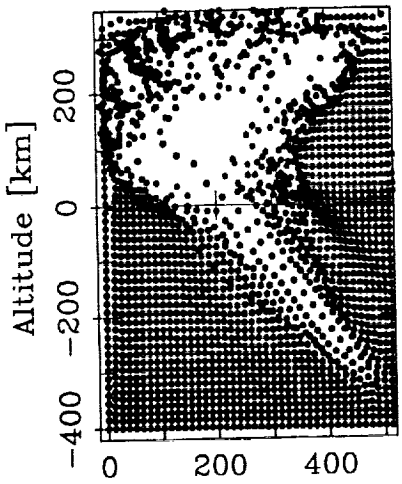

Figure 3. The position of atmospheric particles for the plume expansion of D = 2 km cometary fragment after 82.6 s.

ORTHOPYROXENE WITH DUSTY CORE AND CLEAR RIMS IN ACAPULCO AND ITS RELATED FORMATION PROCESSES TO LODRANITES; Hiroshi Takeda and M. Miyamoto, Mineralogical Institute, Faculty of Science, University of Tokyo, Hongo, Tokyo 113, Japan

Clear orthopyroxene crystals with a dusty core have been known for some lodranites and are taken as a record of melting and crystal growth during the formation of lodranite-acapulcoite meteorites. Similar orthopyroxene crystals 0.37 to 0.62 mm in length have been found in coarse-grained regions in Acapulco. Dusty inclusions are mostly FeNi metal with 5 wt % Ni and troilite. The sizes of the dusty cores are about an half of the crystal and are larger than those in lodronites (e.g. EET84302 and MAC88177). The CaO contents of the core (0.6-0.7 wt %) are lower than those of equilibrated ordinary chondrites. The chemical zoning profiles of CaO, Al_2O_3 and TiO_2 increase towards the clear mantle and slightly dicrease at the rims. The decrease of Fe/(Mg+Fe) indicates that reduction is involved during this process. A proposed formation scenario of such dusty grains suggests that parts of silicates may have been melted and grown around the unmelted cores during the formation of Acapulco.

Acapulcoites and lodranites are rocks consiting of equigranular aggregates of olivine + pyroxene + metal + troilite with or without plagioclase. As McCoy et al. [1] noted, acapulcoites experienced partial melting at the Fe-Ni-S eutectic, while lodranites were heated to somewhat higher temperatures and have experienced silicate partial melting. Acapulco is a representative meteorite of acapulcoites and was studied extensively by Palme et al. [2], who noticed that chromites are somewhat enriched. Because chromite segregation was found in a lodranite closest to acapulcoites (EET84302), we studied Acapulco to find lodranite-like features in it by mineralogical techniques. The CaO contents of orthopyroxene in lodranites (Y74357 and MAC88177) decrease gradually toward the rim, as do the Cr_2O_3, Al_2O_3, TiO_2, and Na_2O in orthopyroxene and augite [3]. These results suggest that interstitial melt was present and was then extracted at a late stage in the formation of these meteorites [3].

A polished thin section (PTS) of Acapulco was prepared from a chip from the Planetary Materials Database Collection of Univ. of Tokyo. The zoning was measured along profiles selected on the basis of back-scattered electron images, and by making spot analyses at every few micrometers from core to rim. The acceleration voltage was 15 kV and the beam current was 24 nA on a Faraday cage. Eleven major elements were analyzed (Si, Mg, Fe, Ca, Na, K, Mn, Al, Ti, Cr, and Ni). Counting times at peak wavelengths were 40 s and the background intensity of each element was counted on both sides of the peak wavelenght.

The dusty cores were found in orthopyroxene crystals in the coarse-grained regions of Acapulco. The metal grains around these regions have rounded shapes along the silicate grain boundaries. Some opaque grains consist of metal, troilite and chromite with clear boundaries as found in EET84302 [4]. The chemical zoning profiles of representative orthopyroxene crystals are given in Fig. 1 for CaO, Al_2O_3, Cr_2O_3 and Fe/(Mg+Fe).

The presence of dusty cores in the mafic silicates of lodranites is similar to that in the partly shock-melted, recrystallized diogenites (e.g. Y74013) [5]. This fact suggests that shock partial melting is responsible for recrystallization, and that total melting did not occur [4]. McCoy et al. [1] suggested that partial melting did not result from local shock

melting. The dusty grains are troilite and metal with 5 wt % Ni. They may have deposited in the remnants of the shocked source materials, which contain low CaO. The clear mantle with high CaO contents may have crystallized from partial melt with high CaO contents. The slight decrease of CaO at the rim may indicate minor loss of the partial melt at the late stage of crystallization. Another scenario with an event taken place in the solid state cannot be ruled out, but is less likely. The finding of such dusty cores in orthopyroxene suggest that lodranites and acapulcoites are not much different in their formation processes, and represent materials from nearby parts of the same body with different degree of migration of partial melts.

We thank the Planetary Materials Database Collection for the sample and Mr. A. Yamaguchi for making the Acapulco PTS. We are indebted to Mr. T. J. McCoy and J. G. Taylor for discussion and Mrs. M. Otsuki for technical assistance.

References: [1] McCoy T. J. et al. (1993) LPSC XXIV 945-946. [2] Palme H. (1981) Geochim. Cosmochim. Acta 45, 727-752. [3] Miyamoto M. and Takeda H. (1994) JGR Planets, in press. [4] Takeda H. et al. (1992) Proc. Japan Academy 68, Ser B, 115-120. [5] Takeda H. et al. (1981) Mem. Natnl. Inst. Polar Res., Spec. Issue 20, 81-89.

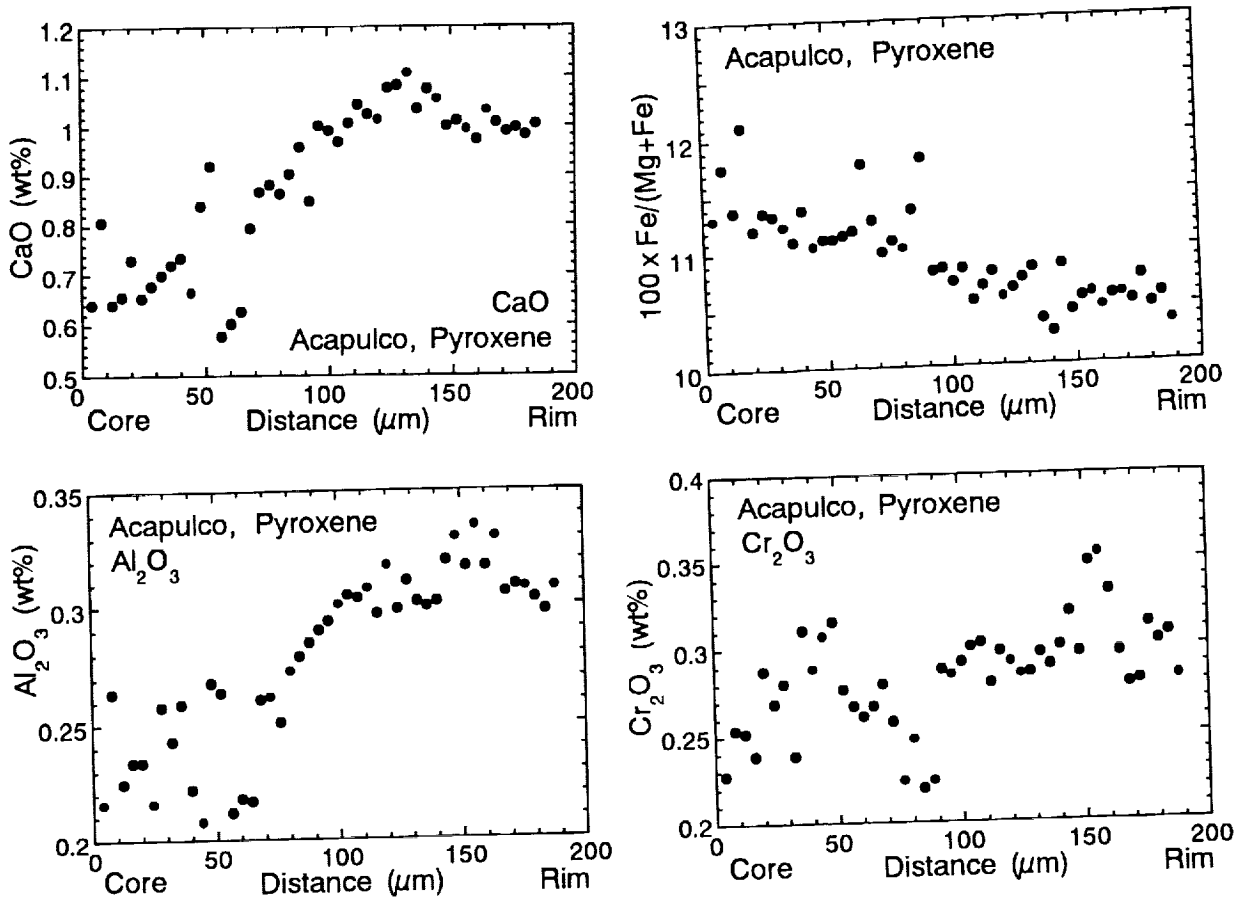

Fig. 1. Representative elemental distribution profiles of CaO, Al_2O_3, Cr_2O_3 and Fe/(Mg+Fe) of orthopyroxene crystals in Acapulco. The wt % of each oxide are protted along the distance from core to rim. Fe/(Fe+Mg) Mol ratios show reduction. Cr_2O_3 wt % do not show increase at the rim.

MINERALOGY OF APOLLO 12 LOW-Ti BASALTS IN RELATION TO LUNAR METEORITES FROM MARE REGION; Hiroshi Takeda, Tomoko Arai and K. Saiki, Mineralogical Inst., Faculty of Science, Univ. of Tokyo, Hongo, Tokyo 113, Japan.

In order to characterize mineralogically a possible new type of low-Ti mare basalts in the Antarctic lunar meteorites, which were formerly classified as VLT basalts, we investigated two low-Ti basalts in the Apollo samples, 12064 and 12031 by mineralogical techniques including chemical mapping analysis utilities (CMA) of SEM and EPMA. The pyroxene chemical zoning trends of an oriented pyroxene crystal along nearly the c-axis of 12064 showed a trend intermediate between the Apollo 12 pigeonite basalts and low-Ti lunar meteorite, Y793169. The spinel chemical variations of chromite-ulvöspinel in 12064 are within one spinel crystal produced during the crystal growth, whereas those of Y793169 and A881757 (YA meteorites) are from grain to grain variations. The Ti/(Ti+Cr) versus Fe/(Mg+Fe) Mol ratios for the 12064 pyroxenes are distinct from the YA meteorites and support the proposal that they represent a new low-Ti type.

Consortium studies of the YA meteorites have indicated that they are intermediate between VLT and low-Ti mare basalts [1,2]. They appear to represent a new type of low-Ti mare basalt that crystallized at about 3.9 Ga [3]. Y793169 contains considerable amounts of Ti-bearing oxides in the mesostasis area. The chemical variations of these phases are not in the same trends as in the low-Ti pigeonite basalts of Apollo 12 and 15 in spite of its higher TiO_2 contents [4]. Rock 12064 has been found to be closest to this basalt in the grain size and mineral assemblages [4,5].

We investigated polished thin sections (PTS) 12031,21 and 12064,9 to compare them with Y793169,51-3 and A881757,51-4 supplied by the National Inst. of Polar Res. (NIPR) for the consortium studies. 12031 is a pigeonite basalt but has not been studied, because it was kept for future studies during the Apollo mission [6]. Mineral chemistries and textures were examined by an electron probe microanalyzer (EPMA) and scanning electron microscope (SEM), JEOL 840A with X-ray CMA utilities. We measured zoning profiles selected on color maps produced by the PXQUD system of Saiki [7].

The 12031,21 PTS consists of one large single crystal 5.2X1.8 mm in size and small aggregates of plagioclase, ilmenite, troilite, a silica mineral are attached. The pyroxene crystal includes small grains of chromite and Fe metal. The CMA data showed that 12031 is a pigeonite basalt inermediate between 12021 and 12037 [4]. Rock 12064 is a ilmenite basalt with a microgabbro texture. Mineralogy and petrography have been reported by Klein et al. [5]. Modal abundances of minerals of 12064 is pyroxene 57 %, plagioclase 33 %, opaques 7 % [4], which are nearly equal to Y793169 with pyx. 56 vol. %, plag. 42 %, ilmenite 1 %, ulvöspinel 1 % etc.

Rock 12064 shows texture and pyroxene chemical zoning trends comparable to those of Y793169. The zoning trend of 12064 was examined on a partly oriented crystal which has an hour glass texture. The trend along the c-axis (Fig. 1, left) is one found in Y793169 [2], and the trend parpendicular to c is similar to those of the pigeonite basalts such as 12031. The Ti/ (Ti+Cr) versus Fe/(Fe+Mg) trend of the 12064 pyroxene is distinct from those of the YA meteorite pyroxenes (Fig. 2). Chemical variations of ulvöspinel and chromite in 12064 are compared with the YA meteorite spinels in Fig. 3. The Ti/(Ti+Cr+Al) versus Fe/(Fe+Mg) variation (Fig. 3) of 12064 represents the core to rim variation but is similar to

LOW-Ti BASALTS IN RELATION TO LUNAR MARE METEORITES: Takeda H. et al.

Y793169. The trend of Y793169 is grain-to-grain variation representing only very last stage of the local differentiation of the mare basalt.

It is to be noted that the YA meteorites show resemblance to 12064, but others are distinct. The variation may represent differece in the condition during crystal growth process and their bulk chemistries. The precipitation of Ti-bearing phases in Y793169 took place at the last stage of the small-scale differentiation. Comparisons of 12064 and 12031 with those of the YA meteorotes support the previous conclusions [1] that the YA meteorites represent a new type of low-Ti basalts not known in the Apollo samples.

We thank NASA and NIPR for the samples, and to Drs. M. Lindsrom, P. H. Warren, and K. Yanai for discussion, and T. Ishii, E. Yoshida, O. Tachikawa, K. Hashimoto, M. Ohtsuki and M. Hatano for their technical assistances.

REFERENCES: [1] Yanai K. et al. (1993) LPSC XXIV 1555-1556. [2] Takeda H. et al. (1991) Proc. NIPR Symp. Antarct. Meteorites 6, 3-11. [3] Misawa K. et al. (1992) ibid, 5, 3-22. [4] Pipike J. et al. (1976) Rev. Geophys. Space Phys. 14, 475-540. [5] Klein C. Jr (1971) Proc. Lunar Planet. Sci. 2nd, 265-284. [6] Takeda et al. (1975) Proc. Lunar Sci. Conf. 6th, 987-996. [7] Saiki K. et al. (1992) Lunar Planet. Sci. XXIII 1201-1202.

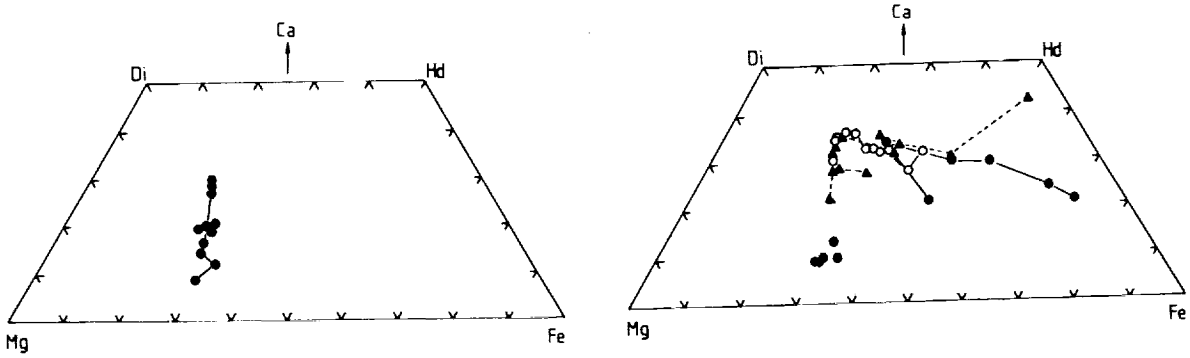

Fig. 1. Pyroxene quadrilaterals of 12064. Left: traverse parallel to the c-axis. Right: perpendicular to c; open circles: trends at the center of the hour glass texture; solid circles: open ends; and triangles: middle.

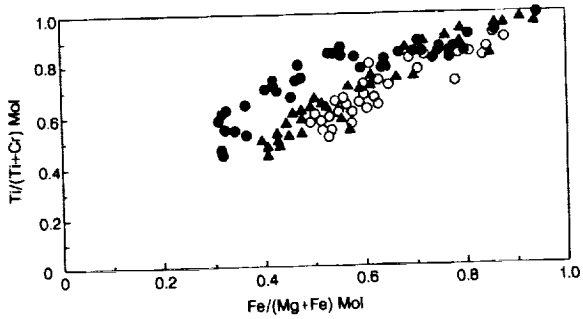

Fig. 2. Ti/(Ti+Cr) vs. Fe/(Fe+Mg) Mol. ratios for pyroxenes in 12064,9 (solid circles), Y793169 (solid triangles), and A881757 (open circles).

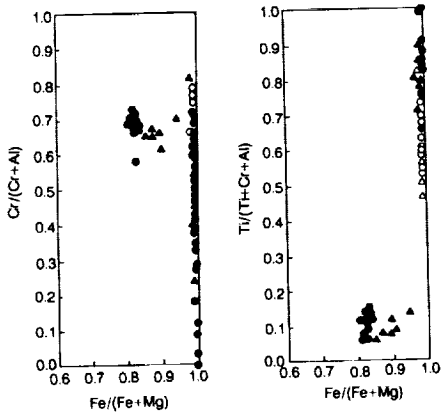

Fig. 3. Ti/Ti+Al+Cr and Cr/(Cr+Al) vs. Fe/(Fe+Mg) diagrams for ulvöspinel-chromite from mare basalt, 12064,9 (solid circles), Y793169 (solid triangles) A881757 (open circles)

P. 2

INHOMOGENEOUS DISTRIBUTION OF MATERIALS IN LODRANITES-ACAPULCOITES AND IAB IRONS AND THEIR COMMON FORMATION PROCESSES; Hiroshi Takeda, Mayumi Otsuki, A. Yamaguchi, M. Miyamoto, Mineralogical. Inst., Faculty of Science, Univ. of Tokyo, Hongo, Tokyo 113, Masayuki Otsuki, JEOL Ltd. 3-1-2 Musashino, Akishima, Tokyo 196 and M. Tomobuchi, Kawasho Hightex Co., Ltd. 2-1-13 Higashiueno, Taito-ku, Tokyo 110, Japan and Takahiro Hiroi, SN3, NASA Johnson Space Center, Houston, Texas 77058.

Two dimensional chemical mapping analysis (CMA) techniques of EPMA and XRF have been applied to a new polished thin section (PTS) of EET84302,28, Acapulco and a 5x3 cm slice of Caddo County to find heterogeneous regional distribution of low temperature fractions in the lodranite-acapulcoite groups and silicate inclusions in the IAB irons. A region richer in metal-plagioclase were found in EET84302,28 and Caddo County. Mineralogy of EET84302,28 is not much different from coarse-grained metal-rich acapulcoite-like mineral assembrage in EET84302,19, which has chromite -orthopyroxene segregation. Nearly uniform Mg/Fe ratios of silicates modified by reduction at regional oxygen fugacity and large difference in modal abundances of minerals in this meteorite group can be explained by regional concentration of materials when the souce materials were partly melted.

Segregation of chromites and metal-silicates has been found in lodranite EET84302,19 [1] and of mafic silicates and plagioclase-augite-metal in IAB iron, Caddo Co. [2]. In order to find distribution of materials in a larger area than that of PTSs, a large sample of Caddo Co. and a new PTS of EET84302 (,28) and Acapulco have been studied by mineralogical techniques including CMA techniques of electron probe microanalysis (EPMA) and microbeam X-ray fluorescent (XRF) analysis.

PTS of EET84302,28 has been supplied from Meteorite Working Group (MWG). This PTS is similar to a part of the previously studied PTS of EET84302 in both texture and mineralogy [3]. Samples of Acapulco and Caddo Co. is from the Planetary Materials Database Collection of Univ. of Tokyo. We have studied PTS EET84302,28 by JEOL Electron Probe Microanalyzer JXA 8900 and scanning electron microscope (SEM) 840A. The CMAs of EET84302,19 and ,28 were performed by JEOL EPMA for 600X1024 points with 8 μm intervals for Si, Mg, Al, Fe, Ca, Ti, Na, Mn, Cr, Ni, S, and P at 15 kV 10.6 nA. Elemental distribution maps of Caddo Co. (5x3 cm) was measured by Kevex Omicron XRF Unit equipped with EDS and microfocus X-ray tube. Concentration of Fe, Ca, Ni, Co, Cr, Mn, and S were measured by XRF with 100 μm collimator, Mo radiation at 40 kV, 0.8 mA in air and those of Mg, Ca, Al, Si with 2 mm collimator at 4.5 kV, 1.0 mA in vacuum and scanned 3 times on an uncoated cut surface.

The CMA of EET84302,28 (e.g. Fig. 1) showed that it consists of abundant metal filling interstices of silicate grains of orthopyroxene (Opx), olivine Fa_8, plagioclase(Plag.) An_{24}, and augite (Aug), but no chromite has been detected. Modal abundances of minerals are: Opx 38.4 %, olivine 18.5 %, Plag. 12.6 %, Aug 0.8 %, FeNi metal 26.8 %, (FeNi oxides 2.1 %), schreibersite 0.7 %, and troilite 0.1 %. EET84302,19 is richer in chromite (17 %) and its grains are interconnected to form a domain of chromitite with rounded inclusions of silicates (Opx 50.7 %). Another area is similar to EET84302,28. Modal abundances of minerals in the metal-rich region of EET84302,19 (Opx 31 vol.%, olivine 21 %, plagioclase 16 %, Aug 1.3 %, metal 22 % and Fe oxides 9 % etc. for 2 mm area in diameter) are similar to PTS

,28, which is enriched in metal and plagioclase (Fig. 1) and depleted in chromite. A large poikilitic olivine (2 mm) with small plagiocalse inclusions are present. An amoeboidal grain of metal-troilite-chromite assemblage as was found in EET84302,19 [1] was detected in Acapulco.

The CMA of 5x3 cm slice of Caddo Co. confirmed the presence of the plagioclase(Al)-rich or augite(Ca)-rich regions [2] in cm scale (Fig. 2). Mafic silicate-rich area as studied by Plame et al. [4] are also found. However, we have to admit that silicate inclusions in the IAB group have different oxygen isotopic abundances from those of lodranites-acapulcoites [5]. Lodranite-like meteorites in mineralogy and bulk chemistry are missing in the winonaite-IAB group and those of Caddo Co. have not been found in the acapulcoites-lodranites group. Although two groups may represent meteorites from two different S asteroids, there may be common processes to form such meteorites from similar source materials. Our fingings suggest that large variation in modal abundance of minerlas with their small compositional ranges in these groups of meteorites may stem from segregation of partial melts and the residues in different regions within two parent bodies in a scale of cm to more than m. The heterogeneous distribution of materials is in line with our proposed model of S asteroids [6].

We thank MWG for the meteorite samples. Drs. H. Ozawa, T. J. McCoy, and Profs. K. Keil and J. G. Taylor for discussions and Mr. H. Yoshida, O. Tachikawa, Mrs. K. Hashimoto and M. Hatano for technical assistance.

REFERENCES: [1] Takeda H. et al. (1992) Proc. Japan Academy, 68, Ser B, 115-120. [2] Takeda et al. (1993) Meteoritics 28, 447. [3] Mason B. (1986) Antarctic Meteorite Newsletter, 9, No.3, p. 18. [4] Palme H. et al. (1991) LPSC XXII, 1015-1016. [5] Clayton R. N. et al. (1992) LPSC XXIII, 231-232. [6] Hiroi T. et al. (1993) Icarus, 102, 107-116.

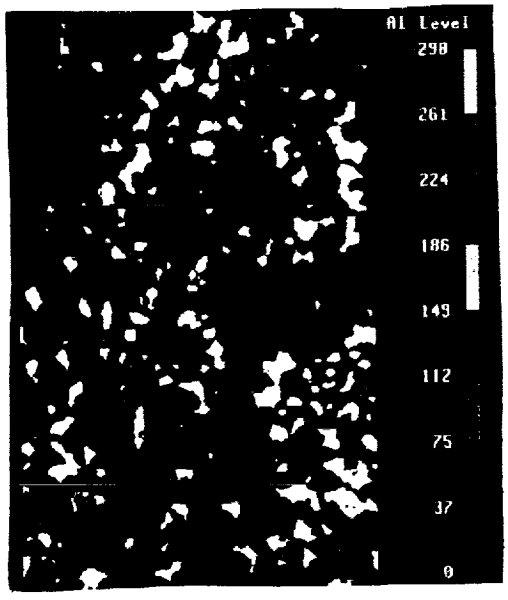

Fig. 1. Example of B&W image of the colored CMA map EET84302,28 for Al. Hight is 8.1 mm. Note appreciable amounts of plagioclase.

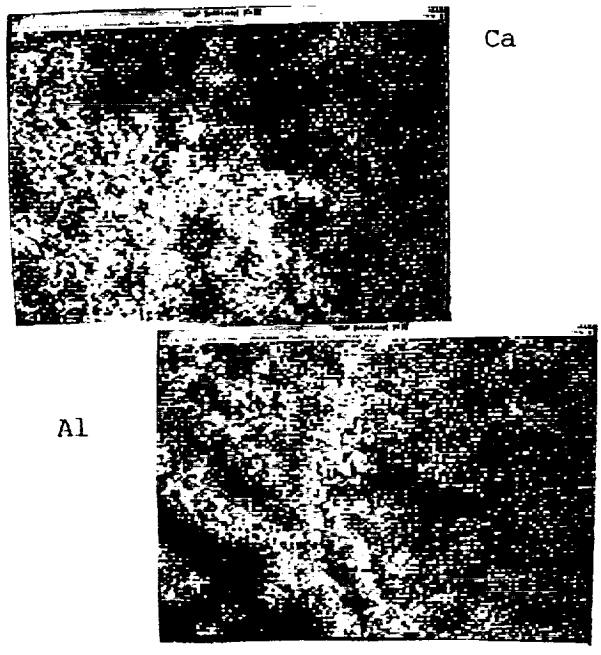

Fig. 2. Examples of B&W images of the CMA maps of Ca and Al by microfocus XRF. Width is 4 cm.

omit to p.1389

STRAIN MEASUREMENTS OF IMPACT CRATERS ON TEMPE TERRA, MARS; **Kenneth L. Tanaka**[1] and **Matthew P. Golombek**[2]; [1]U.S. Geological Survey, Flagstaff AZ 86001; [2]Jet Propulsion Laboratory, Caltech, Pasadena, CA 91109

Introduction. Tempe Terra has undergone several episodes of tectonic deformation, dominated by NW-SE extension along NE-trending grabens and E to NE compression along N- to NW-trending wrinkle ridges [1, 2]. Rough estimates of NW extensional strain range from 8 to 50 km, based on simple approaches [3, 4]. A more comprehensive study using measured slope widths of grabens indicates a total extension of about 17.6±13.4 km, or an average strain of 1.8±1.3% given the 1,000 km average width of Tempe Terra [5]. In agreement with [5], the elongations of 91 impact craters on Tempe Terra yield an average extensional strain of 1.9±1.2%. The elongated craters are crossed by about 400 normal faults and wrinkle ridges, yielding an average of about 100 m of strain per structure, similar to results, based on photoclinometric measurements of grabens and wrinkle ridges, for these feature types in other Martian areas.

Methods and approach. Measurement of crater elongation is a simple task in itself. However, very different results and interpretations of strain can be obtained, depending upon the approach, technique, and assumptions that are used in choosing and measuring craters. In addition, impacts may have formed noncircular craters, or erosional processes may have given them elliptical or irregular shapes [see 4].

To obtain a reasonable estimate of the extensional strain across Tempe Terra from measurements of crater elongations, we used the following methods and approach in this study: (1) to attempt to limit our sample to Noachian-age craters, all large, degraded craters lacking well-preserved ejecta were used to provide the largest possible sample of craters that predated much of the structural deformation; (2) the Mars Digital Image Mosaic (MDIM), displayed on a computer video terminal, was used to ensure consistent projection and resolution of the database (231 m/pixel); a few craters on image boundaries were not measured; (3) fault scarps that cut the crater rims were noted (because of crater fill, not all scarps can be seen to cut the crater floor); (4) wrinkle ridges that deform crater floors were counted (these positive-relief features are generally well exposed); and (5) shortened craters were assigned negative values.

Results. First, we attempted to measure the inherent uncertainty in our crater-strain measurements by determining the statistical elongation of ten craters in the sample set that show no observable signs of tectonic deformation. As expected, their average elongation is near zero (<0.1%). However, the standard deviation of the elongation is 4.7% and the maximum value is 7%. For absolute values of crater strain, the mean and standard deviation is 3.7±2.7%.

Next we analyzed the relation between observed structural deformation and measured crater elongation. Overall, 336 normal faults, most of which bound grabens, and 56 wrinkle ridges were observed to cut across the rims or floors of craters. Figure 1 plots the amount of extension vs. the number of crosscutting structures for each crater. Despite a large uncertainty for each individual measurement of crater elongation (which accounts for the poor correlation in Fig. 1), the least-squares fit line shows generally increasing deformation as a function of number of structures. The overall *average* amount of deformation per fault or wrinkle ridge is about 100 m. This average value is imprecise because of uncertainties in crater elongations and crosscutting observations, but it is likely accurate within a factor of two.

Finally, we estimated regional strain to be 1.9±1.2%. This strain value is an average of individual measurements weighted by crater diameter (measured strain multiplied by original crater diameter and divided by average original crater diameter for the entire sample set). Thus larger craters, which cross more terrain, have correspondingly greater weight in the results. The error given is the 95% confidence interval of the mean.

Discussion and interpretation. Our first result indicates that individual measurements of crater elongation have a high uncertainty due to nontectonic ellipticity acquired during impact or by later modification. This restricts the application of the method for strain purposes to broad statistical inferences; precise, local evaluations are not possible. For our study, we note a sampling bias to areas of older terrain, which preserve a higher density of large Noachian craters. Also,

TEMPE TERRA, MARS: **Tanaka K.L. and Golombek M.P.**

extension is concentrated along the Tempe rifts, which cut across the center of the plateau. Thus the accuracy of our overall strain estimate rests largely on both the degree of spatial randomness and the number of craters in the dataset.

Overall estimated extension across Tempe Terra, whose extended width is 1,000 km, is 19±12 km. This value is much lower than the 50 km of extension (across 500 km) and the 9.8% strain value estimated from the measurement of 13 elongate craters by [4]. In addition to the smaller size of their sample set (which included only craters elongated in the proper direction), other factors also appear to account for the discrepancy, as is seen from our remeasurement of these craters. We measured nine of their craters and obtained significantly less elongation for most of the measurements; the average strain of nine of the craters is 4.1%. (Four of the craters could not be remeasured, because one could not be positively located, two are on MDIM boundaries, and one is missing part of its rim in a critical location.) The reason for the discrepancies with measurements in [4] are unknown.

Our overall results coincide, within reasonable limits of statistical precision, with estimates produced from measurements of fault-scarp widths across Tempe Terra [5], which are assumed to mimic typical scarp geometries associated with grabens in other parts of the Tharsis region [6-8]. Mean extension per narrow graben (each made up of *two* normal faults) and its standard deviation has been estimated at 101±83 m (or about 50 m per normal fault) [9]. In addition, the Tempe rifts are bordered by major normal faults having much higher amounts of extension [5], which would increase the overall average value per fault. Shortening produced by wrinkle ridges in Lunae Planum and Arcadia Planitia has been modeled from photoclinometric data; average strain values per wrinkle ridge in the two regions are 131 m and 57±40 m, respectively [10, 11].

Our examination of crater-elongation measurements shows that they cannot be used for precise strain estimates due to the overshadowing effects of nontectonic vs. tectonic crater elongation and the dependence of meaningful strain estimates on crater distribution. On the other hand, overall crater-strain estimates of Tempe Terra form an independent approach that appears to affirm the methodologies used to obtain more direct strain estimates based on measured dimensions of grabens and wrinkle ridges.

References cited: [1] Scott, D.H., and Tanaka, K.L., 1986, *USGS Map I-1802-A.* [2] Scott, D.H., and Dohm, J.D., 1990, *PLPSC 20,* 503-513. [3] Tanaka, K.L., and Chadwick, D.J., 1992, *LPSC Abstracts XXIV,* 1397-1398. [4] Thomas, P.G., and Allemand, P., 1993, *JGR 98,* 13,097-13,108. [5] Golombek, M.P. et al., *this volume.* [6] Tanaka, K.L., and Davis, P.A., 1988, *JGR 93,* 14,893-14,917. [7] Davis, P.A., and Golombek, M.P., 1990, *JGR 95,* 14,231-14,248. [8] Plescia, J.B., 1991, *JGR 96,* 18,883-18,895. [9] P.A. Davis, 1993, *personal commun.* [10] Golombek, M.P. et al., 1991, *PLPSC 21,* 679-693. [11] Plescia, J.B., 1993, *JGR 98,* 15,049-15,059.

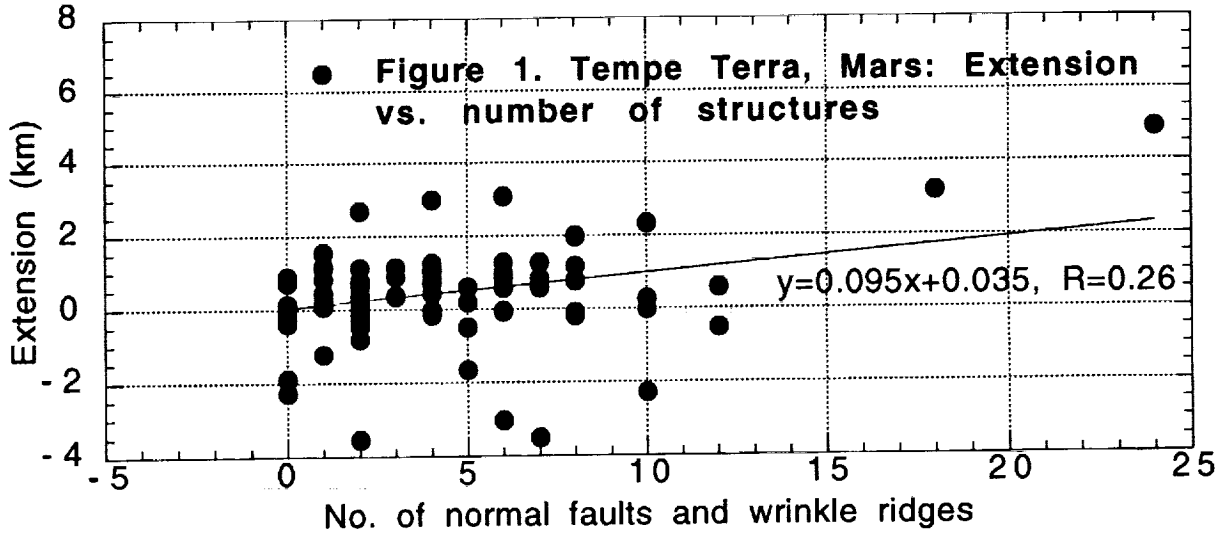

EOLIAN HISTORY OF THE HELLAS REGION OF MARS;

Kenneth L. Tanaka and **Gregory J. Leonard**, U.S. Geological Survey, Flagstaff, AZ, 86001

Introduction. Geologic mapping at 1:5,000,000 scale [1] and other studies indicate that the Hellas region has undergone a long and eventful eolian history. The major factor controlling this history has been the huge impact basin formed during Early Noachian time [2] and largely preserved until the present. This basin, about 2,500 km across, has relief of 9 km [3] and is the deepest basin on Mars. It was partly filled, apparently with eolian material, during the Early Hesperian; the sources of the material probably include volcanic ash and clastic debris generated by erosion of highland materials. We propose that eolian mantles came and went throughout the Hesperian and Amazonian. High obliquities and availability of dust and silt may have been responsible for occasional periods of greater deposition of eolian material. At present, dunes, frost and dust splotches, and high winds evidenced by dust storms indicate that the Hellas region is the site of one of the most active eolian regimes on Mars. We describe here the probable eolian deposits in the Hellas region and discuss their depositional styles and modification histories.

Lower Hesperian interior deposit. On the floor of the Hellas basin, a thick, highly degraded deposit covers about 10^6 km^2. Although its thickness has not been precisely determined, it may be as thick as 2 km. One of the tallest erosional scarps within the unit has a height (determined by shadow measurement) of about 700 m. Erosional landforms within the deposit include steep scarps, hummocky and knobby terrains, and deeply etched margins and hollows. The unit overlies an Upper Noachian ridged plains unit (age determined by density of craters >8 km in diameter), and it is embayed by alluvial and eolian materials of Late Hesperian and Amazonian age. The crater-density distribution for the interior deposit is difficult to interpret because of very deep erosion in most places. Relatively uneroded areas of the deposit generally appear blanketed by the ejecta of larger impact craters; presumably, the ejecta provide armoring against erosion. In any case, Hesperian to Amazonian crater densities are obtained for three mapped subunits of the deposit (these subunits represent varied degradational states of the bulk interior deposit). The crater distributions also show that the smaller the crater-size range, the younger the crater age. This result, along with the observed erosional features, may indicate that initial erosion hundreds of meters deep during the Early or Late Hesperian was followed by relatively modest erosion (typically, tens of meters deep) through the Late Hesperian and Amazonian.

Hesperian-Amazonian rim mantles. On the upper slopes and rim of the Hellas basin, smooth, flat, irregularly shaped mantles are locally preserved. These mantles (tens to hundreds of meters thick) occur (1) in shallow topographic traps (such as within Amphitrites and Peneus Paterae and on smooth plains surrounded by wrinkle ridges), (2) on broad plains (such as south of Hamarkhis and Reull Valles), (3) within large craters, and (4) as pedestals beneath impact ejecta. Because pedestal craters of fairly high density occur on Malea Planum and small craters of moderate density superpose some of the mantles within craters, at least some of the mantles are probably Hesperian [see 4]. However, other mantles appear uncratered (at 200-300 m/pixel resolution) and are likely to be Amazonian. These young mantles commonly appear etched, e.g., the material that thinly blankets the northern parts of Peneus Patera and the dissected slopes of northern Malea Planum. Also, some of the crater-fill mantles have pits hundreds of meters deep (such as in the large crater Terby, lat 28°S., long 286°; see also [5]). Pits and etched features indicate the poorly indurated, friable nature of these mantles.

Hesperian-Amazonian interior mantles. Along the south edge of the floor of Hellas, in a topographic low between the Lower Hesperian interior deposit and the north edge of Malea Planum, deposits of relatively low albedo form a fairly continuous blanket. The blanket is made up of smooth, broad (>70 km across), rolling mounds having mostly gently sloping margins that embay or feather into adjacent units. The blanket appears to be covered locally by dunes, and thus it may be made up of thick sequences of dune material. Its crater density indicates a Late Hesperian or Early Amazonian age. In addition, possible eolian mantles that are wind sculptured and similar in age to the blanket form generally sharp edged, etched, irregular mesas near the center and the northwest edge of the Lower Hesperian interior deposit.

Upper Amazonian dunes. Occurrences of dunes in the Hellas region are indicated by (1) linear, arcurate, and reticulate patterns of low ridges in the central, northern, and western parts of the Hellas floor; (2) a ripple pattern of linear ridges, spaced about 1 km apart, on interior mantle material at lat 51° S., long 291°; and (3) individual ridges (perhaps climbing dunes) on the top and flanks of some irregular mesas within the Hellas basin. Also, dark dunes occur within craters west of the Hellas basin [5].

Transient bright and dark splotches. Some Viking images reveal seasonal, surficial, bright and dark splotches in various areas of the Hellas region; the splotches have been interpreted to be eolian frost and sand deposits [5, 6]. Some of these features are elongated and lineated, indicating prevailing wind directions.

Discussion. We conclude that the Hellas basin has served as a major center of eolian activity on Mars throughout much of the Hesperian and Amazonian. Under present conditions, some of the highest wind stresses are predicted along the southern and northern margins of the basin [7]. These stresses have been attributed to broad slopes, high solar insolation during southern summer, and high atmospheric density within the basin, and they are sufficient to induce saltation of fine sand [7]. Saltation and dust devils are primary mechanisms of kicking up dust into the atmosphere, thereby initiating dust storms [8]. The identification of probable dune fields both within and outside the Hellas basin shows that saltation does occur in this region (which coincides with observations that Hellas is a major source region for regional and global dust storms on Mars [9]). The interior deposit is deeply eroded, perhaps by mass wasting and collapse. Eroded debris was probably removed by eolian transport. If so, the materials of the interior deposit would have been friable, fine, and poorly consolidated (they could include ice), which is in agreement with an interpretation made from Viking IRTM data [10]. However, because of the depletion of fines that would likely result from eolian deflation, much of the interior deposit may now be covered by a lag deposit of largely sand grains that is perhaps indurated [10]. Although at present dust is likely being removed from Hellas [10] and accumulating in equatorial regions [11], depositional cycles of 10^5-10^6 years [8, 11] may reverse this transfer and perhaps result in cyclic formation of dust deposits as much as a few meters thick.

Periods of heightened net deposition and erosion are indicated by our stratigraphic interpretations of the Hellas region. We do not preclude a late (Early to Middle Amazonian) glaciation event in Hellas as proposed by [12]; however, much of the sedimentary and erosional activity at Hellas occurred at different times and periodically over a much broader region than that discussed by [12]. The Hesperian-Amazonian rim mantles throughout the region may have been emplaced during periods of high obliquity, when polar layered deposits may have been deeply eroded, thus making available greater amounts of dust to form extensive, thick mantles. The Hesperian-Amazonian interior mantles coincide in age with the formation of deep valley systems along the northeastern slope of the basin, and thus they may be made up of clastic material derived from that activity. The Lower Hesperian interior deposit has great volume (~10^6 km^3), which could be due in part to pyroclastic activity and erosion of the paterae on the northeast and south sides of the rim. However, erosion of these features (to depths of no more than ~200 m) probably has produced <10^5 km^3 of debris. Thus a much larger source of fines is required. A good candidate would be the eroded rocks along the highland/lowland boundary, where glacial-like erosion and mass wasting may have produced a large volume of fines during the Early Hesperian [2]. Other sources of fines are the many highland valleys of this age [13, 14].

References cited: [1] Leonard, G.J., and Tanaka, K.L., 1993, *work in progress.* [2] Tanaka, K.L., 1986, *PLPSC 17, JGR 91,* E139-E158. [3] USGS, 1991, *USGS Map I-2160.* [4] Tanaka, K.L., and Scott, D.H., 1987, *USGS Map I-1807-C.* [5] Thomas, P., 1984, *Icarus 57,* 205-227. [6] Thomas, P. et al., 1979, *JGR 84,* 4621-4633. [7] Greeley, R. et al., 1993, *JGR 98,* 3183-3196. [8] Greeley, R. et al., 1992, *in Mars (H.H. Kieffer et al., eds.),* ch. 22. [9] Martin, L.J., and Zurek, R.W., *JGR 98,* 3221-3246. [10] Moore, J.M., and Edgett, K.S., 1993, *GRL 20,* 1599-1602. [11] Christensen, P.R., 1986, *Icarus 68,* 217-238. [12] Kargel, J.S., and Strom, R.G., 1992, *Geology 20,* 3-7. [13] Wilhelms, D.E., and Baldwin, R.J., 1989, *PLPSC 19,* 355-365. [14] Craddock, R.A., and Maxwell, T.A., 1993, *JGR 98,* 3453-3468.

EXPERIMENTAL AND THEORETICAL EXAMINATION OF COSMIC DUST GRAIN DECELERATION. W. G. Tanner[1,2], W. M. Alexander[1], and S. Stephenson[1]. [1]Baylor University Space Science Laboratory, Waco, TX 76798 USA, [2]University of Kent at Canterbury, Unit for Space Science, Kent CT2 7NR, UK

OVERVIEW: During the past few years several designs for devices to detect the penetration of a thin metallic film by a dust grain have been tested both in the laboratory and in space. Another crucial component of the analysis has been the theoretical calculation conducted to assess the parameters of the hypervelocity penetration event. In particular theoretical hydrodynamic calculations have been conducted to simuated the hypervelocity impact event where various comsmic dust grain candidates, e.g., ρ = 7.87, 2.70, 1.00, have been utilized to reproduce the events. Theoretical analyses of hypervelocity impact events will be reported which span an extensive matrix of values for velocity, density and size. Theoretical deceleration values have been duduced from the data created by CTH, a Sandia National Laboratory Hydrodynamic computer code (McGlaun et al, 1990). The calculation of the pressure, temperature, and density of the impactor during the high shock events have also been assessed. With these data one can assess the thermodynamic behavior of the material in the interaction, and connect thermodynamic properties in the impactor with the deceleration process.

BACKGROUND: The plasma yielded by the hypervelocity penetration events has been collected and an empirical power law fit made to the normailized data (according to the paritcle mass). That data also may be utilized to assess the deceleration of cosmic dust grain analogs which penetrate the flim and impact the stopping plate or capture foam. A siginficant quantity of data has been taken which illustates the change in the velocity of a dust grain after it has penetrated an ultra thin film. A continuing effort to model hypervelocity impact penetrations has yielded an extensive matrix of data for penetration events consistent with the experimental data. The primary goal of these research efforts has been to establish unequivocally a semi-empirical equation which can relate the penetration hole diameter, D_h with the penetrating particle diameter, D_p. The velocity of the particle will be a parameter of special importance and for theat reason a study of theoretical limits on the deceleration of dust grains has been undertaken. Perhaps the most important results of simulated particle passage through the test films has been the theoretical confimaton of the degree of destruction a cosmic dust grain experiences.

PENETRATION MECHANICS: The principal theoretical approach has been to perform calculations using a hydrodynamic computer code CTH. This tool provides a computational laboratory where hypervelocity impacts may be controlled and observed. The complete perforation of a thin film will create a significant amount of data depicting the event. The most useful utilization of the modelled event has been the determination of the hole size generated by the penetrating dust grain. Provision must be made of the most crucial parameter which controls the simulation, i.e., time to maximum expansion of the penetration hole. That time must be commensurate with the expansion of the shock front and the rarefaction wave. Pressure, density and temperature in the film must also be tracked to assess the progression of the energy in the material. Of equal interest is the strain rate which signals the relaxation of the material following the passage of the shock front through the material. Once the strain rate has reduced in value near the walls of an impact site a commensurate decrease is seen in the other extensive variables of the interaction, and thus confirm that the progression of the crater's diameter has been halted. Penetration mechanics suggests that the more that the diameter of the impactor exceeds the thin film thickness the less will be th erosion of the projectile during passage through the film. Thus, Dp / Tf must be maximized in order that the fragmentation of the dust grain may be minimized. Hydrodynamic computer programs have benefited greatly from the data provided by many experiments designed to assess the effects of high-shock conditions present in materials. Principally the "hydro-code" calculations possess equations of state which describe both the elastic-plastic and the phase transition with melt of the high-shock regime. For several years

research has been underway to assess the association between specific thermodynamic properties of materials and the process of fragmentation, i.e., the catastrophic failure of materials. Using CTH, many properties of hypervelocity particle thin film capture techniques have been theoretically analyzed. Hypervelocity perforation of thin films will fragment glass spheres which have been used to simulate Interplanetary Dust Particles (IDPs). Upon impacting a thin film with hypervelocity a small IDP analog will fragment if and only if the film thickness and the IDP analog's velocity are sufficient. Hence the coupled parameters of velocity and D_p / T_f ratio will determine the degree of fragmentation the thin film will cause in the IDP analog. With a hydrocode calculation one can investigate many different values for velocity and film thickness. CTH has been used to investigate the penetration mechanics of small particles impacting and perforating a thin film. The fragmentation of IDP analogs have been investigated to determine penetration parameters of thin films. The same analysis can be applied to the fragmentation of targets or projectiles or even secondary impacts due to ejecta sprays.

EXPERIMENTAL RESULTS: Results of both two-dimensional (2D) computer simulations of the hypervelocity impact events which penetrate the STS and the EuReCa 1 thin films will be reported. A relationship between the particle diameter, D_p, and the diameter, D_h, of the hole created in a 500 Å aluminum thin film (T_f) for relevant particle and target parameters will be derived and will be compared with empirical equations. That relationship will be used to analyze *in situ* data of the thin film experiments flown in LEO, and to determine the size distribution of grains which penetrate the thin films [2]. Charge liberation events due to hypervelocity impacts which have penetrated an ultra thin film (Al 250Å and 500Å) and are captured in an underdense foam. The velocity of the dust grain allows for the determination of the mass of an assumed sphere. Efficient charge collection immediately in front of the thin film is the result of a focussing potential of -45 volts on the grid wires. The charge collected reflects an jet initiation event and thus will be most pronounced on the front side of the thin film. Charge collected behind the thin film is much more diffuse and thus is broader in time. It should be apparent that the impact into foam liberates charge in excess of the charge measured at the rear of the film. A time of flight between the thin film perforation and the foam impact can be analyzed to determine a change in the velocity of the perforating dust grain. Charge liberated from the carbon containing material in evidence by the excess of charge on the charge collection grid immediately in front of the foam. The proposed ultra thin film experiment has been tested in the laboratory to establish the quantity of charge liberation during an intact capture event. The entire ultra thin film system has proved to be mechanincally sound after experiencing the launch loads of the Shuttle. Also after eleven months exposure to the LEO space environment the HVI/BUSSL 500Å aluminium films exhibited no penetrations due to mechnical effects. Theoretical calculations have facilitated the determination of the penetration efficiency of the thin film materials selected. Subsequent laboratory studies as well as analysis of the thin film experiment flown on EuReCa have demonstrated the optimization process has produced a highly successful combination of materials. These tests constitute an initial calibration of the thin film charge detection system which will provide data depicting the dynamics of grains COMRADE, SOCCER or LDEF II will collect.

CONCLUSION: Data will be utilized to assess the deceleration of cosmic dust grain analogs which penetrate the flim and impact the stopping plate or capture foam. These data which illustate the change in the velocity of a dust grain after it has penetrated an ultra thin film will be compared with theoretical calculations produced by CTH. Of equal importance will be the comparison of thermodynamic properties of a cosmic dust grain analog with those data generated by theoretical calculations.

REFERENCES: [1] McGlaun, J. M., Thompson, S. L, Elrick, M.G. (1989) *Intl. Journal of Impact Engineering*, Vol. 10. [2] Tanner, W. G, McDonald, R. A., Alexander, W. M, Maag, C. R. (1993) *Intl. Journal of Impact Engineering*, Vol 14.

SLOW EMPLACEMENT OF FLOOD BASALTS: EVIDENCE FROM FRACTAL PROPERTIES OF LAVA FLOWS; G. Jeffrey Taylor, Barbara C. Bruno, and Stephen Self, Planetary Geosciences, Dept. of Geology and Geophysics, SOEST, Univ. of Hawai'i, 2525 Correa Rd., Honolulu, HI 96822

Flood basalts, such as the Columbia River Basalt Group and the Deccan Traps on Earth, young flows in Mare Imbrium on the Moon, the Cerberus Formation on Mars, and Mylitta Fluctus on Venus are impressive accumulations of basaltic lava, on the order of 10^5 km^3. The conventional view is that these flow fields formed at enormous eruption rates, up to 10^3 km^3/day [e.g., 1,2]. Such catastrophic eruption rates would have enormous effects on planetary atmospheres. However, as shown by S. Self and co-workers [3,4] evidence is accumulating that large basalt provinces on Earth were emplaced at much more modest eruption rates. The main line of evidence is that flood basalts contain features common in terrestrial pahoehoe flow fields, which are known to form at relatively low eruption rates ($< 10^{-3}$km^3/day [5]). This paper presents independent evidence based on the fractal properties of large lava flow fields on the Moon, Mars, and Venus that supports the revised view of flood basalt emplacement. Specifically, the margins of many large planetary flow fields have fractal dimensions similar to those of pahoehoe lava flows, implying that they formed by similar emplacement mechanisms.

Fractal dimensions and emplacement mechanisms of a'a and pahoehoe

We have shown that the margins of terrestrial basaltic lava flows are fractals in the range 10 cm to over 2 km [6,7]. Furthermore, a'a flows have systematically lower fractal dimensions (a measure of how convoluted a margin is) than do pahoehoe flows (≤ 1.09 for a'a and ≥ 1.14 for pahoehoe). Being able to make this distinction is far more important than distinguishing remotely between these two lava flow morphologies. The margins reflect the internal dynamics of the flows. Thus, the nature of lava flow margins inform us about the emplacement mechanisms of lava flows. There is now strong evidence that emplacement of pahoehoe lava flows involve inflation and lava-rise mechanisms [8,9]. The lava moves from the vent to the margins and flow front inside an insulating carapace, in either tubes or broad sheets. This allows the formation of large, voluminous flow fields at low, but long lasting, effusion rates. In contrast, a'a flows surge across the surface with significant portions of them incandescent, hence losing heat rapidly. Thus, one would predict that flood basalts ought to have fractal dimensions like those of a'a flows (≤ 1.09) if they formed at enormous effusion rates, as conventionally thought. On the other hand, if flood basalts were emplaced at low effusion rates involving complex internal dynamics, then their margins ought to be more like those of pahoehoe lava flows, with fractal dimensions ≥ 1.14. This has implications for the effusion rates during eruption: As noted above, for Hawaiian basalts, a'a forms at rates $> 10^{-3}$ km^3/day, whereas pahoehoe forms at lower eruption rates. (The transition is not really quite so sharp.) If the typical vent is about 10 m long, this suggests that pahoehoe-type emplacement mechanisms require effusion rates of $< 10^{-4}$ km^3/day per meter of fissure. The margins of terrestrial flood basalts are not preserved, but there are numerous large, flood-basalt scale flow fields on other planets, allowing us to measure fractal dimension and assess their emplacement mechanism.

Fractal dimensions of large planetary lava flows

The Cerberus Formation, Mars. Plescia [10,11] has marshaled convincing arguments that the Cerberus Plains in southeastern Elysium and western Amazonis are volcanic. They cover an area of 1.5×10^6 km^2 and have volumes of at least about 3×10^5 km^3 [11]. Available images do not allow estimation of the volumes of individual flow units. A preliminary analysis of the northeast distal end of the Cerberus Formation indicates a fractal dimension of 1.17, in the range observed for pahoehoe

emplacement styles. Plescia has noted that the western part of the field has characteristics akin to "plains style" volcanism [12]. Good examples are found in the Snake River Plain, Idaho. These are pahoehoe flow fields, and the one we have analyzed (Hell's Half Acre) has a fractal dimension of 1.21. Thus, our data and other observations of Cerberus lava flows suggest they were emplaced by an inflation-dominated mechanism at relatively low effusion rates.

Young flows in Mare Imbrium, the Moon. The Moon has few visible lava flow margins. Fortunately, the most well-preserved margins are of the relatively young lava flows (about 2.5 to 3.0 Gy) in southwestern Mare Imbrium [13]. These are extremely long lava flows, extending up to 1200 km from their sources. The minimum volume erupted during the 0.5 Gy time interval was 4×10^4 km^3 [13]. Using the flow model applied the Columbia River basalts [1], Schaber [13] and Schaber et al. [14] calculated that the emplacement of the Imbrium flows as incandescent masses roaring across the lunar surface took place at eruption rates of about 10^2 km^3/day. However, our measurement [6] of the margins of the Imbrium flows indicate that they have fractal dimensions of 1.20, in the pahoehoe range. This suggests that we should examine the alternative idea that the Imbrium flows were emplaced at more modest eruption rates. For a 20-km long fissure [13], this suggests an eruption rate of about 2×10^{-3} km^3/day, five orders of magnitude less than calculated by the Shaw and Swanson [1] model. In turn, this means that a given eruptive event lasted 10^5 times longer. In the case of the Imbrium flows, this implies an eruptive event lasting up to 1000 years. However, given the low viscosities of lunar lavas and the critical relation between viscosity and shear rate needed to transition from a'a to pahoehoe, the event may have lasted only a century, or 10 times longer than the current eruption at Kilauea.

Flow fields on Venus. We have measured the fractal dimensions of 13 large-volume lava flows on Venus. All but two have fractal dimensions > 1.15. This suggests pahoehoe-like emplacement characteristics, consistent with radar observations [15]. On the other hand, the two exceptions (fractal dimensions of 1.04 and 1.09) are in Mylitta Fluctus, which appears to be a flood basalt province [16]. This may indicate that some large-volume flows do, indeed, form at high effusion rates.

Implications

The geometry of the margins of Cerberus and Imbrium flow fields suggests emplacement by an inflation-dominated mechanism. This supports the Self et al. [3,4] hypothesis stemming from field observations that terrestrial flood basalts were emplaced that way, rather than as huge lava flows erupted at enormous rates. This is a case where comparative planetary science clearly contributes to understanding a terrestrial geologic problem. This interpretation may also be significant for understanding the petrology (e.g., crystal size distributions, extent of phenocryst accumulation, vesicle distributions) of samples of lava flows from the Moon and Mars.

References: 1) Shaw, H. R. and Swanson, D. A. (1970) *Proc. Second Columbia River Basalt Symposium*, 271-297. 2) Hooper, P. R. (1982) *Science* **215**, 1463-1468. 3) Self, S. et al. (1991) *EOS Trans. AGU* **72**, 566. 4) Self, S. et al. (1993) *IAVCEI Abstracts*, 98. 5) Rowland, S. and Walker, G. P. L. (1990) *Bull. Volc.* **52**, 615-628. 6) Bruno, B. C. et al. (1992) *Geophys. Res. Lett.* **19**, 305-308. 7) Bruno, B. C. et al. (1993) *Bull. Volc.*, in press. 8) Walker, G. P. L. (1991) *Bull. Volc.* **53**, 546-558. 9) Hon, K., et al. (1993) *Bull. Geol. Soc. Amer.* in press. 10) Plescia, J. B. (1990) *Icarus* **88**, 465-490. 11) Plescia, J. B. (1993) *Icarus* **104**, 20-32. 12) Greeely, R. (1982) *J. Geophys. Res.* **87**, 2705-2712. 13) Schaber, G. G. (1973) *Proc. Lunar Sci. Conf. 4th*, 73-92. 14) Schaber, G. G. et al. (1976) *Proc. Lunar Sci. Conf. 7th*, 2783-2800. 15) Campbell, B. A. and Campbell, D. B. (1992) *J. Geophys. Res.* **97**, 16,293-16.314. 16) Roberts, K. M. et al. (1992) *J. Geophys. Res.* **97**, 15,991-16,015.

PLANAR DEFORMATION FEATURES IN QUARTZ GRAINS FROM RESURGE DEPOSIT OF THE LOCKNE STRUCTURE, SWEDEN; A.M. Therriault[1] and M. Lindström;[2] [1]Geol. Survey of Canada, Geophys. Div., Ottawa, Ont. K1A 0Y3; [2]Stockholm University, Dept. of Geology and Geochemistry, Stockholm, Sweden.

The Lockne structure, located 20 km south of Östersund, Sweden, has a diameter of 7-8 km and was formed in the Middle Ordovician,[1,2] at 455 Ma, based on infilling sediments and sedimentary cover.[3] Strongly shattered Proterozoic crystalline rocks, which form the local basement,[4] and what have been interpreted as fragments of impact melt, and grains of shocked quartz are evidence of its possible origin by impact cratering.[2,5] The proposed impact occurred at sea in an area consisting of Proterozoic crystalline basement covered by several tens of meters of Lower Palaezoic sedimentary rocks.[2] Detailed description of the structure can be found in Lindström *et al.*[5] and Lindström and Sturkell.[3] No optical measurements of the proposed shocked quartz were made, moreover, the occurrence of shock metamorphism has not been confirmed according to the criteria of Grieve *et al.*[6] Accordingly, we have undertaken a preliminary study of the "shocked quartz" to confirm or deny the occurrence of shock features.

Sample FF6, used in this more detailed examination, was collected in an outcrop consisting of thick-bedded Loftarsten, which is the local vernacular name for what was considered to be a tuffaceous lithic greywacke.[7] In more recent interpretations, this deposit is considered to represent the final stages of resurge deposition after the marine impact at Lockne.[3] In this case, the Loftarsten is a coarse arenite with an estimated median grain size between 0.25 and 1 mm and is composed of 10-15% lithic fragments derived from crystalline basement rocks, 15-20% limestone clasts, 10-15% pyroclastics (in the impact interpretation, ejecta of impact melt origin), which are more or less altered, 10-20% fossil fragments (mainly arthropods and echinoderms), about 10% quartz and feldspar grains, and 15-20% matrix.[7] Our sample is about 2 kg, massive (i.e., laminations and other structures are missing on the scale of the sample), and has a uniform composition.

A characteristic feature of quartz grains, found at impact sites, is the development of microscopic planar deformation features (PDF).[e.g., 6,8,9,10,11,12] In the sample studied, single quartz grains reveal from one to five lamellae sets of PDF (Fig. 1). Individual PDF are usually decorated with <1-3 μm isotropic inclusions and have a spacing of 1 to 5 μm between individual PDF. In general, the lamellae sets are sharp, moderately continuous, straight to moderately curved, and cover more than half the length of the grains. In 25 grains of quartz, the orientations of 82 poles of lamellae planes relative to the optical axis were determined using a universal stage. As quartz is weakly biaxial and the grains are weakly to strongly recovered, i.e., show mosaicism and wavy extinction, the precision of measurement did not exceed 5°.

The poles to all sets of PDF and the optic axes of each quartz grains studied were plotted on a stereonet, and then, rotated to a c-axis vertical orientation. This standard projection allows the identification of the poles of PDF with the crystallographic planes of quartz[e.g., 13] by overlaying a template of all rational crystallographic orientations (c-axis vertical orientation) onto the data for each quartz grain and then rotating the template to get a best fit to the PDF. This method, although time consuming, retains the angular separation between multiple sets of PDF, and thus, more confidence may be placed in the assignment of particular PDF to specific crystallographic indices of quartz. Our results are shown in Table 1 and Figure 2. Two marked peaks are obtained: one which corresponds to the ω $\{10\bar{1}3\}$ crystallographic plane of quartz with 39.0% of the measured orientations falling within ±5° of 22°56', and another corresponding to the π plane of quartz $\{10\bar{1}2\}$ with 23.2% of the lamellae sets measured falling within ±5° of 32°25'. Of all the PDF measured, 18.3% did not correspond to rational crystallogaphic planes for PDF in quartz.

The distribution of the orientation of the lamellae sets indicated that their crystallographic arrangement corresponds well with the distributions found at known impact craters with similar target rocks.[e.g., 10,11,13,14,15,16] PDF formed in shock-metamorphosed quartz are commonly oriented parallel to the basal pinacoid, c {0001}, and to the rhombohedral forms ω and π.[e.g., 8,9,10] Recognition of the ω orientation is important because this is not a normal cleavage or twin plane and is rare as a growth plane. Our results show that ω features dominate and that π features are the next most common features in the Lockne sample studied. This would indicate moderate shock pressures of >10 GPa during formation of the PDF.[17] The PDF found in the Lockne structure fulfill the general criteria defined by Alexopoulos *et al.*[12] that must be met for microscopic lamellar features in shock-metamorphosed quartz, i.e., features are well defined and sharp, relatively straight, parallel, and continuous, cover more than 50% of the grain, occur in multiple sets, and have a spacing between features of <5 μm.

PLANAR FEATURES IN QUARTZ FROM LOCKNE, SWEDEN: Therriault, A.M. and Lindström, M.

The Lockne Breccia and Loftarsten are interpreted as having formed after impact in a shallow sea and consist of ejecta brought back int the crater by resurgent water immediately after the impact.[2] Resurge deposition began with the polymictic Lockne Breccia, which has the properties of a debris flow, continued, and ended with the overlaying Loftarsten, which has roughly the composition of the Lockne Breccia except constituted of particles in the silt to fine gravel size range sorted by grain size. Furthermore, a relatively greater content of single quartz, feldspar, and fossil grains follows with the smaller grain size. Fragments of what are believed to be impact melt and shocked grains of quartz are observed in the Lockne Breccia[5] and shocked grains of quartz for certain in the Loftarsten (as shown in this study). We concur with Simon[7] in regarding the Loftarsten as the terminal and finest precipitate of the flow(s) initiated with the introduction of the Lockne Breccia; there are in fact transitions between the two lithologies. However, the further interpretations diverge between Simon[7] and ourselves because the impact hypothesis was not put forward by Simon at the time.

This preliminary study strengthens the previous conclusion by Lindström *et al.*[5] and Lindström and Sturkell[2] that the Lockne structure is an impact crater.

References: (1) Wickman F.E. (1988) *Deep Drilling in Crystalline Bedrock, 1*, 298-327. (2) Lindström M. and Sturkell E.F.F. (1992) *Tectonophysics, 216*, 169-185. (3) Grahn Y. and Nelvak J. (1993) *Geol. Fören. Stockholm Förhandl., 115*, 263-263. (4) Strömberg A. *et al.* (1984) *Sver. Geol. Unders., Ser. Ca, 53*, 4 map-sheets. (5) Lindström M. *et al.* (1991) *Geol. Rundschau, 80*, 201-204. (6) Grieve R.A.F. *et al.* (1990) *Eos, 71*, 1792. (7) Simon S. (1987) *Sver. Geol. Unders., Ser. C, 815*, 156p. (8) Hörz F. (1968) *Shock Metamorphism of Natural Materials*, 243-254. (9) Engelhardt W.V. and Bertsch W. (1969) *Contr. Miner. Petr., 20*, 203-234. (10) Stöffler D. (1972) *Fortschr. Mineral., 49*, 50-113. (11) Walzebuck J.P. and Von Engelhardt W. (1979) *Contri. Miner. Petr., 70*, 267-271. (12) Alexopoulos J. *et al.* (1988) *Geology, 16*, 796-799. (13) Robertson P.B. *et al.* (1968) *Shock Metamorphism of Natural Materials*, 164-184. (15) Robertson P.B. (1972) *Bull. Geol. Soc. Am., 86*, 1630-1638. (16) Grieve R.A.F. and Robertson P.B. (1976) *Contr. Miner. Petr., 58*, 37-49. (17) Robertson P.B. and Grieve R.A.F. (1977) *Impact and explosion cratering*, 687-702.

Table 1: Planar deformation features (PDF) in quartz grains versus crystallographic indices in quartz, for sample FF6 of the Lockne structure, Sweden, as obtained from stereonet plots.

Plane	Miller-Bravais index	Angle with c-axis	Number of PDF	Percentage
c	{0001}	0°	3	3.7%
ω	{10$\bar{1}$3}	22°56'	32	39.0%
π	{10$\bar{1}$2}	32°25'	19	23.2%
ξ	{11$\bar{2}$2}	47°43'	3	3.7%
r	{10$\bar{1}$1}	51°47'	0	-
z	{01$\bar{1}$1}	51°47'	1	1.2%
s	{11$\bar{2}$1}	65°33'	2	2.4%
ρ	{21$\bar{3}$1}	73°25'	1	1.2%
ζ	{22$\bar{4}$1}	76°	1	1.2%
Γ	{40$\bar{4}$1}	79°	1	1.2%
χ	{51$\bar{6}$1}	81°57'	2	2.4%
m	{10$\bar{1}$0}	90°	1	1.2%
a	{11$\bar{2}$0}	90°	1	1.2%
unindexed	-	-	15	18.3%
Total	-	-	82	99.9%

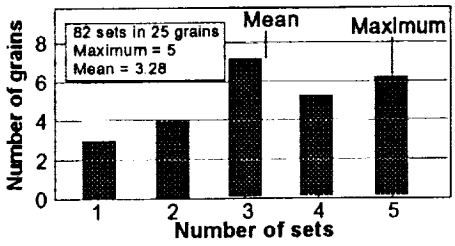

Figure 1: Histogram of the number of sets of planar deformation features per individual quartz grain from the resurge deposit of the Lockne structure, Sweden.

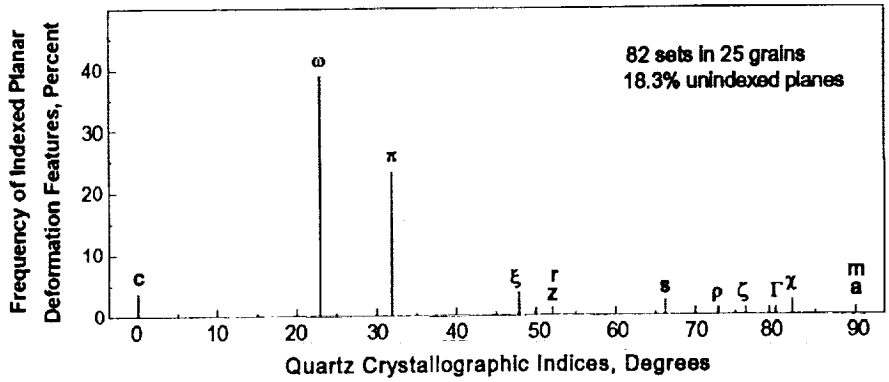

Figure 2: Histogram of indexed planar deformation features of quartz grains in relation to quartz crystallographic indices for the resurge deposit of the Lockne structure, Sweden.

NEW STUDIES OF MASS INDEPENDENT ISOTOPIC FRACTIONATION PROCESSES AND THEIR OCCURRENCE IN THE EARLY SOLAR SYSTEM, MARS AND THE EARTH; M.H. Thiemens, Department of Chemistry, University of California, San Diego, La Jolla, CA 92093.

Since the observation that the same mass independent isotopic composition observed in high temperature inclusions of the Allende meteorite could be produced by a chemical process (1) the question as to the source of the meteoritic composition has remained open. The question is of fundamental importance since oxygen is the most abundant element in stony meteorites and planets, hence the process which produces the observed meteoritic isotopic composition is significant. It has long been a major paradox as to why oxygen is the only element to possess isotopically anomalous behavior on the bulk level; the observed isotopic anomalies are unaccompanied by effects in other elements isotopic composition While it is true that undisputed nucleosynthetic anomalies reside in the CAI's where there is a large ^{16}O enrichment, there is no quantitative relation between oxygen and the isotopes of any other element. In order to assess the possible role of chemical processes in the early solar system there have been several obstacles . Resolution of the mechanism responsible for production of the effect has been particularly important. At present, the effect of temperature (2), pressure (3), excitation (2, 4) and symmetry have been experimentally determined. In addition, it is known that the effect is rather general, and is observed in several reactions and other elements (e.g. recent reviews in 5-6). It is now generally agreed upon that the effect occurs in the recombination reaction and derives from molecular symmetry factors. Thus, the physical-chemical understanding of the mechanism by which chemically produced isotopic fractionation's occur has advanced considerably since the original discovery. In addition, as described in this volume, it is now observed that a ^{16}O enriched silicate condensate may be produced in the laboratory from gas phase precursors, thus demonstrating that condensation reactions may also produce mass independent isotopic compositions.

An early concern regarding the possibility that meteoritic oxygen isotopic anomalies arise from chemically produced fractionation's was that although they are produced in the laboratory they were not observed in nature. Mass independent isotopic compositions have now been observed in several of the most interesting molecules in the earths atmosphere. Ozone in the stratosphere has an isotopic composition with $\delta^{18}O$ approximately equal to $\delta^{17}O$ (7). Stratospheric carbon dioxide is now known to possess a large mass independent isotopic composition (8). Recent rocket collected samples from more than 12 flights demonstrate that a pure $\delta^{18}O=\delta^{17}O$ fractionation is observed, the magnitude of which varies with altitude. Most recently, this laboratory has demonstrated that atmospheric nitrous oxide also possesses a mass independent isotopic signature (9). Thus, at present, at least three of the most important molecules in the earths atmosphere possess a mass independent isotopic composition. As is the case for the meteorites, the observed mass independent isotopic components have provided insight into atmospheric processes which could not have been obtained from either concentration or single isotope ratio measurements. The observations are also important for enhancing insight into how mass independent components are produced in nature.This may ultimately be useful in modeling how these processes may occur in the early solar system.

Recent laboratory experiments have provided further insight into both the different mechanisms by which chemically produced mass independent isotope effects may be produced and how they could occur in the early solar system (10). In a series of experiments it was observed that the simple process of isotopic exchange between atomic oxygen ($O(^1D)$) and ground state carbon dioxide produces a mass independent isotope composition. The most important aspects are: 1) the process is mass independent, with a fractionation of $\delta^{17}O=\delta^{18}O$. 2) the exchanged atomic oxygen is depleted in the heavy isotopes (or ^{16}O enriched) by precisely 40 per mil. 3) the exchange is ***independent*** of the oxygen atoms isotopic

MASS INDEPENDENT ISOTOPIC FRACTIONATION PROCESSES: Thiemens M.H.

composition; e.g. when the atomic oxygen isotopic composition was varied by as much as 76 per mil, the final atomic oxygen is always enriched in ^{16}O with respect to the bulk reservoir by 40 per mil. The source of the mass independent isotopic fractionation is the CO_3^* transition state, which has a lifetime of less than 100 vibrational periods (11). The striking similarity to the meteoritic observations is of interest. First, it is well known that the CAI's have, in the most refractory phases, an isotopic composition which is enriched in ^{16}O by 40 per mil (12) essentially identical to what is observed for the steady state fractionation factor observed in the experiments. Secondly, the process which produces the effect is general, it is simple isotope exchange. Third, the product of the exchange is atomic oxygen, which is highly reactive. The kinetic fate of the exchanged oxygen, as it is in the earth's atmosphere, would be reaction. Thus, this could lead to the earliest products possessing a $\delta^{17}O=\delta^{18}O=-40$ per mil isotopic composition. Most reactions which have been previously studied result in a product which is enriched in the heavy isotopes, while CAI's are depleted. This now provides at least one mechanism by which a condensate could become enriched in ^{16}O, and by the same magnitude as observed in CAI's. The plausibility is further enhanced by the observation that silicate like material may be produced which is mass independently fractionated and ^{16}O enriched. Future investigations of isotopic exchange processes, reaction mechanisms of nebular species and isotopic fractionation processes which occur during heterogeneous grain formation will be of considerable importance in further advancing our understanding of these processes in the early solar system.

The observation that a mass independent component is produced in exchange of atomic oxygen with carbon dioxide may be of importance in the Martian atmosphere. It is possible that CO_2 in the Martian atmosphere is mass independently fractionated as a result of the same process which occurs in the earth's atmosphere . In the stratosphere, the photolysis of ozone produces the atomic oxygen which undergoes exchange with CO_2 to produce the observed mass independent composition. The Martian atmosphere also possesses both CO_2 and O_3 (13) which undergoes photolysis. Since the kinetic fate of the product atomic oxygen in the Martian atmosphere may be to undergo isotopic exchange with CO_2 it is likely that it acquires a mass independent isotopic signature, as does CO_2 in the earth's atmosphere. Since CO_2 and H_2O easily isotopically exchange, particularly on a surface (mineral) this is a physical chemical mechanism by which water in the Martian regolith becomes mass independently fractionated and account for isotopic measurements of SNC meteorites which possess a mass independent composition (14) . It has previously been suggested that interactions between carbon dioxide and water in the Martian regolith are of importance in accounting for the observed isotopic compositions SNC meteorite components (15). The recent observations of mass independent isotopic variations in terrestrial CO_2 coupled with laboratory measurements provides a firmer basis by which the chemistry of the Martian atmosphere, regolith, as well as the early solar system may be studied. Continued laboratory experiments and atmospheric observations will further enhance our understanding.

REFERENCES. (1) Thiemens M.H. and Heidenreich III, J.E. (1983)*Science , 219*, 1073. (2).Morton J. et al. (1989) *JGR, 154*, 143. (3) Thiemens M.H. and Jackson T. (1990) *Geophys. Res. Letters 17*, 717. (4) Thiemens M.H. and Jackson T. (1988) *Geophys. Res. Letters 14*, 639. (5) Thiemens M.H. (1992) in "Isotope Effects in Gas-Phase Chemistry". J.A. Kaye, ed. American Chemical Society, Washington, D.C. 138. (6) S.M. Anderson, et. al. (1992). in " Isotope Effects in Gas-Phase Chemistry" J.A. Kaye ed. American Chemical Society, Washington, D.C. 155. (7) Schueler B. et. al. (1990) *Geophys. Res. Letters 17*, 1295. (8) Thiemens M.H. et. al. (1991). *Geophys. Res. Letters, 18*, 669. (9). Thiemens M.H. et. al. (1993). Submitted to *Science.* (10) Wen J. and Thiemens M.H. (1993) *J. Geophys. Res. 98*, 12,801. (11) DeMore W.B. and Dede C. (1970). *J. Phys. Chem. 74*, .2621. (12) Clayton R.N. (1993) *Annual Review Earth and Planetary Sciences 21*, 115. (13) Blamont J.E. and Chassefiere E. (1993) *Icarus 104*, 324. (14) Karlsson, H.R. et. al. (1992) *Science 255*, 1409. (15) Jakosky B.M. (1991) *Icarus 94*, 14.

P. 2

FIRST OBSERVATION OF A MASS INDEPENDENT ISOTOPIC FRACTIONATION IN A CONDENSATION REACTION;

M.H. Thiemens, R. Nelson and Q.W. Dong, [1]Department Of Chemistry, UCSD, La Jolla, CA 92093-0356. J. A. Nuth, III, [2]Astrochemistry Branch, Goddard Space Flight Center, Greenbelt, MD.

Thiemens and Heidenreich (1983) first demonstrated that a chemically produced mass independent isotopic fractionation process could produce an isotopic composition which is identical to that observed in Allende inclusions.This raised the possibility that the meteoritic components could be produced by chemical, rather than nuclear processes. In order to develop a mechanistic model of the early solar system it is important that relevant reactions be studied, particularly those which may occur in the earliest condensation reactions. This abstract reports the isotopic results for isotopic fractionations associated with condensation processes. A large mass independent isotopic fractionation is observed in one of the experiments.

The condensate smokes were produced utilizing the Goddard Space Flight Center condensation flow apparatus, which has been described by Nelson et al. (1989). The silicon oxide condensates were prepared from mixtures of molecular hydrogen, silane and molecular oxygen. The total pressure was approximately 60 torr with silane and molecular hydrogen in excess of molecular oxygen by approximately a factor of 10. Reaction temperature was about 800 K. The oxygen was obtained from the samples by reaction with bromine pentafluoride as previously described (Nelson et al, 1989). After oxygen extraction all samples were additionally purified by passage through a molecular sieve powder at -122 degrees centigrade. Measurement of the sample background demonstrated that the samples contained no impurities. The measured stoichiometry for the samples was approximately $SiO_{1.5}$-$SiO_{1.8}$.

From the data it is observed that experimental runs II and III produced samples which were essentially isotopically identical, -12.54 and -12.57 per mil ($\delta^{18}O$), respectively. These particular samples were obtained from within the furnace of the flow condensation apparatus. For runs II and III, which were obtained from the collection foils outside the furnace exit, the fractionation is somewhat greater, -16.15 and -15.09 per mil, respectively. The modest difference between the foil and furnace samples likely results from the temperature difference between the furnace and collection surface exterior to the furnace.The magnitude of the observed fractionation reflects the isotopic fractionation associated with the condensation reaction at temperatures of approximately 800 degrees K. For all samples from runs II and II the fractionation is strictly mass dependent.

Sample I reveals a striking and important isotopic difference. The four samples which were collected from the furnace define a straight line with a slope of 0.73 and a correlation coefficient of 0.99, clearly mass independent. This is the first observation of a chemically produced mass independent fractionation in a condensate. At present we may make the following observations. The anomalous composition does not derive from contamination. As described, all samples were processed through a second purification step and the background measurements demonstrated that all were clean. The ratio in the experiments of reduced (silane+hydrogen) to oxidized (molecular oxygen) were similar, with the anomalous samples having a value between samples from runs II and III. The total pressure for run I was approximately 15% higher (70 torr total), thus there could be a different kinetic reaction mechanism though at present we cannot resolve this from the limited data. The greatest difference between the experiments was reaction time. Experiment I was only 13 minutes duration whereas II and III were significantly longer; up to 2 hours for experiment III. It may be possible that secondary reaction between the flow molecular oxygen and the condensate alters the primary condensation isotopic signature. Future studies which determine the temporal characteristics will be of importance in addressing the possible extent of secondary isotopic exchange.

The best fit line determined by experiment I does not pass through the initial molecular oxygen isotopic composition. This requires that there are at least two isotopic fractionation

processes occurring. For the reaction conditions, it is reasonable to presume that gas phase reaction between oxygen and silane produces an isotopic fractionation. If this is the case, then the magnitude of the observed isotopic fractionation (in all three experiments) would be larger since the residual molecular oxygen which reacts to form a condensate would be isotopically heavier. There is also no reason to presume that this does not happen in all three experiments, in which case we would conclude that this initial reaction between silane and oxygen in the flow stream is a mass dependent process as experiments II and II are strictly mass dependently fractionated. This then suggests that the source of the anomalous fractionation could be in the reaction leading to condensation and which is secondarily lost by exchange during passage of molecular oxygen over the solid product. The observed difference isotopically between the foils and the furnace may be a reflection of this as greater extent of exchange would be expected in the furnace.

A most important observation in the products of experiment I is that they are enriched in ^{16}O with respect to the make up gas. In other gas phase reactions which have previously been studied, and where mass independent isotopic fractionations are observed, the stable products have been enriched in the heavy isotopes. This is the first example of a ^{16}O enrichment. Wen and Thiemens (1993) have shown that exchange between atomic oxygen and CO_2 produces a mass independent fractionation, with $\delta^{17}O=\delta^{18}O$. In this instance, the CO_2 is enriched in the heavy isotopes and the atomic oxygen depleted. It appears that the present results are unlike any previous experiments. We rule out ozone formation as being responsible for the observed mass independent component as 1) at these temperatures it is unstable and would not form 2) the conditions are too reducing and 3) ozone is enriched in the heavy isotopes whereas the product is depleted in the heavy isotopes. Thus, it is unlikely that ozone formation is relevant to the present experiments.

In conclusion, the first mass independent fractionation in the formation of a solid has been observed . The fractionation is unlike those observed in gas phase reactions in the laboratory and the atmosphere and may be a new type of isotope effect. Future experiments which control the reaction kinetics and define the reaction mechanisms will be crucial in resolving the source of this isotopic fractionation process.

REFERENCES. [1] Nelson R. et al. (1989) *Proc. 19th Lunar and Planetary Conf.* 559,
[2] Thiemens M.H. and Heidenreich III J.E. (1983). *Science 219*, 1073,
[3] Wen J. and Thiemens M.H. (1993) *J. Geophys. Res. 98*, 12,801.

ANATOMY OF A CLUSTER IDP (II): NOBLE GAS ABUNDANCES, TRACE ELEMENT GEOCHEMISTRY, ISOTOPIC ABUNDANCES, AND TRACE ORGANIC CHEMISTRY OF SEVERAL FRAGMENTS FROM L2008#5;

K.L. Thomas[1], S. J. Clemett[2], G. J. Flynn[3], L. P. Keller[4], D. S. McKay[5], S. Messenger[6], A. O. Nier[7], D.J. Schlutter[7], S.R. Sutton[8], R. M. Walker[6], and R. N. Zare[2]; [1]Lockheed 2400 Nasa Rd. 1Houston, TX, 77058, [2]Dept. of Chemistry, Stanford University, Stanford, CA 94305, [3]Dept. of Physics, SUNY-Plattsburgh, Plattsburgh, NY 12901, [4]MVA Inc., 5500/Suite 200 Oakbrook Pkwy., Norcross, GA 30093, [5]NASA/JSC, SN, Houston, TX 77058, [6]McDonnel Center for the Space Sciences, Physics Dept., Washington University, St. Louis, MO 63130, [7]School of Physics and Astronomy, University of Minnesota, Minneapolis, MN 55455, [8]Dept. of Geophysical Sciences, The University of Chicago, Chicago, IL 60637

In Part I, we described the bulk chemistry and mineralogy of large fragments and fines (<5 μm) from a cluster IDP originally ~ 40-50 μm in diameter [1]. Here we report results from several types of analyses: noble gas measurements (Nier), Synchrotron X-Ray Fluorescence (SXRF) for trace element abundances (Flynn and Sutton), ion probe studies (Messenger and Walker), and trace organic chemistry (Clemett and Zare). The same fragments were analyzed for isotopic abundances and organic compounds.

Noble Gas Content and Release Temperatures He content and the He release temperatures for four samples were determined by step-heating experiments [2]. The average ^{4}He abundance is ~4.1 (cc x 10^{11}) and extraction temperatures for removal of 50% of the He range from 750-1040 °C, with an average at 928 °C (Table 1). The low He content and high release temperatures indicate that all fragments from L2008#5 have experienced heating during atmospheric entry. He measurements have been used to distinguish asteroidal from cometary IDPs in individual, small-sized particles (< 10 μm in diameter) [3]; however these measurements cannot be used to determine sources of cluster particles because higher deceleration heating occurs in large-size particles.

Trace Element Abundances SXRF was used to determine trace element abundances in four fragments from L2008#5 [technique described in 4]. Two fragments show marked depletions in Zn (Zn/Fe < 0.1) indicating they have experienced heating during atmospheric entry (Table 2). Zn/Fe ratios range from 0.2-0.5 for the remaining fragments. All four fragments show deviations by more than a factor of 2 from CI for 3 or more elements (Table 2). The only consistent trends are enrichments in Cu, Se, and Br, and a depletion in Zn relative to CI.

Heating Summary of Cluster Fragments He content and release temperatures of fines suggest they experienced atmospheric entry heating. The large range in 50% He release temperatures suggests that fragments have not been heated equally. Low Zn/Fe ratios show that 2 of 4 fragments were heated during atmospheric entry. Previous TEM studies have shown that the presence of magnetite rims on IDP surfaces is an indication of atmospheric entry heating [e.g., 5]. Magnetite rims were observed in 13 of 20 fragments and fines from this cluster[1]. The He measurements indicate that cluster L2008#5 has not been uniformly heated; trace element abundances and magnetite rims are evidence that heating is seen in selected fragments, probably those located on the exterior surfaces of the cluster.

Isotopic Measurements D/H ratios of eight fragments were measured using an ion microprobe [technique described in 6]. Deuterium enrichments (δD) were observed in all four of the C-rich fragments and range from +322- +822 per mil. Four fragments from Clu37, which had a chondritic C abundance, showed no D enrichment (Table 3). The D enrichments in the C-rich fragments are far in excess of values for terrestrial samples and are another indication that the fragments are extraterrestrial [6]. There is an apparent positive correlation of D enrichment with the abundance of carbonaceous material in our fragments. A larger group of IDPs should be examined to confirm this result.

Trace Organic Chemistry The signatures of polycyclic aromatic hydrocarbons (PAHs) in IDPs have been observed with a microprobe two-step laser mass spectrometer (μL^{2}MS) [7]. All cluster fragments which had been analyzed previously for isotopic abundances were examined for the presence of PAHs (Table 3).

All PAH signatures observed show significant variability between different particles. In fact, intensities of PAH signatures varied in pieces from the same fragments (e.g., Clu19 and Clu37, Table 3). For example, a strong PAH signature was observed in Clu19(β), while essentially no signal was found in Clu19(α) (Table 3). The PAH spectra from all fragments are very different from those of two other unrelated IDPs, Aurelian or Florianus [7]: the range of aromatic species observed is reduced (limited from 1 to 6 ring species) although individual peak intensitites (e.g., naphthalene and the alkyl-phrenathrenes) are in some cases more intense than the most intense peak observed from Aurelian. The spectra are dominated by even mass PAHs with little evidence for odd mass peaks, suggestive of nitrogen substituted aromatic species. Although the distribution of PAHs may be affected by previous exposure to the ion probe (10kev Cs^+ ions), strong PAHs signatures have only been observed in D-rich particles [this work & 7]. PAHs and elemental carbon coexist in some fragments of this cluster; however, there is a lack of correlation in the abundance of C and the presence of PAHs. Considering the mass of the entire cluster, PAHs and elemental carbon are not homogeneously distributed.

In summary, analyses of fragments from one cluster IDP show large variations in He content, He release temperatures, trace element and isotopic abundances, and the presence of organic components.

References: [1] Thomas K.L. *et al.* (1994) This volume. [2] Nier A.O. and Schlutter D.J. (1993) *Meteoritics* **25**, 675. [3].Brownlee D.E.*et al.* (1993) *LPSC* **24**, 205. [4] Flynn G.J. and Sutton S.R. (1991) *Proc. LPSC* **21**, 549. [5] Keller L.P. *et al.*(1992) *LPSC* **23**, 675. [6] McKeegan K.D. *et al.* (1985) *GCA* **49**, 1971. [7] Clemett S.J. *et al.* (1993) *Science* **262**, 721.

Table 1. He measurements of fines from cluster L2008#5.

Sample #	^{4}He (cc x 10^{11})	50% He Release Temp (°C)	^{3}He/^{4}He (x10^{-4})	^{20}Ne/^{22}Ne	^{4}He/^{20}Ne
1	4.5	750	3.3 +/- 0.7	13.3 +/- 1.6	9.9 +/- 0.4
2	6.1	1040	4.7 +/- 0.5	11.5 +/- 1.3	14.3 +/- 1.0
3	3.4	1010	7.2 +/- 1.2	7.2 +/- 1.0	12.0 +/- 3.0
4	2.2	910	5.9 +/- 1.4	10.5 +/- 1.7	6.8 +/- 1.0

Table 2. SXRF trace element abundances normalized to CI of 4 large fragments from L2008#5.

Sample #	Cr	Mn	Fe*	Ni	Cu	Zn	Ga	Ge	Se	Br	Zn/Fe
Clu16	0.2	0.4	1.4	2.0	3.5	0.06	0.4	0.2	6.1	2.0	0.04
Clu18	1.3	1.8	1.3	0.5	1.7	0.06	7.1	0.3	1.8	7.3	0.05
Clu21	0.4	3.1	2.1	2.0	7.4	0.44	1.4	0.6	3.4	7.3	0.2
Clu319	3.5	0.2	1.1	0.9	2.6	0.52	10.0	2.8	5.4	24.8	0.5

*Values from EDS

Table 3. Carbon abundance (Wt.%), Deuterium enrichments (δD), and the presence of PAHs signatures in several large fragments from cluster L2008#5.

Sample	Wt.% Carbon (EDS)	δD (per mil)*	μL^{2}MS (%) **
Clu19(α)‡	a+b=14	+664 +/- 84	>5
Clu19(β)‡	"	+424 +/- 71	100
Clu110	10	+822 +/- 91	43
Clu313†	15	+322 +/- 67	Not measured
Clu37(α)§	a+b+c+d=3	-24 +/- 17	20
Clu37(β)§	"	+25 +/- 22	7
Clu37(χ)§	"	-14 +/- 36	32
Clu37(δ)§	"	+12 +/- 29	13

*Terrestrial range is -200 - +50 per mil **Integrated signal intensity from 80-450 amu normalized relative to Clu19(β) ‡ Clu19 broke into 2 separate pieces (α & β) †3 μm fragment, possibly too small for PAHs analysis § Clu37 fractured into 4 pieces (α, β, χ, δ)

THE ANATOMY OF A CLUSTER IDP (I): CARBON ABUNDANCE, BULK CHEMISTRY AND MINERALOGY OF FRAGMENTS FROM L2008#5; K.L. Thomas[1], L.P.Keller[2], W. Klock[3], J. Warren[1], G.E. Blanford[4], and D.S. McKay[5] [1]Lockheed, 2400 Nasa Rd.1 Houston, TX, 77058, [2]MVA Inc., 5500/Suite 200 Oakbrook Pkwy, Norcross, GA 30093 [3]Institute fur Planetologie, Wilhelm-Klemm-Str.10, 4400 Munster, Germany, [4]University of Houston, Clear-Lake, Houston, TX 77058, [5]NASA/JSC, SN, Houston, TX 77058.

Chondritic anhydrous interplanetary dust particles (IDPs) are among the most pristine solar system materials known, and despite their small size, have been intensely studied. Multidisciplinary studies of IDPs have traditionally been restricted to cluster particles, where individual fragments of the same cluster are allocated to several researchers. In this manner, different analyses can be performed on essentially the same material, assuming that individual fragments are representative of the whole cluster. Our preliminary work, however, indicated that fragments from cluster particles can show mineralogical and chemical heterogeneities at the 10 μm scale [1].

The objective of this study was to determine whether or not cluster particles are sufficiently homogeneous to enable observations from one fragment of the cluster to be extrapolated to the entire cluster. Here we report on the results of a consortium study of the fragments of a large cluster particle. Multiple fragments from one large cluster were distributed to several research groups and were subjected to a variety of mineralogical and chemical analyses including: SEM, TEM, ion probe, SXRF, noble gas measurements, and microprobe laser mass spectrometry of individual fragments. The mineralogy and bulk chemistry of the cluster fragments are discussed below and the trace element geochemistry, isotopic data, and other results are given in a companion abstract [2].

Methods We were allocated ~95% of the fragments from cluster L2008#5 (originally ~40-50 μm in diameter), which contained many large fragments and fines: three fragments are ~15 x 15 μm, six are ~12 x12 μm, 30-40 range from 5-10 μm in diameter, and many fragments (called fines) were <5 μm in diameter. We have determined bulk compositions for elements with Z > 5 of 53 particles from one large cluster. Our procedures and extensive analytical checks for quantitative SEM EDX light element analysis are described in detail elsewhere [3]. Following the chemical analysis, several of the particles were embedded in epoxy, thin sectioned using an ultramicrotome, and examined in the TEM.

Chemistry We analyzed 53 fragments from cluster L2008#5 for major, minor, and light elements (carbon and oxygen). The cluster average and major element ranges for all fragments are shown in Fig. 1. The average element abundances were found to be chondritic (within 2xCI) for L2008#5 with the exception of Na and P which were ~4xCI and 5xCI, respectively. Large ranges for major elements C, Si, Mg, S, Fe, and O suggest that compositional differences exist (Fig. 1). Only 24 (45%) of the analyzed fragments have the "same" composition for major elements (C, O, Mg, Si, S, Fe) within one standard deviation. Of the 29 remaining fragments, 31% have significantly higher Fe or Fe and S with lower O; 17% have significantly higher C.

Mineralogy Table 1 lists mineral assemblages found in large fragments and fines from cluster L2008#5. Fragments have been classified according to the most abundant mineral phase. A variety of mineral phases are present in this cluster particle and minerals with similar compositional ranges are found in large fragments and fines. For example, olivine compositions range from Fo 57-99 in large fragments and from Fo 66-98 in fines. However, several olivine-dominated fragments have very narrow ranges of olivine compositions which differ from one fragment to another. Pyroxenes range in composition from enstatite to those high in Ca. Amorphous material, such as glass and carbonaceous material, is present in some fragments. Glass compositions range from Si-rich to feldspathic with minor amounts of Mg and Fe occasionally present; glass regions can have either a smooth or a vesicular texture. Amorphous, C-rich material is observed in particles with C >3xCI (~11 wt.% C). Mineral grain sizes vary from fragment to fragment: some fragments are predominantly coarse-grained (μm in diameter), some are predominanty fine-grained (<50 nm in diameter) and

some contain a mixture of coarse and fine grains. Partial magnetite rims are present on some fragments, indicating they were heated during atmospheric entry [4]. The relative range of mineral abundances in the large fragments is also duplicated in the fines.

Discussion Cluster L2008#5 is composed mainly of chondritic (within ~2 x CI) fragments that differ significantly in mineralogy (Table 1). Non-chondritic fragments (e.g., those dominated by sulfides or magnetite) make up 25% of this cluster. A representative sampling of material from the cluster for mineralogical and chemical analyses would require analyses of a minimum of four large fragments. Attempts to extrapolate analyses from one fragment to an entire cluster will be misleading if all cluster particles show similar levels of heterogeneity as L2008#5.

References: [1] Thomas K.L. *et al.* (1993) *Meteoritics* **28**, 448. [2] Thomas K.L. *et al.* (1994) This volume. [3] Thomas K.L. *et al.* (1993) *GCA* **57**, 1551. [4] Keller L.P. *et al.* (1992) *LPSC* **23**, 675.

Figure 1. Mean values and range of element abundances for 53 fragments from cluster L2008#5. Chemical heterogeneity of fragments is shown by the ranges for major elements (bars); mean values are represented by lines located to the right of the bars.

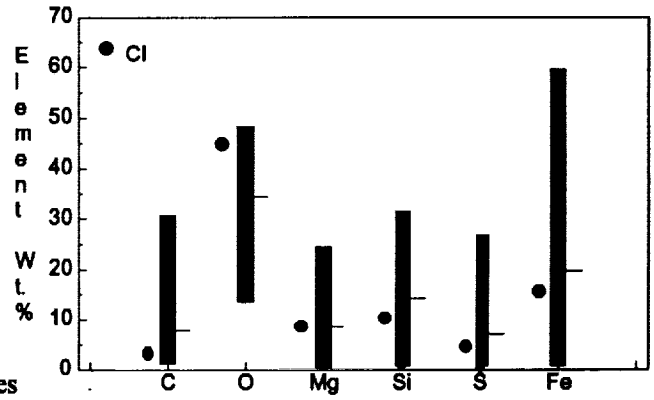

Table 1. Mineralogy of 10 large fragments and fines from cluster L2008#5. Fragments have been classified according to the most abundant mineral phase. Ranges of mineral compositions are given for each group (e.g., olivine-dominated) as a whole, but some individual fragments have narrow ranges of mineral compositions.

Fragments (> 5 μm)	**Fines (<5 μm)**
Olivine-Dominated (4 fragments)	**Olivine-Dominated (3 fragments)**
* Fo 57-84, Glass, Enstatite, high Ca pyroxene, Fe-sulfide with Ni; 3 have magnetite rims. Coarse, fine, and mixed grain sizes.	* Fo 78-86, Glass, Enstatite, high Ca pyroxene, Fe-sulfide with Ni; all have magnetite rims. Mostly coarse and mixed grain sizes.
Pyroxene-Dominated (3 fragments)	**Pyroxene-Dominated (2 fragments)**
* Enstatite, glass, few Fo 88-95, Fe-sulfide with Ni, Carbonaceous material; 2 have magnetite rims. Mostly fine and mixed grain sizes.	* Enstatite, glass, high Ca pyroxene, Fe-sulfide with Ni; all have magnetite rims. Coarse and fine grain sizes.
	Olivine-Pyroxene Mix (1 fragment)
	* Fo 66, Glass, Enstatite, few fine-grain aggregates; Magnetite rim, mixed grain sizes.
FGA (Fine-grain aggregate) Dominated (1 fragment)	**FGA Dominated (1 fragment)**
* Fine-grain aggregates, Fo 79-99, enstatite, glass, Abundant Fe-sulfides with Ni; magnetite rim. Fine grain sizes.	* Fine-grain aggregates, Fo 98, Enstatite, Augite, Fe-sulfide; no magnetite rim, fine grain sizes.
Others (2 fragments)	**Others (3 fragments)**
*Large Fe-sulfide, few Fo 65-76, No magnetite rim, coarse grain sizes.	* 2 Large magnetites, Fo-68-91, few Fe-sulfides with Ni, 1 has lg. kamacite; no magnetite rims, coarse grain sizes.
*Large magnetite grain, few fe-sulfides with Ni, Si-rich glass; magnetite rim, coarse grain sizes.	*Large Fe-sulfide with Ni, glass, kamacite, ferrihydrite; magnetite rim, coarse grain sizes.

IDA: TOPOGRAPHY, SLOPES AND GROOVES: P. Thomas, J. Veverka, Cornell University, M. J. S. Belton, KPNO, and Galileo Imaging Science Team

Topography, slopes, and surface features seen on 243 Ida suggest a single coherent body with only minor structural control on its form and surface. The presence of regolith is indicated by ejecta blocks, crater morphologies, and morphology of linear depressions. Topographic slopes are all below angle of repose values; those near 30° show signs of downslope movement of regolith. Ida's shape is less influenced by planar structural features than is Gaspra's.

a) Size and Shape

Because only about 30% of Ida is visible in the data received, overall size and shape measures are only approximate. The longest visible dimension is 55 km. The images can constrain a part of the shape from limbs and terminators, and a swath about 8 km wide is covered in stereo with a convergence angle of 10°.

Despite the partial coverage, several characteristics of the shape are apparent. Ida qualitatively appears to be one object. Its elongation is consistent with the groundbased predictions of a/b = 1.82 and b/c of 1.15 [1]. There is a decided asymmetry along the long axis, a condition nearly universal for well-imaged small objects (Phobos, Deimos, Amalthea, Gaspra).

Ida does not appear to have areas as flat as some on Gaspra. Most morphology can be related to concave crater forms of different sizes and ages.

b) Topography and Slopes

The elongate form and large craters give the impression that Ida may have some very steep slopes. Slopes relative to radii from a common center tell little of the relation of surface normal orientation to local gravitational acceleration. The partial shape model can be used to calculate gravity vectors and surface normals, using assumptions of the mean density and approximate size of the hidden part of Ida. Techniques are described in [1].

A 10 km crater lies in the zone of stereo coverage. Figure 1 shows two cross sections of dynamic topography on the model. Maximum model slopes in this crater are about 18°. Maximum calculated slopes in areas near limbs are 27°. The density of the asteroid affects these values slightly, but even for densities of 8 gm/cm^3, the slopes would nearly all be well under 30°. The uncertainties in the shape of Ida are not sufficient to alter significantly the effective slope calculations. The interior of one 12 km crater has calculated slopes near 30°, and also shows signs of downslope movement in elongate depressions (craters, slumps?).

c) Grooves

Ida displays a variety of linear features ranging from subtle lineations to substantial linear depressions, here called grooves from their (first order) similarity to those on Phobos and Gaspra. Lengths of continuous segments reach 4 km. Widths are typically 150-200m, maximum widths are about 350 m. Depths appear to be small fractions of the widths, or less than a few tens of meters. Margins of the grooves range from fairly sharp continuous parallel crests to beaded outlines. The forms thus range from strings of coalescing pits to simple elongate troughs. These features are comparable in morphology, if not in length or pattern,

to many grooves on Phobos. They do not show clusters of intersecting members as is prominent in one area of Gaspra and common on Phobos.

The grooves trend at a variety of directions relative to calculated local slopes (Figure 2). They are substantially wider than the blocks visible on the surface, and blocks are not seen within or at the ends of the grooves, so they do not appear to be boulder tracks.

The similarity of the forms to some of those seen on Phobos and Gaspra, suggests similarities in origins, although the patterns of those on Ida are more difficult to relate to structural features of the asteroid. Their smooth forms occurring on a low gravity object suggest the presence of loose material. The material would have to be at least 20 m thick in places to show the observed depths of the grooves.

References: [1] Binzel, R. et al. (1993) *Icarus*, submitted. [2] Thomas, P. C. (1993) *Icarus* **106**, 224.

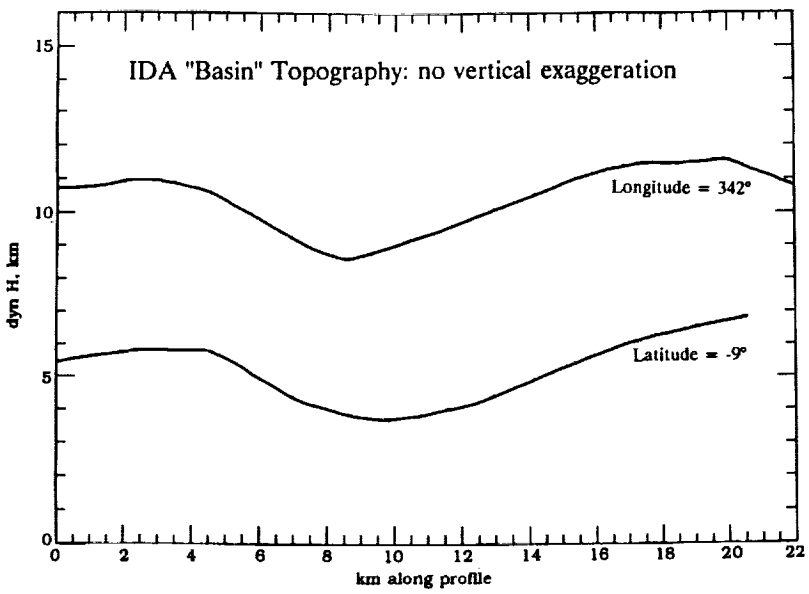

Figure 1. Cross sections of calculated topography in 12 km crater. Shape is controlled from 18 points measured stereoscopically; the dynamic topography is calculated using a mean density of Ida of 3.5 gm/cm^3, and represents the topography relative to local gravity vectors [2]. There are no slopes approaching angle of repose values in this depression.

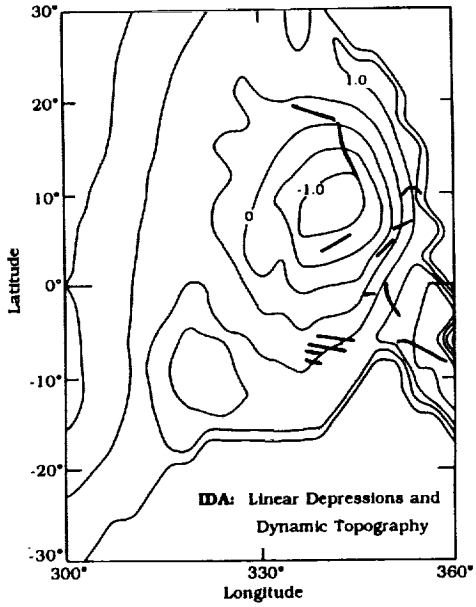

Figure 2. Locations of most prominent grooves superposed on dynamic topography in area of best shape model control. The dynamic topography is the best representation of local slopes relative to effective gravity.

DEFORMATION OF LARGE BOLIDES DURING ATMOSPHERIC PASSAGE: COMPARISON OF SPH AND ANALYTIC MODELS

P.J. Thomas[1], L. Brookshaw[2], and G. Starkey[1]

[1]Department of Physics and Astronomy, University of Wisconsin, Eau Claire, WI 54702 USA; [2]Physics Department, University of California, Davis, CA 95616 USA.

Extraterrestrial objects traversing planetary atmospheres at hypersonic speeds are subject to atmospheric stresses that may easily be sufficient to produce failure in the material from which the objects are composed. Subsequent deformation is controlled by the differential aerodynamic pressures between the object's leading and trailing faces. The leading face of the object is subjected to pressures $\sim C_D \rho_a v^2/2$ (the stagnation pressure), where C_D is the drag coefficient, ρ_a the atmospheric density and v the speed of the object. The trailing face essentially experiences a vacuum, as air does not have sufficient time to fill the void behind the object[1]. Pressures on the side of the object are small in comparison with this pressure difference, so the object deforms in an "pancaking" fashion. This deformation, of course, increases atmospheric drag and so leads to an explosive fragmentation[2]. We report comparisons between analytical and numerical models for this process.

Deformation, leading to explosive fragmentation, accounts for many airburst explosions observed for bolides in the Earth's atmosphere[3], and an analytic model of bolide deformation have been applied to the Tunguska explosion of 1908[4]. The model has also been applied to the upcoming impact of the fragments of comet Shoemaker-Levy 9 with Jupiter[5]. The analytic model represents deformation of the bolide, once the stagnation pressure exceeds the material strength, as the radial spreading of a strengthless cylinder into a squatter version of itself. Hydrostatic equilibrium is assumed throughout the entire body, which may not be correct for objects sufficiently large that the sound speed travel time is comparable to the duration of passage through the atmosphere (objects with diameters larger than $\sim$ 100 m). Furthermore, material behavior is represented by a single strength parameter and material density and compressibility, which may play a significant role in bolide deformation, is ignored[6].

Given the numerous assumptions of the analytic model, it is of interest to compare the results of this model to a more complete numerical simulation of bolide deformation and fragmentation. A Smoothed Particle Hydrodynamics (SPH) model has been constructed to represent the passage of a bolide through an atmosphere. The atmosphere is modeled as a perfect gas, while the bolide physical properties are calculated using the Los Alamos SESAME EOS data base. The SESAME data base allows a more complete representation of material behavior than for the simple analytic model, including compressibility.

Simulations have been performed for a stony, iron and cometary bolides traversing the Earth's atmosphere. The model does self-consistently calculate temperatures of the atmosphere and the bolide, although ablation is not considered in our calculations. Our results to date for objects with low material strengths (such as comets) show pancaking of the bolide in a similar manner and extent to that assumed by the analytical model. A sample of this behavior is illustrated in Figure 1. This result is in contrast to that reported by similar numerical simulations[7], which imply a dominant role for aerodynamic erosion from the leading edge of the bolide, leading to a conically deformed bolide. While such erosion is seen in these simu-

lations (see Figure 1(b)), its effect is small compared to the overall deformation, which produces a global flattening of the bolide.

We are currently examining the role for various forms of deformation (e.g. pancaking vs. leading-edge erosion) for a range of bolide speeds and compositions. In addition, the numerical model is currently being extended to include elastic behavior, by the incorporation of the Grady-Kipp model adapted to Lagrangian hydrocodes by Melosh *et al.*[8].

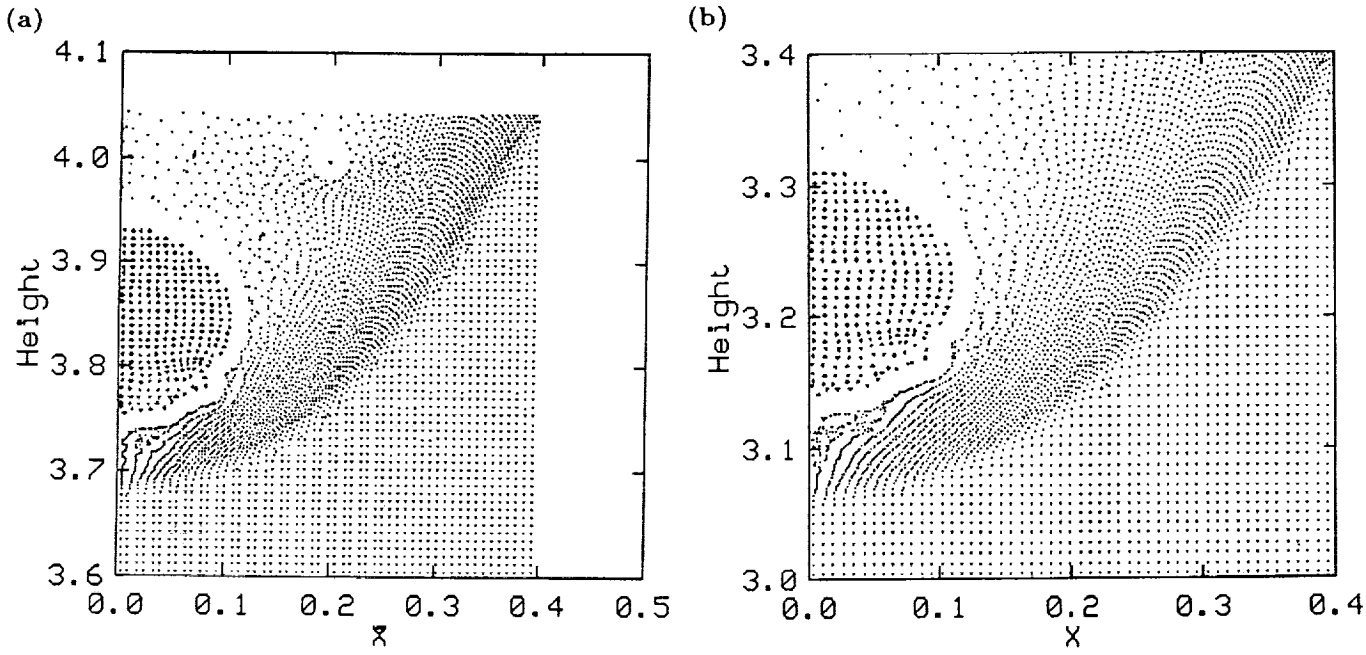

Figure 1. SPH simulation of the vertical entry of a 200 m diameter comet through the Earth's atmosphere. Initial speed of the comet was 5 km/sec. The simulation is shown at (a) 0.23 s, when the comet's vertical axis has been reduced to 83% of its initial value and (b) 0.45 s, when the comet's vertical axis has been reduced to 78% of its intial value.

References:

(1) Seiff, A., (1962) *Gas Dynamics in Space Exploration*, 19-32 (NASA SP-24). (2) Baldwin, B. and Y. Sheaffer (1971) *J. Geophys. Res.*, **76**, 4653-4668. (3) Passey, Q.R. and H.J. Melosh (1980) *Icarus*, **42**, 211-233. (4) Chyba, C.F. *et al.* (1993) *Nature*, **361**, 40-44. (5) Sekanina, Z., (1993) *Science*, **262**, 382-387. (6) Ivanov, B.A. *et al.* (1992) *J. Geophys. Res.*, **97**, 16,167-16,181. (7) Svetsov, V.V. *et al.* (1994) *Icarus*, (submitted). (8) Melosh, H.J. *et al.* (1992) *J. Geophys. Res.*, **97**, 14,735-14,759.

TEACHING PLANETARY SURFACE PROCESSES AND MAPPING TO ADVANCED 5TH AND 6TH GRADE STUDENTS: Pam Thompson, Scott Murchie, Robert Herrick, Ben Schuraytz, and Graham Ryder, Lunar and Planetary Institute, 3600 Bay Area Boulevard, Houston TX 77058-1113.

For the past four semesters, Lunar and Planetary Institute staff members have been teaching a course on "Exploring the Solar System" in the Alpha Program for Gifted and Talented Students of the Clear Creek Independent School District, Houston. In developing the course, we have concentrated on ways to explain "what we know and how we know it—or *think* we know it" to our 5th and 6th grade students. Classes are developed and taught by many of the LPI staff scientists as well as outside scientists invited to share their expertise. The course as a whole is designed to give students a broad background in the space program and spacecraft and an appreciation of the place of humans in the universe—in time and space. Space science is emphasized, including instruments, observations, and measurements. Two of the threads woven throughout the 12-week course involve discovering the basic processes that create planetary surfaces and mapping the surfaces themselves to decipher how these processes have occurred over time. Our educational exhibit will showcase classroom laboratory simulations of surface processes and classroom mapping projects of inner and outer planets.

Students in grades 1-6 are selected by the district to participate in Alpha. Alpha students in grades 4-6 may choose from a catalog of courses ranging from creative writing to computer programming to ecology to marine biology. "Exploring the Solar System" is the only planetary science course offered at present. We have limited classes to 5th and 6th graders to ensure that students have a similar math background, but many of the lessons have proved adaptable to other age groups who have participated in workshops at LPI. The 1-semester class has been fully subscribed (18 students) since the second semester. Classes are three and a half hours, once a week, and are held at the Institute.

Several of the classes concentrate on planetary surface processes. Our exhibit will feature classroom labs that allow students to simulate impact cratering, volcanism, and fluvial erosion using readily available materials. Planetary images are used to compare the surfaces created in the labs with features on the planets themselves. The impact lab introduces concepts of projectile velocity, mass, and density as well as target strength, and shows how impact provides a probe of material beneath a surface. The volcanism lab shows (a few) different eruption styles and emphasizes how terrains are resurfaced. The impact and volcanic experiments are combined to demonstrate how a complex stratigraphy is built up over time and how subsequent impacts may reveal some of this stratigraphy. Determining "what came first," also stressed in mapping exercises, is emphasized. Fluvial erosion is demonstrated with a stream table and the surfaces created are compared with Viking images of Mars.

Mapping exercises complement the surface processes experiments. We use a Lunar Orbiter map of the Apollo 15 site (inspired by a short course taught by R. Greeley and P. Schultz [1]) to introduce photogeologic mapping. A worksheet guides students through a simple mapping project introducing the geologic unit, contact, and the concept of superposition. A simple "sample" return simulation using terrestrial analogs of lunar rocks introduces a few simple rock and mineral types, and, using a geologic map of the Apollo 15 site and their mapping experience, students are able to determine what the samples are, how they may have formed, and what their relative ages are.

Extrapolation of the technique to Mars allows students to arrive at the relative age of martian channels and to discover that the channels record an ancient period in martian history when the climate was much different than it is now.

In addition to surface processes and mapping, the course includes classes in remote sensing techniques, introducing the concept of radar imaging with Magellan data and a hands-on simulation of radar mapping, and discovering how composition can be determined through visible and near-infrared spectroscopy. Computer labs in image processing round out the remote sensing theme.

Many of the concepts presented are integrated at the end of the course when the students plan an exploration program for Mars. Drawing on their geologic knowledge and the different exploration techniques introduced during the semester, student teams define a science objective and plan a strategy to achieve it within strict cost and time limits.

REFERENCES: [1] Activities in Planetary Geology for the Physical and Earth Sciences, *NASA EP-179,* 1977.

MAGELLAN MISSION PROGRESS REPORT: Thomas W. Thompson and Magellan Flight Team, Jet Propulsion Laboratory, California Institute of Technology, Pasadena, California

The Magellan spacecraft was launched from Cape Kennedy on May 4, 1989 and was inserted into orbit around Venus on August 10, 1990. The Magellan science objectives are (1) improve the knowledge of the geologic history of Venus by analysis of surface morphology and (2) improve the knowledge of the geophysics of Venus, principally its density distribution and dynamics. The first objective was supported by radar imaging, altimetric and radiometric mapping of the Venusian surface which commenced on September 15, 1990 and continued until September 15, 1992 (mission cycles 1,2,3). Some 98 percent of the surface has been mapped with radar resolutions on the order of 120 meters. The second objective is still being pursued. High resolution Doppler tracking of the spacecraft in elliptical orbit from September 16,1992 until May 24, 1993 (mission cycle 4) provided gravity observations of Venusian near-equatorial regions. The Magellan orbit was circularized in the summer of 1993. Now, high resolution Doppler tracking of the spacecraft in near-circular orbit (which commenced in August 1993) is providing gravity measurements of all of Venus.

The two years of radar and radiometric observations of Venus constitute three mission cycles. The first misison cycle from mid-September 1990 through mid-May 1993 emphasized the acquisition of radar images from the left side of the orbit, from over the North pole to as far south as possible. Some 84 percent of the surface was mapped in this first mission cycle. The second mission cycle from mid-May 1991 through mid-January 1992 acquired radar images from the right side of the orbit with the goal of mapping the south polar regions of Venus. The third mission cycle from mid-January through mid-September returned to left-side imaging with the goal of stereo imaging. Unfortunately, a transponder failure early in January 1992 curtailed data acquisition throughout the third mission cycle. However, some 24 percent of the surface was observed in this third mission cycle and 98 percent of the Venusian surface was imaged in total.

The processing of the radar data by JPL was completed in late 1993. Over 1200 radar image products are available as analog photographs and digital compact disks (CD-ROMs) at the National Space Science Data Center (NSSDC), Goddard Space Flight Center, Greenbelt, Maryland. In addition, the altimetric and radiometric data products from MIT and the cartographic maps from USGS are available at the NSSDC. The altimeter and radiometer data produced by Peter Ford and Gordon Pettengill at MIT are available as images as well as digital data on 17 CD-ROMs. Also, the United States Geological Survey (USGS) in Flagstaff, Arizona is producing a second generation of radar mosaics that should be available soon. A useful contact for these Magellan data products is the Planetary Data System (PDS) Geosciences Node at Washington University, St. Louis, Missouri.

The first set of high-resolution gravity observations were obtained between late-September 1992 and late May 1993. Some 950 orbits were obtained while Magellan was in an elliptical orbit with a periapsis near 175 kilometers and an apoapsis near 8,000 kilometers. These data were reduced to a 60 degree-by 60-degree harmonic field by Bill Sjogren of JPL. Magellan gravity products, line-of-sight acceleration profiles and spherical harmonic fields for this cycle-4 gravity data are at NSSDC also.

The Magellan spacecraft was aerobraked from late May through early August 1993 by lowering perapsis to about 140 kilometers. During aerobraking the atmospheric drag at periapsis removed a small amount of orbital energy on each pass. The apoapsis was lowered from 8,000 kilometers to 500 kilometers. Magellan now orbits Venus with a near-circular orbit which passes over the polar regions with altitudes of a few hundred kilometers. High resolution Doppler tracking of the spacecraft now provides gravity measurements with near uniform resolutions.

MAGELLAN MILLION PROGRESS REPORT: Thompson T.W. et al.

Magellan has also provided information about the Venusian atmosphere. The high effective isotropic radiated power of the Magellan downlink radio system enabled the deepest probing of the Venusian atmosphere by occultation. Refractivity and absorptivity profiles down to 35 km at 3.8 cm wavelength and down to 34 km at 13 cm wavelength have been obtained near 65-deg North with a solar zenith angle of 108-deg. This in turn yielded vertical profiles of temperature, pressure and density as well as H2SO4 abundances.

Atmospheric drag measurements, particularly during aerobraking, have extended those originally obtained with the Pioneer-Venus spacecraft and have validated the Venus International Reference Atmosphere (VIRA) model. Magellan cycle-4 observations at 180 km periapsis detected a 4-day oscillation in the day-side thermosphere while nightside observations during aerobraking and into mission cycle-5 showed a 5-day oscillation. The new Magellan observations at low solar minimum complement the Pioneer-Venus drag observations during high solar activity. Drag torques during Magellan near-circular orbit will enable extension of these type of atmospheric observations to a larger range of latitudes and will provide these measurements at a relative rapid rate of once every 95 minutes.

Also the high effective power of the Magellan downlink system enables a number of radio and radar experiments. Scintillations in the solar atmosphere close to the Sun are observed during Venus superior conjunctions when the spacecraft passes near the solar disk. Also, bistatic radar observations are being performed by directing the downlink signals toward the surface and observing the echoes with Deep Space Network (DSN) antennas. These "extra" radio and radar experiments as well as the atmospheric drag and occultation observations demonstrate that Magellan is producing useful scientific data beyond that originally specified in the mission objectives.

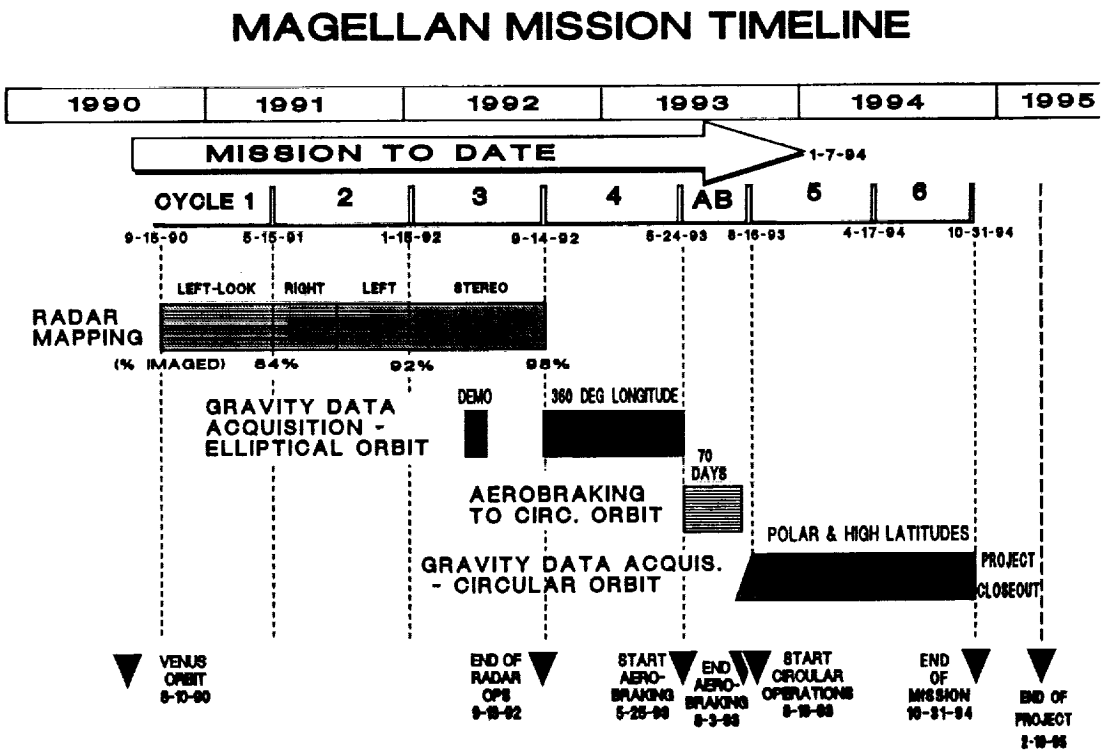

Figure 1 Magellan Mission Timeline

A SIMPLE MODEL FOR PARTICLE SUPPORT IN PYROCLASTIC FLOWS. G. D. Thornhill, Department of Geological Sciences, Brown University, Providence, RI 02912.

Introduction.

A simple model of radial flow, assuming an inviscid fluid, has been used as a basis for examing the support of particles in the early stages of pyroclastic flows, in order to characterise the initial particle sorting process which results in the separation of the flow into a dense basal portion, and a more dilute, frequently convective upper part. The model does not account for any fluidisation in the flow at present. The work represents a preliminary attempt at modelling the evolution of pyroclastic flows, including the particle sorting characteristics, which are important for comparison with field evidence. Results for various combinations of initial parameters are given. Future work will concentrate on tracing particle trajectories within the flow, improving the formulation by addition and examination of other processes, and then modelling the dense part of the flow as it develops from these initial stages.

Method.

The model is based on a simple Navier-Stokes formulation, assuming an inviscid fluid, with a density reflecting the bulk density of the gas and fine particles. An equation of continuity relating the flow velocity, thickness, and radial distance of the flow with the initial quantities is also used [1]. The model also assumes steady-state conditions, so no time-dependence of initial conditions is permitted.

The numerical integration was carried out using a Runge-Kutta 4 numerical integration scheme, and the results checked against the analytical solution for the case with 0° slope. A suitable integration step was selected by checking for convergence as the integration step was reduced.

The particle support is calculated by assuming spherical particles, by calculating the terminal velocity of each particle, and relating this to the friction velocity within the turbulent flow [2,3].

The density of the flow is assumed constant, both with radial distance, and with depth in the flow, although both these conditions will become less valid with distance from the vent, as particles begin to settle out. The effect of various factors on particle support in theearly stages of the flow have been examined, including the initial velocity, underlying slope, particle concentration, and initial temperature (the latter two control the density of the flow).

Results.

The initial parameters will depend on the genesis of the flow from either a collapsing plinian column, or as a low fountain, feeding the flow continuously [1].

In figure 1, the flow velocity as a function of distance from the vent for different particle concentrations (given as mass fraction of particles in the flow). The main effect of the particle concentration is in the density of the flow, which has values of 1.775 kg/m^3, 3.544 kg/m^3 and 7.063 kg/m^3 for the three cases shown. The starting conditions for these examples were an initial velocity of 200 m/s, initial flow thickness of 500m, initial temperature of 1000K, and a slope of 10°.

The velocity initially increases slightly as the flow runs down the slope, but begins to decelerate as the flow thins and the drag coefficient increases as it spreads away from the vent. After the initial rapid deceleration, the velocities decrease more slowly.

In figure 2, the maximum particle diameter (assumed to be pumice, density 1000 kg/m^3) as a function of distance from the vent is plotted. Naturally, the higher density flow supports larger diameter particles, an effect which is augmented by the higher velocity maintained by the denser flow. The denser, faster flow can support particles of 3cm diameter at its peak velocity, compared to 5mm diameter particles in the least dense flow.

Conclusions.

A simple model for calculating particle support in an inviscid, turbulent flow has been developed. The model allows for variation of the initial flow condtions, and calculates directly the maximum size particle supported for any given flow velocity. The effect of parameters such as the particle concentration in the flow on the ability of the flow to carry particles can be investigated, in a preliminary attempt to use particle size characteristics in pyroclastic flows as an indicator of emplacement conditions in a quantitative way.

References. [1] Sparks, R. S. J., Wilson, L., and Hulme, G. (1978) JGR 83, p. 1727. [2] Shreffler, J. H., (1975) Bound. Layer Meteor. 9, p. 191. [3] Wilson, L., Huang, (1979) Earth. Plan. Sci. Lett. 44 p. 311.

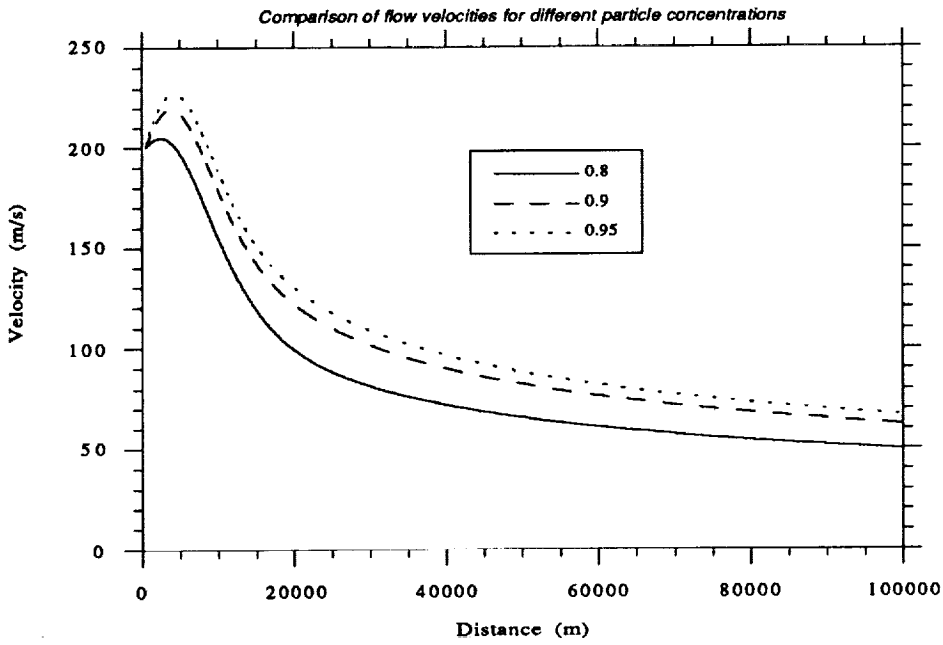

Fig. 1. Graph showing flow velocity as a function of distance for three values of particle concentration (given as a mass fraction). The corresponding densities are 1.775 kg/m^3, 3.544 kg/m^3 and 7.063 kg/m^3.

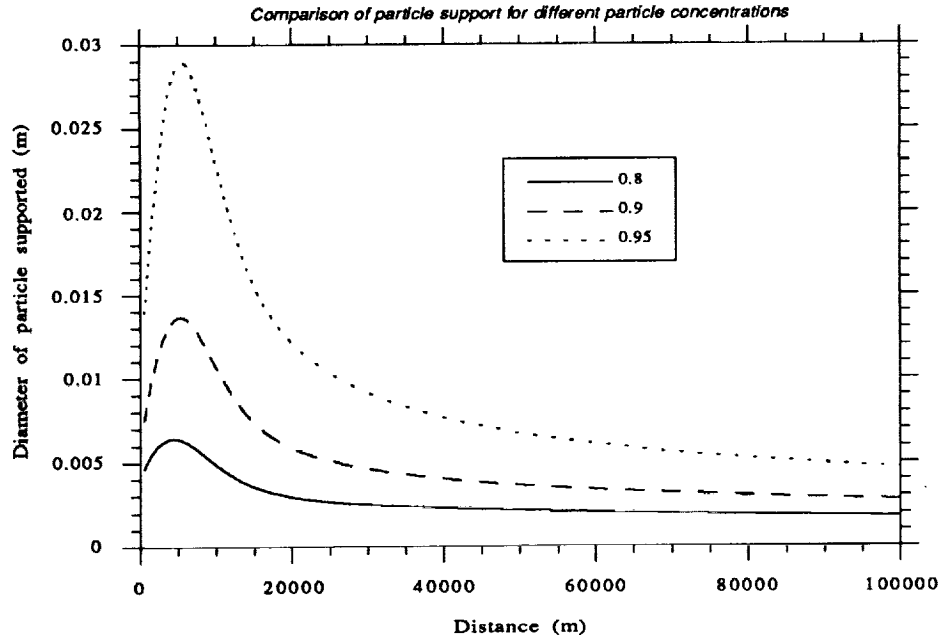

Fig. 2. Graph showing diameter of maximum pumice particle supported (density 1000 kg/m^3) as a function of distance for three particle concentrations. The corresponding flow densities are the same as given for fig. 1.

PROPERTIES OF LAVA FLOWS ASSOCIATED WITH CORONAE IN S.E. APHRODITE TERRA, VENUS; Kerry-Anne Tomkinson, Travers Morgan, Cantelupe Road, East Grinstead, Sussex, U.K. & Lionel Wilson, Environmental Science Division, Institute of Environmental and Biological Sciences, Lancaster University, Lancaster LA1 4YQ, U.K.

Abstract: Morphological properties have been determined for 59 lava flow units found in association with three coronae in S.E. Aphrodite Terra as part of a larger study of the tectonics and volcanics of the area around (215°E, 15°S). Lengths and areas of flows were measured directly on Magellan images and, in most cases, flow thicknesses were inferred from altimetry data in order to obtain volume estimates. Attempts were made to identify flow sources and,wherever possible, to deduce flow directions . Flow length distributions were examined and showed some evidence of compound flow fields formed at near-constant effusion rates in long-duration eruptions. The lava effusion rates corresponding to commonly occurring flow lengths were found (1000-5000 m^3/s), and the flow volume estimates (a few to a few tens of km^3) were used to deduce eruption durations (weeks to months).

Background: As part of a wide-ranging study of the tectonics and volcanics of S.E. Aphrodite Terra [1], systematic morphological data were obtained on all of the identifiable lava flow units associated with three coronae. These features, centered at (215.5°E, 15.2°S), (211.2°E, 12.1°S) and (214.5°E, 9°S), were studied in detail, and are labelled C1, C2 and C3 in what follows.

Observations: Most of the lava flow units associated with these coronae have their sources in radial features which we assume to be the surface expressions of dikes [2], and most of them flow radially away from the centre of the corona, often terminating within the circumferential moat. Lengths and planimetric areas were measured for 59 clearly identifiable flow units, and thicknesses were estimated to lie between 10 and 25 m for the majority of the flows, based on their minimal signatures in the altimetry data. There are several examples of flow units with source vents which appear to be located outside the outer edge of the moat. These units flow towards the centre of the corona, again being channeled into the moat, and the source of one of them appears to be a fissure elongated in a non-radial direction. The length of the fissure in this case is somewhat greater than the width of the flow into which its lava is channeled, a rare instance which allows a good estimate of the length of the active fissure (~8 km) to be made. Other examples, though less well defined, seem to have similar lengths, certainly ~ 5 km.

Analysis: Histograms of the length distribution were drawn up for all of the flows associated with each of the coronae in turn (Fig. 1). These show multiple modes, a phenomenon which may imply [3, 4] that the flows belong to compound flow fields formed over long periods by eruptions which are maintained at roughly constant rates. Under these circumstances, an initial flow unit advances until it reaches its cooling-limited length; a break-out then occurs, at the front or side of the original unit or from the main vent, and forms a second unit of similar length. If the eruption continues for a great enough period, many cooling-limited flows may form in this way. Break-outs from the fronts of earlier flows may not be recognised as such, due either to the finite image resolution or to local variations in radar incidence and emergence angles caused by topographic undulations. Hence, two (or three, etc.) units may be misinterpreted as a single unit twice (or three times, etc.) as long, leading to the multiple modes in the length distribution. Examination of the histograms with this in mind suggests that the fundamental cooling-limited lengths for flows at all three coronae probably lie in the range 50 to 150 km.

These lengths can be used to deduce lava effusion rates at the vent using a model [5] of the cooling-limited flow emplacement process, provided a value is assumed for the mean slope of the ground down which the flows move. Using a value of ~0.25°, the effusion rates corresponding to the above flow unit lengths lie in the range ~1000 to ~5000 m^3/s and are given in Table 1, together with the rates for lengths up to 300 m, the longest apparent flow length measured. These values are high when compared with eruption rates of up to a few hundred m^3/s from modern [6] and recent [7] mafic fissure eruptions on Earth. However, given the ~5 km lengths of the eruptive fissures observed for these flows, the discharge rates per unit outcrop length of fissure would lie in

LAVA FLOWS ASSOCIATED WITH CORONAE: Tomkinson, K.-A. & Wilson, L.

the range 0.2 - 1 m^3/s per metre of fissure length, much closer to terrestrial values [8] and implying quite similar magma velocities through the dyke systems feeding the surface vents [9]. The main differences between these eruptions on Venus and common terrestrial eruptions would then lie in the factors controlling the lengths and widths, at right angles to the direction of magma motion, of the dykes. These factors are probably traceable to the stress conditions around, and the excess fluid pressures within, the magma reservoirs supplying the eruptions [2]. Most of the flows mapped have volumes in the range of a few to a few tens of km^3; division of these volumes by the eruption rates implied by the flow lengths yields eruption durations from a few weeks to a few months.

Conclusions: Even allowing for the complications engendered by the formation of compound lava flow fields, it is hard to escape the conclusion that the fissure eruptions which fed the flows associated with the three coronae examined here took place at relatively high effusion rates, at least 1000 to 5000 m^3/s, from fissure vents several km long. The chief cause of these high rates is most likely to be the magma reservoir pressure/stress conditions defining the geometries of the feeder dykes.

References: [1] Tomkinson, K.-A. (1993) unpubl. M.Sc. thesis, Geophysics Dept., Univ. of Newcastle-upon-Tyne, U.K. [2] Parfitt, E.A. & Head, J.W. (199?) Icarus ? [3] Head, J.W., Magee-Roberts, K., Wilson, L. & Pinkerton, H. (1993) LPSC XXIV, 627. [4] Wilson, L., Pinkerton, H., Head, J.W. & Magee-Roberts, K. (1993) LPSC XXIV, 1527. [5] Pinkerton, H. & Wilson, L. (1994) in press, Bull. Volc. [6] Wolfe, E.W., Neal, C.A., Banks, N.G. & Duggan, T.J. (1988) USGS Prof. Paper 1463, 1-98. [7] Laki, Toby [8] Heslop, S.E., Wilson, L., Pinkerton, H. & Head, J.W. (1989) Bull. Volcanol. 51, 415. [9] Head, J.W. & Wilson, L. (1986) JGR 91, 9407.

Acknowledgements: K-AT thanks the University of Newcastle-upon-Tyne, U.K. for logistic support in this work, and both authors thank J.W. Head and E.A. Parfitt at Brown University for facilitating access to Magellan imaging and altimetry data.

Table 1: Lava effusion rates (dense rock equivalent volume flux) corresponding to flow lengths relevant to the present study (see text for details).

Lava flow unit length in km:	50	100	150	200	250	300
Lava effusion rate in m^3/s:	1400	3280	5380	7640	10040	12540

Figure 1: Histogram of lava flow lengths for each of the three coronae studied.

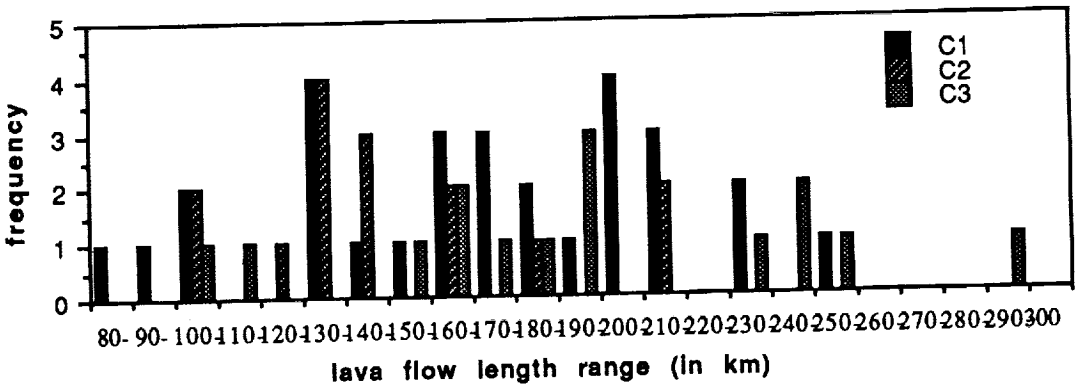

SEMI-OBJECTIVE DETERMINATION OF LITHOLOGIC END-MEMBERS IN A GEOLOGIC ENVIRONMENT (SPECTRAL MIXTURE ANALYSIS) Stefanie Tompkins, John F. Mustard, Carlé M. Pieters, Donald W. Forsyth, Dept. Geol. Sci., Box 1846, Brown University, Providence, RI 02912

Introduction: Spectral mixture analysis (SMA) has been shown to be a powerful tool for the analysis and geological interpretation of planetary multispectral images (1-3). The underlying assumption of SMA is that each pixel on the surface is a physical mixture of several components, and the spectrum of the mixture a linear combination of the end-member reflectance spectra. The spectral variability of a scene is thus modeled as a linear combination of a small number of spectral end-members (which are usually expected to be end-members on the ground, as well). The strength of this approach lies in three major areas: it is a physically based model that transforms reflectance values to physical variables, it provides a means to detect and represent components that occur at a sub-pixel level, and it provides quantitative results that can in turn be incorporated into models of surface processes within the image scene. However, issues remain concerning the selection of spectral end-members and the interpretation of fraction images that must be resolved. SMA results must be repeatable, and the fraction images must describe realistic physical variables of components in the scene. If not, SMA becomes little more than an image classification technique.

End-member Selection: The repeatability and physical interpretation of end-member fraction images depends on the accuracy of the spectral end-members that are used to model the data. End-members are usually selected through an educated trial-and-error process: the analyst selects those areas in an image that are expected to represent end-members, finds the fraction images of those end-members, and uses the error of the model fit to improve the initial end-member selection. The process is highly subjective, often based on *a priori* knowledge of the geologic setting, but may be preferable to the extreme alternative: selection of end-member spectra by purely statistical methods (e.g., principal components, or factor analysis). While the latter method is objective, and is repeatable for a given image, the end-member spectra may not be realistic in a physical sense. An alternative approach is to combine the statistical and subjective methods (as described below, and in detail in 4) to find end-members that are believed to model the mixing of surface materials, and still satisfy statistical requirements imposed by the variance of the spectral data at the sub-pixel level.

Modified SMA (MSMA): The fundamental equations of spectral mixture analysis are:

$$\sum_b R_b = \sum_b \sum_i r_{ib} f_i + \sum_b E_b \quad \text{and} \quad \sum_i f_i = 1.0$$

where f_i is the fractional abundance of end-member i in a given pixel, R_b is the total reflectance of the pixel in band b, r_{ib} is the reflectance of end-member i in band b, and E_b is the residual error in band b. In the classic SMA, the end-members are selected first, and their fractional distribution found within the image scene. In the modified method, both end-member spectra and fractional abundance are treated as unknowns. In order to solve this type of non-linear equation, a starting model is provided, and a solution is found through iteration using a damped least squares stochastic inversion (5). The evolution of end-member spectra and fractions from the starting model to the solution is governed by a number of constraints imposed on the calculations, that are essentially quantitative descriptions of *a priori* knowledge. These constraints are applied in the form of additional equations, the starting model itself, and covariance matrices for both the data (pixel spectra) and the model parameters (end-member spectra and fractions). Exact matches to the derived end-member spectra may not necessarily be found within the original data set. However, these "virtual end-members" appear to represent mixing end-members that are more spectrally pure, and which may be more closely matched to library or reference end-members.

Lunar Crater Example: The modified mixing model has been applied to 8-band CCD images of the lunar crater Bullialdus. In Figure 1, the starting model spectra are shown in solid lines, and the virtual end-members derived by MSMA in dashed lines. The kinds of constraints used to derive this solution should help to clarify the MSMA approach. First, since the geology of Bullialdus had been previously studied (6, 7), the starting model end-members were selected from within the image where distinct units were expected to occur. Thus spectra from the central peaks, floor, walls and immediate ejecta of the crater were selected to be end-members for the starting model. They were then allowed to vary by different amounts, depending on *a priori* information. The central peaks, for example, are known to be distinct from the rest of the crater (6, 7), and to mix very little with other crater materials. Therefore the starting model spectrum for the peaks was assumed to be well known, and allowed to vary less than the other three end-members. The starting model fractional abundances were set at 0.5, and all were allowed to deviate ±0.5 (i.e., the fractions were allowed to vary between 0 and 1). Variances were applied to the data as well, in the data covariance matrix. Standard deviations of 10x10 pixel areas within the image were used to determine the

variance of each channel. The variance was allowed to increase for those channels where problems with image registration were known to add noise. The final solution was reached when a predetermined error threshold was passed. In this example, the virtual end-members better model the image data in that the rms error is lower, and the fraction images are spatially coherent with no negative or superpositive values. However, several questions remain. The most important is whether the virtual end-members represent real materials that exist at sub-pixel levels within the image. This becomes a critical issue if the end-members are not as well known ahead of time as they were for this example. In such a case, one or more end-members could be a straight line in the starting model, and assigned a high variance. The MSMA would then derive virtual end-member spectra (as has been demonstrated for a terrestrial data set, 4), but it remains to be proven that the virtual end-members are truly part of the image scene. Another question concerns the possible uses of constraints. In this example, the different Bullialdus channels were weighted unequally to account for noise in different channels. However, they could also be weighted unequally to examine a specific scientific question. For lunar spectra, this type of weighting could be used to subdue the effects of the 0.40-0.56 μm slope (strongly linked to maturity), and to emphasize the effects of channels in the 1-μm region (where absorptions are linked to composition as well as maturity) when determining spectral end-members. Other constraints may be added in the form of additional equations to the model. In the lunar case, end-member spectra could be required to have a positive slope between 0.40 and 0.70 μm. A broader application would be to constrain the interaction of specific end-members that are known always or never to be located together on the ground.

Simulated Crater Example: In order to answer these questions, and to test more thoroughly the applications of both the traditional SMA and our modified SMA, a simulated lunar crater image is currently being developed. For this simulated crater, the abundances of end-members (representing immature central peaks, wall, a mare component) are predetermined based on simple cratering models, and their spectra mixed together in either a linear or non-linear (8) fashion. A topographic model for the crater is included in the simulation, to explicitly incorporate shade as a variable. The spatial resolution of the image is then degraded, to represent the type of data that is generally available for planetary study, and to ensure that the end-members do not make up 100% of any single pixel. The virtual end-members that are derived for the image can then be compared to the "true" end-members that created the simulation. The first test is focused wholly on the behavior of the MSMA itself: to determine whether or not the true end-members can be derived from this simulated image, and what constraints are required to do so. Both random and non-random noise (such as arise from registration or calibration errors) may be added to the image as well, in order to determine the adjustments that must be made to the constraints under these conditions. Ideally, similar constraints may be applied to a real image, and any inconsistencies between the artificial and true image results can be used to further modify the artificial image and find new constraints.

However, it is simplistic to expect tests such as those described here to directly affect the geologic interpretation of the image data. The model crater is an extremely simple representation of what is obviously a complex geological feature. Therefore, it is anticipated that as research progresses, the simulated image will be further developed in a geological sense to reflect more accurately those lunar processes that are known to occur, such as space weathering, complex mixing on the crater floor, etc. As the development of the simulated image occurs, the use of constraints to examine specific science questions can be further explored as well. Ultimately, the results of SMA and MSMA applied to a simulated image can be directly compared to those obtained from real craters such as Bullialdus or from lunar basins, in order to guide the geologic interpretation of the mixing model solutions.

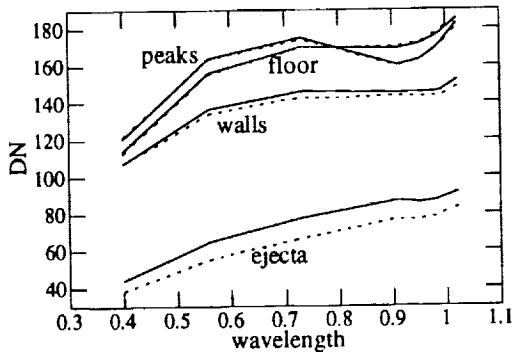

Figure 1: MSMA End-member Spectra. Solid lines represent starting model spectra. Dashed lines are model-derived virtual end-members.

Acknowledgements: This research was supported in part by NASA grant NAGW-28 (CMP) and JPL Contract 959-228 (JFM).

References: (1) Adams et al. (1986) *J. Geophys. Res., 91*: 8098-8112. (2) Head et al. (1993) *J. Geophys. Res., 98*, 17,149-17,181. (3) Adams et al.(1993) in *Remote Geochemical Analysis: Elemental and Mineralogical Composition*, Pieters and Englert, eds., 145-166. (4) Tompkins et al. (1993) *JPL Pub. 93-26, v. 1*, 177-180. (5) Tarantola and Valette (1982) *Rev. Geophys. Space. Phys.*, 20: 219-232. (6) Pieters, (1991) *Geophys. Res. Let.*, 18: 2129-2132. (7) Tompkins et al. (1993) *LPSC 24*, 1433-1434. (8) Hapke (1981) *J. Geophys. Res., 86*, 3039-3054.

4.56 GA U-TH-PB AGE OF MET 78008 UREILITE: Noriko Torigoye[1], Mitsunobu Tatsumoto[1],and Keizo Yanai[2]. [1]US Geological Survey, Branch of Isotope Geology, MS 963 Box 25036, Denver, CO 80225. [2] National Institute of Polar research, 9-10, Kaga 1-chome, Itabashi-ku, Tokyo 173, Japan.

The U-Th-Pb isotopic systematics of MET 78008 Ca-rich ureilite is reported. The extensive acid leaching procedure was used to eliminate terrestrial Pb contamination since the amount of U, Th, and Pb are highly depleted in the meteorite. The Pb-Pb age of the residues is 4527 ± 29 Ma and U-Pb concordia diagram gives upper intercept ages of 4565 ± 46 Ma and 4581 ± 31 Ma. All these ages are significantly older than the Sm-Nd and Rb-Sr age of 4.1 Ga previously reported from the same meteorite. The result strongly indicates that the formation of the ureilite is as old as 4.56 Ga

None of the formation theory of ureilites were completely successful to explain all the characters of ureilites, which show both igneous processes, such as ultramafic mineralogy (olivine and pyroxene) and depletion of incompatible trace elements, and nebular signature, such as oxygen isotopic heterogeneity. As a key to solve the problem, several authors investigated the Sm-Nd and Rb-Sr systems of some ureilites and obtained relatively younger ages of 4.1 Ga for MET 78008 [1], 3.7 Ga for Kenna [2], and 4.2 Ga for PCA 82506 [3] . However, these authors also discussed that original formation age of ureilite might be as old as 4.55 Ga because some of whole rock data of ureilites lie on 4.55 Ga Sm-Nd isochron. Goodrich et al. (1991) explained the younger ages as later metasomatic event to the parent body of ureilites. In our previous work, the U-Th-Pb and Sm-Nd systematics of Goalpara ureilite were examined for the mineral separates by applying acid leaching experiment [4, 5]. For the Sm-Nd system, the linear trend in the Sm-Nd isochron diagram, the same as 3.7 Ga isochron from Kenna [1], was obtained. However, leaching experiment showed that elemental ratios of Th/U and Sm/Nd and isotopic compositions of Pb and Nd in all the acid leachates are contaminated by terrestrial average crustal composition. Even acid residues showed a large amount of excess radiogenic Pb and Pb-Pb system was basically made of mixing of modern terrestrial Pb (MT) and primordial meteoritic Pb (CDT). Because Goalpara is highly depleted in U, Th, Pb, Nd, and Sm (0.001-0.1 times CI chondritic abundance), only a small amount terrestrial contamination affected significantly to the isotopic systematics. Therefore, no meaningful ages could be obtained from U-Th-Pb and Sm-Nd isochron diagram due to a disturbance from terrestrial contamination. However, the U-Pb concordia diagram resolved the effect of contamination from radiogenic composition. Because the U-Pb concordia diagram use two different decay modes of 238U-206Pb and 235U-207Pb, the data from Goalpara plot along the mixing line between terrestrial Pb composition and the radiogenic composition from the decay of U. The intercept of the mixing line to the concordia curve gives the age of 4550 ± 30 Ma. For this reason, we concluded that the formation age of Goalpara is as old as 4.55 Ga and the Sm-Nd young isochron age is artificial by a mixing effect between highly depleted ureilite composition (high Sm/Nd and 143Nd/144Nd isotopic ratio) and terrestrial composition (low Sm/Nd and low 143Nd/144Nd ratio) [5].

MET 78008 allocated from National Institute of Polar Research weighed 4.49 g as a several pieces. One of the pieces showed green color which is different from others and contained a lot of interstitial carbon-metallic phase so that we separated this piece from others (here after called as GR). Under the binocular microscope, GR contained more augite than olivine. The rest of the sample was crushed gently into the powder and sieved into three, 300-150 μm, 150-63 μm and <63μm. From the coarse-grained fraction, olivine and augite grains were hand picked. The middle grain sized fraction was separated by a hand magnet and non-magnetic fraction was further separated into four by Frantz isodynamic separator (here after called as M1, M2, M3, and M4, from the least magnetic to the most magnetic). The fine grained fraction was used as whole rock sample (here after called as WR). Leaching experiment was applied to five mineral separates as follows; Augite, M3, M4, WR, and GR. These samples were washed by ethanol and acetone, and then leached successively by 0.1N HBr (first leach), 1N HNO3 (second leach) and 7N HNO3 (third leach). The final residues were dissolved by HF-HNO3 mixture.

So far, we obtained preliminary results of U-Th-Pb data of second leachates and residues. The concentration of U and Th are 0.3-0.6 ppb and 1.0-2.3 ppb, respectively, which are significantly higher than those in Goalpara. The concentration of Pb in the residues and second leaches are 4.2-6.6 ppb and 1.9-33.3 ppb, respectively. Especially Pb in second leachates are much lower than those of Goalpara of 20-470 ppb, indicating MET 78008 contains less terrestrial Pb than Goalpara. The 206Pb/204Pb ratios of residues are less radiogenic and varies between 11.9 and 21.3. As shown in Fig. 1, all the residues plot along the line which is above the mixing line between CDT and MT, while second leachates are plot close

to the modern terrestrial composition, indicating that the terrestrial Pb component was removed by the leaching procedure. Using Pb-Pb data of the four residues except for WR which plot slightly closer to MT, the Pb-Pb isochron age of 4527 ± 29 Ma is obtained. This isochron passes CDT composition within a error of the regression. Using the two less radiogenic data, GR and Augite, the slightly older isochron age of 4566 ± 25 Ma is obtained.

In Fig. 2, U-Pb and Th-Pb data of three residues, augite, M4 and GR, are shown. The most radiogenic data M4 plots above the 4.56 Ga chondritic isochron, indicating that M4 may contain a small amount of excess radiogenic Pb form terrestrial contamination. The U-Pb concordia diagram of these three data in Fig. 3 also indicates the terrestrial contamination effect on M4. In this diagram Augite and GR plot inside of the concordia curve, while M4 plot outside of concordia curve. Linear regression of these three point gives the intercept of concordia curve of 4565 ± 46 Ma. As discussed in our previous work [5], this line may be explained as a mixing line between radiogenic composition corresponds to 4.56 Ga and CDT corrected 207Pb*/206Pb* value of modern terrestrial Pb (0.567). Since both GR and Augite data plot inside of concordia curve, there might be Pb loss by some late event, such as last evacuation from parent body. These two data gives the discordia line with upper intercept of 4581 ± 32 Ma and lower intercept of 500 ± 2100 Ma. Therefore, if there were some late disturbance to lose Pb, it would not be the same as 4.1 Ga Sm-Nd and Rb-Sr isochron age [1]. According to the present U-Th-Pb data of MET 78008, this meteorite might be formed as old as 4.56 Ga and may not be younger than 4.50 Ga, which is the lower limit of Pb-Pb isochron age. It may be possible that formation age of ureilites are consistent with so-called 4.55 Ga "canonical age" of meteorites. For further confirmation, we are proceeding Sm-Nd dating of the same samples.

[1] Takahashi and Masuda (1990) Meteoritics **25**, 413. [2] Goddrich et al., (1991) G.C.A. **40**, 55, 829-848. [3] Goodrich and Lugmair (1992) LPSC XXIII, 429-430. [4] Torigoye et al., (1993) Meteoritcs **28**, 450-451. [5] Torigoye et al. (1993) submitted to G.C.A.

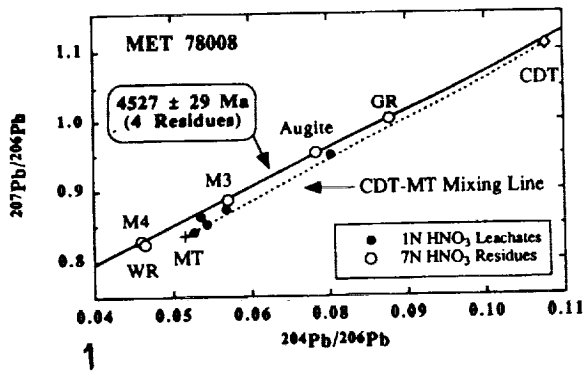

1

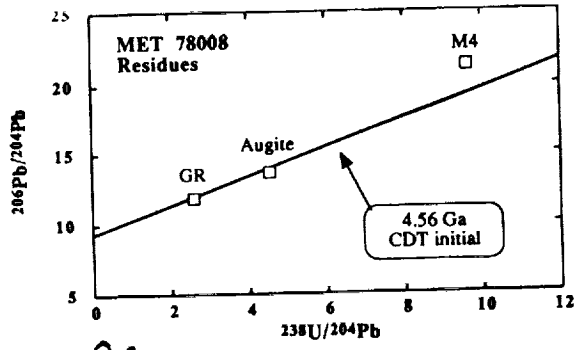

2a

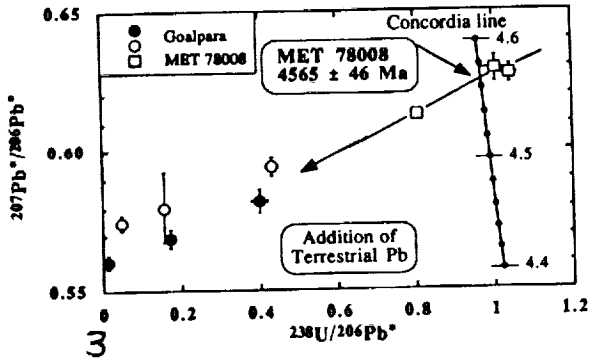

3

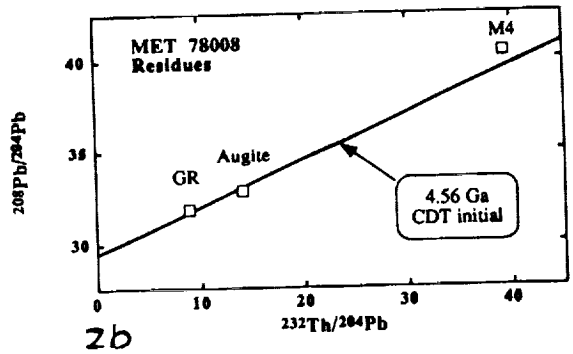

2b

AREAL DISTRIBUTION OF DOUBLE-TYPE CORONAE AND CORONA-LIKE FEATURES ON VENUS, AND THEIR RELATION TO TOPOGRAPHY, TESSERAE AND DEFORMATION BELTS; T. Törmänen and K. Kauhanen, Department of Astronomy, University of Oulu, 90570 Oulu, Finland

Introduction. We have analyzed coronae and corona-like features that are characterized by two linked parts. The overall shape of these features ranges from elongated, peanut- or pear-shaped features that have two parts separated by a narrow neck-like part (e.g. Demeter Corona and Gaia Corona) to distinct double features with two parts joined by a common section of a structural annulus (e.g. Neyterkob Corona). We included also features where two corona annuli appear to be partly overlapping, or where the two corona parts are joined by a more complex central structure. Features were identified from Magellan cycle 1, 2 and a few cycle 3 radar images. We recognized 40 double-type coronae and corona-like features. This population includes features in coronae list in [1] and in the Magellan volcanic and magmatic feature catalog [2]. Also included are several features identified as arachnoids in [2]. Some of our double features were not in either of these lists.

The double-type coronae and corona-like features can be divided into 4 morphological classes based on the shape and structural characteristics of the features. The classification with examples is presented in [3]. 40% of the double-type features (16 out of 40) belong to the class A (a distinct double structure with a section of an annulus joining the two parts); 42.5% (17 features) to class B (elongated two-part structure, no joining section between the parts); 12.5% (5) to class C (two overlapping annuli); and 5% (2) to class D (double structure with a complex central part). In this paper we present the first results of our analysis of the areal distribution of the double-type coronae and corona-like features and their relation to global topography and tectonic patterns.

Areal distribution and relations to topography, tesserae and deformation belts. Only about 9% of the total population of coronae and arachnoids exhibits any kind of double structure (40 features out of the total of more than 430 features [1,2]). The areal distribution of this small population follows the general distribution of coronae on Venus [1,4] with over half of all double-type features located within the area of the anomalously high concentration of volcanic centers in the Beta-Atla-Themis regiones (the BAT anomaly [5,6]; Figure 1.). In the southern hemisphere, there is, however, a noticeable paucity of double-type coronae and corona-like features, also in the areas where other types of coronae are present (e.g. the area south of the equator and east and northeast of Alpha Regio; cf. Fig. 6c in [6]). The double-type coronae and corona-like features form seven groups of two or three features that belong to class A or B (Figure 1.). There are groups whose members belong to only one class and groups where both classes are represented. These groups are located within the BAT area or to the north of it. At the present moment it is not clear whether this is result of pure coincidence or whether these groups point to locations favourable for the formation of double-type coronae.

The double-type coronae and corona-like features are located typically on the plains lying slightly lower than the mean planetary radius (MPR) of 6051.84 km (between -1 km and 0 km elevations; Figure 1.). Only a few features are located above the MPR. Features belonging to different morphological classes do not have markedly different base elevations. Thus slight variations in base elevations do not appear to greatly affect the morphology of the double-type coronae and corona-like features. They do not occur in or near large tessera areas such as Fortuna Tessera and Ovda Regio (Figure 2.). Several of them lie on the plains near smaller and more fragmented tesserae but do not appear to be significantly affected by presence of tessera.

Only two double-type features lie on the plains characterized by regional sets of wrinkle ridges (Figure 3.). Also, the majority of these features are not associated with ridge belts. Many of the double-type features are located near fracture belts (Figure 4.). Partly this is due to their concentration within the densely fractured and rifted BAT area. Most of the features, however, are not located directly on the fracture belts or rifts and are preferentially located adjacent to the belts but mostly outside of them. There does not appear to be any correlation between the morphological class of the feature and its location relative to fracture belts. We can conclude that compressional and/or extensional stresses forming deformation belts do not appear to have a dominating effect on formation of the double-type features. Although double-type coronae and corona-like features appear to favor areas near fracture belts they are mostly absent from areas adjacent to the largest and deepest rifts (e.g. troughs of Aphrodite Terra) i.e. areas of largest extensional strain. Coronae on Venus are thought to originate from upwelling mantle plumes or diapirs [7]. We propose that different types of double coronae and corona-like features may form from 1) elongated mantle diapirs, 2) two closely-spaced roughly contemporaneous mantle diapirs, or 3) closely-spaced secondary diapirs rising from larger mantle upwellings. The relationships of the double-type features to fracture belts and rifts suggests that along the deepest rifts and more deformed fracture belts conditions inhibit formation of the double-type coronae and corona-like features or they may have formed at some earlier time but have been subsequently erased by later intense deformation.

Future work: We are now studying structural and volcanic characteristics of these features and their relation to topography in more detail. A thorough analysis of relationships between the fracture belts and the double-type features will give more insight into formation processes of the double-type coronae and coronalike features.

References. [1] Stofan E.R. et al. (1992) *JGR*, **97**,13347. [2] Crumpler L.S. et al. (1994) *Geol. Soc. Am. Spec. Paper*, manuscript. [3] Kauhanen K. and Törmänen T. (1994) *LPSC XXV*, this volume. [4] Head J.W. et al. (1992) *JGR*, **97**,13153. [5] Crumpler L.S. et al. (1992) *Int. Colloq. on Venus*, 25. [6] Crumpler L.S. et al. (1993) *Science*, **261**, 591. [7] Stofan et al. (1991) *JGR*, **96**, 20933; Squyres et al. (1992) *JGR*, **97**, 13611; Janes et al. (1992) *ibid.*, 16055. [8] Ivanov, M.A. et al. (1992) *LPSC XXIII*, 581. [9] Crumpler L.S. et al. (1993) *LPSC XXIV*, 363.

DISTRIBUTION OF DOUBLE-TYPE CORONAE ON VENUS: Törmänen T. and Kauhanen K.

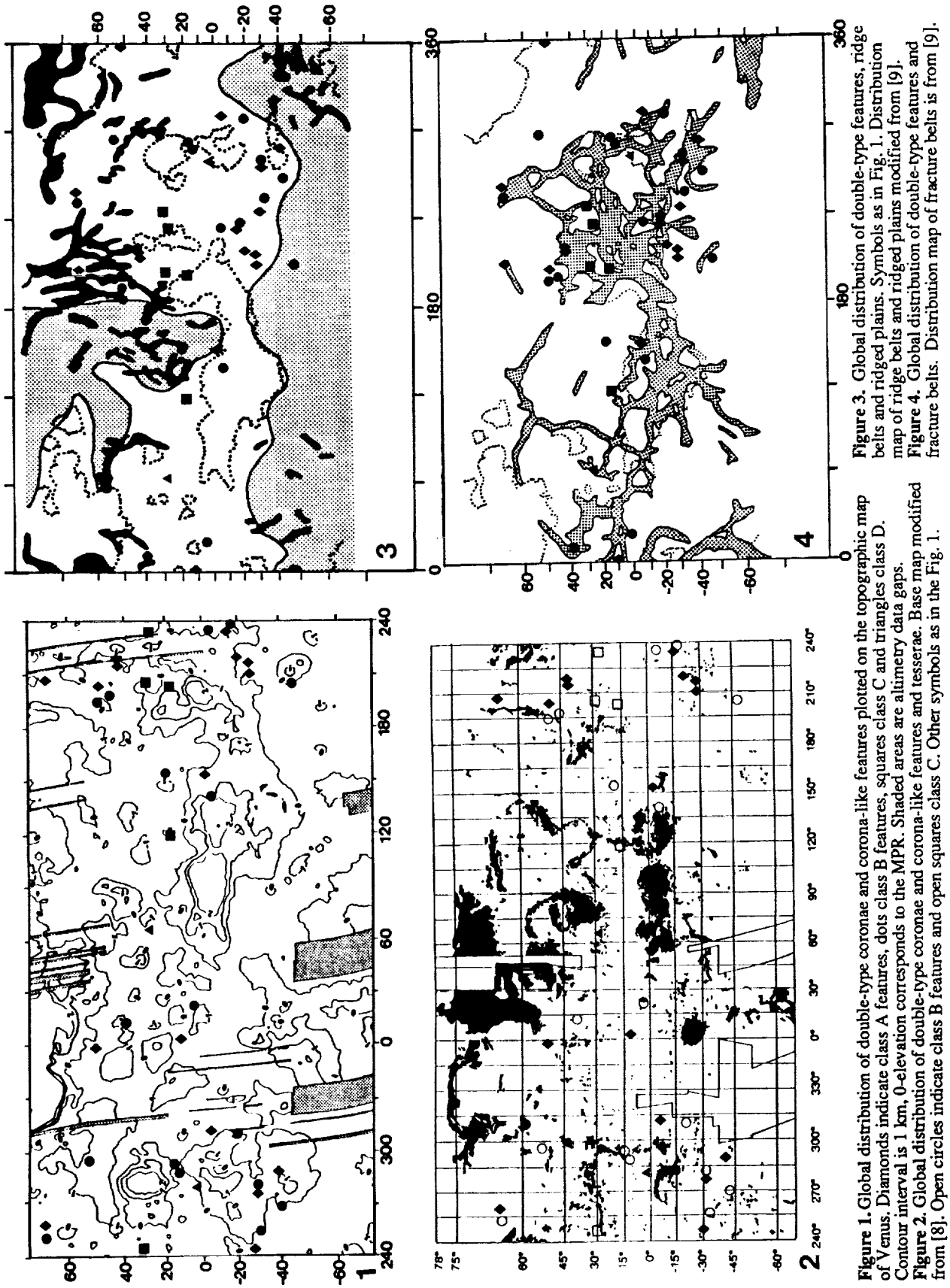

Figure 1. Global distribution of double-type coronae and corona-like features plotted on the topographic map of Venus. Diamonds indicate class A features, dots class B features, squares class C and triangles class D. Contour interval is 1 km, 0-elevation corresponds to the MPR. Shaded areas are altimetry data gaps.
Figure 2. Global distribution of double-type coronae and corona-like features and tesserae. Base map modified from [8]. Open circles indicate class B features and open squares class C. Other symbols as in the Fig. 1.

Figure 3. Global distribution of double-type features, ridge belts and ridged plains. Symbols as in Fig. 1. Distribution map of ridge belts and ridged plains modified from [9].
Figure 4. Global distribution of double-type features and fracture belts. Distribution map of fracture belts is from [9].

TWO SOURCE AREAS FOR THE SNC METEORITES: PETROLOGIC, CHEMICAL AND CHRONOLOGIC EVIDENCE. Allan H. Treiman, Lunar and Planetary Institute, 3600 Bay Area Blvd. Houston TX 77058-1113. [713-486-2117; treiman@lpi.jsc.nasa.gov]

The **SNC** meteorites (Shergottites, Nakhlites, Chassigny) are samples of the Martian crust, and so are of surpassing planetologic importance. The **SNC**s have been inferred to come from a single impact crater on Mars. However, no known crater fits all known constraints. The sum of petrologic, chemical, and chronologic data suggests two distinct sites of origin: **S** from one, **NC** from another.

INTRODUCTION: The **SNC** meteorites are rocks of basaltic parentage, propelled from Mars by meteoritic impact. The **SNC**s have been important in providing "ground truth" to studies of mantle and magmatic processes, the hydrosphere, and atmosphere composition. But their utility is limited because their source(s) on Mars are not known. Most studies have suggested that the **SNC**s were ejected from Mars by a single meteorite impact in or near Tharsis [1-4, but see 5,6]. Nine potential source craters in Tharsis were located by [1], but none are consistent with constraints imposed by all of the **SNC**s. Multiple source craters on Mars have been considered but rejected [4,5], partly on cratering and orbital dynamic bases and partly because all **SNC**s were inferred to have the same crystallization age.

TWO SOURCE CRATERS: S ≠ NC. However, the sum of petrologic, chemical, and recent chronologic evidence suggests that the **SNC**s originated at two distinct sites on Mars. The most important data set is that the crystallization ages for **S** are significantly younger than for **NC** (Table 1). **S** and **NC** are different in most other respects. From Table 1, it appears that **S** and **NC** have been distinct through their whole histories, from source mantle through magma composition through low-temperature aqueous alteration through impact ejection.

TABLE 1. Selected Properties of **SNC** Meteorites, Chronological Order.

	S	**NC**
Effective Mantle Source $^{238}U/^{204}Pb$: 4,500 m.y. [7]	~5	~2
Magma Composition: Rb/Sr, Nd/Sm etc.	≤CI (Depleted) [8]	>>CI (Enriched) [9,10]
Crystallization Age	~180 m.y. [11,12]	~1,250 m.y. [8,9]
Pre-terrestrial Aqueous Alteration of Silicates (where present; all include salts)	Aluminosilicate [13]	Smectite-Iron Oxide [14,15]
Shock Pressure (maskelynite vs. plagioclase)	>> 29 GPa	< 29 Gpa
Cosmic Ray Exposure Age	2.8±0.3, 0.5 m.y. [5]	11±1 m.y. [5]

Constraints on the mantle sources [7,16] are least secure, but it appears that **S** and **NC** sources must have experienced some significantly different geochemical events since 4,500 m.y. The most parsimonious conclusions from these data are that **S** and **NC** had essentially nothing to do with each other, and formed at different sites on Mars.

SINGLE CRATER ORIGIN? The current paradigm for **SNC** origins involves ejection from Mars by a single impact [1-5]. Ejection at ~180 m.y. [1-3, favored by 4] is no longer tenable in that the 180 m.y. event recorded in S is igneous crystallization (Table 1). Ejection of the **SNCs** from a single crater at 11 m.y. (cosmic ray exposure age for **NC**) might be possible if the crater ejection zone overlapped distinct **S** and **NC** terranes, or hit a veneer of **S** over **NC**. But, ejection and subsequent orbit evolution must somehow ensure that 1) of materials exposed to cosmic rays for 11 m.y., only **NC** lithologies arrive at Earth, and 2) of materials exposed to cosmic rays for 2.5 m.y. or less, only **S** lithologies arrive at Earth. Neither scenario seems likely to me. EETA79001 has a younger cosmic ray exposure age, 0.5 m.y. [5], than the other **S**. This age could represent a collision in space [17], but could also represent a third impact event on Mars.

IMPLICATIONS: If the **SNC** meteorites left Mars in two separate impact events, at least some current understandings of Mars and its surface processes must be revised.

1). Some objections to the nine potential source craters of [1] are removed. A single impact need not have had access to all **SNC** lithologies, so meteorite source craters in monolithologic, simple units are permitted. Among the choices of [1], **S** might have come from craters 1, 3, 7, or 9 and **NC** might have come from craters 2 or 4-9.

2). One (or more) of the following must be incompletely understood: mechanics of ejection of meteorites from Mars; absolute ages of Martian surfaces inferred from crater-count statistics; or distribution of craters-forming events in time. The underlying problem here is that **two** meteorite-ejecting impacts are required in the last 11 m.y. This would suggest an embarrassingly high cratering rate on Mars unless: 1) craters smaller than 35 km can eject SNC parent meteoroids [1,4]; 2) Mars surfaces are much younger than in current estimates [18]; or 3) crater-forming events on Mars are not randomly distributed in time (idea from J. Jones).

3). The lack of meteorites from old Martian surfaces becomes a problem. In single-crater models (accepting current estimates of surface ages [18]) the lack of meteorites from surfaces older than 1,300 m.y., >95% of the Mars surface [1], can be ascribed to chance. But the probability of the only two meteorite-forming impacts on Mars avoiding these old surfaces is ≤ 0.0025. So, it becomes likely that older surfaces have experienced impacts that could have propelled meteorites to Earth. Perhaps the physical properties of older surface materials preclude ejection of meteorite-sized fragments, or perhaps materials from the older surfaces terranes do fall to Earth (e.g., altered basaltic rocks, sandstone, conglomerate, granite, rhyolite, or anorthosite [19]) and are not recognized as meteoritic.

ACKNOWLEDGMENTS. Discussions with J. Jones and M. Lindstrom have helped clarify my thoughts and (with luck) this presentation.

[1] Mouginis-Mark P.J. et al. (1992) J.G.R. 97, 10213-10336. [2] Wood C.A and Ashwal L.D. (1981) Proc. Lunar Planet. Sci. Conf. 12th, 1359-1375. [3] Nyquist L.E. (1983) Proc. Lunar Planet. Sci. Conf. 13th, A785-A798. [4] Vickery A.M. and Melosh H.J. (1987) Science 237, 738-743. [5] Bogard D.D. et al. (1984) G.C.A. 48, 1723-1740. [6] Ott U. and Begemann F. (1985) Nature 317, 509-512. [7] Chen J.H. and Wasserburg G.J. (1986) L.P.S. XVII, 113-114. [8] Smith M.R. et al. (1984) Proc. 14th Lunar Planet. Sci. Conf. B612-B630. [9] Nakamura N. et al. (1982) G.C.A. 46, 1555-1573. [10] Nakamura N. et al. (1982) Meteoritics 17, 257-258. [11] Jones J.H. (1986) G.C.A. 50, 969-977. [12] Jagoutz E. (1989) Geochim. Cosmochim. Acta 53, 2429-2442. [13] Gooding J.L. and Muenow D.W. (1986) G.C.A. 50, 1049-1059. [14] Treiman A.H. and Gooding J.L. (1991) Meteoritics 26, 402. [15] Treiman A.H. et al. (1993) Meteoritics 28, 86-97. [16] Jones J.H. (1989) Proc. 19th L.P.S.C., 565. [17] Treiman A.H. (1993) Meteoritics 28, 451. [18] Strom R. et al. (1992) in Mars, 383. [19] Lindstrom M. et al. (1994) This Volume.

CHEMICAL WEATHERING ON VENUS: PRELIMINARY RESULTS ON THE INTERACTION OF BASALT WITH CARBON DIOXIDE. Allan H. Treiman[1] and Carlton C. Allen[2]. [1]Lunar and Planetary Institute, 3600 Bay Area Blvd. Houston TX 77058. [2]Lockheed Engineering and Sciences Co. 2400 NASA Rd. 1, Houston TX 77258.

Chemical reactions between the atmosphere and surface of Venus are thought to exert strong controls on the compositions of both [1-3]. Reactions between Venus atmosphere and basalt may be important because 80% of Venus is surfaced by volcanic units and most of them are basaltic [4]. Preliminary experiments show that basalt glasses react with 1 bar of CO_2 to become coated with thin films of Ca-Mg carbonate (?). However, the rate of this reaction is slower than the rate of reaction with SO_2-bearing gas [5], suggesting that the weathering of basalt is not a likely source of carbonates on the Venus surface.

Samples and Method. Our approach is to subject samples of basalt and basalt glass to model Venus atmospheres and temperatures. Samples were reacted in a vertical tube furnace, in which weight change can be monitored continuously by an electronic microbalance. Before each experiment, the furnace was preheated to the run temperature and purged with CO_2 for several hours. Approximately 200 mg of powdered sample was weighed and placed in an open platinum crucible, which was suspended in the furnace by a platinum wire. The furnace was resealed, evacuated to remove air, and flushed with argon or CO_2. A controlled flow of 5 cm^3/min CO_2, upward past the sample, was then initiated. The sample weight change was monitored periodically during each experiment. At the conclusion of an experiment, the furnace was cooled rapidly to 200°C. The sample was removed and weighed to confirm the weight change indicated by the microbalance. In our experiments, weight changes measured by both methods were identical within error. After reaction, mineral proportions in the samples were determined by X-ray diffraction analysis. Samples were then mounted for SEM/EDX analysis (and eventually transmission EM/EDX). Knowledge of reaction products and rates may eventually be interpreted in terms of reaction mechanisms.

Experimental Results. By Jan. 7, 1994, two experiments have been completed. In both cases, samples reacted with the CO_2 gas and did gain weight. The weight gain was approximately proportional to $\sqrt{\text{time}}$, consistent with diffusion-controlled reactions at grain surfaces.

In experiment VBW2, synthetic glass of Apollo 11 basalt composition (#1 of [6], crushed to 840-149 μm) was reacted at 750°C for 5 days. During reaction, VBW2 partially devitrified to yield augite and gained 0.25% in mass. Its surfaces became coated with an optically thin layer that shows Fizeau interference colors of gray through orange. In SEM, the glass surfaces are coated with a bumpy layer, <10 μm thick, composed of grains ~0.1 μm across. SEM/EDX chemical analyses suggest that the layer is rich in Ca and Mg. The layer did not effervesce under 1-M HCl, but did detach from the underlying glass.

In experiment VBW1, porphyritic tholeiite basalt JSC-1 [7] (crushed to <840 μm) was reacted at 800°C for 4 days. The sample gained 0.7% in mass, and changed color from black to dark ocherous red. Diopside and plagioclase phenocrysts showed no signs of reaction. Crystals of Fe oxide, 10 μm across, were abundant on glass immediately adjacent to phenocrysts and were rare elsewhere. Glass surfaces were covered with a thin bumpy layer similar to that of VBW2; SEM/EDX analyses suggest it was also enriched in Ca and possibly Mg.

Interpretation. Interaction of basalt and basalt glass with CO_2 involved two reactions: oxidation of iron, and formation of a Ca-Mg-rich surface layer. The color of VBW1 (from JSC-1

basalt) suggests that the Fe oxide is hematite. The absence of Fe-oxide from VBW2 is puzzling as its starting material (simulated A11 basalt glass) contained more FeO than did JSC-1 (~13% vs. ~10.5%). The abundance of Fe-oxides adjacent to phenocrysts in VBW1 suggests that formation of Fe oxide is rapid only in the compositional boundary layer that surrounds crystals in basalt. It is possible that these layers in VBW1 were molten during reaction.

The surface layer that formed on the basalt glass could be a carbonate, dolomite or magnesian calcite, given its composition (rich in Ca and Mg) and the mass gains during reaction. Unequivocal identification of the mineralogy of the surface layer will require additional analyses by SEM and TEM/EDX.

Implications. At this point, few conclusions about Venus can be drawn from these preliminary experiments because: 1) temperatures were higher than those at Venus' surface; 2) pressure was much lower than at the Venus surface; 3) the gas lacks reactive minor species of the Venus atmosphere; and 4) effects of basalt composition and crystallinity are uncontrolled.

Most important is that the rates of carbonate (?) formation on basaltic solids under 1 bar CO_2 appear to be significantly lower than rates of sulfate formation under 1 bar $\{CO_2 + 1\% SO_2\}$ [5]. Specifically, [5] found that diopside reacted with this sulfur-bearing gas to form anhydrite crystals (to 15 μm) in 2 days at 833°C. We saw no detectable reaction on diopside, and significantly less reaction on basalt glass, with pure CO_2 in twice as much time. This comparison suggest that basalt glass on Venus may weather directly to sulfate minerals and may not be a source of carbonate for buffering atmosphere composition (as in [1,3]).

Future Work. Future experiments at more realistic pressures, temperatures and gas compositions will yield more complete models of the chemical weathering of basalt on Venus. Experiments at 1 bar can be extended to lower temperature, longer times, and more realistic gas compositions, as in [5]. Experiments at Venus surface pressures, ~90 bars CO_2, can be performed in externally heated (cold-seal) pressure vessels. Through these and similar experiments it will be possible to understand the mutual chemical influences of Venus atmosphere and Venus basalt.

ACKNOWLEDGMENT: We are grateful for the help and support of B. Fegley Jr. and D. S. McKay.

[1] Nozette S. and Lewis J.L. (1982) Science 216, 181.
[2] Zolotov M.Yu. and Volkov V.P. (1989) p. 177 in Barsukov V.L. et al. eds. Venus Geology, Geochemistry and Geophysics. U. Az.
[3] Fegley B.Jr. and Treiman A.H. (1992) p. 7 in Luhmann J.G. et al. eds. Venus and Mars: Atmospheres, Ionospheres, and Solar Wind Interactions. A.G.U.
[4] Head J.W. et al. (1993) Jour. Geophys. Res. 97, 13153.
[5] Fegley B.Jr. and Prinn R.G. (1989) Nature 337, 55.
[6] Allen C.C. et al. (1992) Engin., Constr., Ops. in Space III, 629.
[7] McKay D.S. et al. (1994) Engin., Constr., Ops. in Space IV, in press.

N94-35467

THE PARENT MAGMA OF XENOLITHS IN SHERGOTTITE EETA79001: BULK AND TRACE ELEMENT COMPOSITION INFERRED FROM MAGMATIC INCLUSIONS. Allan H. Treiman[1], David J. Lindstrom[2] and Rene R. Martinez[3]. [1]Lunar and Planetary Institute, 3600 Bay Area Blvd. Houston TX 77058 [2]SN4, Johnson Space Center, Houston TX 77058 [3]Lockheed E.S.Co. 2400 NASA Rd. 1, Houston TX 77258.

The SNC meteorites are samples of the Martian crust, so inferences about their origins and parent magmas are of wide planetologic significance. The EETA79001 shergottite (S of SNC), a basalt, contains xenoliths of pyroxene-olivine cumulate rock which are possibly related to the ALHA77005 and LEW88516 SNC lherzolites [1]. Olivines in the xenoliths contain magmatic inclusions, relics of magma trapped within the growing crystals. The magmatic inclusions allow a parent magma composition to be retrieved; it is similar to the composition reconstructed from xenolith pyroxenes by element distribution coefficients. The xenolith parent magma (assuming a single magma) is similar but not identical to parent magmas for the shergottite lherzolites.

Magmatic Inclusions. Magmatic inclusions in xenolithic olivine in the A lithology of EETA79001 were identified optically in thin sections: ...,367; ...,68; and ...,18. The inclusions, up to 150 μm diameter, consist of high-Ca pyroxene, glasses of feldspar and silica composition, and troilite, chromite, and apatite. They are petrographically similar to magmatic inclusions in olivines in other SNCs and other basaltic rocks [2-5]. Some inclusions are adjacent to or include chromite grains 30-50 μm across, which are not interpreted as having crystallized from trapped magma.

Analytical Method. Chemical analyses of the inclusions were obtained by electron microprobe [5]. Rastered area analyses covering each inclusion were averaged; sums are low because of abundant cracks. Olivine adjacent to each inclusion was analyzed. The proportion of olivine in each analyzed area (18-65%) was determined planimetrically from BSE images; and that proportion of olivine was subtracted from rastered area analyses to yield bulk inclusion analyses and their average (e.g., Table 1). A few inclusions with Cr_2O_3>2%, caused by large chromite crystals in and adjacent to the inclusions, were excluded from further interpretation. To reconstruct the parent magma from the average inclusion analyses, we correct for chemical effects after the inclusions were entrapped: crystallization of olivine from the inclusion onto the host olivine, and Fe/Mg/Mn exchange with and through the host olivine [5]. The parent magma composition was reconstructed by simultaneously: adding to the inclusion composition olivine composition that would have been in Fe/Mg equilibrium (Mg*=0.84) with the most magnesian pyroxenes in the xenoliths (Mg*=0.86); and adjusting the Mg/Fe ratio of the inclusion composition, holding molar Mg+Fe constant. These corrections were iterated until the magma composition: had the correct Mg*=0.61 for equilibrium with the xenoliths' most magnesian pyroxenes; and was co-saturated in olivine and low-Ca pyroxene [6]. The correction involved adding 13.1% mass of olivine and adjusting MgO/FeO from 1.1 to 0.51.

Discussion. The reconstructed parent magma for the EETA79001 xenoliths in Table 1 is provisional, as it is derived from an average of only 9 inclusions (more are being analyzed). Standard deviations of the average are high because the mineral grains in the inclusions are not much smaller than the inclusions themselves; thus, placement of individual mineral grains has a strong effect on an inclusion analysis.

Given these uncertainties, the xenolith parent magma estimated here is quite similar to that estimated by [6] for the xenoliths from pyroxene analyses and mineral/melt partition coefficients

(Table 1). The parent estimated here has higher Mg* than the parent estimated by [6] because we have used a slightly more magnesian pyroxene to fix Mg*. The similarity of these results is gratifying, as they rest on totally independent assumptions and methods [5]. Both estimates of the xenolith parent magma are slightly more siliceous, aluminous, chromian, and magnesian (Mg*) than the host basalt (Eg [6], Table 1). This mix of primitive (high Cr, Mg*) and evolved (high Si, Al) characteristics suggests that the xenolith parent magma is not directly related to the host basalt. The xenoliths are similar in petrography and mineral chemistry to the ALHA77005 and LEW88516 SNC lherzolites, and the xenolith parent magma is in the range of possible parent magmas for the latter ([3] Table 1). However, minor and trace element chemistry and isotopic ratios appear to preclude a comagmatic origin for xenoliths and the SNC lherzolites [7,8].

Trace Element Analyses. Trace element analyses for these inclusions are being measured by micro-INAA [9], following [10] where it was shown that useful trace element data could be derived from magmatic inclusions. Inclusions from ...,367 (including some contained entirely within the section) have been removed from the section by drilling and have been irradiated. Analytical results from these irradiations will be presented at the conference.

This research was supported in part by NASA RTOP 152-14-40-22 to D. Lindstrom.

[1] McSween and Jarosewich (1983) *Geochim. Cosmochim. Acta 47*, 1501. Treiman A.H. (1993) Meteoritics 28, 451. [2] Jagoutz E. (1989) *Geochim. Cosmochim. Acta 53*, 2429. [3] Harvey R.P. et al. (1993) *Geochim. Cosmochim. Acta 57*, 4769. [4] Roeder E. (1979) *Bull. Mineral. 102*, 487-510. [5] Treiman A.H. (1993) *Geochim. Cosmochim. Acta 57*, 4753. [6] Longhi and Pan (1989) *Proc. 19th LPSC*, 451. [7] Wadhwa M. et al. (1994) *Geochim. Cosmochim. Acta*, submitted. [8] Wooden et al. (1982) *LPS XIII*, 879. [9] Lindstrom D. (1990) *Nucl. Instr. Meth. Phys. Res. A299*, 548-588. [10] Lindstrom D. et al. (1993) *Meteoritics 28*, 386-387.

Table 1.Magmatic Inclusion Analyses and Estimated Magma Compositions.

	Representative Anal's. Inclusion EETA 79001 ,367i1	Inclusion EETA 79001 ,367i14	Average 9 Inclusions	Std. Dev. Mean	Derived EETA Xenolith Parent Magma	EETA Xenolith Parent Magma Ex [6]	EETA 79001A Host Basalt Eg [6]	LEW 88516 Parent Basalt [3]*
SiO_2	63.61	47.10	56.5	± 2.4	53.3	51.47	50.67	54.5
TiO_2	0.70	0.76	0.69	± 0.09	0.6	0.62	0.86	0.7
Al_2O_3	12.45	9.30	12.0	± 1.0	10.2	12.21	7.10	7.1
Cr_2O_3	0.20	1.52	0.7	± 0.2	0.6	0.50	0.12	--
FeO	1.24	7.48	7.7	± 1.9	12.7	13.77	18.67	14.2
MnO	0.10	0.26	0.25	± 0.03	0.2	0.50	0.52	--
MgO	1.94	7.75	8.4	± 1.8	11.1	10.32	12.22	10.9
CaO	9.21	10.70	10.4	± 1.1	8.9	9.56	8.74	9.5
Na_2O	2.40	1.31	1.9	± 0.3	1.6	0.93	1.07	1.2
K_2O	0.03	0.02	0.13	± 0.04	0.1	0.08	0.07	0.07
P_2O_5	1.95	1.30	1.4	± 0.2	1.2	--	--	--
Total	93.83	87.50	=100.		=100.	99.96	100.04	99.68

* Average of olivine-pigeonite-cosaturated compositions, Table 3 of [3]

S20 91 ABS. ONLY
3086
P-2

N94-35468

THE TEMPERATURE OF NITROGEN ON PLUTO; K.A. Tryka, Division of Geological and Planetary Sciences, Caltech, R.H. Brown, Jet Propulsion Laboratory, D.P. Cruikshank, NASA Ames, T.C. Owen, Institute for Astronomy, University of Hawaii

Millimeter flux measurements of the Pluto/Charon system [1,2] have placed the temperature of Pluto between 30 and 44 K. This is in conflict with previous infrared flux measurements obtained by IRAS [3,4] which placed the temperature of Pluto closer to 55 K. Recent spectroscopic measurements of Pluto have shown that nitrogen and carbon monoxide exist on the surface of Pluto [5], in addition to the methane previously identified [6]. Laboratory work [7,8] has shown that the 2.148 μm band of solid N_2 is temperature dependent. Using laboratory data of N_2 and groundbased spectral data of Triton [9] Tryka et al. [7] determined a temperature for the nitrogen on Triton which is in agreement with Voyager 2 measurements. Thus, an analysis of the spectrum of Pluto is expected to yield an accurate temperature for the nitrogen on that body.

Solid nitrogen exists in three phases [10]. The cubic α phase exists at temperatures below 35.6 K at 0 pressure; the hexagonal ß phase exists at temperatures above 35.6 K and below the triple point (63.15 K) at 0 pressure. The γ phase exists only at high pressures and is not relevant to planetary surfaces.

There is a dramatic change in the shape of the 2.148 μm band in solid nitrogen as it passes from the ß to α phase [11]. In the ß phase the band is quite shallow and very broad while in the α phase the band is much deeper and very sharp. More recent work has shown that changes in the spectral band are not only a function of the nitrogen phase, but also a function of temperature [7,8]. As ß N_2 is cooled the 2.148 μm band systematically deepens and gets narrower (Figure 1). In addition, between 35.6 K and about 41 K a second feature appears at 2.16 μm. Thus the shape of the spectral band is a reliable indication of the temperature of the nitrogen.

With Hapke scattering theory [12] and absorption coefficients derived from our laboratory measurements of N_2 ice we have modeled the spectrum of Triton [9]. By comparing a Hapke scattering model to the measured spectrum from Triton we determined the temperature of the N_2 on the satellite's surface to be 38 (+2,-1) K which is in accord with the measurements of Voyager 2 [13,14].

Applying this technique to Pluto we find that the temperature of N_2 on that body is 40 ± 2 K (Figure 2). If the distribution of N_2 on the surface and in the atmosphere of Pluto is controlled by vapor pressure equilibrium (as is apparently the case on Triton) the areas of N_2 will be isothermal while areas bare of N_2 could have a significantly higher temperature. By considering Pluto to be a non-isothermal body we were able to create a model which is able to match the millimeter and infrared flux points simultaneously.

Our model Pluto consists of a spherical planet with symmetric, isothermal N_2 polar caps. The equatorial region is bare of N_2 and assigned a bolometric albedo. It's temperature is determined by instantaneous equilibrium [15]. Charon is modeled as a spherical planet with an albedo typical of icy satellites and its temperature is also calculated using instantaneous equilibrium.

Figure 3 shows a sample flux model

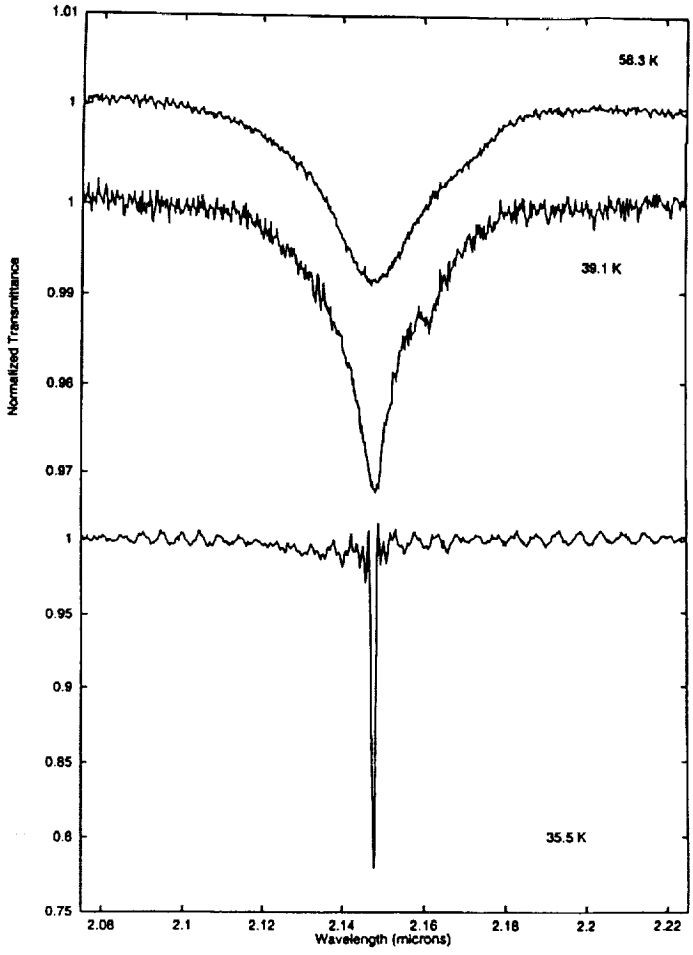

Figure 1

(solid line) along with flux measurements of the Pluto/Charon system (shown with error bars) and upper limits to fluxes determined by non-detections (short horizontal lines). The model has polar caps down to $\pm 20^{\circ}$ latitude, an equatorial albedo of 0.2, and a Charon albedo of 0.4. This model falls within the error bars of all the data points with the exception of the 1200 μm measurement. Models with other parameters also fit the data, but they have these points in common; the polar caps are very large (extending to latitudes of $\pm 20^{\circ}$-$\pm 25^{\circ}$) and the equatorial albedo of Pluto is quite dark (<0.4). Thus, it is possible to match the observed flux points with a simple model of Pluto.

References

[1] S.A. Stern, D.A. Weintraub, and M.C. Festou, *Science*, **261**, 1713-1716 (1993).
[2] W.J. Altenhoff et al., *Astron. and Astrophys.*, **190**, 15-17 (letter)(1988).
[3] M.V. Sykes, R.M. Cutri, L.A. Lebofsky, and R.P. Binzel, *Science*, **237**, 1336-1340 (1987).
[4] H.H. Aumann and R.G. Walker, *Astron. J.*, **94**, 1088-1091 (1987).
[5] T.C. Owen et al., *Science*, **261**, 745-748 (1993).
[6] D.P. Cruikshank, C.B. Pilcher, and D. Morrison, *Science*, **194**, 835-836 (1976).
[7] K.A. Tryka, R.H. Brown, V. Anicich, D.P. Cruikshank, and T.C. Owen, *Science*, **261**, 751-754 (1993).
[8] W.M. Grundy, B. Schmitt, and E. Quirico, *Icarus*, **105**, 254-258 (1993).
[9] D.P. Cruikshank et al., *Science*, **261**, 742-745 (1993).
[10] T.A. Scott, *Phys. Rep.*, **27**, 89-157 (1976).
[11] J.R. Green, R.H. Brown, D.P. Cruikshank, and V. Anicich, *Bull. Am. Astron. Soc.*, **23**, 1208 (1991).
[12] B. Hapke, *JGR*, **86**, 3039-3054 (1981).
[13] A.L. Broadfoot et al., *Science*, **246**, 1459-1466 (1989).
[14] B. Conrath et al., *Science*, **246**, 1454-1459 (1989).
[15] R.H. Brown, D. Morrison, C.M. Tedesco, and W.E. Brunk, *Icarus*, **52**, 188-195 (1982).

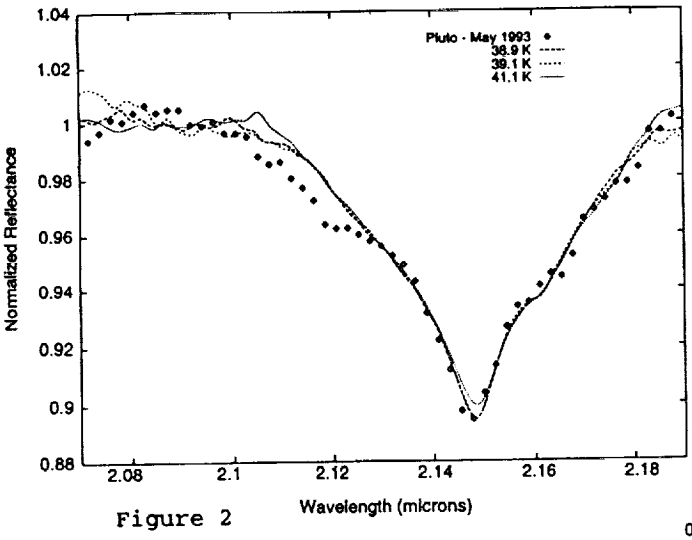

Figure 2

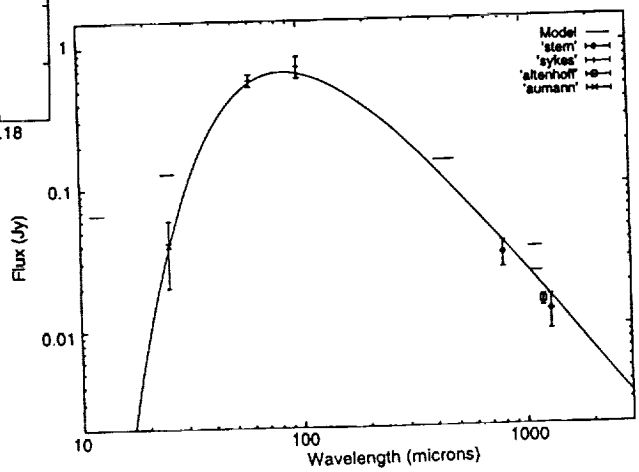

Figure 3

S21-27 ABS ONLY 3087 N94-35469

PURITY & CLEANNESS OF AEROGEL AS A COSMIC DUST CAPTURE MEDIUM

P. Tsou[1], R. H. Fleming[2], P. M. Lindley[2], A. Y. Craig[2], D. Blake[3]
[1]Jet Propulsion Laboratory, [2]Charles Evans & Associates, [3]Ames Research Center

The capability for capturing micrometeoroids intact through laboratory simulations [Tsou 1988] and in space [Tsou 1993] in passive underdense silica aerogel offers a valuable tool for cosmic dust research. The integrity of the sample handling medium can substantially modify the integrity of the sample. Intact capture is a violent hypervelocity event: the integrity of the capturing medium can cause even greater modification of the sample. Doubts of the suitability of silica aerogel as a capture medium were raised at the 20th LPSC [Gibson 1989], and questions were raised again at the recent Workshop on Particle Capture, Recovery, and Velocity Trajectory Measurement Technologies. Assessment of aerogel's volatile components [Hartmetz 1990] and carbon contents [Gibson 1991] have been made. We report the results of laboratory measurements of the purity and cleanness of silica aerogel used for several Sample Return Experiments flown on the Get Away Special program.

Silica aerogel is very suitable for cosmic dust collection and can be easily cleaned to meet biogenic sample requirements. In fact, the purity and cleanness of silica aerogel fabricated at the Jet Propulsion Laboratory (JPL) handled under normal laboratory conditions were found to be comparable to silicon wafers produced for the semiconductor industry under strict clean room handling procedures. Silica aerogel has been shown to be the most suitable nonobstrusive elemental and biogenic intact sample capture medium.

EXPERIMENT A 10 cm x 10 cm x 1 cm piece of 20 mg/ml JPL silica aerogel taken from the fabrication lot flown on STS-57 was cut into smaller pieces (~ 1 cm x 1 cm x .2 cm). One piece was heated at 400°C for two hours. One piece with the internal surface and one with the external surface were mounted in separate sample holders under a normal laboratory environment. Charles Evans & Associates' Time-of-Flight Secondary Ion Mass Spectrometry (TOF-SIMS) and X-ray Photoelectron Spectroscopy (XPS) instruments were used to analyze the aerogel. TOF-SIMS makes use of a microfocused pulsed primary ion beam to sputter the top surface layer of the sample. The secondary ions produced are extracted and injected into a specially designed time-of-flight mass spectrometer. The mass sensitivity range is typically 0 to 5000 atomic mass units at relatively high mass resolutions, > 3000. An image of the lateral distributions of the secondary ions can be generated at spatial resolutions of less than 1 μm. XPS irradiates the sample with Mg or Al X-rays to cause the ejection of photoelectrons. The electron binding energies are used to identify the elements and, in many cases, the valence state(s) or chemical bonding environment of the detected elements.

RESULTS The TOF-SIMS positive ion spectra of the heated, unheated internal and external surfaces of the JPL aerogel are shown in Figures 1a, b & c respectively. The total integral counts were 1,252,803, 1,595,436 & 2,316,377 with acquisition times of 14.6, 15.3 & 15.0 minutes respectively. Figures 1b & 1c show the results of handling with vinyl gloves, wax papers, polyethylene bubble wrap and room contamination. Figures 1a and 1b show that heating pyrolyzed nearly all of the organic components. The cleanness of aerogel is compared to a typical silicon wafer as shown in Figure 2. The JPL silica aerogel is quite pure and clean. The binding energy of the heated sample with Mg X-ray is shown in Figure 3. The sample plane was 45° to the spectrometer with a total acquisition time of 19.7 minutes. XPS reaffirms that the aerogel is as clean as silicon wafer having been exposed to air.

FINDINGS With proper purification of raw materials and due care, silica areogel can be made very pure. The heating in the aerogel critical extraction fabrication renders it inherently clean. With post heat processing, silica aerogel can be made essentially free from organic contamination to enable the preservation of captured biogenic elements and compounds. TOF-SIMS can be an excellent technique to analyze organic and inorganic particles captured in aerogel nondestructively even down to micron size.

ACKNOWLEDGMENT This work was carried out in part by the Jet Propulsion Laboratory, California Institute of Technology, under NASA contract.

REFERENCE Tsou, P., et al, LPSC 19 (1988), Tsou, P., et al, LPSC 24 (1993), Gibson E. K., et al, LPSC 20 (1989), Hartmetz, C. P., et al, LPSC 21 (1990), Gibson E. K., et al, LPSC 22 (1991).

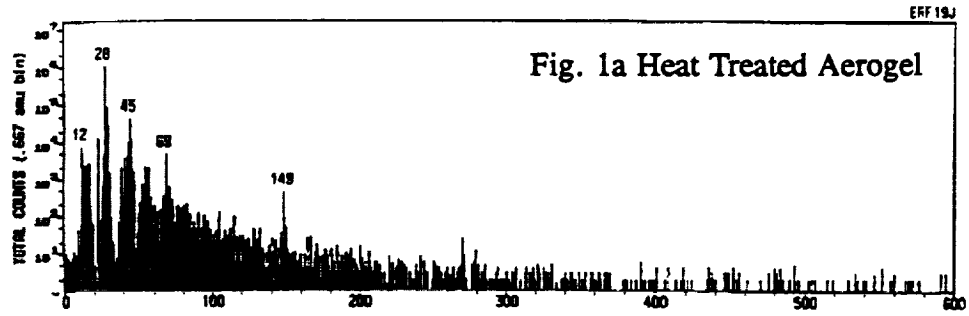

Fig. 1a Heat Treated Aerogel

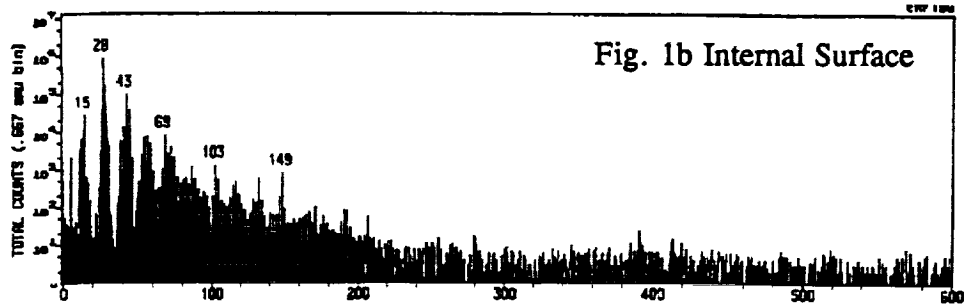

Fig. 1b Internal Surface

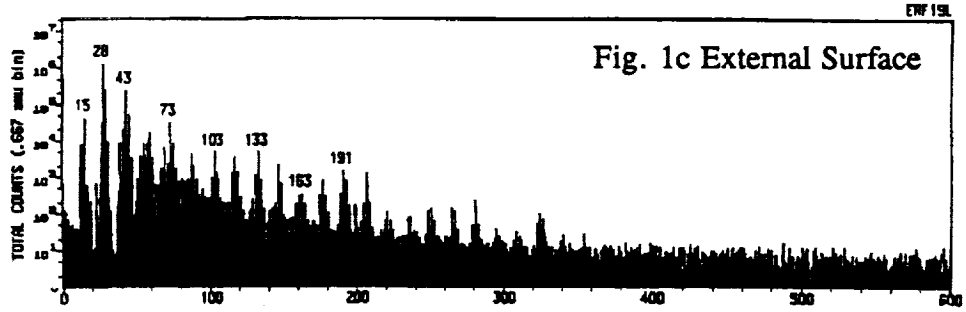

Fig. 1c External Surface

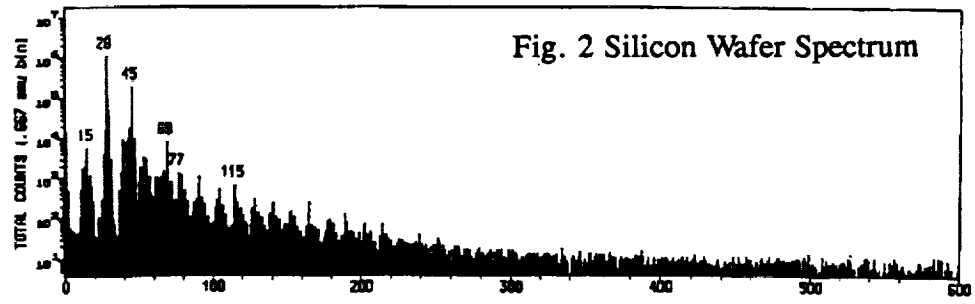

Fig. 2 Silicon Wafer Spectrum

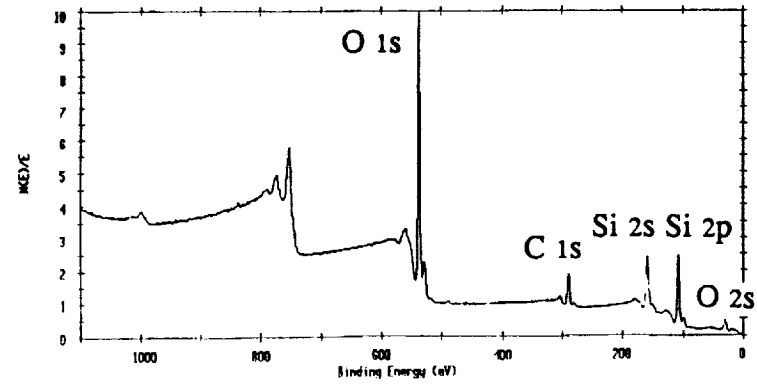

Fig. 3 Bonding Energy of Heat Treated Aerogel

omit to P/439

HOW DOES VENUS LOSE ITS HEAT? D.L. Turcotte, Department of Geological Sciences, Cornell University, Ithaca, NY 14853

On the earth about 75% of the heat flow through the mantle is attributed to subduction of cold lithosphere. In order to understand the tectonic and volcanic processes on Venus it is necessary to understand how heat is transported through the mantle of that planet.. Two general hypotheses have been proposed, the first is a near steady-state loss of heat as on the earth, the second is a strongly time dependent or catastrophic loss of heat. For the steady-state hypothesis the convective heat flux in the mantle must be attributed to either downward movement of cool delaminated lithosphere or upward movement of hot plumes. There is little surface evidence for the high required fluxes of either or both processes. The alternative is that Venus has not been losing significant heat for the last 500 Myrs., the lithosphere has been thickening by heat conduction and the interior is heating due to radioactive heat production.

Based on the near-uniform distribution of cratering on its surface, Schaber et al. [1] postulated that a global resurfacing event occurred on Venus about 500 Myrs. ago. Several authors [2, 3, 4] have argued that the lithosphere of the planet stabilized at that time. The extreme view is that the lithosphere has been thickening conductively since that time with no significant convective heat flux to its base. In this limit the thickness of the lithosphere is now near 300 km. Such a thick lithosphere is consistent with a number of observations:
i. it provides support for the high topography, up to 10 km.,
ii. it is consistent with the high observed geoid-topography ratios, up to 33 m/km [5],
iii. it is consistent with the observed unrelaxed craters [6],
iv. and it is consistent with the thick elastic lithospheres inferred from flexural studies [7].
In this limit the radioactive heat release heats the interior of the planet. Assuming that the concentrations of heat producing elements within Venus are equal to those within the earth the increase in temperature in 500 Myrs. is about 100 ^{o}K.

Based on a scaling with the earth the total heat production within Venus is estimated to be 3×10^{13} W. It is necessary to transport this heat through the mantle by convective processes. One mechanism is the delamination of the base of the lithosphere, the descent of the cool lithospheric rock cools the mantle. Assuming that the temperature difference across the delaminated layer is 400 ^{o}K and its thickness to be 20 km, it is necessary to completely delaminate the entire lithosphere of Venus every 7 Myrs. This could happen if the viscosity of the mantle is very low, near 10^{18} Pa s, but there is no surface evidence for regular global delamination and it is very difficult to envision such a low mantle mantle viscosity.

A second mechanism for the vertical ascent of heat is a high plume flux. The strongest plume on the earth is the Hawaiian and it is estimated to have a heat flux of 4×10^{11} W [8]. Thus nearly 100 Hawaiian strength plumes would be required to transport heat through the mantle of Venus. With a relatively thin lithosphere, it would be expected that both surface swells

and massive surface volcanic eruptions would be associated with strong mantle plumes on Venus. Beta Regio certainly has many of the surficial features associated with a mantle plume, Atla, Eistla, and Bell Regiones may also represent plumes. But the number and volume of surface volcanism would indicate that the vertical flux of heat associated with plumes on Venus would be only a small fraction of the total required vertical heat flux.

The heat flow from the mantle can be reduced if a significant fraction of the heat producing elements are concentrated in a relatively thin crust. Heat can then be conducted through the crust to the surface. Based on concentration measurements taken by Vega and Venera landers [9] a crustal heat production near 1.4×10^{-10} W/kg is indicated, about a factor of 20 greater than the mantle. A global crust 50 km thick would include about 40% of its heat producing elements, the temperature at the base of the crust would be about 1600 ^{o}K. A thinner crust would contain a lower percent of the heat producing elements, a thicker crust would be molten at its base. With such a high crustal temperature, a very low mantle viscosity would be required to extract the remaining heat from the mantle.

Observational evidence appears to strongly favor a thickening lithosphere on Venus. But the question of heat loss from the mantle of Venus remains. As the lithosphere thickens its gravitational instability increases, also the heating of the mantle will have reduced its viscosity by an order of magnitude in 500 Myrs. Both could contribute to a relatively rapid global subduction event.. The cooling associated with such an event would be equivalent to over 50% of the accumulated mantle heating. After a global subduction event a period of very high surface heat flow would be expected to occur. However, conditions for the initiation of subduction on the earth are not established, so applicable criteria are not available.

1. G.G. Schaber, R.G. Strom, H.J. Moore, L.A. Soderblom, R.L. Kirk, D.J. Chadwick, D.D. Dawson, L.R. Gaddis, J.M. Boyce, and J. Russell, J. Geophys. Res. 97, 13,257 (1992).
2. J. Arkami-Hamed and M.N. Toksoz, Phys. Earth Planet. Int. 24, 232 (1984).
3. R.G. Strom, J. Arkami-Hamad, and M.N. Toksoz, Lunar Planet. Sci. XXIII, 1379 (1992).
4. D.L. Turcotte, J. Geophys. Res. 98, 17,061 (1993).
5. S.E. Smrekar and R.J. Phillips, Earth Planet. Sci. Let. 107, 582 (1991).
6. R.E. Grimm and S.C. Solomon, J. Geophys. Res. 93, 11,911 (1988).
7. D.T. Sandwell and G. Schubert, Science 257, 766 (1992).
8. N.H. Sleep, J. Geophys. Res. 95, 6715 (1990).
9. Yu.A. Surkov, F.F. Kirnozov, V.N. Glazov, A.G. Dunchenko, L.P. Tatsy, and O.P. Sobornov, J. Geophys. Res. 92, E537 (1987).

STRESS AND FLEXURAL MODELING OF ALBA PATERA, MARS. E.P. Turtle and H.J. Melosh. Lunar and Planetary Lab, University of Arizona, Tucson, AZ 85721.

Surface fracture patterns are indicative of the regional stress level and of the thickness of the elastic layer in which they are active. The terrain surrounding Alba Patera, one of the shield volcanoes in the Tharsis region of Mars, as well as the flanks of the volcano itself, is cut by numerous graben which are diverted outward around the volcanic cone (Fig. 1, [1]). Wise [2] demonstrated that this deflection could be caused by the interaction of an extensional regional stress with the stresses associated with the load of the volcano on the lithosphere. However, the regional stresses which produced a stress field matching the observed faulting were quite low. This is probably a result of his use of an elastic half-space to represent the Martian lithosphere. Here we present results of a similar study in which we represented Mars as having an elastic lithosphere of finite thickness overlying a fluid interior. This improvement in the model has enabled us to derive not only a better estimate for the amount of stress in this region, but also a value for the thickness of the lithosphere in the vicinity of Alba Patera.

Alba Patera rises about 2km above the Tharsis plateau and has a diameter of about 700km at its base. The surrounding graben cut across volcanic flows from Alba. Drainage from the slopes is not diverted into the faults, indicating that they formed after the growth of the volcano. The graben are thus the result of extensional stress imposed on the region after the formation of the volcano. Wise modeled Alba as a cone 500km in diameter and 5km high with a density of 2900kg/m^3, equal to that of the crust. The stress field from this load on an elastic half-space along with a superimposed regional stress between 5 and 20 bars produced a stress pattern that matched the trajectories of the graben around Alba. This value of stress is quite low compared to stresses thought to be necessary to initiate faulting, probably due the use of the elastic half-space in his model.

We have applied a model which incorporates an elastic lithosphere over a fluid mantle. The same type of model proved successful in describing a variety of fracture patterns associated with coronae on Venus [3]. We assumed a load with a gaussian shape for Alba. First we calculated the flexure of the lithosphere under such a load by varying three parameters: lithospheric thickness, load radius, and load height. The resulting profiles were compared to the most recent Martian topography [4]. The best fit was obtained for a lithospheric thickness of 100±25 km, volcano radius (at base) of 350±25km, and volcano height of 4.0±0.5km. There was little variation of load radius among the group of models which produced good fits. The expected tradeoff between lithospheric thickness and load height was apparent, but parameters were chosen to be in the middle of the range for each variable. Regional gravity has not yet been used to confirm the results of the topographic modeling. It should be possible to compute the gravity associated with the modeled volcanic load and resultant lithospheric flexure. A comparison of this with the observed gravity of the region will serve as a check on the validity of the model. This has not yet been implemented, however, and could lead to some changes in the model parameters.

Stresses due to a combination of the modeled volcanic load and a superimposed regional stress field were calculated out to a distance of three volcano radii for various values of regional stress. The pattern which best fits the observed graben trajectories (Fig. 2) corresponds to a extensional regional stress of 1.4±0.2kbar, significantly higher than the value obtained by Wise. The surface fracture pattern observed around Alba Patera is indicative of an extensional regional stress of 1.4±0.2 kbar acting in an elastic layer about 100±25 km thick.

[1] Scott, D.H. *et al.* (1986-87) Geologic Map of the Western Equatorial Region of Mars, USGS Map I-1802-A.
[2] Wise, D.U. (1975) *International Colloq. of Planetary Geology, Proceedings*, pp. 430-433.
[3] Cyr, K.E. and Melosh, H.J. (1992) *Icarus*, **102**, pp. 175-184.
[4] Zuber, M.T. personal communication

TECTONIC MODELING OF ALBA PATERA, MARS: Turtle, E.P. and Melosh, H.J

Figure 1 (right): Sketch of graben surrounding Alba Patera 90°-120°W and 25°-50°N (from [1]). Same scale as Figure 2.

Figure 2 (below): Model results for a lithospheric thickness of 100km, gaussian load with 700km diameter and 4km thickness, and regional stress of 1.4kbar. Left hand side of figure shows the resultant principal stresses: hourglass shape indicates compression and bars denote tension. Sizes are proportional to the magnitude of the stress. Regional stresses act in the x direction. Orientation of resultant graben are sketched on the right.

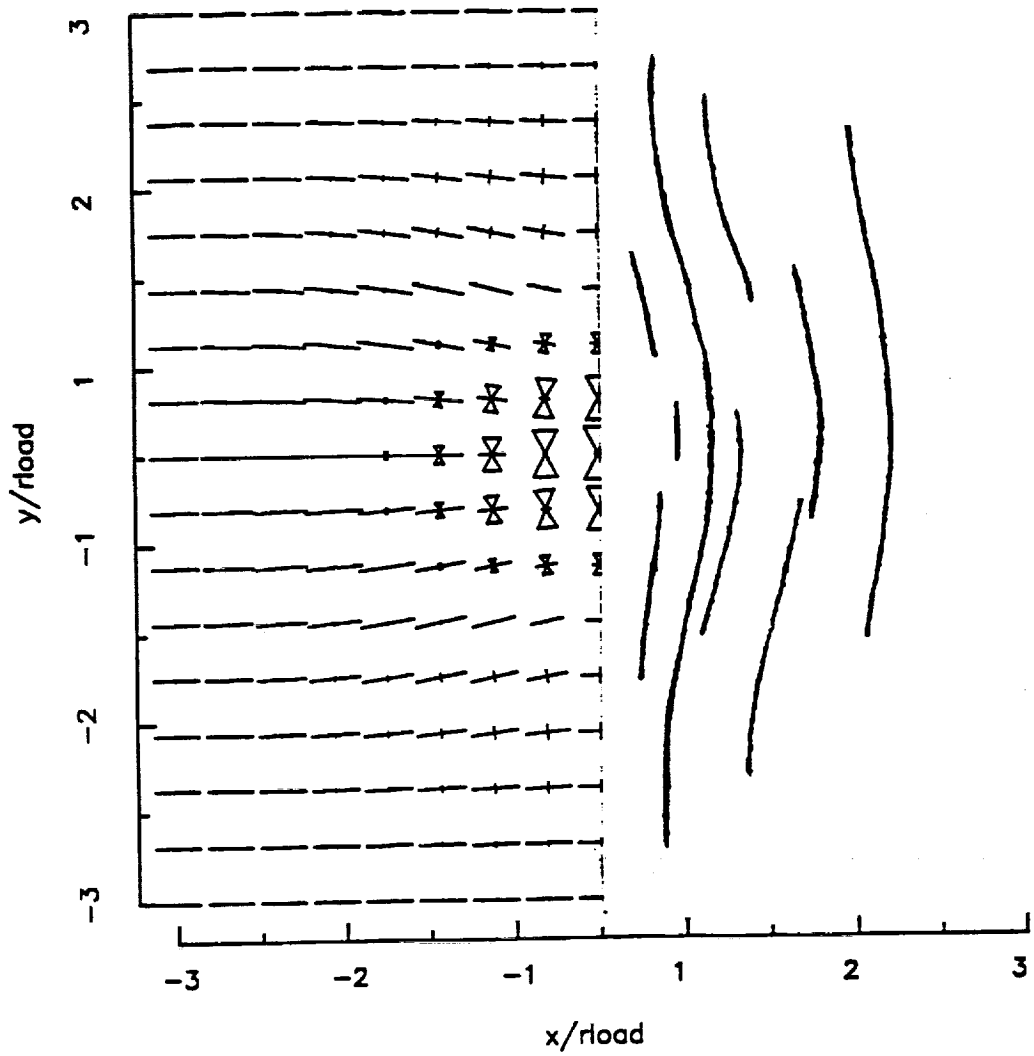

EXCITATION FUNCTIONS OF THE NEON ISOTOPES IN CHONDRITES AND ACHONDRITES; G.K.Ustinova, Institute of Geochemistry and Analytical Chemistry, Russian Academy of Sciences, Moscow 117334 Russia

The composition-weighted excitation functions in chondrites and achondrites for Na-22 as well as for the isotopes of Ne are constructed. The depth distributions of the production multiplicities and fluxes of nuclear-active particles inside those meteorites are demonstrated. Some general peculiarity of their interaction is indicated.

The noble gases, in particular, the neon isotopes are constantly produced in the extraterrestrial matter due to its interaction with the solar (SCR) and galactic (GCR) cosmic rays. Besides of such a direct production, Ne-22 is also generated due to decay in situ of radioactive Na-22. Some meteoritic minerals contain the noble gases formed by energetic particles in the peculiar conditions at the early stage of the solar system. There are trapped gases of both the solar and planetary origin. In addition, some interstellar components could survive in refractory grains. The origin of the noble gases in various processes gives us an opportunity to use them for studying those processes and different characteristics of the extraterrestrial matter. For instance, the radiogenic Ne-22 in the refractory inclusions of chondrites provides us some information about the variable spectrum of energetic particles accelerated in the strong shock waves accompanied many events in the protosolar nebula /1,2/, whereas the cosmogenic Ne-21 is well known to be the most sensitive chronometer of the cosmic-ray exposure age of meteorites, and the cosmogenic Ne-22/Ne-21 ratio can be used as an indicator of the sample screening /3/. Obviously, that knowledge of the excitation functions of the isotopes by SCR and GCR on the main target elements of the meteorites is of paramount importance. A number of good experimental works on the subject have been carried out /4-6,etc./. Their data as well as the ones on Na-22 production /7-9/ and the previously elaborated systematic of nuclear reactions /10/ are utiliz-

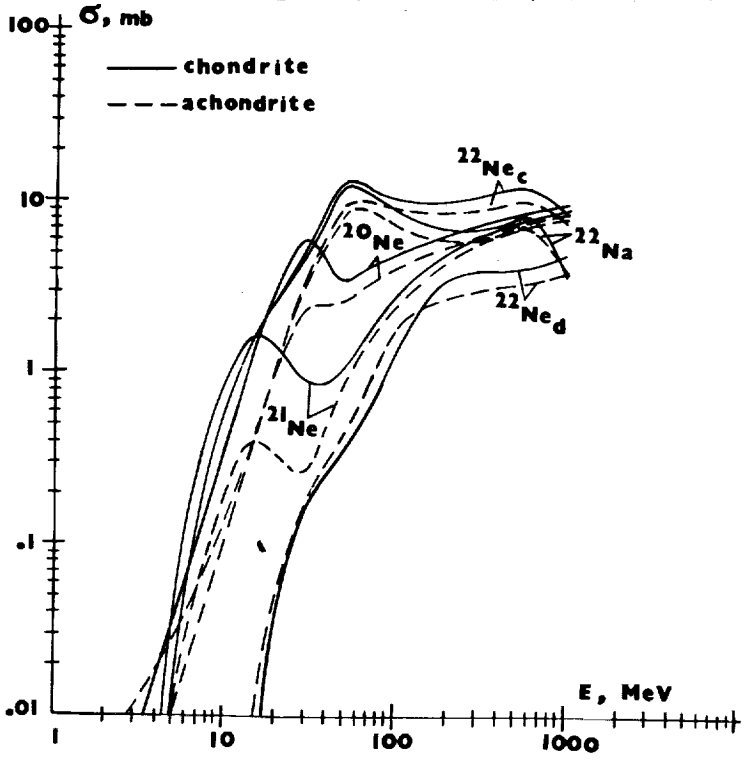

Fig.1- Excitation functions of the neon isotopes and Na-22 in chondrites and achondrites (both the Ne-22 functions of direct production (d) and cumulative one (c) are shown)

NEON EXCITATION FUNCTIONS: Ustinova G.K.

ed to construct the composition-weighted excitation functions of the isotopes in chondrites and achondrites using their average compositions /11/(in %): Na-0.67;Mg-13.9; Al-1.3;Si-17.2 and Na-1.94;Mg-3.3; Al-7.61;Si-20.4,respectively (see Fig.1). The obtained excitation functions turned out to be distinguished from those calculated by Dragovitsch, as described in /6/, especially below 50 MeV. The Na-22 production on Na may be the most crucial factor in that energy range.The neon isotopes are produced by GCRs of some average spectrum, e.g.,similar to it in 1962. The primary particles become exhausted with depth in meteorites, but the nuclear-active secondaries and tertiaries are generated/12/. There are showers (>1000MeV),cascade p, n and π (~100-1000MeV) and low energy neutrons (1-100MeV). Although the multiplicities of their production depend only slightly on depth of the matter /12/(see Fig.2),their fluxes vary so considerably that,on the whole, determine the shape of the total flux distributions inside meteorites (see Fig.3).The shapes of Ne-21 and Ne-22 distributions in chondrites and achondrites are similar to those of fluxes in Fig.3, but the $Ne\text{-}22_c/Ne\text{-}21$ ratio decreases with depth,e.g., the observed range of it in chondrites is 1.3-1.0 /13/. According to the correlations of the functions in Fig.1,this range corresponds to energy of 700-900 MeV that so should be considered as the average energy of the total spectrum of all nuclear-active particles in the meteorites and could be used for some estimations.

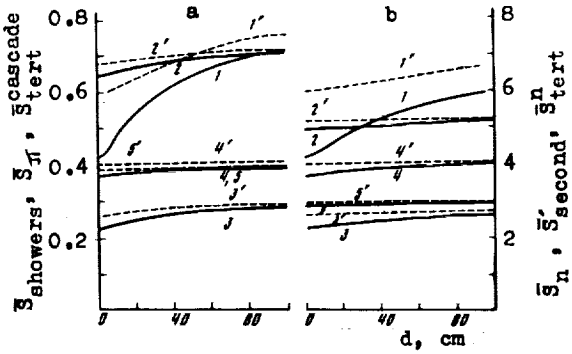

Fig.2- Depth dependence of the spectrum-weighted multiplicities (in particles/interaction) of secondary and tertiary particle production in GCR interaction with Fe(a) and Al(b) ($\bar{S}_{sh,\pi}$-1,1';$\bar{S}_n$(1-100MeV)-2,2';$\bar{S}'_s$(all secondaries)-3,3';$\bar{S}^{casc}_t$-4,4';$\bar{S}^n_t$(1-100MeV)-5,5';solid and dashed curves are for 1965 and 1962 spectra,respectively)

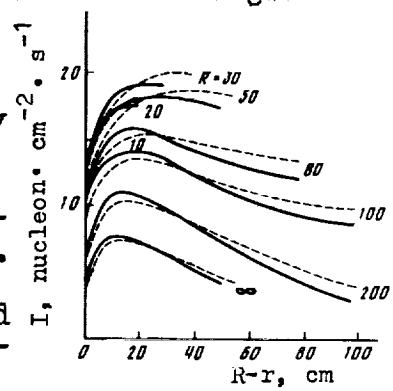

Fig.3- Depth distribution of total fluxes of nuclear-active particles in chondrites (solid curves) and achondrites (dashed curves) irradiated by GCRs of 1962 spectrum /12/

References. [1] Lavrukhina A.,Ustinova G.,LPS XXIII (1992)761. [2] Lavrukhina A.,Ustinova G.,Astron.Vestnik 26(1992)62. [3] Cressy P. Bogard D.,GCA 40(1976)749. [4] Walton J.et al.,JGR 78(1973)6428; 81(1976)5689. [5] Reedy R.et al.,EPSL 44(1979)341. [6] Michel R.et al.,Nucl.Instr.Meth.Phys.Res.B42(1989)76. [7] Furukawa M.et al., Nucl.Phys.A,174(1971)539. [8] Hintz N.,Ramsey N.,Phys.Rev.88(1952) 19. [9] Korteling R.,Caretto A.,ibid.C1(1970)1960. [10] Lavrukhina A. Ustinova G.,Nature 232(1971)462. [11] Dyakonova M.,Kharitonova V., Yavnel'A.,Chemical composition of meteorites,M.Nauka(1979). [12] Lavrukhina A.,Ustinova G.,Meteorites as probes of cosmic ray variations,M.Nauka(1990). [13] Bhandari N.,Potdar M.,EPSL 58(1982)116.

ON POSSIBLE DISTURBANCE OF THE SOLAR MODULATION MECHANISM OVER A LONG TIME SCALE; G.K.Ustinova and A.K.Lavrukhina, Institute of Geochemistry and Analytical Chemistry, Russian Academy of Sciences, Moscow 117334, Russia

Cosmogenic nuclides in chondrites with different orbits as well as in lunar soil cores give evidence on higher galactic cosmic ray (GCR) intensity and absence of their spatial variations in the solar system during a period of 2-6 My ago.

An ever-increasing number of new pages in the cosmic radiation history is being written by investigation of radioactivity of extraterrestrial matter. Great progress is made with studying cosmogenic radionuclides in lunar samples because it turned out to be possible to reveal temporal GCR variations and further, subsequently, studying radioactivity of the cosmogenic nuclides in meteorites with different orbits, to estimate the spatial GCR variations. The radioactive Na-22 ($T_{1/2}$ = 2.6 y) and Al-26 ($T_{1/2}$ = 0.74 My) in the deep specimens of the lunar drill soil cores are the most valuable detectors of the temporal GCR variations. The observed radioactivities of Na-22 and Al-26 are accumulated, successively, during ~4 years and over a million years before removing samples from the lunar surface. One can see in Fig.1 that the experimental depth profiles of both the radionuclides in the soil cores of Luna 24 and Apollo 15 are fitted by the theoretical curves calculated with using the data on the GCR intensity in the contemporary solar cycles. It means that, on the average, at least over a million years, the solar modulation of GCRs is constant in the solar system.

There is very different situation in the case of considering the last ~ 6 My in accordance with the data on radioactivity of Mn-53 ($T_{1/2}$ = 3.7 My). As follows from Fig.2, the experimental profiles of this nuclide inside the soil core of Apollo 15 and in the St.Severin chondrite are fitted by the theoretical curves calculated with using the maximum GCR intensi-

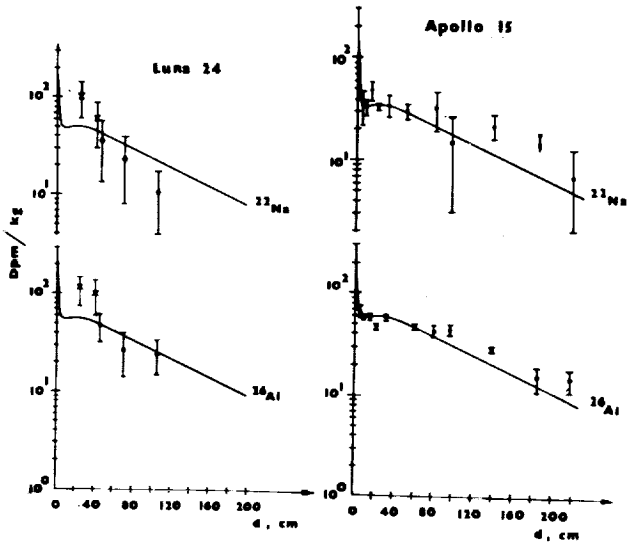

Fig.1- Depth distributions of Na-22 and Al-26 in the Luna 24 and Apollo 15 soil cores /1/. (experimental points are from data /1-3/; curves are calculated by the analytical method /4/ with using the stratospheric data /5/ on the average GCR intensity over ~4 years before the end of exposition (in Na-22 case) and over the contemporary solar cycles (in Al-26 case); d is depth from the lunar surface)

ON MODULATION DISTURBANCE: Ustinova G.K. and Lavrukhina A.K.

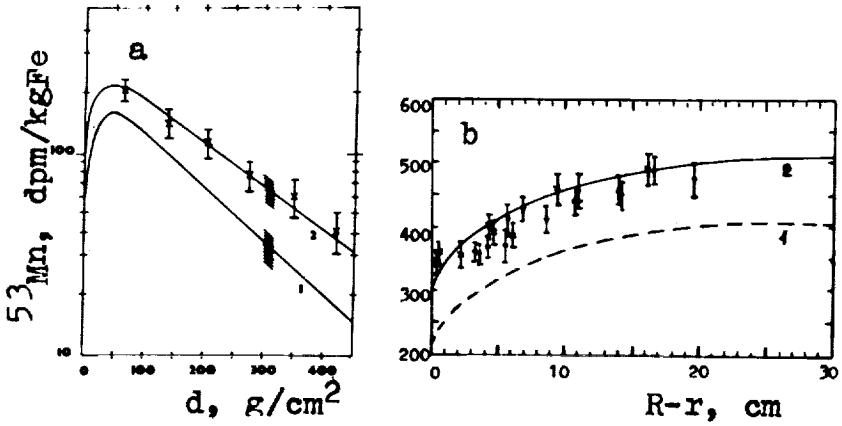

Fig.2- Depth distributions of Mn-53 in the Apollo 15 soil core (a)/6/ and in the St. Severin chondrite (b) (experimental points are from data /7-9/; curves 1 and 2 are calculated, successively, using the average and maximum GCR intensity of the contemporary solar cycles; R is the chondrite radius; r is distance from the center)

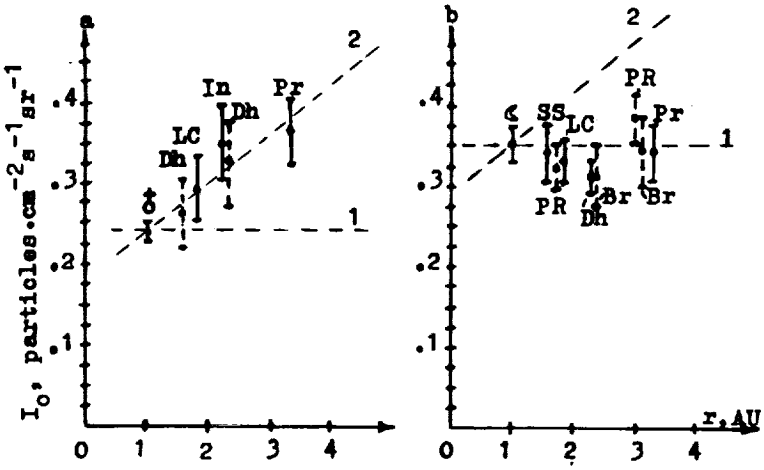

Fig.3- Spatial distribution of the average GCR intensity over ~1 My (a) and over ~6 My (b) along the meteorite orbits /4/ (1 is the average intensity near the earth; 2 is GCR intensity gradient of 20-30%/AU; the available data on Al-26 and Mn-53 in the chondrites Lost City (LC), Innisfree (In), Pribram (Pr), Dhajala (Dh), St.Severin (SS), Bruderheim (Br) and Peace River (PR) are used; r is heliocentric distance).

ty observed near the earth for the periods of solar activity minimum, rather than the average intensity for the solar cycles. It means that, at least, 2-6 My ago the GCR intensity in the solar system was ~40% higher than during the last million years. Moreover, studying the radioactivity of Al-26 and Mn-53 in the chondrites with different orbits shows quite different spatial distribution of the average GCR intensity for ~1 My and for ~6 My in the solar system (see Fig. 3). Indeed, the gradient of 20-30%/AU (R≥0.5GV) conditioned by the solar modulation is characteristic of the average GCR intensity for 1My as well as for the modern solar cycles /4/, while the absence of any gradient is inherent in the average GCR intensity for ~6 My. Thus, the temporal as well as the spatial GCR variations testify to some disturbance of the solar modulation mechanism over a period of 2-6 My ago due to the Sun dynamo breaking.

References. [1] Lavrukhina A.et al.,Kosmich.Issled.22(1984)110. [2] Rancitelli L,et al.,Proc.VI LSC(1975)1891. [3] Surkov Yu.et al., Proc.X LPSC(1979)1401. [4] Lavrukhina A.,Ustinova G.,Meteorites as probes of cosmic ray variations, M.Nauka(1990)262p. [5] Cosmic Data, M.Nauka(1974-1984). [6] Lavrukhina A.,Ustinova G.,Proc.IX LPSC (1978)2399. [7] Bhattacharya S.et al.,EPSL 51(1980)45. [8] Evans J. et al.,JGR 87(1982)5577. [9] Imamura M.et al.,EPSL 20(1973)107.

SHOCK DEFORMATION IN TALC AND ITS POSSIBLE SIGNIFICANCE FOR INVESTIGATIONS OF ASTROBLEMES; A. A. Valter, Institute of Geochemistry and Physics of Minerals, Acad. Sci. of Ukraine, 34, Palladin Ave., 142 Kiev, 252680, Ukraine

Diaplectic talk with the atomic Fe/Mg ratio of 1:9 (talk-1) and 1:2 (talk-2) has been found in the Terny astrobleme /1-3/ of the Krivoi Rog basin, Ukraine, in the rocks which have been subjected to the impulse pressure of 3-4 and 10-12 GPa respectively. The planar cleavage and mechanical twins parallel to (100),(010), (213) and other planes are developed.The width of twin lamellae is supposed to be used for the estimation of impulse action duration.The anomalously strong coloring of diaplectic talk is likely to be applied for its distances diagnostics.

Talk-1 crystals (up to 2 cm) have been ascertained in metasomatic bodies among the microgneiss in the base of ring depression.Talk-2 has been discovered as poikilitic crystals (0,5- 2mm) in blocks of ferruginous quartzites from the denudated uplift.The block size of talk has been distinguished as apr. 10-100 nm and for talk-2 less than for talk-1 by X-ray and electron microscopy methods. Fractures of the shock cleavage systems density makes up 10^2 -10^4 mm. The width of shock twins varies from less than 1 to 100 μm (fig.1,2).The finest twin lamellaes have accomodation bands around them.This bands have an intermediate optical orientation between the host crystal and twin lamella (fig.3).The normal twins are predominant but the axial ones are also present.

In 50 crystals of talk-1 and in 20 ones of talk-2, orientation of twinning and cleavage planes has been measured according to the axis of the optical indicatrix.On the stereographic projection the points of shock features orientations have formed thickenings which were indexed by the comparison with calculated data for the planes with low indexes of talk structure.

The established orientations of the twinning and cleavage planes have coincided with (100) 12%;(010) 10%;(213) 10%;(241) 13%;(403) 6% and others.

The systems of fissures are formed in the rarefaction wave. Evidently,their orientations mark out the planes of the highest stresses which are the twinning and translation gliding planes. With regard for gliding on (001), the gliding direction has been determined as [100] or [010] as well as [210],[201] and others. In talk-2 the part of gliding direction which do not coincide with indicatrix axis exceeds that of talk-1. In some cases the shear plane for twins is near to (010).The shear direction is near to [014].In this direction the one-dimensional Si-O-Mg(Fe)-O chains with high atomic density may be distinguished.

SHOK - DEFORMATION IN TALK

Valter, A.A.

The difference between shock features of talk and micas can be explaned by the low static and dynamic elastic limits of talk, i.e. by the formation of residual twins under relatively low pressures. The rate of mecanical twins lenghth is $n.10^{6}$ mm/s in growth and only near 10^{-1} mm/s in width [4]. Accordingly, the width of twins lamellas in talk may be used for the estimation of shock pressure duration. The widest twin lamellas (up to 100 μm) are discovered in veined impact breccia where the pressure action duration is estimated as 0,n of a second.

The diaplectic talk has an anomalously deep green colouring which is probably due to thin Fe minerals inclusions. The maximumes of absorption measured by Dr. V.M. Khomenko make up 470 and 600 nm (Fe^{3+} in octahedrons), 1050 nm (Fe^{2+} in octahedrons) and the charge transfer band Fe^{2+} oct.-Fe^{3+} oct (680 nm).

The deep colouring of diaplectic talk makes possible its diagnostics at great distances on the planet bodies with the basic silicate crusts.

Ref.: 1. Masazitis, V.L. et al. (1981) LPSC, XII, p.655. 2. Valter, A.A. et al (1987) LPSC, XVIII, p.1032. 3. Valter, A.A. et al. (1989) LPSC, XX, p. 1148. 4. Klassen-Nehludova, M.V. (1960) Mecanical twinning in crystals. Moscow, 1960 (in Russian).

Fig.1. The cross-section of talk near (001). The twins on (010) and cleavage on (100). Ni ×.

Fig.2. The wide twins of talk crystals from breccia. Ni ×.

Fig.3. Twins of talk with accomodation bands

A SILICATE LAVA MODEL FOR IO'S HOTSPOTS. G. J. Veeder, D. L. Blaney, T. V. Johnson, D. L. Matson, and J. D. Goguen, Jet Propulsion Laboratory, California Institute of Technology.

The method of bringing heat to the surface and the relative role of different types of volcanic materials on Io (silicates, sulfur, and sulfur dioxide) are poorly understood. We have analyzed our Io radiometry (4.8, 8.7, and 20 μm) collected at the NASA Infrared Telescope Facility between 1983-1993. In modeling the data to determine the size and temperature distribution of thermal anomalies, we began with a distribution of thermal anomalies based on Voyager data where applicable and extended it as needed to match all the data. We also include the thermal pedestal effect to model the spectrum of the thermal emission caused by the heating of the thermal anomalies by sunlight [1,2]. The areas, temperatures, and power for the model thermal anomalies during each apparition are shown in the figures, binned in 100 K increments. The diagonal lines are contours of constant power (10^9 to 10^{14} Watts). The bulk of the observed power comes from large, relatively cool regions (150 - 200 K). Hot regions are small in areal extent and thus contribute little to the total heat flow. The area/temperature relations derived by McEwen *et al.* [3,4] using Voyager IRIS data are shown in **Figure 1** connected by the dotted line. There is good agreement between McEwen's Voyager based results and our results from earth based infrared radiometry, particularly with respect to the domination of large cool regions in terms of radiated power.

It has been suggested that such a distribution of areas and temperatures is a natural result of continuing, multiple volcanic resurfacing events. Carr [5] used a relatively simple eruption model to match the infrared spectrum from Loki. The model included an active eruption source, an active flow front, and a cooling, inactive flow. His calculations provide a good, although not perfect, fit to Voyager IRIS data for Loki. Interestingly, the distribution of areas and temperatures resulting from this model are qualitatively similar to both our global model and McEwen *et al.*'s Voyager results. **Figure 2** shows Carr's [5] results, multiplied by thirty to match the absolute areas of the global model. A simple interpretation would be that the equivalent of thirty active eruption centers similar to Carr's model could produce more or less the observed suite of hotspot characteristics.

Our data set also provides some insight into Io eruption characteristics. The event we observed on 9 Jan. 1990 is modeled having a very high eruption rate (~10^5 m^3 s^{-1}). This flow increased its area and cooled significantly over the 2.8 hrs we observed it [6]. The rate of area increase (4.3 x 10^4 m^2 s^{-1}) and the frequency of similar events in our data record (~4% of the time) suggetst that eruptions of this sort could produce an accumulated area of old, cooling flows equivalent to our lowest temperature anomalies (~2.7 x 10^6 km^2 at ~150-200K) in about 50 years. Taking Carr's calculation of cooling rates for inactive flows on Io, this is the approximate time for a silicate flow to cool to the observed temperatures. We conclude that the characteristics of Io's thermal anomalies are consistent with global resurfacing at very high rates by silicate volcanism over at least the last 50 - 100 years.

References: [1] Veeder, G J. ,*et al.*, Io's heat flow from infrared radiometry: 1983-1993, *JGR-Planets*,in press, 1994. [2] Matson *et al.*, On the nature of Io's thermal reservoir unit, *EOS*, **74**:43, 392, 1993. [3] McEwen, A.S. *et al.*, Io thermophysics: New models with Voyager 1 thermal IR spectra, *Lunar and Planet. Sci. XXIII*, 881, 1992. [4] McEwen, A.S. *et al.*,, New Voyager 1 hot spot identifications and the heat flow of Io, *Bull. Am. Astron. Soc.*, **24**, 935, 1992. [5] Carr, M. H., Silicate volcanism on Io, *J. Geophys. Res.*, **91**, 3521-3532, 1986. [6] Johnson *et al.*, Implication of the January 1990 volcanic eruption on io for resurfacing rates and energetics, *EOS*, **74**:43, 392, 1993.
(This work was done at JPL/Caltech under contract to NASA.)

IO'S SILICATE LAVA FLOWS: Veeder, G. J. *et al.*

Fig.1 Comparison of Voyager and Groundbased Io Data

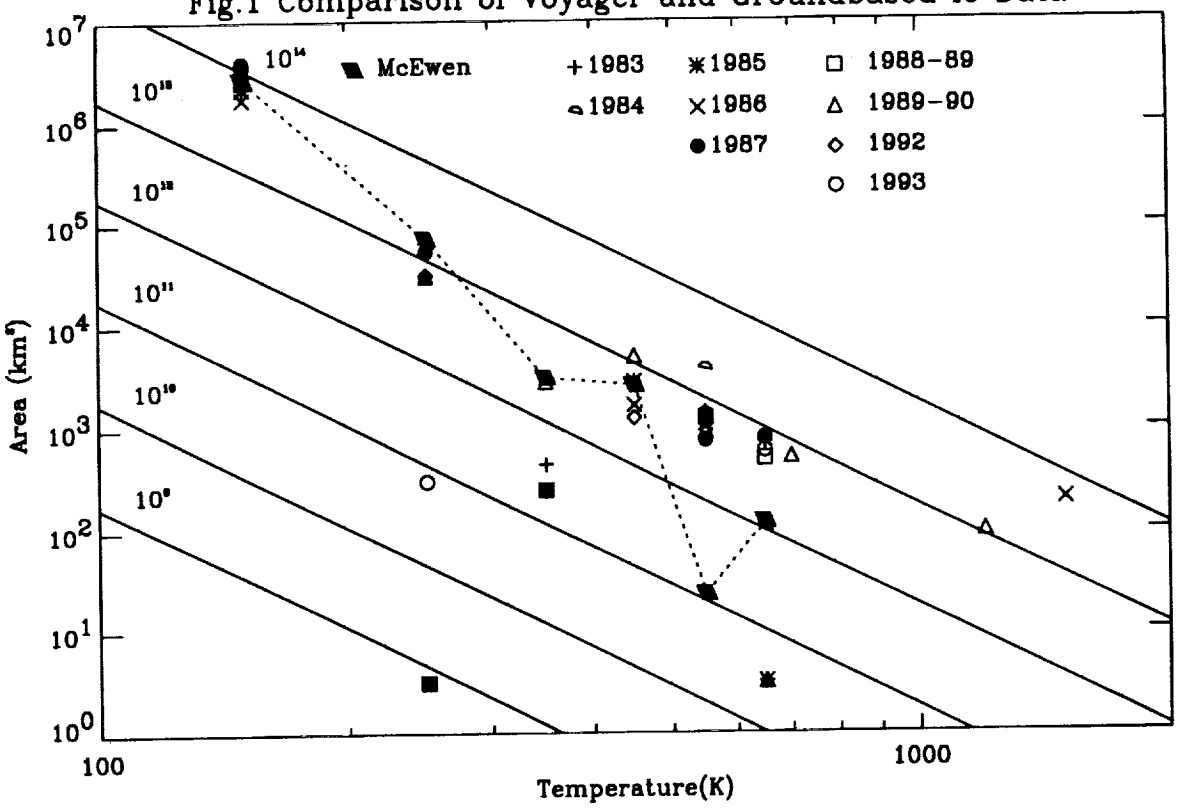

Fig.2 Comparison of Io Thermal Anomalies and Carr Model

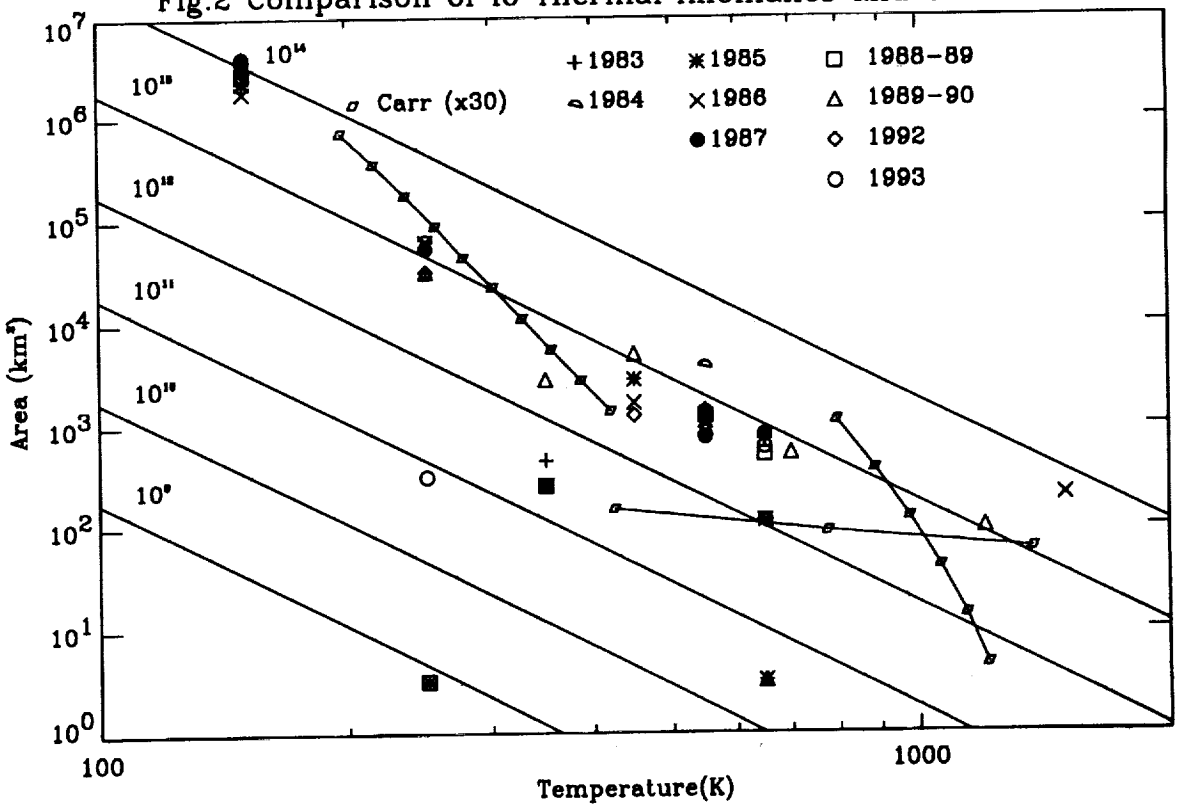

NITROGEN AND CARBON COMPONENTS IN C_δ; A POSSIBLE PRESENCE OF NITROGEN-FREE DIAMONDS IN C_δ; A.B. Verchovsky, J. Newton, I.P. Wright, J.W. Arden[1] and C.T. Pillinger, Planetary Sciences Unit, Dept. of Earth Sciences, The Open University, Milton Keynes MK7 6AA. [1]Dept. of Earth Sciences, Parks Road, Oxford.

The use of quasi-three isotope plot ($\delta^{15}N$ vs. C/N) for data acquired by stepped combustion of C_δ fractions from primitive chondrites may be interpreted in terms of several nitrogen containing components. The preferred explanation of the results however requires diamonds or diamond-like material free of nitrogen.

Variations of the abundance of nitrogen and carbon isotopic composition observed during stepped combustion of C_δ are still not well understood. So far we do not know whether metamorphic processing is involved [1] or if different components are present within C_δ; indirect evidence seems to favour the latter interpretation [2-4]. Unfortunately the two isotope systems of C and N cannot allow resolution of more than two component mixtures. Therefore to find out whether C_δ indeed contains greater than two nitrogen and/or carbon components, it is useful to use quasi-three isotope plots including elemental ratios for example $\delta^{15}N$ *vs.* C/N. Analysis of the stepped combustion data on such a plot surprisingly showed that N-C system of C_δ for some meteorites is rather simple: most of the experimental points define two distinct mixing lines which on occasion (*eg.* Krymka, Fig. 1) are practically ideal with deviation of the points from the lines within experimental errors. Thus, intuitively it would seem that isotopic variations of N in C_δ can be explained in terms of a three component mixture: (i) a $\delta^{15}N$= 0‰ component with low (possibly 0) C/N ratio released at low temperature that could be adsorbed atmospheric nitrogen, (ii) an intermediate lighter ($\delta^{15}N \sim -200$‰) component with high C/N ratio that appears to be a carbonaceous phase; and (iii) a component with very light nitrogen ($\delta^{15}N = -350$‰) and low C/N ratio released at high temperature which, presuming the C/N is finite, could in principle be either carbonaceous or a non-carbon nitrogen rich phase. This interpretation would suggest that both components (ii) and (iii) are presolar in that they have anomalous $\delta^{15}N$ values.

A more detailed look at the data suggest that the above interpretation is over-simplified. First of all considering plots from several meteorites the range of $\delta^{15}N$ for the intermediate component (from the mixing line intercepts) is rather high (from –50‰ to –250‰) to believe that it is a single entity. Likewise then intercept C/N ratio varies from 250 to more than 1000 to support this argument. Secondly, whilst the experimental points lie along the mixing lines for the pure components, they do not always lie within the experimental uncertainties; in such examples however the points are not obviously inside the triangle (Fig. 1). For this to be true the carrier of the lightest nitrogen (with $\delta^{15}N = -350$‰) cannot be oxidised at low temperature at all. It seems very odd for a mixture of three combustible phases whose total range for complete combustion is only from 300°C to 500°C to be so apparently completely resolved.

Another, quite different interpretation of the data is that nitrogen in the samples is a mixture of only two nitrogen containing (light $\delta^{15}N \sim -350$‰ and heav y $\delta^{15}N \sim 0$‰) components, in the presence of a carbonaceous nitrogen-free phase which causes the variability of the C/N ratio. In this case the different intercepts for $\delta^{15}N$ and C/N during stepped combustion can be easily understood as being due to change in the abundance of the nitrogen-free-carbon. In the other words the variations of $\delta^{15}N$ and C/N ratio on the quasi-three isotope plots are mostly independent and controlled by different processes. Analysis of all available data on stepped combustion and pyrolysis of C_δ suggest that the heavy nitrogen itself is complex and probably consists of two

components: a relatively small amount of physically adsorbed air nitrogen on grain surfaces and another more abundant component associated with a small amount of carbon (Fig. 2). Thus both components seem to be a laboratory contamination.

The experimental data also allows calculation of the putative nitrogen free component and its release pattern as a function of temperature. For simplicity we use a C/N ratio for the component containing the lightest nitrogen (–350‰) of 100 and C/N = 0 for the heavy nitrogen component. In some samples the nitrogen-free carbon can be as high as 80%; it is isotopically heavier ($\delta^{13}C$ = –32‰) than carbon containing the light nitrogen (–40‰). More complicated models are needed to take into account the carbon which comes from laboratory contamination.

None of the carbon phases discussed here appear to contain the anomalous noble gases. As we have argued in a previous paper [4] the noble gases have significantly higher release temperatures during stepped heating than light nitrogen. Nitrogen-free-carbon unequivocally has a lower combustion temperature than the other carbon *ie.* that associated with –350‰ nitrogen in the carbon colloquially known overall as C_δ. The relationship with P-type noble gases is unknown. If the nitrogen-free-carbon is also diamond or diamond-like we conclude that it may have been created under different conditions from the diamonds which contains the light nitrogen. The carbon isotopic composition –32‰ is entirely compatible with a solar system origin. There is no other diagnostic isotopic anomaly. N.B. however that the $\delta^{13}C$ value for the nitrogen-free-carbon is also entirely different from other diamonds of believed solar origin [5].

References: [1] Russell S.S. *et al.* (1992) *L.P.S.* **XXIII**, 1187. [2] Russell S.S. *et al.* (1991) Science **254**, 1188. [3] Huss G.R. and Lewis R.S. (1993) *G.C.A.* in press. [4] Verchovsky A.B. *et al.* (1993) Meteoritics **28**, 452. [5] Russell S.S. *et al.* (1992) *Science* **256**, 206.

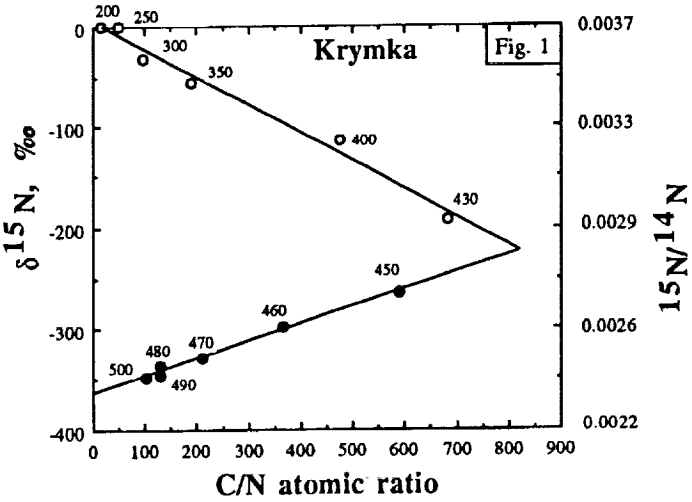

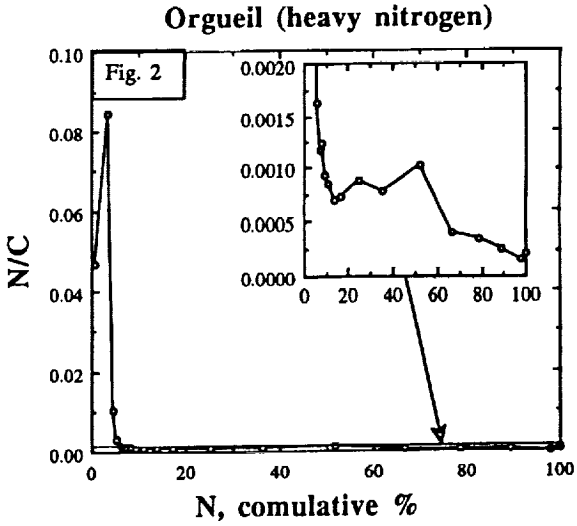

IMPACT EROSION OF ATMOSPHERES; A. M. Vickery, Lunar and Planetary Laboratory, The University of Arizona, Tucson, AZ, 85721

It has been hypothesized for several years that sufficiently energetic impacts can results in the net loss of atmosphere from a planet. Previous models of the interaction between the impact generated vapor plume and the overlying atmosphere indicated that atmospheric erosion may have been important for the evolution of the Martian atmosphere and the atmosheres of the satellites of the giant planets, but was probably not effective on the earth or Venus [1,2,3]. By inverting these models, it was shown that impacts are capable of delivering sufficient volatiles to account for the earth's water inventory [4]. This abstract reports the results of the first detailed hydrocode study of the impact process with respect to atmospheric erosion. The first series of calculations was done for a hypothetical primitive 1-bar Martian atmosphere composed of CO2. The results indicate that atmospheric erosion is less effective than predicted by the simplest analytic model [1], but is roughly comparable to that predicted by the more sophisticated sector model [2].

The earliest model of impact erosion [5] considered only the transfer of momentum from the impactor to the atmosphere during the initial penetration of the atmosphere, and found that this mechanism cannot account for the loss of atmospheres from planets with escape velocities greater than ~10 km/s. This treatment, however, neglects the role of the impact-generated vapor plume, which may contain a significant fraction of the total impact energy. The simplest treatment of the impact plume/atmosphere interaction is that of Melosh and Vickery [1], in which the plume is treated as a hemisphere of highly shocked gas deposited at the base of the atmosphere. It's momentum was then balanced against its own mass plus that of the overlying atmosphere; if the resulting velocity was greater than escape velocity, it was assumed that the atmosphere above a plane tangent to the planet was lost. Combining this model with estimates of the cratering flux on Mars as a function of time concluded that Mars could have been stripped of a ~1-bar atmosphere by this means.

This simple model implicitly assumed that the atmosphere over the expanding vapor plume is distributed isotropically with respect to zenith angle, whereas in real atmospheres, the mass is concentrated rather heavily toward $\theta = 90°$ (the horizon), with the degree of concentration depending mostly on the ratio of scale height to planet radius (H/R). This anisotropy was taken into account [2] by dividing both the vapor plume and the overlying atmospheres into conical sectors based on zenith angle and doing the momentum balance separately for each sector. This type of model showed, not surprisingly, that atmsopheric erosion is less effecient than predicted by the earlier "isotropic" model.

I here report the results of using the 2-D hydrodymic code CSQ to model the impact process, including the flight of the projectile through an exponential atmosphere as well as following the crater formation and vapor plume evolution. The atmosphere was modelled as pure CO_2, an ideal gas with $\gamma = 4/3$. It is assumed to be isothermal (298K), with a surface pressure of 1 bar. (Because all the early models indicate that atmospheric erosion is negligible on present-day Mars, a hypothetical primitive Martian atmosphere was used.) The inferred scale height of this atmosphere is approximately 15 km. Two runs have been completed, one for a 10 km diameter projectile and one with a 20 km diameter projectile. Both were dunite spheres, with an impact velocity of 15 km/s. For the smaller impactor, the isotropic model predicts no atmospheric loss and the sector model predicts negligible loss (~0.03% M_{tp}. where M_{tp} is the mass of atmosphere lying above the tangent plane). The hydrocode results show that no material, either plume or atmosphere, has a final velocity greater than escape velocity. For the larger impactor, the isotropic model predicts complete removal of the atmosphere above the tangent plane, and the sector model predicts loss for zenith angles between 0° and 43° ($M_{lost} \equiv 0.4\%$

M_{tp}). The hydrocode results, carried out until the top of the plume reached 5 scale heights, indicated atmospheric erosion for zenith angles less than about 30° ($M_{lost} \cong 0.1\%$ Mtp).

The numerical results are much more consistent with the sector model results than with those of the isotropic model because both the former take into account the anisotropy of the atmosphere. The numerical results differ from those of the sector model primarily because the upraised lip of the growing crater funnels the vapor plume upward, whereas in the sector model, it was assumed that the vapor was free to expand along the target surface.

References

[1] Melosh. H.J. and Vickery, A.M. (1989)Nature 338 487-489.
[2] Vickery, A. M. and Melosh, H. J. (1990) in: Global Catastrophes in Earth History (,eds.) GSA Special Paper 247, 289-300.
[3] Zahnle, K. at al. (1992) Icarus 95, 1-23.
[4] Chyba, C. (1990) Nature 343, 129-133.
[5] Walker, J. C. G. (1986) Icarus 68, 87-98.

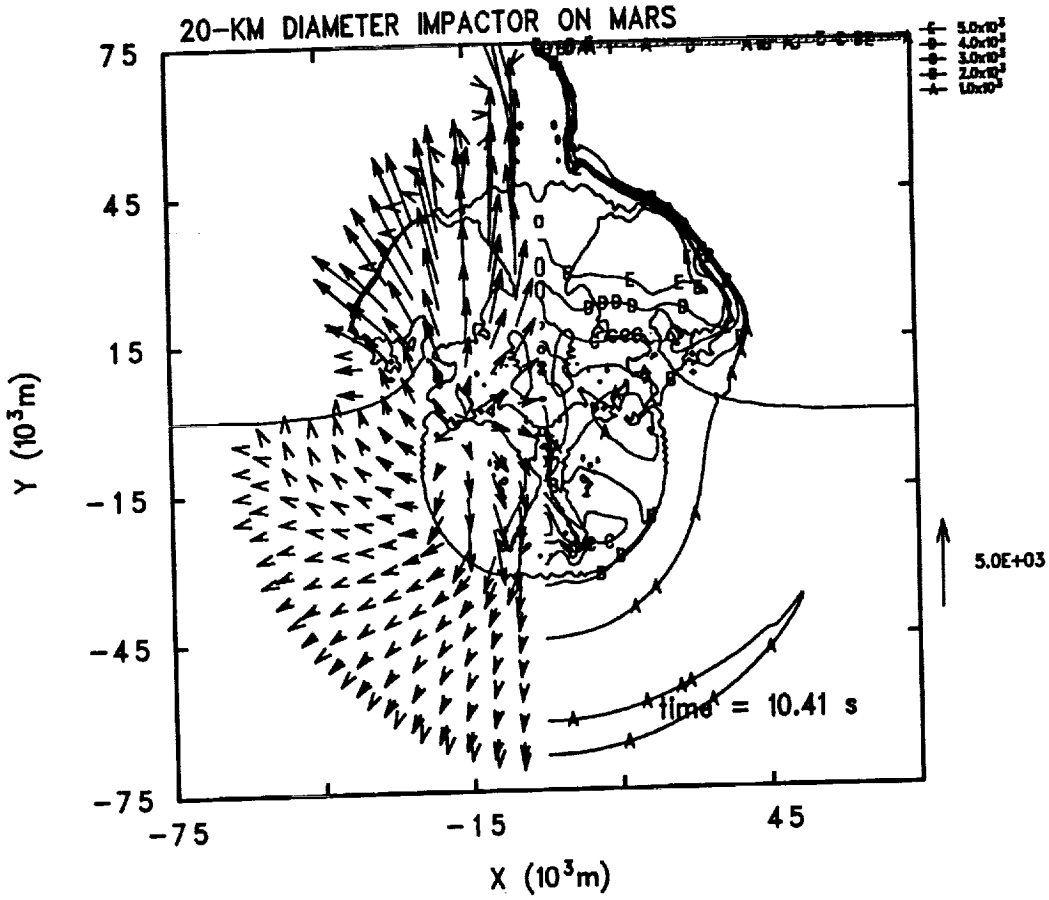

A QUICK LOOK METHOD OF DETECTING WATER OF HYDRATION IN SMALL SOLAR SYSTEM BODIES; F. Vilas, NASA Johnson Space Center, Houston, Texas.

The action of aqueous alteration of the near-subsurface material on asteroids and probably some satellites in the Solar System constitutes part of the formation history of the Solar System. The C-class asteroids (and subclasses B, G and F) were initially believed to have undergone aqueous alteration based on their low albedos and neutral broadband visible and near-infrared colors. These spectra exhibit a sharp drop at wavelengths shorter than 0.55 μm due to a strong ferric oxide intervalence charge transfer transition. This IVCT comprises multiple absorptions that are not uniquely indicative of phyllosilicates, but rather are present in the spectrum of any object containing Fe^{2+} and Fe^{3+} in its surface material. A definitive indication of aqueous alteration came when the broad IR absorption feature having a minimum near 3.0 μm indicative of structural hydroxl (OH) and interlayer and adsorbed water (H_2O) in phyllosilicates was identified in the IR photometry of many C-class asteroids [1]. Additional mineralogical compositional evidence of aqueously-altered asteroids has come as the result of high SNR narrowband spectrophotometry in the visible and near-infrared spectral regions taken using a CCD/spectrograph combination. An absorption feature centered at 0.7 μm indicative of an Fe^{2+} - Fe^{3+} charge transfer transition in oxidized iron in phyllosilicates in spectra of some low-albedo asteroids, especially C and G class, and CM2 carbonaceous chondrite meteorites was identified in the CCD spectra [2,3].

The correlation and covariance of the 0.7-μm and 3.0-μm features were examined by comparing observations of asteroids common to both the CCD reflectance spectra and the 3.0-μm multicolor photometry data sets [1,2,3]. Thirty-one pairs of observations were included in this training group. (Four asteroids were not included in this group: 1 Ceres, 2 Pallas, 72 Feronia and 570 Kythera. The first two objects are large enough to be considered atypical of any asteroid. The latter two objects have extremely unusual properties; classifications when possible are ambiguous.) The results of the statistical study indicate that with a 95% confidence level, 84% of the objects observed either having or not having the 0.7-μm feature will correspondingly have (or not) the 3.0-μm water of hydration feature.

Problems arise when trying to compile a large body of data to study the aqueous alteration history of the Solar System, or the availability of water in minerals as a possible space resource. The infrared observations directly address the question of the availability of water of hydration in clay silicate materials, however, the limitations of available IR astronomical instrumentation and the strong background signal resulting from both the immediate physical environment and the earth's atmosphere limit the objects that can be observed to those having an apparent visual magnitude $m_V \leq 14.5$ [4].

Is there a quick method of determining the presence of water of hydration in the surface material of asteroids that does not rely on IR observations? If one assumes that (1) the presence of H_2O-bearing phyllosilicates indicates the presence of water of hydration in the surface material of the asteroid, and (2) the feature centered at 0.7 μm is due to the Fe^{2+} - Fe^{3+} charge transfer transition in oxidized iron in H_2O-bearing phyllosilicates, then the presence of the 0.7-μm absorption feature in the narrowband spectrum could serve the purpose of identifying hydrated water in minerals. Even with a multiplexing system such as a CCD spectrograph, the long integration times necessary to produce high quality SNR narrowband spectra sufficient to identify the absorption feature preclude this from being a quick look method of determining its presence.

The Solar System can, however, be sampled extensively by applying a simple technique using three ECAS filters in the visible/near IR spectral region. Models of the ECAS filter

ASTEROID WATER OF HYDRATION: Vilas F.

transmission based upon the filter characteristics [5] were developed to simulate ECAS photometry from narrowband spectrophotometry. Simulated v (0.550 μm) , w (0.701 μm) and x (0.853 μm) ECAS filter values were made from narrowband reflectance spectra acquired since 1982 that have sufficient spectral coverage to contain the complete passbands defined by these filters [3], and for which corresponding ECAS photometry exists. The 0.7-μm feature has a lower wavelength edge near 0.57 μm, a minimum reflectance near 0.7 μm, and an upper reflectance edge near 0.83 μm; this varies slightly among asteroid spectra. The passbands for the v and x filters are concentrated primarily (although not entirely) in spectral regions that do not contain the absorption feature. The w filter is centered at the minimum of the absorption feature. In order to delineate this feature in the narrowband CCD spectra, a simple linear continuum defined by a linear least squares fit to the points in the spectrum is removed from the spectrum. Any weak absorption features present remain. This removes the effects of slope on the spectrum.

An empirical relationship was developed by examining simulated ECAS photometry. If the relationship

$$\frac{R_{0.701}-(0.4984(R_{0.853}-R_{0.550}))}{R_{0.550}} < 0.990$$

then the 0.7-μm feature is present. If this ratio is ≥ 0.990, the feature is absent.

This algorithm was applied to the ECAS reflectances for asteroids, Jupiter's and Saturn's satellites [6]. The composite asteroid values show that ~33% B class, ~50% C class and ~80% G-class asteroids indicate the presence of water of hydration. Less than 10% of the F, P, M, and X-class asteroids indicated water of hydration. One S-class asteroid out of 121 sampled had a low ratio, and the feature was absent from photometry of all other classes. The feature was present on Himalia and Phoebe.

CCD spectrophotometry of 52 Europa showed that on 3 nights of observations, the asteroid's spectrum was flat. On a fourth night, the 0.7-μm feature was present [2]. This suggested that variations in surface composition could exist on asteroids suspected of having undergone some aqueous alteration. From the population of C-class asteroids whose ECAS algorithm values were ≥ 0.990, those objects for which photometry exists from more than one night were selected. Algorithm values for individual nights of photometry were calculated. Over 50% of these asteroids show values that indicate the presence of water of hydration on some observing dates.

The M-class asteroid 92 Undina observed to have a 3.0-μm absorption [4] does not test positively for water of hydration using this algorithm. This, coupled with the paucity of M-class asteroids that indicate water of hydration by this algorithm, could indicate a different surface composition.

Acknowledgements: FV was supported by the NASA Planetary Astronomy Program.

References:[1] e.g.,Lebofsky L.A.(1980)*AJ,85*,573; Lebofsky, L.A. et al.(1990)*Icarus, 83*, 16.[2]Sawyer, S.R.(1991)*PhD Thesis, UTexas.*[3]Vilas, F.and Gaffey, M.J. (1989)*Science, 246*, 790; Vilas F. et al. (1993)*Icarus,105*,67. [4]Howell, E., per. comm. [5]Tedesco E. F. (1982) *AJ,87*,1585.[6]Zellner B. et al. (1985)*Icarus,61*,355; Tholen D.J. and Zellner B. (1984)*Icarus, 58*, 246.

FIREWORKS AROUND NAKED T TAURI STARS

A.V.Vityazev and G.V.Pechernikova
United Institute of Physics of the Earth, Moscow,123810, Russia

Our investigations have revealed new possibilities for searches and observations of circumstellar protoplanetary disks at the intermediate stages of planet formations in addition to strategies of discovery and investigation of protoplanetary gas-dust disks and other planetary systems. According to our estimates [1,2] the high-energy collisions of the large 100-1000 km bodies take place in the disks similar to the early circumso- lar disk at the stage of planet formation with protoplanets masses more than $0.1M_\oplus$ ($M_\oplus$ is mass of the Earth). Such collisions are attended with explosive processes with energy in the range $30<\log(Q/erg)<35$.

The result of the collisions of two bodies depends on the impact energy. If the impact energy is sufficient not only for disruption of the bodies but and for other dissipative losses, heating, melting and partial evaporation of the matter take place. It was pointed out earlier by a number of authors that the high-temperature (up to 10000 K) gas jets can be formed at the high-velocity collisions. This effect is of importance to the evaluation of the luminosity fluctuations in the optical, and IR ranges.

The generalized Boltzmann equation with the modified Smoluchowski operator [3] is sufficient to find the distribution function $n(m,v,x,t)$ and to obtain simple relations for intermediate asymptotics in the mass and velocity spectra, which are necessary to make the resulting estimates of the

FIREWORKS: A.V.Vityazev, G.V.Pechernikova

frequency and amplitude of the luminosity fluctuations.

For the standard model of Solar preplanetary disk [1,2] in the zone of giant planets it was obtained:

$\nu(Q) \approx 7.5[\sigma/\sigma_\oplus][R/a.e.]^{-5/2}[\delta/4.5 gcm^{-3}]^{-2/3}[M_p/M_\oplus]^{2/3}[10^{30} erg/Q]$ in year, where σ is the surface density, and δ is the density of bodies matter. For $L \approx Q/\Delta t$, where $\Delta t \approx 10^3 sec$ is the time of the jet life, and supposing that about 50% of Q goes to L we can obtain $\nu(L) \approx \{81[(10^{28} erg/sec)/L]^{5/6} + 2(10^{28} erg/sec)/L\}$ in year

So for the collisions in the vicinity of a star possessed the disk with the mass about 0.1 solar mass the durations of individual flashes are in the range from tens of minutes to several hours and their frequency is in the interval from thousands in a year for the events with Jupiter's luminosity to ones in a year for the events with luminosity about 1000 times higher. Such phenomena named by us "Fireworks" take place in the vicinity of young stars previously possessed gas-dust disks.

This investigation is performed under support of Russian fond of fundamental researches N93-02-17171.

References: [1]Vityazev A. et al."Terrestrial Planets",Nauka, Moscow, 1990,296p.(in Russian), [2]Vityazev A., Pechernikova G. Late Stages of Accumulation and Early Evolution of the Planets in "Planetary Sciences",Eds. T.Donahue, K.Trivers, D.Abramson, Washington, D.C.,1991, [3]Vityazev A. et al. Generalized Coagulation Equation...LPSC 25,1994.

GENERALIZED COAGULATION EQUATION AND MASS-SPECTRUM OF PROTOPLANET

Vityazev A., Kukharenko Yu., Bashkirov A., and Pechernikova G.
United Institute of Physics of the Earth, Moscow 123810, Russia

The classic Smoluchowski equation is valid only in the thermodynamic limit, when a number of the particles N in the volume V is great, so that the concentration of particles $n = N/V$ is finite. However during coagulation n can become as small as one likes. Formal application of the Smoluchowski equation to the case of small values of leads to the difficulties. They lie in the fact that its steady-state solution is identical with zero and all the moments, beginning from the second one, diverge. It is due to an unlimitation and a positive definity of the quadratic form (n,An), where A is the kernel of the Smoluchowski integral operator.

We derived the generalized equation of coagulation which differed from the Smoluchowski one by the presence of the renormalized function $f_{12}(m,m',t)=n(t)(n(t)-\frac{1}{V})\rho_{12}(m,m',t)$ Here m and m' are masses of two coagulating particles and $\rho_{12}(m,m',t)$ is the pair probability function. In this case the renormalized kernel is not positive definite and the equation has the stable steady-state non- zero solution and has the finite moments. At the final stage the relaxation goes on to this solution according to the exponential low. The generalized equation of coagulation makes possible to describe the most interesting stage of relaxation.

For three kernels 1)$A=a$, 2)$A=b(m+m')$, 3)$A=cmm'$, where a,b,c are positive constants, we obtained the concentration $n(t)$ and the second momentum $M_2(t)$ of the mass distribution of particles in the forms

GENERALIZED COAGULATION: **Vityazev A.,Kukharenko Yu. et al.**

$$1)\, n(t)=\frac{n_0}{Vn_0-V(n_0-\frac{1}{V})e^{-\frac{\alpha}{2V}t}},\quad M_2(t)=M_2(0)+2M^2V[1-\frac{1}{Vn_0}][1-e^{-\frac{\alpha t}{2V}}]$$

($n_0 \equiv n(t=0)$, M is the total mass of particles in the unit volume)

$$2)\; n(t)=\frac{1}{V}+(n_0-\frac{1}{V})e^{-bMt},\quad M_2(t)=M_2(0)\left[\frac{n_0}{\frac{1}{V}+(n_0-\frac{1}{V})e^{-bMt}}\right]^2$$

3)the solution represented in the implicit form

$$n(t)=\frac{1}{V}+(n_0-\frac{1}{V})e^{Vn_0-Vn(t)-\frac{c}{2}M^2t},\quad \frac{1}{M_2(t)}=\frac{1}{M_2(0)}+\frac{2}{M^2}[n(t)-n_0]\varepsilon\ln\frac{M_2(0)}{M_2(t)}$$

where ε is infinitezemal positive number putting to zero after relaxation to the steady state.

For coagulation kernel $A \propto (m^{\alpha}+m'^{\alpha})$ we found the intermediate asymptotic solution in the form $n(m,t)=n(t)m^{-q}$, with $q=1+\alpha/2$.

It is well known that the largest bodies have in average smaller eccentricities and inclinations. So in the region of mass m far more the mean mass the effective values of α are smaller than commonly used 4/3. In other words mass-spectrum of largest bodies is more steeper and (in the absence of gas accretion) is determined by surface density distribution of solid material. Our results showed that collisions of large bodies in a forming planetary systems are more frequent and more energetical than previously assumed.

This investigation is performed under support of Russian fond of fundamental researches N93-02-17171.

SURFACE ENERGY MEASUREMENTS OF COMMINUTED SILICATES: IMPLICATIONS FOR COSMOCHEMICAL PROCESSES

R. Voelkel and R. F. Giese, Department of Geology, and C. J. van Oss, Departments of Microbiology and Chemical Engineering, State University of New York at Buffalo, Buffalo, NY 14260.

Interactions at the surfaces of very small particles are fundamentally related to cosmochemical processes. Greenberg [1] and others state that some interstellar grains typically are sub-μm , amorphous silicate particles which act as "seedlings" onto which gaseous atoms and molecules are adsorbed creating core-and-mantle grains of volatile, particularly organic, molecules [2]. Likewise, scenarios proposed for planetary formation assume an adhesive process which commenced particle flocculation in what Dodd [3] refers to as "some means of...getting the first few grains to stick together" when they are too large to be held by static electrical forces and too small to have appreciable gravitational fields [4]. Recent research into interfacial phenomena of very small particles has led to innovative methods of measuring surface energy components for powders and fibers. One application of this line of research currently involves examining the total interaction energy of cohesion of volcanic ash, in liquid media, to predict the potential for this material to form massive mudflows [5]. In extending the application of these same techniques to non-terrestrial phenomena, the surface thermodynamic properties of several common silicate minerals were measured using the thin-layer wicking method. The free energy of cohesion between particles was then calculated from the surface thermodynamic properties.

Enstatite ($MgSiO_3$), forsterite (Mg_2SiO_4), quartz (SiO_2), and antigorite ($Mg_3Si_2O_5(OH)_4$) were incrementally comminuted by percussive grinding for 15, 30, 60, 120, 240 and 480 minutes with the dual purpose of characterizing changes in surface properties in response to progressive crystal structure disorder and creating materials analogous in certain respects to refractory constituents of the interstellar medium. The choice of silicate minerals was based on assessments of primitive materials drawn from a review of recent cosmogony literature, described in [6], plus a desire to examine a variety of silicate structure types. However, particles created during this study are not presumed to be realistic physical analogues of conditions, processes or materials which preceded solar system formation. Rather, data and conclusions drawn from this work are intended to complement present models of particle interactions.

A detailed discussion of the theoretical basis for the thermodynamic property of condensed systems is given by [7]. The total surface free energy of cohesion (ΔG_{ii}^{coh}) of a given (non-metallic) material, i, is given by:

$$-\frac{1}{2}\Delta G_{ii} = \gamma_i^{LW} + \gamma_i^{AB} \qquad (1)$$

where γ_i^{LW} and γ_i^{AB} are the surface tension components of the apolar Lifshitz-van der Waals (LW) and the polar Lewis acid-base (AB) interactions, respectively; the AB component is determined by two parameters, one for the electron acceptor, $\gamma_i^{\oplus}$, and the other for the electron donor, $\gamma_i^{\ominus}$, related by $\gamma_i^{AB} = 2\sqrt{\gamma_i^{\oplus}\gamma_i^{\ominus}}$. The surface tension components and parameters of a solid material, γ_s^{LW}, $\gamma_s^{\oplus}$, and $\gamma_s^{\ominus}$, can be determined from measurements of the contact angles, θ, of drops formed by a series of test liquids, whose surface tension components are already known, deposited on a smooth surface of that solid. The contact angles and the surface tension components are related by the Young equation:

$$\frac{(1+\cos\theta)}{2}\gamma_L = \sqrt{\gamma_S^{LW}\gamma_L^{LW}} + \sqrt{\gamma_S^{\oplus}\gamma_L^{\ominus}} + \sqrt{\gamma_L^{\oplus}\gamma_S^{\ominus}} \qquad (2)$$

However, for many materials, including the powders analyzed for this study, it is not possible to obtain a smooth, non-porous surface upon which to measure contact angles directly. Instead, an indirect method, referred to as thin-layer wicking, is used to determine the contact angle values. In this method, measurements of height as a function of time are made for a series of test liquids as they rise through a thin layer of the powdered material. The contact angle of a particular liquid on the solid is given by the Washburn equation [8]:

$$h^2 = \frac{t\gamma_L R\cos\theta}{2\eta} \qquad (3)$$

where h is the rise of the liquid in time t through the powdered substrate, R is the effective pore radius of the powder being measured, γ_L is the total surface tension of the liquid, and η is the viscosity of the liquid.

Mineral	Grinding Time min	γ^{LW} mJ/m^2	$\gamma^{\oplus}$ mJ/m^2	$\gamma^{\ominus}$ mJ/m^2	ΔG_{ii}^{coh} mJ/m^2	BET m^2/g
antigorite	15	31.43	0.0	25.2	-62.86	36.08
	120	33.21	0.0	19.85	-66.42	33.58
	480	33.75	0.0	40.89	-67.50	16.27
enstatite	15	43.04	0.0	40.41	-86.08	5.81
	120	39.41	0.0	38.17	-78.82	8.42
	480	39.09	0.0	34.31	-78.18	7.71
forsterite	15	36.48	0.15	35.88	-82.24	1.99
	120	33.35	0.23	25.58	-76.40	5.78
	480	33.66	0.0	29.66	-67.32	8.93
quartz	15	39.81	0.0	46.70	-79.62	1.77
	120	46.47	0.0	53.52	-92.94	5.46
	480	33.39	0.0	32.84	-66.78	13.26

XRD analyses showed increasing crystal structure disorder of all comminuted silicates; SEM examinations revealed particle sizes approaching colloidal (<2 μm) dimensions. BET surface area measurements were also made as a function of grinding time. The measured surface tension values (see the table) show that the silicate minerals examined (in common with most oxides materials) are primarily Lewis bases and the magnitude of the Lewis basicity, $\gamma^{\ominus}$, is strongly influenced by grinding. Values for the free energy of cohesion, ΔG_{ii}^{coh} (which is strongly dominated by LW forces, see table), range between -63 to -92 mJ/m^2. For small plate-shaped particles having a contactable surface area between particles as small as 10^{-12} cm^2 there is an energy of attachment of -1575 to -2150 kT per particle pair, *in vacuo*, sufficient for adhesion to occur readily. The energy of attachment will still be on the order of 15-20 kT for particles having a contactable surface area as small as 100 Å^2. Thus, there seems little difficulty in getting small silicate particles to adhere to each other; the adhesion is a natural consequence of interfacial thermodynamic interactions. The analysis to this point assumes that there are no net electrostatic charges on the particles. If the particles are electrically charged (with the same sign of charge), with a surface potential of, say, 25 mV, particles larger than about 0.1 μm can repel one another electrostatically with sufficient strength to obviate further attachment by means of the LW forces. When particles occur with opposite charges (either on the same particle, as in kaolinite [9], or on different particles), much larger agglomerates can occur, due to the electrostatic attraction.

REFERENCES

[1] Greenberg, J. M. (1984) Scien. Amer., June, p. 124-135.

[2] Verschuur, G. L. (1989) Interstellar Matters. Springer-Verlag New York Inc., 320 pp.

[3] Dodd, R. T. (1986) Thunderstones and Shooting Stars: the Meaning of Meteorites. Harvard University Press, Cambridge, Mass, 196 pp.

[4] Wasson, J. T. (1985) Meteorites: Their Record of Early Solar-System History. W. H. Freeman and Company, New York, 267 pp.

[5] Li, Z., Giese, R. F., and van Oss, C. J. (1993) Colloids and Surfaces, in review.

[6] Voelkel, R., (1994) Surface Characterization of Comminuted Silicate Particles. Masters thesis, State University of New York at Buffalo, in preparation.

[7] van Oss, C. J., Chaudhury, M. K., and Good, R. J. (1988) Chem. Rev., 88, 927-941.

[8] Washburn, E. W. (1921) Phys. Rev., 17, 273-283.

[9] Thiessen, P. A. (1942) Z. Elektrochem., 48, 675-681; (1947) Z. Anorg. Chem., 253, 161-169.

DEPOSITIONAL UNITS IN WESTERN MAXWELL MONTES: IMPLICATIONS FOR MOUNTAIN BUILDING PROCESSES ON VENUS R. W. Vorder Bruegge, Science Applications International Corporation, 400 Virginia Ave., S.W., Suite 400, Washington, D.C. 20024

Summary. Structural mapping of western Maxwell Montes, Venus has led to the recognition of a number of units that are best characterized as depositional in nature. These units occur in local topographic lows and tend to embay adjacent structures, indicating their relative youth. While much of eastern Maxwell is blanketed by continuous deposits associated with Cleopatra crater, the western slopes of the mountain belt are characterized by scattered deposits. Several of the patches in western Maxwell exhibit characteristics of fluid flow, including evidence for channel formation. Possible origins include: local debris from landslides and other downslope mass movements; impact crater ejecta and outflow materials; weathering products; wind-blown materials; and volcanic deposits. None of these origins may be ruled out yet. It is critical to determine if volcanism played a role in forming these deposits, since a lack of volcanism would imply the presence of either a cold mantle or cool, thick crust beneath Maxwell, while abundant volcanism would imply a hot mantle beneath the mountain belt. Defining the nature of these deposits may also provide insight into weathering processes at high elevations on Venus.

Observations. The dominant characteristic of western-most Maxwell Montes (defined here as approximately between 359-002°E and 63-67°N) is a ridge-and-valley structure that parallels the topographic trend of the mountain belt and extends from the north-northwest to south-southeast [1-4]. In addition to this structure, the current mapping effort has led to the recognition of a number of units within western Maxwell Montes that may best be characterized as depositional in nature. These units typically are found in local topographic lows and at times embay adjacent structures. They tend to be characterized by a uniform radar backscatter texture that is unbroken over tens to hundreds of square kilometers. In the Magellan SAR images, these units are most often bright, indicating that they either: (1) consist of materials that are rough at the scale of the radar wavelength (10-15 cm); (2) incorporate materials having electrical properties that make them highly reflective to the Magellan radar; or (3) form relatively flat surfaces, which makes them appear bright in contrast to east-facing slopes when viewed by Magellan from the west at incidence angles of 25-35°. The latter factor is least likely since in some cases intermediate-to-low radar backscatter units are also seen, indicating materials that are either less rough or less highly reflective than the brighter materials.

In plan view, these units most often occur as long, narrow 'strips' 25 km or more in length, but no more than 5-7 km in width. The long axis of the strips is oriented parallel to the ridges and valleys within Maxwell. The eastern edge of a strip is usually defined by a sharp discontinuity in brightness which is consistent with deposition against a steep, west-facing scarp. The other edges of individual strips rarely exhibit such sharply defined boundaries. Instead, these edges are often arcuate and tend to be more diffuse, consistent with deposition upon more subdued, east-facing slopes. These units appear to pond within the valleys of the Maxwell Montes ridge-and-valley structure. An example of this type of feature is seen at ~0°E/65.75°N. Individual strips sometimes appear to extend between adjacent valleys and surround intervening ridges. An example of this occurs at ~0.25°E/65.8N. In at least one case (~359.5°E/65.25°N, Figure 1), several very narrow strips radiate from an equidimensional patch of this unit. Magellan stereo data of this area reveal the equidimensional patch to be in a local low, with the strips radiating upslope to the west. Farther west these strips widen and merge before they intercept a graben oriented perpendicular to them. To the south there is also a short channel that appears to cut through existing ridges connecting several smaller patches of bright, ponded material.

A common characteristic of the units described above is their marked embayment of surrounding structures. In a few cases these units occur as shorter swaths (< 20 km) that appear to flow over or cut downslope through the ridge and valley structure from east to west. The swaths appear more diffuse than the ridge-parallel strips and an example may be found at ~0.25°E/65.25°N. In one case (~359.5°E/65.95°N) the eastern end of a swath occurs at a scalloped scarp which is concave to the west, while the distal end is a fan-shape bright region that is convex to the west (downslope). In between, the lateral edges appear bright, while the interior is dark.

Finally, the Magellan SAR images reveal many parts of Maxwell that exhibit a patina of bright material. This patina does not embay underlying structure but, instead, appears to coat ridge crests, their slopes, and intervening valleys. The patina is very diffuse, with indistinct edges, and it does not appear to effect the texture of the underlying materials, just their relative brightness. This patina is most prominent around the edges of Maxwell Montes, where it contrasts sharply with the low-radar backscatter of the surrounding areas. This patina also seems to be absent at the highest elevations of Maxwell, in the central part of the belt.

Potential Origins. The low Magellan SAR incidence angles and steep slopes present at Maxwell Montes make this a prime candidate for occurrences of layover. However, most of these areas can be interpreted as containing depositional units with great confidence. The materials that make up these units may arise from a number of sources including chemical and mechanical weathering, tectonic disruption, impact cratering, and volcanism. The means by which these materials have been emplaced may include downslope (gravitationally driven) movements, ballistic emplacement, *in situ* weathering, and wind-borne transport.

DEPOSITS ON MAXWELL MONTES: Vorder Bruegge R.W.

The specific nature of the depositional units on Maxwell remains to be determined. Much of that observed on western Maxwell may just be the result of downslope material movement associated with the steep slopes there. The morphology of the swath at ~359.5°E/65.95°N (scalloped scarp at eastern edge, with fan-shape deposit downslope at western edge) is consistent with the morphology of rock/block slide avalanches elsewhere on Venus [5]. The ponding of materials associated with the patch at ~359.5°E/65.25°N (Figure 1) is consistent with emplacement through fluid flow, and the channels (?) to the west and south could be indicative of an erosive fluid flow. A number of fluids could form such channels including lavas [6], impact melts and other crater outflow materials and debris [7-8], and water [6]. The most likely of these is the volcanic origin, with the graben to the west serving as a potential source. However, this conclusion must be viewed as preliminary, subject to reinterpretation of the channels (?) as erosive in origin

One interpretation that is in less doubt is that of the fine patina. The distribution of this patina corresponds directly to low-emissivity regions on Maxwell, which Klose et al. [9] interpreted to be due to a change in the surface mineralogy caused by weathering above a critical altitude. The fact that the patina does not alter the observed texture of the surface, just the brightness, indicates that this effect only occurs in the uppermost centimeter to meters.

Discussion. The depositional units in western Maxwell are of interest for the clues they may provide to the sequence of events within the mountain belt and the geodynamics at depth. The majority of these units appear to embay the adjacent structures, indicating they are the more recent features. In western Maxwell a few of the mapped depositional units may have a volcanic association. In one location a graben may represent a volcanic source, but indisputable evidence supporting such an origin is lacking. Should this apparent lack of widespread volcanism in western Maxwell be confirmed, then it could indicate that the crustal column there is still relatively cool, consistent with relatively recent crustal shortening and support at depth by crustal thickening, in which temperatures at depth remained low. If the crustal thickness beneath Maxwell is not large, yet there still is little evidence of volcanism, then a cool mantle is anticipated. However, should the existence of widespread volcanism be confirmed in western Maxwell, then a hot mantle is expected beneath Maxwell.

References. [1] Campbell D.B. et al. (1983) *Science, 221*, 644. [2] Basilevsky A.T. et al. (1986) *PLPSC 16th, JGR, 91*, suppl. D399. [3] Crumpler L.S. et al. (1986) *Geology, 14*, 1031. [4] Vorder Bruegge R.W. et al. (1990) *JGR, 95*, 8357. [5] Malin M.C. (1992) *JGR, 97*, 16337. [6] Baker, V.R. et al. (1992) *JGR, 97*, 13421. [7] Schultz P.H. (1992) *JGR, 97*, 16183. [8] Asimow P.D. and Wood J.A. (1992) *JGR, 97*, 13643. [9] Klose K.B. et al. (1992) *JGR, 97*, 16353.

Figure 1. Sketch map of region in vicinity of ~359.5°E/65.25°N. North is to the top. Depositional unit embays plains and ridge-and-valley structure in east. To the west, linear strips of this unit merge and intersect a graben. To the south are several ponds connected by a channel which cuts through ridges. A volcanic origin is suspected for the unit.

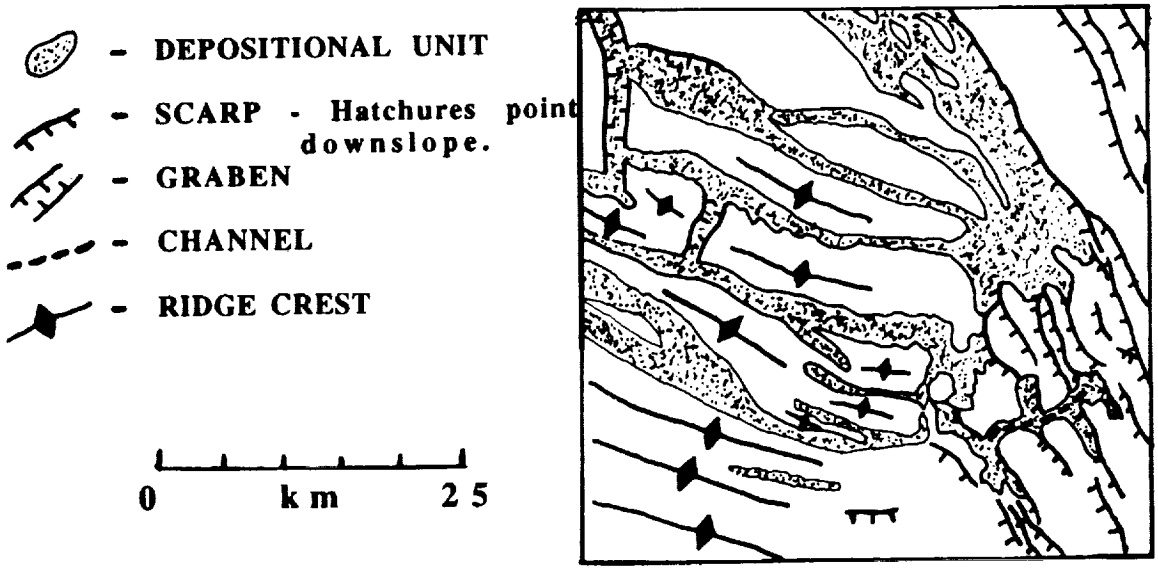

VARIATION IN COMPRESSIONAL STRUCTURES ACROSS MAXWELL MONTES: EVIDENCE FOR A SEQUENCE OF EVENTS IN A VENUSIAN OROGENY R. W. Vorder Bruegge, Science Applications International Corporation, 400 Virginia Ave., S.W., Suite 400, Washington, D.C. 20024

Summary. Structural mapping of Maxwell Montes has revealed a variation in the character of ridges and valleys from the toe of the mountain belt in Lakshmi Planum to the crest of the belt. This variation is interpreted as an evolution in thrust systems from simple fold-bend anticlines as they are incorporated into belt at the toe to steeply dipping duplexes at the crest. A shallow depth of decollement and displacements of several kilometers are indicated. This model may permit gravitational relaxation of the highest part of the mountain belt through normal faulting of the steeply dipping duplexes along pre-existing thrust faults. The mechanism for support of the mountain belt at depth is probably not crustal thickness variations, alone, and its true nature remains elusive. Nevertheless, the evolution of Maxwell Montes can still be interpreted as quite comparable to that of terrestrial fold-and-thrust belts, with a key difference being the lack of erosion on Venus.

Introduction. Structural mapping of Maxwell Montes, Venus, is being performed with Magellan data in order to characterize the tectonic processes associated with the creation and evolution of the mountain belt, their sequence, timing, and overall relationship to the rest of Ishtar Terra. Earlier examination of Venera and Arecibo radar images led a number of workers to interpret the surface deformation as occuring through folding, thrusting, and buckling of the crust [1-4]. More recent examination of Magellan data has led others to confirm this preliminary assessment [5-7]. Suppe and Conners [8] determined that the topography of the western face of Maxwell is consistent with its formation through critical taper wedge mechanics involving the upper-most crustal layers. The purpose of this work is to explictly document the characteristics of individual structures present across Maxwell Montes, incorporate them into an evolutionary sequence of events, and compare that to the evolution of terrestrial fold-and-thrust belts.

Observations and Interpretations. The mapping of western Maxwell Montes has revealed a predominance of structures related to crustal shortening, primarily in the form of thrust faulting and folding. The nature of these features varies from west to east and appears to be correlated with the large-scale topography (Figure 1). Off the western edge of Maxwell Montes, in the smooth, low-lying plains of Lakshmi Planum (~63-64°N), small folds or flat-topped anticlines are observed trending to the north or slightly west of north. These folds are on the order of several hundred meters across and occur at spacings of approximately 5-6 km. They are separated from one another by relatively flat, undeformed plains. An interpretive cross-section of these folds that assumes a shallow depth to decollement is shown in Figure 2A. To the east the surface slopes upward rapidly on the western face of Maxwell, and more north-northwest trending anticlines are observed. In this region, the flat-topped anticlines broaden while the width of flat regions between them decreases to almost zero. On the lower reaches of the toe of western Maxwell, the spacing of the anticlines can be as little as 3 km, or half that observed in the plains (Figure 2B). The increase in fold width and decrease in spacing are interpreted to be the result of large displacements (several km) along the shallow-dipping thrusts. Farther up the slope the spacing increases to approximately 5-6 km (as in the plains) but the width of individual anticlines also increases, so that there are only narrow, flat valleys between anticlines (Figure 2C). This is interpreted to be a result of merging of adjacent anticlines. Near the crest of the mountain belt, the nature of the compressional features changes again. Instead of flat-topped anticlines, the general structure appears to consist of steep west-facing scarps (<1 km wide) and long, shallow east-facing slopes (~10 km wide). The east-facing slopes terminate at the base of a subsequent west-facing scarp. Although radar foreshortening and elongation will tend to exaggerate the relative widths of these slopes, the geometry of these features is consistent with their representing stacked duplexes in an imbricate sheet (Figure 2D).

Synthesis. The cross sections of Figure 2 suggest the following sequence of events in Maxwell Montes from the toe to the crest. Anticlines first form in the plains (Fig. 2A), then become incorporated into the toe of the mountain belt through further shortening along existing thrust faults which increases the width of the existing anticlines and decreases the spacing between them (Fig. 2B). Farther up the wedge the increased width and spacing of the anticlines is interpreted to be the result of further slip along the decollements and merging of adjacent anticlines (Fig. 2C). Finally, at the crest of the mountain belt duplexes are formed and rotated backwards (Fig. 2D). This may ultimately lead to normal faulting along steeply dipping thrust surfaces, which would expose more of the flat, east-facing slopes. Such normal faulting would be indicative of gravitational relaxation and has been observed along pre-existing thrust faults in the Himalaya [9].

The Maxwell cross-sections show good agreement with those of terrestrial thrust systems [e.g., see 10]. A major difference is that the Maxwell cross-sections show no evidence of erosion. Another difference is that the Maxwell cross-sections are not yet balanced from toe to crest. Efforts are being made to produce a balanced cross-section for Maxwell in order to predict relationships at depth and to examine the implications for support of the mountain belt.

References. [1] Basilevsky A.T. et al. (1986) *PLPSC 16th, JGR, 91*, suppl. D399. [2] Ronca L.B. and Basilevsky A.T. (1986) *EM&P, 36*, 23. [3] Crumpler L.S. et al. (1986) *Geology, 14*, 1031. [4] Vorder Bruegge R.W. et al. (1990) *JGR, 95*, 8357. [5] Solomon S.C. et al. (1991) *Science, 252*, 297. [6] Solomon S.C. et al. (1992) *JGR, 97*, 13199. [7] Kaula W.M. et al. (1992) *JGR, 97*, 16085. [8] Suppe J. and Conners C. (1992) *JGR, 97*, 13545. [9] Burchfiel B.C. and Royden L.H. (1985) *Geology, 13*, 679. [10] Boyer S.E. and Elliott D. (1982) *AAPG Bull., 66*, 1196.

Figure 1. Topographic profile across Maxwell from 0.0°E/63.0°N to 3.0°E/64.0°N. Elevations shown are relative to mean planetary radius of 6051.84 km. Letters A-D refer to cross-section locations in Figure 2.

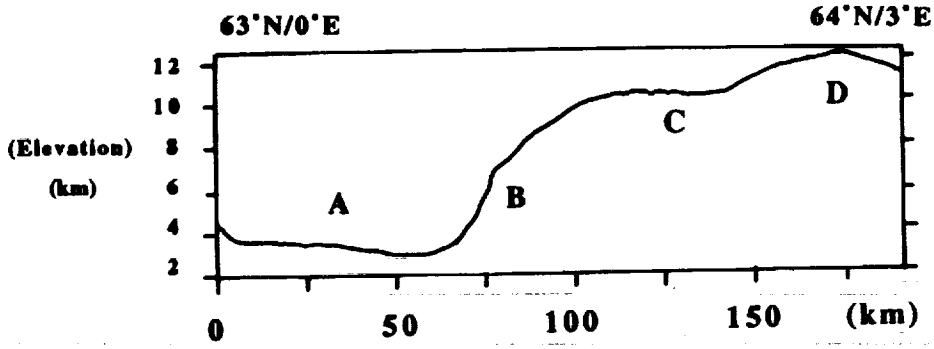

Figure 2. Interpretive cross-sections of different structures on Maxwell Montes. Letters "A" - "D" correspond to locations on topographic profile of Figure 1. East is to the right. Heaviest lines indicate 'active' thrust surrfaces. Note scale change between "B" and "C." D1 and D2 represent the progressive growth of a duplex.

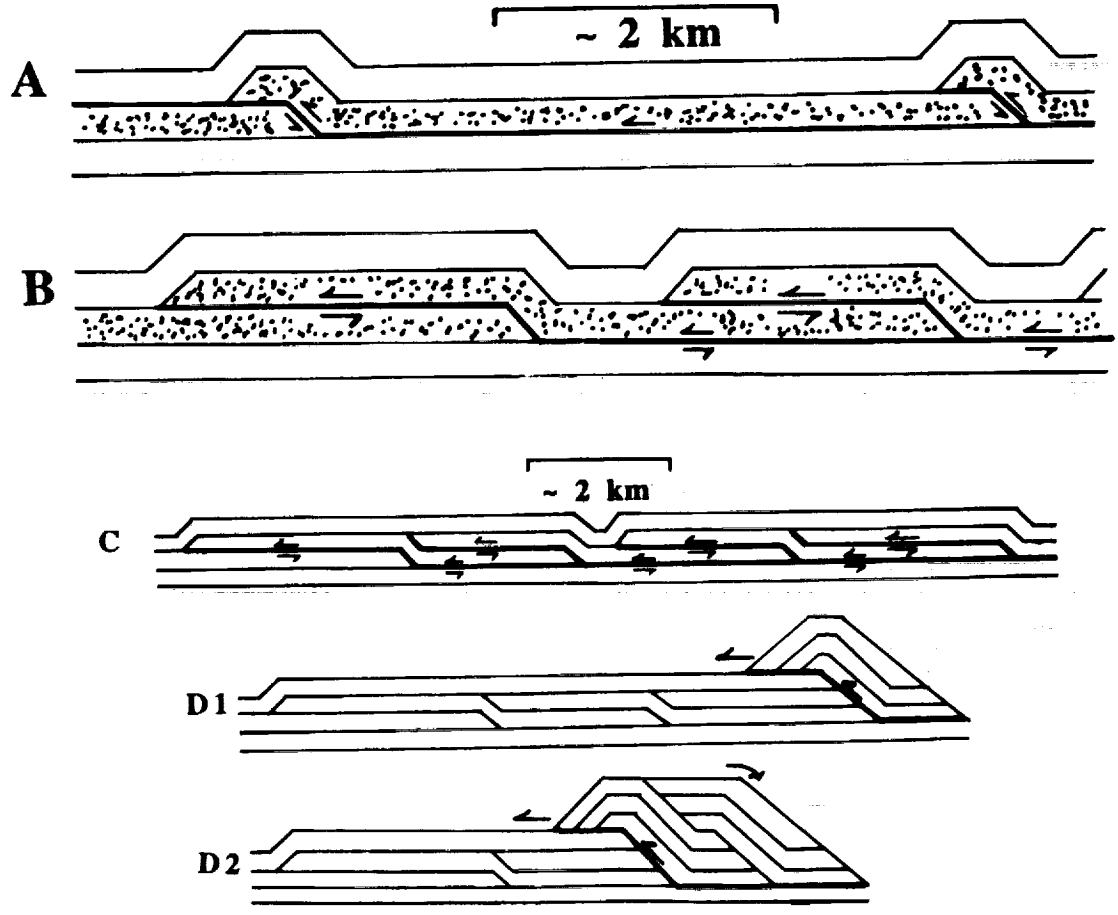

RARE EARTH ELEMENT DISTRIBUTIONS IN CHASSIGNY: CLUES TO ITS PETROGENESIS AND RELATION TO THE NAKHLITES. Meenakshi Wadhwa and Ghislaine Crozaz. McDonnell Center for the Space Sciences and Dept. of Earth and Planetary Sciences, Washington University, St. Louis, MO 63130.

The Chassigny meteorite is a dunite that belongs to the SNC (Shergottites-Nakhlites-Chassigny) group of achondrites; these are believed to be samples of the planet Mars ([1] and references therein). This meteorite is composed predominantly of olivine (~90%), with minor pyroxene and plagioclase and trace phases such as opaques and chlorapatite [2]. Chassigny is the least studied of all the SNC meteorites, and there still remain questions regarding its petrogenesis. By studying the microdistribution of trace elements (in particular, rare earth elements, which are recognized to be indicators of igneous petrogenetic processes) we hope to gain additional information about the formation and crystallization history of this meteorite. Moreover, it has been recognized that Chassigny is closely related to the nakhlite pyroxenites, since it has (a) an igneous crystallization age that is similar to that of the nakhlites (~1.3 b.y.; [3, 4, 5]), (b) an initial Sr isotopic ratio that is identical to that of Nakhla [5], and (c) a whole rock REE abundance pattern that is LREE-enriched, like that of the nakhlites (although absolute REE abundances are approximately an order of magnitude lower in Chassigny compared to Nakhla) [6]. Also, Nakamura et al. [5] performed mineral separate analyses for REE in Chassigny (although results of these analyses were not reported), and calculated that the REE composition of the Chassigny parent melt was similar to that of Nakhla. All these characteristics indicate that Chassigny and the nakhlites may, indeed, be petrogenetically linked. This hypothesis can be further tested by comparing the REE microdistributions in minerals in Chassigny and in the nakhlites. Therefore, we present here *in situ* measurements of REE abundances in Chassigny minerals, including, olivine, pyroxene, plagioclase and chlorapatite. These analyses were made with the Washington University ion microprobe.

Fig. 1 compares chondrite-normalized REE abundances in minerals of Chassigny and of Nakhla (the latter were previously reported by Wadhwa and Crozaz [7]). It is interesting to note the similarity of REE *patterns* for each mineral in these two meteorites. Moreover, REE *abundances* in olivine, plagioclase and apatite in both meteorites are also approximately the same. Chlorapatite is the mineral that has the highest REE abundance in both meteorites, with La ~2000xCI. The most striking difference between REE abundances in minerals in Chassigny and Nakhla is that augites in Chassigny have, on average, higher REE abundances (La ~4.5-9xCI) than those in Nakhla (La ~0.5-2xCI)

Because of the strong similarities between Chassigny and Nakhla, we have assumed that the REE equilibrium partition coefficients used to interpret Nakhla results can also be applied to Chassigny data. To calculate the parent melt composition of Chassigny, augite/melt partition coefficients experimentally determined by McKay et al. [8] were used. Similarly, to estimate the composition of melts in equilibrium with plagioclase and apatite, we used the same REE partition coefficients as in Wadhwa and Crozaz [7]. The most significant result of these calculations is that the REE pattern of the Chassigny parent melt is parallel to that of its whole rock (absolute REE abundances are, as expected, higher in the parent magma than in the bulk rock) and is also identical to the REE pattern of Nakhla's parent melt (as calculated in [7]). This suggests that the observed LREE-enrichment in the Chassigny whole rock is a characteristic of the parent melt from which it crystallized, and that this meteorite was not significantly affected by metasomatic infiltration of evolved, LREE-enriched melts subsequent to crystal accumulation. The crystallization sequence of minerals in Chassigny, i.e., olivine (± augite?)-->augite-->plagioclase-->chlorapatite, is inferred (from REE abundances in calculated mineral equilibrium melts) to be the same as in Nakhla, and is consistent with the observed textural relations. Therefore, based on REE microdistributions, it is likely that Chassigny and the nakhlites are genetically related. The parent melt composition of Chassigny could be related to that of the nakhlites by a process such as olivine fractionation or, alternatively, a different degree of partial melting of the same source.

REFERENCES: [1] McSween (1985) *Rev. Geophys.* **23**, 391-416. [2] Nehru et al. (1983) *Proc. Lunar Planet. Sci. Conf.* 14th; *J. Geophys. Res.* **88**, B237-B244. [3] Bogard and Nyquist (1979) *Meteoritics* **14**, 256. [4] Lancet and Lancet (1971) *Meteoritics* **6**, 81-85. [5] Nakamura et al. (1982) *Meteoritics* **17**, 257-258. [6] Burghele et al. (1983) *Lunar Planet. Sci. XIV*, 80-81. [7] Wadhwa and Crozaz (1992) *Lunar Planet. Sci. XXIII*, 1483-1484. [8] McKay et al. (1993) *Lunar Planet. Sci. XXIV*, 965-966.

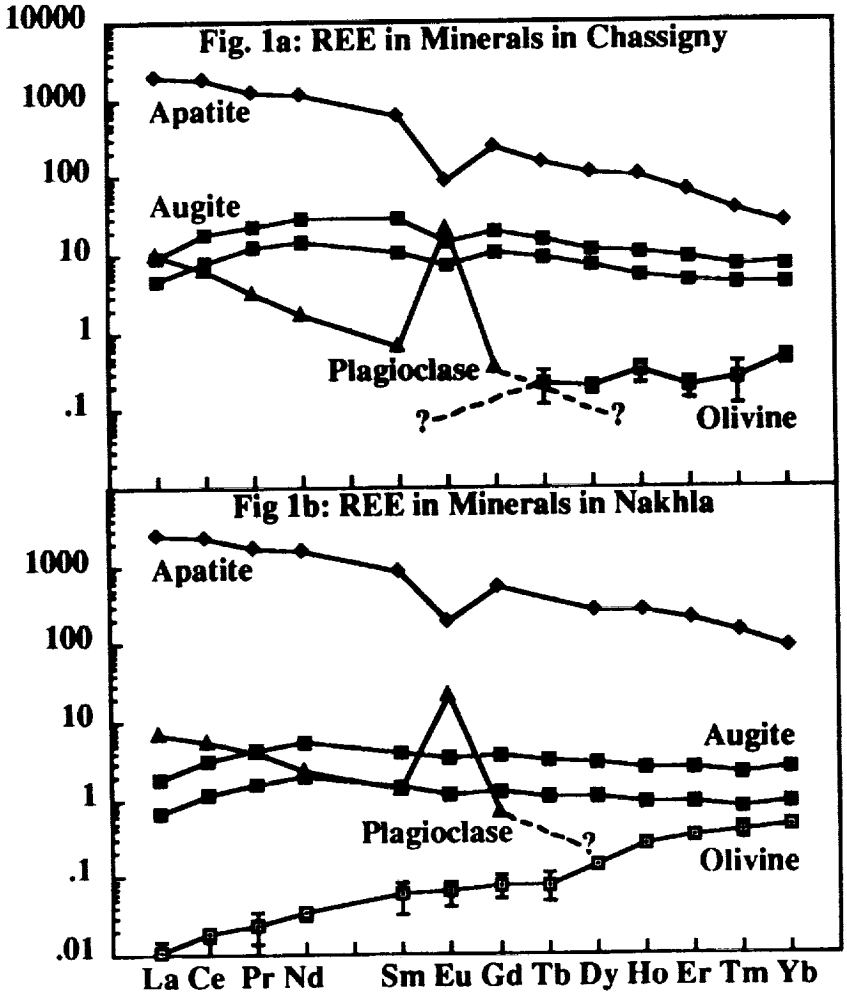

MODELING THE THERMAL INFRARED DIRECTIONAL EMISSIVITY OF LARGE, CLOSE-PACKED, PARTICULATE MEDIA;

A.E. Wald and J.W. Salisbury, The Johns Hopkins University

Because of the presence of strong molecular vibration bands, many common planetary surface materials, such as ices and silicates, are opaque in the thermal infrared (2-14 μm) region of the spectrum, even at relatively small particle sizes. Existing theories of radiative transfer in close packed media, typically derived for the transparent materials common in the visible and near infrared, assume that each particle scatters independently of its neighbors. For opaque particles, such as snow or quartz in the thermal infrared, this assumption is not valid, and these radiative transfer theories will not, in general, be accurate. A modification to standard radiative transfer theory, called diffraction subtraction, is proposed to account for the effect of close packing on the diffraction scattering cross section of large spheres.

When particles are closely packed, the diffraction contribution to the scattering cross section is eliminated [1]. Therefore, the appropriate inputs for radiative transfer theory are not the Mie albedo and asymmetry parameter, but rather these quantities minus the diffraction contribution. In the large particle limit, this contribution is easily derived using Mie theory, geometrical optics and Fraunhofer diffraction theory. Mie theory is used for the single scattering portion of the calculation instead of Hapke theory because the index of refraction of quartz is generally not in the $1.2<n<2.2$ window for which the Hapke theory is valid. With this diffraction subtraction modification, standard Mie theory-plus-radiative transfer accurately predicts the directional hemispherical reflectance (or directional emissivity) of large particulate samples (see figure 2).

If Mie parameters are to be used in Hapke radiative transfer theory (which assumes isotropic scattering), then the diffraction subtraction approximation must be applied to account for diffraction scattering in the forward direction. This is especially true at Christiansen peaks, where almost all scattering results from diffraction and is in the forward direction(see figure 3).

References

[1] Hapke, B. 1981 Bidirectional Reflectance Spectroscopy I : Theory. *J. Geophys. Res.* Vol. 86, No. B4, pg 3039-3054, 1981

DIRECTIONAL EMISSIVITY: Wald A.E. and Salisbury J.W.

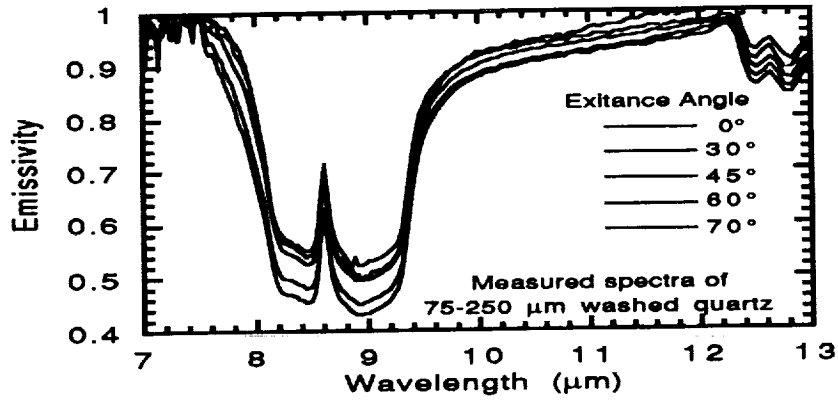

Figure 1 Measured directional emissivity of 75-250 μm quartz grains. Emissivity always decreases with increasing exitance angle.

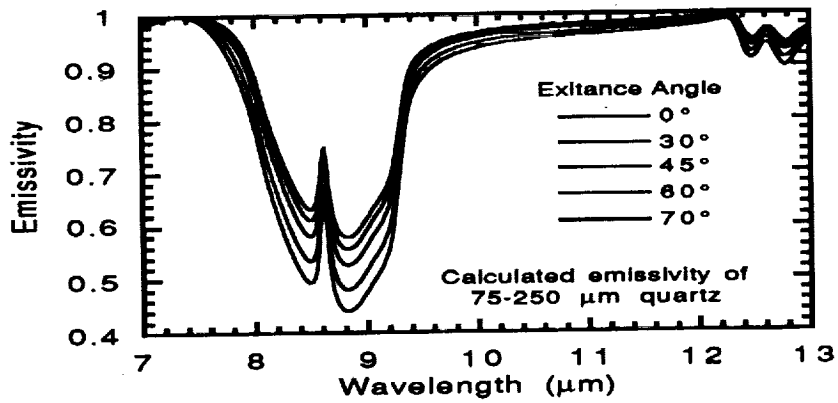

Figure 2 Calculated directional emissivity of large (75-250 μm diameter) quartz grains using Mie theory, diffraction subtraction, plus the doubling method. A Henyey-Greenstein phase function is used to approximate the actual phase function, and both sets of optical constants are included.

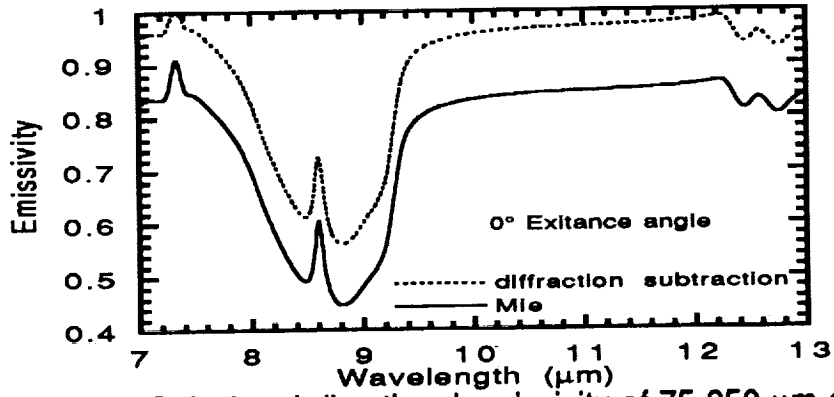

Figure 3 Calculated directional emissivity of 75-250 μm quartz grains using Hapke emittance theory with and without diffraction subtraction.

TEM STUDIES ON THE DISLOCATIONS IN OLIVINE OF TAIZHOU METEORITE FROM JIANGSU PROVINCE CHINA

[1]Henian Wang, [1]Wei Rong, [2]Fusheng Zhang, [2]Chengyi Lin
[1]Department of Earth Sciences, Nanjing University; [2]Centre for Materials Analysis, Nanjing University, Nanjing 210008, PRC

Taizhou Meteorite was formed at high speed of condensation, which are indicated by EDS and SEM study on chemical compositions of its principal mineral olivine. A TEM study shows that there are edge and screw dislocations in olivine with great density, which are thought to be formed as a consequence of an intense impact. The conclusions are drawn according to the following facts.

BACKGROUND:

On June 15th 1989, there, in Taizhou,Jiangsu Province, China, fell a meteorite, which was later named as Taizhou Meteorite. The samples we got are black in appearance, greyish white in section and finely crystallized. Optical microscopy reveals that Taizhou Meteorite mainly consists of olivine and bronzite. The principal matrix minerals are whitlockite, cristobalite, troilite and kamacite besides olivine and pyroxene.What's more characteristic is its chondrule texture. The chondrules have the shapes of fans, bunches, bars (Photo 1) and girdles with porphyritic textures. All these classify Taizhou Meteorite to olivine-pyroxene chondrite. In addition, wavy extinction and cataclasm are also found.

ENERGY DISPERSION X-RAY ANALYSIS:

The EDS data of olivine in Taizhou Meteorite are shown in Table 1. These data were got from HITACHI X-650 SEM and EDAXPV 9100 EDS.

The heterogeneity in chemical compositions of olivines is clearly seen from the table, with the value of Fa% ranging from 21.7% to 46.0%. Of most olivines, Fa% values are below 24%. According to the classification of Van Schemus et al.(1967), Taizhou Meteorite belongs to L-type Ordinary Chondrite. Thus we infer that high speed of condensation occurred in the process of nebulous fractionation and aggregation before the meteorite was formed. After its formation, the meteorite underwent small changes in terms of thermal metamorphism.

TRANSMISSION ELECTRON MICROSCOPY:

By using TEM technique, we find that the olivine in Taizhou Meteorite contains two arrays of supermicroscopic textures(Photo 2), one of which is straight, the other, somewhat curved. Both of them look like exsolution lamellae.

Through a close study, they turn out to be two arrays of dislocations perpendicular to each other(Photo 2). The observed direction of the straight array of dislocations is [001]. It shows edge character with Burgers vector $\vec{b}$=[001]. However, the somewhat curved array of dislocations is of screw character with the dislocation direction in [100] and Burgers vector $\vec{b}$=[001]. Besides, the dislocations in olivine of Taizhou Meteorite have other characteristics:

DISLOCATIONS IN OLIVINE

Wang H. et al.

(1) Most dislocations are parallel to [001] or [100]. Only a small number of dislocations showed mixed characters.
(2) By calculating on 25 electron microscopic photos, the density of dislocations is determined to be 4.13×10^{10} /cm^2.
(3) Occasional jog and flexion of dislocations indicate that interaction between dislocations and climbing in edge dislocations have been developed.
(4) With reference to Phakey's data(1972) on the nature and slide of dislocations varying as the generation temperature, Taizhou Meteorite was generated at about 800°c.

All the above facts show that the dislocations in olivine in Taizhou Meteorite were formed at a temperature of 800°c to 1000°c and by an impact at relatively high strain rates.

Reference: [1] Christie, J.M. et al.,(1976), Electron Microscopy in Mineralogy, Spinger-Verlag; [2] Dodd, R.T. et al., (1965), JGR, 70,3801; [3] Nicolas, A. et al.,(1967) Crystalline plasticity and solid state flow in metamorphic rocks, John Wiley & Sons; [4] Van Schemus, W.R. et al., (1967), GCA 31,747.

Table 1: EDS data of the olivine in Taizhou Meteorite

	SiO_2	FeO	MgO	Total	Fa%
1	38.92	20.21	40.87	100	21.72
2	38.69	21.45	39.86	100	23.75
3	38.45	22.72	28.83	100	32.45
4	37.43	28.16	34.42	100	45.99

Photo 1 : Bar-shaped olivine chondrule, single-polarized light,×30
Photo 2 : Edge and screw dislocations in olivine

Photo 1

Photo 2

C-6.

CHEMICAL AND ISOTOPIC FRACTIONATION DURING THE EVAPORATION OF THE FeO-MgO-SiO_2-CaO-Al_2O_3-TiO_2-REE MELT SYSTEM

Jianhua Wang[1], Andrew M. Davis[2], Robert N. Clayton[1,2,3] and Toshiko K. Mayeda[2]. [1]Department of the Geophysical Sciences, [2]Enrico Fermi Institute, [3]Department of Chemistry, University of Chicago, Chicago, IL 60637

Hashimoto [1] conducted vacuum furnace evaporation experiments on synthetic chondritic material and found that major elements alone were unable to discriminate between the evaporation and condensation evolution paths for CAI formation. Evaporation and condensation may be distinguished by their different isotope fractionation effects in the major elements. Isotopic fractionation is negligible for silicon, magnesium and calcium isotopes during *equilibrium* condensation or evaporation processes. Up to a few percent per a.m.u. mass fractionation of magnesium, silicon, oxygen and chromium isotopes relative to normal (terrestrial) value in CAIs [2] can result from the *kinetic* effects between vapor and liquids due to nonequilibrium evaporation [3]. We performed evaporation experiments on a synthetic solar composition material in a vacuum furnace [4] at 1800 and 2000°C for different durations to study the chemical and isotopic composition of the evaporation residues.

The starting material is a mixture of FeO, MgO, SiO_2, CaO, Al_2O_3 and TiO_2 of chondritic elemental ratios doped with oxides of La, ^{140}Ce, Pr, ^{146}Nd, ^{152}Sm, Eu, Gd, Tb, Dy, Ho, Er, Tm, Yb and Lu. These oxides comprise more than 95 mole % of volatile-free material of solar composition. We used synthetic mixture of oxide reagents rather than natural materials such as CI chondrites to avoid complications due to sulfides and water. The starting mixture of about 200 mg was pressed into a pellet with a hole drilled in the center and suspended in the center of the tungsten heater using an iridium wire. When the sample melts, it moves into the loop and stays in the loop as evaporation goes on. Sixteen evaporation runs were conducted at 1800 and 2000°C with durations of a few seconds to 5 hours. The pressure was maintained at 10^{-6} torr. The mass fraction evaporated ranged from 0.38 to 95.4 %. The melting of the sample usually starts at 1310°C and total melting occurs at about 1450°C. Quenching (radiation cooling) of the sample was done by turning off the heating power when the prescribed duration at desired temperature was reached. The residues were split in half with one half for SEM, electron microprobe and ion microprobe characterization and the other half for oxygen and silicon isotopic analysis. The SEM examination reveals that most residues consist of olivine and glass, with a barred olivine texture. Parallel olivine bars a few microns wide usually run across the entire residue. Major elements were determined using a Cameca SX-50 electron microprobe with a defocused electron beam about 100 μm in diameter. REE abundances and magnesium isotopic compositions were obtained using a modified AEI IM-20 ion microprobe with rastered beam. Primary beam intensities were about 10-20 nA with a rastered area of ~100×100 μm^2. Our ion probe has a precision for magnesium isotope analysis reported as Δ^{26}Mg of ±1‰ (1σ). Oxygen and silicon isotope compositions in the residues were measured by extraction of O_2 and SiF_4 by fluorination followed by isotope ratio mass spectrometry.

There is no significant evaporation of calcium, aluminum and titanium up to 95% mass loss; the evaporation behavior of magnesium, silicon and iron is similar to that found by Hashimoto [1]. Up to a 5×10^{-4} negative cerium anomaly and a 50% negative praseodymium anomaly developed in the residue of 95% mass loss while other REE are not significantly evaporated [5].

EVAPORATION OF SOLAR COMPOSITION MELT

Wang J. *et al.*

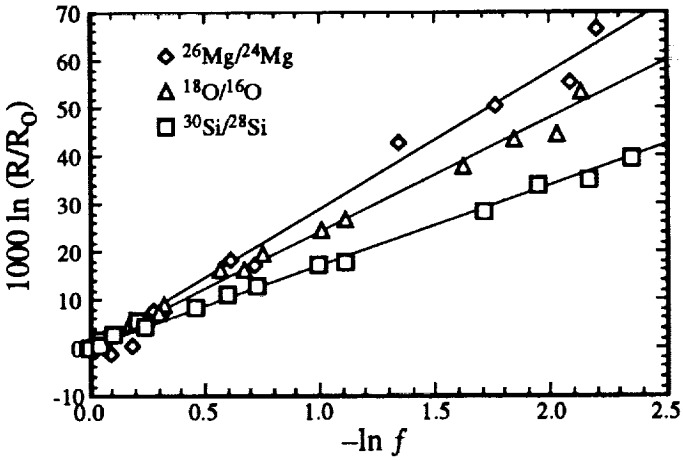

The figure shown is a plot of the isotope ratio R in the residue relative to its starting ratio R_0 versus the fraction (f) of its elemental abundance remaining for magnesium, oxygen and silicon. The linear relationship between 1000 ln (R/R_0) and $-\ln(f)$ is best described by Rayleigh fractionation law: $R/R_0 = f^{1/\alpha-1}$. Values of the inferred fractionation factor α (derived from the slope of the fitted line) between the residue and gas for $^{26}Mg/^{24}Mg$, $^{18}O/^{16}O$ and $^{30}Si/^{28}Si$ are listed in the table. For magnesium isotopes, the fractionation factor is very close to the values for the evaporation of liquid Mg_2SiO_4, 1.0313 [3], and single crystal forsterite, 1.0283 [6]. For oxygen and silicon isotopes, they are higher than those obtained from liquid Mg_2SiO_4 experiments [3]. All fractionations are less than the theoretical values, 1.0408, 1.0308 and 1.0225, assuming magnesium evaporates as Mg, oxygen as O_2 and silicon as SiO, respectively. The reduced fractionation factors deduced from the experiments are partly due to reprecipitation during the evaporation process. Since any possible oxide species leaving the residue will have a fractionation factor lower than the experimental value of 1.0241, O_2 is certainly produced during the evaporation process. This explains the cerium and praseodymium depletions in some of the residues as cerium is much more volatile than the other REE under oxidizing conditions [7]. The four known HAL-type hibonite-rich inclusions, which have large negative cerium and small negative praseodymium anomalies [8], probably formed by evaporation that provided an oxidizing environment. If silicon evaporates as SiO_2, the theoretical fractionation factor for $^{30}Si/^{28}Si$ will be 1.0165, which is smaller than the experimental value 1.0171. This implies that SiO_2 is probably not the principal gas species leaving the liquid residue. Mass dependent heavy isotope enrichment of magnesium, silicon, oxygen, chromium, calcium and titanium in some CAIs suggests that their origin involved evaporation from a melt. The depletion of cerium and praseodymium in these CAIs further constrains their formation to an oxidizing environment caused by the release of O_2 in the evaporation process.

Table. Condensed phase/gas isotopic fractionation factors (α).

	$^{26}Mg/^{24}Mg$	$^{18}O/^{16}O$	$^{30}Si/^{28}Si$
This study	1.0305	1.0241	1.0171
$Mg_2SiO_{4(\ell)}$ [3]	1.0313	1.0198	1.0142
$Mg_2SiO_{4(s)}$ [4]	1.0283	—	—
Theoretical	1.0408 (Mg)	1.0308 (O_2)	1.0225 (SiO)
	1.0247 (MgO)	1.0225 (SiO)	1.0165 (SiO_2)

References: [1] Hashimoto A. (1983) *Geochem. J.* **17**, 111. [2] Clayton R. N. *et al.* (1988) *Phil. Trans. Roy. Soc.* **A325**, 483. [3] Davis A. M. *et al.* (1990) *Nature* **347**, 655. [4] Hashimoto A. (1990) *Nature* **347**, 53. [5] Wang J. *et al.* (1993) *Meteoritics* **28**, 454. [6] Wang J. *et al.* (1993) *LPS* **XXIV**, 1479. [7] Davis A. M. *et al.* (1982) *GCA* **46**, 1627. [8] Ireland T. R. *et al.* (1992) *GCA* **56**, 2503.

KINETIC ISOTOPIC FRACTIONATION DURING THE EVAPORATION OF THE IRON OXIDE FROM LIQUID STATE; Jianhua Wang[1], Andrew M. Davis[2], Robert N. Clayton[1,2,3] and Toshiko K. Mayeda[2], [1]Department of the Geophysical Sciences, [2]Enrico Fermi Institute, [3]Department of Chemistry, University of Chicago, Chicago, IL 60637

Large enrichments in the heavy isotopes of oxygen, iron and nickel have been reported in magnetite-wüstite deep-sea spherules of cosmic origin [1,2,3,4]. These cosmic spherules are thought to have been Fe-Ni metal particles that were oxidized, melted and evaporated during atmospheric entry. The heavy isotope enrichments have been attributed to Rayleigh fractionation during evaporation [2,3,4]. Davis *et al.* [2] inferred that iron and oxygen evaporated as FeO, because of the agreement between the average amount of isotopic mass fractionation of iron and oxygen for all spherules. Assuming that FeO and NiO are the phases involved in the evaporation reaction, Davis and Brownlee [4] obtained a range of 76 to 94% mass loss for iron and 52 to 99.2% mass loss for nickel.

The sample preparation and the evaporation procedures are similar to those described by Wang *et al.* [5]. We evaporated reagent-grade wüstite (Alfa Products) at 1450, 1550, 1650 and 1750 °C for durations of 30 to 420 minutes. Ten evaporation runs produced a weight loss range of 3.5% to 87.2% of the original mass. We calculated evaporation rates of iron oxide by assuming that the density of the liquid residue is the same as that of the final solid residue. We also assumed that the liquid residue was spherical during evaporation. Fig. 1 shows the experimental data compared with evaporation rates (J) calculated from the kinetic theory of gases using thermodynamic data [6]: $J = p/\sqrt{2\pi MRT}$, where p is the equilibrium vapor pressure, M the molecular weight, R the gas constant and T the temperature (K). This equation only applies in cases involving a single solid phase going to a single gas-phase species, whereas many of the possible reactions for evaporation of iron oxide involve two gas-phase species. The evaporation rate (J) can be calculated from each of the gas phase species involved in a reaction. Rates calculated from $Fe_{(g)}$ are generally slower than those calculated from $O_{2(g)}$, so we have calculated rates from $Fe_{(g)}$ for all reactions involving two gas-phase species. The experimental data exhibit a remarkable fit to the evaporation rate calculated for the reaction: $FeO_{(\ell)} \rightarrow Fe_{(g)} + {}^1/_2\ O_{2(g)}$. As this is the fastest of the possible evaporation reactions, evaporation of FeO must not be kinetically hindered.

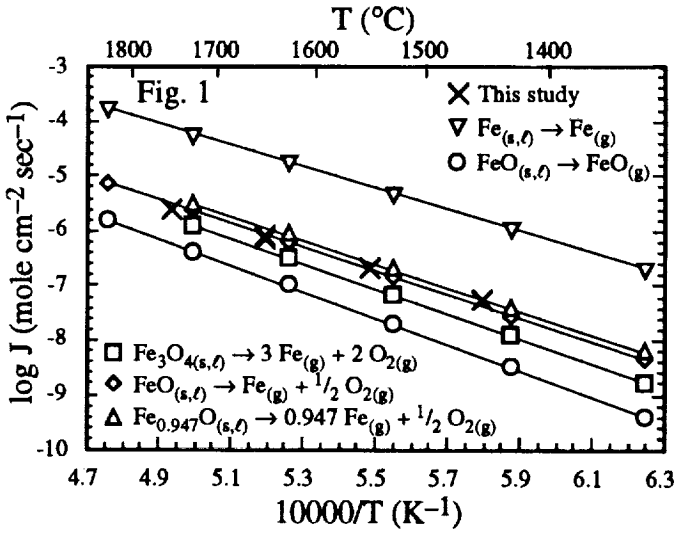

SEM examination of polished FeO residues using backscattered electron imaging indicates that there are two phases in most residues. We dissolved starting iron oxide and residues with 6N HCl and determined their Fe content by atomic absorption spectrophotometry. The starting iron oxide is of wüstite composition ($Fe_{0.947}O$) rather than stoichiometric FeO. The residues usually contain less iron than wüstite, suggesting that the minor phase in the SEM images is magnetite (Fe_3O_4). No systematic relationship was found between the magnetite content and the degree of

evaporation loss. Since most residues have a bubble in their center, we suspect that oxygen is not efficiently evacuated from the residue. This hypothesis is supported by the oxygen isotope fractionation results which will be discussed later. We should point out that the kinetic theory that we used is a crude approximation to this complicated system.

We measured the iron isotopic composition of the residues with a modified AEI IM-20 ion microprobe, using melted starting material as a standard (Fig. 2). The linear relationship shows that the isotopic fractionation obeys the Rayleigh equation ($R/R_0 = f^{1/\alpha-1}$, where R is the isotope ratio in the residue, R_0 is the isotope ratio in the starting material, f is the fraction evaporated and α is the fractionation factor between liquid and gas). The fractionation factors can be obtained from the slopes of linear fits to the data (slope = $1-1/\alpha$). They are 1.0183 for $^{56}Fe/^{54}Fe$, 1.0274 for $^{57}Fe/^{54}Fe$ and 1.0345 for $^{58}Fe/^{54}Fe$. These α's are almost identical to the theoretical values of 1.0184, 1.0274 and 1.0364 (inverse-square-root of mass ratio) assuming iron leaving the liquid as $Fe_{(g)}$. Because the theoretical value of α is the upper limit for the fractionation factor of iron, any species heavier than monatomic $Fe_{(g)}$ would lower the fractionation factor. This confirms our conclusion that $Fe_{(g)}$ rather than $FeO_{(g)}$ is the species evaporated. Using our results, we only need a range of 67 to 89% of Fe loss to account for the iron isotope fractionation found in the deep-sea spherules [2, 4].

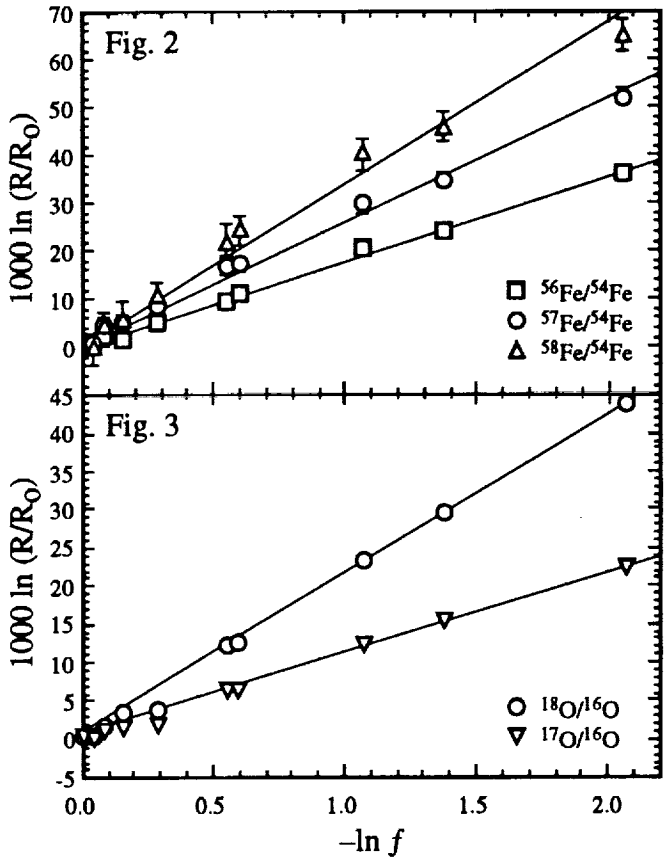

Oxygen isotopic compositions of the residues and starting material were obtained using conventional oxygen extraction by fluorination and mass spectrometry. The results are shown in Fig. 3. The oxygen isotopic data also obey the Rayleigh equation, with α's of 1.0217 for $^{18}O/^{16}O$ and 1.0110 for $^{17}O/^{16}O$. These values are smaller than the theoretical values of 1.0308 and 1.0155 calculated for O_2 as the gas-phase species. Since we have verified that $FeO_{(\ell)} \rightarrow Fe_{(g)} + {}^1/_2\, O_{2(g)}$ from both iron isotopes and kinetic experiments, we think that the kinetically hindered oxygen evaporation rate which makes it inefficient to fractionate isotopes can explain the observed fractionation factors for oxygen. The retention of O_2 gas in the central vesicle of most residues maintains an interaction between oxygen in the gas phase and the liquid residue. This will also reduce the efficiency of fractionating oxygen isotopes as O_2 will not be isolated from the liquid after its formation.

References: [1] Clayton R. N. *et al.* (1986) *EPSL* **79**, 235. [2] Davis A. M. *et al.* (1991) *LPS* **XXII**, 281. [3] Herzog G. F. *et al.* (1992) *LPS* **XXIII**, 527. [4] Davis A. M. and Brownlee D. E. (1993) *LPS* **XXIV**, 373. [5] Wang J. *et al.* (1994) *LPS* **XXV**, this volume. [6] Barin I. (1989) *Thermochemical Data of Pure Substances*, VCH Publ., Weinheim, Germany.

COORBITAL BENDING WAVES AND INCLINATION DECAY. Wm. R. Ward, JPL, Pasadena, CA 91109 and Joseph M. Hahn, Univ. of Notre Dame, Notre Dame, IN 46556.

A secondary orbiting in a self-gravitating disc on an inclined orbit will launch bending waves from vertical resonance sites where the Doppler shifted forcing frequency, $m|\Omega-\Omega_{ps}|$, of an m^{th} order Fourier component of the disturbing potential matches the natural frequency, μ, for vertical oscillations of the disc [1,2]. The pattern speed of an ℓ,m component is $\Omega_{ps} = \Omega_s + (\ell/m - 1)\mu_s$, where Ω_s and μ_s are the mean motion and vertical oscillation frequency of the secondary. The potential amplitudes, $\phi_{\ell,m}$, are of order $|\ell-m|$ in inclination, I; so that the $\ell = m \pm 1$ terms are first order in I and have pattern speeds slightly faster and slower than the perturber's mean motion, i.e., $\Omega_{ps} - \Omega_s = \pm\mu_s/m$. As a result, the inner (outer) resonance of the faster (slower) component falls inside (outside) the perturber's orbit (i.e., at $r_v \approx a(1 -(+)4/3m)$, designated *external*), while the outer (inner) resonance falls at the perturber's semi-major axis ($r_v \approx a$, designated *coorbiting*).

The response of the disc to an m^{th} order perturbation is to launch a spiral bending wave. The attraction of the perturber for this configuration gives rise to a reaction torque on the secondary of magnitude $T_m = \mathrm{sgn}(\Omega-\Omega_{ps})(\pi\sigma\mathcal{H})^2 mGr$, where σ is the surface density of the disc, Ω is the orbital frequency of the resonance site, and $\mathcal{H}$ is the maximum vertical displacement of disc material after the wave has achieved full amplitude [3]. The equations of motion for the perturber are $\dot{L}_\perp = T_m$, $\dot{E} = \Omega_{ps} T_m$, from which one finds the rate of change in the inclination to be [4]

$$(1) \qquad \frac{dI}{dt} = \left[\Omega_s - \Omega_{ps} + 2\Omega_{ps}\sin^2 I/2\right] \frac{T_m}{M(a\Omega_s)^2}$$

The amplitude of an m^{th} order bending wave in a self-gravitating disc is given by Shu et al [1,2]. Substituting their results into eqn (1) we find

$$(2) \qquad \sin I \frac{dI}{dt} = \pm[\cos I \pm 2m\sin^2 I/2]\left(\frac{\pi\sigma r^2}{M}\right) \frac{\pi\langle\partial\phi/\partial z\rangle^2}{a^2\Omega_s|\mathcal{D}|}$$

where $|\mathcal{D}| = |r d/dr\{\mu^2 - m^2(\Omega-\Omega_{ps})^2\}| \sim 3m\Omega^2$, $\langle\partial\phi/\partial z\rangle = |\pi^{-1/2}\int_{-\infty}^{\infty}\partial\phi/\partial z \exp i\xi^2 d\xi|$, $\xi = (r/r_v - 1)\sqrt{(r|\mathcal{D}|/4\pi G\sigma)}$, and the subscripts $m\pm1$, m on ϕ are to be understood. Coorbital torques (lead negative sign) are to be evaluated in the vicinity of the perturber ($r \sim a$) and damp the inclination; while external torques (lead positive sign) are to be evaluated in the vicinity of $r-a \sim \pm 4a/3m$ and excite I. [The second $\pm$ sign refers to slow vs. fast pattern speeds.]

Using the direct portion of the disturbing potential, $\Phi = -(GM/a)\{1+\gamma^2 - 2\gamma\cos\Delta\theta+(z'-z'_s)^2\}^{-1/2}$, the needed forcing amplitudes are

$$(3) \qquad \frac{\partial\phi}{\partial z} = \frac{m}{\pi}\frac{GM}{a^2}\left[I_1(\lambda_-)K_0(\lambda_+) - I_0(\lambda_-)K_1(\lambda_+)\right] \frac{\sin I}{\sqrt{x^2 + \sin^2 I}}$$

where M is the secondary's mass, $\gamma = r/a$, $x = \gamma - 1$, and $\{I_n, K_n\}$ denote modified Bessel functions of the first and second kind with arguments $\lambda_\pm = (m/2)[\sqrt{(x^2+\sin^2 I)} \pm |x|]$.

Substituting eqn (3) into (2) yields the desired expression for the

COORBITAL BENDING WAVES AND INCLINATION DECAY: Ward W.R. and Hahn J.M.

rate of change of the inclination due to m^{th} order vertical resonances

$$(4) \qquad \frac{2}{\sin 2I}\frac{dI}{dt} = \pm \frac{2}{3}\frac{m^3}{r}\frac{M}{M_p}\left|\frac{1}{\sqrt{\pi}}\int_{-\infty}^{\infty}\mathcal{K}_m \exp -i\xi^2\, d\xi\right|^2$$

where M_p is the mass of the primary, $r \equiv (M_p/\sigma r^2)\Omega_s^{-1}$, and $\mathcal{K}_m \equiv [I_0K_1 - I_1K_0]m^{-1}(x^2+\sin^2 I)^{-1/2}$. In obtaining (4), it is assumed that the disc extends far enough interior and exterior to the secondary to contain resonances from both fast and slow pattern speeds for each m, which are then combined while ignoring any "slow" changes in the disc, i.e., for which $d/dr \sim O(1/r)$. If the spatial variation of the forcing potential is slow compared to the oscillation of the exponential, the quantity $\mathcal{K}_m$ can be pulled out of the integral with the remaining part reducing to unity. For $\sin I > \sqrt{(4\pi\sigma r^2/3M_p)}$, this procedure is valid for all orders.

In this case, eqn (4) can be rearranged to read $d/dt\{\ell n(\cos I)\} = \mp (2/3)(m/r)(M/M_p)\{Z\mathcal{K}_m(Z)\}^2$, where the last bracketed quantity on the R.H.S. is a function of $Z \equiv m\sin I$ only. Figure 1 displays the behavior of $(Z\mathcal{K}_m(Z))^2$ as a function of Z for both coorbital and external resonances. We expect these results should apply whenever $a\sin I$ exceeds both the thickness of the disc and the Hill's radius of the secondary. At small I, the inclination excitation rate found by Borderies et al. [4] for external resonances is recovered. However, figure 1 indicates that the damping strength of coorbital resonances exceeds the excitation strength of external resonances for all Z. Hence, if the secondary is embedded in a smooth disc without a local gap in the surface density, bending wave interaction should damp the orbital inclination [5,6].

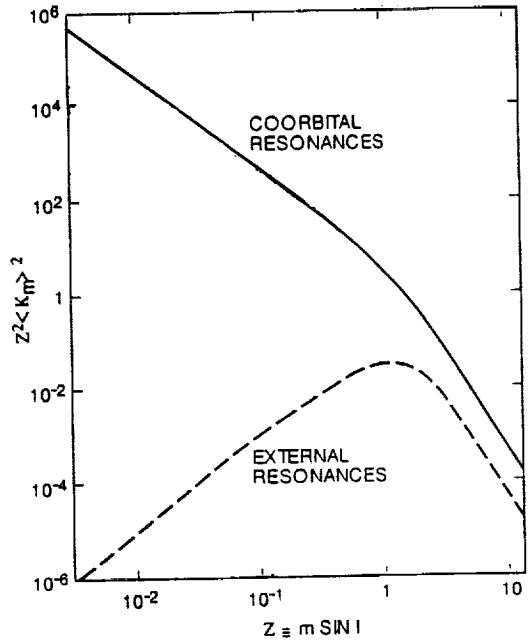

REFERENCES

[1] Shu, F. H., J. N. Cuzzi, and J. J. Lissauer (1983) *Icarus* 53, 185.
[2] Shu, F. H. (1984) in *Planetary Rings* (Univ. of Ariz. Press), 513.
[3] Bertin, G., and J. W.-K. Mark (1980) *Astron. & Astrophys.* 88, 289.
[4] Borderies, N., P. Goldreich, and S. Tremaine (1984) *Ap. J.* 284, 429.
[5] Artymowicz, P. (1993) preprint.
[6] Ward, W. R. and J. M. Hahn (1993) preprint.

PETROLOGIC INSIGHTS REGARDING LUNAR AND PLANETARY METEORITE LAUNCH PROCESSES

PAUL H. WARREN

Institute of Geophysics and Planetary Physics, UCLA, Los Angeles, CA 90024-1567

Précis: The problem of understanding the launch circumstances for lunar and planetary meteorites is addressed by integrating physical modeling constraints, geochemical cosmic-ray exposure (CRE) constraints, and petrologic constraints. The potential source region for lunar meteorites (LMs) is remarkably small compared to the final crater volume. Pre-launch depth tends to be shallow, in part due to the shock-wave interference effect suggested by Melosh [1], although the effect is even more pronounced than Melosh assumed, due to the extremely low compressional wave velocity of the Moon's regolith. The large number of separate LM source craters implied by combined CRE and petrologic constraints implies either the source craters can be much smaller than previously supposed; *and/or* (b) the cratering rate estimates (which have never been claimed to be precise) are much too low.

At latest count [e.g., 2], nine meteorites (12, if one ignores some obvious cases of pairing) have been identified as lunar meteorites. In addition, the 10 mafic-igneous meteorites of the SNC clan are widely believed to be pieces of Mars. Understanding the launch mechanism is clearly important for all attempts to utilize these samples as constraints to study the Moon and Mars. Previous attempts to constrain the process of LM and SNC blast-off have mainly emphasized theoretical physics. Here, I try a two-pronged approach, utilizing some physical modeling as well as observational constraints from geochemistry and petrology.

Complete shielding from cosmic rays requires several meters of rock (Earth's atmosphere is equivalent to ~ 3.4 m of rock). LMs and SNCs, like most meteorites, probably arrive at the Earth as decimeter to meter sized rocks, with virtually their entire volumes enduring isotropic (4π) CRE. In some cases, the meteoritic matter may have earlier experienced an appreciable duration of 2π CRE, by residing close to the surface (less than several meters deep) within a large parent body. By analyzing various ratios of nuclides to their parent and daughter nuclides, taking advantage of the differing half-lives of the CRE spallation products, isotope geochemists are able to gauge several aspects of the histories of meteorites, most notably: (1) the duration and (2) the depth of the 2π CRE (if significant), (3) the duration of the 4π CRE, and (4) the duration of the terrestrial CRE shielding (if significantly long). Assuming no collisional fragmentation en route (safe for LMs, not so safe for SNCs), the sum of (3) + (4) is the blast-off age. These constraints have not been reviewed for LMs in several years [3], but I show an up-to-date summary in Fig. 1. (Data sources are far too numerous to cite here. I apologize to all concerned.) A very interesting aspect of Fig. 1 is that it implies a minimum of 5 separate LM source craters (or 4, if one discounts a $4\text{-}\pi$ datum for ALHA81005 based on TL), all within the past 9 Ma, and most within the past 0.3 Ma. When compared with estimated cratering rates [4], this suggests that most of the source craters are surprisingly small: $\leq$5 km in diameter (D).

CRE constraints on pre-launch depth are summarized in Fig. 2. Remarkably, 5 of the 8 LMs with unambiguous CRE constraints were launched from depths of $\leq$3.2 m. Even for a crater D of just 1 km, 3 m is less than the average depth of all excavated matter by an order of magnitude. The shallow depth-provenance for most LMs was implicitly predicted by the shock-wave interference theory of Melosh [1]. A key variable in Melosh's equation for calculating depth to the base of the zone of interference is the compressional wave velocity c_L. In his calculations, Melosh [1] assumed $c_L \sim 6$ km/s, a value appropriate for solid rocks. However, the Moon's upper crust is far from solid, and its outer few meters has average seismic V_p ($\approx c_L$) consistently close to 0.11 km/s [5]. As shown in Fig. 3, the effect of assuming a c_L of even 0.2 km/s is to drastically reduce the interference zone thickness, to a range that corresponds (in the LM-fertile region close to the impactor, and assuming a typical impact velocity of 10-20 km/s) to only 1-2 m for craters with D of the order 5 km.

The CRE data, by themselves, permit 3 (or perhaps 4) of the most recently launched LMs to be source-crater paired. However, the above conclusion that the source crater was not >>5 km can be factored in with petrologic constraints to test the plausibility of source-crater pairing, on a couple-by-couple basis. Before considering the petrology of these LMs, I adduce a key constraint from cratering physics. Shock pressure gradients, and thus ejection velocities, fall off with distance from the impact point as a function of the impactor radius raised to a power called the "launch-position exponent" e_x. The most likely value for e_x is thought to be ~2.8, and it is almost certainly between 2 and 3 [6]. Given this power law, it is impossible to derive a LM from more than a few impactor radii out from the center of the crater. This constraint means that the potential LM source region is narrower than D by a factor of at least 3. In other words, when contemplating say a 9-km crater, the maximum separation between two LM launch points is conservatively 3 km (and the most probable separation is smaller yet, by 0.7×).

Three of the recently launched LMs (ALHA81005, Y791197, and Y793274) are regolith breccias; the first two are also relatively mature and young (classified as per [7]), implying they probably were very similar in composition to the local (~ km scale) soils of their launch locality(ies). Y793274 consists mainly of mare basalt, and EET87521 is a mare basalt breccia with a small component of KREEPy highland material. The extent to which mare materials mix into highland regolith samples as a function of distance from the mare can be calibrated on the basis of studies of Apollo and Luna 20 samples (Fig. 4). Assuming a 3 Ga age for the mare, this process can also be modeled, à la [8]. Based on abundances of mare clasts and glasses in the meteorites, Y791197 appears to have formed at a distance from the nearest mare comparable to (probably less than) that of Luna 20, namely ~35 km; ALHA81005 formed at a much greater remove, of the order 100 km. Also, ALHA81005 and Y791197 are probably too different in Mg/(Mg+Fe), to be from a single 10-km scale region (the inset in Fig. 1 shows Apollo 16 regolith samples, for comparison). Barring an implausibly large source crater, it seems unlikely that any source-crater pairing exists among the 8 LMs with unambiguous CRE stories, except for probably Asuka-881757 and Y793169, and possibly EET87521 and Y793274. Note that this last conclusion exacerbates the difficulty of accounting for the abundance of LM source craters without assuming either: (a) these craters can be much smaller than previously supposed [1]; *and/or* (b) the cratering rate estimates (which are only claimed to be accurate within a factor of two) [4,9] are much too low.

References: [1] Melosh H. J. (1985) *Geology* 13, 144-148. [2] Warren P. H. and Kallemeyn G. W. (1993) *Proc. NIPR Symp. Ant. Met.* 6, 35-57. [3] Eugster O. (1989) *Science* 245, 1197-1202. [4] Shoemaker E. M. et al. (1990) in *Geol. Soc. Amer. Spec. Pap.* 247, 155-170. [5] Watkins J. S. and Kovach R. L. (1973) *Proc. LSC 4th*, 2561-2574. [6] Housen K. R. et al. (1983) *JGR* 88, 2485-2499. [7] McKay D. S. et al. (1986) *Proc. LPSC 16th*, 277-303. [8] Arvidson R. et al. (1975) *Moon* 13, 259-275. [9] Grieve R. A. F. (1988) *Revista Geofisica* 28, 145-178..

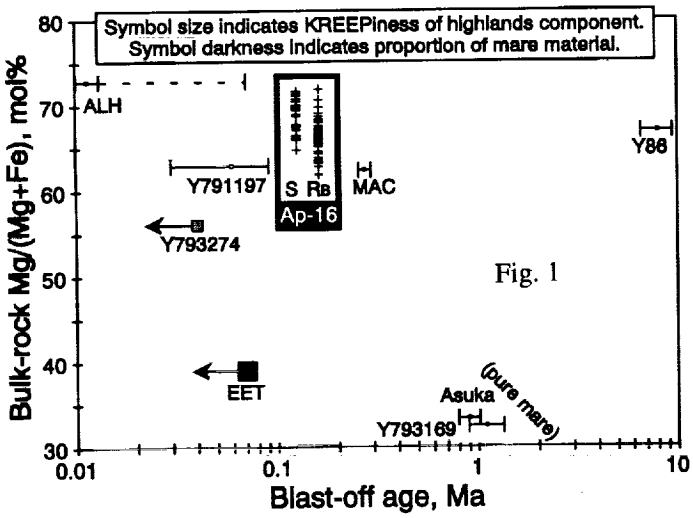

Fig. 1

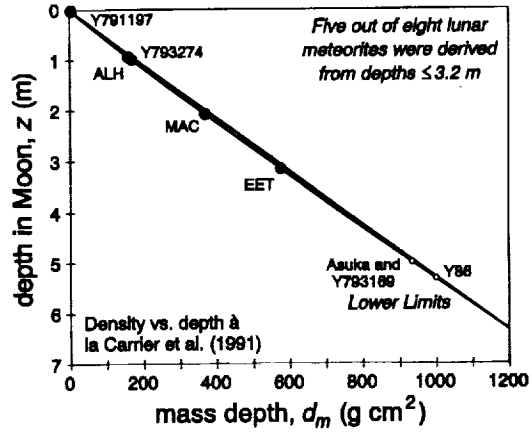

Fig. 2

Fig. 3

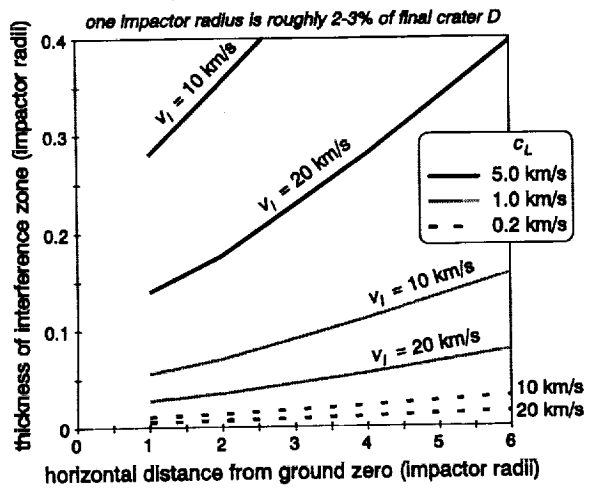

Fig. 4

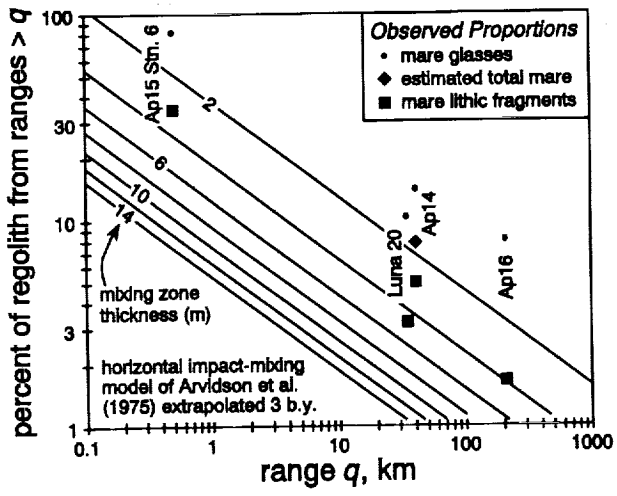

PETROLOGY OF LEW88774: AN EXTREMELY CHROMIUM-RICH UREILITE

PAUL H. WARREN AND GREGORY W. KALLEMEYN
Institute of Geophysics and Planetary Physics, UCLA, Los Angeles, CA 90024-1567

Précis: The LEW88774 ureilite is extraordinarily rich in pyroxene, Cr-spinel, and a Cr-rich, Ni-poor cohenite (carbide). The pyroxene is uncommonly Ca-rich, and has exsolved into coarse lamellae (up to ~50 μm across) and granules of augite ($En_{53}Wo_{33}$) and orthopyroxene ($En_{75}Wo_{4.4}$). Olivine-core CaO is also very low (0.24%), by Fo_{75} ureilite standards. However, the equilibration temperature implied by the pyroxene compositions is still near-solidus (~1300°C), as usual for ureilites, despite the paradoxically coarse-grained texture. The Cr-rich (13-33%) carbide appears to have formed secondarily by a reaction, perhaps triggered by shock-melting, involving the chromite and C-matrix.

Ureilites are a large (~40 stones) class of meteorites that in many ways show great diversity, e.g., in terms of oxygen isotopic compositions. However, in many ways ureilites are remarkably uniform compared to other classes of igneously differentiated meteorites. They are consistently carbonaceous (average C content virtually as high as CI chondrites). Ureilite silicates (except in polymict ureilites) are entirely olivines and pyroxenes, and are consistently coarse-grained, even though ureilites also consistently have unexsolved pigeonites and CaO-rich, Fo-rimmed olivines, implying that they failed to equilibrate to low *T* in the usual manner of coarse-grained igneous rocks [1]. For a few elements that are little-fractionated among carbonaceous chondrites and compatible with mantle olivine+pyroxene assemblages, ureilites tend to have rather uniform composition [2]. The petrologic diversity of ureilites was recently magnified, however, with the discovery of LEW88774 [3]. This mildly weathered (albeit classed B/C) 3.1-gram stone is bizarre, even by ureilite standards.

Roughly estimated, the mode of LEW88774,5 has 70% pyroxene, 14% olivine, 12% C-matrix (which is uncommonly rich in diamond or lonsdaleite), 3% chromian spinel, 1-2% Cr-rich carbide, and <1% Si,Al-rich glass. No other ureilite is so pyroxene-rich [4]. The pyroxene has coarsely exsolved from an original medium-Ca composition into thick lamellae (up to ~50 μm across) and larger granules, yielding roughly equal proportions of low-Ca and high-Ca pyroxene (Fig. 1). Compositions (avoiding rims) cluster tightly around $En_{75}Fs_{21}Wo_{4.4}$ (with 1.3% Al_2O_3 and 0.97 wt% Cr_2O_3) and $En_{53}Fs_{13.7}Wo_{33}$ (2.1% and 1.8%). The olivine (avoiding rims) clusters tightly at $Fo_{74.9}$, with 0.19-0.27 wt% CaO. The rock is mildly brecciated, but apart from the exsolution, the poikilitic silicate texture is not unusual, for an augite-bearing ureilite [4]. Pyroxene optical continuity extends up to 4 mm.

Cr-spinel occurs as numerous (~30) widely scattered grains; mostly 0.5-1 mm, but up to 1.5 mm across. Thus, it seems very unlikely that the mode is a fluke (such that a few cm away chromite is absent); moreover, the bulk rock is extremely Cr-rich [2]. Cr-spinels probed in LEW88774,5 have 54-58% Cr_2O_3, 18-20% MgO, 15-19% Al_2O_3 (the bulk-rock Al distribution is roughly 60% in pyroxene, 40% in chromite), 2-6% FeO, and 0.6-2.8% TiO_2. Many of these grains appear subhedral, but many have a corroded appearance, and are surrounded by complex zones that, where best developed (especially near C-matrix/Cr-spinel boundaries), consist mainly of anhedral Cr-rich cohenite, along with Si,Al-rich glass and several other trace phases [1]. We discovered that the carbide was not Cr-Fe metal, as originally described [1] when we consistently got low sums (mostly 88-90 wt%) from microprobe analyses. Identification of the main unanalyzed element as C was kindly confirmed for us by G. J. MacPherson. This phase is compositionally diverse (although comparatively uniform within grains), with 55-75% Fe, 13-33% Cr (avg. 28%), 0.4-1.8% Ni (avg. 0.7%), and ~0.04-0.2% Co; Si, P and Ti could not be detected.

The detailed origin of this carbide phase is unclear. It seems most likely that it formed as a secondary product of decomposition or shock-melting (along grain boundaries) of the Cr-spinel, which reacted, or became crudely alloyed, with C (from the C-matrix) and Fe^0 (from metal/sulfide veins and reduction of silicate rims). Originally, almost all of the Cr that is now in Cr-cohenite was probably in Cr-spinel. The more profound question concerns how this ureilite originally acquired such a high Cr content [2].

The extensive pyroxene exsolution in LEW88774 is unique among ureilites. Yet a key constraint on ureilite origin, the paradox of their very rapid subsolidus cooling despite their coarse igneous textures, is not much weakened by this development. Despite the scale of the exsolution, application of the two-

pyroxene thermometer [5] indicates that equilibration stopped at ~1250-1300°C; i.e., virtually at the solidus. The olivine-core CaO content (avg. 0.24%) is extremely low, by ureilite standards (especially considering the low *mg*), but still far higher than generally observed for deep-origin igneous rocks [6]; the nearest precedent is perhaps ALHA77005, which McSween [7] stresses is a shallow-origin rock, albeit it contains 2-mm olivines manifestly cumulus in origin. The preservation of reduced rims on the olivines also demonstrates failure to equilibrate far into the subsolidus *T* range.

The coarseness of ureilite textures is not the only evidence against simple models to crystallize them entirely within an environment that is shallow enough to preclude mafic silicate equilibration. Original crystallization (or recrystallization during partial melting) deep in the mantle of the parent asteroid(s) is also evidenced by the simple fact that ureilites hold so much graphite, in conjunction with the (not-so-simple) relationship between graphite stability and pressure at magmatic *T* and ureilite-like oxygen fugacity [8,9]. Oxidation of graphite is favored by a combination of low pressure and low $f(O_2)$; and the latter can be constrained based on olivine-core *mg* ratios. Here, too, LEW88774 is at an extreme for ureilites (Fo_{75}), such that the evidence for deep origin is particularly strong. In this sense, the coarse exsolution features and low olivine-core CaO in LEW88774 are unsurprising. Nonetheless, it seems hard to avoid a major discontinuity in the cooling history of LEW88774, as is true of all ureilites; and the most plausible mechanism is catastrophic impact-fragmentation of the parent asteroid(s) [1,8].

References: [1] Takeda H. (1987) *EPSL* 81, 358-370. [2] Kallemeyn G. W. and Warren P. H. (1994) *LPS XXV*, this volume. [3] Satterwhite C. et al. (1993) *Antarctic Meteorite Newsl.* 16(1), 15. [4] Goodrich C. A. (1992) *Meteoritics* 27, 327-352. [5] Lindsley D. H. and Anderson D. J. (1983) *Proc. LPS Conf. 13th*, 887-906. [6] Warren P. H. and Kallemeyn G. W. (1989) *Proc. LPS Conf. 19th*, 475-486. [7] McSween H. Y., Jr. (1985) *Rev. Geophys.* 23, 391-416. [8] Warren P. H. and Kallemeyn G. W. (1992) *Icarus* 100, 110-126. [9] Walker D. and Grove T. (1993) *Meteoritics* 28, 628-636.

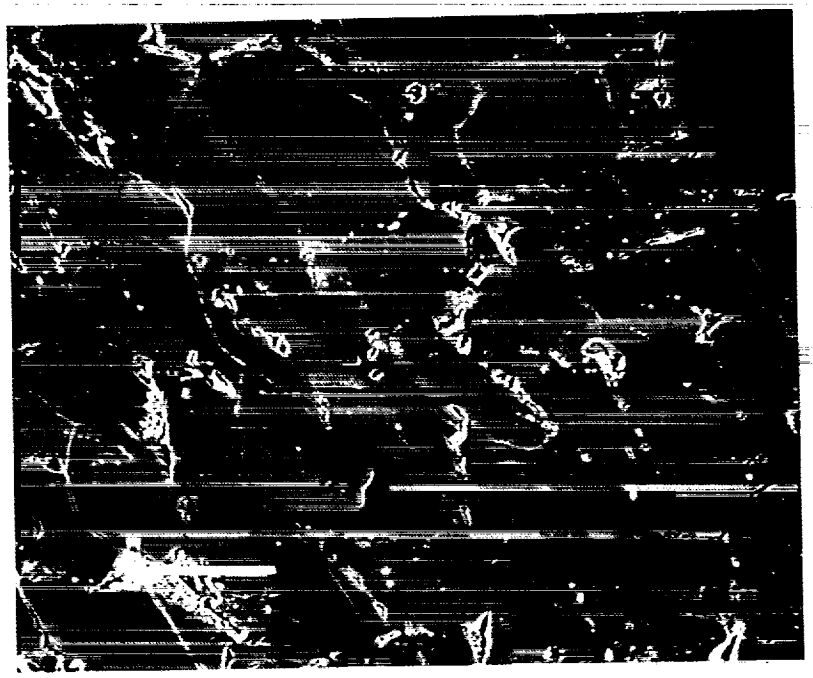

Fig. 1. Back-scattered electron (BSE) image of LEW88774,5: coarse exsolution features in pyroxene. Light = augite, dark = orthopyroxene. Scale bar = 100 μm.

CHONDRULE MAGNETIC PROPERTIES P. J. Wasilewski, and M. V. O'Bryan, Astrochemistry Branch, NASA, Goddard Space Flight Center, Greenbelt, Maryland.

CHONDRULE MAGNETIC PROPERTIES: Magnetically speaking, the chondrules contain a considerable range of ferromagnetic material; the distribution of this material is isotropic to anisotropic with clustering often observed. The NRM (remanence initially measured - 'natural remanence') vector records range from ultra stable to random when demagnetized, and evidence exists for a wide range of magnetic recording scenarios including the need to invoke external fields of at least several milli Tesla (tens of Gauss) to explain the results. The chondrules from each meteorite studied (Allende (C3V), Chainpur (LL3), Bjurbole (L4), and Allegan (H5)) exhibit a wide range of properties attributable to amount and geometric aspects of the ferromagnetic material, and the cooling history (the characteristics of the M shaped diffusion profile in taenite grains). However, the chondrules from each meteorite are different from those coming from another meteorite. These important differences include remanence characteristics that are not easily explained by differences in coercivity spectra (magnetic hardness) or composition of the ferromagnetic fraction.

CHONDRULES FROM THE SAME METEORITE: Regardless of the wide variation in the amount of ferromagnetic material, the chondrules appear to have similar thermomagnetic curves (thermomagnetic curve shapes are mostly defined by tetrataenite and other characteristics of the M shaped diffusion profile - the amount of kamacite is simply background in the thermomagnetic curve). These results suggest, as is often emphasized, that little mixing occurred among chondrules. The thermomagnetic curves for chondrules from one meteorite are characteristically different compared to those from another chondrite.

Saturation remanence (SIRM) demagnetization curves for chondrules are similar or bimodal (essentially reflecting the coercivity spectrum i.e. magnetic hardness due to grain size, tetrataenite and properties of the M shaped profile).

NRM stability to demagnetization is variable, the behavior of the NRM vector direction ranges from ultra stable to random, often these will be definite excursions. This means that during the processing of the chondrules different scenarios for remanence imprinting did indeed exist.

REM values range over 3 orders of magnitude. Some chondrules have REM values >0.1 suggesting that a field of greater than several milli Tesla was required to produce the observed magnetizations. In the terrestrial environment, REM values >0.1 are almost always associated with lightning struck samples.

REM VALUES: REM is the ratio of NRM (remanence initially measured - 'natural remanence') to SIRM (saturation remanence in 1 Tesla field). In Allende chondrules the REM range is 0.0005 (2366) to 0.03 (23); in Allegan the REM range is 0.0004 (2360) to 0.034 (112). The numbers in parentheses are SIRM values ($10^{-4}Am^2K^{-1}$). For Allende and Allegan there appears to be a systematic relationship between REM and the SIRM, which is not related to the size of the magnetic carriers. For example, in Allegan, all chondrules have $Hs^{1/2}$ (field at which one half the saturation remanence is demagnetized) values greater than 100 milli Tesla.

The SIRM for Bjurbole chondrules range from 104 to 27470; those with the highest SIRM values (>10,000) have the smallest REM values (<0.008) but for other chondrules with SIRM (<10,000) the REM values are quite variable ranging from 0.004 to 0.4. REM values for the Chainpur chondrules range from 0.0009 to 0.013 with no relationship to the SIRM.

The SIRM values of a chondrule will not change with time in a museum or laboratory, but the NRM will be subject to change. In handling the chondrules we use copper - Beryllium tweezers which are essentially non magnetic. "Non magnetic" stainless steel tweezers are quite magnetic and can result in contanimation of the NRM.

CONCLUDING REMARKS: The preliminary field estimates for chondrules magnetizing environments range from minimal to at least several mT (tens of Gauss). These estimates are based on REM values and the characteristics of the NRM thermal demagnetization compared to SIRM demagnetization. We expect to have the magnetic recording scenarios for chondrules established and petrologic aspects of the ferromagnetic fraction in the chondrules documented. This will enable interpretations appropriate to chondrule formation.

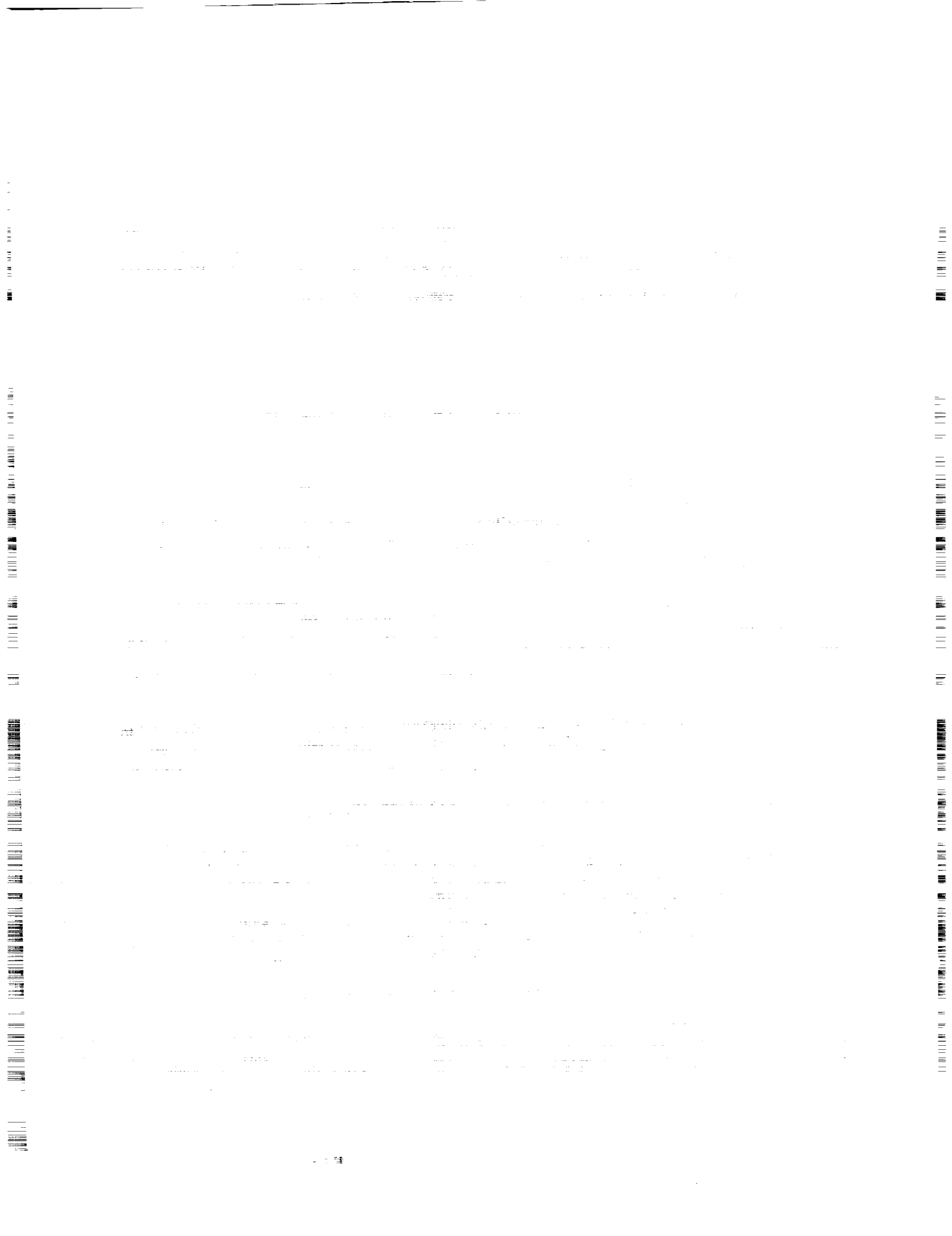

omit to P. 1499

THE EVOLUTION OF NEBULAR SOLIDS: EVIDENCE FROM COMPOUND CHONDRULES AND FROM IGNEOUS RIMS ON CHONDRULES IN ORDINARY CHONDRITES

John T. Wasson* and Alexander N. Krot*+ *Institute of Geophysics and Planetary Physics, University of California, Los Angeles, 405 Hilgard Ave., CA 90024, USA; +Vernadsky Institute of Geochemistry and Analytical Chemistry, Russian Academy of Sciences, 19 Kosygin Str., Moscow 117495 , Russia

Two sets of objects, compound chondrules melted in independent events and chondrules with igneous rims, preserve the record of solids present at different times during chondrule formation in the solar nebula. We had anticipated that the FeO contents of the dominant mafic minerals in the secondaries of independent compound chondrules would either be randomly distributed or consistently FeO-rich; what we observed was that FeO-contents of secondaries are similar to those of primaries, implying formation from the same batch of nebular materials [1]. As shown in Fig. 1, our studies of igneous rims on chondrules show the same trend. We studied ten low-FeO (Fa or Fs <8 mol%) and eight high-FeO (Fa or Fs >8 mol%) chondrules with igneous rims (hereafter shortened to rims) in unequilibrated (type <3.7) ordinary chrondrites. With one exception, the low-FeO chondrules have porphyritic-olivine textures; most of their rims are pyroxene-normative. Most of these rims have experienced high degrees of melting, perhaps 90±10%. In most cases the rims around high-FeO chondrules show appreciably lower degrees of melting; many contain low-FeO relict grains which may have formed by disaggregation of low-FeO chondrules. These rims are mainly olivine-normative. The existence of chondrules with igneous rims supports the conclusion arrived at from our compound-chondrule study, that chondrule-forming high-temperature events took place multiple times.

Rims around chondrules can be divided into two major categories: fine-grained rims, typically opaque and iron-rich [2,3] and relatively coarse-grained rims [4,5]. Fine-grained rims are similar in mineralogy and chemistry to matrix material and consist of micrometer-to-submicrometer-sized grains or amorphous material. It is widely accepted that fine-grained rims did not experience any significant melting [3]. Coarse-grained rims are much coarser than matrix material (e.g., ~4 μm in Semarkona); they surround ~50%, ~10% and <1% of all chondrules in CV3, H-L-LL3 and CO3 chondrites, respectively [4]. Rubin [4] suggested that coarse-grained rims formed by sintering of opaque matrix material by heating to sub-solidus or sub-liquidus temperatures during chondrule formation. Our study of coarse-grained rims in ordinary chondrites showed that these were appreciably melted and can be classified as igneous rims.

Wasson et al. [1] divided the compound chondrules in ordinary chondrites into two categories: sibling chondrules and independent chondrules. Sibling chondrules have essentially identical textures and compositions implying formation in the same flash-heating event. The primary and secondary of independent compound chondrules differ in composition and generally also in texture; the secondaries seem to have formed by melting of materials surrounding the earlier-formed primary. Although the most common type of secondaries are adhering, a significant fraction envelop the primary chondrule. We infer that igneous rims, like independent secondaries, formed by accretion of precursor grains onto chondrules followed by heating and melting during chondrule formation. Thus rims and enveloping secondaries preserve the nebular record of solids present some period after the primary or host chondrule had formed.

These observations are consistent with the canonical cosmochemical picture of nebular solids evolving towards more FeO-rich compositions as the temperature falls. It

THE EVOLUTION OF NEBULAR SOLIDS **Wasson J.T. and Krot A.N.**

seems probable that low-FeO chondrules formed before major low-temperature oxidation of metallic Fe-Ni into fayalitic olivine, high-FeO chondrules formed after the nebula had cooled to lower temperatures (≤500K). Even the low-FeO chondrules contain FeS, an indication that the nebula had cooled to the FeS condensation temperature of 650 K before most of them formed.

The decrease in the inferred degree of rim melting with increasing FeO content is counter-intuitive, since the melting temperature of chondritic matter decreases as FeO increases. Most igneous rims around low-FeO chondrules have been almost completely melted; they contain rounded metallic-Fe-Ni - troilite nodules and euhedral and subhedral olivine and pyroxene phenocrysts in a plagioclase mesostasis; the surfaces of the enclosed chondrules have been partially resorbed. The textures of the rims around high-FeO chondrules indicate lower degrees of melting and do not show evidence of resorption of the host; many contain low-FeO relict grains (Fa_{0-10}, Fs_{1-9}). This offers the important insight that the mean intensity of the chondrule forming-heating events decreased as the temperature of the nebula decreased.

Our observations indicate that formation of primary chondrules, secondaries and rims occurs in a given batch of nebular material, then this set of chondrules is withdrawn from the chondrule-forming region or destroyed by collisions. If we accept the picture that mean FeO increases with time, preexisting low-FeO chondrules were not in the chondrule-forming region when the high-FeO chondrules formed. This is consistent with models [6] e.g., in which chondrule formation is confined to the interface region between the gaseous nebula and the dusty midplane; earlier generations of chondrules could have been stored near the center of the midplane, whereas turbulence could elevate their fragments into the chondrule forming region.

References: [1] Wasson J.T. et al. (1993) GCA, submitted; [2] Ashworth J.R. (1977) EPSL 35, 25-34; [3] Scott E.R.D. (1988) In *Meteorites and the Early Solar System* (eds. Kerridge J.F. and Matthews M.S.) 718-745; [4] Rubin A.E. (1984) GCA 48, 1779-1789; [5] Rubin A.E. and Wasson J.T. (1987) GCA 51, 1923-1937; [6] Wasson J.T. and Rasmussen K. (1984) LPS 15, 896-897.

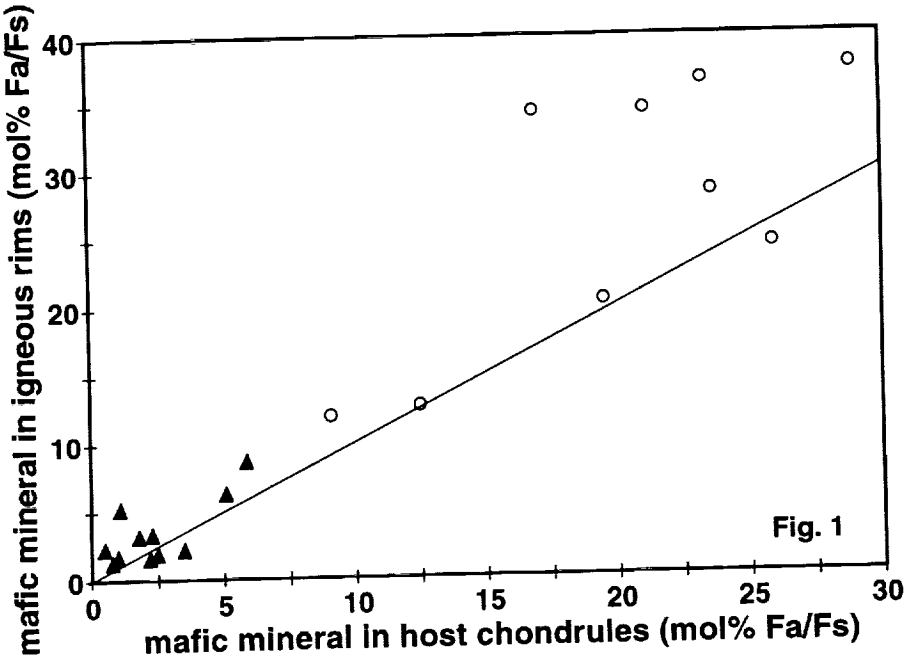

Fig. 1

THE ABUNDANCE AND STABLE ISOTOPIC COMPOSITION OF VOLATILES RELEASED FROM WEATHERING PRODUCTS DURING STEPPED HEATING OF NAKHLA AND LAFAYETTE; L.L. Watson, S. Epstein and E.M. Stolper, Division of Geological and Planetary Sciences, California Institute of Technology, Pasadena, CA 91125.

Overview: As part of our continuing study of hydrogen in SNC phases we report hydrogen isotopic data from water released by stepped heating of Nakhla and Lafayette. Although the water content of Lafayette is greater than three times higher than Nakhla, release patterns and δD values are very similar for both meteorites. Above 200°C both samples release water with δD values greater than terrestrial water, confirming that the alteration of these meteorites was preterrestrial. Due to the presence of a terrestrial component (observable at low temperatures) the highest measured δD values of ~+800 may be a lower limit to the true δD of the original weathering products.

Introduction: We report the latest results of our continuing study of the hydrogen isotope ratios of various SNC phases and their implications for the history of water on the SNC parent planet, which we assume to be Mars [1,2]. Since the D/H of water in the current martian atmosphere is highly distinctive at ~5 times greater than SMOW [3] (corresponding to a δD value of ~+4000, all δD values are reported in units of per mil relative to SMOW), the hydrogen isotopic composition of the water contained in SNC hydrous phases might be a useful tracer of water that once resided in the martian atmosphere or that has isotopically exchanged with it.

Specifically, we report the yield and hydrogen isotope ratios of water released by of stepped heating of aliquots of Nakhla and Lafayette, two of the three nakhlites. In addition, preliminary results of the study of CO_2 also released during heating are reported. The nakhlites contain "iddingsite" [4,5,6], a poorly defined hydrous alteration product of olivine [7]. By studying the volatiles released from these alteration materials we hope to constrain the isotopic composition of the fluids involved in weathering processes in the martian crust.

Previous hydrogen isotopic measurements on various SNCs have yielded highly variable results. A published δD value for Nakhla is -37 with a yield of 2.2 μmoles of H_2 per gram of sample [8], which differs significantly from the reported value of +456 measured on 81.6 μmoles of H_2 extracted from 2.8 g of the Lafayette nakhlite [9]. Our previous studies [10,11] produced preliminary data for Nakhla which also show it to contain water significantly enriched in D (δD values up to ~+500). Published values for Shergotty range from -47 [8] to +878 [9] with yields of 1–7 μmoles of H_2 per gram of sample [8,9,12]. In most of these previous reports, data were obtained after "precombustion" of the sample at temperatures of 350-450°C [8,9,12], which was intended to eliminate terrestrial contamination by organic matter and/or adsorbed water. However, terrestrial iddingsite is typically comprised of a mixture of phases including goethite, smectites, and sometimes carbonates, and it begins to break down at temperatures as low as ~250°C [7]. Thus valuable information on the alteration phases may be lost in the precombustion step employed by previous workers. Our study therefore focuses on gases extracted from the nakhlites by stepwise heating including the low temperatures at which iddingsite is expected to begin to break down. In addition, our work represents the first study of the hydrogen in more than one nakhlite by the same procedure.

Experimental procedure: Two ~1.3 g aliquots of Nakhla (from USNM 5891) and two ~0.6 g aliquots of Lafayette (from the Field Museum of Natural History sample ME 2116) were heated stepwise on a vacuum extraction system specially designed and built for these small samples. For each pair of meteorite aliquots, one was heated in the presence of hot (850°C) copper oxide (referred to as the "combusted" samples), and one was heated under vacuum with no oxygen (referred to as the "pyrolysis" sample). Each meteorite aliquot was coarsely crushed in air immediately before loading on the extraction line. Samples were heated in a quartz boat to temperatures of 120, 200, 300, 400, 600, and 1050°C. During each 2–2.5 hour heating step, gases were frozen in a liquid nitrogen trap. In the pyrolysis experiments, the yield of non-condensable gases was measured. The CO_2 and H_2O released by heating were then cryogenically separated. H_2O was reduced to H_2 in a uranium furnace at 750°C and yields were measured manometrically. Data are reported without corrections for blanks or memory effects, but based on characterization of the extraction line used in this study, we estimate that these corrections will change the δD of our samples by only a small amount (blanks have been measured to be <0.5 μmoles H_2 at each temperature step; at the highest temperature steps where yields are lowest, the reported δD values could increase by a maximum of ~50‰ – the corrections for lower temperature steps would be significantly less). Isotope ratios were measured mass spectrometrically.

Results: Hydrogen yields and isotopic compositions at each temperature step of the four extractions are shown in Figure 1. The amount of water released from both Nakhla samples between 600 and 1050°C was too small for isotopic measurement. The 300–400°C Lafayette combustion sample was lost and thus not analyzed isotopically.

For both Nakhla and Lafayette the integrated total hydrogen yields are very similar for the combustion and pyrolysis and are essentially identical to those of Karlsson [13] with Nakhla containing 60.9 to 63.5 μmoles per gram of sample (corresponding to 0.110 to 0.114 weight % water) and Lafayette containing 209.2 to 215.4 μmoles per gram (0.377 to 0.388 weight % water). The largest amount of water is released at during the 120°C step, and in general, the hydrogen yields decrease with increasing temperature, with the exception of a leveling out or slight peak in the 200–300°C step. In all cases the δD values increase with increasing temperature. The highest δD values for Nakhla are +688 and +706 collected in the 400–600°C step of the combustion and pyrolysis samples, respectively.

Even heavier is the water collected in the 600–1050°C steps of the two Lafayette aliquots, with δD values of +872 and +772 for the combustion and pyrolysis samples, respectively.

Discussion: All samples collected above 200°C have δD values heavier than any known terrestrial hydrogen samples. These data prove unequivocally that the alteration material in the nakhlites could not have formed on Earth. Our new data thus confirm previous conclusions based first on H-isotopic measurements [9,11,12] and later on oxygen isotopic measurements [13] and mineralogical studies [5,6] that the alteration is preterrestrial. The most striking feature of the results is the similarity in release patterns and isotopic compositions of Nakhla and Lafayette, despite a greater than three-fold difference in their total water contents. These results suggest that Lafayette was simply weathered to a higher degree in an environment similar to that in which Nakhla was altered. Although not as high as the present martian atmosphere, the high δD values are consistent with a martian origin for these meteorites.

The water release pattern for the samples is similar to that observed in our previous work [10,11] and in the work of Karlsson [13]. The higher yield and lower δD in the lowest temperature fractions suggest the presence of a component in the low temperature steps of the extractions that has exchanged with terrestrial water. However, the high δD relative to typical terrestrial materials in all but the lowest temperature steps and the progressive increase in δD with temperature indicates that there is still some extraterrestrial component in all but the lowest temperature step (and perhaps even in this one). This observation argues against the practice of discarding water extracted in these low temperature steps. Although the presence of a terrestrial component in the low temperature steps may indicate that even the highest δD values should be taken as lower limits to those actually present in the alteration products at the time of their formation, the observation that both Nakhla and Lafayette, samples with different terrestrial histories and total water contents, contain water of similar isotopic composition, may imply that a δD value of ~+800–900 is close to the true value. This lower limit falls within the range of δD values measured by ion microprobe for amphiboles and biotite (~+500 – +2000) contained in magmatic inclusions in Chassigny and the shergottites [14]. These values have also been postulated to result from interaction of these samples with fluids in the martian crust [14].

In addition to hydrogen, CO_2 was collected at each temperature step. In general our CO_2 results are similar to those previously measured for the nakhlites [15]. We do not report the results in detail at this time due to the presence of additional gas species that follow CO_2 in our extraction procedure. We believe the gas to be largely SO_2, and this is consistent with the presence of S in the alteration material [5,6]. Further investigation of these results is needed to assess adequately the effect of the other gases on yields and isotopic measurements of the CO_2.

REFERENCES: [1] McSween, H.Y. and Stolper, E.M. (1980) Sci. Amer., *242*, 54-63. [2] Bogard, D.D. and Johnson, P. (1983) Science, *221*, 651-654. [3] Bjoraker, G.L. *et al.* (1989) In *Proc. 4th Int. Conf. Mars, Tucson*, 69-70. [4] Bunch, T.E. and Reid, A.M. (1975) Meteoritics, *10*, 303-315. [5] Gooding, J.C. *et al.* (1991) Meteoritics, *26*, 135-143. [6] Treiman, A.H. *et al.* (1993) Meteoritics, *28*, 86-97. [7] Wilshire, H.G. (1958) Am. Min., *43*, 120-147. [8] Fallick, A.E. *et al.* (1983) In *Lunar and Plan. Sci. XIV*, 183-184. [9] Kerridge, J.F. (1988) In *Lunar and Plan. Sci. XIX*, 599-600. [10] Watson, L.L. *et al.* (1991) In *Lunar and Plan. Sci. XXII*, 1473-1474. [11] Watson, L.L. *et al.* (1992) In Workshop on the Martian Surface and Atmosphere Through Time, *LPI Tech. Rept. 92-02*, 156-157. [12] Yang, J. and Epstein, S. (1985) in *Lunar and Plan. Sci. XVI, Suppl. A*, 25-26. [13] Karlsson, H. R. *et al.* (1992) Science, *255*, 1409-1411. [14] Watson, L.L. *et al.*, in preparation. [15] Carr, R.H. *et al.* (1985) Nature, *314*, 248-250.

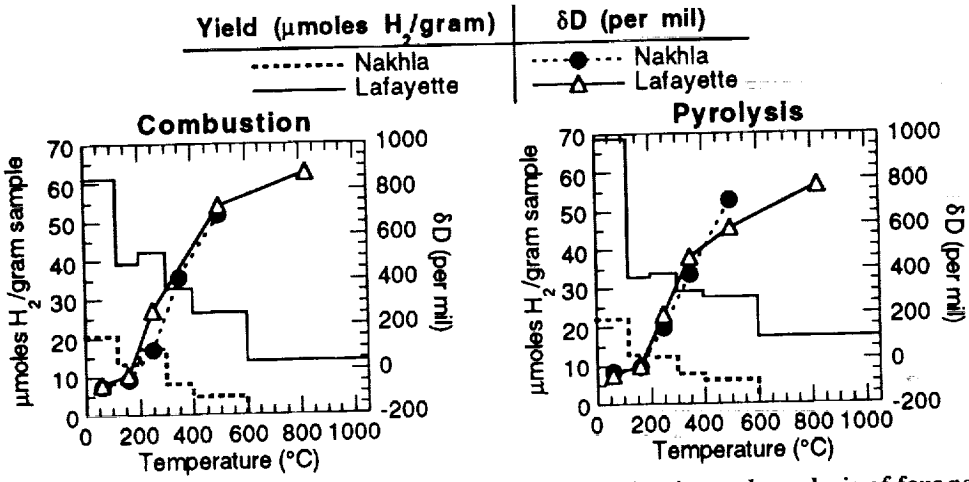

Fig. 1. Yield and hydrogen isotopic measurements for stepwise combustion and pyrolysis of four nakhlite aliquots. Yields (axis to the left) are shown as steps and δD values (axis to the right) as the connected points at the middle temperature of each heating step. Data for Nakhla are displayed with dashed lines and Lafayette with solid lines. Nakhla did not release enough gas for isotopic analysis above 600°C. The δD value of the 300-400°C Lafayette combustion sample was not measured.

MORPHOLOGIC STUDIES OF CONTRACTIONAL FEATURES ON MARS USING PHOTOCLINOMETRICALLY DERIVED ELEVATION PROFILES; T. R. Watters, Center for Earth and Planetary Studies, National Air and Space Museum, Smithsonian Institution, Washington DC 20560, M. S. Robinson, Planetary Geosciences, University of Hawaii, 2525 Correa Road, Honolulu HI 96822

With the loss of Mars Observer and the high resolution altimetry data that would have been provided by MOLA, the extraction of elevation data from Viking Orbiter images using monoscopic photoclinometry and stereogrammetry to characterize the morphology of contractional features has become critical to advancing our understanding of their origin. A variety of landforms on Mars have been characterized using photoclinometrically derived topography [1, 2, 3, 4, 5]. In this study, we attempt to evaluate the sensitivity of elevation data derived through photoclinometry for irregular landforms, such as contractional features, to variations in key parameters. Elevations were derived using the Minnaert photometric function where the surface brightness is assumed to be a function of the solar incidence angle, the spacecraft emission angle, the surface normal albedo, and the Minnaert coefficient [see 1]. Values for the wavelength-dependent Minnaert coefficient were derived by Tanaka and Davis [3] and Thorpe [6]. Two other critical parameters are the haze value and the flat field value. The haze value, determined by the amount of light scattered in the atmosphere and from the surfaces outside the pixel area, must be carefully chosen. A significant error in the estimated haze value will result in an incorrect vertical exaggeration and thus inaccurate slopes. The haze value is estimated by examining brightness values in shadowed areas [see 3, 7]. The flat field value is the brightness of a horizontal surface. It is one of the most important parameters in the asymmetric photoclinometric method [1]. An error in the estimated flat field will result in major distortions in the derived profiles including reversals in the true sense of slope [1, 3].

In order to evaluate the sensitivity of these parameters for features with shallow slopes, profiles were generated across wrinkle ridges in northwest Lunae Planum. This area was chosen because of the availability of medium and high resolution Viking Orbiter images. One of the structures examined is a typical wrinkle ridge assemblage [see 8] consisting of a first- and second-order ridge superimposed on a broad arch (fig. 1). The haze value for this analysis was determined by examining pixels in the prominent shadows cast by the scarp near the terminus of the ridge. The flat field value was estimated by determining the average of a 9x9 array of pixels located near the ends of the profile (west side 686 ± 8, east side 686 ± 6). The results of this run and all the others conducted indicates that the derived elevation profiles are extremely sensitive to small variations in the flat field value (fig. 2). The accuracy of the estimated haze value can be checked by comparing the photoclinometrically derived elevation of the ridge with elevations determined by shadow measurements. It is clear, however, because of the uncertainty in the flat field value (fig. 2), the existence of an elevation change from one side of the ridge to the other can not be verified through photoclinometry alone. In the absence of other topographic data derived through stereogrammetry, the simplest working assumption is to assume that there is no significant elevation difference across the structure and adjust the flat field value until the profile meets this condition. There are problems with this assumption, particularly as applied to wrinkle ridges. A number of factors may contribute to an actual elevation difference across the structure. One important consideration is the presence of lava flows on the ridged plains. Lava flows often occur in proximity to or are ponded along wrinkle ridges (see fig. 1). This could result in significant elevation differences. Another factor is regional slope. A gentle regional slope can result in elevation differences on the order of tens of meters across structures that are up to, and in some cases over, 10 km in width. Photoclinometry is not sensitive to gentle regional slopes. In addition, possible structural offsets must be considered. Elevation difference may result from displacement on thrust or reverse faults associated with wrinkle ridge formation [4, 5, 9].

In conclusion, it should be noted that if elevation differences exist across ridges or similar structures, they can not be resolved using photoclinometry alone. We plan to use photoclinometry to characterize the morphology of other contractional features such as lobate scarps and high-relief ridges [see 10]. This is essential to developing kinematic and mechanical models for their origins.

References Cited: [1] Davis, P.A. and L.A. Soderblom, *J. Geophys. Res. 89*, 9449-945, 1984. [2] Pike, R.J. and P.A. Davis, *LPSC XV*, 194-95, 1984. [3] Tanaka, K.L, and P.A. Davis, *J. Geophys. Res.*, 93, 14893-14907, 1988. [4] Golombek, M.P., J.B. Plescia and B.J. Franklin, *Proc. LPSC XXI*, 679-693, 1991. [5] Plescia, J.B., *J. Geophys. Res. 98*, 15,049-15,059, 1993. [6] Thorpe, T.E., *Icarus, 20*, 482-489, 1973. [7] Robinson, M.S., Masters Thesis, Univ. of Hawaii, 1991. [8] Watters, T.R., *J. Geophys. Res., 93*, 10,236-10,254, 1988. [9] Plescia, J.B., *Geophys. Res. Let., 18*, 913-916, 1991. [10] Watters, T.R., *J. Geophys. Res., 98*, 17049-17060, 1993.

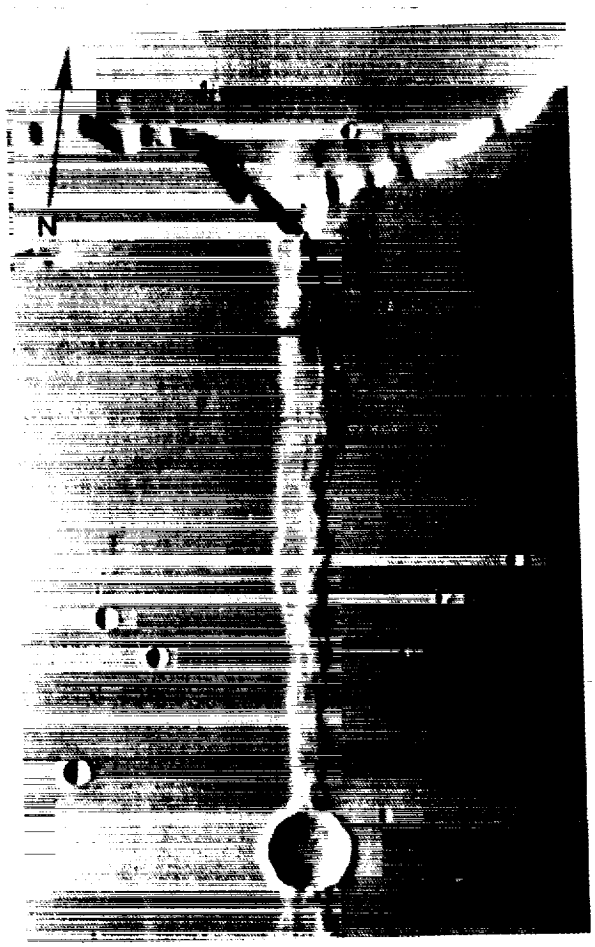

Fig. 1. Wrinkle ridge assemblage in northwest Lunae Planum (Viking Orbiter image 519A06). Black line indicates location of profiles shown in fig. 2. Note lava flow front to the west of the ridge.

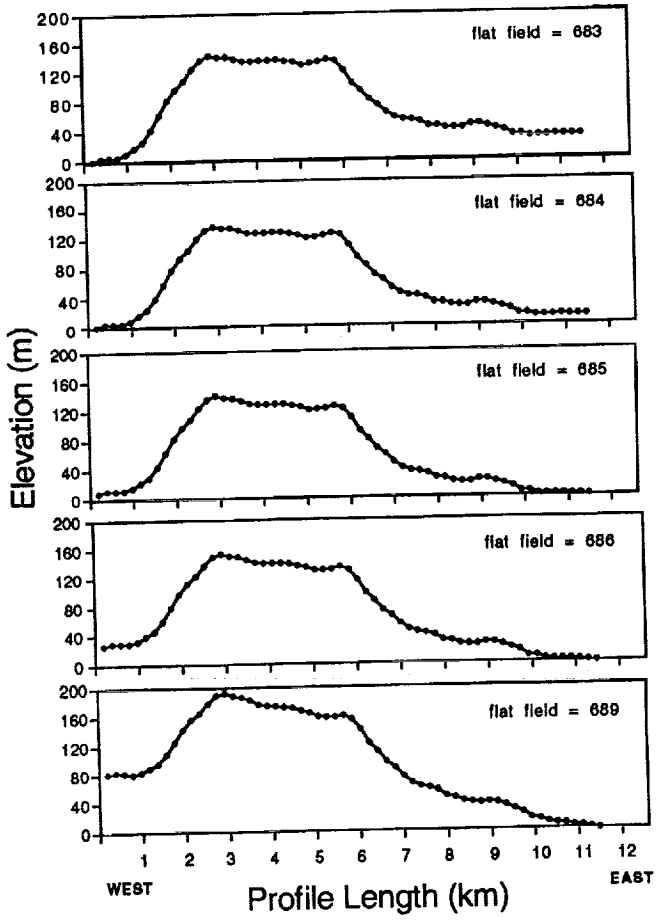

Fig. 2. Elevation profiles derived through photoclinometry. Differences between the profiles are the result of varying the flat field value. The estimated haze value is 455. Vertical exaggeration ~ 20:1.

TRACE ELEMENT AND ISOTOPIC MEASUREMENTS OF REFRACTORY INCLUSIONS FROM THE ACFER 182 CARBONACEOUS CHONDRITE;
D. Weber[1,2], E. K. Zinner[2] and A. Bischoff[1], [1]Institut für Planetologie, Wilhelm-Klemm-Str. 10, 48149 Münster, Germany; [2]McDonnell Center for the Space Sciences, Washington University, One Brookings Drive, St. Louis, MO 63130, USA.

Ion microprobe analyses of 19 Ca, Al-rich inclusions from the CH chondrite Acfer 182 show that most (15) have group II related trace element patterns. Two have group III patterns and two, described in detail, have ultrarefractory patterns. Of 18 CAIs only one has an ^{26}Mg excess corresponding to $^{26}Al/^{27}Al \approx 5 \times 10^{-5}$. These inclusions, most of which contain Ca-dialuminate, must have an origin different from inclusions in other meteorites.

Introduction: The CH chondrite Acfer 182 [1] contains Ca,Al-rich inclusions which differ from most CAIs in other meteorites. Only some of the inclusions resemble those from ALH85085 [2]. Seventeen of 31 inclusions studied contain Ca-dialuminate ($CaAl_4O_7$, CA2) and in many of these CAIs the modal abundance of CA2 exceeds 30 vol% and ranges up to 80 vol%. Comprehensive petrographic and mineralogical descriptions and major element chemistry have been reported previously [1,3,4]. We measured trace element abundances and isotopic compositions of nineteen Acfer 182 inclusions, sixteen of which contain Ca-dialuminate, in continuation of previous work on such inclusions [5].

Results: Fifteen of the inclusions show group II or group II-related trace element patterns. One inclusion has a group III pattern and another CAI shows a group III-related pattern with ultrarefractory characteristics and Ce depletion, similar to the patterns found in HAL and related inclusions [6]. Two CAIs have an ultrarefractory pattern: inclusion 418/P and 418/8; these inclusions are described in more detail below. All inclusions except one have normal Mg isotopic compositions; one object, the CA2-rich inclusion 022/2 described in [1,4], has a ^{26}Mg excess with an inferred initial $^{26}Al/^{27}Al$ ratio close to the canonical value of $5x10^{-5}$. Ca isotopes were measured in nine inclusions and in five out of these we were able to determine also the Ti isotopic compositions. The latter are always normal within errors and in only two inclusions, the ultrarefractory CAI 418/P and a CAI with group II pattern small (4.3 and 3.8 ‰) ^{48}Ca excesses are present.

CAI 418/P: The core of this Ca-dialuminate-bearing inclusion (~100 μm in apparent diameter) consists of an unsystematically zoned Y-, Zr-rich perovskite. The perovskite in the outer parts of 418/P is intergrown with CA2, a Sc-rich, and a Zr-, Sc-rich phase [see also 1,4]. Both the perovskite and the Sc-rich phase have ultrarefractory trace element abundance patterns (Fig. 1). The most refractory REE and the most refractory lithophile elements show the largest enrichments. A striking feature of the patterns is the lack of a Eu depletion in the Sc-rich phase, in contrast to perovskite. The enrichment factors of the refractory rare earth elements reach 15,000 in perovskite and 6,000 in the Sc-rich phase. With the exception of the large Eu depletion in perovskite, the patterns for both minerals are similar to those in other ultrarefractory inclusions, [e. g., 7]. The Ca and Ti isotopic compositions of the perovskite are almost normal; only a small ^{48}Ca excess of 3.8 ± 2.8 (2σ) ‰ was found. When normalized to measurements on terrestrial perovskite [2] the Ca and Ti isotopes in 418/P show no significant intrinsic mass fractionation. Because of the small grain size of CA2 and the Zr, Sc-rich phase we were not able to determine their trace element abundances and isotopic compositions.

CAI 418/8: This 60 μm spherical inclusion consists mainly of CA2 and melilite. The anhedral Ca-dialuminate crystals are concentrated in the center of the inclusion and are intergrown with melilites, some small hibonite laths and spinel. Perovskite occurs both in melilite and CA2. Both CA2 and an about 7 μm large perovskite in the middle of the inclusion have ultrarefractory trace element patterns (Fig. 2). As in 418/P the perovskite is strongly depleted in Eu. Furthermore, the perovskite shows extreme enrichment of Gd, Tb, and Dy, ranging up to 100,000 × chondritic. It contains more than 2 wt% of Gd- as well as Dy-oxide. Remarkable is the decrease of the enrichments from Gd to Er which has not been observed in other ultrarefractory inclusions. The Lu enrichment is only slightly higher than that of Yb and even smaller than the Tm enrichment and is

an order of magnitude below that of Gd. The pattern in CA2 shows no Eu depletion, but a similar decrease of the HREE abundances from Gd to Er. Tm is more enriched than Er.

Discussion: **(I)** The lack of Ca and Ti isotopic fractionation and of a pronounced Ce depletion gives good evidence that, in contrast to HAL-type CAIs [6], inclusion 418/P has never experienced a history of strong distillation. This is in agreement with previous conclusions on UR inclusions from Mighei and Ornans [7]. Furthermore, because of the internal zonation texture of the perovskite, it is safe to assume that this inclusion was never molten. Therefore, CAI 418/P can be considered as one of the first direct gas-solid condensates which remained unprocessed after formation. Despite the round shape and the decreasing abundances from Gd to Er, which seem to indicate igneous fractionation processes, we propose also a direct gas-solid condensation for CAI 418/8. Like for the petrographically similar inclusion 022/14 [4], which shows a group II trace element pattern, perovskite and CA2 in 418/8 probably condensed directly and part of the CA2 reacted with the remaining gas at decreasing temperatures to form melilite and spinel. The difference in the origin of the inclusions 418/8 (ultrarefractory pattern) and 022/14 (group II pattern) is probably to be found in the composition of the gas reservoir and the condensation temperature [8,9]. In a first condensation step inclusions such as 418/P, 418/8 and other ultrarefractory inclusions condensed from a gas reservoir of solar composition. This event occurred at high temperatures, so that the most refractory elements such as Zr, Y, Sc, Gd, Tb, Dy, Ho, Er, and Lu were enriched in the crystallizing solid material and a large fraction of the less refractory elements still remained in the gas reservoir. In a second condensation event the group II inclusions formed from the remaining gas reservoir. Unfortunately, we were not able to determine the REE pattern of melilite in 418/8, so that we cannot conclude from which reservoir the melilite derived. We also cannot explain under which conditions Ca-dialuminate with an ultrarefractory trace element pattern (inclusion 418/8) was formed. Ca-dialuminates in almost all other inclusions in Acfer 182 have group II related patterns. However, MacPherson *et al.* [10] reported a CA2-rich inclusion with an UR REE pattern from ALH85085. **(II)** The large enrichment of ultrarefractory elements in perovskite of 418/P, 418/8 and other ultrarefractory inclusions indicate that perovskite is an important carrier of most refractory elements. However, there are other minerals containing high abundances of refractory elements, such as Sc- and Zr-rich oxides, fassaites and also Ca-dialuminate as shown in Fig. 2. **(III)** Most CA2-bearing CAIs with group II patterns do not contain any ^{26}Mg excesses from the decay of ^{26}Al. This is in marked contrast to hibonite-bearing CAIs in Murchison, where spinel-hibonite (SHIB) inclusions, many of which have group II patterns, usually give evidence for the presence of ^{26}Al [11,12].

References: [1] Bischoff *et al.* (1993) GCA **57**, 2631; [2] Kimura *et al.* (1993) GCA **57**, 2329; [3] Weber and Bischoff (1992) Meteoritics **27**, 304; [4] Weber and Bischoff (1994) GCA, submitted; [5] Bischoff *et al.* (1992) Meteoritics **27**, 204; [6] Ireland *et al.* (1992) GCA **56**, 2503; [7] Davis (1991) Meteoritics **26**, 330; [8] Boynton (1975) GCA **39**, 569; [9] Davis and Grossman (1979) GCA **43**, 1611; [10] MacPherson *et al.* (1989) Meteoritics **24**, 297; [11] Ireland *et al.* (1988) GCA **52**, 2841; [12] Ireland, 1990 GCA **54**, 3219.

Fig. 1: CAI 418/P

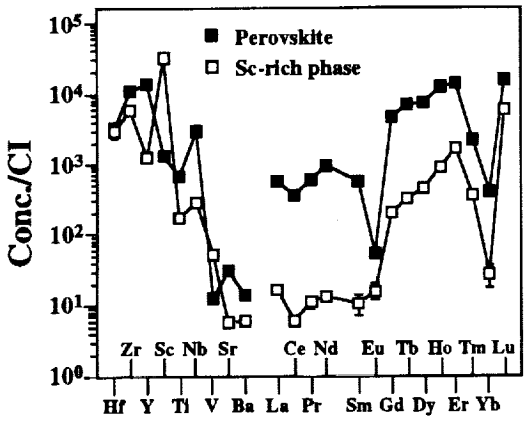

Fig. 2: CAI 418/8

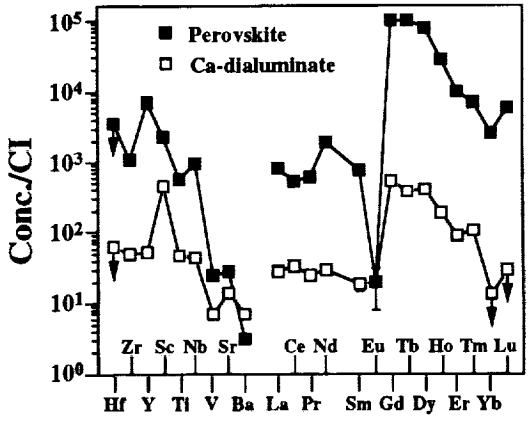

ORIGIN OF "RUBBLE PILE" COMETARY NUCLEI; S.J. Weidenschilling (Planetary Science Institute)

The disruption of comet P/Shoemaker-Levy 9 during an encounter with Jupiter implies that the parent nucleus had extremely low tensile strength, ~10^{-3} bar (1). The number of observed crater chains on the Galilean satellites, if due to impacts of disrupted comets (2), is consistent with comparably low strengths for most, perhaps all, cometary nuclei. Such weak bodies must be "rubble piles" consisting of smaller components held together by mutual gravity and/or weak surface forces. This common structure must be the result of the process(es) that formed them in the solar nebula. I show that a two-stage process of collisional coagulation, followed by gravitational instability of a particle layer, yields weakly bound bodies of cometary size, and is a plausible, perhaps inevitable, result of accretion in the outer part of a low-mass ($\lesssim$0.1 $M_\odot$) nebula.

Icy particles in the nebula will tend to settle toward its central plane, forming a dense layer. A necessary condition for this layer to become gravitationally unstable is that it attain a critical density, $\delta_c \sim 3M_\odot/2\pi a^3$, comparable to the local Roche density at distance a from the Sun. However, it is not possible for a layer of small particles to reach this density, which greatly exceeds the local gas density. The nebular gas, supported by a radial pressure gradient, rotates at less than the local Kepler velocity. If the particles are small enough to be coupled to the gas by drag, the resulting shear between the layer and the surrounding gas generates turbulence and prevents further settling (3,4). Numerical simulations suggest that the mean particle size must grow to $\gtrsim$1 m before the critical density is attained (5).

Reaching the critical density is not a sufficient condition for gravitational instability. The dispersion relation for a differentially rotating, self-gravitating disk implies that density perturbations can grow if the particle velocities are less than a critical value, $c* \sim \pi G\sigma_p/\Omega$, where G is the gravitational constant, σ_p the surface density of the particle layer, and Ω the Kepler frequency (6). For random, isotropic particle velocities, the thickness of the particle layer is $h \sim c/\Omega \sim \sigma_p/\delta_c$, so the two conditions are essentially equivalent. However, in the presence of nebular gas, particle velocities are neither random nor isotropic. For bodies $\gtrsim$1 m in size, the largest velocity component is a systematic radial motion resulting from orbital decay due to gas drag: $V_r = 2a(\Delta V/V_K)/t_e$, where $\Delta V/V_K$ is the fractional deviation of the gas from Keplerian motion, and t_e is a response time of the particle, which depends on its size. For Epstein drag, $t_e = d\rho_p/2\rho\bar{v}$, where d,ρ_p are the particle's diameter and density; $\rho,\bar{v}$ are the density and mean thermal velocity of the gas. For Stokes drag, $t_e = d^2\rho_p/18\eta$, where η is the gas viscosity.

The condition for gravitational instability with an anisotropic velocity dispersion is not clear. I assume that the dispersion of V_r must be less than c^*, regardless of the density of the particle layer. A sufficient condition is that the median-mass bodies have $V_r < c^*$; this implies $d > 4\Delta V\rho\bar{v}/\pi G\rho_p\sigma_p$ for Epstein drag, or $d > 6(\eta\Delta V/\pi G\rho_p\sigma_p)^{1/2}$ for Stokes drag. Using $\rho_p = 0.7g\ cm^{-3}$, and values of ρ,σ_p and ΔV appropriate for a low-mass solar nebula, the critical diameter falls in the range ~10-100 m for a between 5 and 50 AU. Thus, collisional coagulation must produce bodies of this size before

ORIGIN OF "RUBBLE PILE" COMETARY NUCLEI; Weidenschilling, S.J.

gravitational instability can occur. It may be significant that this size corresponds to the mass of material involved in a typical cometary outburst (7).

Once gravitational instability occurs, the largest density perturbations have a size scale $\lambda \sim 4\pi^2 G\sigma_p/\Omega^2$. These would yield bodies of mass $\sim\sigma_p\lambda^2$, corresponding to diameters of several hundred km. However, collapse on these scales is inhibited by angular momentum; direct collapse is possible only on scales that yield solid bodies with $d \lesssim 10$ km. Thus, a typical comet should comprise $\sim 10^6$ components. These collisionally accreted "building blocks" would be fairly compact and more or less uniform in structure. The nucleus itself, bound by gravity and weak contact forces between the blocks, will contain a large fraction of macroscopic void space (8).

Numerical simulations now in progress suggest that the collisional growth stage lasts $\sim 10^5$y at 30 AU. Instability occurs when the median particle size is ~20-30 m and the particle layer has a density $\sim 5\delta_c$; about half of the total solids take part in the instability, with the rest dispersed as smaller particles at larger distances from the central plane of the nebula. Shear-generated turbulence is not strong enough to prevent gravitational instability after particle sizes reach tens of meters; collisional accretion of larger components is unlikely unless there is an additional source of stirring, e.g., global convective turbulence, to delay the onset of instability. The predicted components are smaller than the observed fragments of S-L9, implying that its breakup during its Jupiter encounter was incomplete; further disruption is likely during its final approach in July.

References

1) Scotti, J. and Melosh, H.J. (1993) *Nature*, **365**, 733.
2) Melosh, H.J. and Schenk, P. (1993) *Nature*, **365**, 731.
3) Weidenschilling, S.J. 1980) *Icarus*, **49**, 172.
4) Weidenschilling, S.J. and Cuzzi, J. (1993) in *Protostars and Planets III*, (Eds. E. Levy, J. Lunine, U. of Az. Press), p. 1031.
5) Cuzzi, J. *et al.* (1993) *Icarus*, **106**, 102.
6) Goldreich, P. and Ward, W.R. (1973) *Ap.J.*, **183**, 1051.
7) Larson, H.P. *et al.* (1990) *Icarus*, **86**, 129.
8) Weidenschilling, S.J. (1994), *Nature*, submitted.

PRIMITIVE TRAPPED Xe IN LODRAN MINERALS AND FURTHER EVIDENCE FROM EET84302 AND GIBSON FOR BREAK-UP OF THE LODRANITE PARENT ASTEROID 4 Ma AGO.
A. Weigel and O. Eugster, Physikalisches Institut, University of Bern, 3012 Bern, Switzerland.

We studied trapped Xe isotopic abundances in Fe/Ni-, silicate-, pyroxene-, and troilite-separates of the Lodran achondrite. The isotopic pattern of Xe, that is essentially free of the in-situ produced cosmic-ray- and fission-components, differs from that of trapped chondritic, solar, and atmospheric Xe. This lodranitic trapped Xe is similar to that found in the Tatahouine diogenite. It is fractionated relative to the above mentioned Xe reservoirs favoring the light isotopes. In addition to the five lodranites that we analyzed previously, the EET84302 and Gibson lodranites also yield a cosmic-ray exposure age of about 4 Ma, that is, these seven lodranites were produced by the same impact event on the lodranite parent-asteroid.

We continued the analyses of the noble gas inventory of mineral phases separated by handpicking from a 900 mg sample of Lodran [1]. The Xe concentrations are relatively large, in particular in the Fe/Ni- and FeS-phases. From trace element concentrations, a gas retention age of 4.5 AE, and a cosmic-ray exposure age of 3-4 Ma [1] we estimate that in-situ produced cosmogenic and fissiogenic Xe contributes less than a few permil to all Xe isotopes. This is confirmed by the data for the temperature step fractions of the mineral separates shown in Figs. 1-3. Data representing a mixture of cosmic-ray produced spallation Xe and trapped Xe would plot on mixing lines indicated by the arrows in Figs. 1 and 2. Mixtures of atmospheric Xe with spallation Xe, and chondritic (AVCC Xe or Xe-Q) with spallation Xe, respectively, are shown. It is evident that the spread of the data points is not caused by different mixing ratios of trapped Xe and spallation Xe. Furthermore Fig. 3 demonstrates that the spread of the data in a $^{134}Xe/^{132}Xe$ vs. $^{136}Xe/^{132}Xe$ diagram cannot be explained by varying contributions of Xe from ^{244}Pu fission to a trapped Xe component of chondritic composition.

We have shown in our earlier work [1] that the trapped noble gases in lodranites are not implanted solar particles. All mineral fractions of lodran contain relatively large amounts of primordial Ar, Kr, and Xe that were incorporated when the meteoritic material solidified. In particular, the Fe/Ni phase yields up to 2×10^{-9} cm^3 STP/g ^{132}Xe, comparable to the Xe concentration of C3 chondrites.

Fig. 4 shows the isotopic pattern of Xe relative to that in the terrestrial atmosphere. The data are average values for the mineral fractions displayed in Figs. 1-3. The trapped Xe isotopic composition in Lodran is similar to that found in the 1000°C and 1200°C fraction of the Tatahouine diogenite [2]. It differs from that in chondrites (Xe-Q [3], FVC-Xe [4], AVCC-Xe [5]), in ureilites [6], and in meteorites or lunar surface samples exposed to solar particles [7]. This type of trapped Xe in differentiated achondrites appears to be related to the latter types of trapped Xe by a mass fractionation favoring the light isotopes. The datum point at ^{129}Xe does not follow the general trend because ^{129}Xe is enriched in air by a radiogenic component from ^{129}I decay. The new type of achondritic trapped Xe is isotopically similar to that which was predicted (but not observed in any meteorite), by Takaoka [8] and Pepin and Phinney [9]. We have not yet identified the carrier phase of the achondritic trapped Xe. It appears from the general trend of the data points in Figs. 1-3 that Xe in the carrier phase differs even more from that in chondrites than the average values displayed in Fig. 4. The Ar and Kr isotopic abundances were also determined in these samples and results will be presented later.

As in chondrites, the concentration of primordial trapped Ne is low in lodranites. This fact allows us to derive reliable cosmic-ray exposure ages based on ^{21}Ne. In addition to the five lodranites studied earlier [1], we analyzed the noble gases in Gibson and EET84302. Information on chemical abundances is not yet complete and production rates are, therefore, preliminary. We calculate for all lodranites dated till now by us, EET84302, FRO90011, Gibson, LEW88280, Lodran, MAC88177, and Y-791491, ages of about 4 Ma and conclude that these achondrites originate from the same break-up event and, thus, most probably from the same parent asteroid.

Acknowledgements: We thank R. Hutchison and G. Kurat for the Lodran samples and the NIPR and NASA for the antarctic meteorites. This work was supported by the Swiss NSF.

References: [1] Eugster O. and Weigel A. (1993) LPSC 24, 453. [2] Michel Th. and Eugster O. (1994) Meteoritics, in press. [3] Wieler R. et al. (1992) GCA, 56, 2907. [4] Lavielle B. and Marti K. (1992) JGR, 97, 20875. [5] Eugster O. et al. (1967) EPSL, 3, 249. [6] Wilkening L. and Marti K. (1976) GCA, 40, 1965. [7] Kim J.S. and Marti K. (1992) Proc. LPSC, 22, 145. [8] Takaoka N. (1972) Mass Spectroscopy, 20, 287. [9] Pepin R.O. and Phinney D. (1978), preprint.

PRIMITIVE TRAPPED Xe IN LODRAN: Weigel A. and Eugster O.

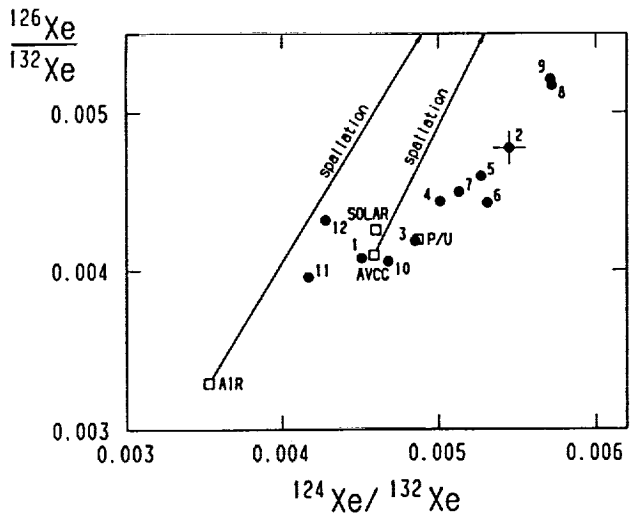

Fig. 1 $^{126}Xe/^{132}Xe$ vs. $^{124}Xe/^{132}Xe$ of pyrolysis step fractions for Lodran and the Tatahouine diogenite: 1 - Lodran Fe/Ni (101.6 mg) 1200°C, 2 - Lodran Fe/Ni (101.6 mg) 1400°C, 3 - Lodran (80.1 mg) 1200°C, 4 - Lodran Fe/Ni (80.1 mg) 1400°C, 5 - Lodran pyroxene 1200°C, 6 - Lodran pyroxene 1400°C, 7 - Lodran pyroxene 1600°C, 8 - Lodran silicates 1200°C, 9 - Lodran silicates 1700°C, 10 - Lodran troilite 1700°C, 11 - Tatahouine bulk 1000°C, 12 - Tatahouine bulk 1200°C. Typical 1σ errors shown for sample 2. These data are compared with those for the terrestrial atmosphere (AIR), trapped solar particles [7] (SOLAR), chondrites (Xe-Q [3], AVCC [5]) and hypothetical primordial Xe (U-Xe [9], primitive Xe [8]). The data are not compatible with a mixing line defined by air Xe or chondritic Xe and typical eucritic spallation Xe.

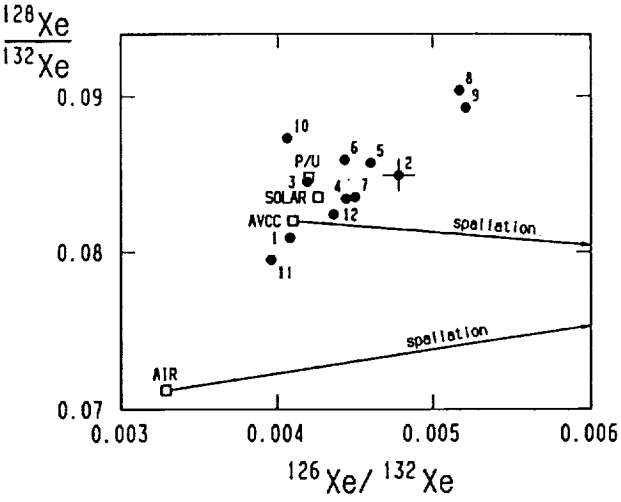

Fig. 2 $^{128}Xe/^{132}Xe$ vs. $^{126}Xe/^{132}Xe$ of pyrolysis step fractions for Lodran and Tatahouine. See also caption to Fig. 1.

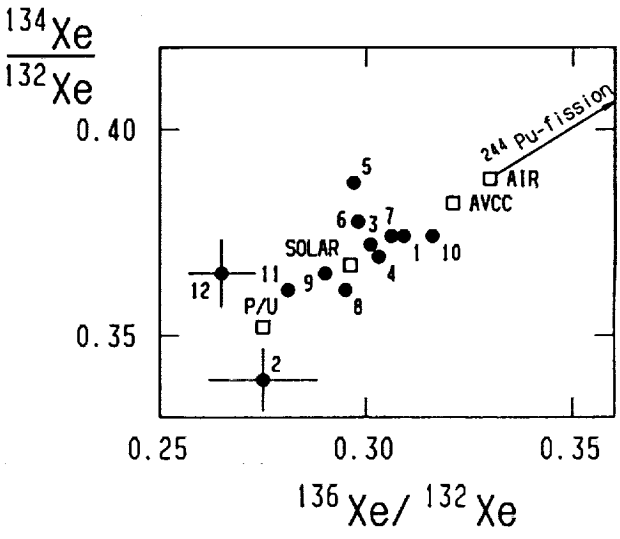

Fig. 3 $^{134}Xe/^{132}Xe$ vs. $^{136}Xe/^{132}Xe$ of pyrolysis step fractions for Lodran and Tatahouine. Typical 1σ errors are about 1% except for data points 2 and 12. Trapped Xe in Lodran and Tatahouine appears to be a mixture of two major components, primitive Xe (P/U) and chondritic Xe (Xe-Q, AVCC Xe). Solar Xe is excluded [1]. See also caption to Fig. 1.

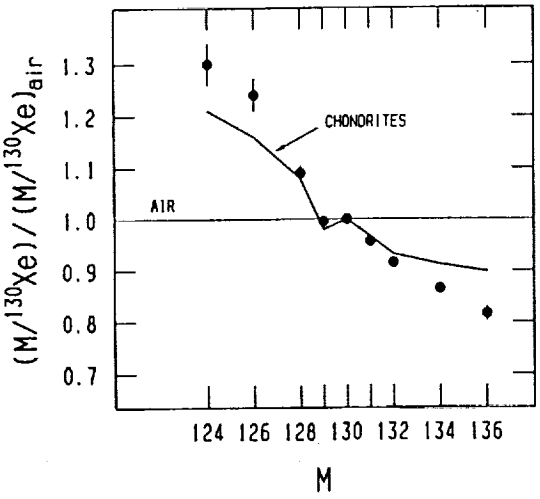

Fig. 4 Isotopic pattern of trapped Xe in primitive achondrites. The data points are average values for the samples shown in Figs. 1-3 relative to Xe in the terrestrial atmosphere. The solid line represents trapped Xe in chondrites (Xe-Q, AVCC Xe, FVC Xe).

AGGLOMERATIC OLIVINE (AO) CHONDRULES IN ORDINARY CHONDRITES.

M.K. Weisberg and M. Prinz. Dept. Mineral Sci., Amer. Museum Nat. Hist., N.Y., NY 10024.

Agglomeratic olivine (AO) chondrules in ordinary chondrites are olivine-rich aggregates of nebular materials which contain olivine and pyroxene crystals, chondrule fragments and refractory inclusions. These chondrules have been heated to a lesser degree or for a shorter time than that of other chondrules. Thus, they provide information about materials that were present in the nebula, prior to and during chondrule formation. AO chondrules have refractory element (Si/Al, Mg/Al) ratios similar to many of the common porphyritic olivine-pyroxene (POP) as well as some barred olivine (BO) chondrules. They appear to represent POP and/or BO chondrule precursor materials that were not heated to liquidus or subliquidus temperatures.

Introduction. Unequilibrated ordinary chondrites (UOC) are mixtures of chondrules, mineral and lithic fragments, and matrix. Chondrules are believed to have formed from molten or partially molten droplets in the early solar nebula, whereas matrix is a mechanical mixture of nebular particles which may include primitive nebular condensates and are not derived from broken chondrules. In addition to matrix, other agglomerational objects in UOCs include dark inclusions, chondrule rims and AO chondrules. AO chondrules were defined by Van Schmus [1] as "a type of chondrule that has internal textures that suggest that they are mechanical mixtures of individual small crystal fragments of silicates, oxides, sulfides, and metal rather than a crystalline assemblage that is the result of crystallization from a melt". Dodd [2] called these chondrules "granular" and Dodd and Van Schmus [3] called them "dark-zoned chondrules". We have studied AO chondrules because they may represent materials that were available in the nebula prior to and during chondrule formation. This is a detailed SEM-petrographic study of AO chondrules in five of the least equilibrated ordinary chondrites: Krymka (LL3.0), Semarkona (LL3.0), Bishunpur (L3.1), Chainpur (LL3.4) and Sharps (H3.4). Our goals are (1) to petrologically characterize these chondrules and compare them to other chondrule types, (2) compare AO chondrules with opaque matrix and chondrule rims, (3) determine if they contain materials that may be precursors of other chondrule types.

Results. A total of 42 AO chondrules were studied. They were found in all the UOCs studied, and make up to ~5 vol.% of the chondrules. **Textures.** AO chondrules are fine-grained (>50% of grains are 2-5μm), olivine-rich (>50% of grains are olivine) objects that are generally similar in size to coexisting chondrules. Their shapes range from irregular to round; many round ones have angular or irregular-shaped silicate-rich cores surrounded by FeS-rich rims that fill irregularities on the surface and render the objects spherical. AO chondrules appear dark to opaque in thin section due to their fine grain size and a high FeS abundance, in some cases. Many contain one or more large (up to 600μm) euhedral to subhedral transparent olivine crystals. The fine-grained olivine ranges from euhedral to anhedral in shape and some occur as blades, similar to some of the olivine in chondrule rims and in the matrix. **Modes.** AO chondrules contain 57-94 vol.% olivine, up to 20% pyroxene, 6-20% plagioclase (glassy to microcrystalline), up to 1% chromite, 1% metal and 5% sulfide. **Mineral compositions.** The fine-grained olivine is Fe-rich and ranges from Fa_{28-51}. Olivine in chondrule rims is similar in composition. Much of the fine-grained olivine (blades and anhedral crystals) in the matrix, however, is more Fe-rich (>Fa_{70}). In some AO chondrules, olivines near the chondrule periphery are finer grained and slightly more Fe-rich. Larger olivines are much more magnesian (Fa_{2-6}), but are rimmed (up to 5μm) by overgrowths of olivine similar in composition to the surrounding fine-grained olivine. These large Mg-rich olivines represent fragments from an earlier generation of chondrule formation. Compositional traverses across large olivine crystals show steep increases in Fe/Mg and Mn at the overgrowth rim, and include sharp spikes of Cr, suggesting the presence of chromite at the core-rim interface. These zoning profiles are reminiscent of those in Allende chondrules [4,5,6] and reflect rapid, disequilibrium growth of olivine. Low-Ca Pyroxene is generally magnesian (Fs_{6-10}) and is in gross disequilibrium with the

Agglomeratic Olivine Chondrules: Weisberg M.K. and Prinz M.

surrounding fine-grained olivine. The plag mesostasis has ~63 wt.% SiO_2, 17 Al_2O_3, 5 FeO, 2 MgO, 4 CaO, 9 Na_2O, and <0.1 K_2O; some plag has up to 1.4 K_2O. The K_2O-rich ones occur near the periphery of the chondrule, in some cases. Chromites occur in clusters of euhedral crystals and are essentially $FeCr_2O_4$. Other minerals include troilite, plus high- and low-Ni, Fe-metal. **Other components.** AO chondrules contain a variety of other components that may be nebular, attesting to the relatively low degree of melting that AO chondrules experienced. These include poikilitic pyroxene inclusions, BO microchondrules, fluffy particles, and refractory inclusions. Poikilitic pyroxene inclusions are irregular-shaped objects consisting of Mg-rich pyroxene (~Fs_2) that contain inclusions of Mg-rich olivine (~Fa_6). These inclusions also occur as isolated objects in the chondrite matrix, and within matrix lumps and chondrule rims. Some AO chondrules contains BO microchondrules (~20μm). Some have portions that are texturally and mineralogically similar to opaque matrix, consisting of fluffy porous masses of submicrometer-sized olivine. One AO chondrule has three spinel-rich inclusions within its FeS-rich rim; these inclusions consist of a core of Fe-Al spinel surrounded by feldspar, and rimmed by Ca-pyroxene. Texturally, they are spinel-pyroxene refractory inclusions, but their Fe-rich spinel suggests that they have reequilibrated with a more oxidizing nebular environment. **Bulk compositions.** AO chondrules have compositions (determined by defocused beam electron probe technique) that are similar to matrix and chondrule rims, having higher Fe and S than most chondrules. Their refractory lithophile ratios, however, (Si/Al, Mg/Al) are similar to those of many of the common POP chondrules and some BO chondrules. Many non-porphyritic (radial pyroxene and cryptocrystalline) chondrules have higher Si/Al ratios.

Discussion: AO chondrules are agglomerations of nebular materials that have been heated to a lesser degree or for a shorter time than other chondrules. Whatever the transient heat source responsible for heating chondrule precursors, AO chondrules must have been far enough from the source to receive relatively little energy. Texturally and compositionally AO chondrules resemble silicate rims on chondrules. AO chondrules and chondrule rims have similar olivine compositions, whereas much of the olivine in opaque matrix is more Fe-rich, suggesting that AO chondrules and matrix differ in their oxidation histories. AO chondrules may have formed by heating of clumps of opaque matrix material to subsolidus and subliquidus temperatures, accompained by reduction of Fe [7]. However, we suggest that the olivine compositions of AO chondrules are primary and formed under different conditions than matrix olivine. Similarities in refractory lithophile abundances between AO and the common POP and some barred olivine chondrules suggest that AO chondrules represent chondrule precursors that were not heated to high enough temperatures to form POP or BO chondrules. If AO chondrules consist of chondrule precursors, the presence of chondrule fragments, BO microchondrules, and refractory inclusions implies that some chondrules formed from material that have had considerable prehistory. Formation of AO chondrules can be summarized in a three stage model. Stage 1: Formation of free-floating or loose agglomerates of fine olivine crystals in the nebula. These crystals may have formed by the reaction of condensed forsterite or enstatite with Fe^0, at lower nebular temperatures. Alternatively, these olivines may have formed at the higher temperatures, in a nebular region with an enhanced oxygen fugacity [6]. Stage 2: Agglomeration of the fine olivines with other nebular components that include microchondrules, poikilitic pyroxene and refractory inclusions. Stage 3: A transient heat source sintered these agglomerations, resulting in small degrees of melting and solid state recrystallization. More intense heating of these agglomerations to liquidus or subliquidus temperatures may have resulted in the formation of POP or BO chondrules. Most of the FeS may have been expelled from the chondrules at their time of formation. Non-porphyritic chondrules (e.g. RP, C) require a somewhat different set of precursors.

References: [1] Van Schmus, W. R. (1969) Earth Sci. Rev. 5, 145-184. [2] Dodd, R. T. (1971) Contr. Mineral. Petrol. 31, 201-227. [3] Dodd, R. T. and Van Schmus, W. R. (1971) Chem. Erde 30, 59-69. [4] Peck, J. A. and Wood, J. A. (1987) GCA 51, 1503-1510. [5] Hua, X. et al. (1988) GCA 52, 1389-1408. [6] Weinbruch, S. et al. (1990) Meteoritics 25, 115-125. [7] Rubin, A. E. (1984) GCA 48, 1779-1789.

RADIOPHYSICAL PROPERTIES OF IMPACT CRATERS ON VENUS. C. M. Weitz, Brown University, Dept. of Geological Sciences, Providence, RI, 02912; J. J. Plaut, Jet Propulsion Laboratory, California Institute of Technology, Pasadena, CA 91109; H. J. Moore, USGS Menlo Park, Menlo Park, CA 94025.

Introduction: We have analyzed 222 large (> 20-km-diameter) impact craters on Venus using Magellan cycles 1, 2, 3 and Venera 15/16 data to determine the radiophysical properties (backscatter cross-section, emissivity, and rms slope) of the craters and to search for correlations with target region properties and subsequent geologic history. On the Magellan SAR images, the crater floors were sampled with boxes that avoided central peaks and inner rings. Backscatter cross-sections were calculated using the average DN values within the boxes and the incidence angle for the crater latitude. Emissivity and rms slope values were taken from the data sets produced by MIT [1]. A rectangular box was selected on each crater floor and the average DN converted to emissivity and rms slope. Because of the poor resolution in emissivity and rms slopes, we are looking at these 2 properties only for craters with diameters greater than 30 km (147 craters).

Backscatter Cross-sections: While the majority of impact craters have radar-dark floors, many have radar-bright floors and several have a mixture of both radar-bright and -dark floors. Radar-dark floors appear to have the same morphology as the adjacent plains and similar radiophysical properties. This suggests that the floors have been filled with lavas similar to those of the plains. Radar-bright floors generally are associated with crater floors that have low emissivities or that are located on rough terrain (i.e. fracture belts, tessera). In many cases, these radar-bright floors may represent the same material (impact melt) that form the outflow deposits. However, there are also examples of radar-bright floors that differ in their emissivity and rms slopes from the outflow deposits.

The crater Stowe was imaged in all three Magellan cycles. Cycle 1 and 2 images show that both the crater floor and outflow deposits are much brighter than the surrounding plains in both the right- and left-looking data at 25° incidence angle. However, the cycle 3 left-looking image taken at 14° incidence angle shows a large increase in the backscatter cross-section of the floor but only a minor increase in the backscatter of the outflow deposits. Cycle 1, 2 and 3 backscatter cross-sections of the floor are -2.72, -3.07, and +5.88 dB, respectively. The outflow deposits from Stowe have a backscatter cross-section of -5.87, -6.07, and -2.32 dB for cycles 1, 2, and 3. Emissivity and rms slopes for the outflow deposits of Stowe are much higher than those of its floor. These observations suggest that the outflow deposits are composed of deposits that are rougher than those of the floor. In contrast, crater floors that have high backscatter cross-sections and low emissivities are probably composed of high dielectric materials. Venera 15/16 data taken at 10° incidence angle also revealed several craters with very bright floors. The craters Cotton and Anya have very bright floors in both the Venera 15/16 and Magellan data compared to other craters at these incidence angles. The floors appear to be flat and smooth so roughness and/or large facets seem unlikely as the cause of the high backscatter. A more likely explanation is that high dielectric materials are present on these crater floors.

In addition to floors with high backscatter cross-sections at low incidence angles, there are examples of crater ejecta with high backscatter in the Venera 15/16 images. Approximately 25% of the craters identified in Venera 15/16 data have bright halos [2]. These halos were attributed to high surface roughness that over time became subdued by external processes [2]. Figure 1 shows a plot of Magellan backscatter cross-sections of ejecta from craters that can be identified in Venera 15/16 data; those craters that have halos visible in the Venera 15/16 data are shown as darkened circles in Figure 1. A linear fit to the Magellan data indicates that the cross-sections of craters with halos lie along a curve with a steeper slope than those without halos. Extrapolation of the curves to 10° incidence angle to match the incidence angle of the Venera 15/16 data suggests that high intrinsic backscatter in some ejecta is possible and may explain the halos around some craters at low incidence angles. The bright halos seen at the smaller incidence angles may be due to high dielectric constants similar to those causing the high backscatter in the crater floors. However, unlike the flat and relatively smooth floors, the crater ejecta is very rough so quasi-specular reflections from facets could also contribute to the high backscatter at small incidence angles.

Low Emissivity Floors: Emissivities of most crater floors lie between 0.8 and 0.9 independent of backscatter cross-sections. However, several craters have emissivities lower than 0.8 in cycle 1 and 2 data. It is well known that above 6053.5 km altitude, emissivities drop to very low values [3,4] and that craters at these elevations also have low emissivities. In this analysis, we are only concerned with craters that have emissivities much lower than the surrounding terrain in order to rule out elevation dependent factors. After completing a search of 147 craters with diameters greater than 30 km, we found 17 craters at elevations below 6053.5 km with emissivities of the crater floor that were much lower than the surrounding terrain. Rms slopes for the crater floors are generally below the average value for Venus of 2.84° [5].

Of these 17 craters, 11 are associated with extended parabolic deposits. A study of backscatter and emissivity for impact craters associated with parabolic-shaped features indicated that the majority of these craters have high

RADIOPHYSICAL PROPERTIES OF VENUS CRATERS: C. M. Weitz et al.

backscatter cross-sections and low emissivities [6]. Campbell et al. [6] suggest that these craters are relatively young and that radar-bright floors are the result of both wavelength scale roughness and high Fresnel reflectivity material. With time, modification processes remove the parabolic deposits and alter the crater floors to lower backscatter cross sections, lower Fresnel reflectivities, and higher emissivities that match those typical of the older craters without parabolic features.

Cycle 1 and 2 data indicate that 15 of the 17 craters have higher backscatter cross-sections than the average scattering curve derived from Pioneer Venus SAR observations [3]. This correlation of high backscatter and low emissivity indicates that the floor materials have high dielectric constants. Figure 2 shows a plot of cycle 1 and 2 backscatter cross-sections for 5 craters. Four of the five craters have similar slopes to each other and the Venus average curve [3]. The slope of the curve for the crater Parra is flatter than the other curves. Parra has a bright floor like the low emissivity craters but the emissivity is normal. This relation may mean that the cause of the high backscatter for Parra's floor is roughness rather than a high dielectric material. Conversely, the high backscatter cross-sections and steeper slopes of the backscatter curves for the low-emissivity craters indicates that high dielectric constant materials are present on their floors.

Conclusions: A strong correlation exists between high backscatter cross-sections and low emissivity on crater floors. Using images taken at different incidence angles, we determined that the crater floors must contain high dielectric materials in order to account for their radiophysical properties and that the floors cannot be made up of the same materials of the outflow deposits (impact melt). Endogenetic lavas with low emissivities (possibly high iron content) that has flooded the crater interiors seems to be the most likely explanation. Lava flows with similar radiophysical properties have been found on Venus by Plaut [7]. Thus, similar high dielectric flows may partly fill the crater. With time, the materials weather to higher emissivities and lower backscatter cross-sections typical of the floors of the older craters. Bright halos found in Venera 15/16 craters may also be composed of high dielectric constant materials, although contributions of quasi-specular reflections from facets in the ejecta cannot be ruled out. Because these radiophysical properties are predominantly a function of crater age, it may be possible to use them to determine stratigraphic relationships between different geologic units on Venus.

References: [1] Pettengill et al., *Science*, **252**, 260-265, 1991; [2] Ivanov et al., *J. Geophys. Res.*, **91**, D413-430, 1986; [3] Pettengill et al., *J. Geophys. Res.*, **93**, B12, 14881-14892, 1988; [4] Klose et al., *J. Geophys. Res.*, **97**, 16,353-16,369, 1992; [5] Ford, P. and Pettengill, *J. Geophys. Res.*, **97**, 13,103-13,114, 1992; [6] Campbell et al., *J. Geophys. Res.*, **97**, 16,249-16,277, 1992; [7] Plaut, J., *EOS Transactions*, **74**, 190, 1993.

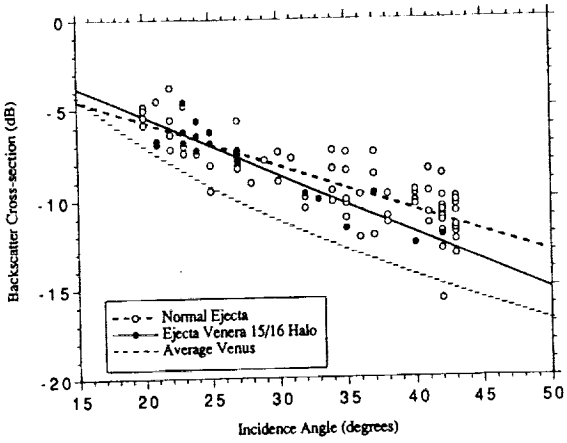

Figure 1. Magellan backscatter cross-sections of ejecta from craters also observed by Venera 15/16. The darkened circles represent craters with halos visible in Venera data.

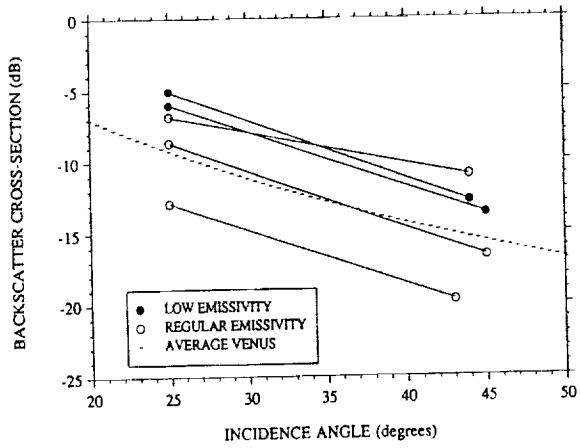

Figure 2. Cycle 1 and 2 Magellan backscatter cross-sections show that slopes of curves for crater floors with low emissivities and high backscatter are similar to the slope of the "average" curve for Venus[3] and crater floors with normal emissivities and backscatter. The slope of the curve for a crater with high backscatter and normal emissivity is much flatter, possibly due to high surface roughness.

DETECTABILITY OF CARBONATE IN UNCONSOLIDATED AND INDURATED SEDIMENTS; M.L. Wenrich and P.R. Christensen, *Department of Geology, Arizona State University, Tempe, Arizona 85287-1404*

Although Mars is predicted to contain carbonate due to possible fixing of atmospheric carbon dioxide or weathering of various silicate minerals [e.g., 1-3] there exist no definitive data which support carbonate being present on the planet. Carbonate, as well as other minerals, may be identified using thermal emission spectroscopy, a technique which utilizes differences in vibrational motions of atoms within a solid to determine mineralogy [4-6]. The primary purpose of this study is to determine the minimum volume percent of carbonate in an unconsolidated sediment mixture that is necessary for detection by a laboratory thermal emission spectrometer. Sediment mixtures consisting of calcite and fine-grained palagonite are used to emulate the possible composition of Martian soil. Additionally, infrared emission spectra of carbonate-bearing terrestrial desert crusts are compared to those of compositionally identical unconsolidated soil to determine the effect of induration on the resultant spectra.

Vibrational spectroscopy, using the thermal infrared 2000 to 400 cm^{-1} region (5 to 25 microns), is useful for determining surface mineralogy and will enable identification of carbonate, if present. This analytical method measures the mid-infrared energy emitted from a surface that varies according to the composition of the material. Fundamental bond vibrations within a crystal lattice produce absorption features that are unique to each mineral such that its spectrum can be used for mineral identification. A typical carbonate mineral, calcite ($CaCO_3$), exhibits diagnostic absorption features at approximately 1530 and 884 cm^{-1}. To provide evidence for carbonate on Mars' surface, a mid infrared spectrum should display these features, singly or in combination.

Large areas of carbonate on Mars, such as those that may exist as crater floor deposits, should be easily recognizable using thermal emission spectroscopy, provided the carbonate represents an adequate portion of the spectrometer's field of view. However, if the carbonate is not present as bedrock, but rather as grains, detection of the carbonate becomes more difficult. Such a situation could exist where carbonate grains are located within the Martian soil from *in situ* weathering of basalt or entrainment into the dust and redeposition associated with Martian dust storms. Under these circumstances carbonate detection will be more difficult due to the decreased volume percent of carbonate and the shallowing of spectral absorption features associated with multiple scattering in soils.

To determine the minimum volume percent of carbonate necessary to be apparent in an emission spectrum of unconsolidated soil, intimate mixtures of optical calcite (Iceland spar) grains and fine-grained Hawaiian palagonite are analyzed. The palagonite endmember is used because previous visible and near infrared reflection analyses of Mars' surface suggest that terrestrial palagonite (an amorphous weathering product of basalt) may be an analog of the Martian soil [e.g., 7]. The palagonite is dry sieved and subsequently the 0 to 63 micron fraction is finely ground using a mortar and pestle to assure that the grains are minimally flocculated. Various amounts of 180 to 250 micron grains of calcite are added to the palagonite and vigorously shaken to produce unconsolidated sediment mixtures containing 0 to 20 volume percent carbonate. After sample analyses are complete, the spectrum of the pure palagonite (0% calcite) sample is subtracted from each of the mixed sample spectra to produce spectra of the difference between the mixture containing carbonate and the pure palagonite endmember. This is done to examine the "contaminant" (i.e., the carbonate) in the palagonite. These spectra are shown in Figure 1 accompanied by a spectrum of pure (100%) calcite grains (180 to 250 microns) for comparison. The deepest calcite absorption feature occurs at ~1530 cm^{-1} but affects the wavelength region between 1585 and 1350 cm^{-1}. It is this broad absorption band that is identifiable in the spectra of the calcite/palagonite mixtures and can be used to indicate the presence of carbonate in an intimate soil mixture. Based on our results, we suggest that the carbonate must be approximately 8 volume percent of the soil to be identified with confidence, according to the parameters of our Mattson Cygnus spectrometer with a spectral resolution of 4 cm^{-1}. It should be noted, however, that this experiment represents a nearly worst-case scenario where the sediment that is fine-grained has a

significant muting effect on the diagnostic spectral features due to multiple scattering and increased blackbody behavior within an unconsolidated sediment. If these grains were present in a coarse-grained mixture, carbonate at less than 5% by volume could be detected, as demonstrated by [8].

Determining how induration (or crusting) of a carbonate-bearing sediment affects the thermal emission spectrum and detectability of carbonate is a second goal of this study. Induration is of interest because images and chemical data acquired from the Viking landers at Chryse and Utopia Planitae reveal a Martian surface comprised of rocks and finer-grained soil that appears crusted at the surface as indicated during sediment trenching by the sampling arms [9]. X-ray fluorescence analyses and investigations by others [3,10-12] suggest that the cementing agent for the Martian crusts are salts such as sulfates and carbonates.

Crusted desert sediment from South Fork Coyote Wash, west of El Centro, California, was collected and broken into small ~2 cm diameter pieces. A few crusts from the sub-divided sample were lightly crushed in a mortar (no grinding was done) and these looser sediments as well as the unaltered desert crusts were spectrally analyzed. The resultant spectra are shown in Figure 2. Although these samples are identical in composition (containing both calcite and quartz) the absorption features are deeper for the indurated sediment than those features associated with the unconsolidated sediment. These data suggest that crusting enhances the mid-infrared spectral features and thus increases the potential for detection and identification of the minerals that constitute the indurated soil. These results are consistent with an increase in spectral contrast associated with a decrease in porosity as demonstrated by [13].

In summary, unconsolidated palagonite soils that may be analogous in composition to soils on Mars would have to contain carbonate at approximately 8 percent by volume for the carbonate to be confidently detected, assuming the spectra were acquired using a spectrometer with similar parameters to the laboratory spectrometer used for this study. However, this carbonate detectability limit may be decreased if the sediment is either coarse-grained or indurated as is proposed for Martian soils [9] which would increase the probability for carbonate identification.

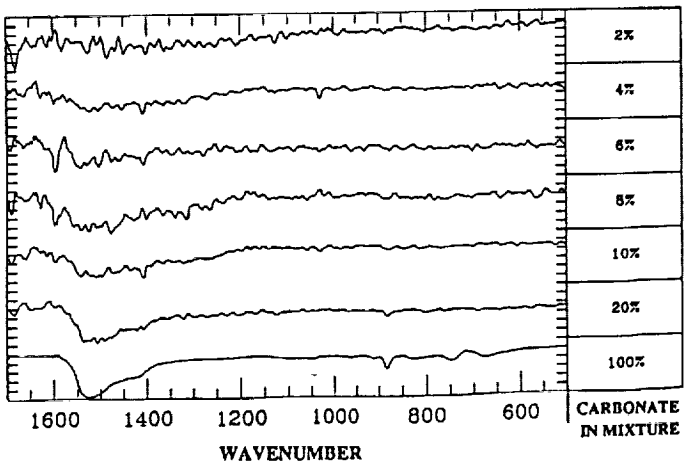

Figure 1. Spectra of the difference between pure palagonite and the sediment mixtures

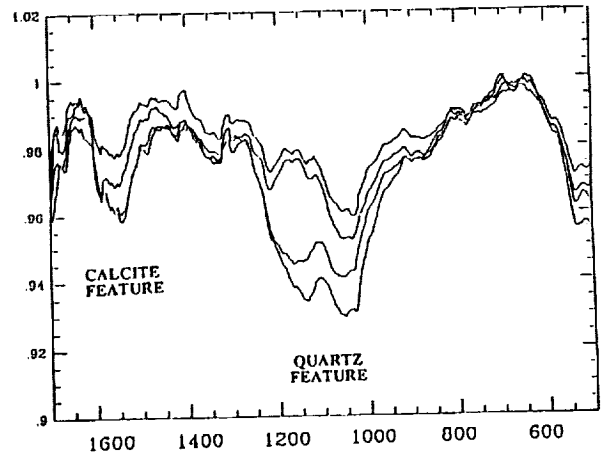

Figure 2. Spectra of unconsolidated (top 2) and indurated (bottom 2) desert sediments

References: [1] Fanale, F.P. (1976) *Icarus, 28*, 179-202. [2] Gooding, J.L. (1978) *Icarus, 33*, 483-513. [3] Clark, B.C. and P.C. VanHart (1981) *Icarus, 45*, 370-378. [4] Conel, J.E. (1969) *J. Geophys. Res., 74*, 1614-1634. [5] Christensen, P.R. and Harrison, S.T. (1993) *J. Geophys. Res., 98*, 19819-19834. [6] Wenrich, M.L. and P.R. Christensen (1993) *LPSC 24th*, 1505-1506. [7] Evans and Adams (1980) *Proc. LPSC 10th*, 1829. [8] Moore, H.J. et al., (1982) *J. Geophys. Res., 87*, 10043-10050. [9] Ramsey, M.S. and P.R. Christensen (1992) *Proc. Third TIMS Workshop, June 1992, JPL Publ. 92-14*, 34-36. [10] Binder, A.B. et al., (1977) *J. Geophys. Res., 82*, 4439-4451. [11] Mutch, T.A. et al., (1977) *J. Geophys. Res., 82*, 4452-4467. [12] Toulmin, P. III et al., (1977) *J. Geophys. Res., 82*, 4625-4634. [13] Salisbury , J.W. and J.W. Eastes (1985) *Icarus, 64*, 586-588.

PROVENANCE OF THE TERRESTRIAL PLANETS; G. W. Wetherill, DTM, Carnegie Institution of Washington, Washington, D.C. 20015

A fundamental problem in geochemistry and cosmochemistry is the location and relative contribution of the source regions in the preplanetary disc from which the present planets are presumed to have formed. This problem has been addressed by use of a more general model for the later stages of growth that simultaneously includes both the terrestrial planet region and the asteroid belt (1). Our Solar System should be considered but one of a number of possible planetary systems of this class. This model succeeds in predicting many of the attributes of the observed Solar System, such as the spontaneous clearing of the asteroid belt, the relative velocities of the surviving asteroids, and the characteristics of the final large bodies in the terrestrial planet region. It is now found that this same model predicts that all of the terrestrial planets receive significant contributions from ~ 10^{26}g "planetary embryos" (2) extending from about 0.5 to 2.5 AU. Nevertheless, there is a correlation between the final heliocentric distance and the average provenance of the planets. The weighted average provenances of "Mercury" and "Venus" are usually between 0.9 and 1.2 AU, whereas that of "Earth" is somewhat larger (~ 1.3 AU), and that of "Mars" usually has an average provenance between 1.5 and 2.0 AU.

59 new simulations of the "nominal model" (1) were used to obtain these results. In my previous work, comparison of 115 nominal simulations with 226 variants of the model show that such differences have little effect on the final results. From these 59 simulations, 13 cases were selected that met assumed criteria for resemblance to our Solar System. The relationship between the final semimajor axes of these bodies and their weighted (by mass) provenance is shown in Fig. 1a. The corresponding relationships with their masses are shown in Fig. 1b. The provenance of "Earth" for a typical simulation is shown in Fig. 2a and that for Mars in Fig. 2b.

In the final asteroid belt, residual test bodies with initial semimajor axes > 2 AU tend to cluster in the outer asteroid belt (2.75 to 3.5 AU), whereas the inner asteroid belt contains a major contribution from bodies having initial semimajor axes between 1 and 2 AU (Fig. 3). The latter may be expected to be more chemically similar to the terrestrial planets than objects now observed in the outer asteroid belt. One may speculate that this could be related to the ~ 1 AU wide "stratigraphy" observed in the asteroid belt (3).

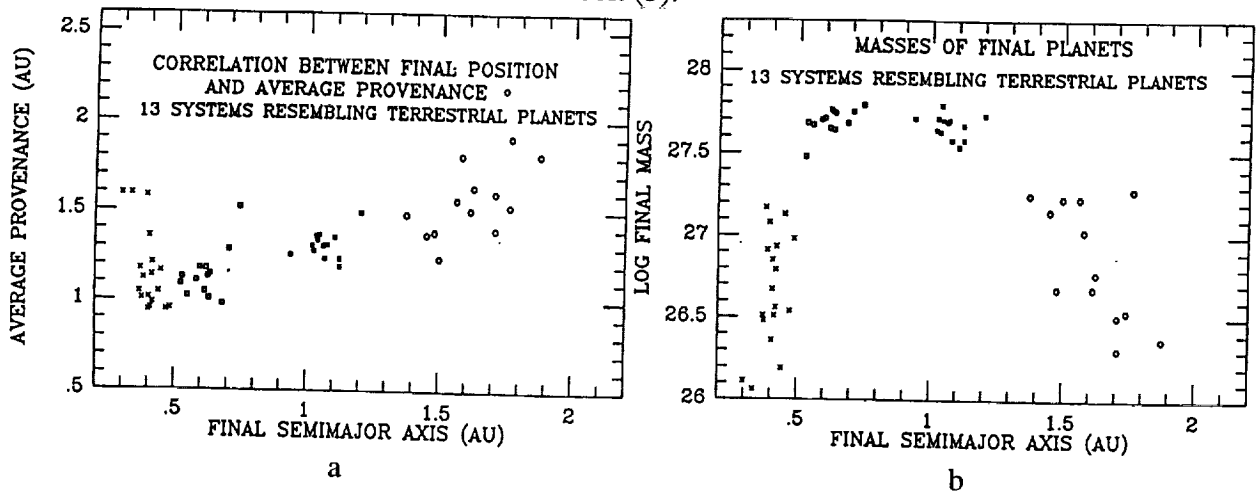

Fig. 1 a. Relationship between average provenance and final semimajor axis. Symbols: "Mercury" (x), Venus (open squares), Earth (solid squares), Mars (open circles).
b. Relationship between final masses and final semimajor axes. Symbols same as in (a).

PLANETARY PROVENANCE: Wetherill, G. W.

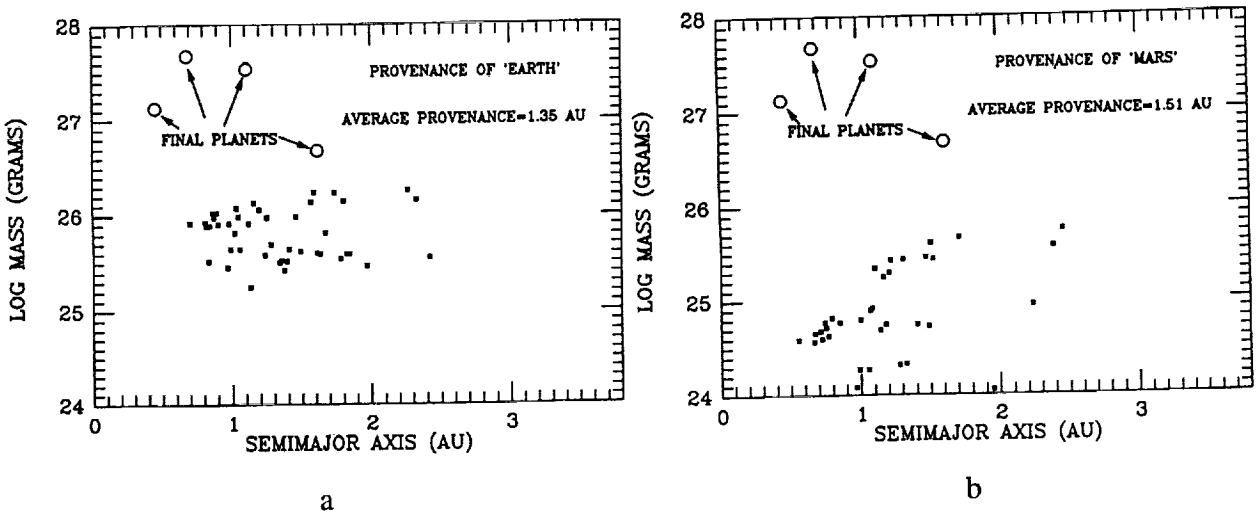

Fig. 2a. Provenance of "Earth" for a typical simulation.
Fig. 2b. Provenance of "Mars" for a typical simulation.

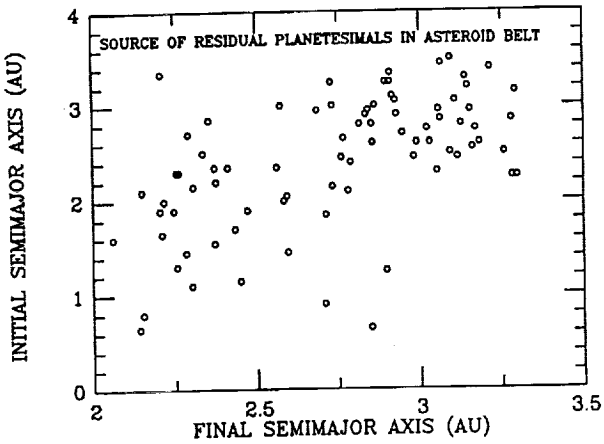

Fig. 3. Final distribution of test bodies in the asteroid belt.

REFERENCES
(1) Wetherill, G. W. (1992) An alternative model for the formation of the asteroids. *Icarus 100*, 307-325.
(2) Wetherill, G. W. (1993) Formation of planetary embryos: Effects of fragmentation, low relative velocity, and independent variation of eccentricity and inclination. *Icarus 106*, 190-209.
(3) Gradie, J. and Tedesco, E.F. (1982) Compositional structure of the asteroid belt. *Science 216*, 1405-1407.

DARK-FLOORED CRATER ELEVATIONS ON VENUS: IMPLICATIONS FOR CRATER-CENTERED VOLCANISM;

R.W. Wichman, Dept. of Space Studies, Univ. of North Dakota, Grand Forks, ND 58202.

Summary: Previous models for impact crater modification by igneous intrusions [1,2] suggest that crater-centered volcanism on Venus should preferentially occur at lower elevations than craters modified by independent, external volcanic flows. Dark-floored craters provide the most likely candidates on Venus for such crater-centered volcanism, and a survey of over 400 craters (D>15 km) indicates that venusian dark-floored craters preferentially occur at elevations between identified floor-fractured craters and craters embayed by external lava flows. Consequently, different styles of volcanically modified craters apparently occur at different elevations on Venus. Further, since young, bright-floored craters are rare at lowland elevations, crater modification by localized, crater-centered lavas appears to be widespread at these lowland elevations and may be relatively recent.

Background: Although most impact craters on Venus exhibit nearly pristine crater rims and ejecta units [3], such observations provide little constraint on the extent or frequency of localized modification inside these craters. The apparent replacement of bright young crater floors with dark crater floor units over time [4,5], however, suggests that either eolian or volcanic processes have produced widespread modification of venusian crater floors without affecting surface units outside the crater rims. Since both mare-filled and floor-fractured craters on the airless Moon exhibit similar cases of localized internal crater modification [6], this abstract favors a volcanic origin for the venusian dark crater floor units.

Previous studies of venusian floor-fractured craters provide a possible test for this hypothesis. Specifically, although floor-fractured craters are rare on Venus, their distribution appears to be elevation dependent and is distinctly different from the distribution of craters embayed by external volcanic units [1,2]. By modeling crater floor-fracturing as a response to crater-centered intrusions, the effects of atmospheric pressure variations on magmatic vesiculation can explain this dichotomy in crater modification [2]. A similar dichotomy can also be predicted in the distribution of crater-centered volcanism as a function of elevation, since the effect of atmospheric pressures on basalt densities should increase regional magma depths at higher elevations over time [7]. Assuming that crater-centered volcanism is most likely when regional magmas are level with near-surface crater breccias, such variations in magma depth should favor crater-filling volcanism at lower elevations and external, crater-modifying volcanism at higher elevations. Further, since magmatic vesiculation increases as atmospheric pressures decrease [7], breccia-centered neutral buoyancy zones should be less stable at higher elevations on Venus as well [2]. Thus, crater-filling volcanism may preferentially occur at higher elevations than the identified floor-fractured craters on Venus. Since conditions on Venus are less favorable for crater-centered intrusions than on the Moon [1,2], however, crater-filling volcanism may also occur throughout the identified elevation range for crater floor-fracturing.

Dark-floored Craters: To test these predictions about the elevation of crater modification on Venus, I have compiled a data set describing the setting, size and character of crater floor units in the Magellan CD-ROM images. This data set expands the crater catalog of Schaber et al. [3] and focuses on variations in the appearance, size and location of dark crater floor units in craters over 15 km in diameter. Crater elevations are derived from the browse version of Venus altimetry in the Magellan CD's. Although many craters show a number of bright, intermediate, and dark crater floor units, the craters are divided into three main groups on the basis of their dominant crater floor albedos. For this division, intermediate crater floors are large smooth surfaces which (1) are brighter than most lowland plains units, (2) generally contain smaller dark floor units, and (3) lack the distinctly radar-bright albedos observed in craters with dark parabolic ejecta deposits.

As shown by Figure 1, dark-floored and bright-floored craters on Venus show distinct differences in their elevation distributions. While dark-floored craters are concentrated at relatively low elevations (mean ~150 m below the MPR of 6051.8 km), the bright-floored crater distribution is centered at somewhat higher elevations (mean ~370 m above MPR) and it shows a pronounced tail extending to elevations over 3500 m above MPR. Using Student's T-test, these elevation distributions are statistically independent at confidence levels exceeding 99%. The intermediate-floored craters (not shown) have a distribution resembling that of the bright-floored craters, but with a slightly lower mean elevation (~250 m above MPR).

In addition, the typical size of dark crater floor units (relative to crater floor size) may vary as a function of elevation. Figure 2 shows that craters in which dark units comprise major fractions (>2/3) of the crater floor typically occur at lower elevations than craters in which dark units comprise minor or negligible fractions (<1/3) of the crater floor. Again, the two distributions are statistically independent at confidence levels of over 99%. Craters in which dark floor units comprise a moderate fraction (>1/3 and <2/3) of the crater floor are concentrated at intermediate elevations, but the distribution is closer to that of the major dark floor units than to that of the minor/negligible dark floor units.

Discussion: The average elevation of floor-fractured craters on Venus is ~580 m below MPR. Thus, although the elevations of dark-floored craters on Venus span the elevation range of the identified floor-fractured craters (figure 1), the dark-floored craters typically occur at higher elevations than the floor-fractured craters. Even the lowest class of dark-floored craters (those with major dark floor units) are statistically independent of the floor-fractured crater elevations (confidence level ~97%). In contrast, the mean elevation of externally modified, volcanically embayed craters (~410 m above MPR) can not be distinguished statistically from the elevation distributions of either the bright-floored craters or craters with minor/negligible dark floor units (confidence levels <<80%). Since the typical size of dark crater floor units apparently decreases as a function of elevation (figure 2), dark-floored craters (like floor-fractured craters) seem to preferentially occur at lower elevations while crater modification by external volcanism is favored at higher elevations.

These observations are consistent with the model for magmatic crater modification derived from previous studies of venusian floor-fractured craters [1,2]. First, the average offset of dark-floored craters to higher elevations than the floor-fractured craters matches the predicted effect of magmatic vesiculation on the stability of crater-centered intrusions. Second, the similarity in the elevations of externally embayed craters and craters with minimal/negligible dark floor units suggests a transition at higher elevations from crater-centered to crater-insensitive volcanism. Such a transition is consistent with the predicted variations in regional magma depths as a function of elevation [2,7]. Lastly, if increased regional magma depths can affect the volume of magma entering a crater [2], variations in regional magma depth also may explain the apparent size reductions of dark crater floor units as a function of elevation.

Implications: Externally modified, volcanically embayed craters are relatively rare (~5% of the observed population) and preferentially occur at highland elevations; thus, previous studies of crater loss and volcanic resurfacing have generally concluded that recent volcanism on Venus is of limited extent and is primarily restricted to the highland regions. The arguments and observations presented above, however, indicate that these views may need some modification. While crater loss appears to be limited to highland regions (eg. 8,9), the apparent transition from floor-fractured and dark-floored craters at lowland elevations to externally modified, volcanically embayed craters at higher elevations strongly suggests that (1) different styles of both volcanism and crater modification occur on Venus as a function of elevation, and that (2) a class of modified craters exists at lowland elevations which have not been included in previous studies. Since young, bright-floored craters appear to be preferentially located at highland elevations, the number of dark-floored craters at lower elevations also suggests that (3) localized, crater-centered volcanism has been widespread in the lowland plains and may be ongoing. In the latter case, recent volcanism may be possible elsewhere in the lowland plains as well.

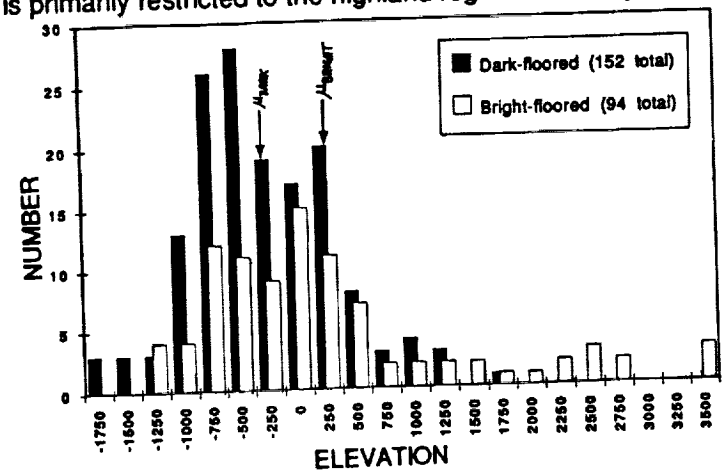

Figure 1. Histogram showing elevation distribution of dark-floored and bright-floored craters on Venus.

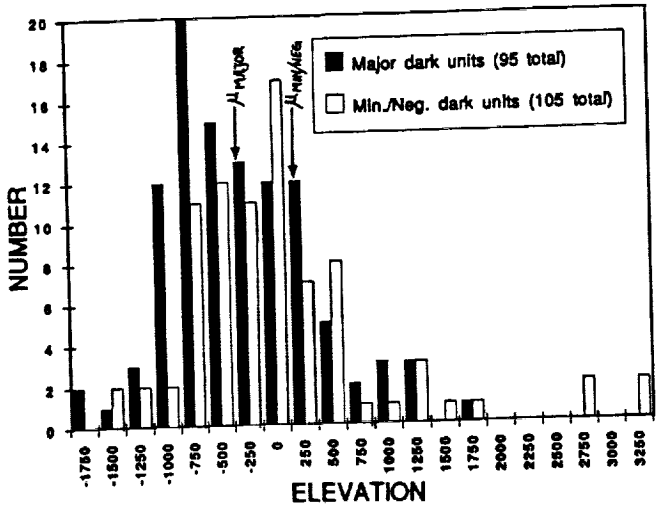

Figure 2. Histogram showing crater elevations for different relative sizes of dark crater floor units.

REFERENCES: (1) Wichman, R.W. and Schultz, P.H. (1992) *Internatl. Coll. Venus, LPI Contrib. No. 789*, 131-132. (2) Wichman, R.W. (1993) *Lunar Planet. Sci. Conf. 24*, 1513-1514. (3)Schaber, G.G. et al., (1992) *J. Geophys. Res. 97*, 13257-13302. (4) Campbell, D.B. et al., (1992) *J. Geophys. Res. 97*, 16249-16278. (5) Izenberg, N.R. et al, (1993) *Lunar Planet. Sci. Conf. 24*, 703-704. (6) Schultz, P.H. (1976) *Moon Morphology* Univ. of Texas Press, Austin. (7) Head, J.W. and Wilson, L. (1992) *J. Geophys. Res. 97*, 3877-3904. (8) Phillips, R.J. et al, (1992) *J. Geophys. Res. 97*, 15923-15948. (9) Price, M.H. and Suppe, J. (1993) *Eos 74*, 379.

COMET DISRUPTION AND CRATER CHAIN FORMATION IN THE EARTH-MOON SYSTEM. R.W. Wichman and C.A. Wood, Dept. of Space Studies, Univ. of North Dakota, Grand Forks, ND 58202-9008.

Summary: Based on the linear array of fragments resulting from tidal disruption of the comet Shoemaker-Levy 9, Melosh and Schenk [1] recently proposed that linear crater chains on the Galilean satellites record previous comet disruption events in the Jovian system. Consequently, the characteristic appearance of these linear crater chains may provide a basis for recognizing past tidal disruption events throughout the solar system. We discuss one such case, the Davy crater chain, which may record an ancient disruption event in the Earth-Moon system.

Introduction: Imagination is never as extravagant as nature. For many decades during this century the idea of impact cratering was rejected because it simply was not conceivable. In the 1970s the proposition that asteroids might have satellites seemed farfetched. And not even a theorist had advocated comet fragmentation as a source of crater chains. But all of these ideas are now forced into our acceptance by observations. And recognition of each new reality prompts reexamination and new explanations for old problems throughout the solar system. Here we investigate whether comet disruption - as spectacularly demonstrated by comet Shoemaker-Levy 9 - can explain anomalous features on the Moon.

Comet Shoemaker-Levy 9 (SL-9) passed inside Jupiter's Roche limit in 1992, tidally shredding the comet into a string of small nuclei in an highly elliptical orbit around Jupiter [2]. The nuclei will sequentially impact Jupiter's atmosphere in June, 1994, depositing immense kinetic energy and causing uncertain turmoil. Jupiter, as the gravitational focus of nearly all short period comets, has captured other comets into temporary satellite orbits [3]. Melosh and Schenk [1] suggest that linear crater chains on the Galilean satellites may provide a record of previous comet disruption events in the Jovian system. They calculate that the travel time between the Roche limit passage and collision with Callisto or Ganymede is lengthy enough, based on the rate of dispersion observed for SL-9, to yield the few hundred kilometer long crater chains seen on those satellites.

Formation of a crater chain by a fragmented comet requires one or two planetary bodies, as well as the suicidal comet. First, a relatively massive planet is needed with a sufficiently extensive Roche limit to have a reasonable statistical probability to intercept and disrupt occasional comets. If the fragmented comet hits the planet immediately it will have had insufficient time to gravitationally disperse and thus will probably cause a single impact crater or perhaps a pair (e.g. Clearwater Lakes). If the comet is captured into an orbit around the planet it may have time to be pulled into a "string of pearls" and make a crater chain on impact. As in the case of Jupiter, a satellite can be a target (or witness plate) for the collision. Although it might seem that the linear crater chains on Phobos could have resulted from such a cometary splintering, the geologic evidence supports the current hypothesis that those chains formed in association with the crater Stickney [4,5].

A lunar example?: But on Earth's Moon there is one anomalous crater chain that has never been convincingly explained. East of Ptolemaeus, near the center of the lunar near-side, the Davy chain cuts the floor of the crater Davy Y. The chain is 40-50 km long and includes 18 or more near-circular craters from 1.5 to 4 km in diameter. Like the crater chains on the Galilean satellites, these craters are closely spaced (rim to rim) and are aligned like "pearls on a string." In the 1960s during the flush of triumph in recognizing the pervasiveness of impact cratering, the Davy chain was sometimes considered to be a secondary crater chain, such as those commonly seen around all young impact craters and basins. Musursky [6] pointed out the obvious flaw: there is no apparent primary crater. We have quantified Masursky's observation by noting that for secondaries 1 to 4 km in diameter, the primary should be ~25 to 100 km in diameter and it should be ~100-200 km from the chain [7]. No such crater of suitable age (Imbrian or younger) exists.

Morphologic evidence does not support a secondary crater origin either. Known lunar secondary craters typically occur as part of an array of chains radiating from the source crater. They are often composed of irregular, relatively shallow craters which are only crudely aligned. The most diagnostic feature of secondary chains is a herringbone pattern of draped downrange ejecta. None of these descriptions are characteristic of the Davy crater chain.

The most favored hypothesis in the Apollo period was that the Davy chain was a tectonically controlled line of volcanic pits [6,8]. On the Moon, collapse pits typically develop along well-defined tectonic trends or rille structures (eg, the rimae Hyginus and Treisnecker pit chains). Additionally, pits appear to develop originally as near-circular features, but continued activity generally produces irregular, coalesced pit features [8]. Lastly, volcanic pit formation presumably results from pyroclastic eruptions which typically produce dark mantling deposits (c.f. the dark halos surrounding endogenic pit craters [9]). Once again, none of these volcanic characteristics are consistent with the Davy chain

Discussion: While the Davy crater chain is distinctly different from other secondary crater chains and pit craters on the Moon, it shows a number of similarities to linear crater chains in the Jupiter system. Like the crater chains on Ganymede and Callisto [1], it is located on the planet-facing side of the satellite, and it cannot be correlated with any major crater- or basin-forming impact. Similarly, the relatively uniform size of the Davy craters resembles the near constant widths of craters in the Jovian crater chains, where crater diameters seldom vary by more than a factor of two within any given chain [1]. Even the near-circularity of craters within the Davy chain has analogs in the Jovian system (eg., Gipul Catena). Thus, we propose that the Davy chain resulted from the impact of a tidally disrupted asteroid or comet in the Earth-Moon system.

Although the crater chains on Ganymede and Callisto are typically wider (~8-40 km) and longer (~40-620 km) than the Davy crater chain, the small size of this lunar example is consistent with a translation of the comet disruption model to the Earth-Moon system. First, the size of the craters in a crater chain should reflect the original size of the tidally disrupted body; hence, the relatively small sizes of most earth-crossing asteroids and comets relative to bodies in the outer solar system should limit the possible size of a tidally generated crater chain on the Moon. Since the Davy crater chain apparently records the impact of a score of objects each several hundred meters in diameter, the diameter of the original parent body was probably on the order of 500-1000 m. This is at the lower end of the inferred initial sizes for the Jovian crater chains (~0.5-10 km, [10]), but it is quite comparable to the size of known Earth-crossing asteroids (typically <2.5 km).

Second, the dispersion rates of a tidally disrupted body should also vary between Jupiter and the Earth. Based on the models for SL-9 [1,10], the linear dispersion of a tidally disrupted body primarily results from variations in the orbital trajectories of material as a function of radial distance within a body at the point of closest approach to the planet. Consequently, dispersion rates and crater chain lengths depend directly on the size of the initial comet, the distance of closest approach to the planet and, to a lesser extent, on the initial cometary velocity [1].Also, the much lower mass of Earth compared to Jupiter would presumably produce lower dispersion rates at Earth. Comparing the terestrial values for this model to those at Jupiter, therefore, all of these factors are consistent with the decreased length of the Davy crater chain relative to those in the Jupiter system. This is especially true when it is recognized that at Jupiter all the observed crater chains which contain more than 10 craters are over 150 km in length.

Based strictly on the increase in average cometary velocities between Jupiter and the Earth, the models of Melosh and colleagues suggest that dispersion rates for the Earth-Moon system should be approximately half of those observed at Jupiter. Since the dispersion rate observed for SL-9 is ~40 km/s [10], a maximum value for the rate near the Earth can be crudely placed at ~20 km/s. A comet travelling 30 km/s can move from Earth's Roche limit to the Moon in ~3-4 hours; thus, the minimum expected value for crater chain lengths on the Moon is ~60-80 km. Considering that this estimate does not account for variations in cometary size, planetary mass, or the vast number of assumptions and extrapolations, this value is remarkably consistent with the observed length of the Davy crater chain.

References: (1) Melosh, H.J. and Schenk, P. (1993) *Nature 365,* 731-733. (2) Chapman, C.R. (1993) *Nature 363,* 492-493. (3) Carusi et al (1982) *Bull. Astron. Inst. Czechosl. 33*, 141-150. (4) Head, J.W. and Wilson, L. (1989) *Lunar Planet. Sci. Conf. 20*, 1211-1212. (5) Murchie, S.L. et al. (1990) *Lunar Planet. Sci. Conf. 21*, 827-828. (6) Masursky, H. (1978) *Apollo Views the Moon, NASA SP-362*, p. 132. (7) Allen, C.C. (1979) *Geophys. Res. Ltr 6*, 51-54. (8) Schultz, P.H. (1976) *Moon Morphology*, Univ. of Texas Press, Austin. (9).Hawke et al, (1989) *Proc. Lunar Planet. Sci. Conf. 19*, 255-268. (10) Scotti, J.V. and Melosh, H.J. (1993) *Nature 365*, 733-735.

ANALYTICAL MODELING OF THERMAL EROSION BY LOW-VISCOSITY LAVA FLOWS AND IMPLICATIONS FOR PLANETOLOGY; D.A. Williams and R. Greeley, *Department of Geology, Arizona State University, Box 871404, Tempe, Arizona 85287-1404.*

The discovery of long, sinuous channels on Venus [1] has renewed the interest in thermal erosion by lava flows. Previous studies suggested that thermal erosion could have produced some lunar sinuous rilles [2] and some channels on Mars [3] and Venus [4,5,6]. However, these models did not evaluate the full range of thermal, rheological, and environmental parameters involved in thermal erosion. Hence, a new analytical model to evaluate thermal erosion potential on the terrestrial planets is required which takes into account all relevant parameters. Figure 1 shows a preliminary model for one-dimensional thermal erosion applied to turbulently-flowing, submarine Archean komatiite flows in Western Australia [7,8]. This model separates a lava flow into surface crust and thermally-mixed inner core [9], and yields estimates of the heat available for thermal erosion by calculating total heat flux (energy per time·area) subtracting heat losses due to radiation, seawater convection, crust formation, thermal convection of the turbulent core, latent heat of crystallization, and viscous dissipation. Requirements for constraining these models and adaptations for applying these models to other planets are discussed.

Thermal erosion potential is dependent on the eruption temperature of the lava, the thermal and rheological properties of the lava and substrate, and the environment in which eruption occurs. Some of the thermal and rheological properties have been measured in the field for terrestrial basalt and carbonatite flows [10,11], but for other lavas (e.g. komatiites, lunar basalts) these properties were determined from laboratory and experimental studies or extrapolated from those values obtained for basalt [8,12-18], and hence are uncertain. Application of a useful analytical model requires good input parameters, and reevaluation of existing values may be in order. Likewise, a good thermal erosion model needs to be calibrated by predicting quantities of erosion determined from field evidence. Unfortunately, good evidence of thermal erosion is not observed in modern basalt flows, and field evidence for thermal erosion by komatiites in Western Australia is equivocal [19]. For example, some of the features observed at or near komatiite/substrate contacts in the field (truncation of underlying stratigraphy, channel-like embayments, presence of interspinifex ore, entrained and partially melted substrate fragments, and geochemical anomalies) offer a good but far from unequivocal case for thermal erosion. These constraints need to be addressed as the development of a new thermal erosion model proceeds. Application of such a model can provide a better understanding of lava flow dynamics on other planets.

REFERENCES

[1] Gulick, V.C., G. Komatsu, V.R. Baker, R.G. Strom, *Lunar and Planetary Science XXII*, LPI, Houston, Texas, 507-8, 1991; [2] Hulme, G., *Modern Geology 4*, 107-117, 1973; [3] Carr, M.H., *Icarus 22*, 1-23, 1974; [4] Baker, V.R., G. Komatsu, T.J. Parker, V.C. Gulick, J.S. Kargel, and J.S. Lewis, *J. Geophys. Res., 97,* 13,421-13,444, 1992; [5] Komatsu, G., V.R. Baker, V.C. Gulick, and T.J. Parker, *Icarus 102*, 1-25, 1993; [6] Gregg, T.K.P., and R. Greeley, *J. Geophys. Res., 98*, 10,873-10,882, 1993; [7] Huppert, H.E., R.S.J. Sparks, J.S. Turner, and N.T. Arndt, *Nature, 309,* 19-22, 1984; [8] Huppert, H.E., and R.S.J. Sparks, *Jour. Pet., 26,* 694-725, 1985; [9] Crisp, J., and S. Baloga, *J. Geophys. Res., 95*, 1255-1270, 1990; [10] Pinkerton, H., in *Active Lavas: Monitoring and Modeling*, C.R.J. Kilburn and G. Luongo, eds., UCL Press, London, 1993; [11] Dawson, J.B., H. Pinkerton, G.E. Norton, D.M. Pyle, *Geology 18*, 260-263, 1990; [12] Jaeger, J.C., *Basalts: Poldervaart Treatise on Rocks of Basaltic Composition,* Wiley Interscience, N.Y., 503-536, 1968; [13] Bottinga, Y. and D.F. Weill, *Am. J. Sci. 272*, 438-475, 1972; [14] Nelson, S.A. and I.S.E. Carmichael, *Cont. Min. Pet. 71*, 117-124, 1979; [15] Usselman, T.M., D.S. Hodge, A.J. Naldrett, and I.H. Campbell, *Canad. Min. 17,* 361-372, 1979; [16] Huppert, H.E. and R.S.J. Sparks, *Cont. Min. Pet. 75,* 279-289, 1980; [17] Arndt, N.T., *Geology 11*, 372-375, 1983; [18] Lesher, C.M., *Ph.D. Dissertation*, University of Western Australia, 318 pp., 1983; [19] Groves, D.I., E.A. Korkiakoski, N.J. McNaughton, C.M. Lesher, and A. Cowden, *Nature 319,* 137-139, 1986.

ANALYTICAL MODELING OF THERMAL EROSION BY LAVA FLOWS:

Williams, D.A. et al

Figure 1. Schematic diagram of analytical model developed in this study.

$$\text{Steady-state Melting Rate} = \frac{H}{\rho_g\left[c_g(T_m-T_a)+L_g\right]}$$

$$H = Q - F_r - F_{cv} - F_{cg} - F_{cc} - F_{xc} - F_{vd}$$ — Heat transfer rate to ground

$$Q = \rho_l c_l T v(1-f)$$ — Heat flux of flow

$$F_r = \varepsilon\sigma\left\{(1-f)(T^4-T_a^4)+f(T_{sc}^4-T_a^4)\right\}$$ — Radiative heat loss from top surface

$$F_{cv} = \rho_w c_w \gamma\left(\frac{\alpha_w g D_w^2}{\nu_w}\right)^{1/3}\left\{(1-f)(T-T_a)^{4/3}+f(T_{sc}-T_a)^{4/3}\right\}$$ — Convective heat loss by seawater from top surface

$$F_{cg} = \rho_l c_l T\frac{x}{t}f$$ — Conductive heat loss through surface crust

$$F_{cc} = \lim_{T\to\theta_{bl}}\left[\rho_l c_l \gamma\left(\frac{\alpha_l g D_l^2}{\nu_l}\right)^{1/3} T^{4/3}\right]$$ — Turbulent flow - thermal convection of inner core

$$F_{xc} = \rho_l\left[c_l(T-T_m)+L_l\right]\frac{x}{t}f$$ — Conductive heat loss of latent heat of crystallization

$$F_{vd} = \frac{k_l}{h}\left(T-T_a+\frac{\mu_l v^2}{2k_l}\right)$$ — Heat loss by viscous dissipation

$$\mu_l = \exp(34.551-0.0226T)$$ — Viscosity changes with temperature and crystal content

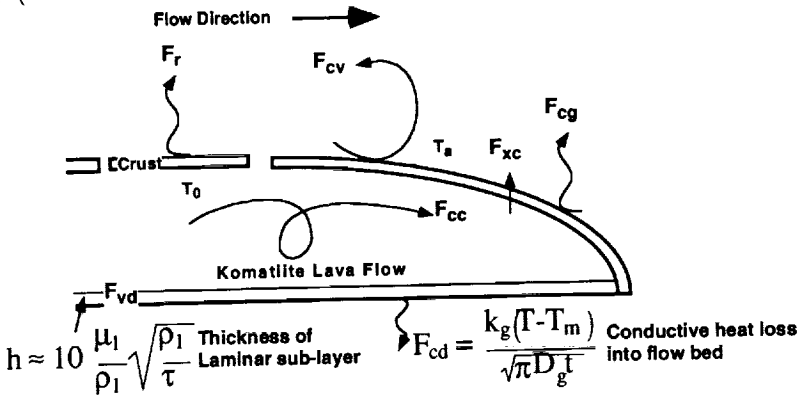

Table 1. Thermal and rheological parameters for analytical model of Figure 1. Subscripts: l - lava; g - ground; w - seawater; m - melting; a - ambient; sc - surface crust; bl - boundary layer.

Symbol	Meaning
H	Heat transfer rate to ground
c	specific heat at constant pressure
L	heat of fusion
f	fraction of surface covered by crust
σ	Stefan-Boltzmann constant
α	coefficient of thermal expansion
D	thermal diffusivity
x/t	crustal growth rate
μ	dynamic viscosity
h	thickness of laminar sub-layer

Symbol	Meaning
ρ	density
T	temperature
v	flow velocity
ε	emissivity
γ	convection parameter
g	gravity
ν	kinematic viscosity
θ_{bl}	mechanical solidus of lava
k	thermal conductivity
σ_w	shear stress

MARS: VOLCANIC ERUPTION THEORY AND RELATIONSHIPS TO OBSERVED LANDFORMS: Lionel Wilson[1,2] and James W. Head[2], [1]Environmental Science Division, Lancaster Univ., Lancaster LA1 4YQ, UK, [2]Department of Geol. Sci., Brown Univ., Providence, RI USA.

Analysis of the images returned from the Mariner and Viking missions has produced abundant evidence for a variety of volcanic landforms on Mars (1). One approach to understanding the styles of martian volcanic activity represented by these landforms has been to compare the morphologies of martian volcanic structures with those of terrestrial analogs. While useful, this method may overlook potentially dramatic effects of differences between the terrestrial and martian environments on eruptive processes (2). As a result, we have concentrated on a different approach, that of initially considering the processes of ascent and eruption of magma on Mars from first principles and developing predictions of the types of volcanic landforms expected to be produced in the martian lithospheric and atmospheric environment. We then compared these predictions with observed landforms (e.g., 3). We followed the basic approach that we have utilized in analyzing the ascent and emplacement of magma on the Earth and Moon (4) and Venus (5). We first examined modes of magma production in the martian interior, then assessed processes of magma ascent, analyzing the shallow density structure of the crust and lithosphere and its potential influence on the production of zones of neutral buoyancy (Fig. 1). Following this, we examined processes of gas exsolution at shallow depths and how the range of eruption products is manifested in the creation and growth of deposits and landforms (Fig. 2). Finally, we compared theoretical predictions with the range of landforms that have been revealed by Mars exploration, and used these observations as a basis to investigate a number of problems in the thermal and volcanological history of Mars (6).

On the basis of this assessment of the crustal configuration of Mars and the theoretical treatment of the ascent and eruption of magma through this crust in the martian gravity and atmospheric environment, we find that the full range of volcanic eruption styles observed on Earth is to be expected on Mars. It is clear, though, that martian environmental conditions operate to modulate the various eruption styles and the morphology and morphometry of resulting landforms. Using these theoretical predictions as a basis we compared observed deposits and landforms and find general agreement. In several cases we find that theory provides new insight into martian volcanological problems. For example, because of the lower gravity, fluid convective motions and crystal settling processes driven by positive and negative buoyancy forces, and overall diapiric ascent rates, will be slower on Mars than on Earth, permitting larger diapirs to ascend to shallower depths. This factor also favors a systematic increase in dike widths on Mars by a factor of two and consequent higher effusion rates by a factor of five. As a result of the differences in lithospheric bulk density profile, which in turn depend on differences in both gravity and surface atmospheric pressure, magma reservoirs are expected to be deeper on Mars than on Earth, by a factor of about four. The combination of the lower martian gravity and lower atmospheric pressure ensures that both nucleation and disruption of magma occur at systematically greater depths than on Earth.

Although lava flow heat loss processes are such that no major differences between Mars and Earth are to be expected in terms of flow cooling rates and surface textures, the lower gravity causes cooling-limited flows to be longer, and dikes and vents to be wider and characterized by higher effusion rates. Taken together, these factors imply that we might expect compositionally similar cooling-limited lava flows to be about six times longer on Mars than on Earth. For example, a Laki-type flow would have a typical length of 200-350 km on Mars; this would permit the construction of very large volcanoes of the order of 500-700 km in diameter.

For strombolian eruptions on Mars, the main difference is that while the large particles will remain near the vent, the finer material will be more broadly dispersed, and the finest material will be carried up into a convecting cloud over the vent. This means that there would be a tendency for broader deposits of fine tephra surrounding spatter cones on Mars than Earth. On Mars, strombolian eruption deposits should consist of cones that are slightly broader and lower relative to those on Earth, with a surrounding deposit of finer material. Martian hawaiian cones should have diameters that are about a factor of two larger and heights that are correspondingly about a factor of four smaller than on Earth; central craters in these edifices should also be broader on Earth by a factor of up to at least five. Grain sizes in martian hawaiian edifices should be at least an order of magnitude finer than in terrestrial equivalents because of the enhanced magma fragmentation on Mars.

Differences in the atmospheric pressure and temperature structure cause martian plinian eruption clouds to rise about five times higher, for the same eruption rate, than terrestrial clouds. Essentially the same relative shapes of eruption clouds are expected on Mars as on Earth and so the cloud-height/deposit-width relationship should also be similar. This implies that martian fall deposits may be recognized as areas of mantled topography with widths in the range several tens to a few hundred km. A consequence of the lower atmospheric pressure is that martian plinian deposits of any magma composition will be systematically finer-grained than those on Earth by a factor of about 100, almost entirely sub-cm in size. Basaltic plinian eruptions, rare on Earth, should be relatively common on Mars. The production of large-scale plinian deposits may not signal the presence of more silicic compositions, but rather may be linked to the enhanced fragmentation of basaltic magma in the martian environment, or the

interaction of basaltic magma with ground water. The occurrence of steep-sided domes potentially formed by viscous, more silicic magma may be largely precluded by enhanced magma fragmentation. Pyroclastic flow formation is clearly inherently more likely to occur on Mars than on Earth, since eruption cloud instability occurs at a lower mass eruption rate for a given magma volatile content. For a given initial magma volatile content, eruption speeds are a factor of at least 1.5 higher on Mars, and so the fountains feeding pyroclastic flows will be more than twice as high as on Earth. Pyroclastic flow travel distances may be a factor of about three greater, leading to values up to at least a few hundred km. Martian environmental conditions thus operate to modulate the various eruption styles and the morphology and morphometry of resulting landforms, providing new insight into several volcanological problems.

REFERENCES: 1) M. Carr, *JGR, 78*, 4049, 1973; R. Greeley and P. Spudis, *RGSP, 19*, 31, 1981; G. Schaber, *JGR, 87*, 9852, 1982. 2) L. Wilson and J. Head, *Nature, 302*, 663, 1983; P. Mouginis-Mark *et al.*, *Mars*, 424, UA Press, 1992. 3) C. Hodges and H. Moore, *USGS PP-1534*, in press, 1993. 4) L. Wilson and J. Head, *JGR, 86*, 2971, 1981; J. Head and L. Wilson, *G&CA, 55*, 2155, 1992. 5) J. Head and L. Wilson, *JGR, 97*, 3877, 1992. 6) L. Wilson and J. Head, Mars: A review of volcanic eruption conditions and relationships to observed landforms, submitted to *Reviews of Geophysics* 1994.

Fig. 1. Diagrams of shallow structure of martian crust.

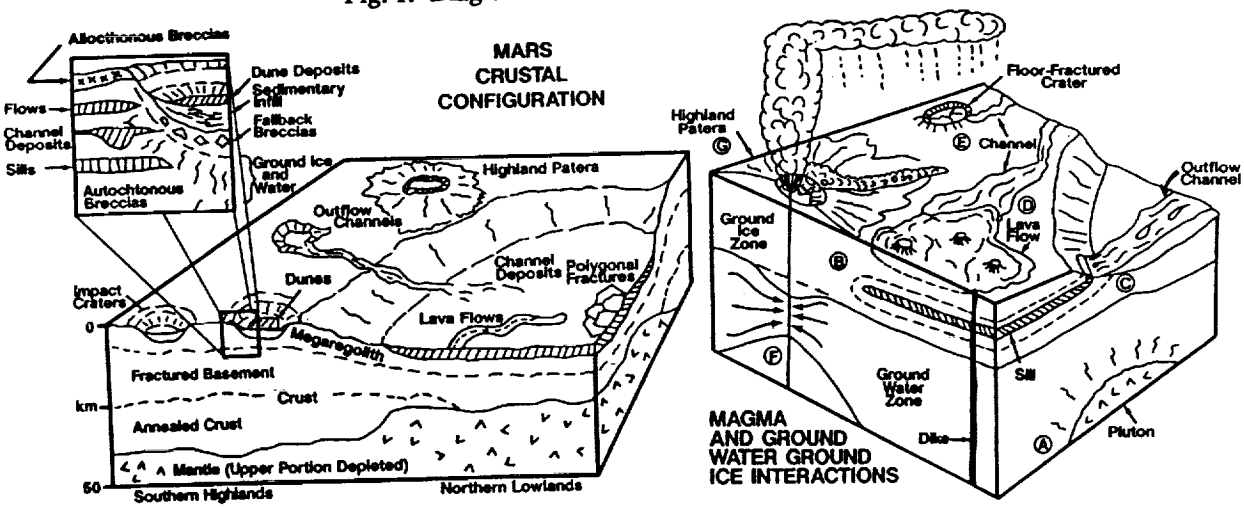

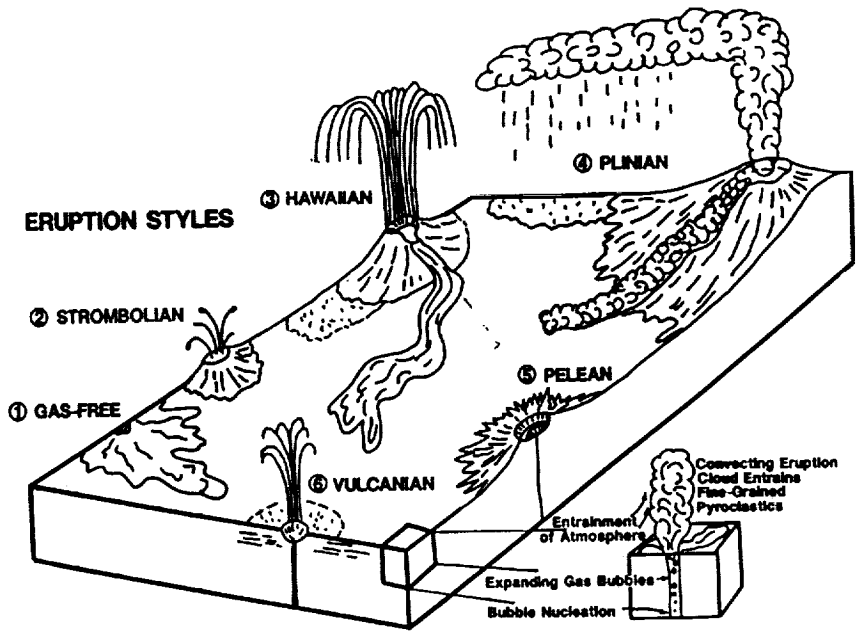

Fig. 2. Typical volcanic eruption styles on Mars.

CLAST SIZES OF BASALTIC EJECTA FROM EXPLOSIVE ERUPTIONS ON ASTEROIDS;

Lionel Wilson[1,2] and Klaus Keil[1] [1]Planetary Geosciences Division, School of Ocean and Earth Science and Technology, Univ of Hawaii at Manoa, 2525 Correa Rd, Honolulu HI 96822, USA [2]Environmental Science Div., Inst. of Env. & Biol. Sci., Lancaster Univ., Lancaster LA1 4YQ, U.K.

Abstract: Heating events took place during the early histories of many classes of asteroids to produce basaltic melts which would have collected in migrating veins and dikes [1]. The likely volatile (mainly CO and N_2) contents of these asteroids were ~ 1000 ppm [2]. This gas, expanding from high pressure in melt veins to the near-vacuum of the surface, would have disrupted the basaltic melt into liquid droplets to be ejected as pyroclasts in explosive volcanic eruptions. The maximum gas speed would have been high enough that eruption speeds of pyroclasts small enough to be locked to the gas motion by aerodynamic forces could readily have exceeded escape velocity on asteroids with radii less than ~100 km [3]. Here we explore the likely sizes and internal pressures of bodies of basaltic melt approaching the surfaces of asteroids and the consequent ranges of pyroclast sizes produced. We then calculate the terminal velocities of clasts with these sizes in the expanding gas streams and thus determine their individual launch speeds from eruption sites to establish if all of the available clasts were in fact able to reach escape speed. We find that clast sizes should commonly have been 30 μm to 4 mm, and that almost all of the clasts would have escaped unless asteroid volatiles contents were unusually low.

Partial Melt Formation in Asteroids: A few volume % partial melting in asteroids produces small (1 μm to 1 mm) melt veins with internal pressures of at least a few tens of MPa [2]. These veins can grow by cracking at their tips , and the gas bubbles which they contain lower the bulk densities of the vein fluids [1] to the extent that they were buoyant, behaving as though their densities were ~2000 kg/m^3 less that that of the asteroid matrix. In principle, therefore, such veins may migrate upwards to erupt at the surface, growing into dikes by capturing other veins as they do so [4].

Melt Migration: Isolated veinlets of a given half-length A will start to grow by cracking at the ends when the internal excess pressure, which increases as the degree of partial melting increases, exceeds a critical value D given by

$$K = D A^{1/2} \quad (1)$$

where K is the apparent fracture toughness of the matrix, ~1 MPa m$^{1/2}$. Large (~1 mm long) vein growth requires a driving pressure of D = 30 MPa, easily achieved for a few % partial melting [1]. Smaller veins accomodate larger internal excess pressures without growing, so when a small vein joins a larger one melt flows from the smaller to the larger [4], helping maintain excess pressure close to the value given by eq. (1). This process is counteracted when two similar-sized veins join tip-to-tip, the excess pressure decreasing to about 70% of the initial value [1].

As a vein grows vertically in a gravitational field, buoyancy forces cause the stress intensites at its upper (K^+) and lower (K^-) ends to become

$$K^+ = D A^{1/2} + 0.5 A^{3/2} [g (\rho_v - \rho_m)] \quad (2) \quad \text{and} \quad K^- = D A^{1/2} - 0.5 A^{3/2} [g (\rho_v - \rho_m)] \quad (3)$$

where g is the acceleration due to gravity, ρ_v is the density of the material in the vein and ρ_m is the density of the asteroid matrix. Thus, K^+ increases and K^-decreases as a vein containing buoyant melt grows, and so growth continues at the upper tip only until A reaches a critical length A_c at which K^- becomes equal to zero:

$$A_c = [2 D]/[g (\rho_v - \rho_m)] \quad (4).$$

The vein then migrates upwards at a speed dictated by the viscosity of the fluid within it. In practice, D decreases as A increases due to vein coalescence events. The extreme extent of driving pressure loss occurs when adjacent veins join together in pairs at their tips as soon as they grow. Let the initial driving pressure be D_0 and the initial vein length be A_0; also, let the driving pressure

Clast Sizes of Basaltic Ejecta from Asteroids: Wilson, L. and Keil, K.

reduce by a factor F (lying between 0.7 and 1.0) in each coalescence event. Then after n events, the driving pressure is $D = D_0 F^n$ and the vein length is $A = A_0 2^n$. If this value of A is identified with A_c, we can substitute into eq. (4) to get:

$$n = \ln\{[2 D_0]/[g (\rho_v - \rho_m) A_0]\} / \ln\{2/F\} \quad (5).$$

Table 1 shows values of n, D, A_c and dike width w for migrating dikes in an asteroid of radius 100 km for 4 values of F and a typical initial vein length of 2 mm and internal pressure of 30 MPa.

Discharge of Melt from Dikes: The lower end (D < 0.25 MPa) of the range of final driving pressures in Table 1 is so low that gas bubbles in the melt would form a froth that would collapse [5], isolating gas in the upper part of the dike and preventing explosive eruption of the bulk of the basaltic liquid. The fact that evidence for residual basaltic liquids in at least some asteroid interiors is lacking [3] then implies that pressures were commonly greater than ~ 0.25 MPa.

When a dike opens at an asteroid surface it discharges melt under choked flow conditions at the exit via the rapid downward passage of an expansion wave [6]. We used a treatment based on [7] to solve for the fluid motion in the region above the level at which the gas volume fraction exceeds 75% and the melt disrupts into a mixture of gas and liquid droplets, where the product of the gas density, viscosity and velocity determine the size of the largest clast which can be supported by the gas flow. The ratio of initial pressure in the fluid below the expansion wave to pressure at the level where disruption takes place determines the amount of gas bubble expansion. The initial sizes of the bubbles will reflect the initial sizes of the pore spaces in which the gas is trapped, assumed to lie in the same (1 μm to 1 mm) range as the matrix grains. The final sizes of the largest bubbles will determine the sizes of the largest liquid droplets (i.e. the erupted pyroclasts) which will be formed in the disruption process, since these will consist of the liquid bodies trapped between closely packed large bubbles. We find that the expected pyroclast sizes are insensitive to the size of the asteroid and range from ~ 30 μm to ~ 4 mm. However, the sizes of clasts supported and transported upwards from the fragmentation level depend strongly on the asteroid radius and very strongly on its gas content. For driving pressures > 1 MPa and gas contents > ~ 500 ppm, all the pyroclasts can be lofted from the fragmentation level and reach a large fraction of the gas speed and escape. However, for gas contents < 300 ppm, it becomes difficult to erupt all the pyroclast size range, and veins of degassed basaltic material should be retained within the asteroid. Again, the apparent absense of such veins implies that gas contents were commonly this high.

References: [1] Keil, K. & Wilson, L. (1993) EPSL 117, 111. [2] Muenow, D.W., Keil, K. & Wilson, L. (1992) GCA 56, 4267. [3] Wilson, L. & Keil, K. (1991) EPSL 104, 505. [4] Sleep, N.H. (1988) JGR 93, 10255. 5] Vergniolle, S. & Jaupart, C. (1990). JGR, 95, 2793. [6] Kieffer, S.W. (1982) pp. 647-723 *in* Satellites of Jupiter, Univ. Ariz. Press. [7] Giberti, G. & Wilson, L. (1990) Bull. Volc. 52, 515.

Table 1. Lengths, mean widths & internal excess pressures in dikes reaching the surface of an asteroid of radius 100 km when the dikes form by the coalescence of veins initially 2 mm long containing melt at a pressure of 30 MPa.

Pressure reduction factor, F, at each coalescence step.	0.6	0.7	0.8	0.9	0.95
Average number of coalescence events, n, before dike migrates.	16.21	18.59	21.30	24.45	26.2
Excess pressure in dike when dike migration starts.	7.59 kPa	39.5 kPa	0.259 MPa	2.28 MPa	7.8 MPa
Half-length of dike when migration starts.	75 m	395 m	2586 m	22.8 km	78.2 km
Average width of dike.	110 μm	3.1 mm	0.13 m	10.4 m	122 m

Lunar LIGO and Gravitational Wave Astronomy on the Moon;

Thomas L. Wilson[1] and Norman LaFave[2]; [1]NASA Johnson Space Center, Houston, Texas 77058. [2]Lockheed Engineering and Sciences Co., Houston, Texas 77058.

Gravitational wave astronomy continues to be one of the exploration concepts under consideration in NASA's strategy for conducting physics and astrophysics from the lunar surface. As with other proposals for new concepts in science and astronomy from the Moon, this one has a number of very interesting features which need to be developed further in order to assess them adequately. The possibility of robotic deployment of a gravitational wave antenna on the Moon in a triangular configuration and the question of closure on the third interferometer leg are discussed here.

The preliminary proposal [1,2] that the Earth-based multi-LIGO system [3-6] can be augmented with a Lunar LIGO appears promising. This consists of emplacing a modest LIGO (Laser Interferometer Gravitational Wave Observatory) optical system [7] on the Moon, proving to be a simple and advantageous application in the vacuum environment of the lunar surface. Emplacement could be accomplished using unmanned robotic landers [8] such as the recent Artemis project [9,10], or by a manned landing program.

The distance between the Earth and Moon provides a long parallax baseline with terrestrial antennas for locating the sources of a gravitational event. Given that the lunar vacuum eliminates the need for long evacuated tunnels, a minimal Fabry-Perot antenna could be placed on the Moon using three robotic landers, one containing the laser source, the beam splitter, the detector, recycle mirrors, cavity mirrors, and other optics. The other two landers would contain the end mirrors of the interferometer arms (Figure 1 and 2), and provide closure phase along the third leg [11,12].

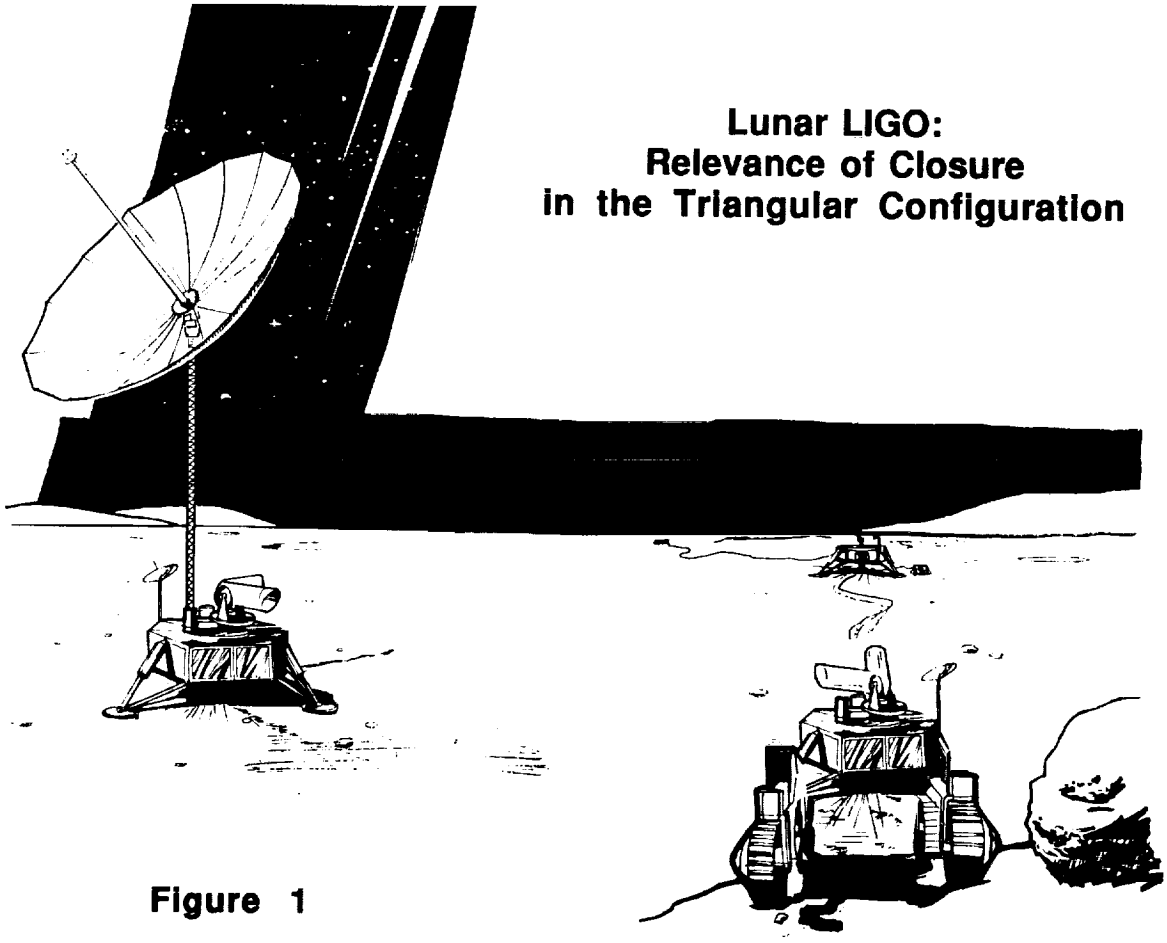

Figure 1

Lunar LIGO, Wilson, T.L., and LaFave, N.

The lack of arm enclosures allows the arms to be extremely long, limited only by a lunar radius of 1738 km. A judicious choice of landing sites could allow for longer arms by taking advantage of local topography. The arms could be easily altered by moving the landers containing the end mirrors.

It is possible that the same three landers could be used to assemble a set of three redundant arrays employing the equilateral concept [13] in Figure 2b. There would be a 13%

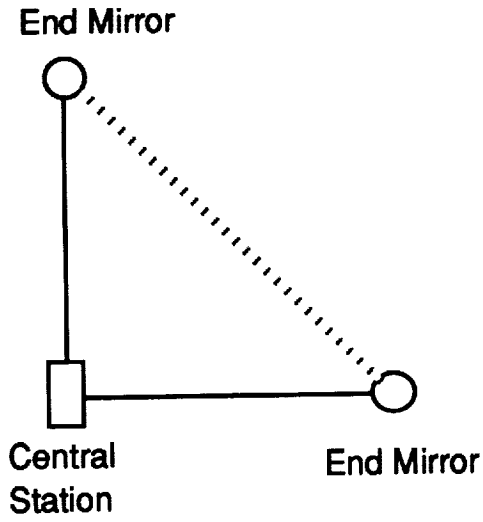

Figure 2a

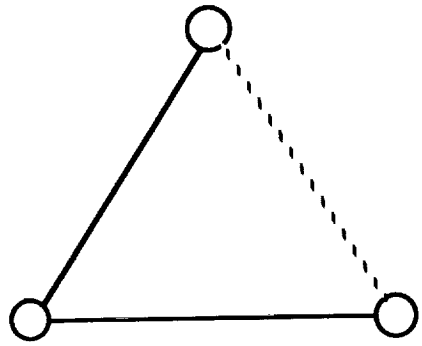

Figure 2b

reduction in the signal strength due to the 60° angle between the arms, but this is not prohibitive. Each lander would have a laser/detector/beam-splitter/ assembly and two end mirrors. This allows the observatory to be redundant and detect both wave polarizations. On the Earth, the third "leg" would require the costly construction and evacuation of a third arm. This is achieved for free on the Moon.

An advanced, man-tended version of the Lunar LIGO would allow for even more flexibility. Detectors and mirrors could be repaired and/or upgraded by the lunar base personnel. The antenna could be actively monitored and seismic data could be screened using gravimeters to aid in the data's noise analysis. For instance, a large array of antennas could be built to allow for better spurious signal elimination by coincidence. A large number of antennas would be easier to build and maintain on the Moon than on the Earth due to the lack of evacuated tunnels.

In conclusion, this investigation shows that a lunar-based Fabry-Perot gravitational wave antenna would provide a valuable complement to the Earth-based systems, both for conclusive, first detection and for continued gravitational wave astronomy. Furthermore, due to unique features of the lunar environment, the life-cycle costs could be competitive with Earth-based antennas.

References

[1] LaFave, N., and Wilson, T.L., *24th Lunar and Planetary Science Conference*, Vol. 2, 841 (Lunar and Planetary Institute, Houston, 1993). [2] LaFave, N., and Wilson, T.L., *23rd Lunar and Planetary Science Conference*, Vol. 2, 751 (Lunar and Planetary Institute, Houston, 1992). [3] Schutz, B.F., *Class. Quan. Grav.* **6**, 1761 (1989). [4] Schutz, B.F., and Tinto, M., *Mon. Not. Roy. Astron. Soc.* **224**, 131 (1987). [5] Tinto, M., and Gürsel, Y., *Phys. Rev. D* **40**, 3884 (1989). [6] Tinto, M., and Dhurandhar, S., *Mon. Not. Roy. Astron. Soc.* **236**, 621 (1989). [7] Abramovici, A., *et al.*, Science **256**, 325 (1992). [8] LaFave, N., and Wilson, T.L., In *Space '94* (Amer. Soc. Civil Engineers, New York, 1994). [9] Artemis, In *LPI Workshop on Early Robotic Missions to the Moon* (Lunar and Planetary Institute, Houston, February 4, 1992) [10] *Artemis Phase 2 Study Results* (NASA JSC New Initiatives Office, March 10, 1992). [11] Jennison, R.C., *Mon. Not. Roy. Astron. Soc.* **118**, 276 (1958). [12] Cornwall, T.J., *Science* **245**, 263 (1989). [13] Winkler, W., Maischberger, K., Rüdiger, A., Schilling, L., and Shoemaker, D., In *Proceedings of the Fourth Marcel Grossmann Meeting on General Relativity*, Ruffini, R., ed., 621 (North-Holland, New York, 1986).

Advanced Technology Lunar Telescope; **[1]Thomas L. Wilson, [2]Wei-Kan Chu, and [3]Peter C. Chen; [1]NASA Johnson Space Center; [2]Texas Center for Superconductivity, University of Houston, Houston, Texas. [3]Computer Sciences Corporation, Calverton, Maryland.**

A new type of telescope pointing system designed specifically for space and lunar applications will be discussed, based upon a prototype advanced technology telescope [1,2] under investigation. The focus here will be the system of hybrid superconductor magnetic bearings (HSMB) used to provide isolation support and steering functions. HSMB's are combinations of high temperature superconductors, permanent magnets, and coils, being passive (requiring no power), noncontact, and essentially frictionless. These also are well suited to long-term unattended operation in the space environment. The characteristics of these subsystems, their expected behavior under space vacuum, and thermal and radiation environments are discussed.

The prospect of important new technology emerging from the discovery in physics of high-temperature superconducting (HTS) materials [3,4] has important implications in its space applications. A recent record-high HTS temperature was 150° K [5], and that has since reached 164° K. Although one common goal of research in HTS material is to find a "room-temperature" superconductor, it has become increasingly obvious that the deep-space "cold-soaked" environment of many spacecraft is within reach of several of the existing record-high HTS temperatures.

One pertinent application would be the Moon or lunar orbit. A summary of the lunar surface temperature environment is given in Table I.

Table I. Approximate Lunar Surface Temperatures

	Apollo 15	Apollo 17[6]	Earth-Based Measurement[7]	Polar[8]
Maximum	374° K	384° K	380° K	84° K
Minimum	92° K	102° K	104° K	

From these data, one can surmise that the ambient thermal environment supports HTS material during the lunar night, but that a telescopic HTS system would have to be actively cryogenic in order to operate during the lunar day. Alternatively, the system could be totally passive and forego daytime operations, provided there were protective conventional bearings (pseudo-bearings) within the design when the HTS components cycle in and out of their superconducting state. For the polar case in Table I, within permanently shadowed craters or with appropriate light baffling/shielding, the ambient temperature may be as low as 40°-50° K.

Based upon early, preliminary prototypes of Meissner quadrupole bearings [9], hybrid superconductor magnetic bearings (HSMB's) have been designed, and are illustrated in Figure 1 for a telescope's azimuth. The proposed ultra-lightweight telescope utilizes such HSMB's. The related telescope structure is made from very lightweight but stiff silica-alumina composite material recently developed by NASA Ames. This will reduce the mass of the instrument considerably, which is estimated to be <20 kg for a fully steerable 1-meter telescope.

Advanced Lunar Telescope, Wilson, T.L. *et al.*

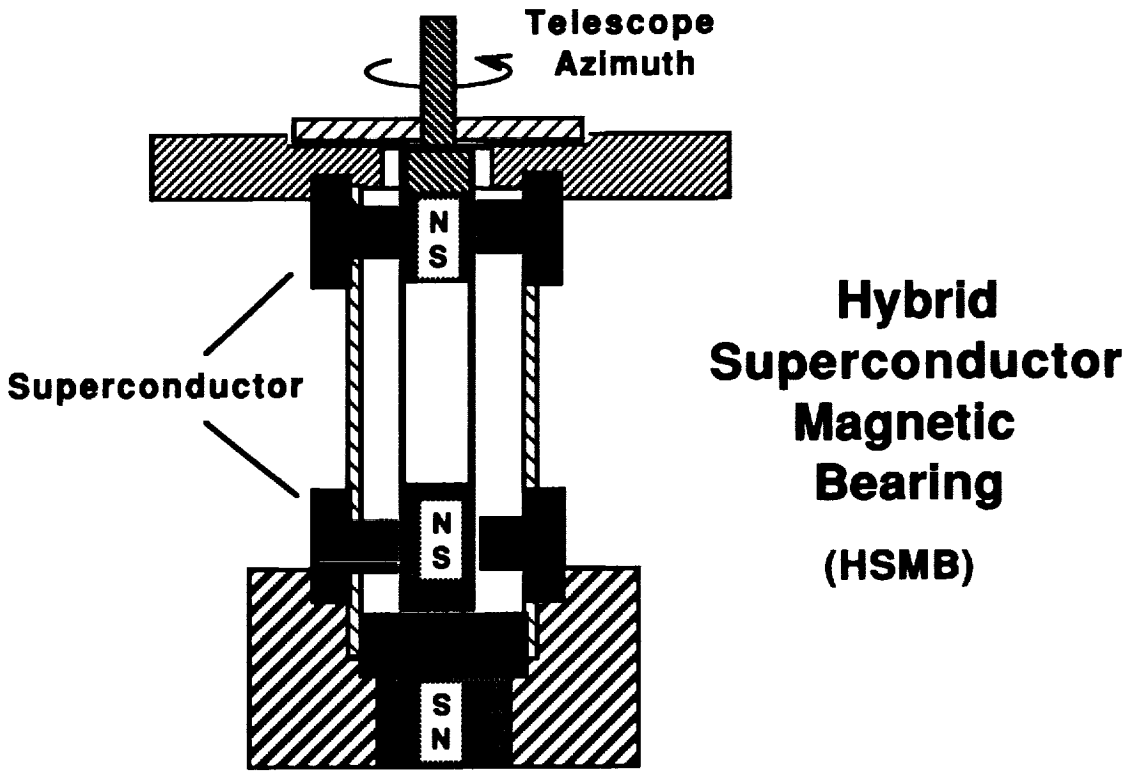

Figure 1

The HSMB's in Figure 1 comprise the three-degree-of-freedom actuation system for pointing the instrument in azimuth and elevation. In the passive thermal mode, they require no power and are frictionless in a vacuum (since only an atmosphere can apply a frictional drag). Due to the light weight or mass of the instrument, a highly accurate pointing capability is envisioned by employing a CD-ROM-drive or disk-drive type of actuation feedback control system on the HSMB's.

In conclusion, this discussion shows that an ultra-lightweight superconducting telescope is a feasible application for several space-based environments. Its reduction in weight and inertia is consistent with the proposal for smaller automated robotic lunar telescopes and light-weight beryllium mirrors, while its improved bearing design preserves the small, classical research telescope as a viable candidate alongside transit concepts [10] or Hubble era technology [11].

References

[1] Chen, P.C., *et al.* in *Space '94* (Amer. Soc. Civil Engineers, New York, 1994). [2] Chen, P.C., *et al.*, "Advanced Technology Lunar Telescopes: I, II, and III" (Abstracts, American Astronomical Society Meeting, January 11-15, 1994). [3] Wu, M.K. *et al.*, *Phys. Rev. Lett.* **58**, 908 (1987). [4] Geballe, T.H., Science **259**, 1550 (1993). [5] Chu, C.W., *et al.*, Nature **365**, 323 (1993). [6] Langseth, M., *et al.*, in *Apollo 17 Preliminary Science Report*, NASA SP-330, P. 9-1 (Washington, 1993). [7] Potter, A.E., and Wilson, T.L., eds., *Physics and Astrophysics from a Lunar Base*, AIP Conference Proceeding **202** (American Institute of Physics, New York, 1990). [8] Heiken, G., Vaniman, D., and French, B.M., *Lunar Sourcebook*, 34 (Cambridge University Press, New York, 1991). [9] Chu, W.-K., unpublished presentation at JSC (June 16, 1993). [10] McGraw, J., in *Astrophysics from the Moon*, Mumma, M.M., and Smith, H.J., eds., AIP Conf. Proc. **207**, 433 and 464 (American Institute of Physics, New York, 1990). [11] Wilson, T.L., Nature **302**, 310 (1990).

NUMERICAL SIMULATION OF SCATTERING BY DISCRETE OBJECTS; P.B. Wong, R.A. Simpson, and G.L. Tyler, Center for Radar Astronomy, Stanford University, Stanford, CA 94305-4055.

Radar scattering by planetary surfaces is controlled both by the properties of the bulk surface material and also by the composite response of discrete objects on or within the surface — if they meet certain criteria for size and electrical properties. In many cases (*e.g.*, nadir reflection to an orbiting altimeter) estimates of the bulk surface properties are sufficient for simple interpretation of backscatter echoes. For more complex surfaces or for surfaces viewed obliquely, an understanding of both the population and behavior of discrete scattering objects becomes important. Scattering by discrete objects can be estimated using numerical models, though there remain significant computational limitations. We have developed a model which allows calculation of scattering in relatively general two-dimensional situations. The model has been tested and yields answers to within a few percent of analytic solutions, where those exist.

Inferring the morphology or geology of a remote surface using radar data requires an understanding of how the radar's electromagnetic waves interact with the surface material. For smooth surfaces, the Fresnel reflection coefficient and knowledge of the angle at which the wave hits the surface may be sufficient. As the surface becomes rougher (relative to the radar wavelength), the undulations change the phase of the echo signal; models such as those by Hagfors [1] have proved useful for interpretation. In extreme cases, when the texture of the surface is rough compared with the wavelength or when the action of discrete elements (*e.g.*, rocks) must be considered in addition to the bulk properties of the surface, there are no satisfactory analytical models.

Instead, with careful modeling, one can accurately simulate the interaction of electromagnetic waves with the surface numerically. Using techniques such as the Finite-Difference Time-Domain approach (FDTD), it is then possible to calculate the fields over a grid at an instant in time and then propagate those conditions to a later instant with due regard to applicable physical laws. The computational complexity of such problems increases rapidly with the size of the region being studied, but we have successfully demonstrated the viability of this approach with two-dimensional discrete objects of a few wavelengths at a dielectric interface. This should prove useful for many important geological cases.

The problem is posed by identifying an object (Figure 1, right — in this case not necessarily geologic) resting on a dielectric half space. Over a region which includes the object, we define a computational grid having both an inner and an outer component. The boundary of the inner region has properties which allow it to "launch" and absorb electromagnetic plane waves. In the absence of the discrete object, all wave activity can be accounted for by the boundary conditions of the inner region. Introduction of the discrete object represents a (significant) perturbation of the fields. The problem then reduces to a search for boundary conditions on the outer region — that is, a description of the field produced by the scattering object. Once the boundary conditions for the outer region have been obtained, those can be used to propagate the waves to great distances by Huygens' equivalence principle.

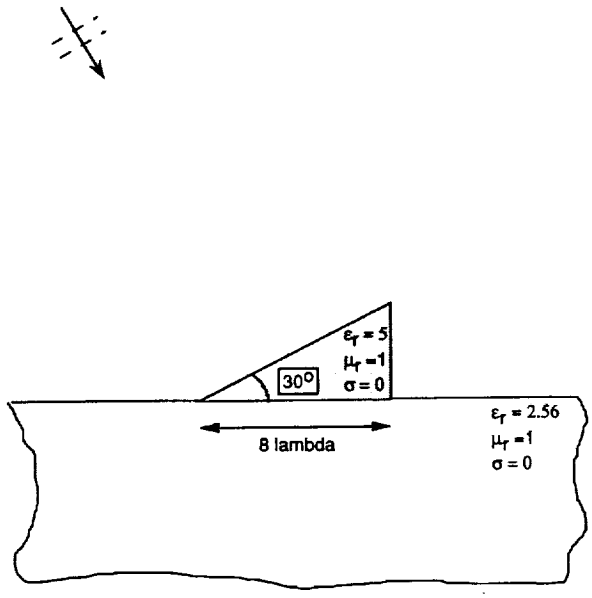

We have modeled the scattering behavior of a wire two wavelengths above a dielectric surface and find that the scattering pattern agrees to within 5% of the analytic solution for the same problem [2]. A wire buried in the dielectric has a computed scattering pattern that never deviates more than 3% from the analytic solution. These results are representative for grids with cell dimensions of 0.02-0.05 times the wavelength using what are known as "second-order absorbing boundary conditions" [3]. They indicate that the computational model meets requirements for simulating scattering by planetary rough surfaces.

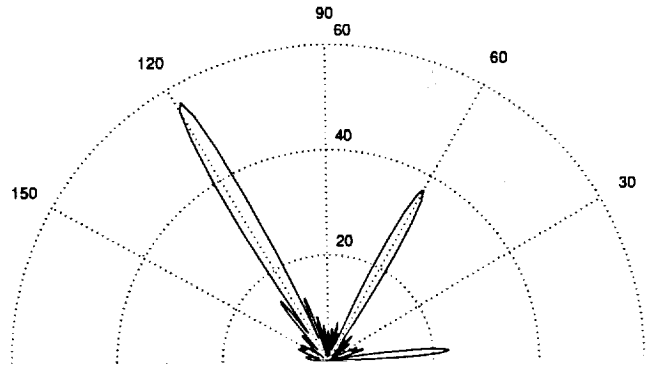

Figure 2 (left) shows the scattering pattern for the wedge-like object illustrated in Figure 1. A strong backscatter lobe is apparent along the 120° azimuth line. The secondary lobe at 60° is an artifact of the computation, representing the "absence" of specular scattering from the surface area now occupied by the wedge.

Neither the wire nor the wedge are likely candidates for discrete objects on planetary surfaces, but the results shown here illustrate the degree to which this tool yields useful results. A set of calculations can now be carried out on a family of 2-D shapes to investigate their behavior as a function of size, shape, and electrical properties. Beyond that, it would then be desirable to generalize the numerical model to handle three-dimensional objects, but the computational requirements and the algorithm complexity increase significantly.

[1] Hagfors T.(1964) JGR, 69, 3779.
[2] Gurrola E. (1993) private communication.
[3] Mur G. (1981) IEEE Trans. EC-23, 377.

A REMOTELY OPERATED PLANETARY SCIENCE OBSERVATORY TO ENHANCE SPACE EDUCATION.

Charles A. Wood and Paul Abell, Department of Space Studies, University of North Dakota, Grand Forks, ND 58201

Planetaria and small observatories are traditional facilities for providing hands-on learning experiences for astronomy students. At the University of North Dakota we have established an observatory with a similar goal but with two significant differences. First, our Department of Space Studies, an interdisciplinary M.S. and undergraduate minor program combining space science and space policy, has a focus on planetary science, not traditional stellar and nebular astronomy. Second, the severity and duration of North Dakota winters limit the time that students can observe from inside the dome. Considering these two factors we have constructed an observing facility which may be of interest to other educators. In particular we have learned a number of lessons concerning observatory design, operations, and appropriate science projects.

Observatory Design and Instrumentation: Teaching at a small state university is reminiscent of living in a third world country. Only a small amount of money and little out of the ordinary technical advice are available. Because of the high cost of a commercial dome (~$35k plus $10k for concrete slab and pier), we chose to have the UND Plant Services group design and build our dome. This had the positive aspects that total cost would be lower ($25k), we could influence the design, and the builder would always be nearby for repairs and to correct any inevitable flaws. We now appreciate that the negative aspects of our decision are also substantial. Neither Plant Services nor we had ever designed or built a dome before and did not fully understand the potential complexities of a rotating building with a floor to ceiling slit in the wall. The dome is converted from a hemispherical silo top, 24' in diameter and 14' high, mounted on a 30' concrete slab. The 24" wide slit is raised and lowered by a garage door opener mechanism, and the dome rotates on 24 nylon wheels using a chain-drive mechanism.

We selected an 18" newtonian reflecting telescope (the NGT-18 made by JMI of Evergreen, Colorado) because of its modern design, integrated computer operation, and excellent value ($10k). A 24" wide pier supports the telescope and extends 4' below ground level. We use the telescope with a 375 x 242 pixel CCD camera with computer-controlled filter wheel (ST-6 camera from SBIG in Santa Barbara, California; $3.5k).

An critical part of our observatory complex is a heated trailer 50' to the west of the dome. An underground conduit brings electrical connections from the dome into an observatory control room in the trailer. Presently, from the control room we can rotate the dome, use electric slow motion controls to refine the pointing of the telescope, and acquire and display CCD images. But we must go into the observatory to open and close it, to initially set the telescope on an object of interest, and to repoint the telescope to another portion of the sky. These functions can not be remotely controlled with the present telescope and dome. An intercom facilitates aiming the telescope on the object of interest.

Science Goals: Although any small university observatory will be used for a variety of public and course-related observing sessions where little more than an eyepiece is necessary, our goal was to define significant research projects with publication potential. Our main research goal is the discovery and characterization of near Earth objects (NEOs - asteroids and comets). This is an important and active field of planetary research for a number of reasons. First, NEOs are small, relatively unmodified (compared to planets and moons) fragments of material left over from the formation of the solar system. Second, near Earth asteroids (NEAs) especially, may be immediate parent bodies of meteorites. Third, NEOS come closer to the Earth than any other celestial body (some pass inside the Moon's orbit!) and are very accessible objects for telescopic and radar investigations and future spacecraft missions. Fourth, NEOs are the projectiles that occasionally hit the Earth, forming impact craters and apparently sometimes dramatically affecting terrestrial life and geology.

In order to discover NEAs we have devised a search strategy that is similar to that pioneered by the Spacewatch project at the University of Arizona. We use a CCD camera at the prime focus of our 18" f/4.5 reflector to image strips of the sky near the opposition point (opposite the sun). A one minute exposure images objects as faint as 18th magnitude, and another minute is required to read the image from the CCD chip onto a computer hard drive. The telescope is then slewed to an adjacent part of the sky and the procedure is repeated continually for approximately one hour. Next, the telescope is slewed back to the original location in the sky and a second strip of images is acquired. At the completion of the night's observing run the stored images are transferred to floppy disks and brought to campus for analysis. The next day each pair of images is coregistered and subtracted (using Photoshop on a Macintosh computer). Stars and other objects which don't move disappear, but asteroids are betrayed by their movement between the two exposures. Based on the size of our telescope and CCD chip we

OBSERVATORY FOR SPACE EDUCATION: Wood, C.A. and Abell, P.

expect to discover one NEA during each 300 hours of observing.

The second part of our program is the characterization of recently discovered NEAs. Most NEAs are so small that they can be easily observed only when near the Earth. Thus if measurements of physical properties are not made during the discovery apparition it may be another 5-10 years before the chance occurs again. Two measurements are important, and possible for a small observatory like ours. First, acquisition of a CCD image through each of the U, B, and V filters provides information on the object's brightness in three wavelengths, allowing classification of its spectral type. Second, a series of brightness measurements over a few hours on a few nights permits determination of the rotation period of the object.

Progress and lessons: The trials and tribulations of this project have been far greater than anticipated, but have increased solidarity between the faculty and students who have been involved. The dome and slit are underpowered and have required a succession of ever larger and more expensive motors. The slit is not weather proof when closed, and telescope and equipment must be protected from wind-blown snow which piles up inside the dome. Vandals have broken all the windows of the trailer and stolen computers and other equipment. Finally, our old trailer was invaded by deer mice during the summer, causing it to be placed off limits due to a hantavirus scare.

If starting over we would be tempted to pursue theoretical astronomy. But if an observing project is envisioned our recommendation would be to find adequate funds to buy a commercial dome that works from the first night. Secondly, we have found that our newtonian design telescope has considerable balance problems when the 4-5 pound CCD camera and filter wheel are attached to the eyepiece holder. A fork mounted schmidt-cassagrain telescope would be easier to add equipment to.

We are having some successes. Two students have completed independent study projects for their M.S. degrees using the telescope, and two others are underway. We are incorporating planet observing sessions into undergraduate and graduate space science courses that were previously classroom-bound. The observatory will also be used by classes in the geology and physics departments and has become the stimulation for the formation of an astronomy club. We have also used the observatory and a weather satellite receiving station as sources of digital data for image processing experiments and as the core for a successful NSF-funded equipment grant to integrate computer based projects in undergraduate teaching. And we still hope to discover an asteroid or two.

The observing facility has been built and outfitted with the support of the North Dakota Space Grant Program, to which we are very grateful.

AN ASTEROID FAMILY AMONG THE NEAs?

Charles A. Wood, Ron Fevig and John Nordlie, Department of Space Studies, University of North Dakota, Grand Forks, ND 58201

A cluster of asteroids has been recognized near $a = 2.18$ AU among the Near Earth Asteroids. Named after its best studied member, the 1981QA family consists of 7 tightly clumped members that are significantly paired according to the D discriminent. These core members are surrounded by 13 additional asteroids with similar orbital elements. Intriguingly, at aphelion members of the 1981QA family pass near the Themis family in the main asteroid belt.

The majority of main belt asteroids travel in independent orbits, but a number of clusters have been discovered in which the members have similar orbital elements. These so-called families are assumed to be fragments from collisions in the asteroid belt; over time, perturbations should disperse family members into 'sporadic' asteroids with totally independent orbits. Apparently there has been little study of possible families among the Near-Earth Asteroids (NEAs), but Drummond [1] discovered that some NEAs have similar orbits and travel in streams that are probably sources of meteors. Since Drummond's work many discoveries have increased the number of NEAs (~280) sufficiently to allow more thorough searches for families among the Earth approaching asteroids.

Valsecchi and others [2] have reviewed definitions and techniques used in prior searches for families among main belt asteroids. In terms of orbital dynamics they note that, "an asteroid family is constituted by a group of asteroids whose proper elements a, e, and i appear to form a cluster distinguishable from the background..." They also added a constraint based on assumptions of family origins: "...these asteroids are genetically related because they come from the disruption of a larger parent body." Proper elements used in the main belt investigations have had the affects of planetary perturbations removed, but NEAs travel on chaotic orbits and have no meaningful long-term proper elements [2]; thus we use osculating elements which change over time. Close approaches to planets can rapidly randomize orbital elements of NEA family members, thus if any NEA families did form by collisions they may only be identifiable for times short compared to the dynamic lifetimes of NEAs.

Our listing of orbital elements of NEAs comes from a compilation by Helin (1993 preprint), augmented by more recent discoveries announced in the *Minor Planet Electronic Circulars*. Actual identification of main belt families has been accomplished by two means: formal computational searches and visual inspection of a, e, i graphs. We first employed the latter technique and then also calculated Southworth's D criteria [3] for each asteroid pair. A problem with the D criteria is that no one knows what a limiting value is in order to accept a clustering as a family. Lindblad and Southworth [3] used D = 0.020; following their recommendation we corrected for sample size and derive a critical value of D = 0.036.

Examination of a-i and a-e distributions for 280 NEAs reveals a number of apparent concentrations of two to four NEAs, some having D<0.036. Most conspicuous, however, is a cluster of asteroids centered near $a = 2.18$ AU, $e = 0.43$, and $\sin i = 0.14$. No other similar size cluster exists among the presently known NEAs. Is this NEA clustering comparable to those accepted for families in the main belt asteroids?

There is much disagreement of what constitutes a family for main belt asteroids, but following the examples given by Chapman et al [4] we accept a group as a family if their orbital elements cluster within a range of 0.07 AU, 0.04, and 0.025 in a, e, and $\sin i$ space, respectively. The NEA group near $a = 2.18$ contains 7 asteroids within this small volume, and 7 more closely surround them in a larger volume defined by a range of a, e, and $\sin i$ of 0.11 AU, 0.05, and 0.07. A more diffuse halo of 6 additional NEAs envelopes these central groups. Six of the 7 asteroids of the inner core group are involved in pairings where the D value <0.036. This core group contains one NEA recognized by Drummond [1] as part of his looser stream, "Association I".

We propose that the innermost NEAs constitute a family (which we christen the 1981QA fam-

ily, after the best known member); including the slightly dispersed extra members makes it an extended family. The third, halo group,are second cousins, maybe twice removed. The members of the central family and extended family (below the line) are listed in the table; most are recent discoveries and do not yet have measured physical properties. Other than brightness (H), only 1981QA has any known properties. With the present lack of data it is impossible to evaluate if the putative family members have similar spectral properties, and hence could have collisionally evolved from a common parent. As a challenge to observers we propose that the majority of these NEA family members will have similar spectral types. Note that in the proposed nomenclature of Farinella et al [5] our core group would be a "cluster" or a "type II family."

The existence of a family within the NEAs may be explained by a collision with another asteroid when an original parent NEA passed through the main asteroid belt. With an average a = 2.18 and e = 0.43, the proposed parent would have Q = 3.12 and thus would pass through nearly all of the main belt. Interestingly, this Q is near the average a for the Themis family (2.14 AU) of main belt asteroids. The obvious speculation that a single collision formed both the Themis family and ejected the 1981QA family into its present orbit is flawed by the observation that although 1981QA has a somewhat uncertain spectral type (QRS; [6]), it is, however, distinctly different from the C types that dominate the Themis family (C.R. Chapman, pers. comm. 1994).

The recognition of an asteroid family among the NEAs provides, if the reality of the grouping is accepted, a family composed of much smaller diameter members than any known in the main belt. Also, the 1981QA family is presumably much younger than the main belt examples, because the dynamical lifetime of its members is only a few hundred million years, and the rate of orbital randomization is higher. 1981QA itself has a rotation period of 148 hrs - one of the longest known [6]. Binzel et al [7] summarize reports that long periods may be due to a torquing by a companion satellite, which is most likely to be captured during a collision. Thus, the 1981QA family and extended family may represent the orbitally coherent fragments from a relatively recent collision. The perihelion distances for these Amor asteroids probably keep them from interacting with the Earth, but they may be a contemporary source of meteorites on Mars.

References:

[1] Drummond, JD (1991) *Icarus 89*, 14-25. [2] Valsecchi, GB et al (1989) in *Asteroids II* (ed. by Binzel, Gehrels, and Matthews), Univ. of Arizona Press, 368-385. [3] Lindblad, BA and Southworth, RB (1971) in *Physical Studies of Minor Planets* (ed. Gehrels), NASA SP-267, 337-352. [4] Chapman, CR, et al (1989) in *Asteroids II* (ed. by Binzel, Gehrels, and Matthews), Univ. of Arizona Press, 386-415. [5] Farinella, P et al (1992) in *Asteroids, Comets, Meteors 1991* (ed. by Harris and Bowell), 167-170. [6] McFadden, L Tholen, DJ and Vedder, GJ (1989) in *Asteroids II* (ed. by Binzel, Gehrels, and Matthews), Univ. of Arizona Press, 442-467. [7] Binzel, RP et al (1989) in *Asteroids II* (ed. by Binzel, Gehrels, and Matthews), Univ. of Arizona Press, 416-441.

Design	q	a	e	sin i	H mag
1990 TR	1.21	2.14	0.437	0.138	14.5
1981 QA	1.19	2.15	0.448	0.146	16.7
1988 PA	1.28	2.16	0.407	0.143	17.5
1990 OA	1.25	2.16	0.422	0.136	17.0
1992 OM	1.30	2.19	0.408	0.143	16.0
1990 KA	1.25	2.20	0.433	0.132	16.5
1991 RJ2	1.26	2.21	0.429	0.155	19.0
1986 NA	1.17	2.13	0.450	0.181	21.0
1988 NE	1.21	2.18	0.444	0.173	18.5
1992 SZ	1.18	2.18	0.460	0.161	20.0
1992 JE	1.18	2.19	0.463	0.102	16.0
1992 AE	1.24	2.20	0.436	0.111	15.5
1993 FS	1.28	2.23	0.425	0.175	20.0
1991 VB	1.32	2.24	0.410	0.111	17.0

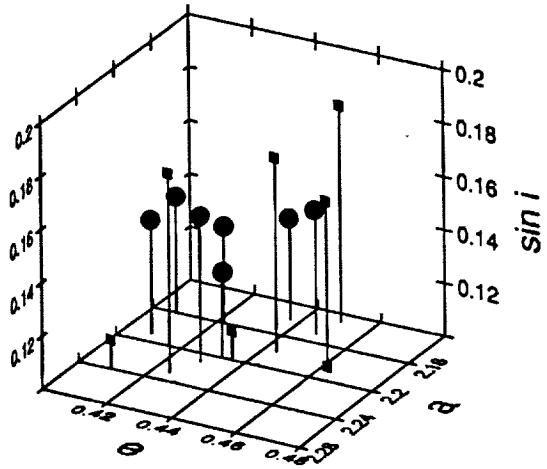

OCCURRENCES OF LOW-EMISSIVITY SURFACE MATERIAL AT LOW ALTITUDES ON VENUS: A WINDOW TO THE PAST; John A. Wood, Harvard-Smithsonian Center for Astrophysics, Cambridge MA 02138

A few craters at plains level on Venus have low-emissivity material in their floors and ejecta. At this altitude the stable weathering product has magnetite as its Fe mineral, and it should display high emissivity. Apparently the craters exhumed pyritic deep crustal material, which has not yet weathered to the stable assemblage. Deep, old crustal material that was weathered by a low-SO_2 atmosphere prior to the ~0.5 Gy resurfacing event would contain pyrite as its Fe mineral.

The radiothermal emissivity of surface material on Venus tends to be high (>0.7) at low altitudes, *i.e.*, over most of the planet, but low (<0.7) on mountain summits. The low-emissivity character of material at high altitudes has been attributed to a mineralogical composition, specifically the presence of the mineral pyrite (FeS_2), that gives it a high bulk dielectric constant [1]. Klose *et al.* [2] showed that, for a plausible atmospheric f_{O2}, the distribution of low- and high-emissivity surface material could result from the position of a phase boundary that controls the composition of the thermodynamically stable weathering product. At high altitudes (hence low temperatures) most Fe resides in the semiconductor mineral pyrite, which is abundant enough to give the bulk surface material (acting as a loaded dielectric) the required high dielectric constant. At low altitudes (high temperatures) the stable Fe mineral is magnetite (Fe_3O_4), which is also a semiconductor but not present in great enough abundance to impart a high dielectric constant to the bulk soil.

A puzzling exception to the above situation is the observation that the floors and ejecta blankets of some impact craters in the plains, such as Boleyn, Stanton, Stuart, and Mead, display anomalously low emissivities [3,4,5]. It appears that the craters excavated high-dielectric-constant crustal material from depth. This raises the question of the expected nature of Venus crustal material at depths of several km.

There is no reason to think the crust to the depths reached by these ≤280-km-diam. craters consists of other than a stacked sequence of old basaltic lava flows. However, primary basalt on Earth does not have an intrinsically high dielectric constant; most of the Fe in igneous basalts on Earth and probably also on Venus occurs in the $FeSiO_3$ components of pyroxenes, not as semiconducting Fe minerals. It is possible that the flows are no longer primary igneous basalts, but were deeply weathered before they were buried; However, as noted above, weathering of basalt by the present Venus atmosphere at plains altitude does not produce a mineral assemblage with a high dielectric constant either.

But it is unlikely that deeply buried basalt weathered under the same conditions that obtain at the Venus surface today. Since Venus has not been very active volcanically since the major epoch of volcanic resurfacing ~0.5 Gy ago [6], deeply buried basalts were erupted before (or during) that epoch. The 0.5-Gy epoch of volcanism must have injected a very large amount of SO_2 into the atmosphere. Only weathering, which probably operates very slowly on Venus, can remove SO_2 from the atmosphere, so it is likely that the present level of atmospheric SO_2 is still enhanced from the 0.5-Gy volcanism. Prior to 0.5 Gy ago there may have been much less SO_2 in the atmosphere than there is now.

It would seem that if deep crustal material weathered in a less sulfurous atmosphere than is present today, this would do nothing to change the character of the weathering product in the direction of a pyritic (hence high-dielectric and low-emissivity) mineral assemblage, but paradoxically this is not the case. Another variable, temperature, affects the stable mineral assemblage: since SO_2 is an important greenhouse gas, its removal from the atmosphere would result in lower surface temperatures [7], and under the circumstances contemplated this favors the stability of pyrite.

I have calculated the ranges of temperature and SO_2 concentration in which pyrite and magnetite are stable, using the energy-minimization program of [2]; the results are shown in Fig. 1, which shows that pyrite stability is affected by both SO_2 concentration and temperature. [7] estimate that removal of all SO_2 from the Venus atmosphere would lower the surface temperature by 52K. The dashed line in Fig. 1 reports this effect, assuming a linear relationship between SO_2 concentration and greenhouse warming. It can be seen that below the present atmospheric SO_2

concentration there is a broad range of concentrations, ~8 to ~130 ppm, where the stable Fe mineral at plains altitudes is pyrite, not magnetite.

I suggest the occurrence of low-emissivity crater ejecta on Venus is telling us this: prior to the 0.5-Gy resurfacing event the SO_2 content of the Venus atmosphere was less than it is now, being in the range ~8 - ~130 ppm, and the surface temperature was commensurately cooler. Basaltic flows at all altitudes weathered to a pyritic mineral assemblage having a high bulk dielectric constant. The planetary surface would have displayed low emissivity and high SAR brightness everywhere to Magellan, if it had been there. The 0.5-Gy resurfacing epoch deeply covered this sequence of soil profiles, and injected large amounts of SO_2 into the atmosphere, raising the concentration of this species far above its present level. During subsequent weathering of 0.5-Gy and later flows, much of this SO_2 was removed (more by formation of anhydrite, $CaSO_4$, than pyrite), but the buried old soil profiles were protected from reaction. Large cratering events have exhumed this high-dielectric-constant material and left it scattered in and around the craters. The low-emissivity signature of this material persists until the debris has had time to weather to the depth sampled by the emissivity measurement (several m), after which it has the same magnetite-bearing, high-emissivity character as other surface material. Thus only the youngest large craters display low emissivities.

REFERENCES. [1] G. H. Pettengill *et al.* (1982) *Science* **217**, 640. [2] K. B. Klose *et al.* (1992) *JGR* **97**, 16,353. [3] R. F. Jurgens *et al.* (1988) *Science* **240**, 1021. [4] G. H. Pettengill *et al.* (1992) *JGR* **97**, 13,091. [5] C. M. Weitz (1992) *LPSC* **XXIII**, 1513. [6] G. G. Schaber (1992) *JGR* **97**, 13,257. [7] J. B. Pollack *et al.* (1980) *JGR* **85**, 8223.

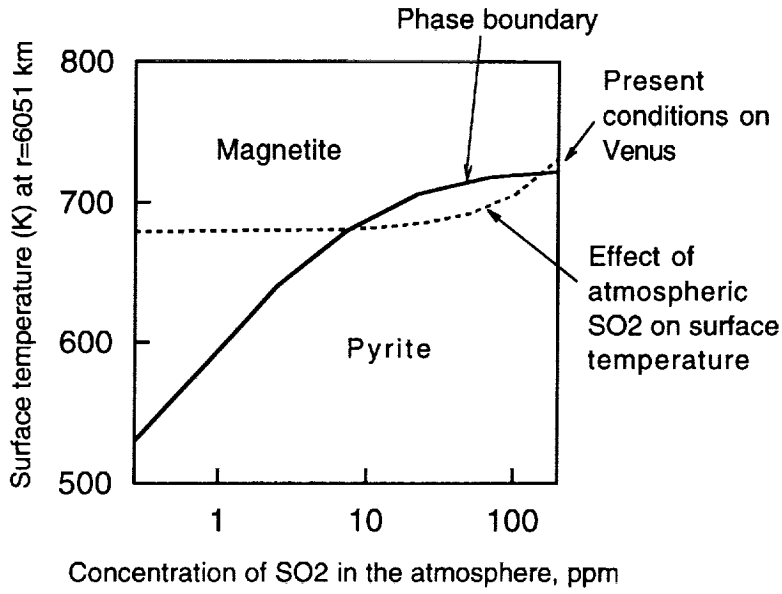

Figure 1. Effect of temperature and SO_2 abundance on the fields of stability of magnetite and pyrite as the major Fe minerals in weathered Venus surface material (computational assumptions: planetary radius, 6051 km; system pressure, 97.6 b; conc. of H_2O, 100 ppm; redox state, δ as defined by [2] = -2.6×10^{-5}). Dashed line shows the greenhouse effect of SO_2 in the atmosphere [7].

IDENTIFYING CONTROLLING MINERAL PHASES IN BASALT CHEMISTRIES: ON BEYOND PEARCE ELEMENT RATIO DIAGRAMS; A. Woronow, Dept. Geosciences, U. Houston, Houston, TX 77004

Conserved denominator (or "Pearce element ratio") diagrams have been used to assess mineral control on the chemistries of basaltic igneous rocks. These diagrams compare two chemical variables that have each been divided by the same third chemical variable. Practical considerations suggest that this approach lacks statistical power—it tends to assert the presence of mineral control where none exists. The cause of this lack of power is spurious correlations introduced by the common divisor. There is no statistical method currently available to remove this spurious correlation or even to quantify it. However, by recasting chemical data into a new form, standard regression analysis can be used to evaluate the same geochemical hypotheses evaluated by conserved-denominator analysis. This new approach devolves from simple geometric relationships among compositional variables confined to a simplex and does not introduce spurious correlations.

Rather than a general development of the conserved-denominator method, we consider an example. Let us consider a suite of chemical analyses on whole-rock specimens from an igneous body that, we postulate, was chemically evolving under olivine + plagioclase control. Say we have expressed the chemical analyses in cation proportions. To construct a Pearce element-ratio diagram for evaluating the postulate of olivine + plagioclase control, we form two new variables. One (to be used on the ordinate of the plot) is [3Na+2Ca+0.5(Fe+Mg)]/K and the other (for the abscissa) is Si/K. The numerators of these ratios contain the critical chemical components of olivine and plagioclase. The denominator is selected to be a component that does not readily partition into olivine or plagioclase. Any chemical element satisfying that criterion would do; K is just one of several possible choices. The denominator variable is called "conserved" because it does not participate in the solid phases that are postulated to control the compositional variations. Consideration of the chemical formulae of olivine and plagioclase reveals that a plot of these two variables should produce a line with a slope of +1 if the putative model is true.

The principal criticisms of the conserved-denominator approach [1] focus upon the fact that the variables on both the abscissa and the ordinate have a common component in their denominator. Any variation in the denominator induces a correlation between the two plotted ratios. Arguments have been made that conserved components cannot cause spurious correlations [2], but these are based upon Chayes' [3] equations which are inappropriate for compositional variables. (There is much misunderstanding about spurious correlation among compositional variables. The equations developed in [3] are inappropriate for this problem because they are based upon the assumption that all the variables involved are independent and not functionally related—this is clearly not the case for compositional variables.) We do not deny the validity of the theoretical basis for conserved-denominator analysis. Woronow [4] showed the equivalence of the conserved-denominator analysis to linear mixing, but it is precisely this linear relationship among the variables that assures spurious correlations are introduced by the common divisor. The presence of spurious correlations is not denied by Pearce [5], although he feels that such correlations can be identified and treated. We disagree with this opinion.

Even practiced advocates of the conserved-denominator analysis can be misled by the spurious correlations; witness the data and analysis published by Russell and Nicholls [6]. They contend that their data support the model that magmas from Diamond Craters, Oregon, are under the simultaneous control of olivine and plagioclase; this finding is based upon the trend shown in Figure 1. However, when only the mean values of the numerators, each divided by K, are plotted along with Russell and Nicholls' common-denominator variables, virtually identical plots result (Figure 1). Clearly, Figure 1 shows that the straight line with slope +1 is caused by the common denominator; namely, it is the result of plotting constant/K vs constant/K—the straight line does not indicate olivine and/or plagioclase control—the numerators contribute almost nothing to the trend.

The new approach proposed here begins by expressing the whole rock analyses as proportions of olivine, plagioclase, Si, and the amalgamation of all other constituents (henceforth "Other"); the simple geometry shown in Figure 2 results. If olivine + plagioclase control is present, the data must lie on a plane such as the shaded plane. In addition, when both Si and Other are equal to zero, the data must lie on the plagioclase-olivine binary join. Therefore, if the data are under olivine + plagioclase control, a regression of Si on Other will indicate that the data lie on a plane that passes through the origin. That is, the intercept will not be statistically different from zero. Furthermore, because the data will lie on a plane (within analytical and sampling uncertainty), the slope will be statistically different from zero.

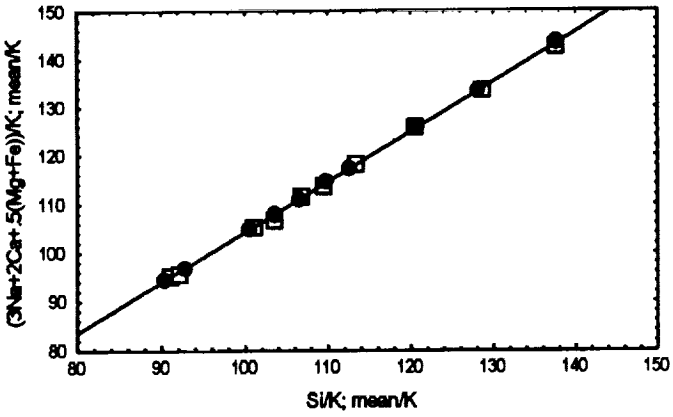

Figure 1: Comparison of a conserved-denominator plot for discerning if olivine + plagioclase is controlling the whole-rock chemistries of data from Diamond Craters, Oregon (open squares). The +1 slope of the line seems to indicate so, but a plot of the mean values of each axes' numerator divided by K (solid circles) yields essentially the same result. Therefore, the plot shows little more than that a plot of 1/K vs 1/K has a slope of +1.

Hence, by regressing Si on Other, the putative geologic hypothesis of olivine + plagioclase can be assessed by the statistical consideration: *reject the geologic model if the regression is not statistically significant (slope not different from zero) or if the intercept is not statistically equal to zero.* Monte Carlo simulations indicate that this approach is far more powerful than the conserved-denominator approach. (An equivalent statistical test for chemical control by a single solid phase is easily constructed from considerations of relationships on triangular diagrams.)

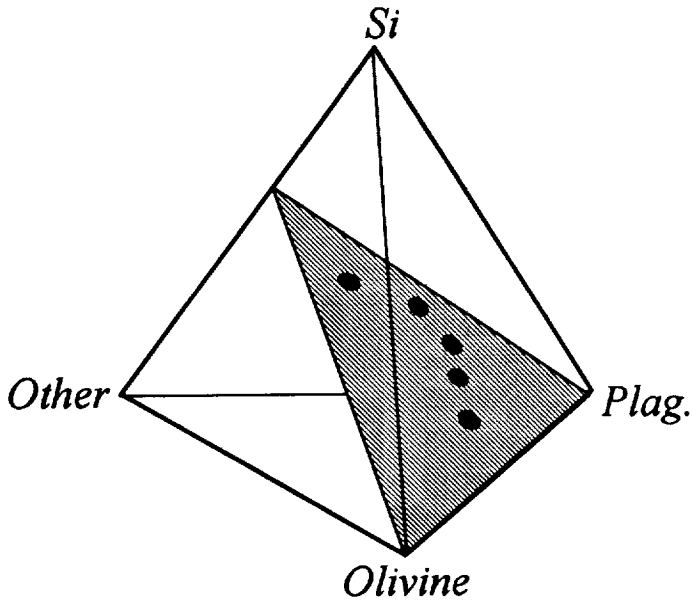

Figure 2: Geometric relationships among whole-rock analyses with chemistries controlled by both olivine and plagioclase. Expressing the whole-rock chemistries as proportions of Olivine + Plagioclase + Si + Other would require that the data lie on a plane such as the shaded plane. Therefore, when the model is correct, a regression of Si on Other will indicate that the data lie on a plane that passes through the origin.

For the Diamond Craters data, neither olivine nor plagioclase (nor a combination of the two) accounts for the observed trends in the data (Figure 1), contrary to the conclusions of Russell and Nicholls [6]. For instance, for the joint control of olivine and plagioclase, the regression of Si on Other yields an intercept with much less than a 0.01 probability of being equal to zero, at odds with the zero intercept required by the model. The difference in conclusions reached by [6] and here is a direct result of the relatively low power of Pearce-element ratio analysis.

REFERENCES: [1] Rollinson, H.R. and Roberts, C.R. (1986) *Contrib. Min. Petrol.*, **93**, 89-97. [2] Vines, K.J. (1987) *Contrib. Min. Petrol.*, **97**, 525-526. [3] Chayes, F. (1971) *Ratio Correlation*, U. Chicago, pp. 99. [4] Woronow, A. (1991) *Geochim. Cosmochim. Acta*, **55**, 2351-2353. [5] Pearce, T.H. (1987) *Contrib. Min. Petrol.*, **97**, 529-534. [6] Russell, J.K. and Nicholls, J. (1987) *Geochim. Cosmochim. Acta*, **51**, 143-154.

PARENTAL MAGMA COMPOSITIONS OF BASALTS USING AN ARTIFICIAL NEURAL NETWORK: THEORY; A. Woronow, A. M. Reid, Dept. Geosciences., U. Houston, Houston, TX 77004; J. H. Jones, JSC, Houston, TX 77058; N. E. Pingitore, Jr., Dept. Geological Sciences, U. Texas at El Paso, El Paso, TX 79968

Expressed in a dissolved fayalite and dissolved forsterite (and dissolved "other") system, a magma crystallizing olivine as its only solid phase evolves along a compositional trajectory unique to the magma's starting composition and its degree of fractionation. From a few samples of derivative magmas along its trajectory, the composition of the parent magma and its fractionation index should be recoverable. The trajectories are nonlinear and have no known closed-form expression, therefore, standard fitting or regression algorithms cannot solve for the unknowns. We are explore the use of an artificial neural network to solve this problem. Thus far the network, trained on computer-generated data and then presented with new (computer-generated) cases, does well in recovering the Mg# of the parent magma as well as its degree of fractionation from as few as three or four well-determined sample compositions.

After a magma arrives at a magma chamber, it may be held there for an indeterminate time before its first eruption, undergoing chemical evolution, perhaps including the segregation of early-formed olivine. If this occurs, the first erupted magma will have a composition different from the original magma. Subsequent eruptions could sample progressive stages in the chemical evolution. Currently, there exists no widely accepted method for determining the degree of chemical change a magma has sustained prior to its first eruption, although a standard method for tracing subsequent evolution is through the magnesium number (Mg#). What we propose here is a new method to infer the chemical composition of the parent magma from chemical analyses of derivative samples. The method can also estimate the average amount of fractionation represented by the derivative compositions. This new method, as currently formulated, assumes that the parent magma had olivine as the sole liquidus phase.

The molar composition of any magma can be expressed in the three components

$$X_{Fa} = x(FeO)_L + \frac{x}{2}(SiO_2)_L; \quad X_{Fo} = y(MgO)_L + \frac{y}{2}(SiO_2)_L; \quad Z = (other)_L,$$

where x and y are, respectively, the mole fractions of FeO and MgO in the melt and Z is the mole fraction of all other components combined. The evolving concentrations of these dissolved components, as olivine crystallizes, follow a trajectory that appears to be uniquely determined by the magma's starting composition. The shape of the trajectory also depends upon the degree of olivine fractionation. Figure 1 shows representative trajectories without fractionation and Figure 2 shows the effects of fractionation on a single starting composition. These computer-generated trajectories use Bradley's [1] thermodynamic equations, although our current approach uses the partitioning relationships of Jones [2] to track magma evolution.

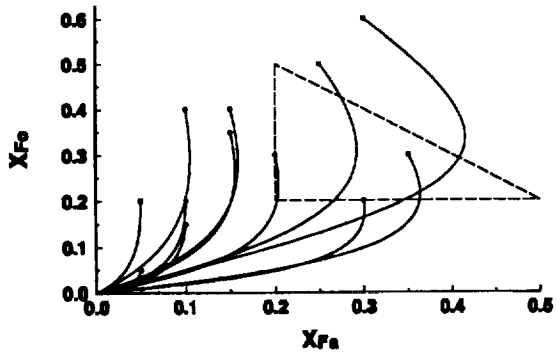

Figure 1: Compositional trajectories for equilibrium crystallization of olivine. The axes express concentrations of dissolved fayalite and forsterite. (See text for discussion of triangular field.)

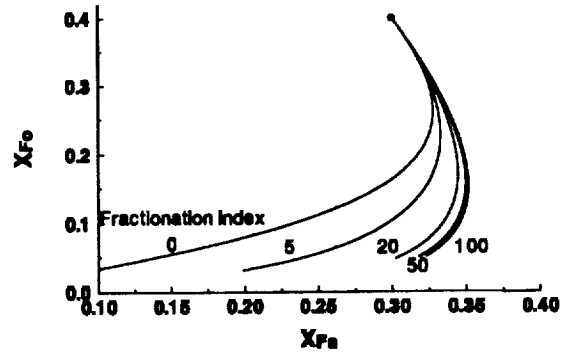

Figure 2: The effects of olivine fractionation on the compositional evolution of a magma in the X_{Fa}-X_{Fo} system.

When applying the neural network algorithm to determine a magma's starting conditions and fractionation index, several thousand simulated trajectories with random starting compositions and random fractionation indices are generated over the range of plausible parental magma compositions and fractionation indices. Along the trajectories, samples are drawn which cover the same range of X_{Fo} as the samples from the magma under analysis. The computer-generated samples' X_{Fa} and X_{Fo} are then perturbed by appropriate random errors simulating analytical error. Stored along with this set of synthetic samples taken from one trajectory are the parent magma's composition (its X_{Fa} and X_{Fo}) and its fractionation index.

Artificial neural networks can solve nonlinear problems even without explicit equations. The crystallization of a magma in our three-component system is such a case. As described above, we can generate a large number of artificial cases and use those cases to "teach" an artificial intelligence program to recognize the response information (the parent magma's X_{Fa}, X_{Fo}, and fractionation index), given the stimulus information (a number of X_{Fa} and X_{Fo} sample pairs taken from the derivative magmas).

A neural network consists of a series of vector-matrix multiplications. Although terminology varies, the components of the vectors are commonly referred to as "units" and the matrices as "weight matrices." The first set of units is loaded with the stimulus variables for a given case. The stimulus variables must be pre-scaled between zero and one. A weight matrix filled, initially, with small positive and negative random values post-multiplies this first vector to produce an output vector. Each component in the output vector is replaced by a value that the component generates through a nonlinear "activation function" thereby producing values to load into the next set of units. Along with the next weight matrix, this vector constitutes a second "layer." Any number of layers can be added to the network. All but the last layer are called "hidden layers" because of the special manipulations needed to update them. The output units from the last layer contain the network's response to the stimulus, scaled between zero and one by the activation function. If the response of the network deviates from the desired response, then the entries in each matrix are adjusted to bring the response into closer agreement. Each subsequent case is presented to the network and the matrices adjusted. By repeatedly cycling the network through the entire suite of cases, the response of the network converges, as closely as possible, to the desired response for the ensemble of training cases.

The above describes a supervised-learning algorithm. We employ a back-propagation algorithm for updating the weight matrices and include a bias term in the input layer. The bias term, always loaded with the value one, serves the same purpose as the constant term in a regression. The activation function,

$$V_{input} = \left(1 + e^{V_{output}}\right)^{-1}$$

automatically produces zero-one scaled values.

Computational time increases rapidly with increasing order of the weight matrices and number of layers, but if the matrices are too small, all the variability in the training data may not be captured. Only through trial and error can the optimal network parameters be determined. We have found that for this problem two layers suffice, with weight matrices of orders (2N+1)x8 and 8x3, where N is the number of X_{Fa}-X_{Fo} stimulus pairs in a case. On a 486/33 PC, learning about 12,000 cases with five X_{Fa}-X_{Fo} pairs may take four or more hours.

To test the network's suitability for recovering a parent magma's composition, we trained it on sets of computer-generated data and then presented it with new data (also synthetic) with known answers. The triangular region in Figure 1 covers one range of parent-magma compositions on which we trained and tested the network. For 1,000 test cases and only three samples per case, the predicted starting magma composition fell within 2% (rms error) of the correct answer for 95% of the cases. Over successively smaller ranges of composition, the errors in the predicted values successively decrease, as they do if more derivative-magma samples are used. Therefore, we have adopted the strategy of successively narrowing the training region about the answer predicted from the previous, broader region.

These verification tests lead us to speculate that trajectories are unique to their starting compositions. As Figure 2 shows, however, very high fractionation indices will probably not be resolvable above the levels of uncertainty usually associated with chemical analyses. We welcome suggestions for natural data sets upon which to exercise this approach.

REFERENCES: [1] Bradley, R.S. (1962) *Am. Jour. Sci.*, 260:550-554. [2] Jones, J.H. (1994) Chapter 3-7, In *Handbook of Physical Constants* (ed., T.J. Ahrens), American Geophysical Union.

ATTEMPTS TO PRODUCE CARBON-FREE SILICA AEROGEL FOR MICROMETEOROID CAPTURE CELLS; I.P.Wright, H-P.Huang and C.T.Pillinger, Dept. of Earth Sciences, Open University, Walton Hall, Milton Keynes MK7 6AA, UK.

In applications where intact micrometeoroids are to be collected from space, it is widely thought that silica aerogel [1,2] offers the best hope for a suitable collection medium [e.g. 3]. For this material to obtain the universal seal-of-approval it should ideally satisfy the constraints of all potential investigations. Thus far it would appear that the implantation of synthetic micrometeoroids into aerogels has been successful [e.g. 4] and, furthermore, the material is chemically pure with respect to its trace element chemistry [5]. However, since a major proportion of micrometeoroids are likely to be carbon-rich or CHON-like, it is imperative that any aerogel selected for a collection cell should not impart any light element contamination to the prospective particles. Since it is known already that aerogel can become coated onto the surfaces of particles during ground-based impact studies [6,7,8], the collection medium itself needs to be free of light element contaminants.

There are two immediate problems with the usage of aerogel. Firstly, by the very nature of its highly porous structure, it tends to adsorb atmospheric water vapor. Fortunately this can be largely removed by heating at relatively low temperatures (a process that has no deleterious effects on the aerogel structure). Secondly, it is clear from a knowledge of the preparation procedures used to manufacture silica aerogel, which commonly involve a substance like tetramethoxysilane, $(CH_3O)_4Si$, and various solvents such as alcohol, CH_3CH_2OH, that complete removal of residual carbon-bearing molecules is difficult. Indeed, a previous study of the carbon contents of aerogel has shown that the element can be present at up to 3.3 % by weight [9]; the exact nature of the compounds has been studied using thermogravimetric analysis and laser desorption-mass spectrometry [10]. Attempts have been made to reduce the carbon content of existing aerogels using either heating [9,10], or a technique known as supercritical fluid extraction [11]. Simple heating techniques (pyrolysis under vacuum conditions) can release about 50% of the total volatile content of aerogel, while supercritical fluid extraction, under optimal conditions, seems to remove >90% of the total carbon content, and presumably most of the water as well.

The biggest challenge for the development of a totally suitable aerogel collection cell is to devise ways of, not only removing the volatiles, but also keeping the material clean once the extraction has been completed. In this respect, simply reducing the concentration of the volatile constituents may not necessarily be what is required because, upon re-exposure of the aerogel to the atmosphere, contaminants may be added to the highly active and clean surfaces of the porous material. Rather, the overall success of a clean-up procedure needs the contemporaneous addition of an inert substance to the aerogel structure during volatile removal. This should then act to terminate any broken bonds, or fill any newly created void spaces, of the devolatilised aerogel. The obvious choice here is oxygen since its addition will effectively purify the Si-O material. For this reason it was decided to evaluate the usage of a combustion technique. A measure of the efficacy of this approach can then be gained by studying the volatiles removed during combustion and then re-appraising the material after exposure to air (in this study, the carbon chemistry of aerogel is used as the monitor). While in principle the idea of combustion sounds fairly straightforward it should be pointed out that previous attempts to remove volatiles from aerogels by heating in air were largely unsuccessful [10]. Furthermore, preliminary experience [9,11] with combusting aerogel by a sealed tube method at high temperature showed that while carbon could indeed be satisfactorily removed, the aerogel structure itself generally collapsed to form a hard coherent material of no value whatsoever, as a collection medium. In the new study, aerogel has been combusted by an

incremental heating technique, using 50°C temperature steps of 40 minutes duration each, from ambient to 1000°C. The benefit of using a stepped combustion technique is that the heating rate experienced by the aerogel is sufficiently slow enough to allow any accompanying structural rearrangements to take place without causing cracking or shrinkage. Indeed, using the technique herein, the aerogel remains, visibly at least, unchanged at the end of a normal experiment.

The extraction system used for the stepped combustion experiments is different to that used in a previous study in the following ways: a wider diameter sample holder is used (8mm i.d. versus 4mm), and a loading stage has been added that enables the sample under investigation to be admitted to the extraction system and evacuated, prior to admission to the combustion furnace. The increased dimensions of the holder mean that with a typical sample size of ~70mg, the depth of aerogel required is only 1-2cm, compared with >5cm in the previous work. This is an important advance since the combustion furnace used previously, and in this study, is only 15cm long, and so a sample depth greater than 3cm is subjected to a large temperature gradient. This could result in volatiles being removed from one part of the aerogel and at the same time becoming adsorbed into another. Loading the aerogel into the extraction system, rather than directly into the reaction vessel as used previously, enables the combustion system to be properly blanked out before the experiment begins (which can now be done without having to open the vessel to the atmosphere).

All experiments were carried out using an aerogel of 0.12 g cm^{-3} density (supplied from L.W.Hrubesh, Livermore, via M.E.Zolensky, NASA-JSC). The carbon released upon stepped combustion is clearly present in two major forms. One variety has a $\delta^{13}C$ of about -28‰ and is released at temperatures less than 500°C. This carbon is certainly not merely a system blank, which would characteristically be present at 2 orders of magnitude lower amounts. The temperature of combustion and the $\delta^{13}C$ value are suggestive of normal atmospheric (hydrocarbon) contamination. The second form of carbon is released above 500°C and has $\delta^{13}C$ of about -36‰; the high temperature of combustion strongly implicates carbon that is in some way bonded to the aerogel (presumably remnant tetramethoxysilane). The ratio of low to high temperature forms of carbon is 0.48.

When removed from the extraction system the aerogel was found to have undergone a 16% loss in weight; since carbon only accounts for 0.1% it is fairly certain that the rest is due to water. Interestingly after exposure to air for 48 hours the weight of the aerogel only increased by ~1%, which seems to imply that only a minimal amount of water was re-adsorbed over this period. Upon re-examination for carbon it was found that the high temperature form of carbon had been effectively removed, while that released at low temperature was present in roughly the same amounts as in the original extraction. Thus, having identified a way of removing the structural carbon with no apparent damaging effects on the aerogel itself, it is now necessary to develop a method of preventing the re-adsorption of low-temperature carbon. In this regard, it was found that simply leaving the material in the extraction system, under vacuum, was not successful. Presumably the aerogel acts to cleanse the vacuum system itself, a possible future application of the material in low carbon blank extraction systems.

References: [1] Kistler,S.S. (1931), *Nature*, **127**, 741; [2] Fricke,J. and Emmerling,A.(1992), In: Chemical Processing of Advanced Materials (eds. L.L.Hench and J.K.West), 3-17; [3] Barrett,R.A. *et al.*, (1992), *Proc Lunar Planet. Sci*, **22**, 203-212; [4] Brownlee *et al.*, (1993), *LDEF Newsletter*, **4** (3), 4-18; [5] Flynn,G.J. and Sutton,S.R., (1990), *Lunar Planet. Sci.*, **XXI**, 371-2; [6] Laurance,M.R., (1989), *Lunar Planet. Sci.*, **XX**, 560-1; [7] Zolensky,M.E. *et al.*, (1989), *Lunar Planet Sci*, **XX**, 1251-2; [8] Zolensky,M.E. *et al.*, (1990), *Lunar Planet Sci*, **XXI**, 1381-2; [9] Gibson,J.E. *et al.*, (1991) *Lunar Planet Sci.*, **XXII**, 441-2; [10] Hartmetz,C.P. *et al.*, (1990), *Lunar Planet. Sci.*, **XXI**, 463-4; [11] Huang,H-P. *et al.*, (1993), *Lunar Planet. Sci.*, **XXIV**, 679-80.

COULD THE ORIGINAL SUDBURY STRUCTURE HAVE BEEN CIRCULAR?

Jianjun Wu; Bernd Milkereit; David Boerner, Blyth Robertson
The Geological Survey of Canada, 1 Observatory Cr., Ottawa, Ontario, K1A 0Y3, Canada

The Sudbury Structure (SS) of the Canadian Shield, one of the oldest (1.85 Ga) and largest (~200 km) impact features on earth, encompasses a unique igneous complex with a closed elliptical surface expression (1-3). Uniform paleocurrent trends observed in the Chelmsford turbidite (4), the upper unit of the sediments filling the igneous complex, have been interpreted to mean the structure was never circular (5,6). As an impact origin would require an initially circular structure, Sudbury's genesis has been controversial for more than a century (7,8). Herein we present new high-resolution seismic images which provide the first evidence for the relative timing of the deformation events that reshaped the initial Sudbury Structure. The seismic images have revealed that the lower unit of the Sudbury basinal fill sediments, the Onwatin argillite, is penetrated by a set of imbricated thrusts, whereas the overlying Chelmsford turbidites are unaffected. By proving that the deposition of the Chelmsford turbidites postdates the major deformation of the SS, our seismic results strongly support the impact origin.

A coordinated geoscience effort, spearheaded by seismic reflection profiling as part of the multidisciplinary Canadian Lithoprobe program was initiated to study the SS during 1991-92. Three high-resolution vibroseis reflection profiles were acquired across the SS. The preliminary results show that the Sudbury Igneous Complex (SIC) is highly deformed and markedly asymmetric at depth, suggesting considerable N-S shortening (9). Intensive reprocessing of the seismic reflection data was rewarded with a substantially enhanced seismic image across the entire SIC to a depth of ~12 km, warranting a new, more detailed, structural interpretation.

Beneath the North Range, most lithologic units are well marked by distinct, south- dipping (20°-30°) seismic reflections, in excellent agreement with borehole logging and geologic data from the vicinity of the seismic profiles. The contact between norite and the Levack gneiss, defining the SIC floor, is the most continuous feature and can be traced to a depth of ~12 km under the South Range, suggesting the original S-W diameter of the SIC could be twice larger.

The South Range is characterized by numerous, steep, south-dipping reflections. Prominent reflectors project updip to surface-mapped faults (10). The deepest reflections can be traced upward to the boundary between the Onaping and Onwatin and project into the Cameron Creek fault (CCF). Considering the surface geologic pattern, the subsurface geometry of these south-dipping reflections, and the manner in which they penetrate the contact between the Onaping and Onwatin, we interpret these faults as part of an imbricate thrust system. The CCF was the basal detachment surface along which NW-SE shortening took place. The observed offset of lithologic contacts by up to 5 km at the southwest closure of the SIC, is the surface manifestation of the thrust-faulting. In contrast to the North Range, correlation of reflections with lithologic units under the South Range is more difficult, consistent with the well-established view that the South Range has undergone deformation.

The Sudbury Basin is conspicuous in the seismic section. The contact between the Chelmsford-Onwatin Formations appears continuous with a steep inward dip (~50°) at the south and a shallow dip (~15°) at the north. The Onwatin-Onaping contact is progressively offset in the south with staircase geometry, consistent with the south-dipping thrusting and indicating that the Onwatin Formation deposition predates the thrusting. The southern contact of the Chelmsford with the Onwatin, however, appears to be unaffected by the thrusting, implying that the Chelmsford turbidites were deposited after the thrusting event or during its final stages.

Two main aspects of the seismic image shed new light on the tectonic history of the SS. First, by clearly defining a major imbricated thrust zone, the seismic data establish that brittle thrust-faulting played an important role in NW-SE shortening of the SS. This brittle deformation has economic implications as the Sudbury Sublayer, an important ore-bearing horizon at the base of the norite, may be duplicated at shallow depths at the southwest corner of the SIC. Second, the relatively undeformed nature of the Chelmsford-Onwatin contact, together with the uniform W-SW paleocurrent trend in the Chelmsford, confirms that the Chelmsford turbidites were deposited in an elongate, not circular, basin. Moreover, the seismic image shows that the discrete thrusting must have taken place after ductile deformation of the SIC, but before the deposition of the Chelmsford. Thus, the paleocurrent direction in the Chelmsford is unrelated to the initial shape of the Sudbury Structure. This, combined with the observed extent of the North Range SIC at depth beneath the South Range, provides quantitative evidence that the initial SIC could have been circular.

Based on the new seismic image and the available geologic data, we speculate the following tectonic deformation sequence (Fig. 1) which created the present Sudbury Structure. The basic assumption underlying the sequence is that immediately after the catastrophic impact event, the SS comprised a stack of horizontal tabular units[4,17] including the Onaping breccia blanket and the molten granophyre, gabbro, and norite of the SIC (a). Subsequent northwest compression deformed the original SS into a tight fold (b), probably during the early stages of the poorly understood 1.8 Ga Penokean Orogeny. This large-scale folding caused the first-order NW-SE shortening of the SS and is manifest today by the South Range shear zone (SRSZ) (11). After the folding, the Onwatin argillite, composed of reworked Onaping, was deposited (c). Discrete NW-SE thrusting (d), took place during the late stages of the Penokean Orogeny, causing further shortening of the SS. The North Range acted as a foreland and largely escaped deformation. The deposition of the Chelmsford turbidite followed the thrusting (d).

REFERENCES (1)Dietz, R.S. *J. Geol.* 72, 412 (1964). (2)Fraggart, B.E. *et al.* Science 230, 436 (1985). (3)Grieve, R.A.F. et al. *J. Geophys. Res.* **96**, 22,753 (1991). (4)Cantin, R. & Walker, R.G. *Geol. Assoc. Can. Spec. Pap.* **10**, 93 (1972). (5)Card, K.D. & Hutchinson, R.W. *Geol. Assoc. Can. Spec. Pap.* **10**, 67 (1972). (6)Muir, T.L. *Ont. Geol. Surv. Spec. Vol.* **1**, 449 (1984). (7)Guy-Bray J.V. (Ed) Geol. Assoc. Can. Spec. Pap. **10** (1972). (8) Pye, E.G., Nakdrett, A.J. & Giblin, P.E. (Eds), *Ont. Geol. Surv. Spec. Vol.* **1** (1984). (9)Milkereit, B. *et al.*, *Geology* **20**, 807 (1992). (10)Thomson, J.E. *Ontario Department of Mines Annual Report 65*, part 3, 1-56 (1957). (11)Shanks, W.S. & Schwerdtner,W.M. *Can. J. Earth Sci.* **28**, 411(1991).

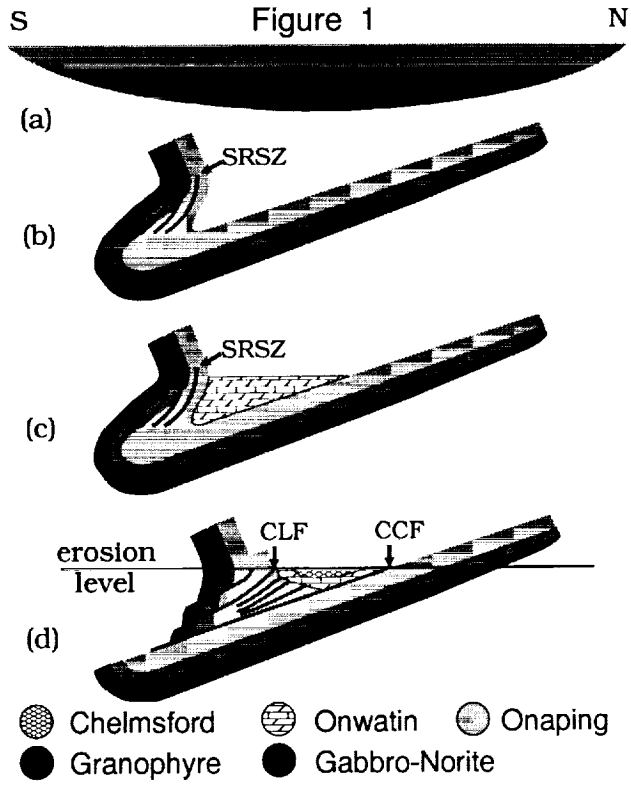

MAGELLAN RADAR DATA FOR VENUS TOPOGRAPHIC MAPPING; Sherman S.C. Wu and Elpis A. Howington-Kraus, U.S. Geological Survey, Flagstaff, AZ 86001

In order to make topographic maps of Venus from Magellan synthetic aperture radar (SAR) stereoimage pairs, we have created a digital radargrammetry workstation and software package called DSWV (Digital SAR Workstation-Venus). DSWV performs the functions of triangulation, digital elevation measurement using automatic correlation techniques, contour mapping, orthophoto rectification, and image mosaicking. Standard image-processing and enhancement techniques can also be applied to the data. We will demonstrate the capabilities of the DSWV package and show results both from our initial test of the software and from more extensive applications now in progress. The hardware used for the demonstration will consist of a SUN SPARCserver 670MP with a Vitec 50B video processor, a Tektronix stereo display, and a three-dimensional trackball used as a measuring device.

During its first three cycles of operation, the Magellan spacecraft obtained radar images of 98% of the surface of Venus. In cycles 1 and 3, about 25% of the surface was covered by usable stereopairs with both views illuminated from the same side. In cycles 1 and 2, about 45% of the surface was imaged in stereo but with opposite-side illumination (Ford et al., 1993). The basic image datasets (one from each orbit of Magellan) are highly elongated, roughly north-south strips called F-BIDRs. The DSWV uses these image strips, rather than the non-orthorectified mosaics that have been produced from them, to maximize stereoradargrammetric accuracy. Enabling the software to read the Magellan F-BIDR data was one of the main steps by which the DSWV was developed from the earlier DSW2 package that had been developed for the analysis of airborne SAR data such as that obtained by the STAR-1 system (Poehler et al., 1993). The other important step in the development of the DSWV was the creation of a mathematical model of the geometric properties of the Magellan observations of Venus, which differ from the properties of airborne SAR. This model allows the DSWV to determine the pixel coordinates (C1, C2) in sinusoidal projection of any point on Venus for which the body-fixed (X,Y,Z) coordinates in the VBF85 system are known; the model can be inverted to determine body-fixed coordinates of a feature from its pixel coordinates in a pair of images. The transformation from body-fixed to pixel coordinates occurs in three steps: (a) an approximate transformation (neglecting the nonzero elevation of the point) is used to locate the feature in the image accurately enough to determine in which burst of Magellan's pulsed operation the feature was imaged most strongly; (b) the position and velocity of the spacecraft at the time of that burst are used to compute the range and Doppler coordinates of the feature; and (c) the range-Doppler coordinates are converted to pixel coordinates by the same transformation that was used in the processing of the Magellan

images. A correction for refraction of the radar beam by the Venusian atmosphere is included in the calculation. The mathematical model also allows for errors in the spacecraft ephemeris for each orbit. The knowledge of spacecraft position (along-track, cross-track, and radial) for each orbit can therefore be improved as part of the triangulation process.

We initially tested the DSWV package with a set of four Magellan F-BIDRs: those from orbits 877 and 878 of cycle 1 and those from orbits 2674 and 2675 of cycle 3. A test area was selected where these images overlap (long 72° 56′ 20" to 73° 30′ 20", and lat -0° 5′ 0" to -2° 58′ 20"). We measured 39 triangulation points with an average residual in the C1 and C2 coordinates of 0.5 pixel and a maximum residual of 1 pixel after the triangulation adjustment. A total of 131 topographic profiles were measured by using both manual and automatic image correlation, and they were used to construct a digital elevation model (DTM). The DTM was then used to produce a topographic contour map of the test area and an orthorectified image mosaic.

We are currently using the DSWV to produce a DTM and derived products for a larger region located on the west flank of Maxwell Montes. The dataset for this application consists of images from orbits 512-536 of cycle 1 and orbits 4075-4106 of cycle 3. The cycle 3 images are special products (FS-BIDRs) with a viewing geometry optimized for stereo viewing of Maxwell. At the 25th LPSC, we will present the results of this analysis along with those of the initial test area, and we will demonstrate the DSWV package.

[1] Ford J.P. et al. (1993) Guide to Magellan image interpretation, JPL Publ. 93-14, 148 p.

[2] Poehler P. et al. (1993) Digital workstation for Venus topographic mapping, Proceedings of SPIE, State-of-the-Art Mapping, v. 1943, 45-56.

3092

P. 2

WINDBLOWN SAND ON MARS: THE EFFECT OF SALTATION THRESHOLD ON DRIFT POTENTIALS DERIVED FROM MARS GCM;

P. Xu, R. Greeley and S. Williams, Dept. of Geology, Arizona State University, Tempe, AZ 85287-1404, J. B. Pollack, Space Science Division, NASA Ames Research Center, Moffett Field, California

INTRODUCTION. The rate at which the wind can redistribute sedimentary material is an important part of any planet's sedimentologic cycle, particularly for Mars, where the competing effects of other gradational processes are less than on Earth. The aeolian drift potential (DP) is a measure of the amount of material capable of being moved through a unit length by the wind for a given period of time [1]. DP is a useful measure of the potential redistribution rate of windblown material on regional scales. The martian aeolian DP was calculated from laboratory studies of sand movement conducted at Martian atmospheric densities and from surface stress, temperature, and pressure values for that region as determined from the Mars General (Atmospheric) Circulation Model (GCM) developed at the NASA/Ames Research Center [2,3]. In our simulations for Mars, DP changes in both magnitude (as expected) and direction if the saltation threshold is altered.

METHOD. The Ames GCM divides the surface of Mars into 7.5° by 9° bins, each with predicted values of pressure, temperature, and surface shear stress. The surface shear vector was used in the saltation flux equation of White [3] to derive DP magnitude and direction for each bin. Seven different values for threshold were used to assess its effect on magnitude and direction of the resultant sand drift. The variation in sand drift direction in a given GCM bin as a function of saltation threshold was analyzed as was the correlation between the calculated sand drift direction and the orientation of aeolian surface features, such as wind streaks.

RESULTS. Threshold shear stresses must be exceeded for a given GCM bin for sand drift to occur. Many bins have no motion, and there is an inverse relationship between the threshold stress and the number of bins reporting sand drift (Figure 1), as well as maximum drift potential value for any given azimuth (Figure 2). Resultant drift directions also change with increasing saltation threshold. The biggest change in direction averaged ~13.25°, which occurs when the threshold increases from 0.008 to 0.016 N/m^2 (Figure 3). The smallest change averaged ~3.6° for an increase in threshold stress from 0.040 to 0.048 N/m^2 (Figure 4). The inverse relationship between saltation threshold and shift in sand drift resultant azimuth reflects the greater variability of gentle winds compared to strong winds.

There is no correlation between the axial orientation of dark (erosional) wind streaks on Mars and the resultant sand drift directions determined in this study (Figure 5). The correlation is much better when bright (depositional) streaks are considered (Figure 6): the best correlation is for a threshold stress of 0.032 N/m^2. The likely explanation for the poor correlation in the case of the dark streaks is that their formation is dominated by local topographic and meteorological conditions that are unaffected by the regional scale parameters utilized by the GCM [5]. Bright streaks form in the aftermath of dust storms when the atmosphere is very stable and less responsive to local conditions [6], hence, bright streak orientation correlate better with the regional sand drift.

CONCLUSIONS. The number of bins which have drift potentials and the maximum drift potential on the planet at one compass direction over the whole year period decrease with increasing threshold. The resultant drift directions also change with increasing threshold. The larger the threshold, the less change in resultant drift direction. The best correlation of bright streaks with resultant drift directions is at a threshold of 0.032 N/m^2.

REFERENCES. [1] Fryberger, S.G. (1979) *U.S.G S. Prof. Paper 1052*, 137-169. [2] Pollack, J.B. et al. (1981) *J. Atmos. Sci. 38*, 3-29. [3] Pollack, J.B. et al. (1990) *JGR. 95*, 1447-1473. [4] White, B.R. (1979) *JGR, 84*, 4643-4651. [5] Greeley, et al. (1993) *JGR, 98*, 3183-3196. [6] Veverka, et al. (1981) *ICARUS, 45*, 154-166.

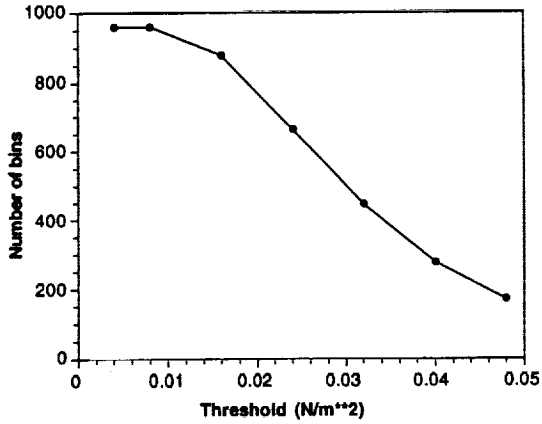

Figure 1. The number of GCM bins which have drift potentials vs. threshold

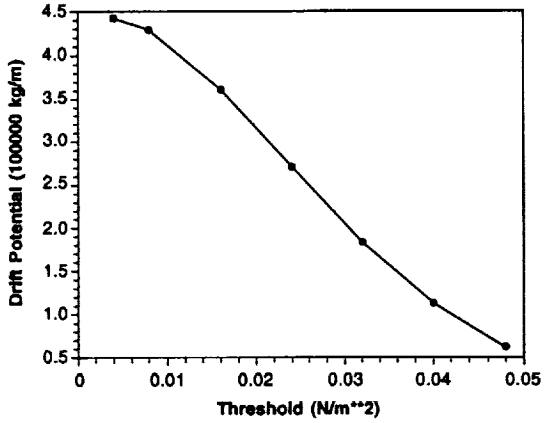

Figure 2. The maximum drift potential on the planet at one compass direction over whole year period vs. threshold

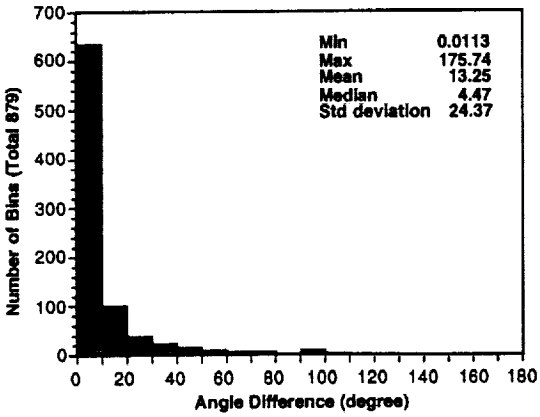

Figure 3. Histogram of angle differences of resultant drift directions from two threshold 0.008 and 0.016 N/m**2

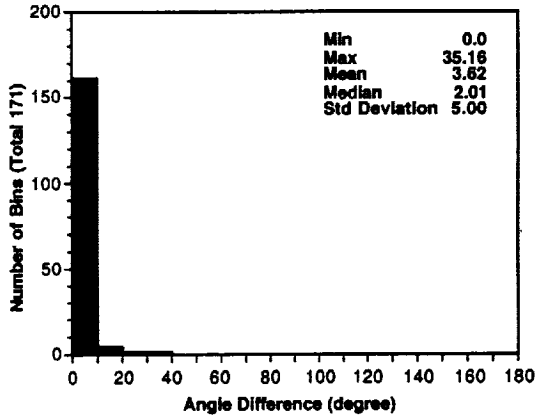

Figure 4. Histogram of angle differences of resultant drift directions from two thresholds 0.040 and 0.048 N/m**2

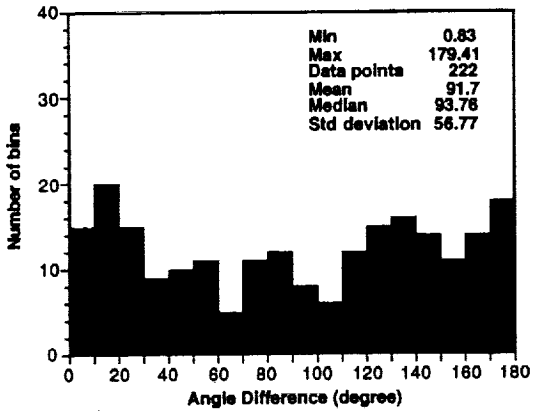

Figure 5. Histogram of angle differences of dark streaks and resultant drift directions at threshold 0.016 N/m**2

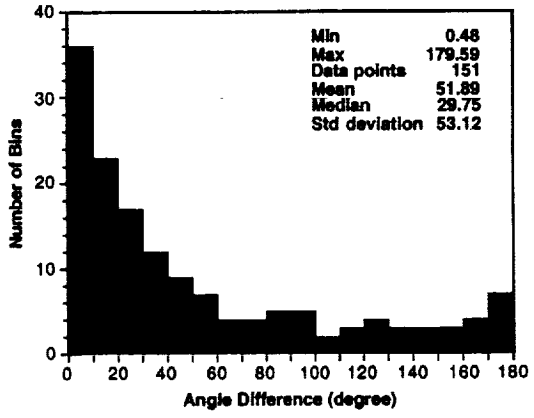

Figure 6. Histogram of angle differences of bright streaks and resultant drift directions at threshold 0.032 N/m**2

^{26}Al AND ^{10}Be ACTIVITIES AND EXPOSURE AGES OF LODRANITES, ACAPULCOITES, KAKANGARI AND PONTLYFNI. S. Xue[1], G.F. Herzog[1], J. Klein[2], and R. Middleton[2]. 1) Dept. Chemistry, Rutgers Univ., New Brunswick, NJ 08903; 2) Dept. Physics, Univ. Pennsylvania, Philadelphia, PA 19104.

Introduction. Many meteorites belonging to the same group have similar exposure ages [1]. This result suggests the importance of a relatively small number of collisional events in determining the nature of much of the extraterrestrial material that arrives on Earth. Among achondrites, the exposure histories of the lodranites, acapulcoites, and winonaites, have received little systematic attention apart from some recent noble gas measurements [2]. We previously reported ^{26}Al ($t_{1/2}$ = 0.71 My) and ^{10}Be ($t_{1/2}$ = 1.5 My) activities for four lodranites [3]. Here we add results for three more lodranites and for some acapulcoites, winonaites and Divnoe. Our main purposes were to search the exposure age distributions for signs of clustering and to determine the degree of shielding experienced by the meteoroids during cosmic-ray irradiation.

Experimental Methods. When sufficient material was available we separated metal-rich and silicate-rich phases by using a hand magnet. We attempted to rid metal-rich material of adherent silicate by etching with HF but met with only partial success (see below). The ^{26}Al and ^{10}Be activities of the samples were determined by accelerator mass spectrometry [4]. The Mg, Al, Ca, Ti, and Fe contents of the silicate-rich samples were measured by DCP emission spectrometry; the Mg contents of the metal-rich samples were measured by ICP/MS [3].

Results and Discussion. The measured ^{26}Al and ^{10}Be activities are shown in Table 1.

Table 1. ^{26}Al and ^{10}Be activities in lodranites, acapulcoites, winonaites, and Divnoe

Sample	ID	^{10}Be (dpm/kg)		^{26}Al(dpm/kg)		Mg (%)
		Bulk or *Silicate*	Metal-rich	Bulk or *Silicate*	Metal-rich	
LODRANITES						
EET 84302	JSC 23	*18.6±0.8*	4.9±0.6	*51.4±1.5*	4.4±0.1	n.d.
FRO 90011	Eu 007	18.2±0.5		51.7±0.8		
Gibson	BE 558	15.0±0.2		32.6±0.6		
LEW 88280[3]	JSC 18	*15.8±0.9*	4.9±0.3	*50.1±2.7*	4.7±0.6	0.2
Lodran[3]	E 2828	*17.4±0.5*	8.0±0.3	*53.7±1.9*	12.1±0.3	11
MAC 88177[3]	JSC 39	*13.4±0.8*	5.7±0.3	*32.4±0.4*	5.2±0.3	0.3
Y 791491[3]	NIPR 63	*17.0±1.2*	6.1±0.4	*47.8±1.1*	5.7±0.2	3.2
ACAPULCOITES						
Acapulco	BM 1978	*20.4±0.2*	5.5±0.1	*50.7±1.0*	4.7±0.2	0.04
ALHA 81187	JSC 20	13.9±0.4	7.0±0.9	39.0±0.5	4.6±0.3	n.d.
ALHA 81261	JSC 16	*14.1±0.3*	5.3±0.1	*49.3±0.5*	4.7±0.3	0.03
ALH 84190	JSC 10	13.9±0.2		40.0±0.9		
WINONAITES						
Kakangari	BM 69062	17.1±0.1	6.5±0.2	55.4±1.6	10.9±0.7	n.d.
Pontlyfni	BM 1975	20.7±0.4	6.1±0.2	67.5±1.4	7.0±0.5	n.d.
Winona[3]	AM 3768	*10.2±0.2*		*42.1±0.6*		
Divnoe	MP	*20.5±0.2*	5.7±0.2	*58.3±4.0*	4.8±0.1	0.4

The stated uncertainties are the 1-σ values for the internal precision. We estimate the overall (external) uncertainties of the ^{26}Al and ^{10}Be activities as 6-8%.

The activities of the metal-rich phases agree with or exceed the values observed in small iron meteorites and the metal phases of stones [5]. The elevations reflect silicate contamination, which normally affects ^{26}Al activities more than ^{10}Be activities. Except for Acapulco, Pontlyfni, and Divnoe, the ^{26}Al and ^{10}Be activities of the bulk samples and silicate-rich phases are lower than the production rates expected for such meteorites under normal shielding conditions and long irradiations. The bulk samples contain more iron and consequently have lower (~10%) production rates of ^{26}Al and ^{10}Be than do the silicate-rich samples. Allowance for this fact must be made when comparing analyses of the various of samples. Acapulcoites ALHA 81187 and ALH 84190 have been paired [6]; their measured ^{26}Al and ^{10}Be activities are indistinguishable.

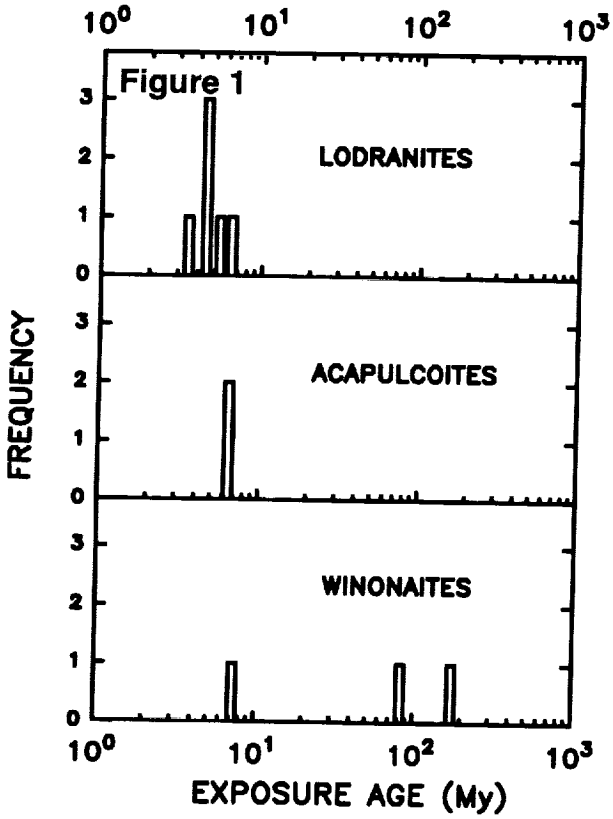

We calculated ^{10}Be/^{21}Ne [7] exposure ages with due allowance for compositional effects by combining our ^{10}Be measurements with noble gas data from the literature. For the purpose we assumed that terrestrial ages of the meteorites are short compared to ^{10}Be half life. Where comparisons are possible ^{10}Be/^{21}Ne and shielding corrected ^{21}Ne ages [8] agree within the ~15% uncertainties of the former. Accordingly, the exposure age distribution of Figure 1 includes shielding-corrected ^{21}Ne ages for Yamato 74063 [9] and Gibson (O. Eugster, pers. comm.), meteorites for which we were unable to calculate ^{10}Be/^{21}Ne ages. The exposure ages of six lodranites cluster in the range from 3.8 to 6.4 My; the average is 5.2±0.9 My. Despite the clear grouping, the data are not now precise enough to claim a common exposure age for all lodranites. The lodranite group age appears marginally lower than the ages for Acapulco (~ 7 My) and ALHA 77081 (6.2±0.4 My [9]) but not enough lower to make a sharp distinction between the two kinds of meteorites. We obtain a ^{10}Be/^{21}Ne age of ~7 My for Kakangari; the ages of Winona and Pontlyfni (^{38}Ar only) are much larger - more like those of mesosiderites [10]. The normalized ^{26}Al and ^{10}Be production rates estimated from our bulk/silicate ^{26}Al and ^{10}Be activities for lodranites and acapulcoites are on average ~25% lower than those of average H chondrites. These results taken together with noble gas data suggest near-surface locations in small bodies for many of the samples [7].

References. [1] Crabb J. and Schultz L. (1981) *Geochim. Cosmochim. Acta 45*, 2152-2160;Marti K. and Graf T. (1992) *Annu. Rev. Earth Planet. Sci. 20*, 221-243; Welten K.C. et al. (1993) *Meteoritics 28*, 459; Eugster O. and Michel Th. (1993) *Meteoritics 28*, 346. [2] Eugster O. and Weigel A. (1993) *Lunar Planet. Sci. XXIV*, 453-454. [3] Herzog G.F. et al. (1993) *Meteoritics 28*, 362-363. [4] Middleton R. and Klein J. (1986) *Proc. Workshop Tech. Accel. Mass Spectrom.*, Oxford, England, pp. 76-81; Middleton R. and Klein J. (1987) *Phil. Trans. Roy. Soc. London A323*, 121-143. [5] Nagai H. et al. (1993) *Geochim. Cosmochim. Acta 57*, 3705-3723; Aylmer D. et al. (1988) *Earth Planet. Sci. Lett. 88*, 107-118. [6] McCoy (1993) *Lunar Planet. Sci. XXIV*, 945-946. [7] Graf Th. et al. (1988) *Meteoritics* **23**, 271. [8] Eugster O. (1988) *Geochim. Cosmochim. Acta 52*, 1649-1659. [9] Takaoka N. and Yoshida Y. (1991) *Proc. NIPR Symp. Antarct. Meteorites 4*, 178-186. [10] Begemann F. et al. (1976) *Geochim. Cosmochim. Acta 40*, 353-368.

GRANULITIC MATRICES IN MONOMICT EUCRITES Akira Yamaguchi and Hiroshi Takeda, Mineralogical Institute, Faculty of Science, University of Tokyo, Tokyo 113, Japan.

The lunar highland breccias have closer textural affinities to some part of eucritic breccias than are found in other meteoritic breccias. The granulitic breccias are recognized as thermally metamorphosed fragmental breccias in early history of the lunar highland. The texture of granulitic breccias are extremely varied, ranging from granoblastic to poikiloblastic, from homogeneous to heterogeneous, and form coarse- to fine-grained [1]. We found that Yamato (Y) -74356,10 and Stannern have textural similarities to lunar granulitic breccias in addition to Millbillillie [2], [3]. The purpose of this study is to investigate "eucritic granulites" and compared with lunar granulitic breccias (67235,5, 76230,12, and 79215,55) mineralogically and petrographically.

Y74356,10. This meteorite was the first monomict eucrite found in Antarctica [4]. This eucrite is composed of ophitic clasts, granulitic pyroxene clasts, comminuted mineral fragments and granoblastic clastic matrix. The granulitic clasts are composed of fine-grained (< 80 μm in diameter) polygonal pigeonite, augite, minor minerals such as ilmenite and silica mineral. Microscopic observation shows granoblastic texture similar to lunar granulite 79215,55. The SEM observation indicates that the clastic matrix of Y74356,10 composed of polygonal mineral fragments with high porosity (~10 %) (Fig. 1a). The fragments in the matrix are usually subrounded to rounded, but some are angular. Many grain boundaries show 120° triple points juncture. Pyroxene compositions fall along a single tie line in the pyroxene quadrilateral ranging from $Ca_4Mg_{38}Fe_{58}$ to $Ca_{37}Fe_{31}Fe_{32}$. Pyroxenes in the ophitic clasts show cloudy appearance. Zoning of plagioclase crystals from An_{86} to An_{94} are preserved.

Stannern. Stannern is a typical example of the ordinary eucrites [4]. The specimen we examined is composed of medium-grained clasts to fine-grained subophitic clasts, and comminuted matrix. The large clasts show subophitic texture of pyroxene and plagioclase. The SEM observation revealed that the clastic matrix of Stannern are comminuted, compacted, and partly recrystallized. Minerals in the matrix are polygonal to subround more than 10 μm (Fig. 1b). Although the pyroxene compositions of the clasts and matrices fall along the single tie line in the pyroxene quadrilateral ranging from $Ca_{2.4}Mg_{36.7}Fe_{60.9}$ to $Ca_{42.8}Mg_{30.1}Fe_{27.1}$, remnant of the Mg-Fe-Ca trend is observed. Plagioclase crystals are zoned from An_{92} to An_{75}.

The petrographic textures of Y74356,10 and the matrices of Millbillillie and Stannern is similar to lunar granulitic breccias. Precursors of the both lunar and eucritic granulitic breccias are fragmental breccias which is derived from impact cratering event. However, in contrast to the lunar granulitic breccias, precursor of Millbillillie, Y74356, and Stannern is not polymict breccia but monomict breccias of non-cumulate eucrites. High porosity (~10%) of Y74356,10 indicates that this rock was not suffered from shock compaction before the thermal annealing.

Y74356, Stannern, and Millbillillie can be classified as eucritic granulitic breccias. Recrystallization of the clastic matrix indicates the post-shock thermal annealing. Presence of the eucritic granulitic breccias implies that extensive thermal annealing generated the ordinary eucrites are related to the brecciation event. However, matrix of Y74356 indicates that the impact cratering events which formed Y74356 have been not so strong as the events formed the polymict breccia.

Similarities in both granulitic textured rocks are textures and thermal histories. However, we conclude that, in contrast to the lunar counterparts, impact and thermal event which produced the eucritic granulitc breccias are not so extensive as those of lunar analogues and the ejecta deposits of the eucritic breccias were thinner than those of lunar granulites. It is interesting to note that these rocks represent products of early crustal evolution induced by cratering. However, the temperature must have been as high as the lunar one to make granulitic textures. The lunar granulites lost their original textures by thermal annealing, but eucritic granulites still keep the original crystallization textures. Thermal metamorphism and impact cratering are intimately related and major events for the early history of relatively large planetary bodies such as the HED meteorites parent body and Moon.

GRANULITIC MATRICES IN MONOMICT EUCRITES: A. Yamaguchi and H. Takeda

We thank to NIPR, NASA, and the Planetary Materials Database Collections of Mineralogical Inst., Univ. of Tokyo for the samples.

REFERENCES. [1] Lindstrom M.M. and Lindstrom D.J. (1986) *Proc.Lunar Planet. Sci. Conf. 16th, in J. Geophys Res.*. 91, D263-D276. [2] Bobe K.D. et al. (1989) *Meteoritics.* 24, 252. [3] Yamaguchi A.et al. (1994) *Meteoritics.* in press. [4] Takeda H. (1979) *Icarus.* 40, 455-470. [5] Takeda H. et al. (1983) *Mem. Natl. Inst. Polar Res. Spec. Issue.* 20, 81-99.

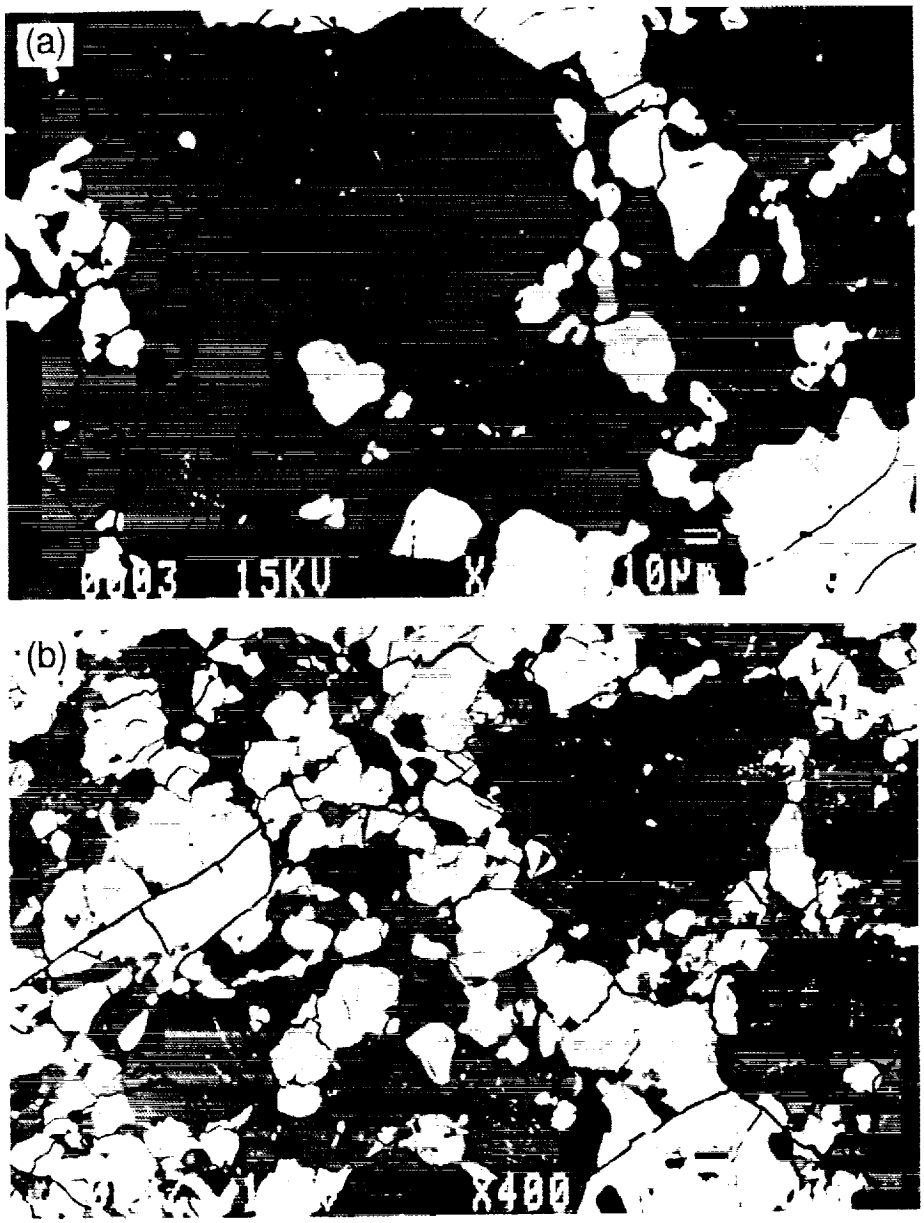

Fig. 1. Back scattered electron images of recrystallized clastic matrix. Dark grey: plagioclase, light grey: pigeonite; back: epoxy.

TIDAL DISRUPTION OF COMET SHOEMAKER-LEVY-9 NUCLEI JUST BEFORE THE IMPACT ON JUPITER;

M. Yanagisawa and T. Konno, Univ. Electro-Communications, Chofu-shi, Tokyo, 182 JAPAN.

Each nucleus of Comet Shoemaker-Levy-9 (SL-9) will be disrupted due to Jovian tidal force just before its impact on the planet. The impact phenomena, for example, impact flash, significantly depend on whether fragments collide with the planet as a single pile or multiple impactors. We modelled the nucleus as being made of non-viscous fluid of 1 g/cm^3 in density and 1 km in diameter. We numerically simulated its tidal deformation during its approach to Jovian surface. The tidal force made the body spheroidal in shape but did not split it. The ratio of the major to minor axes of the spheroid has been shown to be 1.4 at the impact. The fragments of the tidally disrupted real nucleus will be confined in the spheroidal surface and not be scattered at the entry into Jovian atmosphere.

Introduction: SL-9 consists of about 20 nuclei. Its orbital parameters indicate that single cometary nucleus would split during its 1992 close approach to Jupiter due to the planet's tidal forces. Orbital calculations show that these nuclei will impact on Jupiter one after another in July 1994 [1]. If the tidal force exceeds the strength of the nuclei, each of them will be fragmented again and fragments may collide with the planet as multiple impactors. On the other hand, the fragments may play as a single body in the impact phenomena because there may not be enough time for them to be scattered before the impact. Whether the fragments act as a single or multiple impactors depends on how wide they are scattered. Simulated tidal deformation or disruption of a hypothetical strength-less object will give us an idea on the range of fragment dispersion.

Model: We investigated the deformation using 3-Dimensional Smoothed Particle Hydrodynamics (SPH) method [2]. The hypothetical object is represented by 100 particles with a density kernel width of 45 m. Instead of sophisticated equation of state, we adopted isothermal incompressibility of water at room temperature and 1 atm, ie. 2.2 GPa. We do not take temperature into account. This unrealistic equation does not make our results meaningless because pressure has little effect on the deformation. The pressure works just to inhibit the gravitational collapse of the particles and only 10 Pa at most in this case. The equation of motion for each particle has terms for the pressure and gravitational forces due to the other particles and Jupiter. The equations were integrated numerically with time step of 10 sec.. We used the orbital parameters of SL-9 calculated by P. Chodas (personal communication) on the observational data of Mar. 17 - Jun. 6, 1993, that is, a = 380 R_J and q = 0.53 R_J. Here, a, q and R_J are semimajor axis, peri-Jovian distance and radius of the planet, respectively. The positions of the body projected on its orbital plane are shown in Fig. 1 at some instances before the impact. The initial position and velocity of the center of mass of the particles are those at 2 hours before the impact calculated from the orbital parameters. Initial Jovian-centric distance to

TIDAL DISRUPTION OF COMET SL-9 NUCLEI: Yanagisawa, M. and Konno, T.

hours before the impact calculated from the orbital parameters. Initial Jovian-centric distance to the object is 4.3 R_J and the tidal force could be negligible there. The object is initially in hydrodynamic equilibrium without the tidal force. We made calculations for three rotational periods, 20 hours pro-grade (counter clockwise in Fig. 1), 20 hours retrograde, and non-rotation. The axis of the rotation is perpendicular to the orbital plane.

Results and Discussion: The positions of the 100 particles at the impact are projected on the orbital plane in Fig. 2 for non-rotating body. The object that is initially spherical in shape is elongated to spheroidal. However, it does not split. The ratio of the major to minor axes of the spheroid is 1.4. We found that the pro-grade rotation increases the ratio to 1.5 and retrograde one decreases it. This is because the tidal force acts in the same direction of the body for longer time for the pro-grade rotation than non-rotation. The angular velocity of the spin is yet smaller than that of the rotation of Jupiter-nucleus line. Shorter spin period would lead to a little more deformation.

The nuclei of SL-9 will not deform as shown in the simulation but split. The less their strength, the wider range their fragments would disperse. Then, the spheroidal surface of the hypothetical fluid nucleus would limit dispersion range. The results indicate that each nucleus of SL-9 will impact on Jovian atmosphere as a single pile of fragments though it splits due to the planet's tidal force.

REFERENCES: [1] Sekanina, Z. (1993) *Science*, *262*, 382. [2] Benz, W. (1989) in *Numerical Modeling of Stellar Pulsation: Problems and Prospects.*

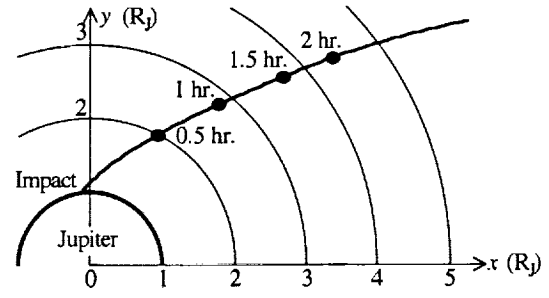

Fig. 1. The positions of one of SL-9 nuclei projected on its orbital plane at 0.5, 1, 1.5 and 2 hours before the impact on Jupiter. Jovian centric x and y axes are parallel and perpendicular to the semimajor axis of SL-9 that is now orbiting the planet.

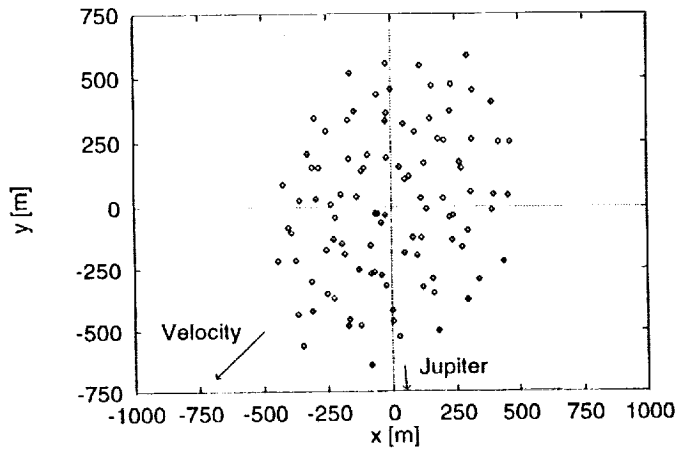

Fig. 2. A hypothetical SL-9 nucleus is represented by 100 particles. They initially formed a spherical body at 2 hours before its impact on Jupiter. The positions of them at the impact are projected on its orbital plane. The x and y axes are parallel and perpendicular to its semimajor axis, and the origin is the center of mass of the object. Also shown are the directions of velocity vector and Jovian center.

AEM STUDY OF THE TETRATAENITE RIM OF METAL PHASES IN METEORITES; C. W. Yang, D. B. Williams, Dept. of Materials Science and Engineering, Lehigh University, Bethlehem, PA 18015, J. I. Goldstein, College of Engineering, University of Massachusetts, Amherst, MA 01003

Three sub-zones have been observed in the tetrataenite rim which is the outermost region of the metal particles in chondrites. We have observed a similar structure in the tetrataenite rim of the mesosiderites. The tetrataenite rim in RKPA 79015 contains a range of Ni contents from 45.6±0.41 wt% Ni to 53.6±0.39 wt% Ni. The ordered structure of the tetrataenite rim and the cloudy zone is a single continuous crystal.

Introduction The retained taenite of meteoritic metal is composed of several structural regions. From the high Ni border moving into the center of the retained taenite, the microstructure includes clear taenite I(CT I), cloudy zone(CZ), clear taenite II(CT II), and martensite(M) along the Ni concentration gradient[1]. In ordinary chondrites, Duffield et al.[2] have observed three sub-zones inside of tetrataenite rim(TR) which corresponds to clear taenite I. It was originally argued that this structure was unique to the non-phosphorus containing metal particles found in the chondrites. In examining the tetrataenite rim in mesosiderites we observed a microstructure containing three sub-zones[3] very similar to that in ordinary chondrites . The purpose of this study is to investigate the microstructure and composition of the tetrataenite rim in the retained taenite using analytical electron microscopy(AEM) techniques.

Experiment Mesosiderites selected for examination include Barea(USNM 1468), Chinguetti(USNM 3250), Patwar(USNM 1243), Pinnaroo(USNM 2312), and RKPA 79015. A combination of electron optical instruments was employed including a JEOL 6300F field emission gun high resolution scanning electron microscope (FEG-HRSEM), a Philips 400T AEM, and a JEOL 733 electron probe microanalyzer(EPMA).

Results and Discussion Fig.1a is a light optical micrograph of a retained taenite particle surrounded by silicate matrix in the Patwar mesosiderite. The micrograph shows three distinct sub-zones in the tetrataenite rim. Since the mesosiderite has been cooled more slowly than other meteorites, the island phase of the cloudy zone is larger (about 350 - 500nm) and the tetrataenite rim is much wider (about 4 - 7μm) than in other meteorites. These larger structures are easily observed in the AEM. Fig. 1b shows a high magnification SEM image of the tetrataenite rim and shows the three sub-zones. All the mesosiderites investigated in this study contain three sub-zones inside of the tetrataenite rim. Fig. 2a is a transmission electron microscopy(TEM) bright field image of the tetrataenite rim and the cloudy zone of the RKPA 79015 mesosiderite at the boundary between the two structures. Fig. 2b shows a Ni composition profile across kamacite and retained taenite in the RKPA 79015 mesosiderite. The data were obtained by X-ray microanalysis using an AEM. The tetrataenite rim in RKPA 79015 contains a range of Ni contents from 45.6±0.41 wt% Ni near the cloudy zone to 53.6±0.39 wt% Ni near kamacite. Using electron diffraction, evidence of an ordered structure ($L1_0$) in the tetrataenite rim was obtained. The twinning structure found in the tetrataenite rim was also observed in other meteorites[5] while there was no twinning structure observed in the kamacite. The twin does not stop at the boundary between the tetrataenite rim and the cloudy zone. In addition, there was no change in crystallographic orientation of the tetrataenite rim and the island phase in the cloudy zone. This observation confirms that the ordered structure of the tetrataenite rim and the cloudy zone is a single continuous crystal. The cloudy zone shows a fluctuation in Ni composition because it is composed of high Ni ordered tetrataenite, called the island phase, which is bright in the bright field image, and low Ni martensite, called the honeycomb phase, which is dark in the bright field image.

References [1] Reuter K. B. et al. (1988) *Geochim. Cosmochim. Acta. 52, 617* [2] Duffield C. E. et al. (1991) *Meteoritics, 26, 97* [3] Yang C. W. et al. (1993) *LPSC XXIV, 1557* [4] Yang C. W. et al. (1993) *Meteoritics, 28, 464* [5] Lin L. S. et al. (1977) *Geochim. Cosmochim. Acta. 41, 1861*

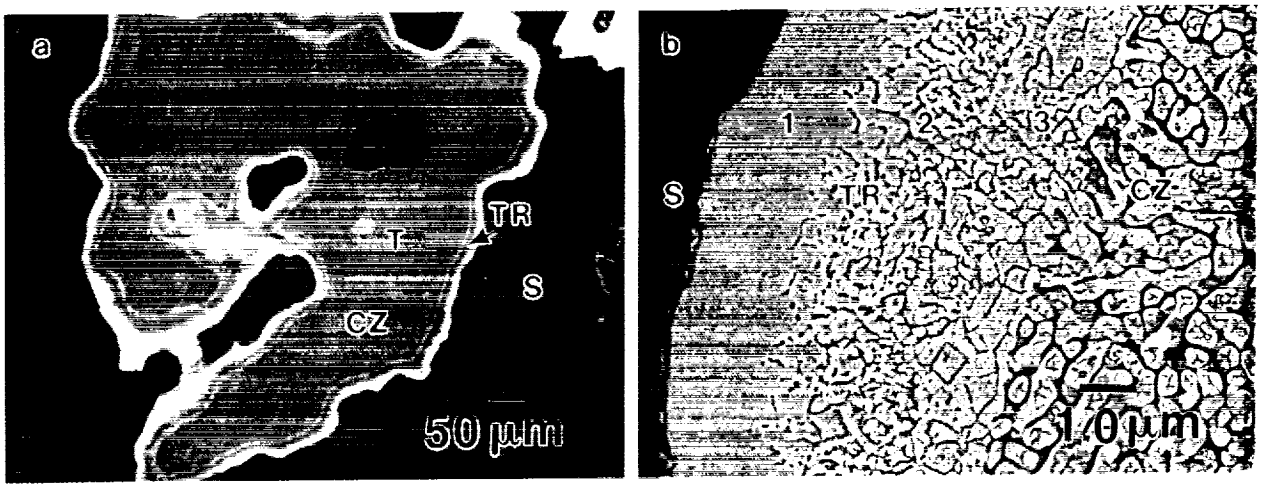

Fig. 1. a) A light optical micrograph of a retained taenite in Patwar mesosiderite. b) A SEM image of the tetrataenite rim which shows three sub-zones(1, 2, 3). T; retained taenite, TR; tetrataenite, CZ; cloudy zone, S; silicate matrix.

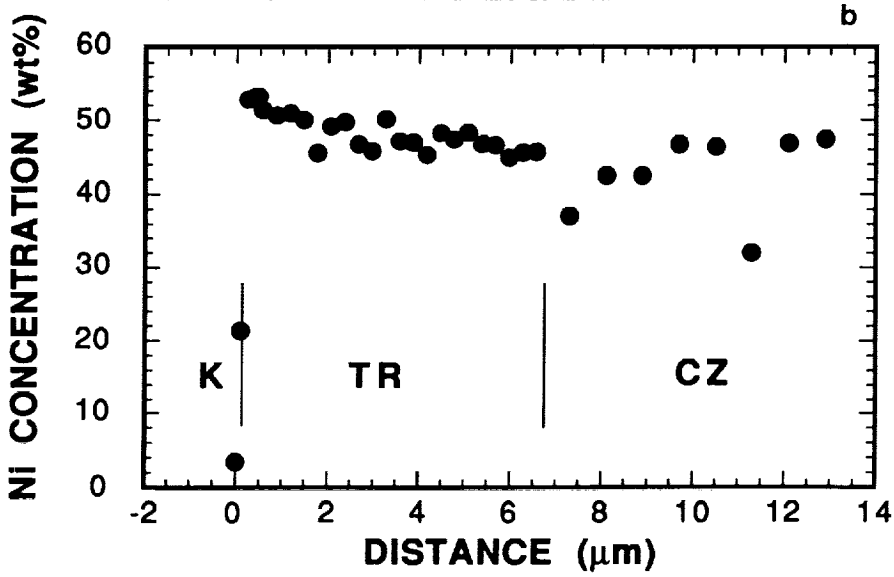

Fig. 2. a) TEM bright field image of the tetrataenite rim(TR) and the cloudy zone (CZ) of RKPA 79015 mesosiderite b) Ni composition profile across kamacite (K) and retained taenite in the RKPA 79015 mesosiderite.

LUNAR MARE DEPOSIT VOLUMES, COMPOSITION, AGE, AND LOCATION: IMPLICATIONS FOR SOURCE AREAS AND MODES OF EMPLACEMENT: R. Aileen Yingst and James W. Head, Dept. Geological Sciences, Brown University, Providence RI 02912 USA

Introduction: Analysis of lunar mare basalts has resulted in intense focus on the petrological aspects of rock characterization and led to a series of mare basalt petrogenetic models (e.g., 1). Analysis of high-resolution images of the mare surface documented the geomorphology of landforms and the stratigraphy of volcanic units (e.g., 2, 3). However, there have been only a handful of analyses focusing on documentation of processes operating between the source regions and the surface features (4, 5). This is particularly true with respect to both conceptual and quantitative assessments of the relation of source regions to surface features, and the interpretation of surface features in terms of the geometry of the conduits delivering magma from the source to the surface. In recent studies we have been working to bridge this gap by establishing the basic theoretical framework for considering the ascent and eruption of magma on the Moon (4), and then developing the principles of reservoir development at neutral buoyancy zones at the base of the highlands crust or at rheological boundaries, the overpressurization of reservoirs, and the general properties of dikes that would be propagated toward the surface from both a theoretical (6) and observational (7) point of view. In this contribution we report on an initial analysis of mare deposit volumes, compositions, ages, and locations, and investigate implications for modes of emplacement and nature of source regions.

Data: In the major lunar maria, analysis of volumes of mare deposits and linkage to their source vents is complicated by subsequent lava flow unit emplacement and burial. To minimize these problems, our intital analyses focus on deposits that occur in isolated patches in the highlands adjacent to the major maria. Although we cannot be sure without supporting evidence that each of these deposits represents a single eruption episode, this approach nonetheless represents better maximum estimates than the more complex deposits of the main maria. We have focused our analysis initially on the mare patches in the western limb and farside area because of the large numbers of patches there (8) and recent data on their composition and ages (9, 10). Although the presence and general characteristics of these mare patches have been known for years (2) recent Galileo multispectral data and impact crater size-frequency distribution data from Lunar Orbiter provide important new information to apply to this problem (9, 10). Mare volumes for 33 lava ponds in the Orientale area have been estimated by Gaddis and Head (8) by measuring flow scarp height, partially buried craters, pre-existing topography and ejecta blanket topography (Fig. 1). In order to examine the evolution of lunar volcanism in this region in space and time, we have placed some of these data in a stratigraphic column (Fig. 2).

Modes of Occurrence, Volumes, and Associated Features: Gaddis (8) found that of the 33 ponds analyzed, 11 occur in association with Orientale basin rings (BR), 10 on the floors of pre-existing craters (CF), and 12 in intercrater areas (IC). Only two of the 33 lava ponds exceed 1280 km^3 (Lacus Veris, 5755 and Grimaldi, 11,250 km^3), and these are likely to have multiple flow units. The remainder fall between 20-1280 km^3 and showed no major differences in average volume relative to mode of occurrence (BR = 385; CF = 250; IC = 542 km^3). Twenty-one ponds were 200 km^3 or less (Fig. 1); of these, the largest group (7 ponds) have volumes 20 km^3 or less, and the next largest (4 ponds) have volumes between 140-160 km^3. For comparison, the terrestrial Laki eruption was ~12 km^3, and the Roza Member of the Columbia River Basalts was ~1200 km^3 (11), approximately at the upper and lower ends of the range of values for the 31 ponds, and orders of magnitude higher than single eruptions associated with shallow magma reservoirs such as Hawaii. Sinuous rilles are associated with 27% of the ponds and linear rilles with 42%; 18% show both linear and sinuous rilles. Sinuous rilles are preferentially associated with basin ring occurrences (BR = 55%; CF = 20%; IC = 0%) and linear rilles show a slight preference for crater floor occurrences (BR = 45%; CF = 50%; IC = 33%).

Interpretation: Typical volumes for dikes bringing melt close to or out onto the lunar surface from source regions at about 100 km depth have been estimated to lie in the range of 200-600 km^3 (6). Thus, if such volumes are required even to establish pathways to the surface it is easy to understand why typical observed lunar volumes would fall more in the terrestrial flood basalt range than in a range typical of shallow magma reservoirs. Observation and analysis of the 31 pond volumes on the western nearside thought to represent single eruptive phases (10-1280 km^3) show that these values range from a small percentage up to about a factor of two of the total estimated dike volumes. In addition, Hulme (12) has estimated that extruded volumes required to erode sinuous rille channels lie in the range of 100 to at least 1000 km^3; 78% of the ponds with sinuous rilles fall in this range. The large number of ponds with associated linear rilles is also consistent with penetration of dikes to the near-surface environment (6,7). The lack of strong correlation of average pond volumes with mode of occurrence suggests that conditions at depth, not in the upper crust, are important. We thus conclude that these data are consistent with dikes that are propagating to the surface from overpressurized source regions at depth.

Stratigraphy: Fig. 2 shows the crater ages of mare deposits analyzed by Greeley *et al.* (9) on the western limb and farside and indicates that mare emplacement occurred over a period of ~1.8 billion years, between ~2.5 and

3.8 b.y. ago. The earliest deposits occurred within ~140 my of the formation of the Orientale basin at ~3.84 Ga, and represent continuation of pre-Orientale mare, now cryptomaria (13), emplacement in the Schiller-Schickard region, and filling of the south-central Orientale basin. Later emplacement (~3.64 Ga) took place in the South Pole-Aitken basin (Apollo and Van de Graff) and following this phase, volcanism continued in Mare Orientale, Lacus Veris, and nearby Riccioli (~3.45-3.5 Ga). Basalts were emplaced in western Grimaldi at ~3.25 Ga. The most recent volcanic activity in this region of the Moon appears to have taken place in Lacus Autumni (~2.85 Ga) and in eastern Grimaldi (~2.49 Ga).

Interpretation: For the most part, there appears to be no strong correlation between time of large crater or basin formation and mare emplacement. Maria in Apollo, Van de Graff, South Pole-Aitken, and Grimaldi postdate these events by many hundreds of millions of years. Although maria began filling Orientale soon after its formation (within ~140 my) nearby deposits were already being emplaced in the Schiller-Schickard region prior to the Orientale event and continued subsequently, contemporaneous with the early Orientale basin fill. In addition, the separation in ages of fill is striking. Maria within Orientale appear to have been emplaced in three phases at ~3.7, ~3.45-3.5, and ~2.85. The total duration is 850 my and the spacing between these phases is 200 my to 650 my, an extremely long time period for a single continuous source region to remain active by terrestrial standards. A similar situation exists in the maria within the crater Grimaldi; on the basis of crater size-frequency distribution data (9) the western flow unit was formed more than 750 million years before the eastern unit and the two units have different TiO2 abundances, suggesting that they may have different source regions. The age difference would seem to indicate different source regions since in 750 million years a diapir/reservoir would almost certainly have solidified. If this is true, the closeness of the two units in such a small basin (about 150 km diameter) suggests a diversity of reservoirs in the same region of the mantle at widely separated time intervals. An alternative is that these deposits represent the surface manifestations of reservoirs in the upper mantle derived from and replenished by long-lasting plume-like instabitities in the deeper mantle (14). We are presently building on this basic data set of individual volcanic episodes in space and time in order to address further the questions of areal extent, compositional variation, and temporal duration of mare basalt source regions.

References: 1) J. Longhi, *G&CA, 56*, 2235, 1992; C. Neal and L. Taylor, *G&CA, 56*, 2177, 1992. 2) D. Wilhelms, *USGS PP-1348*, 302 pp., 1987. 3) J. Head, *RGSP, 14*, 265, 1976; BVSP, Pergamon, 1981. 4) L. Wilson and J. Head, *JGR, 86*, 2971, 1981. 5) F. Spera, *G&CA, 56*, 2253, 1992. 6) J. Head and L. Wilson, *G&CA, 56*, 2155, 1992. 7) J. Head and L. Wilson *PSS*, in press, 1994. 8) L. Gaddis and J. Head, *LPSC XII*, 321, 1981; L. Gaddis, Brown Univ. MSc. Thesis, 1981. 9) R. Greeley *et al., JGR, 98*, 17183, 1993. 10) A. McEwen *et. al., ibid.*, 17207, 1993. 11) S. Reidel and P. Hooper, *GSA SP 239*, 1989. 12) G. Hulme, *Mod. Geol., 4*, 107, 1973. 13) J. Head *et al., JGR, 98*, 17149, 1993. 14) P. Hess and E. M. Parmentier, *LPSC XXIV*, 651, 1993.

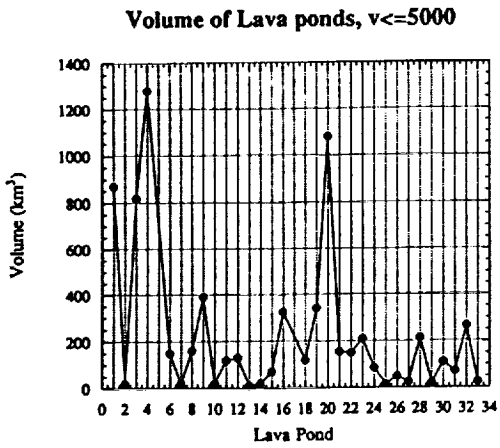

Figure 1.
Volume-frequency distribution for 31 lava ponds (8).

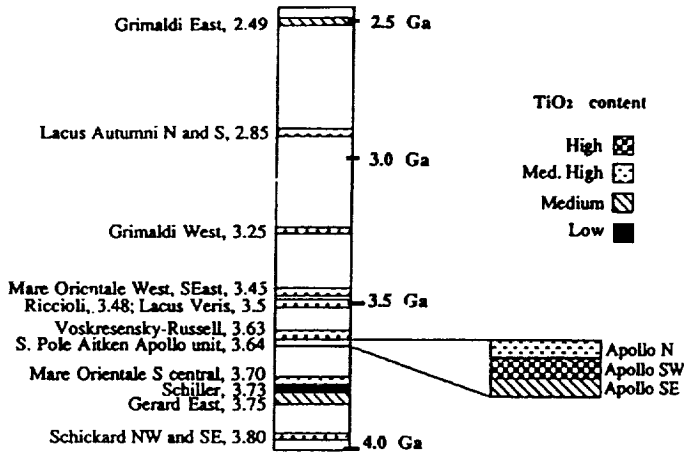

Figure 2.
Stratigraphic column for mare deposit emplacement (9).

ADVANCED GENERATION CONDENSATION CALCULATIONS: COMPOSITIONS OF FASSAITE, SPINEL AND PLAGIOCLASE IN THE SOLAR NEBULA; S. Yoneda[1] and L. Grossman[1,2]. [1]Dept. of the Geophysical Sciences and [2]Enrico Fermi Institute, The University of Chicago, Chicago, IL 60637.

Abstract. An advanced generation of condensation calculations is used to explore the equilibrium gas-solid phase relations in a solar gas, yielding for the first time the expected concentrations of Ti^{3+}, Ti^{4+} and Al in fassaite, and the Fe/Fe+Mg and Cr/Cr+Al ratios in spinel as a function of temperature, along with the compositions of metallic NiFe, melilite, plagioclase, olivine and orthopyroxene. Despite a monotonic decrease in f_{O_2}, the Ti^{3+}/Ti^{tot} ratio in fassaite is predicted to rise from its initial value of .18 at 1449 K to a maximum of .54 at 1366 K, and then to fall steadily, reaching .36 at 1200 K, primarily in response to reactions among Al- and Si-bearing phases. Condensate spinel should contain ≤5.6 wt % Cr_2O_3 and ≤.28 % FeO.

While Ti-, Al-bearing pyroxene is a common constituent of CAIs, and Fe- and/or Cr-bearing spinel is found in a variety of meteoritic assemblages suspected of being condensates or derived therefrom, the expected concentrations of these elements in clinopyroxene and spinel that equilibrated with a gas of solar composition have never been investigated in condensation calculations. New thermodynamic data now make this possible.

Equilibrium condensation calculations were performed by solving systems of simultaneous, non-linear, mass-balance equations for 16 elements by means of a Newton-Raphson convergence technique. The computer program is an extensively modified version of the one used by Lattimer *et al.* [1]. The temperature resolution was improved to 0.1 K, a generalized routine for treating complex, ideal and non-ideal solutions was introduced, a special routine was added for spinel in which solid solution occurs in two sites independently, and the scheme was automated such that, for example, the entire equilibrium description of a solar gas over a 1000 K temperature interval can be computed, without operator intervention, in 15 minutes with a 66 MHz, 486 chip.

Significant improvements were also made to the input data used in [1]. We replaced the solar abundances of Cameron [2] with those of Anders and Grevesse [3], and included He. We updated the thermodynamic data for many gaseous species and some crystalline phases by switching from [4] to [5]. We replaced the free energies tabulated by Robie and Waldbaum [6] for many oxide and silicate phases with those of Robie *et al.* [7] or, preferably, those of Robinson *et al.* [8]. Other literature sources were used for data for phases not considered by [1], and to correct data in [7].

Special attention was paid to calculation of the compositions of three solid solution series, plagioclase, spinel, and Ca-rich clinopyroxene or fassaite, which were not investigated by [1]. Binary plagioclase solid solutions were treated non-ideally using the Al-avoidance model and excess enthalpy of mixing data for high plagioclase from [9]. In the case of spinel solid solutions, free energy data for $MgAl_2O_4$ were taken from [10] and, for each of $MgCr_2O_4$, $FeCr_2O_4$ and $FeAl_2O_4$, were calculated from the enthalpy and entropy of formation from the elements at 298 K and the heat capacity *vs* temperature function of [11]. Ideal solution is an excellent assumption for all spinel compositions encountered in this work, according to Sack (pers. comm.). Because the divalent ion entering the spinel structure is independent of the trivalent ion, thermodynamic data are required for only three of the four spinel components discussed here in order to specify the spinel composition completely. Because of measurement errors in the free energies, however, predicted spinel compositions differ, depending on which three of the four components are used in the computations.

Ideality was assumed for fassaite solid solutions. Free energy data for $CaAl_2SiO_6$ (CaTs) were taken from [8], and for $CaMgSi_2O_6$ (Di) from [7] as updated by [12]. For $CaTi^{+4}Al_2O_6$ (T_4P), the free energy *vs* temperature was based on a single thermochemical measurement of $\Delta G°_f$ at 1460 K and a molar volume estimate by Beckett [13], and estimates of the absolute entropy at 298 K and the heat capacity expression by the methods of Holland [14] and Berman and Brown [15], resp. The same technique was employed for $CaTi^{+3}AlSiO_6$ (T_3P), using a molar volume estimate and the average of three independent thermochemical determinations of [$\Delta G°_f$ (T_3P) - $\Delta G°_f$ (T_4P)] at 1500 K by [13], except that the absolute entropy of Ti_2O_3 at 298 K had to be obtained from the heat capacity data of [16]. According to these data, T_4P is ~11 kJ/mole more stable than its constituents, corundum + perovskite, so stable that pure T_4P condenses at 1700 K. Pure T_4P is unknown. Yagi

and Onuma [17] found a maximum X_{T_4P} of .10 in pyroxenes synthesized along the Di-T_4P join, but Allende fassaite is known with X_{T_4P} up to .20 when X_{CaTs} = .05 and X_{T_3P} = .27 [13]. Assuming that the latter formed at equilibrium, 20 mole % may be the maximum solubility of T_4P in such quaternary pyroxenes. We thus increased $\Delta G°_f$ (T_4P) at 1460 K by ~14 kJ/mole, reducing its stability by just enough that no pyroxene composition calculated herein had X_{T_4P} >.20.

These calculations predict the following sequence of events during equilibrium cooling of a gas of solar composition at 10^{-3} atm total pressure. Corundum condenses at 1770 K and disappears at 1740 K in a reaction with the gas to form hibonite. Perovskite condenses at 1688 K, followed by very gehlenitic melilite at 1628 K. Hibonite reacts completely with the gas to form spinel at 1501 K, and metallic Fe (X_{Ni} = .22, $X_{Co} = 5.6\times10^{-3}$, $X_{Cr} = 1.6\times10^{-3}$, $X_{Si} = 2.2\times10^{-3}$) condenses at 1464 K. At 1449 K, melilite reaches a composition of $Åk_{42}$ and begins to react with the gas to form fassaite whose initial X_{CaTs} = .20, X_{T_4P} = .15 and X_{T_3P}= .033. Fassaite formation consumes perovskite at 1448 K and X_{CaTs}, X_{T_4P} and X_{T_3P} fall to .18, .032 and .0080, resp., at 1444 K where melilite disappears. Forsterite condenses at 1443 K. Fassaite and spinel begin reacting with the gas to form plagioclase ($X_{Ab} = 6.8\times10^{-4}$) at 1415 K, causing X_{CaTs} to fall and X_{T_4P} and X_{T_3P} to rise. When spinel is exhausted at 1408 K, X_{CaTs} = .15, X_{T_4P} = .073 and X_{T_3P} = .025. Plagioclase continues to form at the expense of fassaite below this temperature, causing X_{CaTs} and X_{T_4P} to fall to .088 and .066, resp., and X_{T_3P} to rise to .040 at 1386 K. At this point, T_4P and T_3P begin breaking down to Ti_3O_5 + anorthite, and X_{CaTs}, X_{T_4P} and X_{T_3P} fall to .048, .021 and .026, resp., by 1366 K. At this temperature, forsterite begins to react with the gas to form protoenstatite. X_{Ab} in plagioclase reaches .01 at 1305 K, .10 at 1150 K and .80 at 980 K, below which temperature it remains constant.

The calculated Ti^{3+}/Ti^{tot} ratio in condensate fassaite rises gradually from .18 at 1449 K to .25 at 1408 K, more steeply to .54 at 1366 K, and then falls steadily, reaching .36 at 1200 K, despite a monotonic decrease in log f_{O_2} from -18.16 at 1449 K to -22.05 at 1200 K. These Ti^{3+}/Ti^{tot} ratios are below those seen in fassaite in CAIs, .5-.85 [13,18]. When T_3P is made as stable as possible using the 1σ error, ±2.4 kJ/mole, on [$\Delta G°_f$(T_3P)- $\Delta G°_f$(T_4P)], all calculated Ti^{3+}/Ti^{tot} ratios increase by ~.05, and even the maximum value, .59, still lies below most of the observed ratios. Calculated ranges of X_{CaTs}(.04-.20), X_{T_4P}(.02-.07, except for the very first fassaite) and X_{T_3P}(.01-.04) are all slightly lower than those commonly observed in fassaite in CAIs, .2-.3, .05-.15 and .08-.18, resp. [13]. These discrepancies may be due to our assumption of ideality for clinopyroxene solid solutions.

The spinel solid solution is virtually pure $MgAl_2O_4$ over its entire stability interval. When its composition is calculated from thermodynamic data for $MgAl_2O_4$, $MgCr_2O_4$ and $FeAl_2O_4$, its molar Cr/Cr+Al ratio rises from 9.1×10^{-4} at 1501 K to 2.4×10^{-2} at 1410 K. Its molar Fe/Fe+Mg ratio falls from 8.8×10^{-4} at 1501 K to 5.0×10^{-4} at 1443 K and then gradually rises, reaching 6.3×10^{-4} at 1410 K. When $FeCr_2O_4$ is used instead of $MgCr_2O_4$, Cr/Cr+Al ratios are 2.2-2.5 times higher. When $FeCr_2O_4$ is used instead of $FeAl_2O_4$, Fe/Fe+Mg ratios are 6.4-6.8 times higher. Spinel that condensed at equilibrium from a solar gas should contain ≤5.6 wt % Cr_2O_3 and ≤.28 % FeO.

Old problems persist in applying the results of these new, sophisticated calculations directly to CAIs. For example, while spinel + melilite + fassaite + anorthite is the characteristic mineral assemblage of Type B inclusions, calculations indicate that melilite and fassaite coexist at equilibrium over only a 5 K temperature interval, and that anorthite does not become stable until after condensation of forsterite, which is absent from most CAIs. Similarly, while hibonite + spinel is a common assemblage in CAIs from CM2 chondrites, calculations show that these two phases are incompatible in a solar gas, and that melilite condenses at a temperature intermediate between them.

Refs: [1]Lattimer, J.M. *et al.*(1978) *Ap. J. 219*, 230-249. [2] Cameron, A.G.W. (1973) *Space Sci. Rev. 15*, 121-146. [3] Anders, E. & Grevesse, N. (1989) *GCA 53*, 197-214. [4] *JANAF Thermochemical Tables* (1968) First Ed. & later supps. Dow Chemical Co. [5] *JANAF Thermochemical Tables* (1985) Third Ed. Dow Chemical Co. [6] Robie, R.A. & Waldbaum, D.R.(1968) *U.S.G.S. Bull. 1259*. [7] Robie, R.A. *et al.* (1978) *U.S.G.S. Bull. 1452*. [8] Robinson, G.R. Jr. *et al.* (1982) U.S.G.S. Open-File Rept. 83-79. [9] Newton, R.C. *et al.* (1980) *GCA 44*, 933-941. [10] Chamberlin, L. *et al.* (1991) *LPS XXII*, 195-196; & pers. comm. [11] Sack, R.O. & Ghiorso, M.S. (1991) *Am. Min. 76*, 827-847. [12] Charlu, T.V. *et al.* (1978) *GCA 42*, 367-375. [13] Beckett, J.R. (1986) PhD Thesis, Univ. Chicago. [14] Holland, T.J.B. (1989) *Am. Min. 74*, 5-13. [15] Berman, R.G. & Brown, T.H. (1985) *Contr. Min. Pet. 89*, 168-183. [16] Barin, I. (1989) *Thermochemical Data of Pure Substances*. VCH. [17] Yagi, K. & Onuma, K. (1967) *J. Fac. Sci. Hokkaido U.*, 463-483. [18] Simon, S.B. *et al.* (1991) *GCA 55*, 2635-2655.

RETENTION OF SODIUM UNDER TRANSIENT HEATING CONDITIONS - EXPERIMENTS AND THEIR IMPLICATIONS FOR THE CHONDRULE FORMING ENVIRONMENT. Yang Yu and Roger H. Hewins. Dept. of Geological Sciences, Rutgers University, Piscataway, NJ 08855.

Introduction Natural chondrules show relatively high, though varied, Na concentrations, some even equal to or higher than the primitive CI chondrite [1]. This is contrary to the expectation that much of the Na would have been evaporated during the melting events that formed chondrules. Previous experiments have shown that under isothermal heating conditions, a totally molten droplet does lose significant amounts of Na, and the rate of Na loss depends on the temperature, bulk composition, droplet size, and fO_2 [2]. These lead to the argument that in order to retain the Na content as well as the nuclei needed to form the observed chondrule textures, transient heating is more plausible as a heating mechanism than long duration isothermal heating [1]. Though there are reports on the amount of Na loss during flash heating experiments [3, 4, 5], detailed investigation of how the rate of Na loss is related to different transient heating conditions is still needed to evaluate this argument. The experimental study presented here is aimed at testing this conjecture by studying the rate of Na loss from synthetic chondrules under various transient heating conditions, including different initial temperatures, cooling rates, and fO_2.

Experiments The experiments were conducted on a Deltech furnace at Rutgers University. The samples used were type II/III and type I chondrule analog compositions of [3]. They were put into the furnace at different initial temperatures, and the furnace was immediately cooled down. The maximum heating temperatures were in the range of between about 30°C above and below the sample liquidus. The cooling rates were controlled to follow different non-linear cooling profiles, and the initial cooling rates range from as high as 5000°C/hr to about 500°C/hr. Each charge remained inside the furnace for 35 minutes, and was air quenched at the end of each run. The fO_2 of the furnace was maintained at IW-0.5, -2 and -4 respectively for different runs with a gas mixture of H_2 and CO_2. All the Na analyses of the samples were performed on a DCP-AES at Rutgers University, and parallel runs of some of the samples were also analyzed to check the repeatability of the results.

Results Figure 1 shows the summarized results of the experiments. All of the charges have lost the Na content to some degree, and in general, the higher extent of Na loss is observed at lower fO_2, higher maximum heating temperature, and lower cooling rate. For type II/III chondrule composition, a minimal amount of Na loss was observed at higher fO_2 of about 10^{-10} atm (IW-0.5 at 1500°C), in which case the cooling rate or time at highest temperatures seems to be the major factor affecting the Na vaporization rate: about 91% of Na is retained at the initial cooling rate of about 2500°C/hr regardless of the 60°C difference in maximum heating temperatures, and as much as 94% of Na is preserved if the cooling rate is increased to about 5000°C/hr. Lowering the fO_2 increases the rate of Na loss, and both the cooing rate and the maximum heating temperature show a noticeable effect: e.g. at fO_2 of about 10^{-11} atm (IW-2), the sample retains only 80% of its Na content even under favorable conditions of low peak temperature (30°C below the liquidus) and high cooling rate (2500°C/hr), and only 65% of Na is retained if the peak temperature is raised to 30°C above the liquidus, and the cooling rate lowered to 500°C/hr. At an even lower fO_2 of about 10^{-13} (IW-4), the sample retains less than half of its original Na content with an initial cooling rate of 2500°C/hr. Under the same running conditions, samples quenched at different temperatures during the cooling process (2, 6, and 17 min after cooling started) show identical Na contents, indicating that most of the Na loss occurs at the very early stage of the heating-cooling event. The Na vaporization rate differs among samples with similar textures but different compositions. At the same fO_2 and cooling rate, type I chondrule composition lost 16-23% more Na than type II/III chondrule composition charges.

Discussion While our experiments confirm that the factors affecting the Na vaporization rate from isothermal experiments [2] apply to the transient heating conditions as well, we also discovered that the cooling rate after the instantaneous heating event plays a critical role in affecting the Na content of the chondrules. Up to 94% of the original Na content can survive the flash heating event if the cooling rate is higher than 5000°C/hr and the fO_2 is relatively high. These results suggest that transient heating does dramatically reduce the Na loss, and to retain most of the original Na content, it might require faster cooling rate than that suggested by previous work [3, 6]. The experimentally determined fO_2 favoring the retention of Na is higher than the nebula canonical fO_2 [1]. This suggests that the chondrules with high Na, i.e. type II chondrules, formed in a relatively high fO_2 environment, which is consistent with their FeO-rich silicates. Alternatively, something else might have overridden the effect of fO_2, such as higher partial pressure of the Na vapor [7], though it is difficult to imagine the Na vapor pressure raised sufficiently by localized evaporation. With a cooling rate of 2500°C/hr, the charges with similar textures but different compositions show dramatic difference in their Na loss rates, possibly due to the different maximum temperatures needed to form the similar textures. Whether faster cooling rates can eliminate this effect is unknown, but will be the next step of the experiment. Other further experiments include detailed study of the effect of lower fO_2 and high cooling rate on the Na loss, as well as the possible recondensation of the evaporated Na back to chondrules.

References [1] Grossman J. N. (1988) In Meteorites and the Early Solar System (J. F. Kerridge and M. S. Matthews, eds.), 680-696. [2] Tsuchiyama A. et al. (1981) GCA, 45, 1357-1367. [3] Radomsky P. M. and Hewins R. H. (1990) GCA, 54, 3475-3490. [4] Connolly H. C. et al. (1991) Meteoritics, 26, 328-329. [5] Connolly H. C. et al. (1993) LPSC XXIV, 329-330. [6] Lofgren G. E. (1989) GCA, 53, 461-470. [7] Lewis R. D. et al. (1993) Meteoritics, 28, 622-628.

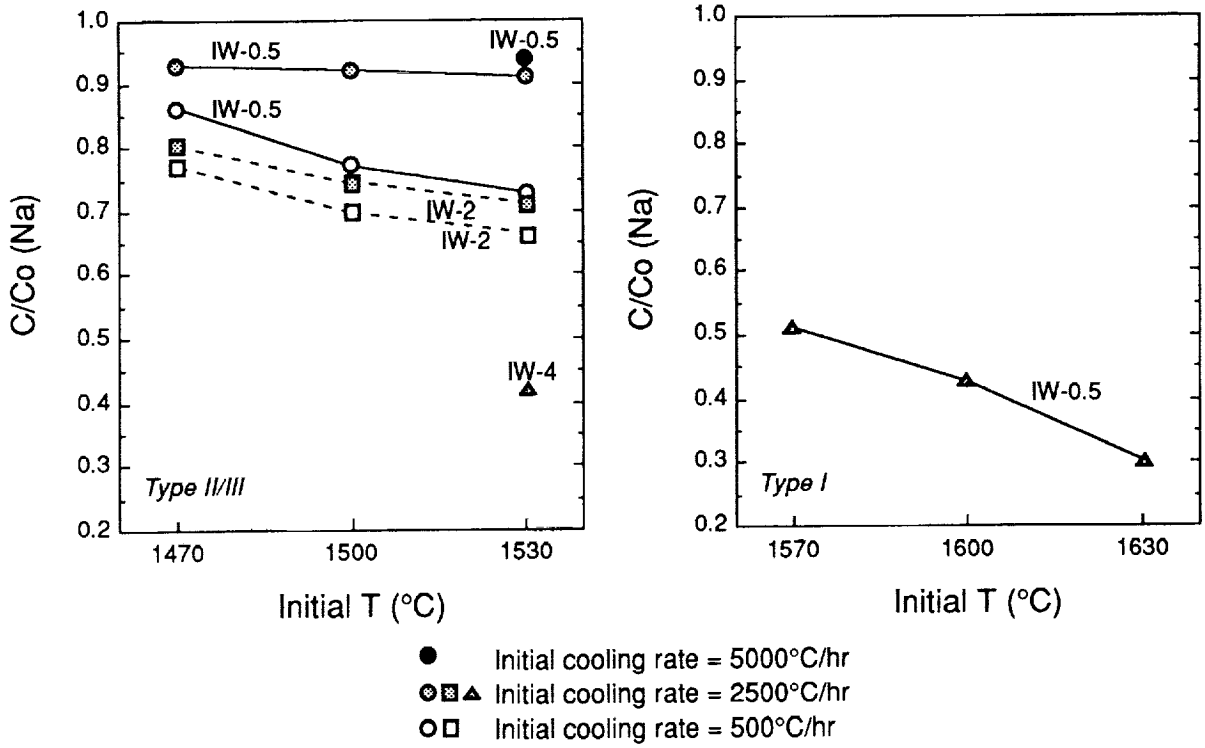

Fig. 1. Experimental results.

CAN SULFIDE MINERALS SURVIVE THE CHONDRULE-FORMING TRANSIENT HEATING EVENT? Yang Yu[1], Roger H. Hewins[1], B. Zanda[2,3], and Harold C. Connolly[1]. [1]Dept. of Geological Sciences, Rutgers University, Piscataway, NJ 08855, USA, [2]Institut d'Astrophysique Spatiale, Paris, France, [3]Museum National d'Histoire Naturelle, 75005 Paris, France.

Introduction The presence of troilite in chondrules has been taken as evidence that chondrule precursors were heated from below its condensation temperature of 650K [e.g. 1], without much agreement on why it has survived melting temperatures approaching 2000K [2]. Retention of moderately volatile elements such as Na in chondrules has suggested very rapid heating [1, 3, 4]. This should apply also to S. Can sulfide minerals survive the heating, and under what conditions and to what degree can chondrules preserve them? The experimental results presented here represent our effort to answer these questions, and include a series of flash heating experiments to see if sulfide can survive different maximum heating temperatures, heating durations, cooling rates, and oxygen fugacities and to consider its implications to chondrule-forming conditions in the nebula.

Experiments The experiments were conducted at Rutgers University with a Deltech vertical muffle tube furnace and at JSC-Experimental Petrology Lab with an Astro furnace. A type II/III chondrule analog composition [5] containing 5% added sulfide (pyrrhotite) was used as the starting material. The experiments at Rutgers University involved both isothermal and flash heating runs. The flash heating conditions were simulated by immediately cooling after the sample was introduced into the hot furnace. The maximum heating temperature ranges from about 30°C above to 30°C below the sample liquidus (~1500°C). The cooling rates were controlled to follow different non-linear cooling profiles, and the initial cooling rates range from as high as 5000°C/hr to about 500°C/hr. Each charge remained inside the furnace for 35 minutes, and was air quenched at the end of each run. The fO_2 of the furnace was maintained at IW-0.5, -2 and -4 respectively for different runs with a H_2/CO_2 gas mixture. The experiments at JSC-Experimental Petrology Lab followed the procedures of [6], in which case the maximum heating temperatures were 150°C to 250°C higher than the sample liquidus, and the fO_2 was maintained at IW-0.5, and -1.5 respectively with a gas mixture of CO/CO_2, . All the charges were later analyzed on a Jeol JXA-8600 electron microprobe at Rutgers University.

Observations Figure 1 shows the results of our observations at different experimental conditions. All the charges run under isothermal conditions with heating times longer than 5 minutes have lost all their pyrrhotite content. However, for the flash heating experiments, some of the charges do retain sulfide as a function of the heating duration and cooling rate. All charges partially retain pyrrhotite if the initial cooling rate was higher than 5000°C/hr, even with the maximum heating temperature of 250°C above the sample liquidus and fO_2 at IW-1.5. However, when the initial cooling rate was decreased to lower than 2500°C/hr, pyrrhotite would be totally evaporated unless the maximum heating temperatures were lower than the liquidus. For the slow cooling runs, higher fO_2 seems to favor the retention of sulfide, but its detailed effect needs further study. For those of the charges that have retained pyrrhotite, the amount of pyrrhotite preserved is less than 1/10 of the pyrrhotite in the original composition. In most cases, the pyrrhotite remains occur in the form of interstitial blebs within the glass between the olivine crystals, but some are enclosed in the latter. Unless the charge is clear glass without olivine crystals, abundant Fe metals are present, which are either embodied within the remaining pyrrhotite grains, or independent interstitial grains between the olivine crystals.

Discussion Many chondrules contain minor to major amounts of troilite, yet all our experiments show extensive loss of S. Very rapid heating of chondrules is one explanation [1, 2, 3].

The flash heating event could be shorter and the cooling profile more curved than in our experiments, reducing the total time spent at high temperature, and preserving more S. Such an origin is likely for weakly melted objects such as dark zoned chondrules which often have abundant troilite. Alternatively, the sulfide in chondrules could be mostly secondary. In Renazzo, the only type I chondrule containing troilite out of about 200 has troilite at the margin which surrounds metal with a very contorted contact between sulfide and metal, suggesting replacement by nebular gas. A similar nebular origin for troilite in chondrule rims in Semarkona was suggested by [7]. In more metamorphosed chondrites such as Tieschitz and Leoville, sulfurization of chondrule metal clearly occurred during metamorphism, as troilite contains inclusions precipitated from Fe metal when it was reheated [8].

Conclusion A very short duration, rapidly decaying heat pulse is required to melt chondrules and retain volatiles such as S. Some troilite may be due to reaction of chondrule metal with S-rich gas.

References [1] Grossman J. N. (1988) In Meteorites and the Early Solar System (J. F. Kerridge and M. S. Matthews, eds.), 680-696. [2] Hewins R. H. and Radomsky P. M. (1990) Meteoritics, 25, 309-318. [3] Yu Y. and Hewins R. H. (1994) LPSC XXV, this volume. [4] Hewins R. H. (1991) GCA, 55, 935-942 [5] Radomsky P. M. and Hewins R. H. (1990) GCA, 54, 3475-3490. [6] Connolly H. C. et al. (1993) LPSC XXIV, 329-330. [7] Huang S. et al. (1993) Meteoritics, 28, 367. [8] Perron C. and Bourot-Denise (1992) LPSC XXIII, 1055-1056.

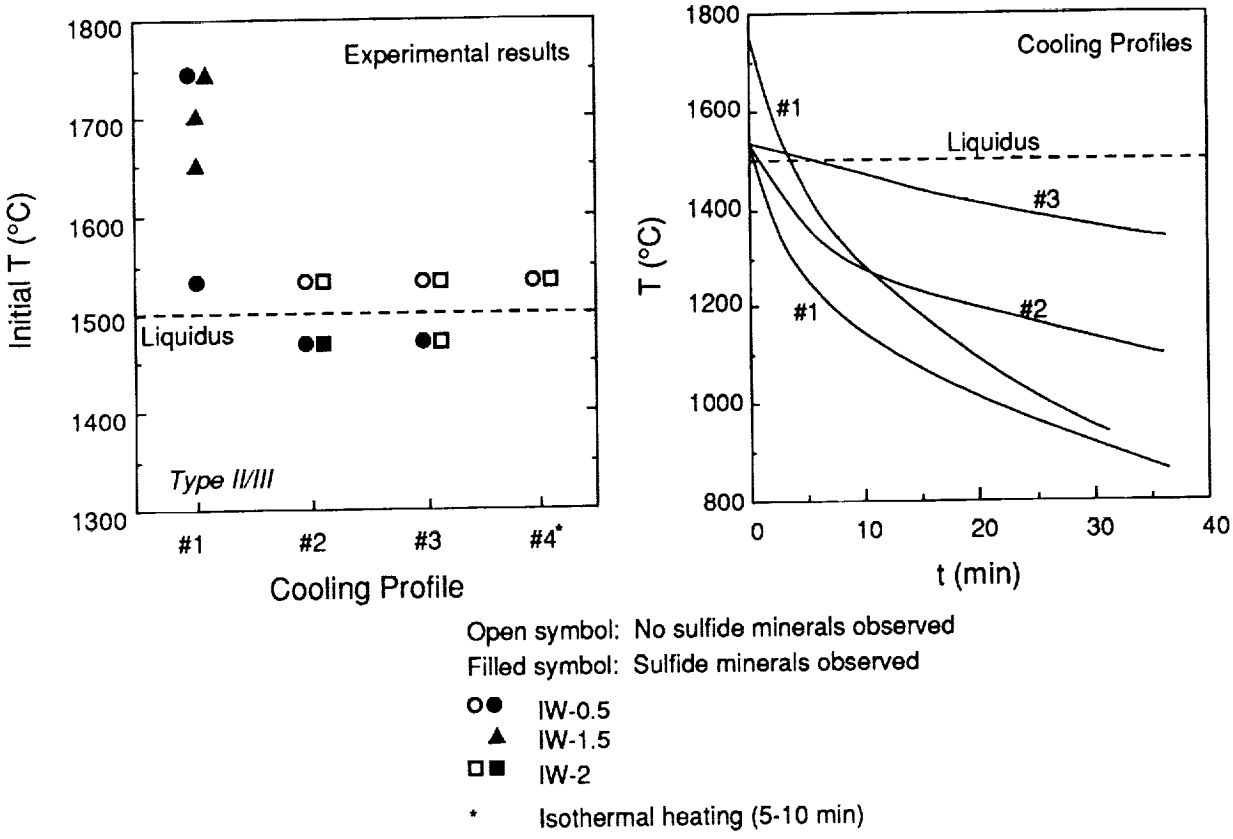

Fig. 1. Experimental results and furnace cooling profiles.

OXYGEN ISOTOPE DISTRIBUTION IN FASSAITE OF ALLENDE CAI;

Hisayoshi Yurimoto [1], Hiroshi Nagasawa [2] and Osamu Matsubaya [3], [1] Institute of Geoscience, The University of Tsukuba, Tsukuba, Ibaraki 305, Japan, [2] Department of Chemistry, Gakushuin University, Mejiro, Tokyo 171, Japan, [3] Mining College, Akita University, Akita 010, Japan.

Calcium, aluminium-rich inclusions (CAIs) from carbonaceous chondrite are believed to be among the first solids to have formed in the early solar system and thus to preserve a record of conditions and processes that prevailed early in the solar nebula. We have measured inter- and intra- crystalline oxygen isotope distribution of fassaite in Type B1 CAI of Allende meteorite. Secondary ion mass spectrometry (SIMS) using negative Au^- primary ion was applied to *in situ* oxygen isotope ratio analysis on an polished thin section of the CAI. Preliminary data and interpretation were given in Yurimoto et al. [1]; the more extensive data presented herein lead to more definitive conclusions than those in our earlier work.

Samples and Experimental Methods: The sample used in this study was a polished thin section (HN3-1c) from Allende HN3-1 Type B1 CAI. Petrological characteristics of the inclusion is described by NAGAHARA et al.[2]. The polished thin section was coated with ~30 nm of gold film for SIMS analysis. Oxygen isotope ratios were measured by the Tsukuba University CAMECA IMS-3F SIMS instrument equipped with BLAKE-V ion source [3]. All O isotopic measurements were made with a focused negative primary ion beam of gold. Primary beam currents were adjusted for each run to obtain a $^{16}O^-$ count rate of ~3 x 10^5 counts s^{-1}. The beam size was 10~20 μm in diameter. A mass resolution power was set to ~2,000 (1% valley), which was sufficient to resolve all significant interferences. Measurements were made by cycling through the mass sequences 16 and 18 in a magnetic peak jumping mode. After the magnetic peak jumping, a precise peak centering of each mass was made by electrostatic peak switching scan. Secondary ion signals were detected with electron multiplier operated in a pulse counting mode. Signals measured in the electron multiplier were corrected for the counting system dead time. The isotopic composition measured by the SIMS differs from true isotopic composition of the sample by the matrix dependent instrumental mass fractionation. In order to correct the instrumental mass fractionation, a terrestrial augite single crystal was prepared as an standard. Oxygen isotope-ratios relative to SMOW for the standard were determined by conventional mass-spectrometry method.

Results and Discussion: Oxygen isotope data for individual minerals after mineral separation in this inclusion were reported by Mayeda et al. [4]. The data were plotted on the slope one Allende mixing line in oxygen three isotope diagram. The $\delta^{18}O$ value of spinel was -40 ‰, whereas melilite and anorthite were around 0 ‰. The $\delta^{18}O$ value of fassaite was -24 ‰ which plot was intermediate from the ^{16}O-enriched spinel position to the melilite/anorthite position. If the CAI was formed originally with ^{16}O-enriched O distributed homogeneously and then O isotopes in minerals were later replaced by heating, diffusion profiles may be observed in the fassaite crystals.

Two distinguished types of fassaite were observed in the CAI. One is the large, blocky fassaite crystals, the other is the fassaite crystals enclosed in melilite in the interiors of the CAI. Fig. 1 shows a blocky fassaite single crystal measured in this study surrounded with anorthite crystals and alteration products. The right bottom part of the fassaite grain was lacked in the thin

section. Oxygen isotope analyses were made on solid circles in the fassaite crystal. The $\delta^{18}O$ data of white and shaded regions in the crystal scatter over the range of -25 to -20 ‰ and -30 to -25 ‰, respectively. The average value of present results is consistent with the previous data of separated fassaite crystals determined by conventional method [4]. The results indicate that there are no evidence of diffusion profile as a result of oxygen isotope exchange after CAI solidification.

In conclusion, present data indicate that O isotope composition is nearly homogeneous inside of fassaite grains in the HN3-1 CAI. The results suggest that the fassaite grains in CAI acquired the peculiar O isotope ratio at crystallization and may be precursor materials like spinel grains.

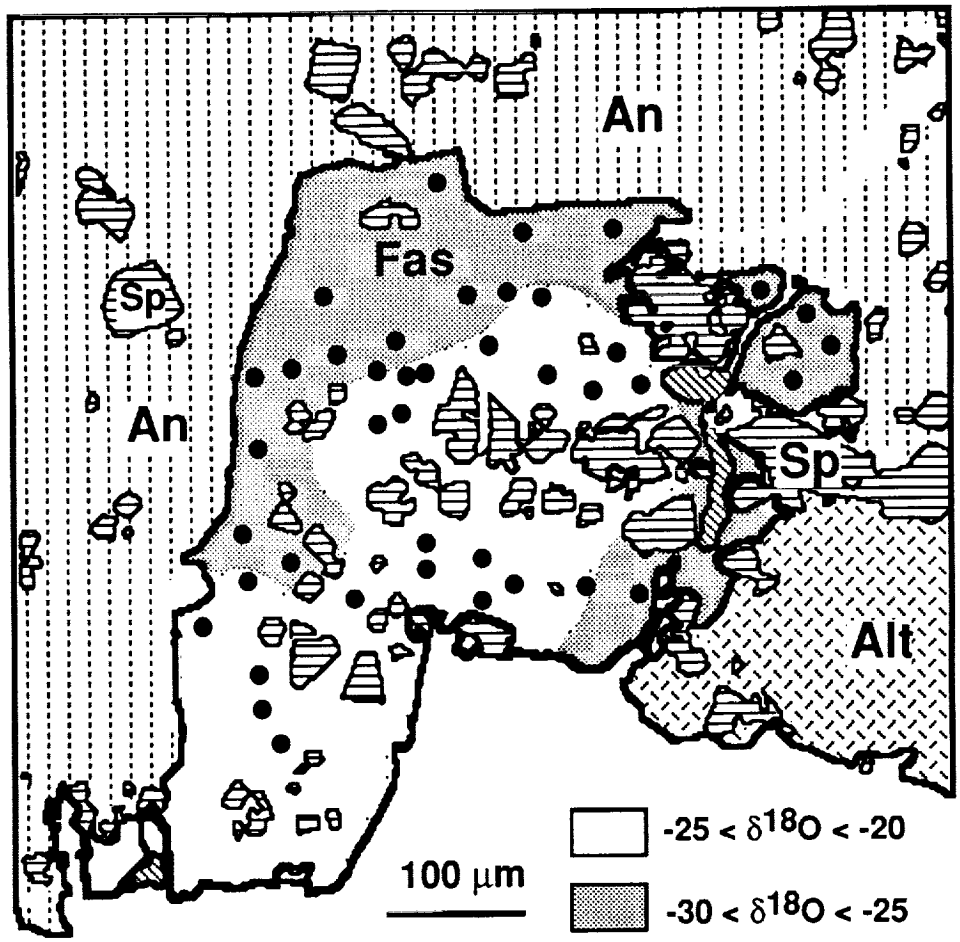

Fig. 1. A large, blocky fassaite single crystal in HN3-1 CAI. Locations of the O isotope analysis by SIMS are shown in solid circles.

References: [1] Yurimoto, H., Nagasawa, H., and Mori, Y. (1993) *Lunar Planet. Sci.* **XXIV**, 1565-1566. [2] Nagahara, H., Nagasawa, H., Nakamura, N., and Matsui, T. (1987) *Lunar Planet. Sci.* **XVIII**, 694-695. [3] Yurimoto, H., Mori, Y. and Yamamoto, H. (1993) *Rev. Sci. Instrum.* **64**, 1146-1149. [4] Mayeda, T. K., Clayton, R. N., and Nagasawa, H. (1986) *Lunar Planet. Sci.* **XVII**, 562-563.

SPECTROPHOTOMETRY OF MARTIAN SATELLITES WITH THE HUBBLE SPACE TELESCOPE. B. Zellner and E. N. Wells, Astronomy Programs, Computer Sciences Corporation, Space Telescope Science Institute, Baltimore MD 21218.

Spectrophotometic observations of Phobos, Deimos, the C-type asteroid 702 Alauda, the D-type asteroid 1144 Oda, and a solar-type star over the wavelength range 0.21 to 0.80 μm were obtained with the Faint Object Spectrograph on the Hubble Space Telescope. The results demonstrate that the Martian satellites are spectroscopically analogous to D-type asteroids, not C-types as has often been assumed.

Table I lists the circumstances of observations. All data were taken with the red channel of the Faint Object Spectrograph (FOS), the prism, and a 1.0-arcsecond focal-plane aperture. The spectral sampling varies non-linearly from 3Å per channel at 0.21 μm to 200Å per channel at 0.80 μm. The Martian satellites were observed near elongation, and skies were measured approximately 3 arcseconds north or south of the satellites. The solar-type star used was Hyades VB64, not 16 Cygni B as erroneously reported earlier [1]. Relative spectral reflectivities were calculated by dividing the satellite or asteroid spectrum by the spectrum of VB64 after corrections for small wavelength shifts caused by geomagnetic effects and imperfect centering in the FOS aperture.

Table I. Observations

Object	Date UT	Notes
1144 Oda	05 Oct 1992 13:28	D-type asteroid
702 Alauda	05 Mar 1993 20:56	C-type asteroid
Phobos-E	18 Jan 1993 22:13	Phobos east of Mars
Deimos-W	28 Feb 1993 10:22	Deimos west of Mars
Deimos-E	28 Feb 1993 21:35	Deimos east of Mars,
Hya VB64	06 Oct 1992 17:05	Solar-type Star

Figures 1 and 2 present the reflection spectra. The spectra of the two asteroids agree well with eight-color results from Zellner et al. [2], and the results for Deimos are in general agreement with groundbased data of more limited spectral coverage from Zellner and Capen [3] and more recently from Fink and Grundy [4]. The leading hemisphere of Deimos is substantially redder than the trailing hemisphere, but the averaged spectrum of Deimos differs only slightly from that of the leading hemisphere of Phobos.

The linear, reddish spectra at wavelengths longer than 0.45 μm are characteristic of D-type asteroids, which are commonly found in the outer main belt and among the Trojans but have no close analogues among known meteorites. Comparisons with spacecraft spectral data for the Martian satellites and with the spectra of some low-albedo meteorites are presented in a companion paper in this volume [4].

References: [1] B. Zellner and E. N. Wells, Bull. Amer. Astr. Soc. 25, 1135, 1993. [2] B. Zellner, D. J. Tholen, and E. F. Tedesco, Icarus 61, 355-416, 1985. [3] B. Zellner and R. Capen, Icarus 23, 437, 1974. [4] U. Fink and W. Grundy, in Asteroids, Comets, Meteors 1991, Lunar and Planetary Institute Contribution No. 765, 991, p. 77. [4] S. Murchie and B. Zellner, this volume, 1994.

Acknowledgments: This work is based on observations with the NASA/ESA Hubble Space Telescope obtained at the Space Telescope Science Institute, which is operated by the Association of Universities for Research in Astronomy, Inc., under NASA contract NAS5-26555. This work was supported by STScI Grant GO-3744.01-91A . In addition to the present authors, Co-Investigators on the approved HST Cycle 2 proposal included P. Thomas and J. Veverka, Cornell University; J. Bell, D. Tholen, and J. Gradie, University of Hawaii; J. Caldwell, York University; K. Pang, Jet Propulsion Laboratory; and U. Fink and W. Grundy, University of Arizona.

MARTIAN SATELLITES. B. Zellner and E. N. Wells

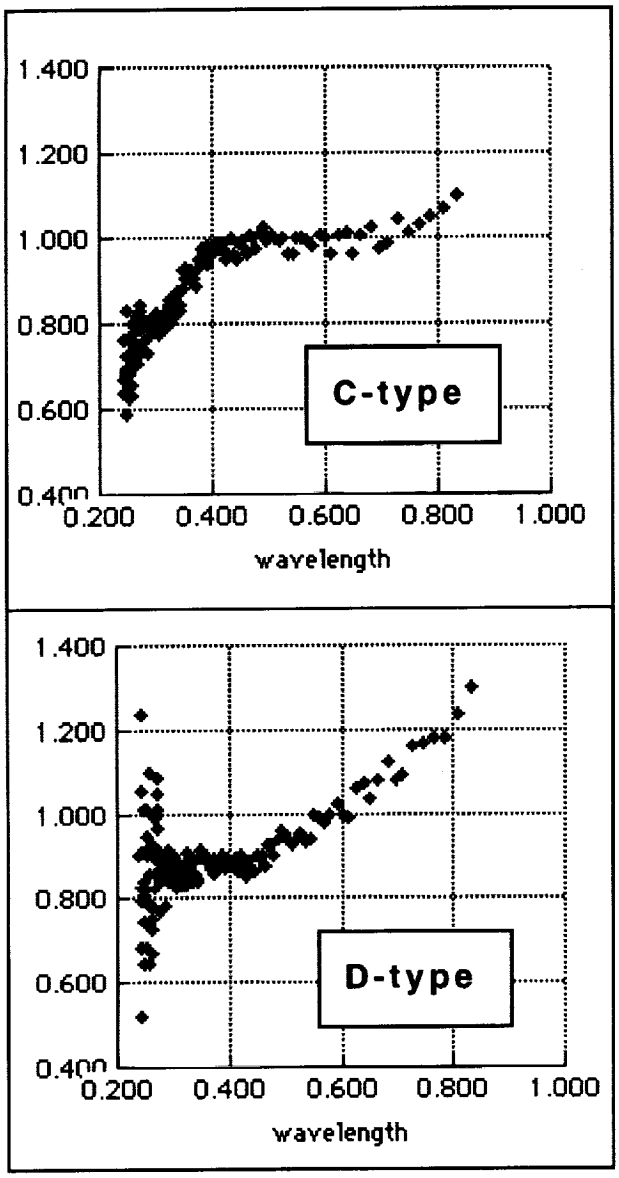

Figure 1 - Spectral reflectance of C-type asteroid 702 Alauda (top) and D-type asteroid 1144 Oda (bottom).

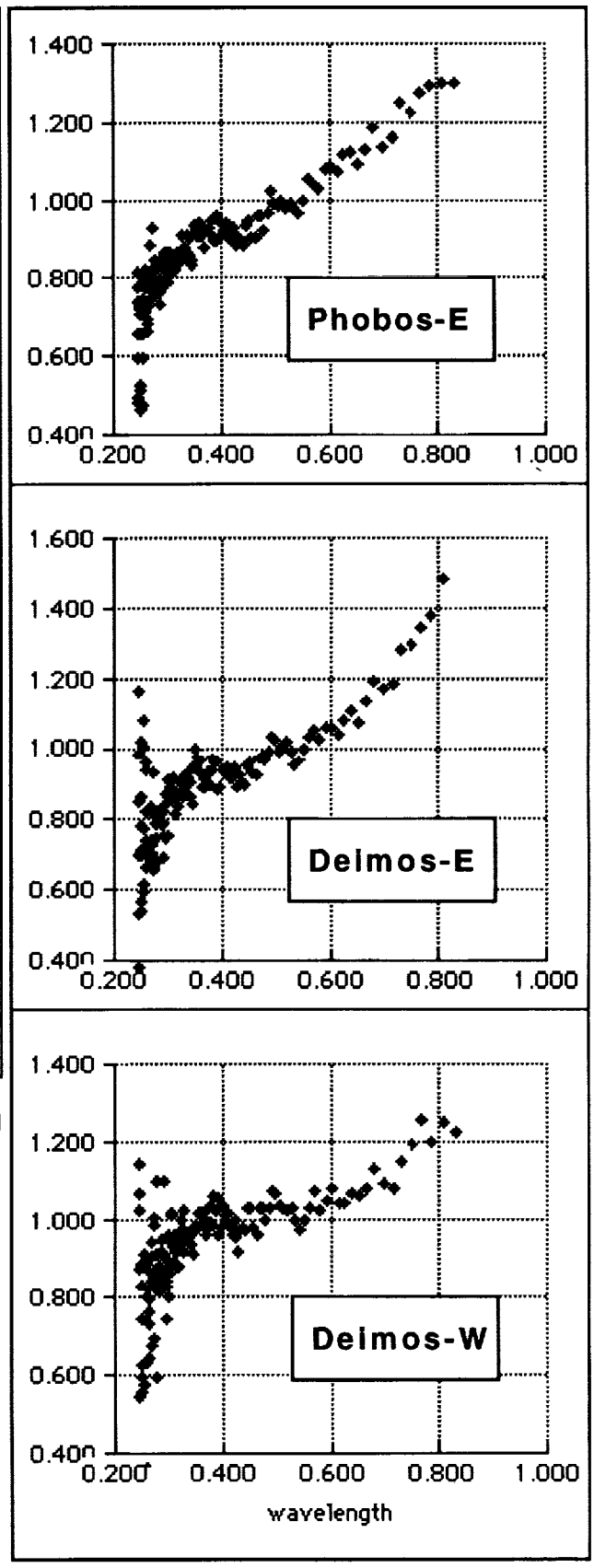

Figure 2 - Spectral reflectance of the leading hemisphere of Phobos (top), the leading hemisphere of Deimos (middle), and the trailing hemisphere of Deimos (bottom).

SIMULTANEOUS ADSORPTION OF CO_2 AND H_2O UNDER MARS-LIKE CONDITIONS AND APPLICATION TO THE EVOLUTION OF THE MARTIAN CLIMATE

Aaron P. Zent, Richard Quinn, SETI Institute and NASA Ames Research Center, Moffett Field CA, 94035.

The martian regolith is the most substantial volatile reservoir on the planet (1-2); it holds CO_2 as adsorbate, and can exchange that CO_2 with the atmosphere-cap system over timescales of 10^5 to 10^6 years. The climatic response to insolation changes caused by obliquity and eccentricity variations depends in part on the total reservoir of adsorbed CO_2. Previous estimates of the adsorbate inventory have been made by measuring the adsorptive behavior of one or more Mars-analog materials, and deriving an empirical equation that described that adsorption as a function of the partial pressure of CO_2 and the temperature of the regolith.

One can solve the heat diffusion equation for annually averaged conditions and determine the temperature profile to any depth of interest. The current CO_2 inventory is that which satisfies a) adsorptive equilibrium, b) observed atmospheric pressure, and c) no permanent CO_2 caps. Atmospheric pressure history over an obliquity cycle can be found by re-calculating the thermal gradient at each obliquity, and balancing the CO_2. If the atmospheric pressure exceeds the vapor pressure at the poles, permanent caps are assumed to exist, and they fix the atmospheric pressure. The adsorbed CO_2 is recalculated in accord with the new atmospheric pressure, and the remainder of the CO_2 is assumed to be in quasi-permanent polar caps (3).

An important assumption has to do with the applicability of the laboratory measurements to the martian regolith. If the assumed adsorption isotherms are wrong, then the CO_2 inventory is wrong, and the climate history is wrong.

There is laboratory evidence that H_2O poisons the CO_2 adsorptive capacity of most materials (4). No consideration of CO_2 - H_2O co-adsorption was given in previous estimates of the martian CO_2 inventory, although H_2O is present in the vapor phase, and so as adsorbate, throughout the regolith.

If CO_2 is substantially displaced from martian materials by H_2O, then the current estimates of the adsorptive capacity of the regolith must be too high. The martian regolith is at or near 100% relative humidity (R_H) throughout the latitude-depth domain in which ground ice is stable. Figure 1 shows a hemispheric map of the subsurface, contoured with predicted adsorbed CO_2 relative concentrations. The stippled area is the domain within which R_H is near unity, and the monolayer coverage of adsorbent surfaces by H_2O is highest. Over 83% of the total CO_2 inventory is adsorbed in the

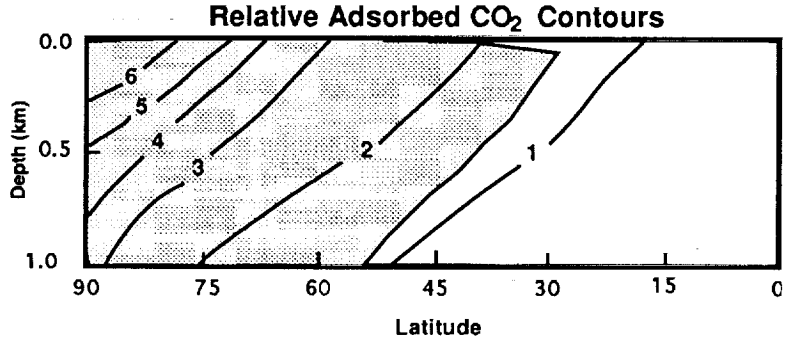

domain in which the H_2O abundance is highest. The potential effect of adsorptive competition by H_2O may be then to decrease estimates of the total exchangeable CO_2 inventory by a factor of 6.

To test the effects of H_2O on the CO_2 adsorptive capacity of the martian regolith, we measured co-adsorption of H_2O and CO_2 under conditions appropriate to the martian regolith. We constructed a manifold that allows us to control partial pressures, and the temperature of the soil sample. We use Mauna Kea palagonite as our Mars analog material, and evacuate it at 120° C overnight.. CO_2 is 99.999%; the pressure is measured by a capacitance manometer. Doubly distilled water is placed in a reservoir in the manifold and evacuated briefly under vacuum to remove dissolved gases.

We control the partial pressure of the H_2O in the manifold, and temperature of the soil, by cryogenic baths. The temperature of the soil is always greater than the temperature of the H_2O ice in order to keep the relative humidity in the soil chamber below unity.

We analyze the adsorbed gases by gas chromatograph (GC); the GC is calibrated every few days for the partial pressure ranges of interest. In all cases, we first measured zero relative humidity isotherms by pressure drop in order to establish a baseline against which to compare the effects of H_2O; the GC was not used. We used these CO_2 isotherms to calculate a BET area of 94.8 m^2/g for the palagonite.

At T_{soil} = 210 K, we found no significant displacement of CO_2 from its R_H= 0 coverage during experiments at R_H = 0.013 and R_H = 0.47; displacement is anticipated at higher R_H, where closer to 0.5 monolayers of H_2O adsorb.

At higher temperatures, (T_{soil} = 242 K) the water poisons CO_2 adsorption at lower R_H. We measured co-adsorption isotherms at $R_H = 9.3\times10^{-3}$ and 0.38, and found up to 30% displacement from the zero relative humidity isotherm.

One can derive the following Langmuir isotherm describing the monolayer coverage of CO_2 as a function of its partial pressure and the measured adsorptive coverage of H_2O. (The adsorption of H_2O is assumed to be independent of the partial pressure of CO_2).

This equation can be fit to the data for α and β

$$\theta_c = \frac{a\left(\alpha T^{-\beta}\right)P_{CO_2}}{\left(1 + a(\alpha T^{-\beta})P_{CO_2}\right)} \qquad 1$$

where a is defined as $(1 - \theta_h)$, where θ_h is the fractional monolayer coverage of water. A least-squares fit to a linearized form of this equation yields $\alpha = 1.002\times10^{17}$ and β = -8.635. These parameters can be expected to change as additional data, particularly at high R_H, are acquired.

Application of this equation to the martian regolith suggests that the effect of H_2O co-adsorption will be to displace a substantial fraction of the CO_2 previously thought to be adsorbed in the high-latitude regolith. As a consequence, the total CO_2 inventory must be revised downward. More quantitative predictions await highest R_H data, and will be presented at the meeting.

References

(1) Toon et al., *Icarus*, **44**, 552-607, 1980; (2). Kieffer and Zent, *Mars*, 1180-1218, 1992; (3) Fanale et al, *Icarus*, **50**, 381-407,1982; (4) Carter and Husian, *Chem Eng. Sci.* **29**, 267-273, 1974

Omit to p 1565

THE COMPLEX THERMAL HISTORY OF ENSTATITE CHONDRITES.

Yanhong Zhang, Paul H. Benoit and Derek W. G. Sears, Cosmochemistry Group, Department of Chemistry and Biochemistry, University of Arkansas, Fayetteville, AR 72701, USA.

The induced thermoluminescence properties of 32 enstatite chondrites have been measured in order to explore the metamorphic history of the EH and EL classes. The EH chondrites show a small increase in TL sensitivity with petrographic type consistent with the increase in blue luminescence as minor elements diffuse out of enstatite during metamorphism. However, the EL chondrites show a much greater range of TL sensitivity and the EL5,6 chondrites appear to be acting independently of the other EL chondrites. We speculate that this is because, unlike the other enstatite chondrites, enstatite is in the ordered structural state in the EL6 chondrites. The TL data provide further evidence, consistent with mineral composition data, that the EL6 chondrites do not constitute a simple monotonic metamorphic series.

Introduction. Induced thermoluminescence (TL) measurements have proved useful in exploring the metamorphic history of ordinary and carbonaceous chondrites and enabling their subdivision into petrographic types 3.0-3.9 [1,2]. The major TL phosphor in ordinary and carbonaceous chondrites is feldspar which is rare in enstatite chondrites [3]. However a number of cathodoluminescence (CL) studies [4,5] have shown that enstatite displays properties which are related to minor element chemistry which are of considerable significance in deciphering the formation and metamorphic history of the meteorites. The enstatite grains may display red or blue CL, of varying intensities, or no CL. Most importantly, the EH and EL chondrites, especially those of higher petrographic type, display very different CL; both EH and EL type 3 chondrites contain a mixture of blue and red CL enstatites but in EH6 chondrites the CL of the enstatite is almost entirely blue while for EL6 chondrites it is a distinctive magenta [6, Zhang *et al.*, this volume]. This is despite current data indicating that minor elements in enstatite decrease in concentration with increasing petrographic type in both classes. In view of the metamorphism-dependence of TL properties and the known CL properties of enstatite chondrites, we have examined the TL of EH and EL chondrites in order to explore their metamorphic histories.

Method and Results. Our apparatus and procedures were as described previously [2], the apparatus being especially sensitive to blue wavelengths. We have measured 12 EH and 20 EL of types 3-6 (and an EL7) [7]. Twelve were falls and 20 were finds displaying various degrees of weathering. The EH chondrites as a group have much lower TL sensitivity than the EL chondrites. The samples generally display two TL peaks, one at ~140°C and one at ~300°C in the glow curve, which both show a small increase in sensitivity from <0.01 to 0.2 (Dhajala = 1) among the EH chondrites. However, there is no systematic trend in TL sensitivity with petrographic type among the EL chondrites. Instead, both TL peaks range from <0.05 to 0.6 for the EL3 chondrites and from <0.01 to 0.9 for the EL6 chondrites (Fig.1).

Acid-washing samples of both classes to remove weathering products increased the TL sensitivity of the falls and finds by factors of 3-4 and 4-10, respectively. However, this treatment did not change any of the trends observed.

The TL data are generally consistent with previous pairing suggestions [8]: PCA 91238 and 82518 (and probably PCA 91085); MAC 88184, 88136 and 88180 (MAC 88180 may be higher than the other two because of limited sample size); LEW 87119, 88135 and 88714.

Discussion. Since we routinely employ filters with a blue bandpass in our apparatus, the trends we see are governed by the abundance of blue luminescing enstatite. The magenta CL of EL6 chondrites apparently reflects the presence of a major red peak in addition to the blue peak, and this is confirmed by spectrometry of the CL photographic negatives [Zhang *et al.*, this volume]. The intensity of the blue CL depends on minor element content, being brighter for grains lower in Cr_2O_3, MnO and TiO_2 [5]. We and others have shown that the concentration of these elements in enstatite decreases with increasing petrographic type in both EH and EL chondrites [3]. We thus have a ready explanation for the TL trends in EH chondrites,

both TL and CL reflecting metamorphism in this class, but not for the more complicated trends observed for the EL chondrites.

We doubt that the spread of TL sensitivities for EL chondrites reflects sample heterogeneity because (1) EH3 chondrites are just as heterogeneous but show very little spread, (2) EL6 chondrites are texturally and compositionally very homogeneous and (3) there is good agreement between paired EL samples. Neither have we found correlations between TL and mineral chemistry which might explain the trends in terms, for example, of considerable variation in metamorphism within a petrologic type, although new high precision EMPA data would help resolve this. We suspect that there is a major component producing TL in the EL5,6 chondrites which is absent from the EL3 and EH3-6 chondrites, in addition to the blue and red luminescencing enstatites present in those classes. We suspect that the component is ordered enstatite, and experiments are in progress to test this idea. Whatever the case, the TL data show clearly that while the EH3-6 chondrites represent a metamorphic series analogous to the ordinary and carbonaceous chondrites, this is not true of the EL chondrites which show a major discontinuity between the EL3 and EL5,6 chondrites.

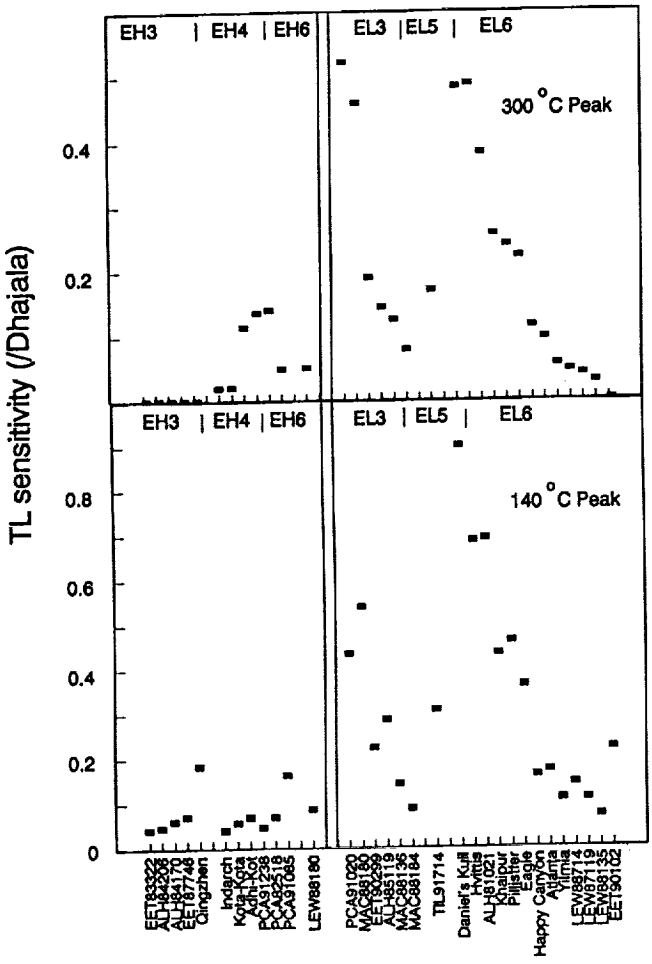

Fig. 1. Plot of the TL sensitivity of enstatite chondrites and the chemical-petrographic class.

1. Sears *et al.* (1980) *Nature* **287**, 791-795. 2. Symes *et al.* (1993) *Meteoritics* **28**, 446. 3. Keil (1968) *JGR* **73**, 6945-6976. 4. Leitch and Smith (1982) *GCA* **46**, 2083-2097. 5. McKinley *et al.* (1984) *JGR Suppl.* **89**, B567-B572. 6. DeHart (1993) *pers. comm.* 7. Zhang *et al.* (1993) *Meteoritics* **28**, 468. 8. Mason (1992) *Antarct. Meteor Newslett.* **12(1), 13(2), 15(1), 16(1)**. Supported by NASA grant NAGW-3519.

THE UNIQUE THERMAL HISTORY OF EL CHONDRITES AND A NEW MEANS OF CLASSIFYING EQUILIBRATED ENSTATITE CHONDRITES.

Yanhong Zhang, Shaoxiong Huang, Paul H. Benoit and Derek W. G. Sears. Cosmochemistry Group, Department of Chemistry, University of Arkansas, Fayetteville, AR 72701, USA.

We have examined the cathodoluminescence (CL) properties of enstatite chondrites as function of petrographic type. The trends displayed by the EH and EL chondrites are very different. In the EH3 and EL3 chondrites the individual enstatite grains display red, blue or no CL, while in EH5,6 chondrites the CL of the enstatite is predominently blue. In contrast, essentially all of the enstatite in EL5,6 chondrites displays a magenta CL. Spectroscopy of the CL negatives indicates that there is a strong red peak in the CL of the enstatite of the EL5,6 chondrites in addition to the blue peak observed in EH5,6 chondrites. The CL of the equilibrated enstatite chondrites is therefore a sensitive method for classification and confirms the EL5 classification of RKPA 80259, which had previously been contentious, and TIL 91714, a newly recovered meteorite. The different CL properties of the equilibrated enstatite chondrites probably indicates different degrees of structural ordering for the enstatite in the EH and EL classes and that the EL5,6 chondrites contain structurally ordered pyroxene. This implies prolonged metamorphism at low temperatures for the EL5,6 chondrites.

Introduction. Enstatite chondrites formed in a very reducing environment and the low concentration of FeO in the enstatite results in intense CL which may be either red or blue [1], and of varying intensities [2], depending on minor element composition. Previous studies have concerned only EH3,4 chondrites, but with the recent discovery of EL3 [3,4], EH6 and EL7 chondrites [5] we thought it appropriate to examine the CL properties of a series of EH and EL chondrites of petrologic types 3 to 7. We are especially interested in thermal histories of the meteorities (*i.e.* cooling rates and equilibration temperatures) which are reflected in the minor element concentrations and crystal structures which, in turn, determine CL color and intensity.

Experimental details and results. We obtained CL mosaics of 0.5x1 cm^2 sections of 11 enstatite chondrites and examined photographs of the CL mosaics of eight enstatite chondrites supplied by John DeHart from work performed at the Johnson Space Center [6]. The samples included EH3-6 and EL3,5-7 chondrites. A Nuclide Luminescope operated at 13 ± 1 kv and 0.8 ± 0.1 mA and Kodak Gold 400 film, exposure times of 20 to 40 s and the C-41 development process were used.

Enstatite grains with red and blue CL, and a few areas of chondrule mesostasis with yellow CL, were observed in EH3,4 and EL3 chondrites. However, the enstatite in Saint-Sauveur (EH5) and LEW 88180 (EH6) displayed almost entirely a blue CL, with only a few magenta CL grains in LEW 88180. The blue CL of EL3 enstatite appeared less intense than that of EH3 enstatite, however essentially all the enstatite grains in the EL6 chondrites displayed a magenta CL, quite different from the EH5,6 chondrites. The EL6 chondrites also contain abundant areas of brown CL material (probably glass). The LEW 87119 (EL7) chondrite and Happy Canyon (EL6 impact melt) contain only red CL grains.

Spectra were obtained from the negatives of typical EH6 and EL6 chondrites (Fig. 1). These showed that the magenta CL in EL6 enstatite is due to a strong peak at red wavelengths which is absent in the spectrum for the EH6 chondrite. The blue peak has roughly the same intensity, and the same fine structure, in the EL6 and EH6 chondrites.

Discussion. The CL properties of enstatite chondrites provide a simple new means of classifying equilibrated EH and EL chondrites, EH5,6 and EL5,6 chondrites containing enstatite with blue and magenta CL, respectively. Thus, TIL 91714, which Mason described as an E5 chondrite [7] and which contains 0.6-0.8% Si in the metal which is characteristic of the EL group [5], contains only enstatite with magenta CL, confirming its EL classification. The RKPA 80259 chondrite, whose

classification is contentious [8,9], also contains pyroxene with the distinctive magenta CL confirming its status as the first EL5 chondrite.

Our EH chondrite results resemble those of McKinley *et al.* [2] who found that as metamorphism increases, the pyroxene in enstatite chondrites assumes an intense blue CL, suggesting that the intense blue CL is a result of metamorphism. It is well-known that the red CL of enstatite in E3,4 chondrites is associated with high concentrations of transition metals (*e.g.* Mn and Cr) which diffuse out of the enstatite with increasing metamorphism [10]. It is possible that the blue luminescence is associated with structural defects, rather than impurities.

The magenta CL of enstatite in the EL5,6 chondrites is associated with very low minor element concentrations and might also be due to structural defects rather than impurities. The X-ray-stimulated luminescence of enstatite achondrites is more stronger at blue wavelengths for disordered pyroxenes but stronger at red wavelength for ordered pyroxenes, especially for grains within a given meteorite [11]. We suggest that while disordered orthopyroxenes are abundant in EH5,6 chondrites, the pyroxenes in the EL5,6 chondrites are in the ordered state (see also ref. 10). The composition of the cubic monosulfides in these meteorites also suggests that the EL5,6 chondrites cooled more slowly than the EH5,6 chondrites [12]. The presence of ordered orthopyroxene in EL5,6 chondrites, and not in the other enstatite chondrites, implies there was a period of prolonged metamorphism at low temperatures for the EL5,6 chondrites but not the others.

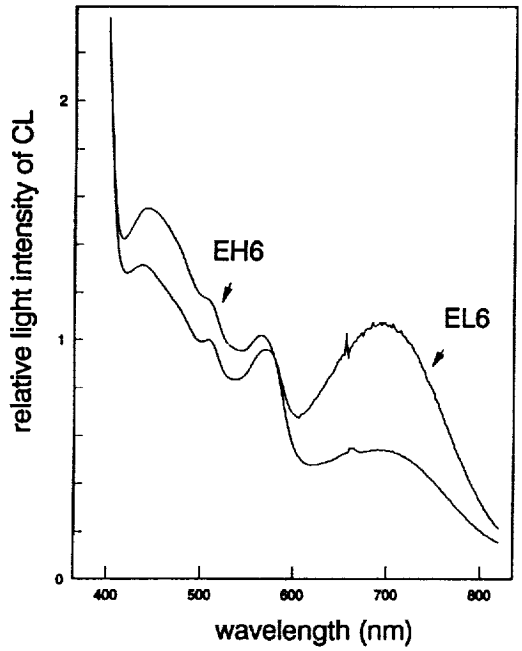

Fig. 1. Visible spectra for the CL of representative regions of EL6 and EH6 chondrites. The spectra were obtained from negatives of the CL photographs, correcting for color reversal in the negatives.

1. Leitch and Smith (1982) *GCA* **46**, 2083-2097. 2. McKinley *et al.* (1984) *JGR* **89**, B567-B572. 3. Lin *et al.* (1991) *LPS* **22**, 811-812. 4. Chang *et al.* (1992) *LPS* **23**, 217-218. 5. Zhang *et al.* (1993) *Meteoritics* **28**, 468. 6. DeHart (1993) *pers. comm.* 7. *Antarct. Meteor. Newslet.* **16** (1). 8. Kallemeyn and Wasson (1986) *GCA* **50**, 2153-2164. 9. Sears *et al.* (1984) *Nature* **308**, 257-259. 10. Keil (1968) *JGR* **73**, 6945-6977. 11. Reid *et al.* (1964) *Nature* **204**, 1292-1293. 12. Skinner and Luce (1971) *Amer. Mineral.* **56**, 1269-1295. Supported by NASA grant NAGW-3519.

Table 1. The CL of enstatite chondrites.

Meteorite†	Class	CL color‡	Data source
Qingzhen	EH3	Red+Blue	DeHart
ALH 84170	EH3	Red+Blue	DeHart
ALH 84206	EH3	Red+Blue	This work
EET 83254	E3	Red+Blue	DeHart
PCA 82518	EH4	Red+Blue	DeHart
PCA 91085	E4	Red+Blue	This work
Indarch	EH4	Red+Blue	DeHart
St.-Sauveur	EH5	Blue	This work
LEW 88180	EH6	Blue	This work
MAC 88136	EL3	Red+Blue	DeHart
ALH 85119	EL3	Red+Blue	This work
TIL 91714	EL5	Magenta	This work
RKPA 80259	EL5	Magenta	DeHart
ALH 81021	EL6	Magenta	This work
Atlanta	EL6	Magenta	This work
Khairpur	EL6	Magenta	This work
Happy Canyon	EL6§	Red	This work
LEW 87119	EL7	Red	This work
LEW 87223	E3	Red+Blue	DeHart

† PCA 82518 and PCA 91085 are paired
‡ "Red+Blue" indicates isolated individual grains, some with red and some with blue CL.
§ Impact melt.

GRAVITATIONAL RELAXATION OF PLANETESIMALS; **I.N.Ziglina,**
United Institute of Physics of the Earth, Moscow, Russia.

The collision integrals for a population of planetesimals with mass m_1 due to gravitational interaction with population m_2 are evaluated by direct integration. The velocity evolution of bimodal collision-free gravitating system with $m_2 \ll m_1$ is considered for the cases when it is controlled a) by large bodies and b) by small bodies.

A triaxial Gaussian velocity distribution, usually admitted for a swarm of planetesimals rotating around the Sun along elliptical orbits with $e,i \ll 1$, seems to be a good approximation [1-3]. In the case under consideration the time between two consequent close encounters is much larger than the period of rotation around the Sun. The distribution function for a population m reads:

$$f(\mathbf{r}, \mathbf{v}) = \frac{N(R)}{(2\pi)^2 \sigma_R \sigma_\varphi \sigma_z h} \exp\left[-\sum_i \frac{v_i^2}{2\sigma_i^2} - \frac{z^2}{2h^2} \right] , \quad (1)$$

where $\mathbf{r}$ is the radius-vector in cylindrical coordinates R,φ,z centered on the Sun, $\mathbf{v}$ is the velocity relative to the circular Keplerian velocity $V_K(R)$, $N(R)$ is the number of bodies in the vertical column with unit basis. We assume that the chaotic velocity dominates the shear velocity at close encounters and impulse approximation is valid. The changes of velocities are taken according to the two body problem. In result of one encounter

$$\Delta v_{1i}^2 = \frac{2 m_2}{m_1 + m_2} v_{ci} \Delta V_i + \left(\frac{m_2}{m_1 + m_2} \right)^2 \Delta V_i^2 , \quad (2)$$

where $\mathbf{v}_c$ is the velocity of the center of mass of the bodies and $\mathbf{V} = \mathbf{v}_1 - \mathbf{v}_2$ is their relative velocity. The first term in the right-hand side of Eq.(2) determines the energy exchange between the bodies m_1 and m_2, the second term redistributes the energy between the degrees of freedom. After integrating over all parameters of the encounters between m_1 and m_2 in a unit of time, these terms convert into the following two:

$$\left. \frac{\partial \sigma_{1i}^2}{\partial t} \right|_{grav} = \left(\sigma_{2i}^2 - \frac{m_1}{m_2} \sigma_{1i}^2 \right) \frac{2 A_i}{\bar{\tau}_{12}} + \frac{\sigma_{1i}^2 + \sigma_{2i}^2}{\bar{\tau}_{12}} B_i , \quad (3)$$

$i = R, \varphi, z$, $\bar{\tau}_{12}$ is analogous (with correction for anisotropic velocity distribution) to the Chandrasekhar relaxation time,

$$\frac{1}{\bar{\tau}_{12}} = \frac{4 G^2 m_2^2 N_2(R) \ln \Lambda}{\hat{\sigma}_R \hat{\sigma}_\varphi \hat{\sigma}_z \hat{h}} , \quad \hat{\sigma}_i^2 = \sigma_{1i}^2 + \sigma_{2i}^2 , \quad \hat{h}^2 = h_1^2 + h_2^2 ,$$

G is the gravitational constant, Λ is the ratio of the maximum impact parameter for encounters to the minimum one.

C-7

GRAVITATIONAL RELAXATION OF PLANETESIMALS: Ziglina I.N.

The coefficients A_i and B_i are elliptic integrals,

$$A_i = \int_0^{\pi/2} \frac{\cos^2\vartheta \sin\vartheta\, d\vartheta}{a_i\, b_i}, \quad B_i = \int_0^{\pi/2} \frac{(1-3\cos^2\vartheta)\sin\vartheta\, d\vartheta}{a_i\, b_i},$$

$$a_i = (\cos^2\vartheta + \sin^2\vartheta\, \hat{\sigma}_i^2/\hat{\sigma}_j^2)^{1/2}, \quad b_i = (\cos^2\vartheta + \sin^2\vartheta\, \hat{\sigma}_i^2/\hat{\sigma}_k^2)^{1/2}.$$

Since the eccentricity and inclination do not change under the Sun's attraction, it follows from (3) that at $e,i<<1$

$$\frac{d\langle e_1^2\rangle}{dt}\Big|_{grav} = (\langle e_2^2\rangle - \frac{m_1}{m_2}\langle e_1^2\rangle)\frac{A_R+A_\varphi}{\bar{\tau}_{12}} + \frac{(\langle e_1^2\rangle + \langle e_2^2\rangle)(B_R+B_\varphi)}{2\,\bar{\tau}_{12}},$$

$$\frac{d\langle i_1^2\rangle}{dt}\Big|_{grav} = (\langle i_2^2\rangle - \frac{m_1}{m_2}\langle i_1^2\rangle)\frac{A_z}{\bar{\tau}_{12}} + \frac{(\langle i_1^2\rangle + \langle i_2^2\rangle)\, B_z}{2\,\bar{\tau}_{12}}. \qquad (4)$$

The gravitation plays a dominant role in velocity evolution of planetesimals, so the consideration of a collision-free gravitating system is of interest. It follows from (4) that in a system of equal bodies the ratio $\langle i^2\rangle^{1/2}/\langle e^2\rangle^{1/2}=\beta$ tends to equilibrium value $\beta^*\simeq 0.55$ found from the condition $B_R+B_\varphi=B_z$. At $\beta=\beta^*$ the values $\langle e^2\rangle^{1/2}, \langle i^2\rangle^{1/2}$ grow proportional to $t^{1/4}$. From comparison of relaxation times in bimodal system we conclude that the velocity evolution is controlled by the larger bodies m_1 when $m_1\Sigma_1 >> m_2\Sigma_2$. Σ denoting the surface density. All the solutions tend asymptotically to $\langle e_2^2\rangle = k\langle e_1^2\rangle$, $\langle i_2^2\rangle = k'\langle i_1^2\rangle$, where the constants $k\simeq 2$, $k'\simeq 1.8$ at $m_2 << m_1$. In the case $m_1\Sigma_1 << m_2\Sigma_2$ when velocity evolution is governed by small bodies $m_2 << m_1$ (the runaway growth situation), we find from (4) that $\langle e_1^2\rangle$, $\langle i_1^2\rangle$ will adjust to the quasi-equilibrium values

$$\langle e_1^2\rangle = \frac{m_2}{m_1}\langle e_2^2\rangle\left(1+\frac{B_R+B_\varphi}{2(A_R+A_\varphi)}\right) = 1.16\,\frac{m_2}{m_1}\langle e_2^2\rangle,$$

$$\langle i_1^2\rangle = \frac{m_2}{m}\langle i_2^2\rangle\left(1+\frac{B_z}{2\,A_z}\right) = 1.23\,\frac{m_2}{m_1}\langle i_2^2\rangle. \qquad (5)$$

One can expect that at the final stage of planetary accumulation there was also tendention to chaotic energy equipartition between the growing planets and planetesimals [4].

References: [1] Goldreich P. and Tremaine S. (1978) *Icarus*, **34**, 227-239. [2] Hornung P., Pellat R. and Barge P. (1985) *Icarus*, **64**, 295-307. [3] Barge P. and Pellat R. (1990) *Icarus*, 85, 481-498. [4] Ziglina I.N. (1991) *Astron. Vestnik*, 25, N 6, 703-721.

COMPUTER SIMULATION OF LAVA FLOW EMPLACEMENT ON THE TERRESTRIAL PLANETS. J.R. Zimbelman, CEPS/NASM, Smithsonian Institution, Washington, D.C. 20560.

A computer program developed to simulate lava flows on volcanoes in Japan (Ishihara et al., 1990 [1]) has been evaluated for its applicability to the simulation of lava flow emplacement under conditions present on various planetary surfaces. A "standard case" for the parameters in the computer code (Table 1) was used as a referent for simulations in which the effects of individual parameters were examined. Results obtained to date indicate that the following general guidelines should be followed when using the Ishihara code: 1) conditions should be restricted to a regime where gravity-driven flow is dominant (slope > 1°), 2) gravitational acceleration should be equal to or greater than lunar gravity ($g > 1.6$ m s^{-2}), 3) effusion conditions should result in a volume-limited rather than a cooling-limited flow, and 4) only basaltic lavas can be simulated with the rheologic parameters provided with the original code. These guidelines eliminate many situations where flows are observed on planetary surfaces. New formulations of the basic flow conditions will be required to obtain simulations relevant to most planetary conditions; it appears unlikely that simple "fixes" can be applied to the Ishihara code to simulate accurately many planetary lava flows.

A computer code was developed to simulate lava flow emplacement on a digital elevation model, and it reproduced both the orientation and the thickness of historic lava flows in Japan [1]. The basic Ishihara code has been modified to keep lava from moving upslope and to allow for limited pressure-driven flow on shallow slopes [2]; this modified program was used to study the effects of individual parameters on lava flows under varying conditions [2-3]. Simulations have been restricted to a uniform inclined plane so that the resultant flow shapes could be directly compared. Lava properties and computational parameters were held constant for each simulation so that effects of four parameters (gravitational acceleration, effusion rate, effusion temperature, and topographic slope) could be examined individually (Table 1). Effusion rate and duration were adjusted to maintain a constant total volume of extruded lava in all simulations. The parameter ranges examined were: gravitational acceleration (0.29 to 29.4 m s^{-2}), effusion rate (31.25 to 125 m^3 s^{-1}), effusion temperature (1000 to 1200°C), and slope (0.5 to 15°). Flow length was observed to increase approximately linearly with slope (Fig. 1) and with effusion temperature. Variations associated with effusion temperature are dependent upon the particular expressions used in the published code for yield strength and viscosity as a function of temperature, relationships based on very limited field measurements. Flow length was observed to increase logarithmically with gravity (Fig. 2), a relationship very consistent for conditions of lunar gravity or greater, but which breaks down for $g < 1.6$ m s^{-2}. Flow length was only weakly influenced by effusion rate. These initial results led to the guidelines listed above for use of the published version of the simulation code. Studies are ongoing to identify formulations that will better accommodate many planetary environments.

REFERENCES: [1] Ishihara K.M. et al. (1990) IAVCEI Proc. Vol. 2, Lava flows and domes (J. Fink, ed.), Springer-Verlag, 174-207. [2] Zimbelman J.R. et al. (1993) LPS XXIV, 1577-1578. [3] Zimbelman J.R. (1993) IAVCEI Abstracts, 129, Canberra, Australia.

Table 1. Standard conditions. Parameters at right were varied individually.

Lava Density	2500 kg m^{-3}	Gravity	9.8 m s^{-2}
Solidus Temperature	800°C	Effusion Rate	62.5 m^3 s^{-1}
Topography Grid Size	25 m	Eruption Temp.	1100°C
Time Increment	1 s	Slope	2°
Total Erupted Volume	1,125,000 m^3		

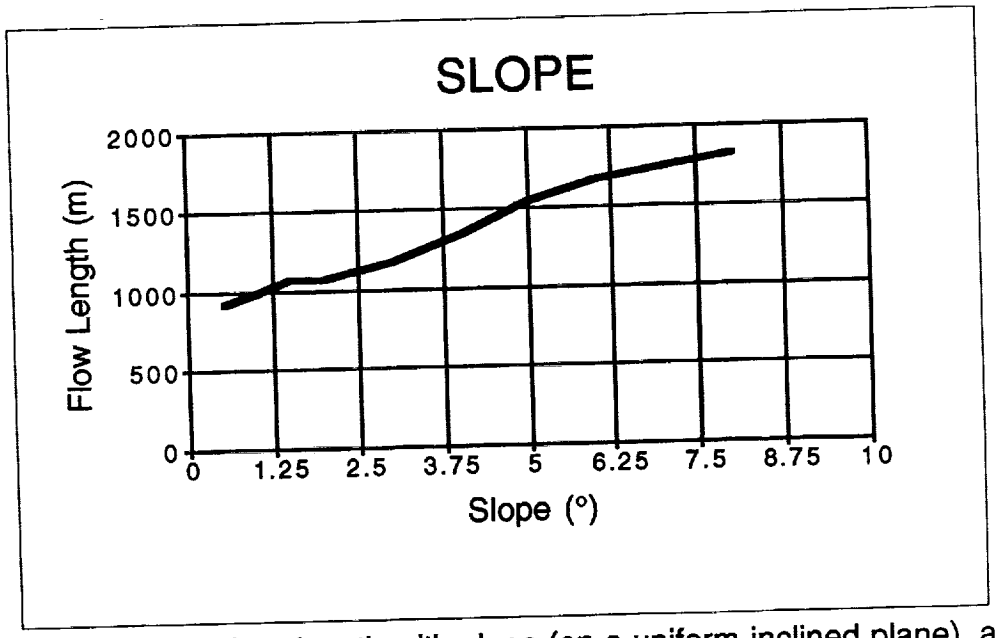

Figure 1. Variation in flow length with slope (on a uniform inclined plane), all other parameters held constant. See Table 1 for standard conditions of simulation.

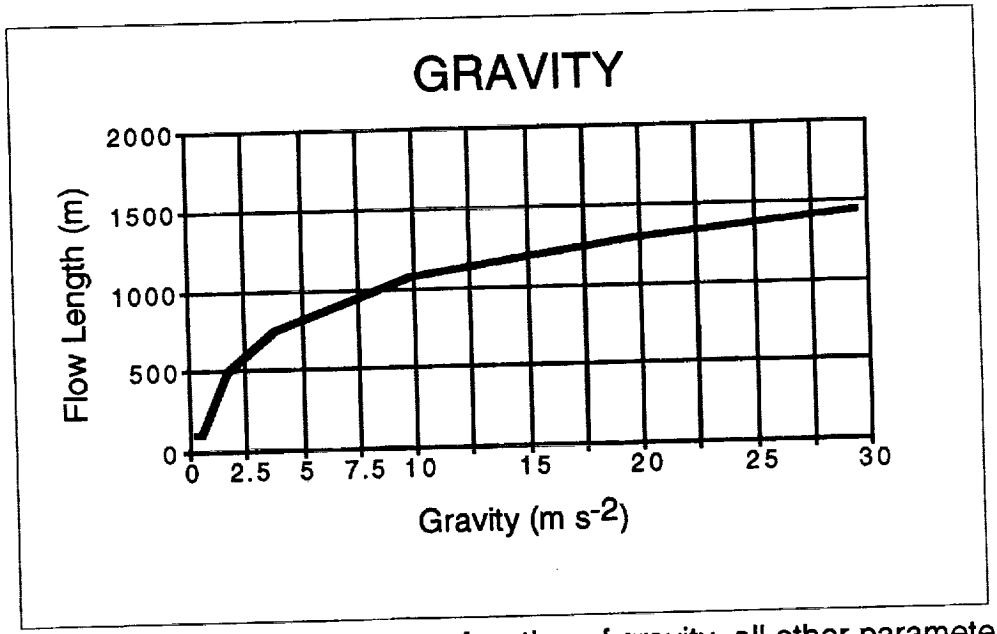

Figure 2. Variation in flow length as a function of gravity, all other parameters held constant. See Table 1 for standard conditions of the simulation.

1:5,000,000-SCALE GEOLOGIC MAPPING OF THE KAWELU PLANITIA QUADRANGLE (V16) ON VENUS. J.R. Zimbelman, CEPS/NASM, Smithsonian Institution, Washington, D.C. 20560.

The Kawelu Planitia (V16) quadrangle covers latitudes 25° to 50°N and longitudes 240° to 270° in the northern lowlands of Venus. Photogeologic mapping of Magellan SAR images has revealed that, along with the Kawelu Planitia plains, V16 also includes several isolated blocks of Complex Ridged Terrain (also called 'tessera'), a broad zone of numerous coronae between 30° to 40°N latitude, and a truly impressive array of intermingled lobate flow fields (Fig. 1). The preliminary mapping carried out for the V16 quadrangle has identified thirteen terrain units representing the complex ridged terrain, the broad plains, the lobate flow fields, and impact-related features. An enormous complex of coalesced flow fields surrounds the volcanic construct Sekmet Mons (44.5°N, 240.5°) and two nearby fields of small domes. The three centers of volcanic activity occur at the intersection of major fracture systems trending N40E, S40E, and N-S through the flow field area. The spatial relationship between the flow fields and the coronae indicates there may a genetic link between these features. Informal discussions have begun with mappers working in other areas on Venus to improve the compatibility of unit definitions.

The V16 photobase of Magellan images at 1:5,000,000 scale was received in early July, 1993, allowing a preliminary assessment of regional units to be made [1]. Thirteen terrain units were identified in the V16 quadrangle representing complex ridged terrain, the broad lowland plains, lobate flow fields, and impact-related features. The stable map base (chronopaque) of V16 was received in mid-December, 1993, allowing revised unit contacts and structural symbols to be placed directly on a representation of the Magellan imaging. Figure 1 is a simplified version of the map; only the complex ridged terrain (black) and the lobate flow fields (lined pattern) are shown in relation to prominent fracture zones and coronae. The spatial pattern and the stratigraphic relationships between units indicates the following general geologic history; the oldest material in the map area is the complex ridged terrain preserved as isolated blocks that are embayed by adjacent units, the plains units are superposed on the complex ridged terrain but the concentric fracturing associated with coronae disrupts the plains materials, and the flow fields consisting of intermixed radar-bright and radar-dark lobate flows are superposed on the other units.

One of the more interesting results to come out of the mapping of the V16 quadrangle involves an enormous complex of coalesced flow fields associated with the volcano Sekmet Mons (44.5°N, 240.5°). Sekmet Mons is a shield volcano with about 2 km of vertical relief spread over an area from 300 to 350 km in width. However, the mapping has revealed that Sekmet Mons is only one of three volcanic centers that were the sources for the lobate flows which extend away from these centers [2]. Both Sekmet Mons and the two newly identified volcanic centers, consisting of a large concentration of small (<10 km) domes, are located at the intersections of major fracture zones which extend along S40E, N40E, and N-S trends. The close association of the fracture zones with the three volcanic centers indicates that the volcanic history of the area must include the entire complex together, rather than as isolated eruptive events. The coalesced flow fields associated with the three

GEOLOGIC MAPPING OF KAWELU PLANITIA, VENUS: J.R. Zimbelman

centers extends into the adjacent V15 quadrangle, covering a total area of 1,200,000 km², which is nine times larger than the area of the Columbia River basalts on Earth [2]. The lobate flows associated with the volcanic centers are surrounded by numerous coronae, which suggests that the source plume feeding the centers may also include segregated magma pods around its periphery, consistent with other observations of lava flow fields and coronae [3-4]. Geologic mapping should help to delineate relationships between volcanic and tectonic features and provide constraints to models of mantle-plume dynamics on Venus [e.g., 5].

REFERENCES: [1] Zimbelman J.R. (1993) Trans. AGU **74(43)**, 379 [2] Zimbelman J.R. (1993) GSA Abs. Prog. **25(6)**, A221 [3] Senske D.A. et al. (1992) JGR **97**, 13395-13420 [4] Stofan E.R. et al. (1992) JGR **97**, 13347-13378 [5] Janes D.M. et al. (1992) JGR **97**, 16055-16067.

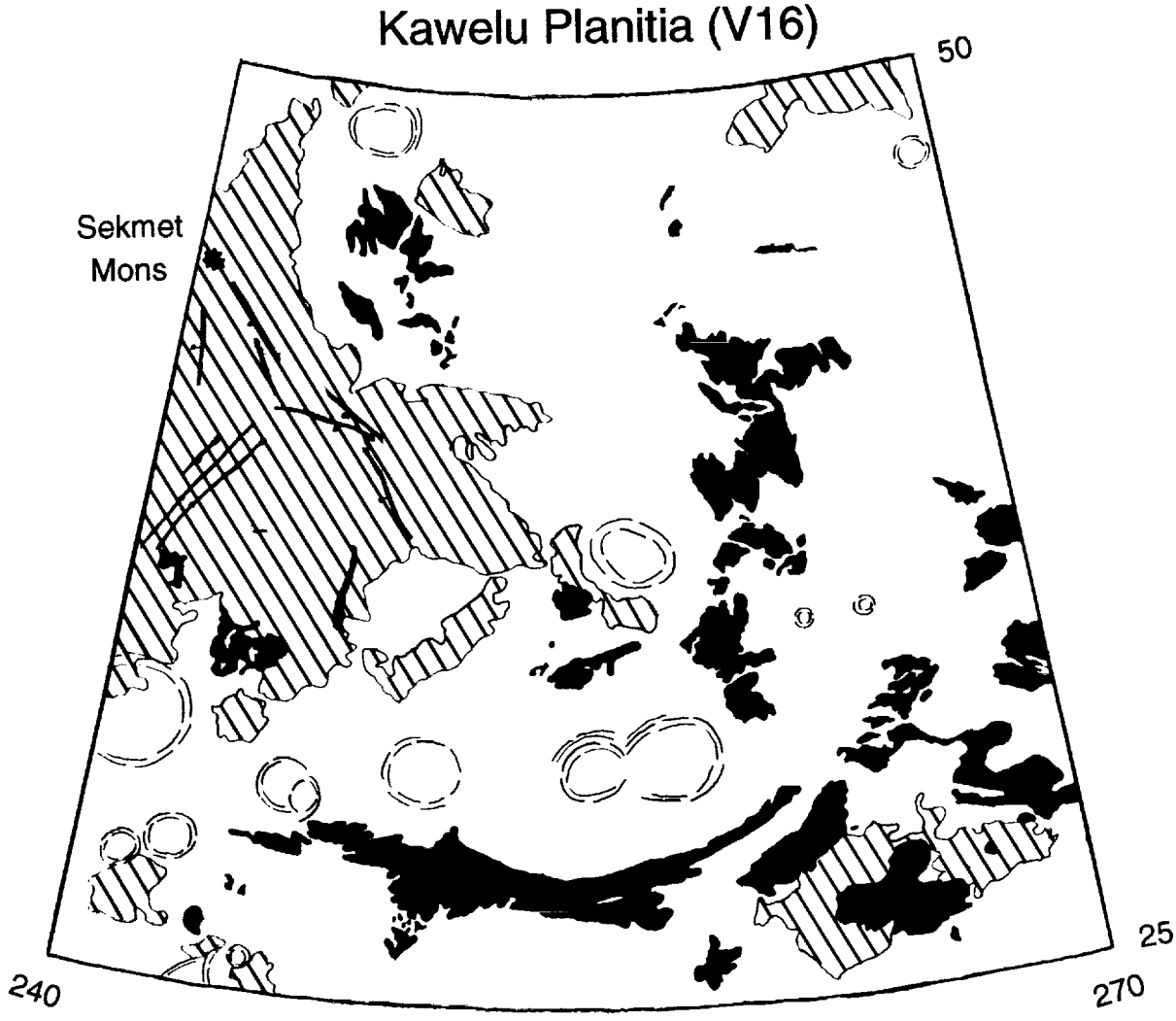

Figure 1. Simplified map of selected geologic units and features in the Kawelu Planitia (V16) quadrangle on Venus. The oldest unit exposed is Complex Ridged Terrain (black), present as isolated blocks embayed by other units. Unpatterned area consists of several types of lowland plains. Flow fields of intermixed lobate flows (lined pattern) are superposed on other units. Coronae are shown as concentric long-dashed lines located near the rim of each feature.

MAFIC MAGNETIC VOLCANICLASTIC DUNES: A POSSIBLE MARS ANALOG IN THE ANDES OF ECUADOR. J.R. Zimbelman[1] and K.S. Edgett[2]; [1]CEPS/NASM, Smithsonian Institution, Washington, D.C. 20560, [2]Dept. of Geology, Arizona State Univ., Tempe, AZ 85287-1404.

A field of dark sand dunes is located in the InterAndean Valley of central Ecuador (1°50' to 2° 10' S, 78°40' to 50' W), approximately 50 km south of the city of Riobamba. The low albedo of the sand results from a predominance of dark grains, a significant fraction of which are strongly attracted to a magnet. The source of the dark sand grains is not readily apparent in the vicinity of the dunes, but an exposure of multi-layered mafic ash 4 km WNW of Riobamba forms piles of loose grains visually identical to the dark dunes further south. No volcanic center is adjacent to the dune field, but both the dunes and the Riobamba ash are located along the predicted fallout direction for eruptions of Sangay volcano, a basaltic-andesite stratovolcano 46 km E of the dunes. The dark dunes in Ecuador are an example of a rare class of mafic volcaniclastic dunes documented on Earth. The Ecuador dunes are of particular interest because both the mafic content and the significant fraction of magnetic grains makes these aeolian-reworked volcaniclastic products candidate analogs to the dark dune fields on Mars.

The country of Ecuador is crossed by the NNE-trending Andes Mountains, the "backbone" of the South American continent. Quaternary volcanoes form the highest peaks of the Ecuadoran Andes; they are divided into two ranges separated by the InterAndean Valley, a graben filled with Cenozoic sedimentary and pyroclastic deposits [1]. The dark aeolian dunes occur at the southern end of the InterAndean Valley along the Pan American Highway, south of Riobamba (Fig. 1). Patches of dark sediment near Guamote and Palmira form sand sheets and isolated transverse and barchan dunes. South of Palmira, dunes of 1-2 m height were sampled and photographed in December 1993. Subsequent study of maps [2] and aerial photographs [3] showed that the sand sheets and dunes cover about 250 km^2 around Guamote and Palmira (Fig. 1). No outcrop of the source material for the dark sand was evident in the vicinity of the sand dunes. However, 4 km WNW of Riobamba, outcrops of 20-30 cm of dark volcanic ash were observed draped over the topography; this ash weathers into piles of dark sand that are visually identical to the dune sand further south. Sieving shows that the ash is poorly sorted relative to the dune sand, but both samples have peak abundances of fine sand (ϕ = 3; 180 to 125 μm) with similar distributions for finer particles. Some particles in all size fractions are strongly attracted to a magnet, as is >30% (by mass) of the bulk dune sand sample.

Where did the dark volcanic ash come from? The closest active volcano is Sangay, 46 km east of the sand locality (Fig. 1). Sangay is one of the most continuously active volcanoes in the world [4], but it's relative inaccessibility has led to only limited study. Sangay is a stratovolcano of basaltic andesite composition (SiO_2 of 56%) which produced a "rain of ash on Riobamba, Guamote, and Palmira" [4]. These towns are in the direction of the most probable ash fall-out from Sangay [5]. Early records of European settlers indicate that the ash layers we sampled in Riobamba may be from violent explosions on Sangay which produced "ash rains in Riobamba" in

1728 [6]. Thus, stratovolcanoes like Sangay may be a source of mafic-rich ash which is then reworked by the wind to form dark sand dunes.

Dunes composed of mafic sands are quite rare on Earth. Some of the best examples of such dunes occur in Washington, Hawaii, Arizona, and Iceland, where the dunes are usually formed from reworked pyroclasts [7]. The Ecuadoran dunes described above are particularly relevant as possible analogs to dunes on Mars because they appear to be linked to a dark volcanic ash from a specific volcano and because they contain an abundance of magnetic materials.

Aeolian dunes on Mars tend to have the lowest albedoes of any Martian surface material [8]. The best spectral evidence suggests that dark regions on Mars include relatively unoxidized mafic materials like pyroxene [9-10]. Most dark dunes on Mars are probably composed of mafic or ultramafic minerals, lithic fragments, and/or glass [7,11-13], but other compositions have also been suggested [12-18]. In particular, Herkenhoff [18] advocates that some dark dunes are aggregates of magnetic dust, consistent with evidence of 1-7% magnetic material (magnetite or maghemite) in the surface fines at the Viking lander sites [19]. The magnetic dark sand in Ecuador provides an analog for an alternative mechanism to account for the magnetic materials in the Martian soil.

Acknowledgments: Logistical support in Ecuador and assistance in sample collection were provided by Ted, Mima, and Kathy Hughes. Pat Jacobberger helped in the sieving analyses carried out at CEPS.

REFERENCES: [1] Baldock J.W. (1982) Geology of Ecuador, 1:1,000,000-scale map, Direccion General de Geologia y Minas, Quito. [2] Instituto Geographico Militar (1991) 1:50,000-scale maps, Guamote and Palmira sheets. [3] Insituto Geographico Militar (1981) 1:60,000-scale aerial photographs, R-62 frames 12091&2. [4] Hall M.L. (1977) El Volcanismo En El Ecuador, Inst. Panamer. de Geographia e Historia, Quito. [5] Salazar E. and Bermudez R. (1982) 1:250,000-scale map, Mapa De Los "Volcanes Activos" Del Ecuador, Minesterio De Energia y Minas, Quito. [6] Hantke G. and Parodi A. (1968) Cat. of Active Vol., XIX, pp. 56-61, Int. Assoc. Vol., Rome. [7] Edgett K.S. and Lancaster N. (1993) J. Arid Envir. **25**, 271-297. [8] Thomas P. and Weitz C. (1989) Icarus **81**, 185-227. [9] Singer R.B. et al. (1979) J. Geophys. Res. **84**,8415-8426. [10] Mustard J.F. et al. (1993) J. Geophys. Res. **98**, 3387-3400. [11] Smalley I.J. and Krinsley D.H. (1979) Icarus **40**, 276-288. [12] Geissler P.E. et al. (1990) J. Geophys. Res. **95**, 14399-14413. [13] Edgett K.S. et al. (1992) LPS XXIII, 327-328. [14] Ksanfomaliti L.V. (1977) Sov. Astron. Lett. **3**, 174-176. [15] Greeley R. (1979) J. Geophys. Res. **84**, 6248-6254. [16] Saunders R.S. and Blewett D.T. (1987) Astron. Vestnik **21**, 181-188. [17] Thomas P. and Veverka J. (1986) Icarus **66**, 39-55. [18] Herkenhoff K.E. (1993) LPS XXIV, 643-644. [19] Hargraves R.B. et al. (1979) J. Geophys. Res. **84**, 8379-8384.

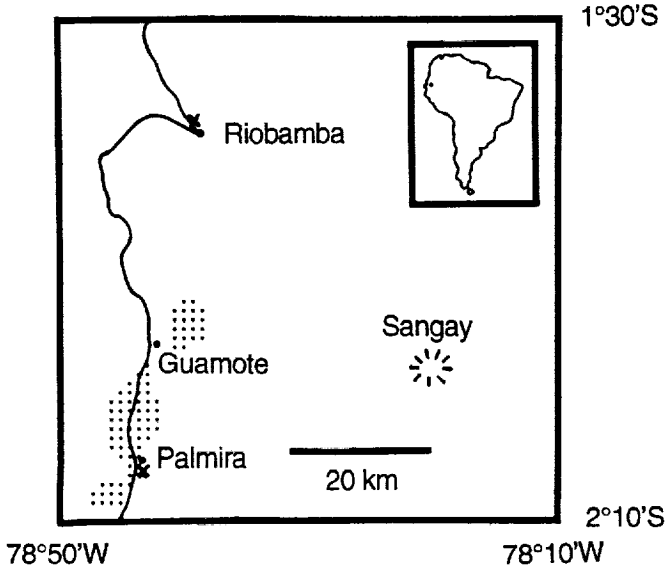

Figure 1. Location map for mafic volcaniclastic dunes in Ecuador. Pattern = dunes and sand sheet; Large dot = Riobamba, Guamote, and Palmira along Pan American Highway; X = sample locations; Hachures = Sangay stratovolcano.

EVIDENCE FOR EXTRANEOUS PEROVSKITES IN CAIs FROM THE EFREMOVKA (CV3) METEORITE: A COMBINED PETROGRAPHIC, TRACE ELEMENT, AND ISOTOPIC STUDY; Ernst Zinner[1] and Ahmed El Goresy[2]; [1]McDonnell Center for the Space Sciences and Physics Department, Washington University, St. Louis, MO 63130, USA; [2]Max-Planck-Institut für Kernphysik, Postfach 103980, D-69029 Heidelberg, Germany.

A petrographic and trace element study of perovskites in several CAIs from the Efremovka CV3 chondrite revealed the presence of several populations of perovskites with different Zr/Y ratios. Zr/Y ratios are higher than chondritic, chondritic, lower, or much lower than chondritic. Perovskites with chondritic, higher, or much lower than chondritic Zr/Y ratios cannot have crystallized from CAI melts and are hence of extraneous origin. Different origins for individual perovskite grains are also indicated by Ca-isotopic heterogeneities.

Equilibrium condensation calculations indicate that perovskite is one of the earliest condensates from a gas of solar composition [1]. In many CAIs from CV and CM chondrites perovskite is believed to have crystallized from refractory liquids [2]. Considerable effort has been devoted to the search for perovskites of extraneous origin, i.e., perovskites which formed elsewhere, were captured by the CAI liquid and survived as relict grains or were incompletely dissolved [3,4]. This search included screening of areas in melilite crystals, in which relict perovskites were believed to have been resorbed [3,4]. This procedure is difficult and trace element data obtained for the analyzed areas were either non-conclusive or the evidence was circumstantial [4]. An additional difficulty arises from the fact that captured and resorbed perovskites may have crystallized from a liquid before their release from the parental CAIs and incorporation into other CAIs. It appears to be of utmost importance to use trace element abundance patterns to establish whether individual perovskites in CAIs formed by condensation from a gas or by crystallization from a liquid [5,6]. In this respect, the relative abundances of the ultrarefractory elements Hf, Zr, Sc, and Y are especially diagnostic for revealing the formation process because crystal/liquid distribution coefficients for these elements differ markedly from one another [4,5] and their relative abundances in igneous perovskites are expected to deviate from chondritic abundances [5,6,7]. Criteria for the identification of extraneous perovskites in CAIs are: **a)** deviation of relative refractory lithophile trace element abundances from abundances predicted for crystal/liquid fractionation, and **b)** occurrence of perovskite in mineral assemblages texturally different from those in which perovskites, whose relative trace element abundances are compatible with the predicted crystal/liquid fractionation ratios, occur [7]. Criterion **b** is important because an assemblage could be a fragment of another CAI and was captured in the host CAI. Trace element abundances are insufficient for deciding whether such perovskites are indigenous or extraneous to the CAI.

We have undertaken a petrologic, trace element, and isotopic investigation of perovskites in several CAIs from the Efremovka (CV3) chondrite. Perovskites were categorized according to occurrence (e.g., in spinel clusters or framboids, in the rim sequence, in xenoliths that petrographically differ from the host CAI and appear to have been captured) Here we concentrate on two Type A inclusions, 101.1 and E2. Efremovka CAI 101.1 contains captured sinuous fragments and perovskites attached to these fragments may be of extraneous origin [7]. In addition, a few perovskites are associated with or enclosed in fine-grained Cr-spinel-bearing xenoliths in the core. Many perovskites in 101.1 are amoeboid in shape and entirely enveloped by reaction rims of Sc-, Zr-rich fassaite [7]. Trace element analyses revealed the presence of different perovskite types: (1) perovskites with higher than chondritic Zr/Y ratios (Per A in Fig.1a), (2) perovskites with chondritic Zr/Y ratios (Per B in Fig. 1a), and (3) perovskites with lower than chondritic Zr/Y ratios. The first two types are probably condensates. Subsequent electron microprobe analyses confirmed the existence of groups 2 and 3 (Fig. 2a). In addition, there appears to be a fourth group with high Y_2O_3 (up to 1.4 wt.%) and very low ZrO_2 (< 0.02 wt.%) (Data points close to the y-axis in Fig. 2a). 40% of the analyzed perovskites belong to this category. Group 1 seems to be very rare in this CAI since no such grain was encountered during electron probe analyses. 21% of the perovskites have close to chondritic ZrO_2/Y_2O_3 ratios (2.7; Fig. 2a). These perovskites must be of extraneous origin. The ZrO_2/Y_2O_3 ratios of group 3 perovskites ($0.15<ZrO_2/Y_2O_3<1.0$) are similar to ratios obtained from crystal/liquid fractionation experiments (0.386 in air and 0.484 at low fO_2 [5]). Perovskites highly depleted in ZrO_2 (members of group 4 plotting close to the y-axis in Fig. 2a) cannot have crystallized

from the host CAI liquid and are probably also extraneous to the CAI. These perovskites and those with higher than chondritic ZrO_2/Y_2O_3 (Per -A in Fig. 1a) are of special interest, since they either condensed from a reservoir with non-chondritic Zr/Y ratio, or formed by fractional condensation. Perovskites coexisting with the Cr-spinel xenoliths fall into groups 1-3, indicating diverse origins (Fig. 1b). Some of these perovskites with low ZrO_2/Y_2O_3 ratios (e.g., Per F in Fig. 1a) are probably of igneous origin, but CAI 101.1 is their second host. The REE and refractory lithophile abundance patterns of three perovskites coexisting with Cr-spinel xenoliths (Fig. 1b) differ from the patterns of perovskites in the host CAI (Fig. 1a) in several ways: a) the former perovskites are more enriched in the light REEs, b) their HREE abundances from Gd to Er do not increase as steeply as those of perovskites A-C, c) compared to the host perovskites, they are much more enriched in Nb. It is remarkable that, although characteristic differences are seen in the abundance patterns of individual perovskites, all of them have the same basic ultrarefractory REE pattern with depletions not only in Eu and Yb but also in Tm. This indicates formation from a common reservoir with an ultrarefractory REE signature but by different processes, causing differences in the abundances of Zr, Y and Nb in individual grains. Different individual formation histories are also indicated by preliminary ion probe measurements of Ca and Ti isotopes in three perovskites. Grain A (Fig.1a) has a clearly resolved ^{48}Ca excess of 9.8±3.4 (2σ) ‰, the others have normal Ca; all Ti-isotopic ratios are normal. Previously, Goswami et al. [8] have reported ^{50}Ti-isotopic heterogeneities among single perovskites from Efremovka inclusion E-50.

In the Efremovka inclusion E2 [9] perovskite occurs in the melilite-rich core, between spinel framboids and clusters in the core, and in a separate layer in the rim sequence. Data points of grains of all three occurrences cluster around the chondritic ratio line (Fig. 2b). ZrO_2/Y_2O_3 ratios of perovskites in the core and in the rim are similar. However, perovskites captured between spinels in the core have distinctly lower concentrations (Fig. 2b). The ZrO_2/Y_2O_3 ratios of perovskites in E2 cannot have resulted from crystal/liquid fractionation during cooling of the E2 liquid. These grains probably condensed from a gas of solar composition. However, the bimodality in their ZrO_2/Y_2O_3 ratios suggests two distinct sources.

REFERENCES: [1] Grossman L. (1972) GCA **36**, 597; [2] MacPherson G. *et al.*(1988) in Meteorites and the Early Solar System, p. 746; [3] Johnson M. L. *et al.* (1988) Meteoritics, **23**, 276; [4] Kennedy A. K. *et al.* (1991) LPS **XXII**, 709; [5] Simon S. B. *et al.* (1993) GCA, in press; [6] Kennedy A. K. *et al.* (1993) LPS **XXIV**, 793; [7] El Goresy A. *et al.* (1993) Meteoritics, **28**, 344; [8] Goswami J. N. *et al.* (1991) Meteoritics 26; [9] Fahey A.J. et *al.* (1987) GCA **51**, 3215.

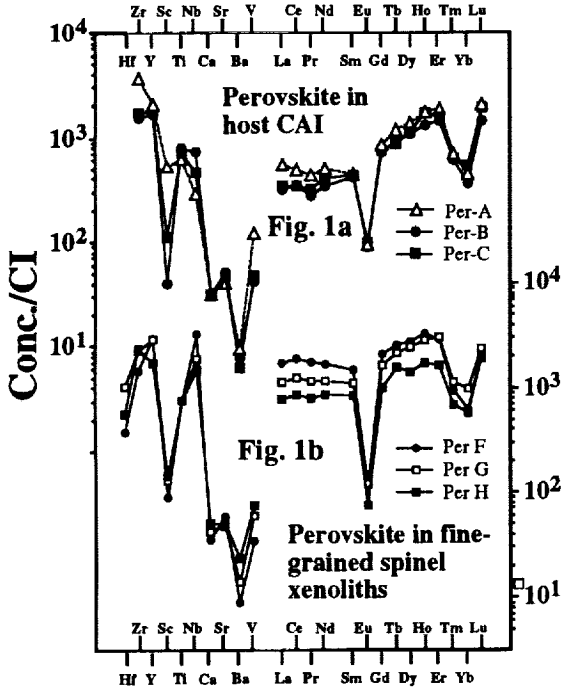

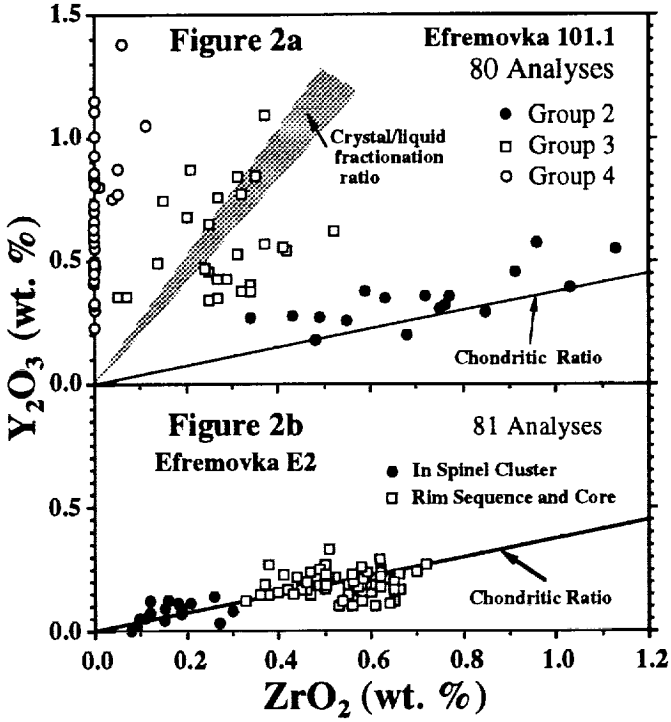

CRYSTALLIZATION IN THE SILICATE PART OF THE EXPERIMENTAL MELTED ORDINARY CHONDRITE TSAREV (L5); N.G.Zinovieva, O.B.Mitreikina and L.B.Granovsky, Department of Petrology, Faculty of Geology, Moscow State University, Lenin Gory, Moscow, 119899, Russia.

The goal of this research was the detailed petrological study on the silicate part of the immiscible sulphide-metallic-silicate melt formed during the partial melting (by microwave-heating, run at vacuum, T=1400±100°C, t=20 min. [1]) of the ordinary chondrite Tsarev (L5). This research showed that there were two immiscible coexisting silicate melts different in chemical composition and crystallization temperature.

The outer part of the sample has a original chondrite structure, while the inner part has a taxite structure, consists of areas of porphyritic (APT) and intersertal (AIT) textures. The formation of these textures shows that this part of the sample has been re crystallized. There are small (up to 1 mm) relicts of the original chondrite material (Fig. 1) in the areas of the both textures.

APT (Fig. 1) consist of idiomorphic 50-150 μm-size tabular olivine crystals, cemented by the glass with fine grains of low-Ca pyroxene, Fe-olivine and sometimes troilite. The tabular (up to 150 μm) grains of olivine have a zonal structure (Fig. 2), and have the constant composition (Fa - 13) of the central parts of the grains. There is the thin (up to 5 μm) rim of olivine rich in Fe around the grains. The composition of the rim changes to the border from Fa - 26 to Fa - 31. There are fine skeletal crystals of Fe- rich (Fa - 33) olivine and needle and dendrite crystals of low-Ca pyroxene embedded in the glass. Low-Ca pyroxene forms also tabular grains <15 μm-size more xenomorphic in comparison with olivine. The tabular grains of low-Ca pyroxene are rich in Fe and Ca on the border of the grains. The cementing glass has nearly equal stehiometry to plagioclase but is quite different in the composition (average composition of the glass: SiO_2 - 60.2; TiO_2 - 0.3; Al_2O_3 - 7.8; Cr_2O_3 - 0.3; FeO - 16.3; MnO - 0.4; MgO - 4.3; CaO - 8.0; Na_2O - 1.2; S - 0.6; n = 11 analyses).

Comparing compositions and shape of crystals of different phases of APT we can make a conclusion that the only liquidus phase of this melt was Mg-rich olivine, forming the tabular constant composition grains. The others phases crystallized during the quenching, had the Fe-rich compositions and formed fine skeletal, needle and dendrite crystals (usual for super cooling systems) in the glass.

AIT (Fig. 3) consist of the tabular grains of olivine (~15x70 μm) and low-Ca pyroxene (~15x30 μm). Moreover, skeletal crystals (~10x200 μm) of olivine occur in the interstices between idiomorphic tabular crystals and all of them are cemented by the glass. The olivine grains have a zonal structure. Fe-content of olivine changes from the center (tabular: Fa - 16, skeletal: Fa - 19) to the border (Fa - 30). Tabular grains of low-Ca pyroxene are situated between more idiomorphic tabular grains of olivine. Low-Ca pyroxene has a heterogeneous composition (center of the grain: Hyp - 30, En - 66, Wol - 3, Bus - 1; border: Hyp - 40, En - 53, Wol - 6, Bus - 1). Skeletal crystals of olivine are more xenomorphic in comparison with tabular crystals of olivine and low-Ca pyroxene. These grains all together are cemented by the glass with fine crystals of low-Ca pyroxene. The average composition of the cementing glass is: SiO_2 - 60.6; TiO_2 = 0.4; Al_2O_3 - 10.3; FeO - 15.0; MnO - 0.3; MgO - 1.8; CaO - 8.0; Na_2O - 1.8; K_2O - 0.2; P_2O_5 - 0.3; S - 0.9; n = 7 analyses. It's necessary to note that the compositions of the glasses of APT and AIT are non-homogeneous, but there are two distinct groups of the compositions (Fig. 4) of the glasses. The APT glass is rich in Ca and Fe and poor in Na and Al in comparison with the AIT glass.

The crystallization of this melt began from the tabular zonal grains of Mg-olivine and Mg-low-Ca pyroxene, which are the liquidus phases of the melt. The others phases (skeletal rich in Fe olivine and needle low-Ca pyroxene) crystallized during the quenching and were cemented by the glass. Fe-rich composition of the tabular grains of olivine and wide-spread skeletal and needle shapes of crystals of AIT in comparison with APT let us conclude that the crystallization of AIT-forming melt began at the lower temperature and was faster than the crystallization of APT-forming melt.

Detailed petrological research on the results of the experiment showed that:

there were two coexisting silicate melts with sharp boundary line [2] and these two melts

were different in chemical composition and temperature of the crystallization;

the melting of the ordinary chondrite even in "dry" (without pressure of fluid components) system shows the specific character of the differentiation of the silicate melt, led to form two coexisting immiscible silicate melts.

ACKNOWLEDGMENTS. We thank Prof. A.V.Vityasev for providing the experimental melted sample of the Tsarev chondrite.

REFERENCES: [1] Zetser Yu.I. et al. (1993) In: *Origin of Solar System*, A.V.Vityasev ed., Nauka Press, 112-115 (in Russian); [2] Zinovieva N.G. et al. (1994) *LPS XXV*, this volume.

FIGURE CAPTIONS: Fig. 1. Relict of the original chondrite material (in the center of the photo) in the area of the porphyritic texture. Black - Mg-rich Ol; white - Fe-rich Ol rim; light gray - cementing glass. Fig. 2. Detail of Fig. 1. Black - Mg-rich Ol; white - Fe-rich Ol rim and skeletal crystals of Ol ; light gray - needle crystals of low-Ca Px; gray - cementing glass. Fig. 3. Area of the intersertal texture. Black - Mg-rich Ol; ; white - Fe-rich Ol rim; gray - low-Ca Px; light gray - cementing glass. Fig. 4. The diagram of compositions (weight %) of the glasses of the areas of the porphyritic (1) and intersertal (2) textures.

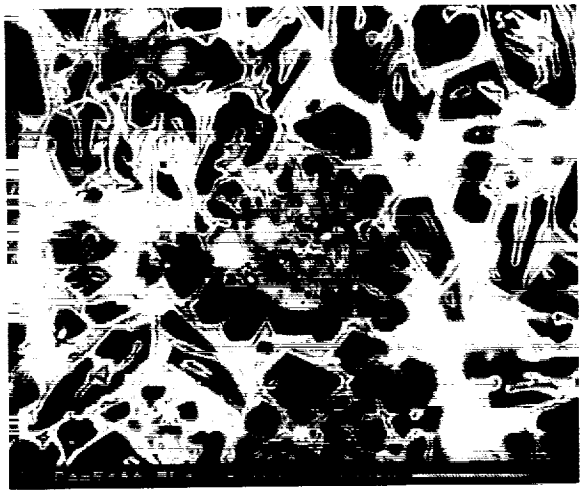

Fig. 1

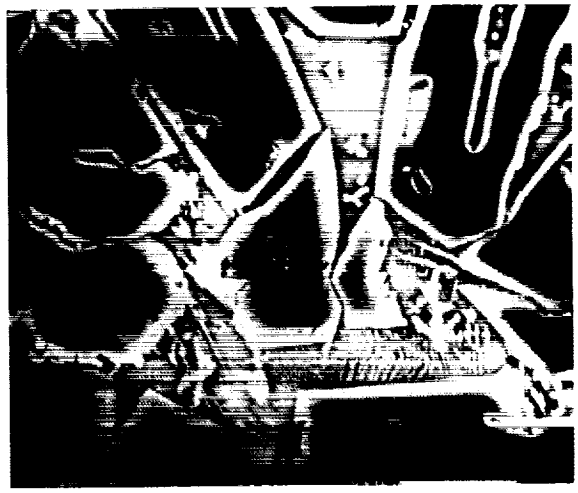

Fig. 2

Fig. 3

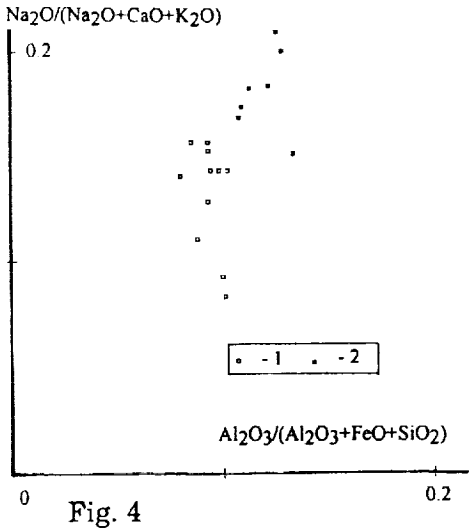

Fig. 4

LIQUID IMMISCIBILITY PROCESS OF THE EXPERIMENTAL MELTED ORDINARY CHONDRITE TSAREV (L5); N.G.Zinovieva, O.B.Mitreikina and L.B.Granovsky, Department of Petrology, Faculty of Geology, Moscow State University, Lenin Gory, Moscow, 119899, Russia.

The goal of this research was the detailed petrological study on the sample (2x2x4 cm) of the partially melted (by microwave-heating, run at vacuum, T=1400±100°C, t=20 min. [7]) ordinary chondrite Tsarev (L5) for understanding the specific character of the sulphide-metal-silicate melt differentiation. This research showed that there was the liquid immiscibility of silicate and sulphide-metallic melts, with the later separation of the silicate melt into two coexisting silicate melts and the sulphide-metallic melt into sulphide and metallic melts.

The outer part of the sample has a original chondrite structure, while the inner part has a taxite structure. It's necessary to note that shapes and sizes of Fe-Ni metal and troilite are quite different in the both structures.

Troilite and Fe-Ni metal grains of the outer not melted part (chondrite structure) of the sample have the irregular, interstitial, xenomorphic shape depended on the boundaries of the chondrules or depended on the silicate crystals inside the chondrules. Sometimes these grains form small (up to first μm) drop-like separations inside the olivine crystals.

Troilite and Fe-Ni metal of the inner melted part (taxite structure) of the sample form only drop-like (from some μm to some mm-size) separations. On fig. 1 we see the separation of the sulphide-metallic drop into troilite and Fe-Ni metal parts. Such things can be formed as a result of the crystallization of the immiscible sulphide and metallic melts.

The inner taxite part of the sample consists of areas of porphyritic (APT) and intersertal (AIT, sometimes with areas of barred texture) textures. The boundary between APT and AIT is sharp and they are different in both the texture and their chemical composition. It's necessary to note that these areas (APT and AIT) form as layer-like as drop-like (Fig. 2) separations one in another. Comparing electron microprobe analyses of bulk compositions of APT and AIT we see that these compositions are different in contents of almost all petrogenic elements (APT[AIT]: SiO_2 - 45.0 [47.3]; Al_2O_3 - 2.4 [3.3]; Cr_2O_3 - 0.6 [0.7]; FeO - 17.3 [18.8]; MnO - 0.3 [0.4]; MgO - 31.2 [24.9]; CaO - 2.0 [2.57]; Na_2O - 0.2 [0.8]; P_2O_5 - 0 [0.4]; S - 0.5 [0.7]) and we can make a conclusion that there were two coexisting silicate melts MP and MI forming during crystallization APT and AIT accordingly. MI is rich in Si, Al, Fe, Ca and alkalis and poor in Mg in comparison with MP. In spite of MI is rich in Si and Al, the ratio Si/Al of MP is higher than MI. We showed [4] that this ratio is important for understanding of the different texture formation.

It's known [6] that even a little (up to 1.0 weight % of P_2O_5) amount of P is favorable for the liquid immiscibility and the decreasing temperature of the crystallization of the melt. MI has a little but constant content (~ 0.4 weight %) of P_2O_5. This fact testify to higher crystallization of MP (poor in P) than MI. It has been confirmed by the mineral compositions and textures of APT and AIT [8]. It's necessary to note that both APT and AIT contain sulphide-metallic drops (from the first μm up to some mm-size) later separated into metallic and sulphide phases (Fig. 1).

Process of the liquid immiscibility of silicate, metallic and sulphide melts is well known [3; 5; et al.]. The experimental research on the melting of the ordinary chondrite Tsarev (L5), run at water-hydrogen fluid pressure [1], showed that there was liquid immiscibility of the chondrite melt into silicate, metallic and sulphide melts. The liquid immiscibility of the silicate part of the chondrite melt is less studied, however examples of the basic - ultra basic layering in the earth rocks are well known [2]. Types of separated (layered) rocks are unusual for the intrusive facies because the crystallization of the phase equalizes the compositions of the coexisting melts and the phase boundary disappears. The situation in the volcanic conditions is quite different because the variolitic structures of the komatiitic formation are wide-spread as in the lava flows as in the dikes. Varioles often consist of boninites or marianites and the matrix consists of komatiites.

The existence of two distinct types of the areas distributed across the melted part of the sample of the ordinary chondrite Tsarev and different in texture (APT and AIT) and their chemical

composition lead us to conclude that there were two immiscible silicate melts. We found that the boundary between these melts is sharp and there were two types of the silicate melt separations: layer-like and drop-like separations.

The conclusions made as a result of the petrological research of the vacuum melting of the ordinary chondrite Tsarev are:

the process of the liquid immiscibility of the sulphide-metallic and silicate melt took place;

the silicate melt later separated into two coexisting silicate melts;

the sulphide-metallic melt later separated into sulphide and metallic melts.

ACKNOWLEDGMENTS: We thank Prof. A.V.Vityasev for providing the experimental melted sample of the Tsarev chondrite.

REFERENCES: [1] Marakushev A.A. and Bezmen N.I. (1983) *Evolution of meteorite substance...*, Nauka Press, 184 pp. (in Russian); [2] Marakushev A.A. (1988) *Petrogenesis*, Nedra Press, 293 pp. (in Russian); [3] Marakushev A.A. et al. (1992) *Space petrology*, Moscow University Press, 325 pp. (in Russian); [4] Mitreikina O.B. et al. (1994) *Petrology 3*, (in press); [5] Ramdohr (1960) *Die Erzmineralien und ihre Verwachsungen*, Akademie-Verlag, 1132 pp. [6] Suleimenov S.T. et al. (1969) In: *Liquid immiscibility in glasses*, Nauka Press, p. 125-128, (in Russian); [7] Zetser Yu.I. et al. (1993) In: *Origin of Solar System*, A.V.Vityasev ed., Nauka Press, 112-115 (in Russian); [8] Zinovieva N.G. et al. (1994) *LPS XXV*, this volume.

FIGURE CAPTIONS: Fig. 1. The drop of sulphide-metallic melt separated into the sulphide and metallic melts. Fig. 2. The drop-like intersertal texture separation inside the area of the porphyritic texture.

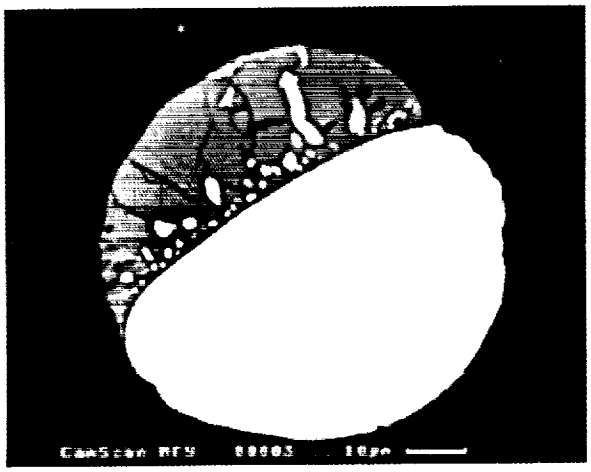

Fig. 1

Fig. 2

THE CHEMICAL COMPOSITION OF ACAPULCO AND ACAPULCOITES; J. Zipfel and H. Palme, MPI für Chemie, Postfach 3060, 55020 Mainz, Germany.

We report here the results of new INA analyses of Acapulco bulk samples and of several other Acapulcoites. Variations in the bulk chemical composition of Acapulco samples are primarily the result of large differences in modal phosphate and chromite contents and, to a lesser degree, in variable sulfide and metal fractions. Elements contained in plagioclase are uniformly distributed. The constant and approximately chondritic K content in all samples analysed excludes loss or gain of partial melts. Variations in the bulk chemistry of Acapulcoites mimic those in individual Acapulco samples. An average Acapulcoite composition derived from these data shows that Acapulcoites form a separate group of chondritic meteorites unrelated to other chondrite groups. Acapulcoites have slightly lower Fe and K and higher Mn, Se and Zn contents than H-chondrites. It appears in the light of several new groups of chondritic meteorites (Acapulcoites, Rumurutiites etc.) that the large fraction of ordinary chondrites among recovered meteorites does not reflect a high ordinary chondrite abundance in the asteroidal belt, but indicates recent break-ups of ordinary chondrite parent bodies.

On the basis of 6 new analyses of Acapulco bulk samples we define a new average Acapulco composition (table 1). The results of the analyses of individual Acapulco samples are graphically shown in Fig. 1, where all data are normalized to average H-chondrites [1]. Samples are arranged according to size. Analyses of [2] are shown for comparison, older analyses from this lab are marked by AP-A and AP-B [3]. Full bars represent an average of all analyses except [2]. Fig. 1 shows higher Mn and Se and lower Fe and K contents in Acapulco compared to H-chondrites. Refractory elements, represented by Sc, and Na, primarily contained in plagioclase, are on the H-chondrite abundance level, while K, almost exclusively sited in plagioclase, is distinctly lower than in H-chondrites. The uniform K-content in all Acapulco samples excludes major mobilisation of partial melts so prominent in Lodranites [4]. The large variability of La reflects large variations in modal phosphate contents. This is supported by similar variations in U and the absence of corresponding enrichments in Th which is, unlike U, not enriched in apatite. The surprisingly large variations in Cr do not allow to define a precise Cr-content for Acapulco. Sulfides, represented by Se, are also rather inhomogeneously distributed (Fig. 1). The elemental pattern in Acapulco is consistent with a large degree of melting and local crystal accumulation of chromite and phosphate. The absence of incompatible element variations (K and Th) and the constant, uniform and chondritic plagioclase content indicate a closed system behaviour except for gains of phosphate which is so obvious in most Acapulco samples.

Similar variations as those of individual Acapulco samples are found in Acapulcoites (see table 1). ALHA 81261 which is probably paired with ALHA 77081 [5,6] is compositionally very similar to average Acapulco. Monument Draw is somewhat different and may have lost a small fraction of a partial melt judging from the low K-content and abundant metal-sulfide veins. ALHA 81187 has obviously suffered a large degree of partial melting which caused a major loss of K and a slight depletion in LREE. This meteorite differs from all other Acapulcoites. In addition, ALHA 81187 is more reduced (Fa 3-4) and has a slightly different oxygen isotope composition than other Acapulcoites. For these reasons ALHA 81187 is not considered in the calculation of the average Acapulcoite composition. The bulk composition of Acapulcoites (AC) is compared to other types of chondritic meteorites in Figs. 2-4 (Chondrite data [1] except CI-data [7], CR-data [8] and solar data compilation in [7]). Chemically, Acapulcoites show some similarity to Rumurutiites (R) [9], although the latter meteorite group is significantly more oxidized. Refractory elements are at a similar abundance level as in ordinary chondrites. Moderately volatile elements of Acapulcoites are distinctly different from ordinary chondrites (Fig. 3). The Se and Zn contents are much higher than in ordinary chondrites while Mn and Na contents are similar. Siderophile elements are basically chondritic in Acapulcoites, although the bulk iron content is slightly below the chondritic value.

Acapulcoites represent a group of chondritic meteorites with basically chondritic abundances but with unique characteristics that distinguish them from other groups of chondritic meteorites. The absence of chondrules and the equilibrated texture of Acapulcoites indicates a thermal history different from other chondrite groups. Acapulcoites were heated to temperatures above the solidus, and have slowly cooled to lower temperatures, although no apparent loss of a low temperature melt fraction is observed implying a closed system during melting. These data demonstrate the importance of classifications based on chemical composition. The increasing number of new meteorite groups with chondritic composition undermines the priviledged position of the ordinary chondrites. Their abundances may reflect the effects of recent collisions of a few Earth crossing asteroids but may not tell us anything about frequency of meteorite types in the asteroidal belt.

THE CHEMICAL COMPOSITION; Zipfel J. and Palme H.

Table 1. Average bulk composition of Acapulcoites (INAA)

	ALHA 81261 (1)	Monum Draw (2)	ALHA 77081 (3)	Acapulco (4)		Acapulcoites average (5)	(6)	ALHA 81187 (7)
%					s.d. in %			
Mg	15.48	14.23	15.70	15.32	3	15.18	3.7	16.31
Al	1.12	1.16	1.20	1.22	3	1.18	3.3	0.99
Ca	1.25	1.04	0.59	1.14	7	1.14	7.5	1.25
Fe	21.81	25.54	24.80	20.69	3	23.21	8.7	18.48
ppm								
Na	6880	6710	7520	6947	3	7014	4.3	5300
K	603	354	690	567	8	553	22.3	192
Sc	8.65	7.43	10.3	8.33	3	8.68	12.0	8.20
V	91.7	70.3	88.7	75.5	3	81.5	10.9	65.8
Cr	5970	2150	7190	3962	3	4818	39.9	3493
Mn	2700	2460	3030	3076	3	2817	8.9	2755
Co	673	900	795	650	3	755	13.3	759
Ni	13600	23400	15600	14333	4	16733	23.4	11600
Zn	243	90.0	306	168	7	202	40.1	119
Ga	9.3	8.6	10.4	6.9	10	8.8	14.4	7.0
As	1.96	3.57	2.14	1.72	10	2.35	30.7	1.96
Se	8.66	10.6	10.3	11.0	5	10.1	8.7	2.0
Br	0.36	1.7	0.35	2.3	5	1.2	72.5	0.8
Sb	0.067	0.10	0.065	0.11	20	0.085	23.0	0.11
La	0.330	0.290	0.290	0.576	15	0.372	32.1	0.225
Sm	0.190	0.119	0.200	0.211	8	0.180	19.9	0.166
Eu	0.094	0.079	0.094	0.097	6	0.091	7.7	0.066
Yb	0.24	0.16	0.30	0.23	25	0.23	22.3	0.21
Lu	0.039	0.030	0.057	0.042	13	0.042	23.1	0.032
Hf	0.15	0.19	0.21		12	0.18	13.6	0.17
Re	0.07	0.10	0.06		35	0.08	24.1	0.077
Os	0.93	1.20	0.95	0.67	15	0.94	20.1	0.928
Ir	0.756	1.07	0.840	0.513	7	0.794	24.9	0.766
Au	0.186	0.344	0.200	0.161	30	0.223	32.0	0.189
U	0.019	<0.06		0.09	15	0.06	65.7	<0.02

(1) Zipfel and Palme, 1993; (2) average Monument Draw; (3) Schultz et al., 1982; (4) average Acapulco, Zipfel et al. in prep.; (5) average of all analyses except (7); (6) variance of (5) in %; (7) this work; < detection limit

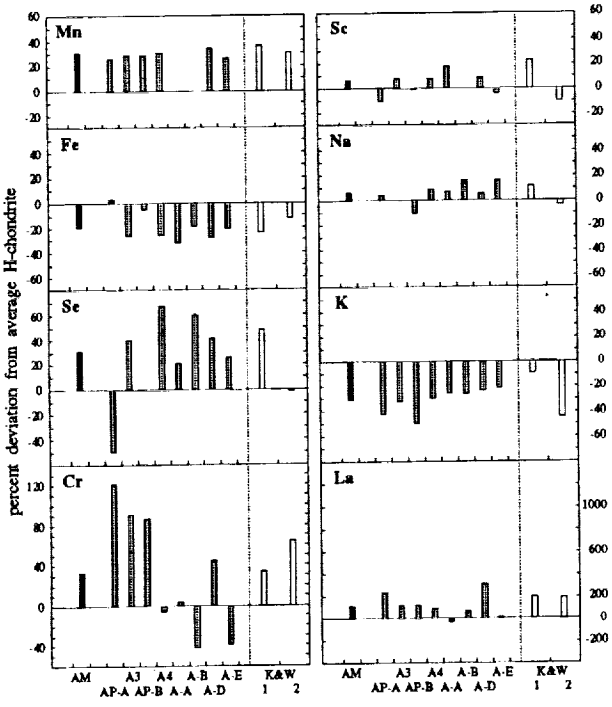

Fig. 2 Refractory Lithophile Elements

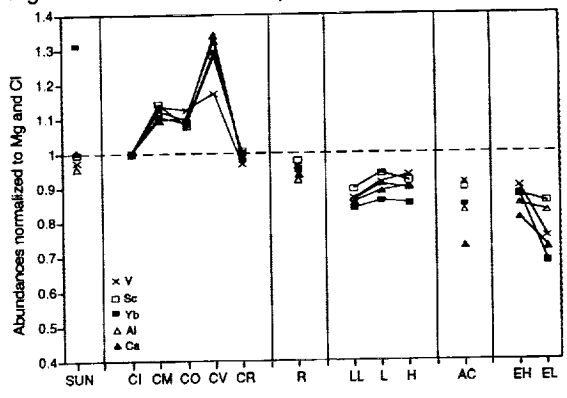

Fig. 3 Moderately Volatile Elements

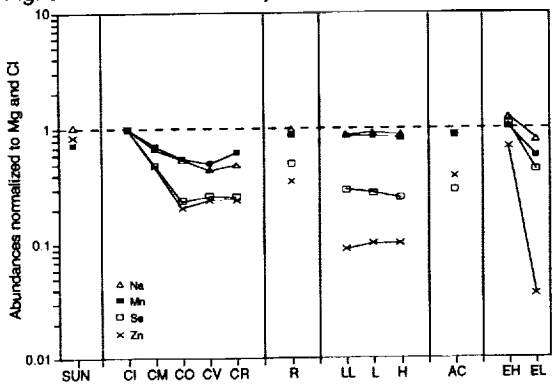

Fig. 4 Siderophile Elements

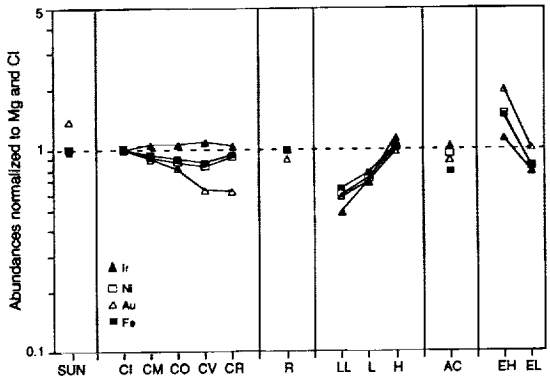

Fig. 1

Ref. [1] Wasson J.T. and Kallemeyn G.W. (1988) Phil. Trans. R. Soc. Lond. A 325, 535-544. [2] Kallemeyn G.W. and Wasson J.T. (1985) Geochim. Cosmochim. Acata 49, 261-270. [3] Palme H. et al. (1981) Geochim. Cosmochim Acta 45, 727-752. [4] Zipfel J. and Palme H. (1993) Meteoritics 28, 469. [5] Mason B. et al. (1998) Smithson. Contrib. Earth Sci. No. 28, 29-59. [6] Schultz L. et al. (1982) Earth Planet Sci. Lett. 61, 23-31. [7] Palme H. and Beer H. (1993) In: Landolt-Börnstein. New Series Vol. VI/3a, 196-221. [8] Bischoff A. et al. (1993) Geochim. Cosmochim. Acta 57, 1587-1603. [9] Schulze et al. (1994) Meteoritics, in print.

MINERALOGY OF AN UNUSUAL CM CLAST IN THE KAIDUN METEORITE

M.E. Zolensky[1], A.V. Ivanov[2], S.V. Yang[3], R.A. Barrett[3] and L. Browning[4]. [1]SN2, NASA Johnson Space Center, Houston, TX 77058, USA; [2]Vernadsky Institute of Geochemistry and Analytical Chemistry, Russian Acad. Sci., Moscow 117975, Russia; [3]Lockheed Engineering Co., Houston, TX 77058, USA; [4]Dept. Geological Sciences, University of Tennessee, Knoxville TN 37996, USA.

ABSTRACT Kaidun is breccia of disparate enstatite and carbonaceous chondrite clasts, and continues to provide real surprises. Many Kaidun clasts have been intensely altered by an aqueous fluid, as evidenced by the widespread occurrence of ferromagnesian phyllosilicates and presence of carbonate- and phyllosilicate-filled veins. In this report we describe an unusual CM lithology containing beautiful aggregates of jackstraw pyrrhotites, not previously reported from any meteorite.

The bulk of this lithology in Kaidun (sample 1.3.18a) consists of serpentine, saponite, and minor clinochlore, frequently intergrown as encountered in CI and CR chondrites and some chondritic interplanetary dust particles. Microprobe analyses of these phyllosilicates are compared to similar materials in Figure 1; the Kaidun phyllosilicates are dominated by Mg-rich serpentines; as verified by subsequent TEM work. The compositional range of Kaidun phyllosilicate is comparable with that in CI and CR chondrites. Although Kaidun phyllosilicate is distinguished from typical CMs by the presence of abundant saponite, it is instructive to note that Kaidun serpentine compositions are comparable with those from the most extensively altered CM chondrites [1]. In fact, the oxygen isotopic composition of this Kaidun lithology indicates it is CM material, being very similar to that of Murchison [3].

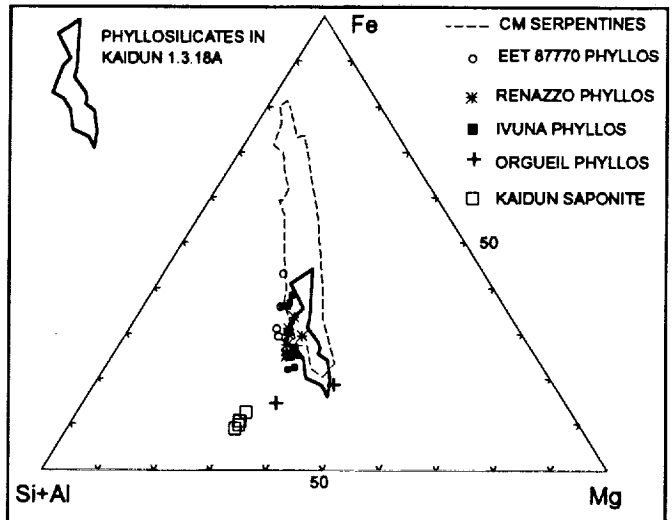

Figure 1 Ternary weight % plot of phyllosilicate compositions from the Kaidun C1 lithology, compared with phyllosilicates from other C chondrites (Renazzo and EET 87770 are CR, Ivuna and Orgueil are CI), including coarse-grained saponite from another Kaidun lithology [2].

Floating in the phyllosilicate-dominated matrix are (1) complex aggregates (see below), (2) abundant acicular, mantled pyrrhotites, identical to those rimming the aggregates (see below), (3) framboidal magnetites, forming in some instances masses adjacent to the exposed ends of pyrrhotite crystals, (4) anhedral to euhedral pentlandites, abundant everywhere within the lithology with the exception of the phyllosilicates lumps, and which generally lack the phyllosilicate sheaths observed about the pyrrhotites, (5) small, hollow apatites, (6) rare, anhedral diopside grains, and (7) homogeneous lumps of phyllosilicate, dotted throughout the matrix, and composed of serpentine, saponite and clinochlore of the same composition as the pyrrhotite mantles; there are no minerals in these lumps larger than 1 μm which makes them readily resolvable from the lithology matrix.

Another interesting component of this lithology are the complex aggregates (Figure 2a), which invariably are rimmed by jackstraw, acicular, pyrrhotite crystals ($Fe_{0.90-.92}Ni_{0.02}S$) (Figure 2b). In one case these pyrrhotites extend to the center of an aggregate, although this may be a projection artifact. All of the pyrrhotites in this lithology (including those in the aggregate rims) are mantled about their long axis by a sheath of phyllosilicate (Figure 2c), in places up to 20 μm thick. Microprobe analyses of these sheaths show that K_2O and Al_2O_3 increase in abundance away from the pyrrhotite, reflecting a gradual increase in the relative amount of saponite and clinochlore, as verified by TEM observations. In many instances phyllosilicate sheets parallel the surface of the enclosed pyrrhotite crystal. In most cases the phyllosilicate sheaths are barrel shaped, as if rounded by abrasion; sheaths are never present at the ends of the acicular pyrrhotite crystals. TEM observation reveals that the sheaths contain scattered submicron-sized pentlandite grains (as for in-situ serpentinization of olivine grains [4], but no fine-grained pyrrhotite. In some instances (Figure 2c) magnetite crystals lie adjacent to embayed pyrrhotite crystals. Everything about these pyrrhotites is exceptional, including (a) their mantling of aggregates in a jackstraw fashion, for which we have not identified a precedent, (b) their acicular crystal habit; plates and laths being far more common morphologies for pyrrhotite, and (c) the phyllosilicate sheaths, which are orders of magnitude thicker than any we have previously observed on sulfide crystals. Several aggregates have discontinuous inner rims of granular andradite garnet. This andradite is very impure (average composition $Ad_{51}Al_{32}Uv_9Gr_5Py_3$), with significant Cr and Ti. The andradite is somewhat porous, with inclusions of serpentine and sulfides; all microprobe analyses yield low totals (96-99%), due to either the porosity or structural water. The interior of the complex aggregates is an assemblage of phyllosilicates and pentlandite; one aggregate also contains endiopside whose texture resembles that of a radial chondrule. The pentlandite most frequently has an irregular morphology, but a delicate skeletal form is present in one aggregate. Two aggregates contain pentlandite-filled veins; which, while cutting through the andradite inner rims, fail to cut the outer pyrrhotite rims (Figure 2d).

This Kaidun lithology completely lacks olivine, glass or objects which can unambiguously be called chondrules, and contains only rare, minuscule clinopyroxene grains. These observations and the abundance of phyllosilicates indicates a classification of C1. Andradite can easily form at temperatures below 400°C, in oxidizing, low CO_2 fluids (as in a skarn), and has even been formed by fumarolitic activity [5]. However, andradite is also stable relative to olivine or clinopyroxene during

low-temperature aqueous alteration, so could also be a residual primary phase. Pentlandite veins, of probable parent body origin, crosscut the andradite, and must be later; hydrothermal pentlandite may indicate temperatures on the order of 450°C.[6] These same veins fail to cut the outer pyrrhotite rims, possibly indicating a later origin for the latter. However, the phyllosilicate mantles may replace a pre-existing silicate mantle, probably olivine (we have observed olivine mantles about *pentlandite* crystals in the Santa Cruz CM chondrite), which could require a condensation origin for the pyrrhotites. Thus, the pyrrhotites themselves could be pre- or post-accretional in origin. The framboidal magnetites, in close association with the exposed ends of pyrrhotite crystals, probably formed through the oxidation of the latter. The phyllosilicate lumps could have formed from the abrasion of pyrrhotite mantles, or simply through the alteration of the same precursor phase as the mantles.

This Kaidun lithology is, in general characteristics, much like the dark, wet clasts frequently observed in CR chondrites, and a large portion of Kaidun is in fact CR. This material has clearly been subjected to an extreme period (or periods) of aqueous alteration, at temperatures sufficiently high (~450°C) for pentlandite veins to form, sufficiently oxidizing (i.e. wet) for magnetite to replace pyrrhotite (log fO_2 = -60 to -65 [4]), and sufficiently long to permit formation of the well-crystalline, thick phyllosilicate mantles. These conditions would also permit andradite to form in-situ from clinopyroxene. This episode of parent-body alteration occurred on a CM parent body, prior to final consolidation of Kaidun.

References: [1] Browning et al. (1993) *Meteoritics 28*, 331; [2] Zolensky et al. (1991) *LPSC XXII*, 1565-1566; [3] Clayton et al., *LPSC XXV*, this volume; [4] Eckstrand (1975) *Economic Geology 70*, 183-201; [5] Varet (1970) *Contr. Mineral. Petrol. 27*, 321-332; [6] Godlevskiy et al. (1971) *Doklady Akad. Nauk. SSSR 196*, 146-149.

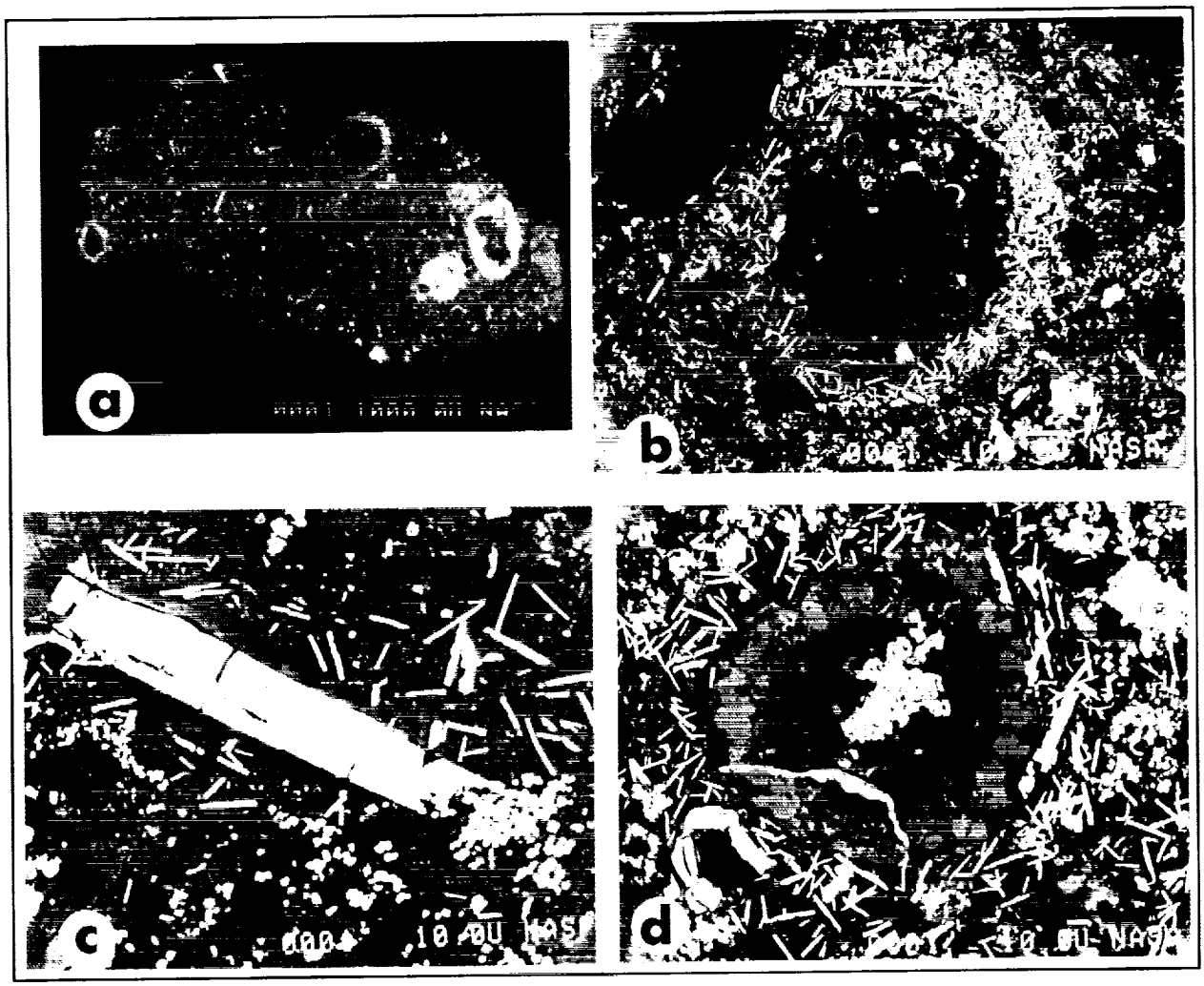

Figure 2 (a) Backscattered electron (BSE) image of a section of the Kaidun lithology, with pyrrhotite-rimmed aggregates plainly visible, (b) BSE image of one complex aggregate, view measures 1200 μm, (c) BSE image of one large acicular pyrrhotite crystal in matrix, with sheath of phyllosilicate and adjacent cluster of magnetite framboids at lower right end of the crystal, crystal measures 200 μm in length, (d) BSE image of a complex aggregate with a core and crosscutting vein of pentlandite (white), inner rim of andradite (gray) and outer rim of acicular pyrrhotites. Cluster of framboidal magnetites are visible at the margins of the image, which measures 500 μm across.

MINERALOGY OF ARTIFICIALLY HEATED CARBONACEOUS CHONDRITES

M.E. Zolensky[1], M.E. Lipschutz[2] and T. Hiroi[1]; [1]NASA Johnson Space Center, Houston, TX 77058; [2]Dept. Chemistry, Purdue University, West Lafayette, IN 47907.

Abstract: We have examined suites of heated Murchison (CM2) and Allende (CV3) samples heated in the range 400-1200°C, in a H_2 atmosphere with a pressure of 10^{-5} bar for periods of 1 to 4 weeks. We used a combination of X-ray diffraction, electron microprobe and TEM analyses to determine the mineralogy of these samples.

Introduction: Several carbonaceous (C) chondrites have been discovered which exhibit evidence of having undergone aqueous alteration followed by a parent body heating event, possibly related to the former process [1]. Our understanding of these heating events is limited by a paucity of information concerning the compositional and mineralogical effects of C-chondrite heating under different environmental conditions. Thus, we have been characterizing suites of C chondrites subjected to laboratory heating under plausible parent body conditions. To date we have examined Murchison (CM2) and Allende (CV3), which together represent the most abundant types of C chondrites. Both suites have been heated in the range 400-1200°C, in a H_2 atmosphere with a pressure of 10^{-5} bar for periods of 1 to 4 weeks. We used a combination of X-ray diffraction, electron microprobe and TEM analyses to determine the mineralogy of these samples. This abstract complements another in this volume which describes the mineralogy of the Murchison samples as determined by Mössbauer spectroscopy [2], and earlier work on their reflectance spectroscopy [3]. Akai has been performing complementary heating experiments on samples maintained in a vacuum [4].

Murchison The CM2 chondrites experienced extensive aqueous alteration, and they typically consist predominantly of phyllosilicates (serpentines ± chlorite), tochilinite, olivine, glass, pyrrhotite and minor pyroxene and Fe-Ni metal. Olivine and orthopyroxene compositions huddle around Fo_{99} and En_{99} (see Fig. 1). We observed the following mineralogical changes in heated Murchison samples (although we examined samples at 100°C steps, only the most interesting changes are noted here).

400°C: Well-crystalline serpentine is now a minor phase; some has been replaced by a poorly crystalline, so-called "intermediate phase" [4]. Tochilinite has been destroyed, some pyrrhotite has been replaced by Fe-sulfate. Olivine is still a minor component of matrix.

500°C: Serpentines are entirely replaced by the intermediate phase.

600°C: Recrystallization (and coarsening) of matrix and chondrule rims is evident.

700°C: The abundance of Fe-Ni metal in the matrix has substantially increased.

800°C: The intermediate phase has now been replaced entirely by olivine. Olivine, now the most abundant mineral (including matrix), has a heterogeneous composition, with a greatly reduced population peak at Fo_{99}; likewise orthopyroxene.

1000°C: Olivine compositions are evenly distributed between Fo_{99}-Fo_{50}; likewise for orthopyroxene. Chondrules are beginning to recrystallize. Matrix olivines and Fe-Ni metal grains continue to coarsen.

Allende The CV3 chondrites experienced minimal aqueous alteration (compared to the CMs), and they typically consist predominantly of olivine, with minor pyrrhotite and/or troilite, pyroxene, Fe-Ni metal, saponite, glass and refractory phases in CAIs. Olivine and orthopyroxene compositions bunch around Fo_{55} and En_{55} (see Fig. 1). The mineralogical changes in heated Allende samples were not as dramatic as those observed in Murchison, until 1200°C. The major observed mineralogical effect (until 1200°C) was a progressive increase in the amount of Fe in olivine, beginning at grain rims and spreading core-ward with increasing temperature, which suggests that the Fe was acquired from matrix phases.

800°C: All olivines have Fe-rich rims; no olivines are observed to be more Mg-rich than Fo_{92}.

1000°C: Fe-Ni metal grains are very abundant in matrix. Chondrules are beginning to recrystallize.

1200°C: The meteorite has completely recrystallized to coarse-grained olivine (Fo_{64-67}), with interstitial augite, chromite, Fe-Ni metal and rare FeS. Large vesicles are evident, presumably from the volatilization of S.

These mineralogical data are being compared to those for naturally heated C chondrites. We are also examining the mineralogy of the Allende samples by Mössbauer spectroscopy, and collecting their optical reflectance spectra. These latter results will then be compared to optical reflectance data of asteroids, in an effort to better understand their evolution.

References: [1] Ikeda (1992) *NIPR Symp. 5*, 49; [2] Morris et al. (1994) *LPSCXXV*, this volume; [3] Hiroi et al. (1993) *Science 261*, 1016; Akai (1992) *NIPR Symp. 5*, 120.

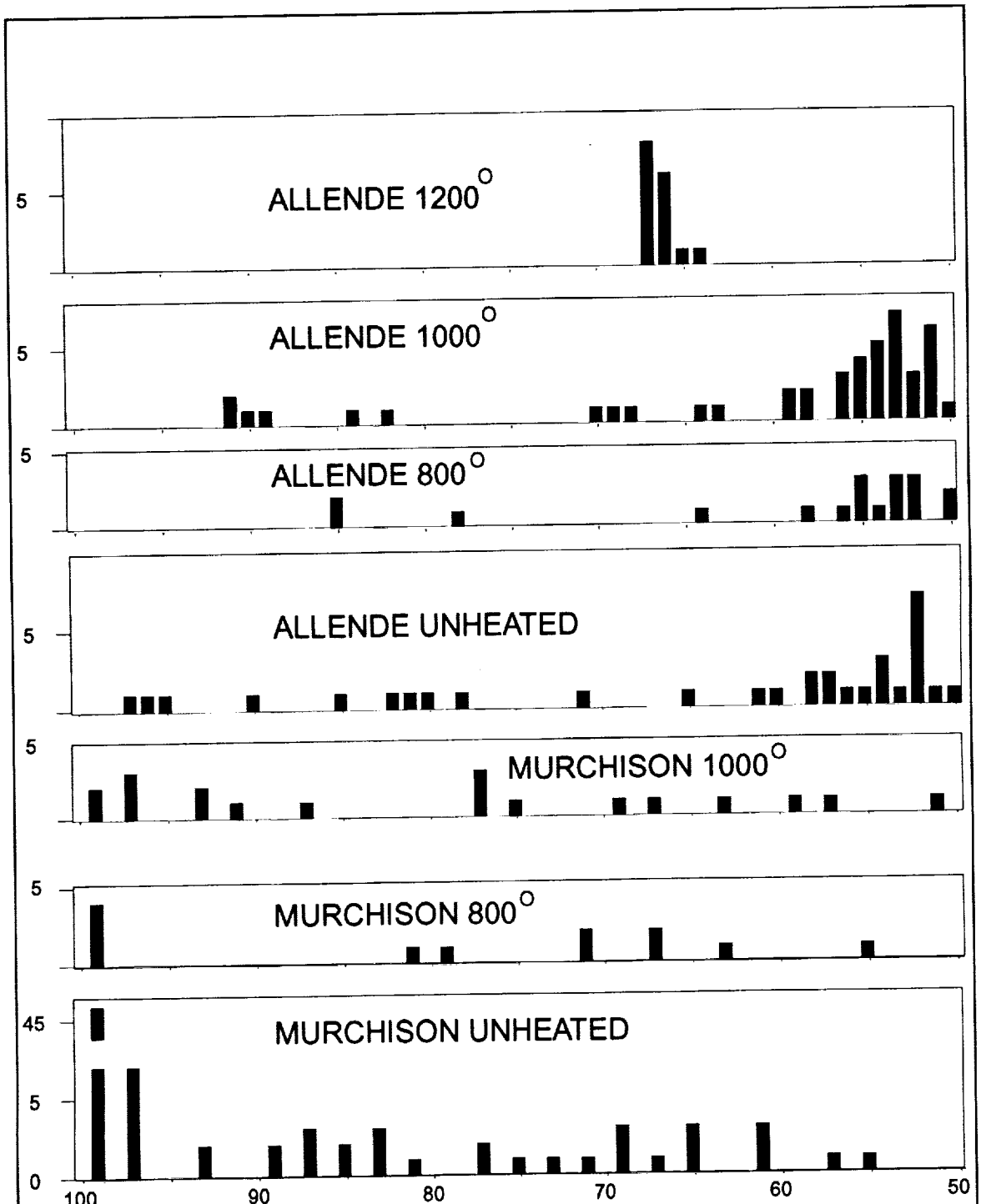

Figure 1. Olivine analyses from unheated and heated samples of Murchison and Allende. Note the height of the Fo_{99} peak for unheated Murchison, which is shown here in a greatly abbreviated fashion.

NEAR-SURFACE ATMOSPHERE OF VENUS: NEW ESTIMATIONS OF REDOX CONDITIONS BASED ON NEW DATA Zolotov M.Yu. Vernadsky Institute of Geochemistry and Analytical Chemistry, Russian Academy of Sciences, Moscow

Atmospheric redox potential at the planetary surface was evaluated providing thermochemical gaseous equilibria on the basis of new spectroscopic estimations of gases content below clouds. The redox potential estimation made based on CO_2, CO, SO_2, and COS content ($\log(f(O_2))$ = (-21.3-(-21.4)) seems to be more reliable. The experimentally expected COS and SO_2 abundance as 15 ppm and <130 ppm respectively do not contradict with the concept of thermochemical equilibrium in the C-O-S system.

Recent estimations of COS, CO, H_2O, and SO_2 abundance obtained from near-infrared spectra of the Venus night side (1,2) enables more precise definition of atmospheric composition (Tab.). The Pollacks' et al. (1) expectation of COS content as 15 ppm and more below 26 km is higher than Pioneer Venus' upper limits (3,4) and appears to be similar with theoretically estimated contents (e.g. 5-8) based on thermochemical equilibrium model for the lowermost part of the atmosphere. That coincidence supports that model at least for the C-O-S system. The new estimations of CO content for the 40-23 km do not contradict the Pioneer Venus (3) and Venera 11,12 data (9). The water vapor content estimated in (1) is essentially lower than recommended in (10) value and similar with the Venera 11,12 spectroscopic data (11). The microwave (12), and Vegas's spectral evaluations (13) showed that SO_2 content below clouds could be lower than 130 ppm. In spite of low accuracy, the latter data might not be accidental. The goal of that work is to test the applicability of these new data to the equilibrium concept.

Results. The atmospheric redox potential was estimated on the basis of recent data providing the following chemical equilibria: $CO_2=CO + 0.5O_2$; $SO_2 = 0.5S_2 + O_2$; $CO_2 + SO_2 = COS + 1.5O_2$; $CO + SO_2 = COS + O_2$; $H_2O + SO_2 = H_2S + 1.5O_2$ (Fig.). The calculations were made at 740 K, 95.6 bar (6051.4 km) on the basis of gases content from Table and thermochemical data for gases mostly from (14).

Discussion. The calculations of redox potential ($\log(f(O_2))$) lead to different results, while this lack of coincidence appears to be lower than has been predicted on the basis of Pioneer Venus and Venera data (e.g. 7,8). This noncoincidence is assumed either to result from lack of total gaseous equilibrium in the C-O-S-H system as suggested in (15), or could be coming from insufficient accuracy of measurements of some gases providing the thermochemical equilibrium. The third possibility is the existence of that equilibrium between two gases (e.g. CO_2 and CO) or a few gases (e.g. CO_2, CO, COS, and SO_2). The latter one seems to be supported by the recent data because of better coincidence of $\log(f(O_2))$ values calculated from these gases (see Fig.). The concentration of CO_2, CO, SO_2, and COS are slightly better known and high enough to determine the redox conditions in contrast with much less abundant gases such as S_2, H_2, and H_2S (see e.g. 10,15). Therefore the redox potential estimations made on the basis of H_2S and S_2 concentration could be considered as less reliable.

The estimation of the redox potential made based on concentration of CO_2, CO, SO_2, and COS (0.965 (10); 17 ppm (17); 60 ppm (12); 15 ppm (1)) results to $\log(f(O_2))$ = (-21.33)-(-21.38). Another words, the redox potential obtained from COS and SO_2 are equal $\log(f(O_2))$ value, which is controlled by CO/CO_2 ratio. That coincidence shows that SO_2 content lower than 130 ppm is not so unusual providing the concept of thermochemical equilibrium (see Fig.). Besides, the COS abundance as high as about 100 ppm (as also was not excluded on the basis of Venus's spectra modeling (1)) does not better corresponded with that concept. Indeed if COS abundance is about 100 ppm the redox potential values estimated from $COS-CO_2-SO_2$ and $COS-CO-SO_2$ equilibria (-21.67 and -21.85 respectively at 130 ppm SO_2, 17 ppm CO, and 0.965 CO_2) is in contradiction with the $f(O_2)$ value obtained from CO_2-CO equilibrium, which supposed to be control the redox potential (15).

The low $f(O_2)$ value obtained from $H_2O-H_2S-SO_2$ equilibrium could be result either of lack of that equilibrium, or the real H_2S content near the surface is much more lower than 3 ppm as measured in (4). At the condition of $CO-CO_2$ equilibrium ($\log(f(O_2))$ = -21.33, 0.965 CO_2, 17 ppm CO) the H_2S content

was estimated as following: 0.02 ppm at 10 ppm H_2O and 60 ppm SO_2; 0.04 ppm at 10 ppm H_2O and 130 ppm SO_2.

These content are even lower than values obtained from previous equilibrium models: 0.3 ppm (5), 0.05 ppm (6), 0.1 ppm (7), 0.08 ppm (15). The redox potential values obtained from SO_2-S_2 equilibrium at the SO_2 content <130 ppm appear to be in accordance with the log(f(O_2)) values, calculated from equilibria between CO_2, CO, COS, and SO_2 If SO_2 abundance is indeed about 130 ppm (2,9) the thermochemical equilibrium concept results to prediction of S_2 abundance as high as 0.3 ppm at log(f(O_2)) = -21.33.

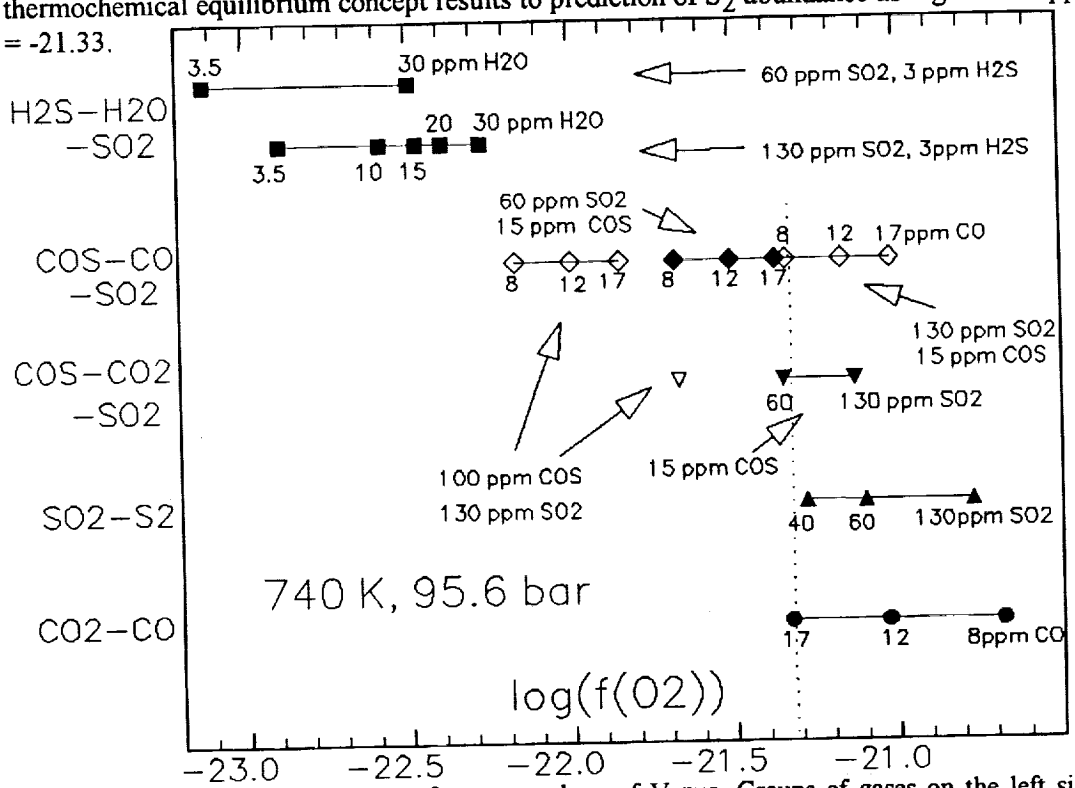

Fig. Redox potential of the near-surface atmosphere of Venus. Groups of gases on the left side of the plot are corresponded to the equilibria mentioned in text. Dot line shows the redox potential, which is controlled by the CO_2-CO eqilibrium at 17 ppm CO and 0.965 CO_2.

Composition of the near-surface atmosphere of Venus

gas	mol. ratio	±	altitude	Ref.
CO_2	0.965	0.008	0-40	(10)
CO	20 ppm	3	22	(3)
	12 ppm	4	23	(1)
	17 ppm	1	12	(9,17)
COS	<3 ppm	-	>22	(4)
	15 ppm	-	<26	(1)
SO_2	185 ppm	43	<40	(3)
	130 ppm	35	<42	(9)
	130 ppm	40	35-45	(2)
	120 ppm	20	42	(13)
	25 ppm	-	0	(13)
	62 ppm	+183/-62	<48	(12)
H_2O	3.5-15 ppm		0	(1)
	20 ppm	-	0	(11)
H_2S	3 ppm	2	<20	(4)
S_2	0.02 ppm	-	0	(16,11)

References: **1.** Pollack J.B. et al. (1993) Icarus 103:1; **2.** Bezard B. et al. (1993) Geophys. Res. Lett. 20:1587; **3.** Oyama V.I. et al. (1980) J. Geophys. Res. 85:7891; **4.** Hoffman J.H. et al. (1980) J. Geophys. Res. 85:7882; **5.** Krasnopolsky V.A., Parshev V.A. (1981) Nature 292:610; **6.** — (1983) *Venus* (Hunten D. M. et al. Eds.), 431; **7.** Zolotov M.Yu. (1991) LPSC 22: 1571,1573; **8.** Zolotov M.Yu., Volkov V.P. (1992) *Venus geology, geophysics and geochemistry* (V.L. Barsukov and V.P. Volkov Eds.), 177; **9.** Gelman B.G. et al. (1979) Cosmic Res. 17:585; **10.** Von Zahn U.et al. *Venus* (Hunten D. M. et al. Eds.), 299; **11.** Moroz V. I. et al. (1983) Icarus 53:509; **12.** Fard A. K., Stefers P.G. (1992) Icarus 87:200; **13.** Bertaux J.L. et al. (1992) Bull. Amer. Astr. Soc. 24:996; **14.** Chase M.W. et al. (1985) JANAF Therm. Tables; **15.** Fegley B.J., Treiman A.H. (1992) *Venus and Mars: Atmosphere, Ionosphere and Solar Wind Intraction.* (J. Luhman, R.O. Pepin Eds.), AGU Chapman Comp.,7; **16.** Sanko N. F. (1980) Cosmic. Res. 18: 437; **17.** Marov M. Ya., et al. (1989) *Venus: Atmosphere, Surface, Interior structure* (V.L. Barsukov , V. P. Volkov Eds.), 25

PHASE RELATIONS IN THE Fe-Ti-Mg-O OXIDE SYSTEM AND HEMATITE STABILITY AT THE CONDITION OF VENUS' SURFACE M. Yu. Zolotov Vernadsky Institute of Geochemistry and Analytical Chemistry, Russian Academy of Sciences, Moscow

Activity-composition relations and miscibility gap of ilmenite-hematite-geikielite solid solution were estimated in the frame of Fe-Ti-Mg-O oxide system for the condition of Venus' surface. The existence of titanhematite-magnetite, titanhematite-rutile, ferrianilmenite-rutile as well as magnetite-rutile or ferrianilmenite-titanhematite assemblages is expected for the surface. Prediction of hematite stability as a Ti-, Mg-bearing solid solution is in accordance with the atmospheric redox potential and with the near-infrared spectral features of the surface. Magnetite-titanhematite assemblage could be considered as a buffer of atmospheric redox potential.

Iron and titanium oxides are minor but critical minerals in igneous rocks and their weathering products (1,2), and could be responsible for the low emissivity features of the Venus' surface (e.g. 3,4). Stability of end members of Fe-Ti oxides on the surface was investigated and reviewed in (5-7). While natural titanomagnetite usually also contains Al, Cr, Mn, and Mg; ilmenite usually contains Mg; hematite (formed as a result of silicates, titanomagnetite or ilmenite oxidation) contains Ti and Mg (2). The aim of that work is to evaluate the stability of solid solutions of Fe-Ti oxides at the conditions of Venus' surface.

The main end members which exist in the Fe-Ti-O system are: hematite, magnetite, ilmenite, ulvospinel, and rutile. Two main solid solution series: magnetite-ulvospinel and hematite-ilmenite exist in the system. The main assemblages which are expected for 700-800 K could be: magnetite-titanhematite, titanhematite-rutile, ilmenite-rutile, and rutile-magnetite or titanhematite-ferrianilmenite (Fig. 1).

The magnetite-titanhematite phase assemblages, which form between magnetite and hematite solid solution are depended on the redox potential (e.g. 1,2). Therefore, the activity of solid phases - redox potential relations could be developed for the condition of Venus' surface (Fig. 2). The activity-composition relations and boundaries of miscibility gap for the ilmenite-hematite solid solution were calculated for the variable geikielite ($MgTiO_3$) content at 740 K on the basis of (8).

Activity of magnetite, which is suggested to be in equilibrium with rutile, titanhematite and ferrianilmenite (compositions for the miscibility gap boundary), was calculated from equilibrium: $Fe_3O_4 + TiO_2 = FeTiO_3(ss) + Fe_2O_3(ss)$ (see Fig. 1) for various geikielite content in hematite and ilmenite solid solutions at the TiO_2 activity given as unity. The magnetite activities obtained from that equilibrium are: 0.82 (at $x(MgTiO_3)=0$, $a_{(ilm)}=0.77$, $a_{(hem)}=0.63$); 0.73 (at $x(MgTiO_3)=0.15$, $a_{(ilm)}=0.67$, $a_{(hem)}=0.64$). The $\log(f(O_2))$ values at 740 K for the condition of magnetite-titanhematite equilibrium were calculated on the basis of hematite activity (for the boundary composition) and estimated magnetite activity: -21.66 and -21.43 (for 0 and 15 mol. % of $MgTiO_3$ in titanhematite respectively). These values of redox potential are suggested as lower limits for the stable existence of titanhematite on the surface.

The redox potential values for the of titanhematite-magnetite equilibrium were also estimated as a function of magnetite activity at the fixed composition of titanhematite on the boundary of the miscibility gap (Fig. 3). The $f(O_2)$ values for the magnetite-titanhematite equilibrium calculated as a function of hematite composition at fixed magnetite activities shown on Fig. 4.

Discussion. The redox potential estimated for the magnetite-titanhematite equilibrium appears to be in a good coincidence with Venus' $f(O_2)$ values, estimated on the basis of atmospheric chemistry (9). Titanhematite with variable composition should be stable at $\log(f(O_2)) = (-20.82)-(-21.66)$, as expected for the nearsurface atmosphere (see Fig. 4). That result is in agreement with the prediction of hematite existence made from near-infrared spectra of the Venus' surface (10). Magnetite ($a_{(Mt)}=0.6$-0.7 and more) - titanhematite ($a_{(Hem)}= 0.63$-0.64 and more) equilibrium could control atmospheric redox condition and composition (e.g. CO_2/CO ratio). That assemblage should form as a result of ilmenite, titanomagnetite and Fe^{2+}-silicates oxidation by $CO_2(g)$ and/or $H_2O(g)$.

Besides, taking into account the hematite and magnetite activities obtained from Fe-Ti-Mg-O system, phase diagrams in the Fe-S-O and Fe-S-O-C systems were developed at 740 K. The advanced position of

the pyrite-magnetite-hematite nonvariant point on these diagrams appears to be quite near to the $P(O_2$, CO, and COS) values, suggested for near-surface atmosphere of Venus (see 9).

The expected buffering of atmospheric redox potential by titanhematite-magnetite (+pyrite?) assemblage should be result of the previous physic-chemical evolution of coupled atmosphere-lithosphere system on Venus. At the present time that equilibrium is considered as a nonvariant point and future evolution (along with pyrite-hematite buffer) will begin only after totally magnetite oxidation in the near-surface soil/rock layer. At the present epoch the full and successful oxidation of magnetite seems to be limited by low rate of hydrogen escape as well as by the ability of relatively fresh basalts.

Acknowledgments. I thank Prof. R. Greeley for the scientific and organizational support. That research was supported by NASA grant No. NAGW-2102, Subgrant No. 93-102SG.

References. **1.** Lindsley D.H. (1976) in Rev. in Mineralogy, Vol. 3, L61; **2.** - (ed.) (1991) Rev. in Mineralogy, Vol. 25, 509p; **3.** Garvin J.B. (1985) Abst. LPSC 16, 262; **4.** Pettengill G.H. et al. (1988) JGR, 88, 14881; **5.** Fegley B.J. and Treiman A.H. (1992) *Venus and Mars: Atmosphere, Ionosphere and Solar Wind Interaction.* AGU Chap. Comp., 7; **6.** Fegley B.J. et al. (1992) Proc. LPSC 22, 3; **7.** Zolotov M.Yu. and Volkov V.P. (1992) *Venus Geology, Geophysics and Geochemisry,* Ariz. Univ. Press, 177; **8.** Ghiorso M.S. (1990) Contr. Miner. Petrol. 104, 645; **9.** Zolotov M. Yu. this volume; **10.** Pieters C. et al. (1986) Science 234, 1379;

Fig. 1. Expected phase assemblages in the system FeO-Fe_2O_3-TiO_2 at 740 K. **Fig. 2.** Redox potential ($\log(f(O_2))$, bar) for the hematite-magnetite equilibrium as a function of hematite and magnetite activity at 740 K. Horizontal lines show the boundaries of miscibility gap for the hematite-ilmenite-geikielite solid solution. Lower horizontal lines indicate the boundaries of miscibility gap at $x(MgTiO_3) = 0$, upper lines indicates these boundaries at $x(MgTiO_3) = 0.15$. **Fig. 3.** Redox potential for the hematite-magnetite equilibrium at the fixed activities of hematite as a function of magnetite activity at 740 K. The fixed activity of hematite is devoted to the boundary titanhematite composition in the hematite-ilmenite-geikielite solid solution. That hematite activity is estimated from miscibility gap boundaries and hematite activity-composition relations for the hematite-ilmenite-geikielite solid solution at $x(MgTiO_3)=0$ and 0.15. **Fig. 4.** Redox potential for the hematite-magnetite equilibrium as a function of hematite molar ratio in titanhematite (hematite solid solution) at 740 K. Fixed magnetite activities were obtained from Mt+Rut=Ilm(ss)+Hem(ss) equilibrium.

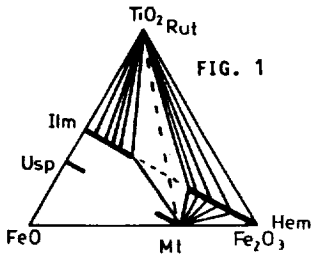

FIG. 1

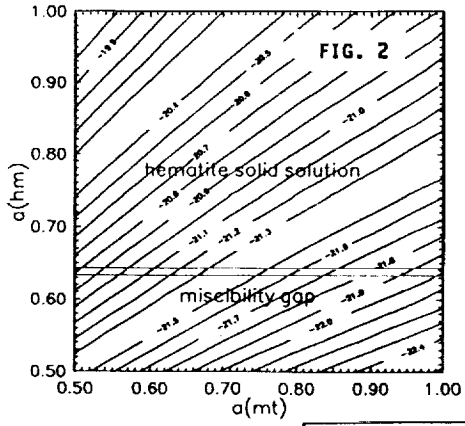

FIG. 2

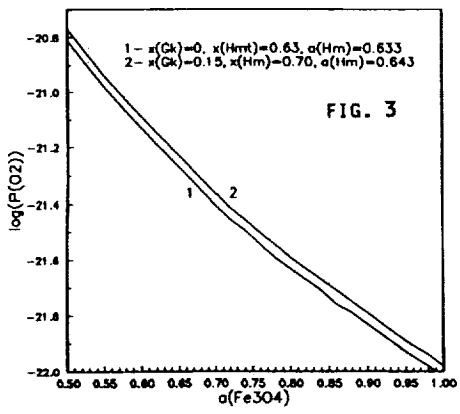

FIG. 3

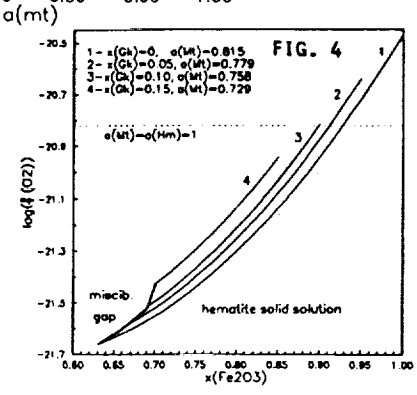

FIG. 4

LUNAR HORIZON GLOW AND THE CLEMENTINE MISSION

H.A. Zook and A.E. Potter, NASA-Johnson Space Center, Houston, TX 77058

Introduction. The Clementine spacecraft is to be launched into Earth orbit in late January for subsequent insertion into lunar orbit in late February, 1994 [1]. There, its primary mission is to produce--over a period of about two months--a new photographic map of the entire surface of the Moon; this will be done, in a variety of wavelengths and spatial resolutions, in a manner greatly superior to that previously accomplished for the whole Moon. It will then go on to fly by, and photograph, the asteroid Geographos. A secondary goal that has been accepted for this mission is to take a series of photographs designed to capture images of, and determine the brightness and extent of, the Lunar Horizon Glow (LHG). One form of LHG is caused by the solar stimulation of emission from Na and K atoms in the lunar exosphere [2]. The scale height of this exosphere is of the order of 100 km. There are also brighter LHG components, with much smaller scale heights, that appear to be caused by sunlight scattered off of an exospheric lunar dust cloud [3,4,5].

Background. The Surveyor V, VI, and VII spacecraft, that were landed on the Moon before the manned missions began, photographed a narrow band of light that glowed along the lunar horizon, and that lasted up to 2 hours after local sunset [3]. The brightness of this LHG ranged up to about $10^{-6}B_o$, where B_o is the mean brightness of the Sun (For comparison, $10^{-6}B_o$ is also about the mean brightness of the full Moon). The source of this LHG was deduced [e.g. 4] to be sunlight scattered by a lunar exospheric cloud of dust with a scale height of 10 to 20 cm. It was further deduced that meteoroid impact ejection of lunar soil grains could not account for the very high spatial density of the exospheric dust cloud that was inferred from the LHG observations; therefore electrostatic ejection of lunar grains from an electrically charged lunar surface was postulated to give rise to this dust cloud [4].

During the Apollo 17 mission, in Dec., 1972, the Lunar Ejecta and Meteorites (LEAM) experiment was placed on the Moon [5]. Over the next 22 months after activation, a remarkable phenomenon was observed: a very pronounced increase in the dust grain impact rate occurred around the sunrise and sunset terminator crossings. This could not be understood as due to impacts by interplanetary meteoroids. Nor was it due to sunrise/sunset thermal noise; the impact rate started increasing as early as 150 hours before sunrise while the Sun was over 70 degrees below the horizon. Berg and co-authors [5] could find no other explanation for these data than that lunar dust grains were being electrostatically transported over the lunar surface; and further that this transport was somehow connected with terminator crossings.

Also, after return from the lunar surface but while still in orbit around the Moon, the three Apollo 17 astronauts sketched various dim light features that they observed when the Sun was occulted from the spacecraft by the Moon. One of the features that they sketched was a glow above the lunar horizon that may have extended as much as 80 degrees along the horizon. This "new" LHG was quite dim and was not recorded with any of the hand-held photography. This glow was later analyzed by Zook and McCoy [6] and found to correspond to a brightness of about $2*10^{-12}B_o$, and to be due, most probably, to an exospheric dust cloud with a scale height of about 10 km (plus-or-minus a factor of 2). Similarly to the previous authors, they also estimated that the dust cloud arises from electrostatic ejection of grains from the lunar surface--as meteoroid impact ejection of lunar soil was deemed an insufficient source.

LUNAR HORIZON GLOW: Zook H.A. and Potter A.E.

In short, three lines of evidence indicate the existence of a surprisingly high spatial density of dust grains above the lunar surface. Estimates of the LHG brightness derived from astronaut sketches are quite uncertain in accuracy, however, and new quantitative data for the high altitude dust are greatly needed.

Capability of the Clementine cameras to sense LHG. The CCD cameras on the Clementine spacecraft are primarily designed to photograph the sunlit lunar surface. Because the Moon is quite bright, long exposures were not necessary; nor was it necessary to actively cool the CCD's. For these, and other, reasons, the longest exposure that can be made with either the f/1.96 UV/Vis camera or the f/1.25 star-tracker camera is 0.77 seconds. Because the backplanes to which the CCD's are thermally coupled are not actively cooled, the CCD temperatures are expected to float between about -20 °C and +10 °C; the corresponding number of electrons expected to be thermally excited to the conduction band per pixel is estimated to range between 1000 and 4000 electrons per 0.77 sec exposure [7]. Along with CCD "read noise", the poisson fluctuation in the number of thermal electrons also creates a background noise. The two sources of noise, coupled together, are expected to range between 50 and 100 electrons per pixel per 0.77 sec exposure. The camera designers, partly with this in mind, digitized the output of the cameras so that one digital unit corresponds to 150 electrons for the UV/Vis camera and to 75 electrons for the star-tracker camera.

Taking all camera characteristics into account, we would expect that a 0.77 sec exposure of a $2*10^{-12}B_o$ bright LHG would result in about 1300 electrons per pixel in either the UV/Vis (through the clear filter) or the star-tracker camera, assuming a solar spectrum. This corresponds to about 8 digital units above background for the UV/Vis camera and about 17 digital units above background for the star-tracker camera. The above exposure duration for the UV/Vis camera through the 340 nm filter would only result in a signal of about 18 electrons; this signal level could not be seen against the noise background (and the same is true of the other narrow band filters). If, however, the LHG is caused by sunlight scattered by particles smaller than about 0.1 μm in radius, then the scattered sunlight will be strongly blue-weighted by the factor $(\lambda o/\lambda)^4$, where λo is the weighted wavelength for the dark-adapted eyes of the astronauts (approximately, λo=500 nm). For this case we could expect about 90 electrons through the UV/Vis 340 mm filter, and this might be detectable--especially if we have underestimated the LHG absolute brightness. Thus LHG should show up as a glow above the lunar horizon with both cameras. The 28deg*43deg field-of-view (fov) of the star-tracker camera will give a good panoramic view of the glow, while the UV/Vis camera (fov=4.2deg*5.6deg) will detail the vertical extent with a sensitivity of about 400 meters per pixel. The LIDAR camera (fov=0.3deg*0.4deg) may also be able to measure the LHG with about 10 times the spatial resolution of the UV/Vis camera. The Na and K LHG, with its much greater scale height, is expected to be significantly above the threshold for detection only in the star-tracker camera; thus, it too may be recorded.

References. [1] NRL internal document "Deep Space Program Science Experiment (DSPSE) Mission Requirements Document", SSD-D-DS001, Rev. 20, 5 Mar., 1993. [2] Potter A.E. and Morgan T.H. (1988) Science, 241, 675. [3] Shoemaker E.M. et al. (1968) Surveyor 7 Mission Report, Part 2. Science Results, JPL Tech. Rep. 32-1264, 66. [4] Criswell D.R. (1972) In: Proc. 3rd Lunar Sci. Conf., 2671. [5] Berg O.E. et al. (1976) In: Interplanetary Dust and Zodiacal Light (H. Elsässer and H. Fechtig, eds.) Springer-Verlag, 233. Zook H.A. and McCoy J.E. (1991) GRL, 18, 2117. [7] Hye-Sook Park (1992) personal communication.

RHEOLOGY, TECTONICS AND THE STRUCTURE OF THE VENUS LITHOSPHERE; *M.T. Zuber,* Department of Earth and Planetary Sciences, Johns Hopkins University, Baltimore, MD 21218, and Laboratory for Terrestrial Physics, NASA/Goddard Space Flight Center, Greenbelt, MD 20771.

Given the absence of ground truth information on seismic structure, heat flow, and rock strength, or short wavelength gravity or magnetic data for Venus, information on the thermal, mechanical and compositional nature of the shallow interior must be obtained by indirect methods. Using pre-Magellan data, theoretical models constrained by the depths of impact craters [1] and the length scales of tectonic features [2,3,4] yielded estimates on the thickness of Venus' brittle-elastic lithosphere and the allowable range of crustal thickness and surface thermal gradient. The purpose of this study is to revisit the question of the shallow structure of Venus based on Magellan observations of the surface and recent experiments that address Venus' crustal rheology.

Both models of viscous relaxation of impact crater topographic relief and the wavelengths of tectonic features made identical assumptions about the composition of the Venus crust and mantle. These include: (1) the Venus mantle is similar in composition to Earth's mantle and therefore the primary constituent is olivine, and (2) the crust in areas where observed impact and tectonic structures used in previous studies are located is similar to the that determined for the Soviet Venera and Vega landers, and is best described by diabase [*cf.* 6]. Knowledge of both the brittle and ductile deformational behavior of these materials is an essential component of these models. Numerous experiments on terrestrial rocks indicate that the brittle strength of near-surface rocks is essentially independent of rock type, strain rate and grain size [7]; strength is dependent almost solely on pressure (depth) and is described in a simple linear relation by Byerlee's Law. The ductile strength of crustal and mantle materials is significantly more problematical, as ductile strength is sensitive to temperature, strain rate, composition, and modal mineralogy. Because of its importance with regard to flow in Earth's mantle, the ductile rheology of single crystal olivine is relatively well-understood [8,9,10], albeit for strain rates 10 or so orders of magnitude greater than characterize the mantle. For Venus, experiments on olivine performed at exceptionally dry conditions are applicable. In contrast, the rheologies of multiphase mineral assemblages such as diabase are not at all well characterized, due in part to the sensitivity of derived flow laws to grain size and mineralogy [11]. Previous studies of the structure of the Venus lithosphere utilized both of the flow laws for diabase that were available at that time [12,13,14], as well as one for websterite [15], although none of these experiments were performed at dry conditions. The results of models based on both impact craters and tectonic wavelengths indicated a range of Venus crustal thicknesses of ~10-30 km and associated thermal gradients of $<25^{o}K\ km^{-1}$. For the assumed rheologies, the shallow Venus lithosphere consisted of a region of brittle flow in the crust to a depth of 2-4 km, underlain by a weak lower crust and a strong brittle or ductile upper mantle (*cf.* Figure 1a).

Fortunately, new experimental data on the rheology of diabase has recently become available [16]. These experiments were carefully performed on thoroughly dried samples of Columbia and Maryland diabase, with these rocks chosen on the basis of their gross similarity to chemical compositions at the Venera and Vega lander sites [6]. The results of these experiments indicate that the rheology of the Venus crust may be much stiffer than previously assumed, with a brittle-ductile transition at a depth of 6-8 km rather than 2-4 km. If this is the case, then the depth averaged strength of the crust may be much more similar to that of the mantle than previously thought. For the new diabase data, depending on the rheology of olivine used, the "strong-weak-strong" rheology illustrated in Figure 1a is much less distinct than indicated by previous experiments (Figure 1b).

A stiffer Venus crust is intuitively appealing given the large values of elastic thickness indicated by Magellan topographic profiles suggestive of lithospheric flexure in association with coronae and other surface loads [17]. However, significant evidence for a ductile lower crust (or other weak subsurface rheological layer) is also present in Magellan images of the surface. Numerous occurrences of tectonic features with multiple tectonic wavelengths are observed -- short wavelength features with spacings of km to tens of km occur pervasively over the planet [18,19,20]. The length scales of these features have previously been interpreted to have been controlled by the depth of the brittle-ductile transition in the crust [3]. Features that display much longer length scales include, for example, the width of the Beta Regio Rift and the width and spacings of ridge belts, which may be controlled by the depth and thickness of a strong upper mantle (or other strong subsurface rheological layer) [3]. The existence of multiple wavelengths of tectonic deformation and their relationship to various rheological wavelengths is well documented on Earth [*e.g.* 21,22]. In addition, the width of terrestrial continental rift zones [30-60 km; 23]

are controlled by the depth of the brittle-ductile transition in the crust [24]. In contrast, the width of Beta Regio is much greater than that of terrestrial rift zones and must be controlled by either a much thicker or deeper layer. The short wavelength faulting on the floor of the rift [19], is may be evidence for a "strong-weak-strong" vertical rheology. Long wavelength deformation on Venus has alternatively been attributed to be a consequence of small-scale convection [25,26,27]. However, while this mechanism can explain the regular development of structures in some ridge belt regions, it cannot explain the width of the Beta Regio Rift.

Further insight into the nature of the structure of the Venus lithosphere will require careful re-evaluation of observations, theoretical models, and experimental data. First, tectonic wavelengths and impact crater depths should be re-measured using Magellan data. Refined observational constraints should be evaluated in models based on the most recent experimental data. Improvements in treatment of the vertical distribution of lithospheric strength in the theoretical models [28] should also be implemented. In addition, for tectonic features, the relationship between tectonic length scales and strong layer thickness should be evaluated for fracture as well as continuum deformation scenarios [29]. Finally, experiments relevant to the ductile strength of the Venus lithosphere should be performed for a broader range of modal mineralogy and grain size, as well as for larger strains. For example, the experiments in [16] were run out to only 1-2% strain. If higher strains characterize relevant tectonic features, such as some Venus mountain belts [8-20%; V. Hansen, pers. comm.], then significant strain softening of the crust is possible [*e.g.* 30]. In addition, the diabase flow laws are highly sensitive to grain size and the feldspar content of the deformed samples [31]; different values could produce significantly different strengths. Consideration of all of these factors will be required to derive a clearer picture of the thermo-mechanical structure of Venus.

References: [1] Grimm, R.E., and S.C. Solomon (1988) *J. Geophys. Res., 93,* 11,911-11,929. [2] Solomon, S.C., and J.W. Head (1984) *J. Geophys. Res., 89,* 6885-6897. [3] Zuber, M.T. (1987) *J. Geophys. Res., 92,* E541-E551, 1987. [4] Banerdt, W.B., and M.P. Golombek (1988) *J. Geophys. Res., 93,* 4759-4772. [5] Zuber, M.T., and E.M. Parmentier (1990) *Icarus, 85,* 290-308, 1990. [6] Surkov, Yu.A., et al. (1987) J. Geophys. Res., 92, E537-E540. [7] Byerlee, J. (1968) *J. Geophys. Res., 73,* 4741-4750. [8] Goetze, C. (1978) *Phil. Trans. R. Soc. Lond. A, 288,* 99-119. [9] Karato, S.-I., et al. (1986) *J. Geophys. Res., 91,* 8151-8176. [10] Kirby, S.H. and A.K. Kronenberg (1987) *Rev. Geophys., 25,* 1219-1244. [11] Kohlstedt, D.L. (1992) in *Workshop on Mountain Belts on Venus and Earth,* 24, Lunar Planet Inst., Houston, 1992. [12] Shelton, G. (1991) *Ph.D. thesis,* Brown University, 146 pp. [13] Shelton, G., and J. Tullis (1981) *EOS Trans. Am. Geophys. Un., 62,* 396. [14] Caristan, Y. (1982) *J. Geophys. Res., 87,* 6781-6790. [15] Ave'Lallement, H.G. (1978) *Tectonophys., 48,* 1-28. [16] Mackwell, S.J., and D.L. Kohlstedt (1993) *EOS Trans. Am. Geophys. Un., 74,* 378. [17] Johnson, C.L., and D.T. Sandwell, D.T. (1992) *Lunar Planet Sci. Conf. XXIV,* 721-722. [18] Solomon, S.C., et al. (1991) *Science, 252,* 297-312, 1991. [19] Solomon, S.C., et al. (1992) *J. Geophys. Res., 97,* 13,199-13,256. [20] Squyres, S.W., et al. (1992) *J. Geophys. Res., 97,* 13,579-13,599. [21] Zuber, M.T., et al. (1986) *J. Geophys. Res., 91,* 4826-4838. [22] Ricard, Y. and C. Froidevaux (1986) *J. Geophys. Res., 91,* 8314-8324. [23] Ramberg, I.B., and P. Morgan (1984) *Proc. 27th Int. Geol. Congress, 7,* pp. 165-216. [24] Zuber, M.T., and E.M. Parmentier (1986) *Earth Planet. Sci. Lett., 77,* 373-383. [25] Kaula, W.M. (1990) *Science, 247,* 1191-1196. [26] Simons, M., et al. (1991) *Lunar Planet. Sci. Conf. XXI,* 1263-1264. [27] Simons, M., et al. (1992) in *Workshop on Mountain Belts on Venus and Earth,* 32-34, Lunar Planet. Inst., Houston. [28] Zuber, M.T., and E.M. Parmentier (1994) submitted to *Geophys. J. Int.* [29] Neumann, G.A., and M.T. Zuber (1994) *Lunar Planet. Sci. Conf.,* this issue. [30] Tullis, J. (1989) in *Deformation Processes in Minerals, Ceramics and Rocks,* ed. D.J. Barber and P.G. Meredith, Unwin Hyman, London, pp. 190-226. [31] Tullis, T.E., et al. (1991) *J. Geophys. Res., 96,* 8081-8096.

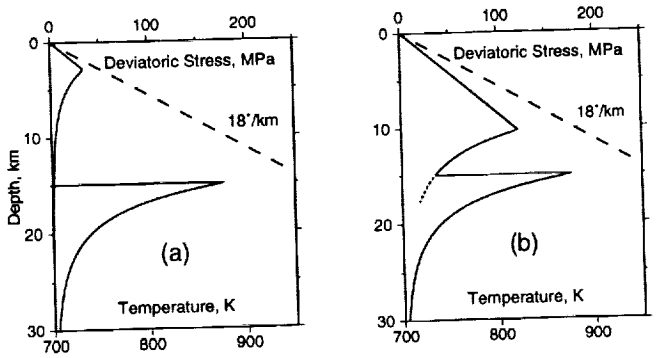

Figure 1. Strength of Venus lithosphere in extension. Ductile strength of crust based on [13] for (*a*) and [16] for (*b*). Both profiles assume ductile strength of olivine from [9], a15-km thick crust, a strain rate of 10^{-14} s^{-1}, and dT/dz=18°K km^{-1}.

FORMATION OF FOLD AND THRUST BELTS ON VENUS DUE TO HORIZONTAL SHORTENING OF A LATERALLY HETEROGENEOUS LITHOSPHERE; *M.T. Zuber*[1,2], *E.M. Parmentier*[3], and *G.A. Neumann*[1], [1]Department of Earth and Planetary Sciences, Johns Hopkins University, Baltimore, MD 21218, [2]Laboratory for Terrestrial Physics, NASA/Goddard Space Flight Center, Greenbelt, MD 20771, [3]Department of Geological Sciences, Brown University, Providence, RI 02912.

An outstanding question relevant to understanding the tectonics of Venus is the mechanism of formation of fold and thrust belts, such as the mountain belts that surround Lakshmi Planum in western Ishtar Terra (*cf.* Figure 1). These structures are typically long (hundreds of km) and narrow (many tens of km), and are often located at the margins of relatively high (km-scale) topographic rises [1-5]. Previous studies have attempted to explain fold and thrust belts in various areas of Venus in the context of viscous [6] and brittle [7,8] wedge theory. However, while wedge theory can explain the change in elevation from the rise to the adjacent lowland, it fails to account for a fundamental aspect of the deformation, *i.e.*, the topographic high at the edge of the rise. In this study we quantitatively explore the hypothesis that fold and thrust belt morphology on Venus can alternatively be explained by horizontal shortening of a lithosphere that is laterally heterogeneous, due either to a change in thickness of the lithosphere or the crust. Lateral heterogeneities in lithosphere structure may arise in response to thermal thinning or extensive faulting, while variations in crustal thickness may arise due to either spatially variable melting of mantle material or by horizontal shortening of the crust. In a variable thickness lithosphere or crust that is horizontally shortened, deformation will tend to localize in the vicinity of thickness heterogeneity, resulting in a higher component of dynamic topography there as compared to elsewhere in the shortening lithosphere. This mechanism may thus provide a simple explanation for the topographic high at the edge of the rise.

To investigate the pattern of deformation, we invoke a finite element approach. We have developed a finite element program that calculates incompressible Newtonian viscous fluid flow using the penalty method [9], and modified it to treat non-Newtonian flow problems [10-12]. We incorporated the strain rate dependence of viscosity by implementing a simple incremental procedure [13] to re-calculate the viscosity $\mu(z,t)$ at each time step. The viscosity takes the form

$$\mu=\mu_0[1/\dot{\varepsilon}_2]^{(1-1/n)}$$

where $\mu_0(z,t=0)$ is the reference viscosity (viscosity at the first time step), z is depth, t is time, $\dot{\varepsilon}_2$ is the second invariant of strain rate tensor, and n is the power law exponent of stress in the stress-strain rate relationship. To simulate the rheology of the lithosphere in the ductile creep regime we used a power law exponent of ~3, while in the brittle regime we invoked the assumption of perfect plasticity in which $n\to\infty$ to approximate a material that deforms by pervasive faulting. In the model the viscosity was constrained to have an upper bound defined by the brittle or ductile strength [14].

We assume that a uniform viscosity layer of thickness h_1 initially contains a thickness perturbation of amplitude Δh and half-width ΔL. We also assume a vertical thermal profile in which the lithosphere cools as a simple half space. For both models we incorporated a strength envelope distribution of lithosphere viscosity, to take into account variation of strength with depth indicated by rock mechanics experiments [*cf.* 15]. For both models, the initial topography of the medium is isostatically compensated and is assumed to shorten at a constant horizontal velocity u. The effect of buoyancy forces in resisting topographic amplification associated with shortening is included via a dimensionless parameter $S=\rho g L^2/\mu_0 u$, where L is the horizontal length scale. Both Cartesian and axisymmetric geometries were explored, where the latter is relevant to the formation of fringing mountain belts at the periphery of the Lakshmi Planum plateau.

Figure 2 shows model profiles for the variable thickness lithosphere model assuming a Cartesian geometry for strains of 0, 0.03 and 0.05. Here it was assumed that the lithosphere was thinned by a factor of 2. The predicted topography is consistent with the general pattern observed across many fold and thrust belts on Venus, such as in the Akna Montes region (Figure 1), both in terms of the change in elevation between the topographic rise and lowland, and the elevation and width of topographic high at the edge of the rise. In this model 80% of the topography associated with the topographic rise is supported by stresses in the lithosphere.

Mountain belt-fringed plateaus with similar patterns of long wavelength topography are also found

on Earth. Prominent examples include the Himalayas at the southern edge of the Tibetan plateau, and the Andes at the western margin of the Altiplano. Mechanisms for the formation of these terrestrial counterparts include lithosphere shortening related to subduction [16], marginal plateau erosion and isostatic uplift [17], and lithospheric shortening not necessarily associated with subduction [18]. Of these mechanisms, subduction may not occur on Venus and mechanical erosion certainly is not important there. It is thus appropriate to question whether similar topographic patterns can be produced by entirely different mechanisms or whether the absence of the first two mechanisms on Venus might point to horizontal shortening of a laterally heterogeneous lithosphere as a mechanism for the formation of fold and thrust belts on both planets.

References: [1] Campbell, D.A. (1983) *Science, 221,* 664-667. [2] Crumpler, L.S., et al. (1986) *Geology, 14,* 1031-1034. [3] Head, J.W. (1990) *Geology, 18,* 99-102. [4] Solomon, S.C., et al. (1991) *Science, 252,* 297-312. [5] Solomon, S.C., et al. (1992) *J. Geophys. Res., 97,* 13,199-13,256. [6] Vorder Bruegge, R.W., and R.C. Fletcher, (1991) *LPSC, XIX.* [7] Suppe, J., and C. Conners (1992) *J. Geophys. Res.* [8] Williams, C.A., et al. (1993) submitted to *J. Geophys. Res.* [9] Bathe, K.-J. (1982) *Finite Element Procedures in Engineering Analysis,* 735 pp., Prentice-Hall, Inc., Englewood Cliffs. [10] Zuber, M.T. and E.M. Parmentier (1992a) *Workshop on Mountain Belts on Venus and Earth,* 49-50, Lunar Planet. Inst., Houston, 49-51. [11] Zuber, M.T. and E.M. Parmentier (1992b) *Lunar Planet. Sci. Conf. XXIII,* 1595-1596, Lunar Planet. Inst., Houston. [12] Zuber, M.T. and E.M. Parmentier (1993) *EOS Trans. Am Geophys. Un., 74,* 546. [13] Desai, C.S., and J.F. Abel (1972) *Introduction to the Finite Element Method,* 477 pp., Van Nostrand Reinhold Co., New York. [14] Chen, Y., and J.W. Morgan (1990) *J. Geophys. Res., 95,* 17,583-17,604. [15] Zuber, M.T. (1987) *J. Geophys. Res., 92,* E541-E551. [16] Wdowinski, and R.J. O'Connell (1991) *J. Geophys. Res., 96* , 12,245-12,255. [17] Masek, J., et al. (1993) submitted to *J. Geophys. Res.* [18] Karner, G.D., and A.B. Watts (1983) *J. Geophys. Res., 88,* 10,449-10,377.

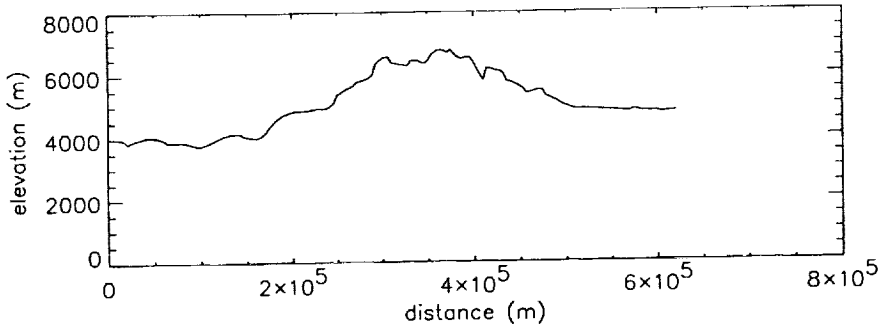

Figure 1. Magellan topographic profile of fold and thrust belt in the Akna Montes region of Venus (long=317^{o}, lon=71^{o}). In this area there is a 1 km elevation difference between the lowland on the left and the topographic rise on the far right. Over 2 km of topography is associated with the high at the edge of the rise.

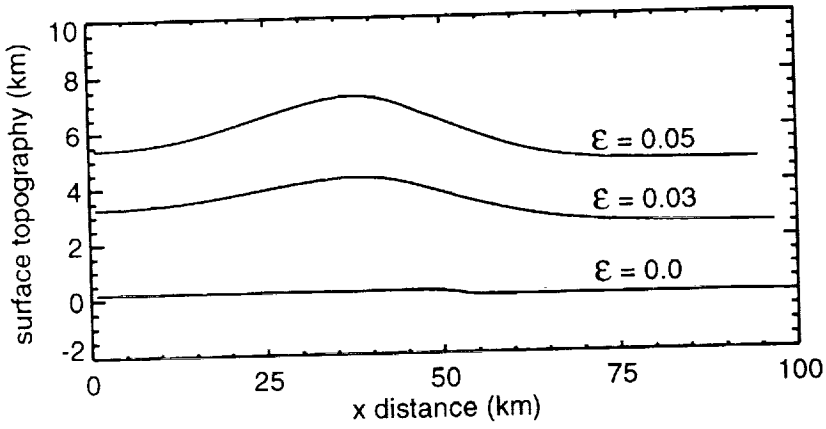

Figure 2. Topographic profiles for variable thickness lithosphere model for strains of 0, 0.03, and 0.05.

AUTHOR INDEX*

Abell P. 1505
Adams J. B. 779, 1181
Aeschliman R. 871
Agerkvist D. P. 1, 819
Agresti D. G. 1261
Aguirre-Puente J. 3
Ahrens T. J. 5, 243, 359, 1023, 1369
Akimov L. A. 1331
Alexander C. 7, 9, 11, 401, 449, 1005
Alexander W. M. 1381
Alexeev V. A. 13, 15, 17, 19
Alexopoulos J. S. 1079
Allen C. C. 21, 23, 937, 1415
Allen J. 795
Allton J. H. 25, 1155
Amari S. 27, 103, 563
Andersen D. W. 119
Anderson F. S. 29
Anderson R. C. 1133
Anderson R. R. 31, 719
Anderson S. W. 33, 1091
Annexstad J. O. 891
Antenenko I. 963
Antoine L. A. G. 847
Antonenko I. 35
Arai T. 1373
Arden J. W. 373, 449, 1435
Ariskin A. A. 37, 1071, 1073
Arndt P. 139
Arnold J. R. 1003
Arriola S. T. 927
Artem'ev V. I. 41
Artem'eva N. A. 39
Arvidson R. E. 157, 481, 605, 815, 1263, 1287
Ash R. D. 279
Asphaug E. 43, 101
Aubele J. C. 45, 47, 305

Bacon R. 837
Badjukov D. D. 601
Bailey S. H. 353
Baines K. H. 1095
Bajt S. 167, 323, 381, 713, 1361
Baker V. R. 627, 629, 631, 727
Baloga S. M. 189
Balogh A. 49
Banerdt W. B. 51, 155
Banin A. 53
Banks M. 55
Bansal B. M. 1015, 1017
Barentine J. C. 57
Barker B. M. 163
Barlow N. 59, 225, 227
Barnouin O. S. 61, 1213
Barrett J. M. 239
Barrett R. A. 1565
Bashkirov A. 1443
Basilevsky A. T. 63, 65, 67
Bass D. S. 69
Basu A. 71
Batchelor J. D. 97
Batson R. M. 871
Baur H. 959
Beard B. L. 73
Beck E. A. 353
Beck P. 75
Becker R. 77, 815
Becker T. 395, 871
Beckett J. R. 79, 755
Begemann F. 849, 1273
Bell J. F. 81, 83, 85, 87, 89, 265, 939, 1161, 1165
Belton M. 237, 453, 469, 787, 1395
Bender K. 91, 463, 1243
Benedix G. K. 865
Benner L. A. M. 93
Bennett M. E. 95
Benoit P. H. 97, 99, 247, 573, 1367, 1545, 1547
Benz W. 43, 101
Ber T. 479
Berg O. 1011
Bernatowicz T. J. 103, 105, 313, 1033
Bernhard R. P. 107, 125, 567, 1233
Bertka C. M. 109
Betts B. 111, 975
Bilotti F. 1105
Bindschadler D. L. 113
Binzel R. P. 1083
Bischoff A. 115, 349, 1475
Bish D. L. 121
Bishop J. L. 117, 119
Blake D. F. 121, 621
Blake G. A. 755
Blake P. 1421
Blanchard D. P. 71
Blaney D. L. 123, 1433
Blanford G. E. 125, 1393
Blewett D. T. 127, 515
Blum J. D. 719
Blumberg D. G. 129, 341
Bobe K.-D. 901
Bobias S. G. 611
Bobina N. N. 131, 1001
Bockstein I. M. 133
Boer R. H. 719
Boerner D. 1517
Boesenberg J. S. 135
Bogard D. D. 137, 403
Bohsung J. 139
Borisov A. 141
Bornhoeft K. 83
Borunov S. 143

*Page numbers refer to the first page of an abstract on which an author appears.

Boslough M. B. 145, 295, 309
Boss A. P. 147, 149, 151
Bottke W. F. Jr. 153
Bourot-Denise M. 543
Bowman D. D. 155
Bowyer S. 749
Boynton W. V. 353
Brackett R. A. 157, 1263
Bradley J. P. 21, 159, 185, 687
Brandstätter F. 979, 981
Brandt D. 161, 847
Brannon J. C. 1033
Brazzle R. H. 163
Brearley A. J. 165, 167, 641, 1069
Bridges J. C. 11
Bridges N. T. 169
Brilliant D. R. 171, 173
Bringol L. A. 589
Britt D. T. 175, 177, 785, 1135, 1293
Brookshaw L. 1397
Brown C. D. 179
Brown R. H. 1419
Brown S. T. 647
Browning L. 181, 645, 1565
Brownlee D. E. 21, 159, 183, 185, 809
Brückner J. 187, 353
Bruno B. C. 189, 1383
Bruno L. 997
Bullock M. A. 191
Bulmer M. H. 193
Bunch T. E. 565
Burba G. A. 131, 195, 1001
Burba G. G. Jr. 197
Burbine T. H. 199
Burch J. 795
Burke K. 201
Burkett P. J. 801
Burnett D. S. 1075
Burns R. G. 199, 203
Burt J. D. 205
Buseck P. R. 345
Bussey D. B. J. 207
Busso M. 209
Butler B. J. 211, 951

Cabrol N. 213, 483, 769
Caffee M. W. 1003
Calvin W. M. 895
Cameron A. G. W. 215
Campbell B. A. 217, 219, 515
Capobianco C. J. 221
Carcich B. T. 453, 787
Carlson R. 453, 807, 863
Carroll J. 227
Casanova I. 223
Cave J. 225, 227
Chadwick D. J. 229, 231, 443, 705, 1199
Chael E. P. 145
Chakrabarti S. 749
Chakravarty N. 353
Challis D. 233
Chamberlain C. P. 719
Chambers J. G. 235, 547
Chapman C. 237, 469
Chapman M. G. 239
Cheeseman P. 241
Chen G. 243
Chen J. H. 245
Chen P. C. 1501
Chen Y. 99, 247
Chevrel S. D. 249
Chibante L. P. F. 251, 545
Chicarro A. F. 253
Choi B.-G. 255
Christensen P. R. 257, 343, 503, 1485
Christoffersen R. 259
Chryukina O. V. 909
Chu W.-K. 1501
Cielaszyk E. 647
Cintala M. J. 107, 261, 567
Clark B. C. 263
Clark B. E. 175, 265
Clark P. E. 267
Clayton R. N. 269, 579, 581, 865, 1063, 1457, 1459
Clemett S. J. 1391
Clifford S. M. 271
Cloutis E. A. 273
Clow G. D. 275
Cobban W. A. 607
Coleman P. 1249
Collins G. 277
Collison W. P. 423
Connolly H. C. Jr. 279, 543, 1285, 1537
Connors M. 281, 283
Consolmagno G. 285
Cook D. 453
Costard F. 3, 287
Cox T. C. 289
Craddock R. A. 291, 293, 857
Craig A. Y. 1421
Crawford D. A. 295
Croft S. K. 297
Crossey L. J. 299, 861
Crowell K. 795
Crown D. A. 33, 301, 1091
Crozaz G. 571, 1451
Cruikshank D. P. 85, 739, 1419
Crumpler L. S. 303, 305
Cuzzi J. N. 307
Cygan R. T. 309

Dale-Bannister M. A. 311
D'Aria D. M. 1191
Daulton T. L. 313, 345
Davis A. M. 315, 1063, 1457, 1459
Davis D. M. 285
Davis D. R. 365, 1175
Davis P. A. 317, 443, 869
Dawidowicz G. 483
Dawson D. D. 1353
Dawson J. B. 1087, 1089
DeAro J. A. 221
DeHart J. M. 319, 801

De Hon R. A. 321
Delaney J. S. 135, 323, 831, 1361
Delano J. W. 325, 505, 639
Dembosky J. 811
Des Marais D. J. 367
DeTroye J. E. 327
Deutsch A. 477, 497, 839, 1031, 1209
Dikov Yu. P. 329, 413, 415
Dobrovolskis A. R. 307
Dohm J. M. 331, 1225
Dolginov A. Z. 333
Dollfus A. 335
Domingue D. L. 337
Donahue D. J. 647, 649
Dong Q. W. 1389
Doose L. R. 1293
Dorofeeva V. 143
Douglas C. 339
Drake D. M. 899
Drake M. J. 221, 551, 873, 1009
Drossart P. 143
Duzheva E. A. 709
Dymek R. F. 1253

Eberhardt P. 563
Ebihara M. 1035, 1269
Edgett K. S. 341, 343, 895, 1555
Edwards K. 453, 1145
Ehlmann A. J. 865
Eisenhour D. D. 313, 345
El Goresy A. 347, 375, 1557
Ellison M. 417, 1187
Emerson S. 55
Encrenaz Th. 143
Endress M. 349
Engel S. 511
Engelhardt W. v. 351
Englert P. A. J. 119, 353
Engrand C. 355
Epstein S. 1471
Erard S. 357
Eugster O. 997, 1479
Evans L. G. 267
Evans N. J. 359
Evergreen High School Research Class 417, 1187
Evlanov E. 709, 819

Fabian U. 187
Fagents S. A. 361
Fahey A. 363, 583, 585
Fanale F. P. 265, 453, 455
Farinella P. 365, 495, 841
Farmer J. 213, 367, 769
Faurschou Hviid S. 819
Fegley B. Jr. 157, 201, 707, 773, 1263
Feldman V. 369
Fevig R. 1507
Fink J. H. 473
Finkel R. C. 1003
Fischer E. M. 371
Fisenko A. V. 373, 775
Fleming R. H. 1421
Flores B. 655
Floss C. 375
Flynn B. 377
Flynn G. J. 379, 381, 713, 1391
Fogel R. A. 383
Foh J. 709
Ford P. G. 67, 1279
Forsyth D. W. 1407
Foster P. N. 151
Fowler G. W. 385, 1043, 1045
Franchi I. A. 171, 173
Franklin B. J. 443
Frawley J. J. 407
Freedman R. 85, 87
Frei R. 997
Frey H. 387, 389, 1345
Fricke S. K. 791, 1291
Friedman R. C. 391
Froeschl H. 119
Fry P. 1195

Gaddis L. 393, 395, 577
Gaetani G. A. 397
Gaffey M. J. 273, 399, 689, 1117
Galileo Imaging Science Team 237, 1395
Galileo NIMS Science Team 575, 807, 863, 1019, 1235
Galileo SSI Team 787
Gallino R. 209, 583
Ganasan J. 555
Gao X. 401, 1005
Garbeil H. 1141
Garrison D. H. 137, 403
Garvin J. B. 405, 407, 409
Geballe T. R. 85
Geiger T. 115
Geissler P. 411
Gektin Yu. M. 133
Gerasimov M. V. 329, 413, 415
Gerlach K. 417
Ghail R. C. 419, 421
Ghiorso M. S. 1183
Gibson E. K. 1155
Gibson R. L. 423
Giese R. F. 1445
Gillis J. 1179
Gilmore M. 425, 529
Gilmour I. 1247
Gladstone G. R. 749
Glass B. P. 427, 1101
Glaze L. S. 429
Gliem F. 1293
Glukhovsky M. Z. 431
Goguen J. D. 433
Golden D. C. 435, 437
Goldsby D. L. 439
Goldstein J. I. 1529
Golombek M. P. 441, 443, 1377
Gooding J. L. 25, 1021
Gorsline D. S. 1053
Gostin V. A. 445, 447
Goswami J. N. 1185, 1325

Grady M. M. 339, 449, 451
Graf Th. 1093
Granahan J. C. 453, 455
Granovsky L. B. 909, 1559, 1561
Grant J. A. 457, 459
Grard R. 49, 461
Greeley R. 91, 129, 213, 233, 237, 463, 465, 467, 469, 769, 787, 1047, 1243, 1493, 1521
Greenberg R. 153, 411
Greenwood J. P. 471
Gregg T. K. P. 473
Grier J. A. 475
Grieve R. A. F. 477, 479, 1085, 1347
Griffith L. L. 481
Grimm R. E. 29, 51, 179
Grin E. A. 483
Grinspoon D. H. 191
Grosfils E. B. 485, 487, 489
Grossman J. N. 929
Grossman L. 223, 315, 1275, 1533
Grove T. L. 397
Guest J. 193, 207, 225, 227, 463, 465, 767
Gulick V. C. 491
Gunnlaugsson H. P. 819
Guofei F. 493
Guseva E. 369
Guyot F. 839

Haack H. 495
Haberle R. M. 517
Hackbarth K. 497
Hackwell J. 123
Hager B. H. 1277
Haggerty P. 525
Hahn J. M. 1461
Haines E. L. 499, 899
Halliday A. N. 1299, 1305, 1307, 1309
Hamilton V. E. 501, 503
Hanner M. S. 123
Hansen O. S. 889
Hansen V. L. 681
Hanson B. 325, 505, 639
Hapke B. 507
Harper C. L. Jr. 509, 613
Harris R. S. 465
Hartmann W. K. 511
Harvey R. P. 513
Haskin L. A. 635, 637, 729, 943, 1149, 1151
Hawke B. R. 81, 127, 219, 515, 1077, 1145
Hayashi J. N. 517
Hays J. E. 519
Hayward T. 925
Head J. W. 35, 65, 205, 237, 249, 305, 425, 469, 485, 487, 489, 521, 523, 525, 527, 529, 675, 677, 679, 821, 823, 963, 1051, 1317, 1329,
Head J. W. (cont.) 1359, 1495, 1531
Hechler M. 49
Held P. 709
Helfenstein P. 453
Helgerud M. B. 531
Henderson B. G. 533
Herkenhoff K. E. 69, 535
Herrick R. 537, 1399
Herzog G. F. 539, 1523
Hess P. C. 471, 541
Hewins R. H. 279, 543, 825, 1535, 1537
Heymann D. 251, 545
Hide R. 243
Higgins J. 173
Higgins S. J. 235, 547
Hildebrand A. R. 549
Hillgren V. J. 221, 551
Hiroi T. 553, 941, 1375, 1567
Hofmann B. 997
Hogan R. C. 307
Hohenberg C. M. 105, 163, 683
Holden T. C. 555
Holmberg B. 557
Holsapple K. A. 559
Honda M. 1269
Hood L. L. 561
Hoppe P. 563, 763
Horan M. F. 929
Horn L. J. 985
Hornemann U. 839
Hornshøj P. 889
Hörz F. 107, 183, 565, 567, 809, 1021
Houck J. 925
Housen K. 569, 1207
Howell E. S. 785, 1135
Howington-Kraus A. 869
Howington-Kraus E. A. 1519
Hrubsch L. 183
Hsu W. 571
Huang H.-P. 1515
Huang S. 573, 1547
Hui J. 575
Hultgrien L. K. 577
Humayun M. 579, 581
Hunten D. M. 337
Huss G. R. 583, 585, 587
Hutcheon I. D. 587
Hutchinson R. 11
Hyde T. W. 589, 591

Iancu O. G. 917
Ip W. H. 1173
Ipatov S. I. 593
Israel E. J. 927
Ivanov A. V. 269, 595, 1565
Ivanov B. A. 41, 67, 597, 599, 991, 1095
Ivanova O. 353
Ivliev A. I. 601, 603
Iwase Y. 1193
Izenberg N. R. 605, 1079

Izett G. A. 607

Jackson A. A. 609
Jackson T. 611
Jacobsen S. B. 509, 613
Jakosky B. M. 517, 533, 615
James O. B. 617
Janes D. M. 619
Jansa L. F. 1085
Jenniskens P. 621
Jerde E. A. 1299, 1301, 1311
Jessberger E. K. 139, 1341
Jha K. 623
Johnson C. L. 625
Johnson G. P. 933
Johnson G. V. 1433
Johnson J. 417, 627, 629, 631, 1187
Jolliff B. L. 633, 635, 637, 729, 1149, 1151
Jones J. H. 615, 639, 651, 653, 879, 1009, 1513
Jones R. H. 641
Jons H.-P. 643
Joseph L. H. 645
Joswiak D. J. 185
Jull A. J. T. 647, 649
Jurewicz A. J. G. 639, 651, 879
Jurewicz S. R. 653
Jurgens R. 655

Kadel S. D. 465
Kadik A. A. 657, 659
Kalinina G. V. 671
Kallemeyn G. 661, 663, 1465
Kamp L. W. 453
Kanefsky B. 241
Kankeleit E. 709, 819
Kano N. 665, 1363
Kargel J. S. 555, 667, 799
Karner J. 1301
Kashkarov L. L. 601, 603, 669, 671, 1185
Kauhanen K. 673, 1411
Kawakami S. 1099
Keddie S. 529, 675, 677, 679
Keep M. 681
Kehm K. 683
Keil K. 495, 865, 1497
Keller H. U. 1293
Keller L. P. 21, 159, 259, 381, 685, 687, 1391, 1393
Kelley M. S. 689
Kelley S. P. 1321
Kenealy D. 897
Kent R. M. 691, 693
Kerridge J. F. 695
Keyser L. F. 1343
Khodakovsky I. K. 143
Khromov V. N. 819
Kidder J. G. 697
Kiefer W. S. 699
Kieffer H. H. 575
Kik A. C. 743
Kilburn C. R. J. 805
Kim J. S. 701
Kim Y. 701, 703
King N. L. 809
Kipp M. E. 295
Kirk R. L. 239, 705
Kirkpatrick R. J. 309
Kissel J. 75
Klaasen K. 237, 453
Klein J. 539, 1523
Klingelhöfer G. 707, 709, 819
Klöck W. 381, 711, 713, 1341, 1393
Knudsen J. M. 1, 819, 1293
Kobayashi Y. 1269
Kochemasov G. G. 715
Koeberl C. 119, 427, 549, 581, 717, 719, 721, 761, 847
Koga A. 723
Kohlstedt D. L. 439, 817
Koike O. 723, 725
Komatsu G. 417, 631, 727, 1187
Konno T. 1527
Kono R. 1193
Kononkova N. N. 595, 905
Konopliv A. S. 1281
Korokhin V. V. 1331
Korotaeva N. 1197
Korotev R. L. 637, 729, 1149, 1151, 1223
Korotkova N. N. 669, 671, 1185
Korotkova Yu. Yu. 603
Kosarev I. B. 731
Koshiishi H. 733, 737
Kotelnickov S. 369
Kotsarenko N. Ya. 735
Kouda R. 733, 737
Kozlowski R. W. H. 739
Kracher A. 719
Krähenbühl U. 741
Kraft R. 241
Kralik C. 119
Kramer J. L. A. M. 743
Kramers J. D. 997
Kransel G. 375
Krasnopolsky V. A. 745, 747, 749
Kraus G. F. 1013
Krauss R. 1195
Kreslavsky M. A. 751, 1109
Kring D. A. 177, 475
Kronrod M. A. 133
Krot A. N. 753, 1469
Kubicki J. D. 755
Kucinskas A. B. 757
Kudo A. M. 299
Kukharenko Yu. 1443
Kuramoto K. 759
Kurat G. 761, 763, 979, 981
Kurokawa H. 1099
Kuzmitcheva M. Ju. 765

Lacchia M. 467
LaFave N. 1499

Lal D. 649
Lancaster M. G. 767
Landheim R. 213, 769
Langenauer M. 741
Lauer H. V. 437, 771, 939
Lauretta D. 773
Lavrukhina A. K. 775, 777, 1429
Lawler M. E. 779
Lawson C. L. 499
Lawson S. L. 781
Layne G. D. 1043, 1257
Le L. 883, 907
Leach R. 467
Leago K. S. 1233
Lebofsky L. A. 783, 785, 1117, 1135
Lebofsky N. R. 783
Lee D.-C. 1299
Lee E. M. 871
Lee M. R. 449
Lee P. 469, 787, 925
Lellouch E. 143
Lemoine F. G. 789, 791, 1291
Leonard G. J. 231, 1379
Lerch F. J. 789
Lewis R. S. 27, 103, 313, 563, 793, 1063
Limaye S. S. 1195
Lin C. 1455
Lindley P. M. 1421
Lindstrom D. J. 1221, 1417
Lindström M. 1385
Lindstrom M. M. 795, 797, 1153
Lipschutz M. E. 941, 1183, 1229, 1567
Lockwood J. 417, 799, 1187
Lodders K. 707
Lofgren G. E. 279, 319, 801
Longhi J. 803
Lopes-Gautier R. 805, 807, 1297
Loseva T. V. 987
Love S. G. 185, 809
Lucchitta B. K. 811
Lucey P. G. 83, 127, 533, 1077, 1145
Lugmair G. W. 813
Luhmann J. G. 615
Luksch R. 795
Lunar Working Group of Japan 915
Luo W. 815
Lynch D. 123
Lynch R. A. 933

Ma Z. 1063
MacIsaac C. 813
Mackwell S. J. 817
MacPherson G. J. 269, 595
Madsen J. 819
Madsen M. B. 1, 819
Maehr S. A. 995
Magee K. 529, 821, 823
Magellan Flight Team 1401
Magellan Science Team 1245
Maharaj S. V. 825
Makalkin A. B. 827
Makhloufi N. 3
Malcuit R. J. 829
Mann J. L. 831
Marchenko A. G. 833
Marín L. E. 1221, 1255
Martel L. 835
Marti K. 347, 701, 703, 1093
Martin P. 837
Martin T. Z. 87
Martinez I. 839
Martinez R. R. 1221, 1417
Marzari F. 841
Masarik J. 843, 845, 1003, 1119
Master S. 847
Mathew K. J. 849, 851
Matson D. 1019, 1433
Matsubaya O. 1539
Matsui T. 759
Matsuzaki H. 665, 853, 1363
Matushima K. 733
Maurer M. J. 855
Maurette M. 355, 761, 763
Maxwell T. A. 857
May L. 549
Mayeda T. K. 269, 865, 1457, 1459
Mazarik J. 899
McBride K. M. 261
McCallum I. S. 859
McCarville P. 299, 861
McCloskey F. C. 353
McCord T. 863, 1235
McCoy T. J. 391, 865
McDonald J. S. 749
McDonnell J. A. M. 183, 867
McEwen A. 395, 453, 869, 871
McFarlane E. A. 873
McGee J. J. 875
McGill G. E. 877
McGlaun J. M. 295
McGovern P. J. 1317
McGuire J. C. 879
McHone J. F. 881
McKay C. P. 491
McKay D. S. 21, 23, 71, 125, 235, 259, 547, 685, 687, 1391, 1393
McKay G. 639, 883, 907, 923
McKinnon W. B. 93
McLeod L. C. 163, 885
McSween H. Y. Jr. 95, 181, 1057
Medveduk S. A. 41
Meeker G. P. 887
Meibom A. 889
Melchior R. C. 891
Melosh H. J. 153, 597, 893, 1201, 1203, 1425
Merényi E. 895
Merrell J. A. 897
Meshcherskaya V. A. 197
Messenger S. 1391
Metzger A. E. 499, 899
Metzler K. 901, 1157

Meyer B. S. 903
Middleton R. 539, 1523
Migdisova L. F. 905
Mikouchi T. 907, 923
Miles J. 925
Milkereit B. 1517
Ming D. W. 435, 437
Minnitt R. C. A. 1121
Misawa K. 935
Mitchell J. 1303
Mitreikina O. B. 909, 1559, 1561
Mittlefehldt D. W. 639, 651, 797, 911, 1167
Miura Y. 913, 915, 917, 919, 1269
Miyamoto M. 921, 923, 1371, 1375
Moersch J. 925
Moholy-Nagy H. 549
Mollard J. D. 1127
Moore B. J. 227
Moore H. J. 927, 1483
Moralev V. M. 431
Morgan J. W. 929
Morgan P. 931, 933
Morgan T. H. 1099
Morikawa N. 935
Morioka M. 967
Morris R. 23, 71, 437, 771, 937, 939, 941, 1165, 1205, 1223, 1261
Morrison D. 237
Morse A. D. 173
Moss B. E. 943
Mostefaoui S. 945
Mouginis-Mark P. J. 947, 949, 1147
Muhleman D. O. 211, 951
Munro D. C. 953
Murchie S. 955, 957, 1399
Murer Ch. 959
Murray B. C. 111, 599
Murty S. V. S. 851
Mustard J. 519, 955, 961, 963, 1407

Nagahara H. 723, 965
Nagao K. 919, 1269
Nagasawa H. 725, 967, 1539
Nakamura N. 935
Nakamura T. 969
Namiki N. 971, 973
Nash D. 897, 975
Nava D. F. 977
Nazarov M. A. 905, 979, 981, 1185
Neal C. R. 983, 1033, 1305
Nehru C. E. 1107
Nelson R. 985, 1297, 1389
Nemtchinov I. V. 731, 987, 989
Neuking K. 713
Neukum G. 237, 991
Neumann G. A. 993
Newmann G. A. 1577
Newsom H. E. 995, 1259
Newton J. 1435
Ngo H. H. 1041
Nguyen T. 1261
Nichols R. H. Jr. 105, 683
Nicholson P. 925
Niedermann S. 997
Nier A. O. 185, 999, 1391
Nikishin A. M. 1001
Nishiizumi K. 1003
Nittler L. 1005
Nogami K. 1363
Nolan M. C. 153
Noll P. D. Jr. 995
Noma M. 1363
Nordlie J. 1507
Norman M. D. 495, 1007, 1009
Nusbaum R. L. 1067
Nuth J. A. III 1011, 1013, 1389
Nyffenegger P. 285
Nyquist L. E. 1015, 1017

Oberbeck V. R. 565
O'Brien H. E. 859
O'Bryan M. V. 1467
Ocampo A. 1019, 1095, 1297
Ocker K. D. 1021, 1039
O'Connor D. J. 265
Okada A. 1269
Okada T. 1269
O'Keefe J. D. 5, 1023, 1369
Olsen E. J. 1025
Opanasenko N. V. 1271
Oran W. A. 1027
O'Reilly S. Y. 931
Orenberg J. B. 1163
Ori G. G. 1029
Orton G. S. 5, 1369
Ostermann M. 1031
Otsuki M. 1375
Ott U. 1033
Owen T. C. 1419
Ozaki H. 1035

Paige D. A. 69, 1037
Palma R. L. 1039
Palme H. 141, 375, 901, 981, 1563
Papanastassiou D. A. 1041, 1253
Papike J. J. 385, 1043, 1045, 1111, 1257, 1259
Pappalardo R. 469, 787, 1047
Parfitt E. A. 1049, 1051
Parker T. J. 1053, 1055, 1205
Parmentier E. M. 205, 541, 623, 1577
Patchen A. 235, 547, 1313
Patel G. B. 789
Paterson B. A. 1057
Pechernikova G. 1441, 1443
Pedroni A. 1059, 1061
Pellin M. J. 1063
Pepin R. O. 77, 1065
Permenter J. L. 1067
Perreau M. 355
Perron C. 945
Petaev M. I. 37, 1069, 1071, 1073
Peters M. T. 1075

Peterson C. A. 1077
Petit J.-M. 411
Pettengill G. H. 1279
Phillips R. J. 697, 885, 1079
Phinney W. C. 1081
Pieters C. M. 117, 119, 371, 1083, 1329, 1333, 1359, 1407
Pilkington M. 1085
Pillinger C. T. 171, 173, 339, 373, 449, 451, 1247, 1435, 1515
Pinet P. C. 249, 837, 1159, 1181
Pingitore N. E. Jr. 1513
Pinkerton H. 691, 693, 1087, 1089
Plaut J. J. 33, 301, 781, 1091, 1483
Plescia J. B. 1323
Podosek F. A. 1033
Polk K. 455
Pollack J. 467
Pollack J. B. 85, 191, 747, 1521
Ponganis K. V. 1093
Pope K. O. 1095
Popov S. P. 989
Popova O. P. 765
Porcelli D. 1097
Potter A. E. 1099, 1573
Povenmire H. 427, 1101
Powell R. A. 721
Pratt S. F. 371
Premo W. R. 1103
Presper T. 711
Price M. 1105
Prilutski O. 819
Prilutski O. F. 709
Prinz M. 1107, 1481
Pronin A. A. 1109
Pun A. 1111
Pybus G. Q. J. 1113
Pyle D. M. 1087, 1089

Quinn R. 1543

Racca G. D. 253
Radocinski R. G. 499
Raitala J. 1115
Raiteri C. M. 209
Rammensee W. 375
Rao M. N. 403, 1039
Rappaport N. J. 51
Rasmussen K. L. 889
Reed K. L. 1117
Reedy R. C. 843, 845, 899, 1003, 1119
Reid A. M. 1513
Reidy A. M. 389
Reimold W. U. 161, 423, 717, 719, 721, 847, 1113, 1121
Reyes-Ruiz M. 1123
Reynolds S. J. 1047
Rice J. W. Jr. 91, 1125, 1127
Richter W. M. 591
Riciputi L. R. 1057, 1311
Rietmeijer F. J. M. 493, 1129, 1131
Riley K. M. 1133
Rivkin A. S. 785, 1135
Roark J. H. 387, 389
Robertson B. 1517
Robertson D. 847
Robinett L. 655
Robinson C. A. 1137, 1139
Robinson M. S. 453, 1141, 1143, 1145, 1147, 1473
Robinson R. 71
Rockow K. M. 637, 729, 1149, 1151
Rode O. D. 1153, 1333
Roedder E. 513
Romanek C. S. 1155
Romstedt J. 1157
Rong W. 1455
Rosenblatt P. 1159
Rossman G. R. 1343
Roush T. L. 87, 1161, 1163, 1165
Rousset A. 837
Rowan L. R. 1167
Rowland S. K. 1147
Rowlands D. D. 791
Rubie D. C. 551, 873
Rubin A. E. 1169
Rud N. 889
Ruff S. W. 1171
Rulle H. 1341
Russell R. 123
Rutherford M. J. 557
Ruzmaikina T. V. 1173
Ryan E. V. 1175
Rybakov V. A. 41
Ryder G. 289, 1177, 1179, 1255, 1399

Sabol D. E. Jr. 1181
Sack R. O. 1183
Safford M. 417
Sahijpal S. 1185
Sahuaro High School Astronomical Research Class 417, 1187
Saiki K. 1373
Sakimoto S. E. H. 1189
Sakurai H. 1363
Salisbury J. W. 1191, 1453
Sammis C. G. 155
Sandwell D. T. 625
Santek D. 1195
Sasaki S. 1193
Saunders R. S. 1055, 1195, 1245
Sazonova L. 369, 1197
Schaber G. 55, 229, 1199, 1353
Schaller C. J. 1201
Schärer U. 839, 1031
Schenk P. 277, 1203, 1205
Scherber D. S. 817
Schlichting F. 709
Schlutter D. J. 185, 999, 1391
Schmidt R. M. 1207
Schmidt S. 343
Schmitt R. T. 1209
Schultz P. H. 47, 61, 457, 459, 1211,

Schultz P. H. (cont.) 1213, 1215, 1355
Schultz R. A. 1217, 1219
Schulz C. K. 125
Schuraytz B. C. 1221, 1255, 1399
Schwarz C. 1223
Scoon G. 49
Scott D. H. 1225
Scott E. R. D. 495, 865, 1227
Sears D. W. G. 97, 99, 247, 573, 1229, 1367, 1545, 1547
Sears W. D. 1231
See T. H. 107, 567, 1233
Segura M. 1235
Sekine T. 969
Self S. 1383
Semenenko V. P. 1237, 1239
Semjenova L. F. 373
Senftle F. 549
Senske D. 463, 531, 1241, 1243, 1245
Sephton M. A. 1247
Sevier J. 1249
Shaffer E. 1075
Shapkin A. I. 1251
Sharma M. 1253
Sharma P. 1003
Sharpton V. L. 201, 537, 1221, 1255
Shearer C. K. 385, 1043, 1045, 1257, 1259
Shelfer T. D. 1261
Shepard M. K. 1263
Shervais J. W. 1265
Shevchenko V. V. 1267
Shih C.-Y. 1015, 1017
Shilobreeva S. N. 659
Shima M. 1269
Shkuratov Yu. G. 1271, 1333
Shukolyukov A. 813, 1273
Shuvalov V. V. 39
Sidorov Yu. I. 1251
Signer P. 959
Simmons E. C. 1303
Simon S. B. 315, 1275
Simonelli D. 453
Simons M. 1277, 1317
Simpson R. A. 855, 1279, 1503
Sims K. W. W. 995
Singer R. B. 895, 1293
Sjogren W. L. 51, 1281
Skinner W. R. 1283, 1285
Slade M. 211, 655, 951
Slavney S. 1287
Smalley R. E. 545
Smith C. B. 161, 1113
Smith D. E. 789, 791, 1289, 1291
Smith M. 925, 1181
Smith P. E. 549
Smith P. H. 1293
Smoliar M. I. 929
Smrekar S. E. 1295
Smythe W. 807, 985, 1297
Snyder G. A. 73, 1299, 1301, 1303, 1305, 1307, 1309, 1311, 1313
Snyder K. D. 739
Socki R. A. 1155
Soderblom L. A. 453, 807, 871, 1293
Solomatov V. S. 1315
Solomon S. C. 971, 973, 1277, 1317
Sonett C. P. 561
Sørensen S. A. 207
Sorkhabi R. B. 881
Souzis A. E. 539
Speidel D. H. 1319
Spettel B. 141, 901, 981, 1061
Spilde M. N. 1043
Sprague A. L. 337, 739
Spray J. G. 1321
Spudis P. D. 127, 1077, 1255, 1323
Squyres S. 619, 925
Srinivasan G. 1325
Sromovsky L. A. 1195
Stadermann F. J. 1327
Staid M. I. 1329
Starkey G. 1397
Starodubtseva O. M. 1331
Starukhina L. V. 1333
Steele I. M. 1025, 1335, 1337, 1339
Stein T. 1287
Stephan T. 1341
Stephens S. K. 1343
Stephenson S. 1381
Stepinski T. F. 1123
Stern S. A. 377
Stevenson D. J. 1315, 1343
Stewart A. D. 1323
Stocco K. 795
Stockman S. 389, 1345
Stofan E. R. 33, 301, 501, 503, 1091, 1245
Stöffler D. 497, 901, 1209, 1347
Stolper E. M. 79, 755, 1471
Stooke P. J. 1349
Strait M. M. 1351
Strange R. 1101
Strebel R. 563
Strobert D. 655
Strom R. G. 55, 1199, 1353
Stutz J. 241
Sugita S. 1215, 1355
Sugiura N. 919, 1357
Sullivan R. 469, 787
Sunshine J. 553, 961, 1235, 1359
Suppe J. 1105
Sutton S. R. 167, 323, 381, 713, 1361, 1391
Suzuki Y. 1363
Svetsov V. V. 1365
Svitek T. 111
Swaby B. 795
Swan P. 401
Swann J. D. 871
Swindle T. D. 475
Symes S. J. 97, 1367

Takano A. 733
Takata T. 5, 1023, 1369
Takeda H. 921, 969, 1371, 1373, 1375, 1525
Talent D. 1099
Tanaka K. L. 231, 317, 331, 443, 1377, 1379
Tanner W. G. Jr. 1381
Tatsumara M. J. 189
Tatsumoto M. 1103, 1409
Taylor G. J. 189, 391, 835, 1077, 1383
Taylor L. A. 73, 235, 547, 983, 1299, 1301, 1303, 1305, 1307, 1309, 1311, 1313
Tejfel V. G. 1331
Tertichnaya B. V. 1237, 1239
Teterev A. V. 989
Teucher R. 709
Thalmann Ch. 997
Therriault A. M. 1385
Thiemens M. H. 611, 1387, 1389
Thomas K. L. 381, 687, 1341, 1391, 1393
Thomas P. 453, 469, 787, 1395, 1397
Thompson P. 1399
Thompson R. N. 1063
Thompson T. W. 1401
Thornhill G. D. 1139, 1403
Thorpe A. N. 549
Tobola K. 795
Tomasko M. G. 1293
Tomeoka K. 969
Tomkinson K.-A. 1405
Tomobuchi M. 1375
Tompkins S. 1407
Torigoye N. 1409
Törmänen T. 673, 1411
Träxler B. 719
Treiman A. 795, 797, 1413, 1415, 1417
Trilling D. 467
Trombka J. I. 267
Trucano T. G. 295
Tryka K. A. 1419
Tsou P. 183, 1421
Turcotte D. L. 757, 1423
Turtle E. P. 1425
Tyler G. L. 1503

Ulyanov A. A. 1325
Ustinova G. K. 19, 777, 1427, 1429

Valter A. A. 1431
Van Cleve J. 925
Vaniman D. T. 121
van Oss C. J. 1445
Vanzani V. 841
Vasavada A. R. 1037
Veeder G. J. 1433
Vempati R. K. 771
Verchovsky A. B. 373, 1435
Verkhoglyadova O. P. 735
Veselova G. V. 709
Veverka J. 237, 453, 469, 787, 1395
Vickery A. M. 153, 1437
Vilas F. 553, 1439
Vis R. D. 743
Vistisen L. 1, 819
Vityazev A. 1441, 1443
Voelkel R. 1445
Vorder Bruegge R. W. 1447, 1449
Vormaier A. 719

Wacker J. F. 1275
Wadhwa M. 1451
Wagstaff J. 883
Wald A. E. 1191, 1453
Walker R. 401, 929, 1005
Walker R. M. 1391
Wallmach Th. 423
Wang H. 1455
Wang J. 1457, 1459
Ward W. R. 1461
Warren J. 1233, 1393
Warren P. H. 663, 1463, 1465
Wasilewski P. J. 1467
Wasserburg G. J. 209, 245, 583, 585, 587, 1041, 1097, 1253
Wasson J. T. 255, 753, 1469
Watson G. 1105
Watson L. L. 1471
Watson W. B. 325
Watters T. R. 1473
Wdowiak T. J. 1143
Weber D. 1475
Weidenschilling S. J. 1477
Weigel A. 1479
Weisberg M. K. 1107, 1481
Weiss J. R. 985
Weissman P. R. 453
Weitz C. M. 67, 1483
Wells E. N. 1541
Wenrich M. L. 1485
Wentworth S. J. 25, 71
Wetherill G. W. 1487
Wharton R. A. Jr. 119
Whitaker E. A. 893
White B. 467
Wichman R. W. 1489, 1491
Wieder M. 187
Wieler R. 959
Wiesmann H. 1015, 1017
Wilhelms D. E. 91
Williams D. A. 465, 1493
Williams D. B. 1529
Williams J. 183, 689
Williams R. S. Jr. 409
Williams S. 233, 327, 1521
Wills E. L. 1261
Wilson D. 1205
Wilson L. 361, 421, 527, 953, 1049, 1051, 1405, 1495, 1497
Wilson T. L. 1499, 1501
Winters R. R. 829

Witteborn F. C. 739
Witzke B. J. 31
Wlotzka F. 329, 363, 413, 415, 1061
Wolbach W. S. 251, 545
Wong P. B. 1503
Wood C. A. 1491, 1505, 1507
Wood J. A. 1071, 1073, 1509
Wood S. E. 1037
Wooden D. 739
Woronow A. 1511, 1513
Wright E. 1195
Wright I. P. 339, 451, 1435, 1515
Wu J. 1517
Wu S. S. C. 1519

Xu P. 1521
Xue S. 539, 1523

Yakovlev O. I. 329, 413, 415
Yamaguchi A. 1375, 1525
Yamakoshi K. 665, 853, 1363
Yanagisawa M. 1527
Yanai K. 917, 935, 1409
Yang C. W. 1529
Yang S. V. 435, 595, 1565
Yaroshevsky A. A. 905
Yen A. S. 599
Yingst A. 529
Yingst R. A. 1531
Yoneda S. 1533
York D. 549
Yu Y. 1535, 1537
Yurimoto H. 723, 725, 1539

Zanda B. 279, 543, 1537
Zare R. N. 1391
Zashu S. 1357
Zbik M. 445, 447
Zellner B. 957, 1541
Zent A. P. 1543
Zhang Y. 1545, 1547
Zheng F. 1455
Ziglina I. N. 1549
Zimbelman J. R. 1225, 1551, 1553, 1555
Zimmerman M. E. 817
Zinner E. 27, 347, 375, 1005, 1475, 1557
Zinovieva N. G. 909, 1559, 1561
Zipfel J. 1563
Zolensky M. 181, 435, 567, 595, 645, 941, 1233, 1565, 1567
Zolotov M. Yu. 1569, 1571
Zook H. A. 609, 1573
Zuber M. T. 789, 791, 993, 1289, 1575, 1577
Zubkov B. 819

SAMPLE INDEX*

10002 1299
10010 1267
10011 1267
10020 97
10049 97
10084 235, 259, 371, 507, 547, 649, 685
10086 173

12002 97
12005 97
12009 579
12011 97
12021 97, 1373
12023 173
12031 1373
12034 1017
12037 1267, 1373
12038 1017
12052 97
12056 1017
12064 1373
12070 507

14066 1305, 1307
14078 1017
14141 1267
14160 1307
14161 633
14163 579, 581
14303 1305
14304 1307, 1311
14305 1265, 1305, 1307
14306 1305
14310 97, 1017
14318 1311
14321 1305, 1307

15001 1119, 1429
15002 1429
15003 1429
15004 1429
15005 1429
15006 1429
15009 1003
15016 579
15041 579
15058 97
15065 579
15076 1017
15125 289
15386 557, 579, 1017
15401 21, 1181
15403 1307
15405 557, 1179, 1307
15415 875, 1103
15427 325
15437 875
15445 1305
15474 289
15495 579
15499 97
15505 579
15555 579, 1017
15556 579
15666 289
15682 289

20001 1267
20002 1267
20003 1267
20004 1267
24080–24102 1429
24105–24114 1429
24118 1429
24143 1153, 1429
24160 1153
24184 1429

60006 125
60009 97, 125, 1267, 1367
60010 97, 1267, 1367
60013 97, 1367
60014 97, 1367
60015 579
60025 1103, 1309
60255 1301
60315 97
60635 1301
60639 1301
61181 71
61221 259, 371
61249 1301
62237 1103, 1309
62245 1301
63321 371
64515 1301
64801 371, 579
65795 1301
65905 1301
67048 1301
67075 859, 1103
67235 1525
67461 371
67513 635
67559 1301
67601 1267
67635 875
67637 875
67701 259, 371, 1267
67747 1301
67915 875
67975 633, 1307
68001 1223, 1313
68002 1223, 1313
68415 97
68501 77, 1065
68815 649, 1003

70001 97, 1367
70002 97, 1367
70003 97, 1367
70004 97, 1367
70005 97, 1367
70006 97, 1367
70007 97, 1367
70008 97, 1367
70009 97, 1367
70051 1181
70135 1017
71055 235
71501 77, 105, 959, 999, 1065
72215 617
72235 617
72255 617
72275 617
72315 617
72395 617
72443 637, 1149, 1151
72503 637, 1149, 1151
73215 617
73221 649
73241 649
73255 617
73261 649
74001 21, 1181
74002 1003
74220 21, 23, 325, 505, 579, 1181, 1267
74240 1267
74241 1181
74255 1017
75061 23
75075 1017
75081 1065
76015 617
76230 1525
76235 617
76255 617
76315 617
76503 637, 1149, 1151
76535 579, 617
77017 617
77035 1045
77135 617
77215 617, 1045
78235 617, 1045
79001 1003
79002 1003
79035 999, 1065
79215 1525
79221 1003

*Page numbers refer to the first page of an abstract in which a sample is mentioned.

METEORITE INDEX*

Abee 449, 617
Acapulco 347, 683, 703, 777, 945, 1071, 1073, 1371, 1375, 1523, 1563
Acfer 094 115
Acfer 111 959, 1061
Acfer 153 1157
Acfer 182 449, 1475
Acfer 214 363
Adhi-Kot 617, 1545
Aioun El Atrouss 385
Al Rais 269
Alais 349, 435, 713
Alende 639
Allan Hills 76004 1339
Allan Hills 76005 647
Allan Hills 77005 403, 797, 911, 1417, 1465
Allan Hills 77011 753
Allan Hills 77081 1523, 1563
Allan Hills 77156 801
Allan Hills 77214 573
Allan Hills 77256 385
Allan Hills 77257 647
Allan Hills 77278 753
Allan Hills 77296 801
Allan Hills 77307 165, 167
Allan Hills 78019 647
Allan Hills 78084 99
Allan Hills 78132 647
Allan Hills 78230 1073
Allan Hills 81005 97, 127, 797, 1463
Allan Hills 81011 647
Allan Hills 81021 801, 1547
Allan Hills 81101 611, 647, 663
Allan Hills 81187 1523, 1563
Allan Hills 81261 1073, 1523, 1563
Allan Hills 82106 647, 663
Allan Hills 82130 647
Allan Hills 84001 451, 647, 797, 911, 919, 1043
Allan Hills 84136 647
Allan Hills 84170 801, 1545, 1547
Allan Hills 84190 1523
Allan Hills 84206 1545, 1547
Allan Hills 85001 647
Allan Hills 85045 1057
Allan Hills 85085 595
Allan Hills 85119 1545, 1547
Allegan 1467
Allende 79, 245, 313, 315, 375, 553, 579, 651, 665, 723, 725, 777, 887, 957, 969, 977, 979, 1075, 1227, 1275, 1283, 1339, 1467, 1533, 1539, 1567
Andreevka 1239
Angra dos Reis 245, 813, 1273
Angrite 923
Arapahoe 475
Asuka 881757 1017, 1373, 1463
Atlanta 1545, 1547
Ausson 95

Bachmut 1237, 1239
Barea 1529
Barringer 913
Barwell 587
Belgica 7904 941
Belle Plaine 1169
Bencubbin 1227
Benld 653
Bennett County 929
Béréba 1273
Bholghati 981, 1015
Bielokrynitschie 1239
Binda 1111
Bishunpur 11, 583, 585, 945, 1229, 1481
Bjurböle 95, 977, 1467
Bogou 245
Bouvante 639, 1273
Bovedy 587
Boxian 247
Brachina 1183
Brenham 701
Bruderheim 1429

Caddo County 1375
Calcalong Creek 797
Cañon Diablo 245, 273, 665
Cape York 245
Carlton 1337
Cat Mountain 177, 475
Cerro los Calvos 865
Chainpur 11, 743, 977, 1229, 1467, 1481
Chassigny 403, 911, 1413, 1451, 1471
Chico 495, 1017, 1169
Chinguetti 1529
Clovis 587
Coolidge 661
Cumberland Falls 611

Daniel's Kuil 1545
Dengli 1185
Derrick Peak 245, 929
Dhajala 573, 1429

*Page numbers refer to the first page of an abstract in which a meteorite is mentioned.

Dioux County 1273
Divnoe 1069, 1523

Eagle Station 777, 1545
Efremovka 1325, 1557
El Sampal 1337
El Taco 849
Elenovka 1237, 1239
Elephant Moraine 79001 339, 403, 451, 911, 1413, 1417
Elephant Moraine 79002 385, 647
Elephant Moraine 79004 647
Elephant Moraine 79005 647
Elephant Moraine 83213 25
Elephant Moraine 83225 647
Elephant Moraine 83230 1025
Elephant Moraine 83235 647
Elephant Moraine 83254 1547
Elephant Moraine 83322 1545
Elephant Moraine 84302 703, 1073, 1371, 1375, 1479, 1523
Elephant Moraine 87503 611, 1015
Elephant Moraine 87511 663
Elephant Moraine 87513 1015
Elephant Moraine 87517 647
Elephant Moraine 87521 97, 797, 1463
Elephant Moraine 87555 95
Elephant Moraine 87720 647
Elephant Moraine 87746 1545
Elephant Moraine 87770 1565
Elephant Moraine 90004 1155
Elephant Moraine 90007 1155
Elephant Moraine 90022 1155
Elephant Moraine 90102 1545
Elephant Moraine 90299 1545
Ellemeet 385
Enon 701
Enshi 247
Erevan 979, 981
Esquel 921

Fayetteville 959, 1061
Flindersites 447
Forest Vale 701, 1057
Frontier Mountain 90011 703, 1479, 1523
Frontier Mountain 90054 663

Galim 543
Gibeon 245
Gibson 1479, 1523
Goalpara 1409
Gorlovka 1239
Governador Valadares 391
Grant 539, 1025

Hallingeberg 95
Happy Canyon 1545, 1547
Haverö 137, 663
Huittis 1545

Ibbenburen 385
Ibitira 651, 1273
Ikhrarene 587
Imilac 921
Indarch 585, 777, 1545, 1547
Inman 585, 945
Innisfree 1429
Ivuna 349, 435, 1565

Jilin 99
Jodzie 979, 981
Johnstown 385, 911
Juvinas 1273

Kaidun 269, 435, 595, 1185, 1565
Kainsaz 165, 167, 641
Kakangari 1523
Kapoeta 37, 981
Kenna 137, 1409
Khaipur 1545
Khairpur 1547
Khohar 945
Knyahinya 843
Kota-Kota 1545
Krymka 573, 1229, 1237, 1239, 1435, 1481
Kuleschovka 1239
Kyushu 95

La Criolla 665
Lafayette 391, 911, 1471
Lakangaon 639
Lancé 641
Laochengzhen 247
Leonovka 1237, 1239
Leoville 969, 1537
Lewis Cliff 85300 981, 1015
Lewis Cliff 85319 99
Lewis Cliff 86001 647, 831
Lewis Cliff 86010 813, 1015, 1017, 1273
Lewis Cliff 86024 1057
Lewis Cliff 87051 907
Lewis Cliff 87119 1545, 1547
Lewis Cliff 87223 319, 801, 1547
Lewis Cliff 87295 647
Lewis Cliff 88008 385
Lewis Cliff 88135 1545
Lewis Cliff 88180 801, 1545, 1547
Lewis Cliff 88280 1479, 1523
Lewis Cliff 88516 403, 647, 797, 911, 1417
Lewis Cliff 88663 1169
Lewis Cliff 88714 1545
Lewis Cliff 88774 663, 1107, 1465
Limerick 1057
Lodran 703, 1073, 1479
Lodranite 921
Lombard 929
Loongana 001 661
Los Martinez 587
Lost City 99, 651, 879, 1429
Lubbock 475

MacAlpine Hills 88104 97, 1463
MacAlpine Hills 88105 97, 1463
MacAlpine Hills 88136 319, 801, 1545, 1547
MacAlpine Hills 88177 1371, 1479, 1523
MacAlpine Hills 88180 1545
MacAlpine Hills 88184 1545
Manegaon 385
Manych 587, 945
McKinney 95
Meghei 957
Messenya 945
Meteorite Hills 78008 1409
Meteorite Hills 78028 99
Mezö-Madaras 245, 753, 945
Mihonoseki 917
Millbillillie 1273, 1525
Moama 1111
Monument Draw 1563
Moorabie 865
Moore County 1111, 1273
Mount Edith 1025
Mount Joy 929
Mundrabilla 25
Murchison 27, 37, 103, 135, 181, 313, 355, 373, 401, 563, 583, 585, 639, 645, 651, 665, 793, 903, 941, 979, 1005, 1063, 1283, 1567
Murray 979

Nakhla 1, 391, 403, 451, 883, 911, 1413, 1451, 1471
Nantan 245
Navajo 929
Negrillos 929, 1041
Netschaëvo 865
Noblesville 795, 1061
Norton County 611
Novo Urei 137
Nuevo Laredo 639, 1273
Nuevo Mercurio 665

Ollague 979
Orgueil 269, 349, 355, 381, 579, 583, 585, 713, 761, 763, 777, 903, 957, 1033, 1435, 1565
Ornans 165, 167, 641
Orvinio 475

Paranaiba 1169
Parnallee 11
Parsa 543
Pasamonte 1273
Patuxent Range 91501 25, 95, 513, 1169
Patwar 1529
Pavlodar 1335
Peace River 247, 1429
Peckelsheim 385
Pecora Escarpment 82502 647, 1273
Pecora Escarpment 82506 647, 663, 1409
Pecora Escarpment 82507 923
Pecora Escarpment 82518 319, 1545, 1547
Pecora Escarpment 86502 137
Pecora Escarpment 91002 1357
Pecora Escarpment 91020 801
Pecora Escarpment 91077 385
Pecora Escarpment 91020 1545
Pecora Escarpment 91085 1545, 1547
Pecora Escarpment 91238 1545
Pesyanoe 1065
Pillistfer 1545
Pinnaroo 1529
Pomozdino 1273
Pontlyfni 1523
Pribram 1429
Pultusk 561

Qingzhen 571, 665, 801, 1545, 1547
Queen Alexandra Range 90210 1057

Ragland 587
Ramsdorf 495, 1169, 1239
Reckling Peak 79015 1167, 1529
Reckling Peak 80259 801, 1547
Renazzo 269, 543, 1537, 1565
Rochester 247
Rose City 1169

Saint Sauveur 543, 617, 1547
Saint-Séverin 99, 639, 651, 843, 879, 1429
Sandia Mountain 929
Santa Cruz 1565
São Julião de Moreira 929
Saotone 917
Saratov 1237, 1239
Semarkona 11, 543, 573, 585, 587, 1227, 1229, 1481, 1537
Sena 1237
Serra de Magé 1111
Severenyi Kolchim 1185
Shallowater 683
Sharps 11, 1481
Shaw 95, 1169
Shergotty 403, 883, 911, 1413, 1471
Shikhote Alin 849
Shirahagi 917
Sioux County 639, 651
Smithsonian 929
Springwater 1335
Stannern 639, 1273, 1525
Suizhou 247
Suwahib (Buwah) 865

Tadjera 957
Tahara 917
Taiban 1169

Taizhou 1455
Tatahouine 385, 1479
Theil Mountains 91714 1547
Thiel Mountain 91714 801
Thiel Mountains 82410 385
Thiel Mountains 91714 1545
Tieschitz 11, 401, 945, 1005, 1057, 1537
Tocopilla 1041
Toluca 509
Torino 1017
Trenton 245
Tsarev 905, 1185, 1239

Ucera 99

Vigarano 79, 223, 1075

Warrenton 165, 167
Weatherford 1227
Weston 77
Wiley 777
Willaroy 865
Winona 1523
Wray 865

Xi Ujimqin 247

Yamato 691 801
Yamato 74013 1371
Yamato 74063 1073, 1523
Yamato 74160 1169
Yamato 74356 1525
Yamato 75011 1015
Yamato 75097 935, 1183
Yamato 790143 1169
Yamato 790964 1169
Yamato 79097 95
Yamato 791197 1463
Yamato 791491 1073, 1479, 1523
Yamato 791493 1071, 1073
Yamato 791538 663
Yamato 792769 1015
Yamato 793164 1015
Yamato 793169 1373, 1463
Yamato 793241 935, 1183
Yamato 793274 1463
Yamato 793421 95
Yamato 794046 935, 1183
Yamato 82162 941
Yamato 82192 97, 1463
Yamato 8451 921
Yamato 86032 1463
Yamato 86720 941
Yamato 92510 1015

Yanzhuang 1169
Yilmia 1545

Zaborzika 1237, 1239
Zagami 1, 403, 911
Zaoyang 247
Zhigailovka 1239
Zvonkove 1239

KEYWORD INDEX*

Ablation 1365
Abrasion 1285
Abriachan 1179
Abundances 1061
Acapulcoites 703, 1071, 1073, 1371, 1375, 1523, 1563
Acapulco metal 347
Accretion 57, 307, 509, 1259
Accretional shock 1173
Achondrites 647, 703, 901
Acid etching 649
Admittance 1277
Adsorption 1543
Aerogel 183, 1515
AGB stars 151, 209, 583, 585
Age dating 997
Ages 19, 813, 1015, 1105
Agglutinates 71, 547, 685, 937
Alba Patera 491, 643, 1425
Albedo 1117
Alkali elements 1009
Alkali suite 1303, 1307, 1311
Alkalies 753
Alkylammonium 435
Alluvium 459
Alpha Regio 425, 463
Alteration 181, 299, 315, 645, 887
Alternative 1027
Altimeter topography 1055
Aluminum oxide, presolar 583
Aluminum-26 27, 363, 539, 587, 1005, 1185, 1475, 1523
Ames Vertical Gun 61, 1211, 1213, 1215
Ammonia 173
Ammonia-water 439, 555
Amorphous rims 105
Analogs 437
Analysis, in situ 75
Ancient atmosphere, Mars 511
Angrite 907
Anhydrite, vaporization 413
Annealing 95, 493
Anorthosites 875, 1077, 1103
Antarctic meteorites 13, 99, 941, 1035, 1155
Antarctica 119, 917, 1125
Antipodal focusing 145
Apatite 881
Aphrodite 229
Aphrodite Terra 1405
Apollo 11 1299
Apollo 14 633, 1305, 1307
Apollo 15 289
Apollo 16 351, 635, 943, 1301, 1313
Apollo 17 617, 637, 1151, 1181
Apollo subsatellites 791
Aqueous alteration 349, 595, 1439
Archeology 549
Archives 1287
Argon 137, 971
Ariel 285, 1193
Arsia Mons 1225
Artemis Corona 179
Artificial intelligence 1513
ARTIST 783
Ascraeus Mons 1225
Asgard 91
Assimilation 1511
Asteroid breakup 1215, 1479
Asteroid families 689, 841, 1507
Asteroid genetic links 689
Asteroids 43, 89, 153, 175, 183, 185, 237, 243, 265, 365, 379, 399, 411, 453, 469, 495, 561, 609, 711, 785, 787, 795, 797, 991, 999, 1083, 1117, 1135, 1175, 1395, 1439, 1487, 1497, 1541
Asteroids, Earth-approaching 153
Astrobleme 369, 1197, 1431
Astronomy 1499, 1501
Atmosphere entry heating 381
Atmospheres 39, 143, 337, 377, 745, 747, 749, 987, 1023, 1093, 1331, 1397, 1437, 1569
Atmospheric chemistry 201
Atmospheric effects 1213, 1215
Atmospheric entry heating 711, 713
Atmospheric evolution 615
Atmospheric stability 429
Aubrites 383
Axial focusing 145
Axtell 1275

Backscatter 627, 1483, 1503
Baddelyite 427
Barberton greenstone belt 717
Barberton Mountain land 717
Barometry 1021
Barringer impact crater 913
Barringerite 979
Basalt-eclogite 205
Basaltic glass 505
Basalts 361, 1301, 1343, 1415, 1511, 1513, 1551

*Page numbers refer to the first page of an abstract in which a term is mentioned.

Beast wave 41
Beneficiation 235
Bistatic 1279
Black chondrites 957
Blanks 983
Blocks 261
Blue CL enstatite 319
Bolides 5, 39, 1023, 1365, 1397
Borealis Basin 293
Boulders 261
Bromine, enrichment 139
Bulk chemistry 981
Bulk composition 1563
Bulk regolith, composition 1153
Bunte breccia 31
Buoyant 623
Bushveld complex 1121

Cadmium 1207
Calcium-aluminum-rich inclusions 79, 223, 315, 363, 471, 587, 725, 763, 825, 887, 965, 1075, 1283, 1475, 1533, 1539, 1557
Calderas 305, 527
Calibration 85, 87, 107, 567
Callisto 91, 455
Camera 1573
Canal 727
Canali 667
Cap 69
Carbide 1465
Carbon 659, 687, 945, 1107, 1435, 1515
Carbon abundance 1391, 1393
Carbon dioxide, trapping 415
Carbon isotopes 339, 373
Carbon-14 647, 649
Carbonaceous chondrites 199, 269, 645, 671, 957, 969, 979, 981, 1567
Carbonaceous material 355
Carbonates 201, 339, 349, 481, 687, 1343, 1485
Carbonatite 667
Carson Quadrangle 463, 1243
Carvon 759
Cathodoluminescence 319, 449, 571, 1339, 1547
CD-ROM 311
Cementation 201
Ceraunius Tholus 947, 1147
Channels 207, 631, 727, 885, 1029, 1493
Channels, depth 811
Channels, floors 811
Channels, walls 811
Characterization 253
Chassigny 1451
Chelmsfold turbidites 1517
Chemical fractionation 1183
Chemical kinetics 707, 773
Chemical mapping analysis 1373
Chemical separations 401
Chemical weathering 707
Chemical zoning 907, 921, 1371
Chemistry 119, 685, 747, 1089, 1221, 1393
Chervony Kut 813
Chicxulub 537, 1095, 1201, 1211, 1221, 1255
Chladniite 1337
Chondrites 11, 181, 279, 645, 661, 865, 905, 945, 1237, 1239, 1357, 1455, 1529, 1559, 1561
Chondritic material 1457
Chondritic meteorites 561
Chondrule formation 573, 1229
Chondrule mesostases 11
Chondrule metamorphism 801
Chondrule rims 1469, 1481
Chondrule texture 801
Chondrules 7, 279, 307, 345, 471, 543, 573, 587, 641, 723, 743, 753, 945, 965, 977, 1173, 1227, 1285, 1467, 1469, 1481, 1535, 1537
Chrometers 683
Chromite 1107
Chromium 907, 1033
Chronology 475, 587, 1409
Cinder cones 317
CK chondrites 1155
Classification 1347
Clays 53
Clementine 21, 1573
Climate 69, 191, 933, 1543
Clinopyroxene 369
Clouds 747
Cloudy zones 1529
CM chondrites 115, 181, 645, 1131, 1565
CM2 chondrites 181, 645, 665
CO3 chondrites 165, 167, 641
Coagulation 1443
Coarse fines 289
Cobalt 657
Cohenite 663, 1465
Coherence 113
Collision experiments 1175
Collision integral 1549
Collisions 569, 841, 1441
Color 1145
Combustion 171, 373, 793, 1435
Comet Halley 1143
Comet Shoemaker-Levy 9 5, 93, 101, 295, 597, 1023, 1369, 1527
Cometary breakup 295

Cometary ionosphere 735
Cometary nuclei 1527
Cometary shells 735
Comets 75, 93, 101, 147, 183, 185, 379, 597, 609, 621, 731, 841, 987, 989, 999, 1369, 1477, 1491
Comminution 1445
Compensation 51
Complex craters 559
Complex ridged terrain 1553
Composition 81, 83, 167, 257, 661, 985, 1363
Condensation 493, 1227, 1251
Condensation, silicates 329
Condensation, sulfur 413
Condensation, trapping 415
Contamination 339, 741
Continental crust 1009
Contractional features 1473
Convection 697, 699, 1277, 1315
Cooling 95, 921
Cooling rate 859, 1315
Core 995
Core formation 141, 397, 509, 551, 653, 759, 1025, 1259
Coronae 179, 239, 419, 421, 501, 503, 619, 673, 751, 823, 973, 1047, 1087, 1137, 1405, 1411, 1553
Correlations 757
Corundum 1005
Cosmic dust 183, 185, 609, 711, 1381, 1515
Cosmic ray exposure 247, 353, 1463
Cosmic rays 19, 125, 845, 1429, 1479
Cosmic spherule 761
Cosmochemistry 1445
Cosmogenic isotopes 15, 17, 403
Cosmogenic material 853
Cosmogenic nitrogen 851
Cosmogenic nuclides 701, 843, 1003, 1119, 1429
Cosmogenic profiles 99
Crater chains 893
Crater morphology 559
Cratering 89, 559, 857, 973, 1213
Craters 43, 55, 237, 511, 599, 627, 629, 809, 893, 953, 991, 1105, 1201, 1355, 1483
Cretaceous-Tertiary 31, 545, 607, 1095, 1221
Crisium Basin 127
Cross-sectional area 1117
Crust 271, 599, 697, 995, 1485
Crustal history 877
Crustal recycling 205
Crustal thickening 205
Cryosphere 271
Cryovolcanism 555
Cryptomare 35, 127, 515, 523, 963, 1077
Crystal fractionation 557
Crystal size 1315
Crystallization 37
Crystals 659
Cumulate eucrites 1111
Curriculum 783
CV3 chondrites 1275
Cydonia Mensae 1053

Danu Montes 681
Dao Vallis 1029
Dark-floored craters 1489
Dating 137
Davy crater chain 1491
Debris 915
Decarbonation 839
Deconvolution 499
Deformation 681, 817
Deformation belts 1411
Degassing 971
Deimos 293, 733, 1291
Delamination 567
Deltas 1029
Density 147
Depletion 995
Deposition 815
Depth distribution 741, 1427
Depth profiles 1119
Detectability 1181
Detection limits 983
Diabese 817
Diagenesis 1131
Diamictite 565
Diamonds 449
Diamonds, presolar 793
Diapirism 619, 751
Diaplectic 369
Diaplectic talc 1431
Differentiated meteorites 813
Differentiation 873, 1185, 1251
Diffuse reflectivity 771
Diffusion 859, 921, 1335
Diffusion coefficient 967
Diffusion profiles 1025
Digital elevation model 1551
Digital imaging 235, 547
Dihedral angle 439
Dike swarms 485, 487
Dikes 523, 527, 693, 1497
Diogenites 385, 639, 651, 1043
Dione Regio 65, 675, 677
Discharge rates 275
Discovery missions 267, 951, 1323
Dislocation 1455
Disruption 495

Dissolution 983
Distinct lithologies 349
Distribution 417
Distribution coefficients 907, 923
Dolomite 839
Domes 193, 1189
Domical uplift 487
Doppler data 1281
Drag 1213
Drift potential 1521
DSC 25, 1021
Dunes 1171
Dunes, linear 341
Dunes, Mars 341
Dunes, star 341
Duricrust 955
Dust 75, 257, 467, 493, 925, 1143, 1363, 1573
Dust collectors 107
Dust grain charging 591
Dust subdisk 827
Dusty plasmas 589, 591
Dynamical evolution 841
Dynamical processes 411
Dynamics 189, 609

E3 chondrites 665
Early crust 1309
Early irradiation 671
Earth 407, 815, 829
Earth, analogs 457
Earth, differentiation 551, 1253
Earth-grazing 283
Earth-Moon system 829, 1009
Earth, origin 215
Eccentricities 593, 1549
Edifices 417
Education 47, 163, 281, 311, 343, 783, 795, 835, 891, 897, 933, 1249, 1351, 1399, 1505
Effusion 1551
EH chondrites 1545, 1547
Eistla Regio 833
Ejecta 35, 41, 359, 459, 549, 787, 1201
Ejecta deposits 565
Ejecta emplacement 61, 1355
Ejection 987
El chondrites 1545, 1547
Electron diffraction 621
Electron energy-loss spectroscopy 687
Electron microscopy 165, 355, 505
Element ratios 1059
Elemental depletions 761
Elemental distribution 1375
Elements 1563
Elysium 225, 227
Emission spectra 1453
Emissivity 217, 503, 605, 781, 1263, 1483
Empirical model 393
Energy partitioning 1175
Enstatite 319, 571, 683
Enstatite chondrites 269, 319, 383, 801, 1545, 1547
Entry 1215
Environment 117
Equation of state 731
Equilibrated ordinary chondrites 99, 247, 1035
Erosion 263, 459, 815, 1437
Eruptions 361, 1051, 1405, 1495, 1497
Eucrites 135, 639, 651, 813, 831, 879, 901, 1015, 1273, 1525
Eureca 867
Europa 1019
European Space Agency 49, 253
Evaporation 375, 723, 755, 965, 1227, 1229, 1457, 1459
Evolution 493, 593
Exercise 281
Exobiology 367, 769
Exopaleontology 367
Exospheres 377, 1099
Experimental chondrules 825
Experimental crystallization 883
Experimental geochemistry 221
Experimental petrology 639
Experimental study 109
Experiments 279, 653, 1343, 1535, 1537
Exploration 733, 1177
Explosion 1369
Exposure ages 15, 17, 475, 539, 1267, 1523
Exsolution 1069, 1335
Extension 29, 443, 993
Extinct nuclides 849, 1185, 1325
Extinct radionuclides 509, 613
Extraterrestrial matter 1429

Fassaite 1533, 1539
Faulting 441, 993, 1217, 1219
Ferric oxides 1165
Ferric oxyhydroxides 1165
Ferroan anorthosites 875, 1299, 1309, 1313
Ferroelectric 1263
Ferromagnetic resonance 71, 937
Ferrous/ferric ratio 323
Festoon flow 1067
Field work 1177
Fillowite 1337
First dredgeup 583
Fission tracks 881
Flash heating 471

Flood basalts 521, 821, 1383
Fluctuation 1441
Fluid dynamics 693
Fluidized 599
Fluidized ejecta blankets (FEB) 627, 629
Fluvial 321
Fluvial processes 213
Fluvial valleys 491
Flux 867
Flyby 1323
Fold wavelengths 473
Folds 331
Formation of giant planets 1123
Forsterite 1339
Found meteorite 917
Fractals 1383
Fractional crystallization 639
Fractional melting 803
Fractionation 375, 385, 723, 761, 873, 1457, 1459, 1511
Fracture patterns 155
Fracture spacing 155
Fractures 1087
Fragmentation 243, 569, 597, 1365
Fragments 1157
Fremdlinge 223
Fretted terrain 327
Friction 1231
FTIR 451

Gabbroic rocks 1077
Gabbronorite 633
Galactic cosmic rays 17, 843, 851, 1003, 1119
Galilean satellites 91, 433, 863
Galileo 237, 243, 395, 411, 433, 453, 575, 807, 863, 869, 1019, 1235, 1359
Gamma rays 499, 845
Ganymede 297, 455, 575
Garnet 803
Gas coalescence 1049
Gas-solid reaction 773
Gaspra 89, 453, 561
GCM 1521
Generation 1427
Geochemical analysis 267
Geochemistry 157
Geochemistry, martian meteorites 911
Geochronology 1113
Geoid 757, 1277
Geologic history 833
Geologic mapping 65, 91, 239, 291, 463, 631, 677, 833, 1225, 1245
Geologic traverse 943
Geological processes 431
Geology 535, 1329
Geology, surface 895
Geometrical transformations 133
Geophysics 1085
Georgia tektite 427, 1101
Geothermal melting 491
Germanium detector 187
Giant impact model 613
Gifted students 163
Giotto 1143
Glaciotectonics 799
Glass 71, 351, 1181
Global 253
Global change 933
Global geology 303
Global properties 407
Global stress 489
Global volcanism 303
Glow 1573
Gold 997
Graben 331
Grain 1239
Grain charging 589
Grain coagulation 591, 1011
Grain size analysis 373
Grain size distribution 1153
Grains 1237
Grains, presolar 151
Granite 557
Granulites 1525
Graphite 27, 103, 945, 1465
Graphite, feathery 347
Graphite, spherulitic 347
Gravitational constants 1291
Gravitational encounters 1549
Gravitational instability 827
Gravitational waves 1499
Gravity 51, 113, 625, 699, 1281, 1295, 1401, 1551
Gravity anomalies 789, 791, 1317
Gravity data 537
Gravity fields 789, 791
Gravity regime 569
Gravity relaxation 1109
Green glass 21, 803
Greenhouse effect 191
Grooves 953
Ground ice 225, 227, 287
Groundwater 271
Group D 1299
Gruithuisen domes 249
Guamote 1555
Guinevere Planitia 301
Gusev Crater 241, 483, 769
GVDR 855
Gypsum, vaporization 413

H chondrites 135, 1209
H3 chondrites 1157
Halogens 741
Hawaiian activity 1049
Heat flow 1423
Heat flux 1159
Heat transfer 691, 693
Heating experiments 713
Heating mechanisms 345
Hecate Chasma, Venus 501
HED meteorites 651, 901, 981, 1083
Helium 999
Hellas 1379
Hertha family 689
Heterogeneity 1393
Hexagonal diamond (lonsdaleite) 313
High pressure experiments 551
High-micrometer sources 1103
Highbury structure 847
Highlands 97, 1265, 1305, 1307
History 1353
Hole size 1207
Hot belt 431
Hot spots 303, 431, 521, 877, 1295
Howardites 603, 979, 981, 1015
HPLC 251
Hubble Space Telescope 957
Hugoniot data 1209
Human exploration 1177
Humorum Basin 1077
Hydrated minerals 381
Hydrocarbons 251
Hydrodynamic effects 1231
Hydrodynamic model 1381
Hydrodynamics 1231
Hydrogen isotopes 1155, 1471
Hydrothermal activity 481
Hydrothermal alteration 861
Hydrothermal systems 299, 491
Hyperion 1349
Hypervelocity impact 1381
Hyprometry 1159
Hypsometry 55

IAB irons 255, 1375
Ice 69, 211, 275, 433, 439, 621, 951, 1037
Ice and frost 975
ICP-MS 983
Icy satellites 285, 555, 863, 1047, 1193, 1205
Ida 89, 237, 411, 469, 787, 1395
Igneous inclusion 935
Igneous intrusion 1007
Igneous processes 635, 1183
IIE irons 865
IIIAB irons 1025
Ilmenite 105, 235, 259
Image analysis 125
Image cube 455
Image errors 779
Image processing 241, 779, 1195, 1407
Imager 1293
Images, color 871
Imaging 81, 239, 655, 1271
IMDR Regio 631
Immiscibility 557
IMP 1293
Impact age 881
Impact basins 293, 387, 389, 537, 1211, 1345
Impact breccias 1169, 1347
Impact craters 59, 67, 201, 225, 227, 411, 559, 719, 721, 781, 847, 947, 1079, 1085, 1137, 1199, 1255, 1321
Impact events 607
Impact flash 5
Impact frequency 1233
Impact glasses 1039
Impact heating 1169
Impact melt breccias 729, 1149, 1151
Impact melts 475, 477, 479, 513, 617, 753, 939, 1007, 1167, 1169, 1255, 1301, 1313
Impact modeling 1095
Impact origin 1121
Impact origin, iron meteorites 255
Impact processes 705, 1095
Impact strength 1175
Impact structures 299, 861
Impact theory 579
Impact, simulation 329
Impactites 445, 447, 1347
Impacts 41, 43, 61, 145, 243, 295, 309, 359, 423, 495, 549, 565, 597, 599, 719, 787, 795, 809, 869, 989, 991, 1175, 1207, 1327, 1347, 1355, 1369, 1385, 1397, 1437
Impacts, giant 215
Implantation 1059, 1093
Inclination 1549
Inclusions 905
Infrared 123, 785, 975, 1135, 1191, 1433, 1453
Infrared spectroscopy 519, 1161, 1163, 1165
Inner solar system 991
Inservice 783
Instrument 1261
Instrumentation 709
Interdiffusivity 967

Interferometers 1499
Interior evolution 541
Interior processes 303
Interior structure 1295
Interplanetary dust particles 139, 159, 185, 379, 381, 687, 853, 999, 1129, 1131, 1341, 1391, 1393, 1515
Interstellar diamond 775
Interstellar dust 621, 1063
Interstellar grains 9, 27, 103, 313, 449, 563, 903, 1005, 1033
Interstellar graphite 401
Intrusives 161
Intrusives, gabbroic 1113
Io 123, 807, 975, 1205, 1433
Ion imaging 1005
Ion microprobe 1057, 1451
Ion probe 763, 1311, 1325
Ionization 149
Iron 1361
Iron grains 1011
Iron meteorites 245, 255, 539, 849, 929
Iron mineralogy 709
Iron oxides 83, 1459
Iron sulfide 773
Irradiation 1157
Irradiation dose 601
Ishihara code 1551
Ishtar terra 1447, 1449
Isidis Planitia 291, 799
ISM instrument 357
Isolated grains 743
Isostasy 489, 757, 1317
Isotopes 173, 375, 903, 1057, 1409, 1457, 1459
Isotopes, carbon 347
Isotopes, magnesium 725
Isotopes, nitrogen 347
Isotopes, oxygen 965, 1389, 1539
Isotopic abundances 1391
Isotopic anomalies 27, 401, 563, 585, 587, 611, 725, 775, 777, 903, 1033, 1185, 1325, 1387, 1389, 1539
Isotopic fractionation 615, 965, 1093
Isotopic ratios 579, 581, 701, 775, 1059
Isotopics, oxygen 1387
Isotopy 75
Isua 1253

Japanese meteorites 917
Johnsomervilleite 1337
Jovian atmosphere 731
Juno Dorsum 1241
Jupiter 143, 295, 597, 1331

Kaapvaal Craton 1113
Kawelu Planitia 531, 1553
Kinetics 755, 1315
Kirchhoff's Law 1191
Klapperkop member 1121
Komatiites 465, 1493
KREEP 557
Kuiper belt 379

L chondrites 95, 495, 513, 1209
L6 chondrites 665
Labrador 1303
Lacustrine plains 321
Lada Terra 821
Lafayette 1471
Lake 213, 483
Lake basins 321
Lakshmi 681
Lamellar structure 1069
Landform relief 927
Large igneous province 521
Laser 683
Laser ablation 1063
Laser fusion dating 1321
Lava 189, 207, 361, 805, 1433
Lava channels 465, 667
Lava compositions 473
Lava domes 33, 169
Lava erosion 465
Lava flooding 525
Lava flows 233, 391, 473, 531, 577, 691, 805, 1087, 1089, 1091, 1193, 1383, 1405, 1493, 1551
Lava folds 473
Lava fountains 1049, 1051
Lava ponds 1531
Lava tube 465
Lavinia 525
Lavinia Planitia 529
Layered deposits 535
Layered materials 955
Lead-205 245
Light lithophile element 1257
Light plains 963
Lineament analysis 1133
Lineaments 277
Linear crater chains 1491
Liquid immiscibility 1559, 1561
Liquidus boundary 803
Lithophile trace elements 1025
Lithosphere 113, 817, 931, 1203
Lithosphere thickness 1159, 1317
LL chondrites 879
Loading 525
Lockne 1385
Lodranites 703, 1071, 1073, 1371, 1375, 1479, 1523

Long Duration Exposure Facility (LDEF) 107, 567, 809, 867, 1207, 1233, 1327
Luminosity 1441
Luna 20 1463
Lunar anorthosite 635, 1081
Lunar basalt 1017
Lunar core 1223
Lunar crust 875, 1007, 1045
Lunar differentiation 1017
Lunar geochemistry 1151
Lunar geochronology 1103
Lunar granites 1179
Lunar gravity 791
Lunar highlands 127, 249, 943
Lunar KREEP 1017
Lunar landing site 915
Lunar mantle 73, 1257
Lunar metal 77
Lunar meteorites 797, 1373, 1463
Lunar orbiters 791
Lunar origin 579
Lunar project 915
Lunar regolith 1223, 1267, 1367
Lunar resources 737
Lunar sample disk 835
Lunar samples 637, 835
Lunar shocked material 915
Lunar soil 23, 547, 685
Lunar surface 533
Lunar symmetric tectonics 715
Lunar volatiles 325
Lunar volcanism 249
Lunar wave tectonics 715

M asteroids 265
Ma'adim Vallis 769
Maat Mons 405, 409, 949, 1139
Macromolecule 1247
Magellan 129, 157, 625, 705, 1195, 1199, 1245, 1281, 1287, 1295, 1401, 1483, 1519, 1553
Magma 361, 527, 1087
Magma chamber 1405
Magma evolution 1511
Magma ocean 875, 1315
Magma recycling 1051
Magma rise speed 1049
Magma sources 1103
Magmatic evolution 541
Magmatism 1497
Magnesian suite 633, 1305
Magnesiowustite 873
Magnesium 1075
Magnesium isotopes 315, 363, 539, 723
Magnesium-perovskite 873
Magnetic fields 149, 333, 561, 1123
Magnetic grains 1011
Magnetic properties 1, 977
Magnetism 709, 1467
Magnetization 243
Mahuea tholus 927
Maja Vallis 1029
Mangala Valles 321
Manson Impact Structure 31, 299, 607, 719, 729, 861
Mantle 657, 659, 699, 751
Mantle convection 489
Mantle flow 205
Mantle mineralogy 109
Mantle plumes 521
Mantle rare gases 1097
Mapping 305, 419, 499, 631, 1297, 1519
Maps 1349
Mare 523, 547, 1359, 1531
Mare basalts 73, 219, 289, 1149, 1257, 1373
Mare Crisium 127
Mare Orientale 715
Marine impact 31
Mariner 6,7 87
Mariner 9 789
Mariner 10 985, 1145, 1297
Marius Hills 1359
Marquez Dome 881
Mars 1, 3, 29, 53, 59, 69, 83, 85, 87, 109, 117, 119, 203, 211, 225, 227, 231, 257, 263, 271, 275, 287, 293, 305, 317, 367, 387, 389, 391, 403, 407, 437, 441, 443, 481, 511, 527, 535, 599, 615, 643, 709, 733, 745, 749, 759, 769, 799, 815, 845, 857, 871, 895, 925, 933, 939, 947, 955, 1043, 1053, 1125, 1127, 1141, 1147, 1171, 1205, 1217, 1219, 1261, 1289, 1291, 1343, 1345, 1377, 1379, 1383, 1413, 1425, 1437, 1473, 1495, 1521, 1541, 1543
Mars, composition 961
Mars, craters 61
Mars, fluvial 457
Mars, gravity 789, 1291
Mars, mineralogy 961
Mars, nitrogen cycle 451
Mars, remote sensing 961
Mars, thermal inertia 517
Mars, thermally derived albedo 517

Mars Observer 353
Mars Observer, gamma ray spectrometer 353
Marsquake 441
Martian meteorites 797, 911
Mass spectrometry 75, 1063
Massif anorthosites 1303
Material extraction, energy cost 737
Mathematical geology 1511, 1513
Matrix 165, 167, 1481, 1525
Maturity 23, 937
Mauna Loa 405, 409
Maxwell Montes 1447, 1449
Mead Crater 51, 537
Mechanical twin 1431
Melilite 79, 825
Melt inclusions 513, 1417
Melting 471, 1185
Melting experiment 923
Melting model 37
Melting reactions 109
Mercury 187, 337, 507, 533, 951, 985, 1037, 1099, 1145, 1203, 1297, 1323
Mercury, surface composition 739
Meroe Patera 291
Merrihueite 753
Mesosiderites 1167, 1529
MESUR 1293
Metal 223, 685, 695, 937, 945, 1061, 1237, 1239
Metal phases 1529
Metal segregation 653
Metamorphism 165, 167, 423, 573, 941, 1169, 1545, 1547, 1567
Metasomatism 11, 641, 1305
Meteor Crater 459
Meteorites 13, 15, 17, 19, 37, 95, 149, 175, 177, 185, 265, 267, 279, 471, 561, 563, 777, 795, 843, 905, 917, 1409, 1427, 1525
Meteorites, gas-rich 959
Meteoritic diamonds 313
Meteoroid 183
Meteoroid and Debris Special Investigation Group (M&G SIG) 1233
Meteors 57, 765, 1397
Methane 1139
MHD 735
Microcrater 867
Micrometeorites 71, 355, 713, 761, 763
Micrometeoroids 809, 1327, 1515
Mineral chemistry 633, 1183
Mineralization 367
Mineralogy 85, 121, 165, 357, 785, 1131, 1135, 1393
Minerals, shocked 309
Minor planets 689
Miranda 1047
Mixing 963
Mixing analysis 1329
Mixing model 479, 1129
Mode of origin 487
Modeling 207, 361, 371, 815, 1403, 1493
Modeling, mineralogic 961
Models 805
Modified Gaussian model 553
Montagnais 1085
Monte Carlo simulation 845
Moon 81, 219, 253, 259, 335, 377, 395, 523, 541, 733, 829, 851, 869, 893, 1145, 1181, 1257, 1259, 1261, 1329, 1333, 1367, 1383, 1407
Moon, age 613
Moon, lunar cores 1367
Moon, meteorites 97
Moon, origin 215, 1259
Moon, soils 97
Morphology 977, 1473
Mossbauer spectroscopy 1, 707, 709, 771, 939, 941, 1261, 1269
Mountain belts 1449, 1577
Mountain building 1447
Multikilometer roughness 407
Multimedia 311
Multiring basin 1255
Multispectral 1145, 1359
Multispectral images 1407
Muong Nong-type tektite 427, 1101

Nakhlites 391, 1451, 1471
Nanodiamonds 313
Nanophase 53
Nanophase hematite 437
Near Earth asteroids 153, 267, 283, 1319, 1505, 1507
Nebula 279, 543, 1251
Nebula heating 1227
Nebular chemistry 773
Nebular processes 345, 827
Nebular solids 1469
Negative polarization 1271
Neodymium-142 613, 1017, 1253
Neon 403
Neon isotopes 1427
Neutral buoyancy 485
Neutron activation 1179
Neutron flux distribution 899
Neutrons 899

Nickel 657
Nickel chromites 717
Nili Patera 291
Nilosyrtis Mensae Region 327
NIMS 453, 575, 807, 1019, 1235
Nitrates 451
Nitrogen 77, 171, 173, 383, 701, 1419, 1435
Nitrogen isotopes 449, 451, 703, 1357
NMR spectroscopy 309
Noachian 457
Noble gases 77, 683, 793, 919, 1039, 1065, 1093, 1269
Noble gases, solar 959
Noble metals 141
Nonisothermal 1251
Nonsteady ionization 765
Norite 633
North Massif 1149
North Ray Crater 635
Nucleosynthesis 563, 665, 777, 903
Numerical modeling 623, 691, 693, 1503
Numerical simulation 843, 1397
Nysa family 689

Oblique impacts 39, 1211
Observing techniques 1505
Oceans 989, 1053
Offset dikes 1031
Oldhamite 571
Olivine 399, 907, 909, 921, 923, 967, 1069, 1335, 1339, 1455, 1481, 1559, 1561
Olivine, isolated 723
Olivine, vaporization 329
Olympus Mons 1225
Optical alteration 371
Orange glass 21, 23
Orbital elements 853
Orbital evolution 247
Orbiter spacecraft 187
Orbits 93
Ordinary chondrite parent bodies 513
Ordinary chondrites 7, 89, 175, 177, 651, 671, 701, 865, 879, 1057, 1169, 1183, 1481
Organic 1247
Organic materials 339
Orientale Basin 515, 1077
Origin 749, 759, 1071, 1073, 1173
Orthopyroxene 385, 1045, 1371
Orthopyroxenite 1043
Oscillation 987
Oscillatory zoning 1339
Outer solar system satellites 863
Outflow 3, 287
Outflow channels 321, 811, 1029
Outreach 163
Ovda Regio 229, 605, 1055, 1067
Oxidation 199, 461
Oxidation state 323, 1361
Oxygen fugacity 323, 657, 923
Oxygen isotopes 269, 583, 1005, 1357

P-sulfide 979
Palagonite 1485
Palagonite, iron clay mixtures 1163
Palagonitic soils 1161
Palimpsests 297
Palisade bodies 1275
Pallasite 921, 1335
Palmira 1555
Pancake domes 169
Parabolic halos 1201
Parent bodies 865
Parent melt 883
Parental magmas 1513
Partial melting 639, 651, 653, 663, 803, 879, 1071, 1073, 1371, 1465
Particle 57, 1251
Particle cohesion 1445
Particle fluxes 843
Particle sorting 1403
Partition coefficients 141, 883, 923, 1081, 1111
Partitioning 79, 873
Pathfinder 1293
Pavonis Mons 1225
Pentlandite 1565
Percussion marks 1121
Permafrost 3, 287
Perovskite 1557
Perseid 57
Petrogenesis 289, 1179
Petrogenesis, martian meteorites 911
Petrography 1269, 1285
Petrology 493, 1129, 1131
Petrology, igneous 1511, 1513
Petrology, martian meteorites 911
Phase equilibria 555, 879
Phobos 43, 111, 293, 733, 953, 957, 1291
Phobos 2 357, 957
Phoebe 1349
Phosphate 1337
Phosphate minerals 1025
Phosphides 595
Phosphorus 143
Photoabsorption 731
Photochemistry 461, 745
Photoclinometry 953, 1053, 1473
Phyllosilicates 435, 763, 1565
Picritic glasses 1257

Picritic magmas 1259
Piece-affine transform 133
Pioneer Venus 1139
Plagioclase 641, 739, 831, 875, 1075, 1081, 1375, 1533
Plains 45, 113
Plains deformation 767
Planar deformation features 847, 1385
Planar three-body problem 593
Planetary accretion 1009
Planetary data system 311
Planetary differentiation 399
Planetary evolution 431
Planetary instrument 121
Planetary mapping 1243
Planetary radar 515
Planetary science 897, 1351
Planetary surface imaging 779
Planetary surfaces 1407, 1453
Planetary wave interference 715
Planetesimal formation 827, 1011
Planetesimals 307, 399, 1283, 1441, 1477, 1549
Planets 797
Plasma instabilities 735
Plasma stratification 735
Plate tectonics 419, 421
Pluto 1419
Plutonium fission xenon 1065
Polar 69, 535
Polar beaches 1125
Polar caps 1323
Polar region 1331
Polarimetry 335, 1271
Polarization 433, 1331
Poles 1037
Polycyclic aromatic hydrocarbons 1391
Polymict material 901
Polyoxymethylene 1143
Post-impact alteration 861
Post-impact processes 299
Potassium 579, 581
Preplanetary bodies 1443
Preplanetary disk 1441
Presolar diamonds 1435
Presolar grains 585
Presolar SiC 373
Pressure indicator 497
Pretoria Saltpan Crater 161
Primitive achondrites 1071
Primitive chondrites 1563
Primitive mantle 995, 1009
Primitive material 355, 1283, 1363
Primitive meteorites 573, 1229
Principal components 1129
Pristine highlands rocks 1007
Procellarum 963
Processes 3
Production rates 851, 1119
Projectile 359
Projectile chemistry 1233
Projectile residues 107
Projective 1221
Proteus 1349
Protoplanetary disk 827
Protoplanetary nebula 333
Protosolar nebula 777
Protosun 333
Provenance 1487
Pseudotachylite 423, 1197, 1321
Pyrite decomposition 707
Pyroclastic flow 1403
Pyroclastic glass 21, 23
Pyroclastics 1495, 1497, 1555
Pyrolysis 171, 793, 1247
Pyrope 909
Pyroxene 497, 859, 883, 909, 939, 1373, 1559, 1561
Pyroxene, plagioclase 669

Q phase 979
Quantitative analysis 251
Quartz 601, 1021
Quartz monzodiorite 557, 1307, 1311

Radar 211, 217, 219, 459, 577, 627, 629, 655, 951, 1091, 1279, 1401, 1503
Radar backscatter 393
Radar properties 927, 1243
Radar scans 483
Radial lineaments 485, 487, 489
Radial pyroxene chondules 801
Radially fractured domes 619
Radiation 1365
Radiation damage 353
Radiation effects 853
Radiative losses 765
Radiative signal 5
Radio tracking 1281
Radioactivity, short-lived 151
Radiogenic Xe 703
Radiometry 1433
Radionuclides 19, 1119
Radiothermal emissivity 1137
Raised channel systems 1127
Rampart craters 287
Rampart ejecta 59
Rare earth elements 315, 571, 725, 935, 1265, 1311, 1451, 1457
Rare gases 13, 997
Rayleigh distillation 375
Recent volcanic activity 1139

Recondensation 1229
Reconnaissance 1323
Red giant stars 583
Redox potential 1569, 1571
Reduction 23, 383, 543, 695, 1107
Reflectance spectra 21, 177, 553, 939
Reflectance spectroscopy 127, 159, 515, 519, 961
Refractive index 507
Refractory 1283
Refractory carbides 103
Refractory elements 375
Refractory inclusion 1325
Refractory inclusions 825, 1275
Refractory siderophiles 1035
Regional highlands 675
Regions 593
Regolith 71, 97, 259, 261, 433, 469, 507, 695, 787, 943, 1059, 1061, 1083, 1157, 1301, 1313, 1333
Regolith breccias 1153
Regolith evolition 1153
Regolith maturity 1367
Regolith processes 175, 177
Regolith properties 1191
Relative ages 503
Relaxation time 1549
Relict enstatite 319
Remote sensing 249, 367, 533, 779, 837, 1191, 1263, 1267, 1407
Remote spectral sensors 737
Reservoir 527
Residue 665
Resolution 241, 625
Resonance ionization 1063
Resources 235
Resurfacing 45, 191, 971, 973, 1079, 1199, 1353
Resurfacing, global 1199
Rhea 1205
Rhenium-osmium dating 1041
Rheology 189, 439, 1089, 1193, 1575
Ridge belts 529
Ridges 1171
Rift zones 1105
Rifting 29, 421, 623, 821, 823, 1047, 1241
Rims 181
Ring vortex 61
Riobamba 1555
Robotic exploration 1177
Robotics 1499
Rock mass 1217
Rocks, pelitic 423
Rocky 1027
Roedderite 753
Rotational variations 1117
Roughness 129, 393
Rubidium-samarium isotopes 1309
Runoff 457
Rusalka Planitia 767
Rutile 771

S asteroids 265, 553
S process 245
Salme Dorsa 1115
Saltation threshold 1521
Samarium-146-neodymium-142 1015
Sample representivity 1179
Samples, lunar 371
Samples, terrestrial 997
Sand 1555
Sandstone 309
Sangay 1555
Sapas Mons 679
Satellites 43, 1541
Satellites, captured 93
Saturn 143
Scaling 359, 559
Scalloped margins 193
Scanning electron microscopy 125, 977
Scapolite 11
Scattering 855
Schiller-Schickard 35
Science payloads 1249
Screen indicator 1427
Sculpture 1237
Seafloor volcanos 169
Seamounts 1189
Secondary cratering 515
Sediment 119
Sedimentary deposits 213
Sediments 1363
Seismic images 1517
Seismic modeling 145
Seismology 441
Sekmet Mons 531, 1553
Semi-automated rover vehicle 737
Semi-major axis 593
Serenitatis melts 617
Serpentine, vaporization 329
Shadow measurements 811
Shatter cones 1121
Sheor-lag model 155
Shergottites 1417
Shergottite meteorites 403
Shield volcanoes 405, 409
Shock 177, 497, 603, 1021, 1209, 1239, 1431
Shock experiments 839, 969
Shock metamorphism 107, 309, 477, 497, 565, 607, 847, 1347
Shock physics code 295

Shock processing 831
Shock recovery 1167
Shock temperatures 1209
Shock waves 39, 731, 777, 987, 1365
Shock, high temperature 969
Shocked graphite 913
Shocked quartz 913, 1385
Shockwave interference 1463
Siderophile elements 397, 551, 617, 663
Siderophiles 983
Sif Mons 949
Silica 641, 753
Silicate condensation 415
Silicate inclusions 849
Silicate liquid immiscibility 1303, 1305
Silicate melts 221
Silicate minerals 603, 701
Silicates 1433, 1445
Silicon carbide 585
SIMS 385, 725, 1043, 1111, 1265, 1341, 1539
Simulation 569
Sinuous ridges 1127
Sirenum 443
Site selection 943
Size analysis 1129
Size distribution 365
Size frequency 1319
Size sorting 307
Slope failure 193, 1127
Small bodies 469, 1027
Small volcanic edifices 1187
Smoothed particle hydrodynamics 1527
SNC meteorites 1, 391, 451, 647, 911, 919, 1043, 1413, 1451, 1463, 1471
Sodium 79, 377, 887, 1099, 1535
Soil 53, 117, 955
Soil, texture 335
Solar cosmic rays 851, 1003
Solar energetic particles 125, 959, 999, 1059
Solar flares 649
Solar modulation 1429
Solar nebula 149, 151, 223, 755, 1123, 1173, 1283, 1469, 1477
Solar protons 403
Solar system 795
Solar transit 1099
Solar wind 77, 105, 171, 173, 259, 649, 959, 999, 1065
Solar wind implantation 1013
Solar wind reduction 1013
Solidification 1027
Solubility 383, 659
Sorting 1061
South Massif 1149
South Pole, Aitken Basin 715
Space debris 183
Space grant program 47
Space science 891
Space weathering 175, 371
Spacewatch objects 153
Spare Environment and Effects Program (SEE) 1233
Speciation 221
Spectra 117, 119, 265, 455, 1329
Spectral analysis 1235
Spectral imaging 895
Spectral mixture analysis 779
Spectral reflectance 249, 837
Spectrophotometry 1135
Spectropolarimetry 1267
Spectroscopy 81, 83, 85, 87, 123, 273, 357, 371, 519, 785, 975, 1333, 1419
Spectrum of masses 1443
Spherule layers 717
Spherules 853, 1459
Spinels 553, 763, 1533
Splotches 705
Sputtering 1143
SSI 453
Stereo 1205
Stereotopography 1055
Stratigraphy 45, 65, 529, 677, 767, 769, 857, 1531
Stratosphere, contamination 139
Stream 57
Strength 1217
Strike-slip faulting 1219
Structural geology 179
Structures 277, 331, 501, 681
Students 897
Subduction 421
Subophitic basalts 1301
Sudbury structure 477, 1007, 1031, 1517
Suevite 479
Sulfide melt 397
Sulfides 273, 1061, 1537
Sulfur 325, 1057, 1155
Sulfur dioxide 123, 429, 975, 1139
Sulfur, condensation 413
Sulfur, isotopes 611
Sun dynamo 1429
Superconductivity 1501
Supernovae 27, 903
Surface composition 187, 1235
Surface mineralogy 837
Surface processes 899, 1263
Surface properties 629
Surface reflection 337
Surface thermodynamics 1445
Surfaces 461, 855, 863, 925, 1237,

Surfaces (cont.) 1239, 1279
Surfacing 335
Surveyor 261
Synthetic aperture radar (SAR) 927, 951
Syrtis Major 291

Taurus Littrow Valley 1149
Teachers 783, 835
Tectonics 29, 113, 179, 285, 441, 673, 697, 817, 877, 885, 993, 1047, 1109, 1115, 1217, 1377, 1411, 1423, 1575, 1577
Tectonism 727, 1105
Tektite-like glaass 1269
Tektites 549, 581, 741, 1039
Telescopic 81, 83, 85
Tellus Regio 425
Tempe Terra 443, 643, 1377
Temperatures 149, 1501
Temporal variations 19
Tephra 1181
Termoskan 111
Terraces 213
Terrestrial age 99, 647
Terrestrial degassing 1097
Terrestrial planets 985, 1487
Tesserae 229, 419, 425, 1001, 1133
Tetrataenite 1529
Textures 825, 1285
Thallium 245
Tharsis 111, 443, 1141, 1147, 1219
Tharsis-Sirenum dichotomy 837
Thaumasia 331
Thermal conductivity 931
Thermal emission 257, 533, 1161, 1163
Thermal erosion 233, 1493
Thermal gradients 1191
Thermal history 223, 247, 1173, 1367
Thermal infrared 925
Thermal isostasy 1159
Thermal models 931
Thermochronology 1113
Thermoluminescence 97, 99, 247, 601, 603, 1367, 1545
Thermometry 25
Three-body calculation 829
Threshold 129
Threshold wind 467
Thrust systems 1449
Thumbprint terrain 799, 1127
Tidal breakup 893
Tidal capture 829
Tidal deformation 1527
Tidal disruption 147, 1491, 1527
Tidal effects 1231
Tidal fracture 101
Tiger spectrography 837
Tikal, Guatemala 549
Tillite 565
Timescales 1325
Titan 1231
Titanium 1075
Titanium isotopes 363, 1063
Titanium-iron-phosphides 595
Topographic slopes 201
Topography 503, 727, 757, 1053, 1277, 1289, 1519
Trace elements 221, 315, 385, 427, 761, 981, 1111, 1417, 1475, 1557
Trace elements, partitioning 1075
Tracks 125, 1157
Trajectory calculation 1327
Tranquillitatis 1329
Transform fault 1115
Transient cavity 479
Transient heating 345, 1535, 1537
Transmission electron microscopy 685, 687, 1455
Trapped gases 997, 1093
Trapped xenon 1479
Triangulation 133
Triton 277, 555, 1419
Troctolitic 935
Troilite 25, 773, 1057
Trojan asteroids 841
Tropospheric circulation 429
Trough 501
Tsunamis 989
Tungsten 995
Turbulence 233, 307
Tusholi Corona 1115
Type B inclusions 79

Ultramylonite 1197
Ultrarefractory inclusions 1475
Ultraviolet 461
Umov effect 1271
Unequilibrated chondrites 1185
Unequilibrated enstatite chondrites 571
Unequilibrated ordinary chondrites 585, 1035
Unique chondrite 115
Uranium-lead dating 1031
Uranium-thorium-lead 1409
Ureilites 137, 663, 909, 1107, 1409, 1465
Ushas Mons 65, 675, 677

Valences 221
Valhalla 91
Valles Marineris 29, 231, 955, 1219

Valleys 331, 457
Vanadium 505
Vapor clouds 1355
Vapor deposit 259, 695
Vapor fractionation 581
Vapor impact 913
Vapor pressure 581
Vaporization 413, 755
Vaporization, silicates 329
Veins 169
Velocity scaling 1207
Venera 15/16 1001, 1483
Venus 33, 45, 55, 63, 65, 67, 129, 155, 157, 179, 191, 193, 205, 207, 217, 229, 239, 301, 303, 405, 407, 409, 417, 419, 421, 429, 463, 485, 487, 489, 503, 525, 529, 531, 537, 577, 619, 627, 629, 631, 667, 673, 675, 677, 679, 697, 699, 705, 707, 727, 747, 749, 751, 757, 767, 781, 817, 821, 823, 833, 855, 877, 885, 927, 949, 971, 973, 993, 1067, 1079, 1109, 1115, 1133, 1137, 1159, 1189, 1195, 1199, 1201, 1213, 1215, 1263, 1277, 1279, 1281, 1295, 1317, 1353, 1355, 1411, 1423, 1447, 1449, 1519, 1569, 1575, 1577
Venus, basalt 1415
Venus, emissivity measurements 1509
Venus, impact craters 1489, 1509
Venus, major resurfacing event 1509
Venus, surface material 1509
Vesta 1083
Vesta Rupes 681
Vibrational (spectroscopy) 1485
Viking 871
Viking missions 953
Viking Orbiter 241, 789
Viscocity 189
Viscosity 699, 1089, 1193
Vitrophyre 289
Volatile elements 617, 663, 713, 741
Volatile loss 579
Volatiles 397, 1535, 1537
Volcanic activity 431
Volcanic glasses 325
Volcanic hazard 805
Volcanic plains 155
Volcanic rise 675
Volcanism 35, 45, 123, 193, 207, 301, 305, 325, 405, 409, 417, 425, 429, 463, 501, 521, 523, 525, 529, 623, 667, 679, 767, 797, 805, 807, 821, 823, 885, 971, 1079, 1087, 1089, 1091, 1105, 1189, 1423, 1447, 1489, 1495, 1531
Volcanology 33, 1189, 1403
Volcanos 227, 305, 317, 679, 807, 947, 949, 973, 1141, 1147, 1317
Vortex flows 41
Voyager 241, 455
Vredefort 423, 1113, 1321

Wake 39, 41
Wanapitei 479
Water 117, 275, 759, 785, 1037
Water of hydration 1135, 1439
Waves 989
Wax modeling 233
Weathering 53, 157, 263, 339, 937, 1035, 1137, 1155, 1415
Wetting behavior 653
White matrix 11
Wildfires 545
Workstation 1519
Wrinkle ridges 63, 1473
Wyoming 1303

XANES 323
Xenoliths 931
Xenon 1065
Xenon isotopes 1097
X-ray absorption spectroscopy 1361
X-ray diffraction 121, 273
X-ray fluorescence (XRF) 1261
X-ray methods 1363

Zimbabwe 847
Zircon 427, 967, 1031
Zodiacal cloud (or dust) 379